Forschungszentrum Karlsruhe
Technik und Umwelt

Wissenschaftliche Berichte
FZKA 6300

Projekt Nukleare Sicherheitsforschung Jahresbericht 1998

B. Mühl (Hrsg.)
Projekt Nukleare Sicherheitsforschung

September 1999

FORSCHUNGSZENTRUM KARLSRUHE

Technik und Umwelt

Wissenschaftliche Berichte

FZKA 6300

Projekt Nukleare Sicherheitsforschung

Jahresbericht 1998

Herausgegeben von B. Mühl

Projekt Nukleare Sicherheitsforschung

Forschungszentrum Karlsruhe GmbH, Karlsruhe

1999

Forschungszentrum Karlsruhe GmbH
Postfach 3640, 76021 Karlsruhe

Mitglied der Hermann von Helmholtz-Gemeinschaft
Deutscher Forschungszentren (HGF)

ISSN 0947-8620

Summary

The reactor safety R&D work of the Karlsruhe Research Centre (FZK) has been part of the Nuclear Safety Research Project (PSF) since 1990. The present annual report summarizes the R&D results of PSF during 1998. The research tasks cover three main topics:

Light Water Reactor safety,

Innovative systems, and

Studies related to the transmutation of actinides.

Numerous institutes of the research centre contribute to the PSF programme, as well as several external partners. The tasks are coordinated in agreement with internal and external working groups.

The contributions to this report, which are either written in German or in English, correspond to the status of early/mid 1999.

Zusammenfassung

Seit Beginn des Jahres 1990 sind die F+E-Arbeiten des Forschungszentrums Karlsruhe (FZK) zur Reaktorsicherheit im Projekt Nukleare Sicherheitsforschung (PSF) zusammengefaßt. Der vorliegende Jahresbericht 1998 des PSF enthält Beiträge zu aktuellen Fragen der Sicherheit von Leichtwasserreaktoren und innovativen Systemen sowie der Umwandlung von minoren Aktiniden. Die konkreten Forschungsthemen und -vorhaben werden laufend mit internen und externen Fachgremien abgestimmt.

An den beschriebenen Arbeiten sind die folgenden Institute und Abteilungen des FZK beteiligt:

Institut für Angewandte Thermo- und Fluiddynamik	IATF*
Institut für Materialforschung	IMF I, II, III
Institut für Neutronenphysik und Reaktortechnik	INR*
Institut für Reaktorsicherheit	IRS
Hauptabteilung Informations- und Kommunikationstechnik	HIK
Hauptabteilung Ingenieurtechnik	HIT
Institut für Nukleare Entsorgungstechnik	INE
Hauptabteilung Versuchstechnik	HVT
Institut für Technische Chemie	ITC

sowie vom FZK beauftragte externe Institutionen.

Die einzelnen Beiträge stellen den Stand der Arbeiten im Frühjahr/Sommer 1999 dar und sind entsprechend dem F+E-Programm 1998 numeriert.

---

*) Das IATF und der größte Teil des INR wurden im April 1999 zum Institut für Kern- und Energietechnik (IKET) zusammengeführt, ein Teil der Arbeiten aus dem INR wurden im neu gegründeten Institut für Hochleistungsimpuls- und Mikrowellentechnik (IHM) angesiedelt. Die in diesem Bericht dargestellten Ergebnisse wurden jedoch vor dieser Umorganisation erzielt, so daß hier noch die alten Institutsbezeichnungen verwendet werden.

Inhalt
Contents

32.21 LEICHTWASSERREAKTORSICHERHEIT

32.21.01 Wasserstofferzeugung,-verteilung und verbrennung

I. Analysis of Hydrogen- and Steam Generation Using the Nuclear Reactor Accident Analysis Code MELCOR1.8.4

(J. Starflinger, INR)

Abstract

The severe accident analysis code MELCOR is described and the results of a MELCOR1.8.4 run for a hypothetical accident chosen as an example for the determination of a hydrogen and steam source term are presented.

Zusammenfassung

Der MELCOR Code zur Analyse von schweren Störfallen wird beschrieben. Weiterhin werden die Ergebnisse eines MELCOR1.8.4-Laufes für einen hypothetischen Unfall, der exemplarisch zur Bestimmung eines Wasserstoff- und Dampf-Quellterms ausgewählt wurde, präsentiert.

At the Institute for Neutron Physics and Reactor Techniques (INR) the severe accident analysis code MELCOR is used to predict the steam and hydrogen sources in course of a nuclear reactor accident. The code mainly simulates the accident progression in the so-called "In-Vessel Phase" (from the initiation to the failure of the reactor pressure vessel), but models are available e.g. for core concrete interaction in the reactor cavity (Ex-Vessel Phase), too.

The main purpose of MELCOR is to simulate typical accident sequences for all components of a nuclear power plant (PWR, BWR) within tenable computer calculation time. Hence, the models implemented in the code are in general based on simplified equations for global mass and energy balances. Many correlations can be adjusted by fitting parameters which enable sensitivity and uncertainty analyses [1].

The main capabilities of the code can be quoted as follows: Core heat-up, oxidation, hydrogen generation, fission product release, melt generation and relocation, thermohydraulic of fluids (steam, water etc), heat transport (conduction in walls, convection, etc). The models for the thermal hydraulic behaviour are based on a so-called 6-equation model, i.e. mass, momentum and energy equation for both the liquid and the gas phases, which are numerically solved on relatively large control volumes [1]. The control volumes representing the coolant lines of a Konvoi-type nuclear power plant are given in Figure 1. In order to simplify the drawing, the nodalisation of the containment building is not depicted.

In Figure 1, control volumes are indicated by bold numbers whereas flow paths connecting control volumes to other ones are provided by numbers in italic style.

The reactor pressure vessel is located in the centre (dark grey) of Figure 1. On the right side, the loop of the primary circuit is depicted, in which the pressurizer (PRZ, light grey) is located. This is by definition the loop, in which a hypothetical accident is initiated. The other three reactor coolant lines (RCL) including the steam generators (SG) are lumped together in one circuit, depicted on the left side.

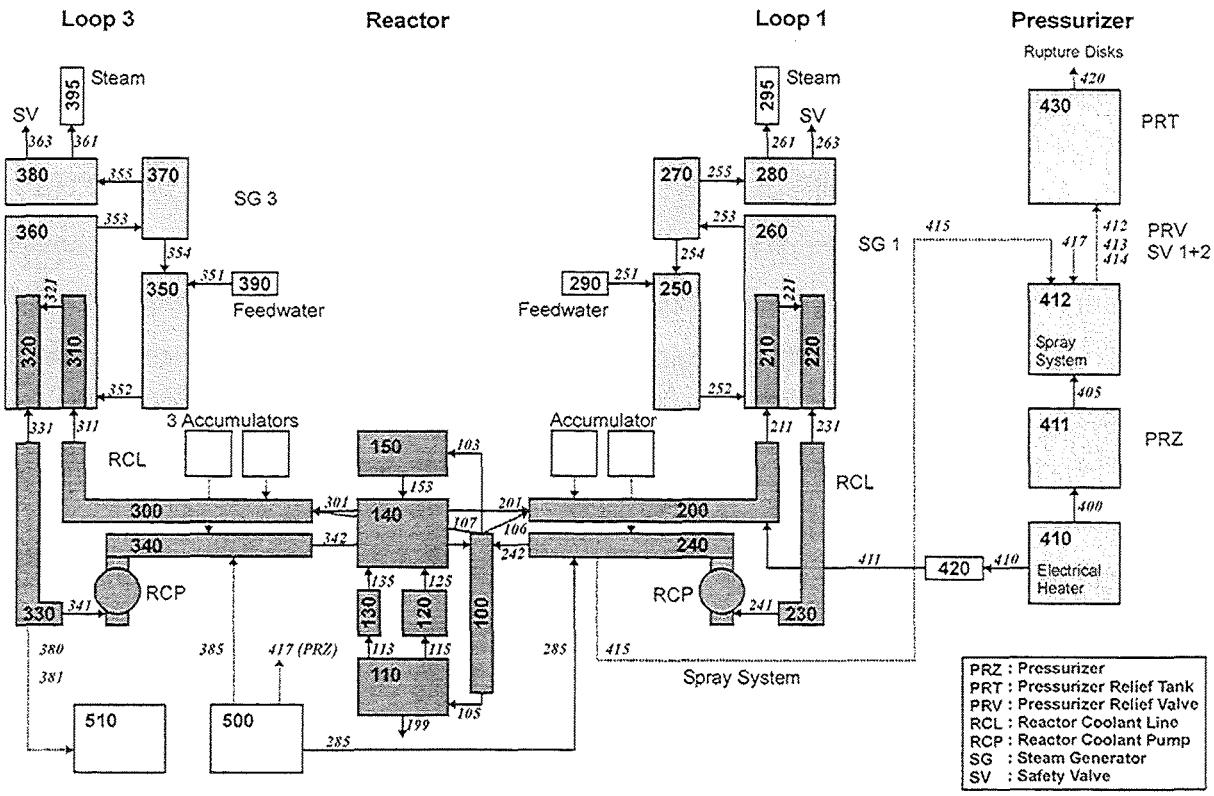

Figure 1: MELCOR-Nodalisation of a Konvoi-type Nuclear Power Plant.

A hypothetical accident (loss of secondary feedwater supply, Konvoi-type PWR) has been chosen here as an example for the determination of a hydrogen and steam source term. An insufficient feedwater supply causes heat-up and subsequent melt of the reactor core. The oxidation of metallic materials, predominantly zircaloy fuel cladding oxidation, generates hydrogen. The steam and the hydrogen pass through flow path 420 (upper right side of Figure 1), representing the rupture disks on top of the pressurizer relief tank (PRT). The new code version 1.8.4 is used to perform this analysis [1].

The following Figures 2 and 3 show the results of a MELCOR1.8.4 run for the accident mentioned above. The total accident time analysed is chosen to 25000s (calculated from the initiation of the accident).
Prior to the release of hydrogen, steam passes through the rupture disks. As depicted in Figure 2, the overpressure in the pressurizer relief tank causes their failure at about 5000s. Lasting about 2500s after the disk break, a two phase mixture of steam (upper graphic) and liquid water (lower graphic) is released into the reactor containment lowering the pressure in the primary circuit. At about 5400s the water level inside the reactor pressure vessel becomes so low that the core is partially uncovered and heats up.

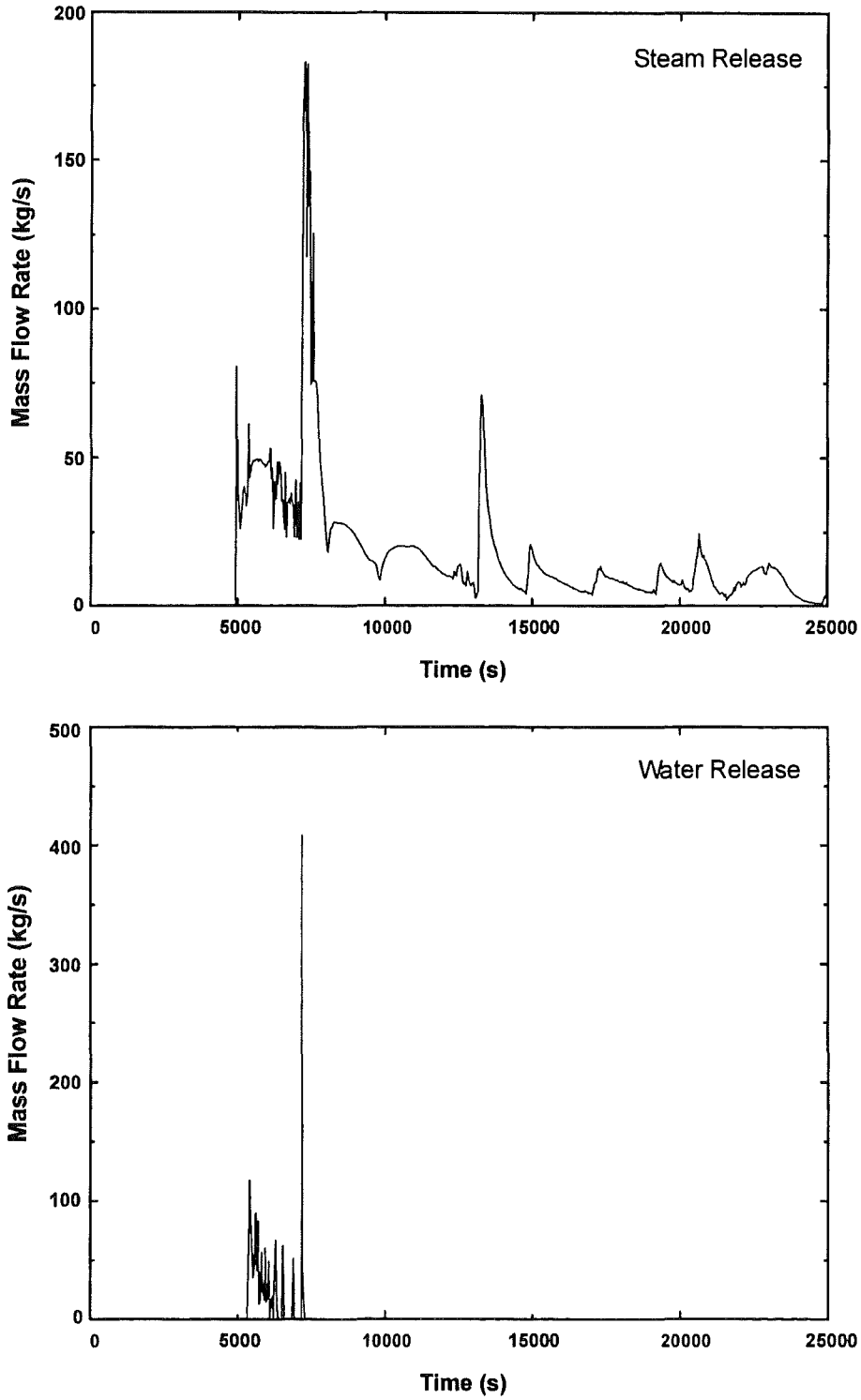

Figure 2: Steam (Upper Graphic) and Liquid Water (Lower Graphic) Mass Flow Rate through the Leak (Flow Path 420).

The hydrogen generation starts at about 7000s as it can be seen in Figure 3. The reactor core is partially uncovered and a slight zircaloy-steam reaction takes place. A temperature escalation and subsequent generation of a large amount of hydrogen occurs at about 12000s, leading to high temperatures and partial melting of the reactor core. In this phase, hot metallic surfaces are exposed to the steam generated by the water from the accumulators, which quickly vaporises in contact with the hot fuel rods.

A hydrogen peak with a maximum of about 0.7 kg/s can be seen in Figure 3. It should be mentioned that a hydrogen source of at least 0.4 kg/s lasts about 1000s.

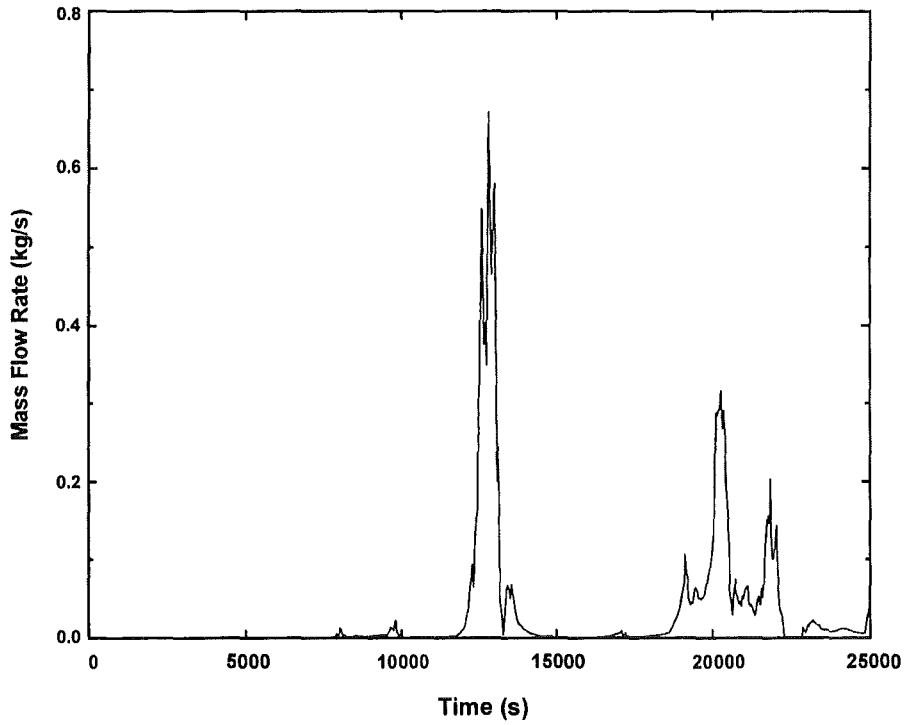

Figure 3: Mass Flow Rate of Hydrogen through the Leak (Flow Path 420).

A second hydrogen peak can be identified between 19000s and 22000s. During this interval, the core support plate fails and relocated corium falls into the water remaining in the lower plenum of the reactor pressure vessel. The maximum hydrogen peak flow rate can be identified to be about 0.3 kg/s. A secondary peak of 0.2 kg/s is visible.

Integrating the flow rates (Figures 2 and 3), about 380000 kg of steam and a total amount of about 800 kg hydrogen are released into the containment atmosphere. The main hydrogen generation mechanisms during this accident can be summarized as the temperature escalation after core uncovery and the contact of the relocated material with water from the cavity.

Future activities will focus on a detailed analysis of different accident sequence with the new MELCOR code version 1.8.4.

[1] R. O. Gauntt, et al.: MELCOR Computer Code Manuals, Version 1.8.4, NUREG/CR-6119, Vol. 1 and 2, Rev. 1, SAND97-2398, 1998.

II. Development and Application of a Dynamic Film Model for Spherical PWR Containments under Hypothetical Accident Conditions

(M. Bottoni, J. R. Travis, INR; P. Royl, IRS)

Abstract

In the frame of safety analysis of water reactors under hypothetical core melt accident conditions, the release of hydrogen and steam, hence the flammability of hydrogen-steam-air mixtures, are a major concern. The code GASFLOW /1/ is applied at FZK to simulate the distribution of steam-hydrogen mixtures in a 3D model of a large reactor containment including the inertization and deinertization effect from steam release and condensation. This contribution describes a method of computing the distribution of velocity, thickness and temperature of a liquid film of water condensing and draining on the inner surface of the containment. Cartesian cells normal to the coordinate axes, approximating a spherical dome, are projected on the dome surface. The film simulation is made in a spherical coordinate system using the "momentum integral method". An ordinary differential equation for the film velocity along the meridian of an azimuthal sector is derived analytically and solved numerically. After computing the heat fluxes to or from the liquid film, the solution of the film enthalpy equation yields the temperature distribution on the inner surface of the containment. Film thickness and temperature distributions are mapped back on the structure nodes that bound the containment in the Cartesian 3D model of GASFLOW. We present the ongoing testing and application of the model, based on the analysis of simple problems, and preliminary results of the simulation of a Loss of Coolant Accident (LOCA) in the Biblis A reactor containment.

Zusammenfassung

Im Rahmen der Sicherheitsanalysen zu hypothetischen Kernschmelzunfällen in Leichtwasserreaktoren kommt der Freisetzung von Wasserstoff und Dampf und der Entzündbarkeit von Wasserstoff-Dampf-Luft-Gemischen große Bedeutung zu. Mit dem Code GASFLOW wird im FZK die Verteilung von Dampf-Wasserstoff-Gemischen in einem 3D-Modell eines großen Reaktorcontainments simuliert. In diesem Beitrag wird eine Methode beschrieben zur Berechnung von Geschwindigkeit, Dicke und Temperatur eines flüssigen Wasserfilms, der an der inneren Ober-

fläche des Containments kondensiert und heruntertropft. Tests und Anwendung dieses Modells zur Filmsimulation werden beschrieben und vorläufige Ergebnisse der Simulation eines LOCA-Unfalls im Containment von Biblis A präsentiert.

1. Introduction

In case of a hypothetical Loss of Flow (LOF) accident within the containment of a light water reactor, a major concern for the containment integrity involves the deflagration or detonation susceptibility of the mixture of hydrogen and steam which may be released. Because the flammability of the mixture of hydrogen and other components is also determined by the concentration of water vapor in the mixture, the calculation of the steam release and distribution and of the water film condensation, evaporation and relocation occurring on the inner surface of a spherical steel shell is important for the safety analysis of the German spherical dry containment of PWRs. The analysis of steam-hydrogen distribution in case of hypothetical accidents in German PWR containments is made in the computational code GASFLOW /1/, which models transport and distribution of hydrogen in reactor containments.

Film condensation of vapor is treated in the GASFLOW code by means of a static model, in which all mass condensing on structure surfaces is assumed to remain in loco, instead of flowing along the surfaces. As an alternative to the static model, we developed a dynamic film model, in which the film flows downwards by gravity. The film behavior controls the mass and temperature distribution of the condensed mass, hence the location and concentration of the water vapor remaining in the mixture with the hydrogen. This report aims at giving an overview of the method used in the dynamic film model and at presenting work ongoing for the validation of the model and for the assessment of its relevance. After discussing some test problems we present preliminary results of the investigation of a LOCA in the simulated containment of the Biblis A reactor.

2. Analytical and numerical models

2.1 Conservation equations for a liquid film

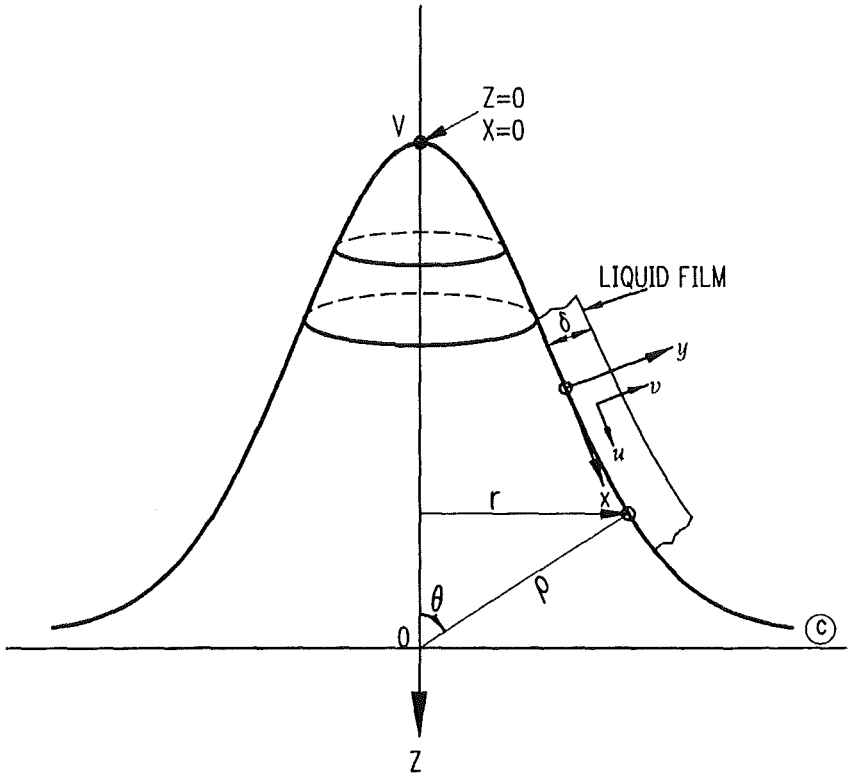

Fig. 1 Geometrical configuration for the simulation of a liquid film on a body of revolution.

Let us consider a body of revolution, as the one shown in Fig. 1, obtained by rotating a curve C around a vertical axis z. The only assumption made is that the analytical equation of the curve C is known. The flow of a liquid film on the inner or outer surface of the body of revolution is described by the following system of mass and momentum conservation equations /2/:

$$\frac{\partial}{\partial x}[r(x,y)u]+\frac{\partial}{\partial y}[r(x,y)v]=0 \tag{1}$$

$$\rho u\frac{\partial u}{\partial x}+\rho v\frac{\partial u}{\partial y}=-\frac{\partial p}{\partial x}+\frac{1}{r(x,y)}\frac{\partial}{\partial y}\left[r(x,y)\mu\frac{\partial u}{\partial y}\right]+\rho g_x \tag{2}$$

$$\frac{\partial p}{\partial y} = 0 \tag{3}$$

In these equations (See Fig. 1), x is a curvilinear coordinate along the curve C. The axis x is tangent to the curve C in a point P(x); y is an axis normal to the tangent to the curve C in P(x) with origin on C; u, v are the components of film velocity along the x and y axes; r is the distance of a point on C from the z axis; p is pressure, ρ and μ are the density and dynamic viscosity of the liquid film and g is the acceleration due to gravity.

Moreover we consider the following enthalpy equation for the liquid film

$$\frac{\partial(\rho h)}{\partial t} + \nabla \cdot (\rho h \vec{u}) = E \tag{4}$$

where h is the specific enthalpy and E is the energy transferred to the film per unit mass and time. As explained later, this enthalpy equation is solved on one azimuthal sector defined on the body of revolution after computing the distributions of the film velocity and thickness along the central meridian of the azimuthal sector.

2.2 Treatment of Mass and Momentum equations

The momentum equation for the y-coordinate axis simply states that the pressure is constant across the thickness of the liquid film. This Eq. (3) can be hereafter neglected, provided the pressure gradient term in Eq. (2) is written as total derivative. Mass and momentum conservation equation for the x-coordinate direction, Eq.s (1) and (2), have been treated analytically with the "Momentum Integral Method". The equations are first integrated over the film thickness and then combined. After a lengthy analytical treatment, which has been documented in detail in Ref. /3/, one derives the following ordinary differential equation of first order:

$$\frac{d}{dx}\left(r u_e^2 \theta_x\right) + \frac{du_e}{dx} r u_e \delta_x^* - r u_e \delta \frac{du_e}{dx} = \frac{r}{\rho}\left(\tau_w - \tau_a\right) - r g \delta \sin\psi \tag{5}$$

with the definitions

$$\theta_x = \int_0^{\delta} \frac{u}{u_e}\left(1 - \frac{u}{u_e}\right) dy \tag{6}$$

$$\delta_x^* = \int_0^{\delta} \left(1 - \frac{u}{u_e}\right) dy \tag{7}$$

of "momentum thickness" and "displacement thickness", respectively. In Eq.s (5)-(7) the subscript "e" refers to quantities defined on the outer film surface, τ_w and τ_a are the wall shear stress and the shear stress on the outer surface (liquid to "air"), respectively. Ψ is the angle between the tangent to the curve C and the horizontal line (normal to the z axis).

By deriving analytically Eq. (5) no assumptions have been made about the physical conditions of the liquid film on the revolution body. Therefore Eq. (5) has general validity. The practical application of the Momentum Integral Method requires however computation of the integrals (6) and (7). Therefore assumptions must be made which allow a calculation of the velocity distribution across the liquid film.

In case of laminar flow regime in the liquid film the velocity distribution across the liquid film is parabolic and given by

$$u(y) = 2u_e\left(-\frac{y^2}{2\delta^2} + \frac{y}{\delta}\right) \tag{8}$$

with u=0 on the structure surface (no slip condition). Using Eq. (8) the integrals (6)-(7) can be computed analytically with the results

$$\theta_x = \frac{2}{15}\delta \tag{9}$$

$$\delta_x^* = \frac{\delta}{3} \tag{10}$$

In case of laminar film the wall shear stress is also known and given by

$$\tau_w = \mu \frac{3\bar{u}}{\delta} \tag{11}$$

where $\bar{u} = 2u_e / 3$ is the mean value of the film velocity in the x direction. In the following we assume τ_a=0, keeping however in mind that this limitation should be removed in future model developments, thus allowing the interaction between film and by-flow of the gas field to be taken into consideration.

Let us consider an azimuthal discretisation of the revolution body in an arbitrary number of sectors of uniform angular width $\Delta\phi$ and define the mass flow along the meridian of a sector by

$$Q_s(x) = \frac{Q(x)}{2\pi} \Delta\phi \tag{12}$$

where Q(x) is the mass flow per unit angular width.

Using Eq.s (6)-(7) and (11)-(12), Eq. (5) becomes

$$\bar{u} \frac{d\bar{u}}{dx} = -\frac{5\mu}{2\rho} \frac{r^2}{Q_s^2} \Delta\phi^2 \bar{u}^3 + \frac{5}{6} g \sin\psi \tag{13}$$

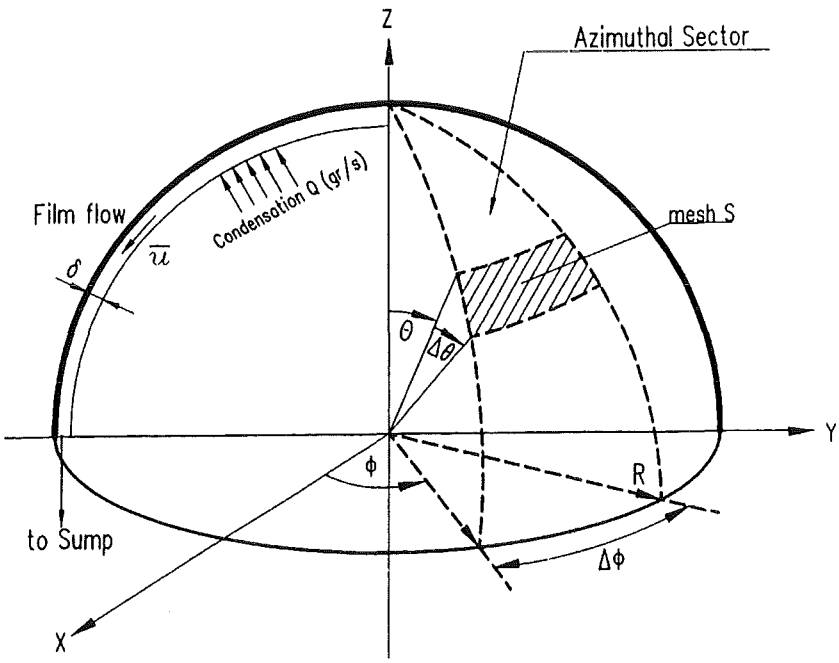

Fig. 2 Definition of spherical meshes on an hemispherical surface.

In case of an hemisphere of radius R, the geometrical configuration is sketched in Fig. 2. The spherical mesh S is obtained by partitioning the azimuthal sector of aperture $\Delta\phi$ in an arbitrary number of latitudinal meshes of uniform aperture $\Delta\vartheta$. In this geometry one has $\psi = \vartheta$, $r = R\sin\vartheta$ and the ordinary differential equation (13) can be directly integrated with initial condition $\bar{u} = 0$ at x=0. The numerical solution yields the distribution of the mean film velocity along the meridian of the body of revolution. The film thickness is then given by

$$\delta(x) = \frac{Q(x)}{2\pi r\bar{u}} \tag{14}$$

The numerical solution of the enthalpy equation for the liquid film, Eq. (4), requires special care because it must be coupled with the solution of the heat conduction equation in the structure of the containment, performed in the GASFLOW program. We discuss this topic together with the analysis of the test cases in section 4.1.

3. Coupling of the dynamic film model to the geometrical representation of the containment in GASFLOW.

In the GASFLOW program the spherical surface of the containment is approximated by means of Cartesian meshes normal to the coordinate axes. For the application of the film model in a spherical coordinate system it is necessary to map the Cartesian coordinate system onto the spherical coordinate system. The method used for this mapping is explained hereafter, with reference to the sketch of Fig. 3.

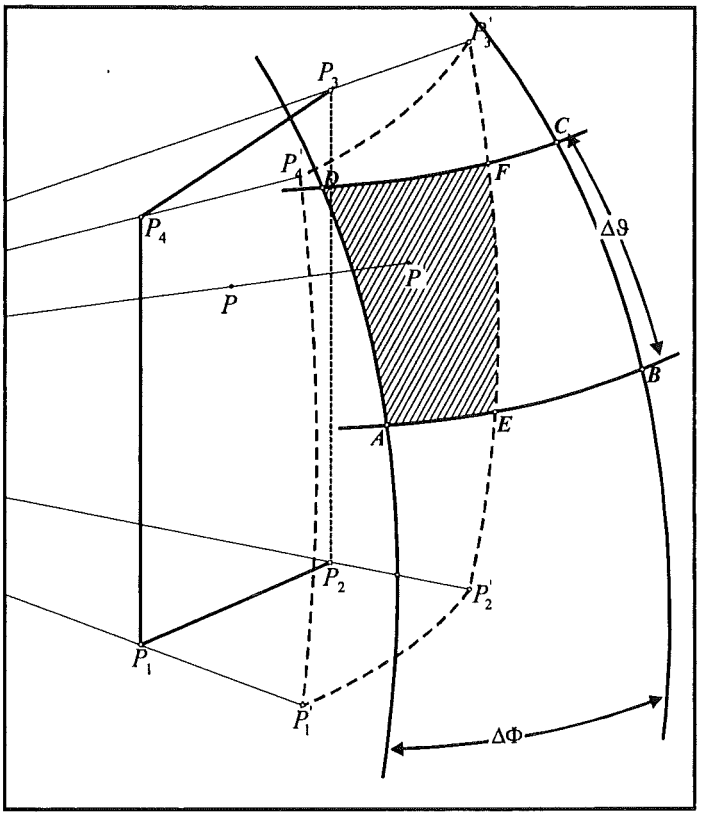

Fig. 3:Sketch showing the mapping of Cartesian meshes upon the spherical coordinate system.

Let P1-P2-P3-P4 be a mesh C defined in the Cartesian coordinate system. The coordinates of the corner points Pi $=(x_{i1}, y_{i1}, z_{i1})$ (i=1, ...4) are known from the program GASFLOW. Let A-B-C-D be a mesh S of the spherical coordinate system with aperture $\Delta\vartheta$ and $\Delta\phi$ in the longitudinal and azimuthal directions, respectively. The Cartesian (x,y,z) and spherical coordinates (ϑ, ϕ) are related by

$$
\begin{aligned}
x &= r\sin\vartheta\cos\phi \\
y &= r\sin\vartheta\sin\phi \\
z &= r\cos\vartheta .
\end{aligned}
\tag{15}
$$

The (ϑ, ϕ) coordinates of the corner points of mesh S are known. Let P'1, P'2, P'3, P'4 be the projections of the points Pi (i=1, ...4) from the center of the spherical coordinate system on the sphere of radius r upon which the mesh A-B-C-D is located. Generally speaking, only a portion of the mesh C will be projected on mesh S. This portion, for instance mesh A-E-F-D in the sketch of Fig. 3, will be denoted as

"mesh(C>S)". The problem of mapping mesh C on mesh S consists in finding the area of mesh(C>S) and therefore the contribution, in terms of condensation or evaporation rate and of heat fluxes, of mesh C on mesh S. This problem has been solved as follows.

Because mesh C lays on a plane parallel to one coordinate plane of the Cartesian coordinate system, without lack of generality we may assume that it lays on a plane y=constant. Let R_1, R_2 be two random numbers in the interval (0-1) and consider the point P= (x_P,y_P,z_P) with coordinates

$$\begin{aligned} x_P &= x_1 + R_1 (x_2 - x_1) \\ y_P &= y_1 \\ z_P &= z_1 + R_2 (z_4 - z_1) \end{aligned} \qquad (16)$$

The latitudinal and azimuthal coordinates of point P in the spherical coordinate system are obtained, inverting equations (16),as

$$\begin{aligned} \vartheta_P &= \arctan\left(\sqrt{x_P^2 + y_P^2} \,/\, z_P\right) \\ \phi_P &= \arctan\left(\sqrt{x_P^2 + y_P^2} \,/\, z_P\right) \end{aligned} \qquad (17)$$

If these spherical coordinates lay in the intervals $\Delta\vartheta = (\vartheta_A - \vartheta_D)$ and $\Delta\phi = (\phi_B - \phi_A)$, respectively, the point P of mesh C will project on point P' of mesh S i. e. point P' will belong to mesh(C>S). We repeat the same operation with say $N = 10''$ (n=3 or n=4) couples of random numbers and count the number of events, say M, in which point P' belongs to mesh (C>S). The ratio M/N gives the fraction of mesh C which projects on mesh S. We sum up all contributions to mesh S from all meshes C and obtain the contributions, in terms of condensation rates and heat fluxes, of the Cartesian meshes upon the spherical meshes. After computing the distributions of film thickness and temperature in the spherical coordinate system the process is reversed and the distributions are mapped back from the spherical to the Cartesian coordinate system of GASFLOW.

The geometrical mapping of the Cartesian meshes upon the spherical meshes and vice versa is performed once per calculation and requires only a few minutes of computational time for a large problem.

4. Computational results

4.1 Test case - Heated and unheated film model.

This test case is a mock-up, on small scale, of a spherical reactor containment of the German PWR type. The computational domain consists of a cube of 60 m edge length, partitioned in 12 x 12 x 12=1728 cells which contains an outer concrete spherical shell of 30 m radius and an inner steel shell of 20 m radius. The steel structure is approximated in the GASFLOW calculation by means of 312 structure nodes positioned on the respective mesh surfaces, 104 normal to each one of the coordinate axes. At the center of the sphere, starting at time t=0, steam is injected with a volumetric rate of $100 m^3/s$ and velocity of 1 m/s. The steam rises in the steel vessel and after a short time starts condensing on the inner surface. Because the problem is axisymmetric and the geometrical configuration, in the discretization made in the GASFLOW code, displays a fourfold symmetry around the vertical z axis, only eight azimuthal sectors have been used in the LINK code. It has been verified that the fourfold symmetry has been preserved in the computational results. For every azimuthal sector the meridian line has been discretized in 40 latitudinal meshes of uniform length. Thus 320 meshes have been used to simulate the film on the steel shell in the spherical coordinate system.

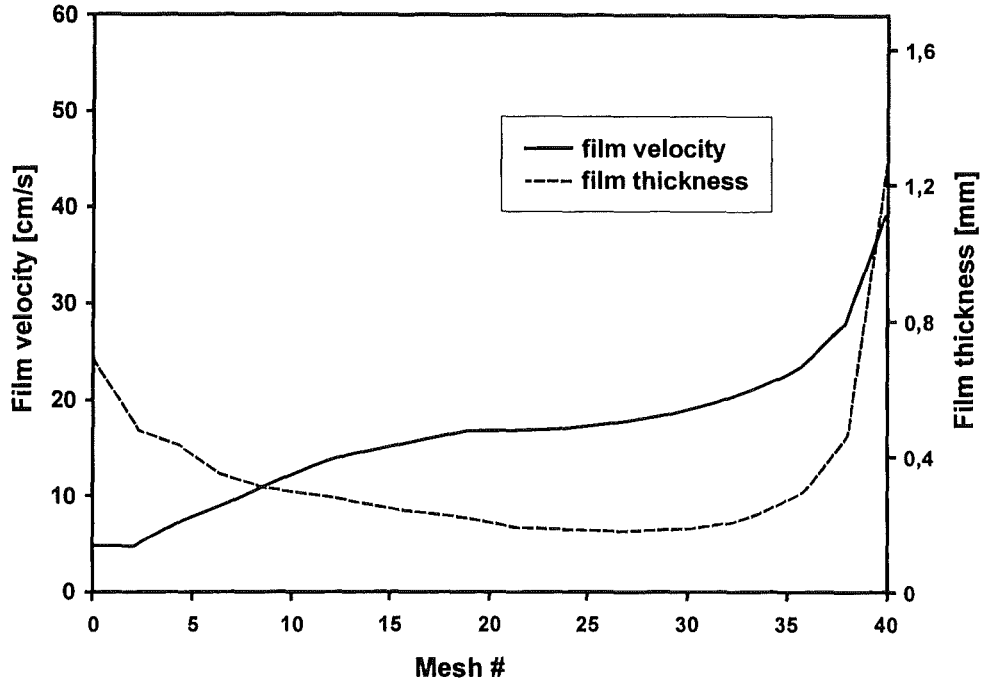

Fig. 4: Distribution of film velocity and thickness computed at t=1000 s for test case 1 (unheated film model used in this case).

The computed results shown in Fig. 4 for this test case are intended to be only a representative example of the distributions obtained for the liquid film velocity and thickness along an azimuthal sector from the top (left) to the bottom of the spherical containment. The mean film velocity ranges from zero to 60 cm/s and, as expected, is a monotonically increasing function of the linear coordinate along the meridian. The liquid film thickness decreases from the top of the spherical vessel due to increasing surface and increasing velocity of the film in the downwards direction, till to the point, around mesh 30, where the decreasing surface at high "south" latitudes of the lower hemisphere dominates with respect to the increasing film velocity.

When not only mass and momentum conservation equations, but also the energy equation is solved for the liquid film we have the "dynamic heated film model". A solution of the enthalpy equation (4) is obtained for an azimuthal sector, after computing the distributions of liquid film velocity and thickness. Integrating Eq. (4) over the film volume V_f in a sector, applying the divergence theorem and discretizing with respect to time (superscript n) and space (subscript k) one obtains for the temperature T of the film in the spherical mesh of index k the following equation

$$T_k^{n=1} = T_k^n + \frac{\Delta t}{V_f}\left(\frac{G_{k-1}}{\rho_k^n}T_{k-1}^n - \frac{G_k}{\rho_k^n}T_k^n + \frac{G_c}{\rho_k^n}T_c + \frac{E}{\rho_k^n c_{pk}^n}\right) \tag{18}$$

In Eq. (18) $G = \rho\bar{u}A_f$ is the mass flow of the liquid film through the cross section $A_f = \delta r \Delta\phi$ and c_p is the specific heat. G_c and T_c are the mass flow source arising in mesh k through condensation and the saturation temperature at which the film condenses. Eq. (18) is solved with a marching technique from the top of the sector for increasing index k to the bottom. Because of the small thickness of the liquid film, the film temperature is assumed, in the GASFLOW code, to coincide with the temperature of the inner surface of the spherical shell. Therefore the solution of Eq. (18) provides the boundary condition for the solution of the heat conduction equation in the structure of the containment.

Analysis of numerical results obtained with this test case has shown that it is important to couple the solution of Eq. (18) with the solution of the heat conduction equation for the structural material of the containment shell. Details of the numerical treatment of the heat conduction equation for the structural material are given in Ref. /1/. It is beyond the scope of this report to recall these details, but it is emphasized that, for future code developments, it would be advisable to solve the film enthalpy equation and the heat conductance equation for the structural material at the same time without having to iterate the separated solutions.

The temperature distribution obtained by solving Eq. (18) for test case is shown in Fig. 5 for one azimuthal sector (results are axisymmetric) at t=1000 s, together with the distributions of condensation rate and of the film thickness. In the uppermost zone of the vessel, between latitudinal meshes 1 and 8 dryout is predicted. In this range the plotted temperature is the inner surface temperature of the spherical shell.

Results obtained with the dynamic heated film model are compared with results of the static film model, the standard solution of GASFLOW, in Fig.'s 6-8. Fig. 6 shows the temperature of the inner surface of the spherical shell in a point just below the equatorial plane, versus time for the static and the dynamic film models. The latter model yields a slightly enhanced temperature (12 K at t=1000 s) with respect to the

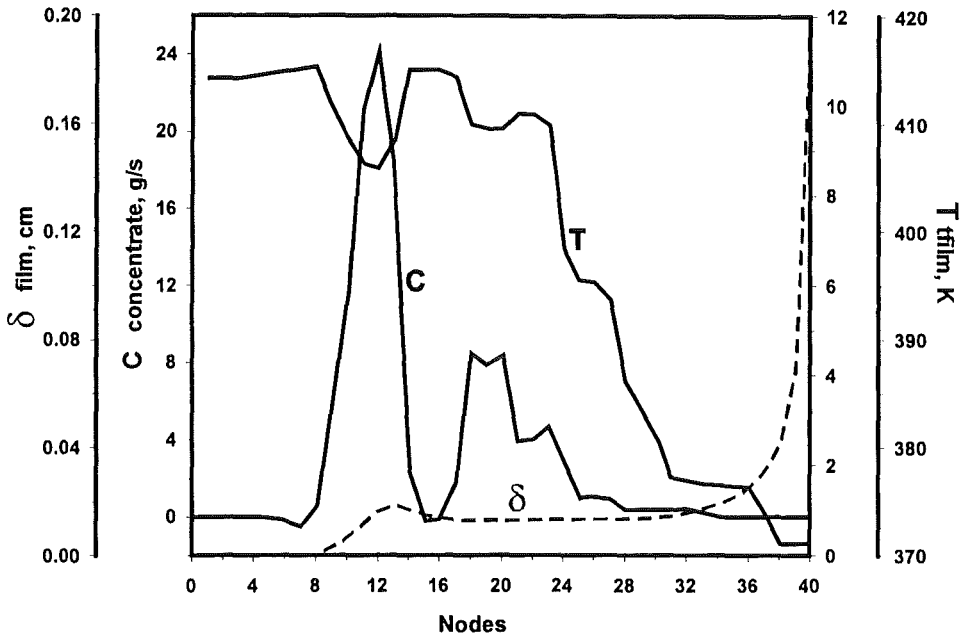

Fig. 5 Distribution of condensation rate, film temperature and thickness along a meridian line (Test case)

static model. Fig. 7 shows a comparison of the two models with respect to the computed condensation rates, integrated over all the inner surface of the spherical shell. Because in the dynamic film model the increased temperature leads earlier to thermodynamic equilibrium of the inner shell surface with the gas mixture of air and steam inside the shell, the condensation rate is somewhat damped. Fig. 8 shows a comparison of the total energy transferred to the shell structure over time. In the dynamic film model the energy stored in the shell is larger than in the static film model. This is consistent with the fact that in the dynamic film model, because of the film draining out rapidly, vaporization cooling occurs far less than in the static film model.

4.2 Containment of the Biblis A reactor

The geometrical configuration of the Biblis A reactor has been represented in the GASFLOW code within an hexahedral domain of 56 m x 56 m cross section and 50 m height, partitioned in 57, 57 and 45 meshes in the x, y an z (vertical) directions, respectively. Including boundary cells the domain consists of 154,744 computational cells. Within this domain, the spherical steel containment and all major components of the reactor plant (reactor vessel, steam generators, pumps, spent fuel storage

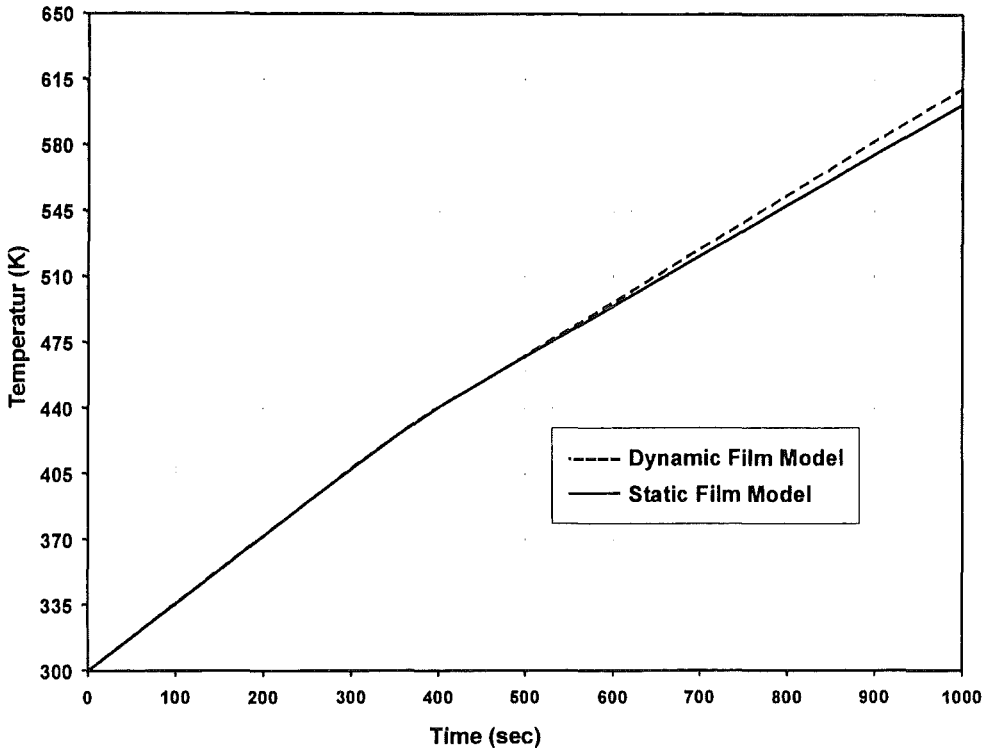

Fig. 6: Comparison between static and dynamic film models for inner temperature of containment versus time.

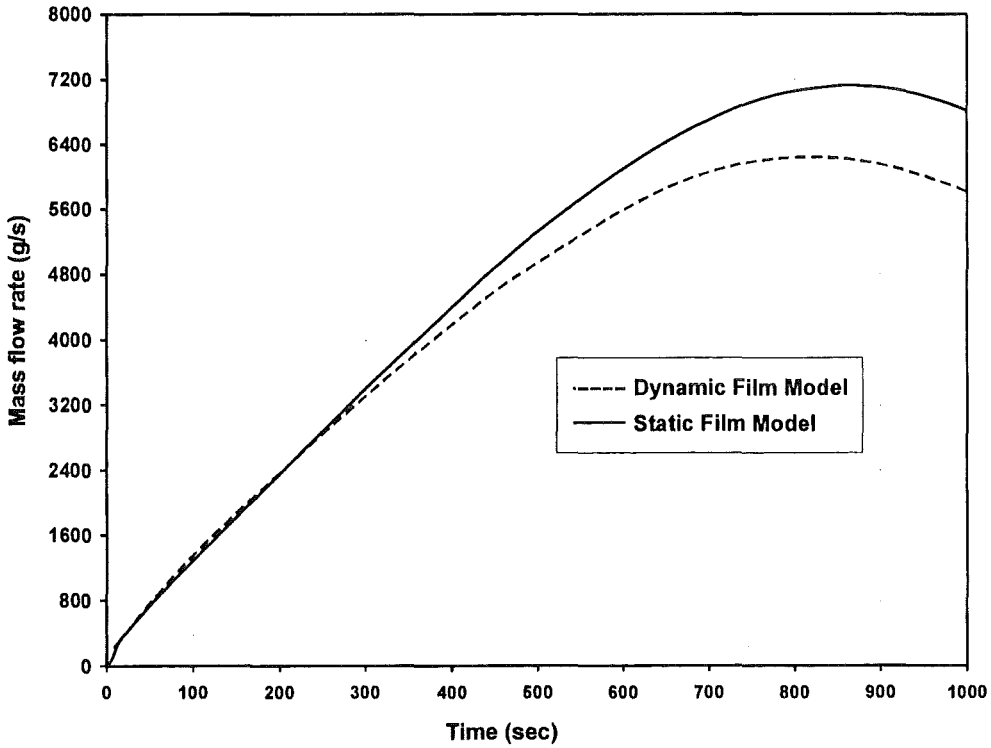

Fig. 7: Comparison between static and dynamic film models for condensation rate versus time.

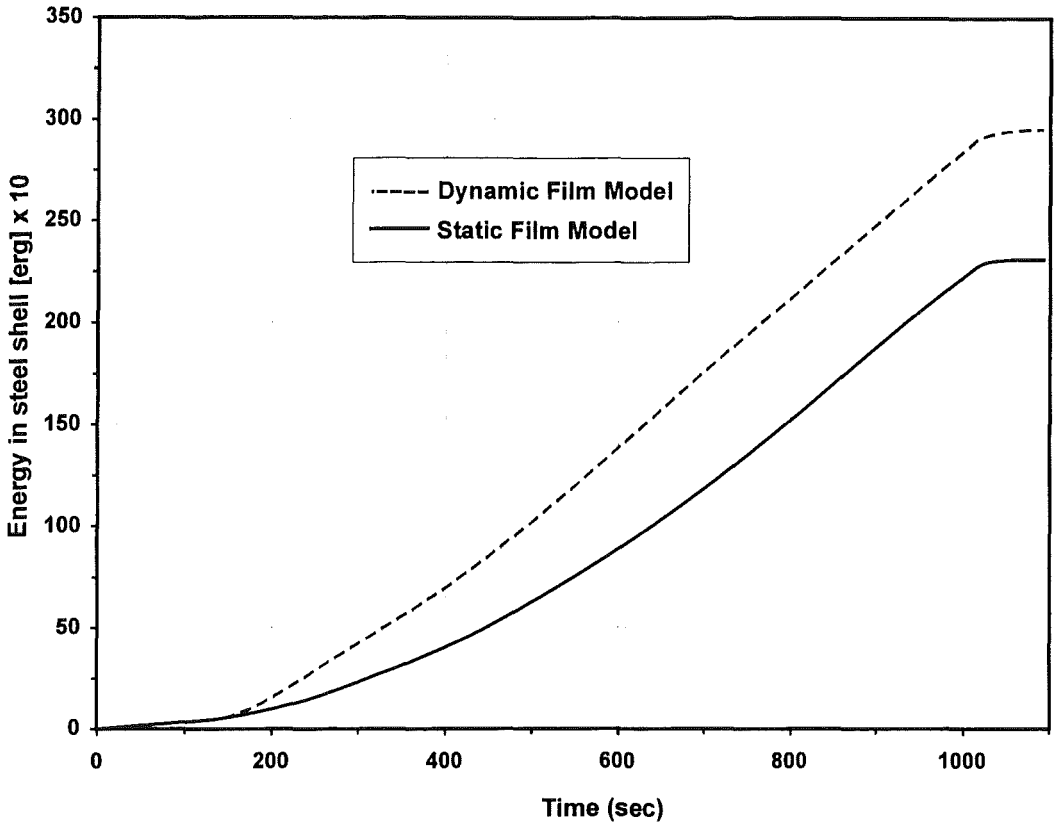

Fig. 8: Comparison between static and dynamic film models for the energy stored in the steel shell versus time.

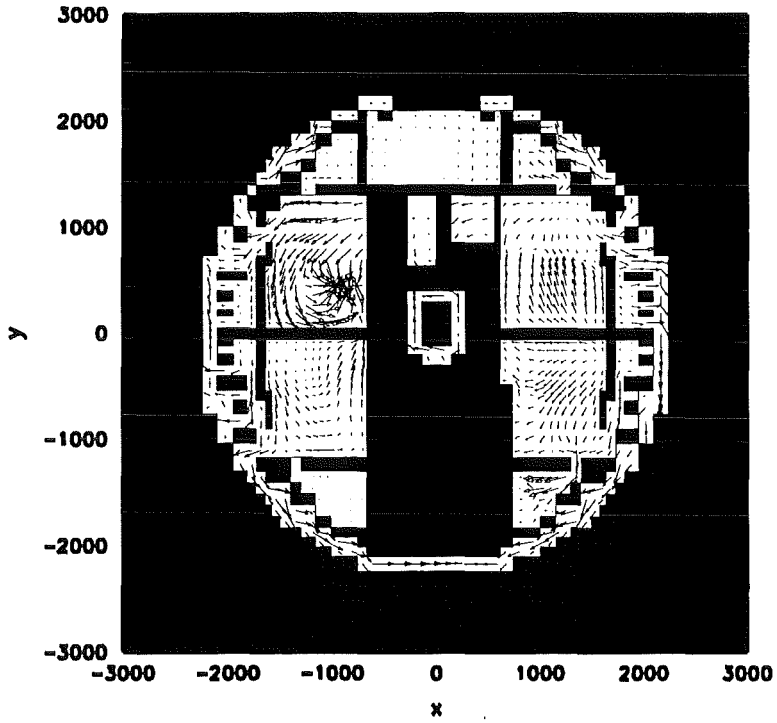

Fig. 9: Horizontal cross section of simulated geometrical configuration for Biblis A reactor.

rooms, biological shield, etc...) are modelled. A detail description of the geometrical model of the Biblis A reactor and results obtained with the static film model have been given in Ref. / 4/. A cross section of the simulated geometrical configuration is shown in Fig. 9.

The spherical steel containment of 56 m diameter and 3.8 cm thickness, extends, with reference to a spherical coordinate system with origin at the center of the spherical shell, from 0 to 135 degrees colatitude. It has been approximated in the code by means of 3066, 3052 and 2696 Cartesian meshes normal to the x, y and z axis, respectively, for a total of 8814 Cartesian meshes. In the spherical coordinate system used for the dynamic film model, the steel shell has been represented by means of 36 azimuthal sectors of 10 degrees aperture, each one partitioned in latitudinal direction with 40 meshes of 4.5 degrees aperture. Meshes 1-30 along a meridian are physical meshes, while meshes 31-40 are dummy meshes. Thus a total of 1080 spherical meshes simulates the real surface of the steel shell. The flow of liquid film draining below the rim of the simulated spherical domain (below latitudinal mesh 30) is assumed to enter a sump domain. The total mass of the sump, accumulated over time, has been computed in the dynamic film model.

The source used for the GASFLOW analysis of the Biblis A reactor simulates a Loss Of Coolant Accident initiated by a surge line break (Surge Line LOCA). In the first 700 s of the simulated problem time 462 tons of water and 39 tons of steam are injected as a mixture into the containment. After 700 s further 50 tons of superheated steam are injected, at much lower injection rate than in the earlier blowdown phase. Injection of hydrogen starts at 1400 s and reaches a total injected mass of 531 kg. Out of this total mass, 120 kg are injected as a sharp pulse around 5900 s. The maximum injection rate of hydrogen is 2.8 kg/s. A source of fission products is simulated after 5000 s through small amounts of Xenon, releasing 8 MW power.

In the course of the blowdown flaps fail in the protection cylinder and a jet of steam impinges against the inner surface of the spherical shell at about the equatorial plane in the azimuthal sectors 16 to 20 of our simulation. In these sectors occur, at first, the largest condensation rates of the steam on the cold inner surface of the shell.

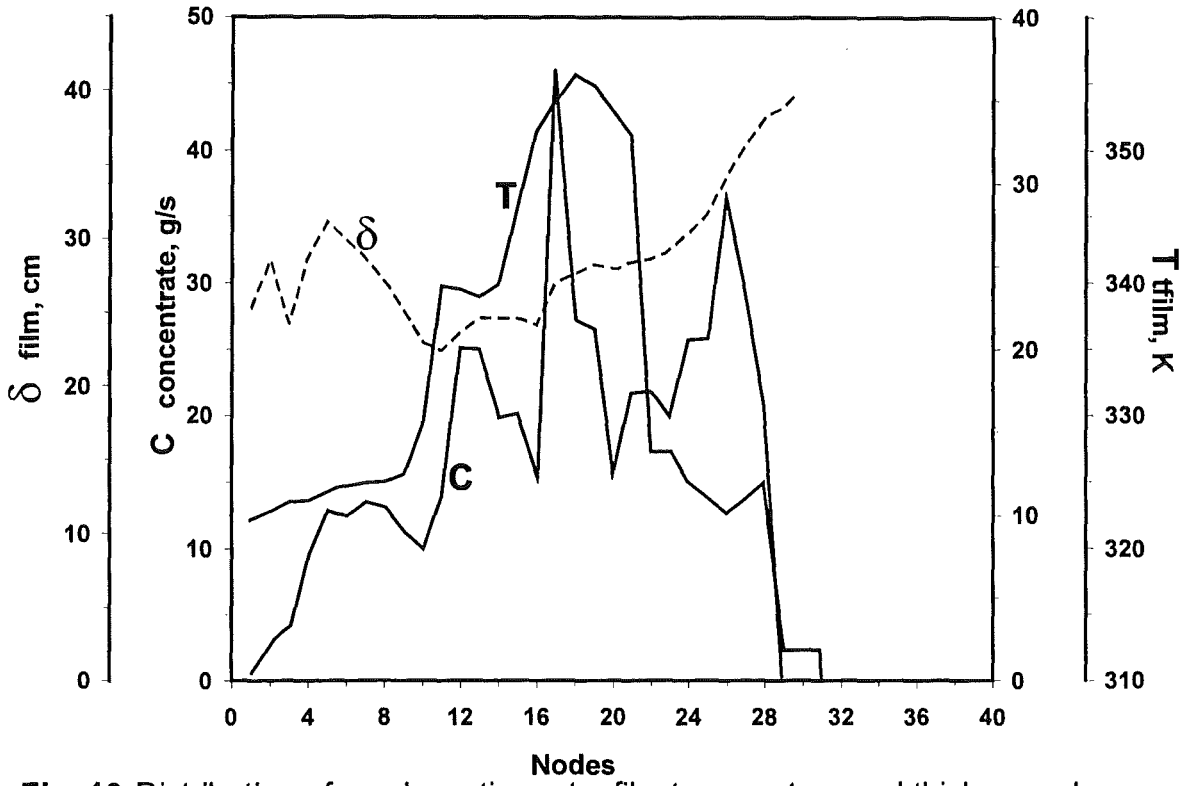

Fig. 10: Distribution of condensation rate, film temperature and thickness along a meridian line for azimuthal sector 18 at t=250 s (Biblis A reactor simulation).

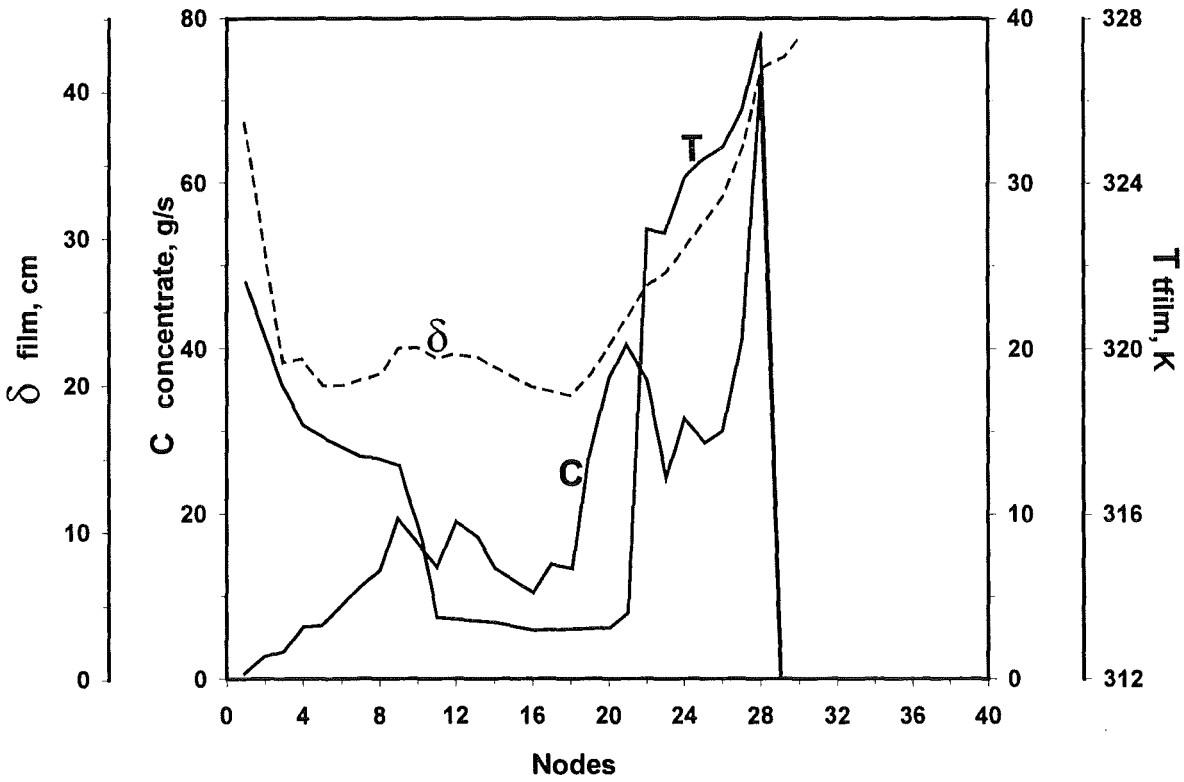

Fig. 11:. Distribution of condensation rate, film temperature and thickness along a meridian line for azimuthal sector 1, at t=250 s (Biblis A reactor simulation).

In Fig. 10 we show the distributions of condensation rate, film thickness and film temperature, coincident, by assumption, with the inner surface temperature, along the central meridian of azimuthal sector 18 at t= 250 s problem time.

Apart from this azimuthal sector, where the jet impinges directly against the spherical shell, vapor condensation during the first few hundreds seconds of problem time occurs, due to the stream pattern, preferentially in the lower ring of the spherical shell, corresponding to the latitudinal meshes 22-30, as shown for the same time point t= 250 s in Fig. 11 for the azimuthal sector 1. Thus, in the first few hundreds seconds of the simulation a hot ring builds up in the lower part of the containment, where temperatures rise in time reaching local maxima of about 410-420 K. The formation of this hot ring in the lower part of the spherical shell is predicted also in the standard static film model of GASFLOW.
Unlike in the static film model, where the mass of the condensed liquid film keeps on accumulating over time, reaching locally thicknesses of several millimeters, in the dynamic film model the liquid film thickness remains rather limited, generally below one millimeter, with at most a local maximum of 2-3 mm at the top of the spherical shell where the film velocity is very small, so that the film is almost stagnant on the spot. As time progresses the full structure of the spherical shell is heated and the outer surface temperature approaches the inner surface temperature. Thus the temperature gradient across the shell structure vanishes and the shell behaves almost as adiabatic. As soon as the inner temperature of the spherical shell approaches the saturation temperature of the steam inside the containment, condensation is suppressed. Because of the reduced source of condensation the liquid film becomes thinner and as the film reaches, in the downward motion, the hot ring below the equatorial plane, it vaporizes completely over large stretches in azimuthal and longitudinal directions. This situation is depicted in Fig. 12 which refers to t=589 s.

Only in the azimuthal sectors where the liquid source due to condensation is still large enough the film can flow to the lower rim of the shell into the simulated sump. One of these is sector 18, where some condensation still occurs in the uppermost part of the shell inner surface at t =1500 s, as shown in Fig. 13. Condensation stops

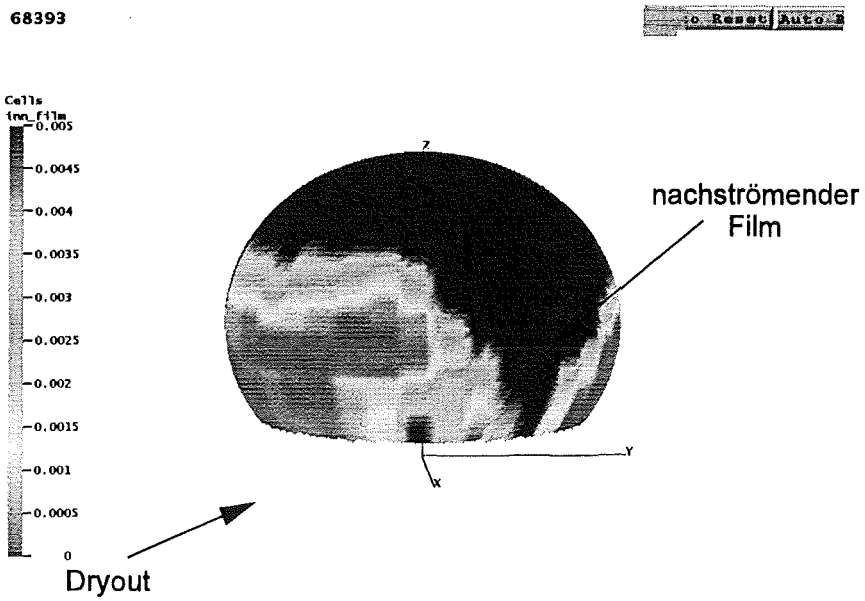

Fig. 12: Distribution of liquid film thickness on the inner surface of the Biblis A reactor containment at t=589 s, computed with the dynamic film model.

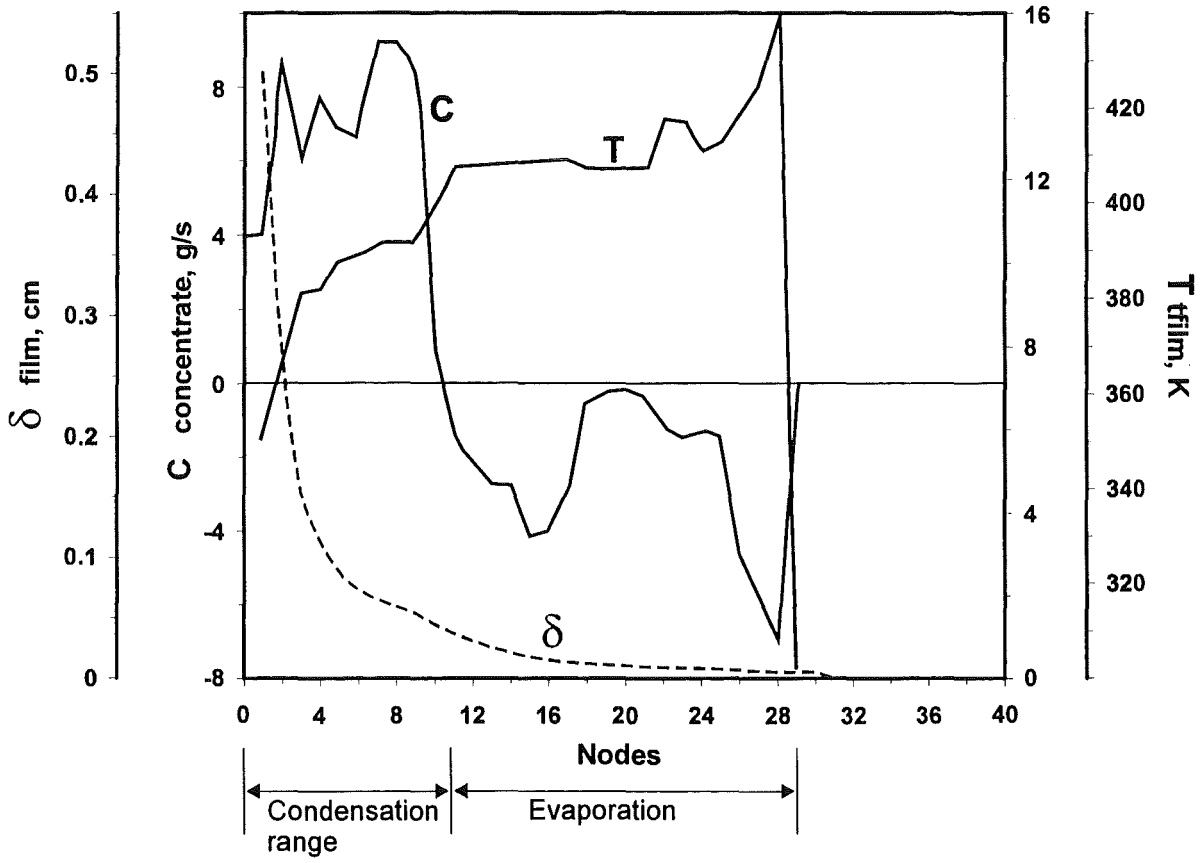

Fig. 13: Distribution of condensation rate, film temperature and thickness along a meridian line for azimuthal sector 18, at t= 1500s (Biblis A reactor simulation).

at latitudinal mesh 11 and reverses to evaporation as the film flows over the hotter lower region of the shell.

Ongoing work aims at evaluating the consequences of the application of the dynamic film model on the space and time distribution of hydrogen and steam concentrations in the containment, especially in comparison with the results obtained with the static film model. Of particular interest is the late phase with superheated steam/hydrogen release, when different preconditioning in the steel shell surface temperatures due to the flowing film will delay the thermal loading of the steel shell.

5. Future work and preliminary conclusions

From all results obtained thus far the most important features of the simulation made with the dynamic film model may be summarized as follows:

a) Because of the downward motion of the film, the maximum film thickness remains rather limited, with peak values around 1-2 mm in the meshes close to the apex of the spherical vessel, but about 0.5 mm or less on most of the spherical surface. As time progresses most of the condensed mass accumulates in a sump at the bottom end of the simulated steel structure. The mass of liquid accumulating in the sump has been computed in the dynamic film model. The enthalpy content of the sump has not been evaluated thus far. It would allow to compute the temperature of the liquid in the sump and the evaporation into the lower regions of the containment. It is estimated that this source of enthalpy and mass arising from sump vaporization will affect the circulation in the course of the simulated accident.

b) Because of the downwards draining of the film the total inventory of condensed mass in the liquid film remains rather limited, compared with the static film model. When the temperature of the inner surface of the containment rises to the saturation temperature of steam inside the containment, and thermodynamic equilibrium is approached, further condensation of the steam is reduced. With reduced condensation and limited film mass inventory, large regions of the containment surface reach dryout conditions and further cooling of these regions

due to evaporation of the film is suppressed. Thus dryout conditions, with correspondingly higher temperatures, are reached earlier than in the static film model.

c) When the film thickness is lower than about 20 microns, due to the wavy condition of the film outer surface, droplets are entrained from the flow and the continuity of the film breaks down. A dryout criterion has been introduced in the code, but, to preserve mass conservation, is application should go along with the use of a droplets transport model which has not been developed thus far.

d) In the application of the momentum integral method done so far the shear stress between the film outer surface and the steam flow within the containment has been neglected. In reality however this shear stress induces a component of the liquid film velocity normal to the meridian, implying a mass flow in azimuthal direction from sector to sector. This effect, and therefore the coupling between azimuthal sectors, should be kept into consideration for future code developments.

e) Treatment of film behaviour should in future also include the large inner concrete surfaces.

REFERENCES

1. J. R. Travis, J. W. Spore and P. Royl, " GASFLOW-II: A Three-Dimensional Finite-Volume Fluid-Dynamic Code for Calculating the Transport, Mixing and Combustion of Flammable Gases and Aerosols in Geometrically Complex Domains". Vol. I: Theory and Computational Model. Vol. 2: User's Manual. NUREG/CR-6570, LA-13357-MS, FZKA-5994, 1998.

2. G. D. Fullford, "The Flow of Liquids in Thin Films". Adv. In Chem. Eng., 5, pp. 151-236, 1964.

3. M. Bottoni, F. C. Chang, T. H. Chien, J. Ding and W. T. Sha, "Liquid Film Tracking Model for Passive Containment Cooling System". NUREG/CR-5895, ANL-92/22.

4. P. Royl, J, R. Travis, H. Rochholz, H. Wilkening, "Verteilung von Dampf und Wasserstoff bei Unfällen in Druckwasserreaktoren". FZK Nachrichten, 4/97.

III. GASFLOW Anwendungsrechnungen

(P. Royl, IRS; H. Rochholz, G. Necker, J. R. Travis, INR)

Zusammenfassung

GASFLOW 2.1 wurde als integriertes Analysewerkzeug zur Beschreibung des Transports von Wasserdampf/Wasserstoffgemischen in LWR Containments in der Version 2.1 bereitgestellt und erstmals erfolgreich zur Analyse von auslegungsüberschreitenden Unfällen mit Einbeziehung von Gegenmaßnahmen (Rekombinatoren) in größerem Umfang eingesetzt. Die Dokumentation von GASFLOW 2.1 wurde gemeinsam mit dem LANL erstellt und als LANL und FZK Bericht veröffentlicht [1].
Die Entwicklung der 3D Geometriemodelle und deren Anwendung in GASFLOW war zeitaufwendig. Die Anwendungsrechnungen wurden im wesentlichen im Berichtsjahr durchgeführt. Die Ergebnisse liegen vor und sind in Detailberichten dokumentiert. Bei den stark auf bestimmte Anlangen konzentrierten Arbeiten konnten viele Erfahrungen und Auswertetechniken entwickelt werden, die die Wissensbasis und die Techniken für solche 3D Untersuchungen mit GASFLOW auch allgemein vorangebracht haben. Wir geben hier eine Zusammenfassung der erzielten Ergebnisse aus den 3D Analysen und ziehen danach Schlußfolgerungen aus den Unterschieden, die sich bei Analysen der gleichen Unfallabläufe mit Lumped Parameter Programmen wie RALOC und Wavco für zwei verschiedene Containmenttypen ergeben haben.

1 GASFLOW Anwendungsrechnungen für 3D Containmentmodelle

Im Mittelpunkt der Arbeiten mit GASFLOW stand die Entwicklung von detaillierten Geometriemodellen für reale Anlagen und Anwendungsrechnungen mit Einbeziehung von Gegenmaßnahmen durch Rekombinatoren. Untersucht wurden je ein Unfall mit großem Leck durch Abriß der Volumenausgleichsleitung (Surge Line LOCA) zwischen Primärkreis und Druckhalter im Kernkraftwerk Neckarwestheim 2 (GKN-2) und in Biblis A. Beispielhaft zeigt Abb. 1 das GASFLOW Geometriemodell für Biblis A, das für diese Analysen entwickelt wurde. Innerhalb eines zusammenhängenden kartesischen Maschennetzes mit 57x, 57y und 45z Maschen wurden die Einbauten des Containments, die Kugelschale und die darum liegende Betonschale definiert, außerdem auch druckabhängig öffnende Klappen bzw. Berstscheiben, die

transient während des Blowdowns Verbindungen zwischen den Anlagen- und den Betriebsräumen im Containment freigeben. Der Blowdown eines Dampf/Wasser-zweiphasengemischs später auch eines Gemischs von überhitztem Dampf und Wasserstoff wird mit einem Quellterm definiert, der aus Rechnungen mit dem Lumped Parameter Code Melcor für dieses Szenario von der GRS bestimmt wurde.

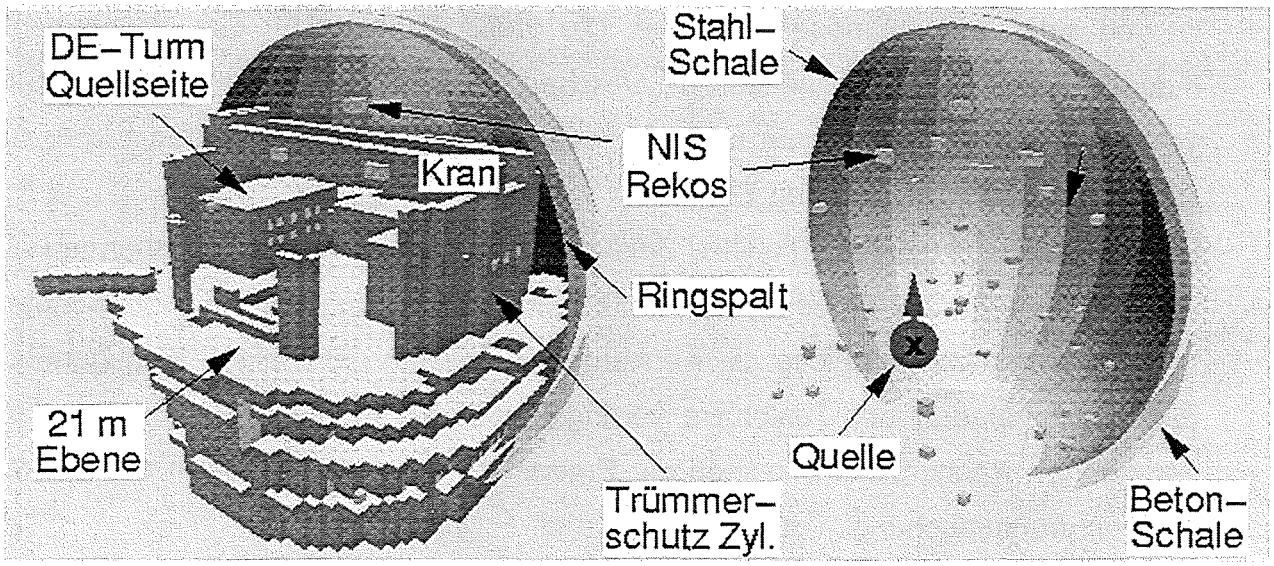

Abb.1: Kartesisches GASFLOW Geometriemodell von Biblis A mit Positionen der NIS Rekombinatoren (146,205 Gitterzellen)

Der Blowdown erfolgt als vertikale Einspeisung mittels einer Geschwindigkeitsrand-bedingung aus einem Quellreservoir, das innerhalb des 3D Maschennetzes von GASFLOW abgetrennt wurde. Die Gasströmung im Containment wird in den verknüpften freien Gasvolumina als vollständige 3D Lösung der kompressiblen Navier Stokes Gleichungen simuliert. Eingetragen in Abb. 1 sind auch die Rekombinatoren, die an verschiedenen Stellen innerhalb und außerhalb der Anlagenräume angebracht wurden, wobei die Einbauten innerhalb der Stahlschale weggelassen wurden und nur die 3D Anordnung der Rekombinatoren im Raum relativ zueinander und zur Quelle erkennbar ist.

1.1 Analysen für den EPR

Im Rahmen des Siemens-EVU-Vertrags und in direkter Zusammenarbeit mit Siemens/KWU wurde parallel zu den Untersuchungen für bestehende Anlagen auch

ein neues EPR Geometriemodell entwickelt. Es wurde zur Simulation des Loss of Off Site Power (LOOP) Unfalls mit aktiven Zündern am Ausgang des IRWST für ein trockenes H_2-Freisetzungs-Szenario im EPR verwendet und auch für ein Szenario mit kleinem Leck und langsamer Dampf/Wasserstofffreisetzung (Small Break Loca). Die Nodalisierung der Containmentmodelle ging an die Grenze dessen, was auf dem verfügbaren VPP Rechner im FZK heute mit einem vernünftigem Aufwand machbar ist und setzt dadurch neue Maßstäbe. Die große Zahl der für die Containmentmodelle verwendeten Rechenzellen (zwischen 120000 und 180000 mittleres Zellvolumen etwa 1 m^3) liegt um mehr als eine Größenordnung über den bisher für solche Analysen verwendeten Zellzahlen, wobei Problemzeiten zwischen 2 und 5 h je Fall untersucht wurden. Die CPU Zeiten lagen zwischen 1 und 2 Wochen je Fall, ein Ergebnis eines verbesserten Zeitschrittschemas und einer überarbeiteten Vektorisierung, durch welche die Rechenzeiten fast um den Faktor 10 gegenüber dem Rechenbedarf der Testphase verringert werden konnten. Wegen der stark verringerten Rechenzeiten konnten die Ergebnisse einzelner Analysen auch durch Parameteruntersuchungen abgesichert werden.

1.2 Analysen für GKN-2 und Biblis A

Die GASFLOW Analyse für den Surge Line LOCA in GKN-2 und Biblis A bezieht die Wirkung von 64 an verschiedenen Stellen im Containment angebrachten Siemens- bzw. 44 NIS-Rekombinatoren ein. Die verwendeten Rekombinatormodelle in GASFLOW wurden zuvor durch Nachrechnung von Rekombinatortests im Battelle Modell Containment validiert. Zum Vergleich mit entsprechenden Untersuchung von GKN-2 und Biblis A mit den Lumped Parameter Programmen RALOC und Wavco wurden die 106 bzw. 102 Kontrollzonen der Lumped Parameter Modelle in den 3D GASFLOW Modellen markiert. Raumweise Mittelungen in GASFLOW für Wasserstoff- und Dampfkonzentrationen sowie für die Temperaturen führten zu direkt mit den Raumdaten der LP Codes vergleichbaren Ergebnissen. Zusätzlich wurden mit GASFLOW in jedem Raum die lokalen Peakwerte zu jedem Zeitpunkt bestimmt.

Die GASFLOW Simulationen für GKN-2 und Biblis A führen ebenso wie die entsprechenden RALOC und Wavco Simulationen zu gut durchmischten Zuständen bei diesem Large Break LOCA und stimmen auch in den berechneten Wasserstoffabbaumengen gut überein. Mit den Siemens Rekombinatoren in GKN-2 werden 40% des freigesetzten Wasserstoffs in den ersten beiden Stunden abgebaut, mit dem untersuchten Anordnungskonzept der NIS-Rekombinatoren etwa 20%. Die Untersuchungen dokumentieren die sicherheitsgerichete Wirksamkeit des Rekombinatorkonzepts für beide Anlagen. Die GASFLOW Simulation beschreibt aber die transienten Übergänge bis zum Erreichen der homogenen Zustände genauer und identifiziert dabei auch Regionen mit temporär zündfähigen Gemischen in den Betriebsräumen, die in RALOC erst durch eine Nachnodalisierung ausgehend von den mit GASFLOW berechneten Strömungsverhältnissen dargestellt werden konnten. Berstscheiben bzw. Klappen, die bei verschiedenen Druckdifferenzen aufgingen, wurden in die Simulation einbezogen. Anhand des berechneten Strömungsfeldes waren die dominanten Strömungspfade aus den 3D Analysen im Unterschied zu den LP Rechnungen direkt ablesbar und sie konnten durch gezielte Verriegelung wichtiger Überströmöffnungen auch unmittelbar von Ihrer Wirkung her quantifiziert werden.

Die in GASFLOW bedeutsamen Phänomene bei diesem Surge Line LOCA sind die transiente Strahlbildung in der dynamischen Phase der Dampf-/Wasserstoffreisetzung, die Vermischung des Strahls, die Wasserstoffstratifikation, die Sedimentation des Wasserstoffs durch Dampfkondensation an den kalten Wänden und die Rekombination des Wasserstoffs.

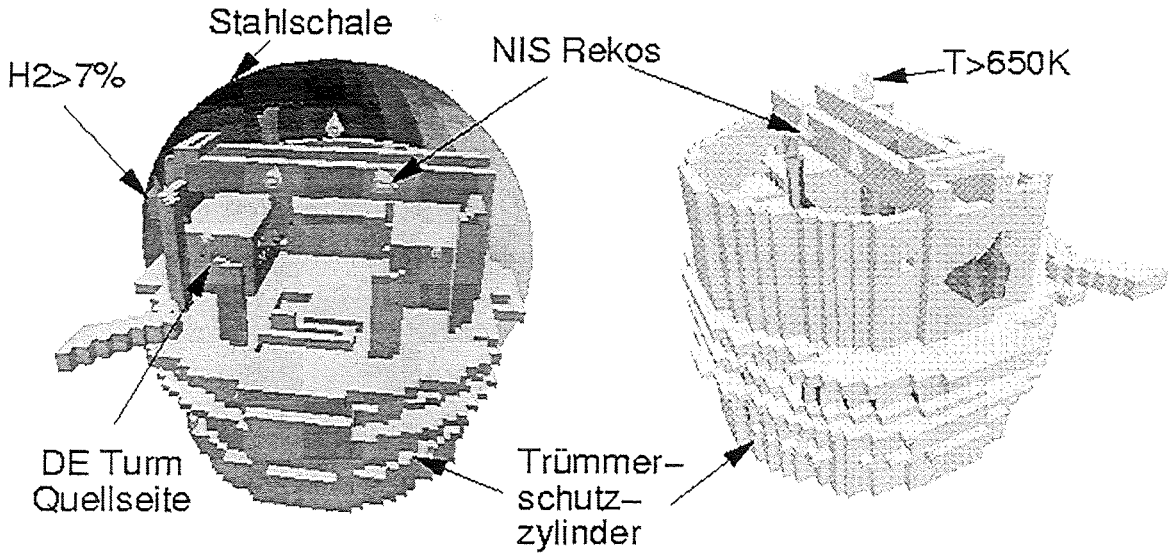

Abb. 2: Berechneter Wasserstoff Quellstrahl aus GASFLOW nach Kernversagen beim Surge Line LOCA in Biblis A (Kismet Darstellung Vorder- und Rückansicht bei 5932 s)

Die GASFLOW Modellierung dieser Phänomene wurde durch die erfolgreiche blinde Vorhersage der Strahlbildung beim Hyjet Test JX7 und die Nachrechnung des Heliumstrahls bei den Whiteshell Tests (s. a. dieser Bericht), die erfolgreiche Interpretation der Stratifikation und Sedimentation des Helium/Wasserstoffgemischs beim HDR Experiment E11.2 und T31.5 und die Nachrechnung der Battelle Rekombinatortests MC3 und GX4, GX6 und GX7 validiert. Die GASFLOW Analysen für Biblis A und GKN-2 haben durch die Validierung für die wichtigsten Phänomene eine gute Vorhersagefähigkeit erreicht und erlauben eine Überprüfung der Vorhersagefähigkeiten auch von alternativ eingesetzten Lumped Parameter Programmen wie RALOC und Wavco bei dem gewählten Unfallszenario mit Gegenmaßnahmen durch Rekombinatoren.

Wichtige GASFLOW Ergebnisse der Simulation für Biblis A und die Unterschiede zu der GASFLOW Simulation des gleichen Unfalls in GKN-2 lassen sich wie folgt zusammenfassen:

Die offenere Bauweise des Biblis A Containments hat bei gleichem freien Gasvolumen verglichen mit GKN-2 um 1/3 kleinere Betonflächen. Verbunden damit ist ein kleineres Kondensationspotential in Biblis A. Daraus ergibt sich ein andauernd höherer Containmentdruck beim Blowdown und ein verglichen zu GKN-2 höherer Dampfpartialdruck. Der berechnete Enddruck ist 4 bar, verglichen mit 2.6 bar bei GKN-2. Bei der gleichen freigesetzten Wasserstoffmasse verringert sich auch der Volumenanteil des Wasserstoffs in Biblis A durch den höheren Druck. Bei hohen Dampfanteilen zwischen 50 und 60 Vol% und mit den verringerten Volumenanteilen des Wasserstoffs ist die Containmentatmosphäre in Biblis A anders als in GKN-2 selbst kurzzeitig nicht zündfähig. Der Quellstrahl aus Dampf und Wasserstoff strömt in Biblis A durch seitlich beim Blowdown öffnende Klappen im quellseitigen Dampferzeugerturm in den Betriebsraum ab und steigt als aufgefingerter Strahl hoch zur Kuppel (Abb. 2).

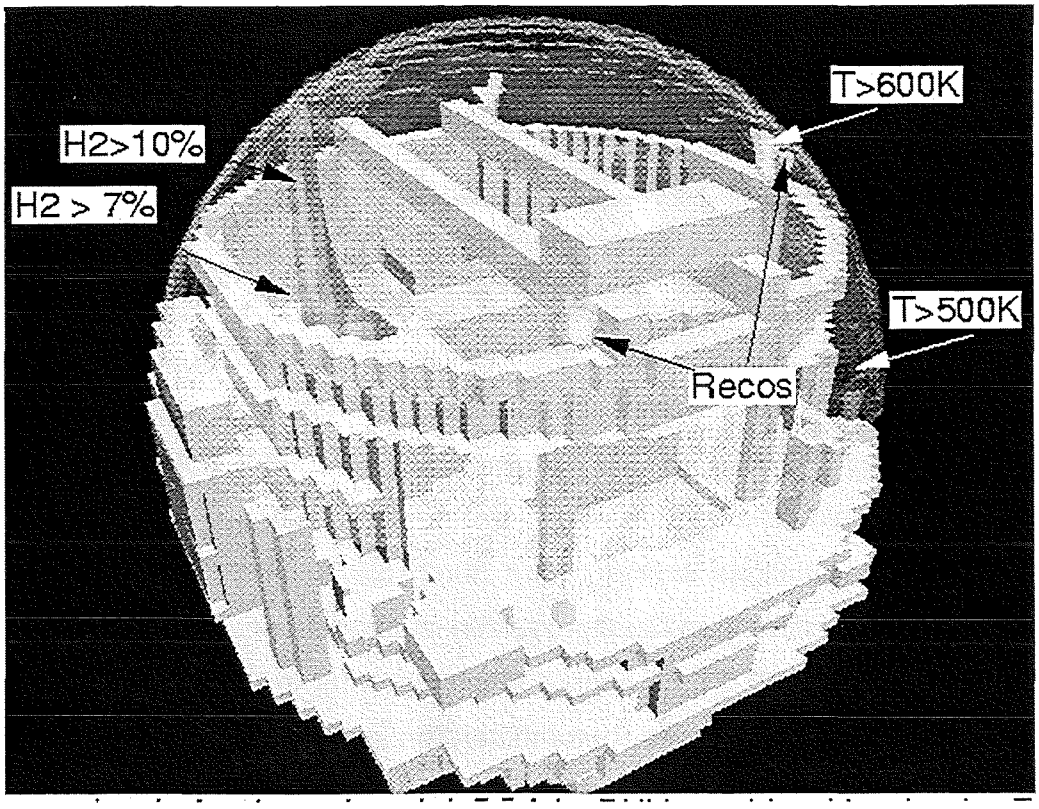

Abb.3 : Wasserstoff im Quellstrahl und Rekombinator Abgase im Dom nach Kernabsturz beim Surge Line LOCA in GKN-2 (3D Kismet Darstellung von GASFLOW Ergebnissen bei 5932 s)

In GKN-2 kam es zum Versagen der Berstfolien auf dem Dach der quellseitigen Dampferzeugertürme und zu einem nicht aufgefingerten direkt aus dem quellseitigen Dampferzeugerturm vertikal abblasenden Quellstrahl (Abb. 3). In beiden Containments vermischen Wirbelbildungen durch Taylorinstabilitäten und Strömungsumlenkungen an der Kuppel den Quellstrahl auf seinem Weg nach oben. In der Kuppel bildet sich danach sowohl in Biblis A wie in GKN-2 eine stratifizierte Schicht mit erhöhter Temperatur und erhöhter Wasserstoffkonzentration. Diese stratifizierte Schicht bleibt in Biblis A länger bestehen, da die Wasserstoffsedimentation durch Dampfkondensation an den kleineren Betonflächen nur langsamer in Gang kommt. Kurzzeitig kommt es wie in GKN-2 zu einer vermischenden Zirkulation durch die Kaminwirkung der quellseitig und quellfern unterschiedlich aufgeheizten Dampferzeugertürme. Überlagert sind auch vermischende Zirkulationen durch die geöffneten Klappen bzw. Berstfolien unten im Rohrkanal. Beide Zirkulationspfade haben in Biblis A und in GKN-2 langfristig keinen großen Einfluß auf die Wasserstoffvermischung und sind am Ende der Analyse bei 7000 s kaum noch erkennbar. Für beide Containments führen die Analysen längerfristig zur Wasserstoffhomogenisierung und letztlich gleichen Zuständen. Am Ende der Analyse bei 7000 s ist der Wasserstoff in Biblis A aber noch etwas mehr stratifiziert mit Konzentrationen zwischen 4 Vol% oben und etwa 3.5Vol% unten, während er in GKN-2 bereits gleichmäßig verteilt ist mit Konzentrationen um 4% . Die Vermischung entsteht wie in GKN-2 durch eine langsame aber großflächig auftretende Sekundärströmung entlang der Betonwände, an denen Dampf lokal auskondensiert und entlang denen das getrocknete Gas aufgrund seines lokal erhöhten mittleren Molekulargewichts absinkt. Die stratifizierte Schicht, die durch das heiße Dampf/ Wasserstoffgemisch im Quellgas entsteht, wird durch die Nachwärme aus den im Quellgas mitgeführten gasförmigen Spaltprodukten zusätzlich erwärmt. In Biblis A ergibt sich verglichen mit GKN-2 eine höhere Gastemperatur in dieser stratifizierten Schicht. Die dichte Anbringung vieler Rekombinatoren an den Kranträgern und im darüberliegenden zentralen Kuppelbereich führt in Biblis A verglichen mit GKN-2 auch zu konzentrierteren Abgasstrahlen, die eine länger anstehende dünne heiße Gasschicht mit T>650K in der Kuppel bilden. Solche gebündelten heißen Abgasstrahlen ließen sich durch eine breiter gefächerte Positionierung der Rekombinatoren am Kranträger vermeiden. Der Wasserstoffabbau erfolgt in Biblis A mit NIS Rekombinatoren, die durch ihre Granulatfüllung eine hohe Wärmekapazität

haben und verglichen mit den Siemens Rekombinatoren, die für GKN-2 untersucht wurden, nur träge anlaufen.

Die Wasserstoffkonzentrationen, die Dampfkonzentrationen und die Gastemperaturen in den Kuppelräumen von GKN-2 und Biblis A wurden in GASFLOW entsprechend den RALOC bzw. Wavco Raumdefinitionen volumengemittelt. Ihr zeitlicher Verlauf ist abhängig von der betrachteten Unfallzeit in den Abb. 4 und 5 dargestellt, oben zusammen mit dem zeitlichen Verlauf des lokalen Maximums der H_2 Konzentration und dem zeitlichen Verlauf der durch die Dampfkonzentration bestimmten Zündgrenze, im unteren Teil zusammen mit dem zeitlichen Verlauf des örtlichen Temperaturmaximums in diesem Raum. Für GKN-2 (Abb.5) sind gestrichelt auch die entsprechenden Ergebnisse ohne Rekombinatoren mit eingetragen. Im ersten Puls der Wasserstofffreisetzung zwischen 1500 und 3000 s werden maximale H_2 Konzentrationen von 7% in GKN-2 und 5% in Biblis A erreicht.

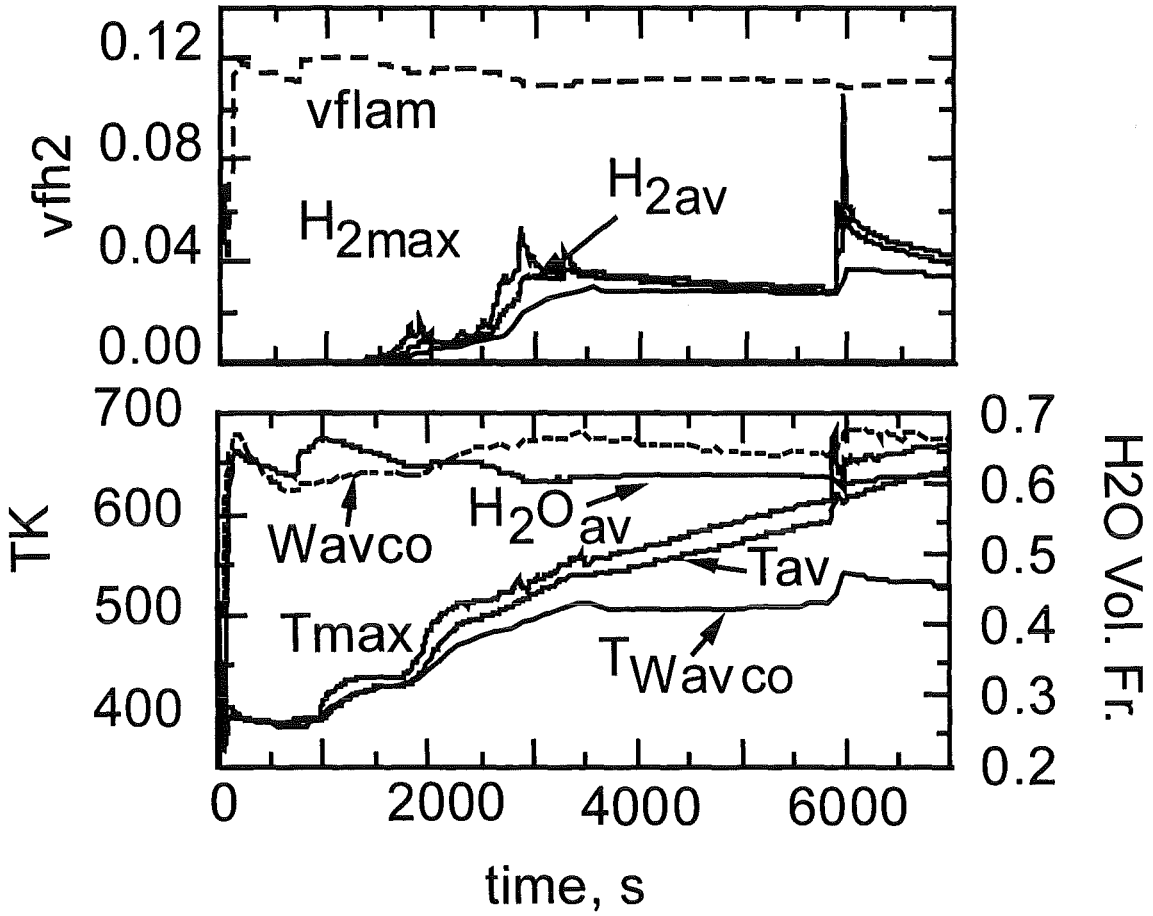

Abb. 4: Wasserstoff-/ Dampfkonzentrationen und Temperaturen im Kuppelraum 99 von Biblis A (Peakwerte und volumengemitttelte Ergebnisse aus GASFLOW verglichen mit Wavco Ergebnissen)

Nach dem Kernabsturz bei 6000 s, wenn in kurzer Zeit weitere 120 kg Wasserstoff freigesetzt werden, erreichen die Konzentrationsmaxima aus GASFLOW Werte von 11% in GKN-2 und 10.5% in Biblis A. Dabei überschreiten die Spitzenkonzentrationen in GKN-2 kurzzeitig die Wasserstoffzündgrenze, die in GKN-2 wegen des niedrigeren Dampfanteils bei ca. 9%, in Biblis A bei 11% Wasserstoff liegt. Das Konzentrationsmaximum liegt in einem der in Abb. 2 bzw. 3 erkennbaren Quellstrahlen, die sich in den Domraum erstrecken. Das Konzentrationsmaximum und der Raummittelwert nähern sich in GKN-2 und Biblis A nach jeder Einspeiseperiode rasch an durch die Vermischung in den Strömungswirbeln, die durch Taylorinstabilitäten und Strömungsumlenkungen im Dom entstehen. Diese Vermischung erfolgt in Biblis langsamer als bei den GKN-2 Analysen und ist nach dem zweiten Freisetzungspuls noch nicht abgeschlossen. Die raumgemittelten Wasser-stoffkonzentrationen aus RALOC bzw. Wavco für die Domräume in GKN-2 und Biblis A sind zusammen mit den GASFLOW Ergebnissen in Abb. 4 und 5 dargestellt.

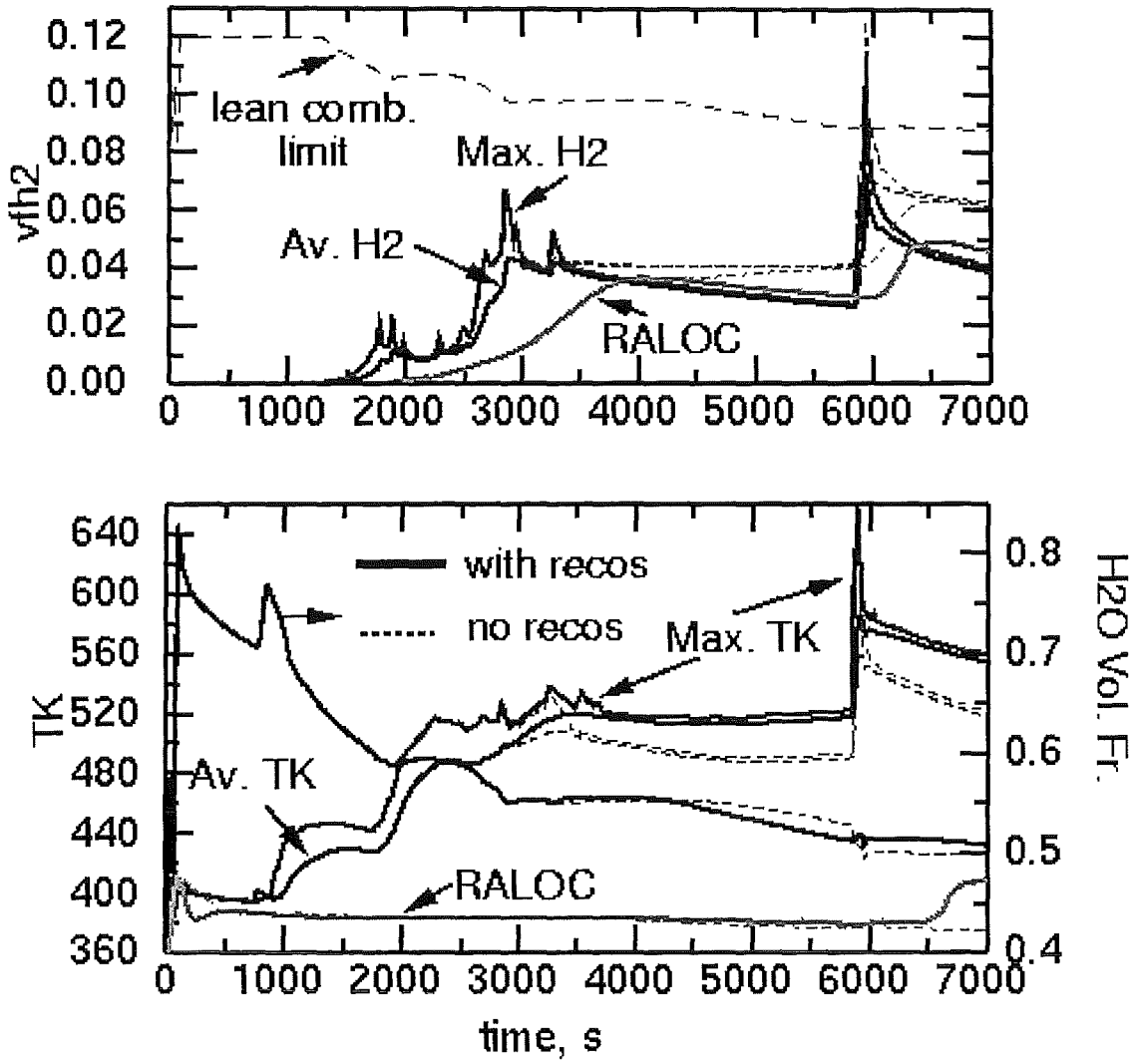

Abb. 5: Wasserstoff-/Dampfkonzentrationen und Temperaturen im Domraum 45 von GKN-2 (Peakwerte und volumengemitttelte Ergebnisse aus GASFLOW verglichen mit Wavco Ergebnissen)

Beide lumped Parameter Programme lösen die temporären Heterogenitäten in der Wasserstoffverteilung aus GASFLOW nicht auf. Durch die integrierende Wirkung der großen Kontrollvolumina (ca. 2000 m^3 in jedem der Domräume) kann die H_2 Konzentration in den Domräumen nur langsam ansteigen. Beim ersten GASFLOW Maximum von 7% H_2 in GKN-2 und 5% in Biblis A berechnen RALOC und Wavco nur Wasserstoffkonzentrationen von 1 bis 2%. Die Konzentrationen steigen dann in den Lumped Parameter Programmen kontinuierlich weiter an und nähern sich asymptotisch dem homogenen Mittelwert aus GASFLOW nach ca. 3000 s. Im

zweiten Freisetzungspuls steigen sie in den LP Programmen wieder nur verzögert an und erreichen für GKN-2 mit RALOC 3%, für Biblis A mit Wavco 3.5% zum Zeitpunkt des örtlichen GASFLOW H_2-Maximums von 11% bw. 10.5%. Erst einige Zeit nach Ende der raschen H_2 Freisetzung aus dem zweiten Puls nähern sich die Wasserstoffkonzentrationen aus RALOC und Wavco den entsprechenden GASFLOW Ergebnissen. Im Endzustand guter Durchmischung ergeben sich nur noch geringe Unterschiede zwischen den LP Analysen und GASFLOW weil in beiden Modellansätzen die Massenbilanz für Wasserstoff eingehalten wird. Die zusätzliche Information aus der 3D Analyse mit GASFLOW ergibt sich aus der Beschreibung der transienten und lokalen Zwischenzustände beim Übergang zu diesem homogenen Endzustand. Der Quellstrahl, dessen Vermischung im Dom, der Aufbau einer temporär stratifizierten Gasschicht und die Homogenisierung des Wasserstoffs durch die Kondensationssedimentation werden in GASFLOW detailliert erfaßt und sind in beiden GASFLOW Analysen die entscheidenden Mechanismen für die gute Durchmischung.

Die mittleren und maximalen Gastemperaturen (unterer Teil der Abb. 4 und 5) erreichen in Biblis A höhere Werte als in GKN-2 wegen der kleineren Strukturflächen und der höheren Nachwärmeleistung aus den mit dem Wasserstoff nach oben getragenen gasförmigen Spaltprodukten. Die Temperaturen steigen auch gegen Ende der Analyse weiter an, während sie in GKN-2 schon abnehmen. Die konzentriertere Anbringung von Rekombinatoren im Domraum von Biblis A trägt mit zum Aufbau einer überhitzten heißeren Gasschicht im Domraum bei, die in GKN-2 nicht auftritt. Die mit den LP Modellen berechneten Gastemperaturen im Domraum sind alle niedriger als in GASFLOW, obwohl Wavco auch überhitzte Bedingungen im Dom vorhersagt. In RALOC ist der Anstieg der Temperatur im Domraum zusätzlich dadurch begrenzt, daß eine Gasüberhitzung wegen der Anwesenheit eines Kondensatfilms auf den Strukturen über lange Zeiträume hinweg nicht möglich ist. Die gegenüber den LP Modellen höheren GASFLOW Temperaturen in der Kuppel sind ein generischer Unterschied der 3D GASFLOW Ergebnisse, der durch die temporär stärkere Stratifikation mit dem Quellstrahl hervorgerufen wird.

2 Allgemeine Schlußfolgerungen aus den Vergleichsrechnungen mit Lumped Parameter Programmen

Aus dem Vergleich der GASFLOW Analysen mit den RALOC und Wavco Analysen geht hervor, daß alle Programme zwar homogene Endzustände für diesen Surge Line LOCA vorhersagen. Weder RALOC noch Wavco können aber die stark heterogenen Zwischenzustände und die temporären Wasserstoffstratifikationen aus den GASFLOW Analysen beim Surge Line LOCA in GKN-2 und Biblis A auf Anhieb vorhersagen. Die H_2 Abbaumengen unterscheiden sich nur unwesentlich zwischen den Codes. Das Ziel solcher aufwendigen 3D Analysen ist aber nicht der Nachweis der homogenen Endzustände sondern gerade der glaubhafte Nachweis, daß diese homogenen Endzustände ohne Zwischenzustände mit größerem Gefährdungspotential erreicht werden. Der Vergleich mit den beiden verschiedenen LP Programmen RALOC und Wavco für GKN-2 und Biblis A zeigt in beiden Anwendungsfällen, daß die Lumped Parameter Programme nur eine begrenzte Vorhersagefähigkeit in dieser Hinsicht haben und von den Ergebnissen her auch nicht konservativ sind.

Die Beschreibung wichtiger Mechanismen für die schnelle Atmosphärenmischung, die in den GASFLOW Analysen identifiziert wurden, (Wirbelbildung, Taylorinstabilitäten und Kondensationssedimentation), stößt auf prinzipielle Schwierigkeiten in RALOC und Wavco, weil die gelösten Modell- Gleichungen stark vereinfacht sind und die entsprechende Physik nicht mehr enthalten. Sie enthalten z.B. keine Richtungsinformation mehr. RALOC hatte zwar zusätzliche wandnahe Räume nachnodalisiert und müßte den lokalen Kondensationseffekt damit eigentlich besser abbilden. Der in GASFLOW identifizierte physikalische Mechanismus der Kondensationssedimentation konnte mit den Lumped Parameter Modellen nicht nachvollziehbar aufgezeigt werden.

Die entscheidenden Mechanismen für die gute Atmosphärenmischung in GASFLOW wurden identifiziert und sind dokumentiert. Die Mechanismen für die gute Durchmischung, die in RALOC und Wavco vorhergesagt wird, sind bisher nicht detailliert ausgewertet und dokumentiert. Es fehlt vor allem die Identifizierung der dominanten Strömungspfade in den Lumped Parameter Analysen. Diese Strömungs-pfade sind

bei den 3D GASFLOW Analysen unmittelbar aus den Geschwindigkeitsfeldern ablesbar und konnten mit einfachen Maßnahmen wie z.B. dem Versperren von Öffnungen in GKN-2 von ihrer Bedeutung her direkt quantifiziert werden.

Bei den 3D GASFLOW Simulationen für GKN-2 und insbesondere für Biblis A ergaben sich mit GASFLOW immer wesentlich höhere Atmosphärentemperaturen im Dom, die auch in engem Zusammenhang mit der stärkeren transienten Stratifikation stehen. Die Aussagen der Lumped Parameter Programme sind daher zumindest beim Surge Line Loca im Hinblick auf die thermische Belastung der Strukturen im Kuppelraum nicht konservativ.

Nun führte der analysierte Surge Line LOCA wegen der gut durchmischten Endzustände und dem erreichten hohen Inertisierungsgrad durch die Dampffreisetzung kaum und wenn dann nur kurzzeitig zu Zwischenzuständen mit Zündpotential. In diesem Punkt zeigen die GASFLOW Analysen für GKN-2 und Biblis A eine generische Übereinstimmung. Mit GASFLOW kann ein solcher Unfall auch wegen des immer noch großen Bedarfs an Rechenzeit mit einem vertretbaren Aufwand nur in einem begrenzten Zeitbereich weiter betrachtet werden. Hier wurde nur die dynamische Phase vollständig in GASFLOW betrachtet. Die Ergebnisse führten zu Endzuständen, die gut mit den Ergebnissen der Lumped Parameter Codes übereinstimmen. Ausgehend von diesen durch die Feldcodeanalyse abgesicherten homogenisierten Zuständen lassen sich die Untersuchungen eines solchen Unfalls, die manchmal noch über viele Stunden und Tage Problemzeit hinweg erforderlich sind, schneller mit Lumped Parameter Codes wie RALOC und Wavco weiterführen, sofern die Natur der Vermischungsvorgänge in diesen Programmen geklärt werden.

[1] J. R. Travis, J. R. Spore, P. Royl, K. Lam, T. W. Wilson, C. Müller, G.. A. Necker, B. D. Nichols, R. Redlinger, E. D. Hughes, H. Wilkening, W. Baumann, and G. F. Niederauer: „GASFLOW: A Computational Fluid Dynamics Code for Gases, Aerosols and Combustion“, Report LA-13357-M , FZKA-5994 Vol. I-III, October 1998

IV. Effects of Oversized Jet Flow Areas in GASFLOW Analyses, Investigations of Canadian Gas Mixing Tests

(W. Baumann, INR)

Zusammenfassung

Mit dem 3D-Code GASFLOW werden auslegungsüberschreitende Unfälle in Leichtwasserreaktoren analysiert, vor allem wird die Wasserstoffverteilung während eines hypothetischen Kühlmittelverlust-Unfalls (LOCA) untersucht. Dazu wird ein Gittersystem erstellt, das – bedingt durch die Dimensionen des Reaktorcontainments – aus rund 10^5 einzelnen Zellen bestehen kann, wobei jede einzelne Zelle nicht kleiner als 1 m^3 ist. Bei dieser Größenordnung stößt man an die Grenzen dessen, was Computer derzeit leisten können. Es stellt sich die Frage, ob GASFLOW auf der Basis eines solchen relativ groben Gittergeflechts noch in der Lage ist, physikalisch vernünftige und zuverlässige Ergebnisse vorherzusagen. Um diese zu Frage klären, wurden kanadische Heliumfreisetzungsversuche analysiert.

1 Introduction

The 3D-code GASFLOW is used to analyze hypothetical LWR accidents, particularly the phenomenon of hydrogen distribution in a containment atmosphere during a postulated loss-of-coolant accident. This is done by setting up a grid system of the calculational domain, which – due to the large dimensions of reactor containments – may attain a total of some 10^5 cell volumes, although one single cell is not smaller than 1 m^3. With transient simulations in mind, this order of magnitude really represents an upper limit of grid nodes for the current standard of available computer performances. Of course, all internal structures and sources, e.g. breaks releasing hydrogen gas, are bound to the extensions of the cell volumes which they are associated to. Here the question comes up whether the GASFLOW code based on such a relatively coarse mesh is still able to predict physically reasonable and reliable results. In order to investigate this issue, suitable helium release tests, carried out at the Whiteshell Laboratories in Manitoba, Canada /1/, have been analyzed.

2 Experiments.

The test facility is a 10.3 m x 8.2 m x 10.95 m concrete enclosure with an internal volume of roughly 1000 m^3 (Fig.1). Helium was injected at a constant rate through a vertically oriented 0.05 m- or a 0.30 m-diameter tube at the bottom (BT) of the facility, as shown in Figs.1 and 2. The injection velocity was calculated based on the injection tube opening area and confirmed by direct measurement using a turbine meter. The interior of the facility was maintained at atmospheric pressure during the test by venting through exhaust location #6 (see Fig.2). Because this location is about 1 m from the floor of the facility, it is expected that only air is vented, and there is no impact on the helium inventory or on the flow pattern inside the facility. In fact, no loss of helium inventory was detected during the entire duration of the experiments. Helium concentrations at 10 different locations inside the facility were monitored by 10 thermal conductivity-type detectors. The probes of these detectors were mounted in two vertically oriented racks. One rack (P1 to P5) was located along the axis of the

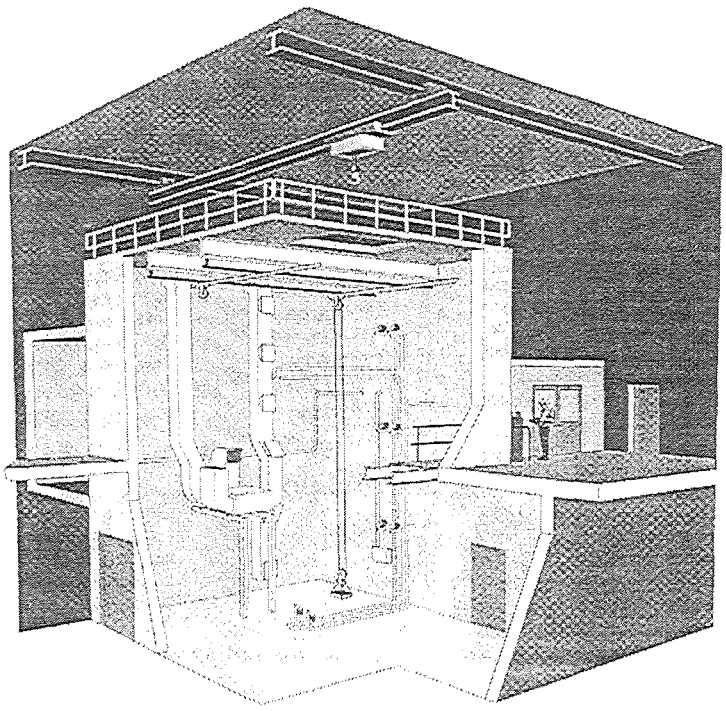

Fig.1: A perspective sketch of large-scale gasmixing facility at Whiteshell Laboratories, Canada.

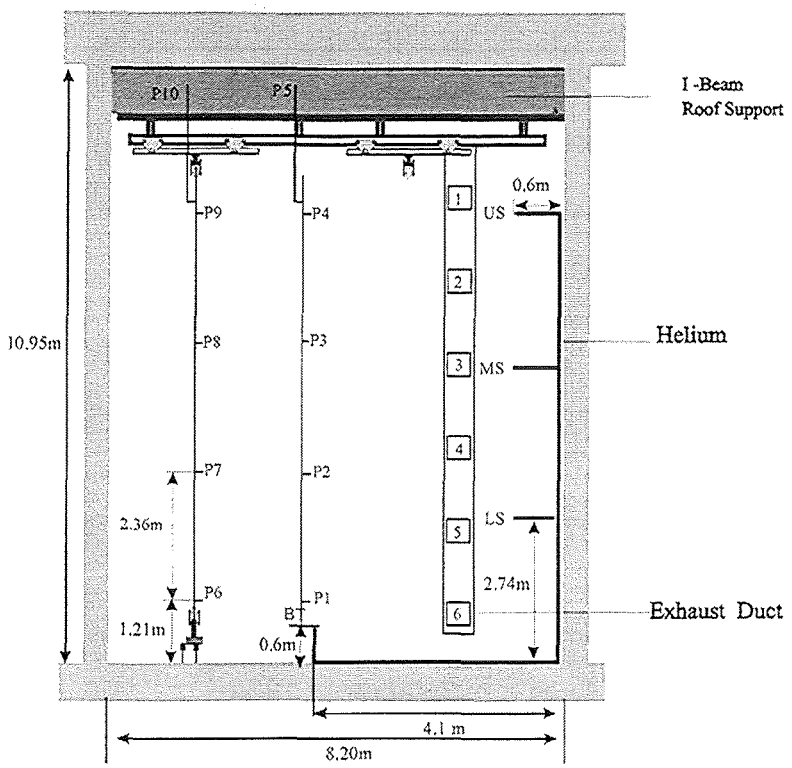

Fig.2: Schematic of the large-scale gasmixing facility

jet, the other one (P6 to P10) at about 2 m aside (Fig.2). Measurements were made by each of the 10 analyzers at a frequency of 1 Hz.

Two tests were performed, one with the 5 cm- and one with the 30 cm-tube. The related helium injection velocities were 8.6 m/s and 0.24 m/s, and in both cases the mass flow rate (2.95 g/s) was kept the same. Each of the tests lasted 600 s.

3 Modelling

The test facility was set up in Cartesian coordinates using ¼ symmetry and 10 x 12 x 25 nodes in x-, y- and z-direction with an expanding mesh, the smallest grid size being 20 cm at the injection point. In order to accurately model the physical jet diameters of 5 or 30 cm in ¼ symmetry, the area of 20 x 20 cm^2 had to be multiplied by 0.01227 or 0.4418, resp. These values therefore were introduced into the input data as so-called area-redefinition factors.

Further calculations were performed to study the effect of oversized jet flow areas. During this effort the jet cross-section was spread over 2 x 2 and 3 x 3 cells, covering 2500 and 9025 cm^2, resp., according to the positions of the grid lines which were

fixed at 50 and 95 cm both in x- and y-direction. For all these cases, the modelled jet cross-section divided by its physical value, which is termed "Jet_{AD} = jet area definition", attains the following values:

Nodes involved	1 x 1	2 x 2	3 x 3
Jet_{AD} (5 cm diam.)	1	509	1839
Jet_{AD} (30 cm diam.)	1	14	51

Tab. I: Jet area definition (Jet_{AD}) values for the various cases.

Here, Jet_{AD} = 1839, e.g., means that the jet cross-section in the computational domain exceeds its physical value by a factor of 1839.
From the structures contained within the enclosure, only the two large I-beams at the ceiling were modelled which was done by blocking the flow convection between the appropriate cell volumes. The exhaust duct was considered negligible, as the total gas volume injected into the enclosure during the 10 min. duration of the test did not amount to more than roughly 1% of the total enclosure volume. All calculations were performed using an algebraic turbulence model. Additionally, only in the case of 3 x 3 cells where the jet area definition (Tab. I) was highest, a calculation without turbulence was conducted for comparison reasons. Care was taken to adjust the vertical grid nodalization to the positions of the He gas concentration detectors in order to have them arranged in the mid of the cell volumes. During the calculation, which was conducted for 600 s real time, gas concentration data of all detector positions were written to a dump file with a selected time-step size of 2 s. In all cases, the jet mass-flow rate was kept constant at a value of 2.95 : 4 = 0.7375 g/s.

4 Results and Discussion

The calculated He gas concentrations from the various cases are plotted vs. time and compared to measurements in Figs.3 and 4. Here, comparisons are only made for the detector positions P6 to P10 which are fixed to the rack 2 m aside from the jet axis. All figures show that the analytical results more or less match the experimental data. For 5 cm jet diameter and Jet_{AD} = 1, the calculated gradients behave distinctly steeper, especially near the ceiling (Fig.3a, P9, P10). In general can be stated that

coincidence improves with increasing jet area ratios, even when no turbulence models are taken into account (Figs.3d, 4d). Major deviations only occur near the floor, e.g. for P6 where some gas concentration was calculated, but the measured values were zero.

The results of this study can be summarized as follows: Close to the jet exit, the results, independent of the jet area definition, are not satisfying. In some distance from the jet, a jet area ratio of several orders of magnitude >> 1 leads to reasonably good results. For these mesh sizes, turbulence modelling is not necessary. Near the floor, the helium gas concentration is over-estimated up to $\approx 0.4\%$. To obtain reasonably good results outside of the immediate jet release region, a fine grid resolution of the jet structure is not needed, because jets, after loosing their initial momentum, are converted into plumes governed by buoyancy forces.

References.

1. C. K. Chan and S. C. Jones, private communication Sept. 1998

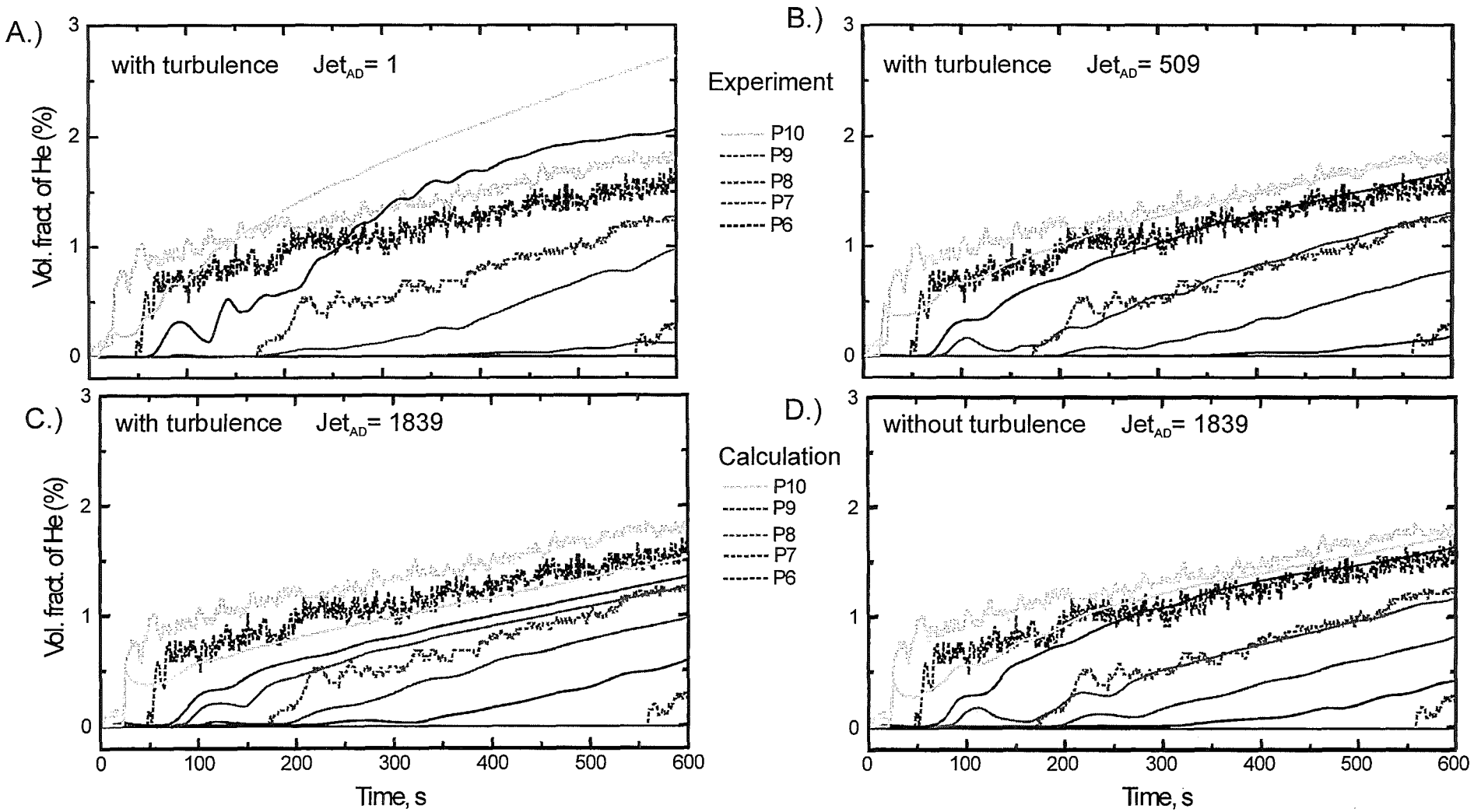

Fig.3: Jet diameter = 5cm, measurement position 2m from jet axis: GASFLOW results compared to measured He gas concentrations from the large-scale gasmixing experiment.

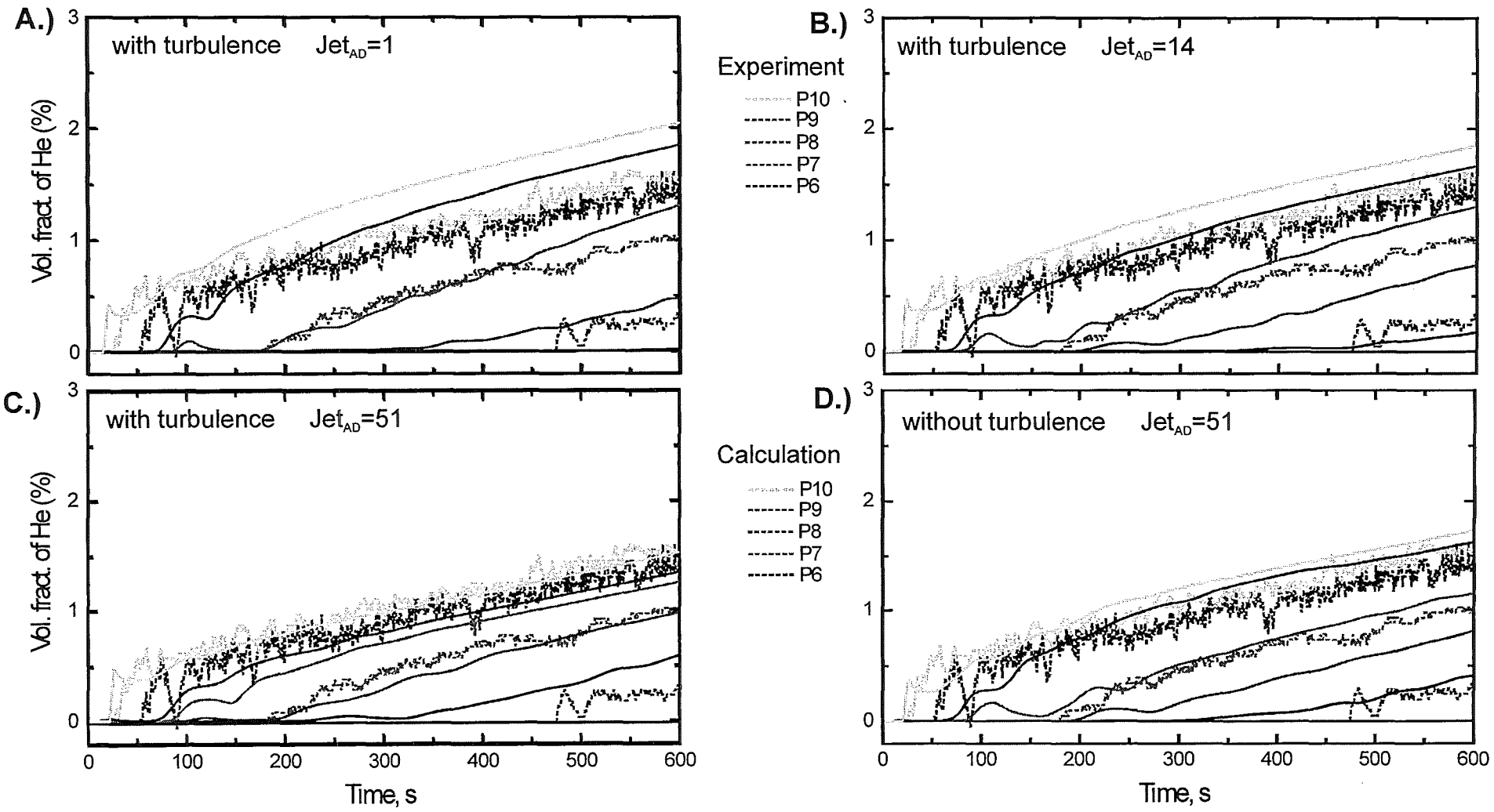

Fig.4: Jet diameter = 30 cm, measurement position 2m from jet axis: GASFLOW results compared to measured He gas concentrations from the large –scale gasmixing experiment.

V. Flame Acceleration Criterion

(W. Breitung, S. Dorofeev, INR)

Zusammenfassung

Die Arbeiten zur Flammenbeschleunigung zielen auf die Entwicklung eines konservativen Kriteriums, das es, erlaubt die Möglichkeit einer Flammenbeschleunigung zu beurteilen. Es hat sich gezeigt, daß nach der ersten Zündung und dem Einsetzen einer langsamen Deflagration zwei Kriterien notwendig sind, um die weitere Entwicklung der Verbrennung zu bestimmen und das geeignete Simulationswerkzeug auszuwählen. Das erste Kriterium betrifft den Übergang zur schnellen turbulenten Deflagration (Flammenbeschleunigung), das zweite den Übergang zur Detonation. In diesem Beitrag wird über die Fortschritte und Ergebnisse berichtet, die im Jahr 1998 für das Flammenbeschleunigungskriterium erzielt wurden, vor allem bei der Ableitung allgemeiner Skalierungsgesetze.

1 Introduction

In the analysis procedure developed for the investigation of hydrogen behaviour in severe accidents (Fig.1 in section 2.9) different codes are used for the simulation of slow quasi-laminar flames, fast turbulent flames, and detonations, because the governing physical processes require different mathematical models and numerical solution algorithms for their effective description (V3D, COM3D, DET3D).

After the first ignition and development of a slow deflagration two criteria are needed to determine the further progress of the combustion and to select the appropriate simulation tool. The first one concerns the transition to fast turbulent deflagration (flame acceleration) and the second one is the transition to detonation. These criteria can also be used to predict directly from the GASFLOW distribution calculation which combustion mode would be physically possible with the given gas composition and scale. This section describes the progress and results obtained in 1998 for the flame acceleration criterion.

2 Scaling law for flame acceleration

To derive general scaling laws for flame acceleration FZK and Kurchatov Institute (KI) have performed joint test series at ambient temperature in obstructed tubes which were geometrically similar on different scales (diameters 170-520 mm). RUT experiments provided data for a channel diameter of about 2400 mm. Optimum conditions for flame acceleration were created to derive conservative criteria (strong turbulence, repeated obstacles, no venting). H_2-air mixtures with mono-, bi-, and triatomic diluents were investigated at FZK and KI (He, Ar, N_2, CO_2). The FZK experiments have been described in the previous Yearly Report [1] and the KI tests were reported in [2]. A joint report will be published in [3].

Systematic analysis of the extensive new data base with different scaling methodologies showed that the expansion ratio σ (= ratio of specific volumes [m^3/kg] of burned to unburned gas at constant pressure) and the non-dimensional length L/δ (L = tube diameter, δ = flame thickness) are the most important parameters determining the flame propagation regime. Also (σ-1) is equal to the ratio of chemical

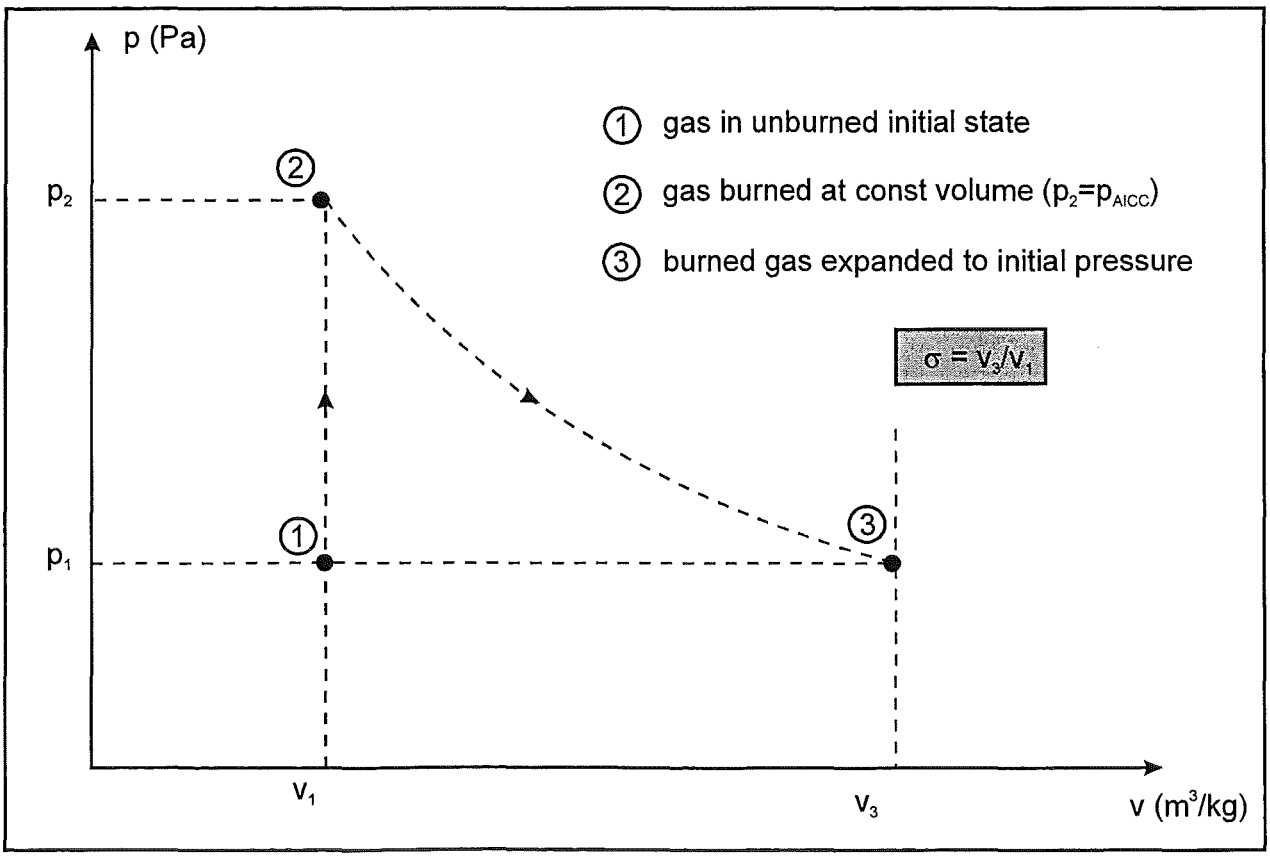

Fig.1: Definition of expansion ratio σ

energy divided by the initial thermal energy. The physical significance of σ is due to the fact that the velocity of an isobaric flame is directly proportional to σ (in simple models). The definition of σ is given in Fig.1. δ serves as a chemical length scale, used to normalize the geometrical scale L. δ is of the order 0.1 mm in hydrogen-air flames.

The results of the scaling analysis are presented in Fig.2. Each point corresponds to one experiment. From the given mixture composition σ and δ can be calculated, and L is the known tube diameter. These values then define the location of the point on the plot.

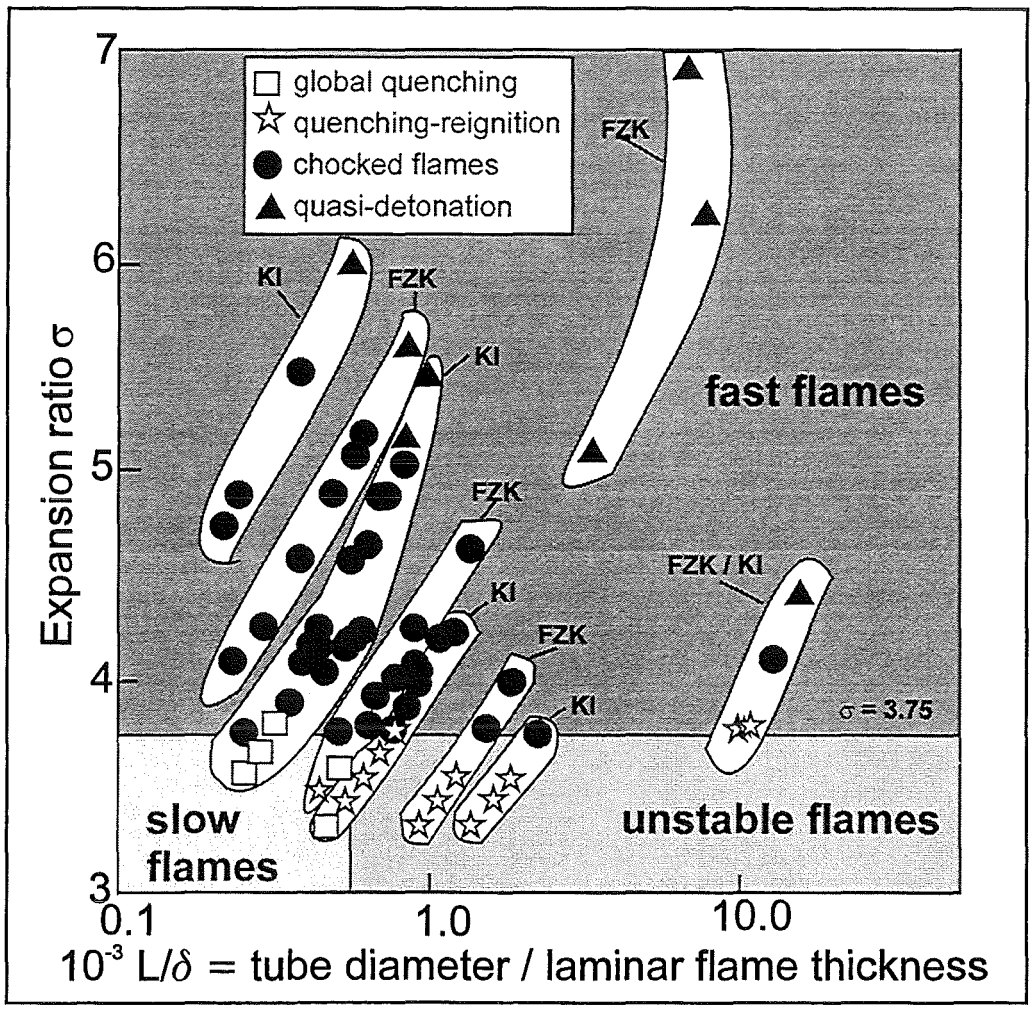

Fig. 2: Measured combustion regimes in obstructed tube/channel geometry with different hydrogen-air-diluent mixtures at ambient initial temperature ($\approx$ 300 K). Acceleration to choked flames or quasi-detonations was only observed for $\sigma > 3.75$, independent of the geometrical scale.

In H_2-air mixtures at NTP conditions this limit corresponds to 11% H_2 on the lean side. Since relation (1) is consistent with RUT-tests in H_2-air mixtures, the experimental data base covers nearly two orders of magnitude in geometrical scale L. In some KI tests done with 0 or 9% blockage ratio in the investigated tubes, relatively „strong" mixtures having a large σ-value were accelerating slowly and did not reach sonic flame or quasi-detonation velocities because of the limited tube length. It is very likely that they would have reached such velocities in longer tubes because the flame speed increased continuously up to the tube end. To get a clearer overall picture, these geometrically limited tests were not included in Fig.2.

In addition to the tests at ambient temperatures (Fig.2), the available literature data on flame acceleration at higher initial temperatures were summarized in [4] with the following results:

- the critical value of σ, which separates slow and fast combustion modes, decreases with increasing initial temperature for <u>lean</u> hydrogen-air-diluent mixtures ($p_{H2} < 2p_{02}$)
- for rich mixtures with $p_{H2} > 2p_{02}$ the critical σ value remains 3.75 for all temperatures investigated experimentally (300-650 K).

For the <u>lean</u> mixtures the results of the individual data analysis are presented in Fig.3 in the σ-T_0 format. Because in all evaluated tests the critical σ - value was independent of the geometrical scale, the data can be plotted as function of this initial temperature only, omitting the variable L/δ used in Fig.2. The critical σ-value decreases with increasing temperature from 3.75 at $\approx$ 300 K to about 2.1 at 650 K.

One possible explanation for the decrease of the critical expansion ratio value (σ_{crit}) with increasing temperature is the fact that the thermal quenching of the chemical reaction in the flame zone by turbulent mixing of cold unburned gas with hot burned gas becomes less efficient with increasing temperature of the unburned gas. Less chemical energy (smaller σ) is therefore needed at high initial temperature to support flame acceleration.

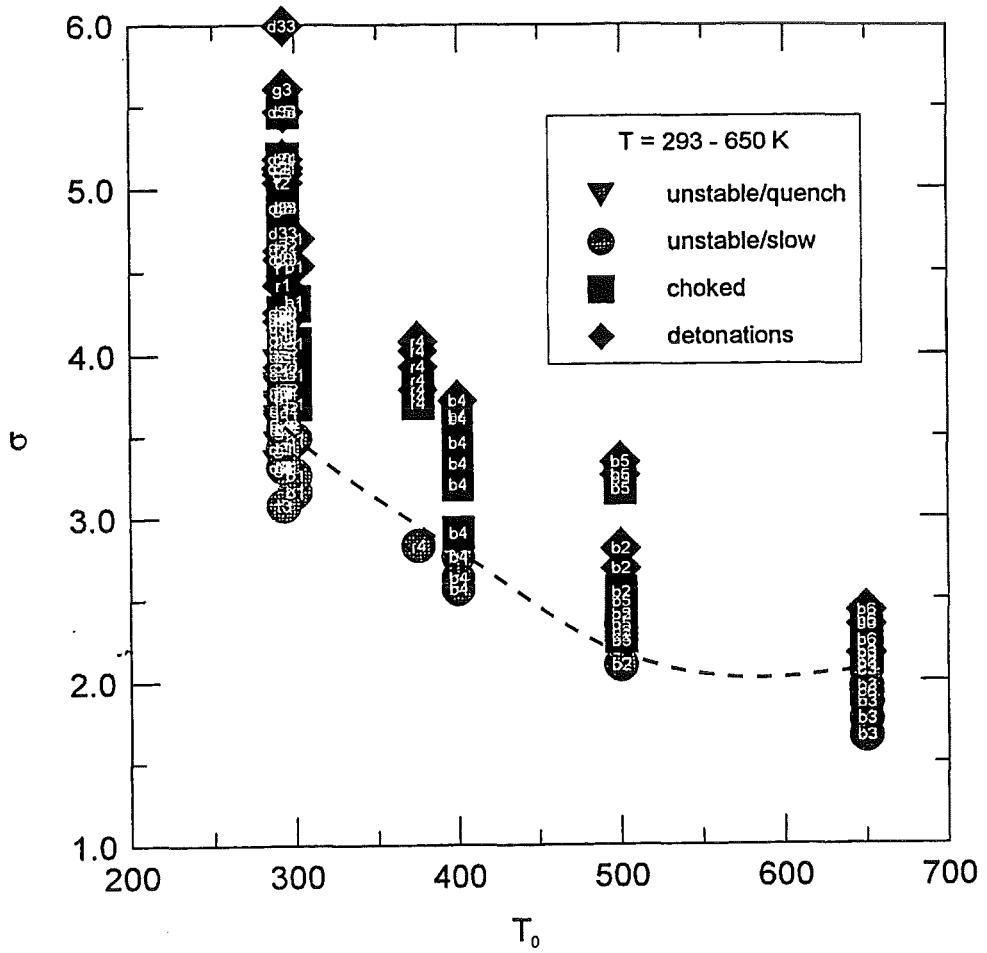

Fig.3: Combustion regime as a function of expansion ratio σ and initial temperature T_0 for lean hydrogen-air-diluent mixtures

3 Expansion ratio data

To evaluate the σ-criterion for containment analysis calculations a program was written which is based on the STANJAN-code and allows to calculate the expansion ratio for a given mixture composition and initial temperature. The data will be incorporated in tabular form into the GASFLOW code in 1999. By comparison with the gas composition and temperature predicted with GASFLOW, the potential for flame acceleration can be evaluated. This GASFLOW extension will be completed early 1999 and applied to future EPR hydrogen analysis work.

References

[1] A. Veser, W. Breitung, G. Engel, G. Stern, page 82-108 in B. Mühl (Ed.), "Projekt Nukleare Sicherheitsforschung, Jahresbericht 1997", Report FZKA-6126 (Sept. 1998).

[2] S. Dorofeev, M. Kuznetsov, V. Alekseev, A. Efimenko, A. Bezmelnitsyn, „Experiments on flame acceleration limits and scaling of turbulent flame propagation", Final report for FZK contract (1997).

[3] S. Dorofeev, M. Kuznetsov, V. Alekseev, A. Efimenko, A. Bezmelnitsyn, Yu G. Yankin, W. Breitung, "Effect of scale and mixture properties on behaviour of turbulent flames in obstructed areas", KI-Report IAE-6127/3 and FZKA 6268 (to be published 1999).

[4] S. Dorofeev, M. Kuznetsov, V. Alekseev, A. Efimenko, "Analysis of experimental data and criteria on flame acceleration limits for nuclear safety applications", Final report for FZK contract (Nov. 1998).

VI. Flame Acceleration and DDT in Obstacle Arrays

(W. Breitung, A. Veser, INR)

Zusammenfassung

Das bereits vor einiger Zeit im Rahmen der FZK-Arbeiten zum Wasserstoffprogramm entwickelte halb-empirische 7λ-Kriterium ermöglicht es, das DDT-Potential in einem bestimmten Unfall-Szenario zu beurteilen (DDT = Detonation, Deflagration, Transition). Zur weiteren Untermauerung dieses halb-empirischen Ansatzes wurden Detailuntersuchungen zu DDT-Prozessen durchgeführt. Im Berichtszeitraum wurden die DDT-Mechanismen anhand dreier verschiedener Testkonfigurationen untersucht. In diesem Beitrag werden die drei im 12 m-Rohr durchgeführten Testreihen beschrieben und die Ergebnisse erläutert.

0 Introduction

An important aspect of hydrogen control in severe accidents is safe implementation of igniters, which excludes initiation of fast uncontrolled combustion processes. Previous experimental and theoretical work within the FZK hydrogen program has led to a semi-empirical scaling methodology (the 7λ-rule) which allows to judge the DDT potential in a given accident scenario. For further justification of this semi-empirical approach, a detailed study on DDT processes was initiated. The principal goal is to connect the 7λ-rule with the microscopic physical process by performing high resolution experiments and numerical simulations.

Different DDT mechanisms were investigated in three test configurations:
- idealised mode A (shock wave focussing in a 3-d reflector)
- prototypic mode A (focussing of flame precursor wave in a 3-d reflector)
- prototypic mode B (accelerating flame in obstacle array).

For DDT by idealised mode A critical Mach numbers were determined for the incident shock as function of the H_2 concentration. At this critical Mach number the ignition

regime changes from slow/weak (= deflagration) to strong/fast (= detonation). Very good reproducibility of individual tests and consistence of the whole data base in terms of ignition modes was observed. The detailed processes in idealised mode A DDT tests are highly mechanistic and seem to be governed by the temperature dependent reaction kinetics.

Prototypic DDT mode A from the precursor wave of an accelerating flame was detected in the FZK-tube at > 16.5% H_2 in air, with a blockage ratio of 60%. At smaller hydrogen concentrations the precursor shock caused only a mild ignition (= deflagration) in the reflector. The tests have clearly proven the significance of DDT mode A in obstructed geometries: a flame which accelerates in a certain part of a complex installation to near sonic velocities emits pressure waves which can trigger a DDT in a distant part of the enclosure, especially if H_2 enrichments should be present in reflecting corners.

DDT mode B was observed in the fully obstructed tube for > 13.5 % H_2 at 30% BR and for > 15 % H_2 at 45 % BR. With 60% BR no DDT occurred for ≤ 15 % H_2 (p_0=1bar). The occurrence of DDT could be clearly identified by four criteria, namely pressure amplitude, pressure profile, wave speed, and coupling of pressure and reaction front.

Pressures developing due to DDT in lean H_2-air mixtures were measured. The highest pressures are generated during the initial ignition phase in the reflector when the reaction starts from a highly pre-compressed state.

The tests have resulted in new data on DDT mechanisms which can be used for model development and verification with increasing complexity. The simplest case are the idealised mode A experiments, which requires only simulation of the compressible flow and the H_2-O_2 reaction but not of turbulence. Numerical models should be first verified on these tests.

1 Summary of experimental methods

Three different series of DDT experiments have been performed in the FZK research facility. Fig.1 shows the FZK-12m-tube, which has an inner diameter of 0.35 m. The three main experimental configurations are given in Figure 2. Mode A refers to DDT processes far in front of the flame, mode B refers to DDT in or near the turbulent flame. The three test series can be summarised as follows.

a) Shock tube with conus (idealised mode A)

The tube was divided by a membrane into a low pressure section (length 9 m) and a high pressure section (length 3 m). The experiments were carried out with a conical reflector at the end of the low pressure section to focus the pressure wave and to reach self-ignition temperatures. The main idea behind this experiment design is the observation that in many tests with fast combustion modes, DDT events are apparently triggered by waves reflected in corners or other converging multi-dimensional parts of the test enclosure. The conus is used to produce local hot spots in the combustible gas as they generally develop from the interaction of a pressure wave with a complex multidimensional target.

After evacuating both sections, the low pressure section was filled up to the desired initial pressure with a defined hydrogen/air mixture. The parameters changed during the experiments were the initial pressure (0.5-1.5 bar) and the composition of the hydrogen/air mixture (9-30 % H_2). The high pressure section was filled with helium up to membrane failure. To detect DDT processes pressure transducers, photo-diodes, and film thermocouples were located along the tube. Ionisation gauges were installed in and near the conus.

b) Partially obstructed tube with conus (prototypic mode A)

In this case a part of the tube was equipped with an array of ring obstacles blocking 30 % of the flow cross section (BR=30%) over a length of 5-6 m to accelerate the flame to a high velocity. The tube also contained a conus to focus the precursor shock wave. It was evacuated and then filled with a defined hydrogen/air mixture (9-20 % H_2) to the initial pressure (1 bar). The mixture was ignited with a glow plug.

Pressure transducers, ionisation gauges, photodiodes and film thermocouples were used to locate the expected DDT events.

c) Fully obstructed tube (prototypic mode B)

The combustion tube was equipped with an array of ring obstacles (BR = 60 %) over its full length of 12 m. The evacuated tube was filled with a defined hydrogen/air mixture (9-20 % H_2) up to the initial pressure (0.5-2.0 bar) and then ignited with a glow plug. To observe the combustion process pressure transducers, photodiodes and film thermocouples were located along the tube.

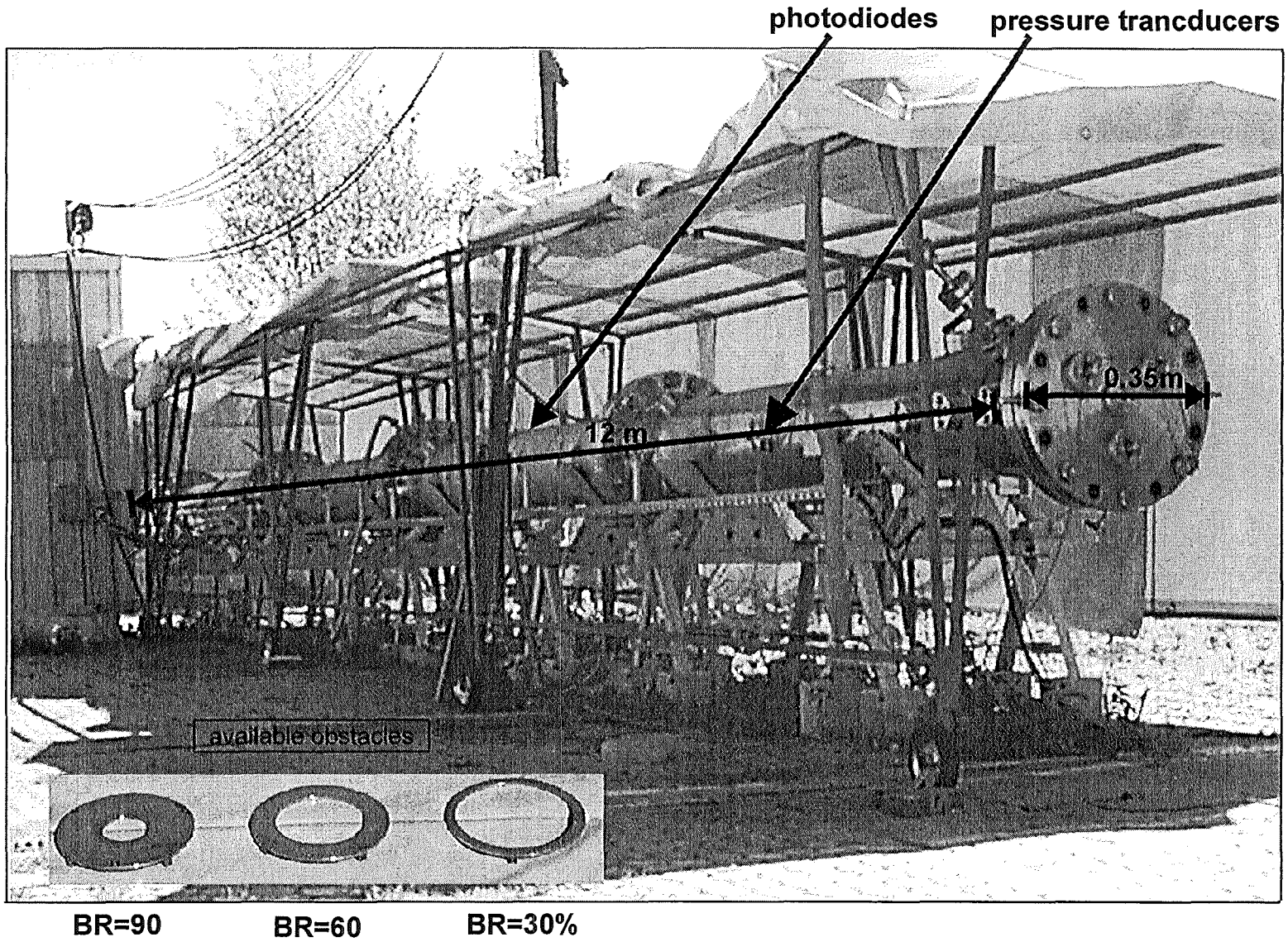

Fig. 1: FZK 12m tube

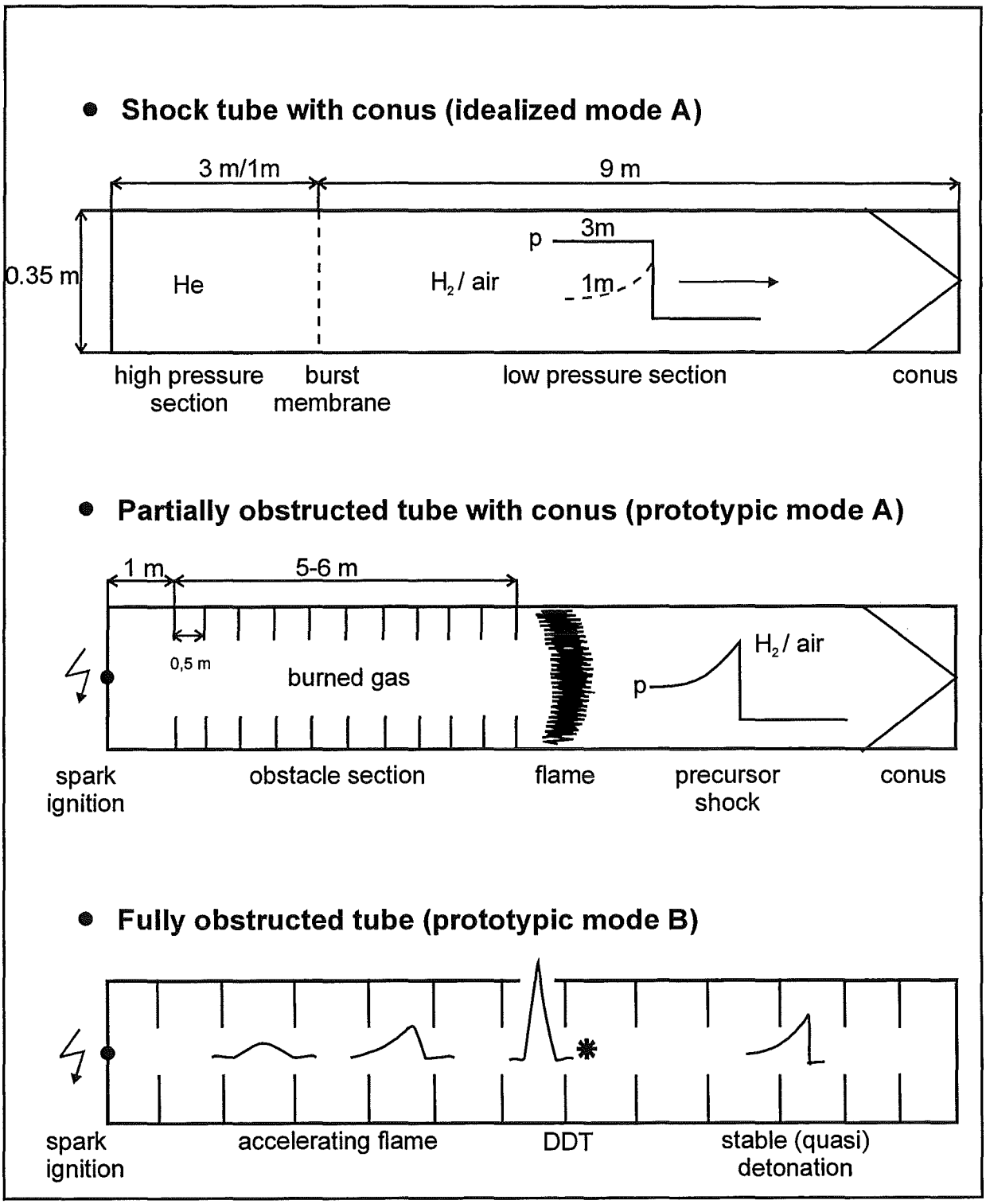

Fig. 2: FZK experiments on DDT mechanisms using three experimental configurations of the 12 m tube. Instrumentation concentrated at expected DDT locations. Pressure transducers, photodiodes, film thermocouples, and ionisation gauges were installed.

2 Results of idealised mode A-DDT experiments

The experiments were carried out with a conus at the end of the low pressure section to focus the incoming pressure wave and to create conditions for self-ignition. The conus is used to produce local hot spots in the combustible gas as they develop in general from the interaction of a pressure wave with a complex multidimensional target. With the rotationally symmetric conus at the end of the tube the incoming shock wave is focused into a certain volume in the center of the conus, as depicted schematically in Figure 3.

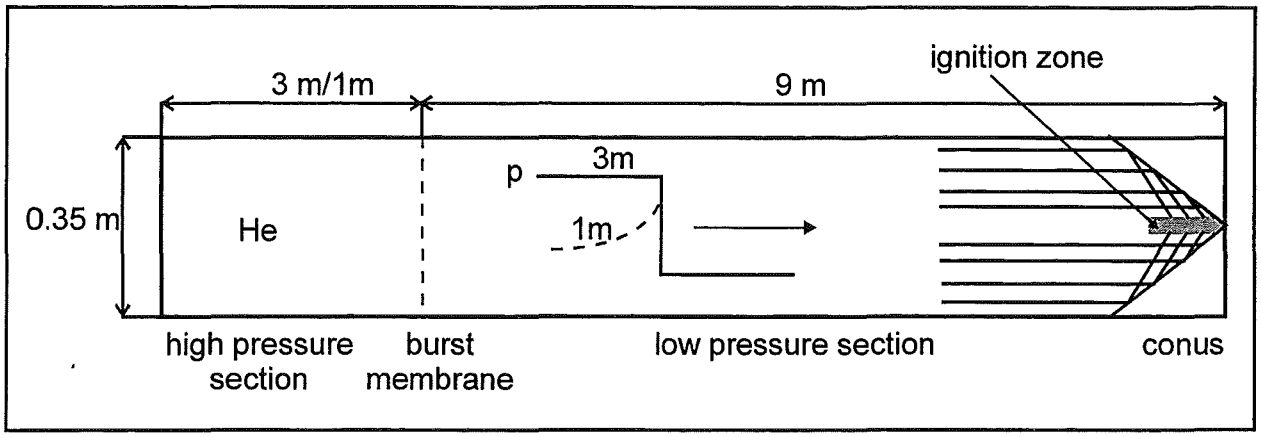

Fig.3: Focusing of the incoming shock wave in the center of the conus

Photographs and a scheme of the used conus are shown in Figures 4 and 5. The conus is 210 mm long with an opening angle of 70°.

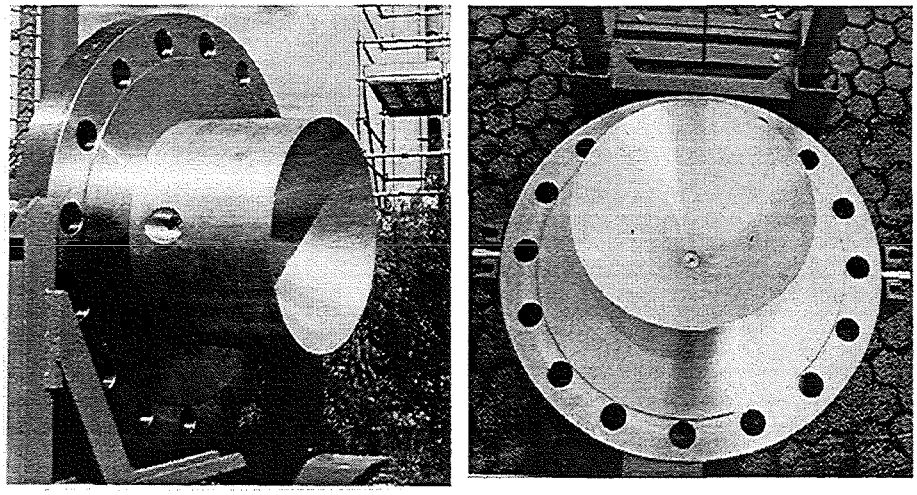

Fig.4: Photographs of the conus used to produce local hot spots for self-ignition of the test gas. Three pressure transducers are installed inside the conus.

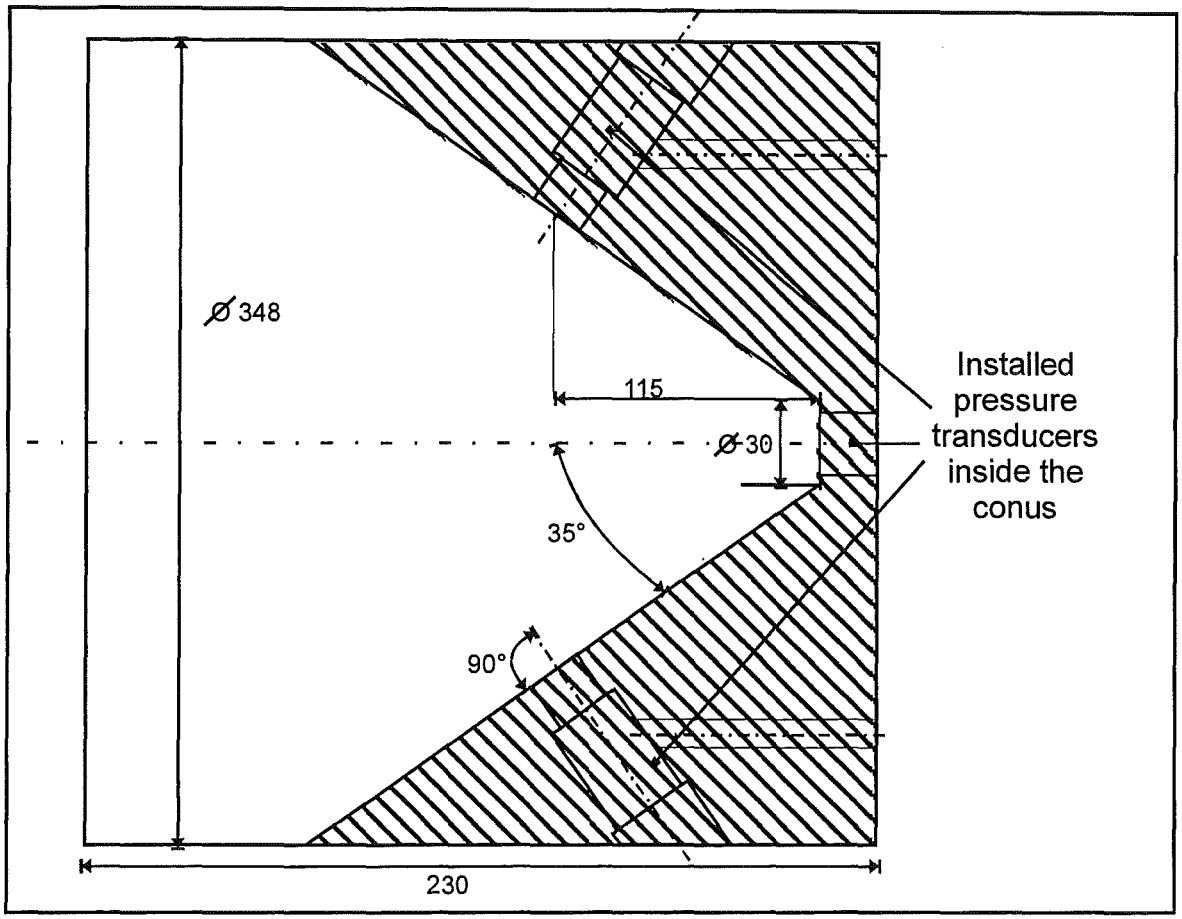

Fig.5.: Scheme of used conus with pressure transducer locations.

A total of 84 experiments were performed with the idealised-mode-A tube configuration. They are listed in Table 1, were p_0 and p_4 designate the initial pressure of the low and high pressure section, respectively. These experiments were carried out with helium as driver gas in the high pressure section (HPS). Aluminium foils with different thicknesses (0.1-0.7mm) were used as membranes. A further parameter was the length of the high pressure section which could be changed from 3m to 1m with an unchanged length of the low pressure section (9 m).

Table 1: Test matrix of DDT experiments in idealised mode A tube configuration

Experiment	Length of HPS (m)	%H_2	p_0 (bar) LPS	p_4 (bar) HPS	Ma-number of incident wave	Velocity of reflected wave (m/s)
R0797_15	0	0	0.3	7	2.55	475
R0797_16	30	30	0.9	14	---	---
R0797_17	15	15	0.45	7.7	2.49	1006
R0797_18	30	30	0.9	7.8	---	---
R0797_19	15	15	1	8	1.99	1087
R0797_20	15	15	1.25	8.2	1.76	438
R0797_21	15	15	1.1	8.4	1.96	1128
R0797_22	0	0	1	8	1.94	414
R0797_23	15	15	1.2	8	2.13	1103
R0797_24	15	15	0.7	7.9	2.14	1086
R0797_25	15	15	1	7.2	---	---
R0797_26	15	15	0.8	5.15	---	---
R0797_27	13	13	1.1	7.9	1.84	430
R0797_28	13	13	1.25	6.8	1.66	436
R0797_29	17	17	1.25	8	1.7-1.72	443
R0797_30	13	13	0.7	7.4	---	---
R0797_31	17	17	1.1	6.9	---	---
R0797_32	14	14	1.1	6.75	---	---
R0797_33	14	14	0.8	6.25	1.902	490
R0797_34	12	12	1.1	6.0	1.72	431
R0797_35	12	12	0.8	6.2	1.8972	430
R0797_36	11	11	1.1	7.4	1.834	441
R0797_37	11	11	0.8	8.5	1.99	441
R0797_38	10	10	0.8	8.4	no measurement	---
R0797_39	10	10	1.1	8	1.815	430
R0797_40	9	9	1.1	8.3	1.839	426
R0797_41	9	9	0.8	7.8	1.94	423
R0598_00	3	15	1	8.3	1.875	410
R0598_01	3	15	0.9	8.3	1.925	1153
R0598_02	3	15	0.950	8.95	1.93	493

Experiment	Length of HPS (m)	%H_2	p_0 (bar) LPS	p_4 (bar) HPS	Ma-number of incident wave	Velocity of reflected wave (m/s)
R0598_03	3	12	0.5	7.7	2.25	931
R0598_04	3	11	0.4	7.6	2.37	949
R0598_05	3	12	0.6	6.1	2.0	961
R0598_06	3	12	0.7	7.7	2.11	1042
R0598_07	3	12	0.8	7.8	1.94	520
R0598_08	3	11	0.5	6.6	2.21	541
R0598_09	3	0	0.5	8.0	2.26	426
R0598_10	3	0	0.75	8.2	2.09	416
R0598_12	3	15	0.97	7.9	1.87	---
R0598_13	3	15	0.970	8.3	2.22	1171
R0598_14	3	12	0.750	7.2	2.07	625
R0598_15	3	11	0.450	7.0	2.265	893
R0598_16	3	12	0.72	7.6	2.15	1007
R0598_17	3	11	0.470	7.4	2.45	943
R0598_18	3	15	0.970	7.4	2.01	1190
R0598_19	3	15	0.97	5.7	1.78	1293
R0598_20	3	15	1.15		1.8	1293
R0598_21	3	15	1	3	1.29	---
R0598_22	3	15	1	0.3	1.96	---
R0598_23	3	11	0.55	5.2	1.98	431
R0598_24	3	11	0.5	5.5	2.2	880
R0598_25	1	15	0.5	6.0	2.04	1172
R0598_26	1	15	0.7	6.5	1.77	480
R0598_27	1	0	0.7	6.0	---	---
R0598_28	1	0	0.5	6.3	1.86	442
R0598_29	1	15	0.6	6.0	1.73	474
R0598_30	1	15	0.5	7.0	1.93	506
R0598_31	1	15	0.45	7.0	2.03	1339
R0598_32	1	15	0.4	6.0	1.96	1230
R0598_33	1	15	0.4	6.0	1.996	1250

Experiment	Length of HPS (m)	%H_2	p_0 (bar) LPS	p_4 (bar) HPS	Ma-number of incident wave	Velocity of reflected wave (m/s)
R0598_34	1	15	0.4	6.4	2.26	1119
R0598_35	1	0	0.4	7.3	2.09	466
R0598_36	1	12	0.4	9.4	2.35	1013
R0598_37	1	12	0.5	8.2	2.05	487
R0598_38	1	12	0.4	9.5	2.27	1041
R0598_39	1	12	0.45	9.9	2.18	1071
R0598_40	1	12	0.5	9.0	2.09	500
R0598_41	1	0	0.6	11	2.05	457
R0598_42	1	0	0.45	12.5	2.26	468
R0598_43	1	11	0.4		2.64	1071
R0598_44	1	11	0.45	11.0	2.45	1056
R0598_45	1	11	0.5	12.0	2.19	514
R0598_46	1	11	0.48	11.8	2.31	1027
R0598_47	1	11	0.49	11.7	---	---
R0598_48	1	10	0.3	6.0		
R0598_49	1	10	0.35	---	---	---
R0598_50	1	10	0.35	7.2		
R0598_51	1	15	1.15	6.0		
R0598_52	1	15	0.93	6.6		
R0598_53	1	15	0.95	6.0		
R0698_00	1	10	---	---	2.07	490
R0698_01	1	10	0.4	12.95	2.8	1042
R0698_02	1	10	0.4	10.0	2.3	962
R0698_03	1	10	0.45	10.0	2.496	974
R0698_04	1	10	0.47	12.2	2.38	949
R0698_05	1	10	0.47	12.0	2.88	939
R0698_06	1	10	0.43	13.2	2.6	948
R0698_07	1	10	0.46	10.0	2.35	947

The different lengths of the HPS result in different flow fields. The principal processes in the shock-tube with a three meter long high pressure section are shown in the upper part of Figure 6. After membrane rupture, a shock wave propagates forwards from the membrane into the low pressure section. At the same time a rarefaction wave runs backwards into the high pressure section. The contact surface, which separates the driver gas of the high pressure section from the flammable mixture in the low pressure section, moves behind the incident shock into the low pressure section. The incident shock wave is reflected at the end of the low pressure section, it interacts with the contact surface and slows it down. The dilution wave propagates into the high pressure section and is reflected at the end of the tube. In this case, the reflected dilution wave reaches the contact surface later than the reflected shock wave. The flammable mixture is located between the contact surface and the end of the low pressure section. Only this part is available for ignition.

The lower diagram in Figure 6 shows the same process with a shortened high pressure section of 1 m. The processes after bursting of the membrane are the same as with the 3m high pressure section, but in this case the dilution wave in the high pressure section is reflected earlier. It arrives at the contact surface before this hits the reflected incident shock wave. The interaction between the reflected dilution wave and the contact surface leads to a velocity decrease of the contact surface. The lower diagram in Figure 6 shows, that the distance between the contact surface and the end of the low pressure section in this case is larger than in the first diagram. Therefore an extended space and time region exists in which the transition from deflagration to detonation could occur. The second effect of the shortened HPS is that the shape of the incident shock wave changes from a flat pressure profile to a triangular profile, which is typical for blast waves. Using the short HPS allowed therefore to investigate the effect of a changed pressure profile (shock wave versus blast wave).

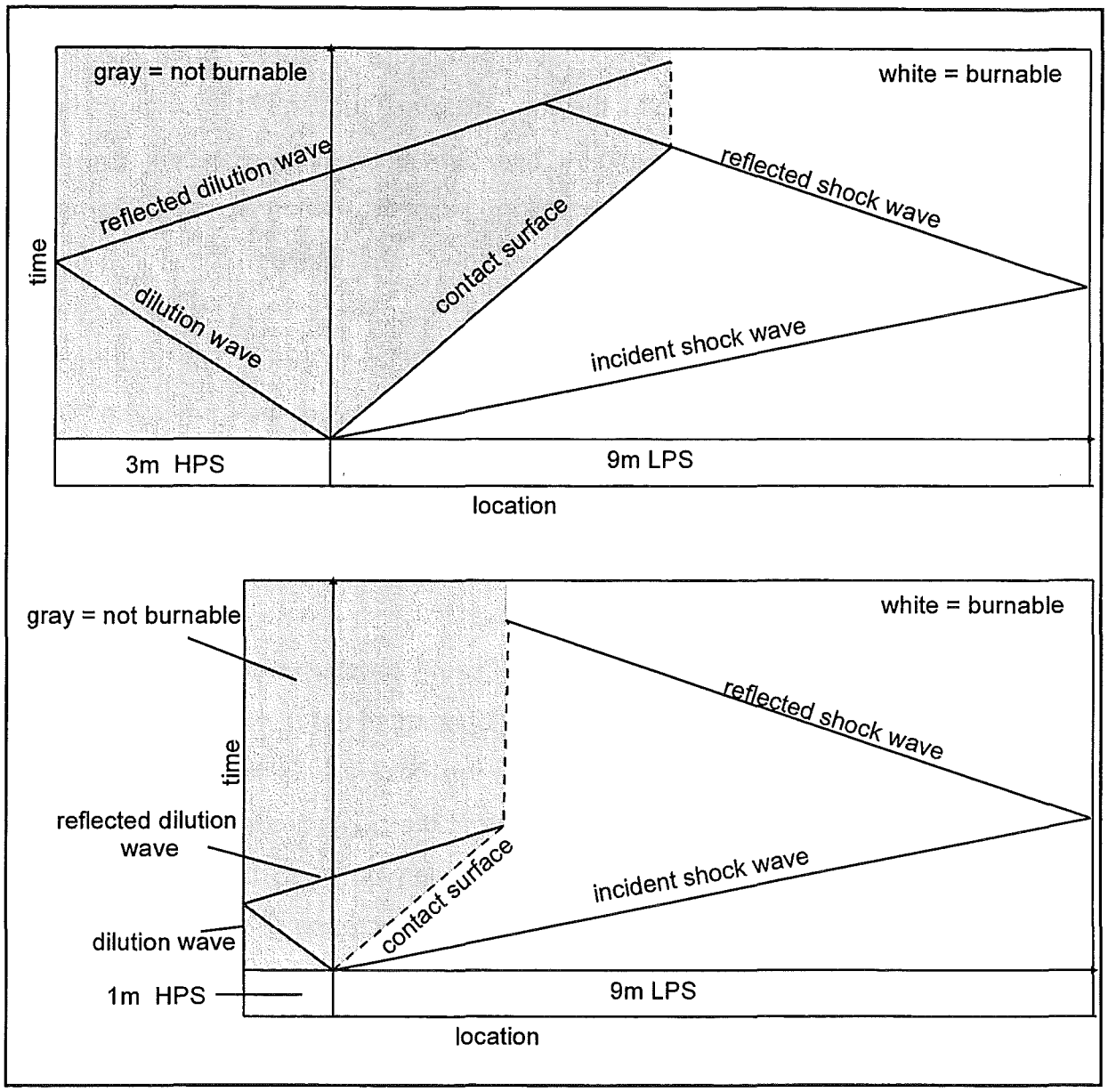

Fig.6: Principle processes in the shock tube with a 3 m and 1 m long high pressure section, respectively.

The main results of the idealised-mode-A tests are presented now by two examples: one for a mild ignition case without DDT, and one for a strong ignition leading to DDT. In both cases the short HPS with 1 m length was used. Figure 7 summarises the results of experiment R0598_26 in the form of an R-t diagram. It shows the incident shock wave (ISW), the reflected shock wave (RSW) and the flame front (FF). The ISW and the RSW were measured with pressure transducers, the FF was detected with photodiodes. The test parameters used in this experiment were 15 %

hydrogen in air with an initial pressure in the low pressure section of 0.7 bar. The high pressure section was filled with helium up to the burst pressure of 6.5 bar, resulting in a Mach number of 1.77. The test lead to self-ignition and a decoupled flame / shock complex without DDT, which can be concluded from the fact that the ISW ignites the mixture, but the RSW moves faster than the FF. For the resulting RSW a velocity of 480 m/s was measured. This velocity is comparable to that of a normally reflected inert shock wave without reaction, again indicating that only a weak combustion pressure was generated by the ignition.

An example for self-ignition and formation of a coupled flame / shock complex, leading to a stable detonation wave (DDT) is shown in Figure 8. This R-t diagram was recorded during experiment R0598_25. The test parameters used in this experiment were 15 % hydrogen in air with an initial pressure of 0.5 bar. The high pressure section was filled with helium up to a burst pressure of 6.0 bar, resulting in a Mach number of 2.04.The triangular shape of the incident shock wave is clearly visible. Again the ISW is focused in the conus thereby igniting the mixture, but this time the resulting RSW and the FF remain coupled. The measured velocity of the RSW is 1172 m/s, which is close to the theoretical detonation speed in the moving H_2/air mixture. (The wave speed w in the laboratory frame is D minus the particle velocity u_2 behind the incident shock, $w=D-u_2$).

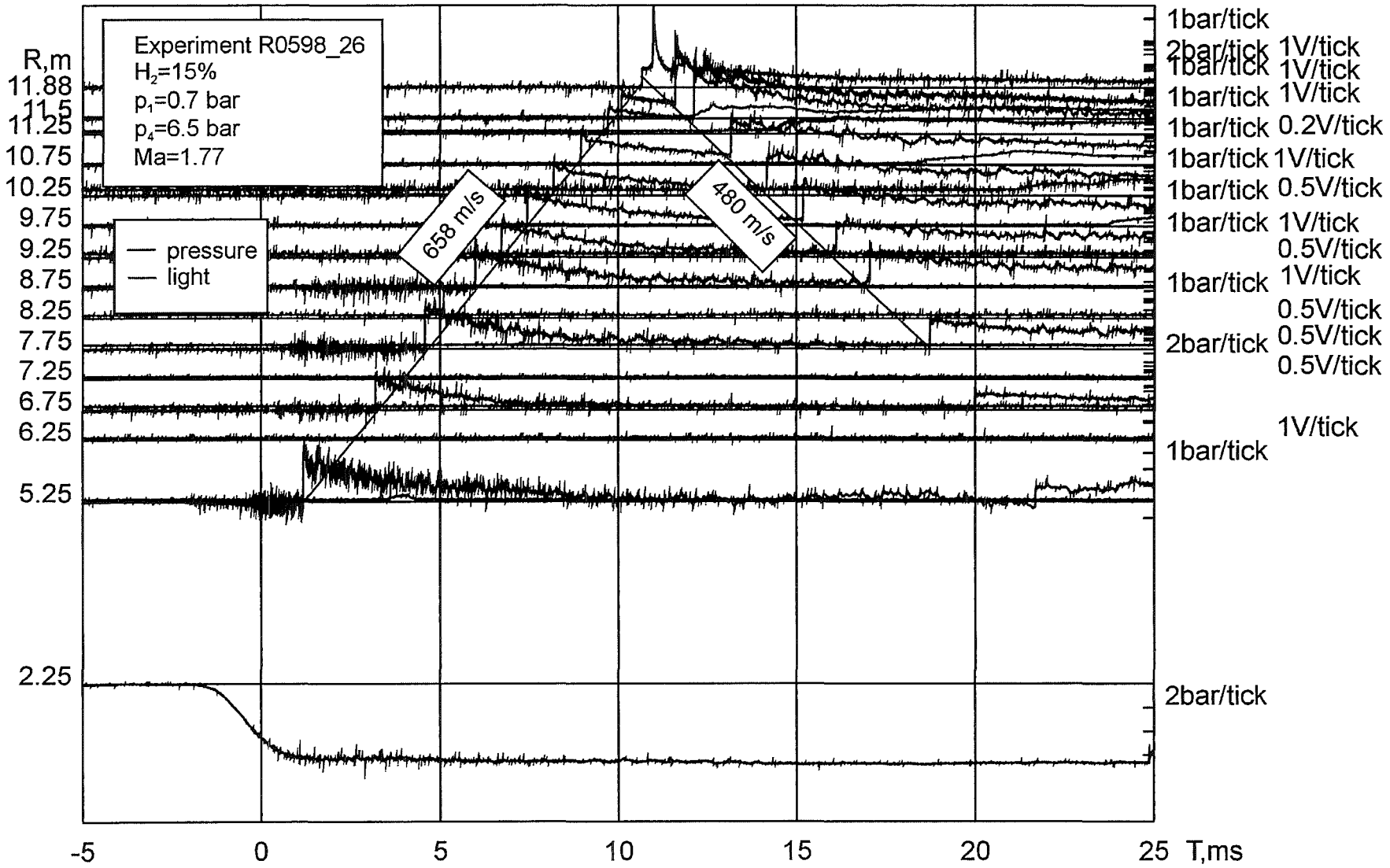

Fig.7: Measured light and pressure signals for experiment R0598_26. Example for mild ignition without DDT.

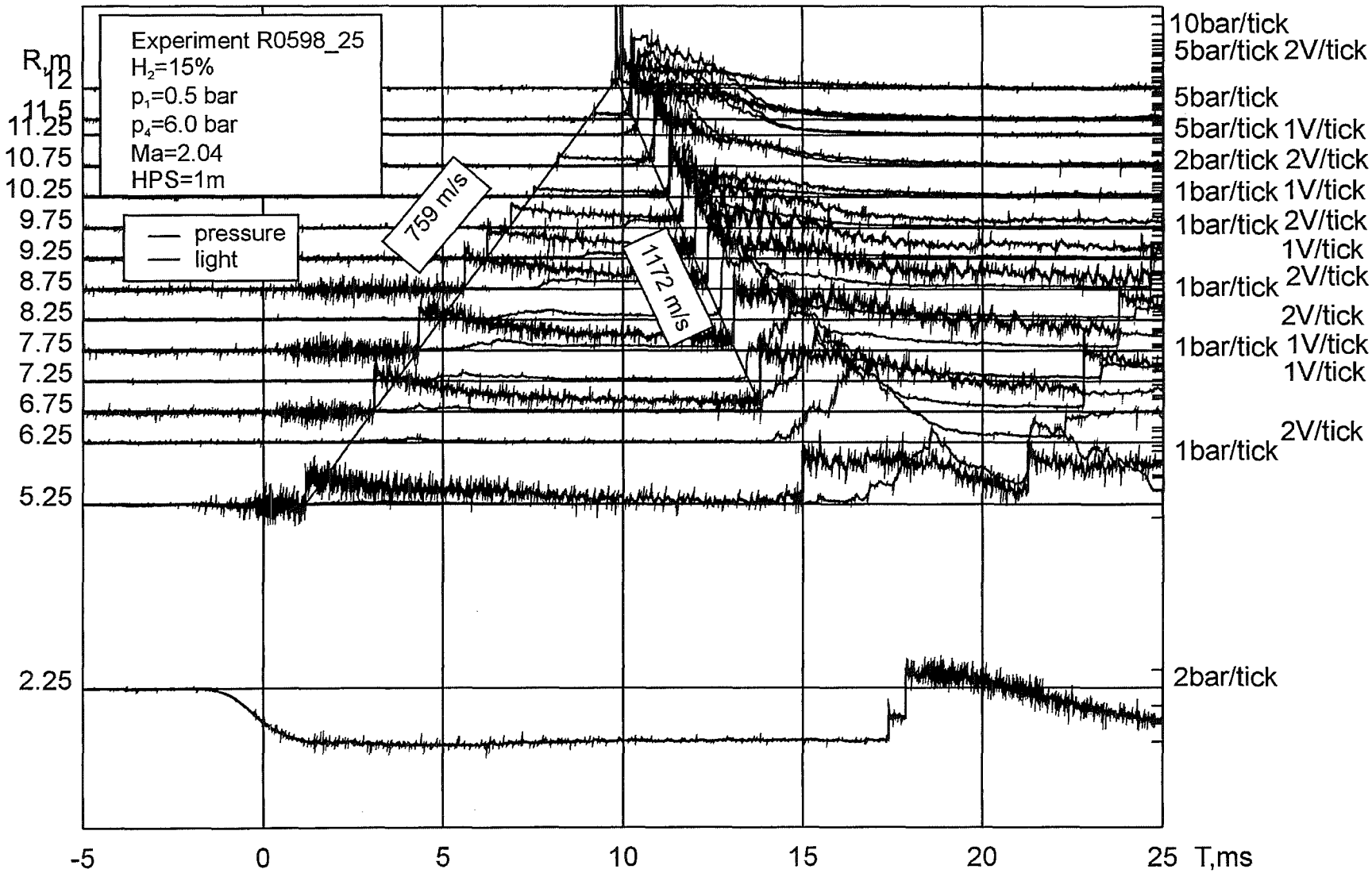

Fig.8: Measured light and pressure signals for experiment R0598_25. Example for strong ignition with DDT.

To verify if the shock wave velocities measured in the experiments correspond to theoretical shock wave velocities, calculations with the KASIMIR code were performed.

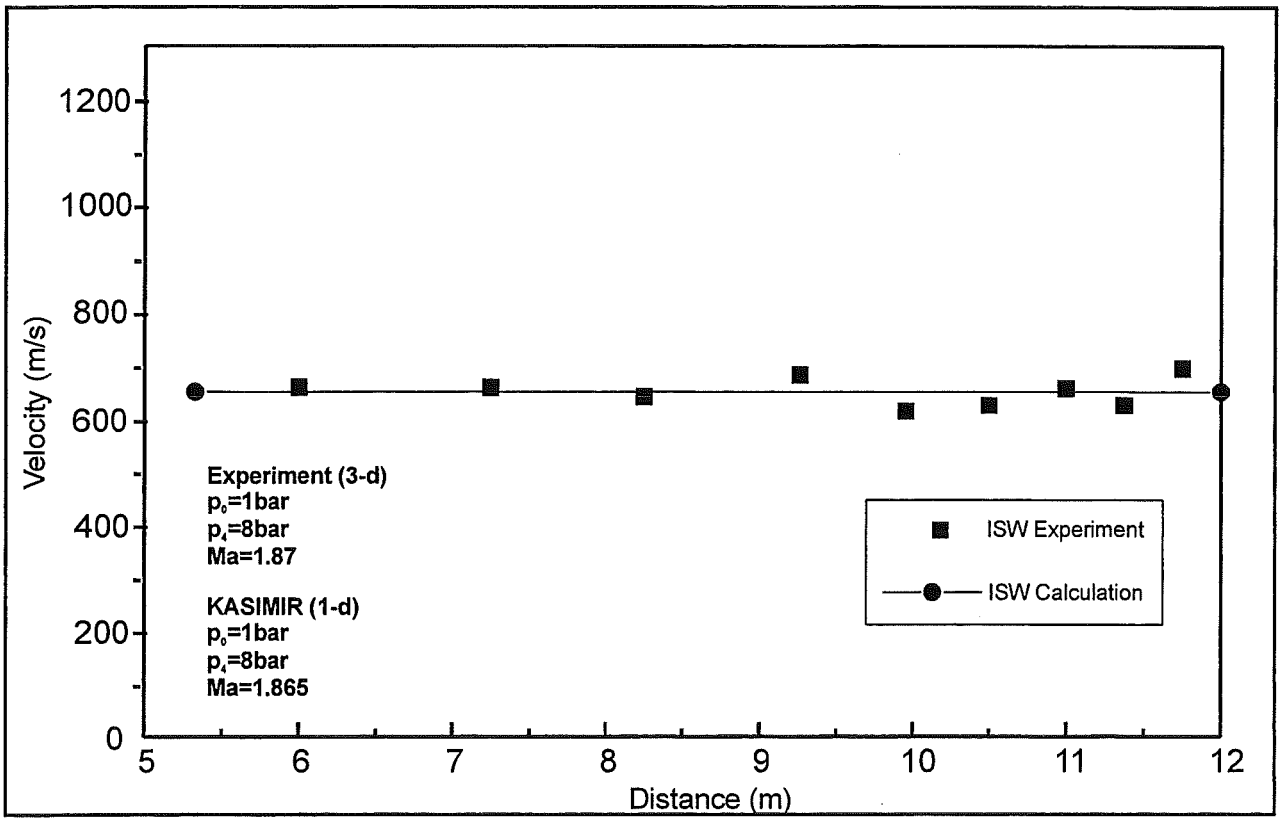

Fig. 9: Comparison between KASIMIR calculation and FZK tube experiment.

KASIMIR is a one-dimensional program which was developed at the Shock Wave Laboratory of RWTH Aachen to describe the dynamics of waves in shock tubes. Figure 8 shows a comparison between the calculated velocity of the incident shock wave with KASIMIR and the velocity of the shock wave in the experiment under equal conditions. Although the experiments are of three-dimensional nature the average shock wave velocity agrees well with 1-d KASIMIR calculations. Contrary to the calculation, the membrane fails in the experiment not as a flat surface , but rather as a hemispherical surface, which creates additional transverse waves in the tube.

Based on the R-t diagrams of the experiments t-x diagrams were constructed for the different observed wave trajectories. Figures 10, 11 and 12 show examples for experiments with different hydrogen concentrations and Mach numbers of the ISW.

Figure 10 shows the t-x diagrams for two experiments with 11 % hydrogen. The upper experiment resulted in a Mach number of 2.19 for the incident shock wave. The ISW travels with a velocity of 870 m/s through the shock tube, is focused in the conus and thereby ignites the mixture. The measured velocity of the RSW is 514 m/s. This velocity is comparable to that of a normally reflected inert shock wave without reaction. The RSW and the FF decouple very early, about 1m away from the conus. The lower test gave a Mach number of 2.48 for the incident shock wave (900 m/s). The velocity of the RSW was measured to 1056 m/s which is close to the theoretical detonation speed in the moving gas. The RSW and the FF remain coupled over a distance of 4.5 m from the conus. A separation of the flame / shock complex appears only after arriving near the contact surface (He/H_2-air interface) where the combustion is necessarily quenched.

Figure 11 shows the t-x diagrams for two experiments with 12 % hydrogen in air and different Mach numbers of the ISW. The experiment with the lower Mach number again leads to a velocity of the RSW (500 m/s) which is comparable to an inert RSW. Again the RSW and the FF decoupled close to conus ($\leq$ 1m). The experiment with the higher Mach number leads to a velocity of the RSW (1041 m/s) which is close to the theoretical detonation speed. In this case FF and RSW decouple about 4m away from the conus.

The t-x diagrams for two experiments with 15% hydrogen in air and different Mach numbers of the ISW are shown in Figure 12. Similar to Figures 10 and 11 the lower Mach number (1.93) of the ISW leads to a RSW with a velocity characteristic for inert behaviour (506 m/s), where as the higher Mach number of the ISW (2.01) leads to a typical detonation velocity of the RSW (1333m/s). Also in this case the decoupling of RSW and FF is earlier in the experiment with lower ISW Mach number of (2m after conus) than in the experiment with higher Mach number (4m after conus).

To check whether the detonation mode of the experiment is stable or unstable the position of the contact surface was calculated with the one-dimensional KASIMIR program (shown in Figures 10, 11 and 12). In the experiment with 11 % H_2 and an ISW Mach number of 2.48, the detonation seems to be stable because the RSW and

FF decoupled only after arrival of the contact surface. In the experiment with 12% hydrogen in air (Mach number of 2.28) and in the experiment with 15 % hydrogen in air (Mach number 2.01), the RSW and the FF decouple somewhat before the calculated arrival of the contact surface. Therefore in these cases the detonation may not to be fully stable, or may transit into a galloping regime.

Three criteria can be used to determine weather DDT occurred or not. The first is the velocity of the reflected wave, the next coupling or decoupling of pressure and light signals, and a further method is to analyse the pressure amplitudes and profiles along the tube. Therefore at given times the pressures at each pressure transducer location were collected and depicted as function of tube location. This was done for different times in each experiment. The spatial distribution of the pressure gives clear indications about the existence of DDT-processes.

An example for pressure profiles along the tube without ignition and combustion (inert case) is given in Figure 13. The upper part shows the measured pressure histories of experiment R0598_35 with the following initial conditions: 0 % hydrogen, p_0=0.7 bar, p_4=7.3 bar. The short HPS section was used. The measured Mach number of the ISW was 2.09 and the reflected wave speed was 466 m/s. The times at which the pressures along the tube were evaluated from the R-t diagram correspond to the arrival times 1 to 7 of the shock at the transducer locations.

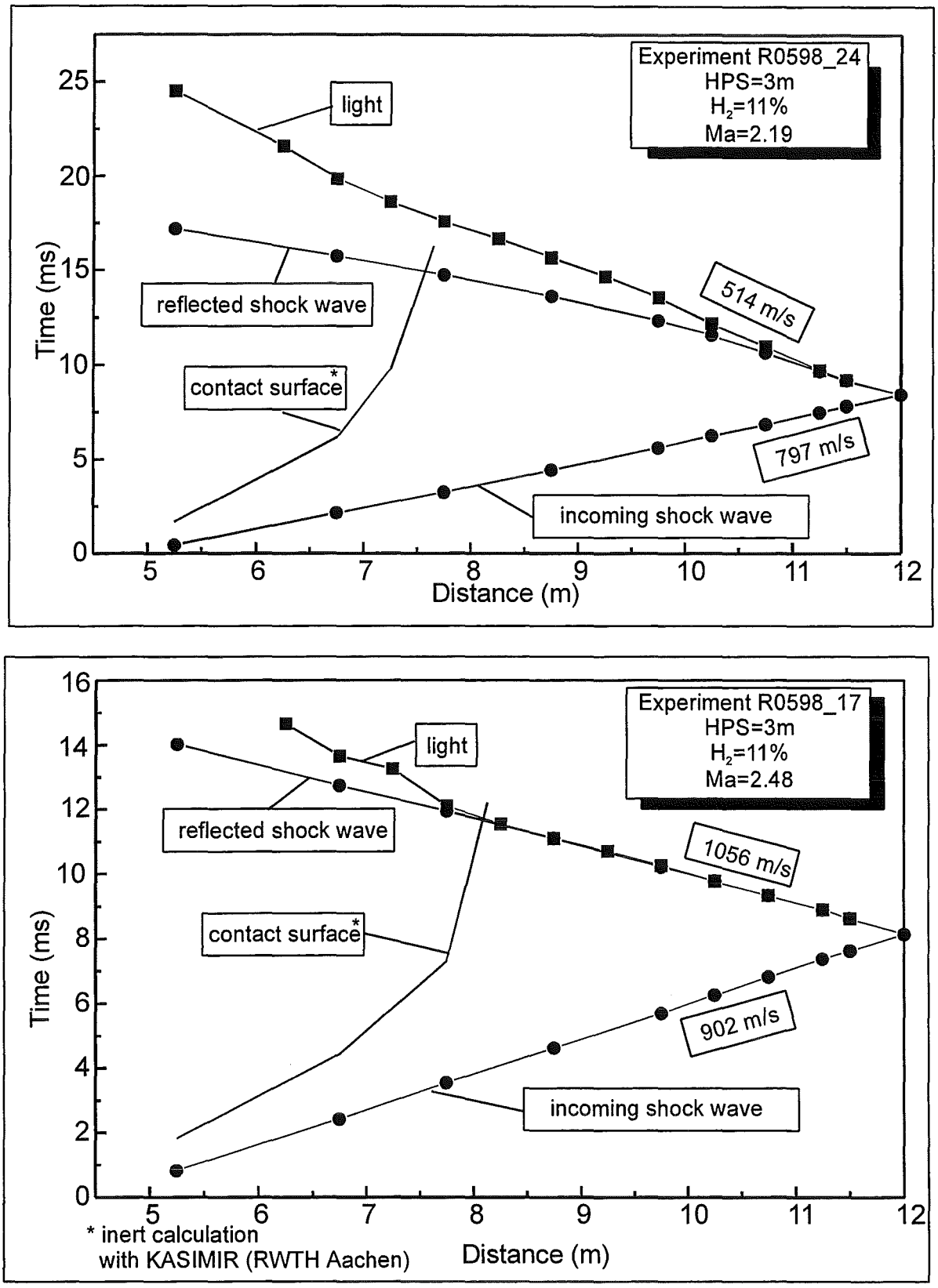

Fig.10: Example for measured light and pressure trajectories with for 11% hydrogen. Upper case weak ignition without DDT, lower case strong ignition with DDT.

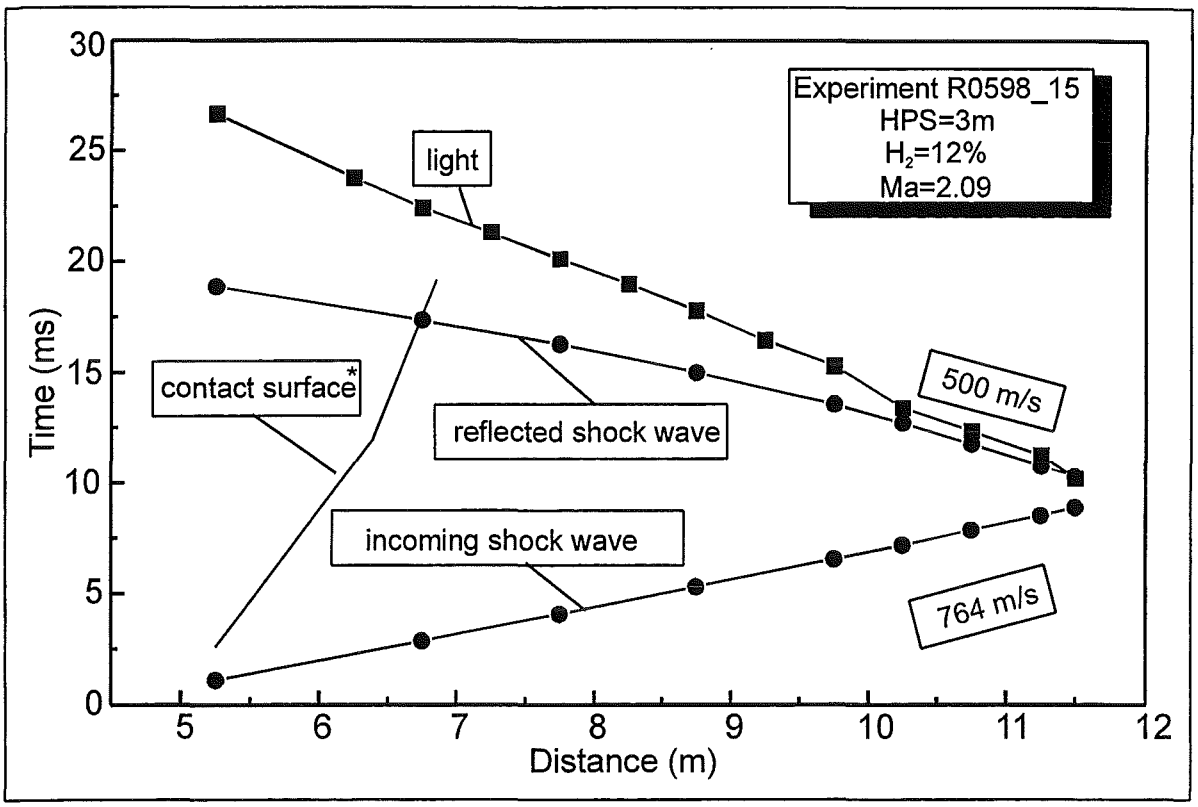

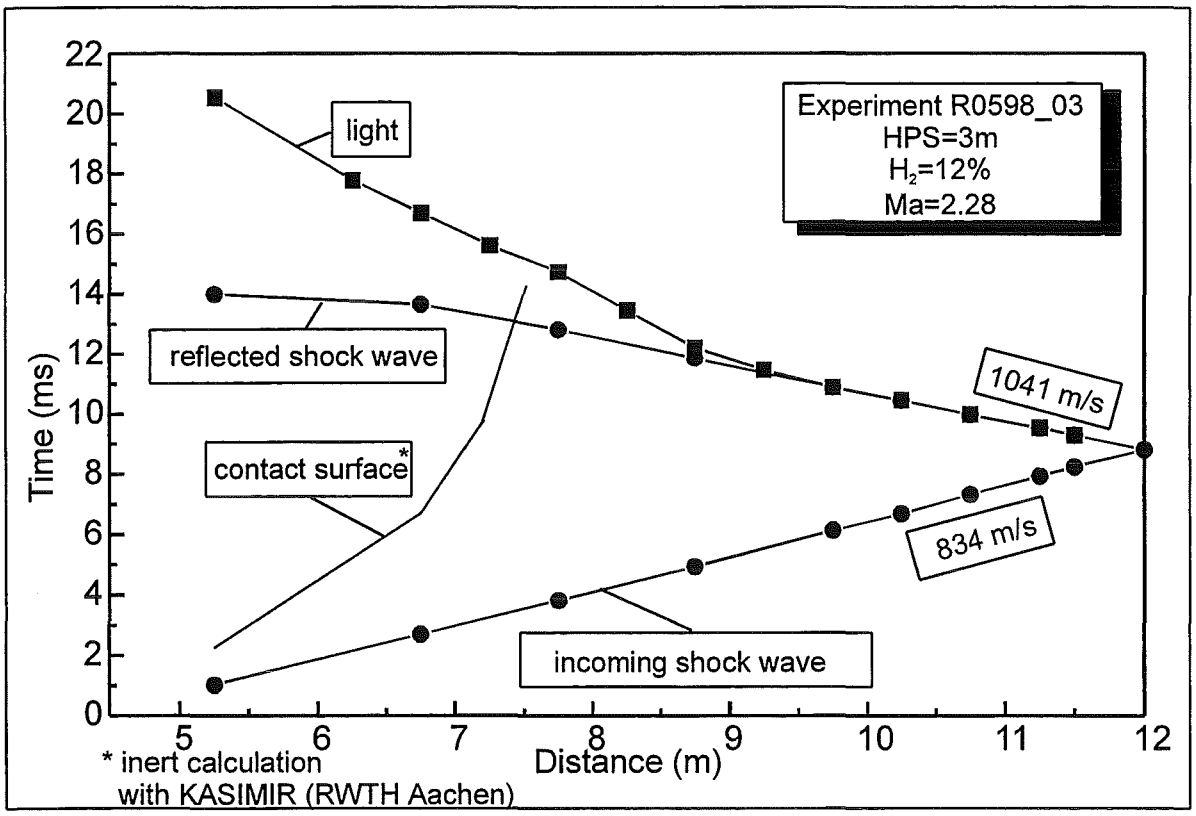

Fig.11: Example for measured light and pressure signals with 12% hydrogen. Upper case weak ignition with uncoupling of pressure and flame front (no DDT), lower case strong ignition with coupling (DDT).

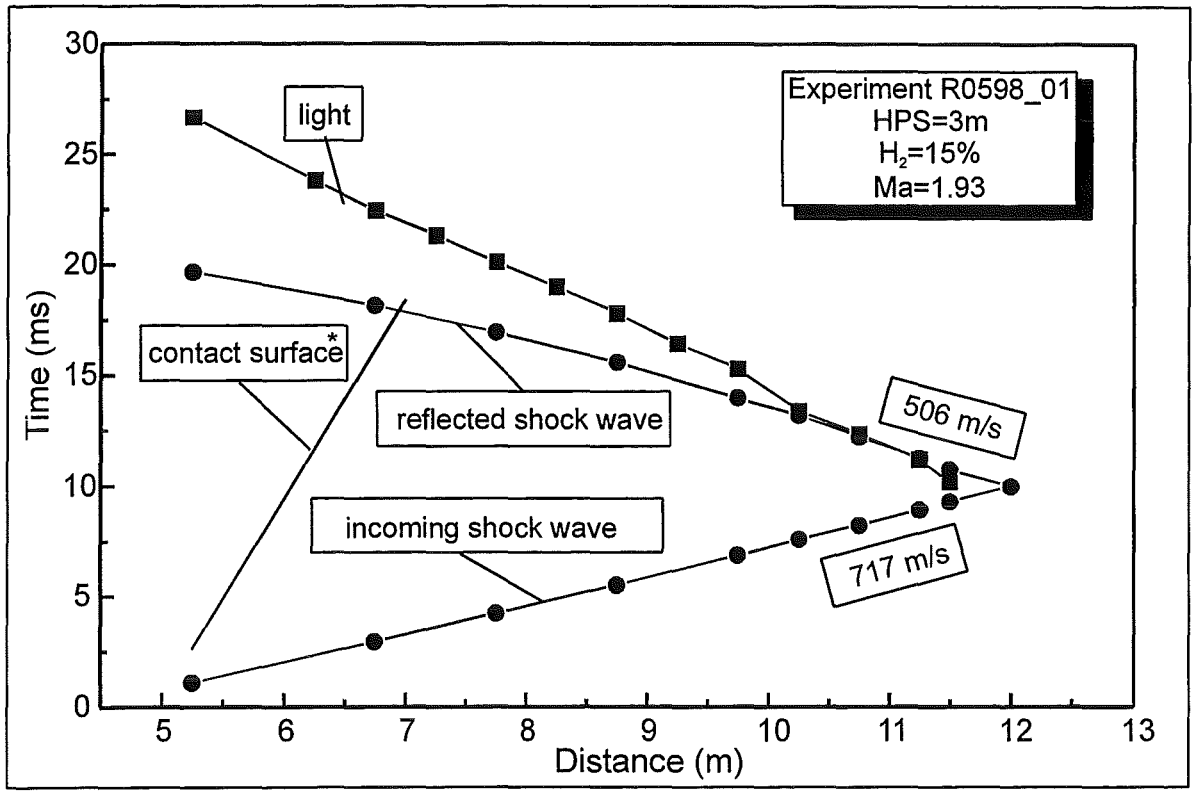

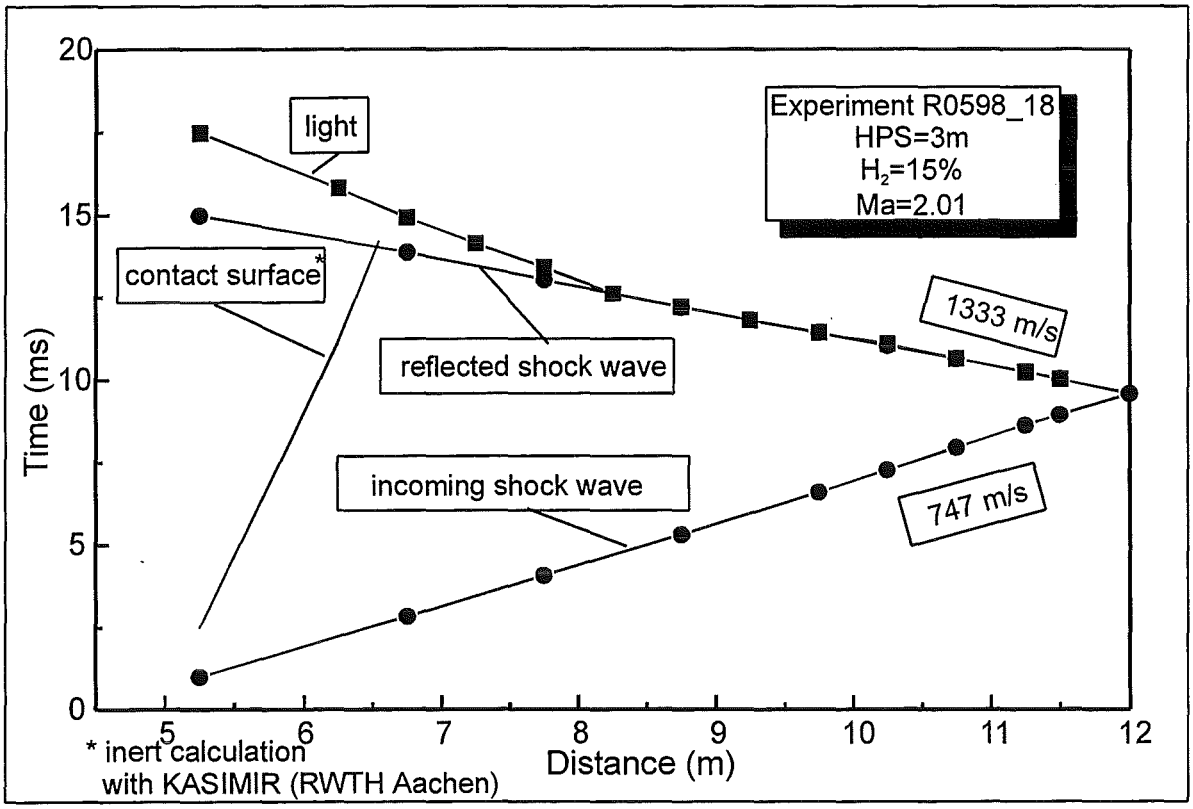

Fig. 12: Example for measured light and pressure signals for 15%. hydrogen. Upper case with weak ignition (uncoupling of pressure and flame front), lower case with strong ignition and DDT (pressure/flame complex, detonation typical speed or RSW).

Curves 1 and 2 in the lower part of Fig.13 show the typical incoming shock front pressures in an inert case. Curves 3-7 in the lower part of Fig.13 show typical reflected shock pressure distributions for an inert case. The maximum pressure which is created by focusing in the conus decays rather fast with increasing distance from the conus. Although the shown pressures scatter somewhat from the noise in the p(t) data, they show typical reflected pressure profiles for the case of an inert mixture. The low pressures of reflected waves inside the conus are due to the change of cross section area in this reflector.

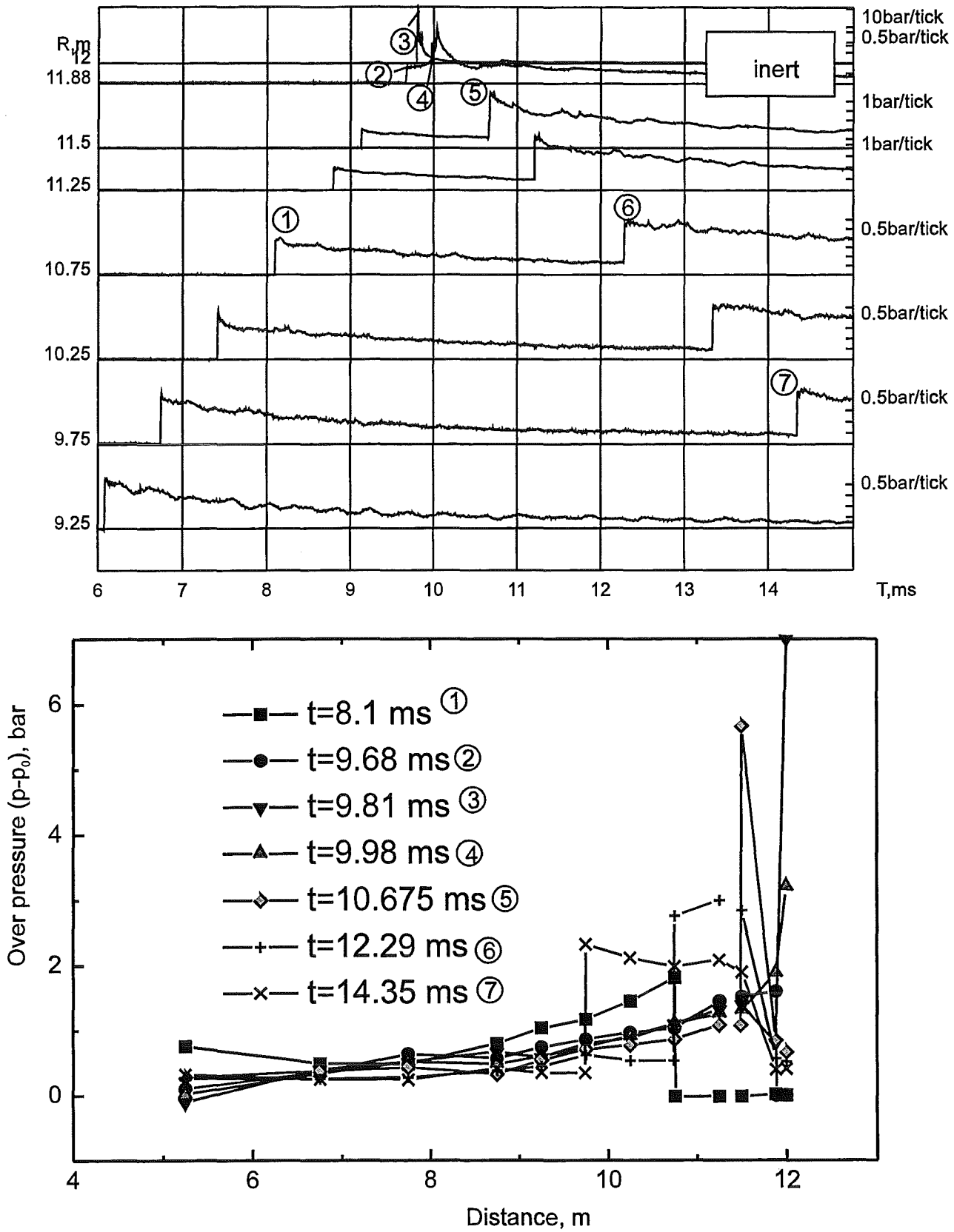

Fig.13: Measured pressure histories of experiment R0598_ 35 (top) and pressure profiles along the tube at given times (bottom). Inert test without hydrogen.(Initial conditions: 0% hydrogen, p_0=0.7 bar, p_4=7.3bar, Ma=2.09. Measured velocity of RWS=466 m/s).

An example for nearly the same initial conditions (p_0=0.7, p_4=6.4, Ma=1.77, RSW=480 m/s) but with 15 % hydrogen is given in Figure 14. The curves 1 and 2 in the lower part of Fig.14 show pressure profiles of the incoming shock wave. Curves 3-6 show reflected pressure profiles, but in comparison to the experiment without hydrogen, the maximum measured pressure in the conus is much higher (8 bar inert case, 40 bar with hydrogen). Also the reflected pressures outside of the conus show higher values. These higher pressures are an effect of the deflagrative combustion process which started inside the conus.

The pressure histories of experiment R0598_31(initial conditions: Ma = 2.03, RWS = 1399 m/s) which is given in Figure 15 shows a rather different behaviour in comparison to the inert experiment (R0598_35) and the experiment with mild ignition R0598_26. The pressure profiles of the incoming shock show of course the same behaviour as in an the inert case, but the shape of the reflected pressures resembles closely that of CJ-detonations. Note that the initial pressure in the LPS was only 0.45 bar which indicates that the detonation decays from an overdriven state towards CJ-conditions as it propagates away from the reflector. In addition the higher velocity and also the coupling between light and pressure leads to the conclusion that DDT occurred in this experiment.

Based on these three indicators (reflected wave speed, coupling between light and pressure, magnitude and shape of pressure distribution) the experiments could be grouped clearly into cases with and without DDT.

Figure 16 (3m high pressure section) and Figure 17 (1m high pressure section) summarise all FZK-experiments as function of the Mach number of the ISW and the hydrogen concentration in air. These data were obtained in joint FZK/RAS measurement campaigns. The experiments can be classified into two groups:

- The first (lower) area describes an uncoupled propagation of RSW and FF with time and length differences of dt = 1-2 ms and dL=0.5-1m. Measured reflected pressure amplitudes and profiles along the tube are comparable to inert cases, indicating absence of DDT.

-The second (upper) area describes a regime of coupled propagation of RSW and FF with $W + u_2 \approx D$, which confirms DDT (W=measured wave speed in laboratory frame, u_2 = particle velocity, D= CJ detonation speed in stationary gas). DDT is further supported by the pressure amplitudes and typical detonation pressure profiles along the tube.

The small triangular region in Fig. 16 between no-DDT and DDT- conditions shows the remaining parameter space which was not covered by experiments. This narrow gap demonstrates that a well defined critical Mach number exists for a given hydrogen concentration in air above which DDT occurs.

Figure 17 summarises the experiments with a shorter HPS (1m) The shadowed area in the middle again depicts the range in which the critical Mach number can be anticipated. Additional experiments would be required to further narrow down the borderline between DDT and no DDT behaviour in the investigated geometry.

Figure 18 summarises the dependence of the RSW velocity from the Mach number of the ISW for 10%, 11 %, 12 % and 15 % H_2 in air. For 10 % hydrogen in air the

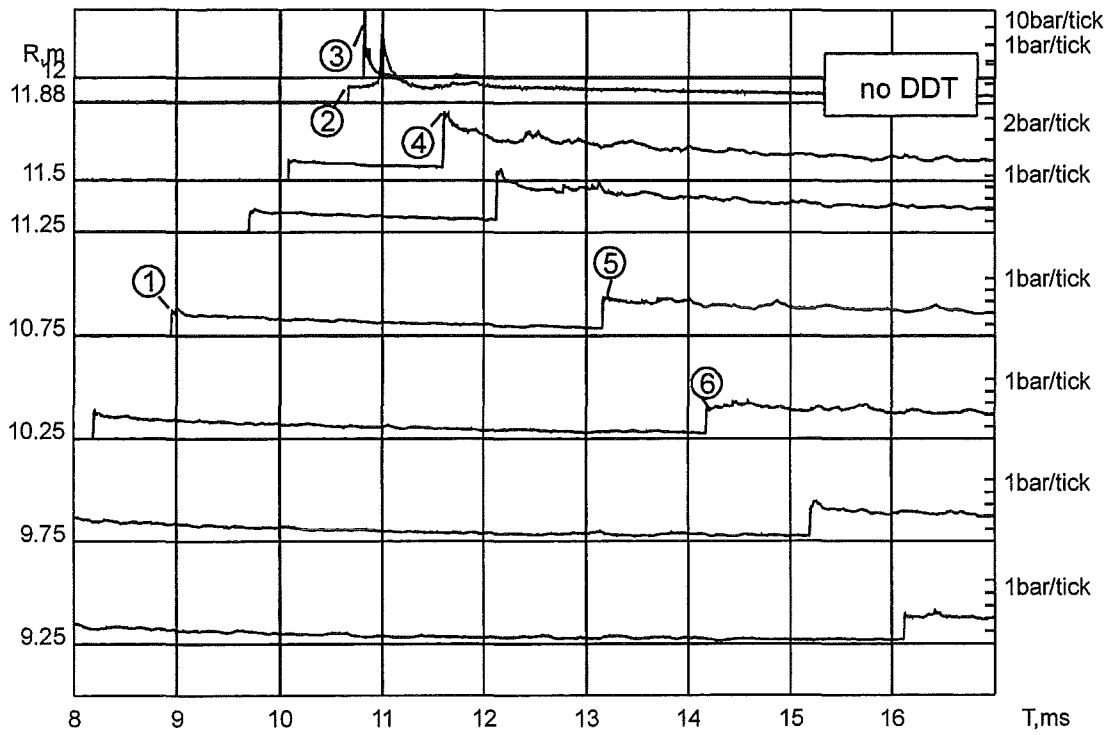

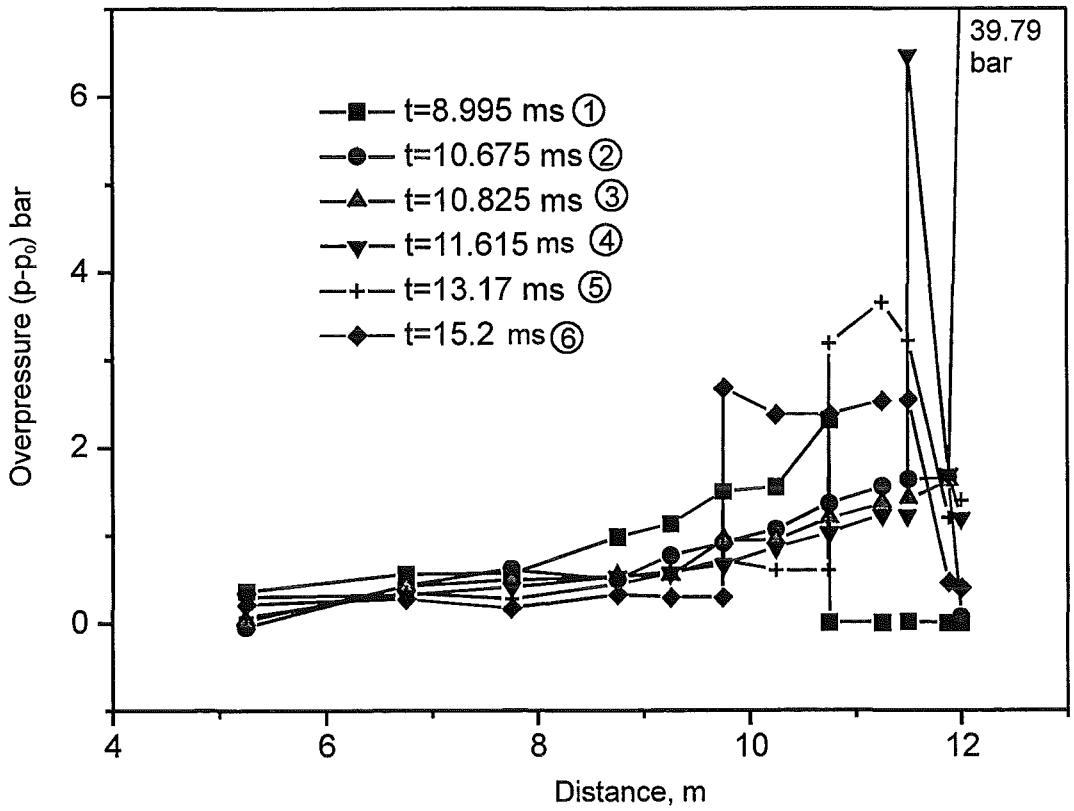

Fig: 14 Measured pressure histories of experiment R0598_ 26 (top) and pressure profiles along the tube at given times (bottom). Initial conditions: 15% hydrogen, p_0=0.7 bar, p_4=6.7 bar, Ma=1.77. Measured velocity of RWS=480 m/s).

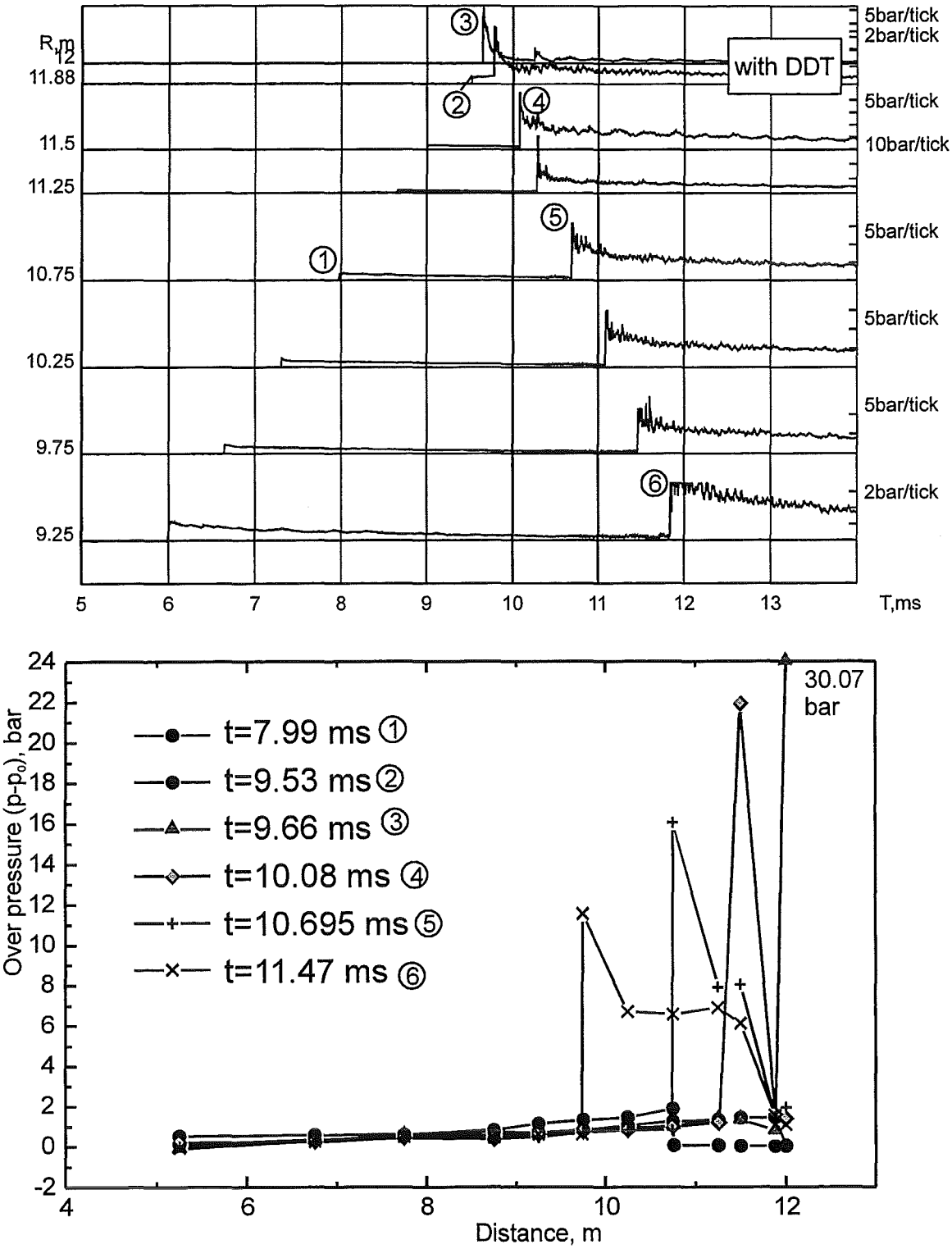

Fig: 15 Measured pressure histories of experiment R0598_ 31 (top) and pressure profiles along the tube at given times (bottom). (Initial conditions: 15% hydrogen, p_0=0.45 bar, p_4=7.0 bar, Ma=2.03, RWS=1399 m/s

critical Mach number of the ISW is between 2.1 and 2.3, for 11 % hydrogen in air it is near 2.2, for 12 % hydrogen in air it is 2.1 and for 15 % hydrogen it is 1.93. We find that the critical Mach number of the IWS decreases with increasing hydrogen concentration, probably because smaller temperature increases are required for triggering a successful DDT.

Figure 18 demonstrates that no substantial difference could be observed between the experiments with 1 m and 3 m length of the HPS, respectively. Obviously the change in the pressure profile of the ISW obtained with the shorter high pressure section, causing a more triangular pulse with the 1 m length than with the 3 m length, did not substantially influence the overall DDT process. Recent numerical simulations [2] have indicated that the temperature gradients which are produced by the triangular incoming pressure pulse using a 1m long HPS (in HPS) are too small to create an additional SWACER mechanism, compared to the 3m HPS.

Figure 19 shows a summary plot containing the data points from Fig.18 and additional test results with more sensitive H_2-air mixtures (22 and 30% H_2). The dashed lines indicate the critical Mach numbers for the respective mixtures at which the reflected wave velocity suddenly switches from inert reflection values (lower line) to detonation like values (upper line). A very low Mach number was found for stoichiometric H_2-air mixtures, demonstrating that DDT by mode A can be easily achieved if such mixtures should be present in a multidimensional enclosure and a pressure wave should be generated by a fast flame or by other means.

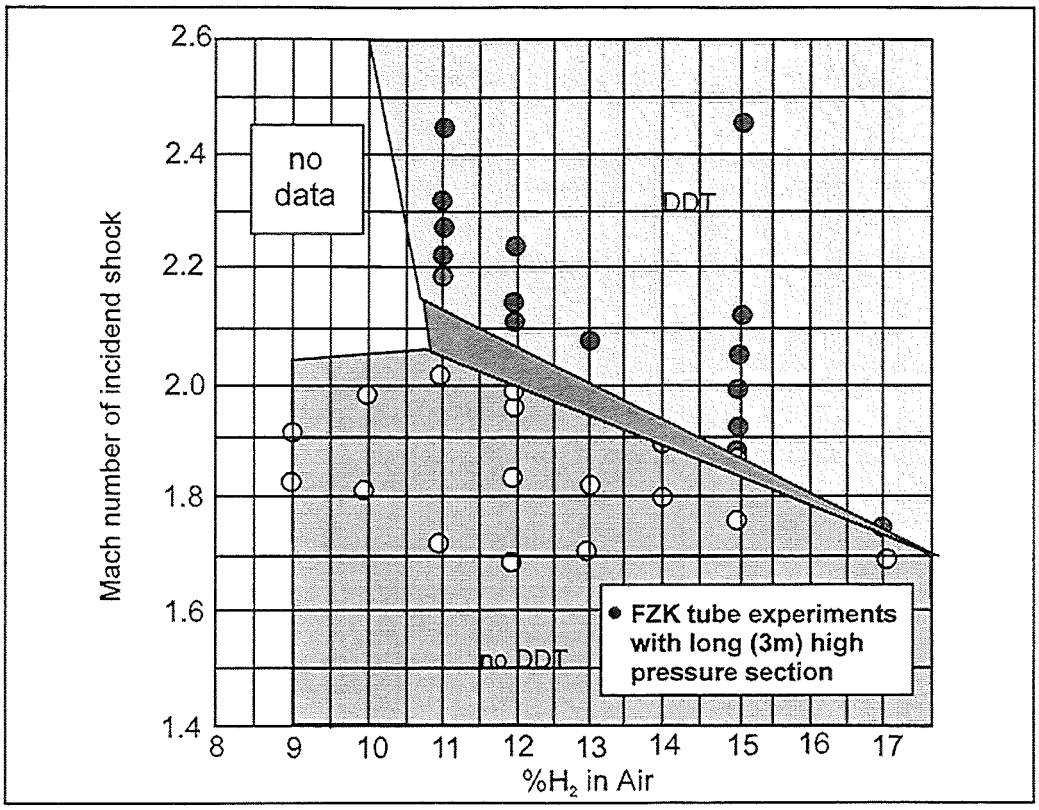

Fig 16: Critical Mach number for DDT in hydrogen -air mixtures (3m HPS)

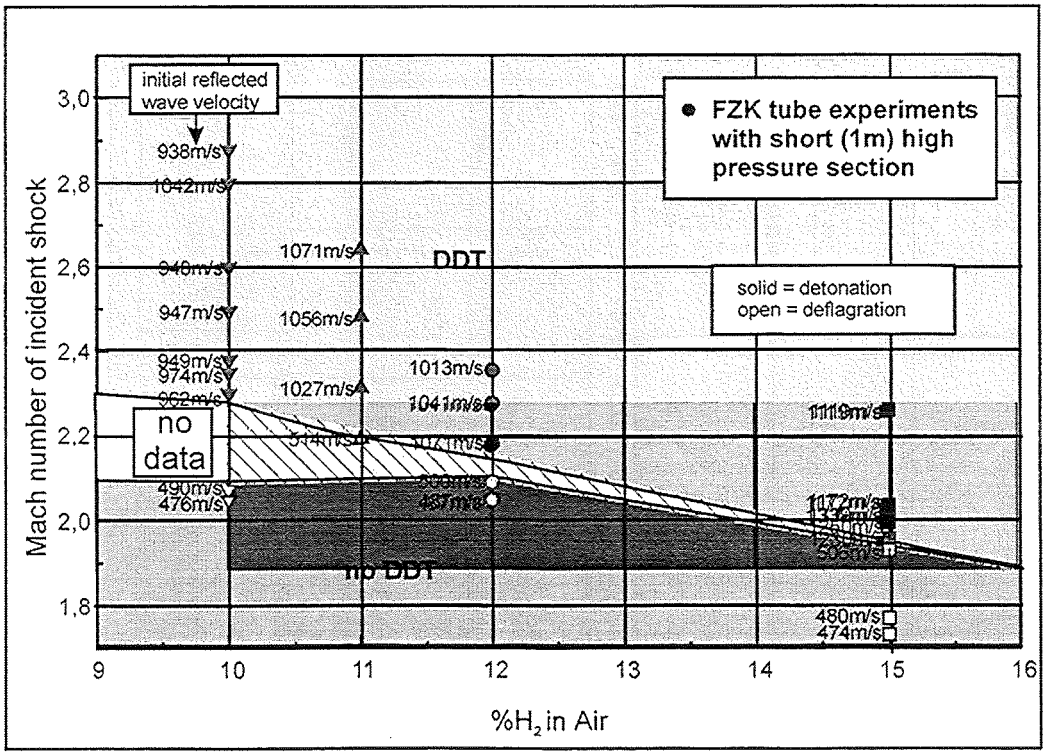

Fig.17: Critical Mach number for DDT in hydrogen -air mixtures (1m HPS). For each test the velocity of the reflected wave is included as indicator for deflagration (no DDT) or detonation (DDT).

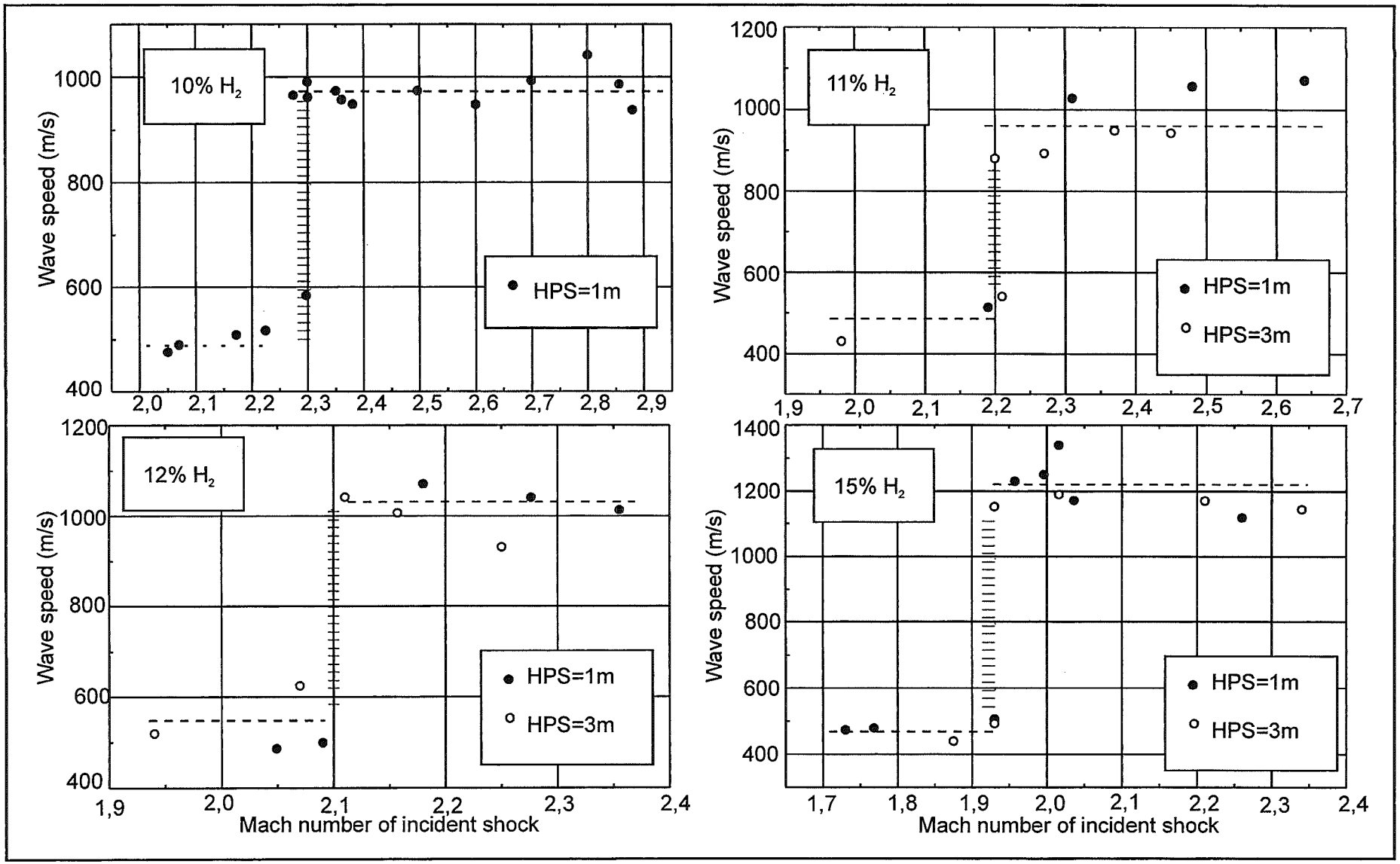

Fig.18: Measured reflected wave speeds in idealised mode A-DDT-experiments. Tests with different pulse shapes (length of HPS) resulted in the same critical Mach number for DDT.

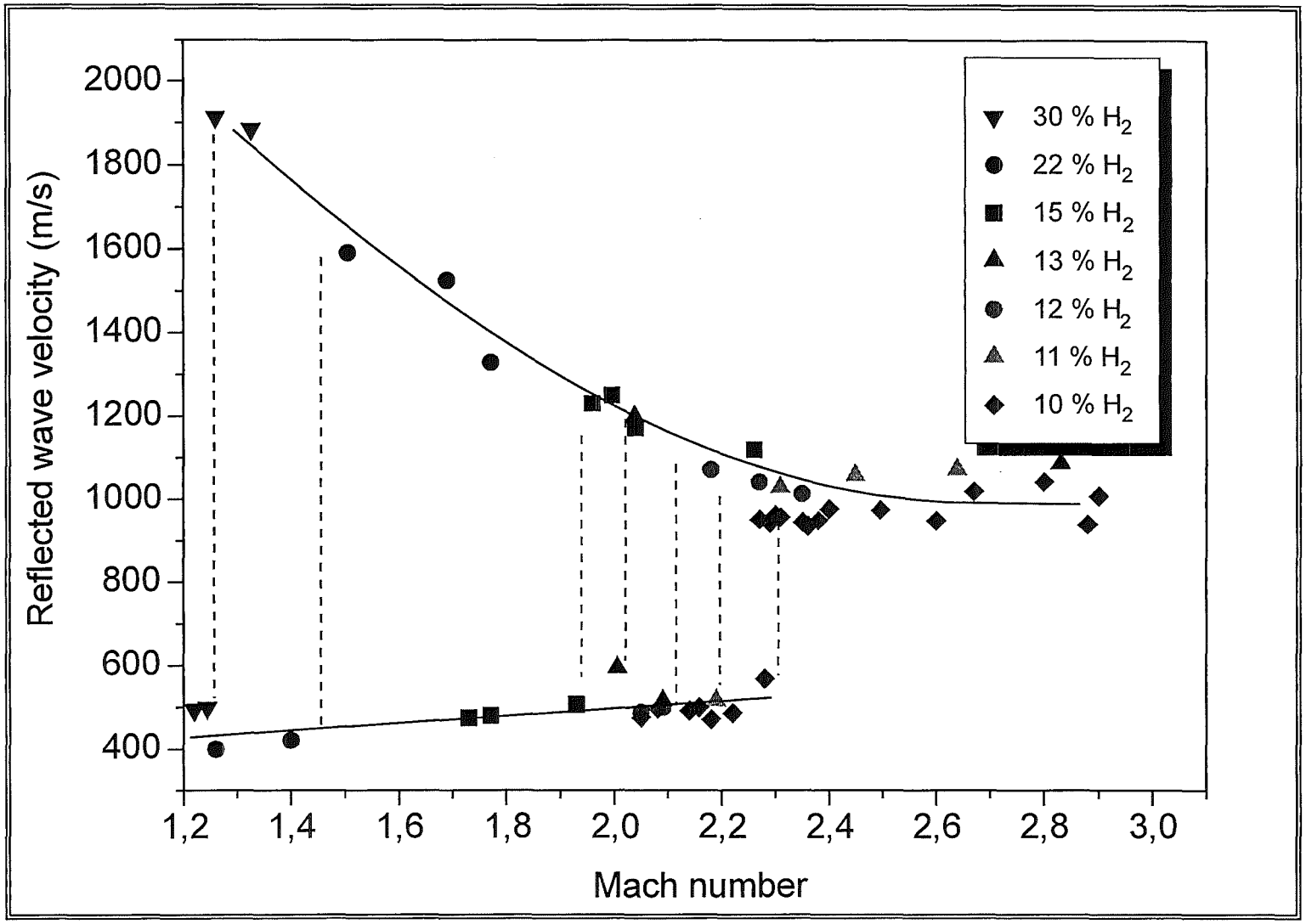

Fig. 19: Critical Mach numbers for idealised mode A- DDT in FZK- tube experiment

3 Results of prototypic mode A-DDT experiments

All experiments that were performed in the prototypic mode A arrangement are listed in Table 2. The main idea behind this experimental set-up is that after a weak spark ignition, the propagating flames reaches a highly obstructed region in which it can accelerate due to intense turbulence generation. This fast flame then emits precursor pressure waves which propagate through a relatively open region until they are reflected from the enclosure. In most practical cases the precursor wave will not simply be normally reflected from a flat wall but rather be focused by two walls (2-d wedge) or three walls (3-d corner). Such focussing geometries in industrial buildings were simulated in the tube tests by a conical reflector situated at the end of the tube, opposite to the ignition location (Fig. 4). The investigated tube geometry contains therefore all characteristic elements of a combustion sequence in a complex industrial installation:

- a combustible gas,
- a weak ignition source,
- a partly blocked region with flow obstacles producing high turbulence levels,
- an open region which permits pressure wave propagation without significant losses,
- and a multidimensional reflector as part of the enclosure.

Table 2: Test matrix of DDT experiments in prototypic mode A tube configuration

Experiment	BR [%]	p_0 [bar]	$[H_2]$ [%]	Obstacle separation
R0797_00	60	1	15	x =50cm
R0797_01	60	1	20	x =50cm
R0797_02	60	1	18	x =50cm
R0797_03	60	1	17	x =50cm
R0797_04	60	1	17	x =50cm
R0797_05	60	1	17	x =50cm
R0797_06	60	1	16	x =50cm
R0797_07	60	1	16,5	x =50cm
R0797_08	60	1	16,5	x =50cm
R0797_09	60	1	16,5	x =50cm
R0797_10	60	1	16,5	x =50cm
R0797_11	60	1	16,5	x =50cm
R0797_12	60	1	16,5	x =50cm
R0797_13	60	1	17	x =50cm
R0797_14	60	1	15	x =50cm

The main results obtained in this prototypic mode A configuration will be described by two examples. Figure 20 shows the R-t-diagram of experiment R0797_14. The test parameters of this experiment were 15.0 % hydrogen in air with an initial pressure of 1 bar. After ignition, the flame accelerated early in the obstacle section and a stable pressure /flame complex propagated in the blocked region. After transition into the smooth part of the tube, the flame decelerates, a shock separates from the flame, and propagates towards the conical reflector.
Figure 21 shows an enlarged part of the R-t-diagram for the tube section close to the conus (9.75 m - 12.0 m). No photodiode and ionisation signals were recorded close to the incident shock, which shows that the turbulent flame has not yet reached this tube section. The measured velocity of this precursor shock wave is about 680 m/s. This precursor shock wave is focussed and reflected in the conus, but the absence of photodiode signals shows that no selfignition has taken place in the conus. The reflected wave seems to have initiated a restricted local explosion at the 10.75 m position as indicated by the short pressure excursion and the corresponding photodiode signal. This local ignition did not propagate along the tube . The sudden increase in light at the 9.75 m position (19ms) is due to the compression of burned gas because the flame arrived at this location already at about 15 ms. The average velocity of the reflected shock wave is measured to 650 m/s, which indicates that no DDT event occurred in this test.

Experiment R0797_10, which was performed with 16.5 % hydrogen in air and an initial pressure of 1 bar lead to different results. The measured R-t-diagram is shown in Figure 22. This diagram also shows an acceleration of the flame in the obstacle section and a separation of shock and flame in the smooth part of the tube. A triangular blast wave, similar to the idealised mode A test with 1m-HPS, is emitted towards the reflector.
Figure 23 is again an enlarged part of the R-t-diagram near the conus (9.75 m - 12.0 m). This time the focussed precursor shock wave causes a strong selfignition, which is due to the higher wave speed and the more sensitive mixture. This ignition is detected simultaneously by the photodiodes, the ionisation gauges and the pressure transducers. The measured pressures are significantly higher than in the previously discussed case (Fig.21) and the values initially exceed the theoretical CJ-

pressures indicating an overdriven detonation. ($p_{cj}/p_0 \approx 11.2$ for 16.5 % H_2 in air). The flame front and the reflected shock wave remain coupled and travel with a measured velocity of 1360 m/s. Such a velocity is typical for a detonation in the counterflowing gas, indicating that a DDT event has occurred.

All experiments performed in the partly obstructed geometry can be grouped in three regimes with respect to the flame/pressure wave interaction:

- At low hydrogen concentrations ($\leq$ 11%) the speed of the propagating flame in the obstructed zone remains much smaller than the sound speed in the unburned gas. The flame emits a set of acoustic waves, and the pressure increases practically uniformly in the tube according to the fraction of gas burned at any given time.

- In the second regime, which occurs for hydrogen concentrations from about 12 to 18 % (at p_0 = 1bar, T_0=300K) a coupled flame/shock complex is emitted from the section with obstacles. Due to the flame declaration in the smooth part of the tube, a shock wave proceeds the flame. The shock is faster than the flame. Depending on the Mach number, the precursor wave can trigger a weak (deflagrative) or a strong (detonative) ignition when it is reflected at the tube end.

- A third regime is observed when the hydrogen concentration exceeds 18%. In this case flame and shock remain coupled after the complex leaves the obstructed region, at least for the distance available in the present test set-up. Flame and shock have the same velocity. The interaction of this complex with the tube end causes only a reflected wave back into combustion products, and contrary to regime II, no secondary ignition can occur.

DDT by mode A is only possible in the second regime where the shock velocity exceeds the flame speed. The corresponding measured range of hydrogen concentrations (12-18%) is not universal, it will generally depend on the tube dimensions and details of the obstacle section (length, blockage ratio). Experiments in a geometrically similar but scaled down facility of the Russian Academy of Science

(linear scale 1:6) have identified the same three regimes but at hydrogen concentrations which were several percent higher than in the FZK-tube tests [1].

The three described regimes lead to different load mechanisms and load magnitudes. In the first case ($v_{flame} << c$) the pressure increases nearly uniformly in the tube. The pressure increase at a given time is proportional to the fraction of burned gas at that time. Shape and size of the reflector have no influence on local pressure loads.

In the second regime ($v_{flame} < v_{shock}$) two effects lead to higher loads compared to the first regime:

1. directed flow with particle velocities of the order of several 100 m/s,
2. secondary ignition after reflection in the multidimensional target at the tube end.

For low shock velocities, which only trigger a deflagration, the additional loading from the secondary ignition is not substantial. The pressure loads are comparable to that of an inert reflection. However in case of sufficiently high shock speed the strong secondary ignition causes very high local pressures because the chemical reaction proceeds from a precompressed state.
Compared to the loads in the second regime, the third regime ($v_{flame}=v_{shock}$) produces lower pressures and impulses. The particle velocities of the directed flow increase, but this is more than compensated by the fact that no secondary ignition can occur from the reflection process.

In summary, the highest loads were observed inside the 3-d reflector under DDT conditions. In this case the directed flow into the conus precompressed unreacted gas which then ignited rapidly. An overdriven detonation propagates away from the reflector into the rest of the unburned gas.

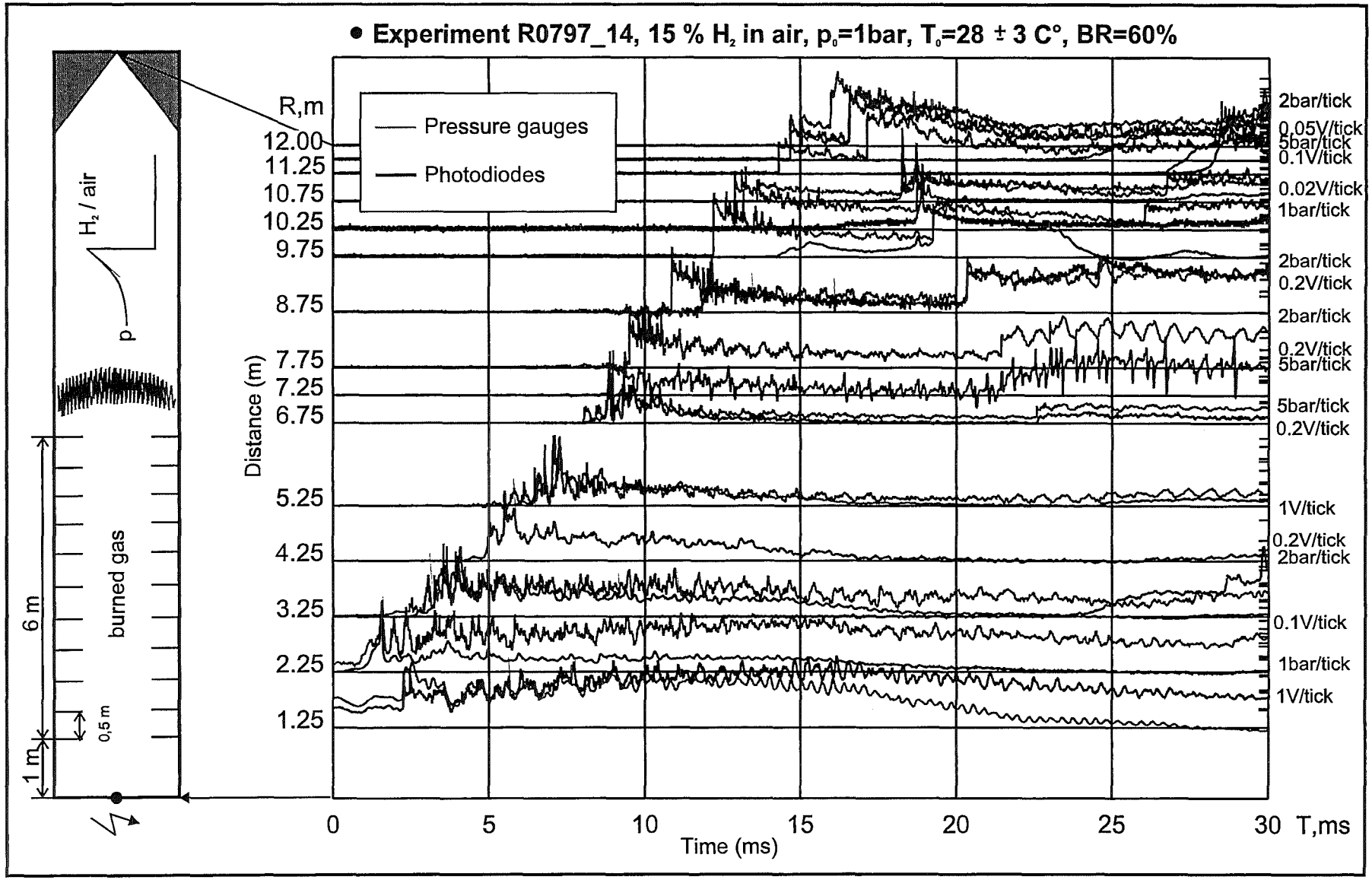

Fig. 20: Measured pressure and photodiode signals of experiment R0797_14

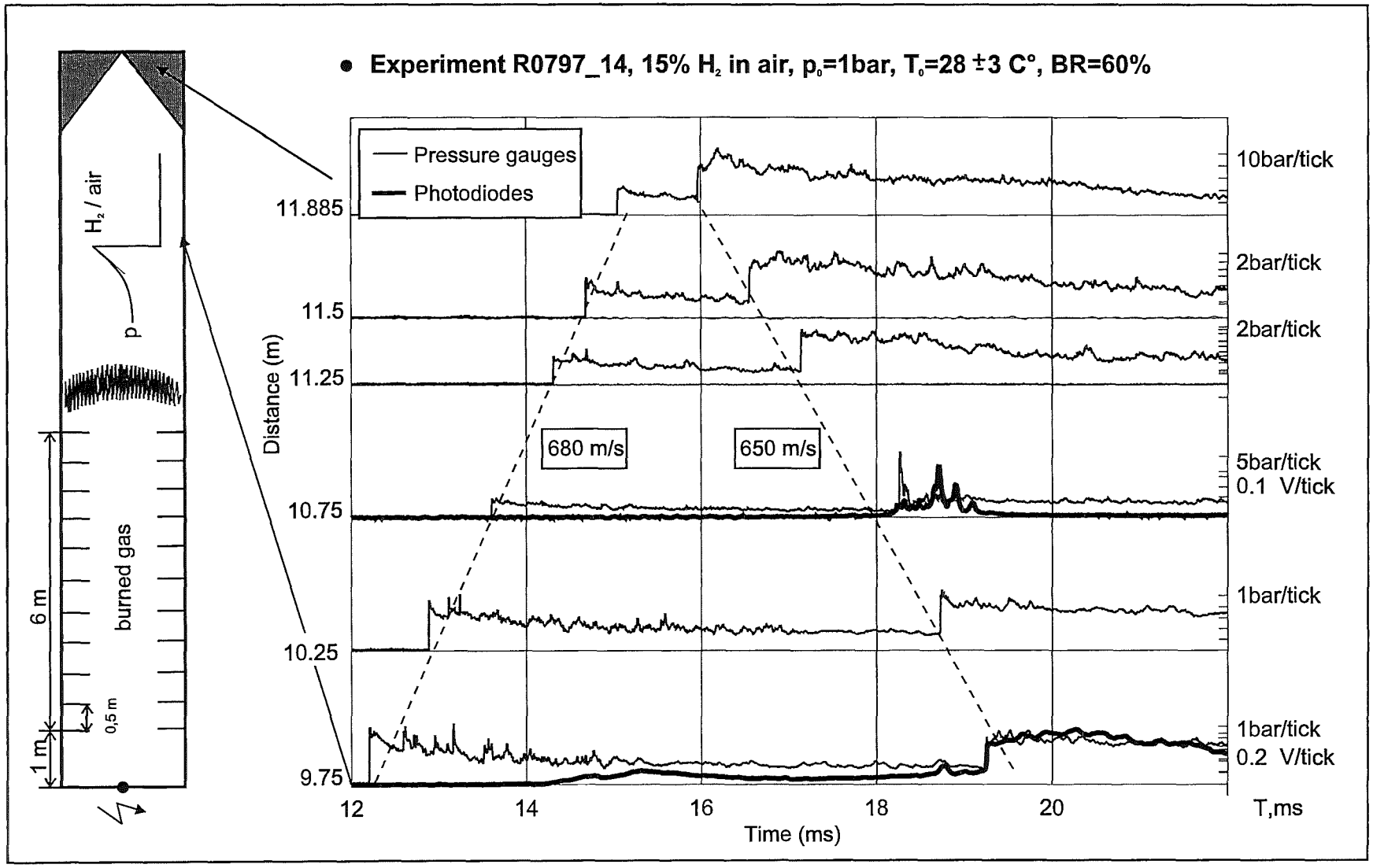

Fig. 21: Measured pressure , photodiode and ionisation signals of experiment R0797_14. Enlarged part of the R-t diagram near the conus (9.75-12.0m)

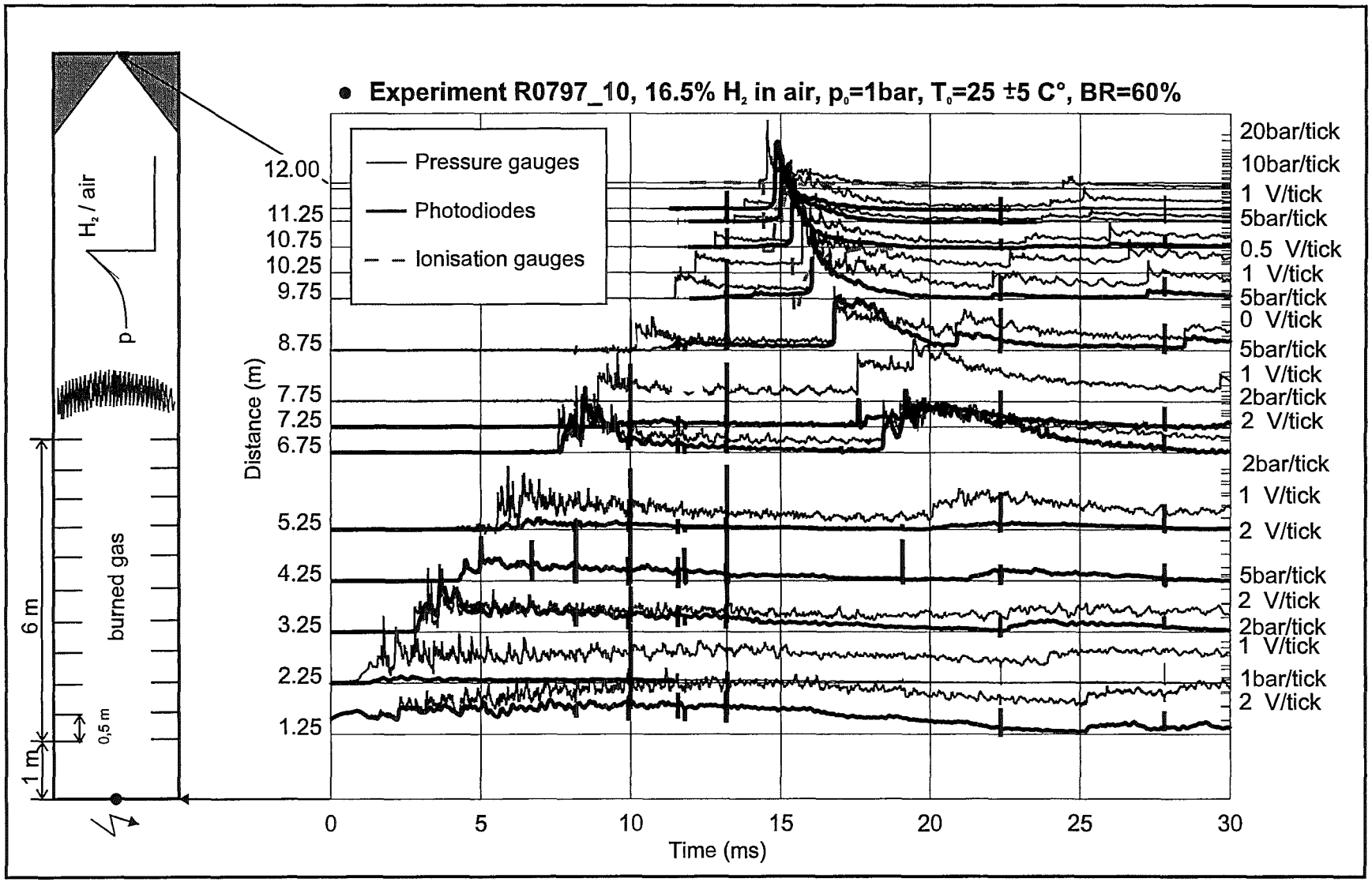

Fig. 22: Measured pressure, photodiode and ionisation signals of experiment R0797_10.

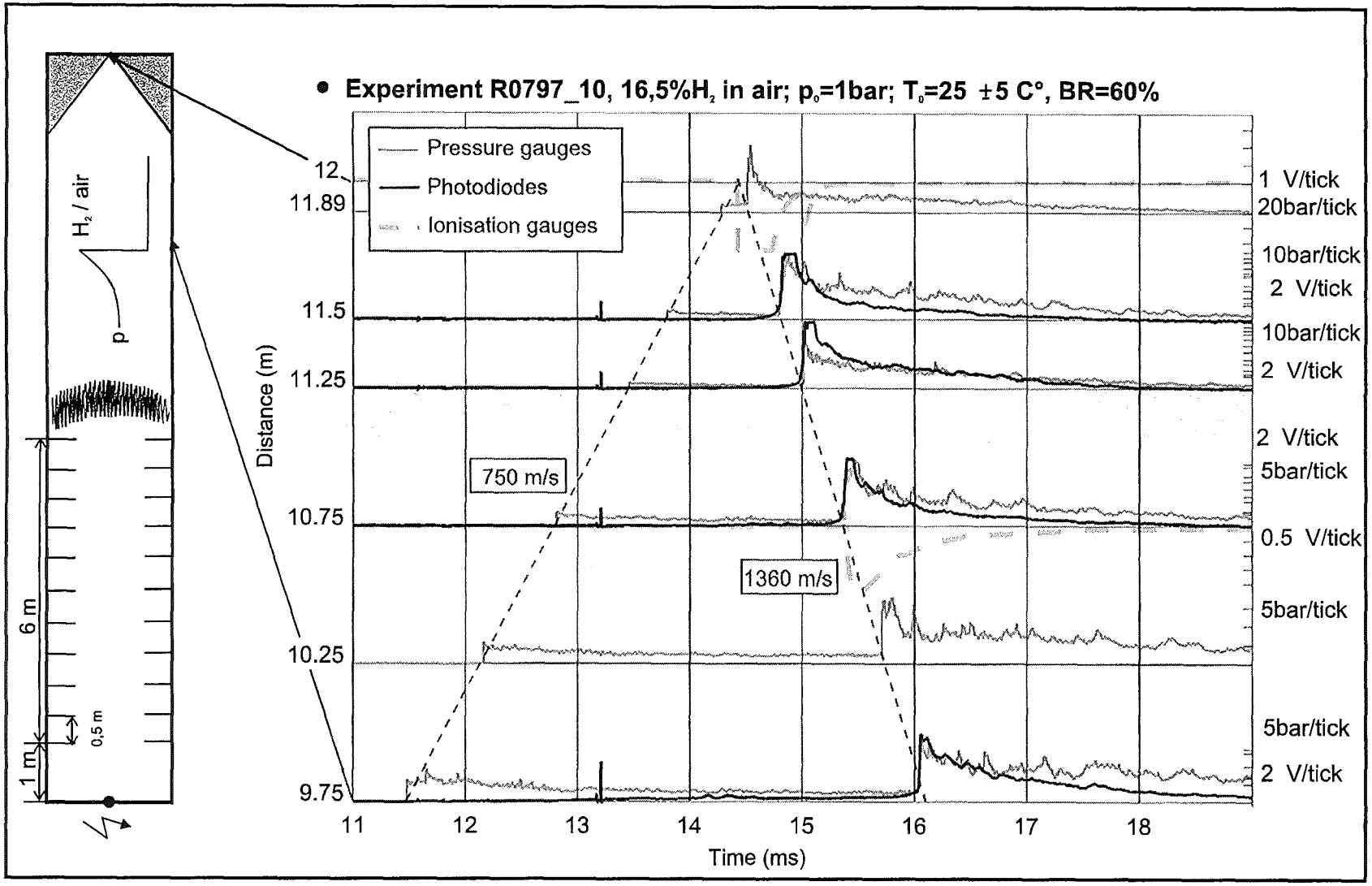

Fig.23: Measured pressure, photodiode and ionisation signals of experiments R0797_10. Enlarged part of the R-t diagram near the conus (9.75-12.0m)

4 Results of mode B-DDT experiments

All experiments performed on mode B-DDT are listed in Table 3. The experimental parameters of the 32 tests were the hydrogen concentration (9-20 % H_2) and the blockage ratio (BR=30 and 45 %). The "+" and "-"signs in the last column of the Table 3 indicate whether a DDT was observed ("+") or not ("-").

The measured pressure and light-signals of experiment R0498_02, which was a typical experiment without DDT, is shown in Figure 24. This experiment was performed with a blockage ratio of 30 % and a hydrogen concentration of 11 % in air. The photodiode signals show that the flame velocity is slow in the beginning (<100 m/s). It accelerates up 450 m/s towards the end of the tube but clearly stays below the quasi-detonation velocity. The pressure signals obtained in this experiment also indicate a rather slow combustion because at first only a smooth pressure increase is observed when the flame passes the pressure transducers. The pressure level rises towards the end of the tube, but stays well below typical detonation pressures.

If this experiment is compared with experiment R0498_13, which used a higher hydrogen concentration in air (13.5 %) but an unchanged blockage ratio, a completely different sequence of events is observed (Fig.25). In this experiment there is again an initial slow acceleration phase in which the flame front velocity reaches 250 m/s, but it then accelerates very fast up to 600 m/s (at the 5 m location), and finally reaches up to 1500 m/s (near the 8.5 m location). This velocity is close to that of a stable CJ-detonation. The pressure signals also show, after an initial acceleration phase, from 8 m on a shock-type pressure history, which is typical for a quasi-detonation. Another indication for detonation is the close coupling of the pressure and light fronts, which agreed after DDT within a few µs. Figures 24 and 25 were plotted on the same time scale to allow a direct visual comparison of the flame acceleration and terminal flame speed. The relatively small increase in the hydrogen concentration from 11 to 13.5% caused a reduction in the total combustion time of almost a factor of 3.

The flame trajectories of the experiments with 12, 15, 16.5 and 20 % hydrogen in air for a blockage ratio of 30 and 45 % are shown in Figure 26. The numbers in Figure

26 indicate the local flame velocity, which was determined from the arrival time of the flame between adjacent photodiodes. Note the different time scales used for different H_2 concentrations. The experiments with 12 % hydrogen in air show a much longer extended slow acceleration phase (0-5 m) than the experiments with a higher

Table 3: Experiments performed on prototypic mode B-DDT in fully obstructed combustion tube.

Experiment	BR	H_2%	DDT observed
R0498_00	30	11	-
R0498_01	30	11	-
R0498_02	30	11	-
R0498_03	30	12	+
R0498_04	30	12	+
R0498_05	30	12	+
R0498_06	30	10	-
R0498_07	30	10	-
R0498_08	30	15	+
R0498_09	30	15	+
R0498_10	30	20	+
R0498_11	30	16,5	+
R0498_12	30	15	+
R0498_13	30	13,5	+
R0498_14	30	13,5	+
R0498_15	30	9	-
R0498_16	30	9	-
R0498_17	45	11	-
R0498_18	45	11	-
R0498_19	45	12	+
R0498_20	45	15	+
R0498_21	45	20	+
R0498_22	45	10	-
R0498_23	45	9	-
R0498_24	45	16,5	+
R0498_25	45	14	+
R0498_26	45	16	+
R0498_27	45	18	+
R0498_28	45	10	-
R0498_29	45	10	-
R0498_30	45	20	+
R0498_31	45	16,5	+

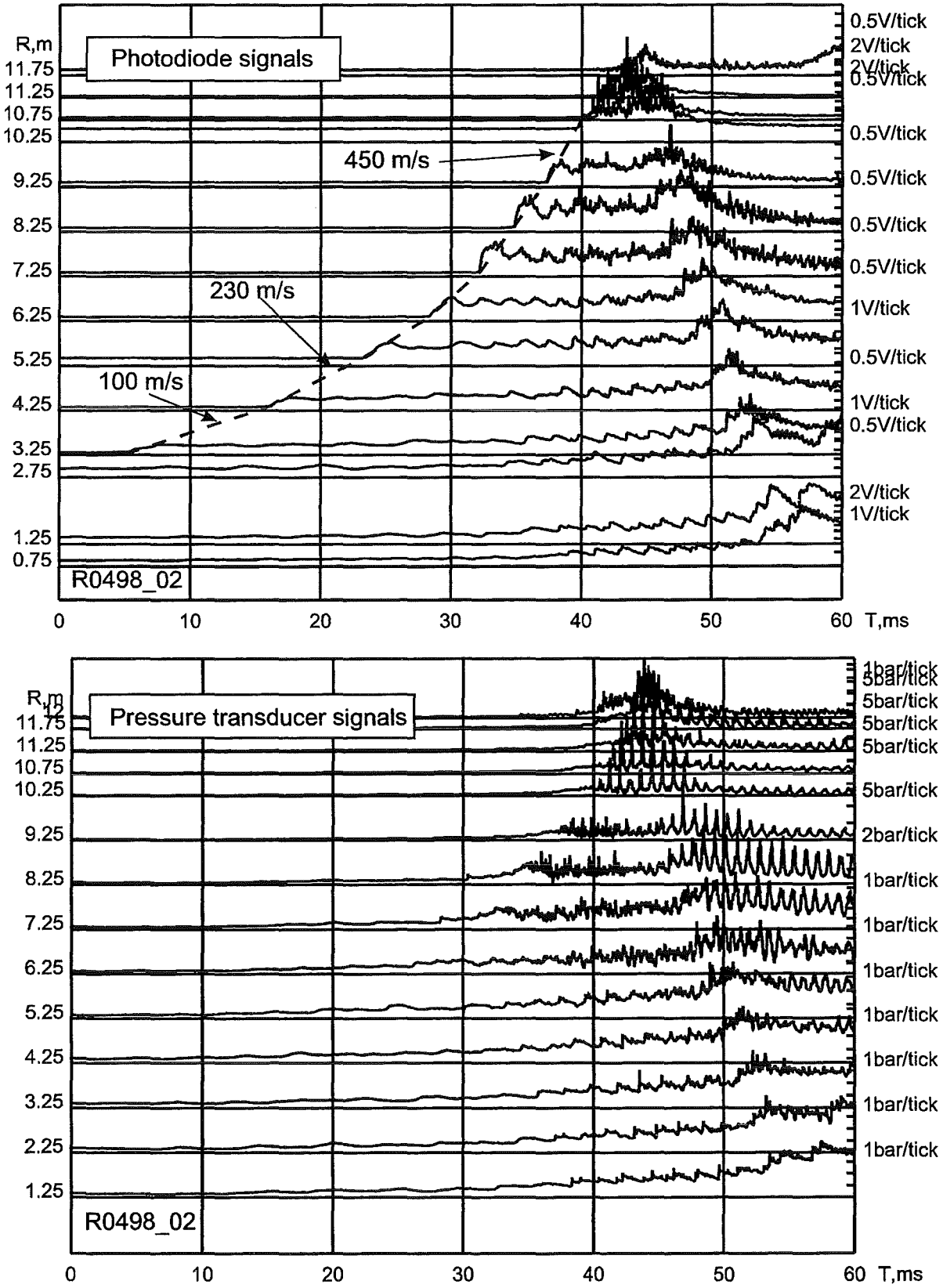

Fig. 24: Experiment on mode B-DDT. Photodiode and pressure signals show that no DDT occurred with 11 % H_2 in air.

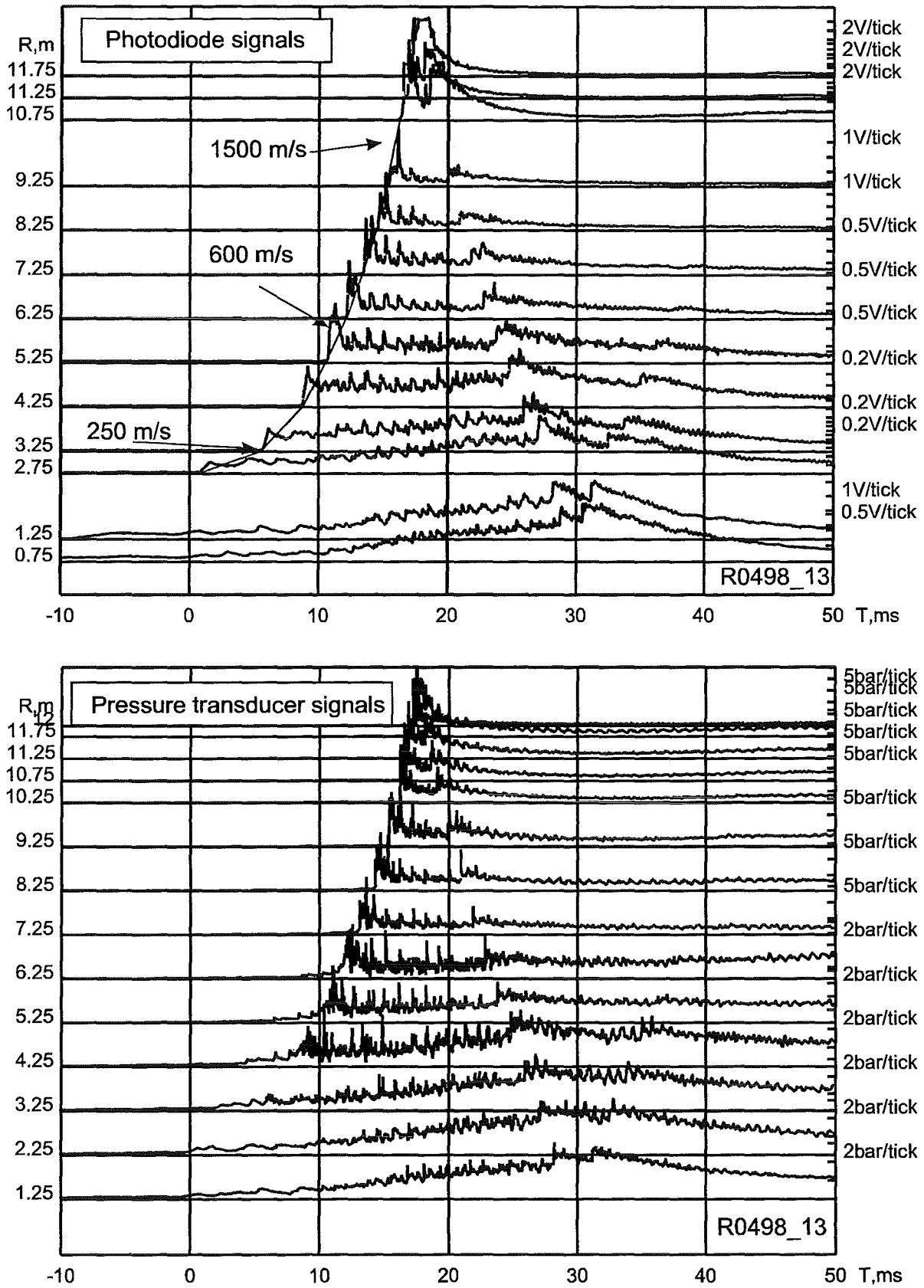

Fig. 25: Experiment on mode B-DDT. With 13.5 % H_2 in air a fast flame acceleration and DDT was detected by photodiodes and pressure transducers.

hydrogen concentration (0-2.5 m). A comparison of the measured local flame velocities in experiments with different hydrogen concentrations, shows that the experiments with 12 % hydrogen reach lower maximum velocities than those with a higher hydrogen concentration. These velocities are much smaller than the theoretical CJ- detonation velocity. For 15, 16.5 and 20 % hydrogen the corresponding CJ-velocities are reached, although in different distances from the ignition point. In the present test facility DDT was observed for more than 13.5 % hydrogen in air.

In addition to the flame velocities the occurrence of DDT can be confirmed from the recorded pressure and light signals. The light and pressure signals of the experiment with 12 % (R0498_5), shown in Figure 27, and the signals of the experiment with 16.5 % (R0498_11) shown in Figure 28, were analysed in more detail.
A comparison of the two cases shows first of all, that the experiment with 16.5 % hydrogen reaches much higher pressures than the experiment with 12 % hydrogen (bottom part of Figures 27 and 28). Furthermore it is observable that in the experiment with 16.5 % hydrogen the flame front catches up with the shock and couples to it at a distance of about 5-6 m from the ignition point (top of Fig.28). This is also the point, where the pressure profile changes from a slowly rising combustion pressure to a shock-like detonation pressure. Also the corresponding x-t-diagram in Fig.26 (bottom, left) shows at this location a sudden acceleration from 900 m/s up to 1500 m/s. This velocity remains approximately constant to the end of the tube, and corresponds to the CJ-detonation velocity. In the experiment with 12 % hydrogen no coupling of light and pressure is observed (Fig.27). The pressure profiles show a shape which typical for a chocked flow deflagration. This leads to the result, that for this kind of tube configuration a transition from deflagration to detonation can be observed and located for concentrations >13.5 % hydrogen in air. The transition locations were found for 15 % hydrogen at 7m , for 16.5 % hydrogen at 6 m, and for 20 % hydrogen at 3.5 m from the point of ignition.

Comparison of the experiments with a different BR but constant hydrogen concentration shows the same point of transition for 16.5 and 20% H_2, however the maximum velocities of the experiments with 30 % BR are slightly higher than with

45 % BR. At 15% hydrogen DDT occurred with 30% BR, but not with 45% BR. A longer tube may have permitted DDT also with 45% BR. Compared to the 30 % BR, the increase to 45 % BR produces a faster initial flame acceleration (more turbulence) but on the other hand only permits lower terminal flame speeds (increased flow resistance).

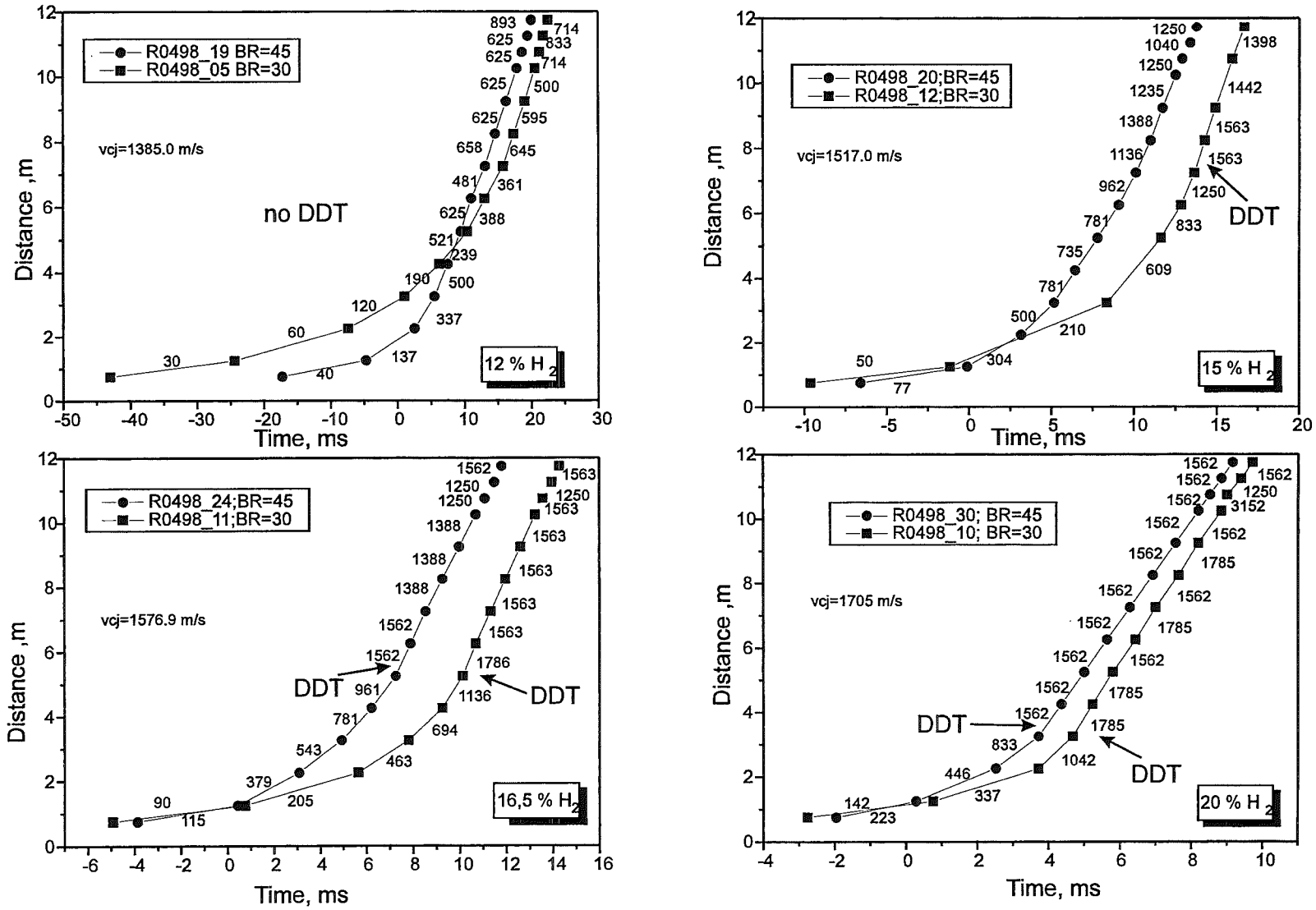

Fig. 26: Measured flame trajectories and local flame speeds in mode B-DDT experiments.

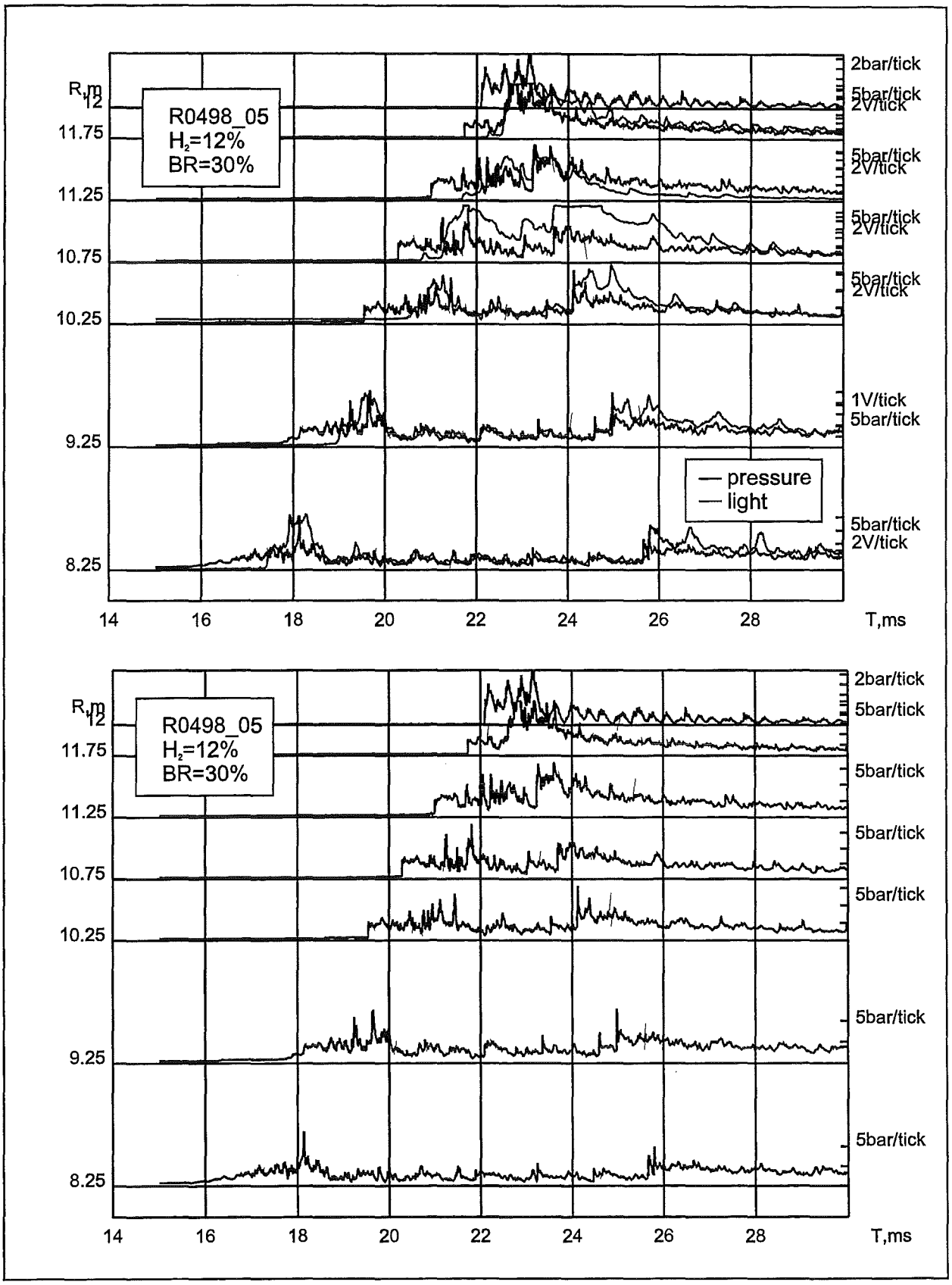

Fig.27: Pressure and light signals in case of an experiment without DDT. Top: no coupling of pressure and flame front. Bottom: deflagration type pressure amplitudes and profiles.

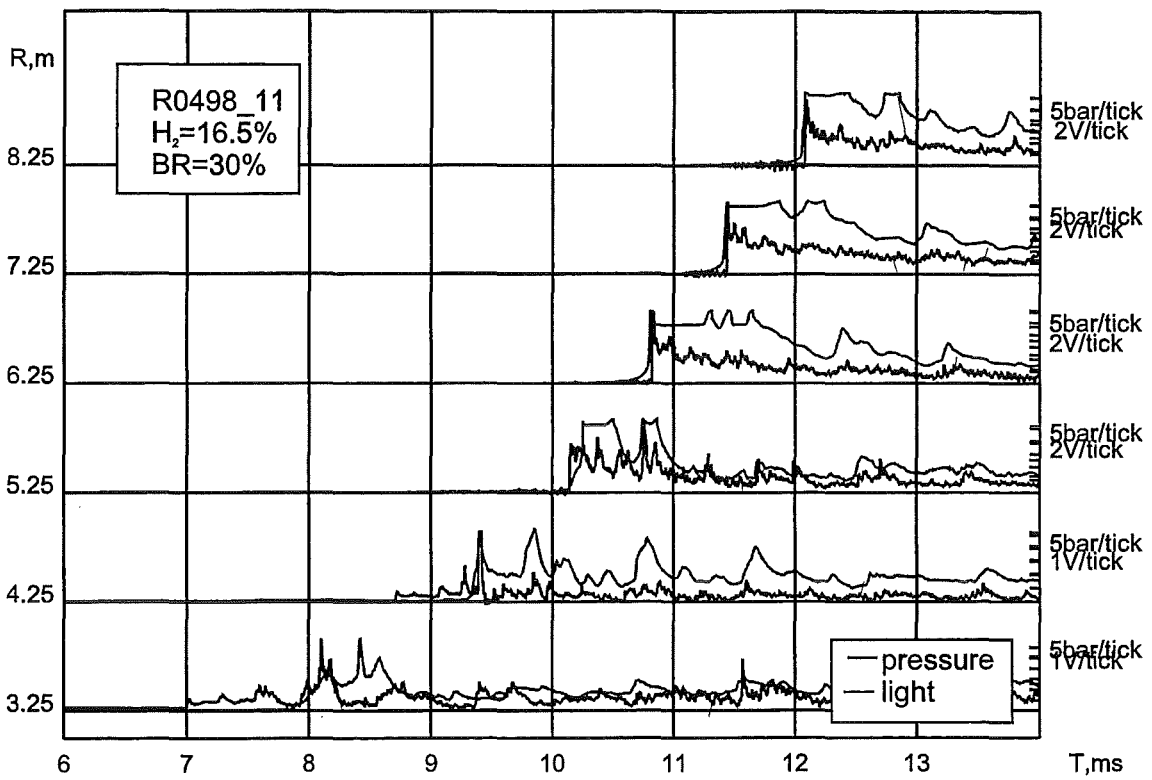

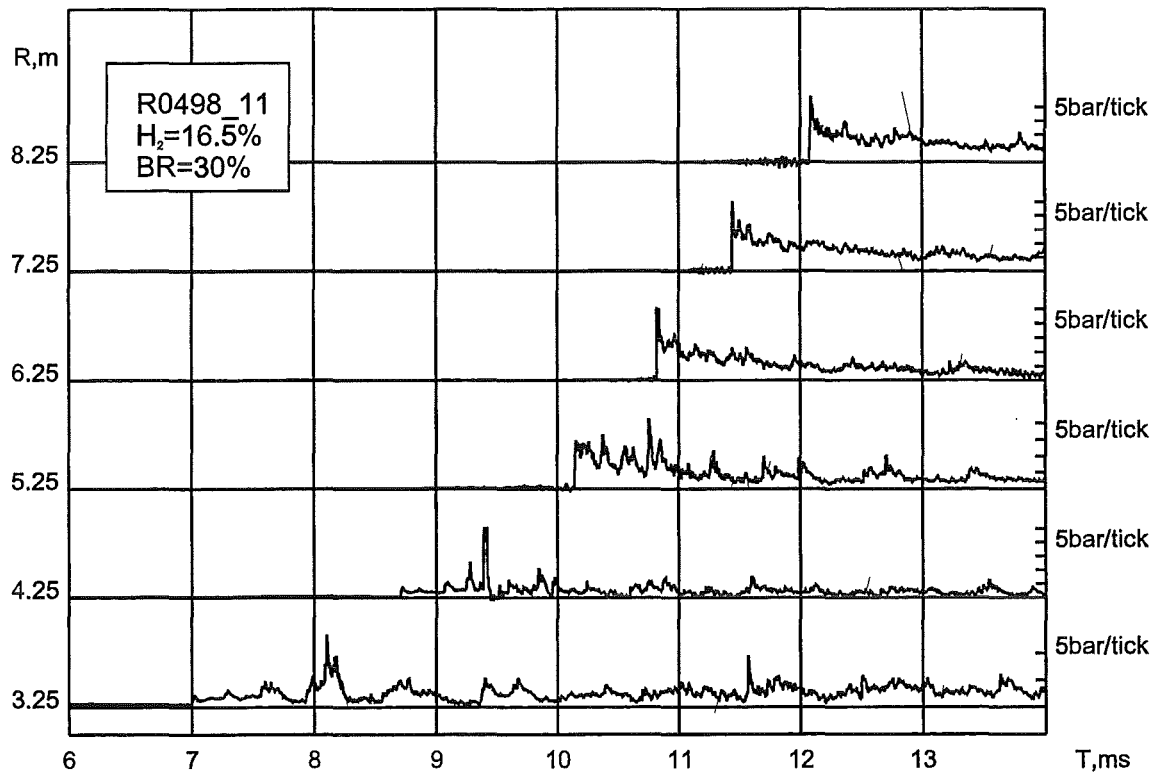

Fig.28: Pressure and light signals in case of an experiment with DDT by mode B. Top: coupling of shock and flame front between the 5 and 6 m positions. Bottom: change from deflagration-like to detonation like pressure amplitudes and shapes.

References

[1] Gelfand B.E., Khomik S.V., Investigation of Hydrogen + Air Fast Flame Propagation and DDT in Tube with Multidimensional Endplates, Report Russian Academy of Sciences, Moscow (1998)

[2] Gelfand B.E., Khomik S.V., Polenov A.N., DDT Experiments with Focusing of H_2 + Air Blast Waves, Report Russian Academy of Sciences, Moscow (1997)

Acknowledgement

An important part of the idealized mode A-DDT experiments was performed jointly with Prof. B. Gelfand and his co-workers during a stay in May 1998. Their experimental and theoretical contributions are highly appreciated.

VII. Validation of COM3D code for fast turbulent H_2-air-steam combustion

(A. Kotchourko, W. Breitung, A. Veser, INR)

Zusammenfassung

Die Entwicklung von einfacheren Modellen zur Beschreibung turbulenter Verbrennungsvorgänge gewinnt an Bedeutung, wenn es um kürzere Rechenzeiten geht. Bei der Wahl des Modells müssen Kosten und mögliche Nutzen gegeneinander abgewogen werden. Zu den wichtigsten Fragestellungen gehört die Abschätzung der Heftigkeit eines Explosionsprozesses unter vorgegebenen Parametern. Das Problem ist nicht, die turbulente Flammenausbreitung in allen Details vorherzusagen, sondern Vorhersagen zu treffen bezüglich der maximalen möglichen Flammengeschwindigkeiten und der Drücke, die während der Explosion entstehen können. Der einfachste und kostengünstigste Ansatz verbindet ein k-ε-Modell für die Turbulenz mit einem Eddy-brak-up-Modell (EBU-Modell) für die chemische Reaktionsrate. Dieser Ansatz hat sich bereits als leistungsfähig erwiesen, es zeigte sich aber auch, daß eine weitere Verbesserung und Erweiterung des EBU-Modells möglich und erforderlich ist. Die bestehenden Arbeiten hierzu werden fortgeführt mit dem Ziel, das Verbrennungsverhalten von mageren Wasserstoff-Luft-Gemischen systematisch zu untersuchen. Die Ergebnisse numerischer Verfahren werden mit experimentellen Daten verglichen.

0 Introduction

The development of simplified models for description of turbulent combustion is of interest when solutions are necessary in practical computing times. Depending on the purpose of the calculations, type of the flow, and the quantities to be predicted, a balance between cost and potential benefit can be achieved by a choice of the model. One of the important practical problems is an estimation of the severity of an explosion process under given geometrical configuration, scale, and composition of combustible mixture.

Such estimates are required for the containment of a nuclear power plant. The problem is not to predict details of the turbulent flame propagation under given initial conditions, but rather to give estimations for the maximum possible flame speeds and the corresponding level of overpressures which might be generated during explosion.

The most simple and least expensive modelling approach combines a k-ε model for turbulence and an eddy-break-up model for the chemistry. This approach has demonstrated its capabilities (e.g. Kotchourko et al., 1997a,b), and it has been shown that further improvement of the EBU model are possible and required. First estimates have shown that the extension of the EBU proposed by Said and Borghi (1988) appeared to be rather promising.

The present work is a continuation of the work cited above on the use of simple and extended EBU models with the aim to study systematically the combustion behaviour of lean hydrogen-air mixtures. The results of numerical modelling are compared with experimental data to define the space of mixture and geometrical parameters where the simple turbulent combustion models could be used for the calculation of accelerated flames in obstructed areas.

1 Experimental data

Two types of experiments were used for testing the turbulent combustion model. The first type of tests are carried out in a cylindrical combustion tube of 12 m length with an inner diameter equal to 35 cm, closed at both ends. The combustion tube was equipped with pressure transducers spaced 1 m apart along the total length of the tube. The instrumentation included also time-of-arrival diagnostics using infrared photodiodes spaced 1 m apart as well. Annular obstacles with circular openings were located inside the tube. In all tests the distance between obstacles was kept constant and equal to 50 cm. The experiments were performed for blockage ratios (BR) equal to 0.30, 0.45, 0.60 and 0.90, (a series with BR equal to 0.75 is underway) while the H_2 concentration was varied from 10% to 20%.

The second type of tests is experiments on hydrogen-air-steam combustion at large scale (Dorofeev et al., 1997a,b). The tests were made in the RUT 2200

facility – which is a large multi-compartment concrete building. This test series included hydrogen-air-steam combustion experiments with lean and nearly stoichiometric hydrogen concentration and steam contents ranging from 6 to 45%. Detailed data on different combustion modes including slow (shock-less) deflagration and fast turbulent deflagration are available.

Test	Average concentration H_2 % vol. (dry)	Average concentration H_2O % vol.	Maximum flame Speed, m/s
STH 6	29.9	45.0	780
STH 9	10.1	6.6	250

Data on turbulent flame propagation in a long channel of the facility (2.5 x 2.3 m in cross-section and ≈ 34.6 m long with obstacles, BR equal to 0.3) were simulated in the present work. Two experiments from this series STH 6 and STH 9 were chosen. These two experiments exhibit different modes of flame propagation involving different physical phenomena, appearing to be a good benchmark for the numerical model under consideration. In the first test a 'sonic' (or 'choking') deflagration regime was identified in which the maximum velocity achieved about 800m/s. In the second test a slow deflagration was observed with a maximum flame speed of about 250m/s. The initial conditions of the tests are listed in Table 1.

2 Result and discussion

Earlier simulations of the medium scale tests in the 12 m combustion tube showed that the classic EBU model has serious problems to describe the flame propagation at low velocities, which is connected with the assumption made in the EBU derivation. In the experiments with BR equal to 30% for the concentrations below 12% H_2 the model produces too fast flames for the reasonable values of the model constant C_{EBU}.

Simulations of the tube experiments with an extended Said-Borghi EBU model give remarkable results: all experiments are reproduced with a good accuracy using the same value of $C_{EBU} \approx 5\text{-}6$.

Figures 1 and 2 show measured and calculated pressure histories along the tube (0-12m). Important is that the numerical calculation also predicts the slow initial phase of the combustion process very well. A comparison of the measured and calculated light signals is given in Figures 3 and 4. The trajectory of the initially slow and then accelerating flame front is also well predicted. The calculated light signal is proportional to the black body radiation of all computational cells i, which are in the line of sight of a given photodiode ($\sim \sum_i \sigma T_i^4$)

For simulations of the large-scale tests in the RUT facility, the geometry of the facility was approximated by a cubic numerical grid with relatively high degree of detailization (cell size 12.5 cm; grid 44 x 50 x 501 $\approx$1.100.000 cells). In the calculations the gas compositions were supposed to be uniform with the values equal to their measured average values. Comparison of the simulation results with corresponding measured values demonstrates good agreement in the details of the process development: flame acceleration in the obstructed channel, and thereafter following propagation with the varying flame speed in other parts of the facility.

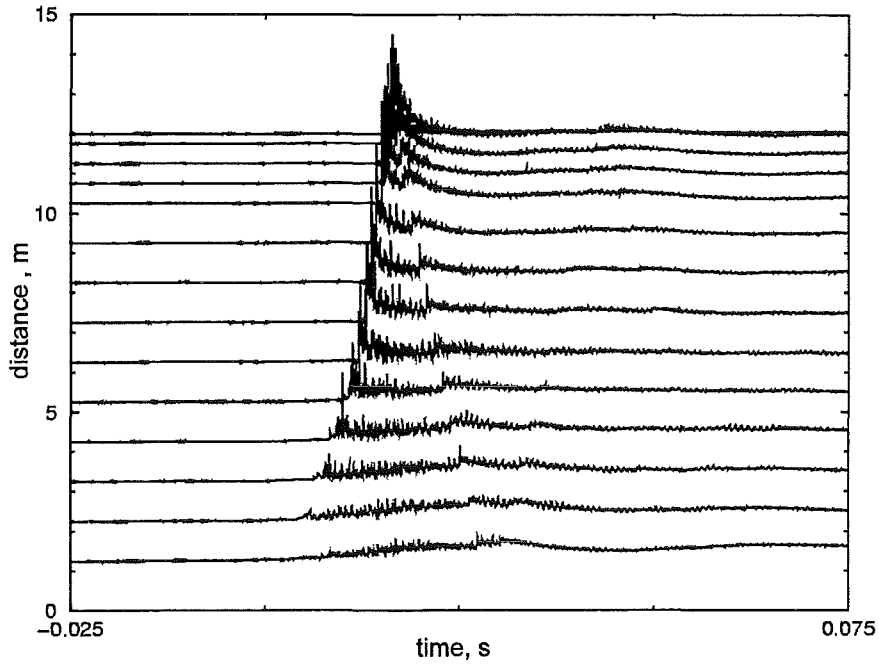

Fig.1: Measured pressure history in test R0498_09 (BR=30%, H_2=15% in air, p_0=1bar, T_0=298 bar)

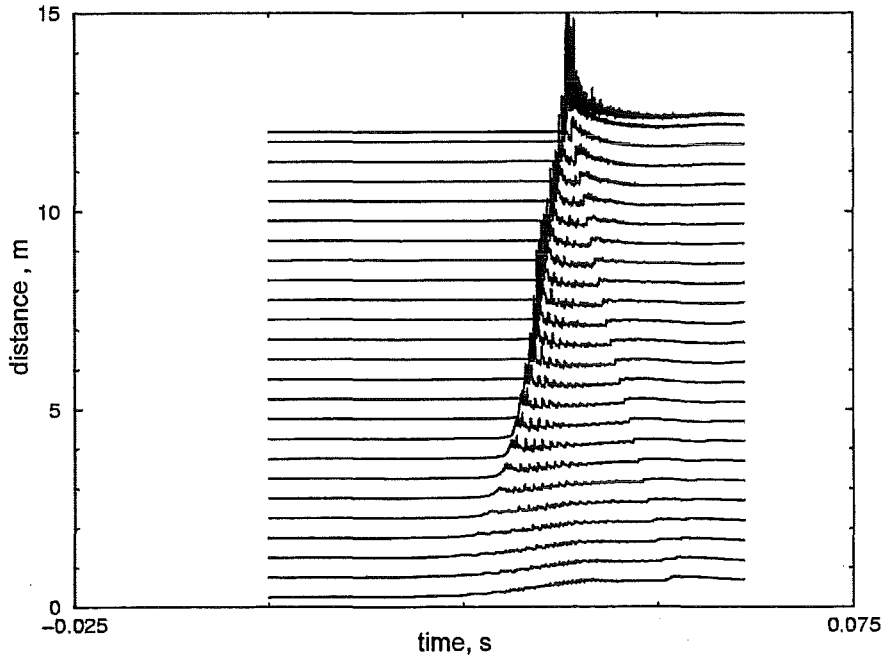

Fig.2: Calculated pressure history in test R0498_09 (BR=30%, H_2=15% in air, p_0=1bar, T_0=298 bar)

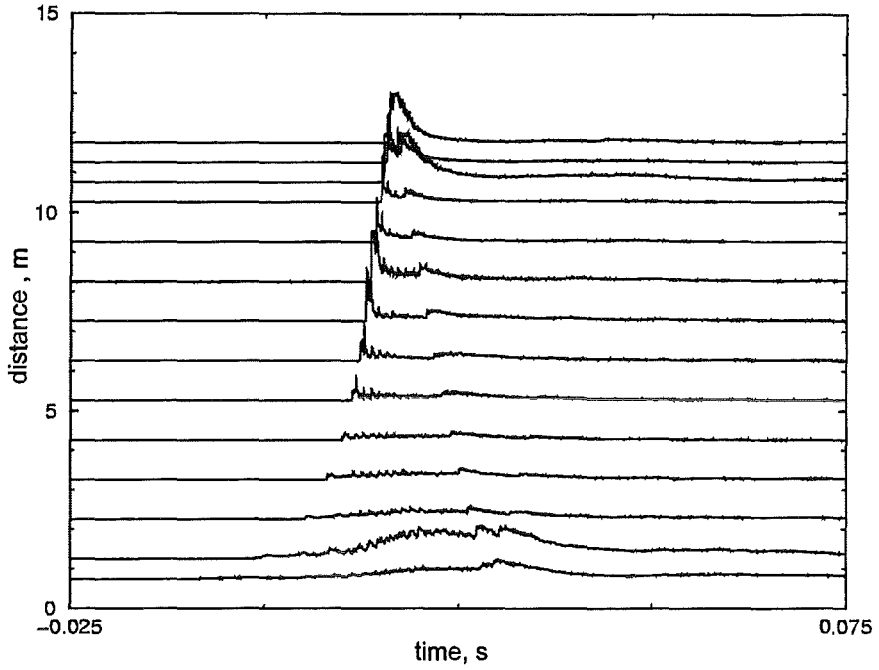

Fig.3: Measured light signals from collimated photodiodes in test R0498_09 (BR=30%, H_2=15% in air, p_0=1bar, T_0=298 bar)

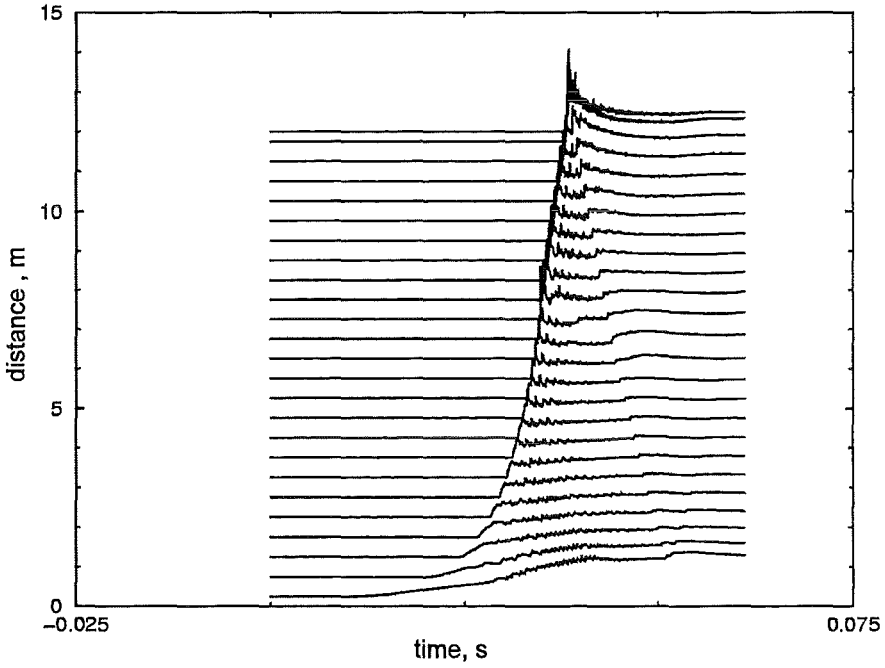

Fig.4: Calculated light signals for test R0498_09 (BR=30%, H_2=15% in air, p_0=1bar, T_0=298 bar)

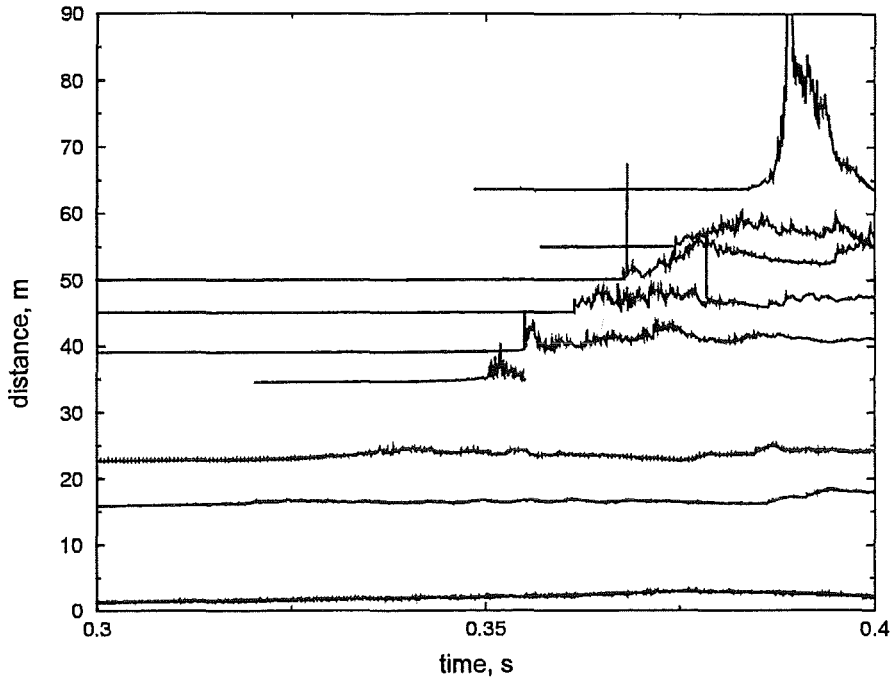

Fig.5: Measured pressure signals in RUT test STH6 (H_2=29.6%, steam=45%, T_0=383 bar)

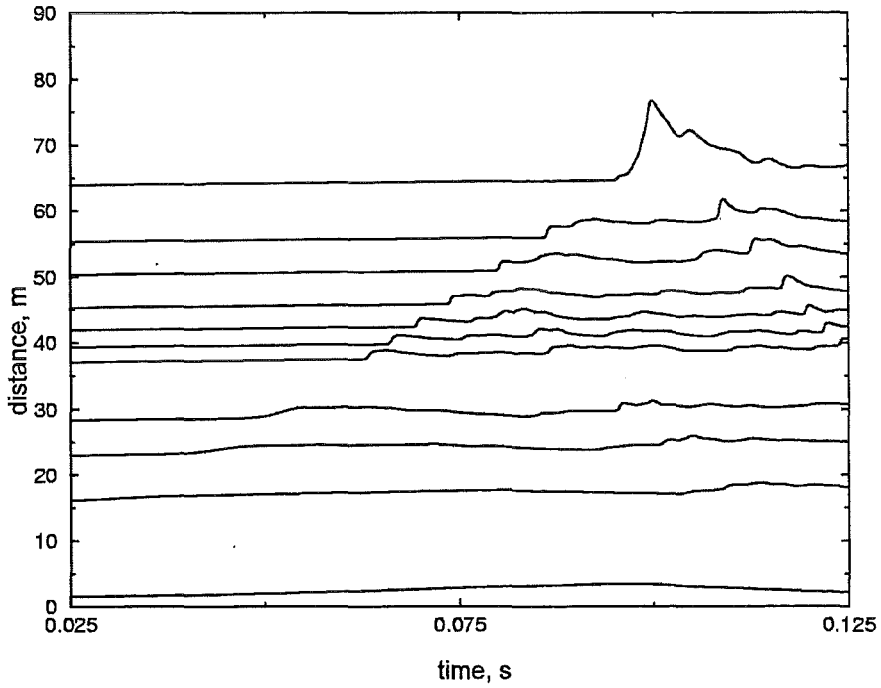

Fig.6: Calculated pressure signals in RUT test STH6 (H_2=29.6%, steam=45%, T_0=383 bar)

Figures 5 and 6 compare measured and calculated pressure histories for locations in the RUT facility up to 64m away from the point of ignition. The simulation was performed with $C_{EBU} = 6$, as in the previously shown case. The calculation reproduces the initial slow pressure rise with respect to amplitude and timing, the reflection of the wave from a vertical wall in RUT facility (at ≈ 50 m) and the reflections from the end wall (at ≈ 64m).

Comparison of experimental and calculated results demonstrated that the extended EBU model can be used for the channel-like combustion simulations for fast deflagrations before DDT, in the 'choking' regime and for medium-slow flames (above 100 m/s) for a range of mixture compositions and details of obstruction.

Compared to the standard EBU model, the extended version gives a possibility to use a fixed C_{EBU} constant for modelling of combustion processes in a wide range of propagation speeds and mixture reactivities. This allows predictive safety related calculations and estimates of severity of explosion processes. Such calculations are now able to describe the dominant effects of scale, geometrical configuration, and mixture composition on the resulting combustion mode and corresponding loads. The shown improvement of the eddy-break-up model broadens its applicability and makes it possible to use the extended model for the description of a relatively wide class of combustion processes having practical interest for containment simulations.

References

SB Dorofeev, VP Sidorov, W Breitung, and Kotchourko AS. Large-scale combustion tests in the RUT facility: Experimental study, numerical simulations as analysis on turbulent deflagrations and DDT. In transactions of 14th International Conference on Structural Mechanics in Reactor Technology, volume 10, pages 275-283, Lyon, France, 1997a.

SB Dorofeev, VP Sidorov, A Dvoinishnikov, A Denkevits, A Efimenko, and A Lelyakin. Large scale hydrogen-air-steam DDT experiments in the RUT

facility. Test series 1996. Report RRC KI 80-05/16, Russian Research Centre " Kurchatov Institute", 1997b.

A Kotchourko, W Breitung, A Veser, and SB Doroveev. Tube experiments and numerical simulation on turbulent hydrogen-air combustion. In Twenty Symp. (Int.) on Shock Waves, pages 3220. 1-3220.6, Great Keppel Island, Australia, 1997a.

AS Kotchourko, SB Dorofeev, W Breitung and Sidorov VP. Experiments and numerical simulation on turbulent hydrogen-air combustion in large enclosure. In 16th Int. Colloq. On the Dynamics of Explosions and Reactive Systems, University of Crakow, Poland, July 1997b.

R Said and R Borghi. A simulation with a cellular automation for turbulent combustion modelling. In 22th Symp. (Int.) on Combust., pages 569-577, University of Washington –Seattle, USA, 1988.

VIII. Implementation of a parallel AMR algorithm

(U. Bielert, B. Burgeth, R. Redlinger, INR)

Abstract

In order to improve the usability and efficiency of our present code generation (COM3D, DET3D, V3D) an adaptive grid refinement procedure (AMR) should be included into these codes. For the codes to run on actual hardware the codes must be parallelized to run on distributed memory architectures. Work was started to address both issues. First design decisions and performance estimates are presented.

Zusammenfassung

Um die Brauchbarkeit und die Effizienz der aktuellen Code-Generation (COM3D, DET3D, V3D) zu verbessern, sollten diese Codes mit einem Gitter-adaptionsverfahren (AMR) gekoppelt werden. Die Codes, die auf der derzeit verfügbaren Hardware laufen, müssen parallelisiert werden, damit sie auch auf verteilten Speicherarchitekturen laufen. Mit den Arbeiten zu diesen beiden Aufgabenstellungen wurde im Berichtszeitraum begonnen. Erste Ergebnisse werden hier vorgestellt.

1 Introduction

The present version of the and combustion codes at FZK (COM3D, DET3D, V3D) is optimized to execute on few processors of fast vector computers. All three codes use a structured grid with a fixed cell size. The calculation domain is limited to closed systems.

This leaves three main topics to be addressed in the further development of these codes.

- Implementation of open boundary conditions

  The implementation of inflow and outflow boundary conditions provides a means to solve problems in a sub domain of the containment. This modification is also useful in situations where only a solution in a relatively small domain is required and the external flow conditions are known (e.g. flow through a section of a pipe).
- Parallelization using message passing

  Further increases in the problem complexity requires large increases in computational power which can only be achieved through parallel processing. Future hardware will most likely combine multiple powerful processors (e.g. Cray T3E). To harvest the power of such hardware the codes must be adopted to the communication requirements of these machines.
- Adaptive grid refinement

  The high temporal and spatial resolution required by combustion modelling can realistically be only achieved by local grid refinement procedures. With such an AMR technique the computational domain is covered by a relatively large grid. Areas of interest (e.g. shocks, reaction zones) are covered by additional grids with finer resolution. The instationary character of the combustion problems requires adaptive techniques for these refinement procedures.

Since all three topics require modifications to the core data structures of the codes they should be addressed simultaneously. The purpose of the present work is to develop a frame work which incorporates an adaptive mesh refinement method into a parallel communication structure. This frame work should be capable to use either of the three codes as solver for the governing equations.

On a single grid without adaptive grid refinement parallelization can usually be achieved by a domain decomposition. The domain of interest is split into several parts that can be solved in parallel on different processors.

Communication between different blocks is only needed at the block boundaries and only once in every time step.

The implementation of an AMR strategy introduces a sequential solution strategy: the governing equations on a fine grid are solved after the solution on the underlying coarse grid is known (see Figure 1). This sequential approach is necessary since the coarse grid data is used as boundary condition for the fine grid. Computations on finer grids are performed with a smaller time step and thus more computations need to be performed on these grids.

The domain decomposition for a single grid with constant cell size is a static structure that is only created once. The communication pattern between processes is fixed and the efficiency of the decomposition algorithm is thus not important. In AMR the structure of the refined regions changes dynamically. This requires a data and communication structure that can adapt dynamically. As a consequence the distribution of the load to different processors must be controlled at the run time.

Computation costs for each block increase with number of cells in this block, communication costs increase with the number of surface cells of the block. Thus with increasing block size relative communication decreases but total computation time increases. As a result a optimum block size for a given computer architecture must be determined.

2 Parallelization strategies

2.1 Domain Decomposition

Without AMR parallelization can be achieved most easily by a domain decomposition. The domain of interest is simply divided into smaller sub domains and the problem is then solved for each sub domain in parallel on different processors. The different sub domains have to exchange boundary data after each time step.

Since the number of cells in the problem is constant the size of the sub domains can be determined to give the same computational effort in each sub

domain while minimizing communication between sub domains. This decomposition is constant during the whole simulation and a good load balance between processors can be determined in advance.
AMR can now be performed independently in each of the sub domains. As a result additional grids will be added and deleted in the different sub domains. As a result the computational effort varies widely between the different sub domains and also changes during the simulation. It is generally not possible to find a domain decomposition which balances the loads between the different processes during the whole simulation. This makes it necessary to change the domains at run time.
It must be noted that in the general case communication can occur between grids on all levels. To investigate the performance of this parallelization strategy we consider an example.

2.1.1 Example Problem with domain decomposition

In order to evaluate the parallel performance that can be expected from a domain decomposition we consider a simple example with the following parameters.

Coarse grid	40 x 50 x 50 = 100000 cells
all other grids	40 x 25 x 20 = 20000 cells
Initial configuration	1 block each on level 0, 1, 2, 3
Additional grids	2 on level 1, 3 on level 2 and 4 on level 3

This gives a total of 4 blocks and 160000 cells for the initial case and 13 blocks with 340000 cells after the refinement.
This example is schematically shown in Figure 2.
We now consider the number of cells each processor has to calculate in each time step as function of the number of available processes NPROCS.
The worst situation we can encounter is that all refined blocks fall within one sub domain. Thus the process for this sub domain has to perform 12 * 20000

+ 100000/NPROCS calculations while the other processes perform only 100000/NPROCS calculations.

In the best case all refine grids are distributed as well as possible over the different processors. This means that the fully loaded processes (here 3) perform 4*20000 + 100000/NPROCS calculations per time step and the additional processes perform 100000/NPROCS calculations.

Figure 3 shows the ratio between maximum and minimum cell numbers for these two configurations as function of available processors.

This figure indicates that even with load balancing a significant amount of CPU time is wasted for massive parallel applications. Such an approach can only utilize as many processors as there are separate regions that need refinement.

In Figure 3 we have neglected the communication between the different processes. If we assume that communication is only performed between level 0 blocks we can estimate the effort needed for communication. If we further assume that the sub domains have a cubic shape we can calculate the number of cells in one side face of a sub domain. Communication is proportional to this size with

$$C_1 * (100000/NPROCS)^{**}2/3$$

The total amount of data transferred between all blocks is

$$C_1 * (100000/NPROCS)^{**}2/3 * NPROCS$$

These functions are plotted in Figures 4 and 5 for our example. While the message size (given in number of cells) decreases with the number of sub domains the total amount of transferred data increases.

2.2 Ready queue

The strategy described so far can be thought of as a vertical partitioning of the stack of grids of different refinement levels. The approach of Colella and Crutchfield [colella3] can be thought of as a horizontal partitioning. Each patch or refined grid is thought of as an independent job that has to be executed. All these jobs are stored in a list. The available processors take a

job from the list, process that job, return the result and than fetch a new job from the list until no more jobs are left. As a result all the processors are busy as long as there are further jobs in the list. Only when the list is exhausted the processors have to wait until the last job terminates.
The procedure is depicted in Figure 6.
This parallelization strategy was implemented by Colella and Crutchfield on a Cray C-90 with shared memory and was tested for up to 16 processors.
Since there is no fixed correspondence between a grid and a processor all data must be available to all processors. This implementation depends on the shared memory architecture. For a MPI architecture each grid has to be transferred to a processor and back into some common memory.
The processors are busy as long as the list of jobs is not empty. Once the list is exhausted all processors have to wait for the last process to terminate. Obviously this wait state can only be neglected when the list of jobs contains much more entries than the number of available processors. Again this seems not appropriate for massively parallel applications.
Coming back to the example grid from section 2 we can at most use 13 processors. All others stay completely idle.

.2.3 Predescribed process structure

Another approach is to associate each patch or refined grid with a processor in advance. With this approach we have the opportunity to perform a domain decomposition and also a decomposition on different grid levels.
We can also reserve additional processors if we expect that additional grids will be generated during the calculation.
Since the grids reside on different processors, data that remain valid from one time step to the next can stay on that processor. There are fixed relationships between parent grids on coarse levels and their children grids on finer levels. Thus communication now takes place between the different processes rather than between a process and some master memory. This makes this approach more useful for distributed memory architectures.

Unfortunately the calculations on the different refinement levels are not independent. The solution of a coarse grid is needed for the boundary conditions on the next finer grid and the solution from the finer grid is needed as correction for the coarse level solution. As a result processes on different levels are inherently waiting for each other.

We can develop different variants of this procedure. We could reserve additional processors for certain grid levels to be used later. Or we could reserve a pool of processors which is then used for what ever grid level is required.

However the main disadvantage of this approach is that the different levels can not be processed in parallel.

Another problem exists if we have more grids than processors. This could be solved by starting several processes (one for each grid) on one processor. However this introduces additional overhead for context switches between these processors.

2.4 Patch based balancing

From the previous strategies we can deduce that we should have a structure where each process calculates approximately the same amount of cells on each refinement level as all other processors. Thus we divide the grid cells of one level in to a series of patches, were a patch is a set of cells that can be solved by the present single grid numerical method. These patches can then be distributed over the available processors and solved in parallel. All processors solve level 0 patches , communicate, switch to level 1 patches, communicate and so on. Since the load is balanced on each level all processors are busy almost all the time. As a consequence communication efficiency becomes important.

This procedure is shown in Figure 7. Patches calculated on the same processor are shaded in the same way. It seems that this approach is most promising and is chosen for further evaluation.

In order for this strategy to work the patches must be constructed carefully. If patches become to large it takes a long time to solve that patch. Thus the efficiency becomes very poor when the other processes do not have similar patches to solve. If small patches are used the number of patches increases and thus more communication is needed.
We can conclude that we need a sufficient number of patches to load all processes and that the size of the patches of the same level should not be too different.

3 Implementation of patch based approach

3.1 Manager worker concept

For the implementation of the algorithm we choose a manager worker concept (see Figure 8). The manager program is a process that takes care of the user interface and controls the program flow in all other process. This program also distributes the load on the other processes. Since no patches are solved on the manager process, computing resources are available to search for an optimal load distribution.
The solution of the numerical scheme is performed in worker programs. There can be as many workers as there are processors available. Each worker has a list of patches that are solved on that worker and a list of messages that are needed to solve these patches. During refinement each worker generates a list of new patches that should be created due to some refinement criteria. The lists of patches are processed by the manager program to find an optimal distribution of the new patches to the available processes.
The criteria used by the manager program to distribute the patches should take into account the load of the worker processes and also the locality of communication. It is much more efficient to solve a patch on a worker were the required initial and boundary data is already available. But this is only true when computational power is available.

3.2 Solution procedure for AMR

The AMR procedure requires to solve the patches of different refinement levels in a certain order as indicated in Figure 8. This sequence is best described as a recursive process as described in the following pseudo code.

```
make_step(int level) {
        for (i=0; i< refinement_ratio(level); i++) {
        for_all          // KeLP loop that executes in parallel for all patches on
                                 // this level
                advance(patch);  // execute numerical solver on a single patch
                refine(patch);   // refine data from this patch to next finer level
                                 // if necessary
                                 // this includes modifying the necessary movers
        end_for_all
        Mover_next;  // KeLP construct, that performs the necessary data
                     // transfer between processes. Data needed on the
                     // next level and that resides on the same processor is
                     // copied, data needed on other processors is sent
        make_step(level+1);          // recursion to next level
        update_solution;       // apply additional information from finer level
                               // to this level
        mover_same;            // exchange data with peers
        }
        Mover_prev;  // Return data after the full time step of previous level;
}
```

3.3 Communication between patches

For the regular communication between patches the concept of a mover was taken from the KeLP project.

A mover is the routine that performs the regular data transfer between different patches. The mover is executed on each worker and manages all

data transfer for this worker. That is one call to mover transfers the data for all patches of that worker between the given refinement levels. Since the mover is executed on each worker it also serves to synchronize the different workers.

There are three different types of messages between patches which are exchanged at different stages of the program execution.

- mover(n, n+1)

  Before the AMR algorithm recourses to the next finer level the boundary conditions on the refined level must be updated. These boundary conditions are the solution on the coarse grid at the end of the present time step. Since the finer level grid has to perform several time steps the boundary conditions for the flow solver are interpolated between the coarse patch data and the boundary data. As a consequence the boundary data must be stored separately in the refined patch. Note that only the two outer layers of the refined region must be transferred to the child patch.

- mover(n, n)

  Once a time step is performed patches of the same level must exchange data at common interfaces. The boundary region of one patch is updated with the solution from the interior of the other patch. Note that the region to be exchanged is always two cells thick. Note also that this transfer is symmetrical. Data is transferred in both directions requiring two messages.

- mover(n, n-1)

  After a coarse time step has evolved on the fine grid the solution must be transferred back to the coarse grid. Here only the interior of the patch data is transferred back.

4 Performance estimates for patch based approach

AMR permits a shift of the computational effort from the less interesting parts of the computational domain towards the more important ones. This means that we use a coarse grid with cell size D_0 and several refined grids (cell size D_j) instead of a single grid (cell size d) alone. D_0 and D_j are practical parameters to estimate the effect of AMR. They depend upon many other quantities which are listed in the table below.

4.1 List of parameters

dim	space dimension
f	refinement ratio
n	total number of refinement levels
p	ratio $\frac{\text{cells to be refined}}{\text{all cells}}$ in each level
Vol	Volume of the containment
D_j	length of the edge of a cell in refinement level $j \in \mathbb{N}$
d_0	length of the edge of a cell if no AMR is employed
ΔT_0 // Δt_0	time step a cell with//without AMR
P_0	performance of the CPU
P_k	performance of a CPU with k processors
$\Delta\tau$	computational time unit
Δt_j	time step of the physical time at the j-th refinement level
α	ratio $\frac{\text{parallelizable part of program}}{\text{complete program}}$
β	ratio $\frac{\text{time spent on communication}}{\text{total computation time}}$ in a multiprocessor computer
k	number of processors
~	a tilde indicates influence of parallelization

4.2 Formulae

Without AMR we can handle cells of size

$$d = \left(\frac{Vol}{P_0 \cdot \Delta\tau} \right)^{\frac{1}{dim}} . \tag{3}$$

Using AMR entails an increase in the cell size of the underlying coarse grid

$$D_0 = d \cdot F_{AMR}, \tag{4}$$

where the factor F_{AMR} is given by

$$F_{AMR} := \left(\frac{\left(p \cdot f^{1+dim}\right)^{n+1} - 1}{p \cdot f^{1+dim} - 1} \right)^{\frac{1}{dim}}$$

This factor measures the effect of AMR. Coarsening in some areas allows an concentration in other parts of the computational region:

$$D_j = \frac{D_0}{f^j}$$

is the cell size at refinement level j. The effect is displayed in Figure 9.

AMR allows larger physical time steps

Since the physical time step Δt_0 is proportional to D_0 (CFL-condition) we can conclude

$$\frac{\Delta T_0}{\Delta t_0} = F_{AMR} .$$

This implies that AMR allows to proceed faster in physical time compared to CFD-calculations without AMR. When using AMR F_{AMR}-times more physical time can be covered with a given computational time than without exploiting AMR.

But we have to be aware of the fact that a small T_0, and hence small D_0, is preferable since it gives way to a more accurate resolution of the complex geometry in a containment than a larger D_0 does. Also some important physical phenomena might not be captured in their early stage of evolution by a calculation based on a coarse mesh size D_0 that is too large.

4.3 Influence of Parallelization

According to Amdahl's Law (2] the increase in computer performance can be described roughly by a factor

$$F_{Amdahl} := \frac{1}{\alpha + \beta \cdot k + \frac{(1-\alpha-\beta)}{k}}$$

Thus parallelization can be incorporated in the above context by replacing P_0 by $P_k = P_0 \cdot F_{Amdahl}$ in (3) and hence indirectly in (4). We obtain

$$\tilde{D}_0 = \left(\frac{Vol}{p_0 \cdot \Delta\tau}\right)^{\frac{1}{dim}} \cdot F_{AMR} \cdot (F_{Amdahl})^{\frac{-1}{dim}} \tag{5}$$

$$= \left(\frac{Vol}{P_0 \cdot \Delta\tau}\right)^{\frac{1}{dim}} \cdot \left(\frac{(p \cdot f^{1+dim})^{n+1} - 1}{p \cdot f^{1+dim} - 1}\right)^{\frac{1}{dim}} \cdot \left(\alpha + \beta \cdot k + \frac{(1-\alpha-\beta}{k}\right)^{\frac{1}{dim}} \tag{6}$$

for the cell size of the coarse grid and

$$\tilde{D}_n = \frac{\tilde{D}_n}{f^n}$$

in case of the finest grid.

Unfortunately the parameters α and β have to be estimated in the current state of development.

It should be emphasized that the parameters α and β are quantities that do not directly depend upon the size of a problem that has to be treated numerically. By their definition they are intrinsic parameters describing to what degree the code can be parallelized. So it cannot be expected a priori that it pays off to employ the more processors the larger the computational task is. It is a consequence of Amdahl's law that, depending on α and β, there is a optimal number of processors to obtain best performance results. This can be seen from Figure10. In this figure based upon (5,6) we assume $\alpha = 0.2$, $\beta = 0.01$, dim = 3, f = 2, n = 3, p = 0,1, Vol = 10^5 [m^3], $\Delta\tau = 1$.

5 Status of the development

In order to test the concept of the patch based approach a test program has been developed that allows to test the communication between manager and worker. The core AMR sequences are also included into the program. However the test program operates without actually solving the fluid dynamic equations.

This test program will allow to examine the influence of the problem parameters (e.g. patch size, number of patches, number of workers, α, β) on the efficiency of the calculation. This program will also allow to examine different load balancing strategies.

Base AMR algorithms have been implemented and will be linked to V3D to allow first evaluations of the grid refinement accuracy.

References

[1] P. Colella and W.Y. Crutchfield. A parallel adaptive mesh refinement algorithm on the c-90. http://www.nersc.gov/research/CCSE/publications/wyc/wyc94a/paper.html, 1996.

[2] J. Schwabe. Team-probleme. c't magazin für computer technik, Heft 26:80-81, 1998.

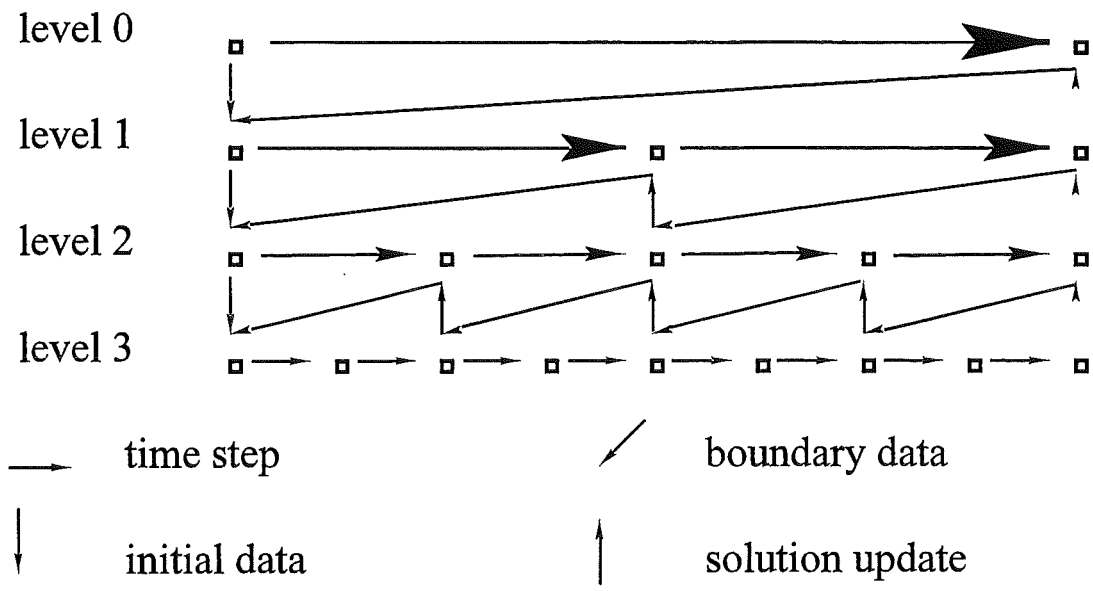

Fig.1: Communication pattern between refinement levels

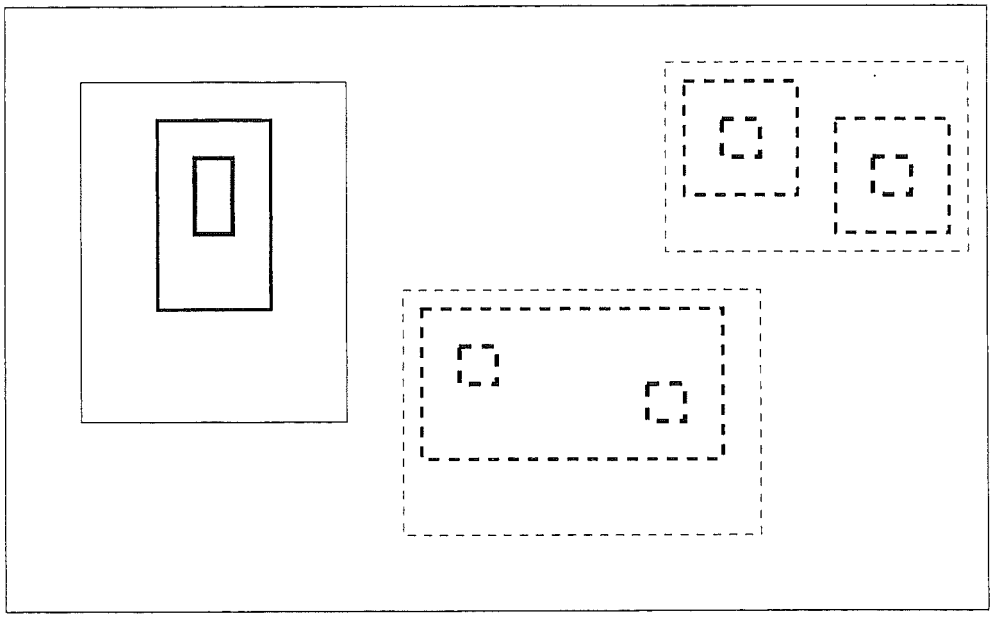

Fig.2: Example: 4 initial blocks (solid) and 9 additional blocks added during calculation (dashed)

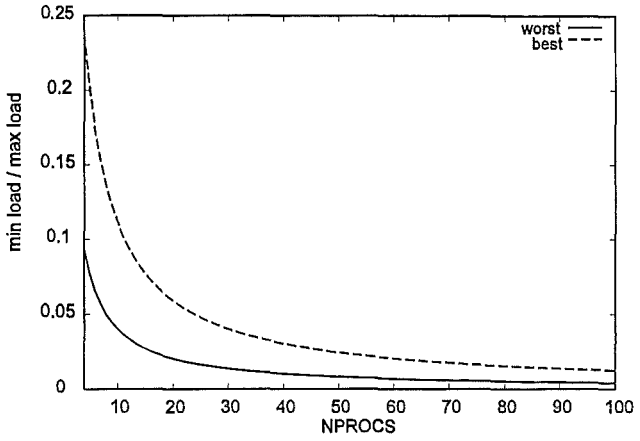

Fig.3: Ratio of processor loads as function of processor number

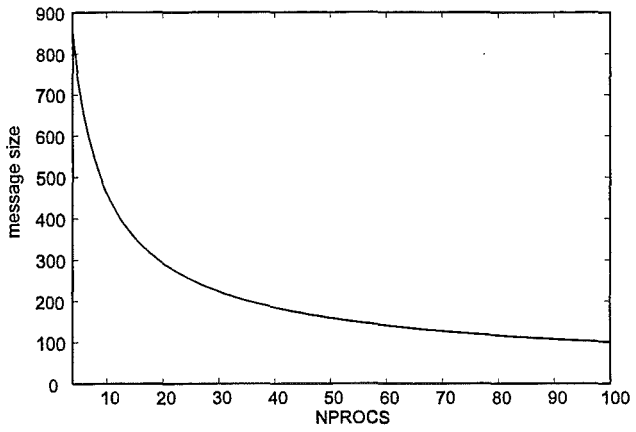

Fig.4: Communication per side of block

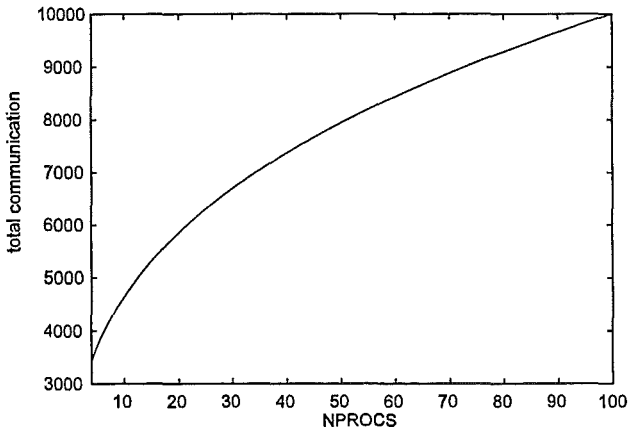

Fig.5: Total communication over all blocks

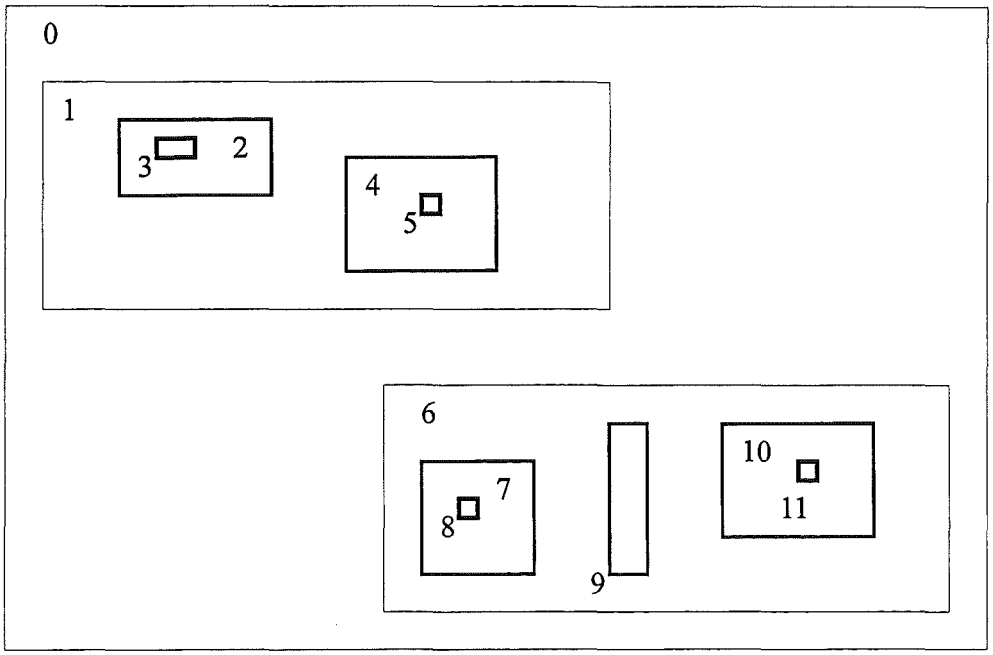

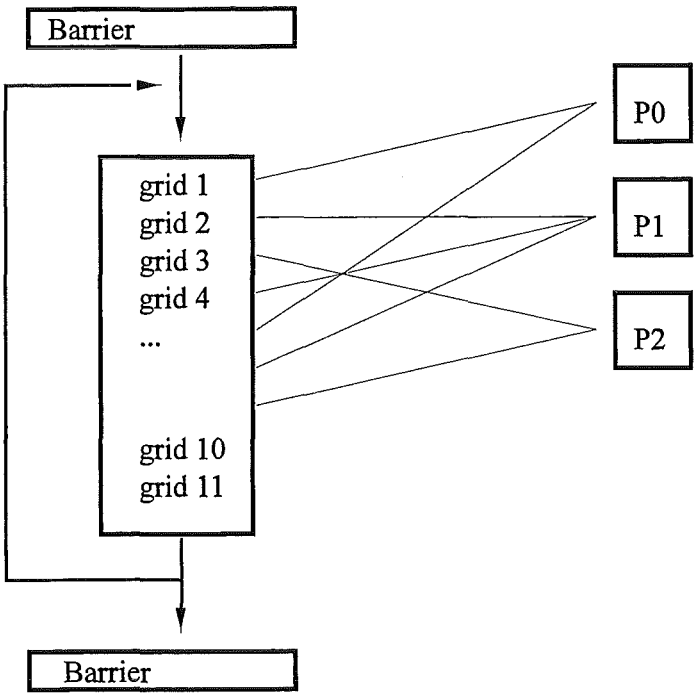

Fig. 6: Parallelization using ready queue

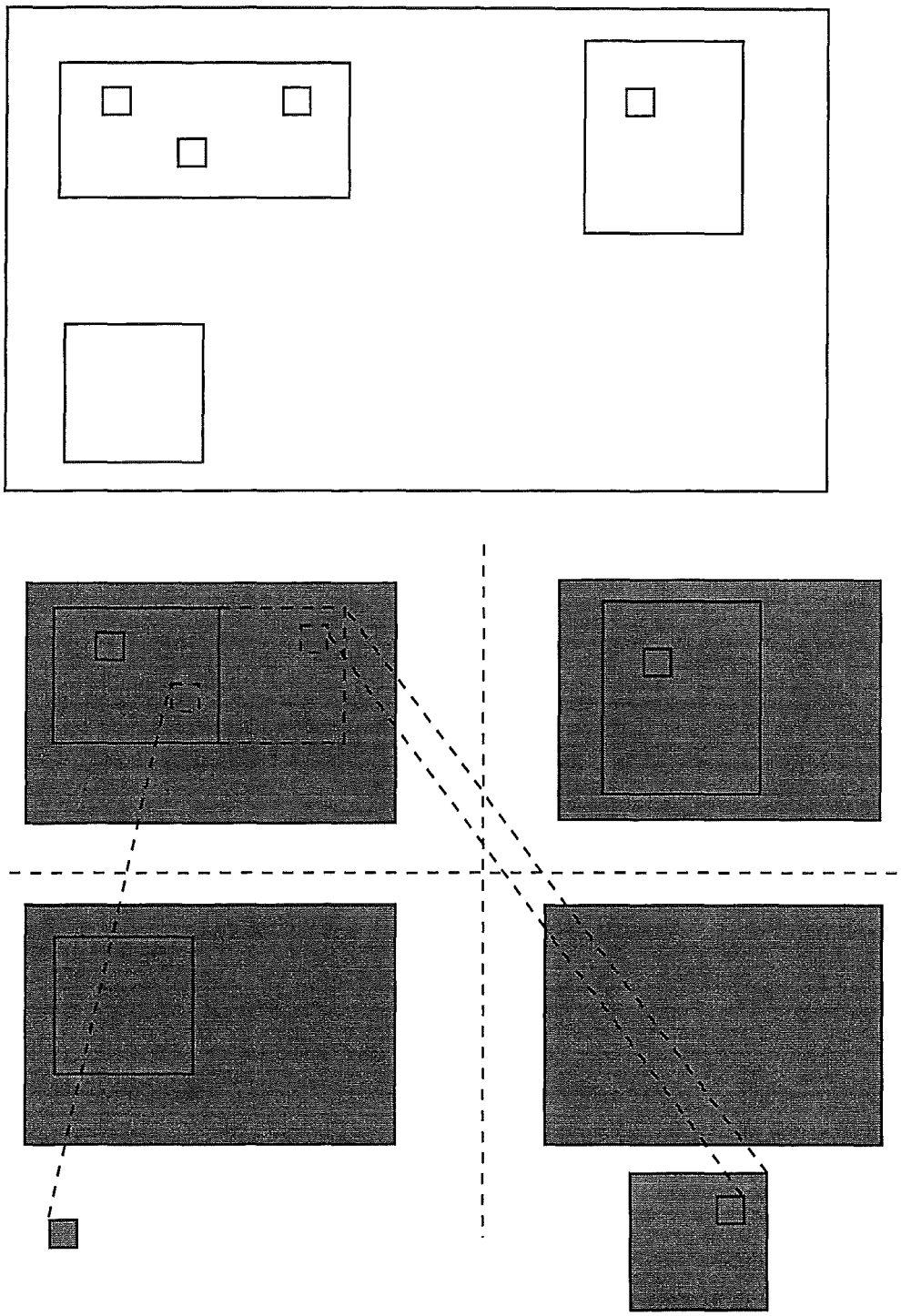

Fig.7: Example grid and distribution on different processes

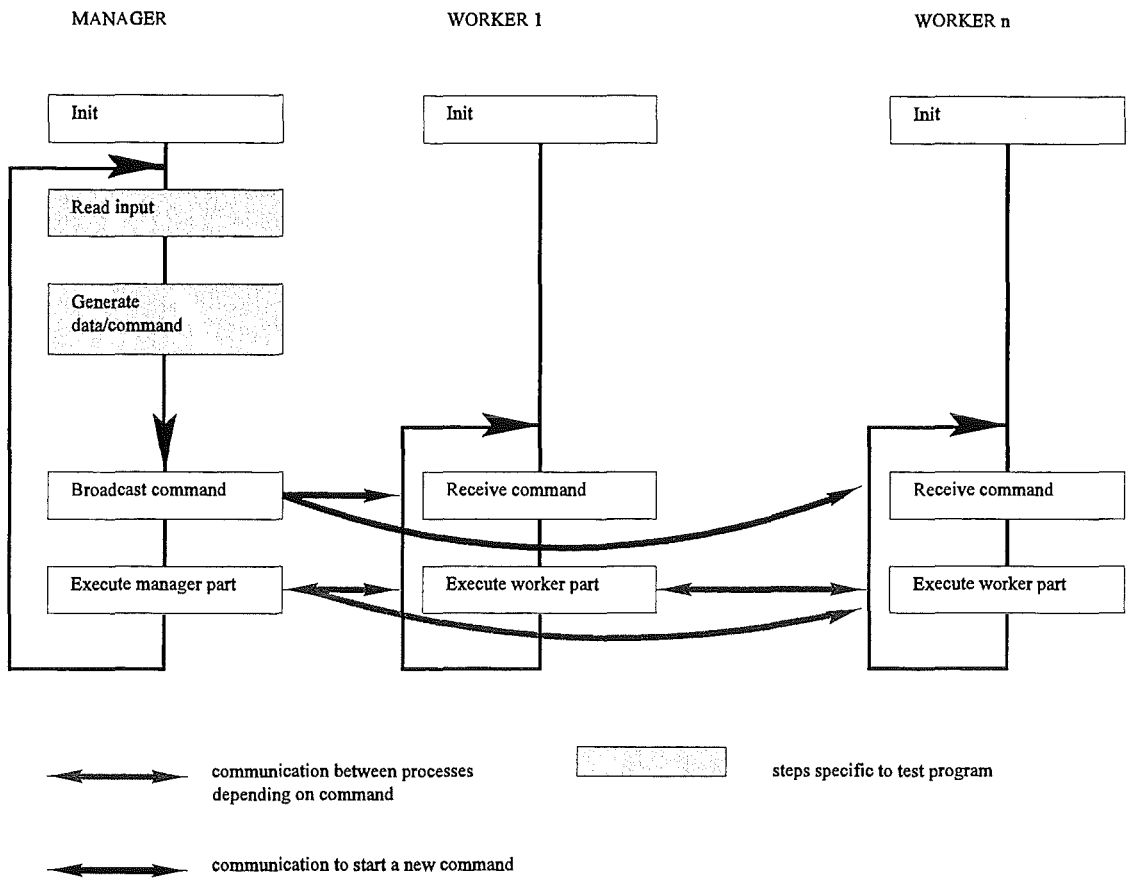

Fig.8: Messages between Manager and Workers

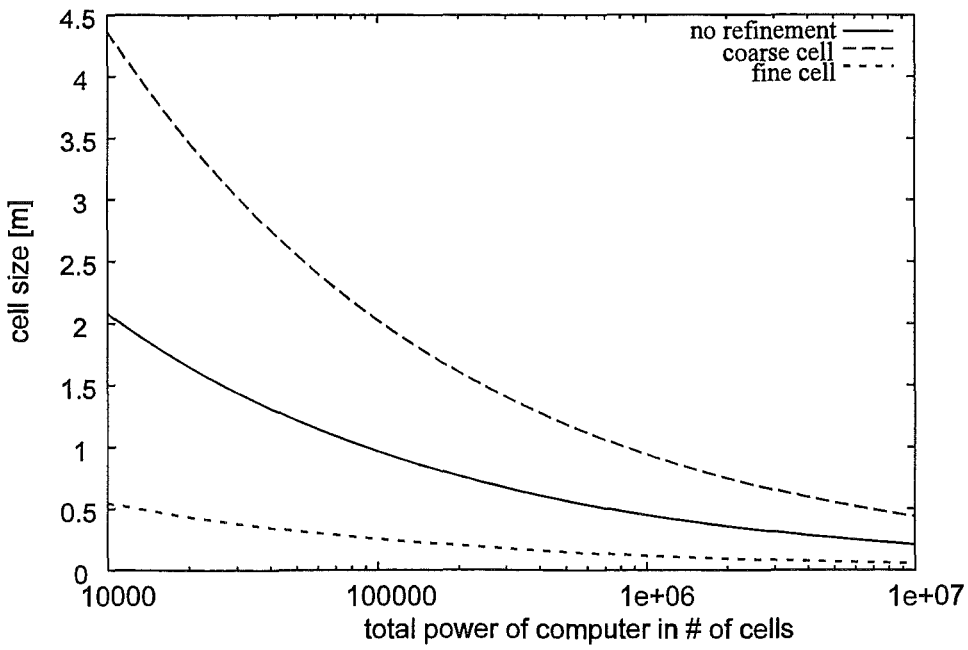

Fig.9: The effect of AMR on possible cell size as function of available computer power

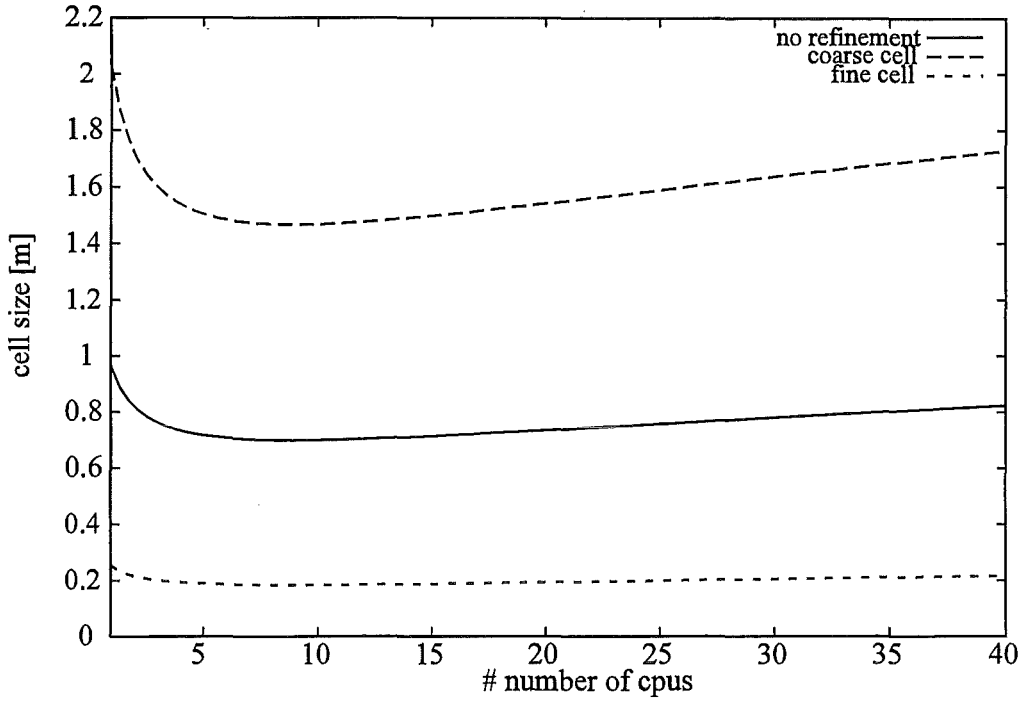

Fig. 10: The influence of parallelization on obtainable cell size.

IX. Summary of EPR analyses

(W. Breitung, INR)

Zusammenfassung

In den vorangegangenen Abschnitten wurden die Arbeiten auf den Gebieten Codeentwicklung, Versuche und Codeverifikation beschrieben. In diesem Abschnitt werden die für die EPR-Designstudien durchgeführten Rechnungen zu Wasserstoffverteilung, Verbrennung und Lasten zusammengefaßt.
Wichtigstes Ziel der EPR-Wasserstoffarbeiten ist die Entwicklung eines Wasserstoffkontrollsystems, das den hohen Sicherheitsanforderungen für zukünftige LWRs genügt. Es muß nachgewiesen werden, daß bei einem schweren Unfall die maximale vorhandene Wasserstoffmenge im Containment zurückbehalten werden kann, ohne daß das Containment beschädigt wird. Im Prinzip hat man beim Wasserstoffmanagement zwei Möglichkeiten. Erstens kann ein neues, stärkeres Containment entworfen werden, das den maximalen möglichen Lasten standhält, zweitens können bei einem bestehenden Containmentdesign Wasserstoffkontrollsysteme zur Reduzierung der Lasten eingebaut werden. Das EPR-Projekt basiert auf dem zweiten Ansatz. Gegenwärtig werden dabei zwei mögliche Optionen (Rekobinatoren und/oder Zünder) untersucht.
Im Berichtszeitraum wurde das zuvor entwickelte schrittweise Analyseverfahren zur Wasserstoffkontrolle im EPR angewandt. Hierzu wurden zahlreiche Rechnungen durchgeführt.

0 Introduction

The preceeding chapters have described the work in the fields of code development, experiments, and code verification. This chapter summarizes the application calculations which have been done on hydrogen distribution, combustion and loads for EPR design studies.

The central goal of the EPR hydrogen work is to derive hydrogen control systems which fulfil the RSK-GPR safety requirements for future LWR's, namely to show that the maximum amount of hydrogen which could be present during a severe accident, can be confined without loss of containment integrity. In principle, there are two possibilities for hydrogen management. The first one is to increase the strength of the new containment design to the maximum possible combustion load. The second, more evolutionary way, is to use an existing containment design and install hydrogen control systems for load reduction, so that the original design load (LOCA) will not be exceeded. The EPR project follows the second approach for which at present two major options exist:

1. LOCA design for 6.5 bar static pressure with catalytic recombiners.
2. LOCA design for 6.5 bar pressure static with recombiners and igniters.

The advantage of the first option would be smaller costs for installations, maintenance and testing, as well as wider acceptance in the German and French industry and licensing authorities. However larger combustion loads must be expected than for the second option. To quantify and compare the loads of both options, a number of 3-d CFD simulations were performed.

During the first and second EVU-Siemens-FZK contract FZK has developed through extensive experimental and theoretical investigations a stepwise analysis procedure which was applied in 1998 to hydrogen control in the EPR. This complete and self-consistent analysis procedure consist of the following steps (Fig. 1):

- definition of the hydrogen control system in the EPR,
- selection of an accident scenario,
- calculation of hydrogen, steam and fission product sources released from the primary system,
- simulation of distribution and mixing in the containment,
- definition of time and location of the first ignition,
- computation of the initial slow deflagration,

- application of flame acceleration and DDT criteria to determine the type of further combustion mode and modelling
  a.) slow deflagration, V3D-code
  b.) fast turbulent deflagration, COM3D-code
  c.) detonation, DET3D-code,
- resulting local, global, dynamic or quasi-static loads, depending on scale and velocity of combustion process,
- structural response and evaluation of containment integrity.

Using this systematic approach a number of calculations were performed for the EPR (Table 1). The arrangement of the columns in Table 1 follows the above given sequence of analysis steps. For a complete overview also the IPSN/GRS lumped parameter calculations with RALOC are included.

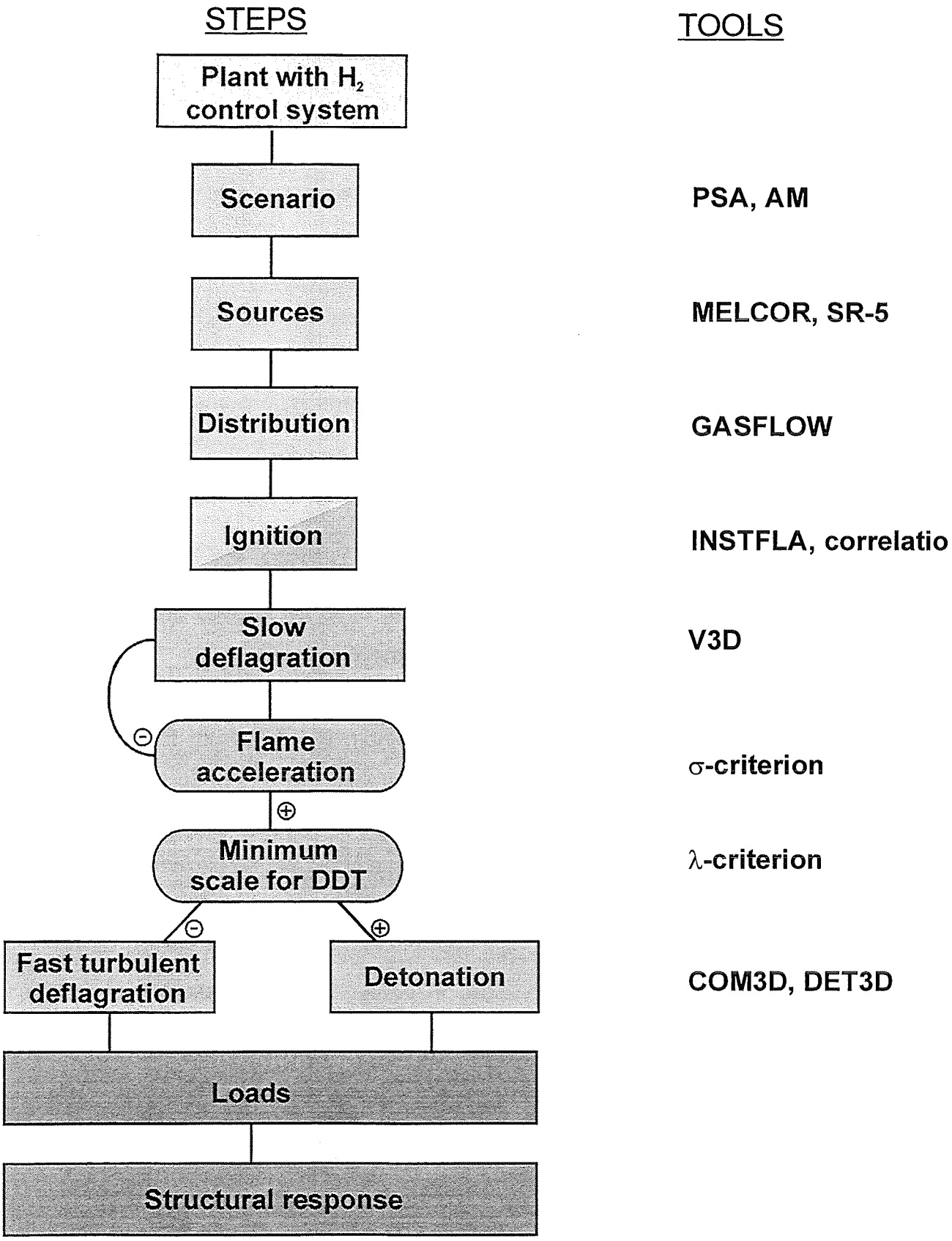

Fig. 1: Stepwise analysis procedure developed and used for the systematic and self-consistent investigation of EPR hydrogen control systems.

1 Base case

First a base case analysis without any hydrogen mitigation was performed for the LOOP scenario to quantify the hydrogen situation in the EPR and to establish a baseline against which the need for and the effectiveness of hydrogen control measures can be compared.

The source terms were calculated with MAAP by Framatome. Siemens developed the GASFLOW input file for the EPR distribution calculation. FZK extensively tested and improved the EPR input file and supervised the production run on the fast VPP vector processor of FZK. Several modifications and extensions of the GASFLOW code were specifically made for the EPR analysis, e.g. generalised source directions, description of the decay heat in the gas phase (Xe), and a more flexible code control scheme.
Further optimizations of numerical algorithms in GASFLOW with respect to degree of vectorization resulted in a speed-up of a factor of six on the VPP-400, allowing now the analysis of several hours problem time within one week.

In this dry LOOP scenario with only little steam injection from the IRWST water evaporation, a hydrogen stratification in the containment was predicted, ranging from about 9 to 13 % H_2 (Fig.2). According to the criterion based on detonation cell size scaling (7λ-rule), a large detonation in the dome could not be excluded. The analysis was made for 90.0000m^3 of free containment volume. This base case analysis with a detailed 3-d containment model confirmed the development of hydrogen stratification in dry scenarios which was observed in earlier EPR calculations with a coarser computational grid (12000 cells, [1]). The possibility of stratified containment atmospheres, together with the relatively large ratio of Zircalloy mass (core size) to free containment volume in the EPR design, makes additional hydrogen control measures mandatory.

Mitigation	Scenario	Sources	Distribution	Combustion	Results
• none	• LOOP	• 900 kg H_2, MAAP a) no steam (worst case) b) ≤ 17 kg/s steam location IRWST	• GASFLOW-2 (Siemens/FZK) 130.000 nodes 3-d	---	• potential for global detonation (12-14% H_2 dry in dome)
• recombiners (44, 4 in dome) layout adaption	• LOOP	• 900 kg H_2, MAAP ≤ 17 kg/s steam	• GASFLOW-2 (Siemens /FZK)	• COM3D (FZK) • DET3D (FZK)	• ≤ 720 kg H_2 potential for fast deflagr. and local detonation • 8.5 bar, 50 ms locally • 20 bar, 10 ms locally
(40)		• 920 kg H_2 ≤ 6 kg H_2/s	• RALOC (IPSN/GRS) 81 zones 0-d	---	• >10 % H_2 in nearly all zones, detonation potential in lower zones
(44, 4 in dome) layout adaption	• SB-LOCA	• location + 6.1m , RCP2 820 kg H_2+ steam, MAAP ≤ 0.46 kg H_2/s	• GASFLOW-2 (Siemens/FZK)	• GASFLOW-2 (FZK, Siemens)	• ≤ 565 kg H_2 in cont. • 560 kg H_2 burn by self- ignition in recos
(40)		• 860 + 500 kg H_2 ≤ 0.7 kg H_2/s	• RALOC (IPSN/GRS)	---	• > 10 % H_2 in 12 zones, ≤ 23 min
(62)	• LB-LOCA	• surge line break 535+515 kg H_2, MAAP < 0.6 kg H_2/s	• RALOC (IPSN/GRS)	---	• ≤ 400 kg H_2 in cont. • ≥ 10 % H_2 in lower zones
• recombiners with igniters (44&4) layout adaption	• LOOP	• 900 kg H_2 steam from IRWST location IRWST	• GASFLOW-2 (Siemens/ FZK) 4 igniters at IRWST exits	• GASFLOW-2 (FZK, Siemens)	• ≤ 110 kg H_2 in containment, standing flames

Table 1 : Summary calculations for EPR hydrogen control in severe accidents

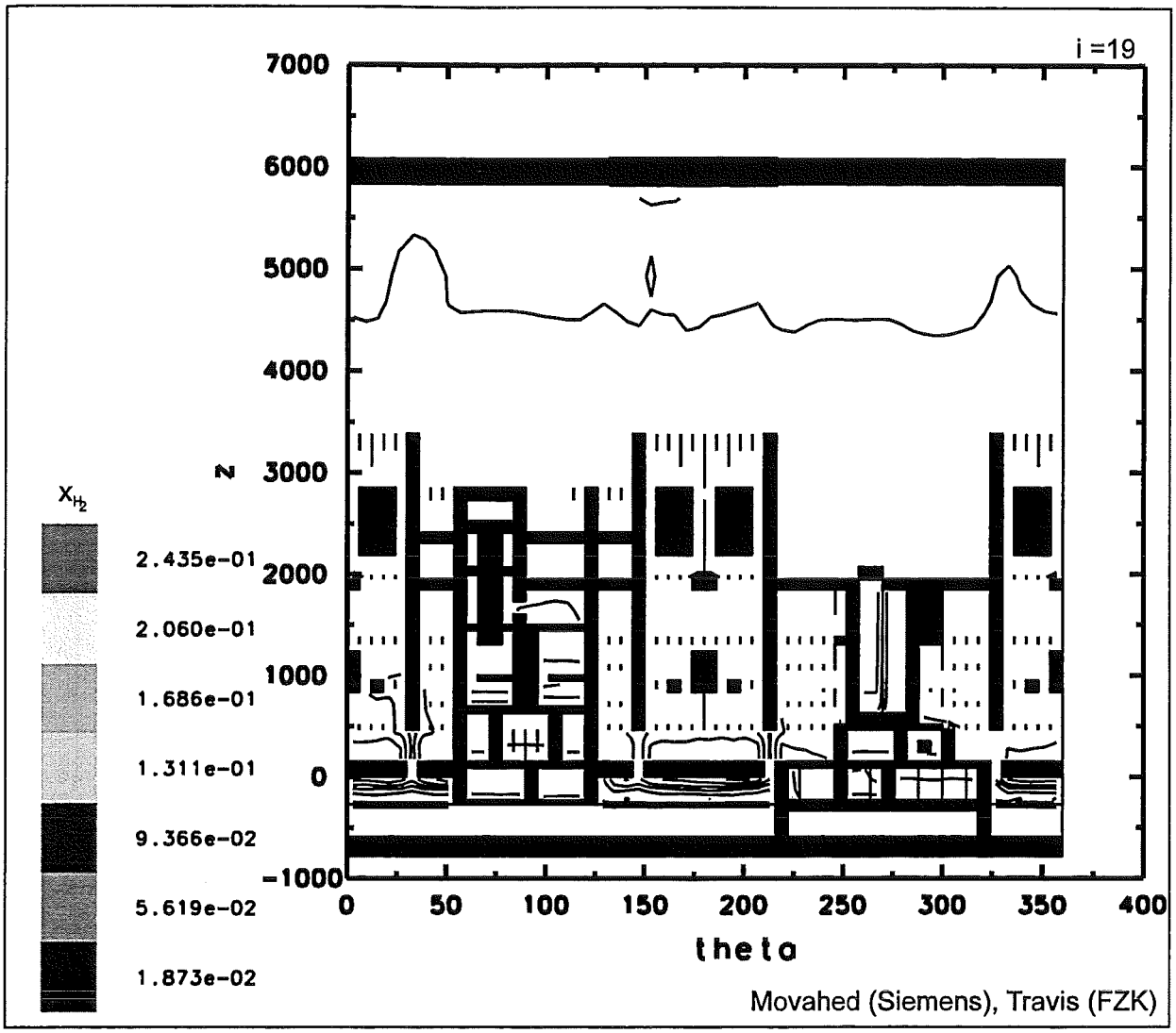

Fig. 2: GASFLOW prediction for hydrogen distribution in LOOP scenario, MAAP sources, base case without hydrogen mitigation. The dry release leads to a stratified containment atmosphere (≈ 9 to 13 % H_2).

2 Mitigation with recombiners

2.1 Distribution

The next step in the analysis of hydrogen behaviour was to include 44 catalytic recombiners of the Siemens design. Siemens selected the recombiner positions. The implementation in the GASFLOW model was done jointly by Siemens and FZK. Test and production calculations were done on the FZK VPP-400 computer (second line in Table 1). The same hydrogen and steam source was used as before (LOOP scenario, MAAP sources).

The inclusion of this recombiner arrangement lead to a decrease of the maximum H_2-inventory in the containment from previously ≈ 900 kg to about 720 kg hydrogen. This relatively small decrease is due to the fact that the H_2-release during the first heat-up of the core is much faster (10 min) than the recombiner removal time (1-2 h). The relatively slow acting recombiners, which remove typically several g H_2/s, cannot significantly reduce the high initial release rate (≤ 6000 g H_2/s in the LOOP scenario). A rapid initial H_2-source occurs in practically all severe accident scenarios because the large chemical heat release of the autocatalytic Zr-steam reaction causes a fast temperature excursion during which initially large surfaces and masses of reaction partners are available.

The investigated 44 recombiners caused a substantial hydrogen reduction on the time scale of hours, but still allow the accumulation of up to 720 kg of hydrogen in the containment. The next question is therefore what combustion mode and what structural loads would develop after ignition of the resulting containment mixture.

2.2 Turbulent combustion

The flame acceleration criterion, recently developed in joint work with the Kurchatov-Institute (see Section 2.5), predicts that the mixture existing in the upper half of the containment (>11% H_2), would be able to support flame acceleration. A COM3D calculation was therefore performed using the stratified H_2 distribution from the GASFLOW-calculation as initial conditions (9-13 % H_2).

The EPR containment model of the COM3D code uses a cubic Cartesian grid with 40 cm cell size, a total of 1.1 million computational cells, and about 80.000 m^3 free volume, close to the current EPR value. The turbulent combustion is simulated with a recently developed and verified extended Eddy-Break-Up model. The model performed well on different scales (FZK 12- m- tube, RUT facility) and for different H_2-air- steam mixtures. The computation was made on the FZK-INR Cray J-90 using 4 of the 8 vector processors in parallel, allowing for the first time a 3-d analysis of a turbulent combustion on full reactor scale.

Fig. 3 shows a plot of the H_2- concentration field 0.4 seconds after ignition on the right hand side of the containment. The results are quite surprising and non-trivial. The highest flame speeds (150 m/s) occur not in regions of highest H_2-

concentration, e.g. the dome, but rather in regions with both sufficient hydrogen concentration and turbulence generation, which is below the operating deck, and along the stair cases. The highest loads to the outer containment wall (≤8.5 bar) develop on the containment side opposite to the ignition point, because two propagating flame fronts meet here , leading to pressure wave superposition (top part of Fig. 4). The right wall near the ignition point is loaded quite uniformly with pressures up to about 4 bar (bottom part of Fig. 4). Since this pressure rise time is much longer than the typical containment wall period, this represents a quasi-static load to the structure which is within the static design limit (<6.5 bar).

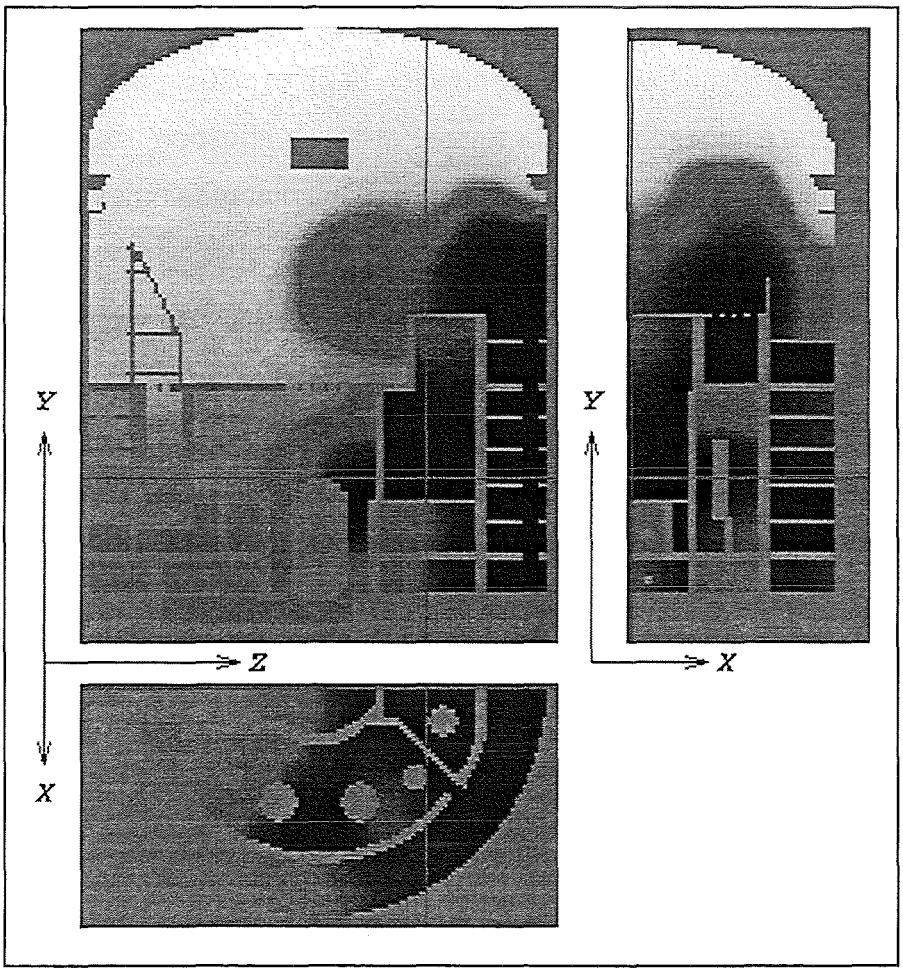

Fig. 3: Simulation of turbulent combustion in the EPR with the COM3D code, 1.1 million computational cells, parallel computation on the FZK-INR Cray J90. The highest flame velocities (150 m/s) develop in regions where both sufficient hydrogen concentration and turbulence generation exist. Initial conditions from GASFLOW calculation, LOOP scenario, 44 recombiners.

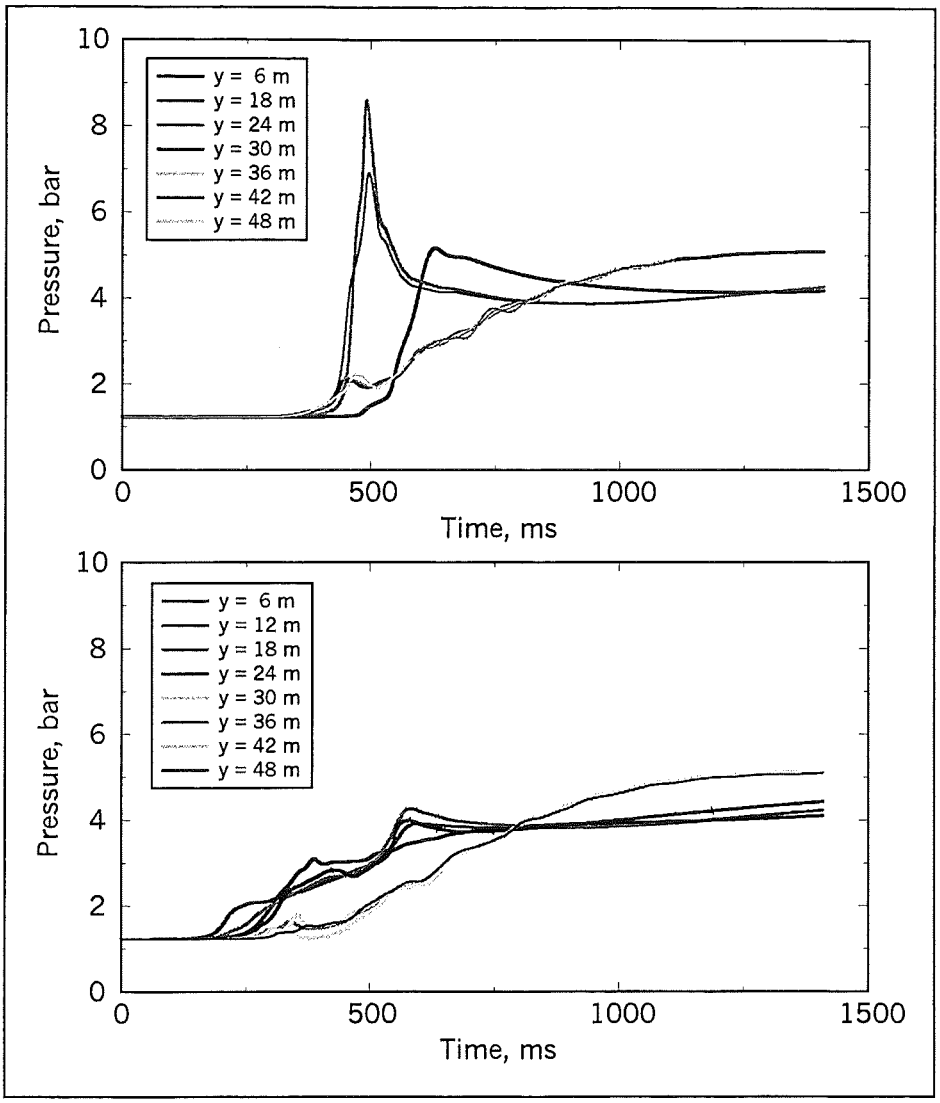

Fig. 4: Containment loads from fast turbulent combustion in EPR, 3-d COM3D calculation, initial gas distribution from GASFLOW, LOOP scenario, 44 recombiners installed. Top: pressure on the left containment wall, opposite from ignition point. Bottom: pressures on right containment wall near ignition point.

The characteristic loading times of the left and right containment wall are quite different, about 50 ms and 300 ms, respectively. When compared to the typical natural response times T_{cont} of a dry PWR concrete containment [2], the first case represents a dynamic load ($T_{load}/T_{cont} << 1$) and the second case a load regime which is in the transition from dynamic to quasi-static ($T_{load} / T_{cont} \approx 1$). In the first domain the deformation is proportional to the wave impulse, where as in the quasi-static domain it is proportional to the peak pressure reached.

2.3 Local detonation

Application of the DDT criterion, according to Fig.1, to the calculated hydrogen distribution, leads to the result that the mixture in the dome is sufficiently sensitive and large enough to support a detonation, provided a local flame acceleration would take place. The loads from such an event were estimated by a DET3D calculation (Fig.5). The same computational grid as in the COM3D calculation was used. The origin of the detonation was assumed near the crane support on the left hand side of the building where some turbulence generating structures are located. This scenario should result in an upper limit for fast local combustion loads which could be possible with the hydrogen inventory in the containment under the present conditions (LOOP, MAAP sources, GASFLOW distribution, 44 recombiners). A linear H_2 gradient from 7 to 13 % was assumed, leading to a total H_2-mass of 690 kg. The initial temperature was 47°C, and the initial pressure 1.23 bar. Figure 6 shows the predicted pressure loads at different points along the upper edge of the containment cylinder (1 to 7). Ignition is initiated at point 1. In points 2,3 and 4 basically side-on pressures are generated, whereas in points 5,6 and 7 higher reflected pressures appear. Due to the short loading times of typically 10 ms, these loads clearly fall into the impulsive regime, where the building deformation is proportional to the wave impulse. The calculated impulses in the detonation wave range from about 5 to 20 kPas.

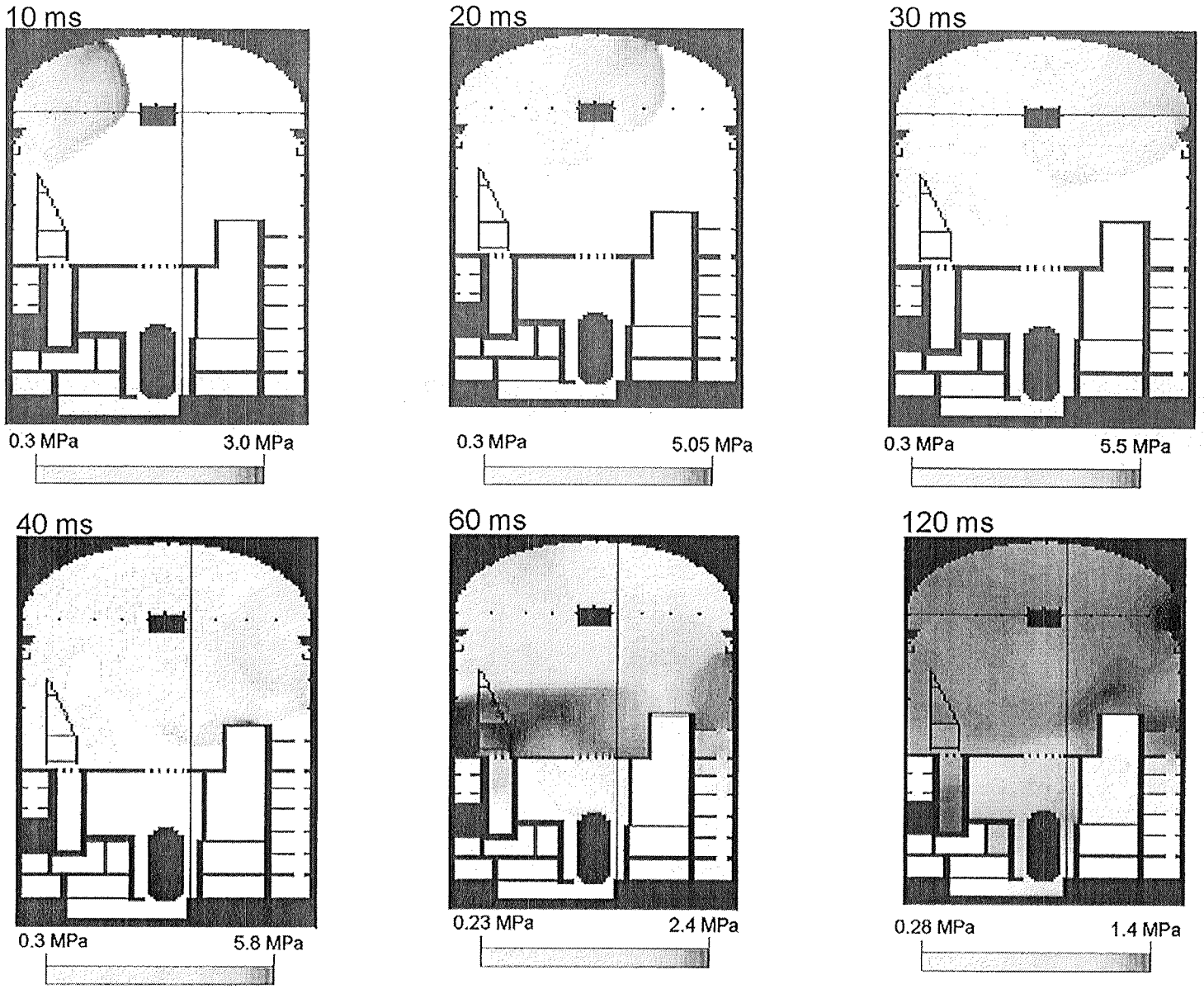

Fig.5: Simulation of a local detonation in the containment dome.

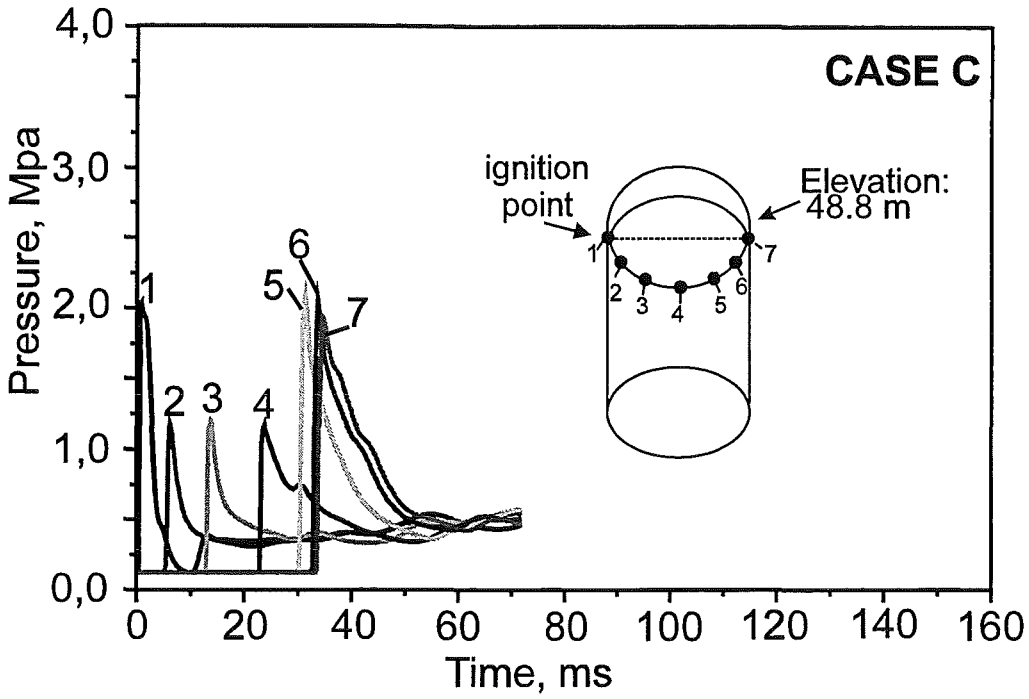

Fig.6: Calculated pressures from a local detonation in the containment dome. Total H_2 inventory in the building 690 kg H_2, vertical H_2 gradient from 7 to 13% H_2, initial pressure 1,23 bar, initial temperature 47°C, LOOP scenario with 44 recombiners .

2.4 Structural response

The inner containment of the EPR will be a pre-stressed concrete containment with two layers of tendons similar to the N4 plant. The design load of the EPR containment is a static internal pressure of 6.5 bar. The above calculations indicate that in case of mitigation by recombiners alone, new dynamic load regimes could not be excluded. The structural response of the complicated pre-stressed concrete containment to new transient loads has not been investigated. The major questions that arise concern the strain in the tendons (elastic or plastic) and resulting crack distribution (crack width, penetration depth). The undisturbed parts of the containment structure could probably be investigated with a single-degree of-freedom oscillator model, the areas around penetrations (cables, pipes, locks) will require detailed FEM analysis to evaluate the structural integrity. Using the response data of a typical pre-stressed concrete containment as an basis for damage estimates [2], it will probably not be easy to show that at least the EPR containment regions near

penetrations can certainly withstand the above calculated loads. The high hydrogen inventories leading to these loads should therefore be avoided.

2.5 Results

The described calculations have shown that mitigation with recombiners alone still allows accumulation of up to roughly 700 kg H_2 in the containment, and that combustion of this hydrogen mass could lead to significant dynamic loads.
Although these loads may not endanger the containment integrity in the undisturbed areas, they would certainly require extensive analysis of containment integrity in regions around penetrations. Furthermore, these dynamic loads would have severe consequences for safety systems which are needed for further management of the accident. Especially vulnerable are the structurally weak recombiner boxes and the spray system.

The general conclusion from these investigations is that igniters appear necessary for further reduction of the maximum possible hydrogen inventory and of the corresponding pressure loads. Recombiner systems alone will not allow to fulfil the GPR-RSK recommendations at least for dry LOOP scenarios. Therefore an analysis with recombiners and igniters was performed.

3 Mitigation with recombiners and igniters

In addition to the 44 recombiners one igniter was installed at each of the four IRWST exits from which the hydrogen / steam mixture would emerge in dry scenarios (last line in Table 1). Again the MAAP sources for the LOOP scenario with reflood were used as input to GASFLOW.

In the simulation the first ignition occurred at an hydrogen inventory in the building of 110 kg. Thereafter a continuous burn was predicted, with one large standing flame at each IRWST exit (Fig.7). The evaluation of the 7λ-criterion, which is implemented in GASFLOW, showed that at no time a DDT possibility existed and that a safe implementation of igniters is possible for the LOOP scenario. The early ignition, with most of the hydrogen actually still in the IRWST as a non-flammable mixture, reduced the maximum combustion pressure effectively to insignificant values.

The use of igniters basically transforms the previously large containment pressure load to a thermal load. The combustion energy is not released in a short event (seconds), but rather over a long time period (several 1000s). The total combustion energy of the 900 kg hydrogen used in this LOOP sequences, corresponds to roughly 100 GJ (900 kg x 120 MJ/kg). The thermal power of the diffusion flames can be quite high (1kg H_2/s ≡ 120 MW). Experimental investigations at the Russian Academy of Sciences on the stability limits of H_2-air-steam diffusion flames, which were specifically initiated for the EPR investigations [3] have shown that the flame length will be in the range of 20 to 200 times the fuel gas exit diameter, depending on the Froude number. The flame length is governed by the exit velocity of the fuel gas (plume or jet).

Because of the potentially large thermal power and geometrical extension, the thermal effects of standing diffusion flames should be investigated in future work. The results can then be used to avoid thermal overloads to safety systems (igniters, recombiners, spray, liner) by design modifications if necessary .

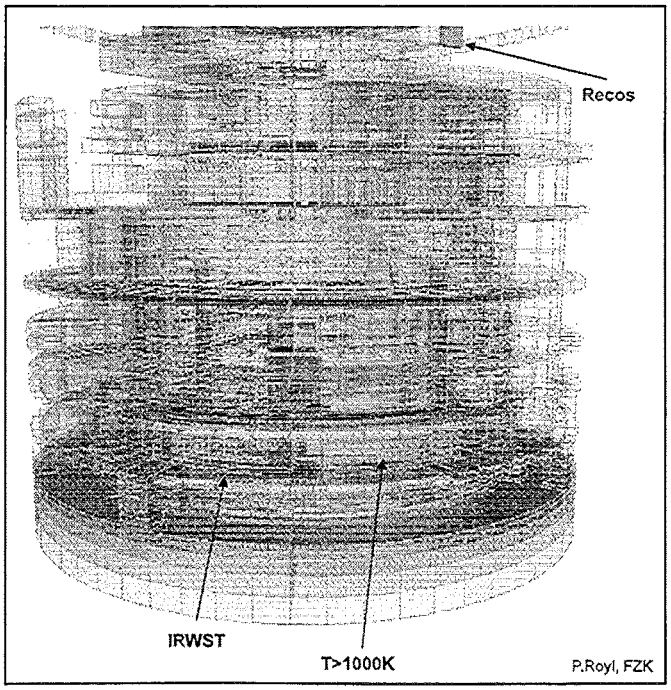

Fig.7: GASFLOW analysis of LOOP sequences with 44 recombiners and 4 igniters at the IRWST exits. Low hydrogen inventories, low pressure loads and standing flames are predicted.

4 Conclusions

A systematic and self-consistent procedure was developed for the comprehensive analysis of hydrogen behaviour in severe accidents, covering hydrogen sources, distribution and different combustion modes. For each step in the analysis, codes or criteria were developed and verified by a large new experimental data base on different scales (Fig.1).

The theoretical tools were used to investigate the effectiveness of different options for EPR hydrogen mitigation systems. The goal is to fulfil the GRS/RSK safety requirements for future reactors, which require control of the maximum amount of hydrogen which can be present in the containment building during a low pressure scenario. Although a mitigation system consisting only of recombiners would be attractive for acceptance and cost reasons, the magnitude of the still possible combustion loads calls for installation of additional igniters. The calculations done so far, have shown that igniters can be safely positioned and that they reduce the pressure loads very effectively.

There is strong evidence that in-depth analysis and detailed layout of a recombiner/ igniter hydrogen mitigation system will allow to control also the thermal loads from standing diffusion flames.

Literature

[1] R. Hüper (Ed),
"Projekt Nukleare Sicherheitsforschung, Jahresbericht 1995";
Report FZKA 5780 (August 1996) p. 14

[2] E.Studer, M. Petit,
"Use of RUT large scale combustion test results for reactor applications", SMIRT-14, Lyon, France, August 17-22, 1997

[3] B.E. Gelfand, S.P. Medvedev, B.E. Popov,
"Flame stabilization and flammability limits of H_2+air+steam (fog) mixtures"
Final report to FZK, contract 315/20089955/INR, (Dec. 1998).

32.21.02 Thermische Wechselwirkung von Kernschmelze und Kühlmittel

I. Experimente zur Vorvermischungsphase (QUEOS)

(R. Huber, M. Kirstahler, D. Kuhn, L. Meyer, A. Roth, M. Schwall, E. Wachter, G. Wörner, INR)

ZUSAMMENFASSUNG

Die QUEOS-Experimente wurden mit drei kurzen Versuchsreihen abgeschlossen. Bei Experimenten mit Wolframkugeln wurde die Zieltemperatur von 2600 K erreicht. Sechs Experimente mit Kugeln aus Zirkonoxid bei 2000 K wurden mit offenem und geschlossenem Wasserbehälter durchgeführt, jeweils mit und ohne Anfangsunterkühlung des Wassers. Wenige Grad Unterkühlung, für die eine Drucksteigerung von wenigen Zehntel Bar ausreicht, führen zu einer starken Rekondensation, so daß keine großen Dampfblasen entstehen und auch nachfolgende Partikel gut mit Wasser vermischt werden. Schließlich wurden Versuche mit drei dünnen Kugelstrahlen anstelle eines dicken durchgeführt, ähnlich wie bei PREMIX 11, bei dem eine Dampfexplosion stattgefunden hat. Hierbei war die Bestimmung des Dampfanteils zwischen den Strahlen von besonderem Interesse. Die Messungen mit Voidsonden und die Bilder der Hochgeschwindigkeitsfilme zeigten, daß sich Wasser zwischen den Strahlen nur entlang einer kurzen Strecke an der Front der Mischzone befindet. Dahinter wachsen die drei Dampfkanäle zu einem einzigen großen Dampfkanal zusammen. Nach Abschluß des QUEOS-Programmes liegt jetzt eine umfangreiche Datenbank von 60 Experimenten mit einem großen Parameterfeld zur Code-Validierung vor.

1. EXPERIMENTELLES PROGRAMM

Das experimentelle Programm zur Untersuchung der Vorvermischungsphase einer Dampfexplosion mit heißen Kugeln anstelle von Schmelze ist abgeschlossen. Während in einer ersten Versuchsserie ein Kugelstrahldurchmesser von 180 mm verwendet wurde, wurde in der zweiten Serie der Durchmesser auf 100 mm reduziert, was bei gleicher Kugelmenge zu längeren Strahlen geführt hat. Die zweite Versuchsserie wurde mit den drei Kugelsorten (ZrO_2, ∅ 5 mm und 10 mm und Mo ∅ 4.3

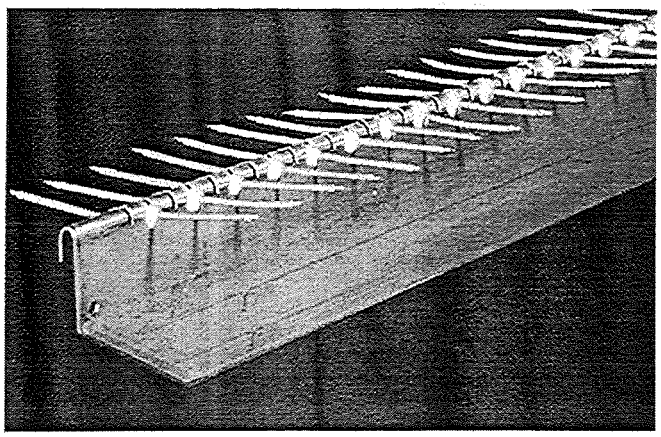

Abb. 1 Voidsonden mit Sondenhalter

mm) bei hohen Temperaturen (2100-2550 K) beendet. Bei diesen Versuchen wurde der Dampfblasenanteil mit einer neu konstruierten Meßeinrichtung zum erstenmal zuverlässig gemessen. In einer Tiefe von 60 cm unterhalb der Wasseroberfläche (40 cm über dem Behälterboden) befindet sich ein horizontaler Sondenträger genau in der Behälterachse (Abb. 1). Der Träger ist 5 mm breit und ca. 50 mm hoch und trägt an jeder Seite 25 Meßsonden im Abstand von 20 mm zueinander. Die Kugelwolke wird durch diesen Träger geteilt, so daß unterhalb dieses Trägers keine sinnvolle Messung möglich ist. Die Meßmethode, die im letzten Jahresbericht im Detail beschrieben wurde, wurde auch bei den diesjährigen Versuchen angewendet.

Das experimentelle Programm wurde mit einigen speziellen Versuchen beendet, die im folgenden beschrieben werden. Dies waren Versuche: (1.) mit Wolframkugeln, mit denen die höchste Temperatur von 2600 K erreicht wurde, (2.) mit einem geschlossenen Versuchsbehälter, bei denen durch die starke Druckerhöhung und die daraus folgende Unterkühlung des Wassers die transienten Kondensationseffekte stärker zum Tragen kamen, und schließlich (3.) mit drei dünnen Kugelstrahlen anstelle des einen dicken Strahles, ähnlich wie bei PREMIX 11, bei dem eine Dampfexplosion stattgefunden hat. Für die Versuche mit drei Strahlen wurden die Sonden an zwei Sondenhaltern montiert, die im rechten Winkel zueinander angeordnet waren. In Abb.2 ist die Position der 3 Strahlen zu den Voidsonden gezeigt. Die Linien durch die Meßspitzen laufen genau durch das Behälterzentrum. Der Abstand zwischen den Meßspitzen ist 16.5 mm.

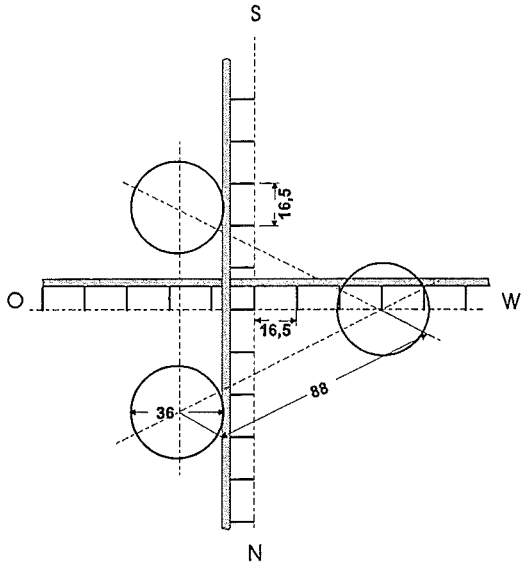

Abb. 2 Anordnung der Sondenhalter für das 3-Strahlexperiment

2. ERGEBNISSE

Die Tabelle 1 zeigt die Daten der durchgeführten Versuche. Die unterschiedlichen Kugelmengen bei den Versuchen mit Zirkonoxid haben sich durch das Zusammenbacken der Kugeln im Ofen ergeben. Der Strahldurchmesser betrug bei der 50er Serie 180 mm, während die 60er Serie mit drei Strahlen mit jeweils 36 mm Durchmesser durchgeführt wurde. Die Dichte der gesinterten Wolframkugeln ist 16.3 g/cm³, die der Zirkonoxidkugeln ist 6.06 g/cm³.

2.1 Experimente mit Wolframkugeln

Da die Kugeln aus Zirkonoxid und Molybdän bei hohen Temperaturen zunehmend im Ofen zusammenklebten, wurden Kugeln aus Wolfram benutzt, um die Zieltemperatur von 2600 K zu erreichen. Gleichzeitig wird der Parameter der Dichte zu hohen Werten variiert, was bei einer Masse von 20 kg allerdings zu relativ kleinen Volumina

Tabelle 1 Versuchsparameter

No.	mass [kg]	vol. [cm³]	number of spheres -	material and sphere diameter [mm]	water temperature [1] ±0.3 [°C]	furnace temp. ±20[°C]	sphere temp. above water ±30 [°C]	duration of pour ±5 [ms]	length of pour[2] ±3[cm]	average volume fraction[3] ±0.02	Vesel open / closed
51	20	2100	2100	W-10	97	-	20	36	18	0.27	open
52	20	2100	2100	W-10	100	1600	1580	60	30	0.16	open
53	20	2100	2100	W-10	100	2360	2350	60	30	0.16	open
57	9.87	2580	25580	ZrO_2-5	100.1-101.0	1950	1860	95	47	0.14	closed
56	13.94	3640	36125	ZrO_2-5	99.8 -100.8	1950	1860	100	50	0.18	closed
55	6.86	1800	17777	ZrO_2-5	97.5 - 98.1	1860	1740	85	43	0.10	closed
58	10.84	2830	28090	ZrO_2-5	97.0 - 97.7	1940	1850	110	55	0.13	closed
54[4]	7.60	1990	19700	ZrO_2-5	100.6-101.4	1780	1700	155±15	78	~0.06	open
59	12.03	3140	31180	ZrO_2-5	96.8 - 97.6	1750	1730	95	47	0.17	open
60	7.00	1830	18140	ZrO_2-5	20.0	-	20	200	100	0.30[5]	open
61	4.95	1300	12830	ZrO_2-5	100.0	1600	1550	310	165	0.13	open
62	8.61	2240	22300	ZrO_2-5	100.0	1850	1750	420	210	0.18	open

[1] the first value gives the temperature of most of the water, the second value is true for the lower 200 mm in the vessel.

[2] above the water surface; it is calculated by velocity at water surface times duration of pour, which gives a virtual length over a time period; the real length at a certain time is shorter (app. 8%).

[3] average volume fraction = mass / density / (flow area * length), with flow area of a 180-mm-jet diameter

[4] In Q54 the pressure relief valve above the sliding door did not work properly. A differential pressure of app. 0.3 bar existed when the sliding doors opened, therefore a gas flow pushed the spheres downward. The arrival of the spheres at the pyrometer, 0.25 m above the water level (1.05 m below the sliding doors) was at 0.30 s. The initial velocity was determined to v_{ini} = 2.0 m/s, with the velocity at the position of the pyrometer v_p = 5.0 m/s. The first spheres reached the water level at t_{imp} = 0.35 s with a velocity of v_{imp} = 5.25 m/s. The duration and length of the pour cannot be defined precisely, because the jet starts and ends with a thin cloud of spheres. This applies to the other jets also, but to a lesser extend.

[5] flow area of 3 times a 40 mm jet, (not 36 mm because of some spreading)

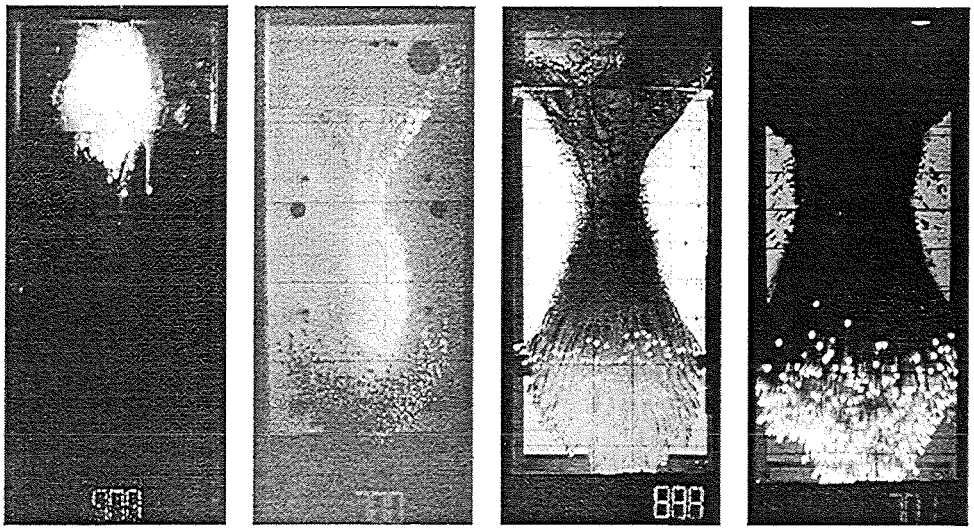

Q53 t=500 ms **Q51** t=700 ms **Q52** t=700ms **Q53** t=700 ms

Abb. 3 Wolframkugeln bei verschiedenenTemperaturen

und Kugelzahlen führt. Die hohe Dichte führt zu hohen Geschwindigkeiten im Wasser, die Kugelwolke bleibt kurz (Abb.3). Die Kugelfront erreicht den Behälterboden schon bei etwa 700 ms, während das sonst nie vor 800 ms der Fall war. Mit der Kugeltemperatur von 2600 K erreicht der Druck mit 1.44 bar den höchsten Wert (Abb.4), der bisher im offenen Behälter gemessen wurde, wie bei Q17, wo 10 kg Molybdänkugeln (Durchmesser 4.3 mm, 24000 Stück) bei einer Temperatur von 2200 K verwendet wurden. Bei Q17 ist die Gesamtoberfläche der Kugeln aber etwa doppelt so groß wie bei Q53, so daß trotz geringerer Gesamtmasse und niedrigerer Temperatur die Dampfproduktion in etwa gleich war.

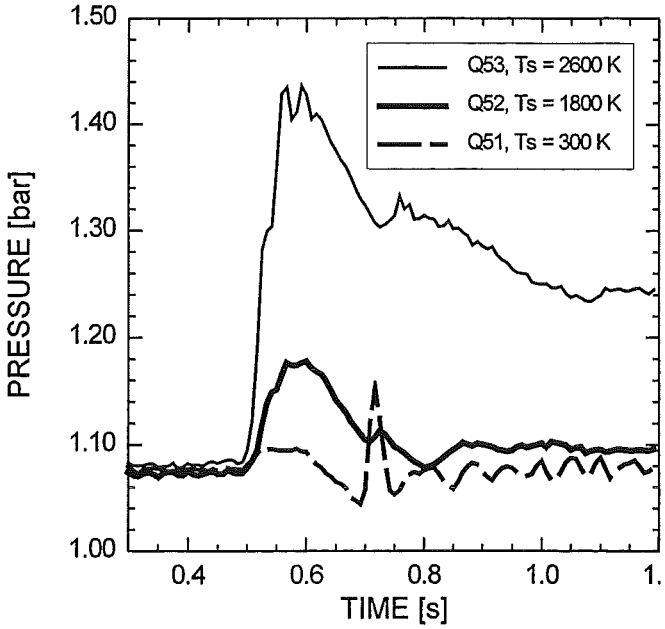

Abb. 4 Die Druckverläufe im Wasser bei den drei Versuchen mit Wolframkugeln

2.2. Experimente mit geschlossenem Behälter

Die Ausströmbedingungen durch das Abdampfrohr sind in den Rechnungen schwierig zu modellieren. Deshalb bestand der Wunsch Experimente im geschlossenen Wasserbehälter durchzuführen mit einfach zu modellierenden Randbedingungen. Es wurden deshalb jeweils zwei Experimente bei siedendem Wasser und zwei mit einer leichten Unterkühlung von ca. 2-3 K im geschlossenen Behälter durchgeführt. Zum Vergleich wurden zwei Experimente mit ähnlichen Bedingungen aber bei offenen Behälter durchgeführt. Abb.5 zeigt die Druckverläufe über einen längeren Zeitraum. In den Fällen mit unterkühltem Wasser bleibt das Druckniveau relativ hoch, was auf das Vorhandensein von einem höheren Anteil von nicht-kondensierbarem Gas (Luft) zurückzuführen ist. In den anderen Fällen ist durch das intensive Sieden wahrscheinlich die meiste Luft aus dem Wasserbehälter ausgetrieben worden. Die Gasanteile vor dem Versuch wurden nicht bestimmt.

Ein Vergleich der Voiddaten zeigt den großen Einfluß der zusätzlichen Unterkühlung durch den größeren Druckanstieg im geschlossenen Behälter (Abb.6 und 7). Während mit offenen Behälter im Zentrum ein Gasraum über ca. 100 ms besteht (Q59), ist im geschlossenen Behälter dieser nur für kurze Zeit vorhanden (Q58). Besonders ausgeprägt ist der Unterschied am Rand der Vermischungszone, hier ist bei geschlossenem Behälter kaum noch Dampf vorhanden.

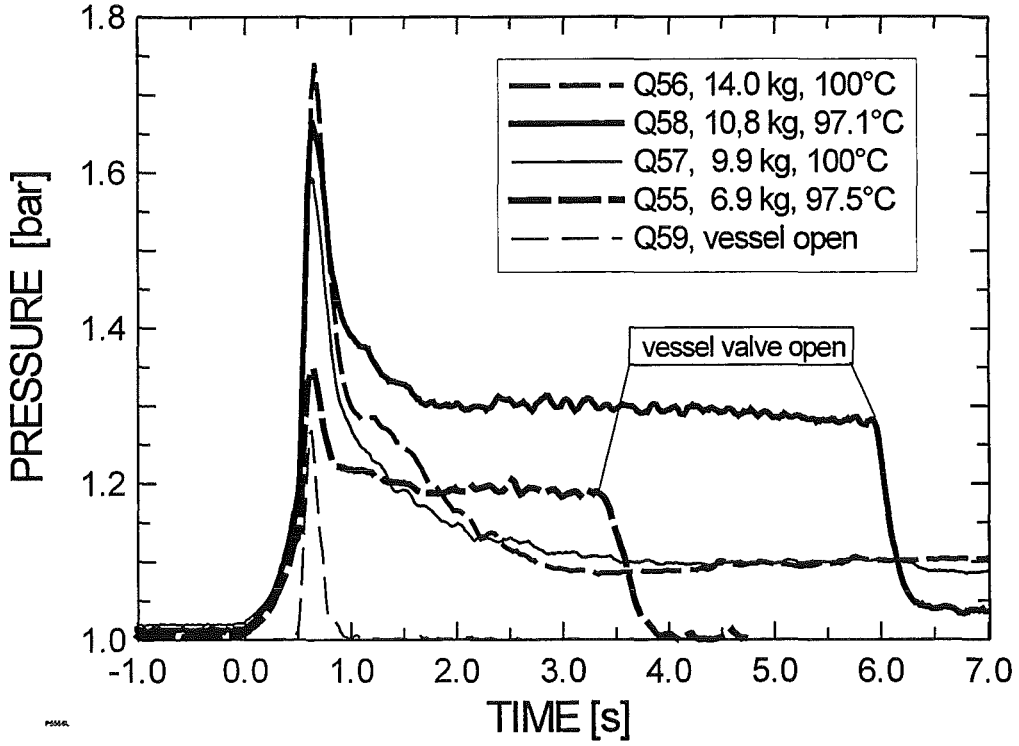

Abb. 5 Druckverläufe bei den Experimenten mit geschlossenem Wasserbehälter

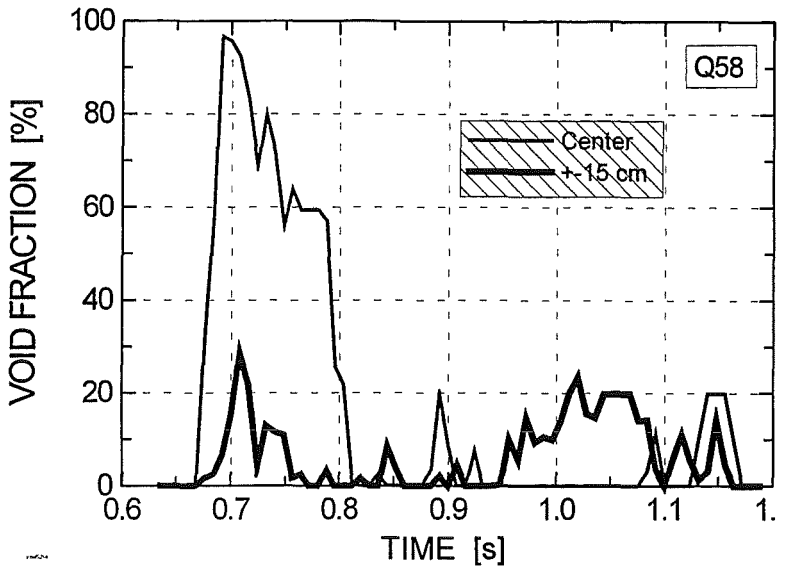

Abb. 6 Gasanteil in der Mitte und am Rand der Vermischungszone bei geschlossenem Behälter

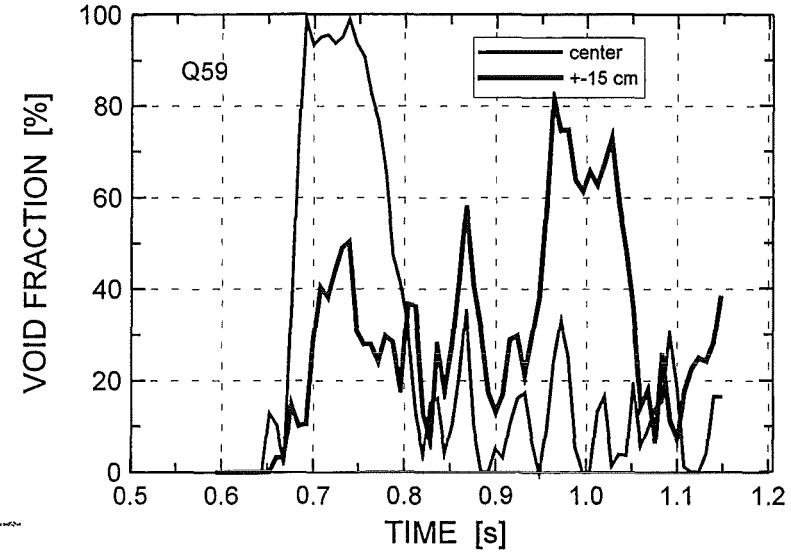

Abb. 7 Gasanteil in der Mitte und am Rand der Vermischungszone bei offenem Behälter

Die Versuche Q54 bis Q59 wurden mit dem MATTINA–Code nachgerechnet und sind in [1] ausführlich beschrieben.

2.3 Experimente mit drei Strahlen

Die Experimente Q60 bis Q62 wurden mit dem Ziel durchgeführt, Einblick in die Wechselwirkung von mehreren Kugelstrahlen, besonders im Hinblick auf die Dampf-Wasser-Verteilung, zu bekommen. Die drei Strahlen waren im gleichseitigen Dreieck angeordnet (Abb. 2), ähnlich wie im Experiment PREMIX 11, bei dem mit Eisen-Aluminiumoxid-Thermit eine Dampfexplosion stattgefunden hat. Voidmessungen

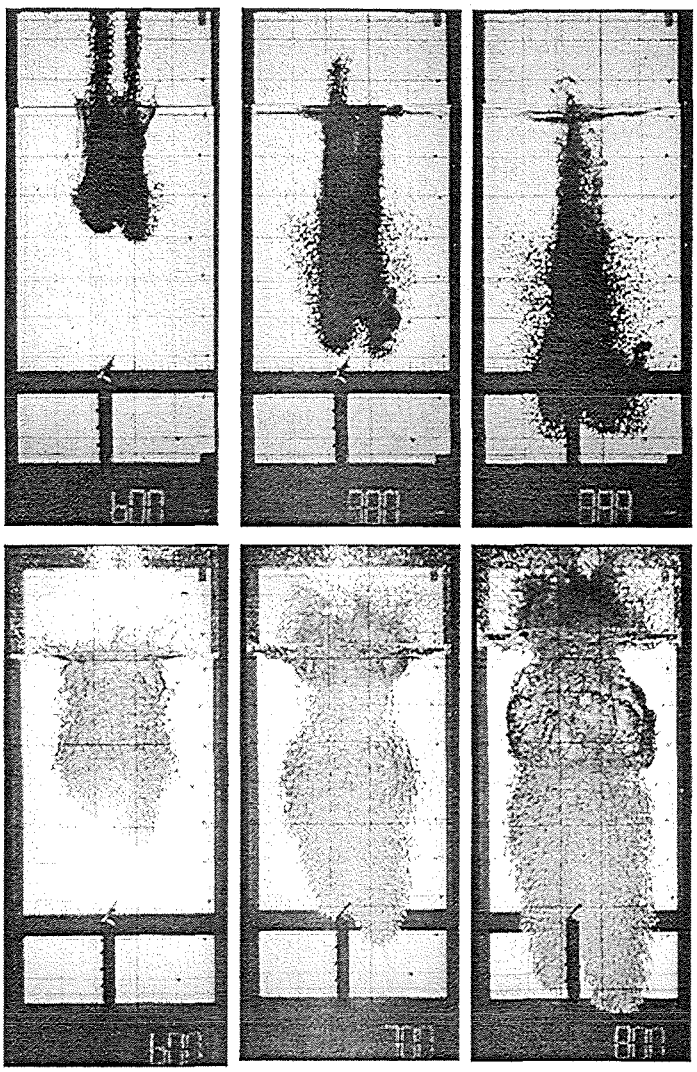

t = 600 ms t=700 ms t=800 ms

Abb. 8 Kugelwolken von Q60 und Q61

hatten hier Wasser in der Nähe der Schmelze am Behälterboden angezeigt, unmittelbar vor der Dampfexplosion. Die drei QUEOS-Experimente wurden bei Kugeltemperaturen von 20°C, 1550°C und 1750°C durchgeführt. Die Maximaltemperatur wird durch die Tendenz des Zusammenbackens der Kugeln im Ofen mit steigender Temperatur begrenzt. Die Schmelzetemperatur bei PREMIX betrug dagegen etwa 2300°C und die Schmelzemasse lag bei 20 kg, mehr als die doppelte Masse von Q62. Ein direkter Vergleich von PREMIX-11 mit QUEOS-62 ist deshalb nicht sinnvoll.

Auf den Fotos in Abb. 8, die von Norden aufgenommen wurden, sieht man zwei Strahlen, der dritte Strahl ist verdeckt hinter dem Strahl auf der linken Seite. Die Kugeln links (O) fallen etwas später als rechts (W), weil die Schiebetüren des Schiebers, auf dem die Kugeln liegen, in N-S-Richtung öffnen. Der W-Strahl liegt im Zentrum und wird zuerst freigegeben. 200 ms nachdem die ersten Kugeln ins Wasser gefallen sind, kann man die einzelnen Strahlen an der Kugelfront 60 cm unterhalb der Wasseroberfläche noch unterscheiden. Etwa 10 cm hinter der Kugelfront wachsen die einzelnen Gasräume zu einem großen Gasraum zusammen. Das zeigen auch die Voidsonden an. Die Gaskanäle sind umgeben von einer Wolke von Einzelkugeln, im Fall von heißen Kugeln zusammen mit den individuellen Gasschleppen, die langsamer zu Boden sinken als die Kugelfront. Bei heißen Kugeln sind die Gaskanäle breiter und wachsen schneller zusammen.

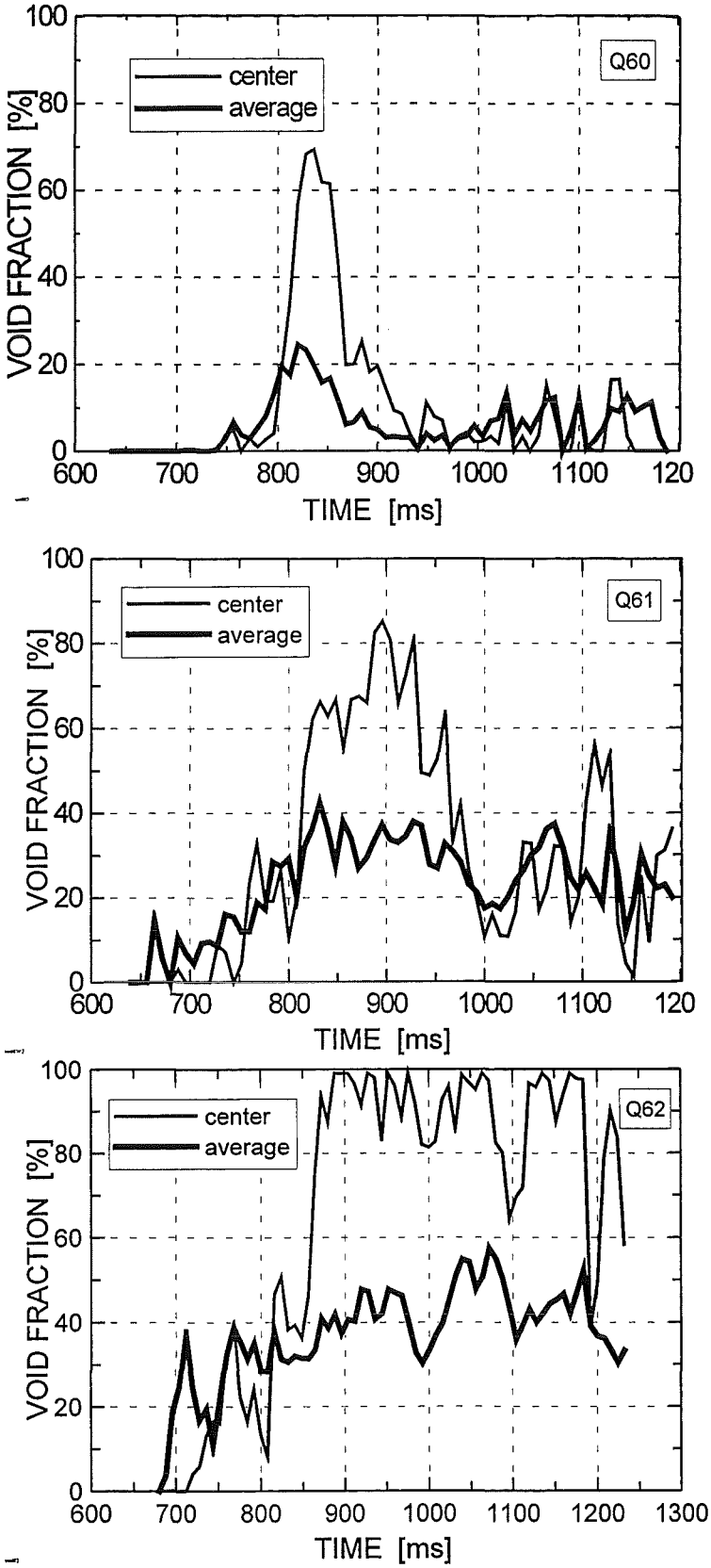

Abb.9 – 11 Gemittelte Blasenanteile der Dreistrahlexperimente

Die Abb.9–11 zeigen gemittelte Blasenanteile der Dreistrahlexperimente. Eine Kurve zeigt den Mittelwert von jeweils drei Sonden jedes Sondenhalters im Zentrum. Die zweite Kurve zeigt den Mittelwert aller Sonden bezogen auf die Anzahl der Sonden, die innerhalb der Vermischungszone liegen, wie man es aus den Hochgeschwindigkeitsfilmen von zwei Richtungen entnehmen kann. Sie gibt also den mittleren Gasanteil in einem horizontalen Schnitt durch die Vermischungszone 60 cm unterhalb der Wasseroberfläche an. Ähnlich wie bei Einzelstrahlversuchen liegt der mittlere Gasanteil bei Versuchen mit hohen Kugeltemperaturen bei 40%, während sich im Zentrum über längere Zeit ein Gasraum mit nur wenig Wasseranteil hält.

Abb.12 zeigt die Drücke der beiden heißen Dreistrahlexperimente im Vergleich mit dem Druck eines Einzelstrahlexperimentes mit ähnlichen Anfangsbedingungen. Der Druck-

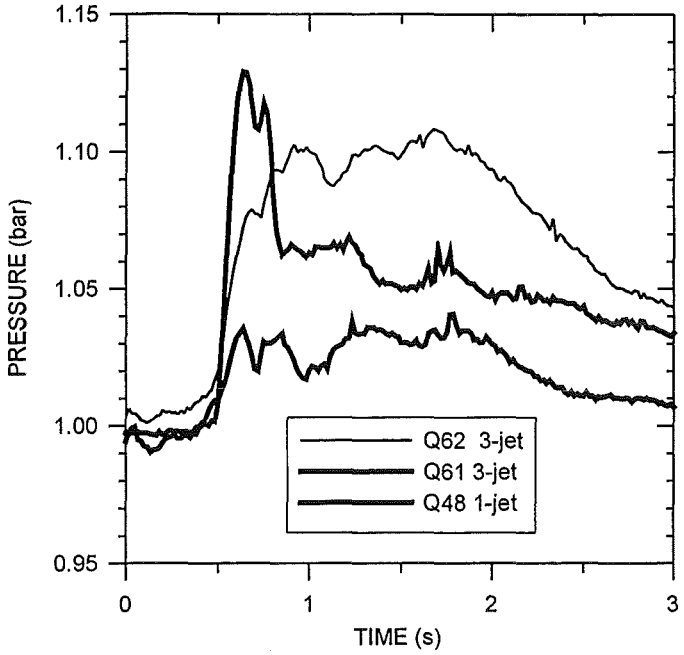

Abb. 12 Vergleich der Drücke im Gasraum zwischen 3-Strahl- und 1-Strahlexperimenten

anstieg ist viel steiler bei dem Einstrahlexperiment, da etwa die gleiche Menge Kugeln in einem Drittel der Zeit ins Wasser fallen wie bei Q62 (140 ms bei Q48, 420 ms bei Q62). Die Dampfproduktion und damit der Druck bleibt aber im Dreistrahlexperiment für längere Zeit höher, lange nachdem alle Kugeln ins Wasser gefallen sind. Durch die starke turbulente Bewegung des Wassers wird ein großer Teil der Kugeln im Wasser in der Schwebe gehalten.

Eine ausführliche Dokumentation und Diskussion der Dreistrahlexperimente findet sich in der Referenz [2]. Nachrechnungen dieser Experimente haben noch nicht stattgefunden, wegen der Notwendigkeit eine 3-D-Rechnung durchführen zu müssen.

3. SCHLUSSBEMERKUNG

Nach Abschluss der letzten drei Versuchsreihen liegt jetzt eine umfangreiche Datenbank von 60 Experimenten vor, die ein großes Parameterfeld abdecken. Die Daten wurden und werden zur Validierung von mindestens fünf verschiedenen Rechenprogrammen benutzt. Der Versuchstand wird noch einige Zeit betriebsbereit gehalten, für den Fall, daß noch spezielle Fragestellungen auftauchen.

REFERENZEN

1. L. Meyer, H. Jacobs, *A study of the water depletion effect in melt water mixing,* Ninth Int. Topical Meeting on Nuclear Reactor Thermal Hydraulics (NURETH-9), San Francisco, 3.-8. Oktober 1999.
2. L. Meyer, D. Kuhn, *The interaction of very hot particles falling into water*, 2nd Int. Symp. on Two-phase Flow Modelling and Experimentation, Pisa, Italien, 23.-25. Mai, 1999.

II. Experimente zur Vorvermischungsphase (PREMIX)

(H.-H.-Brüggemann, E. Jenes, A. Kaiser, I. Kornelson, N. Prothmann, D. Raupp, W. Schütz, H. Will, IRS)

Abstract

The PM12 – PM14 test series aiming at evidencing and demonstrating reproducibility of PREMIX results was completed by the third experiment (PM14) performed under equal initial conditions. It could be shown that the pressures differ only by about 10 % and the steam generation rate as well as the particle size distribution are rather similar. Significant differences only exist in the times when substantial rises in the pressure and steam generation, respectively, occur after the first melt/water contact. It is believed, that inevitable small deviations in the starting conditions, such as the speed of melt on contact with the water, are the reason for these differences. The results of the first two test have been reported in the last period. A summary report on the three tests is under way [1].

The PREMIX experiments were continued by the PM15 test performed with an elevated system pressure of five bars. All other parameters were set equal to those of the preceding PM14 test.

The measurements clearly show the influence of the larger system pressure on the two major measurements. The steam volume flow as well as the pressure increase developed at a significantly smaller rate in case of the larger system pressure. An important result is that the maxima of the steam mass flow rates agreed in both cases after about one second.

The post-test particle size distribution showed a small shift towards larger melt fragments in case of the larger system pressure. This result agrees with observations made in the films that show less boiling intensity in this case. Under the presumption that the particle size distribution found after the test was approximately given also during the initial period of time, one can conclude that the total melt surface and with it the steam production rate were smaller during that time. This conclusion is supported by the integrated steam masses giving smaller values up to the time of one second.

A separation of the influence of the small water subcooling from that of the larger system pressure on the results in PM15 can only be done by parametric code calculations.

The consistent continuation of the investigation of the premixing phenomena is the measurement of the conversion rate of thermal to mechanical energy in case of a steam explosion. For this purpose a new test facility was designed and fabricated using essential components of the PREMIX facility. After finishing the defined PREMIX test series the new ECO (energy conversion) experiments will start mid of 1999.

Zusammenfassung

Die Versuchsserie zur Überprüfung und Nachweis der Reproduzierbarkeit von PRMIX-Ergebnissen (PM12 - PM14) wurde mit dem dritten Versuch (PM14) abgeschlossen. Es konnte gezeigt werden, daß die Drücke sich in der Höhe lediglich um 10 % unterscheiden und die Dampfproduktionsrate und Partikelgrößenverteilung nur geringfügig unterschiedlich sind. Wesentliche Unterschiede bestehen lediglich in den Zeiten nach dem ersten Schmelze-Wasser-Kontakt, nach denen substantielle Anstiege des Druckes und der Dampfproduktion erfolgen. Es wird vermutet, daß unvermeidliche kleine Unterschiede in den Anfangsbedingungen, wie z. B. die Geschwindigkeit der Schmelze beim Eintritt in das Wasser, hierfür verantwortlich sind. Das Ergebnis der ersten beiden Tests wurde im letzten Fortschrittsbericht gegeben. Ein zusammenfassender Bericht erscheint in Kürze [1].

Die PREMIX-Versuche wurden fortgeführt mit dem Test PM15 unter erhöhtem Systemdruck. Alle anderen Parameter wurden denen des Versuchs PM14 gleichgesetzt.

Die Messungen zeigen deutlich die Wirkung des höheren Systemdrucks auf zwei der wichtigsten Meßdaten. Der Volumenstromrate des Dampfes und die Druckänderung nahmen unter dem Einfluß erhöhten Drucks geringere Werte an. Ein weiteres wichtiges Ergebnis ist, daß die Maxima der Massenstromraten des Dampfes in den Versuchen mit unterschiedlichem Systemdruck ungefähr übereinstimmen.

Die nach dem Versuch gefundene Partikelgrößenverteilung zeigt eine leichte Verschiebung in Richtung auf größere Partikel im Falle des höheren Systemdrucks. Dieses Ergebnis stimmt mit den Beobachtungen in den Filmen überein, die auf eine deutlich weniger heftige Wechselwirkung hinwiesen. Unter der Annahme, daß die nach dem Versuch gefundene Verteilung auch während der Anfangsphase der Wechselwirkung gegeben war, kann man schließen, daß die Gesamtoberfläche der Schmelzetropfen und damit auch die Dampfproduktionsrate in diesem Zeitraum klei-

ner waren. Diese Schlußfolgerung wird gestützt durch das Ergebnis der etwas geringeren Masse des über die erste Sekunde integrierten Dampfes.
Eine Separierung des Einflusses, den die geringe Unterkühlung des Wassers ausübte, von dem des erhöhten Systemdrucks auf die Ergebnisse des Versuchs PM15 kann nur mit Hilfe eines Rechenprogramms unter Variation der Parameter erfolgen.
Die folgerichtige Fortsetzung der Experimente zur Vorvermischung ist die Messung der Konversionsrate von thermischer zu mechanischer Energie im Falle einer Dampfexplosion. Hierfür wurde eine neue Testeinrichtung konstruiert und gefertigt, die wesentliche Teile der PREMIX-Anlage verwendet. Nach Beendigung des definierten PREMIX-Versuchsprogramms, werden die neuen ECO (energy conversion) Experimente ab Mitte 1999 beginnen.

1. PREMIX

INTRODUCTION

Release of a hot melt into water may occur during a severe core-melt accident in a nuclear light-water reactor. In the course of the accident, the melt may drain down into the lower head of the reactor vessel which is filled with water at that time. Such an event implies the possibility of a steam explosion, whose energetic mainly depends on the extent and characteristics of mixing. Research work in the field of molten fuel/coolant interaction is done at several laboratories /2/.

At the Forschungszentrum Karlsruhe, an experimental programme called PREMIX is performed in which the mixing of a hot melt discharged into water is investigated on a small to medium scale. Strong safety directions as well as similarity considerations led us to choose alumina as a simulating material instead of corium. To date, 15 experiments, PM1 to PM15, have been performed under various starting conditions.

The results are firstly used to identify the phenomena that dominantly control the premixing. The information helps in improving multi-phase computer codes presently under development, i.e. MC3D at CEA Grenoble and at FZK, MATTINA at FZK; and IVA5 at SIEMENS. Secondly, the quantitative results are used to validate the codes. Up to PM11, the results have already been published /3/. This report gives the results of the last two experiments, PM14 and PM15, in which the influence of the system pressure on the mixing behaviour was investigated.

EXPERIMENTAL FACILITY

The melt is provided by an exothermal reaction of powdered aluminium and iron oxide. The crucible located in the upper part of the test facility (Fig. 1) was designed to retain the liquid iron and to allow mostly alumina to be released into the water pool. The test vessel is closed except for the four venting lines through which the steam formed during the mixing escapes. The test facility is extensively instrumented with pressure gauges, level meters, thermocouples, and void detectors distributed over the height as well as the azimuthal co-ordinate. The glass windows enable video and high-speed filming which help to identify the characteristics of the mixing process. The test facility is housed in a 200 m^3 steel vessel which primarily serves as a safety container. It can also be pressurised so that experiments under elevated system pressures can be performed.

EXPERIMENTAL PARAMETERS

The two experiments were performed under equal test conditions except for the system pressure (Table 1). PM15 was the first test to be performed under elevated pressure (0.5 MPa). Small variations in some of the parameters which are inevitable, such as the initial water level (which determines the melt falling height), the speed of melt, or the water subcooling are assumed to exert no marked influence on the results.

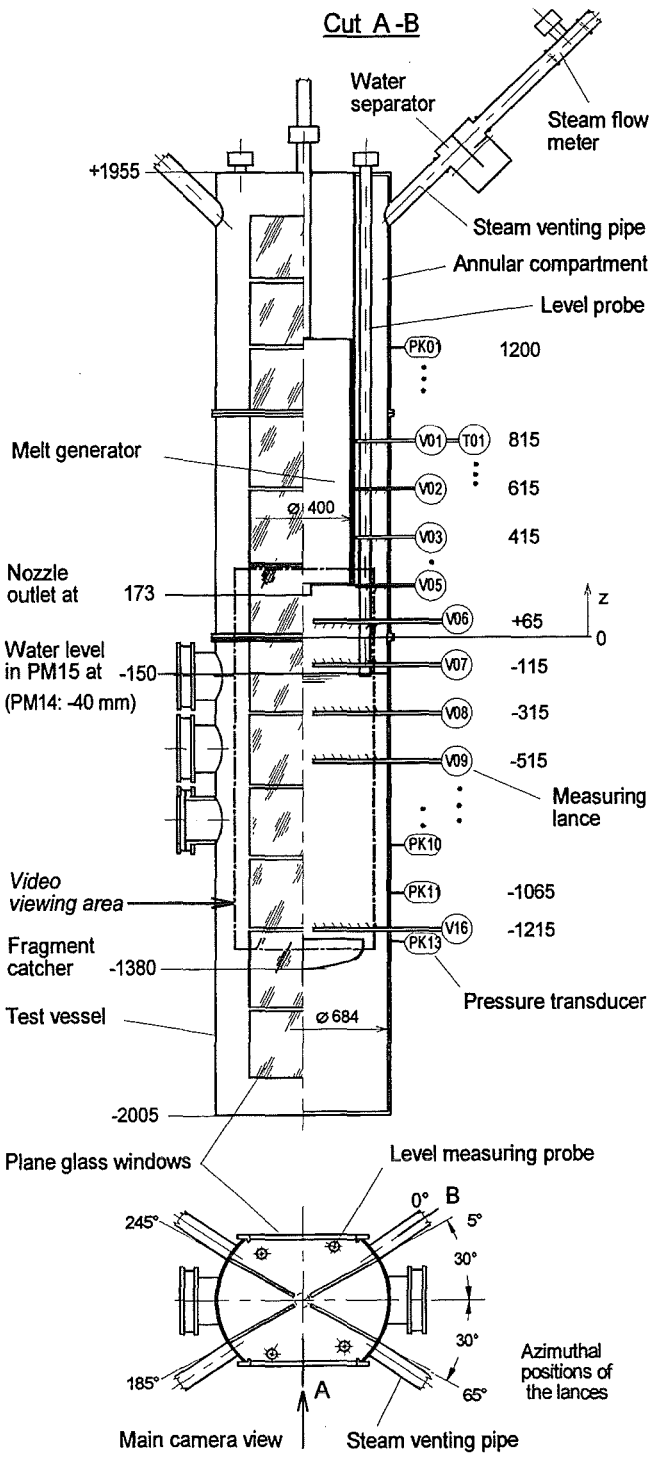

Fig. 1: Test facility used for PM14 and PM15. Dimensions are given in mm.

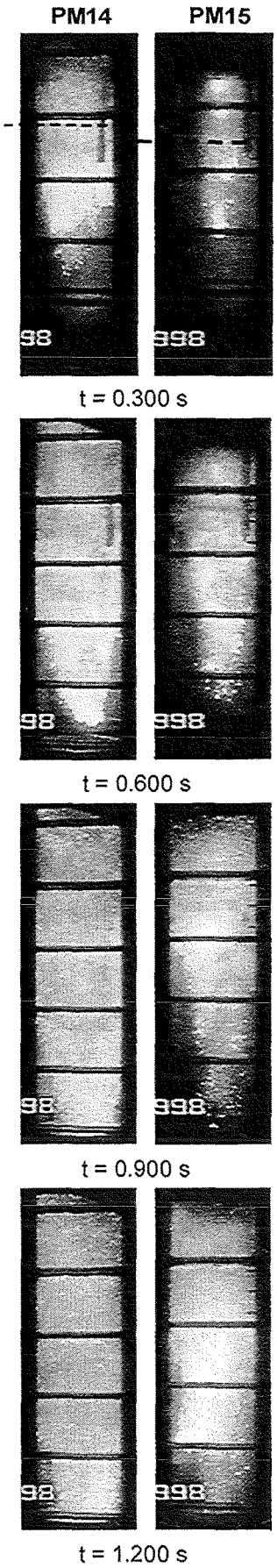

Fig. 2: Development of the interaction zone at selected times showing the influence of the system pressure (PM14: atmospheric pressure, PM15: 0.5 MPa). The initial water level is marked by dashed lines in the top pictures.

TEST RESULTS

Table 1. Test conditions

		PM14	PM15
Melt			
Mass	kg	23.2	23.1
Temperature	K	2600	
Composition		>90% oxides, <10% iron	
Melt release			
Orifice diameter	mm	60	
Init. driving pressure	MPa	0.06	0.03
Speed †	m/s	5.8 – 3.0	3.4 – 3.7
Falling height	mm	193	323
Water			
Depth	mm	1340	1230
Temperature	K	373	416
Subcooling	K	0	8 ±1
System pressure		0.1 MPa	0.5 MPa

†Calculated on the basis of the actual driving pressure data

General course of events

By the penetration of the melt into the water an interaction zone is formed which is composed of melt, steam, and water. The formation of steam which goes along with a pressure rise displaces the water which in turn leads to an increase in the water level. The melt stream fragments due to hydrodynamic interactions with the water and steam, respectively. The boundaries of the interaction zone expand in axial and radial directions. The steam flow occurs from the interaction zone through the annular compartment and the venting lines into the surrounding vessel. Due to the long travel distance, the melt particles solidify or get at least a solid crust before they are collected at the fragment catcher.

Detailed results

Progression of the interaction zone The video and high-speed films give good information about the course of events. To better compare the test results, zero time defines the time of the first melt/water contact. Figure 2 gives the extensions of the interaction zones for four selected times. The pictures show the interaction zone advanced faster in axial and radial directions in PM14 than in PM15.

The development of the interaction zone derived from void data are shown in Fig. 3 with the water depth as the axial co-ordinate in a mirror-inverted form for both tests. In the construction of the contour lines (i.e. lines of constant time) which represent the envelope of outermost steam/liquid interfaces toward the water pool, the instants of the first changes from "water" to "steam" of the void sensors were taken as an input to a small numerical routine based on the interpolation method. Note that rotational symmetry has been assumed in the presentation since, because of the limited number of measuring lances, the data of all sensors were used in the construction regardless of the different azimuthal positions of the lances.

The films show, as in previous experiments, that the melt sometimes proceeded intermittently as well as somewhat non-symmetrically related to the vessel axis. Non-symmetrical advance can also be concluded from the void measurements (Fig. 3) on closer examination. Two examples are given: (1) The films (Fig. 2) show the axial speed was markedly faster in PM14 than in PM15 whereas approximately equal penetration rates along the vessel axis can be derived from the lines in Fig. 3 for both tests up to the time of 0.4 s. We conclude that the melt penetration was non-symmetrical in PM14 initially. (2) The contour lines regarding 0.5 to 1.2 s in PM15 are more closely packed below the -700 mm co-ordinate than above it. We conclude from this that the leading edge of the melt advanced for some time in a section of the vessel cross section that was not monitored by the void measurements.

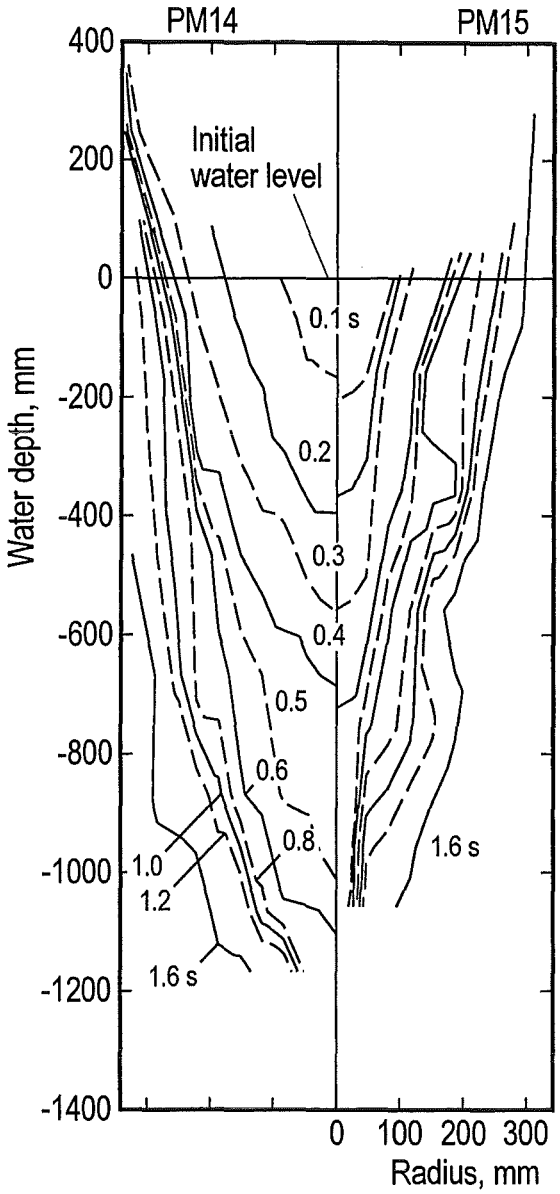

Fig. 3 Progression of the interaction zone into the water with the time as a parameter; the times are identical for both tests.

Note that the upper ends of the contour lines (up to time 0.3 s in PM14 and 0.8 s in PM15) correspond to the water level data. One can deduce from the shape of the lines that it was the smaller steam volume production rate in PM15 (see below) that caused less water displacement which in turn resulted in a smaller water level rise.

The advance of water drops carried with the steam into the annular gas compartment can be pursued in the respective void measurements (not shown). The data show that the front of the water particles moved much faster towards the exit in the case of the smaller system pressure (PM14). In both tests, the water fraction was overwhelmingly concentrated in the outermost regions, i.e. in the vicinity of the vessel wall.

Pressure and steam flow measurements The time histories of the pressure and the steam production rates are compared in Figs. 4 and 5. Due to the larger system pressure in PM15, the pressure increase as well as the steam volume rate were smaller in this test than in PM14 by factors of 1/4 to 1/5; these numbers approximately agree with the ratio of the actual steam densities which is about 0.22. On the other hand, the steam mass flow rates in both tests are comparable (Fig. 5b). While starting to increase later, the integrated steam mass in PM15 attained the same rate as that in PM14 from about 0.7 s on. It should be noted that the break-downs occurring in the PM14 flow signal between 1.3 and 1.8 s are caused by excessive fractions of water droplets carried with the steam that temporary plugged two of the venting pipes. Leaving apart other influencing variables, one can presume from this result that the heat transfer between melt and water was only little influenced by the system pressure.

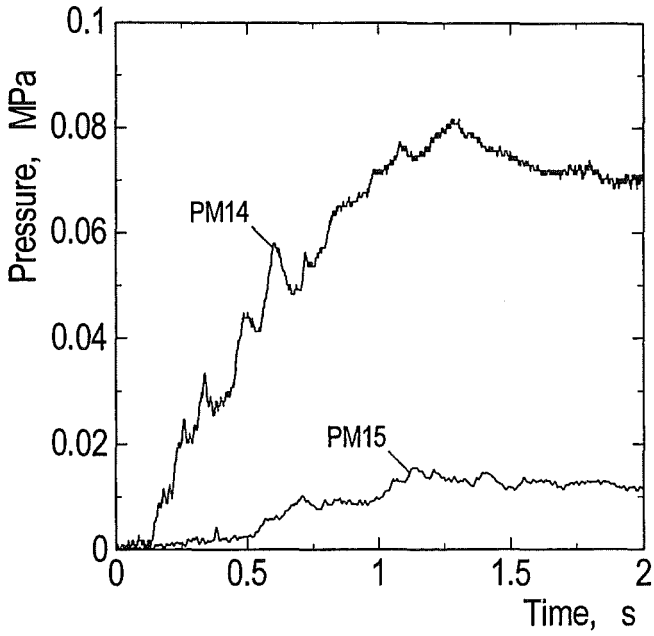

Fig. 4 Dynamic pressure data obtained from the PK11 gauges located in the water at –1065 mm height.

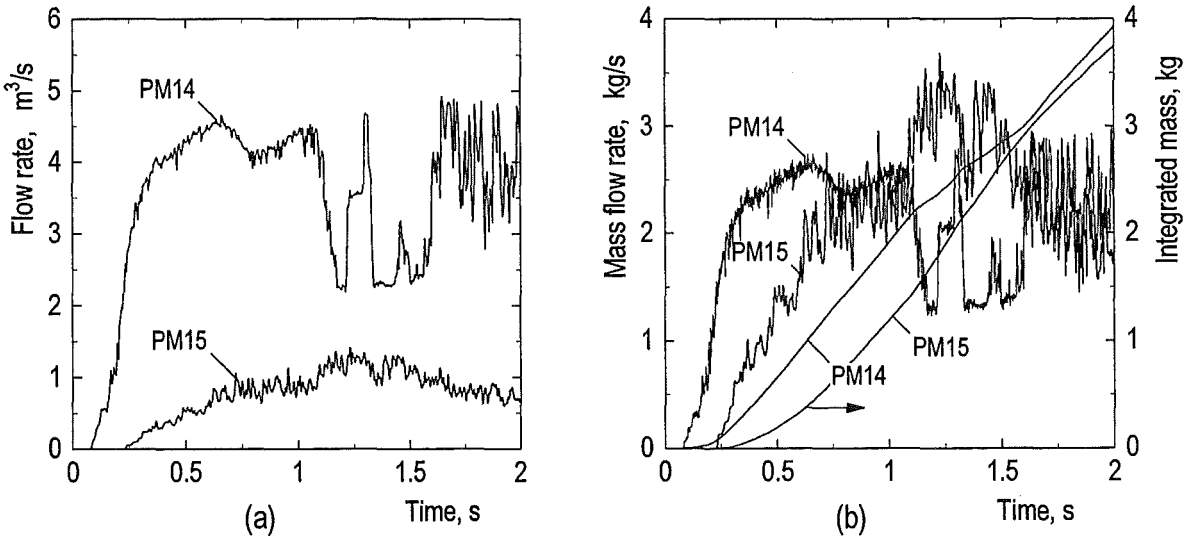

Fig. 5 Steam volume flow rates (a) and mass flow rates (b).

Substantial rises in the pressure and steam flow rates occurred with short delay times around 0.15 to 0.25 s after the first melt/water contact. This is a typical result of all PREMIX experiments. It is conceivable that the small subcooling of the water (eight Kelvin) in PM15 has additionally extended the delay. At the times of the marked pressure rises, the melt streams had penetrated distances of about 420 mm (PM14) and 450 mm (PM15) into the water.

Melt stream fragmentation The melt stream which appeared compact at the beginning fragmented on its way down. Fragmentation took place at the leading front as well as at the circumference of the jet where the actual fragmentation processes, e.g. jet break-up due to shearing flow of steam along the jet (Kelvin-Helmholtz instability) will not be discussed here. Anyhow, it is presumed that the core of the jet remained compact for a certain period of time. The life time of a compact jet was estimated on the basis of the penetration speed derived from the films. We conclude that a compact jet existed as long as the speed was large, i.e. typically 2.5 m/s. This was given during the first period of time. The value of 0.7 m/s estimated for the following period of time is presumed to be evidence for the existence of a melt stream that was largely fragmented in its leading part.

Additional evidence is provided by the consecutive destruction of the thermocouples. These were located at various depths in the water close to the vessel axis. It is concluded that the thermocouple tips were destroyed as long as the melt jet was compact; they were not destroyed in case the jet was largely fragmented. The respective couples of data (water depth and time of change) are about 1100 mm and 0.75 s in PM14, and 1050 mm and 0.70 s in PM15.

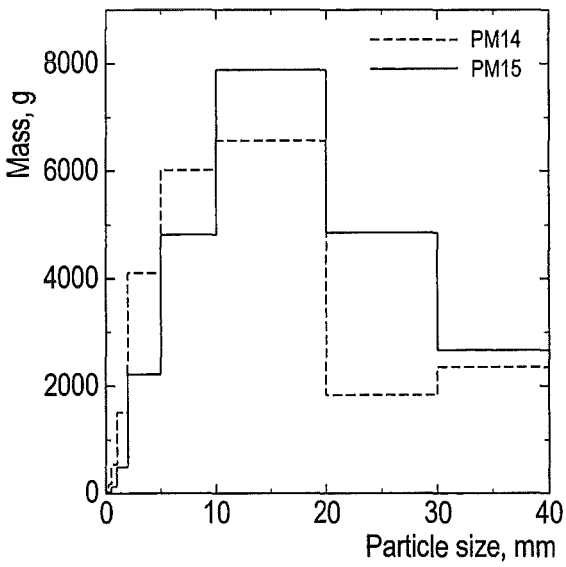

Fig. 6 Post test particle size distribution

The particle size distribution of the melt fragments (Fig. 6) collected after the test from the various sites (fragment catcher, water separator, and vessel basement) shows a shift towards larger sizes for the test with the larger system pressure (PM15). One can conclude from this result that, if the

total surface of the fragments was also smaller in PM15 during the first second, the steam mass production rate was smaller, too. This result must be taken into account in the judgement of the steam generation rate.

Volumes due to interaction Various sorts of volumes generated as a consequence of the interaction are shown on top, average volume fractions of the three components within the interaction zone at the bottom of Figure 7. The volumes of the interaction zone were estimated from the lines in Fig. 3 assuming rotational symmetry; the volumes due to the level rise (i.e. level rise times vessel cross section) are auxiliary data used in the calculation; the melt volume flow entering the interaction zone is best estimated. The steam mass flow rates (liquefied steam, labelled exit) are comparatively small. For more details of the calculation see Ref. 3.

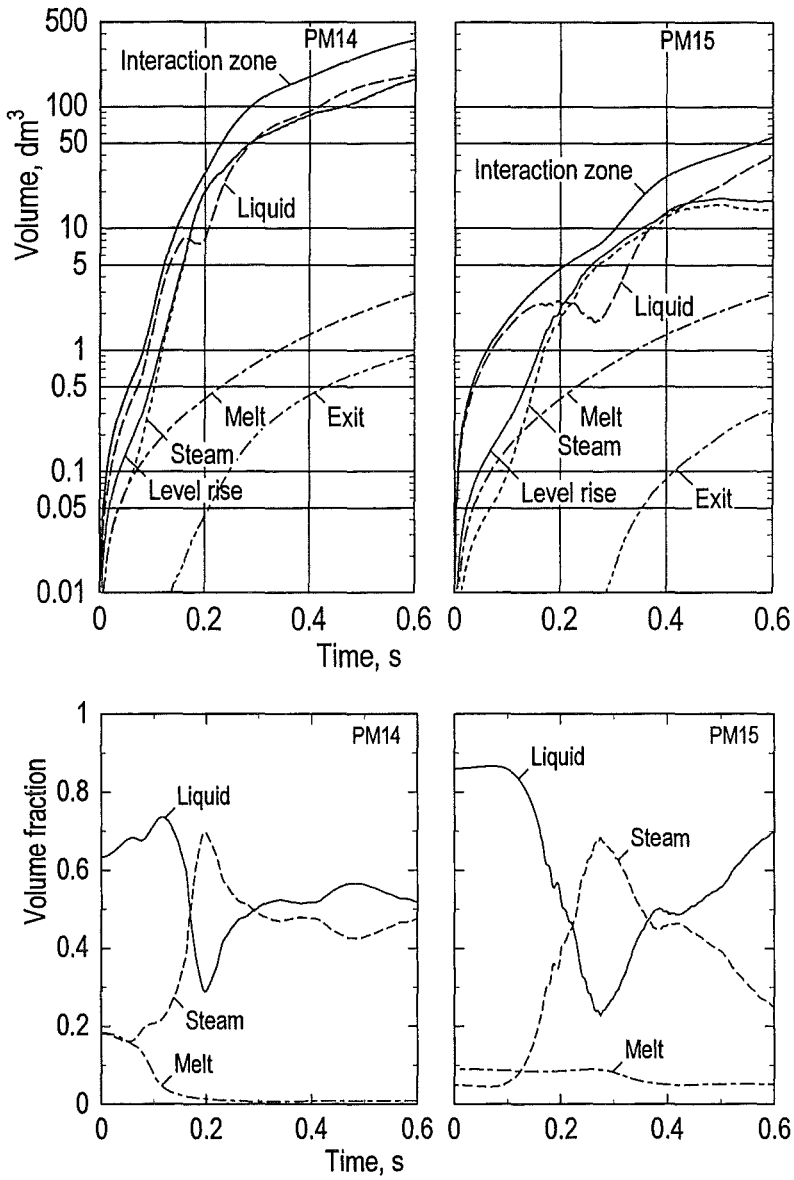

Fig. 7 Various volumes resulting from melt/water interaction and partial volumes of the interaction zone (steam, liquid, and melt) versus time (top). Average volume fractions of the components inside the interaction zone (bottom).

The considerable effect of the larger system pressure (in PM15) found above in the steam volume flow rates, is likewise found in the time histories of the volumes presented in Fig. 7. The differences in the two tests predominantly developed after the time of about 0.1 s. For example, the ratio of the steam volumes within the interaction zones amounted to 1/8 at the time

0.3 s. It should be noted that reasonable results can generally be obtained only up to the time of about 0.5 s since afterwards the error in the measurements and the error due to the assumptions made become large.

The time histories of the average volume fractions which were estimated using the volume data give additional information. Both the steam and melt volume fractions were small in the initial periods (i.e. up to the time of 0.1 s) of both tests. The melt volume fraction decreased with time; the decrease was more rapid in PM14 due to the rapid increase of the absolute interaction volume. The liquid volume fraction was large in the beginning because the initial melt release occurred as a shower of drops and the volume of the interaction zone included the volume of the water between these drops. After having passed relative minimum and maximum values the initial period of time, the steam and liquid fractions in both tests approached average values between 0.4 and 0.6.

REFERENCES

[1] A. Kaiser, H. Will, and W. Schütz, PREMIX, Documentation of the results of experiments PM12, PM13, and PM14. FZKA report to be published

[2] D. Magallon, G. Berthoud, W. Schütz, N. Kolev, A. Alemberti, R. Seghal, M. Bürger, G. Colombo, B. Turland, S. Zero, 1998.Characterisation of processes which govern quenching of molten corium in water including steam explosions, Proc. FISA – EU research on severe accidents, Luxembourg, Nov. 1997, EUR 18258 EN

[3] A. Kaiser, W. Schütz, H. Will, PREMIX, Experiment on steam explosion, Jahrestagung Kerntechnik, Aachen, May 1997

ACKNOWLEDGEMENT

This work is partly funded by the European Community (under contract FI4S-CT96-0037), SIEMENS and a consortium of German electricity utilities.

2. ECO

The PREMIX test series will be completed in agreement with the partners by two or three tests until June 1999. Additional experiments on demand will be postponed to the time a series of ECO tests have been performed.

The ECO experiments are directed to measure the conversion of thermal to mechanical energy in case of a steam explosion under well defined conditions. For this purpose a new test facility was designed, which is based on the PREMIX-tests. Substantial parameters (Table 1) are similar, e.g. dimensions of the facility, melt mass and melt temperature, release, water inventory, test procedure. By this, it is possible to use the results gained from the PREMIX-tests for the definition of conservative starting conditions. Furthermore, the experiences are worthwhile for the interpretation of the measurements because of the missing possibility for observation. The facility mainly consists of a piston/cylinder-system (Fig. 1). The melt generator is part of the cylinder. The energy resulting from the steam explosion causes the movement of the piston against a well defined constraint. The energy is measured by three independent and diverse principles:

- force
  - a) Strength of the crushing material
  - b) reaction force in the frame by means of strain gauges
  - c) pressure inside the facility by means of diverse gauges
- movement
  - a) high speed cinematography
  - b) deflection meters
  - c) compression of the crushing material

The main parts are already fabricated, and construction will start soon. After termination of the PREMIX test series in autumn 1999 the ECO facility will be mounted inside the FAUNA vessel. This thick-walled vessel will act as safety container in case of an unexpected high energy release. The crushing material as designed presently allows for an energy dissipation of 7.2 MJ. This is 17 % of the thermal energy of 10 kg alumina at 2600 K.

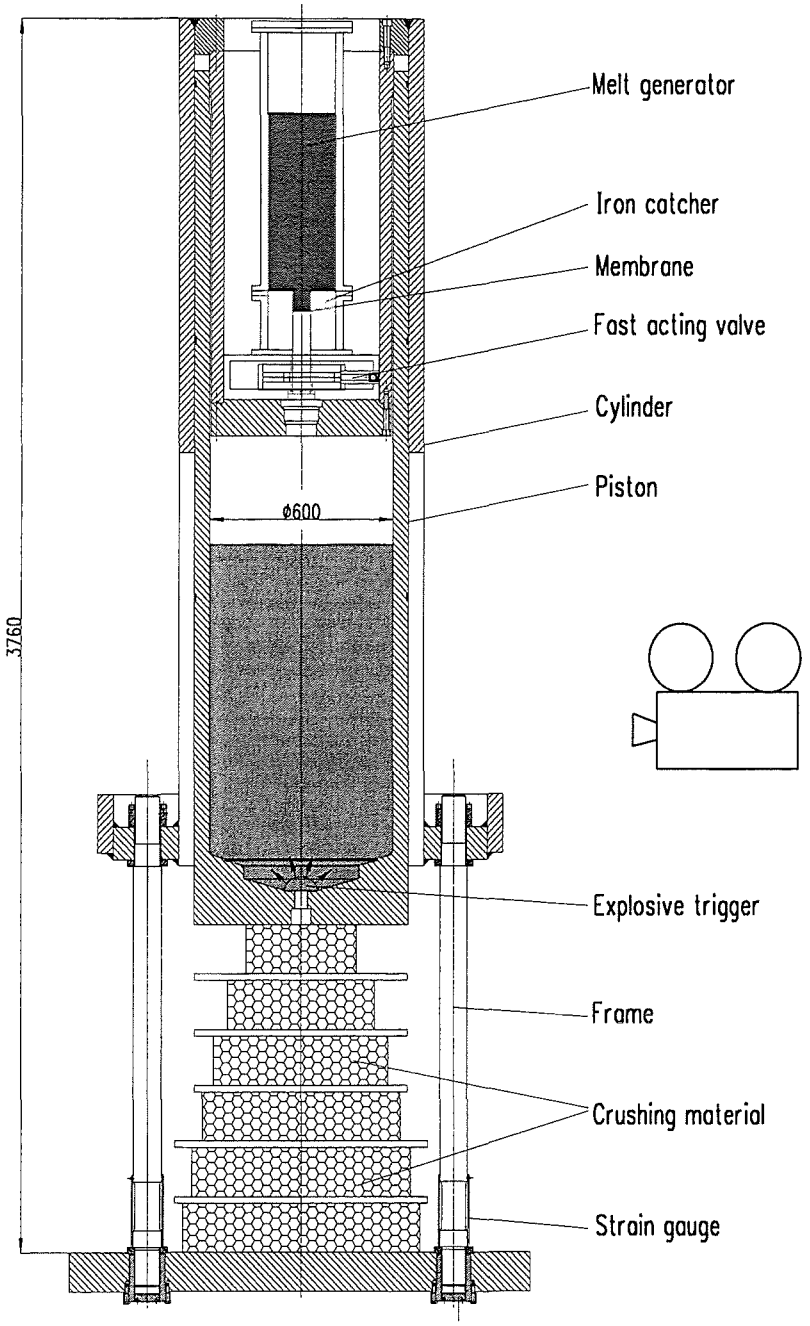

Fig. 1: ECO-facility

III. Theoretische Arbeiten zur Schmelze-Kühlmittel-Wechselwirkung

(H. Jacobs, B. Stehle, K. Thurnay, L. Väth, INR; M. Böttcher, U. Imke, M. Lummer, D. Struwe, IRS)

Abstract

Work in 1998 concentrated on using the multicomponent-multiphase codes MATTINA and MC3D to evaluate the consequences of in-vessel fuel coolant interactions in the European Pressurised Water Reactor. Besides that the codes were further tested and partially verified by calculations of experiments of the programmes QUEOS, PREMIX and FARO.

Zusammenfassung

Der Schwerpunkt der Arbeiten lag 1998 auf der Anwendung der Mehrkomponenten-Mehrphasen-Codes MATTINA und MC3D zur Abschätzung der Folgen der Schmelze-Kühlmittel-Wechselwirkung im European Pressurized Water Reactor. Die Codes wurden getestet und teilweise auch durch Nachrechnungen von QUEOS-, PREMIX- und FARO-Experimenten verifiziert.

Code validation

MATTINA and the three field application of MC3D were intensively used for theoretical interpretation of experiments performed in the programmes QUEOS [1], FARO [2], and PREMIX [3]. Though progress has been made when simulating the high pressure FARO experiments and some of the QUEOS experiments, difficulties in interpretation of the low pressure FARO- and the PREMIX experiments are not yet resolved. Current understanding of these difficulties is that they arise from numerical difficulties, simplified modelling of physical phenomena and insufficient knowledge of experimental boundary conditions. One identified problem is numerical diffusion which is due to the first order difference schemes in space and time used in both codes. In some cases, the codes appear to overestimate water displacement from the mixture zone with the consequence of stronger separation of melt and water and the reduction of the thermal interaction during premixing.

To get more insight into numerical characteristics of MC3D calculations, a series of test cases were investigated. Results are reported in [4]. For the present calculations, the version 3.1 (September 1997) was used including some changes made by FZK-IRS, which are partly described in [4]. The QUEOS experiments, which give low evaporation rates at low pressure (1 bar) and do not cover the phenomena of fragmentation can be calculated with satisfying precision for the first 0.2 s as shown for QUEOS12 in Figure 1. For later times a large pressure peak is calculated caused by water pushed into the cross-section outlet. The FARO-experiments at high pressures like the L-14 test (50 bar) defining the international standard problem ISP-39 [5] can be recalculated to give a satisfactory pressure curve using an initial melt drop diameter of 7 mm (see Figure 2). The total surface of fragments found at the end of the experiment is underestimated

All calculations for the EPR are done at a low pressure level of 2.5 bar, so validation of the code for low pressure experiments becomes very important. PREMIX is an experimental FZK-program to investigate mixing behaviour of hot alumina melt which is discharged into water at low pressure levels [3]. All calculations for 1 bar experiments show that a large vapour bubble is created around the penetrating melt. Water is pushed strongly apart from the melt reducing interaction and leading to an early blocking of the outlet cross-section. Those effects are not seen in the experiments. A lot of calculations were made changing boundary conditions and code parameters to cover a variety of unknown experimental conditions and poorly modelled physical processes. The result is that vapour bubble expansion and strong vapour outlet blocking are generic effects in the calculation of low pressure experiments with large vapour production. That is confirmed by first calculations for FARO low pressure experiments like L-27 and L-28. The reason is the large difference in density between water and vapour. The mass of 100 g vapour needs place of 167 kg water (1 bar). If the transport of vapour from the mixture zone to the outlet cannot be described with high precision, the balance of vapour production and removal from the interaction zone can lead to an overestimation of vapour in the interaction zone pushing away water. That leads to some isolation of hot melt from cold water reducing premixing.

To overcome the problem of outlet blocking, an additional boundary condition is introduced around the outlet. Water is released at the top of the test chamber and the outlet is not disturbed by intense two phase flow. The amount of water released is some measure how strong water is removed from the interaction zone and how far we are from experimental conditions. It was seen that it is very important to simulate the fast radial expansion of the interaction zone, which was observed in the experiment. To reach such strong radial expansion is difficult with the present modelling. Three measures were taken to reproduce the experimental observations:

- smearing the melt jet by expanding the diameter by a factor of two
- start with large particles
- reduce the surface tension by a factor of about ten

So we start with a spray of large particles which have strong momentum coupling with its environment and high fragmentation rates due to low surface tension. That helps to transport more melt droplets in radial direction. The melt evaporates water at those locations resulting in some counter-pressure for the big bubble around the spray type jet. The graphics given in Figures 3 and 4 show the pressure curve and the integrated steam release dependent on time in comparison to the experimental curves of PM13 [6]. The good agreement of the calculation with those experimental findings is achieved by choosing the initial melt droplet diameter to 2 cm and using a droplet-droplet heat transfer model. About 110 kg water left the vessel during 0.5 s in the calculation, which is a lot for the short time. 220 kg water were missing after the whole experiment.

With MATTINA [6], the validation has been continued by simulating experiment QUEOS 48. This is an experiment in which the local void fraction has been measured with many probes in two horizontal lines 65 mm apart that crossed the centre of the test vessel at a height of 40 cm. The test has been performed with 10 kg of molybdenum spheres at 2000 K in a jet with 100 mm diameter and with saturated water. Here again the simulation started with a sphere column that was assumed in accordance with the experiment just above the water surface. As was to be expected, leading front penetration, pressure rise (cf. Fig. 3.6) and the distribution of particles in the multiphase mixture where quite close to the experimental findings. The steam

flow rate, see Fig. 3.7, agreed with the measurement in the maximum but was somewhat too high later on, because the pressure losses were too low. The calculated local void conditions were compared with the experiment in two small volumes, one in the centre of the test vessel and the other one at a radius of 15 cm from the centre, see Fig. 3.8. Initially the calculation reproduced correctly that the void almost jumped to one in the centre immediately and rose more gradually at the outer position. But after about 0.2 sec both calculated values were close to one while the experimental values were between 0.4 and 0.5. So the void was overestimated by about a factor 2 during about half the transient. The comparison becomes slightly better when taking into account that actually the water was slightly subcooled (up to 2 K at the bottom) in the experiment. One can conclude that the void distribution is very sensitive to details of the modelling and that deviations from the experimental values are observed. It should be noted that this void condition is expected to have a strong influence on the 'efficiency' of steam explosions. Therefore it is used to decide whether corium present in the neighbourhood is to be considered as premixed or not – if such a decision is required.

The situation is much less satisfactory in the case of the PREMIX experiments [3]. Here, experiment 13 [7] has been studied. A straight forward simulation leads (until now) to completely wrong results. It is, e. g. observed that the melt penetrates for quite some time (0.2...0.4 sec) into the water without much pressure rise and a slow rise of the water surface. This phase is then followed by a steep pressure rise. In a standard simulation, however, the pressure would rise gradually from the very beginning and the water surface would rise besides the melt jet, thus blocking soon the initially 20 cm high vapour space between water and melt generator. This then prevents that steam can escape into the annular space besides the melt generator so that water is pushed into that gap. This is partly due to the fact that a 'standard' simulation does not describe properly the rather complicated (and not too well known) conditions of initial melt release and melt-water contact. In this case, the wrong behaviour has partly been avoided by assuming a slow start of the melt ejection and by spraying sideways the initial part of the melt as it is observed in the experiment. With such modelling the flow path towards the venting lines was blocked by water only intermittently. In this context it might also play a role that the actual situation is really three-dimensional while axial symmetry is assumed in the

calculations. So one shouldn't expect too much from the simulations. But in addition (and one could say: in spite of that), the pressure rises much less steeply than in the experiment and still, after about 0.7 sec, the inlet to the venting lines (1.8 m above the initial water level) is blocked by liquid water which does not occur before 1.3 sec in the experiment (at one of the four vent lines initially). At 0.7 sec, the pressure is underestimated by about 40 % and the steam flow by about 55 %. An obvious explanation for such underestimation would be a too small heat transfer area (melt drop surface). In the calculation described here, we assumed an initial particle size of 60 mm in the melt 'jet' (similar to the orifice diameter) and relied on the code to describe the break-up into smaller drops. As a result we obtain the 'jet' with 60 mm particle diameter and particles of 6...7 mm diameter in the surrounding. This doesn't look unreasonable.

This problem needs further evaluation and at the moment it is not possible to judge on the fitness of MATTINA for premixing studies on the basis of comparisons with the PREMIX experiments.

Reactor application

In a first tentative application of both codes to an accident analysis, the premixing of corium pouring into residual water in the lower plenum of the EPR was investigated. A simplified geometry including the heavy reflector, the lower core support plate and the flow distribution plate was chosen to describe the most important structure components of the reactor vessel internals. A low pressure scenario was assumed with a system pressure of 2.5 bar and a large corium pool of 110 t at 3000 K located directly on the lower core support plate. The level of saturated water reached the upper edge of the lower core support plate. Axial relocation of melt in the center of the core was considered as a compact jet through a large failure or as a distributed outflow through the porosity of the lower core support plate. Radial melt relocation through heavy reflector and core shroud into the downcomer was simulated at the bottom or at the top of the molten pool. The basic free cross section was assumed to be about 0.2 m^2.

Parameter studies were done to cover a band of uncertainties. A very strong influence on the results is recognised for the variation of the initial size and the transient increase of the melt release area. The initial droplet size is a key value for the strength of the thermal melt water interaction. The pressure losses at the distribution flow plate in the lower plenum influences the mixing of corium with water considerably. The spatial discretization has a strong impact on the overall result due to the nonlinear behaviour of most of the simulated processes and the utilization of a first order scheme for the convective terms in the basic equations. Feedback of pressure losses at coolant inlet and outlet and at the junction between downcomer and lower plenum is of minor importance. Moderate variations of the system pressure give similar results. For MC3D the change in melt surface tension does not give large differences due to the used combination of fragmentation and drag models.

The maximum mass and thermal energy of premixed corium is determined by summation over all mesh cells with a water volume fraction greater than 0.1, thus attempting to compensate the strong water depletion effect observed during recalculation of experiments. The average water volume fraction in the premixing zone is calculated by summation of all mesh cells containing water volume fractions greater than 0.1 and melt volume fractions greater than 0.01.

The calculations indicate that the water of the lower plenum is displaced rapidly into the downcomer by vapour for axial and radial outflow scenarios. Radial outflows should be investigated by 3D-simulations, to avoid an artificial enclosure of water in the lower plenum. Generally premixing is intensified by large melt release cross sections, large initial droplet diameters and pressure loss in the lower plenum flow distribution plate. The conservatively oriented evaluation of all investigated cases leads to a maximum of thermal premixed energies of 3 GJ and an average water volume fraction of about 0.5 to 0.6 in the premixing zone. In the majority of the calculated cases the thermal premixed energies vary between 0.5 to 2.0 GJ and the values of the respective average water volume fraction between 0.2 to 0.5. The total amount of melt in the lower plenum can be much larger than the premixed melt mass with a considerable water inventory still available. In the end, water is stratified above a compact molten corium pool.

Generally the two codes show similar results. MATTINA gives lower thermal premixed energies due to stronger water displacement, which is caused by stronger evaporation events after intensive fragmentation of melt droplets. The presently used MC3D version simulates a more moderate fragmentation behaviour leading to less evaporation and water depletion. Both codes predict removal of non negligible amounts of fragmented core material into the primary circuit, if radial outflow scenarios are considered.

Figure 8 shows the thermal energy of premixed melt for axial fuel relocation into the lower plenum calculated by MATTINA and MC3D. In this case, the plenum is filled with saturated water at 2.5 bar. Coherent failure of the molten pool crust with a radius of 0.45 m is assumed corresponding to about 14 cross sections of a subassembly. In that region the permeability of 0.33 of the lower core support plate forms the total cross section available for melt outflow, which is driven by gravity of a 110 t molten pool of corium. As initial droplet diameter the large value of 5 cm is used representing the order of magnitude of the holes in the support grid. The thermal energy calculated by MATTINA is more than a factor of two smaller than the result given by MC3D even for the maximum values. In the MATTINA calculation only one maximum appears and the mixing energy tends to zero for the late phase, which is not the case in the MC3D calculation.

The evaluation of the possible mechanical loads from a steam explosion with 3 GJ of thermal energy available has shown that such explosion can be contained within the reactor pressure vessel without failure of the vessel head. Further work will be required to remove existing uncertainties, to reduce the conservatisms that these uncertainties required in the present study, and to evaluate other possible consequences of in-vessel steam explosions.

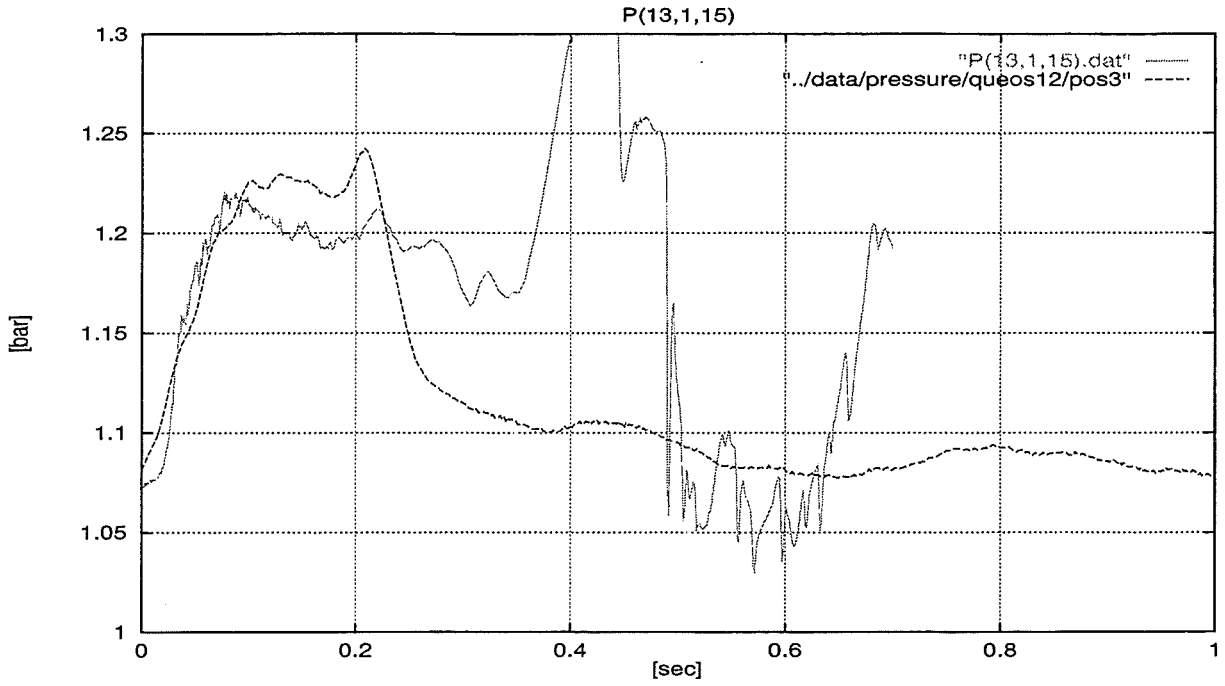

Figure 1: Calculated (P(13,1,15).dat) and measured pressure curve in QUEOS12.

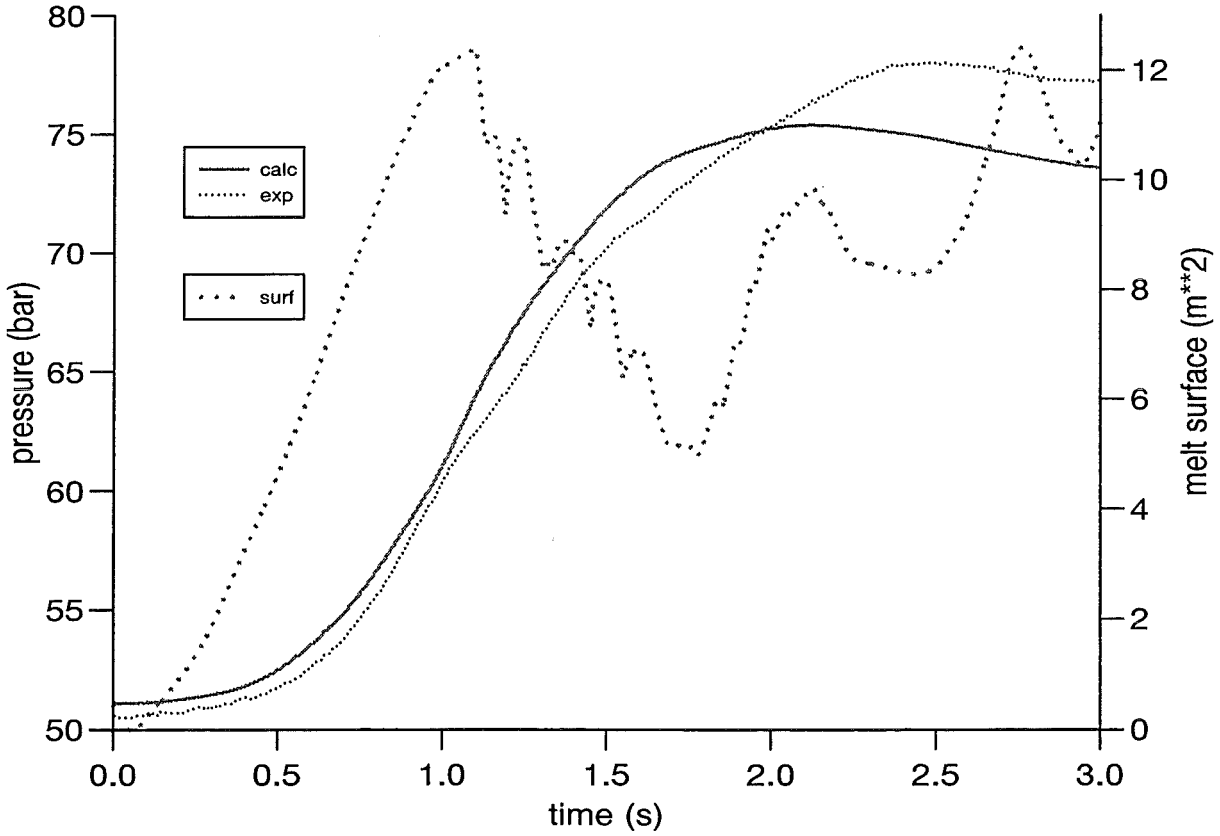

Figure 2: Pressure in the gas dome and total heat transfer surface for FARO L-14.

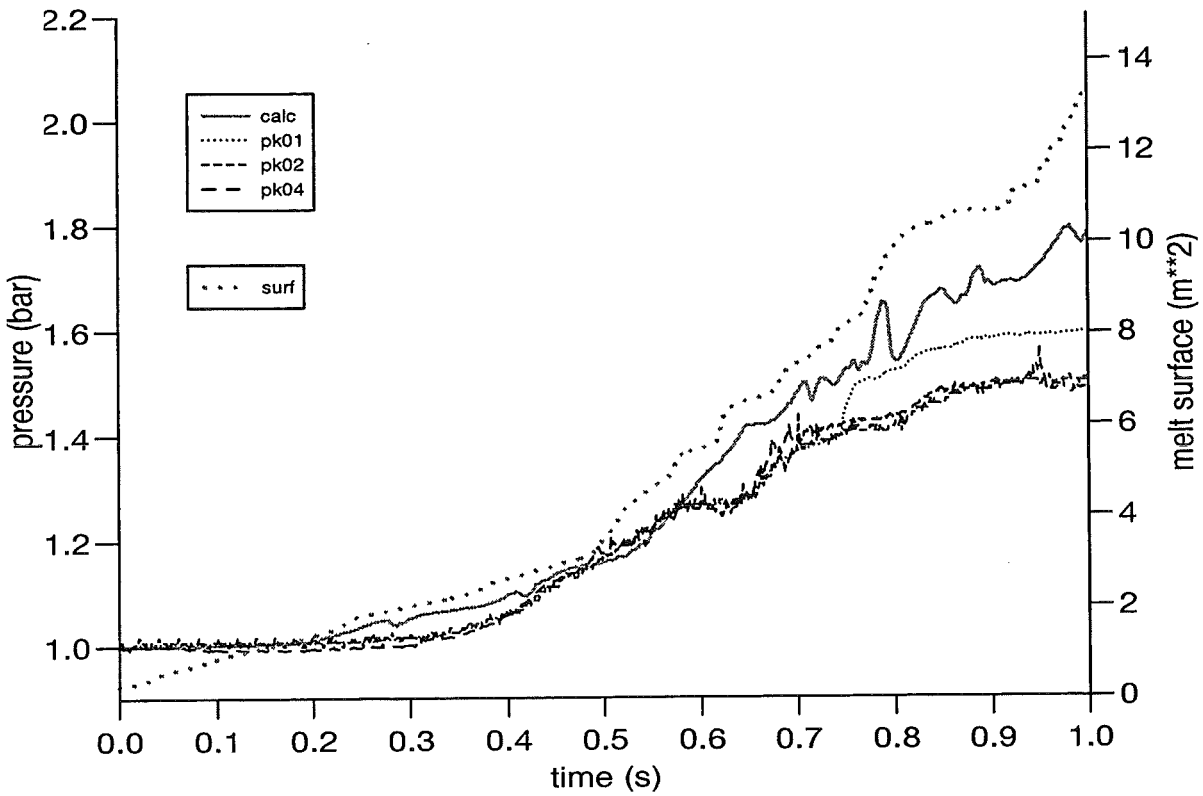

Figure 3: Pressure above initial water level and melt surface for PREMIX PM13 with water sink at the top.

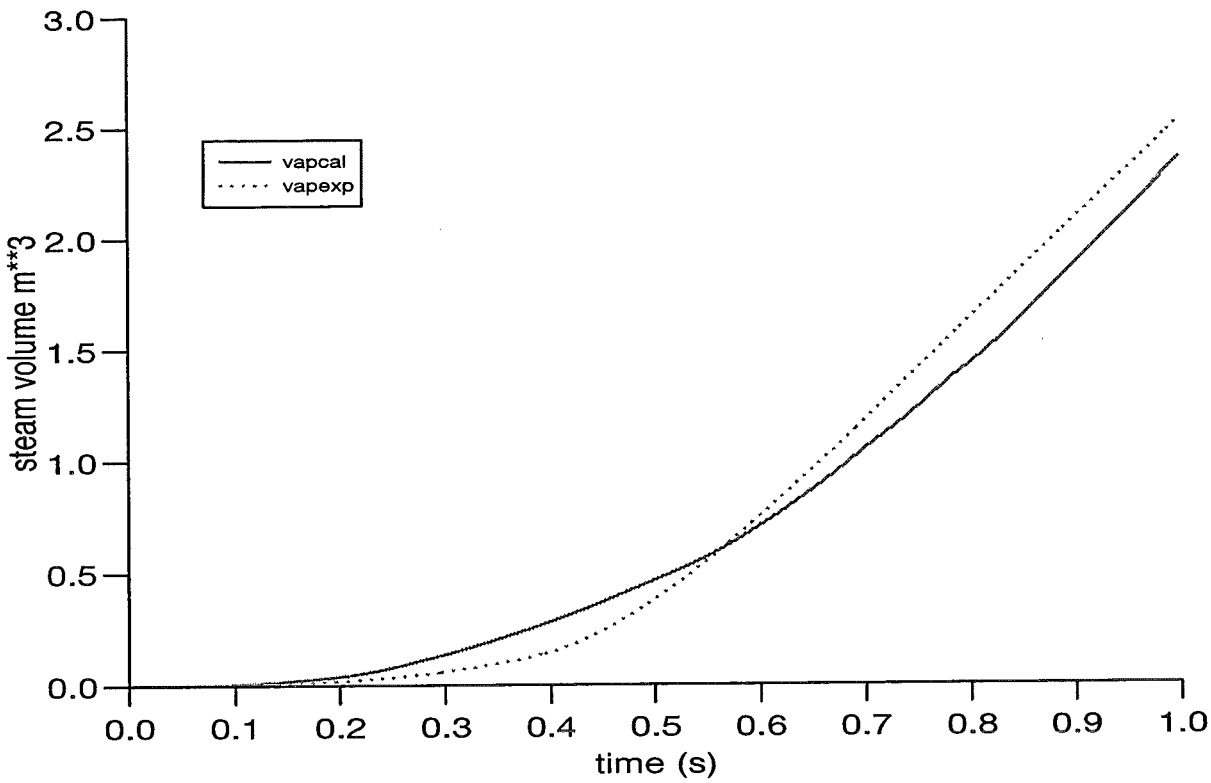

Figure 4: Integrated vapour volume released from the venting pipes for PREMIX PM13 with water sink at the top.

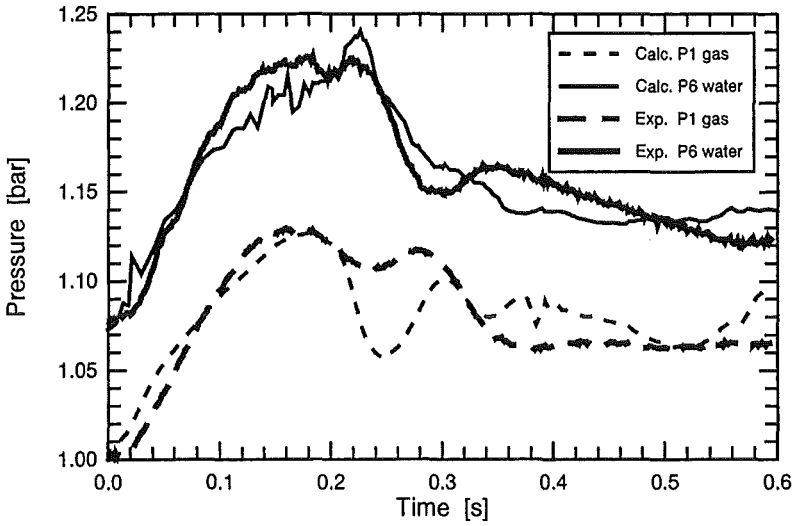

Figure 5: Experimental and calculated (MATTINA) pressure histories of QUEOS 48

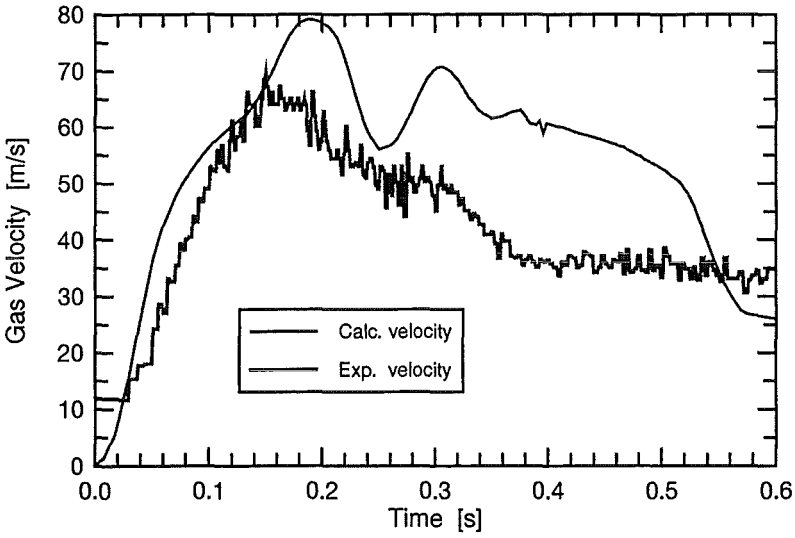

Figure 6: Experimental and calculated (MATTINA) gas velocities in the vent pipe for QUEOS 48

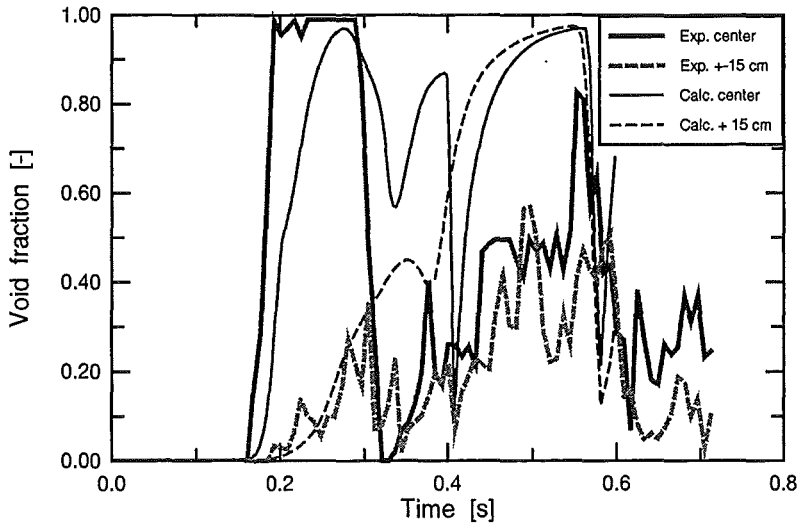

Figure 7: Experimental and calculated (MATTINA) void fraction histories for QUEOS 48

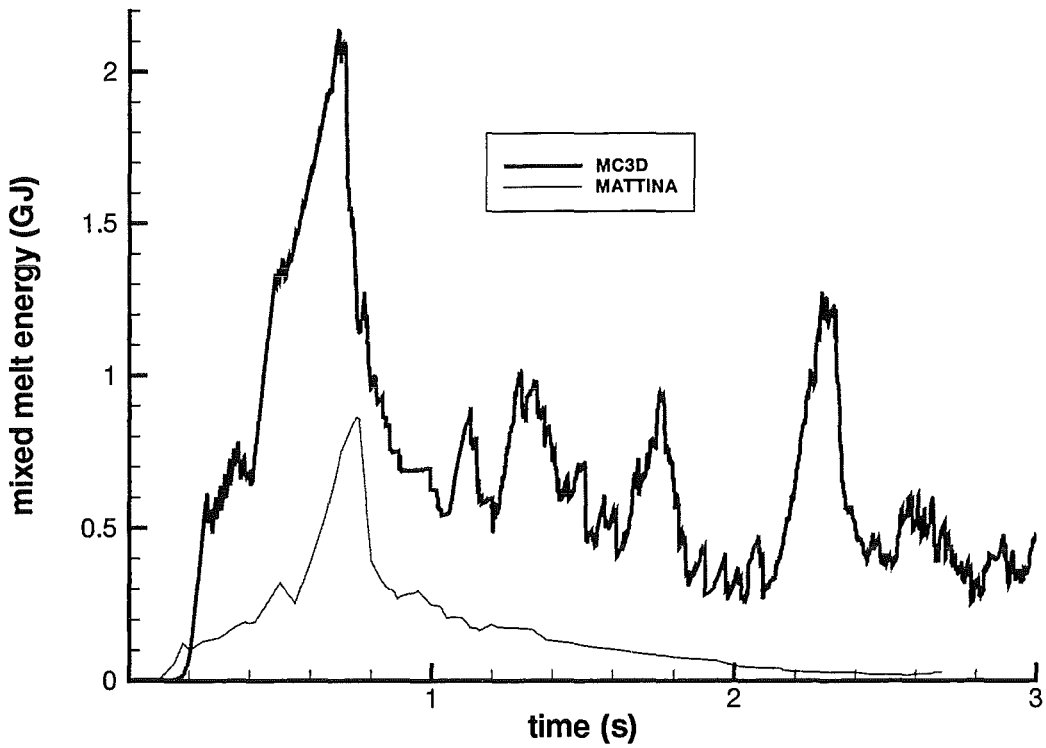

Figure 8: Thermal energy of premixed corium mass for the 0.1 limit of water volume fraction.

References

[1] L. Meyer, G. Schumacher, QUEOS, a Simulation-Experiment of the Premixing Phase of a Steam Explosion with Hot Spheres in Water Base Case Experiments, Forschungszentrum Karlsruhe, Wissenschaftliche Berichte, FZKA 5612, 1996

[2] D. Magallon, H. Hohmann, High Pressure Corium Melt Quenching Tests in Faro, Nucl. Eng. Des. 155 (1995) 253

[3] F. Huber, A. Kaiser, M. Steinbrück, H. Will, PREMIX, Documentation of the Results of Experiments PM01 to PM06, Wissenschaftliche Berichte, FZKA 5756, Forschungszentrum Karlsruhe, 1996

[4] U. Imke, Application of MC3D to simple test cases and fuel coolant interaction experiments, IRS-1 Notiz 1/98, Institut fuer Reaktorsicherheit, Forschungszentrum Karlsruhe, 1998

[5] A. Annunziato, C. Addabbo, G. Leva, OECD/CSNI International Standard Problem No. 39 on FARO Test L-14, Reference Specification, Institute for Systems, Informatics and Safety, Joint Research Centr, Ispra, Technical Note No. 1.96.64, April 1996

[6] L. Meyer, G. Schumacher, H. Jacobs, K. Thurnay, "Investigation of the premixing phase of a steam explosion with hot spheres, Nuclear Technology **123** (1998) 142-155

[7] A. Kaiser, W. Schütz, H. Will, PREMIX-13 Description and First Results, IRS-4-Notiz Nr. 1388/97, Institut für Reaktorsicherheit, Forschungszentrum Karlsruhe, 1997

32.21.03 Versagen des Reaktordruckbehälters und Dispersion der Kernschmelze

I. On the Identification of Material Parameters by Means of Neural Networks
(H. Lämmer, Ch. Tsakmakis, IMF II)

Kurzfassung

Das im vergangenen Jahr vorgestellte Verfahren zur Bestimmung der Materialparameter des finiten Thermoviskoplastizitätsmodells wurde im Berichtszeitraum modifiziert. Ausgehend von einer vereinfachten Version des Modells wurden für Temperaturen von 500 °C –1300 °C neue Parametersätze bestimmt, wobei Zug- und Kriechkurven des franösischen Reaktorbaustahls 16 MND5 zugrunde gelegt wurden. Anders als im vorhergehenden Jahresbericht beschrieben, wurden die Daten aus den Zug- und Kriechkurven allerdings getrennt trainiert. Daher wurden pro Temperatur zwei verschiedene neuronale Netze benutzt. Dies erleichterte den Trainingsprozeß und führte zu geringeren Fehlerraten, so daß sowohl Zug- und Kriechkurven in zufriedenstellender Weise beschrieben werden konnten. Um die Einflüße charakteristischer Parameter zu separieren und den gesamten Parametersatz eindeutig zu identifizieren, bedarf es jedoch Experimente mit komplizierteren Lastgeschichten. Deshalb wurden für den deutschen Reaktorbaustahl 20 MnMoNi 55 dehnungsgesteuerte zyklische Versuche mit zwei Haltezeiten für Temperaturen zwischen Raumtemperatur und 650 °C durchgeführt.

Abstract

The procedure, presented in 1997, to identify the material parameters of the finite deformation thermoviscoplasticity model by means of neural networks was modified. Starting from a simplified version of the model, new sets of parameters were determined in a temperature range from 500–1300 °C using the data from tensile and creep tests on 16 MND5 reactor pressure vessel steel. Contrary to the way described in the previous progress report, tensile and creep data were trained separately. Therefore, two different neural networks for each temperature were used. This facilitates the training process for the neural networks, leads to lower error measures and allows to describe both tensile and creep curves in a satisfactory way. To separate the effects of some characteristic parameters and to determine the whole set of parameters properly, uniaxial tests with more complex loading histories are necessary. Therefore, strain-controlled cyclic experiments with two relaxation phases on 20 MnMoNi 55 reactor pressure vessel steel in a temperature range from room temperature up to 650 °C were performed.

1 Introduction

To properly describe the failure behavior of the reactor pressure vessel (RPV) lower head after severe core melt accidents a finite deformation thermoviscoplasticity model with damage was developed and implemented in the ABAQUS finite element code. The model exhibits nonlinear isotropic and nonlinear kinematic hardening, where static recovery is taken into account. In a first step a simplified version of the constitutive equations was considered. The remaining 7 material parameters were determined by means of neural networks using the data from the tensile and creep tests on 16 MND5 RPV steel performed by CEA-Saclay[1] in a temperature range from 500–1100 °C.

It became obvious, that simple tension and creep tests are usually not sufficient to determine the material parameters properly. To identify the whole set of material parameters, uniaxial tests with more complex loading histories are necessary to separate the effects of some parameters. For example, cyclic tests are useful to distinguish between isotropic and kinematic hardening, whereas relaxation phases give information on the viscosity parameters and the parameters describing static recovery. For this reason, strain-controlled cyclic experiments with two relaxation phases on 20 MnMoNi 55 RPV steel at different temperatures were carried out. Some of these tests are presented in Section 4.

2 Constitutive equations

The constitutive equations, adopted in the present work, describe finite deformation thermoviscoplasticity with nonlinear kinematic hardening and static recovery. They represent a special case of the constitutive model described in [3]:

$$\overset{\nabla}{\mathbf{S}} = \dot{\mathbf{S}} - \mathbf{L}\,\mathbf{S} - \mathbf{S}\,\mathbf{L}^T = c\,[\mathbf{D} - \mathbf{D}_t - \mathbf{D}_p] \tag{1}$$

$$\mathbf{D}_t = \left\{\alpha + \frac{\partial \alpha}{\partial \theta}\,(\theta - \theta_{Ref})\right\}\dot{\theta}\,\mathbf{1} \tag{2}$$

$$\mathbf{D}_p = \dot{s}\sqrt{\frac{3}{2}}\,\frac{(\mathbf{S}-\mathbf{Z})^D}{\|(\mathbf{S}-\mathbf{Z})^D\|}\,, \quad \dot{s} = \frac{\langle \mathsf{F}\rangle^m}{\eta} \tag{3}$$

$$\mathsf{F} = \sqrt{\tfrac{3}{2}\,(\mathbf{S}-\mathbf{Z})^D \cdot (\mathbf{S}-\mathbf{Z})^D} - \mathsf{k} \tag{4}$$

$$\dot{\mathsf{k}} = \frac{\partial \mathsf{k}_0}{\partial \theta}\,\dot{\theta} \tag{5}$$

$$\overset{\nabla}{\mathbf{Z}} = \dot{\mathbf{Z}} - \mathbf{L}\,\mathbf{Z} - \mathbf{Z}\,\mathbf{L}^T = c\,\mathbf{D}_p - b\,\dot{s}\,\mathbf{Z} - p\,\|\mathbf{Z}\|^{\mathrm{w}-1}\,\mathbf{Z} + \frac{1}{c}\,\frac{\partial c}{\partial \theta}\,\mathbf{Z}\,\dot{\theta}\quad . \tag{6}$$

[1] Commissariat à l'énergie atomique, Department de Mecanique et de Technologie (CEA/DMT), F-Saclay

In these relations, boldface capital letters denote second-order tensors, while $\mathcal{C}$ is the fourth-order isotropic tensor

$$\mathcal{C} = \frac{E}{1+\nu}\mathcal{I} + \frac{E\,\nu}{(1+\nu)\,(1-2\nu)}\mathbf{1}\otimes\mathbf{1} \quad , \tag{7}$$

with E and ν being Young's modulus and Poisson ratio, respectively. In the case of viscoplasticity, F represents an overstress, which is used to define the rate of the arc length $\dot{s}$ directly, by means of relation $(3)_2$. For simplicity, only kinematic hardening (6) was taken into account. Thus, the constitutive equation responsible for isotropic hardening reduces to (5), where k_0 is the temperature dependent initial yield stress. For given E and ν, the number of parameters to be identified reduced to seven. For a more detailled description of the model and the meaning of the remaining variables see e.g. [3, 4].

For uniaxial tension with constant nominal strain rate $\dot{\varepsilon}_n$, the inelastic strain-stress relation is deduced from equations (1) – (6) to be

$$\sigma = S_{11} = \mathsf{F} + \xi + \mathsf{k}_0 \quad , \tag{8}$$

with the overstress being approximated by

$$\mathsf{F} = (\eta\,\dot{\varepsilon}_n)^{\frac{1}{m}} \tag{9}$$

and the contribution of the kinematic hardening by

$$\xi = \frac{c}{b-2}\left(1-e^{-(b-2)s}\right) + \frac{c}{2\,(b+1)}\left(1-e^{-(b+1)s}\right) \quad . \tag{10}$$

Characteristic properties of the hardening behavior may be obtained by considering two limiting cases

$$\Delta\Sigma := \lim_{s\to\infty}\sigma = \mathsf{F} + \mathsf{k}_0 + \frac{3}{2}\frac{c}{b}\frac{b^2}{(b^2-b-2)} \tag{11}$$

$$= \mathsf{F} + \mathsf{k}_0 + \frac{3}{2}\frac{c}{b}\,f(b) \tag{12}$$

and

$$\sigma' := \lim_{s\to 0}\frac{\mathrm{d}\sigma}{\mathrm{d}s} = \frac{3}{2}c \quad . \tag{13}$$

Of course, for characterizing hardening properties, one may omit the nonlinear function $f(b)$ in equation (12). Therefore, the stress

$$\Delta\sigma := \mathsf{F} + \mathsf{k}_0 + \frac{3}{2}\frac{c}{b} \quad , \tag{14}$$

will be used to characterize the hardening response.

3 Identification of the material parameters

Artificial neural networks represent a qualified tool for solving complex inverse problems in computational mechanics. They have been used sucessfully for parameter identification in the past (see e.g. [1, 2, 6, 8]). As outlined in [5] and illustrated in Figure 1 (right), a neural network consists of neurons connected with links to a highly parallel structure. Each neuron has multiple inputs and a single output value to mimic the biological brain neuron (see Figure 1 (left)). By supplying the network with training patterns, which consists of the input values and the corresponding desired output values, the error of each pattern can be calculated. This error is minimized by adjusting the synaptic weights w_{kj}, which represent the links between the neurons, by means of a so-called resilient backpropagation learning rule. After sucessful training, the network has been teached a relation between input and output values.

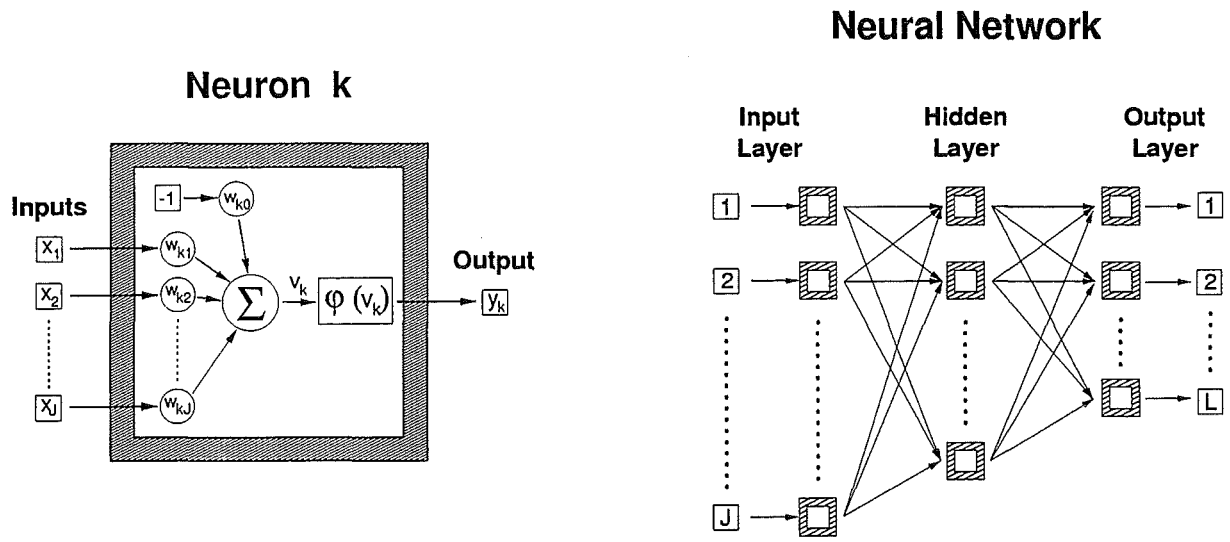

Fig. 1: Unit (left) and topology (right) of a multilayer perceptron (feed-forward neural network).

The simulation and training of the neural networks was performed by means of the neural network program SNNS (Version 4.1) [7], written and distributed by the Institute for Parallel and Distributed High Performance Systems (IPVR) of the University of Stuttgart. Contrary to the way described in [5], tensile and creep data were trained separately and two different neural networks for each temperature were used. First, characteristic properties describing uniaxial tension were determined from the strain-stress response. Then, this *a priori* knowledge was used for uniaxial creep to define suitable output quantities characterizing the time-strain responses.

3.1 Tensile curves

As illustrated in Figure 2, characteristic properties describing uniaxial tension are the initial yield stress k_0, the upper limit of the kinematic hardening approximated by $\frac{3}{2}\frac{c}{b}$, the slope of the kinematic hardening at the onset of inelastic deformation $\frac{3}{2}c$, and the overstress F approximated by (9). These properties have an essential influence on the strain-stress behavior, especially on the ultimate strength and the corresponding nominal strain.

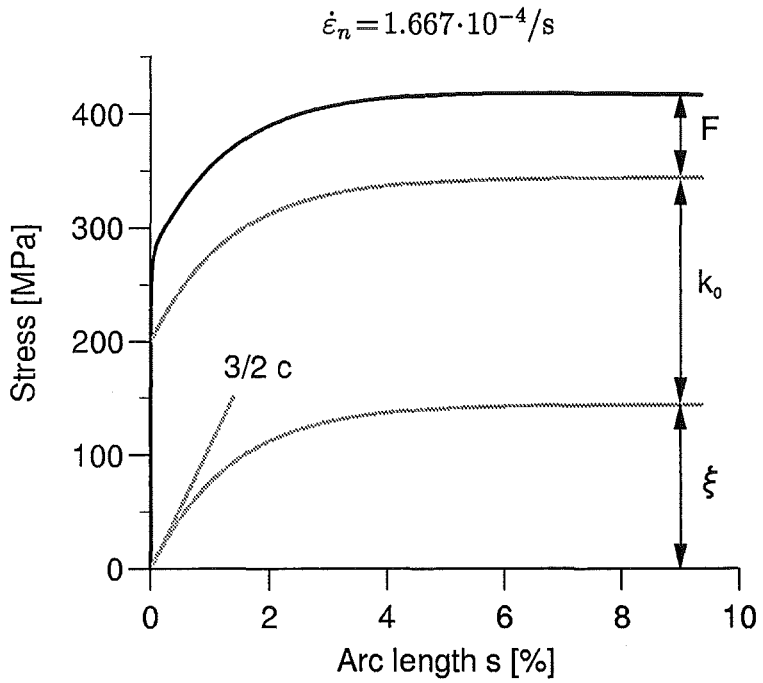

Fig. 2: Characteristic properties describing uniaxial tension.

The viscosity parameters m and η itself could not be determined from a monotonous tensile test with constant strain rate because they do not significantly affect the strain-stress behavior, provided that F = const.. To determine the viscosity parameters, additional information are necessary, resulting e.g. from tensile tests at different strain rates or tensile tests with relaxation phases. Thus, only the parameters k_0, $\frac{c}{b}$, c and F could be determined from the strain-stress response. For the training of the network the following input and output data were used:

Input:	Stress values at plastic strains between 1% and 8% (maximum 8 values)
Output:	Stress values $k_0+\frac{3}{2}\frac{c}{b}+F$, $\frac{3}{2}\frac{c}{b}+F$, $\frac{3}{2}c$, F.

3.2 Creep curves

From the time-strain responses the recovery parameters w and p were determined. Therefore, a common quantity

$$\zeta_i = p\,(\sigma_{n,i} - \mathrm{k}_0)^{\mathrm{w}-1} \quad , \tag{15}$$

was chosen, which characterizes static recovery. In this expression $\sigma_{n,i}$ represents the nominal stress, which belongs to the i-th creep curve. The effect of the parameters w and p on the time-strain response is shown in Figure 3, where w and p are chosen in a way that ζ=const..

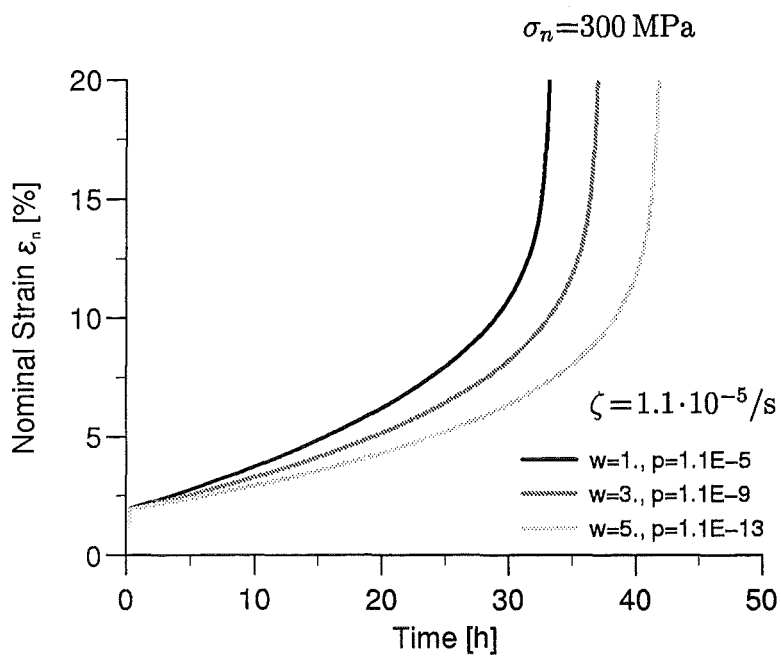

Fig. 3: Effect of the recovery parameters on the time-strain response.
(k_0=200 MPa, c=7200 MPa, c/b=95 MPa, m=1, η=4.799·10^5 MPa^m s)

By means of two creep curves, the recovery parameters could be determined. The input and output data to the network were as follows:

Input:	Logarithmic holding times at nominal strains ε_m, $0.8\,\varepsilon_m$, $0.6\,\varepsilon_m$, $0.4\,\varepsilon_m$ of the creep curves, which belong to the lowest nominal stresses $\sigma_{n,4}$ and $\sigma_{n,3}$ (8 values)
Output:	Logarithmic quantities $\log\zeta_4$, $\log\zeta_3$.

These two logarithmic quantities lead to the following expressions for the parameters w and p:

$$\mathrm{w} = 1 + \frac{\log \zeta_4 - \log \zeta_3}{\log(\sigma_{n,4} - \mathrm{k}_0) - \log(\sigma_{n,3} - \mathrm{k}_0)} \quad , \tag{16}$$

$$p = \frac{\zeta_4}{(\sigma_{n,4} - \mathrm{k}_0)^{\mathrm{w}-1}} \quad . \tag{17}$$

Since it was not possible to identify the viscosity parameters m and η in a satisfactory way, neither from the tensile curve nor from the creep curves, m was determined by trial and error and η according to (9) by

$$\eta = \frac{\mathrm{F}^m}{\dot{\varepsilon}_n} \quad , \tag{18}$$

so that the calculated material responses are in accordance with the experimentally observed material behavior.

The identified parameters are shown in Figures 5 and 6 of the appendix, where the parameters are plotted versus the temperature. Note that in Figure 6 instead of p and η the quantities $\log(p/c)$ and F are plotted versus the temperature. Contrary to p and η, these quantities show a monotonous evolution with respect to the temperature and can be used for interpolation. Only the identified parameter set for θ=500 °C goes its own way, even if these parameters describe the experiment well. The comparison of the tensile and creep tests with the simulated tensile and creep tests on the basis of the identified parameters is shown in Figures 7 – 9. Contrary to [5], these new sets of parameters also describe the tensile tests in a satisfactory way.

4 Uniaxial cyclic tests with relaxation phases

It became obvious, that simple tension and creep tests, as performed by CEA, are usually not sufficient to determine the parameters properly. To determine all 17 material parameters of the finite deformation thermoviscoplasticity model, described in [3], additional information are necessary. Therefore, strain-controlled cyclic experiments with two relaxation phases on 20 MnMoNi 55 RPV steel at room temperature (RT) and 400 – 650 °C (each 50 °C) were carried out. These tests were performed on a servohydraulic closed-loop ± 100 kN MTS-machine. A load cell with a fatigue rated capacity of ± 100 kN was used. The specimens were cylindrical with a uniform diameter of 5 mm and a useful length of 30 mm, as shown in Figure 4.

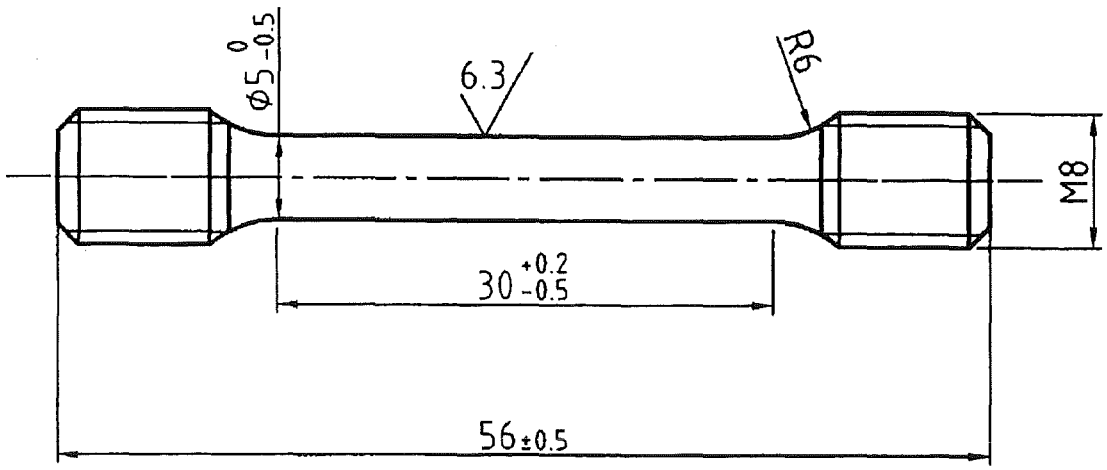

Fig. 4: Specimen geometry.

A radiant heating chamber allows to heat the specimen up to approximately 800 °C. This furnace focuses radiant energy onto a cylindrical target area in the middle of the furnace (where the specimen is mounted) by means of four elliptically shaped specular aluminium reflectors. The temperature in the furnace was controlled and monitored by a thermocouple welded slightly below the thread. For the strain measurement a ceramics extension rod with chisel edge contacts was used, which minimizes thermal expansion error and conduction losses from specimens.

Some experimental results are shown in Figures 10 – 17 of the appendix. All tests were performed with a strain rate of $\pm 10^{-3}$/s and two relaxation phases of 1 and 2 h, respectively. To ensure homogeneous deformations during the three cycles, different strain levels according to the different temperatures were prescribed. The tests performed at higher temperatures, show a stronger decrease of stress during the relaxation process. At 650 °C the stress even drop down to almost zero during the second relaxation phase (see Figure 17). In this case, effects like static recovery play a dominant role. To investigate the reproducibility of the experiments a second test was performed at 500 and 600 °C with the same loading histories. The corresponding stress responses, shown in Figures 12 – 15, are in good accordance.

5 Concluding remarks

The present work has shown a possibility to determine material parameters by means of neural networks using data from tensile and creep tests. In a first, but most promising step, a simplified version of the model was used, which consists of 7 parameters only. Contrary to way in [5], tensile and creep data were trained separately, which allows to describe both tensile and creep curves with sufficient accuracy. Nevertheless, it became obvious, that these tests are not suitable to identify

the parameters of our finite deformation thermoviscoplasticity model. To get more information about characteristic material properties, more complex loading histories, including different strain rates or relaxation phases, are necessary. In our special case, strain-controlled cyclic experiments with two relaxation phases on 20 MnMoNi 55 RPV steel at different temperatures were carried out. These tests show a strong decrease of stress during the relaxation process, especially at higher temperatures, which underlines the importance of a static recovery term in the constitutive equations. By means of these tests, it should be possible to determine accurately the parameters describing the isotropic and kinematic hardening behavior.

References

[1] HUBER, N. and CH. TSAKMAKIS: *Determination of constitutive properties from spherical indentation data using neural networks - Part I: The case of pure kinematic hardening in plasticity laws.* J. Mech. Phys. Solids, 47, 1569–1588, (1999).

[2] HUBER, N. and CH. TSAKMAKIS: *Determination of constitutive properties from spherical indentation data using neural networks - Part II: Isotropic and kinematic hardening.* J. Mech. Phys. Solids, 47, 1589–1607, (1999).

[3] LÄMMER, H.: *Thermoplastizität und Thermoviskoplastizität mit Schädigung bei kleinen und großen Deformationen.* Thesis, Universität Karlsruhe (TH), (1997).

[4] LÄMMER, H., B. RITTER, and CH. TSAKMAKIS: *Thermodynamisch konsistente, finite Thermoviskoplastizität mit Schädigung.* In MÜHL, B. (editor): *Projekt Nukleare Sicherheitsforschung - Jahresbericht 1996*, pages 161–182, FZKA-Report 5963, Forschungszentrum Karlsruhe, (1997).

[5] LÄMMER, H., B. RITTER, and CH. TSAKMAKIS: *Zur Bestimmung der Materialparameter des Modells der finite Thermoviskoplastizität mit Schädigung.* In MÜHL, B. (editor): *Projekt Nukleare Sicherheitsforschung - Jahresbericht 1997*, pages 176–191, FZKA-Report 6126, Forschungszentrum Karlsruhe, (1998).

[6] SUMPTER, B.G. and D.W. NOID: *On the design, analysis and characterization of materials using computational neural networks.* Annu. Rev. Mater. Sci., 26, 223–277, (1996).

[7] UNIVERSITY OF STUTTGART, INSTITUTE FOR PARALLEL AND DISTRIBUTED HIGH PERFORMANCE SYSTEMS (IPVR): *SNNS Stuttgart Neural Network Simulator, User Manual, Version 4.1.* Report No. 6/95.

[8] YAGAWA, G. and H. OKUDA: *Neural networks in computanional mechanics.* Archive of Computational Methods in Engineering, 3, 435–512, (1996).

Appendix: Figures

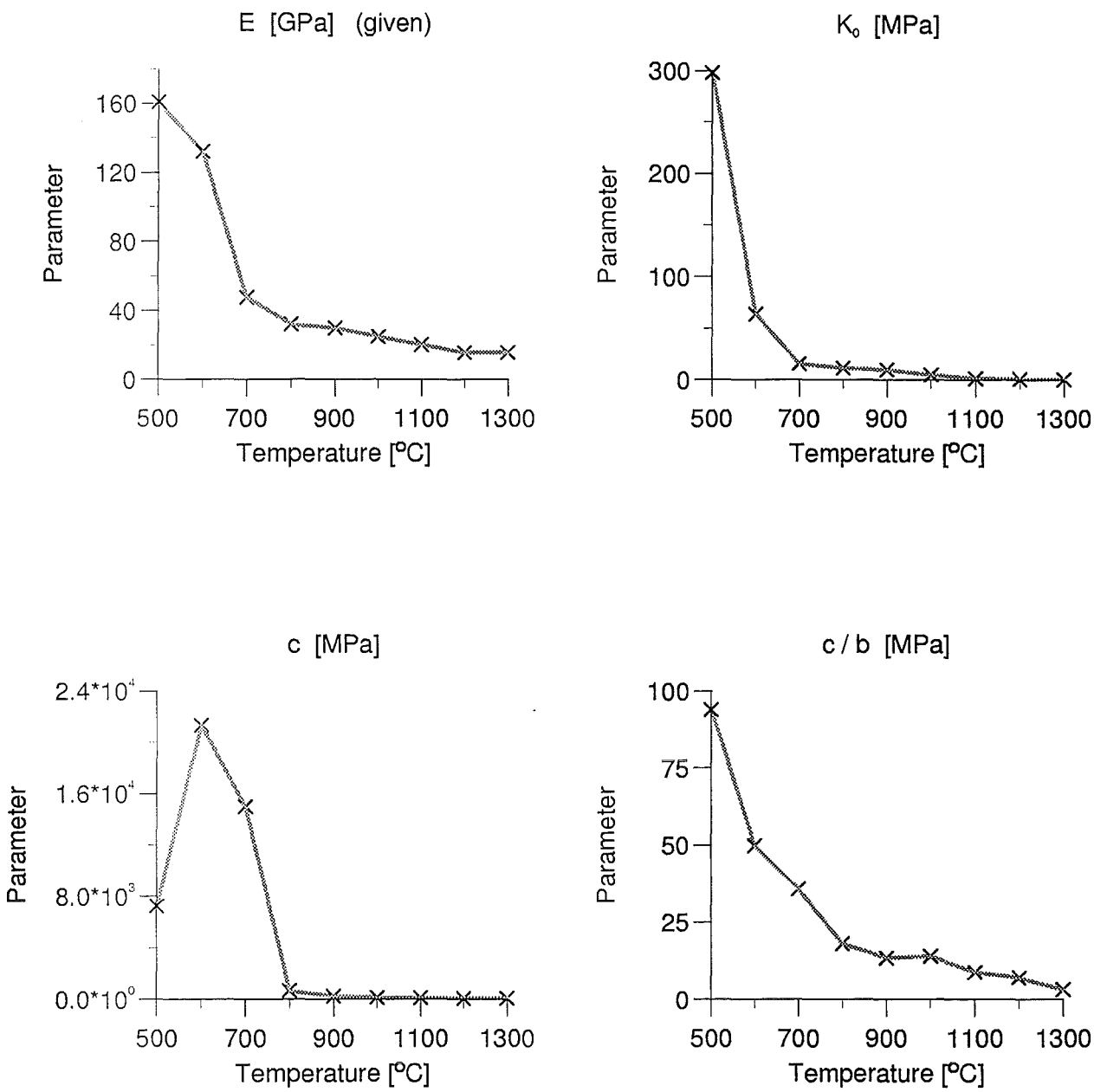

Fig. 5: Young's modulus and identified parameters k_0, c, c/b.

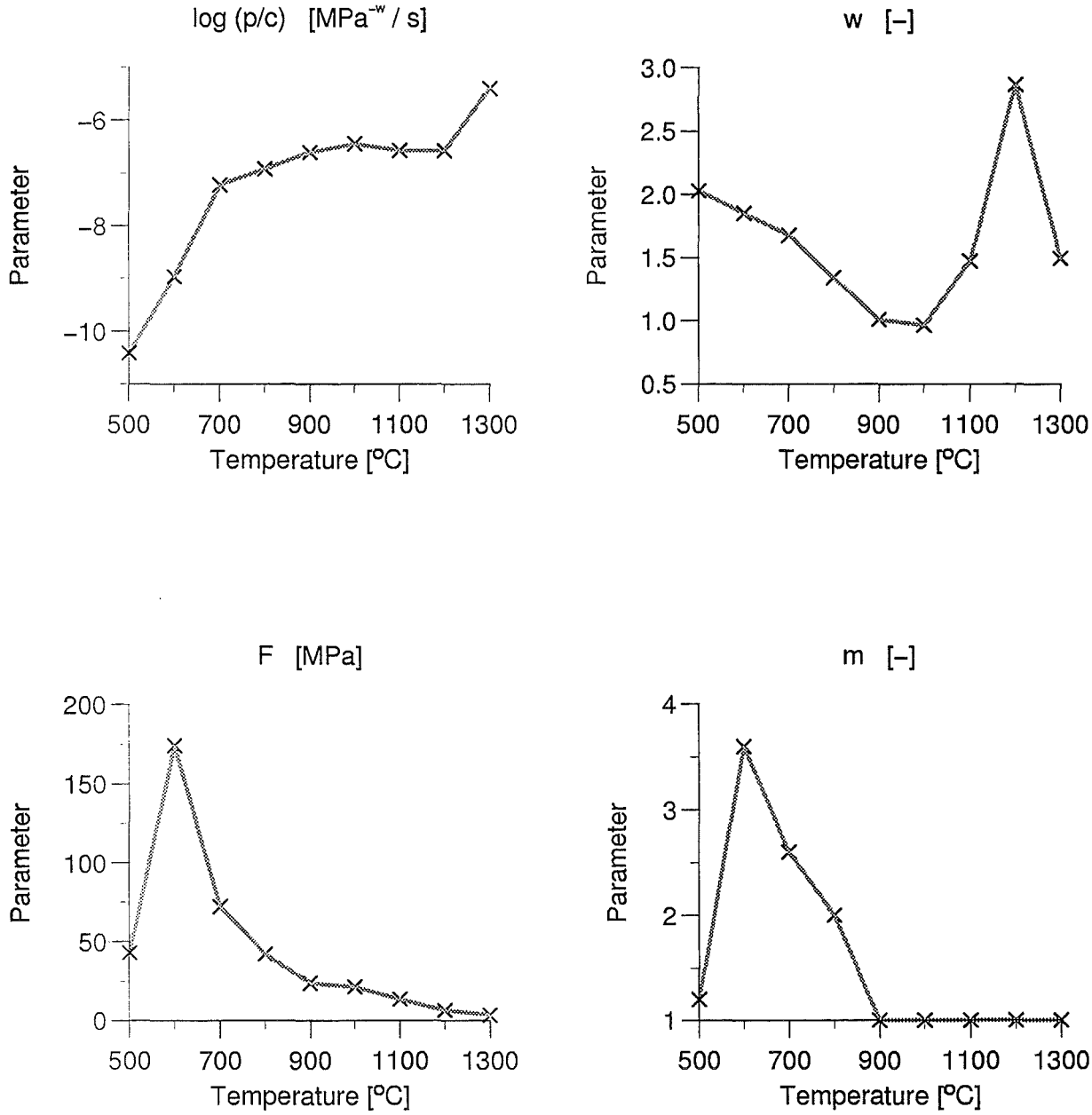

Fig. 6: Identified parameters log (p/c), w, F, m.

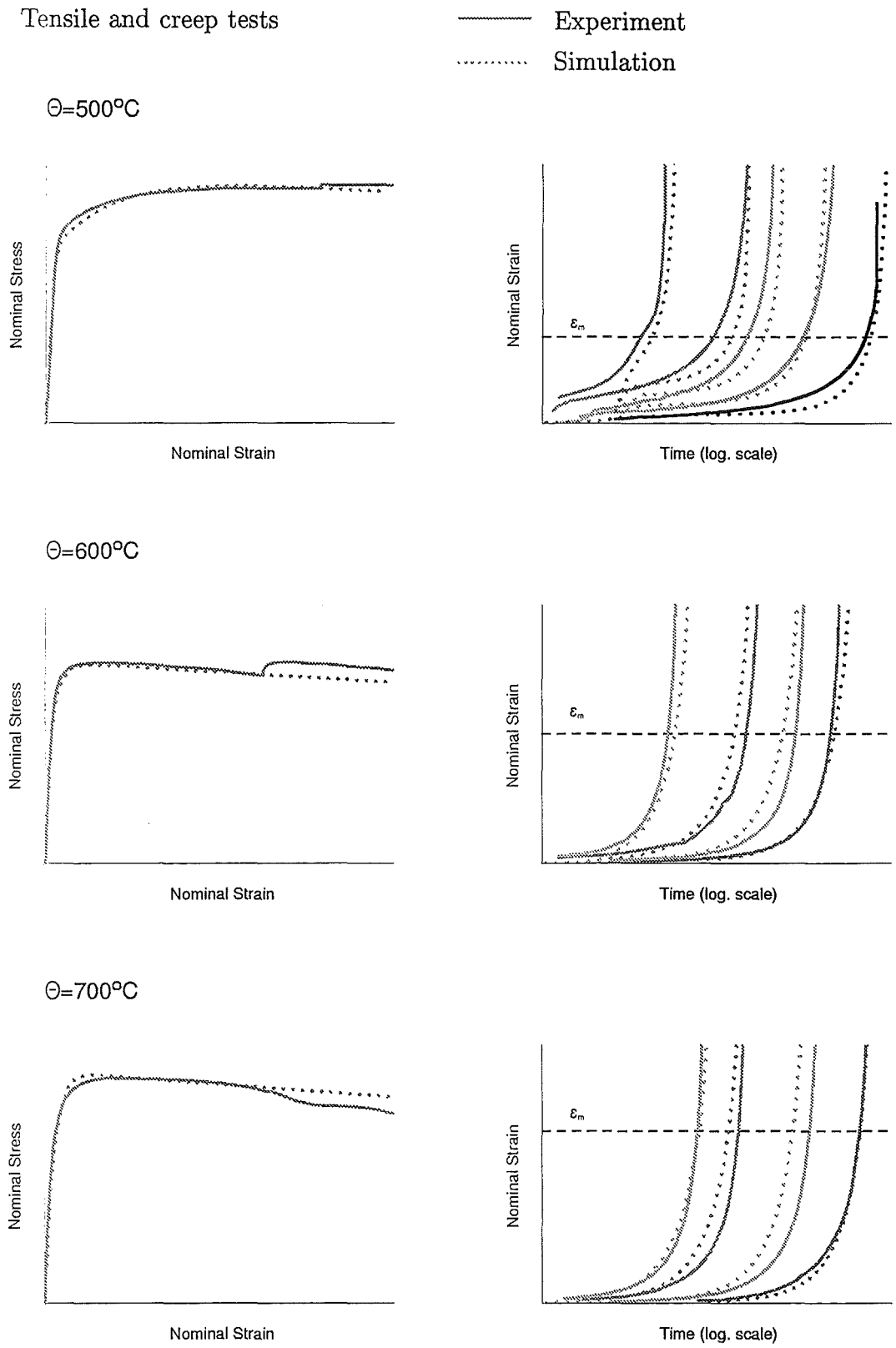

Fig. 7: Experimental and simulated tensile and creep curves for 500 °C, 600 °C and 700 °C.

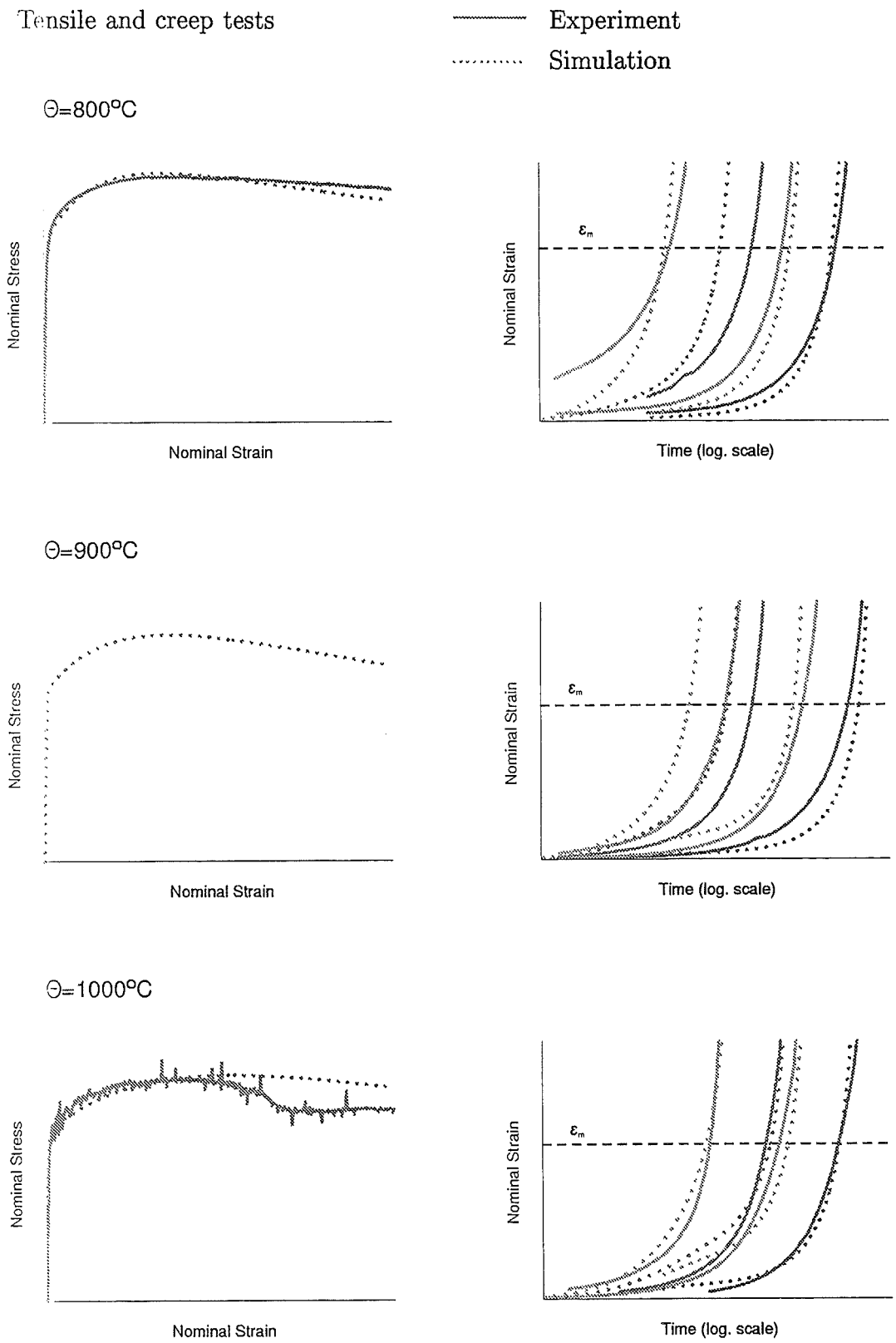

Fig. 8: Experimental and simulated tensile and creep curves for 800 °C, 900 °C and 1000 °C.

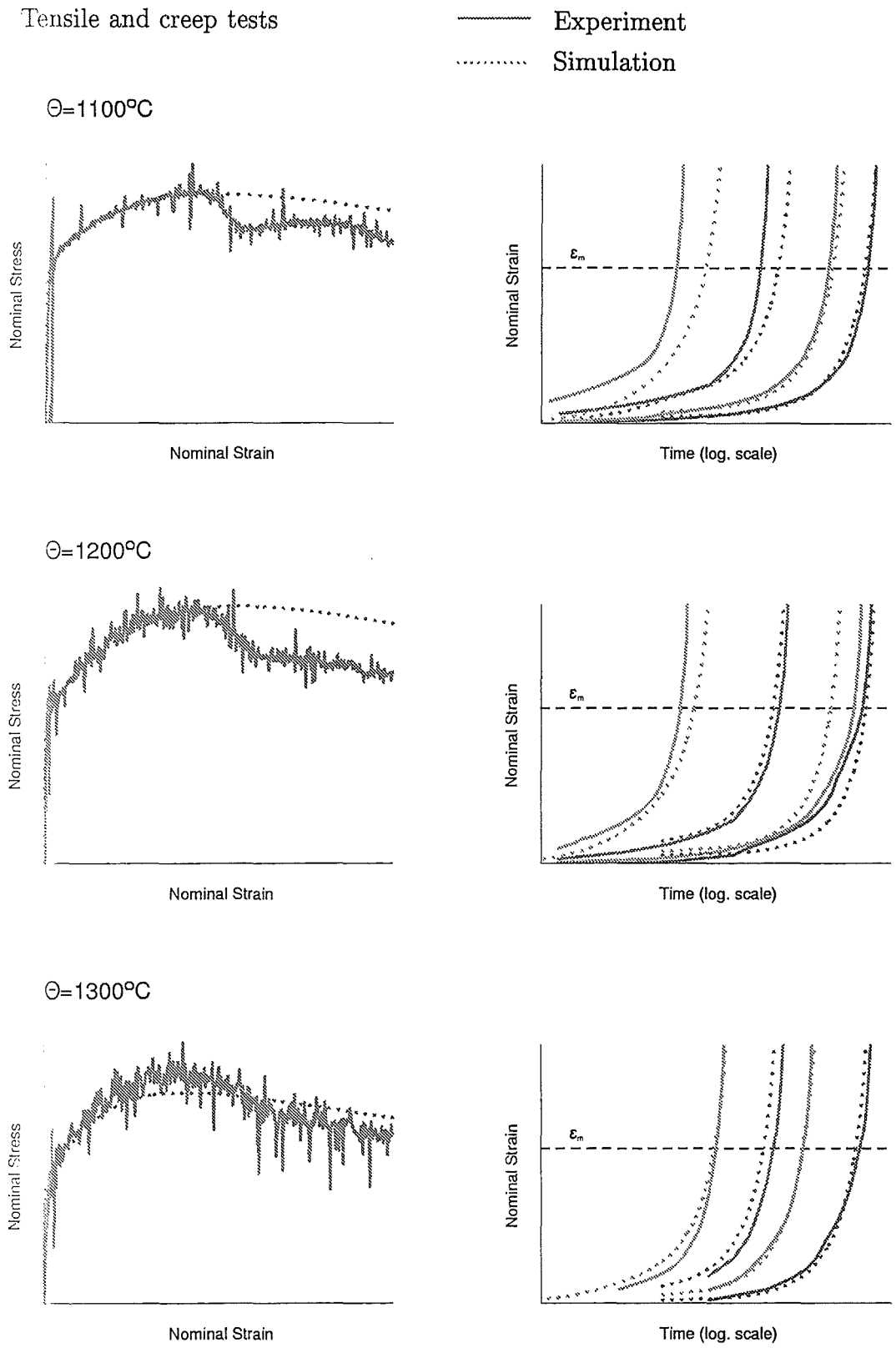

Fig. 9: Experimental and simulated tensile and creep curves for 1100 °C, 1200 °C and 1300 °C

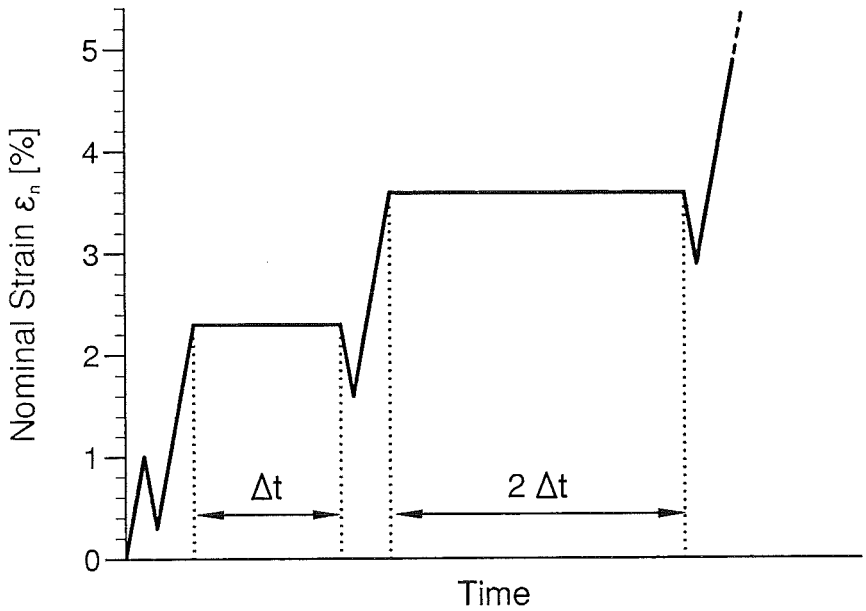

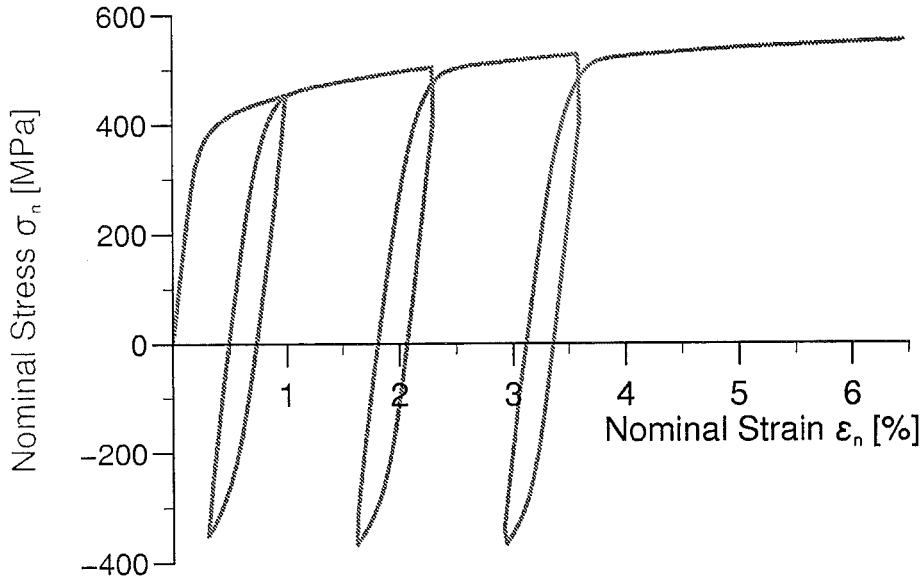

Fig. 10: Loading history and strain-stress response at 400 °C.

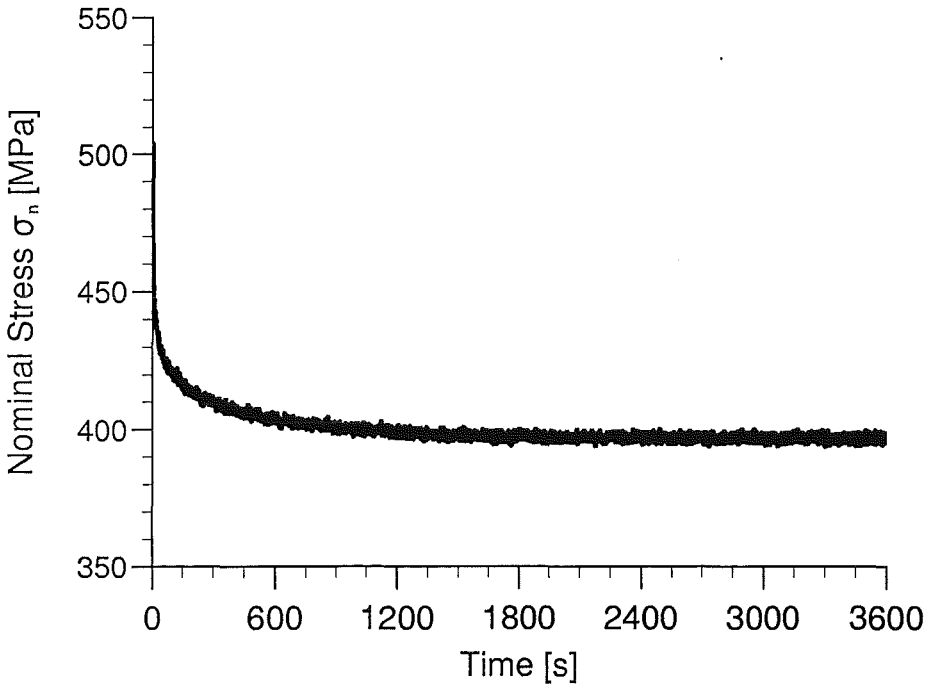

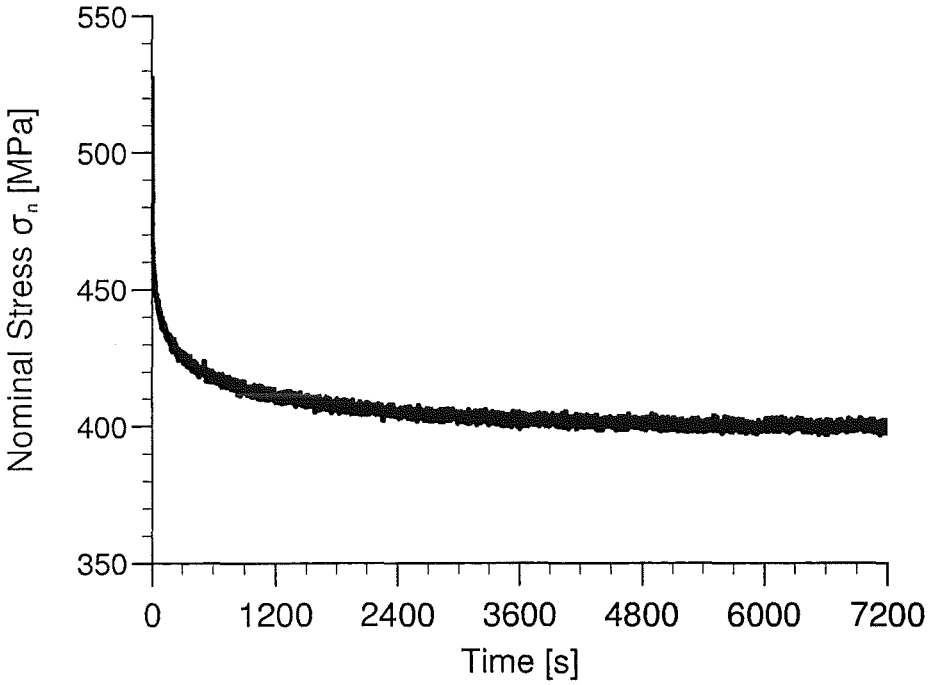

Fig. 11: Time-stress responses during the relaxation phases at 400 °C.

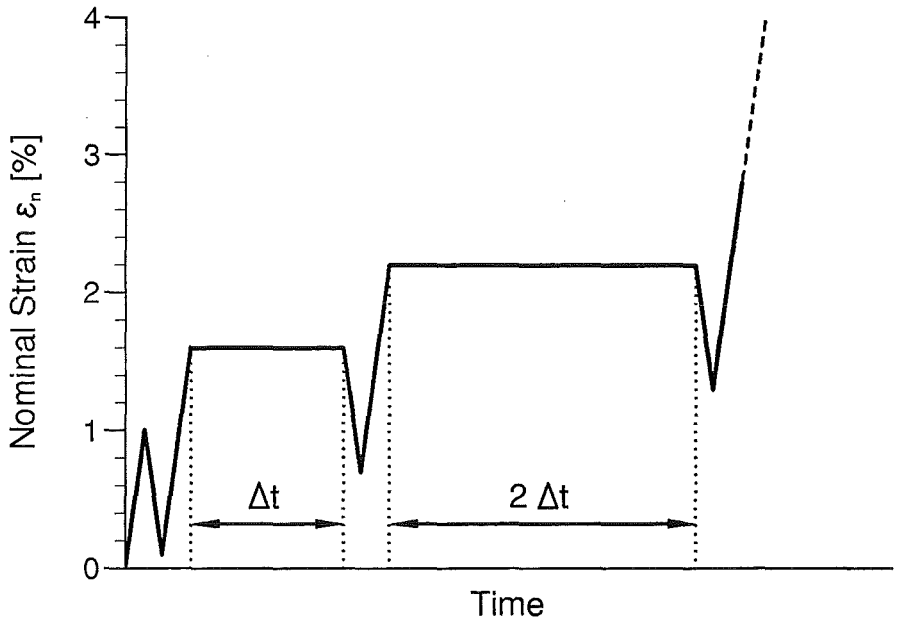

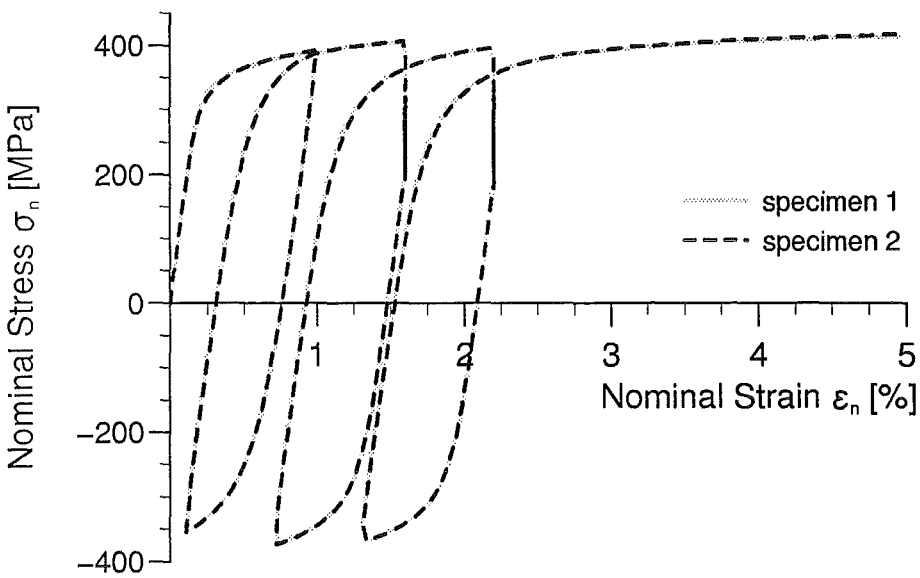

Fig. 12: Comparison of the strain-stress responses of two tests with the same loading history at 500 °C.

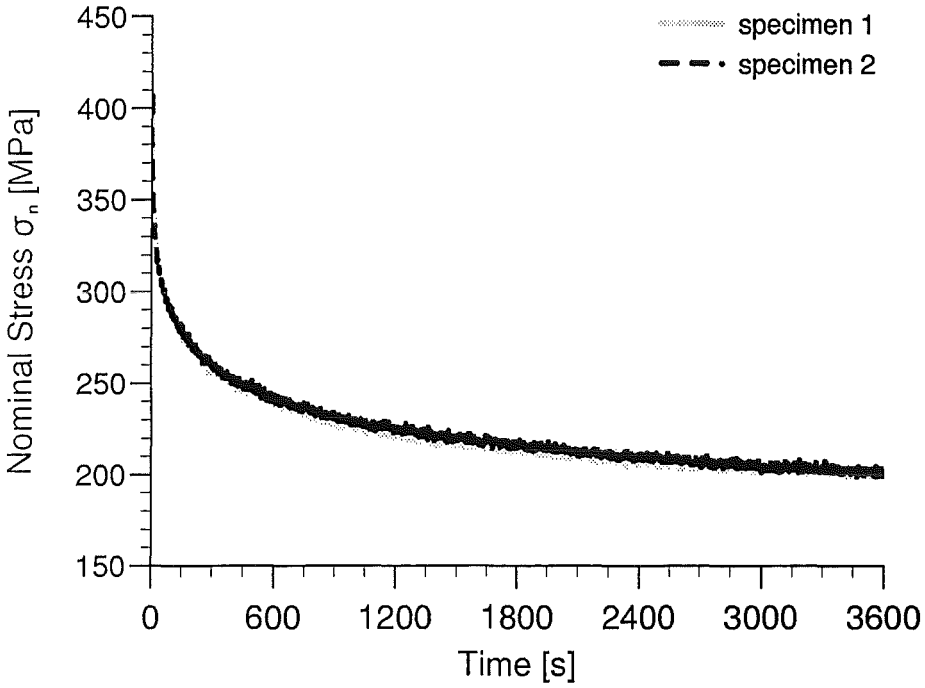

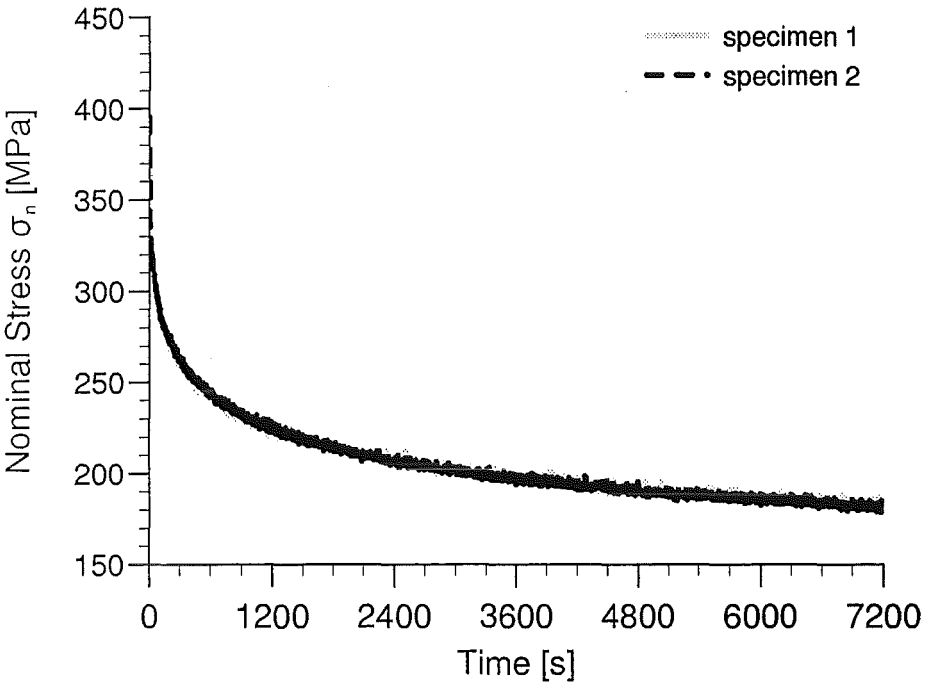

Fig. 13: Comparison of the time-stress responses during the relaxation phases of two tests with the same loading history at 500 °C.

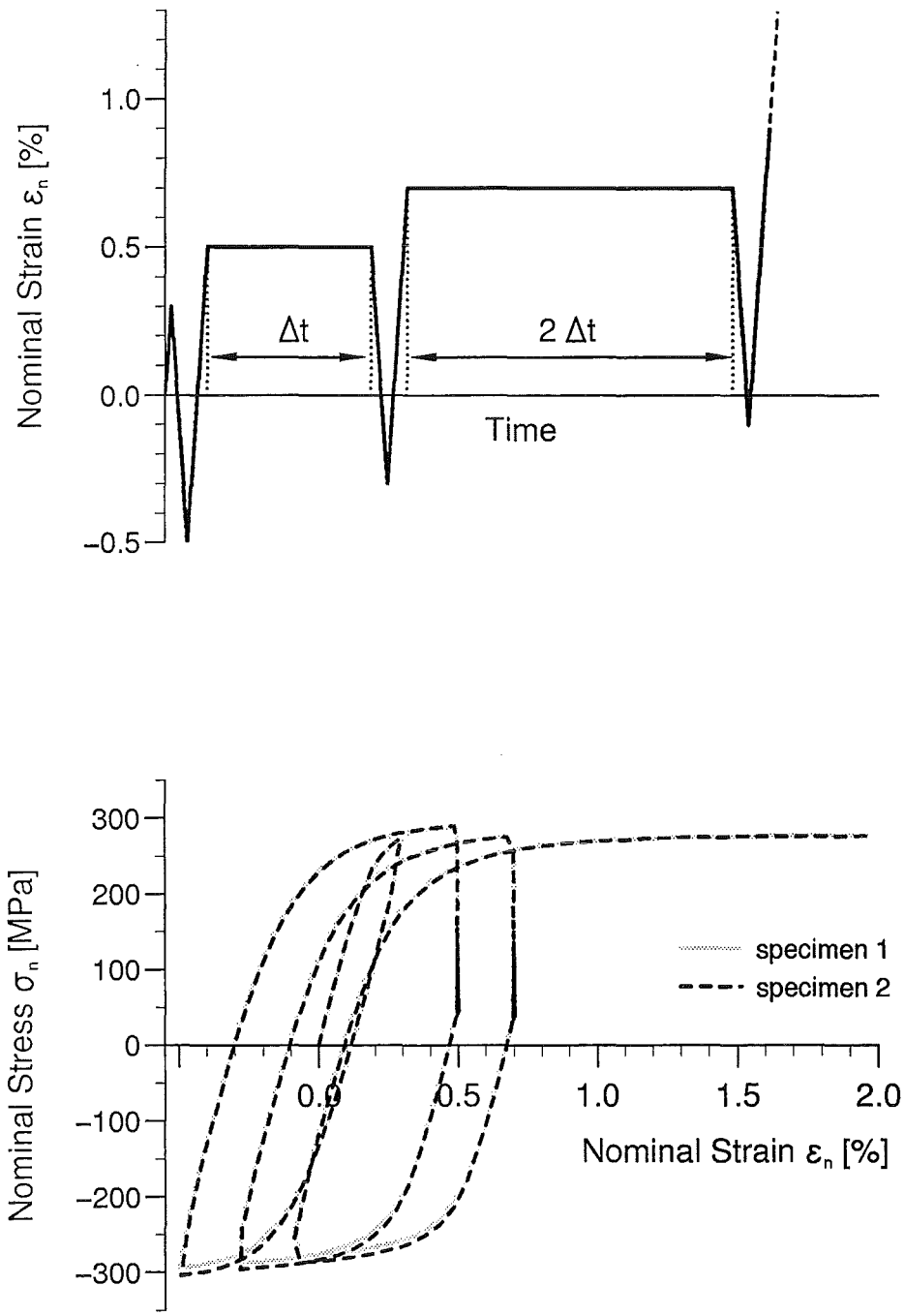

Fig. 14: Comparison of the strain-stress responses of two tests with the same loading history at 600 °C.

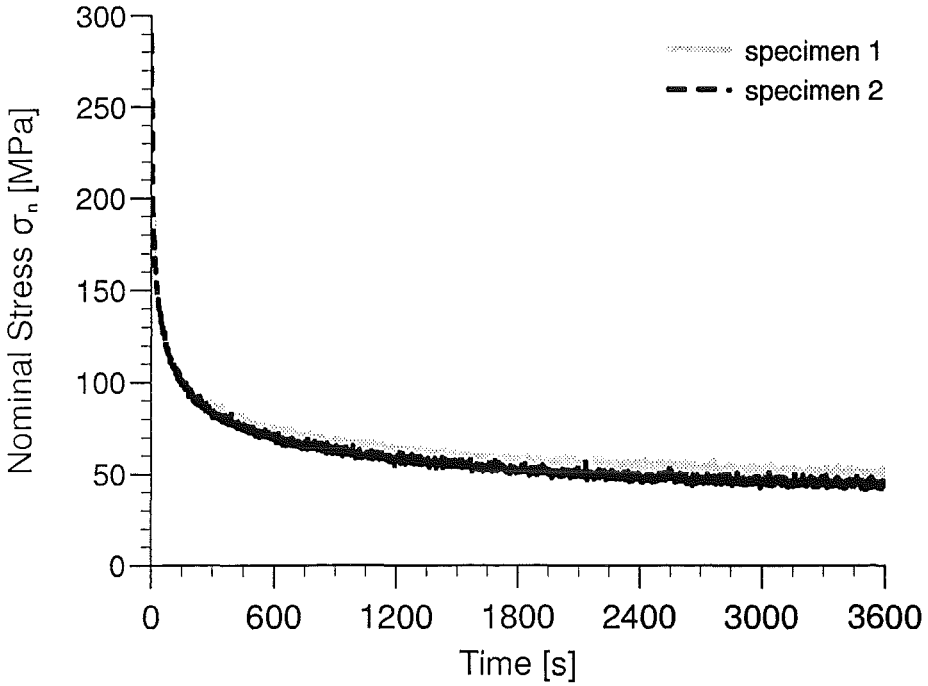

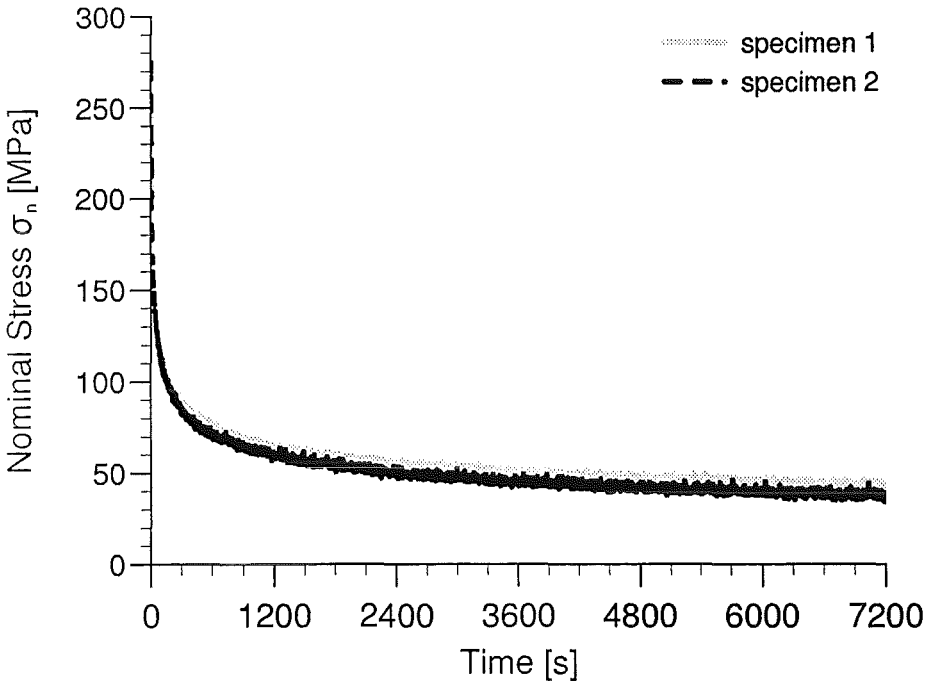

Fig. 15: Comparison of the time-stress responses during the relaxation phases of two tests with the same loading history at 600 °C.

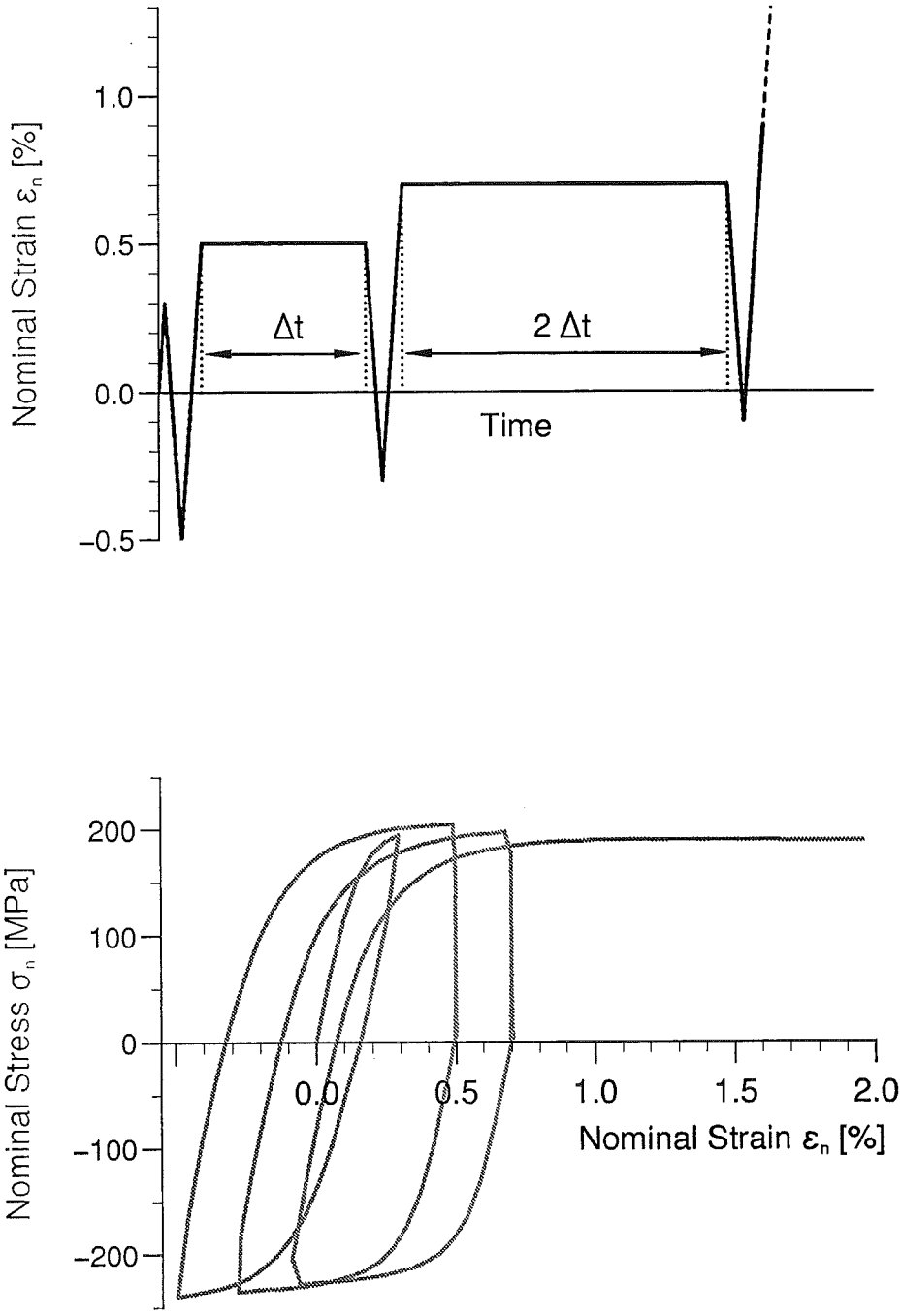

Fig. 16: Loading history and strain-stress response at 650 °C.

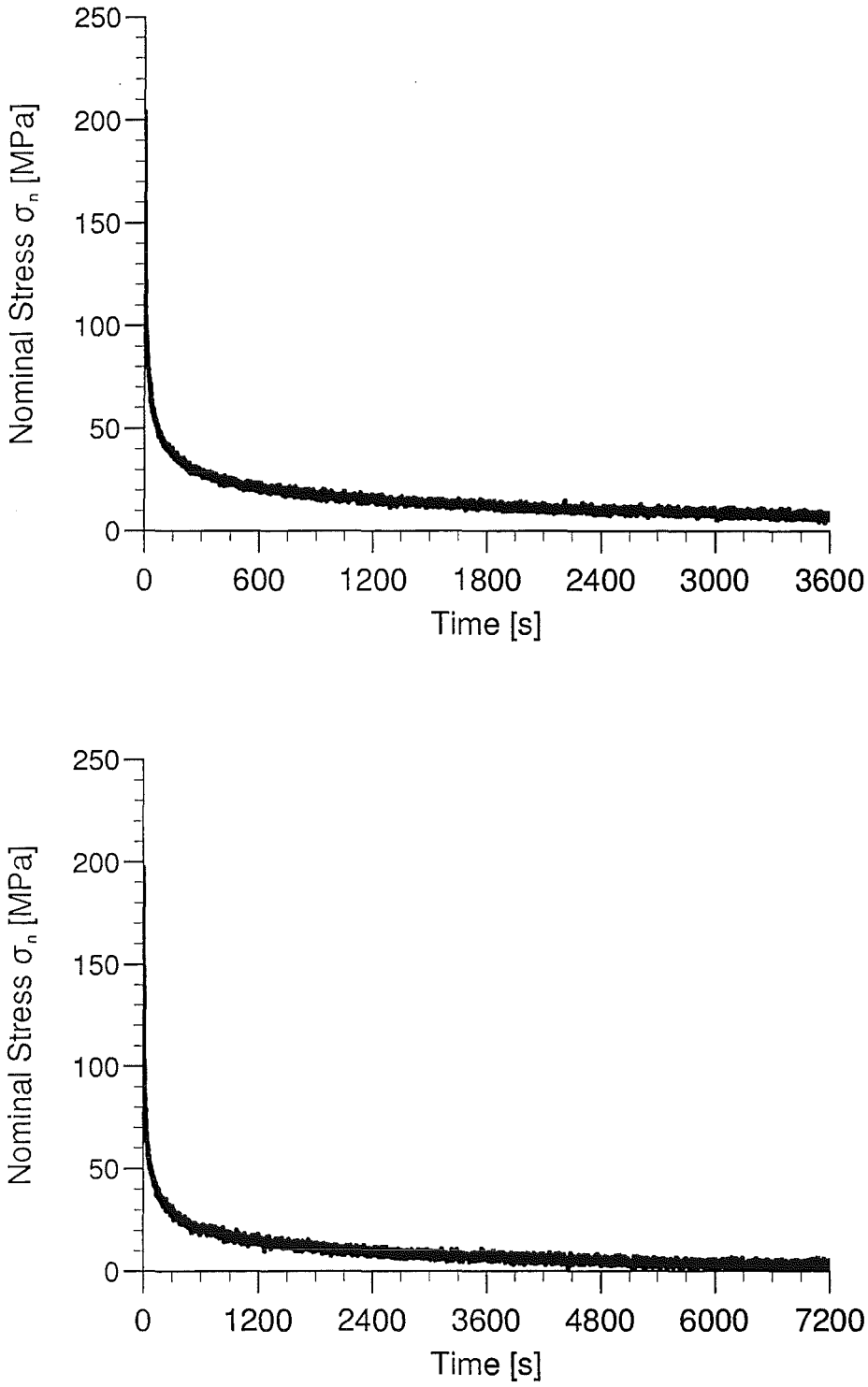

Fig. 17: Time-stress responses during the relaxation phases at 650 °C.

II. Experimente zur Dispersion von Corium

(M. Hartnagel, M. Kirstahler, L. Meyer, A. Roth, M. Schwall, E. Wachter, G. Wörner; INR; T. Blanchat, SNL)

Zusammenfassung

Die diversen Aspekte der Schmelzedispersion bei moderatem Versagensdruck (< 20 bar) werden experimentell für den Europäischen Druckwasserreaktor (EPR) untersucht, um zu einer soliden Datenbasis zu kommen, speziell für die Beurteilung der Rückhaltefähigkeit der Reaktorgrube. Zwei integrale Referenzexperimente mit Thermit und Dampf wurden in der Surtsey Anlage im Maßstab 1:10 im SNL durchgeführt. Bei einem Anfangsdruck von 11 bar im RDB und 2 bar im Containment und einer skalierten Lochgröße in der RDB-Kalotte von 1 m Durchmesser wurden 78 % der Schmelze aus der Reaktorgrube ausgetragen. Der Druck im Containment stieg für wenige Sekunden auf 6 bar, hervorgerufen durch das Aufheizen der Atmosphäre durch die Schmelzepartikel, die Oxidation des Eisens und die Wasserstoffverbrennung. Bei einem kleineren Lochdurchmesser (0.5 m skaliert) wurden nur 21 % ausgetragen. Diese Ergebnisse zeigen die Notwendigkeit, das RDB-Versagen bei niedrigen Drücken zu untersuchen.

Im Versuchsstand DISCO-C, der die EPR-Reaktorgrube und die anschließenden Räume im Maßstab 1:18 modelliert, wurden die ersten Versuche mit Wasser und Stickstoff als Simulationsfluide für Schmelze und Dampf durchgeführt. Bei 10 bar Anfangsdruck im RDB und einer skalierten Lochgröße von 90 cm wurden hier 80 % der Flüssigkeit aus der Grube ausgetragen. Bei einem kleineren Lochdurchmesser (45 cm skaliert) wurden noch 68 % ausgetragen. Die Versuche werden unter Variation der Parameter Druck, Fluide, Lochort und -größe, und Grubengeometrie fortgesetzt.

1. THE SURTSEY EXPERIMENT AT SNL

1.1 Test Summary

Figure 1 shows a cutout of the Surtsey vessel with the 1/10th scale CE-like structures resting on the lower floor. Figure 2 shows a cross section of the concrete structures, cavity and RPV, and steam accumulator which represents the total volume of the RCS. Figure 3 shows a cross-section of the cavity and RPV. The melt generator (or crucible) is attached to the lower part of the RPV. The bottom of the melt generator holds a graphite disk machined with a 10-cm I.D. or 4-cm I.D. hole, respectively, a brass melt plug fits within the graphite and provides a pressure barrier during the thermite reaction interval. In case of the 10-cm hole, the 4-inch pipe connecting the accumulator to the crucible limits the blow down due to a 9.3 cm I.D. Figure 4 shows a top view of the operating deck, refueling canal, and cavity exit with the RPV model in-place and attached to the steam accumulator.

After installing a crucible containing 62 kg of compacted iron oxide/aluminum thermite to the RPV model and modified-CE cavity, the Surtsey vessel was sealed. Following leak checks, the vessel was vented to atmospheric pressure (0.084 MPa). The vessel was then heated by filling with steam until the vessel pressure reached app. 0.21 MPa. The average gas temperature inside the Surtsey vessel was 372 K (279 K in test 2) at the end of the heat up. About 200 moles of hydrogen gas were added to the vessel near the end of the heat up. Water condensed on the vessel walls and the CE structures during the 16-hour heat up and the condensate was manually drained from the cavity and vessel floors during the steaming process. The initial conditions for both tests are summarized in Table 1.

After taking the pretest gas grab samples and verifying camera and data acquisition systems operating, a thermite initiator ignited the thermite powder. About 12 s (9 s in test 2) after ignition, an explosive charge was used to fail the burst diaphragm separating the accumulator and the crucible, pressurizing the crucible with steam. About 1 s (4 s) later, the brass melt plug failed, initiating the melt ejection (defined as t = 0 s).

1.2 Video Interpretation

Four CCD cameras were used to view the inside of the Surtsey vessel. Two cameras (one heavily filtered) looked down from the window port in the Surtsey upper head and two cameras (one heavily filtered) looked across the operating deck directly at the cavity exit through a level 3 window port. At t = 0 s, glowing orange molten particles exited the cavity.

Test 1: The melt first impacted the dome at about t = 0.5 s. The molten particle stream out of the cavity lasted about 0.3 s. A glowing-orange cloud indicating a hydrogen de-

flagration reached the top of the vessel almost immediately and pulsed and glowed orange for an additional seven to eight seconds. Glowing particles rained down on the operating deck for about 3 s after the start of the ejection.

Test 2: The melt stream out of the cavity did not appear to be as vigorous as in the previous test. The stream had more of a liquid sparging or jetting structure as compared to a fine spray droplet structure. The video showed most of the melt rising, peaking at about 0.6 s, and then falling back without striking the vessel dome. The molten particle stream out of the cavity lasted about 1-2 s. Glowing particles rained down on the operating deck for about 3 s after the start of the ejection. A glowing-orange cloud indicating a hydrogen deflagration reached the top of the vessel in about 1-2 s. Combustion in the dome region ended at about 5 s.

Table 1 Initial conditions for the two DCH / EPR Experiments at SNL

		Test 1	Test 2
Thermite composition (kg)			
iron oxide		44.41	44.41
aluminum		13.81	13.81
alumina		3.79	3.79
Mass of the thermite charge (kg)		62.00	62.00
Accumulator pressure (MPa)		1.106	1.53
Accumulator gas or steam temperature (K)		467	483
Accumulator volume (m^3)		0.2544	0.2544
Moles of accumulator steam (moles)		74	80
Time between thermite ignition and LPME (s)		13	13.7
Exit hole diameter (m)		0.10	0.04
Exit hole area (m^2)		0.0079	0.0013
Annular gap area (m^2)		0.0825	0.0825
Vessel pressure (MPa)		0.213	0.2184
Vessel temperature (K)		372	379
Vessel gas moles (moles)		6308	6351
Gas composition	Steam	47.9	45.2
in the Surtsey vessel (mole %)	N_2	38.3	40.1
	O_2	10.3	10.7
	H_2	3.2	3.3
	Other	0.3	0.7
Freeboard volume inside subcompartment structures (m^3)		21.5	21.5
Freeboard volume in upper dome (m^3)		70.1	70.1
Total freeboard volume (m^3) [1]		91.6	91.6

[1] The Surtsey empty volume is 98.9 m^3.

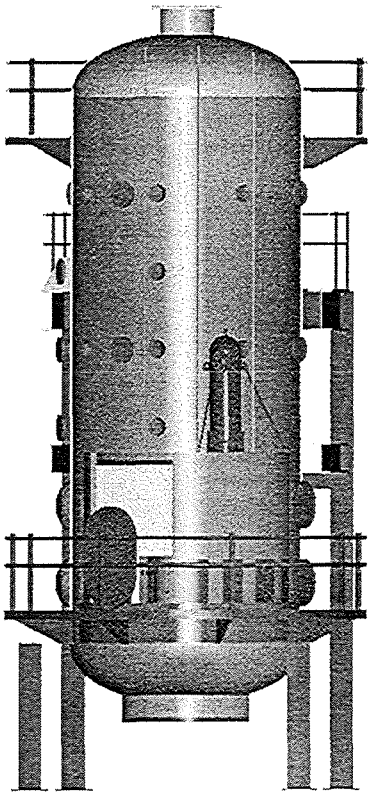

Fig. 1 The Surtsey vessel with the structures on the lower floor

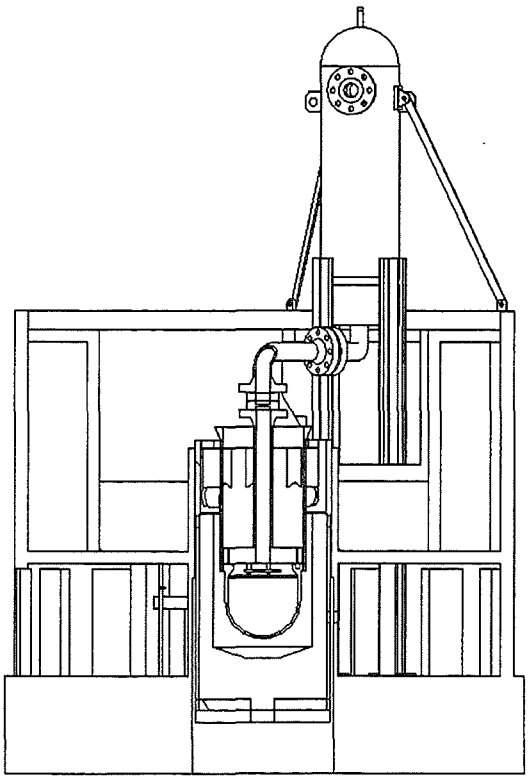

Fig. 2 The concrete structures, cavity, RPV and steam accumulator.

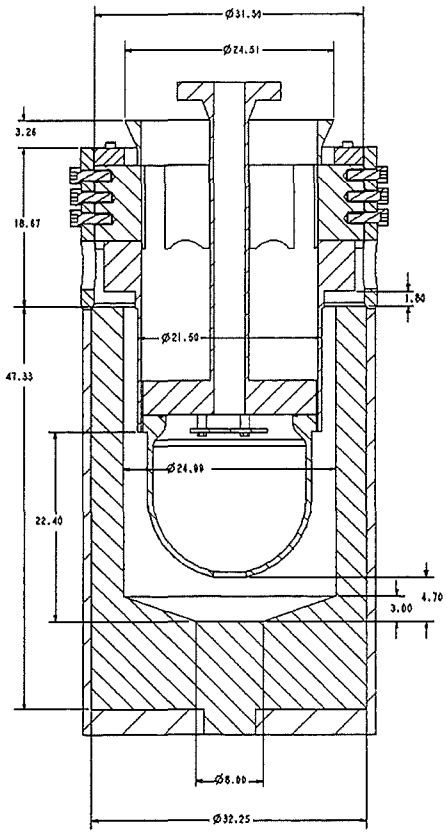

Fig. 3 The RPV model in the scaled cavity (in inch).

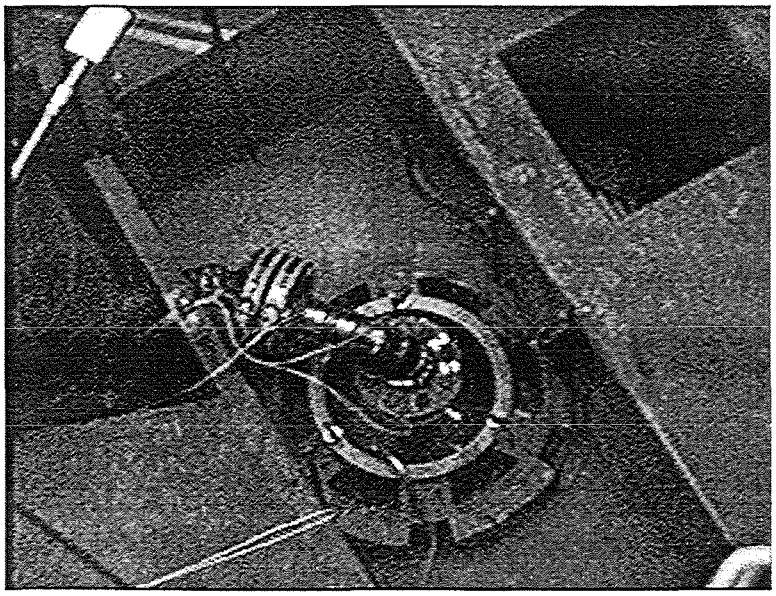

Fig. 4 A top view of the operating deck (upper deck), refueling canal (lower deck) and cavity exit with the RPV model in-place and attached to the steam accumulator.

1.3 Measured Data

Figures 5 and 6 give the pressure history of the crucible (RPV), cavity and vessel, and pyrometer temperature (with the pyrometer focused on the cavity exit). The thermite was ignited about thirteen seconds prior to melt ejection, verified by increasing crucible pressure. The burst diaphragm separating the accumulator and the crucible was failed about one second prior to ejection in test 1 and 4.5 s in test 2, equilibrating the accumulator and the crucible.

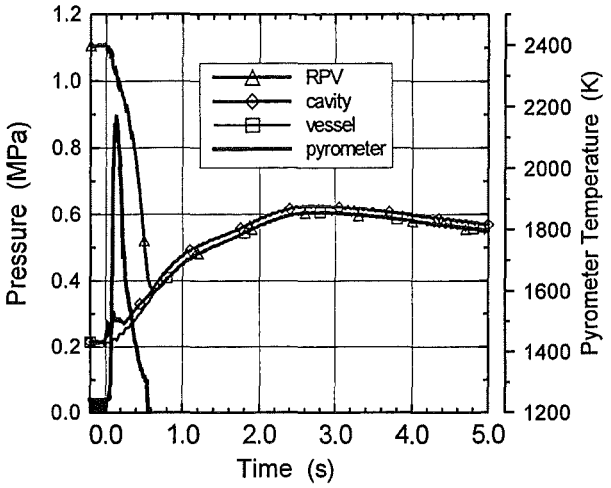

Fig. 5 Pressures and pyrometer temperature at cavity exit in test 1

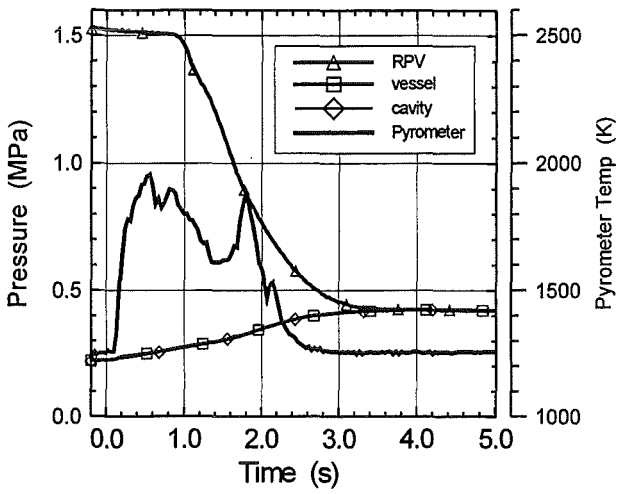

Fig. 6 Pressures and pyrometer temperature at cavity exit in test 2

A pressure controller was used to fill and maintain the accumulator with steam between 1.0 MPa and 1.2 MPa, automatically operating the steam boiler fill and accumulator vent valves. Receipt of the melt plug breakwire signal at melt ejection would automatically close the fill and vent valves. In test 1, the accumulator was at 1.1 MPa just prior to melt ejection. In test 2, the system functioned as designed during the accumulator fill process until thermite ignition. However, a transient voltage pulse (from the thermite igniters) tripped the pressure controller circuit, closing the fill and vent valves. Therefore, no automatic venting of the accumulator occurred when pressure started to increase. After the burst diaphragm was failed and prior to melt plug failure (about a 5 s interval), the equilibration of the accumulator with the crucible produced a steam/melt interaction that caused system pressure to rise from about 1.2 MPa to about 1.5 MPa.

Zero time was set at the initiation of the melt ejection, verified by the melt plug break wires and the start of the accumulator depressurization. The accumulator and crucible blow down commenced at t = 0 s. Accumulator and crucible pressure (RPV pressure) dropped immediately in test 1 while it stayed at the initial value for almost 1 s before falling in test 2. This implies that in test 1, with the large hole, a blow through with a two-phase flow occurs instantaneously, while with the small hole in test 2 there is a single-

phase liquid flow first and a two phase flow later. The RPV pressures reached a minimum of 0.4 MPa in both tests, then equilibrated and tracked the increasing vessel pressure. Vessel pressures peaked to 0.606 MPa in test 1 and to 0.42 MPa in test 2.

In test 1, the debris entrainment interval probably occurred from t = 0.1 s to t = 0.4 s, based on the failure of the cavity exit break wire, the very quick rise and fall in the pyrometer signal, the small over pressures registered by the cavity gages near t = 0.1 s, and the camera video interpretation. In test 2, the debris entrainment interval probably occurred from t = 0.1 s to about t = 2.0 s, based on the very quick rise and slow fall in the pyrometer signal and the camera video interpretation.

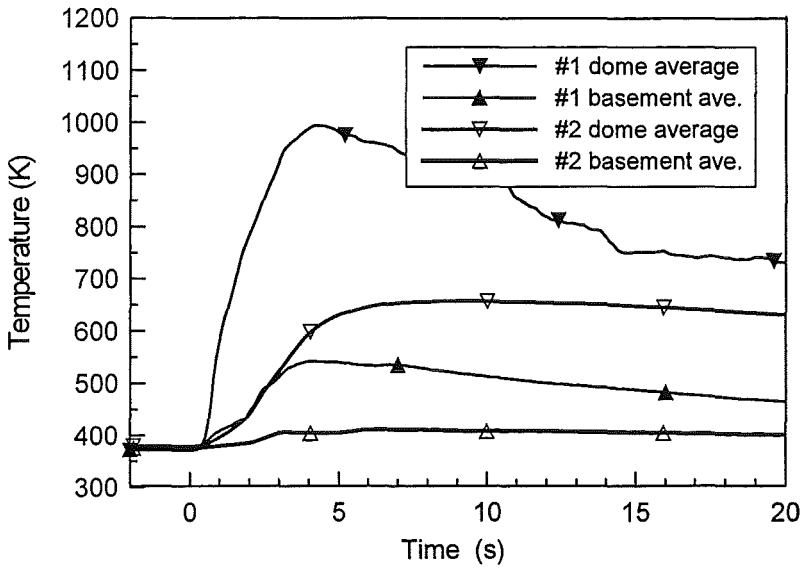

Fig. 7 Average gas temperatures in the vessel

Figure 7 shows the vessel gas temperatures averaged from three thermocouple arrays. The average basement gas temperatures were measured in the subcompartments. Specific thermocouples indicated temperatures up to 400 K higher.

1.4 Debris Recovery

The debris recovery focused on several areas; the structure basement, the operating deck (upper deck), the refueling canal (lower deck), the RPV/cavity area, and the Surtsey vessel. The crucible recovery showed that the melt plug was completely gone and that the graphite disk showed no ablation or erosion. The final exit hole was round with a 10-cm, respectively, a 4-cm diameter. A small part of the lower section of the steel crucible inner liner was melted by the thermite.

Table 2 Debris recovery results

MASS BALANCE (kg)	Test 1	Test 2
Initial thermite charge, M_d^o (a)	62.00	62.00
Crucible (b)	-2.05	-0.22
Cavity (c) [1]	15.18	58.00 [3]
Inside structures (d) (d = f - e - c)	5.93	0.56
Outside structures (e)	47.50	14.61
Total Recovered (f) [2]	68.61	73.17
Recovery fraction, $f_{recovery} = f/a$	1.11	1.18
THERMITE TRANSPORT FRACTIONS		
Ejected into cavity, $f_{eject} = 1 - b/a$ (only if < 1)	1.00	1.00
Dispersed from cavity, $f_{disp} = (d+e)/(c+d+e)$	**0.779**	**0.207**
Transported outside subcompartment, $f_{dome} = e/(d+e)$	0.889	0.963
Transported to dome, $f_{trans} = f_{eject} * f_{disp} * f_{dome}$	0.693	0.199
Thermite transported to dome, $M_d = M_d^o * f_{trans}$ (kg)	42.94	12.34
Particle size SMMD (mm)	3.40	1.54

[1] Cavity mass in Sup-2 includes the 1.44 kg debris found inside the loop piping.

[2] The molten mass available for dispersal into the vessel is greater than the initial thermite charge due to melting of the inner wall of the crucible (if used), vaporization of the fusible brass plug (1.675 kg for test 1), ablation of concrete in the cavity, contaminants (break wires, thermocouples, etc.), and oxidation of metallic debris by steam.

Table 2 shows the debris recovery and the mass balance and transport fractions. The cavity dispersal fraction in the test-1 experiment was 0.78 with driving pressure at 1 MPa and using a 0.1 m diameter hole. The test-1 cavity dispersal fraction was identical to the average cavity dispersal fraction in the CE experiments, most of which were performed with driving pressure at 8 MPa and using a 0.04 m diameter hole. The cavity dispersal fraction in the test-2 experiment was 0.21 with driving pressure at 1.5 MPa and using a 0.04 m diameter hole. The test-2 cavity dispersal fraction was much less than the average cavity dispersal fraction for both the CE experiments and the test-1 experiment.

The debris recovered from the upper deck was sieved. This debris covered the deck uniformly and consisted of small particles of iron and alumina. The appearance of the debris in the two tests in the lower deck (so-called refueling canal) was different. In test 2 the debris appeared to have been laid down rather than sprayed down (as if due to a low pressure "burp" of material out of the cavity). The thickness of the larger pieces was 2-5 mm. The outer RPV wall and the inner cavity wall was coated with a layer of alumina. The thickness of the layer was 1-4 mm (thicker near the cavity floor). This layer

was chipped off yielding a total weight of 37.76 kg in test 2. In addition, an iron slug weighing 18.80 kg was recovered from the bottom of the cavity.

The sieve analysis (in test-2 only that debris recovered from the upper deck) yielded a particle sieve mass median diameter (SMMD) of 1.54 mm in test-2, compared to the SMMD of 3.40 found in the test 1. This was large but consistent with the CE tests in that the particle size increased with lower driving pressure. Note that the CE-4 test (with the driving pressure reduced by a factor of 2) yielded the highest cavity retention and the largest particle size of all the CE DCH experiments. Figure 8 shows that the SMMD of the debris recovered from the operating deck in the new experiments were much larger than that found in the CE experiments.

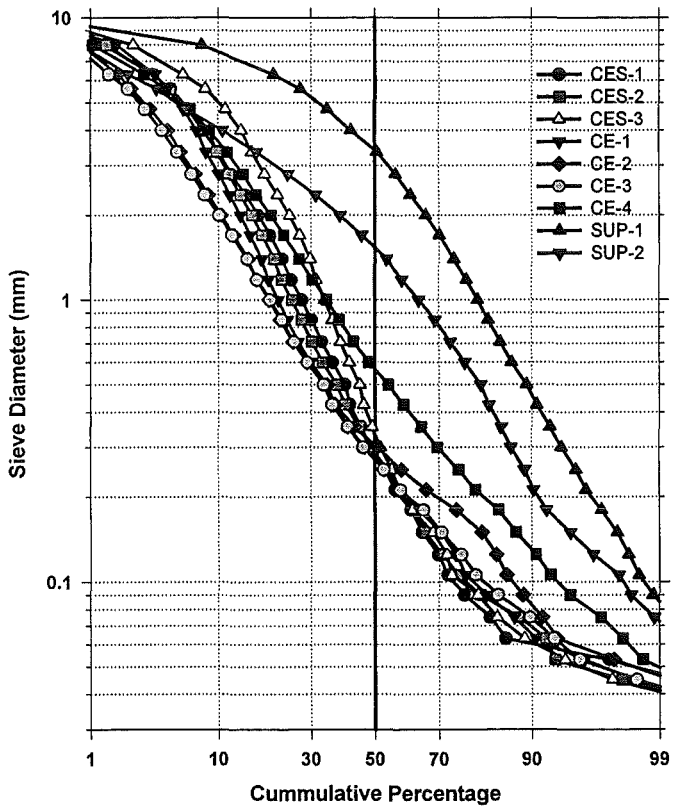

Fig. 8 Sieve analysis of debris recovered from the upper deck.

1.5 Gas Analyses

Gas grab samples used to measure the vessel atmospheric composition were taken near the top of the Surtsey vessel, above the upper deck, and also in the basement. The times of the samples were background, 20 s, 240 s, and 52 min. All samples (except the 20 s) were taken following a 30 s line purge. Mixing fans attached to the underside of the Surtsey vessel upper head were operated prior to taking the background samples and the 240 s and the 52 min. posttest samples. Table 3 shows the initial and the 52-min-posttest gas composition together with the key results of both tests.

Table 3 Key results from Surtsey experiments

		Test 1		Test 2	
Initial vessel pressure (MPa)		0.2133		0.2184	
Initial vessel temperature (K)		372		379	
~3 s (#1), resp. 4 s (#2) after melt ejection		**Peak**	Δ	**Peak**	Δ
Pressure (MPa)		0.6062	0.3929	0.4175	0.1991
Subcompartment gas temperature (K)		523	151	405 (411)[1]	26 (32)[1]
Dome gas temperature (K)		967	595	607 (656)[1]	228 (277)[1]
Vessel average gas temperature (K)		806	434	543 (575)[1]	164 (196)[1]
Cavity ΔP (MPa) at 0.12 s		0.07		-	
Thermite cavity dispersal fraction		0.779		0.207	
Thermite transport fraction (to dome)		0.693		0.199	
Initial gas composition in the Surtsey vessel (mole %)	Steam	45.2		47.9	
	N_2	40.1		38.3	
	O_2	10.7		10.3	
	H_2	3.3		3.2	
Posttest gas composition in the Surtsey vessel (mole %)	Steam	51.1		53.7	
	N_2	40.6		36.2	
	O_2	6.1		7.1	
	H_2	1.1		1.9	
Moles of preexisting combustible gas (moles)		211		201	
Moles of combustible gas produced (·moles)		442		269	
Moles of combustible gas burned (·moles)		586		345	
Net difference between production and combustion		-144		-76	
Fraction of available combustible gas that burned ($N_{burn}/(N_{pre} + N_{prod})$)		0.90		0.73	

[1] Peak vessel average gas temperature occurred at 7.81 s.

The two main mechanisms that cause DCH are efficient debris-to-gas heat transfer and hydrogen combustion. Speculation has been that combustion of preexisting hydrogen is a relatively slow process, and may not contribute significantly to peak containment pressurization. Measurements and interpretation of data taken in these experiments support this conclusion. Table 4 shows the event timing taken from the breakwire signals and the video interpretation.

In test 1, there is a marked inflection in the rising vessel pressure (Fig. 5) at about 1 s (when the melt first impacted the dome) and the pressure peaked near 3 s (when the melt had stopped falling onto the upper deck). However, the video showed hydrogen continuing to burn in the upper dome region until t = 8 s, with decreasing vessel pressure. Pressures in test 2 show a similar behavior (Fig. 6); vessel pressurization is

nearly complete at 3-4 s, with the cavity melt ejection complete and all of the debris fallen back onto the structure surfaces, while the video showed hydrogen continuing to burn until t = 5 s.

Table 4 Event timing by breakwire and video

Event	Test 1 Time (s)	Test 2 Time (s)
Wire breaks at melt plug	0.0	0.00
Wire breaks at cavity exit	0.1	0.63
Melt stops rising		0.6
Debris ejection ends	0.4	1 - 2
Flame plume impacts dome		1 - 2
Melt impacts dome	1.0	-
Debris stops falling	3.0	3.0
Dome combustion ends	8.0	5.0

2. THE DISCO EXPERIMENT

The test facility DISCO-C has been built at FZK for performing dispersion experiments with cold simulant materials in an EPR-geometry in a 1/18 scale. The fluids are water or gallium alloy instead of melt, and nitrogen or helium instead of steam. There are three possible flow paths out of the cavity. The path (1) straight up into the refueling canal through 8 openings with a total cross section of 3 m² (92 cm² scaled down) may not exist in the final EPR design. Than the main flow path (2) would be the free flow area around the 8 main coolant lines into the pump and heat exchanger rooms with a total flow area of 10 m². However, there is a flow constriction below the nozzles (upstream) at the RPV support structure with an minimum flow area of only 6 m². The third way out of the reactor pit (3) will be through the four ventilation openings in the lower part of the cavity leading to the spreading compartment via an annular channel around the pit, and a vertical channel.

The first experiments in the DISCO-C facility have been performed with both the first and third flow path closed, the only paths were the flow areas along the main coolant lines into the pump and heat exchanger rooms. Five experiments have been performed up to now, with a hole diameter of 50 mm (90 cm scaled) and 25 mm, and water and nitrogen as fluids.

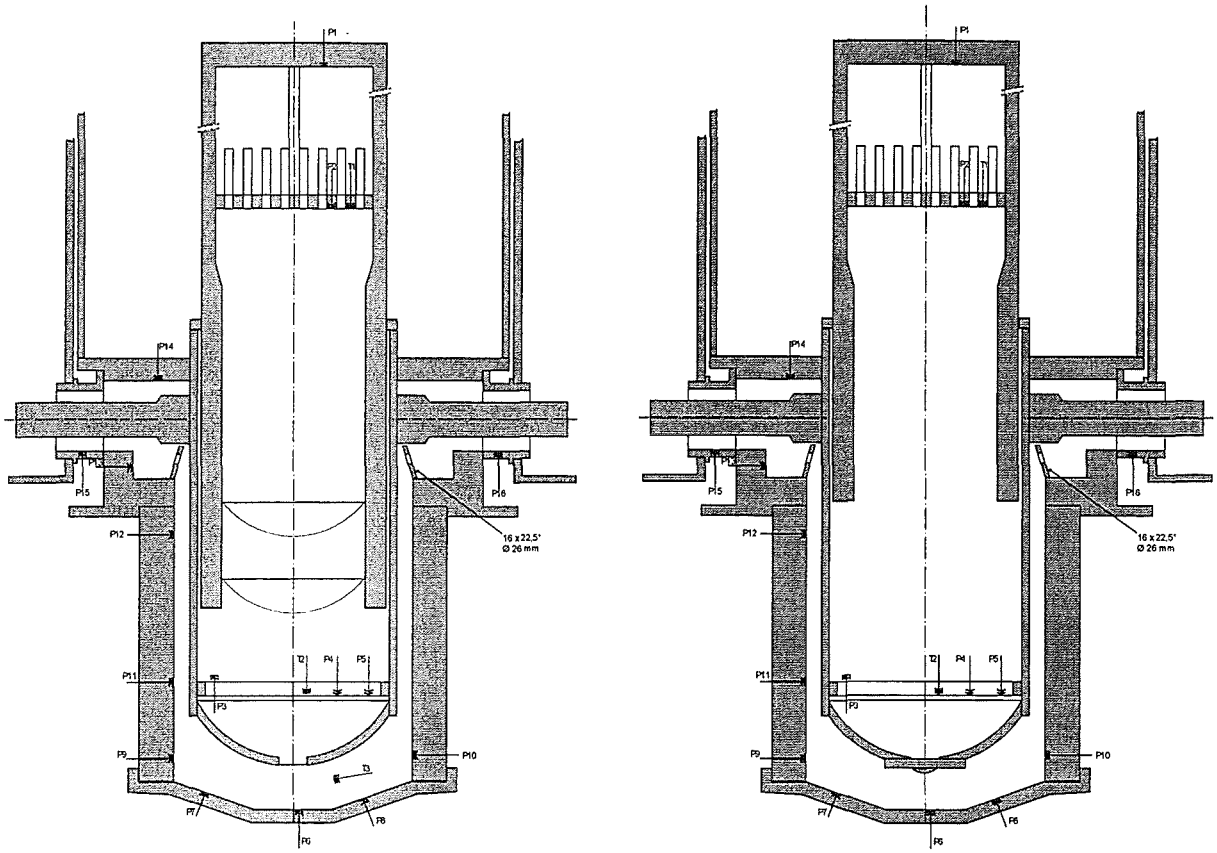

Fig. 9 The original configuration of the pressure vessel with two rupture disks and a thin foil at the hole in the lower head (left), and the modified configuration with one rupture disk at the lower head.

We investigated the effect of the pressure shock that occurs in the original configuration of the pressure vessel, where the high pressure region is separated from the low pressure region (atmospheric pressure) above the liquid in the lower head by a double rupture disk (Fig. 9). The test was started by either venting or pressurizing the space between the two disks, thereby breaking first the upper and than the lower disk, or vice versa. This guaranteed a precise starting time that is necessary for the high speed film cameras. Also, with this technique, any hole shape at any position of the lower head is possible. In the modified configuration there is a small rupture disk at the bottom of the lower head and the whole vessel is pressurized close to the failing limit of the disk. The experiment is started by quickly filling more gas into the vessel until the disk breaks. The results in both cases differed notably (Table 5). In the two experiments with the double rupture disks the water ejected into the compartments (8 boxes simulating the pump and heat exchanger rooms) was only about 52% and 56% of the total mass versus 80% in the second case. Also the blow down pressures and the pressure in the cavity were different in both cases (Fig.10 and 11). In the first case the jet started as a single phase liquid jet while in the second case a distorted jet was observed (Fig.12). Whether or not it was a two-phase jet could not be determined.

Table 5 Parameters and dispersed liquid fractions in DISCO-C experiments

Exp. No.	hole size (mm)	pressure (MPa)	gas	liquid	mass (g)	rupture disk	fraction in subcomp.	fraction in cavity
D00	50	1.00	N_2	H_2O	3400	double	0.518	n.a.
D01	50	1.00	N_2	H_2O	3400	double	0.557	0.20
D02	50	1.12	N_2	H_2O	3400	one	0.804	0.012
D03	25	1.13	N_2	H_2O	3400	one	0.668	0.056
D04	25	1.16	N_2	H_2O	3400	one	0.698	0.053

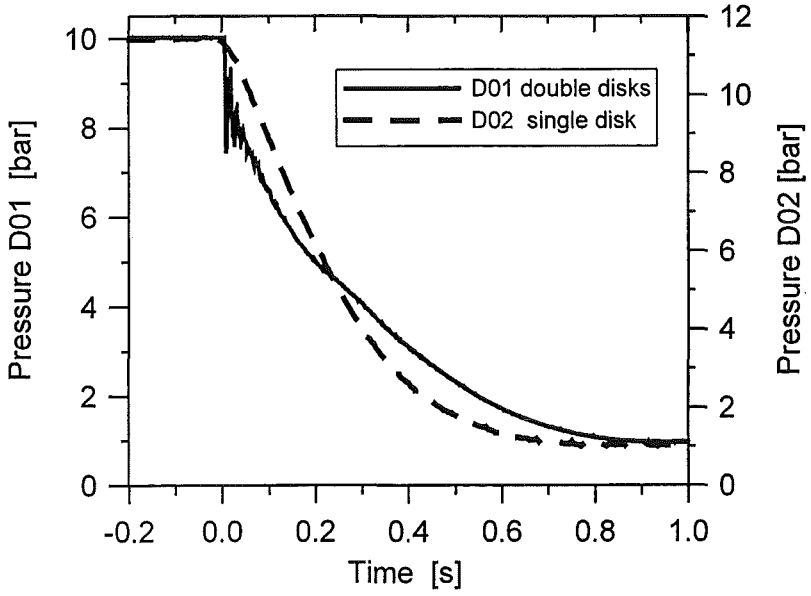

Fig. 10 Blow down pressures in the upper part of the pressure vessel in the case with double disks and a foil at the lower head and the case with one single disk at the lower head

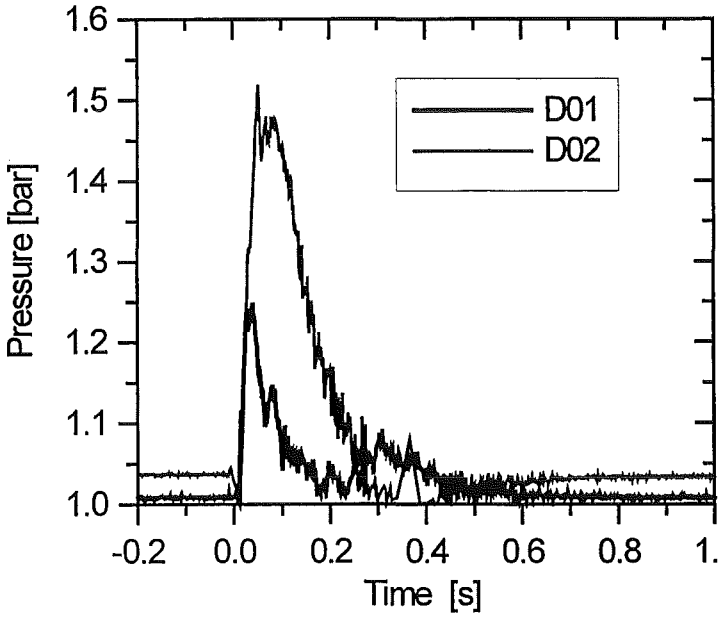

Fig. 11 Pressures in the in the cavity

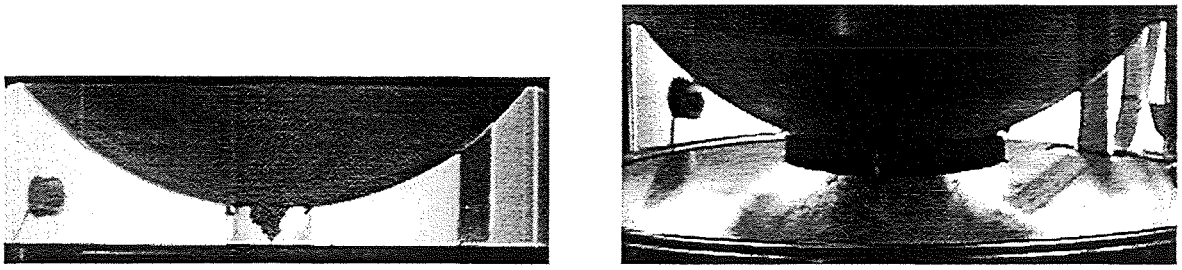

D01 D02

Fig. 12 Jet configuration in the two cases of blow down

The case with a shock wave is obviously less prototypic than the case with a constant pressure above the liquid, therefore we intend to do most experiments with the second technique or a similar one. During the blow down the gas temperature drops by approximately 75 K (Fig. 13). This is a non-reversible thermodynamic process where the temperature can be determined by

$$\frac{T_2}{T_1} = \frac{\frac{p_2}{p_1} + \frac{1}{\kappa - 1}}{1 + \frac{1}{\kappa - 1}} ,$$

with the index 1 and 2 denoting the state before and after the blow down, respectively. This causes the formation of a thick fog that obscures the view into the cavity and some ice formation at the walls. It also makes measurements of the gas velocity by particle imaging velocimetry almost impossible. To reduce the fog formation we tried a third method of initial conditions.

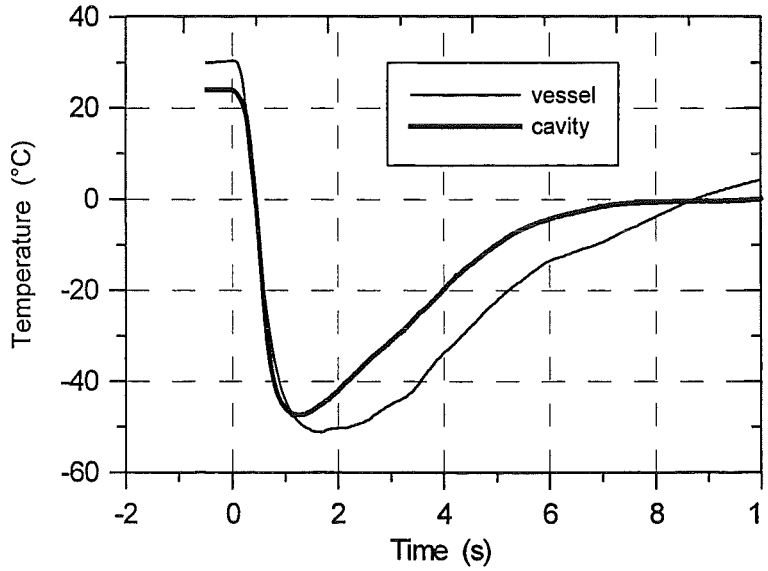

Fig. 13 Gas temperature during blow down in test D02

In order to avoid a temperature drop below freezing we must heat the gas to at least 80°C before the test. On the other hand, the water must stay at room temperature or colder to avoid evaporation. To achieve this, the pressure vessel is divided into two volumes by a thin diaphragm. The walls above the diaphragm are heated, while the lower part remains cold. Both volumes are filled with hot gas at a pressure slightly lower than the failing pressure of the lower rupture disk. The blow down is initiated by pressurizing the upper space until first the upper thin diaphragm breaks and immediately thereafter the lower disk fails. Thereby a shock wave does not occur, because the pressure ratio in the two compartments of the vessel is close to one. This was done in test D03 for the first time. Although the temperature still dropped below freezing in D04, the fog formation was reduced (Fig.14 and 15).

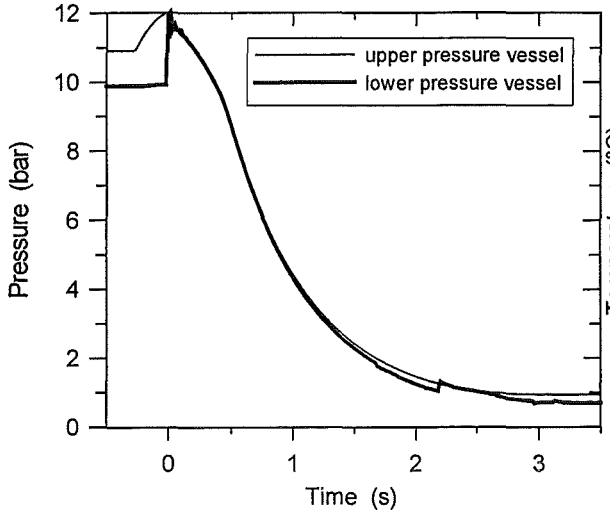

Fig.14 Pressures in the pressure vessel in test D04 with heated gas

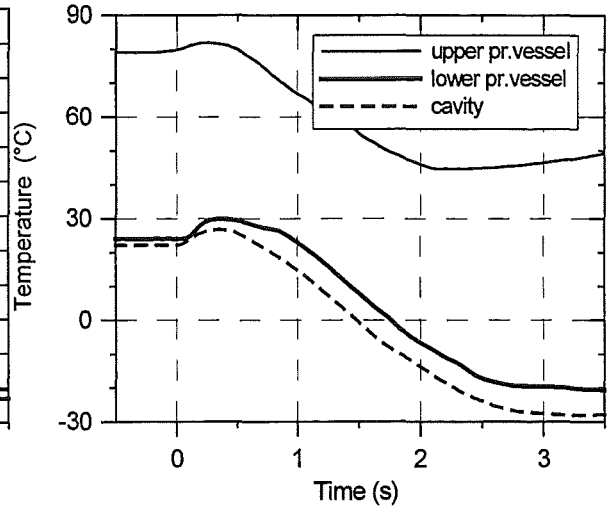

Fig.15 Temperatures in the pressure vessel and in the cavity in test D04 with heated gas

3. CONCLUSIONS

Even at low pressures below 20 bars, corium dispersion out of the cavity may be high. If a direct path exists, large fractions can reach the dome. Otherwise the melt mass is ejected into the pump and heat generator rooms via the flow path around the main coolant lines.

More experiments and analysis are required to investigate the possible implications for the EPR. Studies are required to assess the realistic hole size for low pressure scenarios.

III. Nachrechnungen der DISCO-Versuche mit RELAP5

(G. Jacobs, INR)

Zusammenfassung

Die ersten DISCO-Versuche, die mit Wasser als Schmelze-Ersatz durchgeführt wurden, sind mit dem Thermohydraulik-Programm RELAP5 nachgerechnet worden. Die Untersuchungen prüften die Anwendbarkeit von RELAP5 für die Dispersions-Versuche. Die bisherigen Rechenergebnisse zeigen, dass Vorhersagen mit dem Programm ohne bestimmte Eingabevorschriften problematisch sind.

Einleitung

Es wurden die ersten DISCO-Versuche (Vorversuche), die mit Wasser als Schmelze-Ersatz durchgeführt wurden, mit dem Thermohydraulik-Programm RELAP5 **[1]** nachgerechnet. Benutzt wurde die beta-Version von mod 3.2.2 **[2]**. Berichtet wird hier über Parameter-Variationen der Eingabe, die sich auf die beteiligten, hydraulischen Modelle auswirken. Die Ausführungen beschränken sich auf den Versuch D02 **[4]**. Zweck der noch nicht abgeschlossenen Untersuchungen ist es, die Anwendbarkeit von RELAP5 auf diese Dispersionsversuche zu prüfen und gegebenenfalls Empfehlungen zur Eingabe zu geben. Diese Arbeiten sind als Ergänzung der Skalierungsanalyse **[5]** zu sehen.

Eingabemodell

Nodalisierung

Das geometrische Model versucht, DISCO **[3]** eindimensional abzubilden. Das Modell besteht aus 18 Kontrollvolumen (**Abb. 1**). Auf Wärmeleitstrukturen kann wegen der Kürze des ablaufenden Abblase- und Dispersionsvorganges verzichtet werden. Auf der Primärseite (Hochdruckkessel) sind die Längen der Kontrollvolumen gleichmässig etwa 20 cm lang. Wegen eines durchgehenden Länge/Durchmesser- Verhältnisses von etwa 1 empfiehlt sich eine feinere Nodalisierung nicht. Auf der Con-

tainmentseite ergeben sich günstigere Länge/Durchmesser-Verhältnisse mit Ausnahme des Grubenbodens (KV# 30) mit der geringen Höhe von 6,2 cm. Die acht Auffangkästen werden zu einem Kontrollvolumen (KV#42) zusammengefasst, die anders als im Versuch hängend angeordnet sind, um das Zurückfliessen des Wassers in die Grube zu verhindern.

Anfangsbedingungen

Die Eingabe der Anfangsbedingungen für das untere Plenum (KV#20), wo 3.4 kg flüssiges Wasser, Wasserdampf und nichtkondensierbares Gas (Stickstoff) koexistieren, erfordert einige Nebenrechnungen. Die übrigen Anfangsbedingungen, 300 K und 1.14 MPa primärseitig sowie 300 K und 0,1 MPa auf der Containment-Seite sind unproblematisch. Für das Kontrollvolumen # 20 sind aus den gegebenen Anfangsbedingungen Gesamtdruck, Gas- und Flüssigkeitstemperatur, Voidanteil und Massenanteil des nichtkondensierbaren Gases (Gasqualität) die spezifische Energie des Mischgases und der Flüssigkeit zu berechnen. Auf Einzelheiten der Rechenschritte möchte ich hier nicht näher eingehen. Benutzt werden dabei die NBS/NRC-Wasserdampftafeln **[7] [8]**.

Zeitschrittbestimmung

Für die Stabilität des verwendeten halbimpliziten Lösungsverfahrens ist es notwendig, die maximale Zeitschritt kleiner als das Verhältnis "minimale Schrittweite/ maximale Schallgeschwindigkeit" zu halten, weil das im Programm verwendete Courantsche Stabilitätskriterium auf der Fluidgeschwindigkeit basiert und für Rechnungen, bei denen Druckwellen auftreten, nicht ausreicht.

Hydraulische Modelle

Hinsichtlich der relevanten hydraulischen Modelle werden verschiedene Varianten ausprobiert. Im einzelnen handelt es sich um

1. die kritische Strömung an der Berststelle (Knoten# 25) und am Lochring im Grubenkopf (Knoten# 3601),
2. die abrupte Querschnittsänderung an der Berststelle (Knoten# 25) und am Lochring (Knoten# 3601),
3. die Gegenströmungsbegrenzung (CCFL) im Ringspalt (Knoten# 3601)
4. die vertikale Schichtung und Mischspiegel im unteren Plenum (Volumen# 20) und
5. die Energie-Erhaltung an der Berststelle (Knoten# 25).

Die Einflussnahme auf die wichtigen Modelle der Reibung zwischen den Phasen und des Entrainments innerhalb der vorherrschenden Strömungsregime (dispersive Ringströmung, Nebelströmung) sind ohne direkten Eingriff in das Quellprogramm nicht möglich. Davon wurde vorerst abgesehen. Es werden zunächst die Möglichkeiten der Eingabe-Schnittstelle genutzt.

Zu den vorgenannten Modellen ist folgendes zu ergänzen.

Ad 1: Bei Rechnungen für den AP600 hat man beobachtet, dass das Modell für kritische Strömung einen unrealistisch niedrigen Massenfluss und eine zu niedrige statische Qualität bei Drücken unter 3 MPa errechnet. Das führt dazu, dass die Bedingung der kritischen Strömung aufrecht erhalten bleibt bis hin zu einem viel zu kleinen Druckverhältnis von 1.1. Die Ursachen hierfür sind zu finden in einer Inkonsistenz bei der Ableitung des Kriteriums und in einem relativ grossen Schlupf bei der Reibung zwischen den Phasen bei niedrigen Drücken. Deshalb wird von den Entwicklern empfohlen, nur dort das Modell zu aktivieren, wo kritische Strömung erwartet wird und für die betreffenden Knoten die Option der homogen Strömung zu wählen. Als weitere Alternative wird in mod 3.2.2 angeboten, eine modifizierte Form des Henry-Fauske-Modells (HFM) zu verwenden. Bei Wahl des HFM ist von der Spezifizierung der homogenen Option abzusehen, um Schlupf zu ermöglichen wenn das Modell gerade nicht aktiv ist. Das Henry-Fauske-Modell verlangt auch nicht die Verwendung des Modells für die abrupte Querschnittsänderung. An den Knoten # 25,3601 und 3602 ist kritische Strömung zu erwarten.

Ad 2: Soweit das Modell der abrupten Querschnittsänderung nicht aktiviert wird, werden an den betreffenden Knoten Druckverlust-Beiwerte eingegeben. Die Eingabe orientiert sich an dem Handbuch von Idelchik **[6]**.

Ad 3: Das Modell für die Begrenzung einer Gegenströmung (engl. countercurrent flow limitation = CCFL) , das in mod 3.2.2 eine Überarbeitung erfuhr, könnte bei unserem Problem eine gewisse Rolle spielen. Zum besseren Verständnis der Modellparameter sei das CCFL-Model kurz vorgestellt. Das aus dem TRAC-P Programm übernommene Modell hat die Form

$$H_g^{1/2} + mH_f^{1/2} = c$$

$$H_g = \alpha_g v_g \left[\frac{\rho_g}{gw(\rho_f - \rho_g)}\right]^{1/2}$$

$$H_f = \alpha_f v_f \left[\frac{\rho_f}{gw(\rho_f - \rho_g)}\right]^{1/2}$$

$$w = D^{1-\beta} L^{\beta}$$

$$L = \left[\frac{\sigma}{g(\rho_f - \rho_g)}\right]$$

Es bezeichnen:

α Volumenanteil

D Hydraulischer Durchmesser

g Erdbeschleunigung

H Fluid-Fluss (dimensionslos)

L Laplace Zahl (Kapillaritätskonstante)

ρ Fluid-Dichte

σ Oberflächenspannung

v Fluid-Geschwindigkeit

Index f für Flüssigleit

Index g für Gas

β, c und m sind Eingabeparameter. Für $\beta = 0$ erhält man die Wallis-Form, für $\beta = 1$ die Kutadeladze-Form der CCFL-Beziehung und für $0 < \beta < 1$ Kombinationen von beiden.

Grundsätzlich ist es so, dass passende Parameter nur aus entsprechenden Daten (Filmströmung, Entrainmentrate et c.) der untersuchten Anlage gewonnen werden

können. In Anbetracht noch fehlender Daten von DISCO werden alternativ zwei Parametersätze verwendet, die sich an den Untersuchungen von Tien et al. und Wallis orientieren (**Tab. 1**).

Tab.1 : CCFL-Parameter

	D		c	m
Satz 1, nach Wallis	0.156	0.0	0.7	1.0
Satz 2, nach Tien et al.	0.156	1.0	1.0	0.7

Ad 4: Das Modell zur Beschreibung des Mischspiegels im Falle vertikaler Schichtung ist neu in mod 3.2. Es hat u. a. Einfluss auf den Void-Anteil ober- und unterhalb des Spiegels.

Ad 5: An der Berststelle (Knoten# 25) entlädt sich ein Wasser/Gas-Gemisch aus einem Kontrollvolumen mit hohem Druck in ein Volumen mit niedrigem Druck. In den Vorgänger-Versionen von mod 3.2 war die Energiebilanz in den Differenzengleichungen hier fehlerhaft. In mod 3.2 wurde dies Problem korrigiert, indem im konvektiven Energieterm die Enthalpie strömungsgerichtet (engl. "donored") verwendet wird.

Ergebnisse

Rechenfälle

Es werden zehn verschiedene Eingabesätze, E bis N, betrachtet, die sich nur in wenigen modellbezogenen Parametern unterscheiden (**Tab. 2**), aber zum Teil grosse Unterschiede in den Ergebnissen zur Folge haben. Der Platz reicht hier nicht aus, um auf alle Unterschiede und ihre Ursachen in den Rechnungen einzugehen. Ich beschränke mich auf die auffälligsten.

Tab. 2 : Rechenfälle

Fall		Kontrollvol. 20		Kontrollknoten 25				Kontrollknoten 3601						Kontrollknoten 3602			
	HFM [a]	v=0 c1o=66 [b]	v=0 l=1 [c]	a=1 [d]	c=0 [e]	e=1 [f]	h=2 [g]	a=1	c=0	e=1	h=2	f=1 set1 [h]	f=1 set2 [i]	a=1	c=0	e=1	h=2
E		✓		✓	✓	✓	✓						✓		✓	✓	✓
F	✓	✓		✓	✓	✓							✓		✓	✓	✓
G	✓			✓	✓	✓							✓		✓	✓	
H	✓		✓	✓	✓	✓		✓	✓		✓				✓	✓	✓
I					✓	✓	✓		✓							✓	✓
J	✓		✓		✓	✓		✓	✓		✓				✓	✓	✓
K		✓	✓		✓	✓							✓		✓	✓	
L			✓		✓	✓							✓		✓	✓	
M			✓		✓	✓						✓			✓	✓	
N			✓	✓	✓	✓	✓	✓	✓		✓				✓	✓	✓

a. HFM ist Henry-Fauske-Model für kritische Strömung, Relap5-Modell ist Default.
b. v=0 ist vertikale Schichtung, c1o=66 ist zusätzlich Karte 1 Option 66, d.h. im oberen Knoten nur Gas, im unteren Knoten nur Flüssigkeit.
c. v=0 ist vertikale Schichtung, l=1 ist Mischspiegel-Modell.
d. a=1 ist Modell für abrupte Querschnittsänderung, eingegebene Druckverlust-Beiwerte ist Default.
e. c=0 ist Modell für kritische Strömung aktiv (Default), c=1 ist Modell nicht aktiv.
f. e=1 ist Modell zur Energieerhaltung bei grossem Druckunterschied.
g. h=2 ist homogene Strömung.
h. f=1 ist CCFL-Model aktiv, set1 ist Parameter nach Wallis.
i. f=1 ist CCFL-Model aktiv, set2 ist Parameter nach Tien et al..

Wasseraustrag

Im Versuch D02 wurden etwa 80 % des Wassers aus der Grube in die Kästen ausgetragen. Wie aus **Tab. 3** zu ersehen ist, wird dieser Befund in der Rechnung in den Fällen E, F und I ganz gut bestätigt, wo der Anteil zwischen 63 und 71 % beträgt. Für den Fall E ist in **Abb. 2** die Verteilung des Wassers in den verschiedenen Kontrollvolumina gezeigt. Das übrige Wasser sammelt sich am Boden der Grube. Im Versuch wurde fast überhaupt kein Wasser auf dem Grubenboden gefunden. Den drei Fällen E,F,I ist gemeinsam, dass die Option 'homogene Strömung' an dem Knoten zwischen Grubenkopf und Kästen gesetzt ist. Die homogen Bedingung lässt keinen Schlupf zu, was den hohen Austrag erklärt. Zugleich aber deuten die anderen Fälle mit den viel zu niedrigen Austragsanteilen darauf hin, dass die Zwischenphasenreibung im Programm in diesem Druckbereich zu niedrig berechnet wird. Die eindimensionale Nodalisierung lässt sogar ein Zurückschwappen des Wassers in das KV # 20 zu, wie **Abb. 3** z.B. im Fall K zeigt, in dem in allen Knoten die nichthomogene Zweiphasenströmung zugelassen wird. Die Fälle H und N fallen aus dem Rahmen und werden hier nicht weiter betrachtet. Sie haben gemeinsam, dass sowohl das neue Mischspiegelmodel als auch das Modell der abrupten Querschnittsänderung aktiv sind. Ich schliesse daraus, dass diese Modelle nicht zusammen harmonieren. Hinsichtlich des CCFL-Models lässt sich durch Vergleich der Fälle E (mit CCFL) und I (ohne CCFL) nicht behaupten, dass ein grosser Einfluss besteht. Auch ist nicht zu sehen (vergl. Fälle L und M), dass die Unterschiedlichkeit der Parametersätze eine erkennbareAuswirkung auf den Wasseraustrag haben.

Tab. 3: Anteil des ausgetragenen Wassers

Fall	E	F	G	H	I	J	K	L	M	N
F_d	0.71	0.68	0.04	0.0	0.63	0.06	0.15	0.06	0.06	0.0

Druck

Der Vergleich der primärseitigen Druckkurven mit der Messung ist in **Abb. 4** dargestellt. Die gemessene Kurve wird von den berechneten eingehüllt. Die Abblasezeit von etwa 0.7 s wird von allen betrachteten Rechnungen einigermassen getroffen. Die Entlastungsraten weichen allerdings voneinander ab. Die Fälle E,F,G und I zeigen bis zur Mitte der Entlastungszeit eine schwächere Druckabnahme, bei K,L,M ist es umgekehrt. Bei der ersten Gruppe (E,F,G,I) wird die homogene Ausströmung (auch bei Henry-Fauske) erzwungen und das Mischspiegelmodell ist nicht aktiv, d.h. es findet eine zweiphasige Ausströmung mit gleicher Geschwindigkeit für Gas und Wasser statt. Das ist der Grund für einen anfänglichen geringeren Druckabfall. Dagegen findet in der anderen Gruppe nichthomogene Ausströmung bei Vorhandensein eines Mischspiegels statt. Zunächst wird schwallartig Wasser ausgetrieben, dann folgt ab etwa 100 ms eine reine Gasströmung. Fall J mit homogener Henry-Fauske-Ausströmung und aktivem Mischspiegelmodell liegt dazwischen und zeigt im Vergleich mit den Fällen K,L,M den Einfluss des Henry-Fauske-Modells.

Die in **Abb. 5** im Vergleich mit der Messung an der Pos. 11 (Eintritt in den Ringspalt) dargestellten Druckkurven lassen eine ähnliche Gruppierung der Rechenfälle erkennen wie bei der zuvor diskutierten Druckentlastung. Allen gerechneten Kurven gemeinsam ist die etwas spätere Ausbildung der Druckspitze, was vermutlich auf eine Schwäche der angewandten Modelle für die kritische Strömung hinweist. In der Höhe des Druckes liegen bis auf den Ausreisser I (Druck zu gross) alle Kurven ganz gut zusammen. Die hohe Druckspitze ist sicher bedingt durch eine zeitgleiche, kritische Strömung am Lochring zwischen Ringspalt und Grubenkopf (Kontrollknoten # 3601).

Temperatur

Infolge der Expansion des Treibgases ist ein starker Abfall der Gastemperatur zu beobachten. In **Abb. 6** sind die gerechneten Kurven mit der gemessenen an der Position T1 (im Kessel direkt unterhalb der Rohrstutzenplatte dargestellt). Während im Versuch der Temperaturabfall maximal etwa 80 K beträgt, zeigen die Fälle E,F,G und I eine Erniedrigung von 150 K. Offenbar wird im Programm mit einer isentropen Ausdehnung eines idealen Gases mit konstanten spezifischen Wärmen gerechnet, wofür die Beziehung

$$\frac{T_2}{T_1} = \left(\frac{P_2}{P_1}\right)^{(\kappa-1)/\kappa}$$

gilt. In der Tat lässt sich hiermit der relap5-gerechnete Temperaturabfall bestätigen. In Wirklichkeit handelt es sich vermutlich um einen polytropen Prozess, der mit derselben obigen Beziehung beschrieben wird, allerdings hat dann κ die Bedeutung eines polytropen Exponenten, der deutlich kleiner ist als der Quotient der spezifischen Wärmen. Sobald in den betreffenden Volumina allerdings Wasserdampf anwesend ist, wie in den übrigen Fällen J, K, L und M, stellen sich die Gastemperaturen auf der Basis der realen Zustandsdaten von Wasser ein. Die Gastemperaturen können allerdings örtlich sehr schwanken in Abhängigkeit vom Dampvolumenanteil..

Gasgeschwindigkeit

Wichtig im Zusammenhang mit der Dispersion (z.B. Entrainment, CCFL) ist die Gasgeschwindigkeit in der Grube, insbesondere im Ringspalt. **Abb. 7** zeigt die berechneten Gasgeschwindigkeiten im mittleren Knoten im Ringspalt. Ein Vergleich mit dem Experiment ist nicht möglich, weil Gasgeschwindigkeiten bislang noch nicht gemessen werden konnten. Die Rechnungen zeigen Maximalwerte von über 100 m/s und Mittelwerte von etwa 50 m/s während der Abblasephase. Relap5 verwendet die Entrainment-Korrelation von Ishii und Mishima **[9]**. Die Korrelation, die von Luft-Wasser-Daten abgeleitet wurde und die den DISCO-Bereich gut abdeckt, lautet:

$$E = \tanh(7.25\times10^{-7} \cdot We^{1.25} \cdot Re_f^{\,0.25})$$

E ist hierin der Volumenanteil der Tröpfchen am gesamten Flüssigkeitsfluss, We die Weber-Zahl für Entrainment und Re_f die Reynolds-Zahl für die Flüssigkeit. Die Gasgeschwindigkeit geht hier mit dem Exponenten 2.5 ein.

Schlussfolgerung

Festzustellen ist bei den RELAP5-Rechnungen eine starke Abhängigkeit der Ergebnisse von den Optionen der wichtigen, hydraulischen Modelle. Eine gute Vorhersage ist daher nicht ohne weiteres möglich. Der hohe Wasseraustragsanteil im Versuch D02 beispielsweise ist nur zu erreichen, wenn an den entscheidenden Kontrollknoten homogene Strömung per Eingabe erzwungen wird, d. h. wenn Gas und Flüssigkeit dieselbe Geschwindigkeit haben. Für entsprechende Eingabeempfehlungen sind weitere DISCO-Versuche nachzurechnen.

Referenzen

[1] The RELAP5 Code Development Team, RELAP5/MOD3 Code Manual, 7 volumes, Idaho Nat. Eng. Lab., NUREG/CR-5535,1995.

[2] Relap5/MOD 3.2.2 Beta User Guidelines, Idaho Nat. Eng. Lab., July 1998.

[3] Meyer,L., A.Roth, DISCO, Experiment zur Dispersion von simuliertem Corium, FZK Int. Bericht, INR 1972, 199

[4] Hartnagel,M., Kurzbericht DISCO-Experiment D02, 21.09.98, FZK, Sept. 1998.

[5] Jacobs,G., Low Pressure Corium Dispersal (LPCD) - Scaling Analysis for the Isothermal Melt Dispersal Experiment DISCO, FZK Int. Bericht, INR 1977, 1998.

[6] Idelchik, I.E., Handbook of Hydraulic Resistance, Hemisphere, 2. Ed., 1986.

[7] Haar, L., J.S. Gallagher, G.S.Kell, NBS/NRC Steam Tables, Hemisphere Press, New York, 1984.

[8] Thurnay,K., Thermal Properties of Water, FZK Wiss. Berichte, FZKA 5588, 1995.

[9] Ishii,M. and K. Mishima,"Droplet entrainment correlation in annular two-phase flow," Int. J. Heat Mass Transfer, Vol. 32, 1989.

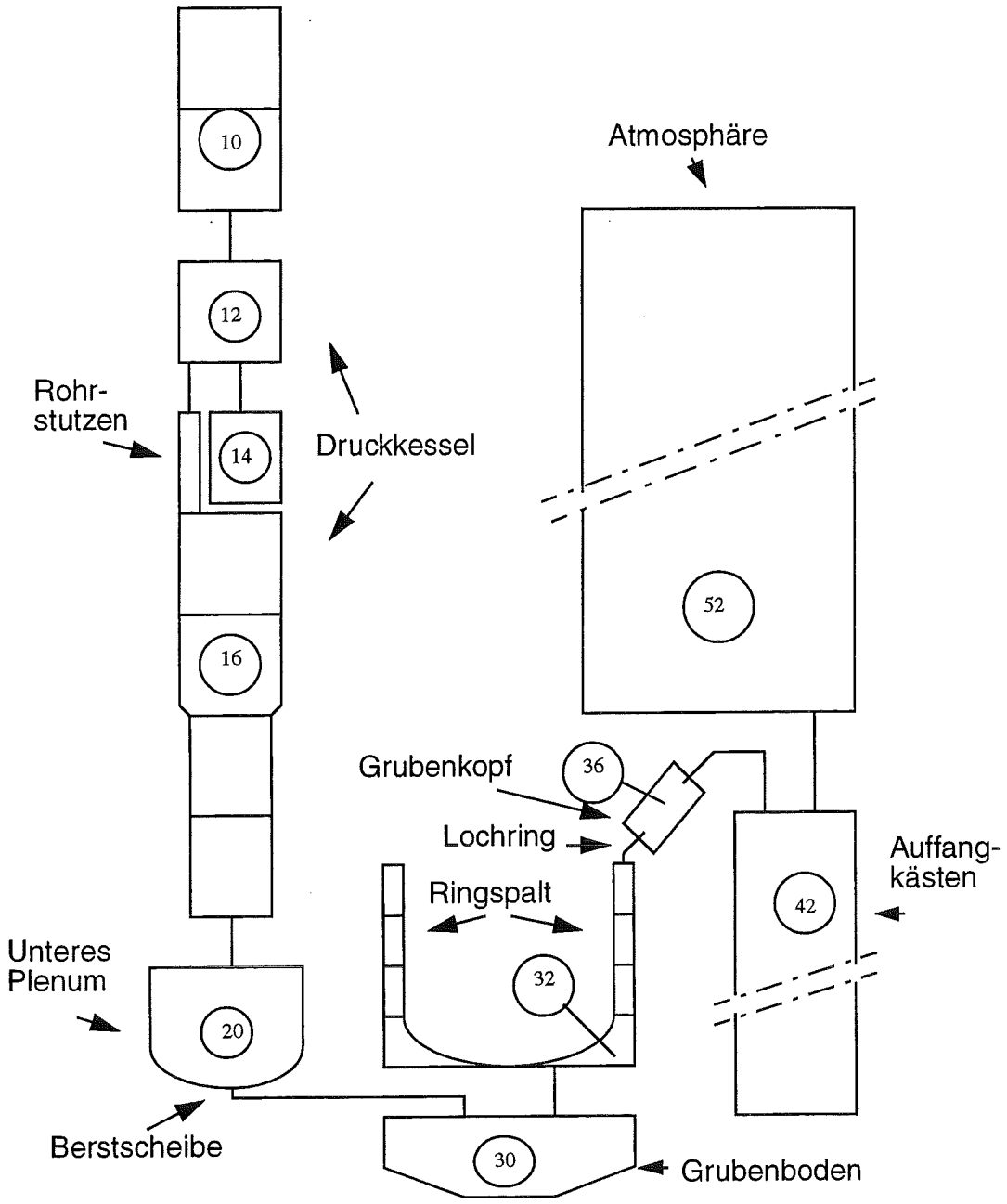

Abb. 1: DISCO-Nodalisierung für relap5

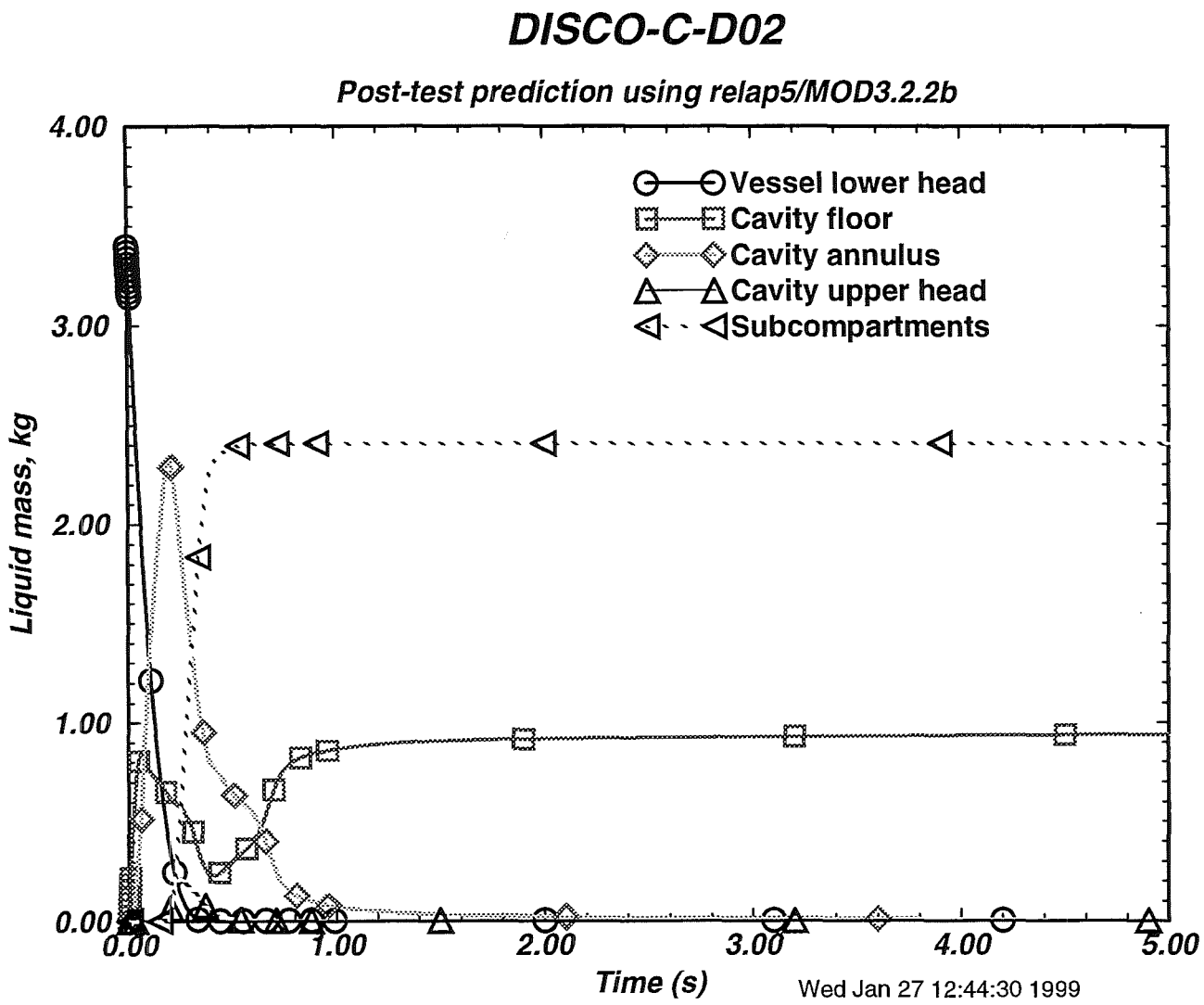

Abb. 2 : Verteilung des Wassers im Fall E

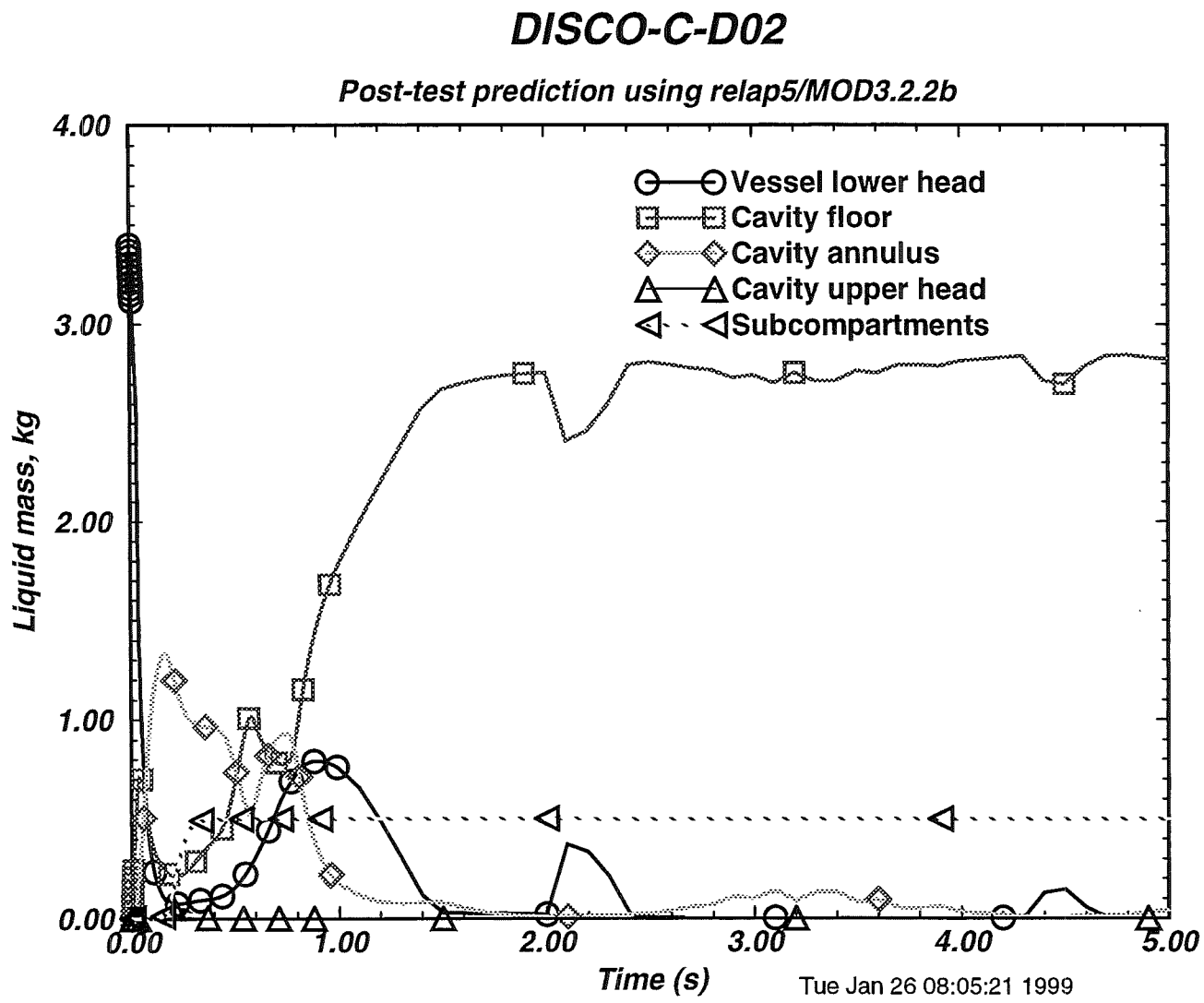

Abb. 3 : Wasserverteilung im Fall K

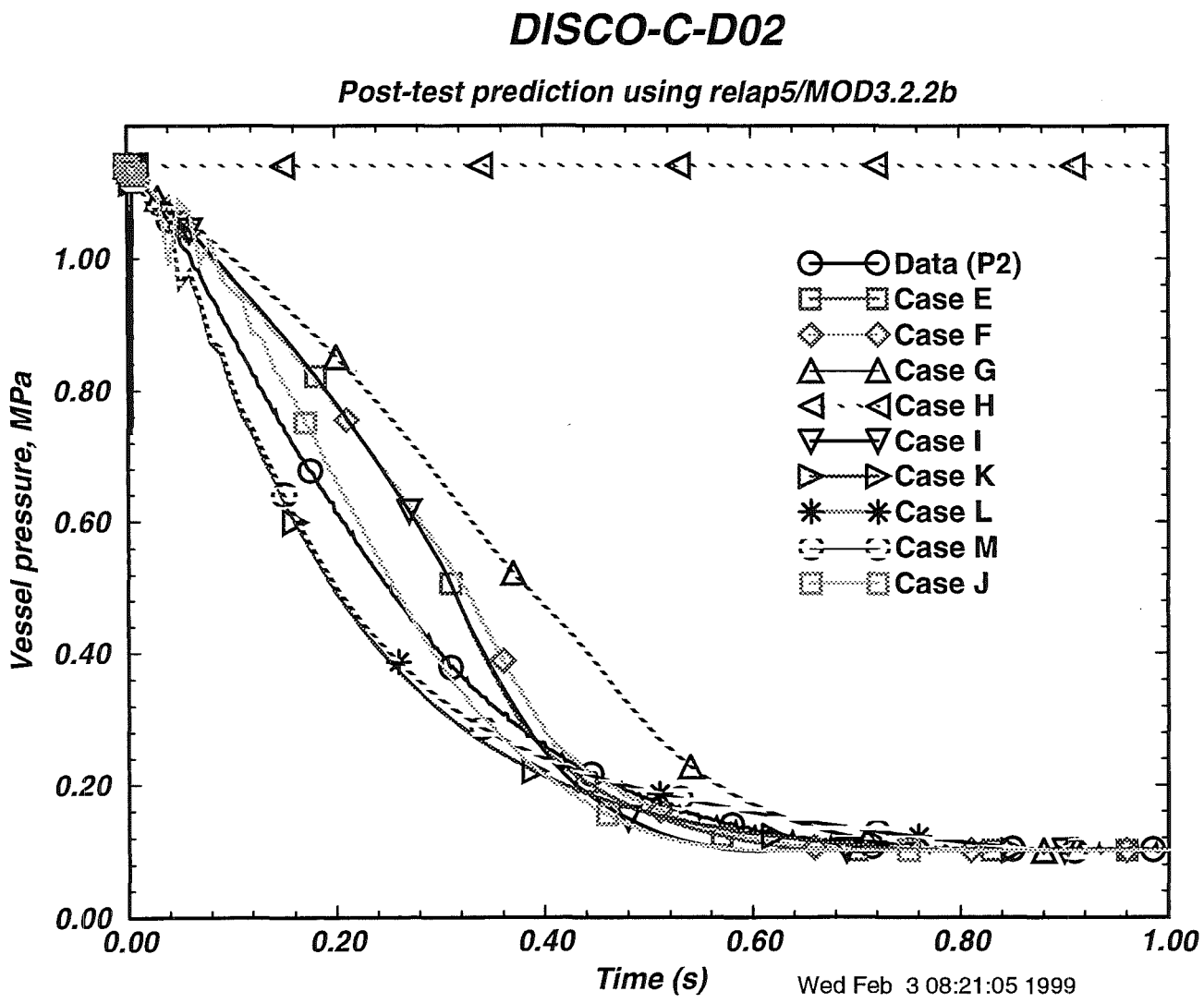

Abb. 4 : Primärseitiger Druckabfall im Vergleich mit der Messung

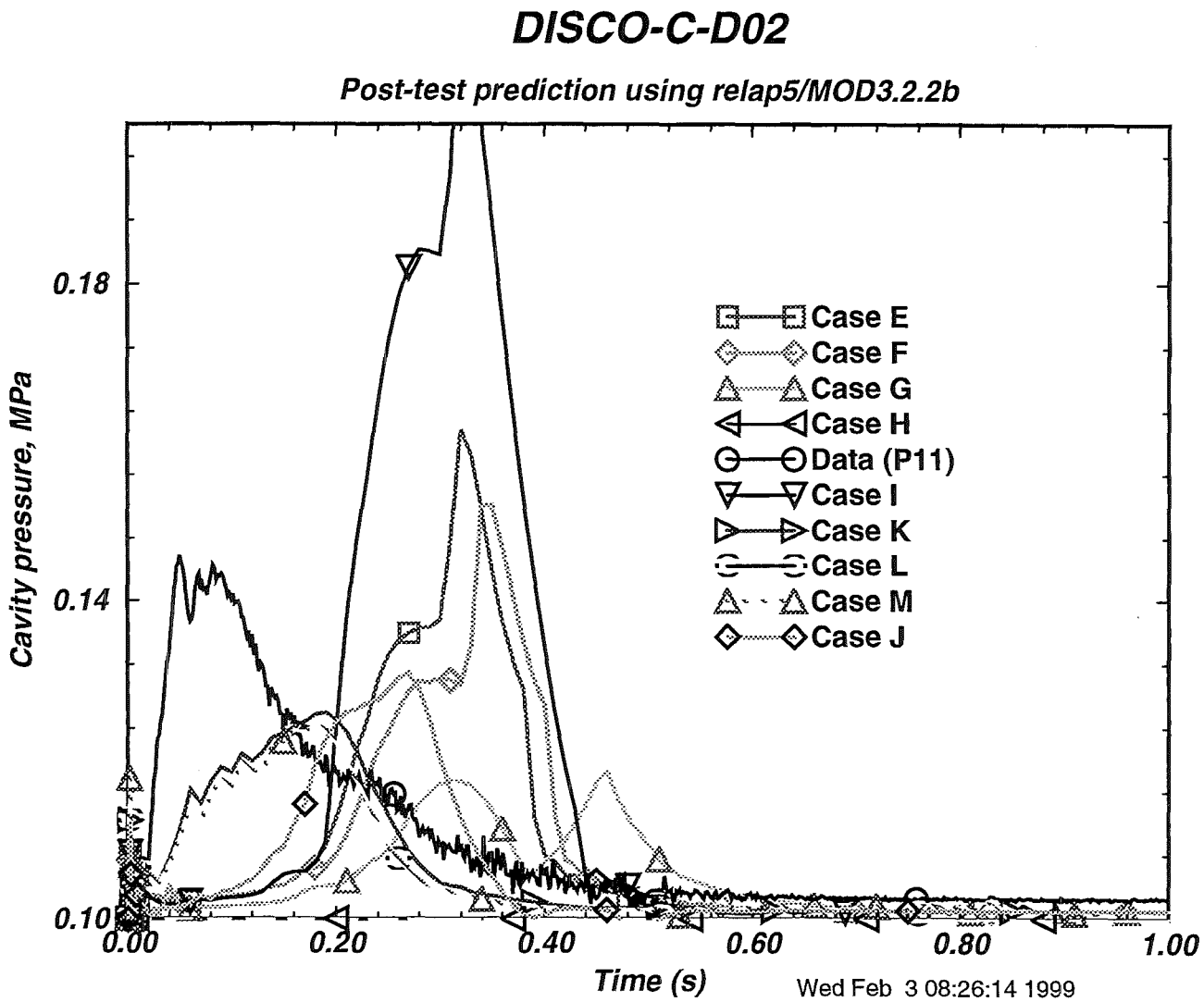

Abb. 5 : Druckaufbau in der Grube im Vergleich mit der Messung

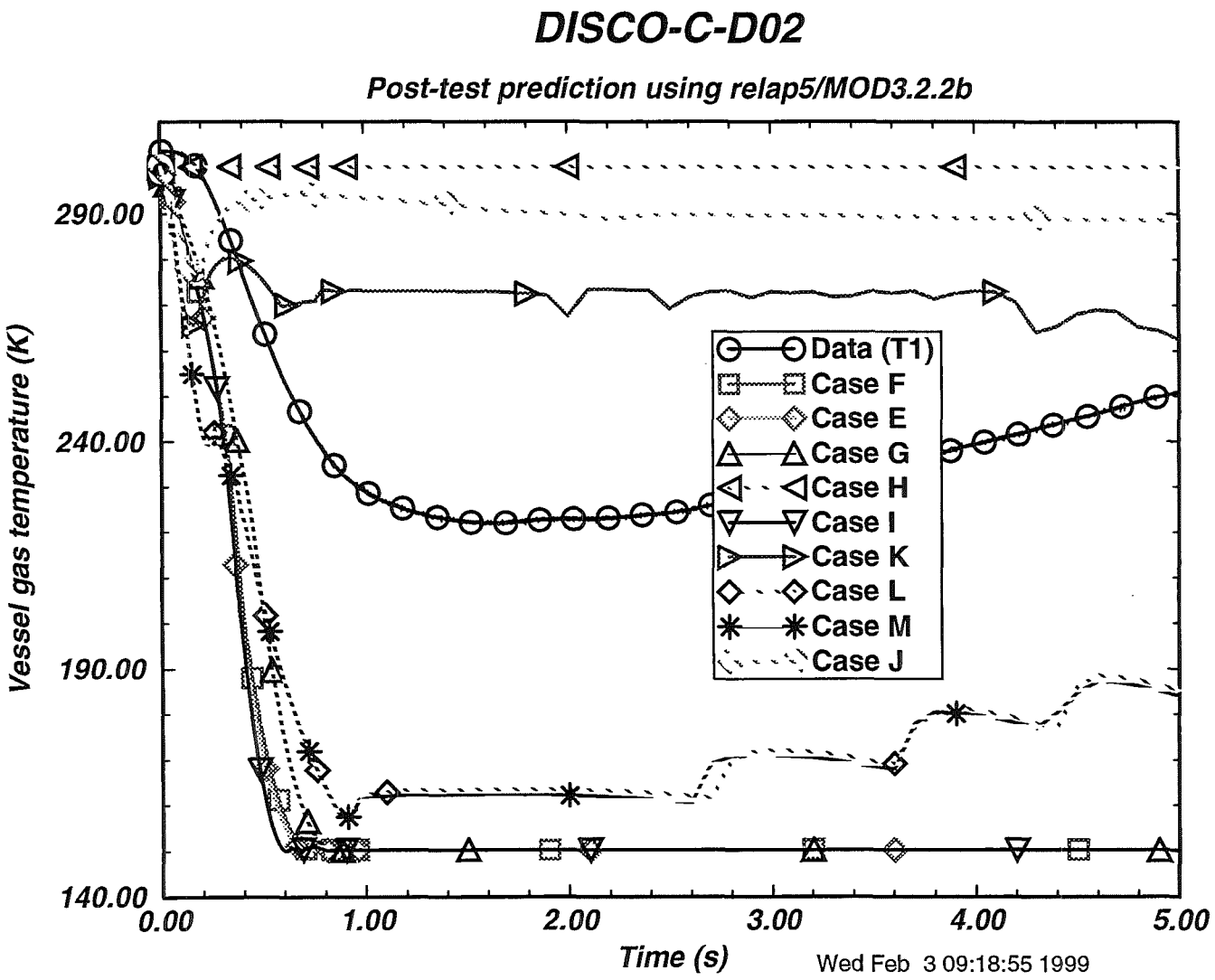

Abb. 6 : Temperaturverläufe im Kessel im Vergleich mit der Messung

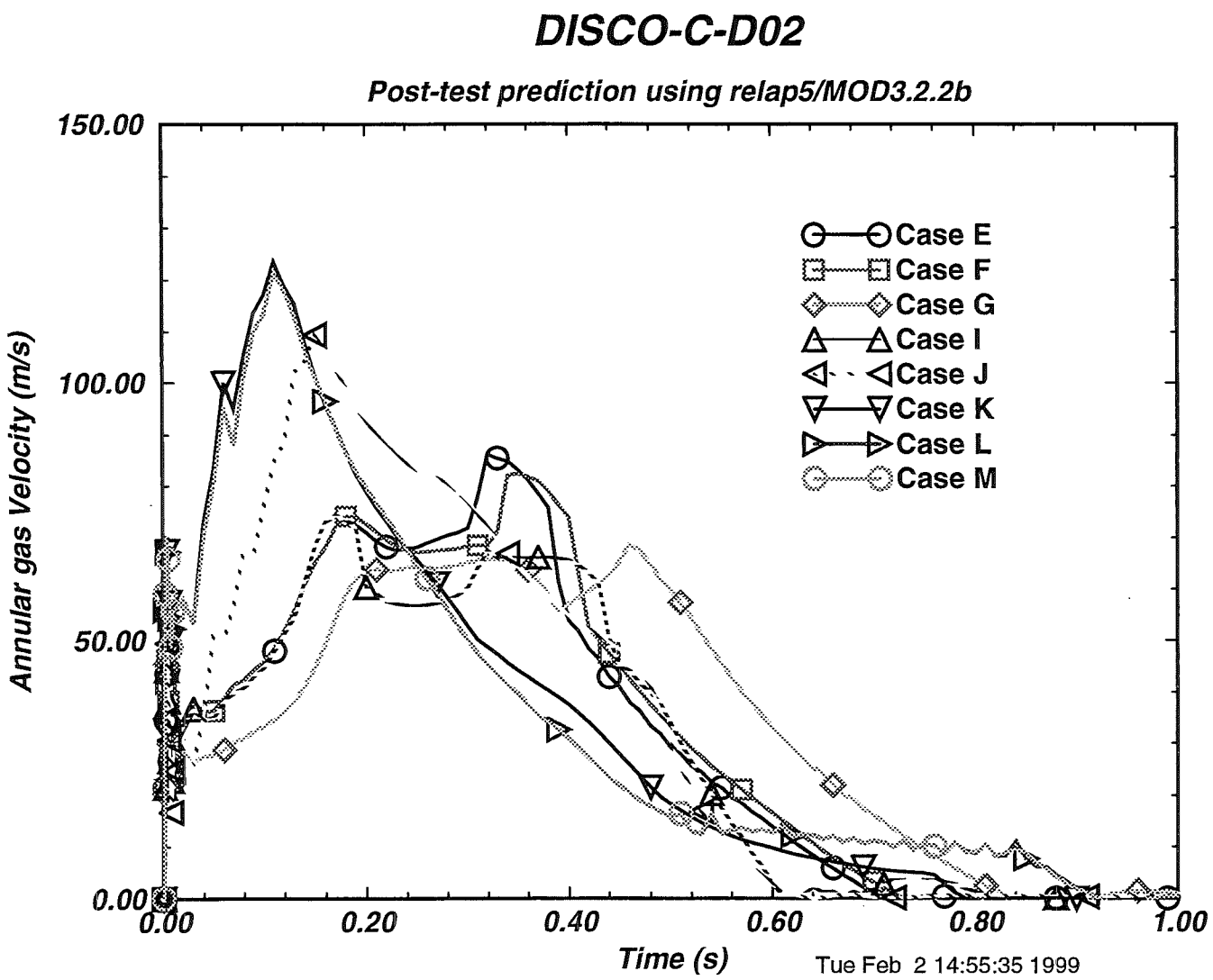

Abb. 7 : Gasgeschwindigkeiten im Grubenringspalt

32.21.04 Thermischer Angriff durch Kernschmelzen und deren langfristige Kühlung

I. COMET-Konzept

H. Alsmeyer, T. Cron, S. Schmidt-Stiefel, H. Schneider, W. Tromm, T. Wenz, IATF; F. Ferderer, KIKI; C. Adelhelm, IMF I; H.-G. Dillmann, H. Pasler, ITC-TAB; W. Schöck, IMK; G. Schumacher, INR; H. Benz, C. Grehl, G. Merkel, W. Ratajczak, HVT)

Zusammenfassung

Die Kühlung der Schmelze nach dem COMET-Konzept beruht vor allem auf dem passiven Zutritt des Kühlwassers von unten in die Schmelze. Der Schwerpunkt der Untersuchungen im Zeitraum 1998 lag bei der Kühlung von Schmelzen unter extremen Bedingungen, um damit die Funktionsfähigkeit auch unter eventuell schwierigen EPR-Situationen zu prüfen. Mit diesen Experimenten wurde die Versuchsreihe zum COMET-Konzept abgeschlossen. Alle bisher durchgeführten Untersuchungen wurden in einem zusammenfassenden Bericht dokumentiert und der Industrie im Hinblick auf eine Bewertung des Einsatzes im EPR übergeben. Danach ist das Kühlkonzept gekennzeichnet durch eine schnelle und vollständige Erstarrung der Schmelze. Für seinen sicheren Betrieb im Reaktor wird bei Schmelzenhöhen um 50 cm ein wirksamer Druck des Flutwassers von 0,2 bar oder höher vorgeschlagen.

Nach einem Vorschlag von Siemens scheint eine Vereinfachung des COMET-Konzepts möglich, indem die Wasserzufuhr in die zu kühlende Schmelze statt über Kühlkanäle durch eine wasserführende, poröse Schicht erfolgt. Hierfür wurde eine grundlegende Lösung konzipiert und ihre Funktionsfähigkeit in 5 transienten Experimenten mit Thermitschmelzen bestätigt. Danach läßt diese Variante bei einem einfachen und kostengünstigeren Aufbau ein erhebliches Potential sowohl bezüglich der Kühlung wie auch bezüglich der Sicherheit gegen Durchschmelzen nach unten erwarten. Eine Fortführung der Qualifizierung dieses Konzepts durch Experimente mit nachbeheizten großen Schmelzen ist in Vorbereitung.

1 Einführung

Die Kühlung der Schmelze nach dem COMET-Konzept beruht vor allem auf dem passiven Zutritt des Kühlwassers von unten in die Schmelze, nachdem diese eine Opferschicht erodiert und die darin eingebetteten Kühlkanäle geöffnet hat. Durch die schnelle Verdampfung des Wassers in der Schmelze bricht die Schmelze in ein poröses Bett auf, so daß große innere Oberflächen entstehen, über die die Wärme kurz- und langfristig sicher abgeführt werden kann. Diese sehr wirksame Wärmeabfuhr läßt die Schmelze schnell erstarren, so daß die angrenzenden Strukturen auf sehr niedrigen Temperaturen bleiben.

Als wichtiges Ergebnis im Jahr 1997 war durch Experimente mit Uran-haltigen Schmelzen deren sichere Kühlbarkeit nachgewiesen worden. Damit ist gezeigt worden, daß das COMET-Kühlkonzept im Hinblick auf die Kühlbarkeit von Corium-Schmelzen ebenso leistungsfähig ist wie bei Simulationsschmelzen, wie sie in den FZK-Experimenten auf der Basis von Eisen-/Aluminium-Thermit zur Simulation verschiedenartiger Unfallbedingungen eingesetzt werden. Weiterhin wurde in großskaligen Experimenten mit simulierter Nachwärme, die die Kurz- und Langzeitkühlbarkeit untersuchen, gezeigt, daß auch die ungleichmäßige Erosion des Opferbetons beherrscht wird, und daß auch Schmelzen mit einem repräsentativen Anteil an metallischem Zircaloy sicher gekühlt werden, ohne die Strukturen anzugreifen.

Der Schwerpunkt der Untersuchungen im Berichtszeitraum 1998 lag bei der Kühlung von Schmelzen unter extremen Bedingungen, um damit die Funktionsfähigkeit auch unter eventuell schwierigen EPR-Situationen zu prüfen. Mit diesen Experimenten wurde die Versuchsreihe zum COMET-Konzept abgeschlossen. Alle bisher durchgeführten Untersuchungen wurden in einem zusammenfassenden Bericht dokumentiert und der Industrie im Hinblick auf eine Bewertung des Einsatzes im EPR übergeben.

Nach einem Vorschlag von Siemens scheint eine Vereinfachung des COMET-Konzepts möglich, indem die Wasserzufuhr in die zu kühlende Schmelze statt über Kühlkanäle durch eine wasserführende, poröse Schicht erfolgt. Hierfür wurde eine grundlegende Lösung konzipiert und ihre Funktionsfähigkeit in 5 transienten Experimenten mit Thermitschmelzen überprüft.

In den folgenden Abschnitten wird über die 1998 erzielten Ergebnisse berichtet.

2 COMET-H Experimente mit Nachwärmesimulation

Bei den zwei im Jahre 1998 durchgeführten COMET-H Experimenten wurden die Versuchsbedingungen so gewählt, daß extreme Kühlungsbedingungen im Reaktor simuliert wurden: Bei einer vergrößerten Anfangshöhe der Schmelze von 50 cm wurde gleichzeitig der wirksame Druck des Kühlwassers auf 0,1 bar abgesenkt, gegenüber 0,2 bar in früheren Experimenten. (Der wirksame Druck ist der Überdruck des Flutwassers gegenüber dem statischen Druck der flüssigen Schmelze auf der Höhe der Öffnung der Kühlkanäle unter der Opferschicht). Von beiden Maßnahmen ist zu erwarten, daß die Kühlung erschwert wird. Mit diesen Experimenten soll das Potential der Kühlung unter diesen erschwerten Bedingungen oder eventuell auch seine Grenzen aufgezeigt werden. Die Höhe der hier erzeugten Schmelze liegt um etwa 35 % über der Höhe, die im EPR erwartet wird.

Kühlungs-Experiment COMET-H 3.3

Der Aufbau dieses Experimentes entspricht den früheren Großexperimenten mit induktiver Nachbeheizung der Schmelze. Die Kühlfläche von 0,92 m Durchmesser besteht aus einer Opferschicht aus Glasbeton von 110 mm Höhe (Abb. 1). Darunter befindet sich eine 50 mm hohe Schicht aus vergossenem Aluminiumoxid, in die 112 Kühlkanäle zum Zutritt des Kühlwassers so eingebettet sind, daß sie mit der Oberkante der Schicht abschließen. Das quadratische Raster der Kanäle hat 80 mm Kantenlänge. Die Kühlkanäle haben den in früheren Experimenten erprobten Aufbau: Der Drosselquerschnitt zur Begrenzung des Wasserzutritts ist 5 mm; das obere Ende der Kanäle ist mit einer Kappe verschlossen, die bei Annäherung der heißen Schmelze abbrennt und damit den Strömungsquerschnitt freigibt. Der Aufbau wird getragen von einem Kasten aus Epoxid-

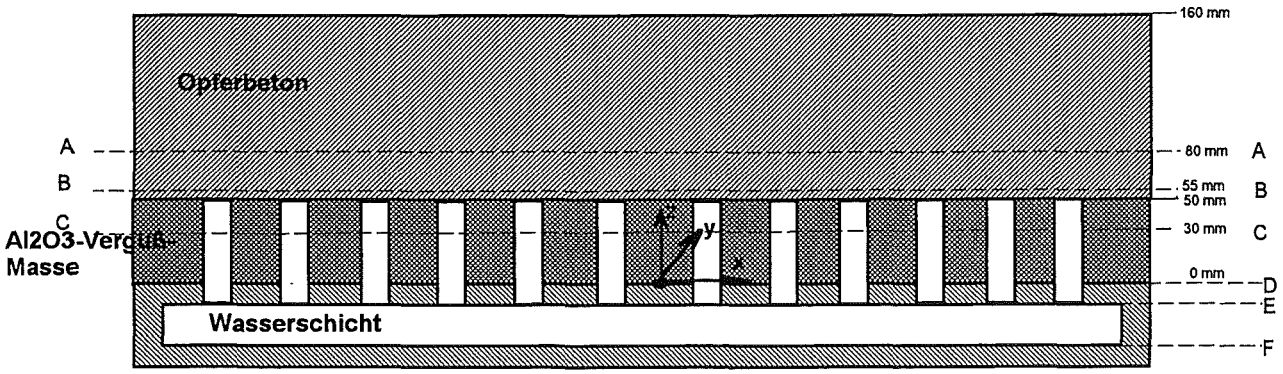

Abb. 1: Schematischer Aufbau des Kühlungseinsatzes mit Opferbeton in Experiment COMET-H 3.3

Kunststoff, der auch die Wasserschicht zur Bespeisung der Kühlkanäle enthält. Die Verwendung von Kunststoff als Strukturmaterial anstatt der im Reaktor vorgesehen Stahlstruktur ist notwendig, damit die induktive Beheizung der Schmelze durch die unter dem Kühlungseinsatz liegende Induktionsspule erfolgen kann. Natürlich ist damit eine wesentlich niedrigere Versagenstemperatur der Tragstruktur von ca. 300 °C verbunden. Dies kommt jedoch nur dann zum Tragen, wenn die Kühlung der Schmelze nicht zuverlässig erreicht wird und die Schmelze weiter nach unten vordringt. Die Bespeisung der Kühleinrichtung erfolgt passiv aus einem hochliegenden Wasserreservoir, das den erforderlichen Überdruck von 0,1 bar vorgibt.

Um die notwendige Höhe der Schmelze von 50 cm zu erreichen, ist eine Schmelzenmasse von 1294 kg erforderlich. Sie wird erzeugt durch Vorlegen von etwa 20 % Metall- und Oxidpartikeln im Tiegel, die durch Betrieb der Induktionsheizung über 10 Minuten vorgeheizt werden. Auf dieses vorgeheizte, teilweise erschmelzendes Material werden die weiteren 80 % der Schmelze aufgegossen, die aus einer Thermitreaktion in einem externen Tiegel erzeugt wurden. Durch Aufschmelzen und Vermischen der beiden Schmelzenfraktionen entsteht die erwünschte Schmelze mit einer Temperatur von etwa 1700 °C und 52 % Metall- und 48 % Oxid-Anteil. Die Höhen der Metall- bzw. Oxidschicht sind 15,7 bzw. 34,3 cm. Der spezifisch schwerere Metallanteil liegt unter der Oxidschmelze und bestimmt daher wie im Reaktorfall die Erosion des Opferbetons.

Die erste Versuchsphase ist durch die trockene Betonerosion der 110 mm hohen Opferschicht gekennzeichnet. Die Leistungseinspeisung in die Schmelze entspricht mit einigen Schwankungen dem angestrebten Nachwärmeniveau von 300 kW. Die Erosion der Betonopferschicht ist jedoch stark ungleichmäßig und konzentriert sich auf je eine Stelle in

den Sektoren SW und NO der Opferschicht. So setzt bereits nach 8:15 min der erste passive Zutritt von Kühlwasser im Süd-West-Sektor der Kühleinrichtung mit einer Zutrittsrate von 65 ml Wasser/s ein. Verantwortlich hierfür ist das Öffnen eines einzelnen Kühlkanals. Nach 10:22 min verdoppelt sich der Wasserzutritt durch Öffnen eines weiteren Stopfens im Nord-Ost-Tiegel auf 120 ml/s, bedingt durch die zweite "heiße Stelle". Zu diesem Zeitpunkt zeigen die Thermoelemente in anderen Bereichen der Betonschicht noch niedrige Temperaturen und damit noch eine Restbetonschicht über den Stopfen von einigen Zentimetern an.

Die bisher wirksam gewordene, lokale Kühlung stoppt zwar das weitere Vordringen an den "heißen Stellen", sie hat aber mit ihrem geringen Wasserstrom noch wenig Einfluß auf den integralen Zustand der Schmelze: Die von oben sichtbare Oxidschmelze ist noch recht dünnflüssig. Sie wird von den aufsteigenden Gasen aus der Betonerosion sowie dem verdampfenden Kühlwasser gut gerührt. Die anfangs schwache Aerosolfreisetzung ist zurückgegangen und der Blick in den Tiegel ist klar.

Der lokale Zutritt des Kühlwassers mit seiner begrenzt wirkenden Kühlung reicht noch nicht aus, um die Nachwärme aus allen Bereichen der Schmelze abzuführen. Im Normalfall würde die Betonerosion in den nicht gekühlten Bereichen weitergehen, bis weitere Stopfen des Kühleinsatzes geöffnet haben und damit die notwendige Kühlung erzeugen, wie es in Experiment COMET-H 2.2 untersucht und nachgewiesen wurde. Bei diesem Experiment jedoch wird zum Zeitpunkt 11:05 min nach Einguß der Schmelze die Induktionsheizung durch ein Kontrollsignal selbsttätig abgeschaltet. Grund hierfür ist eine Störung im Versorgungskreis der Induktionsheizung, die nicht mit dem Zustand der Schmelze in Zusammenhang steht. Dadurch ist eine weitere Nachwärmesimulation nicht mehr möglich, und die Schmelze beginnt an der Schmelzfront des Beton innerhalb kurzer Zeit zu erstarren. Lediglich ein weiterer Kühlkanal wird noch während der Phase der Erstarrung geöffnet.

Die nicht mehr beheizte Schmelze kühlt langsam weiter ab. Der maximale Kühlwasserstrom in die Schmelze beträgt 240 ml/s. Nach 25 min wird die Schmelzenoberfläche durch das von unten zuströmende Wasser überflutet. Sie ist an allen Rändern erstarrt, wogegen sie im Innern zunächst noch überwiegend flüssig ist. Da die Schmelze aber versuchsbedingt in wesentlichen Bereichen eine nur geringe Porosität aufweist, dauerte die Entspei-

cherung der Restwärme aus der Schmelze mehrere Stunden, obwohl ausreichend Wasser auf der überfluteten Schmelze verfügbar ist. Die volle Erstarrung der Schmelze wurde sicher erreicht, ohne daß eine Gefährdung für die Anlage bestand.

Die niedrige Abkühlungsrate, die in der letzten Phase dieses Experiments beobachtet wird, erklärt sich im wesentlichen durch die schlechte Wärmeleitung in der kompakten Oxidphase. Die Wärmeabfuhr ist damit wesentlich geringer als in anderen COMET-Experimenten, in denen die Schmelze durch den ausreichenden Wasserzutritt von unten porös aufgebrochen wurde und einen intensiven Kontakt mit dem Kühlwasser zuließ. Damit macht dieses Experiment den Unterschied der Kühlbarkeit einer kompakten und einer porösen, wasserdurchströmten Schmelze gut sichtbar.

Obwohl das Experiment bezüglich der Kühlvorgänge nach dem COMET-Konzept nicht repräsentativ ist, da die Nachwärmesimulation in einer charakteristischen Phase des Experiments ausgefallen ist, lassen sich zusammenfassend zwei wichtige Aussagen gewinnen: 1. Eine ungleichmäßige Erosion der Opferschicht durch die Schmelze kann auftreten und muß beherrscht werden, wie dies in Versuch COMET-H 2.2 gezeigt wurde. 2. Bei unzureichendem oder fehlendem Wasserzutritt von unten ist die Fragmentierung der Schmelze so gering, daß die Entspeicherung der Schmelze im wesentlich über die wenig wirksame Wärmeleitung in der kompakten Oxidphase erfolgen muß.

Kühlungsexperiment COMET-H 3.4

Das Experiment COMET-H 3.4 ist eine Wiederholung des oben geschilderten Experiments, nachdem die Ursache für die Störung beim Betrieb der Induktionsheizung erkannt und beseitigt wurde. Aufbau des Experiments und Schmelzenmassen sind identisch. Es wurde lediglich die Schmelze vollständig im externen Tiegel durch eine Thermitreaktion erzeugt und in den Versuchstiegel mit 1700 °C eingegossen.

Mit Einguß der Schmelze begann bei kontinuierlicher Beheizung der Schmelze von etwa 300 kW (entsprechend 450 kW/m²) (Abb. 2) die Phase der trockenen Erosion der Betonopferschicht. Diese Erosion, bei Temperaturen der Schmelze um 1500° C, ist anfangs, wie zu erwarten, begleitet von der Freisetzung von Wasserstoff und geringen Aerosol-

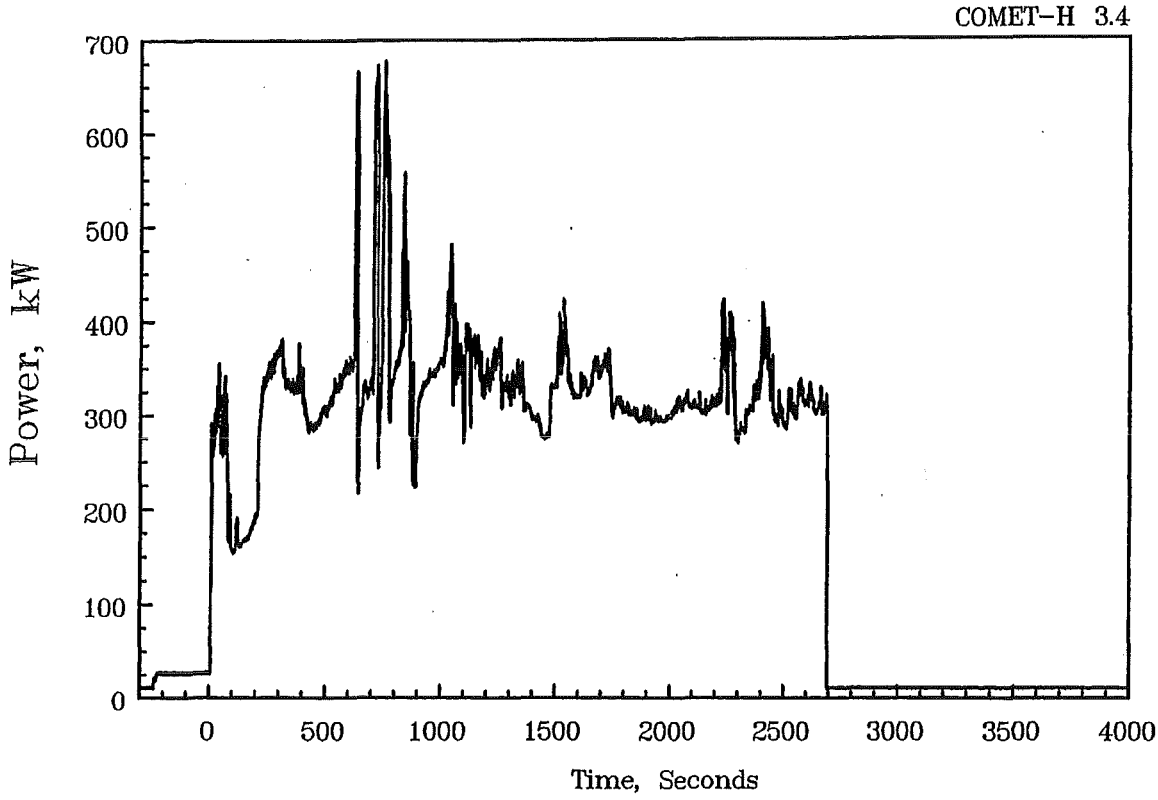

Abb. 2 : COMET-H 3.4, Leistungseinspeisung in die Schmelze (Nachwärme)

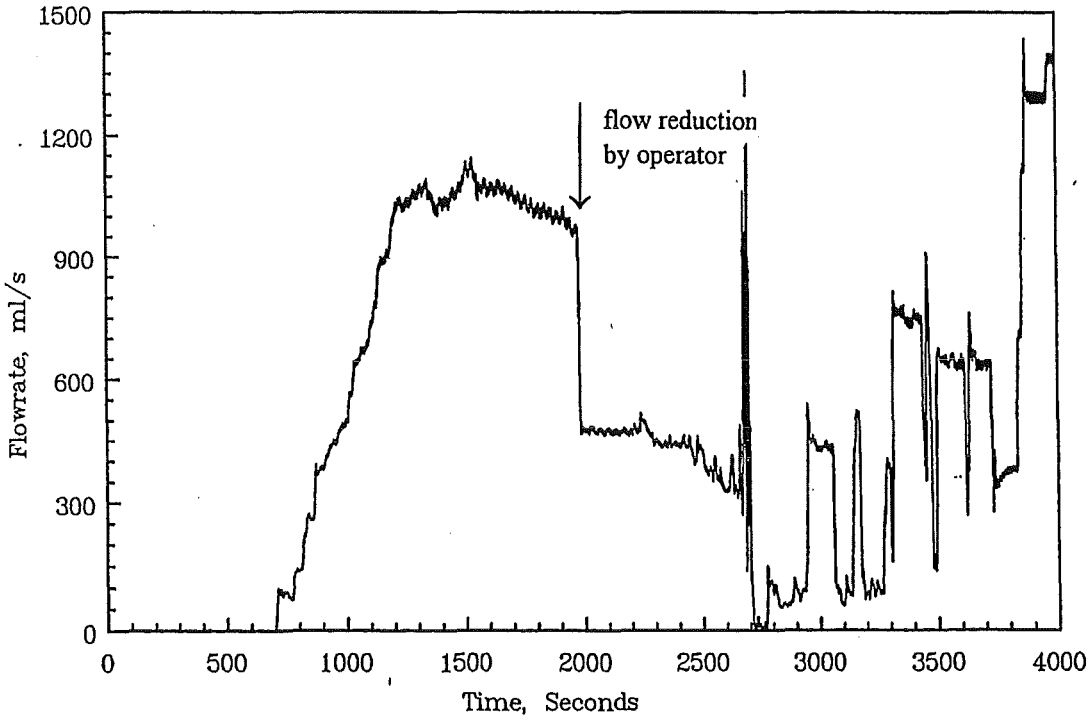

Abb. 3: COMET-H3.4, Wassereinspeisung in die Schmelze

mengen (überwiegend Na_2O und K_2O). Die Betonerosion verläuft jedoch auch in diesem Experiment sehr ungleichmäßig. Sie erfolgt in einigen Bereichen um den Faktor 2 schneller, als bei einem gleichmäßigen Angriff der Opferschicht zu erwarten wäre. Aus nicht bekannten Gründen erhöht sich auch mehrfach im Experiment in deutlicher Weise die Leistungseinkopplung in die Schmelze. Dies deutet vermutlich auf eine Umverteilung/Konzentrierung der Metallschmelze hin, die den Wirkungsgrad der Induktionsheizung erhöht, aber eventuell auch zu einer ungleichmäßigen Verteilung der Metallschmelze und der Leistung führt.

Bereits nach 12 Minuten öffnet ein erster Kühlkanal am nördlichen Rand der Kühlfläche. Der einsetzende Kühlwasserstrom (Abb. 3) beträgt zunächst nur 100 ml/s, natürlich mit sehr begrenzter Kühlwirkung. Durch Öffnen weiterer Stopfen in den Nachbarbereichen steigt der Wasserzustrom bei 16 Minuten auf etwa 0,4 l/s, wodurch der Schmelze etwa 1 MW thermische Leistung entzogen wird und die Bildung erster schwimmender, instabiler Oberflächenkrusten einsetzt. Das Öffnen weiterer Stopfen ab 17 Minuten in allen 4 Quadranten der Kühleinrichtung läßt den Wasserzustrom auf etwa 1 l/s steigen, die maximal abgeführte Leistung durch die zunächst vollständige Verdampfung des Flutwassers beträgt 2,4 MW. Den Verlauf der Kühlung im Vergleich mit der in der Schmelze simulierten Nachwärme zeigt Abb. 4. Man sieht, daß die Wärmeabfuhr wesentlich höher liegt als die eingespeiste Leistung. Daher beginnt in gewohnter Weise die poröse Erstarrung der vom Dampf durchströmten Schmelze.

Nach 22 Minuten ist die Oberfläche der Schmelze von einer stabilen, dunklen Kruste bedeckt, und die Schmelze wird durch das von unten einströmenden Wasser überflutet. Mit der Abkühlung sinkt auch die mit dem Dampf aus der Schmelze abgeführte Leistung. Die Einströmrate des Wassers ändert sich nicht mehr. Sie liegt bei 1 l/s und ist damit wegen des niedrigeren Flutwasserdrucks um 30 bis 50 % niedriger, als sie bei Zuströmdrücken von 0,2 bar gemessen wurde. Der Wasserzufluß wäre aber, gleichmäßige Kühlung der Schmelze vorausgesetzt, mehr als ausreichend, um die Nachwärme abzuführen. Aus Temperaturmessungen in der Schmelze und aus der weiteren Freisetzung einer geringen Wasserstoffmenge ist jedoch zu schließen, daß einige metallische Bereiche der Schmelze noch nicht aus reichend gekühlt sind, da sie offenbar schlechter von Wasser beaufschlagt sind.

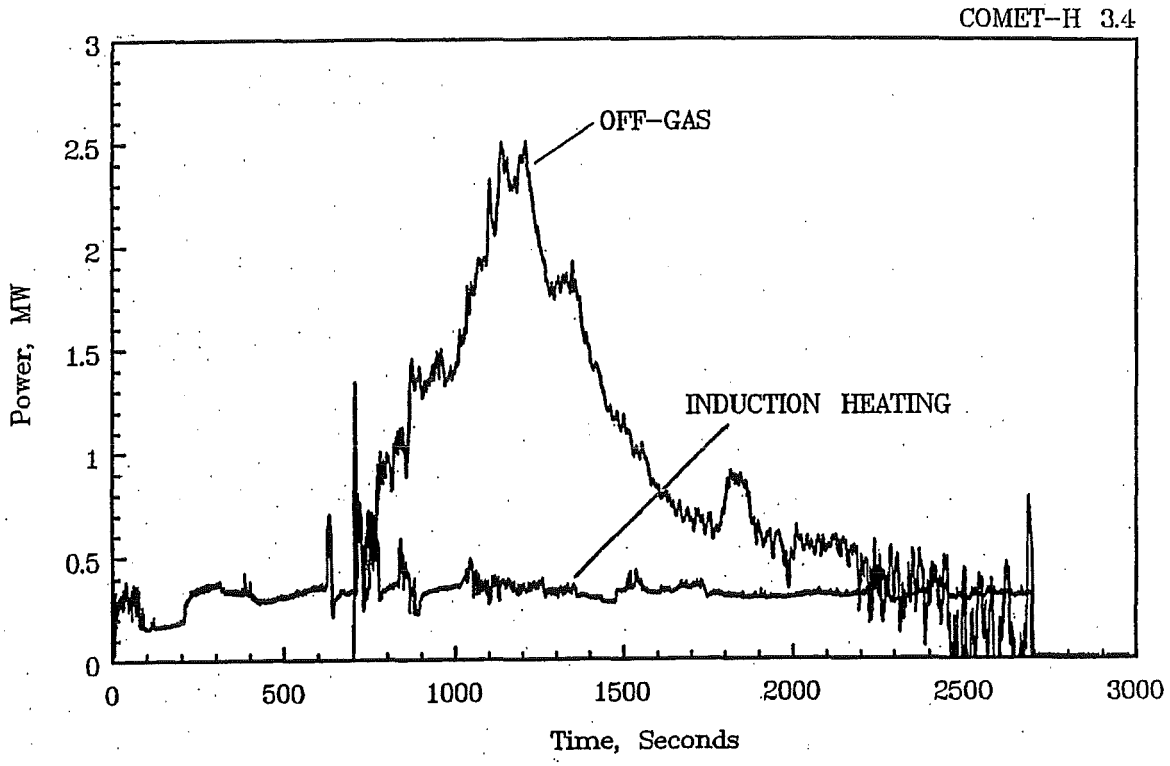

Abb 4: Simulierte Nachwärme (induction heating) im Vergleich mit der durch Verdampfung abgeführten Leistung (off-gas)

So kommt es bei 30 Minuten für die Dauer von 100 s zur Ausbildung eines Unterwasservulkans: Glühende Schmelzepartikel werden, getrieben durch das verdampfende Wasser, aus dem Inneren der Schmelze in das überschichtete Wasser ausgetragen, wo sie schnell erstarren, ohne daß heftige Reaktionen mit dem Wasser entstehen. Dadurch verbessert sich, wie dem kurzzeitigen Anstieg der abgeführten Leistung im Abgasstrom zu entnehmen ist, die Kühlung der Schmelze. Nach Erlöschen des Vulkans wird nach 33 Minuten von Hand die Zufuhr des Kühlwassers auf 50 % reduziert, um eine Überspeisung des Versuchsbehälters zu vermeiden. Trotz weiter steigendem Wasserstand und Überdeckung der (teilerstarrten) Schmelze durch mehr als 50 cm Wasser sind aber, wie aus dem weiteren Verlauf des Experiments folgt, noch Teilbereiche der Schmelze im flüssigen Zustand. So tritt unerwartet zum Zeitpunkt 45 Minuten (2700 s) im zentralen Bereich der kreisförmigen Kühlfläche Schmelze durch zwei Kühlkanäle in die wasserführende Schicht der Kühleinrichtung.

Die durchgetreten Schmelze ist metallisch mit einer Masse von 2 mal 8 kg, und verteilt sich in 2 der 4 wasserführenden Sektoren der Kühleinrichtung. Dadurch wird automatisch die Beheizung der Schmelze unterbrochen, die bis zu diesem Zeitpunkt in Betrieb war. Durch die schnelle Verdampfung des Wassers in dieser Schicht strömt Dampf rückwärts

in die Zulaufleitungen aus Plastik, die daraufhin versagen. Durch zusätzliche Wasserzufuhr wurde die Schmelze schließlich vollständig gekühlt. Der Kühleinsatz aus Epoxid wird durch diesen Vorgang beschädigt. Die Induktionsspule mit dem zugehörigen Aufbau bleibt aber vollständig intakt.

Die Abbildungen 5 zeigen u. a. den gemessenen Verlauf der Wasserstofffreisetzung während des Versuchs. Man erkennt zunächst im ersten Wasserstoffpeak die Erosion des Opferbetons. Der zweite Peak entsteht durch die Einspeisung des Kühlwassers in die Schmelze, die so lange Wasserstoff erzeugt, wie die Metallschmelze noch ausreichend heiß ist und durch das Wasser oxidiert werden kann. Diese Reaktion kommt unter normalen Kühlungsbedingungen innerhalb kurzer Zeit zum erliegen, wenn das Metall erstarrt ist. So folgt aus Abb. 5, daß mit der Abnahme der Wasserstofffreisetzung nach 1500 s das Metall weitgehend erstarrt ist, daß aber wegen der verbleibenden niedrigen H_2 - Freisetzung auch nach 2000 s einige Bereiche der Metallschmelze nicht voll erstarrt und unzureichend gekühlt sind, was schließlich, wie oben beschrieben, den Durchtritt von Schmelze auslöst.

Die Inspektion der erstarrten, geschnittenen Schmelze, die in Abb. 6 wiedergegeben ist, wie auch der Oberfläche des Kühleinsatzes ergeben den folgenden Aufschluß über den Kühlvorgang:

- Die weitaus größte Teil der Schmelze ist porös erstarrt und daher gut kühlbar.
- Der nicht erstarrte Anteil der Schmelze, der in die untere Wasserschicht eingetreten ist, entspricht mit 16 kg 1,3 % der Gesamtschmelze. Dieser Anteil ist metallisch und aus dem zentralen Bereich der Schmelze abgelaufen. Demzufolge weist die geschnittene Schmelze einen geringeren Metallanteil im Zentralbereich auf.
- Die schlechte Kühlung dieses Anteils der Schmelze resultiert aus der großen Schmelzenhöhe und dem gleichzeitig niedrigen Zulaufdruck des Kühlwassers. Trotz Öffnen der Kühlkanäle bei Annäherung der Schmelze haben sich in einigen Fällen keine stabilen Strömungskanäle in der Schmelze ausgebildet. Statt dessen ist Schmelze in die betreffenden Kühlkanäle eingedrungen und hat diese blockiert. Dies führt dazu, daß trotz integral ausreichender Wasserzufuhr, vorwiegend über die Außenbereiche der Schmelze, ein im Zentrum befindlicher, linsenförmiger Metallbereich keinen ausreichenden Wasserkontakt hatte und so ungekühlt blieb. Diese metallische Linse, weiterhin beheizt durch die simulierte Nachwärme, liegt auf der keramischen Al_2O_3-Schicht und dringt schließlich durch zwei wiederaufschmelzende Kühlkanäle.

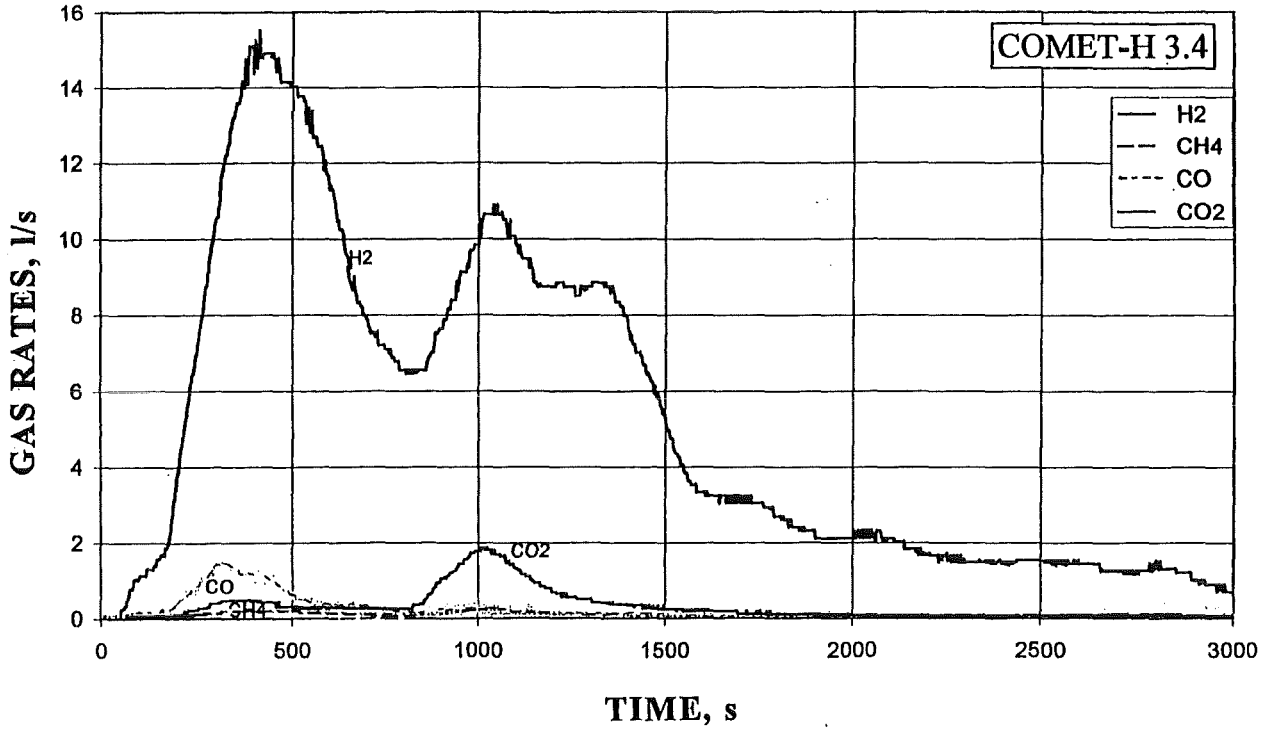

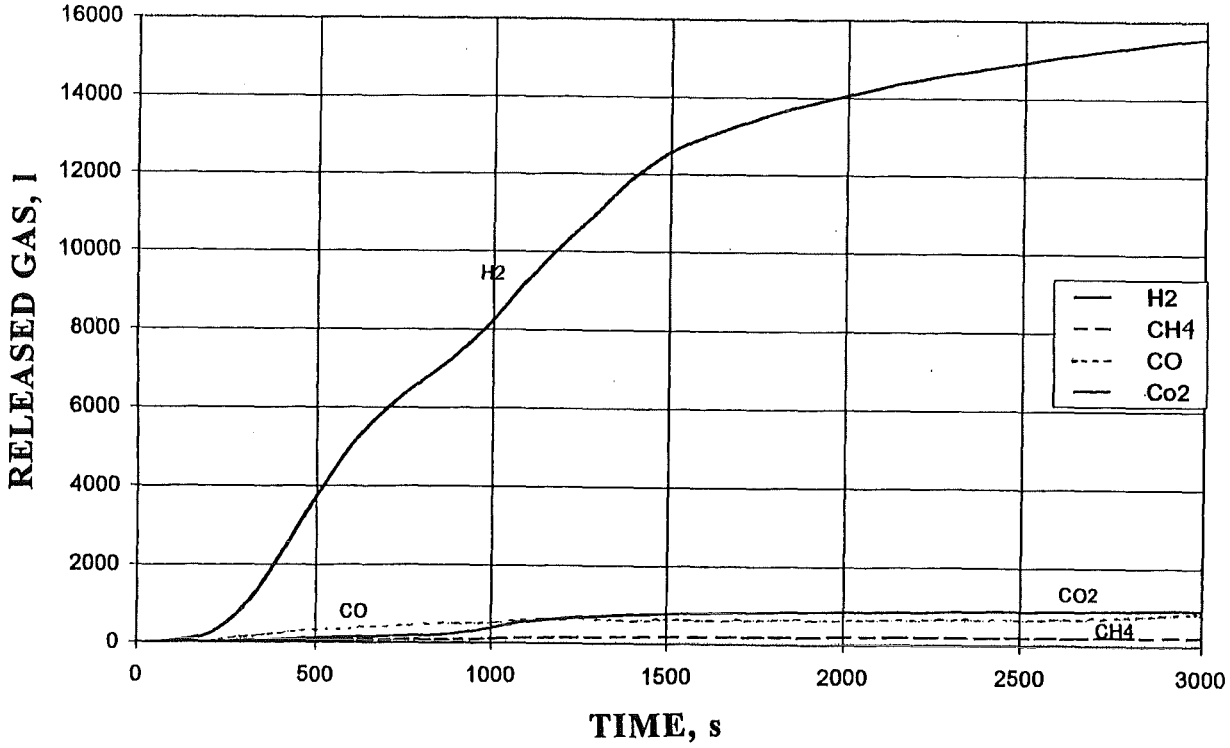

Abb. 5: Freisetzung von Wasserstoff und weiterer Gase in Experiment COMET-H 3.4.
oben: Freisetzungsraten, bezogen auf Normzustand der Gase
unten: integrierte Freisetzung

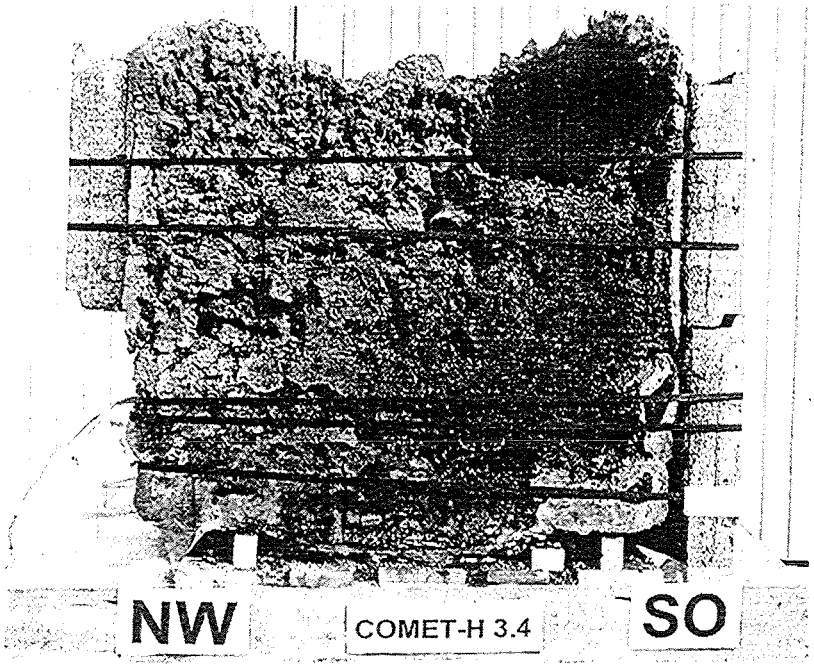

Abb. 6: Schnitt durch die porös erstarrte Schmelze in COMET-H 3.4

- Die beobachtete Bildung von Vulkanen, wodurch noch flüssige Schmelze nach oben ausgetragen wird und dann im Wasser in kühlbarer Form erstarrt, trägt zur Verbesserung der Kühlung bei. Jedoch ist wie in vorliegendem Experiment nicht sichergestellt, daß dieser Vorgang eine ausreichende Kühlung erzeugt.

In diesem Experiment wurden also in der Kombination hohe Schmelze und niedriger Wasserdruck die Grenzen des COMET-Kühlkonzepts überschritten, weil trotz integral ausreichender Wasserzufuhr Teilbereiche der Schmelze ungekühlt blieben, in denen die Fragmentierung unzureichend war und ein zu geringer Wasserkontakt existierte. Es sei hier darauf hingewiesen, daß auch im Experiment COMET-H 3.2, das mit demselben niedrigen Kühlwasserdruck, aber nicht ganz so hoher Schmelze durchgeführt wurde, geringe Mengen von Schmelze (Mengen bis 100 g) durch die geöffneten Kühlkanäle durchgetreten sind, ohne allerdings die Kühlung zu beeinträchtigen. Durchtritt von Schmelze bzw. Blockade der Kühlkanäle sind also die Mechanismen, die bei Überlastung der COMET-Kühleinrichtung auftreten. Durch Verwendung eines ausreichenden Flutwasserdrucks läßt sich aber eine sichere Funktion erreichen.

Das hier beschriebene COMET-Experiment weist einige Besonderheiten auf, die die Langzeitkühlung der Schmelze gegenüber dem Realfall erschweren und die den ungün-

stigen Ausgang des Experiments mit begründet haben. Dies sind die Verwendung von Strukturen aus Kunststoff an Stelle von Stahl und die Einbringung der Nachwärme nur in das Metall und damit verbunden ein höherer Wärmestrom nach unten. Trotz dieser Nachteile erscheint es jedoch im Hinblick auf einen sicheren Betrieb der Kühleinrichtung sinnvoll, bei höheren Schmelzen Flutwasserdrücke > 0,1 bar bereitzustellen.

3 Bewertung der Experimente zum COMET-Konzept

Das COMET-Konzept wurde in den vergangenen Jahren durch verschiedenartige Experimente in Hinblick auf die grundlegenden Fragmentierungs- und Kühlvorgänge sowie auch auf seine reaktorbezogene Verwendung sehr detailliert untersucht, so daß weitere Experimente zur Zeit nicht für notwendig erachtet werden. Die Zielsetzung der Experimente läßt sich in folgender Weise zusammenfassen:

- COMET-P-Experimente: Fragmentierung und Kühlung von heißen Kunststoff- und Metallschmelzen. Mit transparenten Schmelzen von etwa 200 °C wurde die Kopplung von Verdampfung des zutretenden Wassers und das Ausbrechen der Schmelze sichtbar gemacht.
- COMET-T-Experimente: Transiente Experimente mit Thermitschmelzen von ca. 1800 °C Anfangstemperatur mit den Zielsetzungen: Funktionsfähigkeit, Optimierung der Schmelzstopfen, Auswirkungen eventueller Dampfexplosion, Einfluß des Flutwasserdrucks, Kühlbarkeit rein oxidischer Schmelzen, Einfluß metallischen Zircaloys, Kühlbarkeit nachlaufender Restschmelzen.
- COMET-U-Experimente: Transiente Experimente mit einer hoch UO_2-haltigen Schmelze im Hinblick auf Kühlbarkeit und Übertragung von Experimenten mit Thermitschmelzen.
- COMET-H-Experimente: Experimente mit Simulation der Nachwärme zur Kurz- und Langzeitkühlung der Schmelze in einem 1-d Ausschnitt aus der realen Geometrie unter Einsatz von Thermitschmelzen bis 1300 kg. Zielsetzung: Quantifizierung des Kühlvorgans und der H_2-Freisetzung, kühlbare Höhe, ungleichmäßige Erosion der Opferschicht, Einfluß von Zr-Metall, Einfluß niedrigen Flutwasserdrucks

In der folgenden Tabelle 1 sind die durchgeführten COMET-H - Experimente zusammengestellt.

Tabelle 1 COMET-H Experimente mit nachbeheizten Schmelzen (1995 - 98)

Versuch	Zielsetzung	Ergebnis
COMET-H 0.1 28. 1. 95	Inbetriebnahmetest, 300 kg Schmelze	erfolgreich mit kurzzeitiger Induktionsbeheizung
COMET-H 1.1 8. 7. 95	reguläre Geometrie, 500 kg, H = 19 cm	Kühlung erreicht, Induktions-Heizung noch nicht ausreichend stabil
COMET-H 1.2 18. 11. 95	reguläre Geometrie, 650 kg, H = 25 cm	sichere Kühlung, Langzeitkühlung nachgewiesen
COMET-H 1.3 20. 4. 96	reguläre Geometrie, 800 kg, H = 32 cm	sichere Kurz- und Langzeitkühlung bei kontinuierlicher Beheizung erreicht
COMET-H 2.1 12. 10. 96	Einfluß lokaler Erosion 650 kg, H = 26cm	Eindringen geringer Schmelzemengen in untere Wasserschicht
COMET-H 2.2 8. 3. 97	Einfluß lokaler Erosion 650 kg, H = 26 cm	keramische Unterschicht sichert Kühlbarkeit
COMET-H 3.1 28. 6. 97	Einfluß von Zr-Metall, 885 kg, H = 34 cm	zunächst vollständige Zr Oxidation während Betonerosion, danach Wasserzutritt mit vollständiger Kühlung
COMET-H 3.2 29. 11. 97	Einfluß von Zr-Metall, reduzierter Wasserdruck mit veränderten Stopfen	Flutwassermenge ausreichend, Eindringen geringer Metallmengen in untere Wasserschicht
COMET-H 3.3 9. 5. 98	extreme EPR Bedingungen mit 1300 kg (niedriger Wasserdruck, hohe Schmelze)	nach Beginn der Kühlung Ausfall der Nachwärmesimulation, Experiment nicht gültig bezüglich Kühlvorgängen
COMET-H 3.4 11. 7. 98	Wiederholung von COMET-H-3.3	stark lokale Erosion der Opferschicht, trotz ausreichender Kühlwasserrate nach 45 Min. Eindringen von ca. 16 kg noch nicht erstarrter Metallschmelze in Wasserschicht

Wegen einer ausführlichen Darstellung der experimentellen Ergebnisse wird auf den vorgelegten Bericht verwiesen [5] . Es wird die folgende abschließende Bewertung gegeben:

Das COMET-Kühlkonzept wird charakterisiert durch eine schnelle und vollständige Erstarrung der Schmelze, die beim Einsatz im EPR in einem Zeitraum von 30 bis 60 Minuten abgeschlossen sein dürfte. Danach liegt die Schmelze als ein porös erstarrtes, mit Wasser geflutete Schicht niedriger Temperatur vor, aus der die Nachwärme wegen der großen inneren Oberfläche über stationäre Siedevorgänge sicher abgeführt wird. Damit bleibt der Angriff der Schmelze auf einen klar definierten örtlichen und zeitlichen Bereich des Opferbetons beschränkt. Die Temperaturen der Tragstrukturen der Kühleinrichtung und ihrer Umgebung bleiben kalt, so daß hier keine besonderen Materialbeanspruchungen auftreten.

Durch die schnelle Entspeicherung der Schmelze entsteht eine hohe Freisetzung von Dampf. Der daraus folgende, kurzzeitige Maximaldruck im Sicherheitsbehälter, der für einen angenommenen Kernschmelzunfall mit der Annahme ermittelt wurde, daß die Gesamte Energie der Schmelze in nur 15 Minuten entspeichert wird, beträgt etwa 6,5 bar. Dieser Druck nimmt durch die Kondensation des Wasserdampfs an den kalten Strukturen des Sicherheitsbehälters schnell ab. Druckdifferenzen zwischen Ausbreitungsraum und Sicherheitsbehälter sind trotz der hohen Dampfströmung so klein, daß sie den Kühlvorgang nicht behindern.

Für das Kühlkonzept wurde gezeigt, daß Dampfexplosionen und die Anwesenheit von Zirconium-Metall in der Schmelze kein Problem darstellen. Die Freisetzungen von Wasserstoff und Aerosolen enden kurz nach Einsetzen der Kühlung. Die freigesetzten Wasserstoffmengen entsprechen etwa 40 bis 70 % der Molzahl an Wasser, das im Opferbeton vorhanden ist.

Für den sicheren Betrieb der Kühleinrichtung wird nach den durchgeführten Experimenten ein wirksamer Wasserdruck von 0,2 bar oder höher vorgeschlagen. Unter den Bedingungen kontinuierlicher Nachwärmesimulation bei niedrigeren Wasserdrücken (0,1 bar) hat sich gezeigt, daß für hohe Schmelzen eventuell Teilbereiche der Schmelze unzureichend gekühlt bleiben, die dann die Schmelzstopfen durchdringen und in die untere Wasserschicht einlaufen können.

Für 0,2 bar Wirkdruck des Wassers wurde auch gezeigt, daß lokal ungleichmäßige oder höhere Erosionen der Opferschicht und das daraus folgende Einsetzen einer zunächst nur lokalen Kühlung durch die bessere Beständigkeit der keramischen Unterschicht beherrscht werden. Oberflächenkrusten, die sich unter diesen Bedingungen bilden, werden aufgebrochen, bis die notwendige Fragmentierung und Kühlung der Schmelze erreicht sind.

In Experimenten wurde auch das Auflaufen einer spät abstürzenden Schmelze auf die bereits erstarrte erste Schmelze während des Flutvorgangs untersucht. Die Kühlung der ersten Schmelze bleibt voll erhalten, und die nachlaufenden Schmelze erstarrt in sehr gut kühlbarer Form. Diese Experimente können bei Bedarf erweitert werden auf solche Bedingungen, bei denen die erste Schmelze bereits von Wasser überflutet ist.

Die Frage nach der Auswirkung eines frühen, massiven Wasserzutritts auf die Oberfläche der Schmelze vor Einsetzen des Wasserzutritts von unten kann jedoch nicht beantwortet werden. Im Hinblick auf weitere Komplikationen, die sich wegen möglicher Dampfexplosionen bei einem solchen Szenario ergeben würden, scheint ein Ausschluß eines solchen unkontrollierten Wasserzutritts von oben notwendig.

Auf der Basis dieser Ergebnisse erscheint damit heute eine zuverlässige Auslegung und Funktion der COMET-Kühleinrichtung im EPR möglich.

4 Modifikation der COMET-Kühlung: CometPC

Angeregt durch die positiven Resultate der Kühlbarkeit sekundärer Schmelzen hat Siemens vorgeschlagen, daß Stopfenfeld in der COMET-Anordnug durch eine poröse, wasserführende Schüttung zu ersetzen. Den schematischen Aufbau zeigt Abbildung 7.

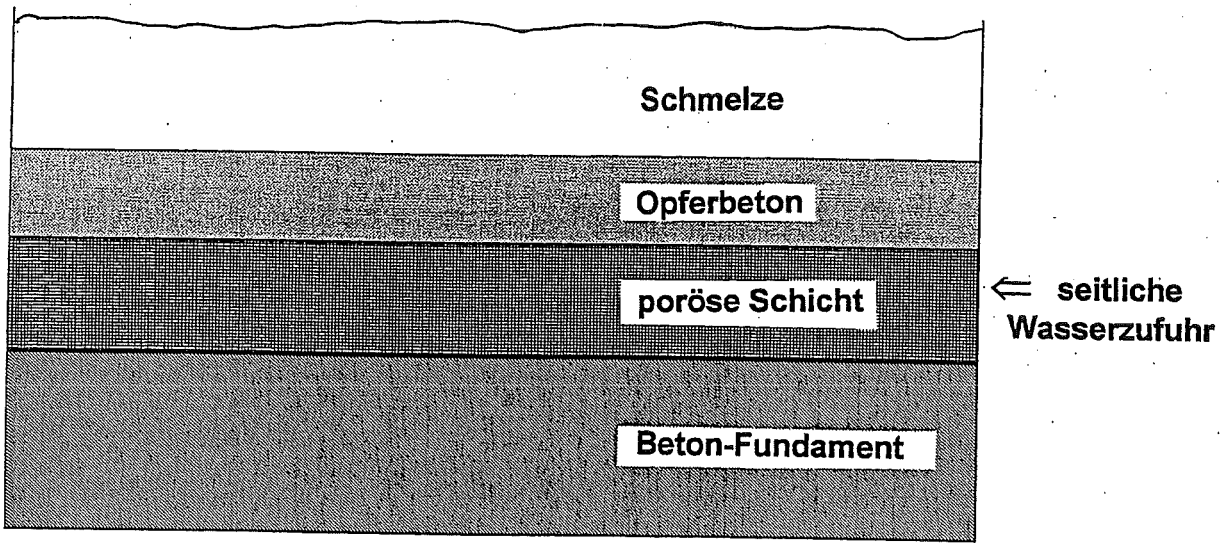

Abb. 7: Grundprinzip des modifizierten COMET-Konzepts mit Verwendung einer wasserführenden, porösen Schicht

Nach weiteren Überlegungen von FZK und ersten orientierenden Experimenten muß die poröse Schicht die folgenden Eigenschaften haben:

- hohe Durchlässigkeit für Wasser in Querrichtung zur gleichmäßigen Wasserversorgung unter der gesamten Kühlfläche
- Begrenzung des Wasserdurchtritts nach oben auf etwa 1 - 2 l / m² s
- ausreichende Stabilität gegen mechanische Lasten und gegen das Eindringen von Schmelze

Eine solche Schicht kann aus 2-lagigem, porösem Beton aufgebaut werden (Abb. 8):

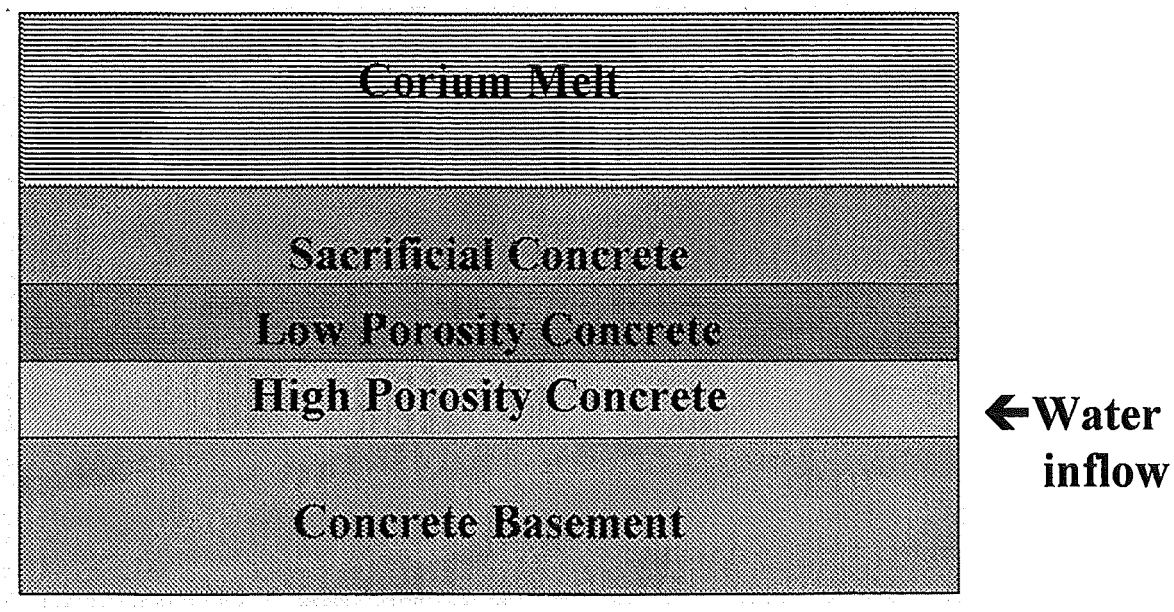

Abb. 8: CometPC-Konzept mit wasserführendem porösem Beton

Die untere Lage hat eine grob poröse Struktur und daher die notwendige hohe Durchlässigkeit für die horizontale Verteilung des Flutwassers. Die darauf aufgegossene Schicht aus Beton der niedrigen Porosität mit einer Schichthöhe von etwa 100 mm begrenzt den Wasserstrom nach oben. Ihre Druckfestigkeit beträgt etwa 15 N/mm^2, liegt also bei 50 % von Normalbeton und ist damit voll ausreichend zur Abtragung mechanischer Lasten. Darüber befindet sich in gewohnter Weise eine Schicht Opferbeton zur Konditionierung und Förderung der Ausbreitung der Schmelze vor Wasserzutritt.

Vorteil dieser Anordnung mit der Bezeichnung **CometPC** (Coolability of melt by Porous Concrete) ist der extrem einfache Aufbau. Die sichere Funktion muß unter Optimierung der Eigenschaften der porösen Schichten für die verschiedenen Anforderungsfälle durch Experimente untersucht werden. Dabei kann in vielen Aspekten von den Ergebnissen der bisherigen Experimente Gebrauch gemacht werden. Es erscheint jedoch wahrscheinlich, daß dieses Konzept eine erhöhte Sicherheit gegen den Durchtritt von Schmelze nach unten aufweist.

Ergebnisse aus transienten Experimenten zu CometPC

Für das CometPC - Konzept wurden bisher 5 transiente Experimente durchgeführt, die in der COMET-T Versuchsanlage mit Thermitschmelzen von 54 bzw. 180 kg bei Anfangstemperaturen der Schmelze um 1800 °C durchgeführt wurden (Tabelle 2). Für die Experimente wurden verschiedene poröse Schichten eingesetzt, zunächst eine Schichtung aus Sand und Kies im ersten Experiment, danach dann Schichten aus porösem Beton, der nach verschiedenen Methoden hergestellt wurde. In allen Experimenten war angestrebt, die Durchlässigkeit der porösen Schicht so klein zu halten, daß allein durch sie der Wasserzutritt in die Schmelze auf etwa 1 - 2 l/m^2 s begrenzt wird. Dies erreicht man, wie abschätzende Rechnungen zeigen, nur durch Verwendung feinporöser Schüttungen. Übliche Kiesbettschüttungen mit ihrer Porosität von etwa 50 % erlauben demgegenüber einen viel zu hohen Wasserzutritt.

Beim ersten Experiment CometPC-T1 mit einer mechanisch nicht gebundenen Sand/ Kies-Schüttung zeigte sich, daß die Fragmentierung und Kühlung der Schmelze zwar schnell erfolgt, daß sich aber die feine Schüttung bei Anwesenheit von Wasser teilweise in die grobere Schüttung verlagert und auch Schmelze in die Sandschüttung in Form von

Tabelle 2: Versuchsparameter der transienten Experimente CometPC-T1 bis T5

	CometPC - T1	**CometPC - T2**	**CometPC - T3**	**CometPC - T4**	**CometPC - T5**
wirksamer Wasservordruck	0,1 bar	0,1 bar	0.1 bar	0.1 bar	0.0 bar
Schmelzenmasse	54 kg	180 kg	180 kg	180 kg	180 kg
Schmelzbadhöhe	31 cm	45 cm	45 cm	45 cm	45 cm
Tiegeldurchmesser	23 cm	35 cm	35 cm	35 cm	35 cm
Anfangstemperatur der Schmelze	ca. 1800°C	ca. 1800°C	ca. 1800°C	ca. 1800°C	ca. 1800°C
Höhe der Betonopferschicht	25 mm	30 mm	30 mm	30 mm	30 mm
pöröse Schicht	Sand/Kies-Schüttung	por. Beton, (handgefertigt)	por. Beton, (handgefertigt)	por. Beton (ausZwangsmischer)	por. Beton (ausZwangsmischer)

Zungen vordringen kann. Dies wurde zwar bei diesem ersten Experiment durch ungleichmäßiges Vordringen der Metallschmelze begünstigt, eine Stabilisierung der porösen Schüttung erscheint aber notwendig.

Die Stabilisierung gelingt durch die Verwendung porösen, offenporigen Betons. Poröser Beton wird dadurch erzeugt, daß die Sieblinie des verwendeten Sand- Kies- Gemisches gezielt verändert wird. Der Feinanteil wird so weit verringert wird, daß nicht mehr alle Poren zwischen dem groben Kies gefüllt werden. Der Beton wird mit nur wenig Anmachwasser homogen vermischt und so als Schicht aufgebracht, daß er sich nicht entmischt und sich der Feinanteil nicht nach unten verlagert. Eine auf diese Weise hergestellte Betonschicht wurde in den Experimenten CometPC-T2 bis T5 verwendet. Die Mischung der porösen Betonschicht erfolgte zunächst von Hand für die Experimente CometPC-T2 und T3. Für die Experimente CometPC-T4 und T5 wurde die Herstellung des Beton mit einem Zwangsmischer vorgenommen. Dadurch wurde eine sehr gute Reproduzierbarkeit der

Betoneigenschaften erreicht, insbesondere bezüglich des Durchlaßwiderstands für das Kühlwasser.

Der Versuchsaufbau für diese Experimente ist in Abbildung 9 wiedergegeben. Man erkennt oberhalb der porösen Betonschicht die Opferschicht von 30 mm Höhe, die in gewohnter Weise aus Glasbeton gefertigt ist. Der lichte Durchmesser des zylindrischen Versuchsbehälters ist auf 350 mm vergrößert, um den Einfluß der Wände zu vermindern. Die Anfangshöhe der Schmelze wurde mit 45 cm so gewählt, daß sie der Situation im EPR entspricht. Der wirksame Druck des Kühlwassers beträgt in der Mehrzahl der Experimente 0,1 bar. Dieser Druck erweist sich bisher als ausreichend, um eine sichere Kühlung zu erreichen. In CometPC-T5 wurde zur Überprüfung der Kühlungsreserven der Druck auf 0 bar abgesenkt.

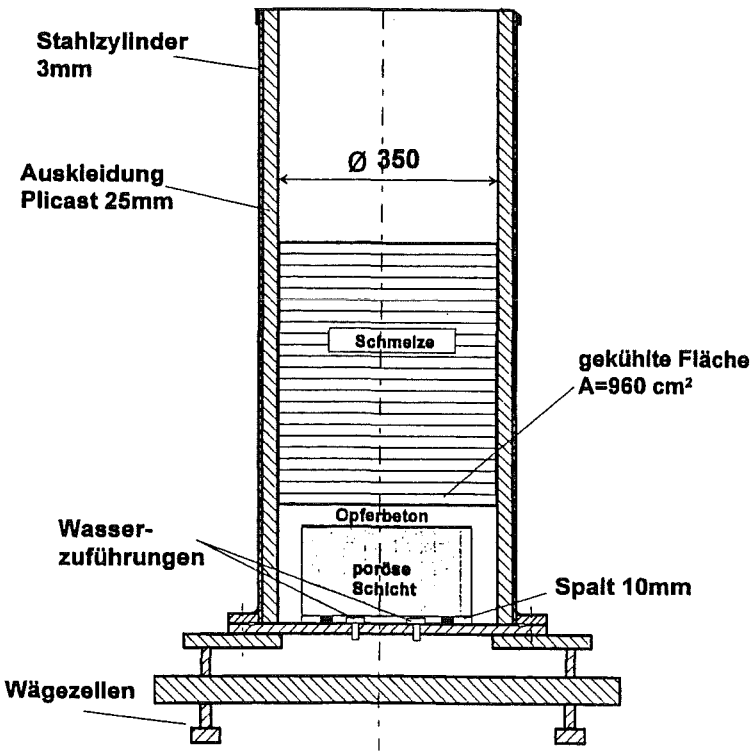

Abb. 9 Versuchsaufbau CometPC-T mit wasserführender poröser Betonschicht

Alle Experimente zeigen in ähnlicher Weise wie die früheren Experimenten mit Wasserzutritt durch die Schmelzstopfen eine gute Kühlbarkeit der Schmelze. Nach Erzeugung der Schmelze durch die Thermitreaktion im Tiegel erfolgt zunächst über einen Zeitraum von etwa 2 Minuten die trockene Erosion der Betonopferschicht. Dann beginnt der passive Zutritt des Kühlwassers aus der porösen Betonschicht, der nach einer kurzen Anlaufphase einen stationären Wert von etwa 300 ml/s erreicht, wie Abb. 10 für CometPC-T4 zeigt. Die Kühlwasserzufuhr entspricht damit den Werten früherer COMET-T Experimente. Damit setzt die schnelle Kühlung ein, die zur porösen Erstarrung der Schmelze führt. Die Überflutung der Schmelzenoberfläche beginnt nach etwa 4 Minuten. Um ein Überlaufen des Versuchsbehälters zu vermeiden, wurde die Wasserzufuhr jeweils nach 950 s

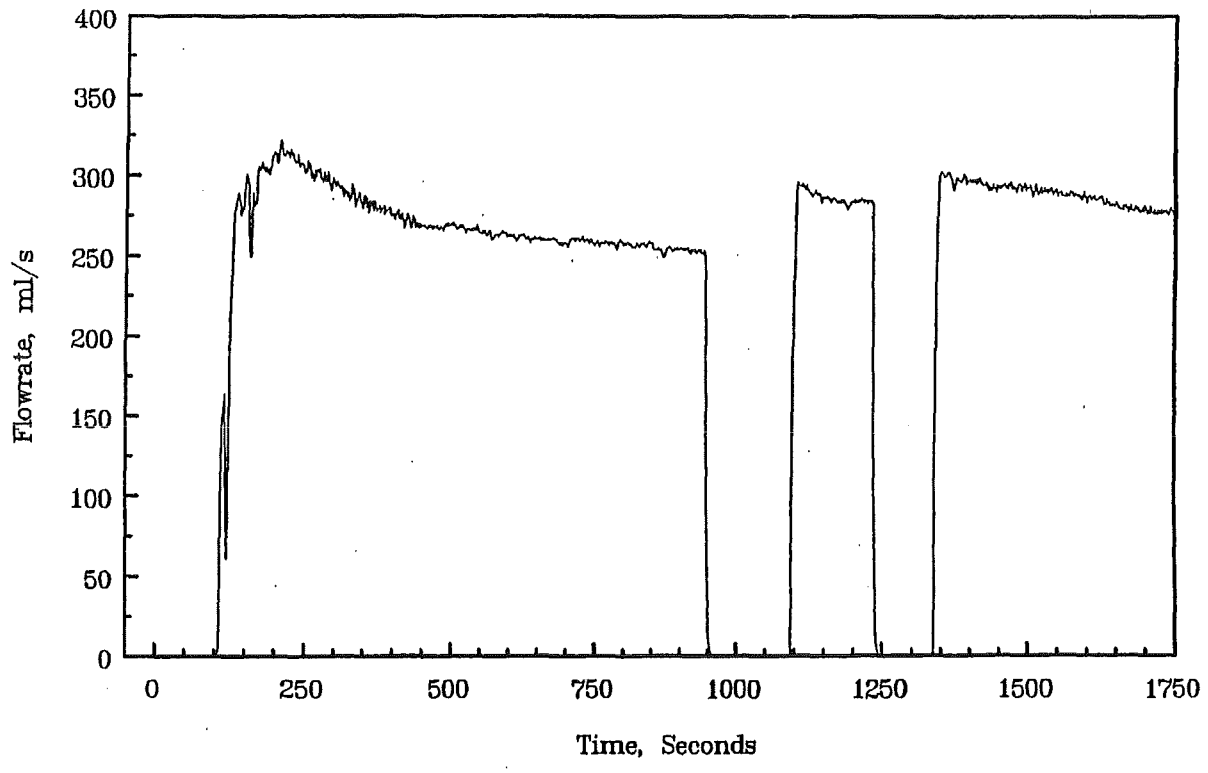

Abb 10: Passiver Kühlwasserzutritt durch die poröse Betonschicht in CometPC-T4

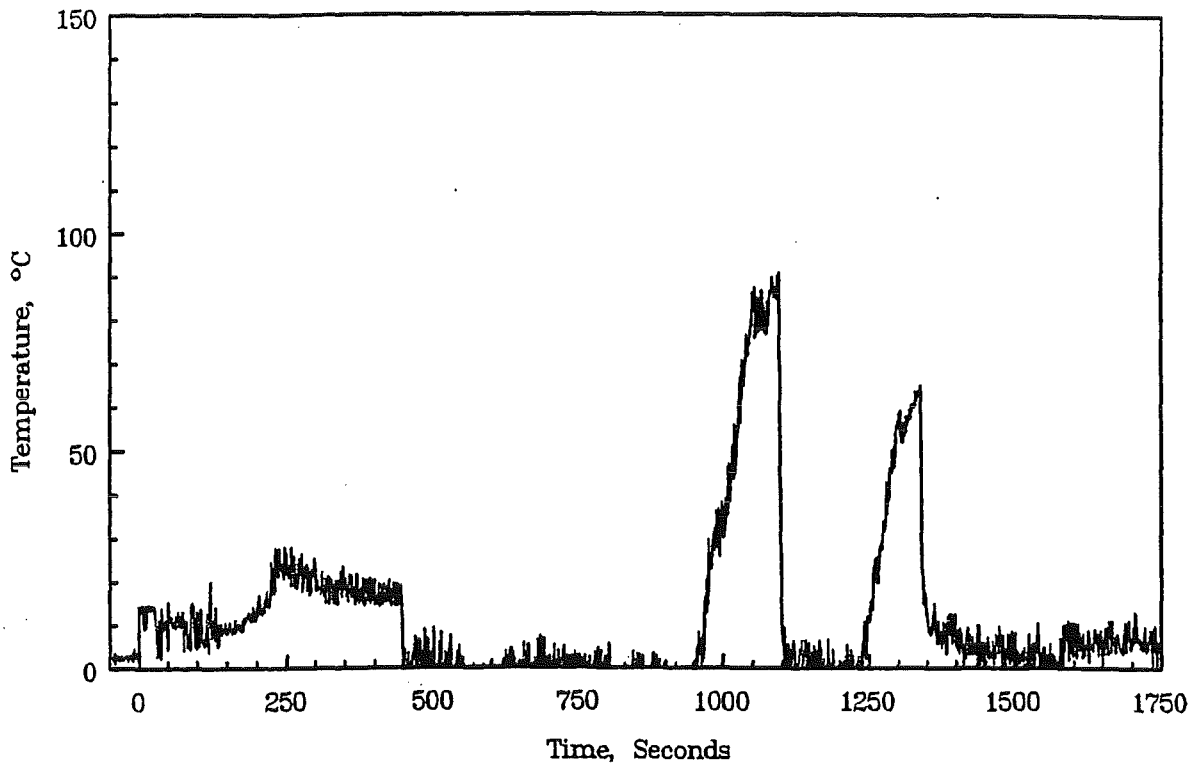

Abb 11: Temperaturverlauf (PT 1) 2 mm unter der Oberfläche der porösen Betonschicht in CometPC-T4

und 1250 s unterbrochen. Zu diesem Zeitpunkt ist die Schmelze bereits vollständig erstarrt.

Den Temperaturverlauf direkt unter der Oberfläche der porösen Betonschicht zeigt Abbildung 11. Die Temperatur bleibt auch bei Annäherung der Schmelze nahe Raumtemperatur, da, wie die Nachuntersuchungen an der erstarrten Schmelze zeigen, die poröse Schicht wegen der sehr wirksamen Wasserkühlung praktisch nicht von der heißen Schmelze angegriffen wird. Lediglich bei Unterbrechung der Kühlwasserzufuhr steigt die gemessene Temperatur erwartungsgemäß bis maximal Siedetemperatur des Wassers bei 1000 s bzw. 1300 s. Damit erweist sich die poröse Betonschicht als mechanisch und thermisch sehr stabile Barriere, die zudem wegen ihrer großen Höhe ein erhebliches Sicherheitspotential darstellt.

Die Nachuntersuchungen zeigen, daß zwischen poröser Betonschicht und der erstarrten Metallschmelze "Inseln" nicht erschmolzenen Opferbetons existieren können, die wenige mm hoch sind. Dieser Restbeton behindert jedoch weder den Wasseraustritt aus der porösen Betonschicht noch die Kühlung der Schmelze, da offenbar genügend andere Strömungswege vorhanden sind.

In dem Experimente CometPC-T5 ereignete sich bei Beginn des Wasserzutritts eine schwache Wechselwirkung zwischen heißer Schmelze und Kühlwasser, die etwa 30 % der Schmelze aus dem Tiegel auswarf. Solche Ereignisse könnten wegen des andersartigen, großflächigen Wasserzutritts häufiger auftreten als bei dem ursprünglichen COMET-Konzept. Jedoch erscheint auch hier eine Gefährdung der Kühleinrichtung wegen der geringen verfügbaren Wassermengen, die in einem reaktionsfähigen Zustand sind, ausgeschlossen. Durch diese Wechselwirkung könnte auch ein schwacher Angriff der porösen Betonschicht verursacht sein, da maximal 5 mm der porösen Betonschicht thermisch angegriffen wurden, natürlich ohne diese Schicht von 150 mm Höhe zu gefährden.

Die Porosität der erstarrten Oxidschmelze wurde zu etwa 50 % ermittelt. Demgegenüber ist die Porosität in der Metallschmelze mit 10 bis 20 % zwar gering, aber offenbar ausreichend, um einen genügenden Wasserzufluß und die schnelle Kühlung in diesen Experimenten zu erreichen.

Ausblick für CometPC

Aus der Bewertung der bisher durchgeführten transienten Experimente zur Funktionsfähigkeit des modifizierten Kühlungskonzepts CometPC folgt, daß diese Variante ein erhebliches Potential sowohl bezüglich der Kühlung wie auch bezüglich Sicherheit gegen Versagen aufweist. Es erscheint daher angebracht, nach den bisherigen, erfolgreichen transienten Experimenten Experimente mit Nachheizung durchzuführen. Solche Experimente sind zur Zeit in Vorbereitung: In etwa 5 Experimenten mit Thermitschmelzen von 600 bis 1000 kg und einer kontinuierlichen Nachwärmesimulation soll die Leistungsfähigkeit der Kühleinrichtung optimiert und überprüft werden.

Die wesentlichen Fragestellungen dieser Experimente sind die Kurz- und Langzeitkühlbarkeit, die ausreichende Fragmentierung der Schmelze und die Stabilität der porösen Betonschicht gegen ungleichmäßigen Angriff der Schmelze. Schließlich sind die zulässige Schmelzenhöhe und der notwendige Flutwasserdruck für eine sichere Funktion zu bestimmen.

Literatur

1 Alsmeyer, H., Spencer, B., Tromm, W.; The COMET Concept for Cooling of Ex-Vessel Corium Melts, 6th International Conference on Nuclear Engineering ICONE-6, San Diego, May 10-15, 1998, New York, N. Y.: ASME, 1998, CD-ROM

2 Alsmeyer, H., Fieg. G., Tromm, W., Werle, H., FZK Investigations on Ex-Vessel Melt Behavior, Technical Meeting on Fuel Assembly Engineering - Core Design - Reactor Operation of the German Nuclear Society (KTG), Febr. 3-4, 1998, Forschungszentrum Karlsruhe

3 Alsmeyer, H., Adelhelm, C., Benz, H., Cron, T., Pasler, H., Schöck, W., Schumacher, G., Tromm, W., Spencer, B. W., Farmer, M.T., Das COMET-Kernfängerkonzept: Experimente mit Nachbeheizung und mit Uranschmelzen, Jahrestagung Kerntechnik, 26. - 28. Mai 1998, München Bonn: Inforum GmbH, 1998, p. 157-60

4 Tromm, W., Alsmeyer, H., Cron, T., Ferderer, F., Transiente Experimente zur Untersuchung des Verhaltens später Schmelzen aus dem RDB für das COMET-Kernfängerkonzept, Jahrestagung Kerntechnik, München, 26. - 28. Mai 1998, Bonn: Inforum GmbH, 1998, p. 153-56

5 Alsmeyer, H., Tromm, W.: Das COMET-Konzept zur Kühlung von Kernschmelzen: Bewertung der experimentellen Untersuchungen und des Einsatzes im EPR, Draft Report, Forschungszentrum Karlsruhe, Sept. 1998

6 Alsmeyer, H., Cron, T., Foit, J.J., Schmidt-Stiefel, S., Schneider, H., Tromm, W., Wenz, T., Ferderer, F., Adelhelm, C., Dillmann, H. G., Pasler, H., Schöck, W., Schumacher, Benz, H., G., Grehl, C., Merkel, G., Ratajczak, W., COMET-Konzept. Projekt Nukleare Sicherheitsforschung, Jahresbericht 1997, FZKA-6126 (Sept. 1998) 229-55

7 Tromm, W., Experimentelle Untersuchungen zum Nachweis der langfristigen Kühlbarkeit von Kernschmelzen, Wissenschaftliche Berichte, FZKA-6176 (Nov. 1998), Dissertation Universität Karlsruhe 1998

II. Investigations for the EPR Concept – KAPOOL and KATS Experiments

(G. Engel, F. Fellmoser, G. Fieg, H. Massier, H. Werle, INR; N. Prothmann, D. Raupp, W. Schütz, U. Stegmaier, IRS; J. Foit, IATF; G. Stern, A. Veser, Fa. Pro-Science)

Abstract

The objective of the KAPOOL and KATS experiments is to investigate basic phenomena in connection with the EPR melt spreading and cooling concept. High-temperature Al_2O_3- and Fe-melts produced by the thermite reaction are used to simulate the oxidic and metallic components of the core melt. Three KAPOOL tests have been performed to study the behaviour of the core melt in the reactor cavity and its release through the gate into the spreading compartment. Erosion rates of two different concretes by a metallic melt have been determined as a function of melt temperature. In addition, a preliminary estimation of the opening time of the EPR gate by a metallic melt has been made. In a series of three KATS tests, one- and two-dimensional spreading with low pouring rate on ceramic and concrete has been studied. Comparisons of one-dimensional spreading data of oxidic and metallic melts on ceramic with CORFLOW predictions are encouraging.

Zusammenfassung

In den KAPOOL- und KATS-Experimenten werden grundlegende Phänomene des EPR-Konzepts zur Ausbreitung und Kühlung der Kernschmelze untersucht. Die oxidische und metallische Komponente der Kernschmelze werden dabei durch mittels der Thermit-Reaktion erzeugte Al_2O_3- und Fe-Schmelzen simuliert. In drei KAPOOL-Experimenten wurde das Verhalten der Kernschmelze in der Reaktorgrube und ihr Austreten durch das "Gate" in den Ausbreitungsraum untersucht. Für zwei verschiedene Betonsorten wurden die Erosionsraten durch Eisenschmelzen als Funktion der Schmelzentemperatur bestimmt. Darüber hinaus wurde eine vorläufige Abschätzung der Öffnungszeit des EPR "Gates" durch eine metallische Schmelze durchgeführt. In einer Serie von drei KATS-Experimenten wurde die ein- und zwei-dimensionale Ausbreitung auf Keramik und Beton bei kleinen Schmelzeausflußraten untersucht. Vergleiche der ein-dimensionalen Ausbreitung oxidischer und metallischer Schmelzen auf Keramik mit CORFLOW-Rechnungen sind ermutigend.

1. Introduction

Next generation LWR's shall incorporate the ability to control and retain ex-vessel corium melt after a postulated core meltdown accident with subsequent penetration of the lower head of the pressure vessel (RPV), to exclude significant radioactive release to the environment. In the case of the European Pressurized Reactor (EPR), an ex-vessel core-catcher is foreseen to meet these requirements [1 – 3]. The corium melt shall first be collected temporarily (~ 1 h) in the reactor cavity under the RPV, to ensure that practically all core masses are gathered. The cavity is covered on all sides with a sacrificial concrete of relatively low water content, consisting mainly of Fe_2O_3 and SiO_2. The zirconium present in the corium will be oxidized by the iron oxide during the concrete erosion phase. The heat production of this strongly exothermic reaction adds to the decay heat. The eroded concrete partly mix with the UO_2/ZrO_2, thereby reducing the liquidus and solidus temperatures as well as the density of the oxide melt. Eventually, the oxide density falls below the density of the metallic phase. This may result in a flipover of the two phases, if gas driven convection allows separation.

The bottom of the cavity consists of a thick (~ 50 cm) layer of sacrificial concrete resting on a 40 mm thick steel plate ("gate"). After melt through of the gate, the melt is released on the spreading area (~ 170 m^2). After spreading, the melt is flooded with water from top to extract the stored and the decay heat.

It is important for this concept that the melt spreads pretty homogeneously over the spreading area. To achieve this, it is favorable if the melt is released in a short time (i.e. a fast opening of the gate over a large area) and the melt viscosity is low.

In the KAPOOL tests, mainly the processes in the reactor cavity, i.e. erosion of the sacrificial concrete, meltthrough of and melt release through the gate are studied. In some tests, in addition, succeeding phenomena, i.e. spreading and flooding of the melt have also been investigated [4, 5] (and previous progress reports).

The main goal of the KATS tests [4, 6, 7] (and previous progress reports) is to provide a broad experimental basis of spreading data of oxidic and metallic melts for code verification, especially CORFLOW [8]. In some tests, in addition, flooding of the spread melt has also been studied.

2. KAPOOL Experiments

The exothermic thermite reaction $8Al+3Fe_3O_4 \rightarrow 4Al_2O_3+9Fe$ is producing an iron and an alumina melt, each with ~ 50 wt% and with temperatures up to 2400 °C. Thermite charges of 100 to 150 kg are ignited in the reaction vessel. The bottom (or part of it) of the crucible consists of a layer of sacrificial concrete on top of a steel plate, which simulates the gate of the reactor cavity. The test parameters and results of the KAPOOL experiments are summarized in table 1.

In the reporting period, three tests, KATS-7, -8 and –9 have been performed. In KATS-7 and –8 erosion of sacrificial concrete, in KATS-9 gate behaviour has been studied.

Erosion of sacrificial concrete.

The erosion rate of the sacrificial concrete is important because it determines the residence time of the melt in the reactor cavity. The experimental erosion data are primarily used to validate the COSACO code [9], developed by Siemens/KWU to describe the melt behaviour in the reactor cavity. In addition, the homogeneity of the horizontal erosion front at the bottom of the reactor cavity is of interest, because it determines the meltthrough behaviour of the steel gate (see next section).

In KAPOOL-7 and –8 (table 1), 150 kg thermite were ignited in crucibles with melt-resistant sidewalls of porous Al_2O_3 and a bottom consisting of a 200 m thick layer of EPR-representative sacrificial concrete type VM281Q (47 %wt Fe_2O_3, 42 wt% SiO_2, 8 wt% cement and ~ 3 wt% water, grain size ≤ 1 mm) above a 10 mm thick steel plate. In KATS-7, 5 kg of Zr particles were placed on top of the concrete and in KATS-8, 10 kg of Zr particles were placed into the upper 10 mm concrete layer to simulate the Zr content of the core melt. A series of thermocouples is located at various positions within the concrete layer to determine the progression and the homogeneity of the erosion front. The thermite reaction lasts ~ 15 s and a few s later, the two phases are separated. The much denser metallic phase is at the bottom and reacts with the concrete. The temperature of the iron melt is measured in intervals of ~ 30 s by W/Re-thermocouples which are dipped into the melt from above.

In both tests, KAPOOL-7 and –8, the first measurement indicated an iron melt temperature of ~ 2200 °C. After ~ 400 s and an erosion depth of ~ 170 mm, the erosion stopped at a melt temperature of ~ 1500 °C.

In fig. 1 the erosion rates from all KAPOOL tests are shown as a function of the temperature of the iron melt. In the first tests (KAPOOL-2, -3, and –5), the glass concrete (82 wt% borosilicate glass, 16 wt% cement and ~ 2 wt% water, grain size ≤ 10 mm) of the COMET core-catcher concept was used. It is evident, that the erosion rates of the EPR sacrificial concrete are, independent from the melt temperature, about a factor two larger than those of the glass concrete. The reason for these very different erosion rates is not clear at the moment, it is tentatively assumed that the very different grain sizes (glass ≤ 10 mm, EPR-type ≤ 1 mm) play an important role.
The melt thickness of the residual concrete layer was 20 – 30 mm in KAPOOL-7 and 30 – 40 mm in KAPOOL-8. The inhomogeneity of the erosion front of ≤ 10 mm is in agreement with the thermocouple results of KATS-6, -7 and –8, which indicate that the maximum inhomogeneity of the erosion front first increases slowly with time and erosion depth, but achieves essentially an asymptotic value of ~ 10 mm after an erosion of ~ 50 mm.

Gate meltthrough by metallic melts

The effective thermal energy of the thermite melt is too small to erode in one test both, a representative thick concrete (≤ 100 mm) and steel layer (40 mm). On the other hand, from the erosion studies of the sacrificial EPR concrete by iron melts it is known, that at the moment of first local contact of melt and steel gate, the thickness of the residual concrete on other places of the gate is ≤ 10 mm.
These initial conditions have been modeled in KATS-9 (thermite mass 150 kg), where the melt through of a representative thick (40 mm) steel gate by an iron melt has been studied (table 1). With exception of a 200 mm ∅ central region, the steel gate at the bottom of the crucible was covered with a 10 mm thick layer of EPR sacrificial concrete (spallation of concrete was prevented by a steel wire grid embedded in the concrete and fixed to the plate). The side walls of the crucible consisted again of melt-resistant porous Al_2O_3 (fig. 2).
The temperature of the iron melt was determined in ~ 30 s intervals by dip-in W/Re-thermocouples. The steel plate was instrumented with thermocouples to determine the erosion front. The released melt jet and the lower surface of the steel plate were observed with normal and an infrared video camera. In addition, the mass rate of released melt was determined from the weight of the crucible, which was measured by force sensors.

The sequence of events observed (or estimated) in KAPOOL-9 is summarized in the following table:

KAPOOL-9, sequence of events

Time after ignition (s)	Iron melt temp. (°C)	Event
15 25 61	2300 1900	Start erosion Concrete completely eroded (estimated) Melt penetration through plate center
61 – 64	1900	Release of iron melt (~ 75 kg ≙ ~ 11 l); strong increase with time of - melt jet (hole) diameter from several to ~ 100 mm - release rate from zero to ~ 35 kg/s (~ 5 l/s)
64 – 69	1900	Release of oxide melt (~ 75 kg ≙ ~ 21 l); slightly decreasing release rate (max 30 kg/s ≙ 8 l/s) through hole of essentially constant diameter (~ 10 mm)
After test	--	- Sacrificial concrete completely eroded - Surface of steel plate eroded; thickness of eroded layer increases continuously towards the center from zero (at the boundary, ~ 350 mm ∅) to about 24 mm at 200 mm ∅; central hole 109 mm ∅ (at lower surface)

It is of interest to note, that the hole in the steel plate is only increased by the outflowing metallic, but not by the oxidic melt.

In table 1, for those KAPOOL-tests (no. 1, 3, 5, 6 and 9), where gate meltthrough was studied, the numbers of release holes, the eroded area and the thickness and inhomogeneity of the residual concrete layer are given. Except in KAPOOL-3, no residual concrete is left on the gate and the eroded area is pretty large (82 – 100 cm^2). KAPOOL-3 was quite different: only a small area (10 cm^2) was eroded and there was a residual concrete layer of 2 – 5 mm thickness, although the melt release lasted for 23 s. Based on the release duration, the melt temperature and the erosion rates of fig. 1, the thickness of the concrete layer at the time of first melt/gate contact is estimated to be ~ 30 mm. The only reasonable explanation for this huge, local inhomogeneity of erosion is local failure (large porosity or gap) in the concrete layer (large grain glass concrete). Therefore the results of KAPOOL-3 are considered to be not representative.

Based on the hitherto performed KAPOOL-tests, the meltthrough behaviour of the EPR gate by a metallic melt (this would be the case after a flipover of the two phases) can be described as follows: at the first local contact of the melt with the steel gate, the other parts of the gate may still be covered by a layer of residual sacrificial concrete with a thickness between zero and a maximum value, which is determined by the inhomogeneity of concrete erosion and was observed to be ≤ 10 mm over an area of 400 mm ∅ for the fine-grain EPR-type sacrificial concrete. The time required to erode this residual concrete essentially determines the time lag between start and complete opening of the gate (opening time). To heatup and erode the gate after melt contact, according to KAPOOL-9, ~ 45 s are required for a cold 40 mm thick steel plate and somewhat less for a hot plate. This effect will delay the opening and might reduce the opening time slightly.

To erode a residual concrete layer with a maximum thickness of ~ 10 mm by a metallic melt with a temperature of ~ 2000 °C (estimated temperature of EPR melt after layer flipover [3]), only about 14 s are required. Assuming that he inhomogeneity of concrete erosion for the larger EPR gate is similar as observed here, it is concluded that the EPR gate, after contact with a metallic melt, will open over the whole gate area within a few ten s. Such a short opening time is very advantageous for a homogeneous spreading.

Conclusions and future work

Erosion rates for two types of sacrificial concrete by a metallic melt have been determined as a function of melt temperature. In addition, based on a model for the meltthrough behaviour of the EPR gate by a metallic melt, a preliminary estimation of the opening time yielded values of only a few ten s. Experiments are under way to study gate meltthrough by an oxidic melt, which is important in the case that no layer flipover occurs in the reactor cavity.

3. KATS Experiments

Description of tests performed

Iron and oxide (alumina) melts are generated by a thermite reaction. Generally about 320 kg of thermite powder with an addition of 20 kg quartz sand are ignited in a reaction crucible. After the reaction is completed, the heavier iron melt (~150 kg) is released first through a swivelling pipe into a container from where it flows over a dam either into the 1-dim spreading channel or onto a 2-dim spreading area. The pipe is then swivelled to direct the lighter oxide melt to a second container and a separate spreading area. With this experimental set-up, the volumetric flow rate for spreading of both melts is limited by the nozzle diameter of the crucible outlet and is in the range between 1 and 2 l/s.

Thermocouples of the types W/Re and NiCr/Ni are installed at several locations on the spreading surfaces. The first is to measure the melt bulk temperature, the latter is to record the arrival time of the spreading front. Several video cameras are installed to record the spreading process, and an infrared camera measures transient surface temperatures of the spreading oxide melts.

The special characteristics of the EPR oxide melt (admixture of eroded sacrificial concrete) are simulated by adding ~8 wt% SiO_2 to the alumina melt, resulting in a solidus temperature of ~1600°C and a liquidus temperature of ~1925°C. The temperatures of the oxide melt at the onset of spreading were between 1950°C and 2030°C in the tests discussed here. Iron temperatures were in the range of 2150 – 2200°C which is ~600 K above solidification temperature.

Three tests have been performed in the reporting period to investigate the spreading with low pouring rates. The first (KATS-14) is a 1-dim spreading experiment on ceramic and is comparable with respect to the geometry to a previous test (KATS-12) with higher pouring rate. A second 2-dim spreading experiment on ceramic (KATS-15) was performed. The influence of the pouring rate can be seen in comparison to the previous test KATS-8, where higher pouring rates were employed with otherwise similar geometry. In the last experiment (KATS-16), finally the 2-dim spreading on silicate concrete with low pouring rate and an oxide temperature close to liquidus was studied. Table 2 lists experimental parameters of all the mentioned tests. It should be mentioned that in KATS-15 and –16 the pouring rate was experimentally determined from the weight of the reaction crucible, which is measured by force sensors.

The experimental results of 1-dim oxide spreading are shown in fig. 3 ($\dot{V}$ is the volumetric pouring rate). Because the initial melt temperatures of KATS-12 and –14 were similar (difference ~ 70 K, see table 2), the differences in spreading distance and melt height distribution are attributed to the different pouring rates. The oxide melt of KATS-12 (high pouring rate) spreads 11.3 m with an average height of 30 mm, whereas in KATS-14 (low pouring rate) the oxide spreads 7.2 m with a melt height between 30 and 60 mm. Both melts have already reached ~ 85 % of their final spreading length at the moment when pouring stops. The last half meter of spreading is in both tests dominated by slowly spreading melt fingers.

It is known, that the spreading length increases with increasing melt temperature. Therefore, considering the 1-dim spreading of the iron melts (fig. 4), it is surprising, that although the initial melt temperature in KATS-12 (high pouring rate) is considerably lower than in KATS-14 (low pouring rate) (1900 and 2180 °C, respectively, table 2), the spreading length is larger in KATS-12 (11.2 m) than in KATS-14 (9.4 m). This indicates a pretty large influence of the pouring rate on the spreading length for metallic melts. Regarding the pouring duration, the spreading of the iron melts takes a longer time than spreading of the comparable oxide melts. At the moment when pouring stops, both iron melts have just reached 60% of their final spreading length.

The spreading results of the 2-dim experiments for iron and oxide are shown together in fig. 5. For the oxide melts the time dependent spreading is shown and for the iron melts the maximum spreading area is given.

For the oxide melts too the pouring rate (KATS-8 high, KATS-15 low pouring rate) and in addition the type of spreading surface (KATS-15 ceramic, KATS-16 concrete) have a big influence on spreading. The oxide melt of KATS-8 spreads faster and covers a bigger area (3.9 m²) than the oxide melt of KATS-15 (2.5 m²). When the pouring in the KATS-15 stops after 26 s, the spreading is not yet finished but ~ 88 % of the final area are already covered at this time. On the concrete surface (KATS-16), the oxide melt spreads over a final area of only ~ 1 m². It should be mentioned that in KATS-16 the temperature of the oxide melt was remakly lower than in KATS-15 (1950 and 2030 °C, respectively).

The maximum area covered by the iron melt is quite similar in the three different experiments (2.3 – 2.6 m²) (fig. 5). This shows that the iron in all tests is able to spread to its maximum area and minimum thickness corresponding to the surface tension of the liquid melt. The outstanding difference is that the iron melt that spread on the

concrete surface (KATS-16) gathered near the melt outlet and did not reach the opposite walls of the spreading area as did the iron melts on ceramic. Because the initial temperature of the iron melt in this test was essentially equal to that in the other two tests, this indicates, that the different spreading behaviour in KATS-16 is due to the melt/concrete interaction.

In fig. 5 (bottom), for the 1- and 2-dim tests discussed here, the area covered by the oxide melt is shown as function of time. The data indicate that the final covered area increases with increasing pouring rate and is generally higher for 2-dim (full lines) than for 1-dim spreading (broken lines).

Conclusions and future work

Concerning spreading on ceramic, for the1-dim case a pretty comprehensive data base (high/low flow rate, high/low superheat) is available. In addition, two 2-dim tests with high and low pouring rate, respectively, have been performed. Comparisons of 1-dim spreading with CORFLOW predictions are encouraging (see section 4). CORFLOW calculations for 2-dim tests are in progress.

On concrete several 1-dim and one 2-dim test have been performed. Spreading behaviour is observed to be remarkably different compared to ceramic. A few more 2-dim tests are planned. Spreading on concrete can, at the moment, not be described by CORFLOW, but this would be very important because of its relevance for the EPR.

4. Comparison of KATS Experiments and CORFLOW Calculations

Introduction

In the framework of large-scale KATS experiments the non-isothermal spreading of metallic and oxidic melts on ceramic or concrete surfaces under various conditions, e. g. melt overheat and melt release rates, is studied. The metallic and oxidic components of the melt are generated by the thermite reaction. The oxidic melt is composed of about 85 wt % Al_2O_3, 10 wt % SiO_2 and about 5 wt % FeO. For the above melt mixture there is only a limited data base of material properties available. Using an estimated phase diagram, the Stedman correlation [10] was applied to evaluate the viscosity within the solidus-liquidus range. Above the liquidus temperature the experimental data of Elyutin et al. were used [11, 12]. An experimental program to

measure the viscosity of the oxidic KATS melts below the liquidus temperature is under way.

The KATS experiments can be classified according to the melt release conditions. In KATS-7 [12] and KATS-14, the melt was poured into a small cavity. As soon as the cavity was filled, the melt began to spread across the channel with a flow rate defined by the diameter of the pouring nozzle in the reaction crucible. In this way an almost constant mass flux was achieved which lasted 12 s in KATS-7 and 37 s in KATS-14. The melt front propagation stopped at 49 s in KATS-7 and at 57.6 s in KATS-14.

In KATS-5 [13] and KATS-12, on the other hand, the melts were gathered in a container. Spreading into the channel was initiated by opening a gate in the container. The outflow of the oxidic melt from the container was completed after 3.7 s and 10.4 s in KATS-5 and KATS-12, respectively. The stop of the melt front was detected at 15 s in KATS-5 and 40 s in KATS-12.

CORFLOW results

One can expect that the discrete phase transition model together with the variable viscosity approach used in the CORFLOW code [8] will predict a stop of the melt front if almost all nodes at the free boundary reach the temperature at which the value of the viscosity becomes large and if the floating crust is connected to the basemat at the melt front. Because there is no crust failure criterion in CORFLOW, the results can depend strongly on the grid used for the simulations. The sensitivity on the grid size will generally depend on the viscosity behaviour as a function of the temperature and on the initial condition of the melt release.

In fig. 6 the melt front progression calculated by CORFLOW using a fine grid and a coarse grid with double mesh size along the channel and triple mesh size in the vertical direction for the oxide melt of KATS-5 is shown together with the experimental data. Both CORFLOW calculations underpredict the velocity of the melt front considerably during the melt release phase. On the other hand, the time of melt front stopping and the final front position agree well with the measurements in both simulations.

The simulation of KATS-12 was performed only with a quite coarse grid (dx = 0.1m, dz = 0.025m). The calculated front positions as a function of time is compared with the measured data in fig. 7. As for KATS-5 the melt front progression in the first stage

of the spreading is underpredicted while the final front position agrees very well with the experimental one.

The results of the CORFLOW analysis of KATS experiments with a small and almost constant mass flux, KATS-7 and KATS-14, are shown in fig. 8 and fig. 9, respectively. The calculated evolution of the melt front during the melt release phase for the KATS-7 agrees very well with the measured curve in contrast to the previous cases. The time at which the melt front stops is predicted to be much shorter than in the experiment: 23 s in the fine grid and 27 s in the coarse grid calculation, whereas in the experiment it was observed at 50 s (fig. 8). The discrepancies between the CORFLOW predictions and the measured front progression in the KATS-14 experiment (fig. 9) during the melt release phase might be due to incertainties in the mass flux caused by an increase of the diameter of the pouring nozzle due to ablation. Both simulations underpredict the final front position. The stop of the melt front is predicted at 60 s in the fine grid and at 48 s in the coarse grid calculation. In the experiment the stop of the melt front progression was detected after 58 s.

Conclusions and future work

After the numerical deficiencies in the treatment of non-isothermal flows with increasing viscosity have been eliminated in CORFLOW, there is a need for validation of the achieved modifications.

The variable viscosity used in CORFLOW seems adequate for the prediction of the final front position of the oxide KATS experiments. The CORFLOW code will predict a stop of the melt front if almost all nodes at the free boundary reach the temperature at which the value of the viscosity becomes large and if the floating crust is connected to the basemat at the melt front. Because there is no crust failure criterion in CORFLOW, the results can depend strongly on the grid used for simulations. The sensitivity on the grid will generally depend on the viscosity behaviour as a function of the temperature and on the initial condition of the melt release.

Even though the progression of the front and the final position of the front calculated for the oxidic KATS experiments are insensitive to the mesh size, i. e. to the resolution of the thermal boundaries and the partition of the energy losses, caution must be exercised if a coarse grid is used. Pronounced discrepancies are observed with respect to other details of the experimental findings such as the velocity of the melt front during the melt release and the time of stop of the front progression. The nu-

merical procedure in CORFLOW does not contain a condition which ensures the continuity of the tangential component of the stress at the free surface. Therefore, it cannot be expected that CORFLOW will generally provide correct velocity profiles.
When compared with the whole available experimental database, the CORFLOW code agrees well with some experimental data, but there are also pronounced discrepancies with other experimental results. The agreement with some experimental data should not be interpreted as justifying the underlying physical processes in the code (the experimental data itself may not be fully qualified or the agreement might have been obtained because of a fortuitous choice of input parameters). Therefore, additional validation is needed in order to reach a status in which one can rely on CORFLOW predictions for the spreading of the ex-vessel melt in a postulated meltdown accident. In addition, a sufficiently qualified data base of material properties for the ex-vessel core melts is required.

References

[1] H. Alsmeyer et al., "Studies on the Core Melt Retention Concepts for the EPR", Proc. SFEN/KTG Conf. on the EPR Project, Strasbourg, November 1995, p. 204.

[2] H. Alsmeyer et al., "Ex-Vessel Melt Behaviour in the EPR", Proc. SFEN/KTG Conf. on the EPR Project, Cologne, October 1997, p. 161.

[3] M. Fischer, Siemens/KWU, private communication.

[4] H. Alsmeyer et al., "Beherrschung und Kühlung von Kernschmelzen außerhalb des Druckbehälters", FZK Nachrichten 4/97, p. 327.

[5] F. Fellmoser, G. Fieg, H. Massier, H. Werle, "Simulation Experiments on the Corium Melt Behaviour in the EPR Reactor Cavity: KAPOOL-Tests", Annual Meeting on Nuclear Technology, Munich, May 1998.

[6] F. Fellmoser et al., "Simulation Experiments on the Spreading Behaviour of Corium Melts", Annual Meeting on Nuclear Technology, Munich, May 1998.

[7] P. Ehrhard et al., "Spreading of the Core Melt in the Spreading Area of the EPR", ICONE-6, May 1998.

[8] R. Wittmaack, ""Numerische Simulation von Strömungen mit freier Oberfläche und diskreten Phasenübergängen", FZKA 6129 (1998).

[9] M. Nie, Siemens/KWU, private communication.

[10] S.J. Stedman, et al., J. Material Sci. 25 (1990), 1833.

[11] V.P. Elyutin, et al., Russian Journal of Physical Chemistry 43 (1969) 3.

[12] G. Fieg, F. Huber, H. Werle, "Simulation Experiments on the Spreading Behaviour of Core Melts: KATS-7", FZKA 6005 (1997).

[13] G. Fieg, H. Werle, F. Huber, "Simulation Experiments on the Spreading Behaviour of core Melts: KATS-5 (1-dim spreading of an oxide melt into a dry channel)", FZKA 5920 (1997).

Table 1 KAPOOL tests

		Thermite		Melt temp. (°C)		Gate								
Test No.	Date	Type	Mass (kg)	Start	End	Dim (cm)	Concrete type	Thickness (mm) Conc.	Steel	Melt release duration (s)	No. of holes	Eroded area (cm^2)	Residual concrete (mm) Thickness	Inhomog.
1	26.6.96	R70SSH	100	2100	1970	15x15	Glass	20	10	6	1	84	0	--
2	10.7.96	"	100+30	2070	1640	40x40	"	50	20	Melt not released				
3	8.10.96	10AlSSH	100+9	2450	2070	20x20	"	40	15	23	1	10	2-5	≤3
4	14.11.96	"	150	2450	--	20x20	"	40	15	Melt release through side wall				
5	16.1.97	"	150	2550	2060	22.5 ∅	"	40	15	8	4	82	0	--
6	15.12.97	R70HC	150	2200	1700	40 ∅	Fe_2O_3	100	10	9	2	100	0	≤10*
7	26.2.98	"	150+5 Zr	2200	1550	40 ∅	"	200	10	Melt not released			20-30	≤10,≤10*
8	27.4.98	"	150+10 Zr	2200	1500	40 ∅	"	200	10				30-40	≤10,≤10*
9	2.11.98	"	150	2300	1880	40 ∅	"	10 center 0	40	8	1	93	0	--

Concrete type Glass: 82 wt% borosilicate glass, 16 wt% cement, ~ 2 wt% water; grain size ≤ 10 mm

Fe_2O_3: 47 wt% Fe_2O_3, 42 wt% SiO_2, 8 wt% cement, ~ 3 wt% water; grain size ≤ 1 mm

* from thermocouples

Table 2 Test parameters for KATS-12, KATS-8 and the new tests KATS-14 to –16

Test	Spreading area / surface	Spread oxide melt	Pouring rate / duration oxide	Spread iron melt	Pouring rate / duration iron
KATS-12 24.7.1997	1-dim 0.25 × 12 m / 0.15 × 12 m ceramic (cordierite)	186 kg 2030°C	12.8 l/s – 0 l/s (linear decrease) 10.4 s	135 kg 1900°C	6.8 l/s – 0 l/s (linear decrease) 6.6 s
KATS-14 26.3.1998	1-dim 0.25 × 12 m / 0.15 × 12 m ceramic (cordierite)	176 kg 1960°C	2 l/s – 1.2 l/s 37 s	154 kg 2180°C	1.2 l/s – 2 l/s 16 s
KATS-8 24.4.1996	2-dim 2.8 × 1.8 m ceramic (cordierite)	158 kg 2100°C	7.5 l/s –0 l/s (linear decrease) 16 s	155 kg 2100°C	6.7 l/s –0 l/s (linear decrease) 7 s
KATS-15 30.7.1998	2-dim 2.8 × 1.8 m ceramic (cordierite)	144 kg 2030°C	~2 l/s 26 s	145 kg 2200°C	1 – 2 l/s 17 s
KATS-16 26.11.1998	2-dim 2.8 × 1.8 m silicate concrete	129 kg 1950°C	~1.1 l/s 45 s	~150 kg 2150°C	1 — 1.6 l/s 21 s

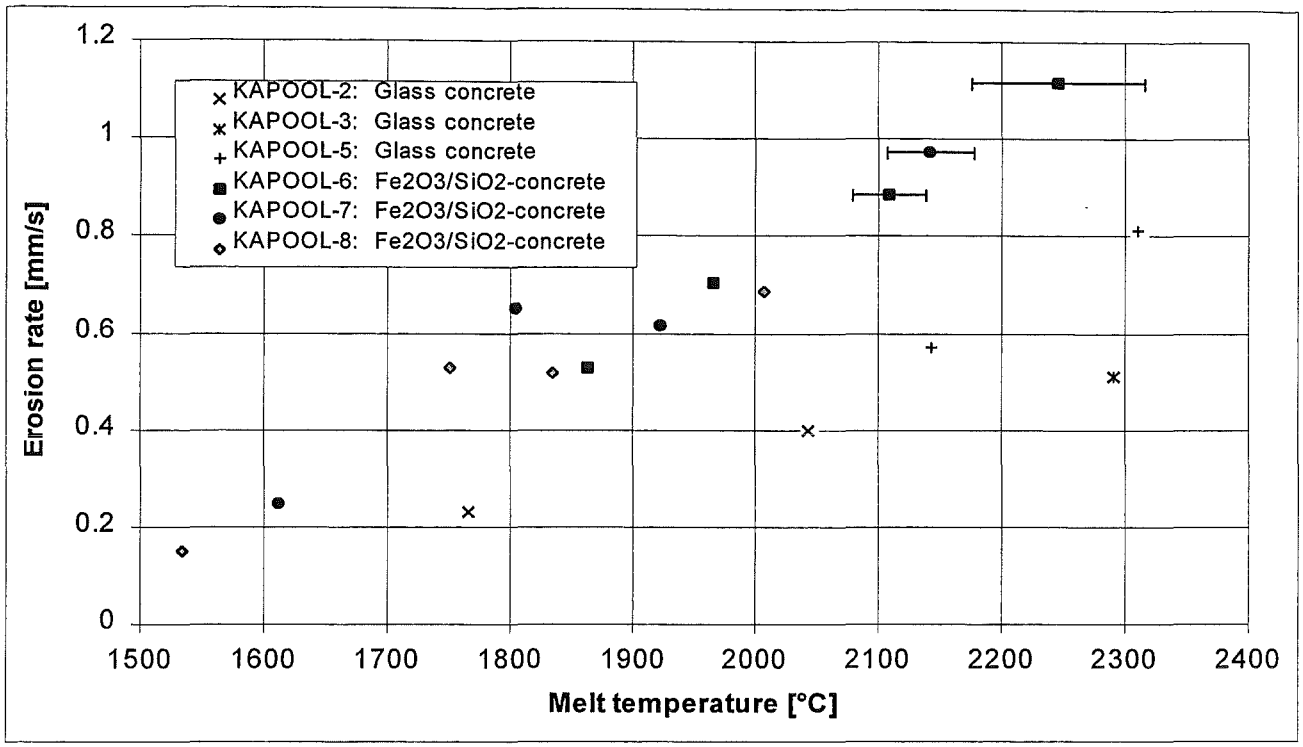

Fig.1 Erosion rates of glass concrete (KAPOOL-2/3/5) and the sacrificial concrete VM281Q (KAPOOL-6/7/8) in dependance of the temperature of the iron melt

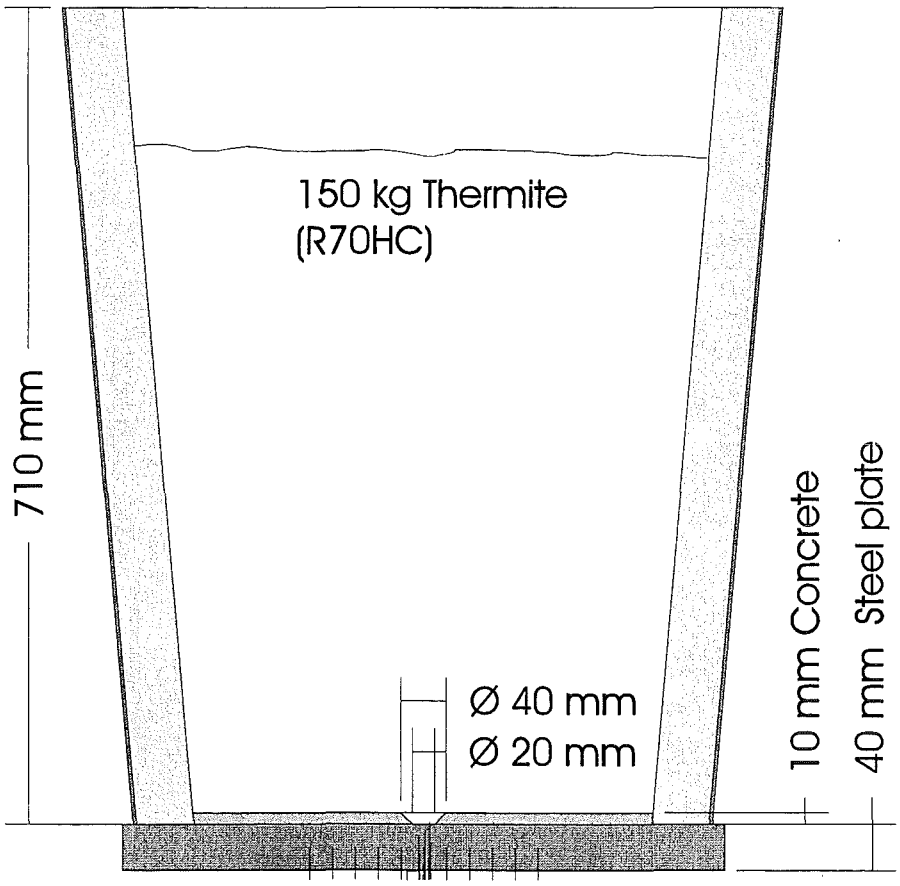

Fig.2 Experimental Setup of the KAPOOL-9 Test

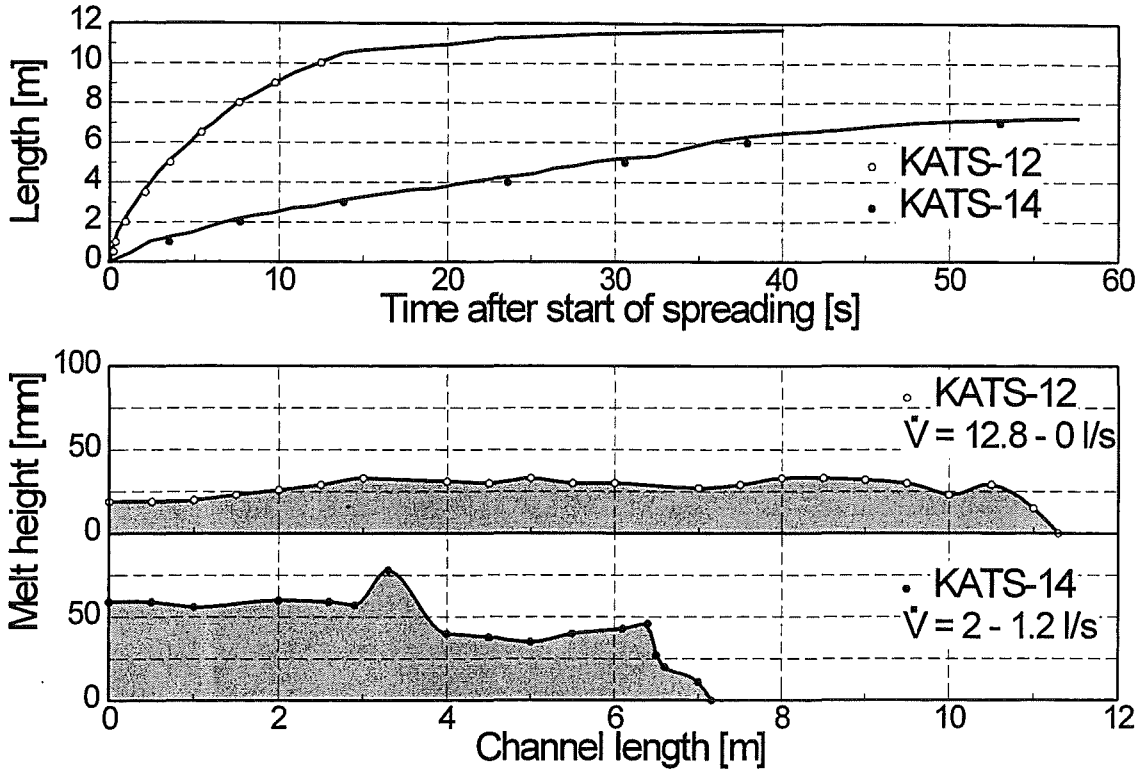

Fig. 3 Oxide melt spreading with different pouring rates

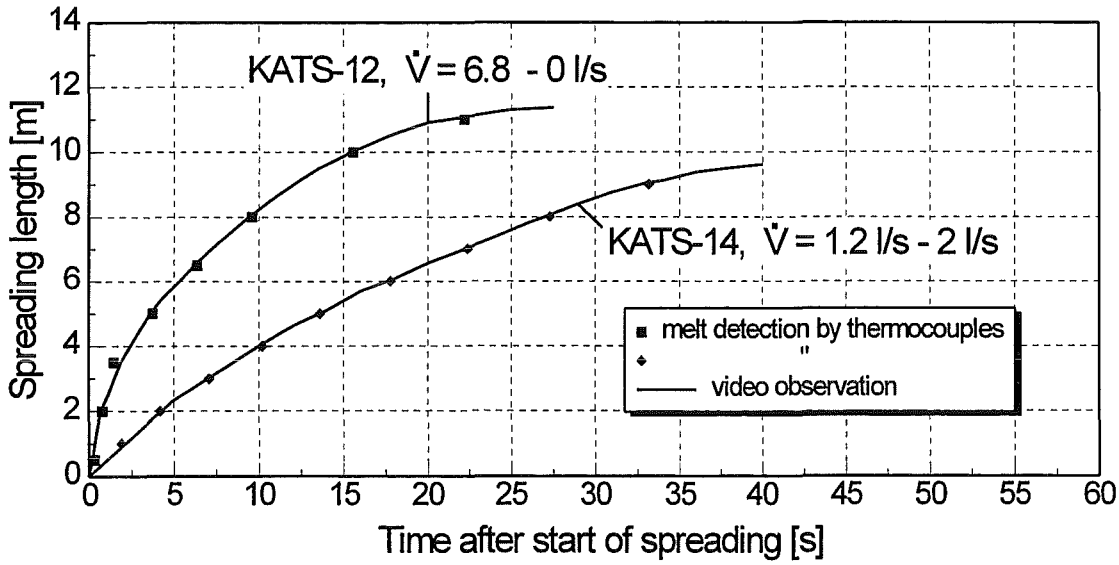

Fig. 4 Iron melt spreading with different pouring rates

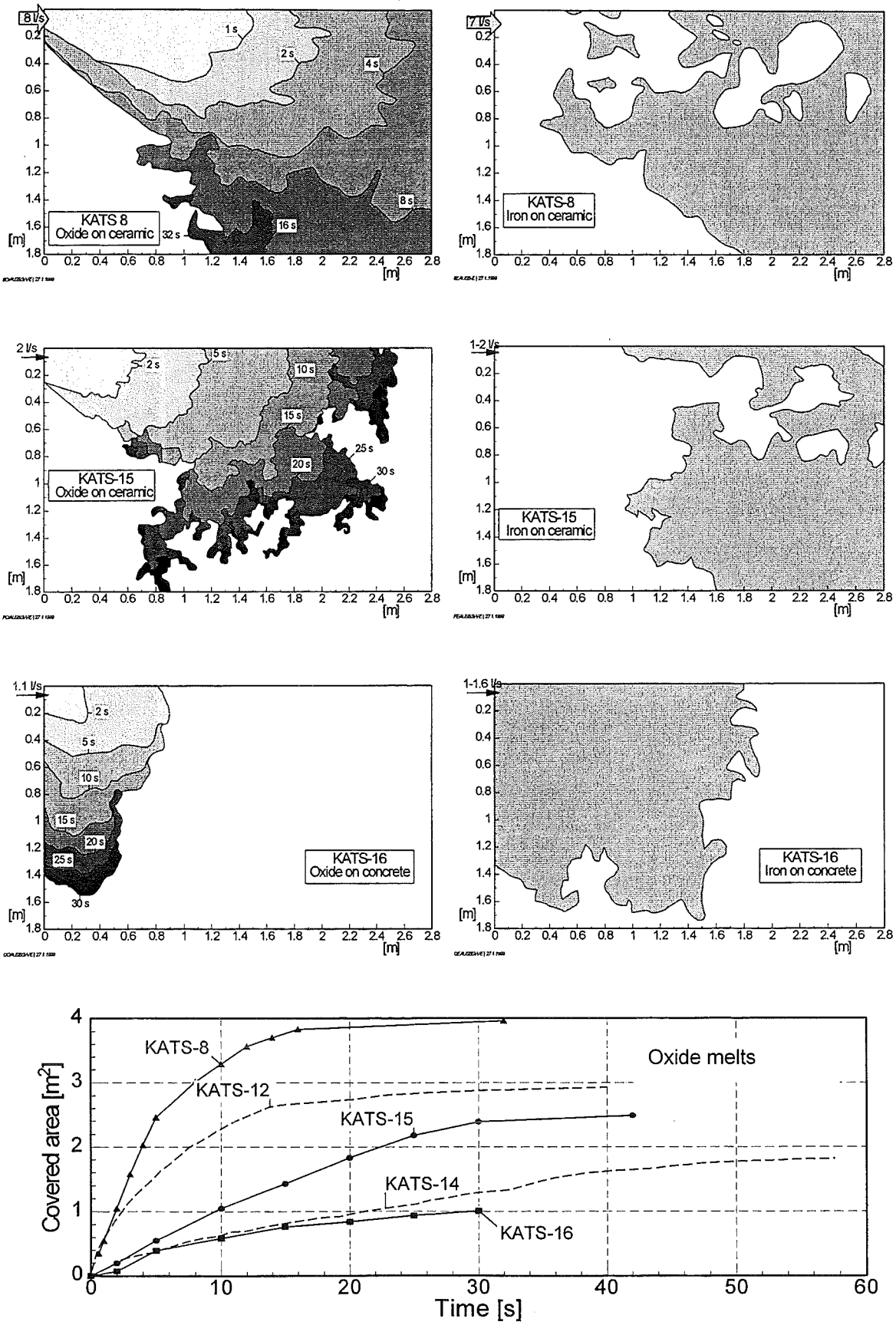

Fig. 5 Oxide and iron spreading with different pouring rates on two substrates

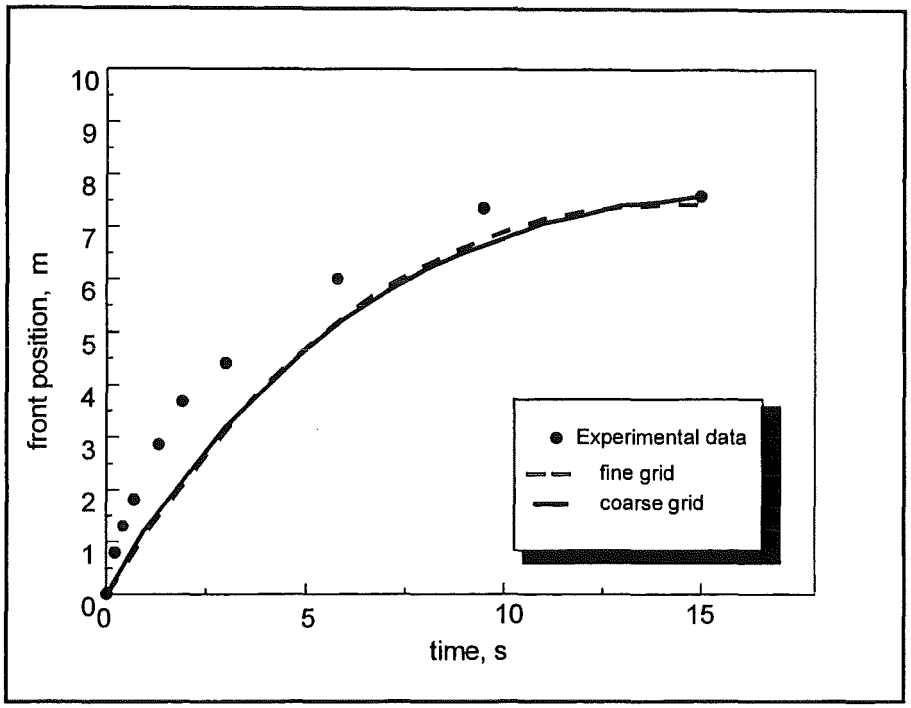

Fig. 6 Melt front progression of the oxide melt in KATS-5

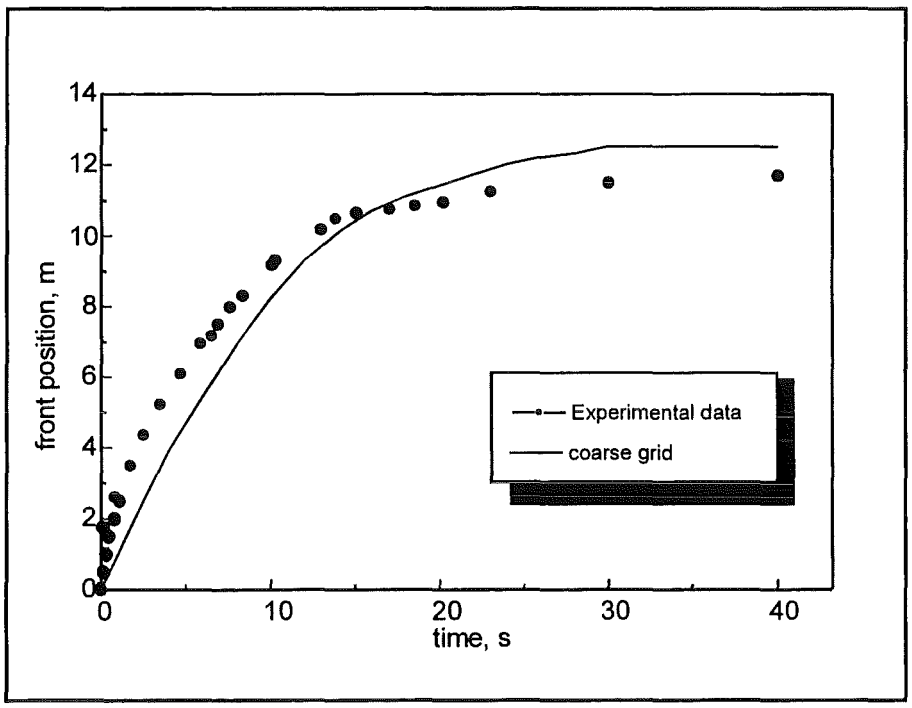

Fig. 7 Melt front progression of the oxide melt in KATS-12

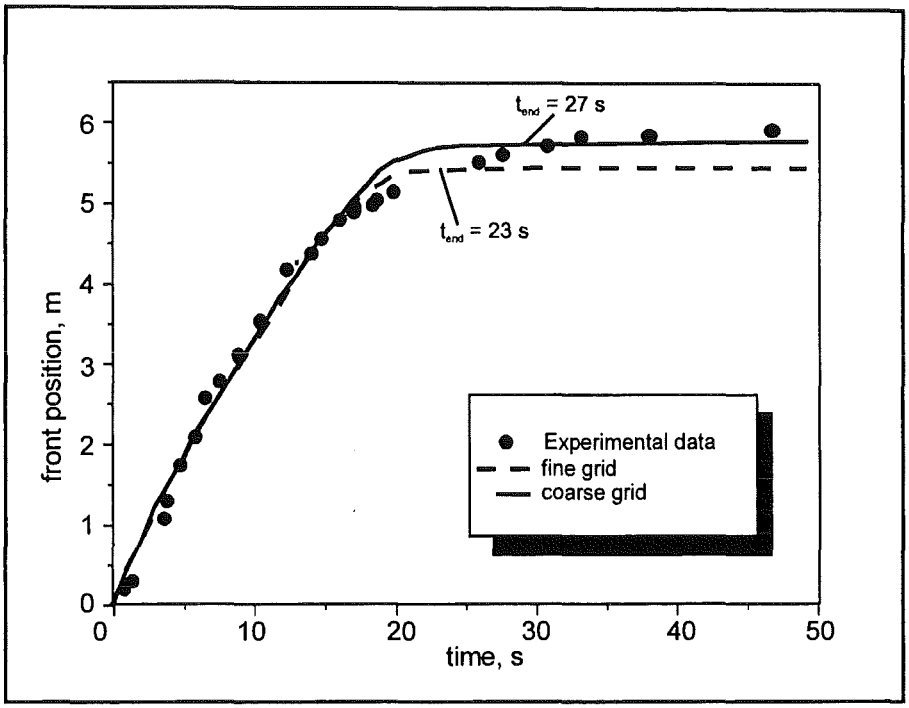

Fig. 8 Melt front progression of the oxidic melt in KATS-7

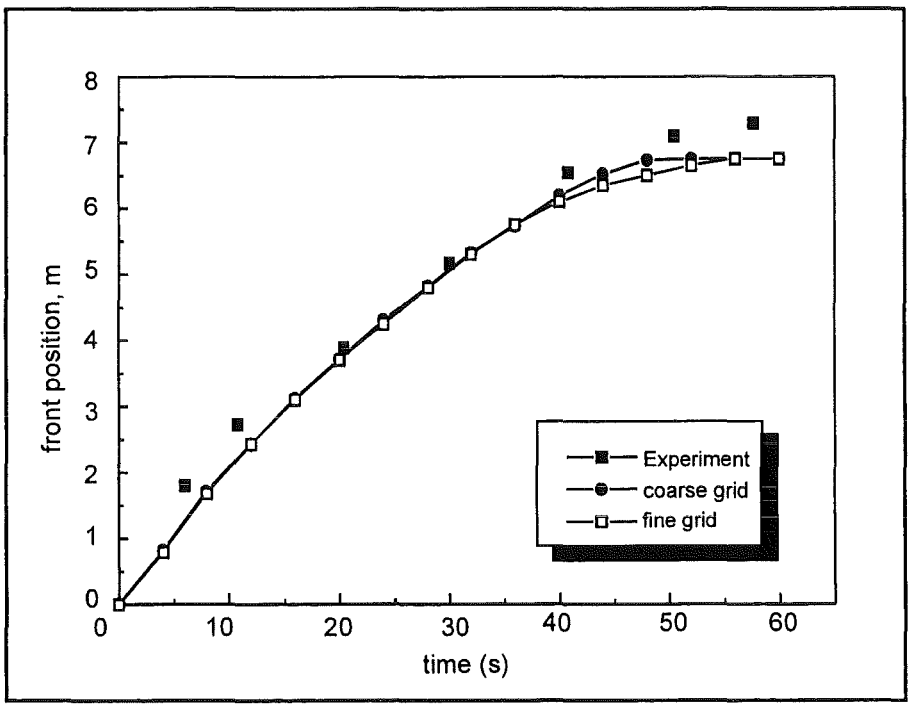

Fig. 9 Melt front progression of the oxidic melt in KATS-14

III. Untersuchungen zum EPR-Konzept — KAJET-Versuche

(G. Albrecht, H. Brüggemann, F. Huber, D. Raupp, W. Schütz, IRS)

Abstract

In the sequence of a core melt accident it is assumed that, after melt through of the reactor pressure vessel, the molten corium is released as a high-pressure melt jet which interacts with the protective liner of the reactor pit. This interaction is investigated in the KAJET experiments in which the molten corium is simulated by thermite melts. In the period reported, the influence of the driving pressure on the jet behaviour and the influence of a modified nozzle geometry were investigated. Melt masses of up to 40 kg were used in the new KAJET test facility. The tests aimed at achieving a compact melt jet with a velocity of up to 25 m/s as well as testing the working life of the nozzle.

1. Einleitung

In den KAJET-Versuchen wird mit Thermitschmelzen als Simulationsmaterial die Wechselwirkung eines Hochdruckschmelzestrahls (2 MPa) auf die in der Diskussion befindlichen Auskleide- und Opfermaterialien untersucht. Eine wichtige Voraussetzung dieser Untersuchungen ist die Herstellung eines möglichst kompakten Schmelzestrahls, der mit einer Geschwindigkeit von bis zu 25 m/s auf das zu untersuchende Material auftrifft. In den bisherigen Versuchen (VJ01-VJ06) wurde gezeigt, daß mit der eingesetzten Düsengeometrie (Düsenwinkel 30°, Auslaufstreckenlänge 110 mm) in einem Druckbereich von 0 bis 1,5 MPa kompakte Schmelzestrahle mit oxidischer Schmelze (Al_2O_3) erzeugt werden können.

Im Berichtszeitraum wurde die KAJET-Anlage für die zukünftigen Erosionsexperimente aufgebaut und in Betrieb genommen. Außerdem wurden zwei weitere Versuche zum Strahlverhalten durchgeführt. Beim Versuch VJ07 wurde untersucht, ob mit der bisher eingesetzten Düsengeometrie auch mit Eisenschmelze die Erzeugung eines kompakten Schmelzestrahls möglich ist. Der darauffolgende Versuch KJ01 wurde bereits in der neuen Anlage durchgeführt. Da die bisher eingesetzte Düsengeometrie im Reaktorfall sehr unwahrscheinlich ist, wurde hier eine Düse eingesetzt, deren Geometrie der angenommenen Form einer durchmolzenen Wand ähnlicher ist.

2. Versuch mit metallischer Schmelze

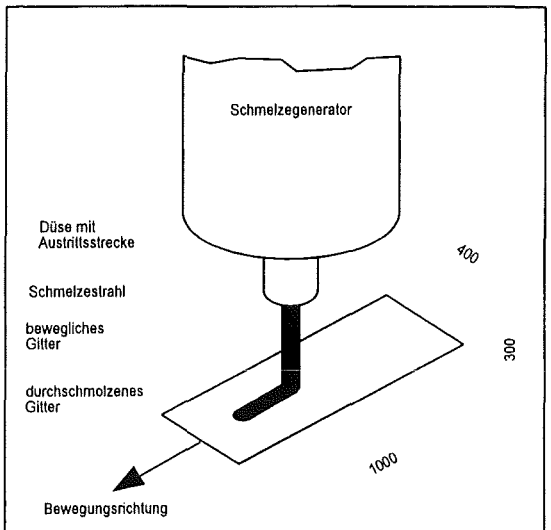

Bild 1. Schema der Versuche

Ziel des Versuchs VJ07 war es, das Strahlverhalten der Eisenschmelze unter ähnlichen Bedingungen zu untersuchen wie bei VJ05 und VJ06, bei denen nur das Oxid austrat. Dazu wurde der KAJET-Generator Typ 20 so modifiziert, daß bei diesem Versuch sowohl die metallische als auch die oxidische Schmelze austrat. Durch den Dichteunterschied der beiden Schmelzen tritt zuerst das Eisen und danach das Oxid aus. Durch den Einbau einer kleineren Drossel (5,6 statt 9,5 mm) in die Druckleitung zum Generator, konnte ein langsamerer Druckanstieg (0-1,5 MPa) realisiert werden (VJ06 = 0,9 s, VJ07 = 1,2 s). Durch die größere Schmelzenmenge (insgesamt ca. 40 kg statt bisher 20 kg) und die genannten Änderungen, mußte auch der zeitliche Ablauf modifiziert werden. Die geometrischen Bedingungen und der maximale treibende Druck (max. 1,5 MPa) blieben unverändert. Um auch unter schlechten Sichtbedingungen eine Information über das Strahlverhalten zu bekommen, wurde eine bewegliche Drahtgitterfläche (Bild 1) im Abstand von 300 mm unter dem Schmelzenaustritt montiert. Diese konnte unter dem austretenden Schmelzestrahl mit konstanter Geschwindigkeit horizontal verschoben werden. Anhand der zeitlichen Zuordnung der durchschmolzenen Breite im Gitter läßt sich der Strahldurchmesser in Abhängigkeit vom treibenden Druck rekonstruieren.

3. Versuch mit modifizierter Düsengeometrie

Ziel der bisherigen Versuche (VJ01-VJ07) war die Erzeugung eines möglichst kompakten Schmelzestrahls. Die Versuche wurden daher mit den in Vorversuchen ermittelten Düsenwinkeln von 30 ° und Auslauflängen von 110 mm durchgeführt (Bild 2a). Da im realen Fall nicht mit einer solchen Geometrie gerechnet werden kann, wurde beim Versuch KJ01 untersucht, ob auch mit einer Düsengeometrie (Düsenwinkel 90 °, Auslauflänge 25 mm, Bild 2b), die eher dem Durchschmelzen einer dicken Wand entspricht (Bild 3), annähernd kompakte Strahle erzeugt werden können. Die Versuche der KJ-Serie werden in einer neuen Versuchsanlage (Bild 4) durchgeführt, die mit dem

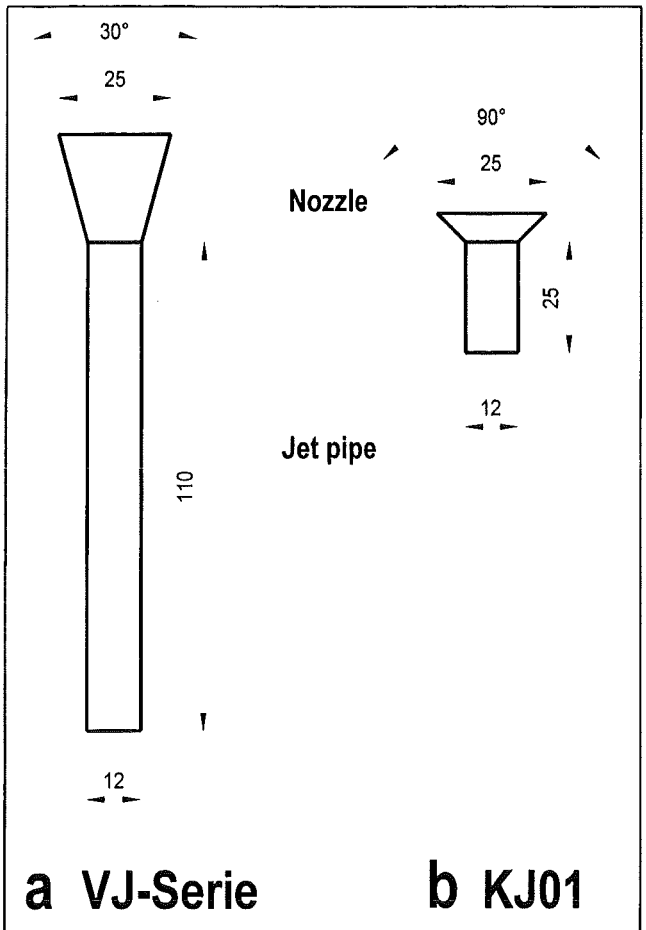

Bild 2. Bei KAJET eingesetzte Düsengeometrien

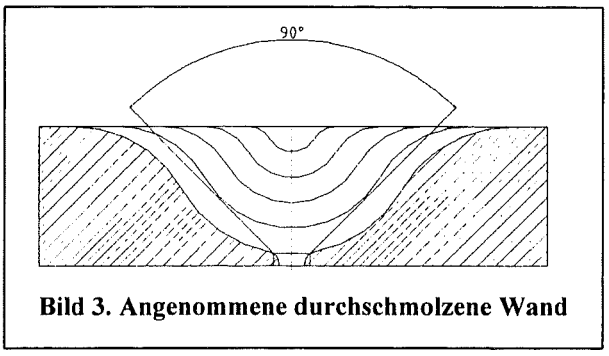

Bild 3. Angenommene durchschmolzene Wand

Versuch KJ01 zum erstem Mal eingesetzt wurde. Im Gegensatz zu den bisherigen Versuchsaufbauten handelt es sich um ein im wesentlichen geschlossenes System, das an eine Absauganlage angeschlossen ist. Mit dieser Anlage können sowohl reine Strahlversuche als auch Versuche zur Erosion durchgeführt werden. Im Falle der Erosionsversuche entfällt der Schlitten mit der Gitterfläche. Statt dessen wird im Inneren des Versuchsbehälters eine drehbare Halterung für die Probenkörper eingebaut.

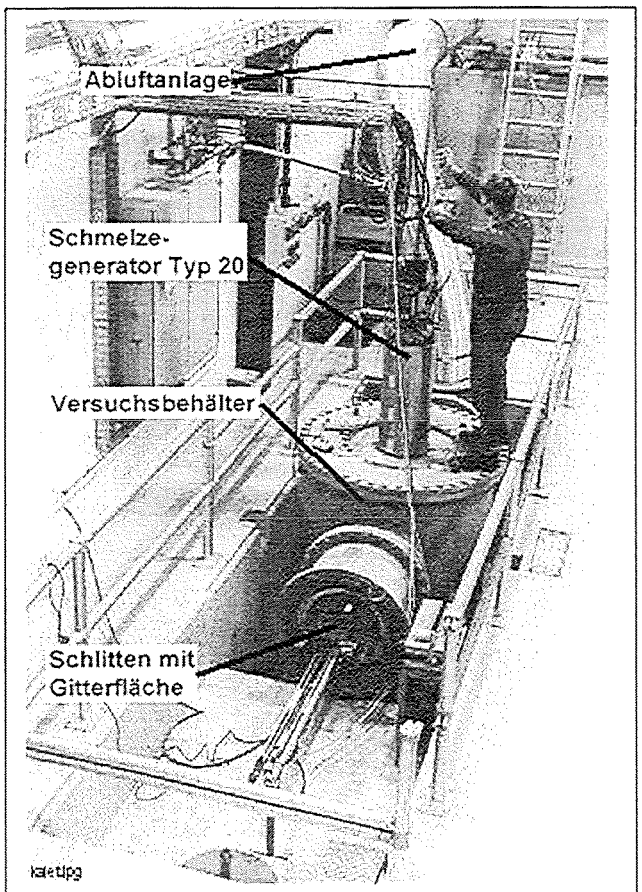

Bild 4. Neue KAJET-Anlage

4. Ergebnisse

Der Versuch VJ07 lieferte gute Ergebnisse zum Strahlverhalten von metallischer und oxidischer Schmelze beim Austritt unter Druck. Im Gegensatz zu den Versuchen VJ01 bis VJ03, bei denen die Düsen vorzeitig versagten, konnte hier erstmals der Austritt der Eisenschmelze beobachtet und aufgezeichnet werden. Der Strahldurchmesser 300 mm unter dem Austritt war über dem gesamten untersuchten Druckverlauf annähernd konstant, es konnte keine Abhängigkeit vom Druck festgestellt werden. Die Eisenschmelze trat deutlich kompakter aus als die oxidische Schmelze. Bei der oxidischen Schmelze kam es auch zu kleineren Aufplatzern des Strahls, was vermutlich von expandierenden Gasblasen hervorgerufen wird. Gas-Einschlüsse in der im Generator verbliebenen Oxidschmelze erhärten diese Vermutung.

Der Versuch KJ01 zeigt, daß auch mit Düsengeometrien, die eine realistischere Durchschmelzöffnung simulieren, kompakte Schmelzestrahle erzeugt werden können. Im Vergleich mit dem Versuch VJ07 sind die ermittelten Strahldurchmesser bei KJ01 sogar um den Faktor 2 kleiner. Auch hier waren im Bereich der beobachteten Länge von 300 mm die Schmelzestrahle über dem untersuchten Druckverlauf annähernd konstant und es konnte kaum eine Abhängigkeit vom treibenden Druck festgestellt werden. Wie bei VJ07 trat die Eisenschmelze deutlich kompakter aus als die oxidische Schmelze. Das Verhältnis Strahldurchmesser in 300 mm Abstand zu Düsendurchmesser (D/d) für die Versuche VJ05 bis VJ07 sowie KJ01 und zum Vergleich die Vorversuche mit Wasser sind in Tabelle 1 aufgetragen.

Tabelle 1. Bedingungen und Daten der wichtigsten Versuche

	Versuche mit Wasser	VJ05 Oxid	VJ06 Oxid	VJ07 1.Eisen + 2.Oxid	KJ01 1.Eisen + 2.Oxid
Ausgetretene Masse (kg)	14	10	10	20 + 20	20 + 20
Düse L/d	15 + 30	10	10	10	2,1
Temperatur[1] (°C)	Umgeb.	2000	2000	(keine Daten)	2050
Max. treibender Druck (MPa)	0,5 - 2,5	0,92	1,5	1,5 1,1	1,5 1,1
Max. Strahlgeschw. (m/s)	20 - 50	20,5	25	17 22,3	17 22,3
Strahlaufweitung[2] D^*/d	1,5 - 2,9	2,5	3 - 5,8	2,5 5	1,5 2,5

[1]Mit Pyrometer gemessen.
[2]Verhältnis der Strahlaufweitung auf einer beobachteten Strecke von 300 mm (200 mm im Fall von Wasser).

5. Weiteres Vorgehen

In den folgenden Versuchen stehen die Wechselwirkungen des Schmelzestrahls mit Auskleidungs- und Opfermaterialien im Vordergrund. Diese Versuche finden in der neu aufgebauten Anlage statt, in der bereits KJ01 durchgeführt wurde. Für den ersten Erosionsversuch (KJ02) wird die gleiche Düsengeometrie eingesetzt wie bei KJ01. Um mit der zur Verfügung stehenden Schmelzenmenge von 40 kg eine ausreichende Austrittsdauer für die Erosion zu erhalten, wird ein treibender Druck von 0,3 MPa eingestellt. Die beiden zu beaufschlagenden Probenkörper sind aus silikatischem Beton und werden um 90° versetzt auf einer drehbaren Halterung unterhalb des Strahlaustritts eingebaut. Die erste Probe wird von der Eisenschmelze beaufschlagt. Nachdem die Eisenschmelze ausgetreten, ist wird die zweite Probe in den Strahl des nun austretenden Oxids gedreht. In weiteren Versuchen wird die Schmelzenmasse schrittweise auf max. 300 kg erhöht. Dabei können der treibende Druck, die Substratmaterialien und in gewissen Grenzen die Schmelzentemperatur variiert werden.

IV. Similarity solutions for non-isothermal spreading and CORFLOW validation

(J.J. Foit, IATF)

Abstract

Recently, the spreading under gravity has received much attention in the field of nuclear safety research. In the case of a postulated melt down accident with a failure of the reactor pressure vessel, the ex-vessel melt will first be collected in the reactor cavity until a melt-through of a gate. Afterwards the gate opens, the corium melt is released into a spreading compartment. The current concept of the EPR (European Pressurised Water Reactor) relies on a sufficiently homogeneous spreading of the melt in order to ensure its coolability after a passive initiation of flooding by water. The conditions under which a complete spreading can be expected are the subject of current theoretical and experimental studies.

Zusammenfassung

Im Rahmen der nuklearen Sicherheitsforschung wird in letzter Zeit die Ausbreitung von Kernschmelzen unter Schwerkraft verstärkt untersucht. Bei einem hypothetischen Kernschmelzunfall mit Versagen des Reaktordruckbehälters sammelt sich die Schmelze zunächst in der Reaktorgrube, bis es zum Durchschmelzen des „Gate" kommt. Danach tritt die Schmelze in einen Ausbreitungsraum aus. Das derzeitige EPR-Konzept geht von einer ausreichend homogenen Ausbreitung der Schmelze aus, so daß diese nach dem passiven Eintritt der Flutung mit Wasser sicher gekühlt werden kann. Die Bedingungen, unter denen eine vollständige Ausbreitung zu erwarten ist, werden derzeit theoretisch und experimentell untersucht.

1. Introduction

In many applications the cooling process will lead to variable flow properties such as viscosity and, consequently, to a coupled system of the temperature and flow equations. It is impossible to satisfactorily treat this problem analytically. The lubrication approximation for low Reynolds-number-flow leads to an equation for which similarity solutions for various conditions have been found by many authors. The present paper gives the similarity solutions for the non-isothermal spreading of a volume of liquid which increases as a power law of time. The effect of cooling on the viscosity is represented by the time-dependent viscosity. The conditions under which these solutions can be applied are also discussed.

The numerical simulations are performed with the CORFLOW code which was developed at Siemens (Germany). The code allows to treat three-dimensional non-isothermal free surface flow. The influence of cooling on the spreading is modelled by a temperature dependent viscosity. The increase of the viscosity in the thermal boundary layer of the melt can eventually lead to a stop of the melt front. The above similarity solutions are used to validate the CORFLOW code. In the framework of large-scale KATS experiments (FZK, Germany) the non-isothermal spreading of metallic and oxidic melts on ceramic or concrete surfaces under various conditions are studied, e. g. melt overheat and melt release rates. The experimental findings from the KATS series and CORFLOW results are analysed.

2. Spreading with variable viscosity

2.1 Spreading of a constant volume

Using the lubrication theory the following evolution equation for the fluid shape $h(x,t)$ holds (Buckmaster, 1977):

$$\frac{\partial h}{\partial t} - \frac{1}{3}\frac{g}{\nu}\frac{\partial}{\partial x}\left(h^3 \frac{\partial h}{\partial x}\right) = 0 \quad \text{in} \quad \boldsymbol{R} \times (0,T) \tag{1}$$

where ν is the kinematic viscosity and g the gravity constant. The spreading of a fluid droplet with the shape $h_0(x)$ and the volume $\int_{\mathbf{R}} h_0(x)dx$ is described by Eq. (1) and the initial data

$$h(x,0) = h_0(x). \tag{2}$$

There is a well-established mathematical theory of the problem (1), (2) (Friedman, 1988).

One of the most important differences between the solutions of Eq. (1) and the solutions of the linear diffusion equation is the existence of solutions which vanish outside a closed and bounded set. Furthermore, the interface propagates with finite speed except possibly at $t = 0$.

The instantaneous release of the volume q of the fluid is described by the initial data given by

$$h(x,0) = q\delta(x) \tag{3}$$

where $\delta(x)$ denotes the Dirac distribution. A self-similar solution of the above problem was obtained by Zel'dovich and Kompaneets (1950).

In (Friedman, Kamin, (1980)) it was proven that the solution of Eq. (1) with the initial data given by Eq. (2) behaves asymptotically for $t \to \infty$ like the similarity solution with initial data (Eq. 3), i. e.

$$h_{h_0}(x,t) \xrightarrow[t\to\infty]{} h_\delta(x,t) \tag{4}$$

The above property allows to compare the long-term behaviour of the release of a fixed volume of fluid with predictions of the self-similar solutions as well it can be used for code validation.

In many applications the cooling process will lead to variable flow properties such as viscosity and, consequently, to a coupled system of the temperature and flow equations. It is impossible to satisfactorily treat this problem analytically. Assuming the viscosity to be a function of time of the form

$$\nu = \gamma t^\beta,\ \gamma = \frac{\nu_0}{t_0^\beta},\ \beta \geq 0 \tag{5}$$

where ν_0 is the initial viscosity of the fluid, self-similar solutions of Eq. (1) with initial data given by Eq. (3) were obtained by Sakimoto, Zuber (1995) and Foit (1997). To

derive the similarity solution in the axisymmetric geometry, Sakimoto and Zuber (1995) used instead the relation (5) the formula $\nu = \nu_0 t^{\beta}$ which cannot be correct for dimensional reasons. The solution of Eq. (1) with the initial data given by Eq. (3) and the fluid viscosity described by Eq. (5) can be written as

$$h(x,t) = \begin{cases} \left(\frac{3}{10}\right)^{1/3} \left(\frac{3q^2\gamma}{g}\right)^{1/5} \eta_f^{2/3} (1-\beta)^{\frac{\beta-1}{5}} \left[1 - \left(\frac{3\gamma}{gq^3}\right) \eta_f^{-2} x^2 t^{\frac{2}{5}(\beta-1)}\right]^{1/3} & \text{for } x_f^- \le x \le x_f^+ \\ 0 & \text{for } x_f^+ < x < x_f^- \end{cases} \tag{6}$$

where

$$x_f^{\pm} = \pm \eta_f \left(\frac{gq^3}{3\gamma}\right)^{1/5} t^{\frac{1}{5}(1-\beta)} \tag{7}$$

describes the position of the interfaces as a function of time. The constant η_f is given by

$$\eta_f = 2^{-3/5} \left[\frac{3}{10}(1-\beta)\right]^{-1/5} \left[\frac{1}{5}\pi^{1/2} \frac{\Gamma\left(\frac{1}{3}\right)}{\Gamma\left(\frac{5}{6}\right)}\right]^{-3/5} . \tag{8}$$

The right-hand side of Eq. (1), $\frac{\partial}{\partial x}\left(h^3 \frac{\partial h}{\partial x}\right)$, is not defined at the free boundary where $h = 0$ so that Eq. (6) is not a solution of (1) and (2) in the classical sense. The solution given by Eq. (6) may only be regarded as a generalized solution of equations (1) and (2) (Friedman, 1988).

2.2 Spreading with variable mass flux

The spreading of a liquid with a volume which increases as a power law of time is described by the following boundary-value problem:

$$\frac{\partial h}{\partial t} - \frac{1}{3}\frac{g}{\nu}\frac{\partial}{\partial x}\left(h^3 \frac{\partial h}{\partial x}\right) = 0 \ \ in \ \ \Omega = \boldsymbol{R} \setminus \{0\} \times (0,T) \tag{9}$$

$$h(x,0) = 0, \tag{10}$$

$$-\frac{1}{3}\frac{g}{\gamma} t^{-\beta} h^3 \left.\frac{\partial h}{\partial x}\right|_{x=0\pm} = f_{\pm}(t) \tag{11}$$

where $f_{\pm}(t)$ is the mass flux in the positive and the negative direction, respectively, and is given by

$$f_{\pm}(t) = \pm \frac{1}{2} \alpha q t^{\alpha-1}, \ \alpha > 0. \tag{12}$$

The integral of Eq. (9) over Ω together with Eq. (11) and Eq. (12) leads to

$$\int_{\mathbf{R}} h dx = q t^{\alpha}, \alpha > 0. \tag{13}$$

which is the global continuity equation.

The above boundary-value problem has an exact solution for every $\alpha = \frac{4}{3}(1-\beta)$ with $0 \le \beta < 1$:

$$h(x,t) = \begin{cases} \eta_f^{2/3} c_1 \left(\frac{3q^2\gamma}{g}\right)^{1/5} t^{\frac{1}{5}(2\alpha+\beta-1)} \left(1 - \frac{|\eta|}{\eta_f}\right)^{1/3} & \text{for } x_f^- \le x \le x_f^+ \\ 0 & \text{for } x_f^+ < x < x_f^- \end{cases} \tag{14}$$

with

$$\eta_f = \left[\frac{2}{3\alpha} c_1^4\right]^{-3/5}, \quad c_1 = \left[\frac{3}{5}(3\alpha - \beta + 1)\right]^{1/3}, \tag{15}$$

$$\eta = \left(\frac{3\gamma}{gq^3}\right)^{1/5} x t^{-1/5(3\alpha-\beta+1)} \tag{16}$$

and the positions of the interfaces

$$x_f^{\pm} = \pm \eta_f \left(\frac{gq^3}{3\gamma}\right)^{1/5} t^{-1/5(3\alpha-\beta+1)}. \tag{17}$$

Huppert (1982) used the global continuity equation (13) instead of the boundary-value condition (11) to determine approximate self-similar solutions of Eq. (9) for the

constant viscosity $(\beta = 0)$. In (Foit, 1997) the same approach was used to derive approximate similarity solution for all $0 \le \beta < 3\alpha + 1$, $\alpha > 0$. An approximate solution of Eq. (9) for $\alpha > 0$ and $0 \le \beta < 3\alpha + 1$ with the initial data (10) which fulfil the boundary condition (12) can be written as

$$h(x,t) = \begin{cases} \eta_f^{2/3} c_1 \left(\dfrac{3q^2\gamma}{g}\right)^{1/5} t^{\frac{1}{5}(2\alpha+\beta-1)} \left(1 - \dfrac{|\eta|}{\eta_f}\right)^{1/3} \left[1 + c_2\left(1 - \dfrac{|\eta|}{\eta_f}\right) + \ldots\right] & x_f^- \le x \le x_f^+ \\ 0 & x_f^+ < x < x_f^- \end{cases} \tag{18}$$

where

$$c_2 = \frac{3\alpha + 4\beta - 4}{24(3\alpha - \beta + 1)}, \tag{19}$$

$$\eta_f = \left[\frac{2}{3\alpha} c_1^4 (1 + c_2)^3 (1 + 4c_2)\right]^{-3/5} \tag{20}$$

and c_1, η and $x_f^{\pm}$ are given by Eqs. (15), (16) and (17), respectively.

The parameter range for α and β for which the solution (14) exists, is exactly the range for which $c_2 = 0$. If the condition (13) is used to determine the solution, the following relation for the constant η_f will be obtained (Foit, 1997):

$$\eta_f^{gl} = \left[\frac{3}{2} c_1 \left(1 + \frac{4}{7} c_2\right)\right]^{-3/5}. \tag{21}$$

The ratio $\dfrac{\eta_f}{\eta_f^{gl}}$ is a measure of the deviation from the mass conservation and can be used to determine the validity of the approximate solution (18) for given values of α and β.

The theory presented here is anticipated to be valid only if the viscous forces are much larger than the inertial forces. Using the arguments established in (Huppert, 1982) one can show that for flows for which $4\alpha - 3\beta - 7 < 0$ the viscous forces are dominant for all $t >> t_{tr}$. In the opposite case, i. e. for $4\alpha - 3\beta - 7 > 0$ the viscous forces are dominant for all $t << t_{tr}$. t_{tr} is the transition time at which the inertial and

viscous forces are equal. In (Foit, 1997) it was shown that if the parameter t_0 in Eq. (5) is chosen to be $t_0 = \tau_{tr}$,

$$\tau_{tr} = \left(\frac{1}{\eta_f^{10}\big|_{\beta=0}} \frac{q^4}{g^2 v_0^3} \right)^{-\frac{1}{4\alpha-7}} \tag{22}$$

which is the transition time for spreading with constant viscosity and flow rates determined by α, the transition time t_{tr} is given by

$$t_{tr}(a, \beta) = \left(\frac{\eta_f^{10}\big|_{\beta=0}}{\eta_f^{10}} \right)^{-\frac{1}{4\alpha-7}} \tau_{tr} \tag{23}$$

provided that $4\alpha - 7 \neq 0$. The following relation holds in case of $4\alpha - 7 = 0$

$$t_{tr}(a, \beta) = \left(\frac{\eta_f^{10}\big|_{\beta=0}}{\eta_f^{10}} \right)^{\frac{1}{3\beta}} \tilde{\tau}_{tr}^{-1} t_0. \tag{24}$$

$\tilde{\tau}_{tr}$ is obtained from Eq. (22) by setting $\alpha = \frac{3\beta + 7}{4}$. For $4\alpha - 3\beta - 7 = 0$ the condition under which the spreading is dominated by viscous forces for all times is given by the following inequality:

$$t_0 << \left(\frac{q^4}{\eta_f^{10} g^2 v_0^3} \right)^{-\frac{1}{3\beta}}, \ \beta \neq 0. \tag{25}$$

3. KATS experiments and CORFLOW results

3.1 Code description

The CORFLOW code (Wittmaack, 1996) simulates the free surface flow of an incompressible fluid in a 3-dimensional geometry. In addition to the fluid, several structure materials can be considered as hydrodynamic obstacles or thermodynamic heat sources. The fluid is assumed to possess Newtonian or non-Newtonian rheology. The free surface is determined by an equation which results from the free interface kinematic boundary condition and an integration of the continuity equation in the vertical direction. The free interface is represented as a height function either as a step

function or a second-order polynomial. Internal heat transport by conduction and convection as well as heat generation (decay heat) and heat transfer to the surroundings are modelled. The material properties, except the surface tension, may depend on temperature. A discrete phase transition model is available to simulate solidification and melting of the fluid and phase transition of the structure materials. The influence of the solidification process on the spreading is modelled by an increase of the viscosity. The increase of the viscosity in the thermal boundary layer of the melt can eventually lead to a stop of the melt front.

3.2 CORFLOW validation

CORFLOW has been validated using a variety of available analytical solutions. In addition, quite a few non-isothermal spreading experiments like KATS (Fieg et al., 1997a; Fieg et al, 1997b), COMAS (Steinwarz et al., 1997), CORINE (Veteau, 1995) have been simulated with variable success. In this paper, the solutions presented in Chapter 2 are used for validation.

Consider the spreading of a constant volume and the spreading of a constant flux, i. e. for $\alpha = 1$. The flow parameters, i. e. v_0 and q are chosen such that the transition time Eq. (22) τ_{tr} is equal to 1 s for both cases. Setting $t_0 = \tau_{tr}$ in Eq. (5) and shifting the time $t \to t + t^*$, $t^* = \max_{\beta \in [0, 3\alpha+1)} t_{tr}(\alpha, \beta) = t_{tr}(\alpha, 0) = \tau_{tr}$, one ends up with the initial data $h_0(x) = h(x, t + t^*)|_{t=0} = h(x, t^*)$ where h is given either by Eq. (6) or Eq. (18). The initial shape $h_0(x)$ is used to determine the initial conditions for CORFLOW simulations. The comparison of the evolution of the interfaces $x_f^+(t + t^*) - x_f^+(t^*)$ for the spreading of a constant mass flux and the spreading of a constant fluid volume for various values of β with the CORFLOW results are shown in Fig. 1 and Fig. 2, respectively. The CORFLOW results are in good agreement with the theoretical predictions for the spreading of a constant flux with increasing viscosity represented by $0 \le \beta \le 2$, whereas, the agreement in the case of the spreading of a constant volume can be stated to be good only for $0 \le \beta < 0.5$. For faster viscosity increase, i. e. for $0.5 \le \beta < 1$ CORFLOW overpredicts the front propagation considerably.

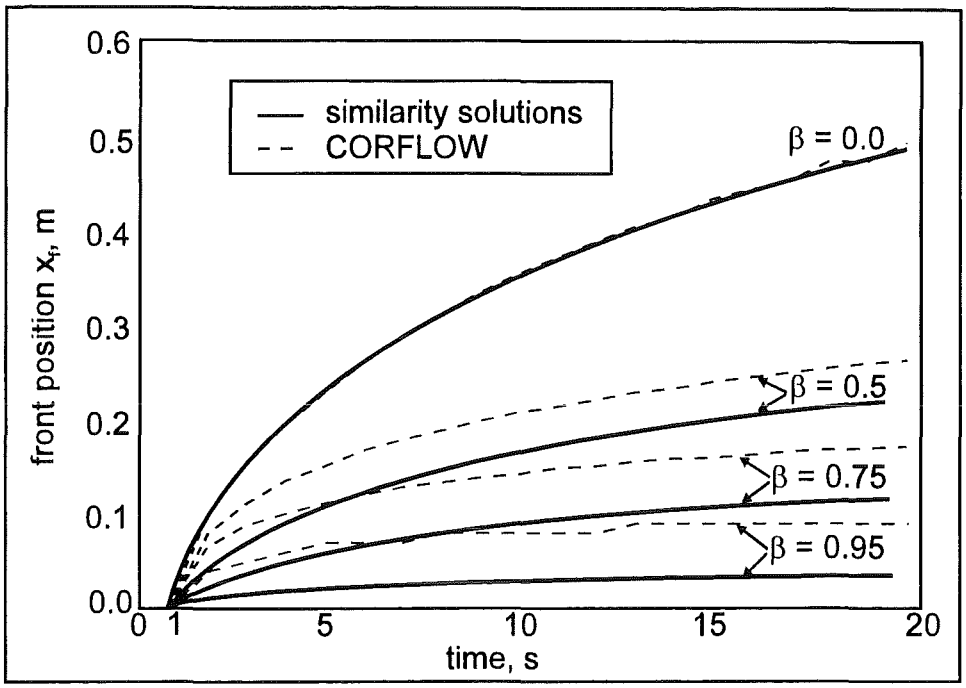

Fig. 1: Spreading of a constant volume

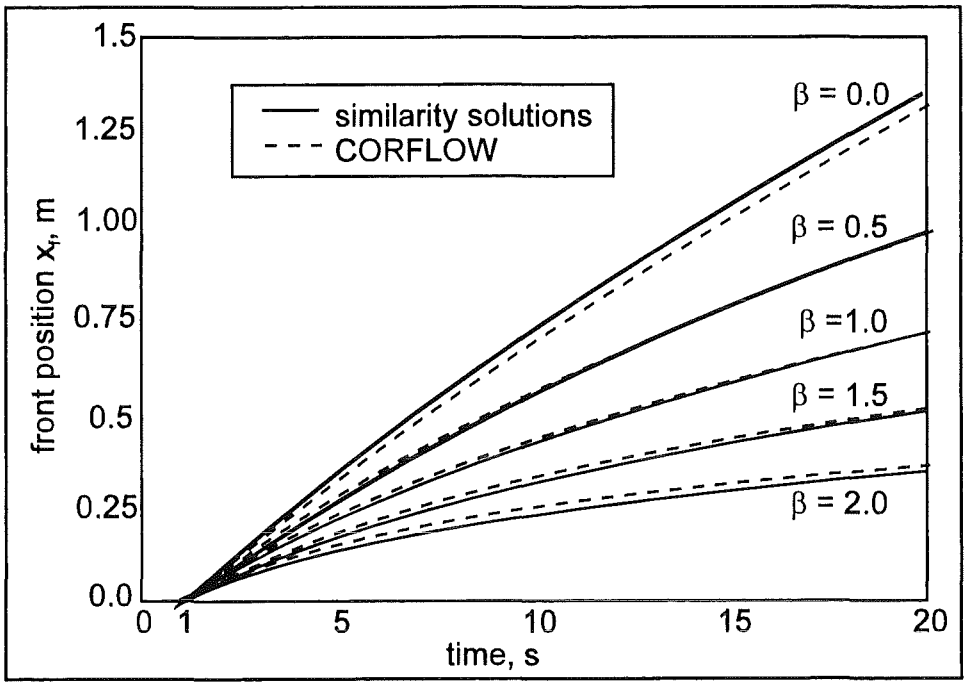

Fig. 2: Spreading of a constant mass flux

3.3 Analysis of the KATS experiments (oxidic melts)

In the framework of large-scale KATS experiments (FZK, Germany) the non-isothermal spreading of metallic and oxidic melts on ceramic or concrete surfaces under various conditions are studied, e. g. melt overheat, melt release rates. The metallic and oxidic components of the melt are generated by the thermite reaction. The oxidic melt is composed of about 85 weight % Al_2O_3, 10 weight % SiO_2 and about 5 weight % FeO. For the above melt mixture there is only a limited data base of material properties available. Using an estimated phase diagram, the Stedman correlation (Stedman, 1990) was applied to evaluate the viscosity within the solidus-liquidus range. Above the liquidus temperature the experimental data of Elyntin et al. (1969) were used (Fieg et al., 1997b). An experimental program to measure the viscosity of the oxidic KATS melts below the liquidus temperature is under way.

The KATS experiments can be classified in accordance with the melt release conditions. In KATS7 and KATS14 the melt was not collected but it was poured into a cavity. As soon as the cavity was filled, the melt began to spread across the channel with flow rates defined by the diameter of the pouring nozzle. In this way an almost constant mass flux was achieved which lasted 12 s in the KATS7 test and 37 s in the KATS14 test. The melt front propagation ended at 49 s in the KATS7 and at 57.6 s in the KATS14 test.
In the KATS5 (Fieg et al., 1997a) and KATS12 experiments, on the other hand, the melts were gathered in a container before spreading into the channel was initiated by opening a gate in the container. The outflow of the oxidic melt from the container was completed after 3.7 s and 10.4 s in the KATS5 and KATS12 tests, respectively. The stop of the melt front was detected at 15 s in the KATS5 and 40 s in the KATS12 experiment. This class of experiments is suitable for comparison with the results obtained for the isothermal spreading given in Eq. (7) in order to see the effects of the melt cooling on the melt front propagation. According to the asymptotic property (Eq. 4) this can be done for times which are larger than the outflow time from the container (Fig. 3).

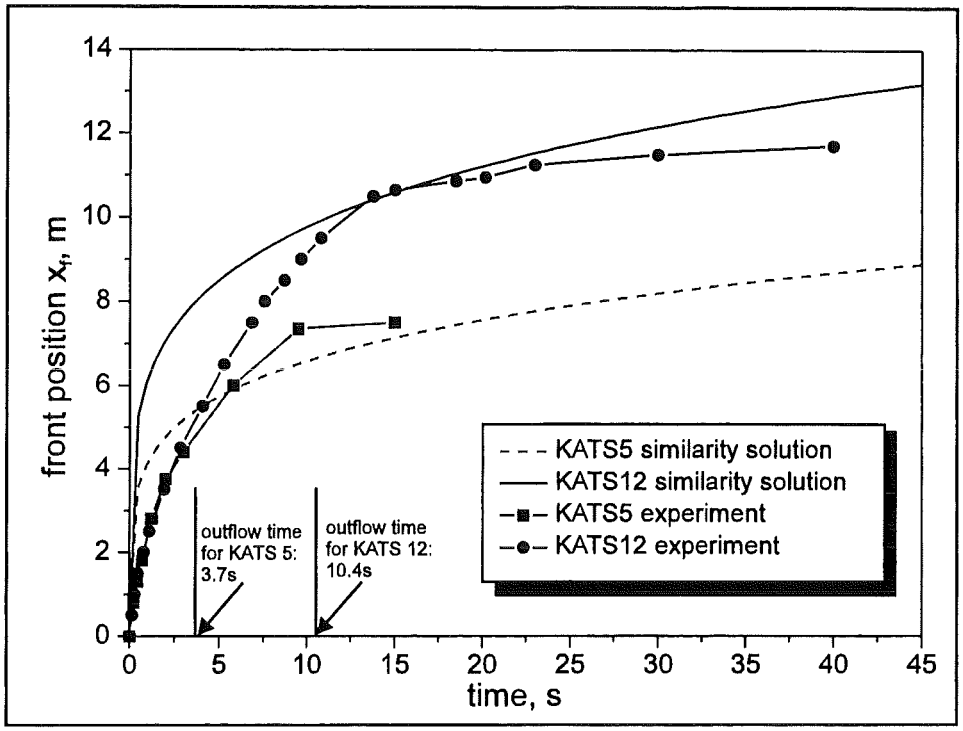

Fig. 3: *Comparison of the front propagation in KATS5 and KATS12 with the self-similar solution for isothermal spreading of a constant volume*

In both experiments the final front position is located in the neighbourhood of the isothermal curve. Due to the fairly large Péclet number for the oxidic melt under consideration, the spreading melt develops only a thin thermal boundary layer at the cooled boundaries. Consequently, the influence of this thin crust on the front propagation is weak until the time at which the buoyancy force is balanced by the strength of the developing crust.

4. Conclusions

The lubrication approximation for the spreading under gravity leads to a nonlinear degenerate parabolic equation. This equation admits solutions which have important properties, namely, they are zero outside a closed and bounded set and the interfaces propagate with finite speed. In many applications (e. g. the spreading of the oxidic core melt in the case of a melt down accident with a failure of the reactor pressure vessel) the cooling process will lead to an increase of the viscosity during the

spreading. Assuming that the increase of the viscosity can be represented as a power law of time, i. e. $\nu = \gamma t^{\beta}$, $\beta \geq 0$, self-similar solutions are derived for the spreading of a given volume of liquid and the spreading of a volume of liquid which increases with time as qt^{α}, $\alpha > 0$. The first case leads to a Cauchy problem with a well-established mathematical theory. The later case is described in terms of a von Neumann boundary-value problem which has an exact solution for every $\alpha = \frac{4}{3}(1-\beta)$ with $0 \leq \beta < 1$. For other values $\alpha > 0$ and $0 \leq \beta < 3\alpha + 1$ approximate similarity solutions are also given. The global continuity equation is used to determine the validity of the approximate solution for given values of α and β. The presented solutions are expected to be valid only if the viscous forces are much larger than the inertial forces. Some of the KATS experiments are suitable for comparison with the self-similar solutions for the isothermal spreading $(\beta = 0)$ of a constant fluid volume in order to see the effects of the melt cooling on the front propagation.

After the numerical deficiencies in the treatment of non-isothermal flows with increasing viscosity have been eliminated, there is a need for validation of the achieved modifications. For this purpose the self-similar solutions for spreading with variable viscosity are used. The CORFLOW results are in good agreement with the theoretical predictions for the spreading of a constant flux for a weak as well as for a strong increase of the viscosity with time. The agreement in the case of the spreading of a constant volume can be stated to be good only for a slow increase of the viscosity as a function of time. For faster viscosity increase CORFLOW overpredicts the front progression considerably.

5. References

Buckmeister, J.: J. Fluid Mech., 81, 735 (1977).

Elyntin, V. P. et al.: Russian Journal of Physical Chemistry 43, 3 (1969).

Fieg, G. et al.: FZKA-Report 5920, Forschungszentrum Karlsruhe (1997a).

Fieg, G. et al.: FZKA-Report 6605, Forschungszentrum Karlsruhe (1997b).

Foit, J. J.: FZKA-Report 6006, Forschungszentrum Karlsruhe (1997).

Friedman, A.; Kamin, S.: Trans. Amer. Math. Soc. 262, No. 2, 551 (1980).

Friedman, A.: "Variational Principles and Free Boundary Problems", Robert E. Krieger Publishing Company, Malabar, Florida, 589 (1988).

Huppert, H. E.: J. Fluid Mech., 121, 43 (1982).

Sakimoto, S. E. H.; Zuber, M. T.: J. Fluid Mech., 301, 65 (1995).

Stedman, S. J. et al.: J. Material Sci. 25, 1833 (1990).

Steinwarz, W. et al.: FISA-97-EU Research on Severe Accidents, EUR 18258EN (1998).

Veteau, J. M. et al.: FISA-95-EU Research on Severe Accidents, EUR 16896 EN (1996).

Wittmaack, R.: Nuclear Technology, 119, 158 (1997).

Zel'dovich, Ya. B.; Kompaneets, A. S.: Collection Commemorating the 70th Anniversary of A. F. Joffe, Izv. Akad. Nauk. SSR (1950).

32.21.05 Langfristige Containmentkühlung

I. SUCO-Programm

(G. Janssens-Maenhout, M. Daubner, J.U. Knebel, IATF)

Abstract

One possible concept for the decay heat removal from the containment of a future LWR after a core melt accident is based on passive sump cooling. The core-melt would spread as a dry melt and stabilise in the reactor sump, as in the reference concept for the European Pressurised Water Reactor EPR. After a number of plugs melt by passive means, water from the IRWST would flood the core melt with a low flow rate from above. The sump cooling is achieved by a stable natural circulation flow which transports the decay heat from the core melt to condensers and heat exchangers located within the sump area. The passive heat transfer mechanisms within the containment are vaporisation/condensation, convection and conduction.
The main objective of the sump cooling programme SUCO is to attain results on the feasibility of the sump cooling concept. The experimental and numerical work on this programme has progressed very well.

Zusammenfassung

Eine Möglichkeit der Nachwärmeabfuhr aus dem Containment eines zukünftigen LWR's nach einem Kernschmelzunfall basiert auf dem Sumpfkühlkonzept. Beim Referenzkonzept für den EPR wird davon ausgegangen, daß sich die Kernschmelze im Reaktorsumpf trocken ausbreitet und dort stabilisiert wird. Nachdem eine Reihe von Stöpseln passiv durchgeschmolzen sind, wird die Kernschmelze von oben langsam mit Wasser geflutet. Die Sumpfkühlung erfolgt durch eine stabile Naturkonvektionsströmung, die die Nachzerfallswärme von der Schmelze zu Kondensatoren und Wärmetauschern im Sumpfbereich transportiert. Die passiven Wärmetansportmechanismen innerhalb des Containments sind Verdampfung/ Kondensation, Konvektion und Übertragung.

Hauptziel des SUCO-Programms ist es, Aussagen über die Machbarkeit des Sumpfkühlkonzept zu erhalten. Die experimentellen und numerischen Arbeiten zum SUCO-Programm sind im Berichtszeitraum gut fortgeschritten.

1. Introduction

In the safety concept of the European Pressurised Water Reactor (EPR) the decay heat removal for the ex-vessel core melt down accident has to be analysed from Weishäupl and Bitterman (1993). For licensing purposes it has to be proved that a safety system can remove the decay heat from a flooded core in the sump out of the containment with a sufficient heat transfer rate so that the containment integrity remains unaffected. Thereby passive safety systems are envisaged because of their automatic, inherently safe operation, independent of human reliability. A passive cooling system can be designed based on boiling induced natural convection. Moreover subcooled nucleate boiling offers the potential of removing heat with a high heat transfer rate at low temperature differences. The behaviour of such a cooling system with subcooled boiling has been investigated by the test facility SUCOT, constructed at IATF (FZK).

2. Experiments

2.1. Large-Scale Experiments in the test facility SUCOT

The test facility is sketched in fig.1 and consists of a L-shaped slab geometry with a length of 4.5 m and a height of 5.5 m. Two operations modes, mixed convection and natural circulation, are possible. Here the mixed convection operation mode has been envisaged, in which subcooled water is pumped into the horizontal lower duct and heated up by the hot bottom plate. After a single-phase entrance length, vapour bubbles are generated (at the bottom plate) and transferred to the bulk fluid. There the bubbles are dragged with the saturated fluid flow, establishing a disperse two-phase region. Some bubbles may condense in a subooled region, others may reach the chimney, where they can rise up and continue to grow in size.

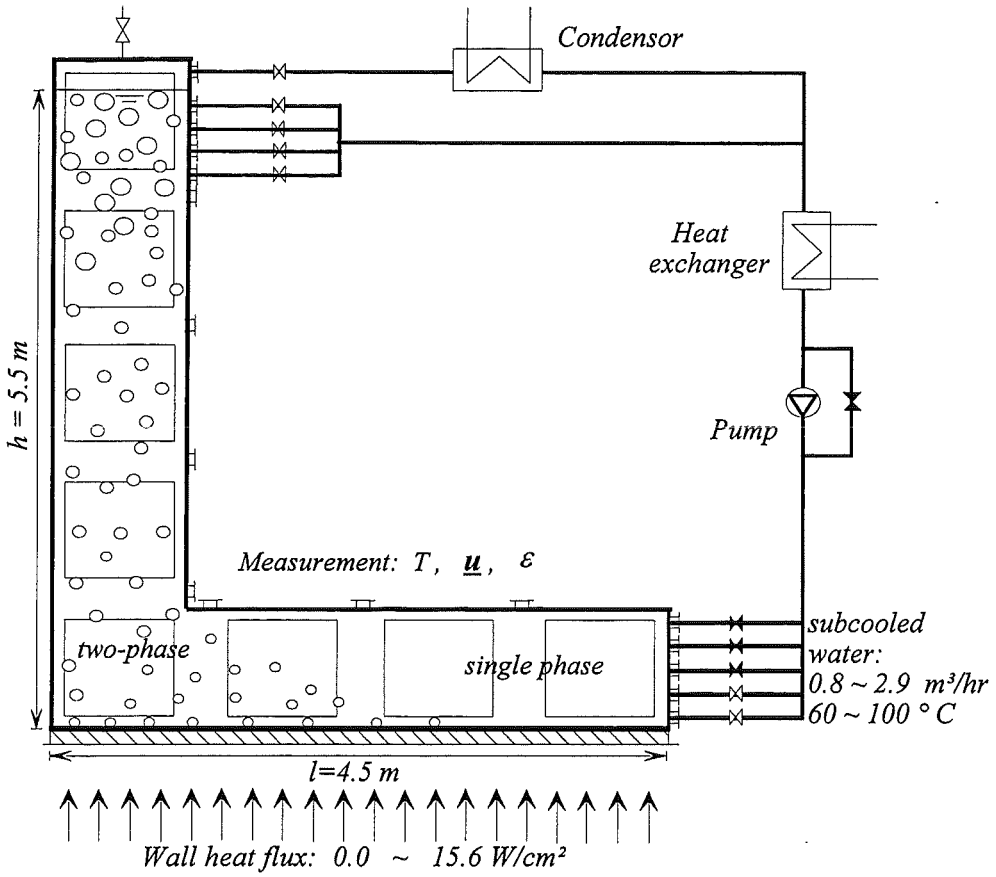

Figure 1: Sketch of the SUCOT test facility at the Forschungszentrum Karlsruhe.

The behaviour of the mixed convection in a partially single phase flow and partially disperse two-phase flow can from Ishii and Zuber (1970) be characterised by the Phase Change Number N_{PCh} and the Subcooling Number N_{Sub} , so that the stability of the operation mode can be defined.

The Phase Change Number describes the ratio of the inlet mass flux to the evaporation mass flux and is for a given inlet mass flow rate M_L *(kg/s)* and a given wall heat source Q_W *(W)* given here. The Subcooling Number describes for a given inlet temperature T_{Lin} *(°C)* the ratio of the inlet subcooling to the latent heat.

$$N_{PCh} = \frac{\dot{Q}_W \Delta\rho}{\rho_G \Delta h_{LG} \dot{M}_L} \quad \text{and} \quad N_{Sub} = \frac{\Delta\rho \, c_{pL} (T_{LPool} - T_{Lin})}{\rho_G \Delta h_{LG}}$$

With the different tests ran by the test facility SUCOT the operation diagram has been performed, presented in fig.2.

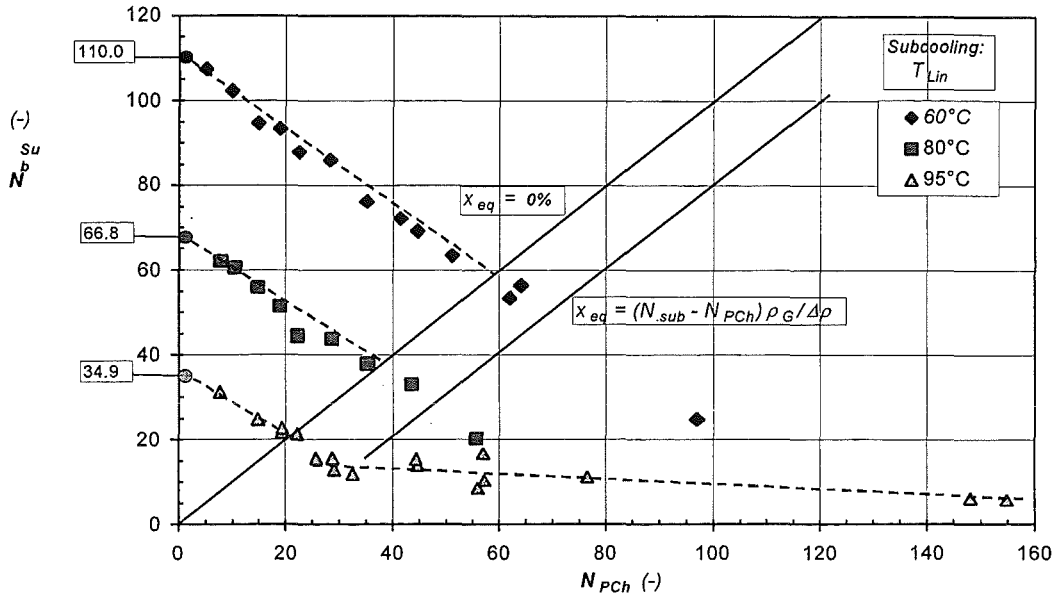

Figure 2: Operation diagram with working points of the test facility of SUCOT.

Almost all working points of the tests in the operation diagram are situated above the limit with zero equilibrium quality x_{eq}=*0%.* They correspond to the mixed convection flow of subcooled water. In this subcooled single-phase flow region, for each class of tests with a certain inlet temperature a linear dependency between the Subcooling Number and the Phase Change Number has been found. This linear function allows us with the chosen scaling to determine the temperature of the almost stagnant water in the upper layer of the horizontal lower duct, defined as the pool temperature. Further tests have to be run in order to investigate the region of higher Phase Change Number, corresponding with higher heat input boundary condition at the bottom plate. Therefore the heating bottom plates need to be replaced. Then the extended operation diagram can be used to determine a stability map for the cooling system.

In the horizontal lower duct temperature profiles have been measured by 6x18 NiCrNi-thermocouples and the void profiles have been determined by gamma densitometry with a ^{137}Cs source. The measurement techniques applied are described by Knebel et al. (1998). An example of typical temperature and void profiles are given in fig.3 for two different distances from the inlet.

The profiles at the position more close to the inlet, *x=3182mm* away from the left bottom corner, indicate a homogeneous temperature behaviour and void generation of *6%* at the heated bottom plate. The vapour bubbles formed at the heated wall are after detachment dragged with the fluid downstream so that in the bulk region no

void is left. The profiles at the position of *x=1400mm* represent a uniform distribution of the bubbles with an almost constant void of *4%* but an inhomogeneous temperature profile.

The fluctuation in the temperature profile at a height of *y=1400mm* is caused by the flashing effect in the vertical chimney. During the flashing phenomenon the direction in which the bubbles formed at the position *x=400mm* detache was reversed. The detachment in the opposite flow direction and the trajectories of dust particles in the water let state that the flashing induces a recirculation flow from the chimney downwards to the horizontal duct and around the inner corner of the L-shape upwards. In order to cope with the strong influence of the non stationary flashing phenomenon, additional tests with higher heat input and with void observations using fibre optic probes in the vertical chimney are needed.

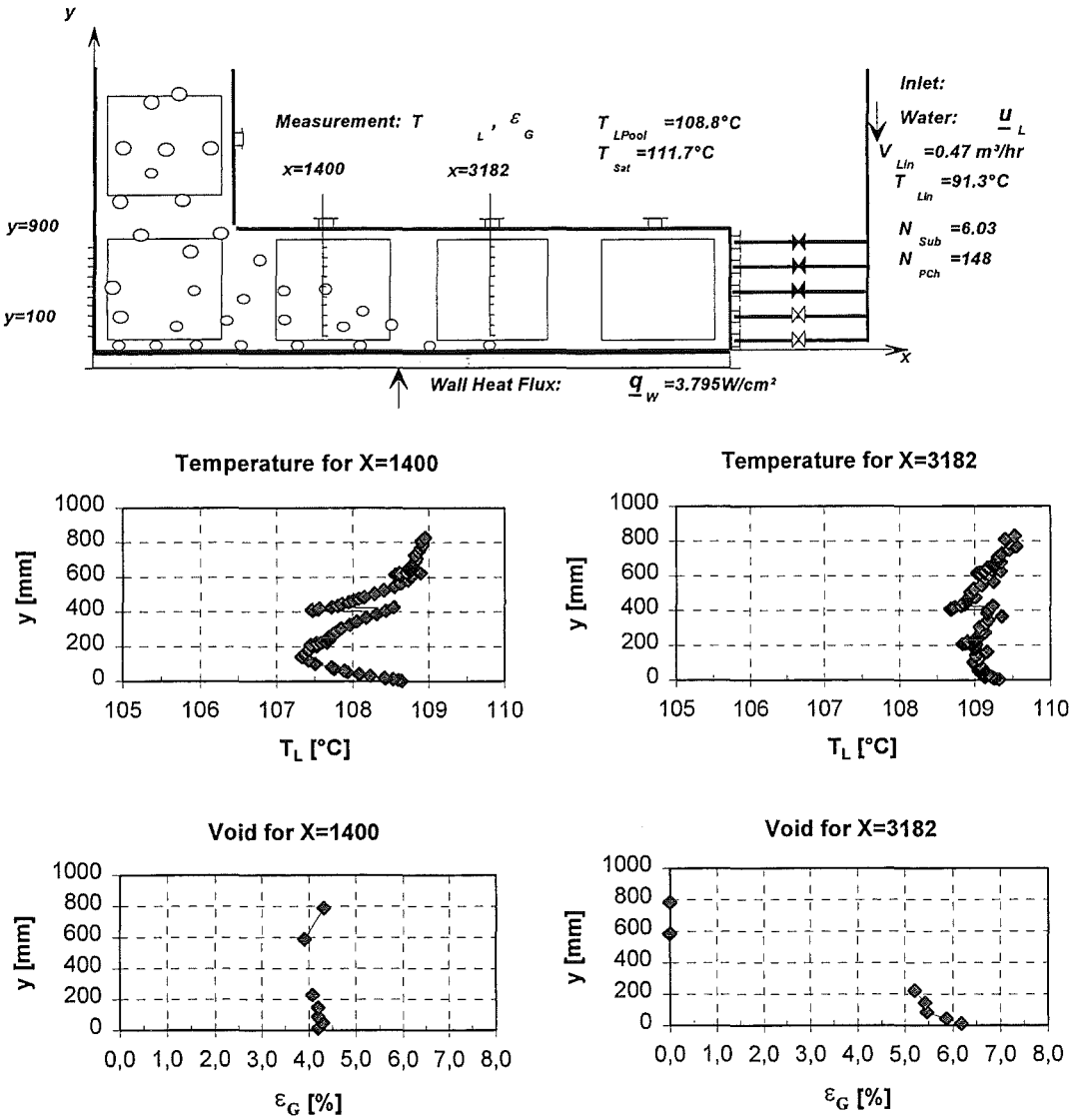

Figure 3: Temperature and void profiles at positions *x=1400mm* and *x=3182mm*.

2.2. Small-scale experiments

In the horizontal lower duct subcooled boiling establishes a transition of a single-phase to a disperse two-phase flow, whereas in the vertical chimney a bubbly plume is developed. Both phenomena have to be investigated, decoupled from each other, by means of two fundamental small-scale experiments. In a first experiment an extending bubbly plume of small air bubbles in stagnant water in a tube of *200mm* diameter and *1200mm* length will be investigated for different air injection systems at the bottom plate with a double fibre-optic probe. In a second subcooled boiling experiment with only the lower horizontal duct of the test facility SUCOT it is planned to derive the temperature diffusivity in the heated boundary layer with bubble formation using particle image velocimetry.

3. Numerical simulation

3.1. Modelling

Although for the scaling of the test facility SUCOT the drift flux model is used, it is common to numerically simulate test facilities of this size by means of the Eulerian two-fluid model form Yadigaroglu and Lahey (1976). The two-fluid-model describes the water and the vapour phase by two interpenetrating fields, yielding a compromise in the description between detailed bubble behaviour and global system response. Although single bubbles along their trajectories or an non stationary density waves may not followed, the two-fluid model is capable to describe a disperse two-phase flow in large detail and to treat a global change in bubble behaviour.

The two-fluid-model has been extended with physical models for the interfacial mass, momentum and energy transfer, as outlined in Janssens-Maenhout et al. (1998). Thereby a ideal dilute bubbly flow with bubbles as spherical particles has been assumed. The following phenomena were modelled in the commercial software package CFX4 : Interfacial forces for drag, lift, virtual mass and turbulent diffusion and a boiling model with a vapour source term at the heated wall and a condensate source term in the subcooled fluid bulk.

The models of the interfacial forces are validated by simulating the void redistribution in a turbulent bubbly flow experiment, in which radial void profiles for different symmetric and non-symmetric local air injections at the inlet of an upwards-directed air-water bubbly flow in a vertical tube have been measured. The boiling model is

validated by simulating the void generation of subcooled nucleate boiling in an internally heated annular water flow. The extended two-fluid-modelling has been documented by Janssens-Maenhout (1999).

Since in the test facility SUCOT a large number of non-spherical bubbles and a strong influence of non stationary flashing effects are observed, some modifications of the models for the interfacial forces and the subcooled boiling are needed. To cope with these deviations of the assumptions from the reality, it is under investigation to extend the two-fluid model with an additional transport equation for the interfacial area density. Such an equation for the interfacial area density has been proposed by Ishii et al. (1998) and yields with source and sink terms for the interfacial area density a more flexible handling of the bubble behaviour with deformation, coalescence or partitioning.

3.2. Verification by single phase flow simulation

A verification of the single phase flow with heat transfer in the test facility SUCOT has been performed. The high Rayleigh Number, up to 10^{12} is expensive in computational time. Since the heat diffusion has a characteristic time scale of 7.10^7, a calculation for a real time of the order 10^8 is required to solve fully the unstable layer. A two-dimensional grid with 44114 cells and a horizontal cell width Δx_C varying between 5mm and 20mm and a vertical cell height Δy_C varying between 5mm and 50mm. In the calculation processus a stepwise approach is followed: starting from single phase forced convection flow, simulated with the two-fluid-model, including the Low-Reynolds-Number turbulence model, and then increasing the heat flux, adding buoyancy and the interfacial exchange terms of a dispersed two-phase flow. First simulation results are represented in fig.4.

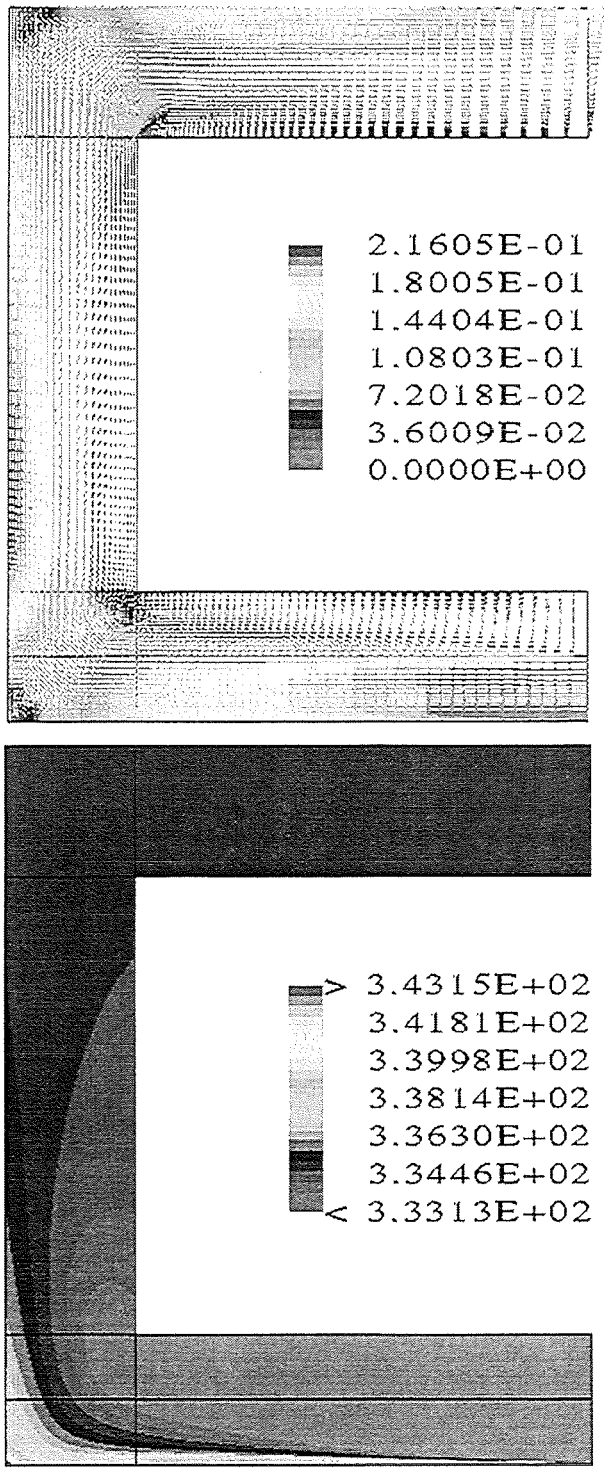

Figure 4: Typical velocity vectors and temperatures shaded contours in SUCOT.

A verification of the single-phase flow, simulated with the two-fluid-model is needed in order to guarantee good initial conditions for a smooth transition two the dispersed two-phase flow. Further validation can be carried out by comparing the measured temperature profiles for working points with low Phase Change Number.

3.3. Perspective for two phase flow simulation

First attempts to model the boiling flow indicated that a time-dependent analysis of the interfacial area is needed. Therefore the two-fluid model extension with the interfacial area density transport equation form Ishii et al. (1998) should be considered. Further an improvement of at IATF developed boiling model will be required, to fix the for the test facility appropriate empirical correlations.

4. Conclusions

In the safety concept of the EPR a passive cooling system has to be designed, with a sufficient heat transfer capacity for a decay heat removal from a flooded core in the sump out of the containment without containment integrity loss. A variety of investigations, such as large-scale and small scale experiments, extension of the two-fluid-model, code validation and development is pursued to achieve the overall goal of a reliable simulation of such a passive cooling system.

The SUCOT test facility scales with the full height of the prototype, so that buoyancy effects and bubbly flow development of such passive cooling system under fairly reactor-typical conditions can be demonstrated. During the operation of the test facility regimes with quiescent subcooled boiling as well as regimes of sudden flashing are observed. Additional tests must be run for higher Phase Change Number, for which bottom plates with higher heat fluxes are needed. The small-scale experiments concentrate on single effects and therefore can give detailed information on the development of a bubbly plume and on the temperature diffusivity of a heated boundary layer with generation of vapour bubbles.

The two-fluid-model in the software package CFX4 is extended for flows with subcooled boiling by physical models, which describe interfacial mass momentum and heat transfer and are thoroughly validated by Janssens-Maenhout (1999). To cope with the non stationary strong change in bubbly flow behaviour, the evolution of the interfacial area density should additionally be taken into account.

5. References

CFX Int. Services (Harwell Lab.), *CFX4.1 Flow Solver User Guide*, AEA Technology plc, Oxfordshire, 1995

Ishii, M., Wu, Q. Assad, A. and Uhle, J., "Interfacial Area Transport Equation for Two-Fluid Model Formulation", *Proc. Of the ImuST Meeting (Santa Barbara),* November 1998

Ishii, M. and Zuber, N., "Thermally Induced Flow Instabilities in Two Phase Mixtures", *Proc. 4th Int. Heat Transfer Conf. (Paris),* B-5.11, 1970

Janssens-Maenhout, G., *Beiträge zur Modellierung und numerischen Simulation von Zweiphasenströmungen mit Wärmeübertragung,* PhD Thesis, University of Karlsruhe, FZKA 6228, 1999

Janssens-Maenhout, G. Knebel, J.U. and Müller, U., "Subcooled Nucleate Boiling at Low Pressure and Low Heat Flux", *Proc. Of the 3rd Int. Conf. On Multiphase Flow (Lyon)*, pp.1-8, 1998

Knebel, J.U., Janssens-Maenhout, G. "Boiling Induced Mixed Convection in Cooling Loops", *Proc. 36th European Two-Phase Flow Group Meeting (Portoroz),* June, 1998

Weishäupl, H. A. and Bitterman, D., "Large Spreading of Core Melt for Melt Retention / Stabilization", *Proc. of 5th Int. Seminar on Containment of Nuclear Reactors, (Karlsruhe),* pp.347-355, August 1993

Yadigaroglu, G. and Lahey, Jr. R. T., "On the Various Forms of the Conservation Equations in Two-Phase Flow", *Int. J. of Multiphase Flow*, N° 2, pp.477-494, 1976

II. Analyse der einphasigen Langzeitkühlung des Sumpfes mit dem Rechenprogramm FLUTAN

(G. Grötzbach, L. Carteciano, B. Dorr, IRS)

Zusammenfassung

Das FLUTAN-Rechenprogramm wird für die numerische Interpretation und für die quantitative Übertragung der Ergebnisse der SUCOS-Experimente, SUCOS-2D und 3D, zur einphasigen Langzeitkühlung der Kernschmelze im Sumpf des Europäischen Druckwasserreaktors EPR nach einem optionalen SIEMENS-Konzept eingesetzt. Nach der erfolgreichen Nachrechnung und Interpretation der zweidimensionalen Modellversuche SUCOS-2D wird hier über die Vorbereitung zur Nachrechnung der dreidimensionalen Experimente SUCOS-3D detailliert berichtet. Es wurden die Gitterspezifikation und die FLUTAN-Eingabe entwickelt. Eine „quasi-transiente" Rechnung von einer Stunde Realzeit wurde erfolgreich durchgeführt. Die Felder der Geschwindigkeit und der Temperatur werden qualitativ richtig wiedergegeben. Die quasi-transiente Rechnung soll bis ungefähr 4 Stunden Realzeit fortgesetzt werden, um dann die transiente Rechnung anschließen zu können.

Einleitung und Zielsetzung

Das Rechenprogramm FLUTAN [1] wird im Forschungszentrum Karlsruhe für die quantitative Übertragung der Ergebnisse der SUCOS-Experimente [2] zur einphasigen Langzeitkühlung der Kernschmelze im Sumpf des EPR eingesetzt. Die erfolgreichen zwei- und dreidimensionalen Nachrechnungen der zweidimensionalen Experimente SUCOS-2D wurden kurz in [3,4,5] vorgestellt. Über erste Versuche, die lokale Gitterverfeinerung an diesem Anwendungsbeispiel zu überprüfen, wird unter 32.22.02 berichtet [6]. Der nächste Schritt der Interpretation der einphasigen SUCOS-Experimente mit FLUTAN ist die Nachrechnung der dreidimensionalen Experimente SUCOS-3D. In diesem Bericht wird über die Vorbereitung zur Nachrechnung von SUCOS-3D detailliert berichtet. Noch in diesem Jahr soll die Nachrechnung von SUCOS-3D und dessen Interpretation abgeschlossen werden

und damit die Eignung von FLUTAN für die Interpretation der entsprechenden Modellexperimente SUCOS nachgewiesen werden.

Vorbereitung für die Simulation von SUCOS-3D.

Die mit FLUTAN durchgeführten numerischen Analysen von SUCOS-2D wurden mit der Aussage abgeschlossen, daß diese Testanlage nicht zufriedenstellend mit einer zweidimensionalen Rechnung simuliert werden kann, da bedeutende dreidimensionale Vorgänge im Experiment auftreten. Diese Effekte werden im Experiment SUCOS-3D wegen der geringeren Flächenanteile der Zuleitungsrohre zu den Kühlern im Grundriß des Modells einen geringeren Einfluß haben. Für die Nachrechnung des dreidimensionalen Experimentes SUCOS-3D heißt das, daß diese quantitativ kaum abschätzbaren Effekte, auch wenn sie teilweise von relativ geringerer Bedeutung sind als in SUCOS-2D, dennoch erfaßt werden müssen. Der numerische Aufwand für solche Rechnungen wird also erheblich sein.

Im Rahmen der Vorbereitung der dreidimensionalen Nachrechnung der Testanlage SUCOS-3D wurde die Gitterspezifikation und die FLUTAN-Eingabe entwickelt. Die Abbildung 1 zeigt die Komplexität der Geometrie von SUCOS-3D mit verschiedenen Strukturen, die bis ins Detail modelliert werden müssen. Wegen der Symmetrie der Anlage reicht es aus, die Hälfte des Behälters zu simulieren. Die Geometrie enthält schräge Ränder, die in FLUTAN mit Hilfe von sogenannten irregulären Zellen modelliert werden können. Die Gitterrichtung wurde so ausgewählt, daß möglichst wenige Wände als schräger Rand modelliert werden und daß die Strömung überwiegend parallel zur Gitterrichtung fließt. Die Draufsicht des ausgewählten Gitters ist in der Abbildung 2 dargestellt. Die Maschenweite des Grundgitters in der Draufsicht beträgt 4 mm. Die Maschenweite variiert von 8 mm bis 1 mm bei den vertikalen Kühlern. Hier ist eine feine Auflösung der Grenzschichten des Geschwindigkeitsfeldes und des Temperaturfeldes notwendig. In der vertikalen Richtung variiert die Maschenweite von 1,5 bis 8 mm. Alle Änderungen der Maschenweiten sind so abgestimmt, daß die Änderungen der Maschenweiten zwischen zwei Nachbarzellen den Faktor 2 nicht überschreiten. Es wird so gewährleistet, daß der Fehler im

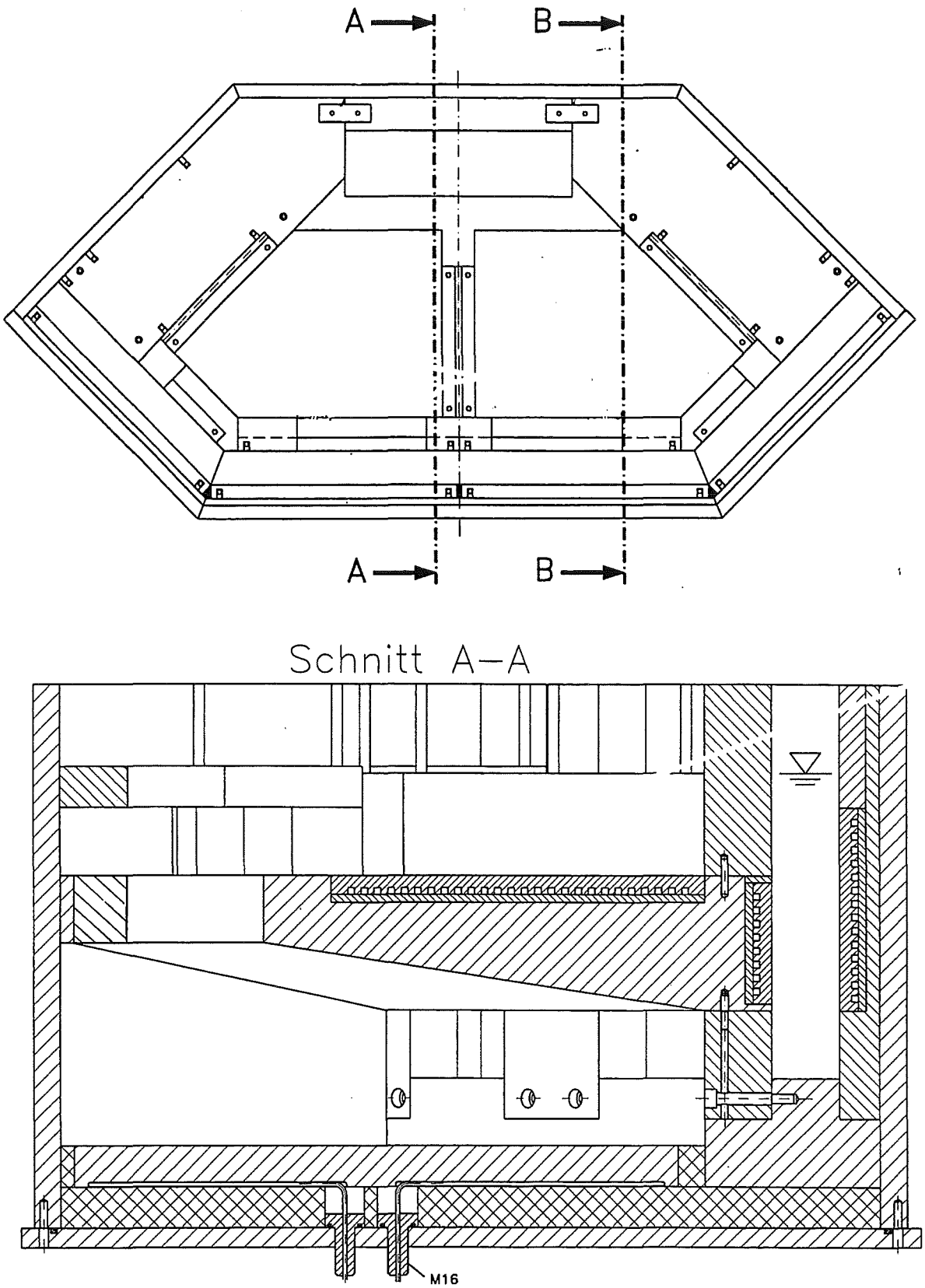

Abb. 1: Draufsicht und Schnitt A-A der Testanlage SUCOS-3D [7]

Diffusionsterm durch nicht-äquidistante Maschenteilung gering bleibt. Für die ersten Rechnungen wird keine lokale Gitterverfeinerung benutzt, da die Implementierung dieses Verfahrens noch vervollständigt werden muß [6]. Das Gitter besteht aus 691 000 Fluidmaschen und 99 500 Oberflächenelementen.

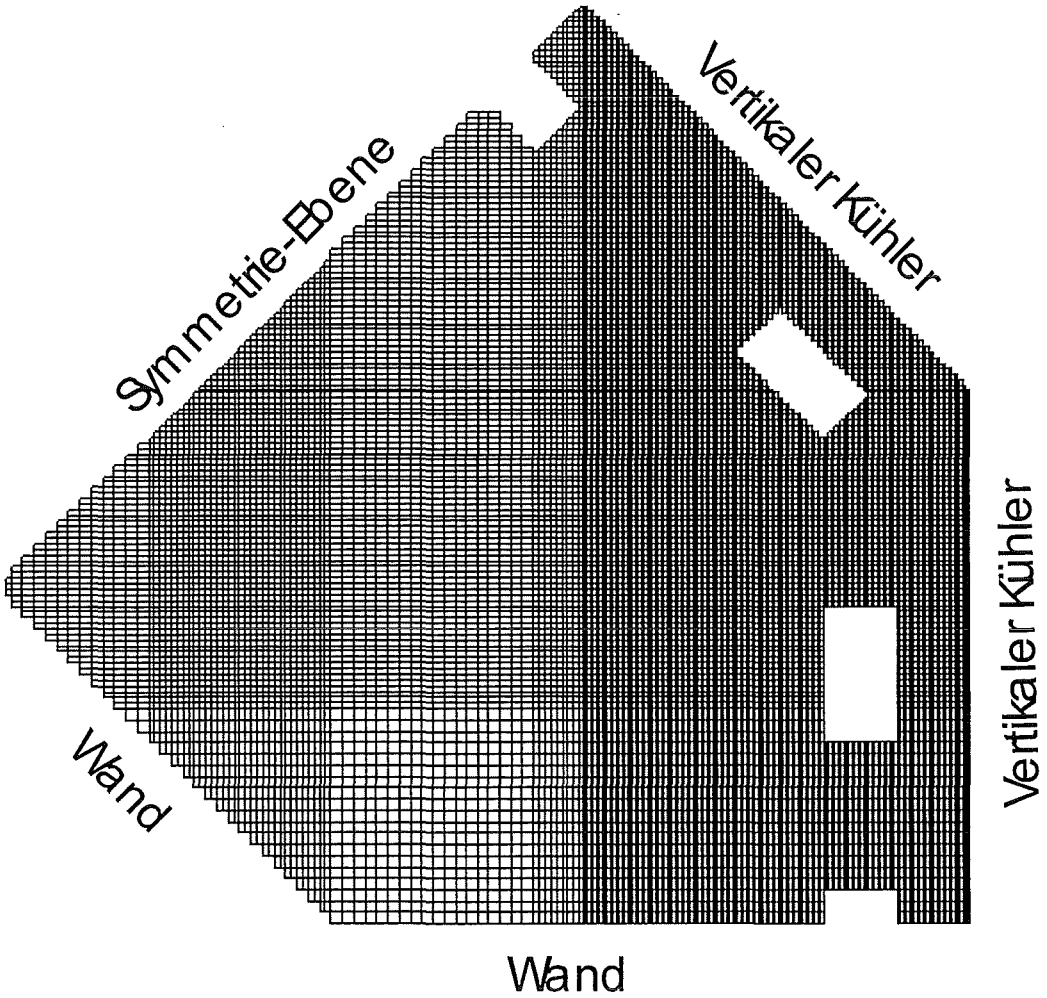

Abb. 2: Draufsicht auf das Rechengitter für SUCOS-3D

Die thermischen Randbedingungen für die Simulation von SUCOS-3D wurden mit Hilfe der Erfahrung aus der numerischen Interpretation von SUCOS-2D entwickelt. Alle Wände werden adiabat betrachtet, da die Nachrechnung von SUCOS-2D gezeigt hat, daß die Wärmeverluste durch das Strukturmaterial der Wände vernachlässigbar klein bleiben. Die vertikale mittlere Ebene der Anlage wird als Symmetrieebene ohne Haftbedingung betrachtet. In SUCOS-3D sind vertikale, horizontale und aufrecht stehende Kühler vorhanden. Es wurde ein Experiment ausgewählt, bei dem alle aufrechten Kühler und der ‚innere'

vertikale Kühler nicht in Betrieb waren. Dieses Experiment ist dann vergleichbar mit dem Experiment in SUCOS-2D, das bereits numerisch untersucht wurde. Die Nachrechnungen von SUCOS-2D haben gezeigt, daß eine detaillierte Simulation der Kühler mit dem Wärmetauschermodell nicht notwendig ist. Die Simulation der Kühler mit einer Temperaturverteilung auf den Kühleroberflächen ist ausreichend. Die aktiven vertikalen Kühler werden in SUCOS-3D mit einer Temperaturverteilung auf der Kühleroberfläche simuliert. Für die horizontalen Kühler wird eine konstante Temperatur als Randbedingung vorgegeben, weil der Unterschied der Aus- und Eintrittstemperatur des Kühlmittels im Experiment kleiner als ein Grad bleibt. Die Kühleranschlußrohre werden auch bei SUCOS-3D im Detail modelliert.

Die Heizplatte aus Kupfer wird mit dem dreidimensionalen Wärmeleitungs-Strukturmodell modelliert, um die Umverteilung der Wärme in der Struktur zu simulieren. Die Platte wird mit einem Gitter diskretisiert, das an das angrenzende Maschengitter des Fluidraumes angepaßt wird. Dadurch ergeben sich alle Randbedingungen an den Kontaktflächen zwischen Fluid und Struktur automatisch. Die Heizleiter unter der Heizplatte werden mit einem konstanten Wärmestrom von 630 W als Randbedingung für diese Struktur modelliert. In der Kupferplatte wird die diskretisierte dreidimensionale Wärmeleitungsgleichung gelöst. Der aufrechte Kühler, der an der Seitenwand steht, wird auch mit dem Strukturmodell modelliert. Im Gegensatz zu den anderen aufrechten Kühlern steht dieser Kühler aus Kupfer auf dem horizontalen Kühler ohne thermische Isolation. Die Heizplatte und der aufrechte Kühler werden mit 58 000 Strukturmaschen modelliert.

Eine stationäre Ausgangssituation wird mit einer "quasi-transienten" Rechnung errechnet, die als Start für die echte transiente Rechnung mit ausiterierten Ergebnissen pro Zeitschritt dient. Wie in der Rechnung von SUCOS-2D wird sowohl auf den Gleichgewichtszustand der bilanzierten Wärmeströme als auch auf die Temperaturentwicklung im Fluidraum geachtet, um die Ausgangssituation für eine transiente Rechnung zu erkennen.

Für die "quasi transiente" Rechnung zum Erzielen der stationären Anfangslösung wird ein implizites Zeitintegrationsverfahren mit einem Zeitschritt von 5 s benutzt. Das Druckgleichungssystem wird mit dem iterativen CRESOR Solver gelöst, während das Energie-

gleichungssystem mit dem iterativen SOR-Solver gelöst wird. Für die Behandlung der konvektiven Terme wird das Upwind-Differenzenverfahren 1.Ordnung eingesetzt. Ein Turbulenzmodell braucht nicht angewendet zu werden, weil die Strömung laminar ist.

Die "quasi-transiente" Rechnung wurde bisher für eine Stunde Realzeit durchgeführt. Diese Realzeit entspricht ungefähr 90 Stunden CPU-Zeit. Die Rechnung wird auf einer CRAYJ916 mit einem Hauptspeicherbedarf von 2.7 Gbyte durchgeführt. Obwohl 8 Prozessoren verlangt wurden, lief die Rechnung wegen der schlechten Parallelisierbarkeit des Programms dominant nur auf einem Prozessor. In der Abbildung 3 wird das berechnete Temperaturfeld dargestellt. Aus diesem Bild kann man die Komplexität der simulierten Geometrie erkennen und wie diese Geometrie mit FLUTAN im Detail bis zu den Kühleranschlußrohren modelliert wird (enge Gebiete mit niedrigerer Temperatur). Die numerischen Ergebnisse haben gezeigt, daß das Konvergenzverhalten bisher erwartungsgemäß ist. Die Felder der Geschwindigkeit und der Temperatur werden qualitativ richtig wiedergegeben. Ein quantitativer Vergleich mit dem Experiment ist noch nicht möglich, da die Rechnung fortgesetzt werden muß.

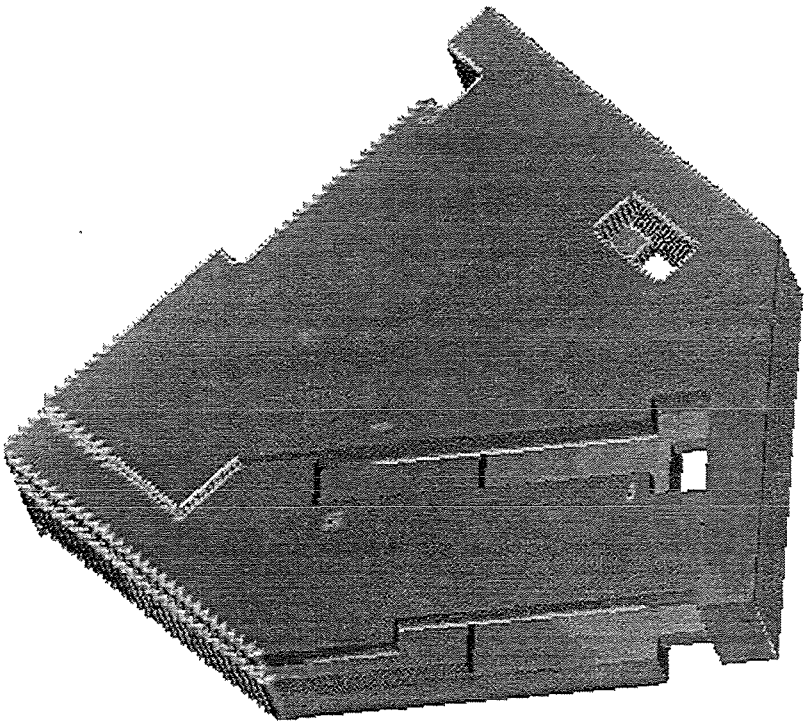

Abb. 3: Temperaturfeld auf den Strukturoberflächen der dreidimensionalen Rechnung nach 1h Realzeit der quasi-transienten Rechnung.

Schlußfolgerung

Das FLUTAN-Rechenprogramm wird für die numerische Interpretation und für die quantitative Übertragung der Ergebnisse der SUCOS-Experimente zur Analyse der einphasigen Langzeitkühlung der Kernschmelze im Sumpf des Europäischen Druckwasserreaktors EPR nach einem optionalen SIEMENS-Konzept eingesetzt. Das experimentelle SUCOS-Programm zur Untersuchung des einphasigen Langzeitverhaltens wurde mit einer zweidimensionalen skalierten Testanlage SUCOS-2D und mit einer dreidimensionalen skalierten Testanlage SUCOS-3D durchgeführt. In einem ersten Schritt wurde die Nachrechnung und die Interpretation eines zweidimensionalen Modellversuches von SUCOS-2D erfolgreich abgeschlossen. Aufbauend auf diesen Erfahrungen aus dem letzten Berichtszeitraum wird nun ein dreidimensionales SUCOS-3D Experiment untersucht. Hier wurde über die Vorbereitung zur Nachrechnung der dreidimensionalen Experimente SUCOS-3D detailliert berichtet. Es wurden die Gitterspezifikation und die FLUTAN-Eingabe (Randbedingungen) entwickelt. Mit einer genauen numerischen Abbildung der Testanlage wird eine möglichst gute Reproduktion des Experimentes versucht und die Mechanismen in der Strömung detailliert analysiert. Eine „quasi-transiente" Rechnung wurde erfolgreich begonnen. Nach einer Stunde Realzeit zeigen die numerischen Ergebnisse, daß das Konvergenzverhalten bisher erwartungsgemäß ist. Die Felder der Geschwindigkeit und der Temperatur werden qualitativ richtig wiedergegeben. Die quasi-transiente Rechnung soll bis ungefähr 4 Stunden Realzeit fortgesetzt werden, um dann die transiente Rechnung durchführen zu können. Die Interpretation der einphasigen SUCOS-Experimente mit FLUTAN wird mit der Auswertung der transienten Rechnung und mit der Interpretation von SUCOS-3D beendet und mit einem Bericht abgeschlossen werden.

Literatur

1 G. Willerding, W. Baumann,
FLUTAN 2.0 - Input Specifications
Forschungszentrum Karlsruhe, FZKA 5712, Mai 1996

2 J. U. Knebel,
SUCO-Programm
Projekt Nukleare Sicherheitsforschung Jahresbericht 1995,
Forschungszentrum Karlsruhe, FZKA-5780, August 1996, S. 224 - 239

3 G. Grötzbach, M. Wörner, A. Blahak, L. Carteciano, B. Dorr, W. Olbrich, W. Sabisch, Q. Ye, M. Alef, St. Genz, G. Janßen, M. Linder, N. Lehmann, A. Müller, X. Jin,
Entwicklung von Thermofluiddynamikprogrammen und ingenieurtechnischen Anwendungen.
Projekt Nukleare Sicherheitsforschung, Jahresbericht 1997,
Forschungszentrum Karlsruhe, FZKA 6162, September 1998, pp. 486 - 504

4 L. Carteciano, B. Dorr, G. Grötzbach,
Theoretical interpretation of the thermal and fluiddynamical conditions in single-phase SUCOS-experiments with the FLUTAN code.
9th IAHR Working Group Meeting on Advanced Nuclear Reactor Thermal Hydraulics, Grenoble France, April 7-9,1998

5 G. Grötzbach, L. Carteciano, B. Dorr,
Interpretation der einphasigen SUCOS-Experimente mit FLUTAN.
In: Zusammenarbeit FZK/EVU/Siemens, Untersuchungen zu auslegungsüberschreitenden Ereignissen (Unfällen) in Leichtwasserreaktoren, S. 398 – 411,
Forschungszentrum Karlsruhe, interner Bericht, März 1998

6 G. Grötzbach, L. Carteciano, M. Wörner, A. Blahak, B. Dorr, S. Mitran, W. Olbrich, W. Sabisch, M. Alef, E. Aronskaia, T. Dunker, U. Gentner, St. Genz, N. Lehmann, A. Müller, D. Seldner; X. Jin,
Entwicklung von Thermofluiddynamikprogrammen und ingenieurtechnische Anwendungen.
Dieser Bericht unter 32.22.02

7 J. U. Knebel, M. Daubner, persönliche Information 1998

III. PASCO-Programm

(X. Cheng, H.J. Neitzel, He. Schmidt, J.U. Knebel, IATF)

Abstract

In addition to the sump cooling concept explained in detail in a preceding chapter, the Forschungszentrum Karlsruhe and the Universität Karlsruhe have proposed a composite containment concept, which copes with severe accidents in a completely passive way. One essential of this concept is the decay heat removal from the containment by natural air convection coupled with thermal radiation. This passive containment cooling concept is investigated in the PASCO program.
The main objective of the containment cooling programme PASCO is to attain results on the feasibility of the passive containment cooling concept. The experimental and numerical work on this programme has progressed very well.

Zusammenfassung

Neben der Möglichkeit der Sumpfkühlung, die ausführlich im Kapitel 7.1 dargestellt wird, wurde von FZK und der Universität Karlsruhe ein weiteres Konzept vorgeschlagen, bei dem nach schweren Unfällen die Containmentkühlung völlig passiv vonstatten geht. Charakteristisch für dieses Konzept ist die Tatsache, daß die Nachwärmeabfuhr vom Containment durch Naturkonvektion plus Wärmestrahlung erfolgt. Dieses Konzept wird im Rahmen des PASCO-Programms untersucht.
Hauptziel des PASCO-Programms ist es, belastbare Aussagen über die Machbarkeit der passiven Containmentkühlung zu gewinnen. Die experimentellen und numerischen Arbeiten hierzu sind im Berichtszeitraum gut fortgeschritten.

1. Introduction

The PASCO program consists of model experiments performed in the PASCO test facility, that are backed up by numerical calculations. A detailed description is given by Erbacher et al. (1996).

The objectives of the experimental and numerical investigations are to

- Simulate the natural air convection coupled with thermal radiation present in the prototype with the help of a model geometry,
- Simulate the model experiment using numerical computer codes,
- Enhance the heat transfer characteristics by passive means,
- Develop heat transfer correlations for containment design,
- Comment on the coolability limit of the passive containment cooling concept.

2. Results

2.1 Experimental results

The test facility PASCO, as shown in fig. 1, has been built at the Forschungszentrum Karlsruhe. It consists of a vertical rectangular channel of which one wall is electrically heated. The other three walls are thermally insulated from the ambient surrounding.

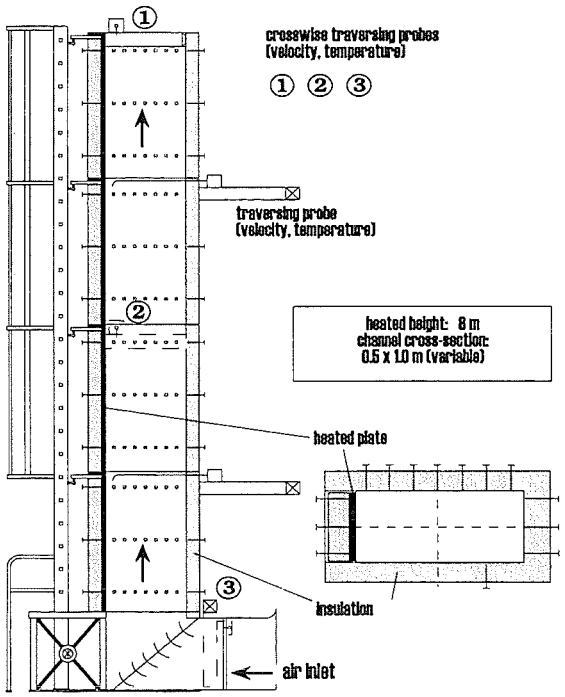

Figure 1: Test facility PASCO at the Forschungszentrum Karlsruhe.

During the experiment the heated wall is kept at a uniform temperature distribution. Fluid temperature and velocity profiles at different elevations, wall temperature distribution and heat power removed from the heated wall are measured. During the period of 1998 experiments have been performed with channel inserts at the following conditions:

- channel depth 1.0 m
- channel height 8 m
- wall emissivity 0.9
- heated wall temperature 100°C - 175°C

Two different kinds of channel inserts have been used, i.e. circular rods and ribs. Figure 2 shows the arrangement and the geometric parameters of the channel inserts.

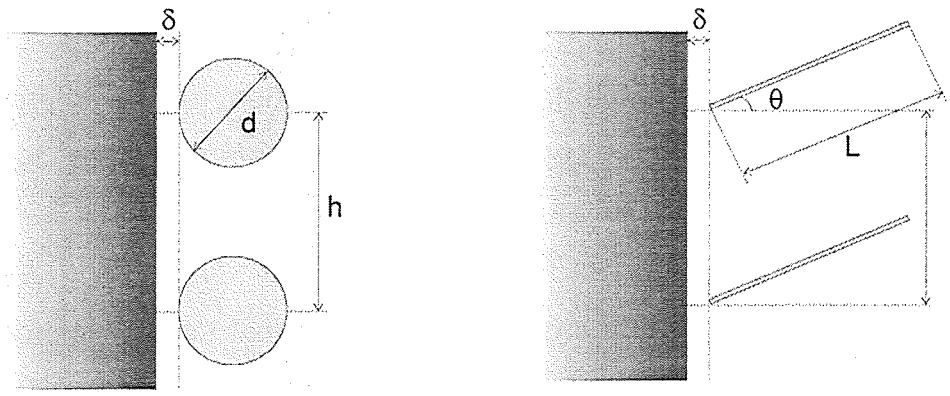

(a) circular rods: d = 10 mm, h = 1, 2 m, δ = 0, 5, 10 mm

(b) ribs: L=100, 150, 200 mm, h=1, 2 m, δ = 10, 20, 30 mm, θ = -45°, 0°, 45°

Figure 2: Arrangement and geometry of channel inserts

For evaluating the effect of channel inserts on heat removal, a heat removal enhancement factor is defined as follows:

$$\Delta Q = \frac{Q_i - Q_0}{Q_0}$$

Herein Q_i and Q_0 stand for heat power transferred with and without channel inserts, respectively.

Figure 3 summarizes the results obtained with <u>*circular rods*</u> as channel inserts. It is seen that for all test conditions the introduction of the channel inserts leads to an increase in the heat power removed. The maximum enhancement of heat removal has been obtained at a gap size of 5 mm and an interval of neighbouring rods of 1 m. With the circular rods a heat transfer enhancement up to 10% can be achieved.

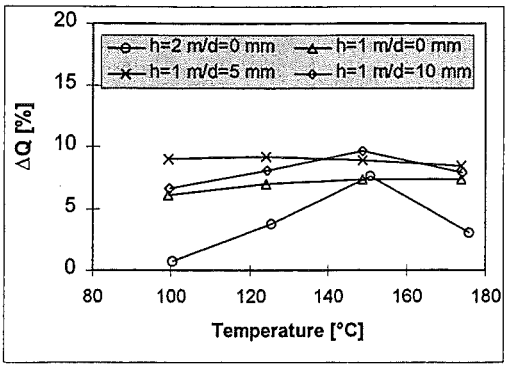

Figure 3: test results with circular channel inserts

(ps.: In the figure the letter d stands for the gap size δ)

Figure 4 shows the effect of the rib interval *h* on the heat transfer improvement. It is seen that for the condition considered a short interval leads to a stronger enhancement of heat removal.

Figure 5 shows the effect of the gap size δ on the heat transfer improvement. The interval between neighbouring ribs is 1 m, the height of the ribs is 200 mm and the inclination angle is -45°. The maximum heat transfer enhancement has been achieved at a gap size of 20 mm.

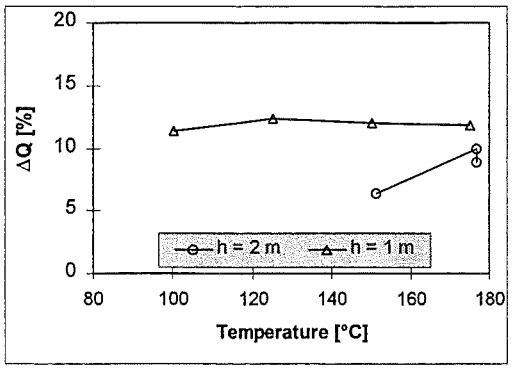

Figure 4: effect of ribs interval

L=200 mm, δ=20 mm, θ=0°

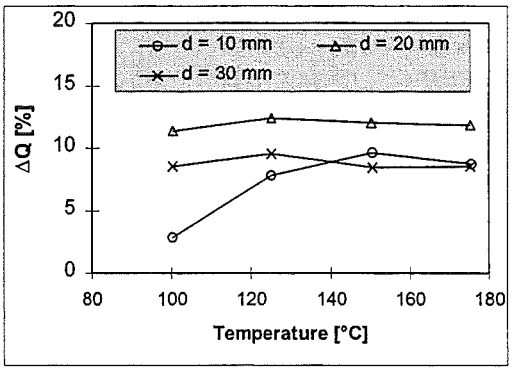

Figure 5: effect of gap size

L=200 mm, h=1 m, θ=-45°

Figure 6 shows the effect of the inclination angle on the heat transfer enhancement at the following conditions: ribs interval 1 m, rib height 150 mm and gap size 20 mm. It is seen that the horizontal arrangement (0° inclination) results in a stronger heat transfer improvement than other cases. A heat transfer enhancement of nearly 20% is obtained for the horizontal arrangement of the channel inserts.

Figure 7 shows the effect of the rib height on the heat removal improvement for horizontal arrangement of ribs with an interval of 1 m and a gap size of 20 mm. Heat removal enhancement at a rib height of 150 mm is more significant than at a height of 100 mm or 200 mm.

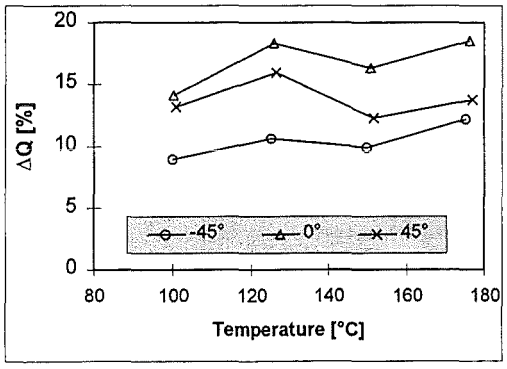

Figure 6: effect of rib inclination

L=150 mm, δ=20 mm, h=1 m

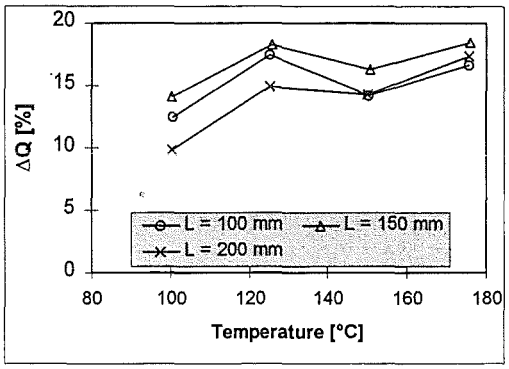

Figure 7: effect of rib height

h=1 m, δ=20 mm, θ=0°

2.2. Theoretical analysis

During the report period efforts have also be made to develop physical models for the heat transfer in a flow channel, as indicated in fig. 8, where heat is transferred from the heated wall by both thermal radiation and convection. The total heat flux on the heated wall consists of the convective heat flux and the radiative heat flux:

$$q_t = q_c + q_r = q_c\left(1+\frac{q_r}{q_c}\right)$$

The average ratio of radiative to convective heat flux on the heated wall has been derived as following:

$$\frac{q_r}{q_{c,}} = (1+2l)\,\frac{a\cdot R_s}{1+b\cdot R_s}$$

with

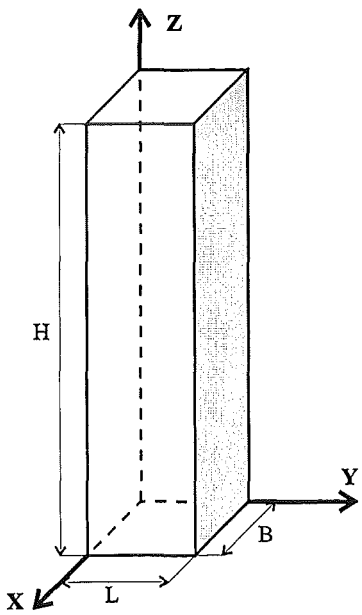

Figure 8: Flow channel

$$R_s = \frac{1}{2 + 2l - \varepsilon} \cdot \frac{St}{Nu_c}$$

$$St = \frac{4\sigma \cdot \varepsilon \cdot T_1^3 \cdot l_0}{\lambda}$$

$$Nu_c = \frac{h_c \cdot l_0}{\lambda}$$

The coefficients *a* and *b* are optimized by using experimental and numerical results.

3. Main progress

- The passive containment cooling concept could be significantly improved by introducing channel inserts which break up the boundary layer along the heated wall, thus enhancing the convective heat transfer. The total heat power removed is increased by about 20%.
- A semi-empirical equation has been derived for the heat transfer of turbulent natural convection in a rectangular channel with asymmetric heating.
- Next experiments are directed in studying the heat transfer improvement by water film evaporation.

References

Erbacher, F.J., Harten, U., Just, W., Neitzel, H.J., Schmidt, He., Langfristige Containmentkühlung, in: B. Mühl (Hrsg.), Projekt Nukleare Sicherheitsforschung Jahresbericht 1995, Wissenschaftliche Berichte FZKA 5780, Forschungszentrum Karlsruhe, pp. 240-245, 1996.

32.21.06 Dynamische Beanspruchung von Reaktordruckbehälter und Containmentstrukturen

Mechanische Auswirkungen auf den Reaktordruckbehälter
(B. Dolensky, B. Göller, G. Hailfinger, O. Jonatzke, J. Jordan, I. Kornelson, R. Krieg, K.H. Lang, T. Malmberg, G. Messemer, E. Stratmanns, G. Vorberg, IRS)

ABSTRACT

The load carrying capacity of the pressure vessel head to withstand an in-vessel steam explosion is investigated. First, as a key problem, the impact of molten core material against the vessel head is studied by model experiments scaled down 1:10. Structural details are considered. The results are converted to reactor dimensions using similarity theory. This approach was checked by simplified liquid-structure impact experiments in different scale. Second, the upward acceleration of molten core is studied by computational models. As results admissible mechanical energies which the vessel head can withstand are presented.

1. INVESTIGATION STRATEGY

During a postulated in-vessel steam explosion molten core material may be accelerated as a liquid slug against the upper vessel head. If the head would fail, fragments of it could be hurled against the containment and endanger its integrity [1, 2]. Therefore, it is required that the liquid slug impact must not cause failure neither of the vessel head nor of the bolts connecting the head to the vessel flange.

In a first step – called BERDA I – the kinetic slug energy which can be carried by the vessel head and the bolts is determined. It is called the admissible kinetic slug energy E_{slug}. Assessments of the impact process revealed two mechanisms which are expected to mitigate the loads and therefore to increase the admissible kinetic slug energy considerably [3]: The liquid character of the slug and the upper internal structures underneath the vessel head. Due to these facts, the impact duration will be increased and thus for a given slug momentum the impact force is expected to

decrease. Therefore, in our investigations, the slug is modeled as a liquid and the upper internal structures are considered.

In a second step - called BERDA II - the mechanical energy which must be fed into the upward acceleration of the core support plate, such that the admissible kinetic slug energy can be reached, is determined. It is called the admissible mechanical energy input E_{plate}. Here it is important to consider that the molten core material which is assumed to become the liquid slug is located on top of the core support plate. Thus, only a fraction of the mechanical energy input will be transferred into kinetic energy of the liquid slug.

Now, if the admissible mechanical energy input E_{plate} is higher than the mechanical energy release from the steam explosion, investigated elsewhere, then the above requirement is fulfilled: The vessel head and its bolts will not fail during a steam explosion and the containment integrity will not be endangered.

2. DESCRIPTION OF THE MODEL EXPERIMENTS BERDA I

Since reliable computational methods for the slug impact problem are not available yet, the model experiments BERDA I are aimed to simulate the reactor scenario as close as possible, such that the results may be directly transferred to reactor conditions. Therefore, the vessel head and its bolts are represented by models made of the original materials. In most of the tests also models of the upper internal structures are considered; in some cases they were made of the original material, in other cases, they were made of red brass in order to simulate the reduced material strength and ductility under accident conditions. All the models are precisely scaled down by 1:10. The molten core is simulated by liquid metal with about the same density but with a much lower melting temperature. So the test can be carried out close to room temperature. The liquid metal is contained in a crucible and accelerated against the model of the head using a pneumatic drive mechanism as shown in Fig. 1. Prior to the liquid slug impact the crucible is decelerated by a crash cylinder, thus the crucible does not participate in the impact process. To carry the dynamic loads, the whole facility is mounted on a heavy base plate of 38000 kg which is supported by springs.

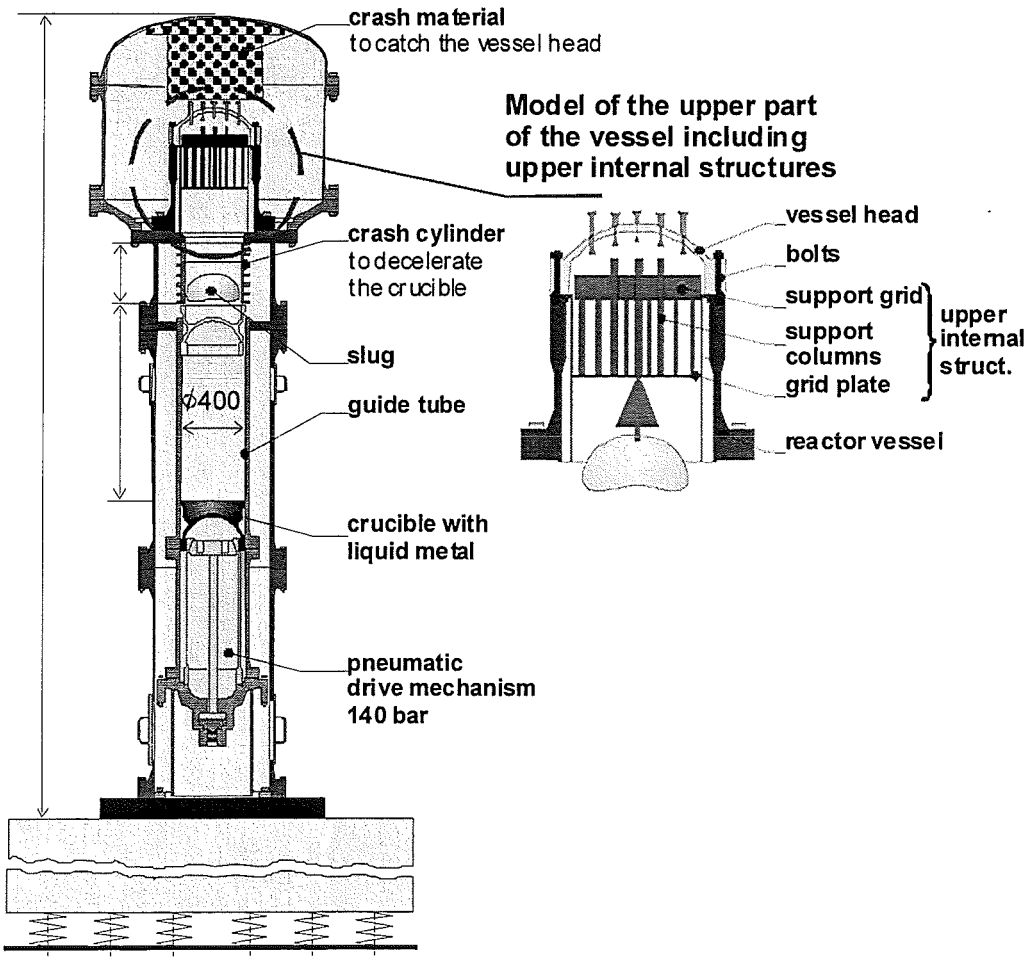

Fig. 1: Facility for the model experiments BERDA I

The liquid slug velocity is measured by photoelectric beams located at different positions along the slug path. The impact force is measured by strain gauges mounted at the bolts connecting the vessel head to the vessel flange. During the test the head deformation is also measured by strain gauges and afterwards by a three-coordinate measuring machine.

3. RESULTS OF THE MODEL EXPERIMENTS BERDA I

3.1 Impact of Slugs Consisting of Lead Spheres, Upper Internal Structures Neglected, Test 01 and 02

In the first and second test lead spheres of 10 mm diameter were filled in the crucible and accelerated against models of the head. The total mass of the spheres was

65 kg, the measured impact velocities were 78 m/s and 101 m/s, respectively. For simplicity, there was only a central hole of 12 mm diameter in the heads (beside the holes in the flange). The maximum impact force linearly converted to a slug mass of 80 kg and the permanent head displacements are shown in Fig. 2. In addition, for test 02 the force history is shown in Fig. 3. In both cases the time integration yielding the momentum transferred to the head approaches the initial momentum given by the product of slug mass and slug velocity. This is in line with the principle of momentum conservation, if one considers, that for the impact of lead spheres significant rebound effects are not expected. Here, one should refer to Fig. 4 showing strong plastic deformations of the spheres after the impact. Thus, we have additional evidence that the measurements are correct.

3.2 Impact of a Solid Slug, Upper Internal Structures Neglected, Test 03

For comparison in the third test a steel projectile with a spherical surface was hurled against the head; radius of the spherical surface 160 mm; radius of the inner surface of the head 278 mm. The mass of the projectile was only 26 kg, the measured impact velocity was 101 m/s. Again, there was only a central hole of 12 mm diameter in the head. The maximum impact force linearly converted to a slug mass of 80 kg and the permanent head displacement are shown in Fig. 2. Consider that for the solid projectile the maximum impact force is much higher than for the test 02 with lead spheres, although the velocity was the same. Comparison of the momentum transferred during the first force peak with the initial momentum led to a rebound factor of 1.4.

3.3 Impact of Liquid Metal Slugs, Upper Internal Structures Neglected, Test 04 to 07 and 09

In order to simulate worst case conditions, rather compact slugs are desired. Therefore, the liquid metal was contained in a second, very thin walled crucible, which was carried in the stronger crucible mentioned above. The second crucible was not decelerated by the crash tube but it moved on together with the liquid metal till the impact occurred. Thus, the slug mass consisted of the liquid metal of 80 kg plus the second crucible and the heater of 2.4 kg.

In test 04 the strong crucible failed during the deceleration by the crash tube. Thus, the impact mass was additionally increased by a crucible fragment of about 2.6 kg. Furthermore, the determination of the impact velocity was very difficult and ambiguous; it was assumed to be 118 m/s. The force history consists of several moderate peaks. The maximum force linearly converted to a slug mass of 80 kg is shown in Fig. 2. We assume that this result was largely influenced by the failed crucible which probably caused enhanced slug dispersion.

In test 05 to 07 and 09 the crucible remained intact. The impact velocities reached 110 m/s, 107 m/s, and two times 61 m/s, respectively. The maximum impact forces linearly converted to a slug mass of 80 kg and the permanent head displacements are shown in Fig. 2. For these last tests, heads were used with a pattern of control rod holes similar to that of German PWR of Convoy type; diameter of the central hole 12 mm, of the other holes 10 mm. As an example, for test 05 the force history is shown in Fig. 5. Now, the force histories contain only one major peak. The maxima are much higher, but the impact durations are shorter than obtained for test 04. The rebound factor was between 1.12 and 1.18. In order to give an impression of the head deformations, for test 05 the shape of the head before and after the impact is shown in Fig. 6. In comparison with test 01 and 02, where slugs of lead spheres are used, the impact forces are a little bit higher; the impact durations are about the same. However, in comparison with test 03 with the solid slug the impact forces are much lower.

In test 06 an additional hole of 10 mm diameter was drilled close to the central hole. Thus the material between these holes had a width of only 33 mm. Here, high strain peaks occurred and a through wall crack developed, as shown in Fig. 7. Before the tests the holes were closed by plugs with threads similar as for German PWR. During the slug impact of test 05 and 06 many plugs were expelled reaching velocities up to about 80 m/s.

3.4 Impact of Liquid Metal Slugs, Upper Internal Structures of Original Steel Considered, Test 08, 10, 12 and 15

The details of the liquid metal slugs were the same as before. The impact velocities were 106 m/s, 121 m/s, 131 m/s and 129 m/s, respectively. The upper internal structures before the impact are shown in Fig. 8. Also the control rods inside the

tubes were roughly simulated. Now the maximum impact forces linearly converted to a slug mass of 80 kg are shown in Fig. 9. As an example, for test 12 the force history is shown in Fig. 10. The impact forces are much lower and the impact durations are much longer than in the tests without upper internal structures. The rebound factor was between 1.08 and 1.14. Permanent head deformations did not occur, although in most of the tests the impact velocities were higher than before. However, the upper internal structures were heavily deformed as shown in Fig. 11.

3.5 Impact of Liquid Metal Slugs, Upper Internal Structures of Red Brass Considered, Tests 11, 13 and 16

The details of the liquid metal slugs were the same as before. The impact velocities were 130 m/s, 128 m/s and about 160 m/s, respectively. However, in test 16 the crucible failed, and therefore, the determination of the last velocity is questionable. Also the geometry of the upper internal structures was the same as before, however, now the material was red brass and for test 16 the material of the control rod guide tubes was lead. The force histories were similar as before, except test 13, where the maximum force occurred as a peak with a very short duration of only about 0.4 ms. Therefore, it is called the peak maximum. The remaining force history reached a smaller maximum called bulk maximum. The maximum impact forces, linearly converted to a slug mass of 80 kg are shown in Fig. 9. For test 11 and 13 the force histories are shown in Fig. 12. It turns out that the weaker and more brittle upper internal structures made of red brass have no significant influence on the loads, except the narrow peak discussed above. The rebound factors were 1.26 and 1.28, which is noticeable higher than before. In all cases permanent head deformations did not occur. The upper internal structures broke into many pieces. Thus the resulting fragments are very different from the large deformations observed for structures made of steel. For test 11 the fragments are shown in Fig. 13.

3.6 Impact of a Liquid Metal Slug, only an Upper Support Grid of Steel Considered, Test 14

The liquid metal slug was similar as before. The impact velocity was 108 m/s. However, the thickness of upper support grid had been reduced to 75 % of its nominal value. The maximum force linearly converted as before, and the very small permanent head displacement are shown in Fig. 9. One can see that the maximum force is about twice the corresponding value obtained with the complete upper internal structures, but it is still considerably lower than the values without any upper internal structures.

3.7 Impact of Liquid Metal Slugs, only Upper Support Grids of Red Brass Considered, Test 17, 19 and 20

Again, the liquid metal slugs were similar as before. The impact velocities were 126 m/s, 106 m/s and 103 m/s, respectively. The maximum forces occurred as peaks like observed for test 13. Both, the peak and the bulk maxima linearly converted as before and the permanent head displacements are shown in Fig. 9. As an example, for test 19 the impact force history is shown in Fig. 14. Comparison of test 19 and 20 with test 14 reveals, that the weaker and more brittle support grid made of red brass can be assumed to have caused the relatively high peak maxima, probably by the impact of upper grid fragments. However, the weaker and more brittle support grid has increased the permanent head deformations only slightly.

One can confirm that the peak maxima have not the same effect as the other maximum forces: For test 19 and 20 the peak forces reach about the same values as for test 05 and 06 the maximum forces; but for test 19 and 20 the permanent head displacements are much lower than for test 05 and 06.

4. INTERPRETATION OF THE MODEL EXPERIMENTS BERDA I

4.1 Application of Computational Models

Analysis of the liquid structure impact process was carried out with the code PLEXUS [4]. The liquid was modeled by a large number of particles, the vessel head by finite elements. Using about 20 000 particles the test 07 could be reasonably simulated. However, despite of this high number requiring large computational effort convergence was not obtained. So the reliability of the predictions is questionable. Furthermore, modeling of the upper internal structures is still an unsolved problem.

The deviation between test 07 and 09 was studied with the finite element code ABAQUS. It turned out that the somewhat higher impact force and the smaller head displacement of test 09 may be caused by increasing the impact area at the head. This might be due to slightly varying slug acceleration conditions leading to increased radial slug dispersion. It is interesting to note, that with upper internal structures severe deviations between similar tests have not been observed.

For better understanding of the various impact phenomena the code SimSIC was developed [5]. It must be mentioned, however, that this code needs some input obtained from experiments shown in Fig. 2. The curve describing the maximum impact force as a function of the impact velocity could be explained with SimSIC. The change of the inclination of this curve at a velocity of about 60 m/s is due to plastic head deformation.

4.2 Transfer of the Results to the Reactor Scale

Conversion of the test results to the reactor scale was accomplished using similarity theory. The length scale λ_ℓ is given by the ratio between the reactor dimensions and the corresponding model dimensions. For BERDA I it is $\lambda_\ell = 10$. The stress scale λ_σ is given by the ratio between the stresses in the stress-strain diagrams for the reactor and the corresponding stresses in the diagrams for the model. Considering that the reactor vessel head has a temperature of 300 – 400 °C, while the model head is at room temperature, one finds $\lambda_\sigma = 0.87$.

Now using the conventional basic equations including the equilibrium conditions, the constitutive equations for time-independent elastic-plastic material behavior, etc., the scales for other quantities can be derived:

$$\text{time scale} = \lambda_\ell / \sqrt{\lambda_\sigma} = 10.7; \qquad \text{velocity scale} = \sqrt{\lambda_\sigma} = 0.93;$$

$$\text{force scale} = \lambda_\ell^2 \lambda_\sigma = 87; \qquad \text{energy scale} = \lambda_\ell^3 \lambda_\sigma = 870.$$

The strains are the same for both the reactor and the model.

Since the basic equations allow only an approximate description of the problem, the scaling rules have also an approximate character. To check the deviations, the similarity experiments FLIPPER had been carried out, where a simple liquid-structure impact process was investigated in three different scales [6]. For the ferritic steel of the vessel head a moderate deviation was found which could be explained by the known strain rate effect on the stress-strain diagram. This effect was considered when defining the above values. However, for austenitic steel, where the upper internal structures are made from, a strong deviation was found indicating that the conventional constitutive equations are not adequate. Fortunately, this doesn't matter, since the influence of the material properties of the upper internal structures on the head response had turned out to be rather low.

The scaling rules apply also to non-linear processes and plastic deformations. However, material damage and fracture could not be taken into account, as adequate theoretical models do not exist. That means, failure strains obtained in the model tests cannot be expected to occur in the reactor components. Therefore, only those results of model experiments BERDA I were converted to the rector, where the plastic head deformations are so small that fracture can be ruled out even for reactor dimensions.

4.3 Determination of the Admissible Slug Energy E_{slug}

Following the above rules, the admissible slug energy could be determined for three cases:

Case **A**, all upper internal structures are molten. Fig. 2 (test 07 and 09) yields

$$\mathbf{E_{slug} = 0.1\ GJ.}$$

Case **B**, only the support grid is available. Fig. 9 (tests 14, 19 and 20) yields

$$\mathbf{E_{slug} = 0.4\ GJ.}$$

Case **C**, all upper internal struct. available. Fig. 9 (tests 14, 19 and 20) yields

$$\mathbf{E_{slug} = 0.8\ GJ.}$$

5. ASSESSMENT OF THE MODEL EXPERIMENTS BERDA II

The model experiments BERDA II are aimed to simulate the upward acceleration of the core support plate and the molten core material on top of this plate. Of special interest is, how this molten core material will form a liquid slug. Currently, the test facility is going to be erected. Since test results are not available yet, assessments by computational models are presented.

The problem is sketched in Fig. 15. The kinetic slug energy E_{slug} of the molten core material hurled upwards is

$$E_{slug} = \int F_0 \, ds_0 = m_0 \int a_0 ds_0$$

with the acceleration force F_0, the mean acceleration path s_0, the molten core mass m_0 and the mean acceleration a_0.

During acceleration, the geometrical form of the core melt may change. In particular, radial acceleration components may occur leading to a radial liquid dispersion. Thus the energy input E_0 into the molten core mass may be higher than E_{slug}

$$E_0 = \int F_0 \, ds_1 = m_0 \int a_0 ds_1 .$$

Due to equilibrium reasons, the applied force must be equal to the acceleration force F_0. During radial liquid dispersion, however, the acceleration path s_1 and the acceleration a_1 of the support surface of the molten core mass may be larger than the mean acceleration path s_0 and the mean acceleration a_0 of this mass.

The kinetic energy of the core support plate is

$$E_1 = \int F_1 \, ds_1 = m_1 \int a_1 ds_1$$

with the acceleration force F_1 and the plate mass m_1.

Neglecting the compression of the core barrel, the mechanical energy input E_{plate} at the core support plate is

$$E_{plate} = E_0 + E_1$$

In case of an unrestricted radial core melt dispersion, the acceleration ratio χ causing approximately the same path ratio

$$\chi = a_0/a_1 \approx s_0/s_1$$

above all depends on the core melt geometry and can be calculated by an available code.

Then, using the above equations one obtains

$$E_{plate} = E_{slug}\left(\frac{1}{\chi} + \frac{1}{\chi^2}\frac{m_1}{m_0}\right).$$

It should be mentioned that the deceleration of the core support plate by compression of the core barrel does not contribute to the maximum impact of the vessel head and its bolts. The cross section of the core barrel limits the force transferred to the bolts. Furthermore, this force occurs prior to the liquid slug impact against the vessel head.

Four cases **a, b, c, d** as indicated in the left hand column of Fig. 16 were studied. For case **a** no radial melt dispersion is assumed, i.e. $\chi = 1.0$. For the other cases radial melt dispersion possibly causing core barrel expansion is allowed and the acceleration ratios $\chi < 1.0$ were calculated. The resulting admissible mechanical energy input E_{plate} for the three different slug impact cases at the vessel head A, B, C are listed in Fig. 16.

REFERENCES

[1] G. Keßler, J. Eibl, "Severe Accident Containment Loads and Possible Design Concepts of Future Large Pressurized Water Reactors", *Nucl. Technol.,* 111, 358 (1995)

[2] G.E. Lucas, W.H. Amarasooriya, T.G. Theofanous, "An Assessment of Steam-Explosion-Induced Containment Failure, Part IV", *Nucl. Sci. Eng. 97*, 316 (1987)

[3] R. Krieg, T. Malmberg, G. Messemer, T. Stach, E. Stratmanns, "Slug Impact Loading on the Vessel Head during a Postulated In-vessel Steam Explosion in Pressurized Water Reactors", *Nucl. Technol. 111*, 369 (1995)

[4] H. Bung, P. Galon, M. Lepareux, A. Combescure, "PLEXUS, A new Method for the Treatment of Impact and Penetration Problems", *SMIRT 12*, Stuttgart 1993, paper B02/1

[5] A. Hirt, "Rechenmodell zum Aufprall von Kernschmelze auf die oberen Einbauten und den Deckel eines Reaktordruckbehälters", PhD thesis, Universität Karlsruhe (1997)

[6] T. Stach, T. Malmberg, R. Krieg, "Scaled Experiments for a Simple Deformable Structure under Liquid Slug Impact", *SMIRT 14, Lyon 1997*, paper P02/1

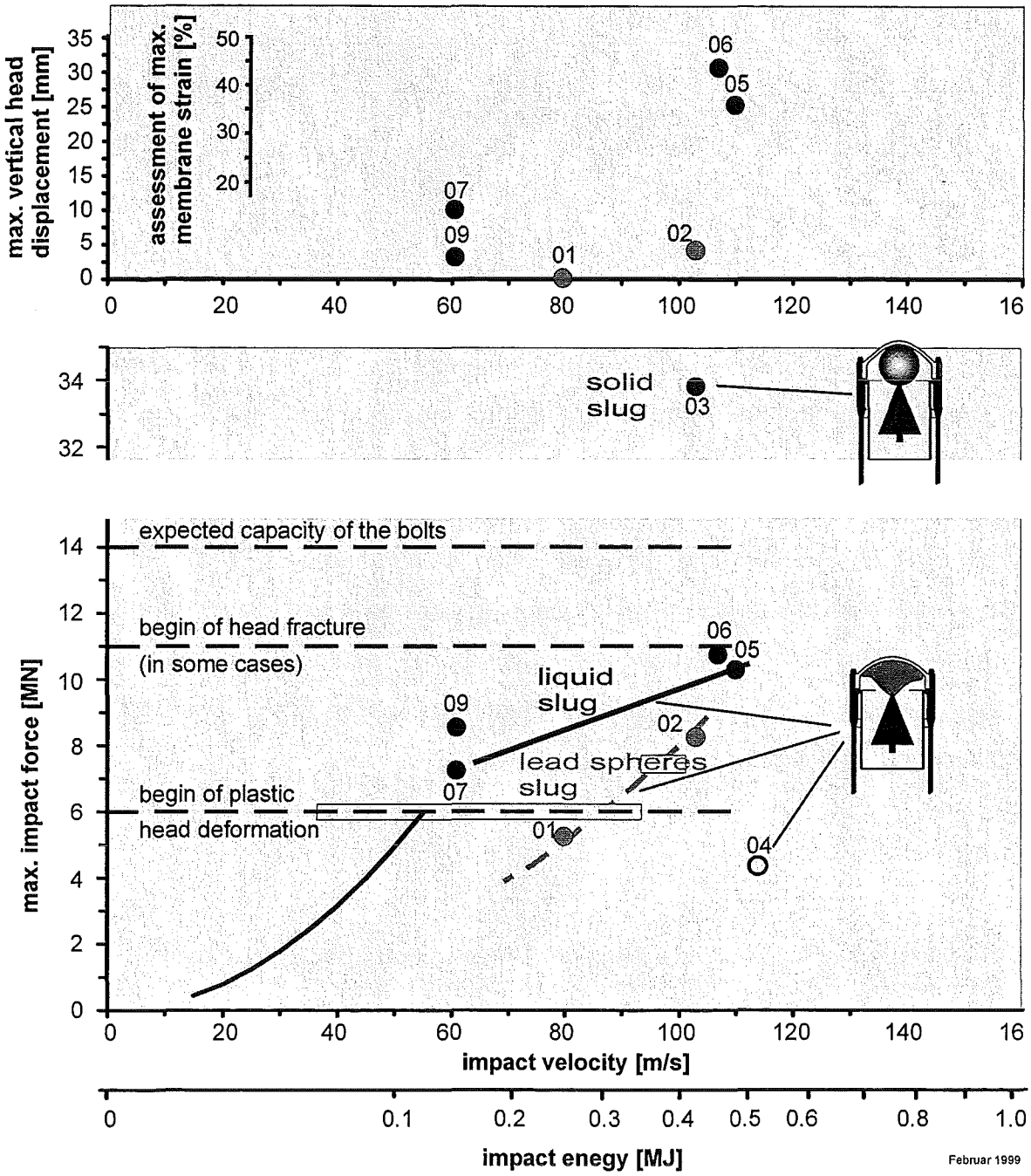

Fig. 2: Results for liquid slug impact tests with upper internal structures

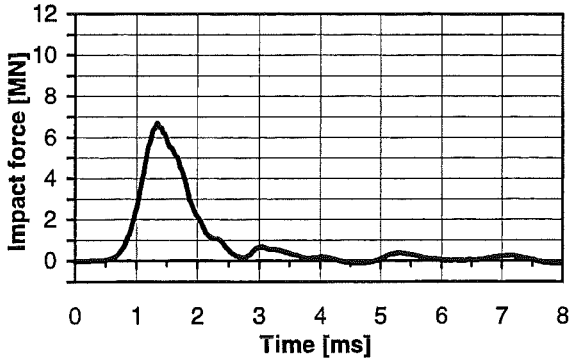

Fig. 3: Test02, lead spheres, 65 kg, 101 m/s, upper internal structures neglected.

Fig. 4: Test02, plastic deformations of the lead spheres after the impact.

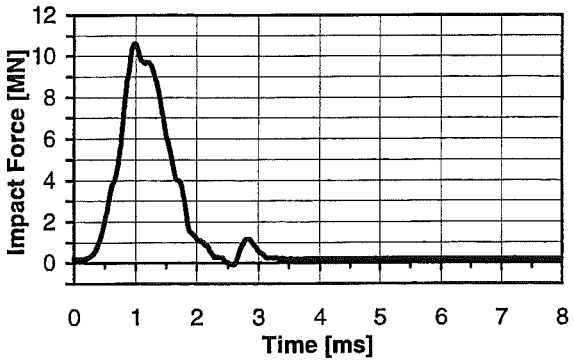

Fig. 5: Test05, liquid metal, 80 kg, 110 m/s, upper internal structures neglected.

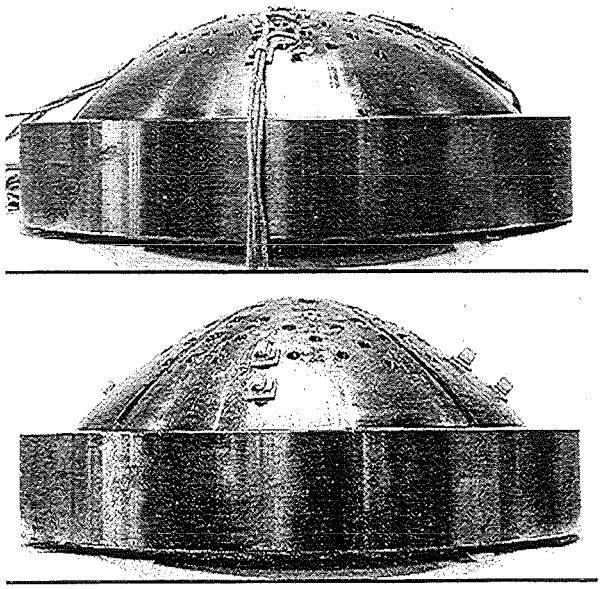

Fig. 6: Test05, shape of the head before and after the impact

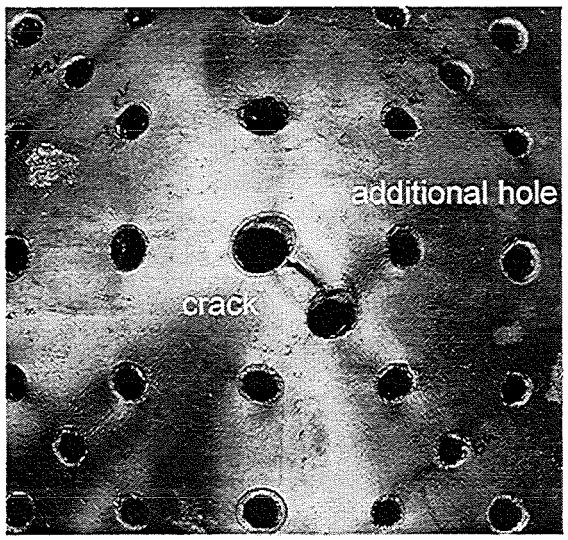

Fig. 7: Test06.
During the head deformation a crack developed.
In addition, the holes in the head were increased and many plugs which had closed the holes were expelled.

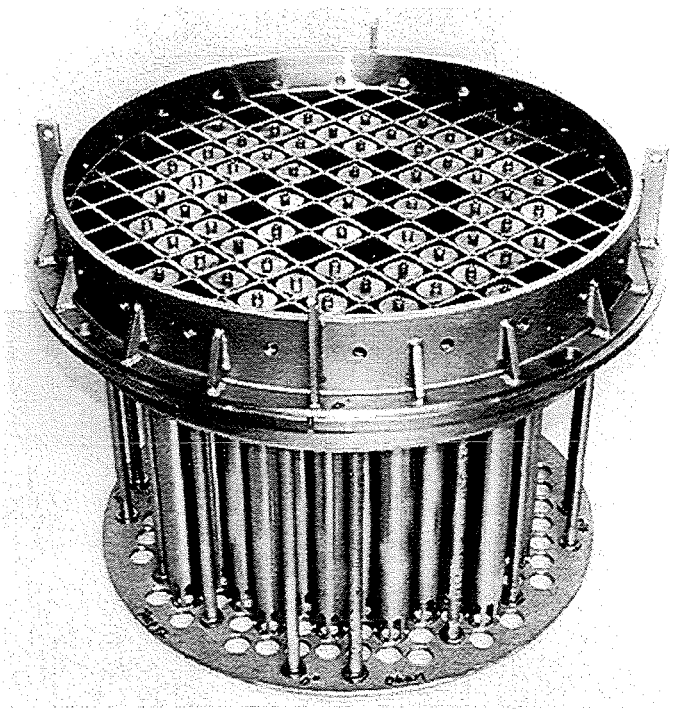

Fig. 8: Model of the upper internal structures prior to the slug impact

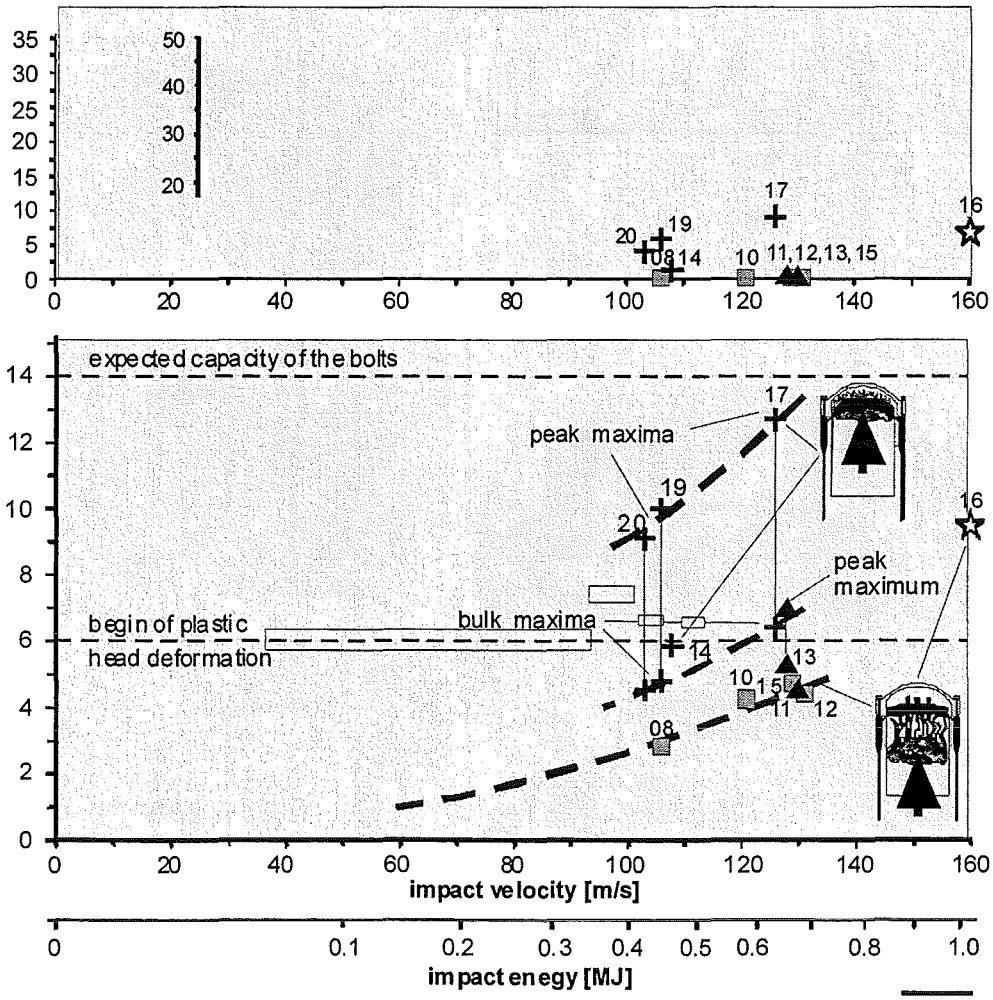

Fig. 9: Results for liquid slug impact tests with upper internal structures

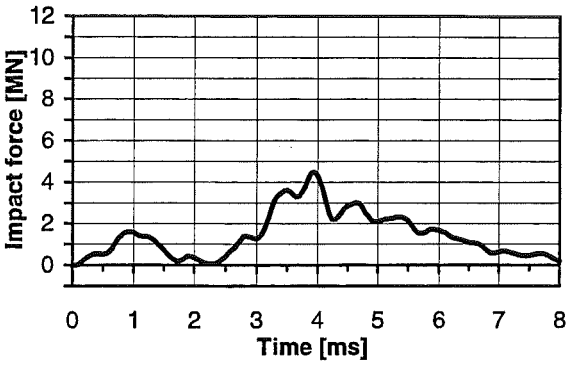

Fig. 10: Test12, liquid slug, 80 kg, 131 m/s, upper internal structures of steel.

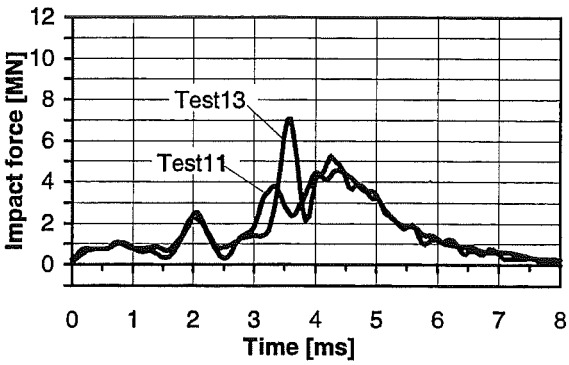

Fig. 12: Test11 and 13, liquid slug, 80 kg, 130 m/s and 128 m/s, upper internal structures of brass.

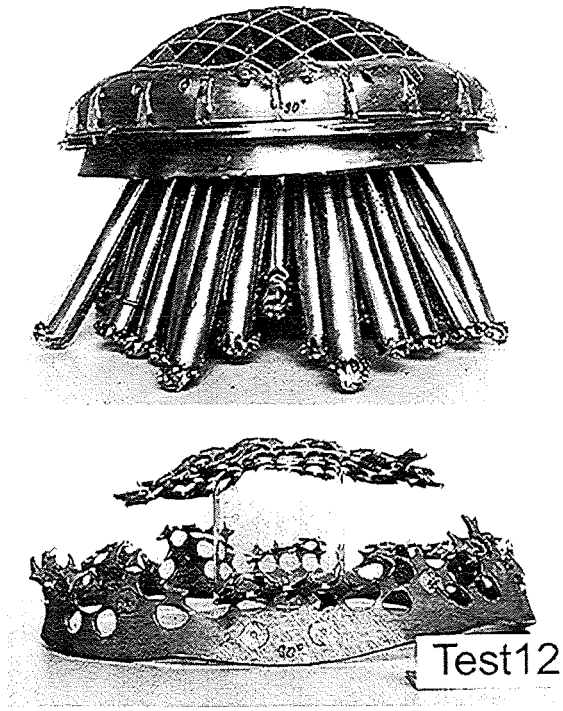

Fig. 11: Test12, upper internal structures of steel after the slug impact.

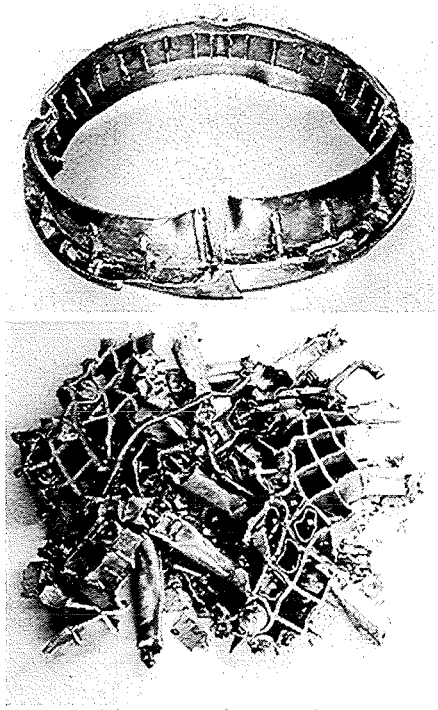

Fig. 13: Test11, upper internal structures of brass after the slug impact.

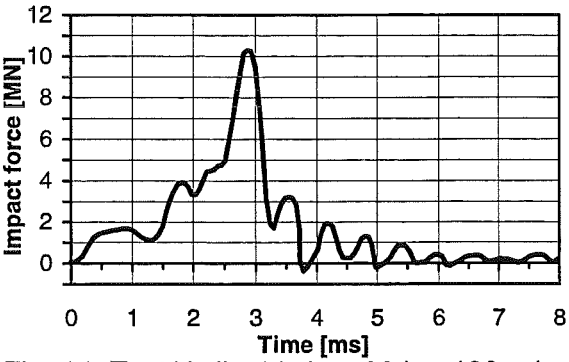

Fig. 14: Test19, liquid slug, 80 kg, 106 m/s, only upper support grid considered.

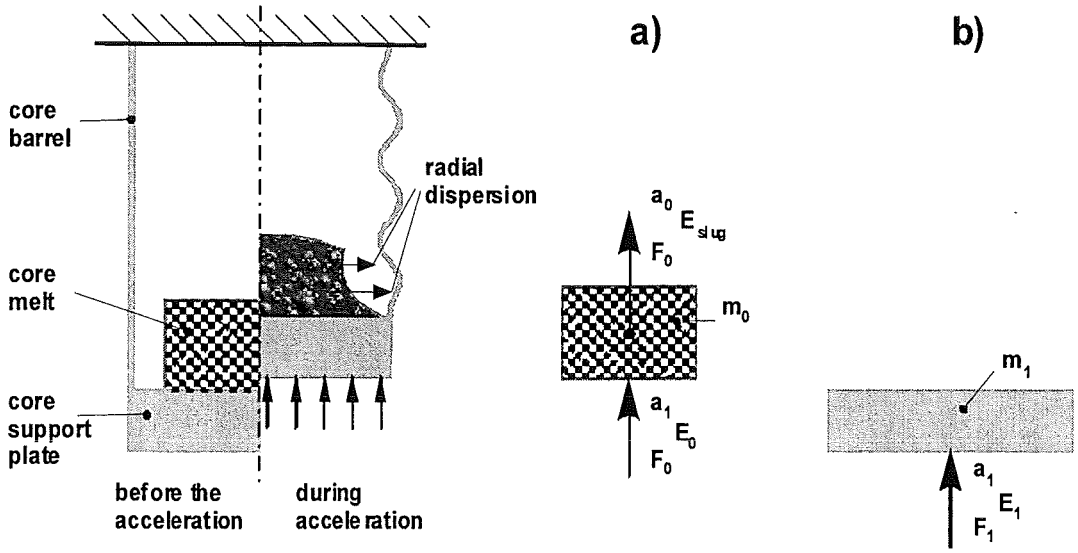

Fig. 15: Computational model to accelerate the core support plate and the molten core

upper line: mass of the heavy reflector not considered lower line: half of the mass of the heavy reflector added to the mass of the support plate	A Upper int. struct molten E_{Slug} = 0,1 GJ	B Only uppergrid available E_{Slug} = 0,4 GJ	C Upper int. struct. available E_{Slug} = 0,8 GJ
a (3,9 m Ø, concertina mode)	E_{plate} = 0,15 GJ 0,20	For case B and C concertina mode not expected	
b (3,9 m Ø, radial expansion)	For case A rad. expansion not expected	E_{plate} = 1,0 GJ 1,4	2,0 2,8
c (3,3 m Ø)	0,4 0,6	1,6 2,4	3,2 4,8
d (conical)	0,5 0,8	2,2 3,5	4,4 7,0

Fig. 16: Calculated admissible mechanical energy input E_{plate}

32.21.07 Analysen zum Containmentverhalten

I. Parameterstudien für den EPR

(G. Henneges, INR)

Einleitung

In den letzten Jahren wurden in Zusammenarbeit mit Siemens/KWU Untersuchungen zu hypothetischen Störfällen am EPR mit verschiedenen Rechenprogrammen durchgeführt. Siemens verwendet meist MAAP in Kombination mit FIPLOC, FZK rechnet mit MELCOR und CONTAIN. Da sich die Auslegungsdaten für den EPR mehrfach änderten, die meisten Rechnungen aber der Vergleichbarkeit wegen, auf ähnliche Geometriemodelle und Eingabedaten abstützten, war es nötig Parameterstudien zum EPR durchzuführen. Dieser Bericht faßt einige der Ergebnisse zusammen.

Studien

Das in /1/ beschriebene Geometrie- und Rechenmodell für einen LBLOCA Störfall wurde für die unten beschriebenen Parameteruntersuchungen verwendet (Abb. 1). Untersucht wurde der Einfluß von

- 20% Volumenerhöhung der Zelle 5
- 20% Volumenreduktion der Zelle 5
- 20% Reaktorleistungserhöhung
- 20% Reaktorleistungserniedrigung
- Inbetriebnahme eines Spraysystems nach 12h (p > 5.1b)
- Inbetriebnahme eines Spraysystems kurz nach SP-Freisetzung (T > 414K)

auf die wichtigsten physikalische Größen im Reaktorgebäude.

Dies waren u.a.

- Gas- und Sumpftemperatur in den Zellen 1 bis 5
- Druck in Zelle 5
- Luftgetragene Aerosolmassen in Zelle 5

Verwendet wurde das Rechenprogramm CONTAIN 2.0 /2/. Im Rahmen dieser Studie wurden die MELCOR-Rechnungen, die die thermohydraulischen und Aerosolquellen aus dem Primärkreis liefern, nicht modifiziert und wiederholt. Es wurde vielmehr davon ausgegangen, daß sich die Parametermodifikationen in erster Näherung nur auf die Verhältnisse im Reaktorgebäude auswirken werden. Dies ist allerdings nur bedingt richtig, wenn die Reaktorleistung verändert würde. Dennoch geben diese Studien einen groben Überblick auf die zu erwartenden Einflüsse.

Im folgenden werden einige der Ergebnisse diskutiert.

1.) Volumenänderung der Zelle 5 (plus/minus 20%)

Abb. 2 zeigt den Einfluß auf den *Druck* im Reaktorgebäude. Die durchgezogene Linie (Mi7) ist der Referenzfall. Wie zu erwarten, steigt bei Reduktion des Volumens (0.8*V5) der Druck etwas an. Das entgegengesetzte Verhalten bei Volumenvergrößerung (1.2*V5) ist der Abb. 2 ebenfalls zu entnehmen. Zu beachten ist, daß beide Kurven nicht symmetrisch zur Referenz liegen.

Die *Temperaturen* (Abb. 3) in den Zellen 1 bis 5 hängen viel stärker von den Volumenänderungen ab. V+ zeigt die Werte bei Volumenerhöhung und V- bei Verminderung an. Im IRWST (Zelle 2) wirkt sich die V+ in einer deutlicheren Temperaturabsenkung, als bei V- aus. Interessant ist die berechnete Temperaturerhöhung in Zelle 4 bei V+, während für V- in dieser Zelle erst nach ca. 8h eine Erhöhung bestimmt wird.

Abb. 4 zeigt beispielhaft das Absetzverhalten luftgetragener Cs-Aerosole in Zelle 5. Man erkennt, daß dieses durch eine Volumenvergrößerung anfänglich (bis ca. 4h) kaum geändert wird, während die Verkleinerung sich sehr wohl schon in der frühen Phase mit schnellerem Absetzen der Aerosole (dies liegt an der höheren Wahrscheinlichkeit für Koagulation) auswirkt.

2.) Änderung der Nachzerfallsleistung (plus/minus 20%)

Abb. 5 zeigt den Einfluß auf den *Druck* im Reaktorgebäude. Die durchgezogene Linie (Mi7) ist wieder der Referenzfall. Wie zu erwarten, fällt bei Reduktion der NZL (0.8*P) der Druck deutlich ab. Das entgegengesetzte Verhalten

bei NZL-Vergrößerung (1.2*P) ist der Abb. 4 ebenfalls zu entnehmen. Diese wirkt sich allerdings anfänglich nicht so stark aus. In den ersten Stunden sind beide Kurven asymmetrisch zur Referenz.

Die *Temperaturen* (Abb. 6) in der Zelle 5 zeigen ein dazu passendes Verhalten. Aus Abb. 7 lassen sich die Temperaturen im Schmelzeausbreitungsraum (Zelle 1) und im IRWST (Zelle 2) ablesen. Durch den 20% höheren Leistungseintrag in Zelle 1 verdampft nach ca. 3h das gesamte Sumpfwasser, was zu einer 50 Grad höheren Atmosphärentemperatur führt. Dies ist eine Folge des hier gewählten CONTAIN-Modells. (Der IRWST speist in diesem Modell die Zelle 1 mit Wasser erst, wenn der Wasserstand 4,4 m überschreitet. In einem modifizierten Modell, das die Verbindung der beiden Zellen z.B. durch ein kommunizierendes System beschreibt, würde es nicht zum Verdampfen des gesamten Wassers kommen können, da dann sehr viel mehr Wasser über der Schmelze stehen würde.) Eine Reduktion der NZL um 20% ergibt dagegen eine ca. 10 Grad niedrigere Temperatur. Im IRWST wirkt sich die NZL-Erhöhung in den ersten 8h kaum aus, eine NZL-Reduktion führt viel schneller zu einer Temperaturabsenkung.

Abb. 8 zeigt das Absetzverhalten luftgetragener Aerosole in Zelle 5. Man erkennt, daß dieses durch eine NZL-Vergrößerung kaum geändert wird, während die NZL-Verkleinerung sich deutlicher auswirkt.

3.) Änderungen durch Einschalten eines Spraysystems

Für den EPR ist nach 12h das Einschalten eines bisher noch nicht genau festgelegten Spraysystems vorgesehen. Für CONTAIN wurde ein Spraysystem modelliert, welches auf folgende Weise arbeitete: Sumpfwasser wird über einen Wärmetauscher (HEX) um 50 Grad abgekühlt. Die Einspeiserate wurde variiert (83.3kg/s und 150kg/s), sowie der Aktivierungszeitpunkt (ca. 12h bzw. 2h nach Unfallbeginn). Das Spraysystem ist an der Decke der Reaktorkuppel angebracht, die Tröpfchenfallhöhe beträgt 60m, die Tröpfchengröße wurde zwischen 1mm und 5 mm variiert.

Man kann den Abbildungen 9 bis 11 entnehmen, daß das Einschalten eines Spraysystems einen großen Einfluß auf die wichtigsten physikalischen Größen hat:

- Starke Reduktion der Gas- und Sumpftemperaturen in den Zellen 1 bis 5
- Starke Reduktion des Drucks in allen Zellen
- Starke Reduktion luftgetragener Aerosolmassen im Reaktorgebäude und dadurch starke Reduktion des Quellterms an die Umgebung

Die Wirksamkeit des Spraysystems ist um so größer, je früher es eingeschaltet wird, je höher die Wasserdurchsatzrate ist und je mehr das Spraywasser abgekühlt wurde.

Zusammenfassung

Die Untersuchungen zum Einfluß verschiedener Parameter auf das thermohydraulische Verhalten und das auf luftgetragene Aerosole im EPR Reaktorgebäude zeigen, daß bei Änderung des Containmentvolumens um plus/minus 20% Druck und Zelltemperaturen relativ wenig verändert werden. Die Aerosolmassen in der Luft werden dagegen stärker beeinflußt.
Modifikation der Reaktorleistung um plus/minus 20% hat größeren Einfluß auf die Thermohydraulik und ist stark vom betrachteten Ort und der Modellierung abhängig (Sumpfaustrocknung usw.)
Wird ein Spraysystem aktiviert, finden sich starke Auswirkungen sowohl auf die thermohydraulischen Größen als auch auf die Massen der luftgetragenen Aerosole mit einer Reduktion um den Faktor 10^4 bis 10^5.

Literatur

/1/ R. Frutos, R.G. Gido, G. Henneges, P. Schmuck
Spaltproduktausbreitung vom Primärsystem an die Umgebung bei einem schweren Störfall im EPR, FZKA 6126, 1998

/2/ K.K.Murata et al.,
Code Manual for CONTAIN 2.0: A Computer Code for Nuclear Reactor Containment Analysis to be published

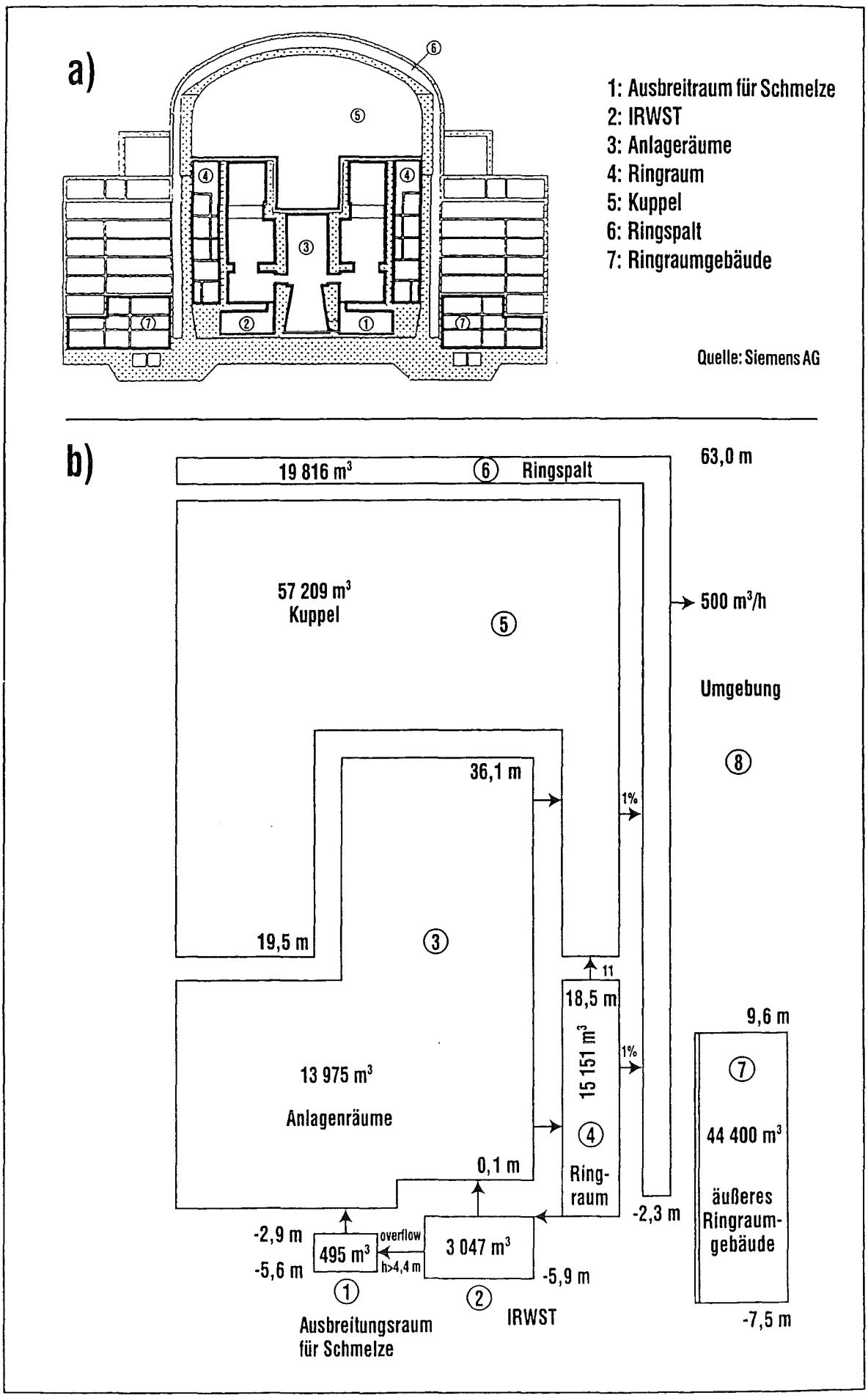

Abb. 1: a) EPR Benchmark: Reaktorgebäude mit Zellnummern
b) EPR Nodalisierung

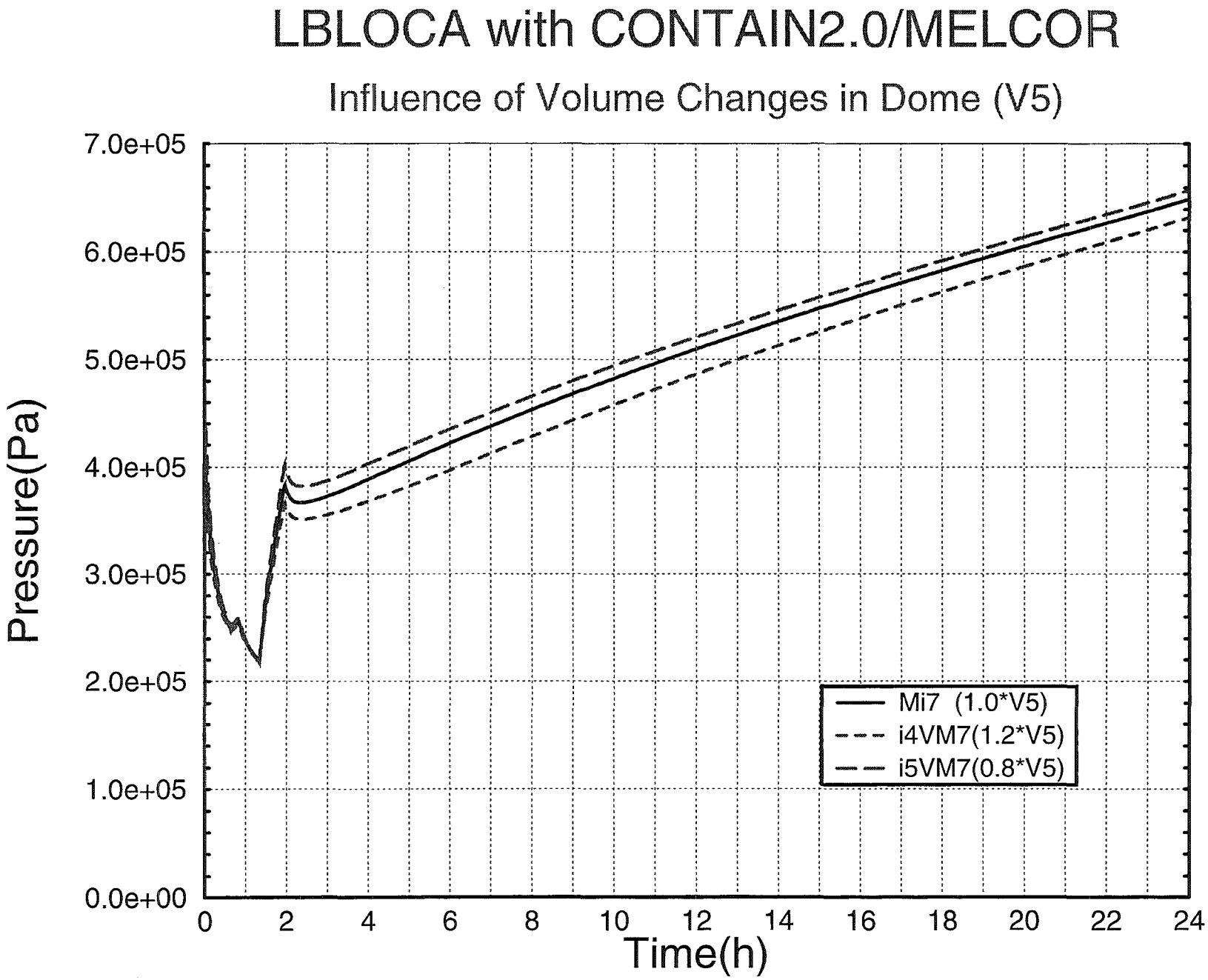

Abb. 2 Druck als Funktion der Volumenvariation

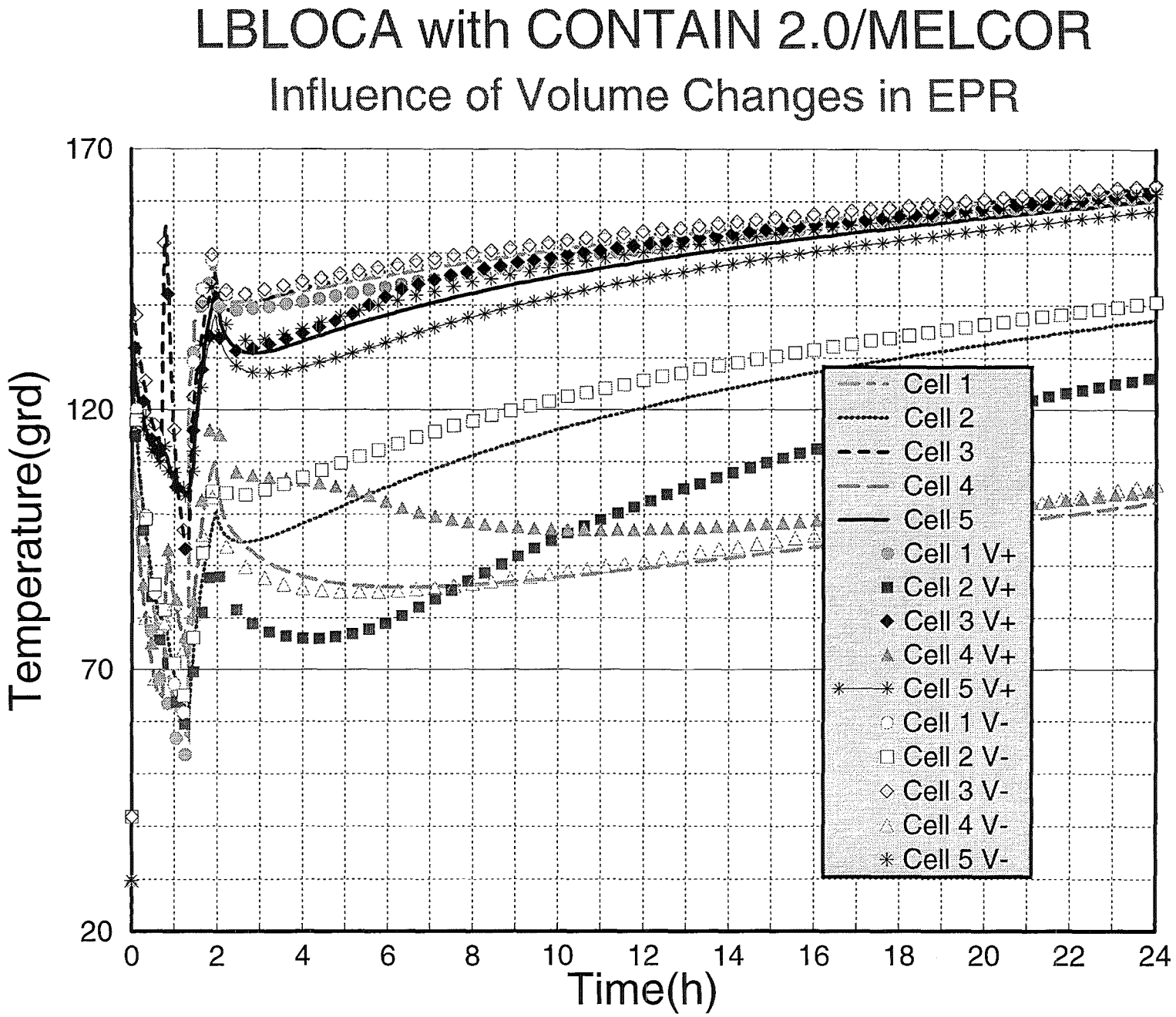

Abb. 3 Temperatur als Funktion der Volumenvariation

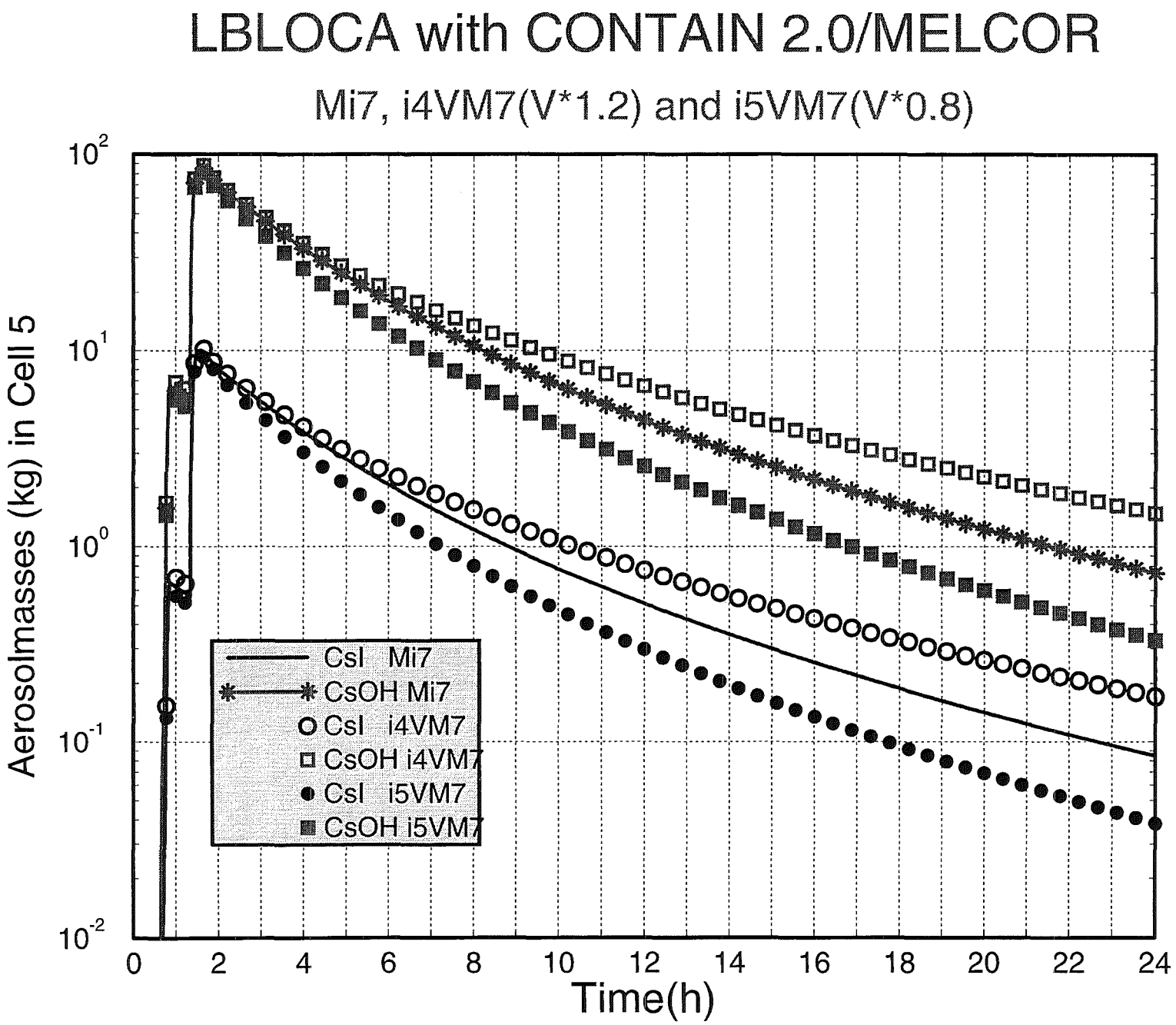

Abb. 4 Luftgetragene Aerosolmassen als Funktion des Volumens

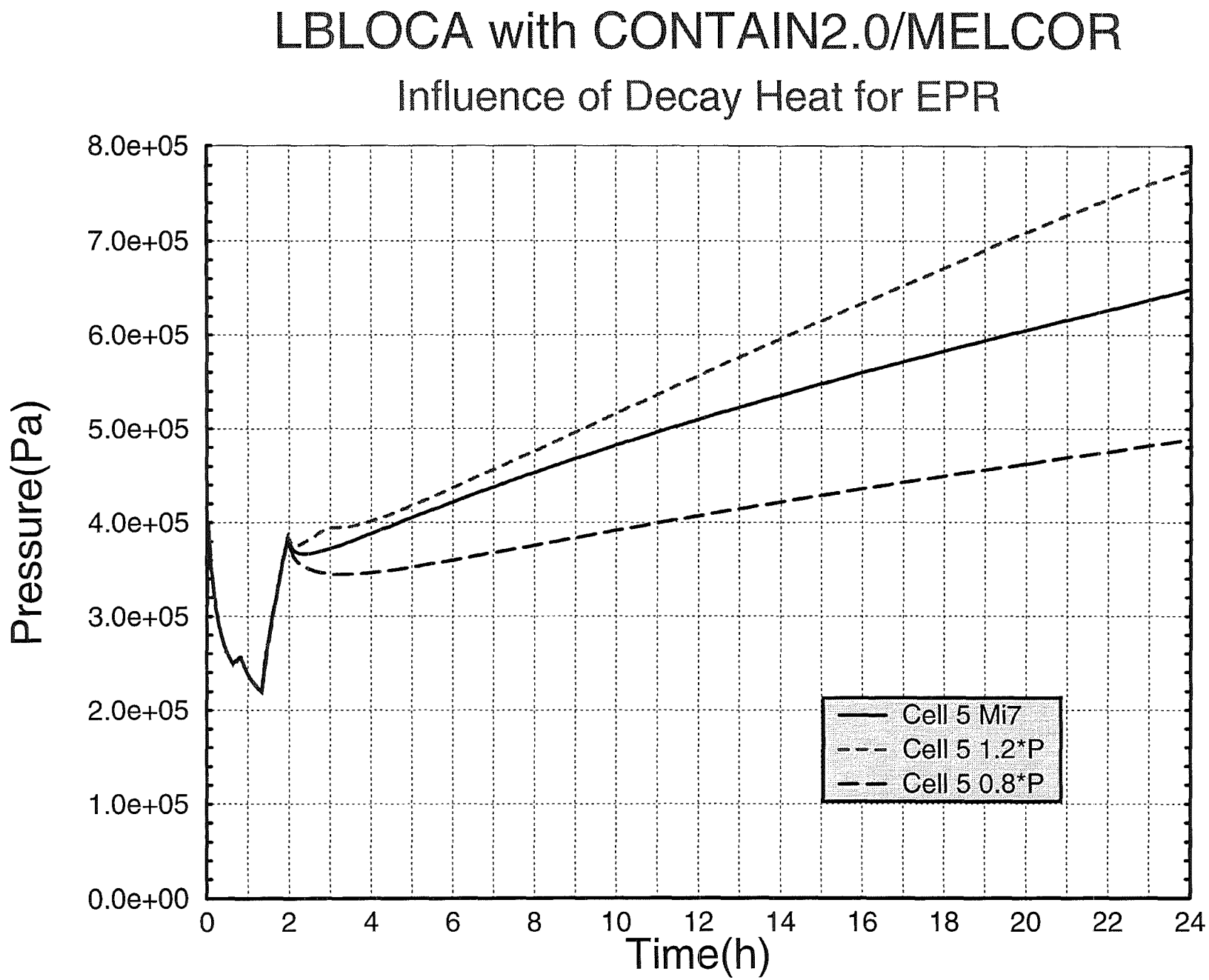

Abb. 5 Druck als Funktion der Reaktorleistungsvariation

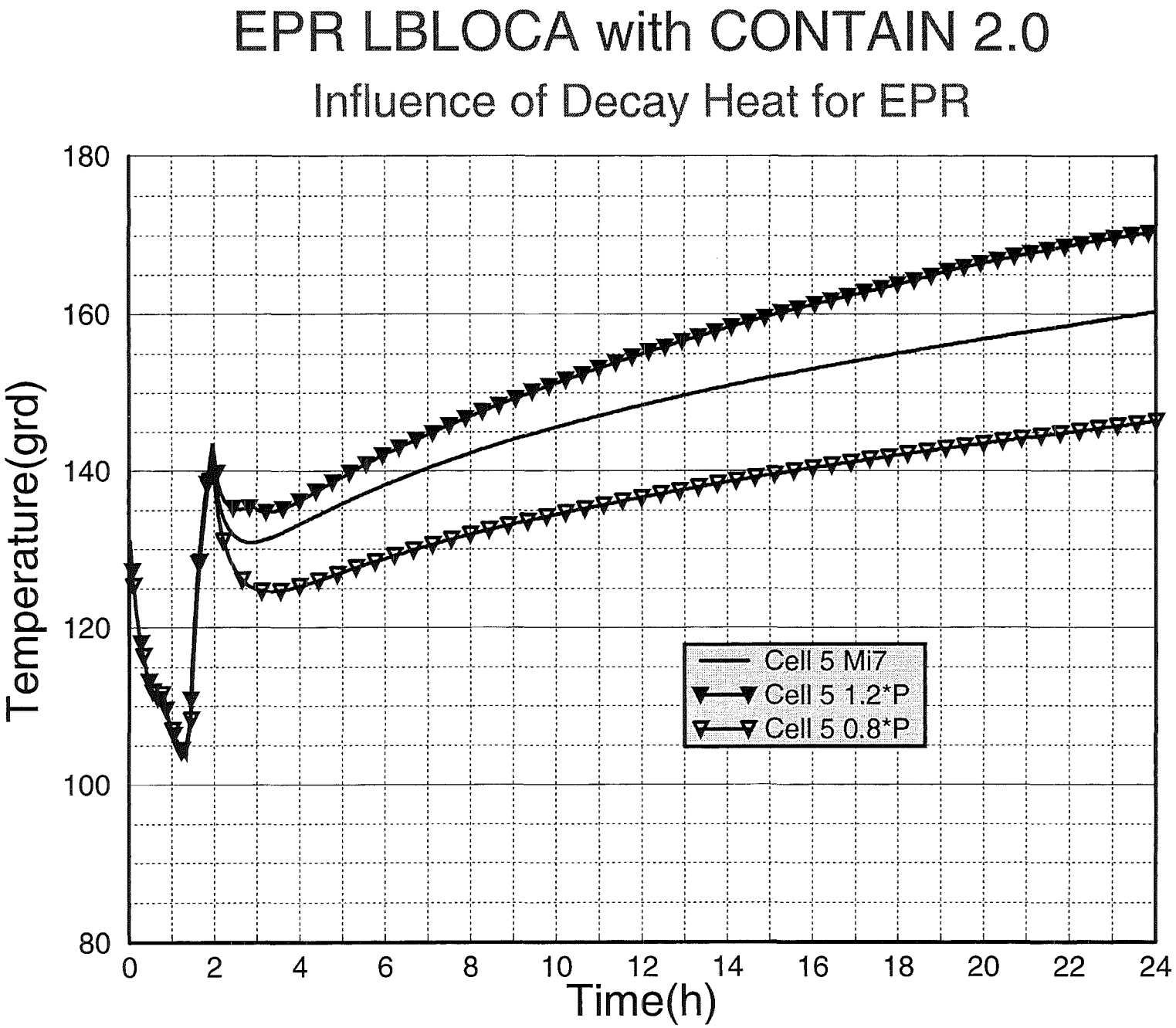

Abb. 6 Temperaturen in Zelle 5 als Funktion der Reaktorleistung

EPR LBLOCA with CONTAIN 2.0

Influence of Decay Heat for EPR

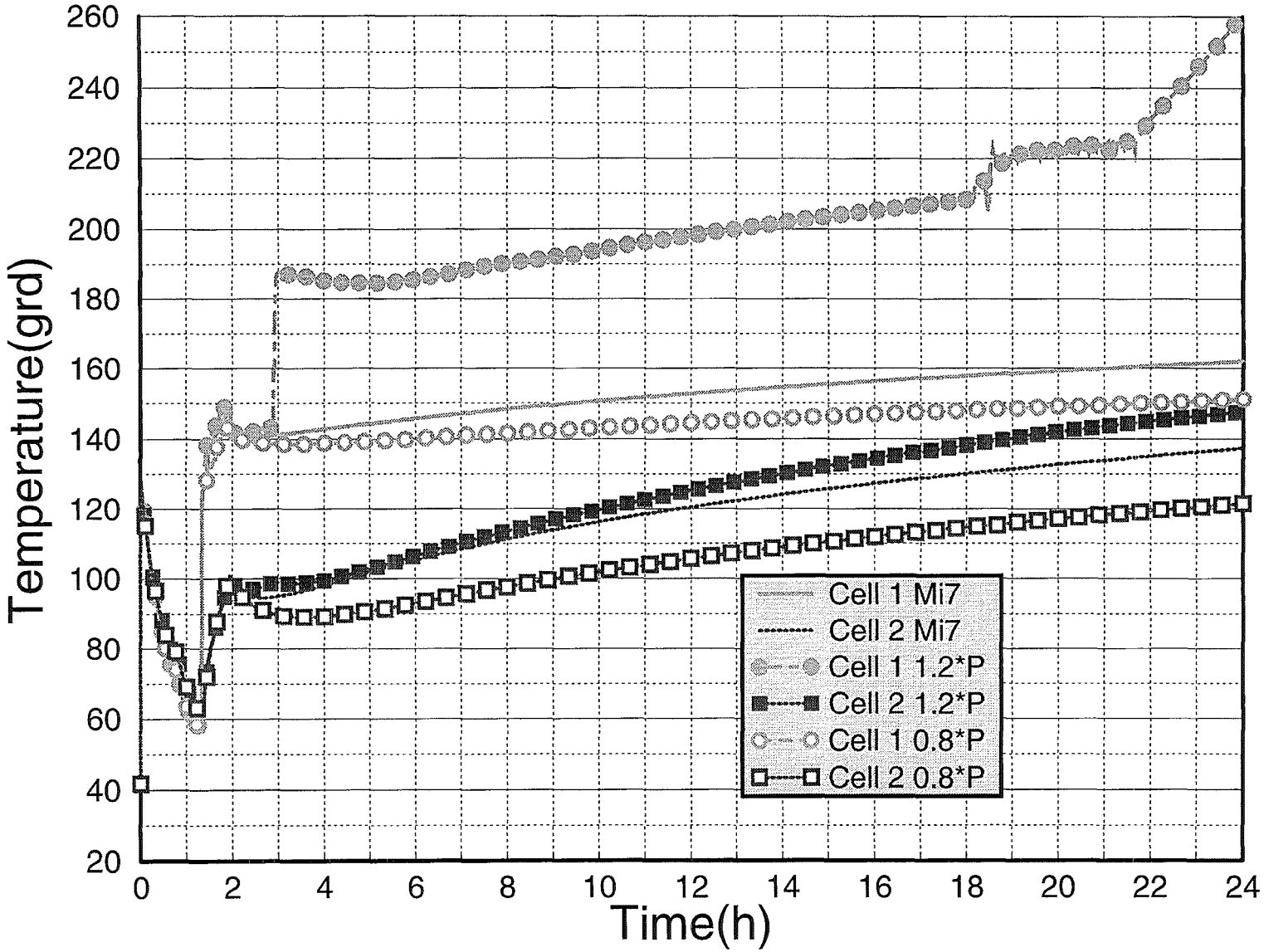

Abb. 7 Temperaturen in Abh. von Reaktorleistung

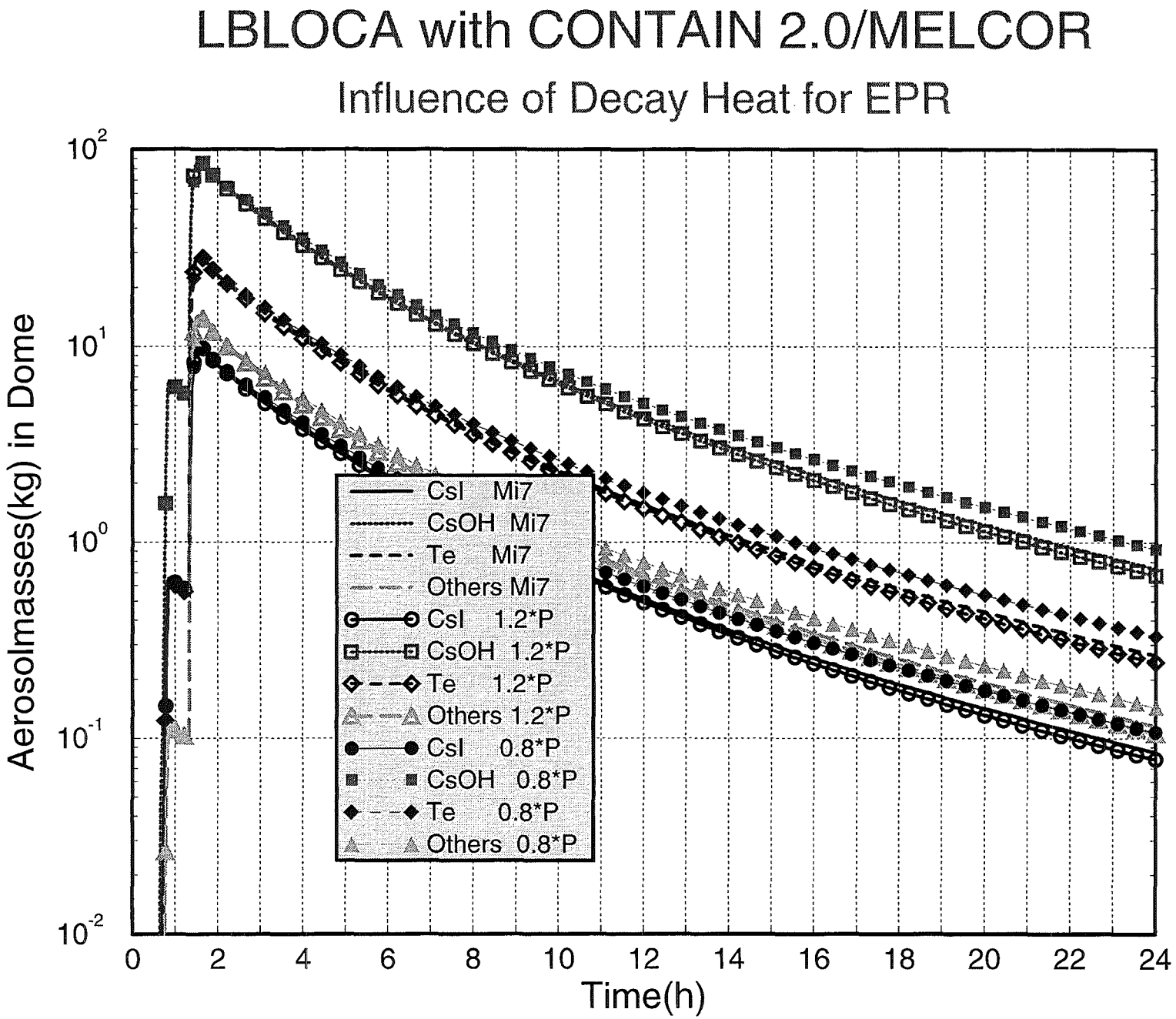

Abb. 8 Massen der luftgetragenen Aerosole als Funktion der Leistung

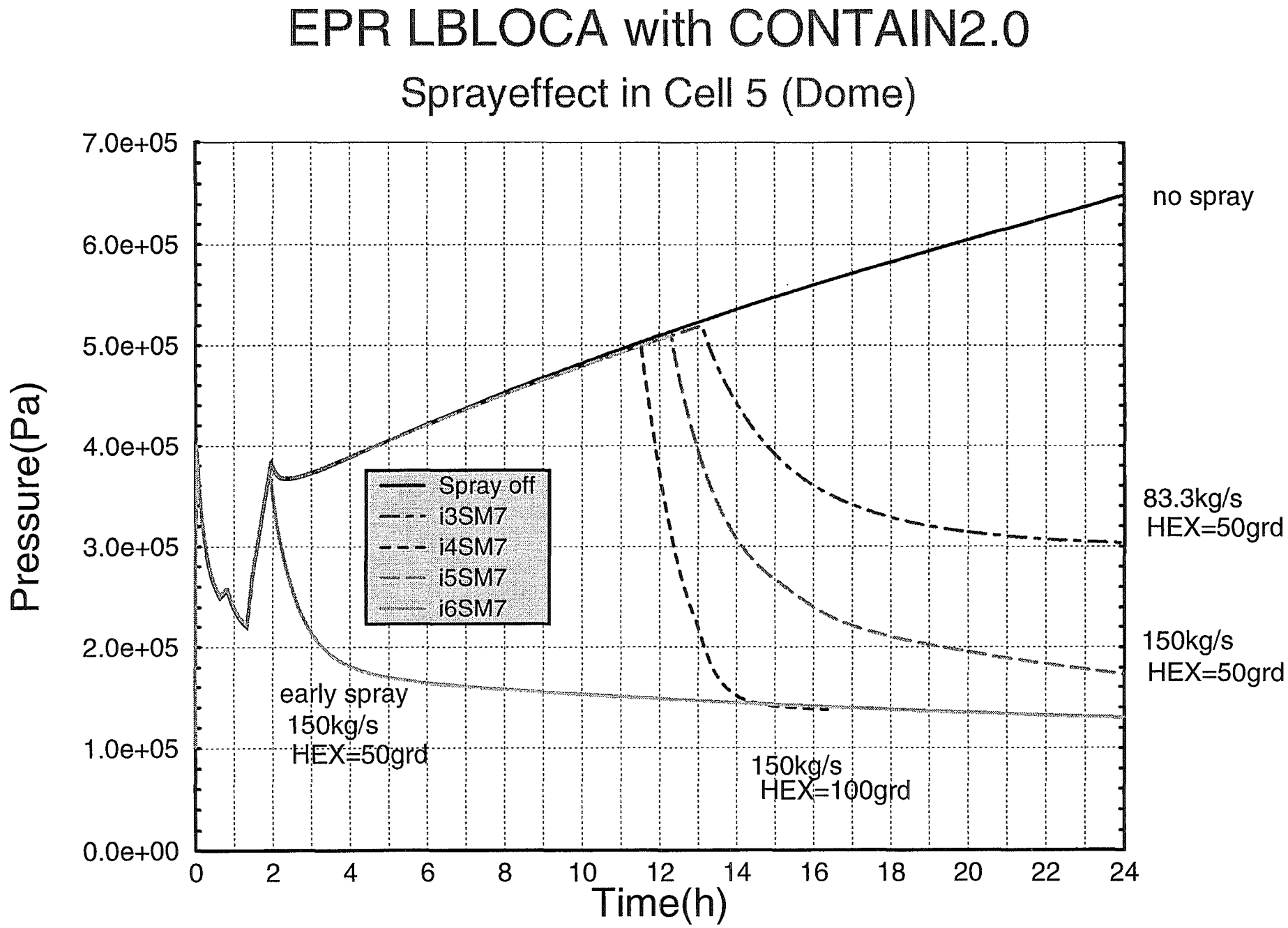

Abb. 9 Einfluss der Spraysystem-Parameter auf den Druck

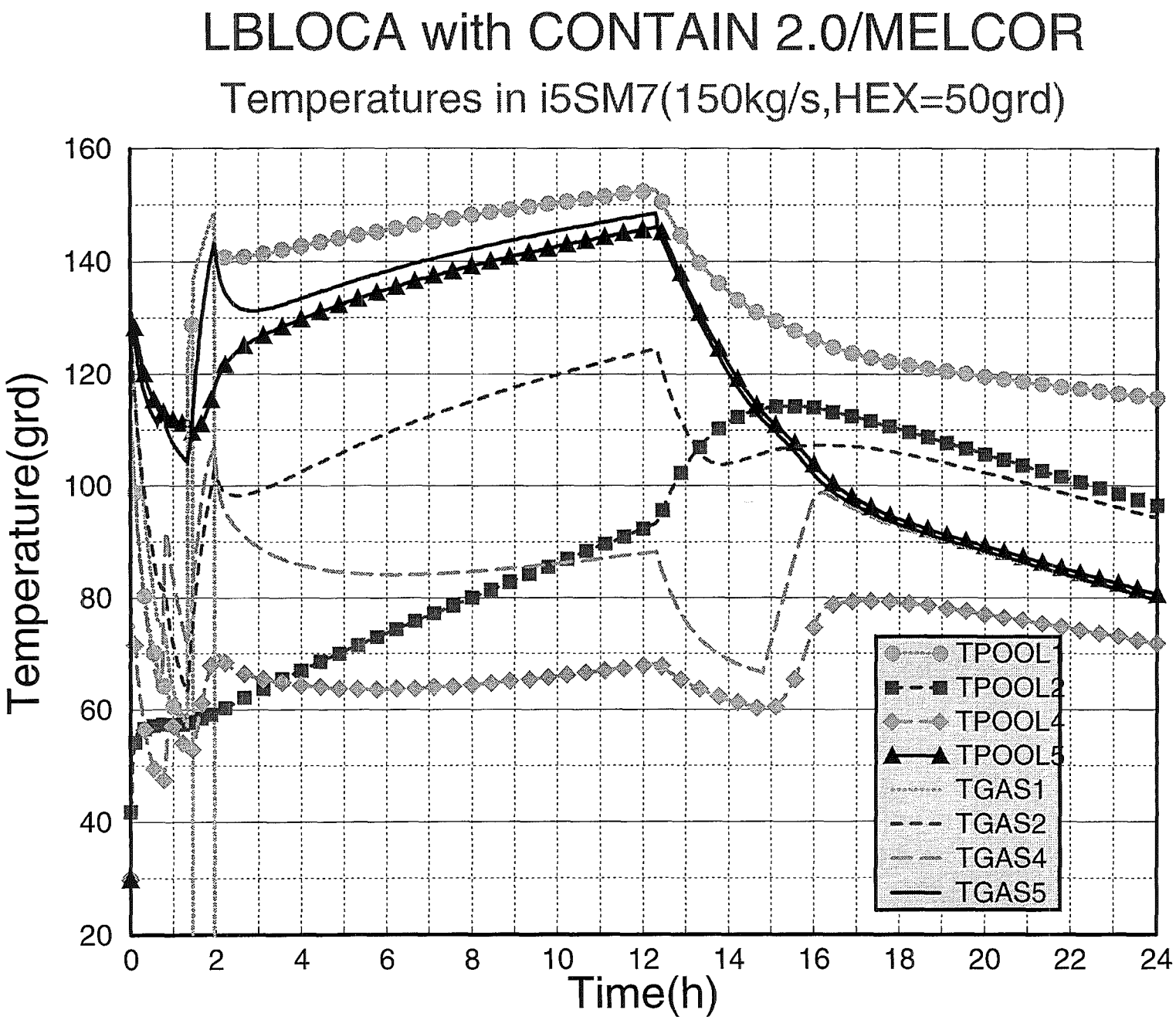

Abb. 10 Einfluss des Spraysystems auf Gas- und Sumpftemperaturen

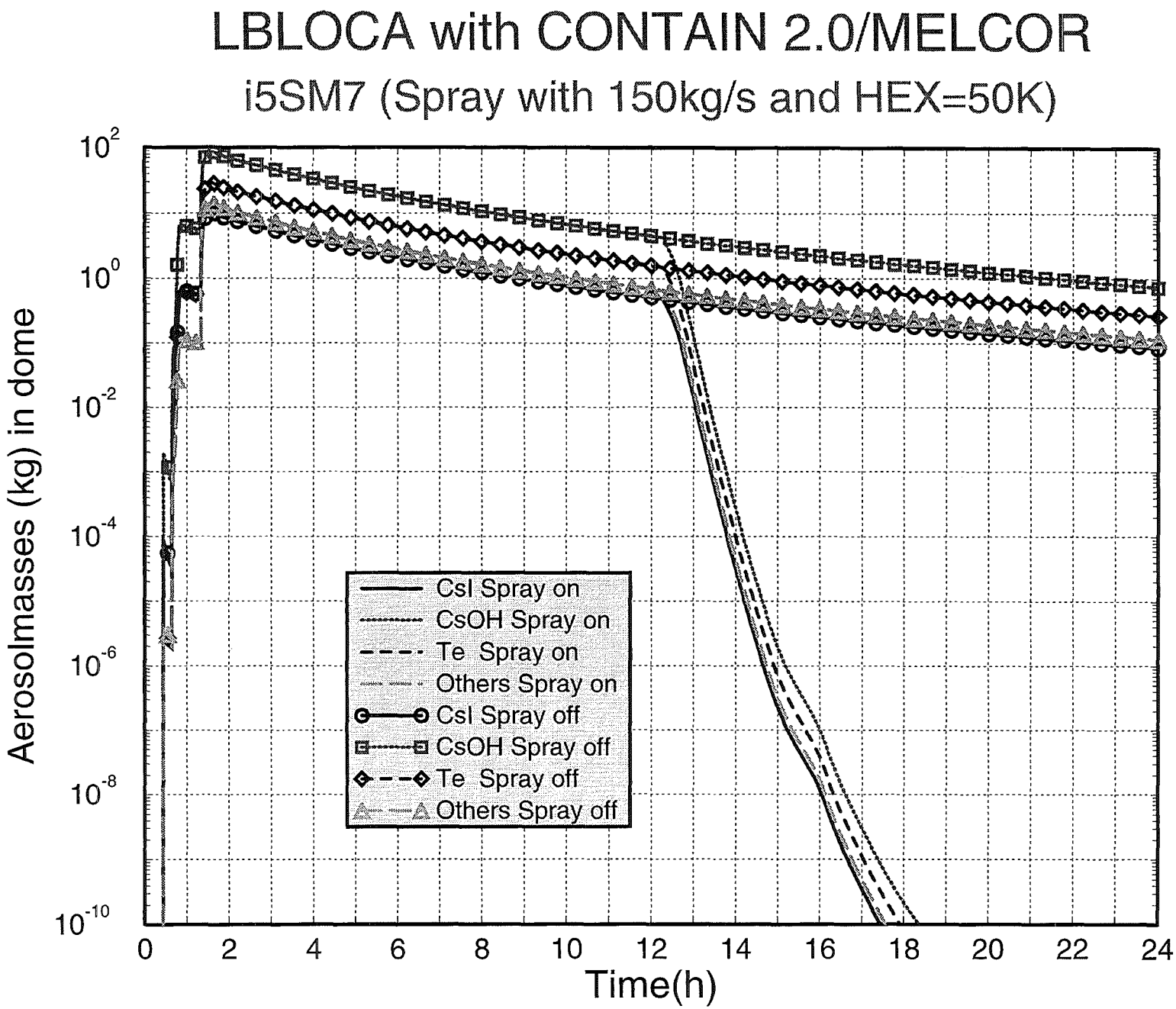

Abb. 11 Einfluss des Spraysystems auf das Aerosolverhalten

II. Iodine Analysis for a One-Cell EPR Model with CONTAIN/CONTI/IMPAIR

(V. Krautschick, G. Henneges, INR)

Zusammenfassung

Die Analyse hypothetischer Störfälle hat eine große Signifikanz bei der Sicherheitsbewertung von Kernkraftwerken. Fundiertes Wissen über die Freisetzung radioaktiver Spaltprodukte ist dabei wesentlich für die Abschätzung radiologischer Konsequenzen postulierter Störfälle. Aus radiologischer Sicht ist das Element Iod ein wichtiges Spaltprodukt, verantwortlich besonders für frühe radiologische Effekte. Dieser Bericht beschreibt die Iodanalyse für ein Einzonenmodell des EPR-Containments nach einem hypothetischen LBLOCA. Die Programme CONTAIN, CONTI und IMPAIR sind die Mittel dieser Untersuchung. In dieser Studie wurden Iodid-Ionen (I^-) und elementares Iod (I_2) entsprechend des hypothetischen LBLOCA in die Gasphase des Containments eingegeben. Das meiste Iod wird als Iodid (I^-) in der Wasserphase gelöst bzw. auf der Farbe abgelagert. Die dominierenden Produkte in der Gasphase sind I^- und organisches Iod. I_2 ist auf Grund seiner Flüchtigkeit von Bedeutung. Die Art und die Menge gasgetragener Iodspezies ist entscheidend für weitere Studien zur Umgebungsfreisetzung. Mit dem Einzonenmodell des EPR steht ein Werkzeug für die weitere Untersuchung von Iodparametern mit vereinfachten Randbedingungen zur Verfügung.

Abstract

The analysis of hypothetical accidents has a great significance for the safety evaluation of nuclear power plants. Profound knowledge about the release of radioactive fission products is essential to estimate the radiological consequences of postulated accidents. From radiological point of view the element iodine is a major fission product. This paper describes an iodine analysis for a one-cell containment model of the EPR after a LBLOCA. The programs CONTAIN, CONTI and IMPAIR are the tools of this investigation. For this study I^- (iodide ions) and I_2 (elemental iodine) were sourced into

the gas phase of the containment due to a hypothetical LBLOCA. Most of the iodine is solved in the water phase as iodide (I^-) or deposited on paint. The dominating products in the gas phase are I^- and organic iodine. I_2 is essential because of its volatility. The type and the amount of gasborne iodine species is decisive for further studies of iodine release to the environment. The one-cell EPR model gives a tool for further iodine parameter investigations with simplified boundary conditions.

1. Introduction

The investigation of hypothetical accidents has a great significance for the safety evaluation of nuclear power plants (NPP). Profound knowledge about the release of radioactive fission products is essential to estimate the radiological consequences of postulated accidents. From radiological point of view the element iodine is a major fission product. Iodine is especially responsible for the early radiological effects. It is chemically very active and reacts with another substances under complex conditions.

This paper describes the iodine analysis for a one-cell containment model of the European Pressurized Reactor (EPR) after a hypothetical large break loss of coolant accident (LBLOCA). The tools used for this study are the programs CONTAIN, CONTI and IMPAIR. IMPAIR is an analysis code to model the iodine behavior in a compartment, the iodine transport to other compartments or to the environment after a severe accident in a NPP. It calculates the chemical behavior of iodine and its compounds. This behavior is based on thermal-hydraulic conditions in the containment. There are different codes (e.g. CONTAIN, MELCOR) available to analyse the physical performance. These programs compute the thermal-hydraulic, fission-product and aerosol conditions which are partly used by IMPAIR. The data transfer from the thermal-hydraulic program to IMPAIR is organized by the interfacing program CONTI. IMPAIR calculates the local concentrations of iodine species in gas and water space and the deposition on the structures. These iodine concentrations are the basis for further investigations of iodine released to the environment.

This report provides a study of the properties of CONTI and the one-cell EPR model gives a tool for further iodine parameter investigations with simplified boundary conditions.

2. CONTAIN 2.0 Calculation

CONTAIN is a containment analysis code to determine the containment thermal-hydraulic and fission-product behavior after a postulated accident. It was developed at Sandia National Laboratories. A one-cell-model of EPR was derived based on the eight-cell-model described in (Hen98) to perform a simple investigation of iodine behavior in the containment. The computation is based on an assumed hypothetical LBLOCA. The one-cell-model was chosen in order to:

- study the interfacing properties of the data transfer program CONTI
- get a tool for further parameter studies with reduced boundary conditions as basis for the determination of iodine released to the environment.

2.1 One-Cell-Model

The new one-cell-model combines cells 1 to 5 of the eight-cell-model to the new cell 1. For that purpose the gas volumes are summarized and the variables of the global control block are adjusted. The flow connections between the cells are taken away with exception of the pool overflow from IRWST to the Spreading Room (mentioned below). The material and energy sources are summarized with the exception of a special treatment of the IRWST (Table 1). Some sources had to be modified to match linear or interpolated input. The summation of heat structures of cell 1-5 gives 32 structures in the one-cell-model. Inner heat structures in the cells are kept as inner heat structures as in the eight-cell-model.

Table 1a Sources of Energy and Mass Input Values of the Eight-Cell-Model

value\cell Nr.	cell 1	cell 2	cell 3	cell 4	cell 5
h2o/h2/ar			*		
decay-heat	low cell	discarded			
q-vol (stored heat)	low cell				low cell

Table 1b Sources of Aerosol and Fission Products of the Eight-Cell-Model

value\cell Nr.	cell 1	cell 2	cell 3	cell 4	cell 5
aerosol mass					
mgo			*		
naoh			*		
zr	*		*		
zro2	*		*		
inactive	*	*	*		
h2ol	*	*		*	*
fission product mass					
csi			*		
csoh	*		*		
te2	*		*		
sro_plus	*		*		

Heat structures which were between cells 1 to 5 in the eight-cell-model were now defined as inner heat structures with non adiabatic outer boundary conditions (bcouter, icell). Heat structures to cell 6 of the eight-cell-model were also defined as inner heat structures but with constant outer temperature of 30 °C as boundary condition (Table 2). That is possible because no relevant temperature increase is realized in cell 6 in 12 h time interval (Schol95).

The water mass of $2*10^6$ kg in IRWST is uncoupled in the one-cell-model. Consideration

of this water mass would result in an overestimation of the evaporation water mass because of the different nodalization. Only the overflow 4.4 m from IRWST to Spreading Room is modeled like in the eight-cell-model. The energy put into the IRWST is treated by the temperature increase to 80°C with the overflow to the Spreading Room (Hen98).

Table 2 Conversion of Eight-Cell-Model Heat Structures into One-Cell-Model Heat Structures

cell	1	2	3	4	5	6
1	1,4 (4)	1,3+2,6 (3)	1,1+3,4 (1) 1,5+3,13 (5)	-	-	1,2 (2)
2		2,4 (9)	2,1+3,5 (6) 2,5+3,2 (10) 2,7+3,9 (11)	2,3+4,6 (8) 2,8+4,8 (12)	-	2,2 (7)
3			3,3 (14) 3,6 (15) 3,10 (18) 3,11 (19) 3,12 (20)	3,1+4,4 (13) 3,7+4,7 (16) 3,14+4,9 (21)	3,8+5,7 (17) 3,15+5,1 (22) 3,16+5,8 (23)	-
4				4,1 (24) 4,2 (25) 4,5 (27)	4,10+5,2 (28)	4,3 (26)
5					5,3 (29) 5,4 (30)	5,5 (31) 5,6 (32)
6			not	Modeled		

X,X eight-cell-model heat structure number

(X) one-cell-model heat structure number

2.2 Results

The calculation is stopped at 12 h (43200 s) because then a spray system would be started. Figures 1 and 2 show the pressure and temperature progression in the gas phase in comparison to cell5 of the eight-cell-model (Hen98). Cell5 is the biggest room in the containment and representative for the pressure progression. The pressure and temperature trend in the one- and the eight-cell-model are qualitatively comparable. Quantitative differences result from different nodalization. The heat sources and with it the gas temperatures are different. Heat structures in cells with lower temperature (especially cell4) will be heated less and so they withdraw a smaller heat amount from the containment atmosphere. This cannot be described within the one-cell-model. Equal distribution of heat sources in containment is assumed in the one-cell-model. All heat structures of the whole inner containment are heat sinks in the *same* temperature environment. Due to that there is an overestimation of heat removal from the containment atmosphere which causes mainly the differences shown in Fig. 1 and 2. A further chemical analysis of iodine behavior with the IMPAIR code uses these thermal-hydraulic results as a physical basis (volumes of gas and water, pressure and temperature values, as a function of time).

3. CONTI Data Transfer

The data transfer between accident analysis codes like CONTAIN with the iodine chemistry code IMPAIR is managed by CONTI. This interfacing program was developed at FZK by W. Scholtyssek (Schol98). The following data could be transferred:

- gas- and water space volumes
- gas- and water space temperature
- gas flow between compartments, (not used because one-cell-model)
- gas flow and material transport to the environment, (not used in this analysis)
- material transport between water- and gas phase and between compartments, (not used in this analysis)

CONTI reads data from the CONTAIN input- and output files and an user specified CONTI input file. This CONTI input file provides additional information like control data, IMPAIR geometry, deposition areas etc. After these data are processed with CONTI it writes the three IMPAIR input files: inpf, ntim, ntnaim.

input (CONTAIN)				inpf
pltfil (CONTAIN)	======>	CONTI	======>	ntim
cont.inp				ntnaim

The contents of the IMPAIR input files is organized by the following items:

- inpf — general data as user input (control data , deposit areas),
- ntim — thermal-hydraulic data (geometrical and time dependent thermal-hydraulic data from CONTAIN),
- ntnaim — iodine species data,

Table 3 Special CONTI Input Data

CONTI input data	area	data from CONTAIN input
sedimentation area	3527 m^2	area floor $_{concrete}$
dep. area of gas space epoxy paint	20183m^2	0.9*(area wall and roof) $_{concrete}$
deposition area of gas space steel	4730 m^2	(area roof, wall and floor) $_{steel}$
dep. area of gas space concrete	2243 m^2	0.1*(area roof and wall) $_{concrete}$
dep. area of water space epoxy paint	3174 m^2	0.9*(area floor) $_{concrete}$
deposition area of water space steel	0 m^2	
dep. area of water space concrete	353 m^2	0.1*(area floor) $_{concrete}$

The multiplication factors are rough estimations. The iodine released into the containment reacts mainly with cesium. It is assumed that 99% of iodine is present as CsI. 1% is elemental iodine I_2 (Keßl93). The CsI amount is taken from CONTAIN input file and split into 99% I^- (about 11 kg iodide) and 1% I_2 (about 0.1 kg) sourced into the

gas phase of containment atmosphere. To be sure to transfer all time steps between CONTAIN and IMPAIR correctly the variable "nthtx" in CONTI program file "params" was changed from 250 to 2222. If one needs more time steps for convergence in IMPAIR one has to adjust the variable nthtx. After this CONTI has to be compiled again.

4. IMPAIR 3 Calculation

IMPAIR is an iodine chemistry analysis code to model the iodine behavior in a compartment (atmosphere, sump and deposition), the iodine transport to other compartments or to the environment after a postulated LWR severe accident. IMPAIR was programmed at FZK and further developed at PSI (Switzerland). IMPAIR describes the chemical reactions and the distribution of the most important iodine compounds (28 species). IMPAIR considers 69 reactions. Every reaction is represented by a reaction rate constant at 25°C. The temperature dependence of the reactions is given by activation energy (Günt92). IMPAIR considers the following mechanisms:

- homogeneous reactions in gas phase
- heterogeneous reaction in gas phase
- transport of iodine species at the gas-water interface
- homogeneous reactions in water phase
- heterogeneous reactions in water phase

Homogeneous reactions are reactions between iodine species, reactions with organic residuals and silver and radiolysis reactions. Heterogeneous reactions are reactions on concrete, steel and paint surfaces.

4.1 Results in Gas Phase

The various iodine species in gas phase considered by IMPAIR are shown in Table 4. Iodide (I^-) and elemental iodine (I_2) are input in ratio 99 to 1 into the gas phase between 1000 - 5000 s. Figure 3 shows the seven largest amounts of iodine species in the gas

phase of cell 1 as results of the IMPAIR 3 calculation. The mass of the iodine species are different by some orders of magnitude. The most frequent iodine species is I^-. I_2 deposits on paint, steel and concrete. Iodine reacts with the organic paint of the component surfaces and with airborne particles of hydrocarbons to form organic iodine. These organic iodine compounds are especially CH_3I (methyl iodide) and CH_3 (methyl residues). With time progression there is a reduction of airborne I^- by more than one order of magnitude caused mainly by solution in water phase. The elemental airborne I_2 is reduced by more than three orders of magnitude. Additionally the deposited I_2 decreases with time progression.

Table 4 IMPAIR 3 Iodine Species in Gas Phase (Günt92)

name of species	IMPAIR Id. number
I_2 (elemental iodine)	1
I^- (iodide)	2
IO_3^- (iodate)	3
CH_3I (methyl iodide)	4
I_2 deposited on painted walls	5
AgI (silver iodine)	6
HMWI (higher molecular weight iodines)	7
I_2 deposited on steel walls	8
I_2 deposited on concrete walls	9
I^- droplets	10
IO_3^- droplets	11
HOI droplets (hydroiodous acid)	12
CH_3 (methyl residues mw=15)	13
CH_3R (methyl residues mw=30)	14

The amounts of organic iodine formed by reaction with paint increase in contrary to all other iodine species whereby the amount of CH_3I stays relative constant after 4h. All other iodine species in the gas phase considered by IMPAIR are smaller than 10^{-7} g or

not produced at all. The type and the amount of gasborne iodine species is decisive for further studies of environment release. The filters available have different effectiveness for various iodine compounds. It is 99% for aerosols, 90 % for elemental iodine (Keßl93) and it is assumed much less for organic iodine. So elemental iodine and organic iodine especially get more significance with regard to iodide.

4.2 Results in Water Phase

The various iodine species in water phase considered by IMPAIR are shown in Table 5. Figure 4 shows the nine largest amounts of iodine species in water phase of cell 1 as results of the IMPAIR 3 calculation. The mass of the iodine species are again different by some orders of magnitude. The most frequent iodine species is I^- (iodide). If the airborne I^- comes in contact with the water phase (sump or condensed water on structures) it is solved there. Here is the main iodine sink. Additionally I^- may be deposited on painted surfaces and react chemically to CH_3I. I_2 decreases after input time as well as the on concrete deposited I_2 and HOI (hydroiodous acid). Organic iodine is build up whereby CH_3I reaches saturation at t = 9 h. I_2 deposited on paint and IO_3^- are relative constant after 3h. All other compounds are smaller by some orders of magnitude or not produced.

Table 5 IMPAIR 3 Iodine Species in Water Phase (Günt92)

name of species	IMPAIR Id. number
I_2 (elemental iodine)	15
I^- (iodide)	16
IO_3^- (iodate)	17
AgI (silver iodine)	18
CH_3I (methyl iodide)	19
Ag (silver)	20
CH_3 methyl residues mw=15	21
HOI (hydroiodous acid)	22
I_2 deposited on paint walls	23
HMWI (higher molecular weight iodines)	24
I_2 deposited on steel walls	25
I_2 deposited on concrete walls	26
CH_3R (methyl residues mw=30)	27
I^- deposited on paint	28

5. Conclusions

For a simplified EPR containment an iodine analysis was performed for a postulated LBLOCA with the code IMPAIR for the first 12 h. The calculation is based on thermal hydraulic data which were supplied by CONTAIN. The data transfer from CONTAIN to IMPAIR was organized by the interfacing program CONTI. The EPR containment was simplified to a one-cell-model to get a tool for fast iodine parameter studies with reduced boundary conditions as basis for the determination of environment release.

IMPAIR calculates iodine behavior which cannot be done so accurately by CONTAIN. In the studies with containment codes it is assumed for example that iodine compounds

which reached the sump are no longer effective as a radiological source. No resuspension or revolatilization is taken into account. With IMPAIR elemental iodine can be calculated which is produced in the sump due to radiological effects and sourced to the gas phase.

For this study I^- (iodide ions) and I_2 (elemental iodine) were sourced into the gas phase of the containment due to a hypothetical LBLOCA. Most of the iodine is solved in the water phase as iodide (I^-) or deposited on paint. The dominating products in the gas phase are I^- and organic iodine. I_2 is essential because of its volatility.

Filters available have different effectiveness for various iodine compounds. The filter effectiveness is higher for aerosols than for elemental iodine and that again higher than for organic iodine. The type and the amount of gasborne iodine species is decisive for further studies of environment release.

References

Hen98 G. Henneges, R.G. Gido, "Containment Analysis of a Nuclear Power Plant Similar to the European Pressurized Reactor (EPR) with Contain 2.0", INR-1982, Forschungszentrum Karlsruhe, Juni 1998

Schol95 W. Scholtyssek, "CONTAIN Analyse zum thermohydraulischen Verhalten im EPR Containment nach einem Kühlmittelverluststörfall", INR-1922, Forschungszentrum Karlsruhe, Juli 1995

Schol98 W. Scholtyssek, "CONTI - a FORTRAN Program for IMPAIR Input Preparation and Coupling to Thermal-Hydraulic and Aerosol Codes", Forschungszentrum Karlsruhe

Helm97 F. Helm, "Untersuchungen mit IMPAIR zum Iodverhalten im Containment", INR-1954, Forschungszentrum Karlsruhe, Januar 1997

Günt92 S. Güntay, R. Cripps, "IMPAIR/3: A COMPUTER PROGRAM TO ANALYSE THE IODINE BEHAVIOR IN MULTI-COMPARTMENTS OF A LWR CONTAINMENT", PSI-128, Paul Scherrer Institut, September 1992

Keßl93 G. Keßler, B. Kuczera, J. Ehrhardt, G. Henneges, W. Scholtyssek, H.W. Wiese, "On the Confinement of the Radiological Source Term during Beyond Design Basis Events in Future Pressurized Water Reactors", KfK 5199, Kernforschungszentrum Karlsruhe, August 1993

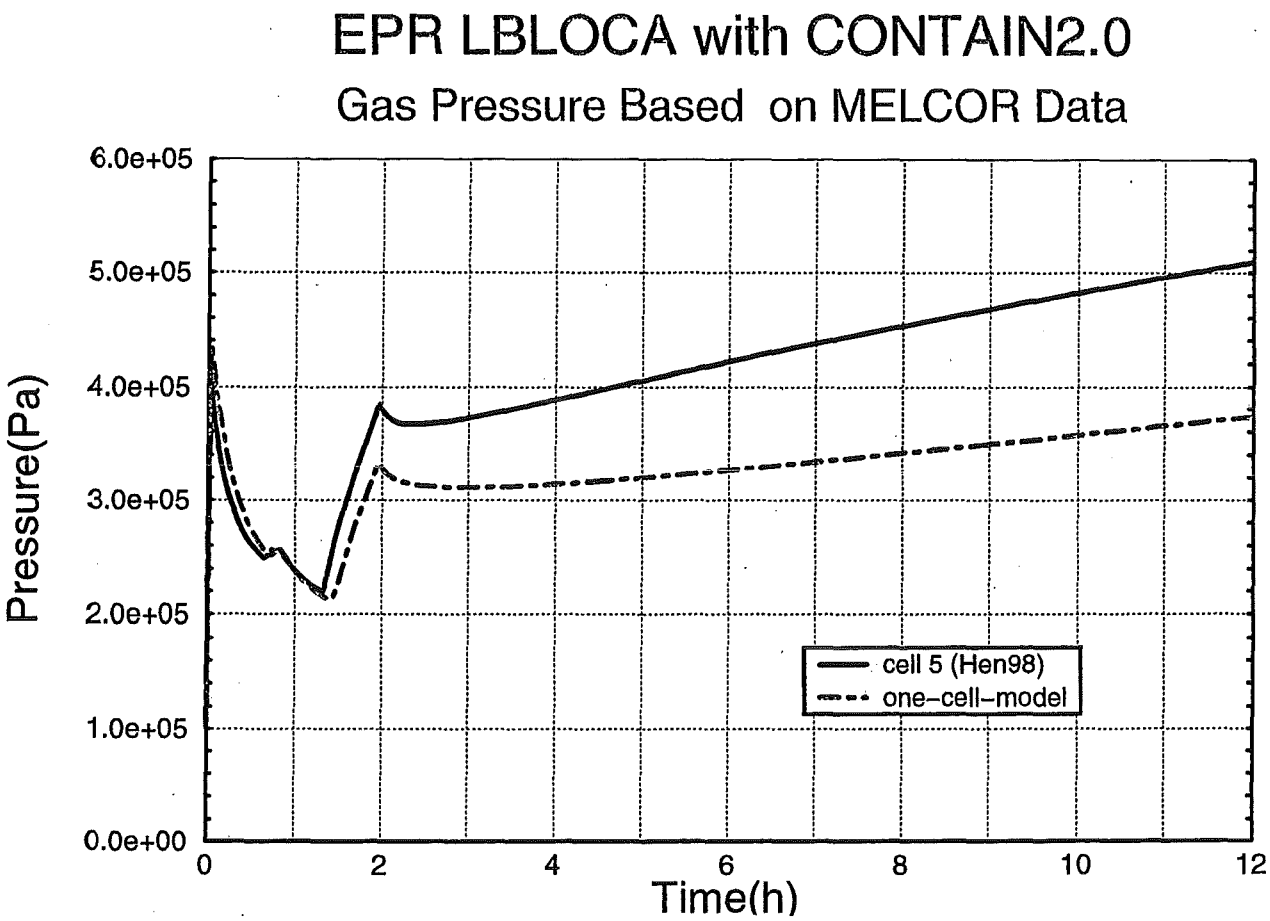

Fig.1 Gas Pressure in One-Cell-Model and Cell 5 of Eight-Cell-Model

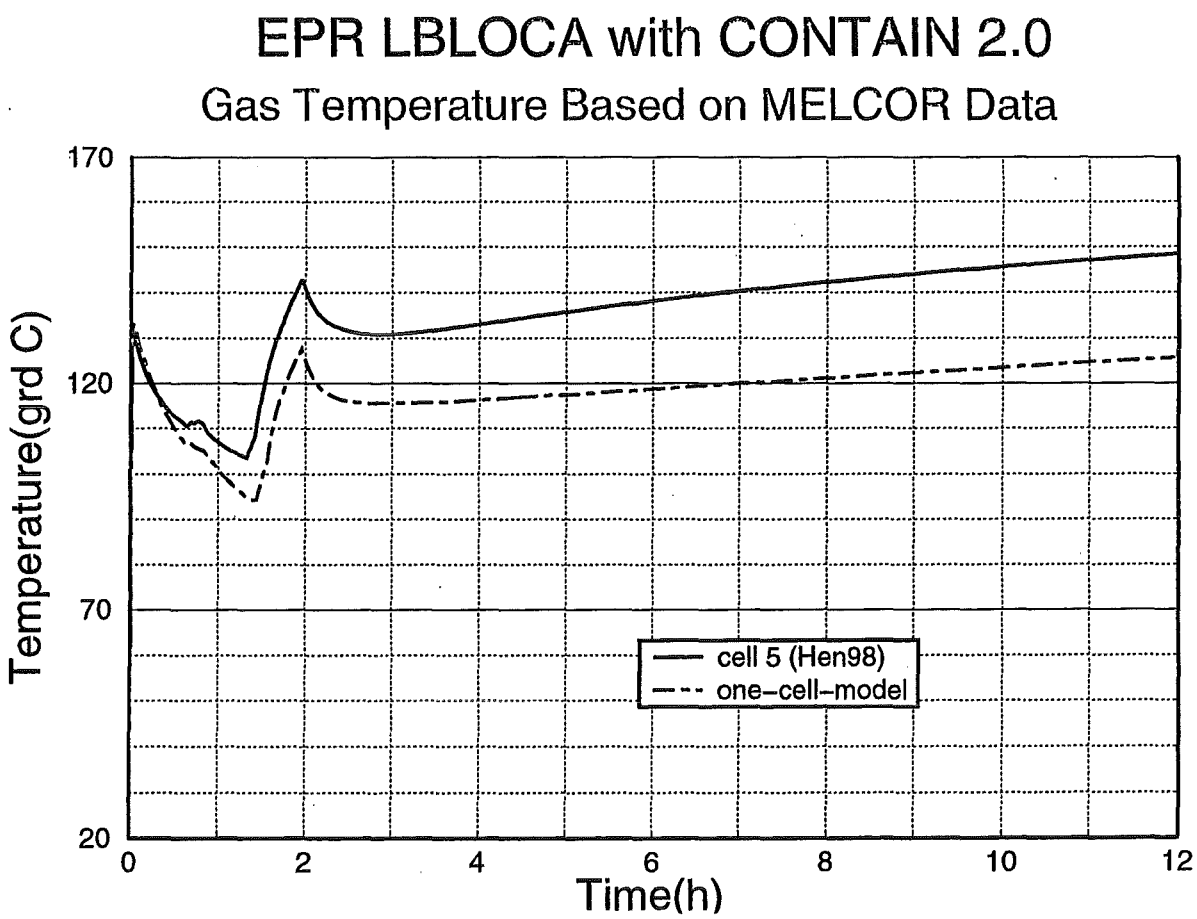

Fig.2 Gas Temperature in One-Cell-Model and Cell 5 of Eight-Cell-Model

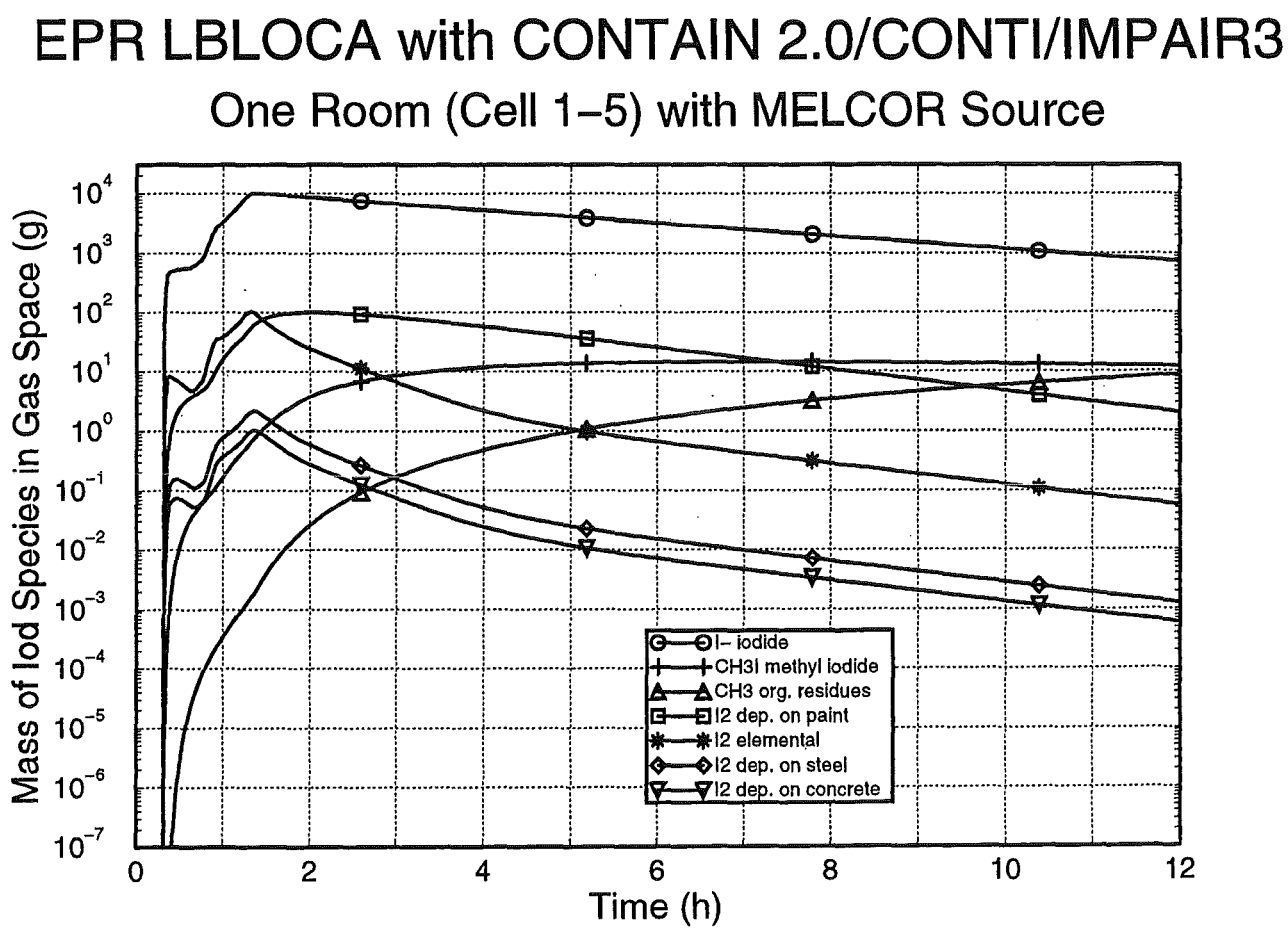

Fig.3 Mass of Iodine Species in Gas Phase of One-Cell-Model

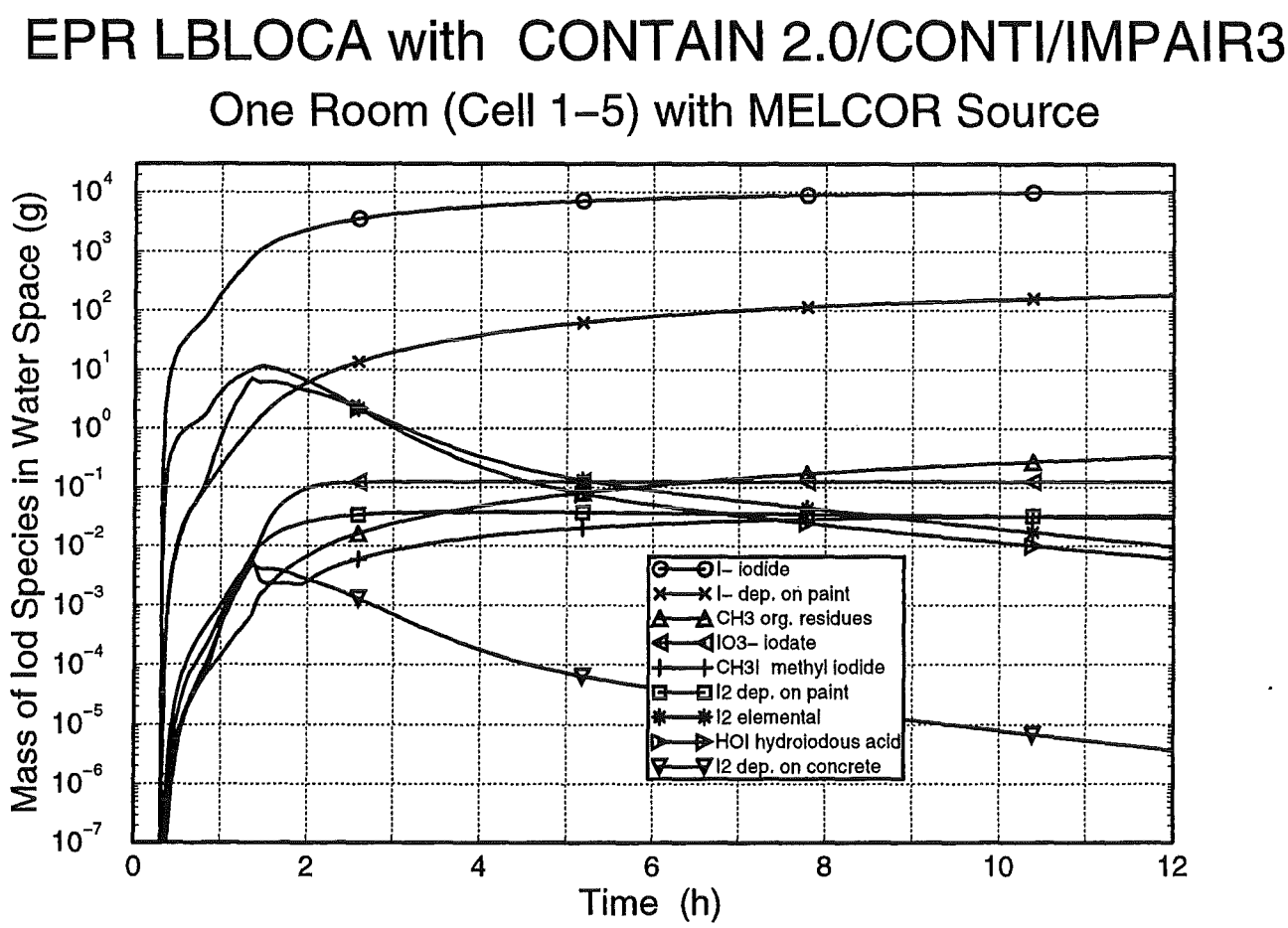

Fig.4 Mass of Iodine Species in Water Phase of One-Cell-Model

III. Analyses of Severe Accidents for the EPR using MELCOR

(P. Schmuck, B. Toth, INR)

Abstract

The MELCOR code is used to study the progression of severe accidents in the EPR. Early 1998 the new version 1.8.4 was released by SNL. This version has been used to reconsider accident scenarios calculated already with earlier MELCOR versions. In this contribution selected results are shown for a LBLOCA which demonstrate that version 1.8.4 provides a more consistent picture of the radioactive source term for severe accidents. Also some remarks related to the EPR optimized design data are made.

Zusammenfassung

Mit dem Code MELCOR wird das Fortschreiten von schweren Unfällen im EPR untersucht. Im Frühjahr 1998 brachte SNL die neue Version 1.8.4 heraus. Mit dieser Version wurden dann bei FZK Unfallszenarien nachgerechnet, die bereits mit früheren MELCOR-Versionen untersucht worden waren. In diesem Beitrag werden ausgewählte Ergebnisse für einen LBLOCA-Fall präsentiert, aus denen hervorgeht, daß die Version 1.8.4 ein konsistenteres Bild des radioaktiven Quellterms liefert. Darüber hinaus befaßt sich dieser Beitrag auch mit den optimierten Designdaten für den EPR.

Generalities

At FZK investigations with MELCOR concentrated on accident sequence studies for the European Pressurized Water Reactor (EPR). MELCOR is a very flexible and versatile tool to perform such system studies. During the reporting period the new version 1.8.4 of MELCOR has been released by SANDIA National Laboratories and was installed and tested on FZK computers.

No prefabricated modelling for the EPR subsystems of the primary and of the secondary circuits and of the reactor containment components is available in

MELCOR. This feature is in contrast to other accident codes, like e.g. MAAP, where generally possibilities are provided by the code to model directly components of the reactor system, e.g. the pressurizer, the steam generators, etc. Therefore, using MELCOR, the EPR system has to be modelled and represented in very great detail by the MELCOR input data themselves. A systematic modelling of the EPR in MELCOR needs about 7000 input records, which should still be more refined for special investigations. These input data have been developed during the last years at FZK and have been transferred (together with the code itself) to SIEMENS/KWU in Erlangen, where the data have been checked to represent correctly the EPR system. In addition, SIEMENS/KWU is doing now own accident simulations using the MELCOR input developed by FZK.

The validation of the input data was done at FZK by checking the operation of various technical components of the reactor systems in steady and transient states. This includes heat transfer in the core, the functioning of the primary circuit, the pump performance of the main primary system pumps, and the heat transfer from the primary to the secondary circuits in the steam generators.The thermal hydraulics of the various subsystems had to be checked always in detail before an accident sequence calculation was started.

Three main scenarios (including some variants) have been widely investigated for the EPR project with the MELCOR code : the LBLOCA, the SBLOCA and the LOOP sequences.

The numerical results were evaluated for different purposes including :

- Hydrogen production and distribution
- Radionuclide release and transport
- In- and ex-vessel steam explosions ..

The results were communicated to four (of the common six) cooperative working groups, for which MELCOR results play an important role.

The general applicability of the MELCOR code to severe accidents in PWRs has been demonstrated by many investigations (see Ref. 1, where a long list of assessment reports is given). FZK takes part in the ongoing assessment of MELCOR in the

international MCAP (**M**ELCOR **C**ode **A**ssessment **P**rogram) efforts. Ref. 2 represents the most recent FZK contribution to MCAP.

EPR accident sequence calculations were done at FZK over the years with three different versions of MELCOR: 1.8.2, 1.8.3 and 1.8.4. Always significant changes in accident modelling were observed from one version to the next, and consequently the numerical results changed also. Version 1.8.4 is characterized by changes to model core degradation more realistically by using the information which comes from the PHEBUS FP experiments. Therefore in this new version improved models for core heatup, core uncovery, core degradation and meltdown have been implemented.
Only a few numerical results of the FZK work will be discussed here and we will concentrate on comparisons of the LBLOCA scenario for versions 1.8.3 and 1.8.4, respectively.

Specific results

The EPR system, as represented in the MELCOR code for accident simulations, is shown in Fig. 1, where the control volumes (nodes), the flow path linking the control volumes and the heat structures are displayed. All the calculations explained here are performed for the basic design data of the EPR. As can be seen in Fig. 1, the primary system and the containment are modelled quite in detail, while only parts of the secondary system (which are important for accident simulations) are represented. In order to study severe accidents leading to core melt-down we assume that the active emergency core cooling systems (medium head safety injection and low head safety injection systems of the EPR) do not operate. This is quite improbable, but the assumption is made to investigate the consequences of failures of the injection systems and to assess the design margins of the EPR.

As mentioned above, the LBLOCA sequence is used to demonstrate some important capabilities of MELCOR. A few significant results are shown in the following which refer to the in-vessel phase and to the early ex-vessel phase, when the hot core debris relocates to the reactor cavity. The total accident time for the LBLOCA

considered is 5000 seconds. In order to facilitate the comparisons between the 1.8.3 and 1.8.4 results, the input data changes necessary for the 1.8.4 runs were kept simple, but we tried to apply some of the more important features of the new code version. For example, the melting of heat structures and a more exact representation of flow blockages in the core during melt-down was taken into account for the 1.8.4 runs.

The LBLOCA sequence is initiated by a break of the surge line (which connects the hot leg with the pressurizer) at time t = 0 , with a break size of 962 cm^2. Automatic reactor scram is actuated by the primary system pressure which decreases rapidly during the first seconds after the break occurrence, so only decay heat is responsible for heating up the core materials later. The hot coolant of the primary circuits is blown out through the large leakage in the surge line to the containment, and in a short time period core uncovery starts.

The accumulators come into play after about 75 seconds, when the primary system pressure decreases below 45 bar. For a while they can replace the coolant lost with water stored in the accumulator tanks, but after 110 seconds they are empty and the final core uncovery and heatup process starts.

When the fuel temperature gets larger than 2000 K, fission products (FP) in the fuel are released to the gap (located between fuel and cladding). Volatile elements are released first (e.g. Xe, Cs) and only at higher temperatures the refractory elements (e.g. Ba, Sr, Ru) will follow. When the fuel can fails (at cladding temperature 1173 K), the FP are transported from the gap into the primary circuit, to the large break leak and from there to the containment.

Core materials will melt also at high temperatures, starting with the EPR control rod materials (Ag, In, Cd) at about 1075 K. At still higher temperatures, the clad materials (Zr, ZrO_2) melt down together with the fuel during a few thousand seconds.

The relocating core debris settles first on the core support plate which is a heavy steel structure. After failure of this plate, the hot debris falls down and accumulates on the lower head.

The timings of structural failures are important for accident damage progression and compare as follows:

	Core support plate	Pressure vessel
MELCOR 1.8.3	3182 s	3856 s
MELCOR 1.8.4	3479 s	3589 s

After failure of the core support plate only a few hundred seconds are needed with version 1.8.3 (and only about one hundred seconds with version 1.8.4) to reach the failure conditions of the lower RPV head. From this time point the hot core debris will relocate to the reactor cavity and interact with the concrete of the cavity floor.

Some interesting results of versions 1.8.3 and 1.8.4 are compared in the Figures 2 to 6, up to the problem time of 5000 seconds. Fig 2. shows the total mass of radioactive materials released from the fuel during the time of the accident and some related quantities (the total mass of radioactive aerosols in the atmosphere and the pool regions, and the total radioactive mass deposited on all heat structures).
The FP release from the fuel is calculated by the CORSOR Booth model for high burnup fuel in both versions. It seems that the 1.8.3 release is correct only after vessel breach, before only a quite low fraction of FP is released, and the large change of the radionuclide masses released at the time of vessel breach is not justified by thermal and pressure conditions in the primary circuit. In contrast, version 1.8.4 leads to a continuous release of FP before and after breach of the vessel in accordance with the temperature of the fuel in the core. To illustrate this feature in more detail we show in Fig. 3 the release of the radionuclide group 1 (noble gases like Xe, Kr) and group 2 (alkali metals like Cs, Li) to the containment. The same characteristics as in Fig 2. can be detected, so in the 1.8.3 results also the noble gases are retained for a long period, which is not realistic.

Figs. 4 to 6 show the hydrogen occurrence in the primary system and in the containment. From Fig. 4 it can be seen that the production of hydrogen in version 1.8.4 is much higher. This is connected with the new core melt-down model which is adapted to the PHEBUS FP experiments. Fig. 5 shows the hydrogen in different compartments of the containment. The dome exhibits the highest amount of hydrogen because of the very large volume of the containment dome.

Fig 6 shows the hydrogen masses in the reactor cavity and the hydrogen flow rates from there to the main compartments of the containment (equipment rooms, dome, annular compartments). About 50 kg hydrogen is produced totally in the reactor cavity up to 5000 s. This can be seen from Fig. 5, where the amount of hydrogen in the containment is depicted (the increase of 50 kg are observed between 4000 and 5000 seconds).

In general it can be said, that the 1.8.4 results differ from the earlier 1.8.3 results because in version 1.8.4 there are more realistic:

- Criteria for core melt-down and collapse:
  As oxidized fuel rods collapse now at the approximate temperature of the UO_2/ZRO_2 eutectic temperature, the core is much hotter at the time when loosing integrity.

- Models for melting the large steel structures surrounding the core:
  Heavy reflector and core top plate; this option was not available earlier.
- Possibilities to simulate blockages of the settling core debris:
  pressure correlations according to flow through porous media are used, so the debris bed is modelled more realistically.

Work in progress

Design data for the EPR optimized design (with a 15% higher nominal reactor power) were distributed in January 1998 by Siemens/KWU. The MELCOR input data were changed and updated accordingly and first MELCOR calculations done for steady state conditions and for the LBLOCA sequence. It was found that these first data were inconsistent in some respects, with a too low nominal flow rate through the core as the main defect. Therefore in the steady state the coolant temperatures in the core get quite high and the coolant state is near to bulk boiling. Early during the LBLOCA progression the fuel clad temperatures becomes so high, that clad failure happens and gap release of radionuclides to the primary circuit occurs.

Only mid of December 1998 revised data were obtained from Siemens/KWU which will used in future investigations.

References

1. B. Boyack et al., MELCOR Peer Review, Report LA-12240, March 1992

2. P. Schmuck, Analysis of Severe Accident Sequences of an Innovative PWR of the 1500 Mwe Class, 1998 Annual MCAP Meeting, Bethesda, MD, May 1998

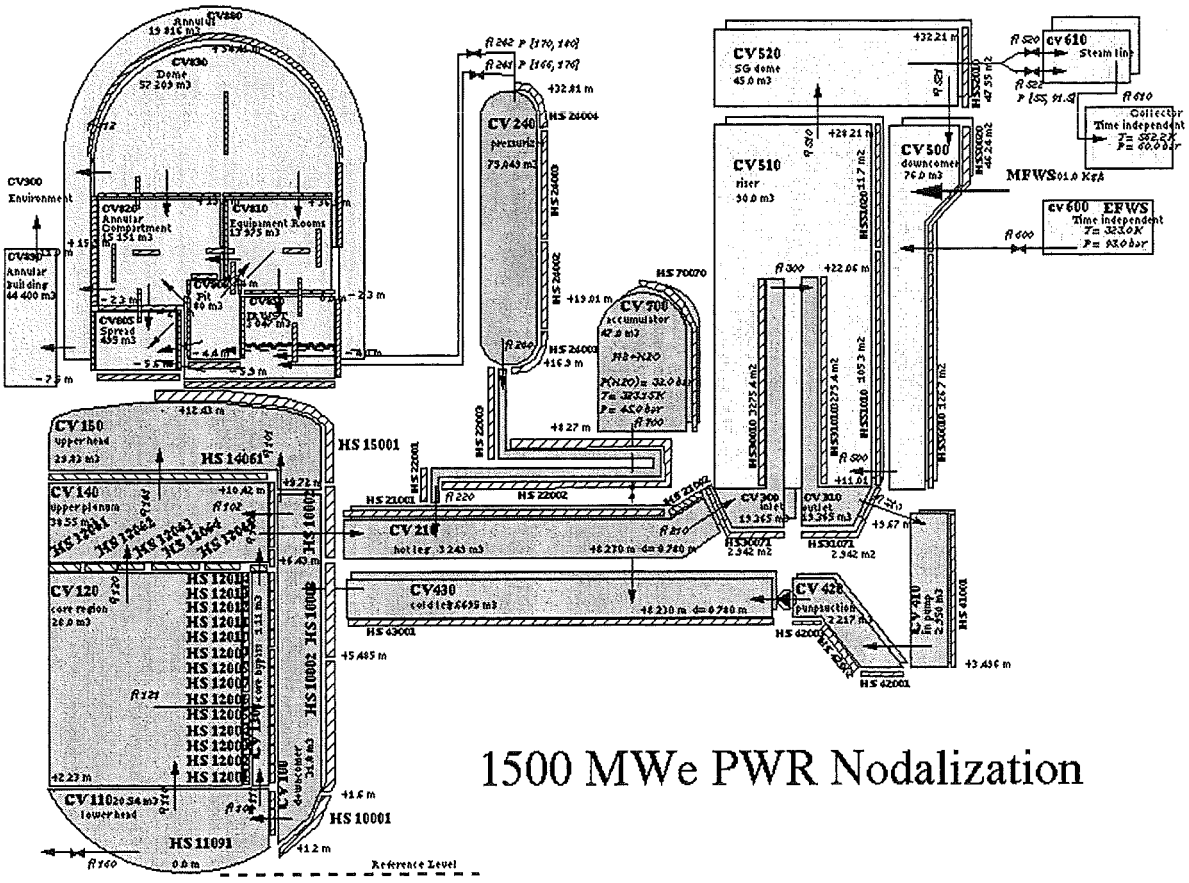

FIG. 1: Nodalization of the EPR primary and secondary system and the reactor containment

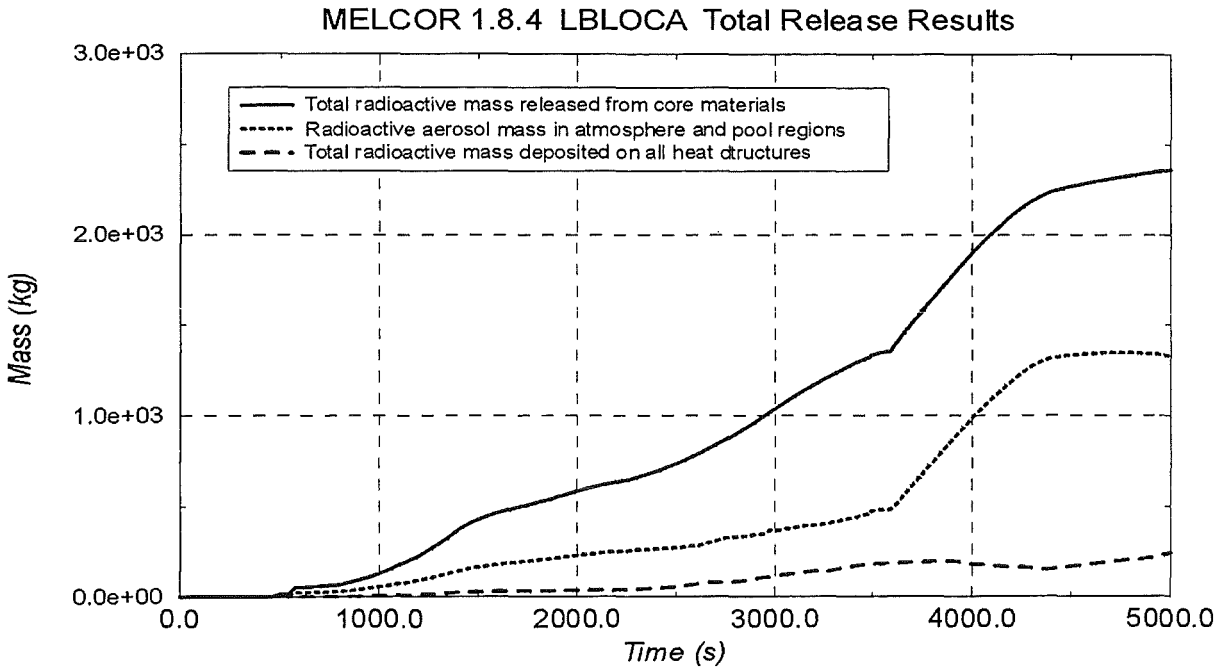

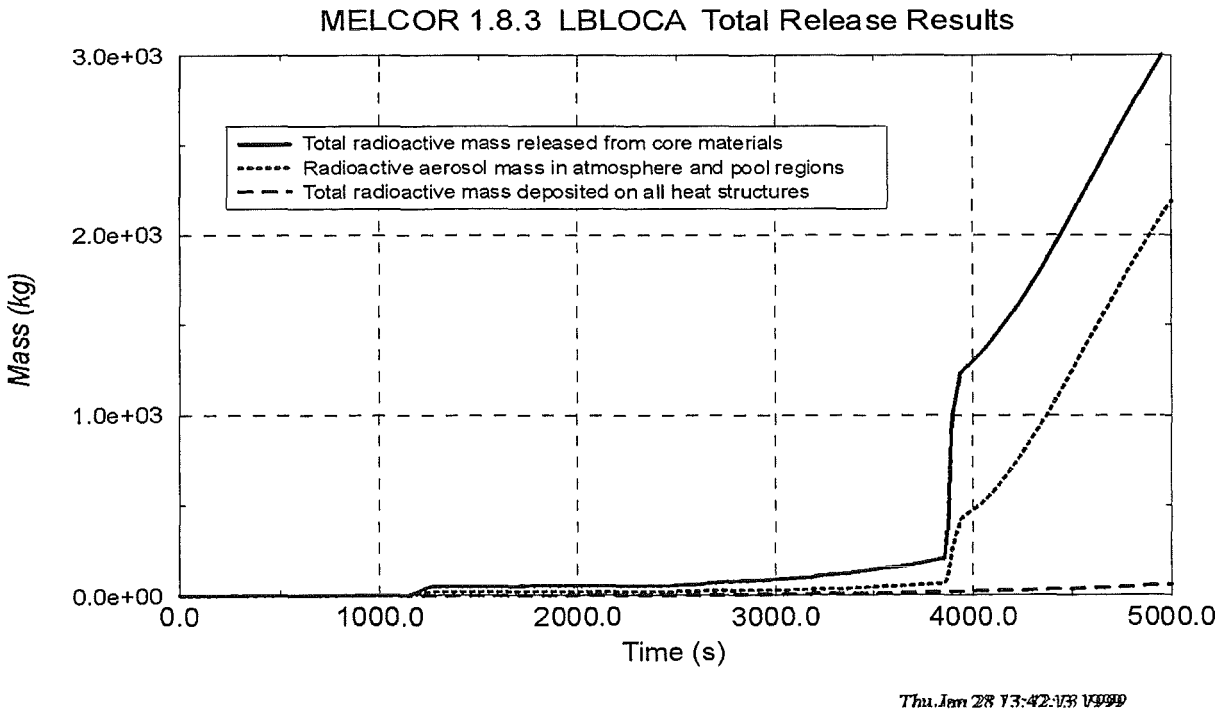

FIG. 2: Total masses of radioactive materials released and distributed in the primary system and containment

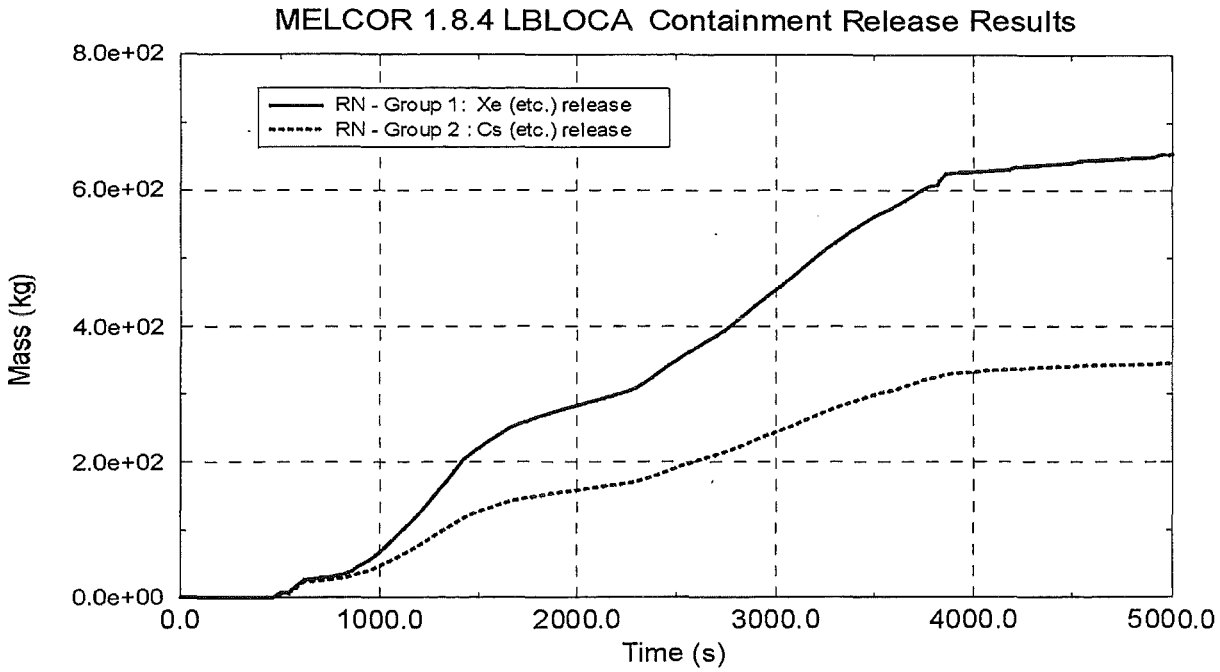

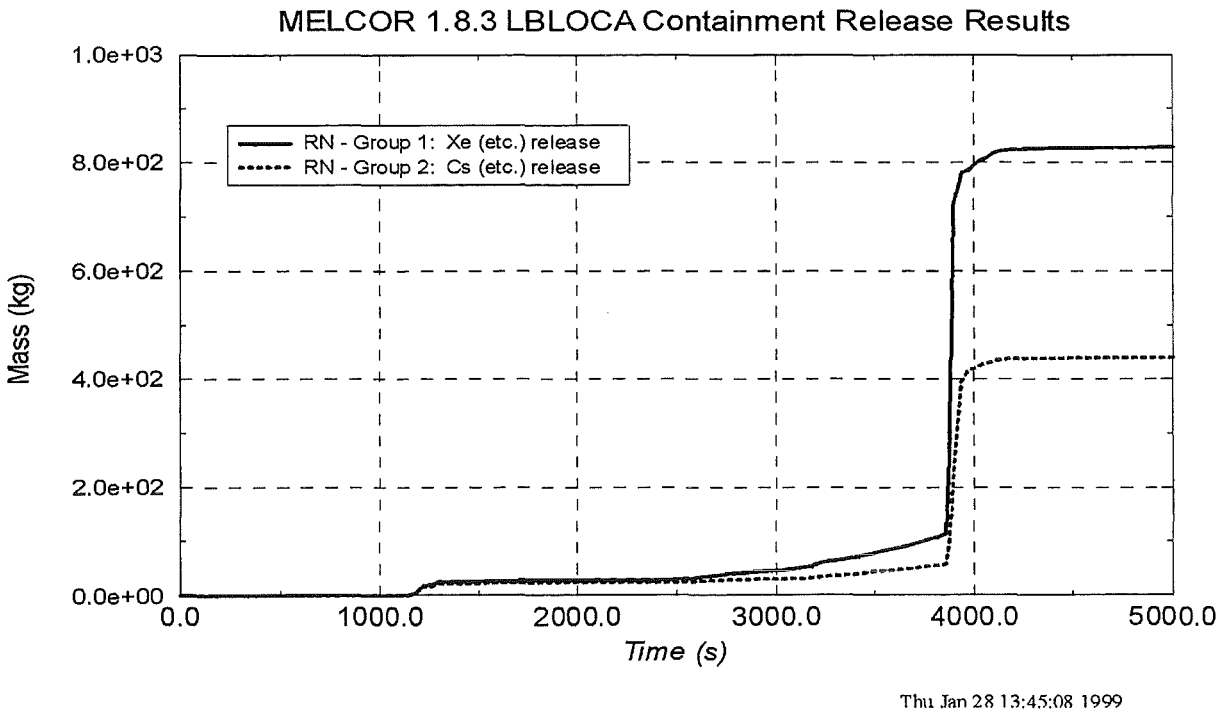

FIG. 3: Radioactive masses of volatile materials (noble gases, alkali metals) released to the containment

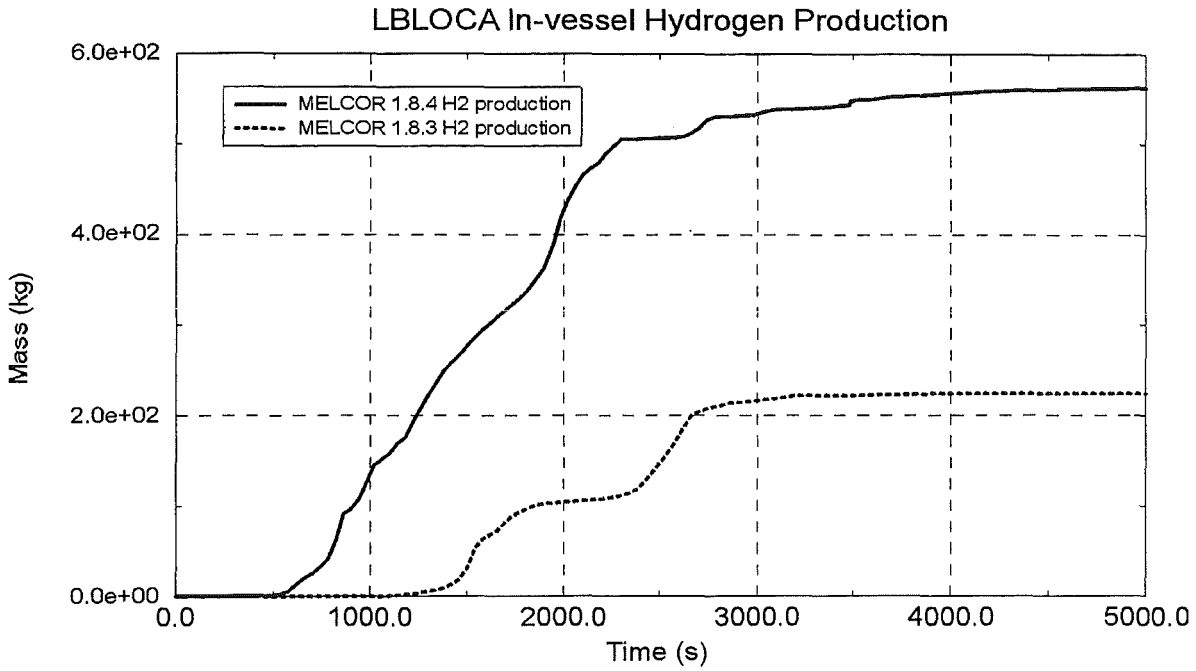

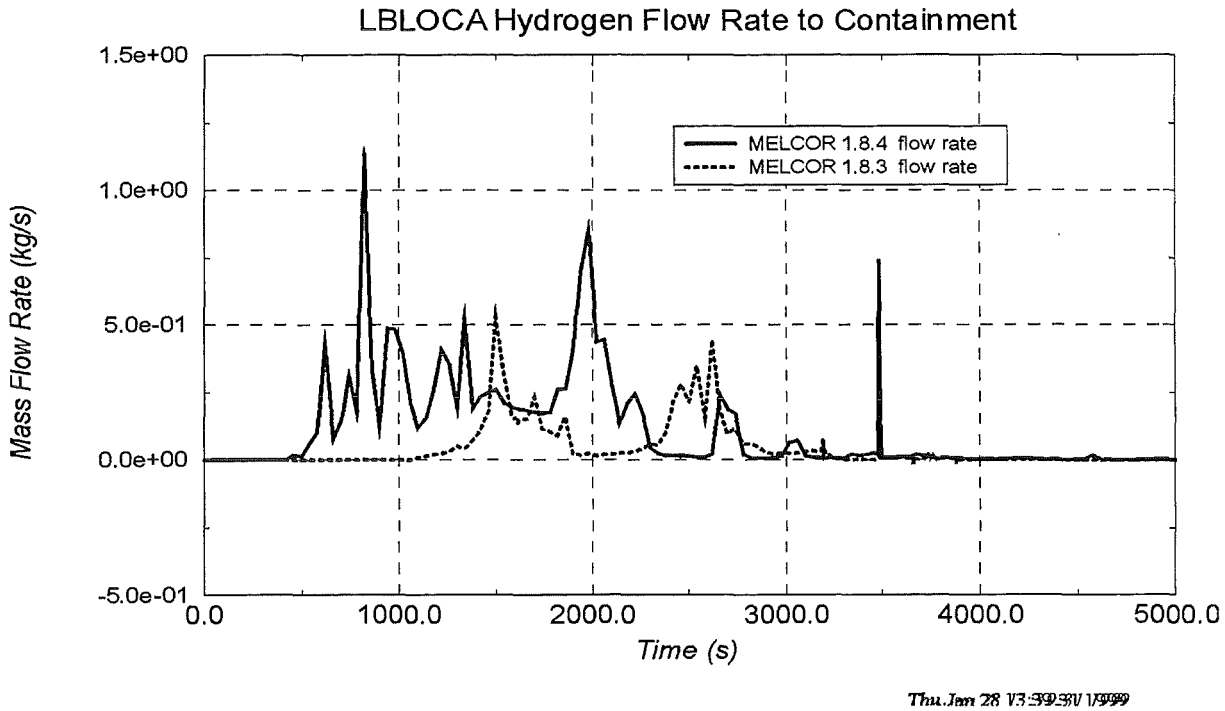

FIG. 4: Hydrogen production in the core and flow to the containment

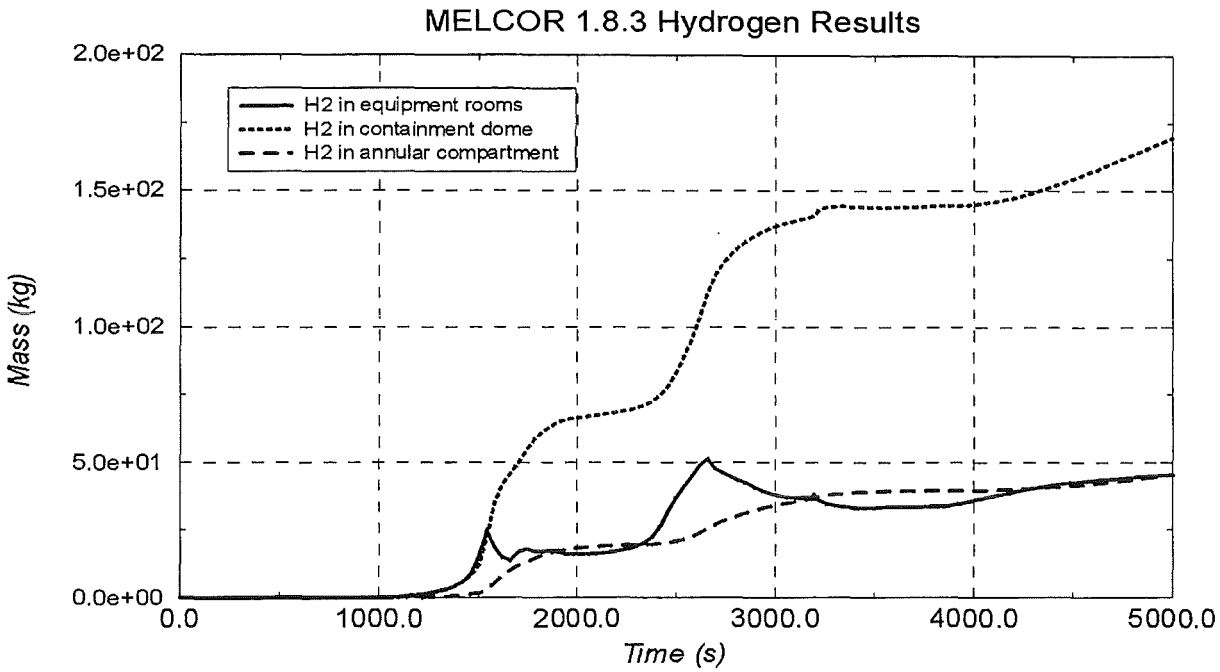

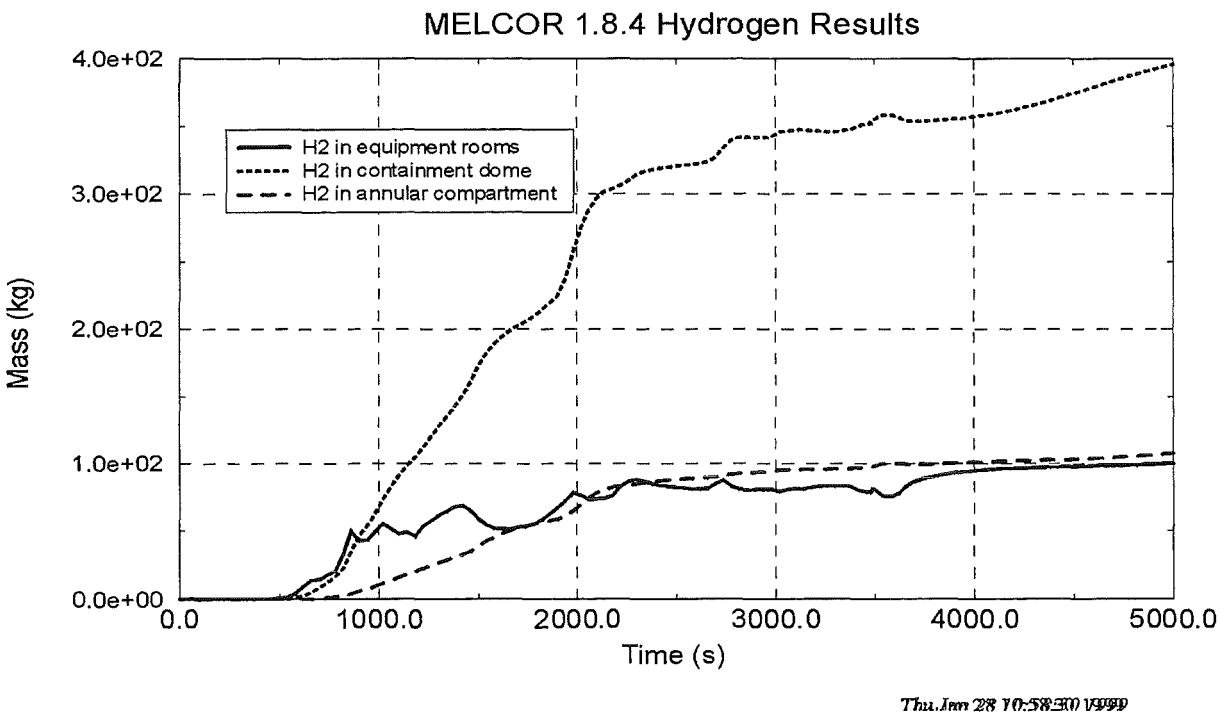

FIG. 5: Hydrogen in the various compartments (shown in Fig. 1) of the containment

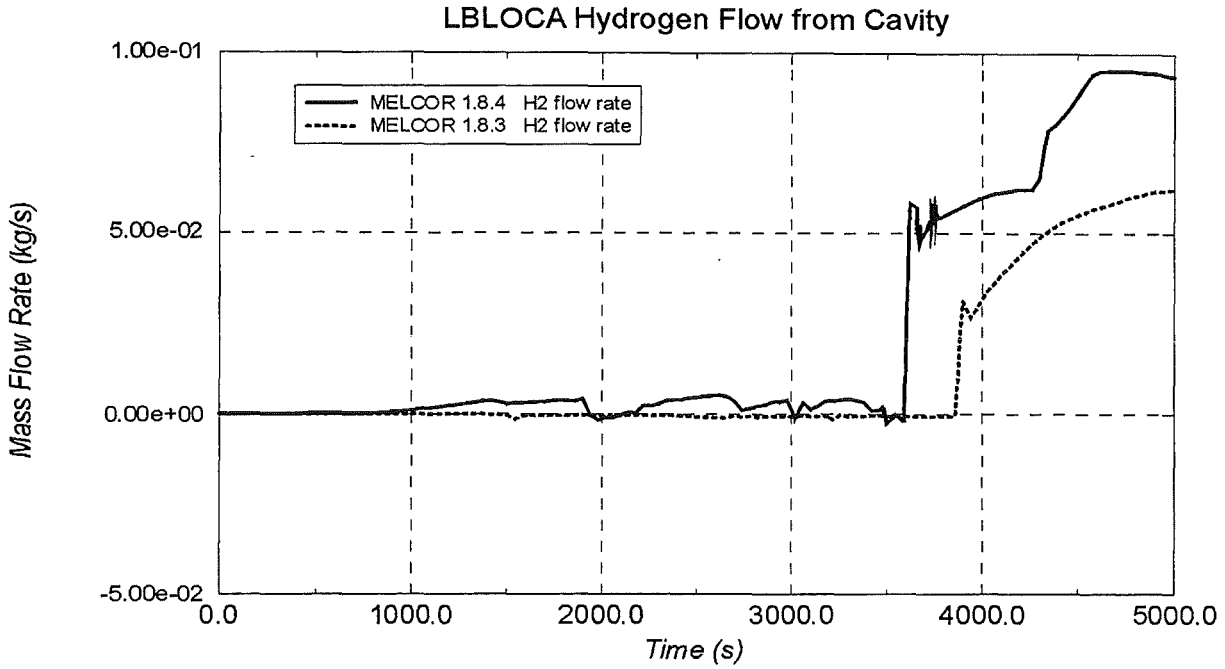

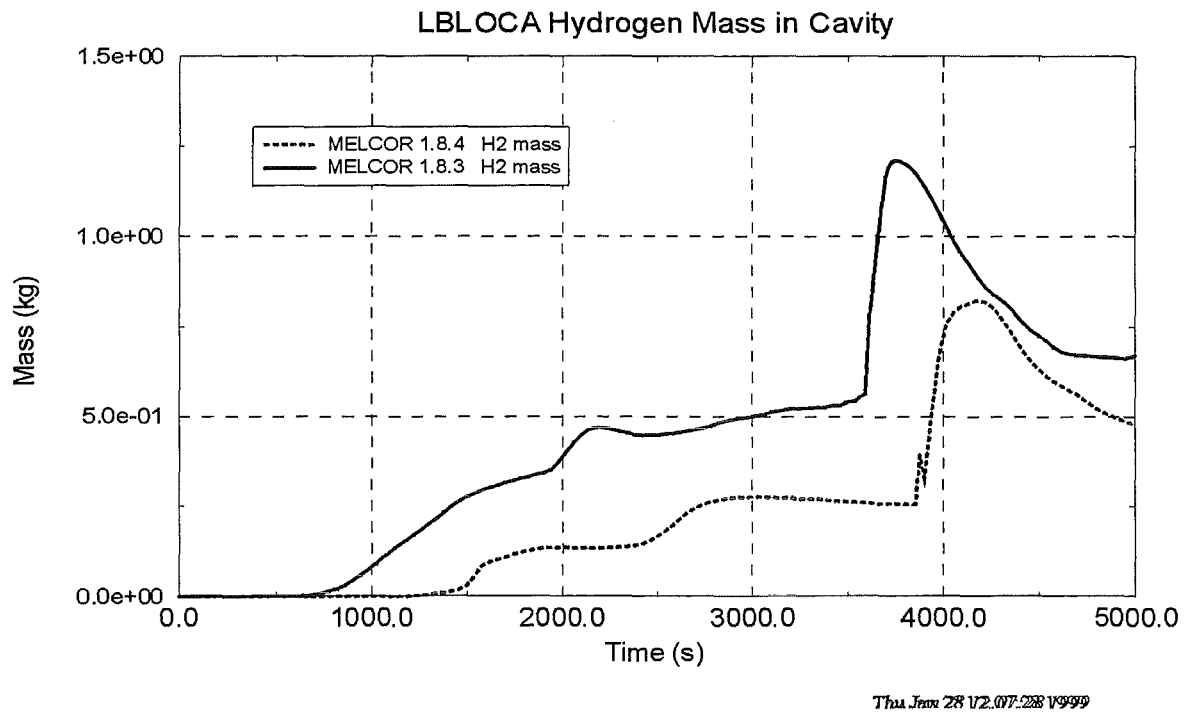

FIG. 6: Hydrogen content in the EPR reactor cavity and transport (flow) to the main parts of the containment

32.21.08. Untersuchungen zur Kernzerstörung

I. QUENCH Experiments

(P. Hofmann, A. Miassoedov, M. Steinbrück, IMF I; L. Schmidt, D. Piel, IMF III; L. Sepold, W. Leiling, HIT)

Abstract

New results of separate-effects tests, namely of single rod quench tests and hydrogen absorption tests of zirconium alloys are described. Furthermore, a description of test conduct and main results obtained during the first two bundle tests QUENCH-01 and QUENCH-02 is given.

Zusammenfassung

Neue Ergebnisse von Einzeleffektuntersuchungen, insbesondere von Einzelstab-Abschreckexperimenten und von Versuchen zum Wasserstoffabsorptionsverhalten von Zirkoniumlegierungen werden vorgestellt. Außerdem wird eine Beschreibung des Versuchsablaufs und der wichtigsten Ergebnisse der ersten beiden Bündeltests QUENCH-01 und QUENCH-02 gegeben.

1. SINGLE ROD QUENCH TESTS

The tests in the small-scale QUENCH rig in which it is possible to quench short Zircaloy fuel rod segments by water or steam have been continued [1]. The principal investigated experimental parameters are the extent of pre-oxidation and the temperature of the tube before cooldown. The experiments are supported by theoretical work at the Nuclear Safety Institute (Russian Academy of Sciences), where modelling of the main processes taking place during reflooding (heat exchange, oxidation of Zircaloy, mechanical behaviour of the cladding) is carried out. In particular, the main objectives of the experimental program are:

- to provide an extensive experimental database for the development of detailed mechanistic quench models;

- to investigate the physico-chemical behaviour of the overheated fuel elements under different flooding conditions;
- to determine the cladding failure criteria, cracking of the oxide layer which results in oxidation of the new metallic surfaces and additional hydrogen production.

The tube specimen of a length of 150 mm, filled with ZrO_2 pellets, is suspended inside a quartz tube which is surrounded by an induction heating coil (Fig. 1.1).

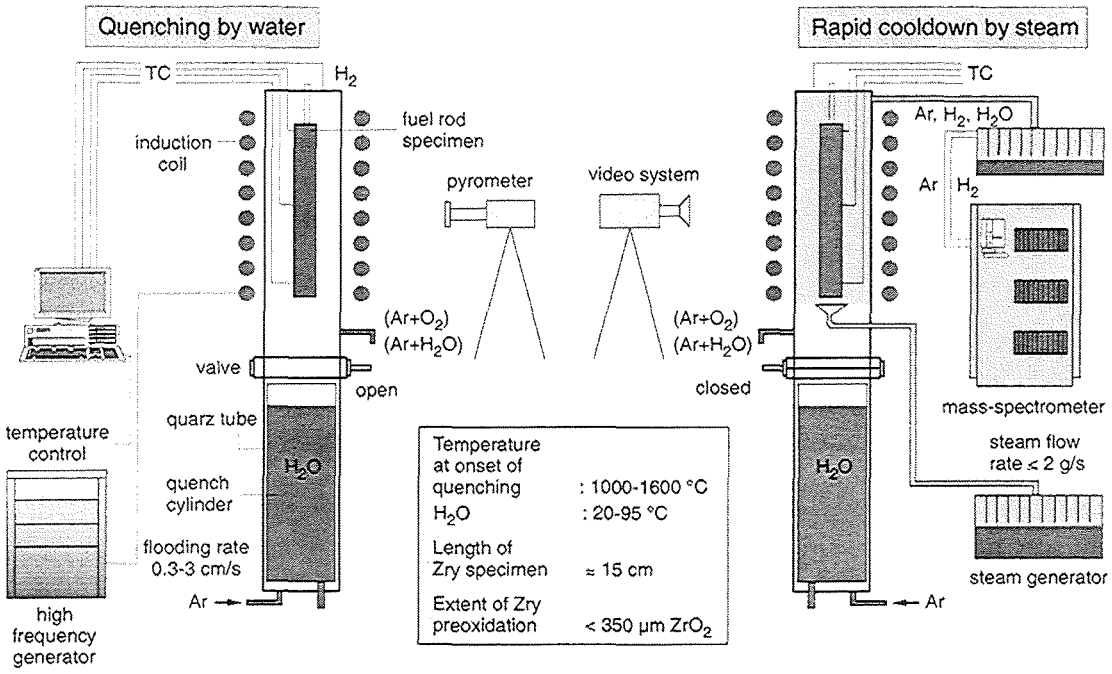

Fig. 1.1: Quench apparatus simulating flooding conditions of a degraded LWR core.

Pre-oxidation of the Zircaloy tube specimen (0≤300 µm ZrO_2 layer thickness) is executed at 1400 °C by a steam/argon gas mixture in the QUENCH rig before quenching. The specimen is then rapidly cooled down by injected steam of 1.0 g/s (Fig. 1.2). During the quench test the temperature of the specimen at three elevations and the hydrogen generation are continuously recorded. The thermocouple readings, the hydrogen generation rates detected by both a Caldos device and a mass spectrometer, and the system overpressure for the whole test sequence are given in Figure 1.3 on the basis of the experiment with 216 µm ZrO_2 pre-oxidation and 1200 °C temperature at onset of rapid cooldown by steam. The two pressure peaks correspond to the injection of 0.08 g/s steam at the beginning of the experiment and an

increased injection of 1.0 g/s steam into the test section 30 s before the power is shut-off. The injection of the 1.0 g/s steam 30 s before power shut-off causes temporary decrease of the specimen temperature in all the experiments performed, because of the better cooling. This temperature drop is soon compensated by increased electrical heating.

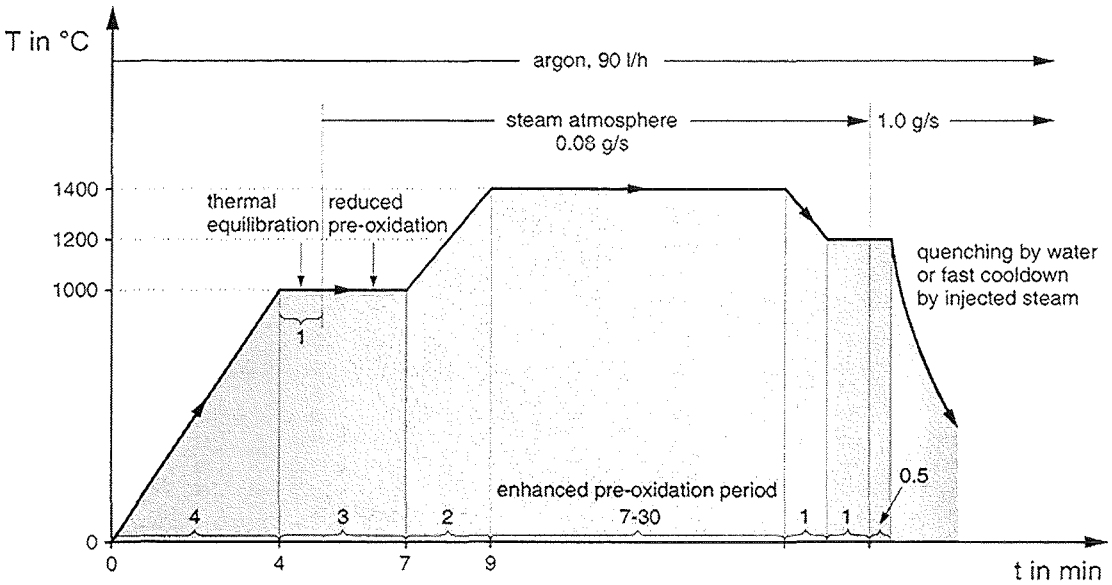

Fig. 1.2: Test conduct of single rod quench experiments.

A total of 24 experiments have been performed with specimens with oxide layer thicknesses varying from 100 µm to 350 µm which were rapidly cooled down by steam from 1100, 1200, 1400 and 1600 °C. The results of the experiments are summarised in Table 1.1.

A temperature deviation from the regular cooldown curve during the quench phase was observed in all experiments with quench temperatures less than 1600 °C when the ZrO_2 layer thickness was larger than 200 µm (Fig. 1.4). No temperature increase was observed in experiments with 1600 °C even for large ZrO_2 layer thicknesses. The mechanical behaviour of the cladding tubes depends on the quench temperature and the extent of pre-oxidation. Formation of macroscopic through-wall cracks can be observed in steam quenched experiments with ZrO_2 layer thicknesses larger than 200 µm. Crack formation is more pronounced at lower specimen temperatures at onset of cooldown (Fig. 1.5). The surfaces of the cracks in the remaining metallic part of the cladding tubes are oxidised. Oxidation of crack surfaces increases with decrease of the specimen temperature at onset of quenching. Due to the

experimental conduct it is not possible to prove the crack oxidation during quench on the basis of measured hydrogen generation which was clearly demonstrated in the experiments performed before (pre-oxidised in an Ar/O_2 mixture) [2].

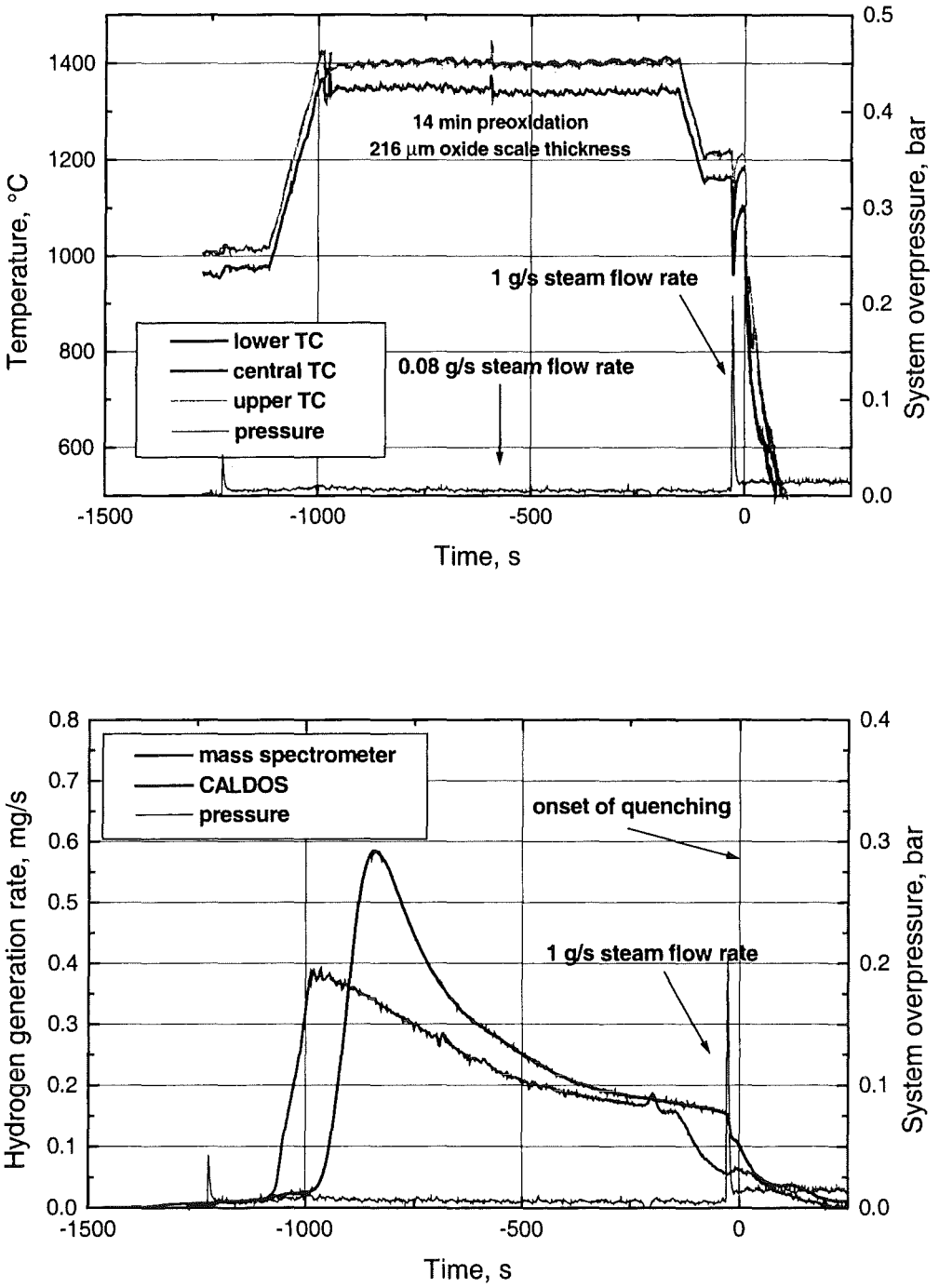

Fig. 1.3: Temperature history and corresponding hydrogen release; steam cooling from 1200 °C.

Test ID	Time of pre-oxidation at 1400 °C, min	Precalculated oxide layer thickness at onset of cool-down, µm	Tempera-ture peak	Total H_2 production, mg	Crack length, mm	Measured oxide layer thickness, µm
cooldown from 1100 °C: 4 experiments						
04038_2	4	135	No	114.7	0	-
05038_1	19	270	UC	244.5	203	270[1], 255[2]
05038_2	12	215	UC	184.4	-	210[2]
06038_1	7	170	No	131.8	0	175[1]
cooldown from 1200 °C: 8 experiments						
09028_1	30	315	UC	379.7	0	290[1]
09028_2	3	113	No	120.1	0	-
10028_1	12	201	U	239.5	1095	212[1], 210[2]
11028_1	9	176	U	203.0	734	185[1], 190[2]
11028_2	14	216	UC	246.4	1368	-
12028_1	7	157	No	184.8	255	167[1]
13028_2	25	287	UC	295.0	1362	-
04038_1	5	137	No	122.9	0	-
cooldown from 1400 °C: 6 experiments						
17028_1	26	290	UC	330.0	437	-
18028_1	7	150	No	145.8	165	160[1]
18028_2	12	195	UC	203.7	300	-
19028_1	19	246	UC	232.3	908	260[1]
25028_1	19	246	UC	255.1	1689	265[1]
25028_2	4	116	No	82.0	136	-
cooldown from 1600 °C (pre-oxidation at 1400 °C, then cooldown): 3 experiments						
16028_1	5	260	No	170.8	579	380[2]
16028_2	6	290	No	170.2	700	370[2]
26028_1	2	240	No	129.2	582	-
Cooldown from 1600 °C (pre-oxidation during heatup from 1000 °C to 1600 °C, then cool-down): 3 experiments						
27028_1	3	139	No	20.1	10	163[1]
02038_1	7	201	No	65.1	315	296[1]
03038_1	5	173	No	39.2	291	-

Table 1.1: Experiments with cooldown by steam. UC: Deviation from the regular cooldown curve was registered by [C]entral and/or [U]pper thermocouple. [1]oxide layer thickness measured at elevation 65-85 mm; [2]oxide layer thickness measured at elevation 105-125 mm.

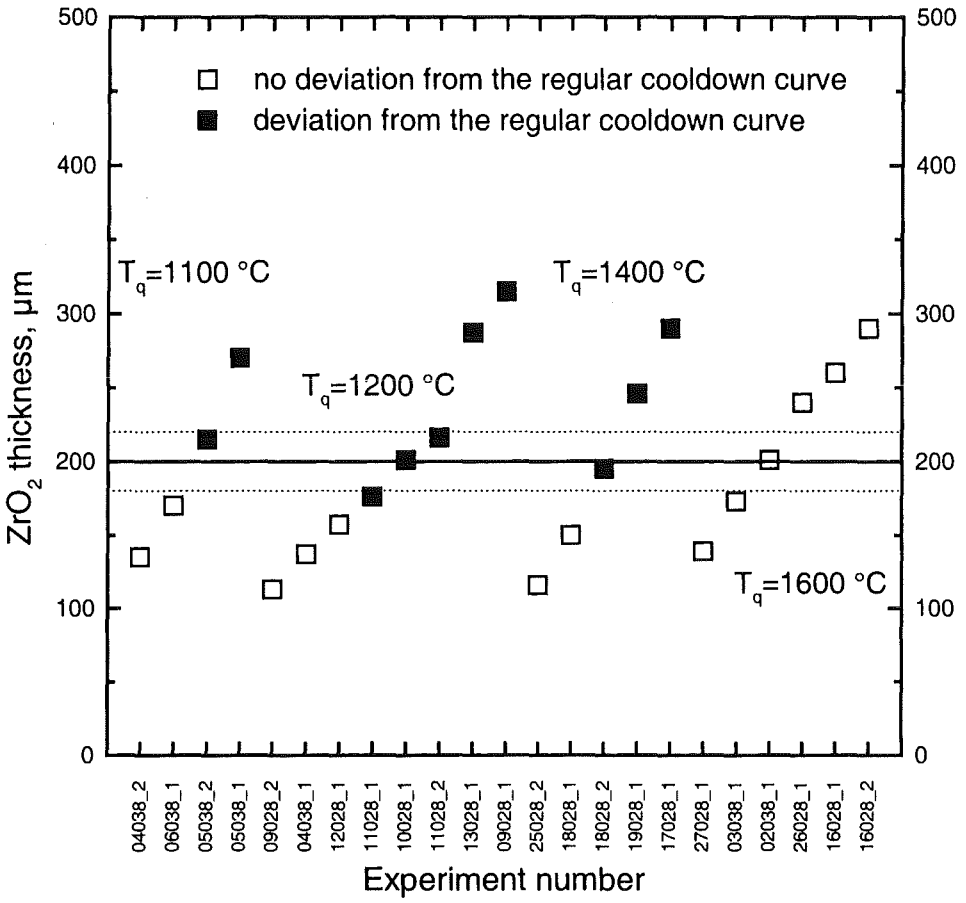

Fig. 1.4: Temperature deviation from the regular cooldown curve in small-scale experiments.

During pre-oxidation in steam as well as during the quench process the hydrogen produced by the steam oxidation of the Zircaloy can be partially absorbed by the remaining metal phase. Separate-effects tests at high temperatures have shown a remarkable capacity of the zirconium for the storage of hydrogen.

The amount of absorbed hydrogen in specimens of the test series was analysed in the so-called LAVA equipment. For the analyses about 2 cm long cladding tube segments were used, mostly taken from the middle part of the tube. From three tubes further specimens from the upper and lower part were also analysed.

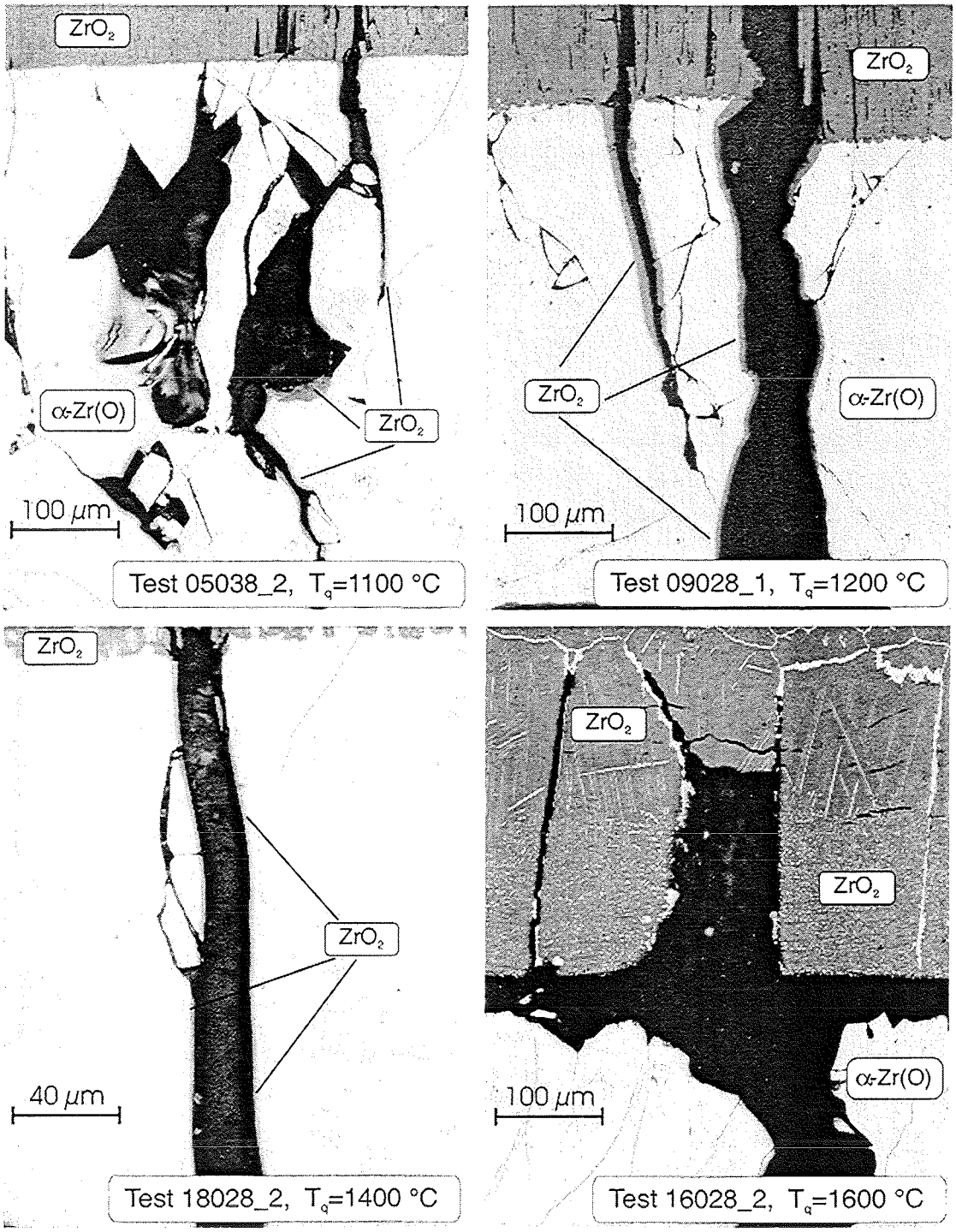

Fig. 1.5: Oxidation of crack and Zircaloy tube surfaces during rapid cooldown by steam.

The results of the measurements are summarised in Table 1.2 and presented in Fig. 1.6. In general, the analysis of the results shows that after reaching certain oxide layer thicknesses (about 200 μm) and crack density, the amount of hydrogen absorbed in the metallic part of the Zircaloy tube increases considerably. In case of cooldown from 1100, 1200 and 1400 °C the amount of hydrogen absorbed in the specimen with pre-oxidation larger than ~200 μm

is significantly larger than for the specimens with pre-oxidation lower than 200 µm ZrO_2 layer thickness.

Test ID	Time of pre-oxidation at 1400 °C, min	Measured oxide layer thickness at onset of cool-down, µm	Hydrogen concentration (referred to metal mass), weight %	Hydrogen concentration (referred to metal mass), mole %	Position of the probe, mm
cooldown from 1100 °C					
06038_1a	7	175	0.0018	0.16	65-85
05038_1a	19	255	0.0150	1.35	105-125
05038_1b	19	270	0.0164	1.47	65-85
cooldown from 1200 °C					
12028_1a	7	167	0.0024	0.22	65-85
10028_1a	12	210	0.0246	2.19	105-125
100281_b	12	212	0.0159	1.43	65-85
11028_1a	9	190	0.0239	2.13	105-125
11028_1b	9	185	0.0089	0.81	65-85
090281_a	30	290	0.0142	1.28	65-85
cooldown from 1400 °C					
180281_a	7	160	0.0015	0.13	65-85
19028_1a	19	260	0.0229	2.05	65-85
25028_1a	19	265	0.0537	4.67	65-85
cooldown from 1600 °C					
16028_1a	5	380	0.0341	3.02	96-115
27028_1a	3	163	0.0002	0.02	65-85
02038_1a	7	296	0.0057	0.51	65-85

Table 1.2: Results of the analysis of the hydrogen absorbed in the Zircaloy cladding tubes from the small-scale experiments.

The measurements of the absorbed hydrogen in the experiments 10028_1 and 11028_1 were performed at two different locations. In these two experiments the deviation from the regular cooldown temperature was registered only by the upper thermocouple and exactly at this elevation more hydrogen was absorbed. A possible explanation is, that the temperature escalation at the upper elevation was triggered by the exothermal hydrogen absorption process; this needs to be investigated further in the future.

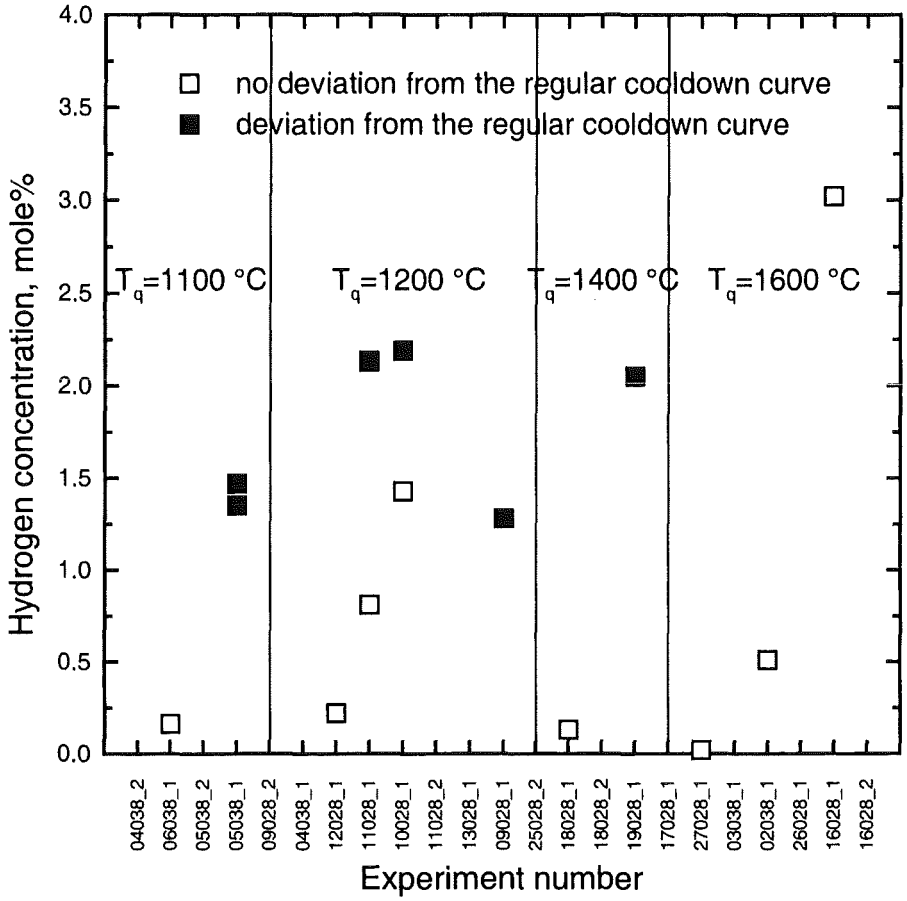

Fig. 1.6: Hydrogen concentration in the metallic part of the Zircaloy cladding tube after rapid cooldown by steam.

Quite a different physico-chemical behaviour of the specimen is observed in the experiments with 1600 °C initial temperature at onset of cooldown. For the small pre-oxidation the amount of absorbed hydrogen is very low and increases with increasing extent of the pre-oxidation. But even for large oxide layer thickness ~300 µm in the experiment 02038_1 this amount is still relatively low in comparison with similar specimens cooled from 1100, 1200 and 1400 °C. Only for a very large oxide layer thickness ~380 µm in the experiment 16028_1 the amount of absorbed hydrogen is significant (Fig. 1.6). The difference in the amount of the absorbed hydrogen could be explained by the different crack length (315 mm in 02038_1 and 579 mm in 16028_1).

It seems that the amount of the absorbed hydrogen correlates not only with the extent of the pre-oxidation of the Zircaloy cladding tube at onset of cooldown, but also with the total crack length. It is still not clear why the same

conditions in the two experiments 19028_1 and 25028_1 lead to different crack patterns and consequently to different content of the absorbed hydrogen. The possibility of the hydrogen absorption process to trigger the temperature escalation must be studied in detail in the future.

2. HYDROGEN ABSORPTION IN ZIRCALOY

In the frame of the QUENCH program the physico-chemical behavior of Zircaloy fuel rod cladding during quenching of an overheated reactor core is investigated at FZK. Besides the oxidation of Zircaloy by steam the interaction of hydrogen produced by this reaction with the remaining Zircaloy metal is of interest.

It is well known that zirconium and Zircaloy, respectively, can dissolve large amounts of hydrogen. This reaction may have important consequences on the course of events during and after quenching of an overheated core. So, Zircaloy may act as a sink or source of hydrogen, depending on the prevailing conditions. In this way, the hydrogen solubility of the cladding material can alter the hydrogen source term.

The tests are performed in a simultaneous thermal analysis (STA) apparatus coupled with a mass spectrometer. This arrangement allows an on-line registration of the interaction between Zircaloy and the hydrogen containing atmosphere. Specimens used are customary Zircaloy-4 cladding tube segments.

The following experimental objectives have been investigated in separate-effects tests within the reporting period:

- Investigation of the influence of oxygen on the hydrogen solubility of Zircaloy-4.
- Comparison between the both internationally used cladding materials Zircaloy-4 and Zr1%Nb.
- Investigation of the transient behaviour of hydrogen uptake and release.
- First tests on hydrogen uptake during oxidation in steam.

Additionally, the hydrogen content in specimens of single tube and bundle QUENCH tests has been analysed. Therefore, a new method for the analysis of hydrogen in oxygen containing Zircaloy specimens has been established.

The influence of oxygen on the hydrogen absorption has been investigated in two ways: (a) with regard to an oxide scale and (b) with regard to dissolved oxygen in the β- as well as in the α-phase.

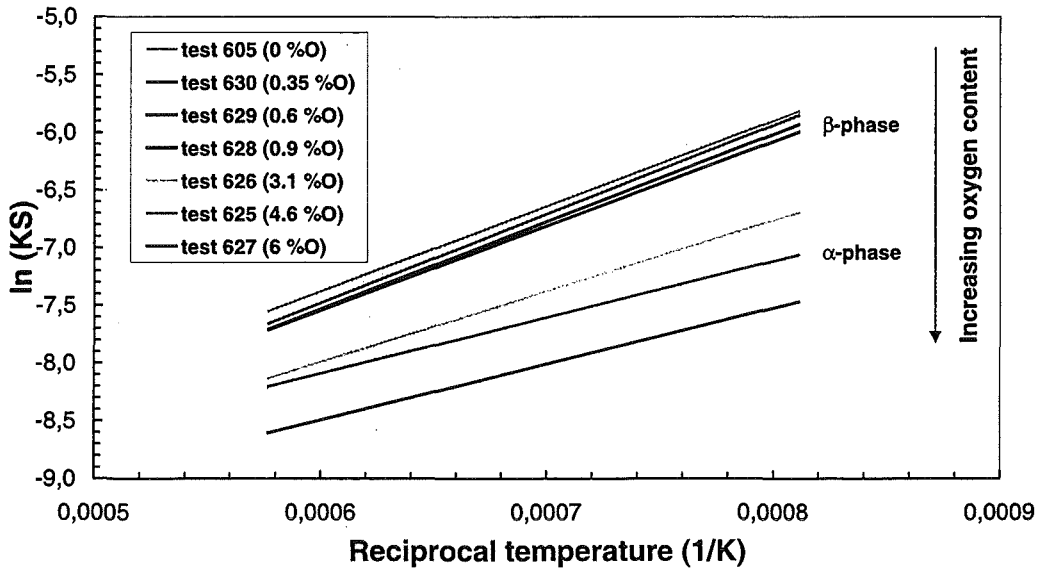

Fig. 2.1: Effect of dissolved oxygen on the hydrogen absorption of Zircaloy-4.

As it was shown in the 5th Progress Report an intact oxide scale on the Zircaloy surface significantly impedes the hydrogen uptake of the metal phase. For the investigation of the influence of dissolved oxygen on the hydrogen solubility of Zircaloy-4 the specimens were pre-oxidised to a well defined amount and then homogenised in the furnace of the thermobalance. The samples were loaded with up to 6 wt% oxygen which is near saturation of the α-phase. It was found that the hydrogen solubility decreases with increasing oxygen content in the β- as well as in the α-phase (Fig. 2.1).

Comparing the behaviour of Zircaloy-4 and Zr1Nb cladding material, no significant influence of the alloying elements was found. Within the experimental scattering the same parameters of the Sieverts constant as for Zircaloy-4 have been determined for Zr1Nb.

The transient behaviour during uptake and release of hydrogen has been investigated in various tests. It was shown that the uptake of hydrogen during switching the hydrogen pressure from 0 to e.g. 0.5 bar is much faster than the release in the opposite case. This behaviour could be well described by a computer program produced by the Russian IBRAE team which includes models for hydrogen diffusion in the solid and gaseous phase and modelling of Sieverts' law and Stefan's flow. Figure 2.2 shows a comparison between experimental and calculated results of a test where the hydrogen flow was interrupted during each level of constant temperature.

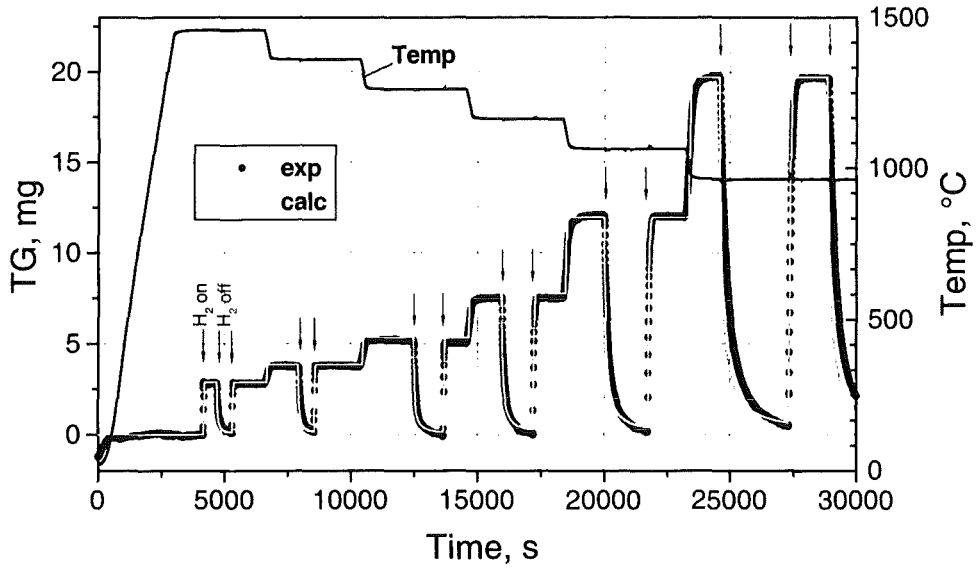

Fig. 2.2: Transient behaviour of hydrogen uptake/release during switching between 0 and 0.5 bar hydrogen partial pressure. Comparison between experimental results and calculation with IBRAE model.

First tests have been performed to determine the hydrogen uptake during oxidation of Zircaloy-4 cladding specimens in steam. Therefore, the samples which were oxidised in steam have been rapidly cooled in argon atmosphere in the small scale QUENCH rig. A certain amount of hydrogen has been taken up by the Zircaloy which was in the same order of magnitude as the amount of hydrogen analysed in specimens after single rod QUENCH tests with pre-oxidation lower than 200 µm, but much lower than the hydrogen concentration in specimens with thicker oxide scales. The hydrogen concentration in such specimens is very well correlated with the temperature behaviour during cooldown and the crack densities determined in post-test examinations.

The axial distribution of hydrogen absorbed by the cladding material in the large scale bundle QUENCH tests has been analysed using one cladding tube per test which was removed from the bundle before embedding in epoxy. The hydrogen concentration is correlated with the oxide layer thickness determined at the same rod. There was no indication for the uptake of hydrogen in other parts of the bundle, e.g. near the upper plenum.

3. BUNDLE QUENCH TESTS

To investigate the in-vessel hydrogen source term that results from the water injection into the core to cool it down a new test facility "QUENCH" was built at FZK. In the following a description of the test facility, conduct and experimental results of the first two QUENCH tests is given.

Design and construction

The main component of the QUENCH test facility [3] is the test section with the test bundle (Fig. 3.1). Superheated steam from the steam generator and superheater together with argon as a carrier gas enter the test bundle at the bottom. The argon, the steam not consumed, and the hydrogen produced in the zirconium-steam reaction, flow from the bundle outlet at the top through a water-cooled offgas pipe to the condenser where the steam is separated from the non-condensable argon and hydrogen gases. The quench water enters the test section through a separate line at the bottom. At the inlet of the test section the quench water has reached approx. 395 K, i.e. saturation temperature at 0.2 MPa.

The test bundle is made up of 21 fuel rod simulators approximately 2.5 m long. The design characteristics of the test bundle are listed in Table 3.1. Twenty fuel rod simulators are heated over a length of 1024 mm, the central fuel rod simulator is unheated. The unheated fuel rod simulator (Fig. 3.2) is built with ZrO_2 pellets (bore size 2.5 mm ID) and a Zircaloy cladding tube but without a tungsten heater and electrodes. Two thermocouples are inserted in its center, one thermocouple from the bottom and one from the top.

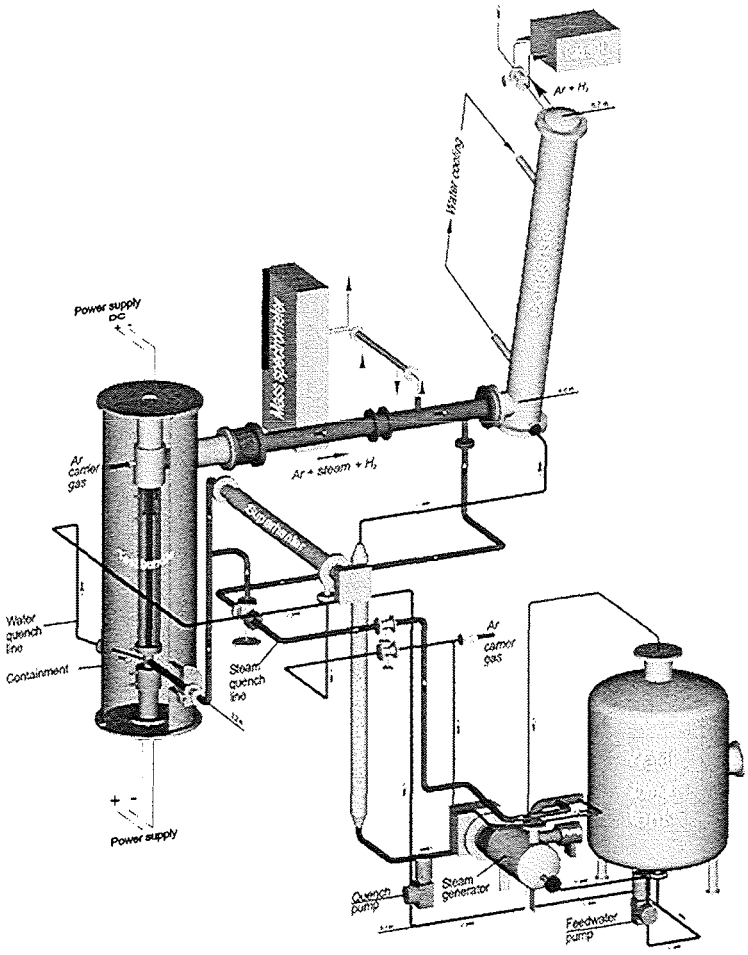

Fig. 3.1: QUENCH test facility with the main components.

Heating is electric by 6-mm diameter tungsten heaters installed in the rod center and surrounded by annular ZrO_2 pellets and the Zircaloy-4 cladding (Fig. 3.2). Electrodes of molybdenum and copper are installed axially between the tungsten heater and the cable connected to the electric power supply (DC). The total heating power available is 70 kW distributed between two groups of heated rods. The usual distribution of the electric power within the two groups is as follows: 40 % of the power is released in the inner ring of rods (eight fuel rod simulators), 60 % in the outer ring (twelve fuel rod simulators). The fuel rod simulators are held in position by five grid spacers, four made of Zircaloy and one made of Inconel at the bottom. Rod cladding is identical to that used in LWRs with respect to material and dimensions (Zircaloy-4, 10.75 mm outside diameter, 0.725 mm wall thickness; see also Table 1). The rods are filled with argon (QUENCH-01) or Ar-5%Kr (QUENCH-

02 and subsequent tests) at a pressure of approx. 0.22 MPa. (The krypton additive allows test rod failure to be detected by the mass spectrometry).

The test bundle is surrounded by a shroud of Zircaloy with a 37 mm thick ZrO_2 fibre insulation and an inner and an outer cooling jacket of stainless steel (Fig. 3.3). The 9.7-mm annulus of the cooling jacket is cooled by argon. Above the heated zone, i.e. above the 1024-mm elevation, both the test bundle and the shroud are uninsulated. This region of the cooling jacket is cooled by water. Both the absence of an ZrO_2 insulation above the heated region and water cooling are to force the axial temperature maximum downward.

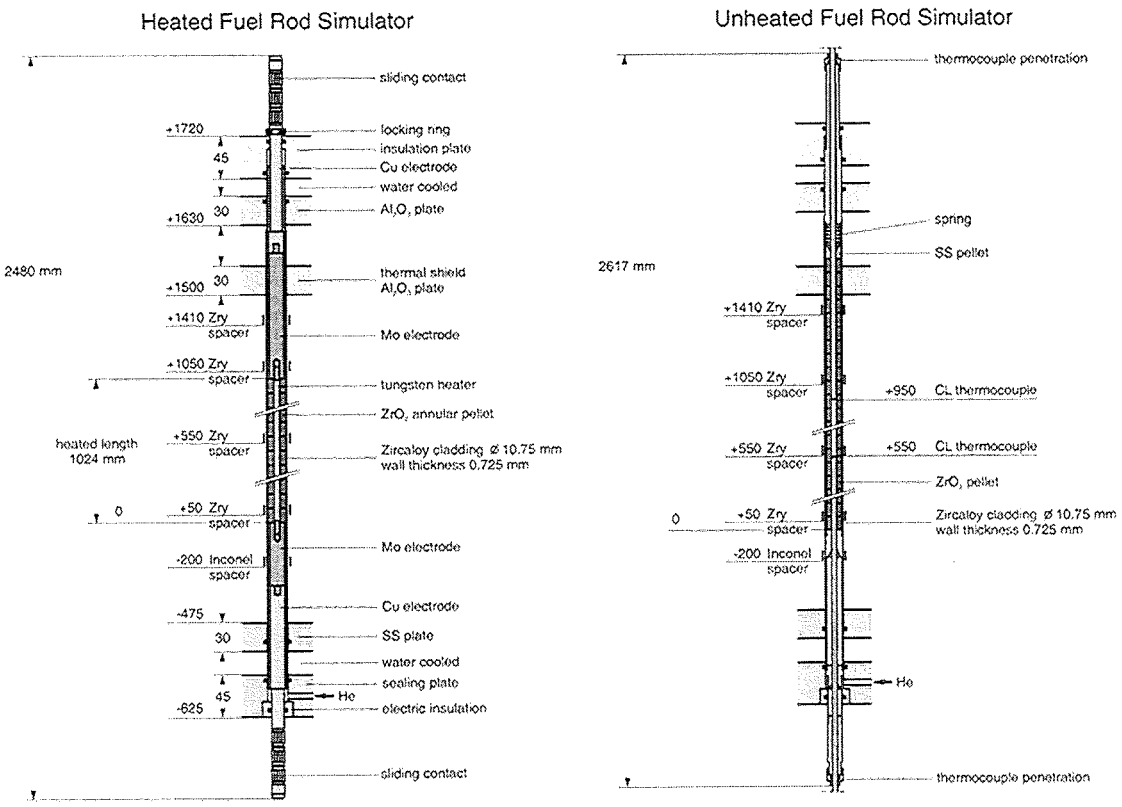

Fig. 3.2: Fuel rod simulators used in the QUENCH test bundle.

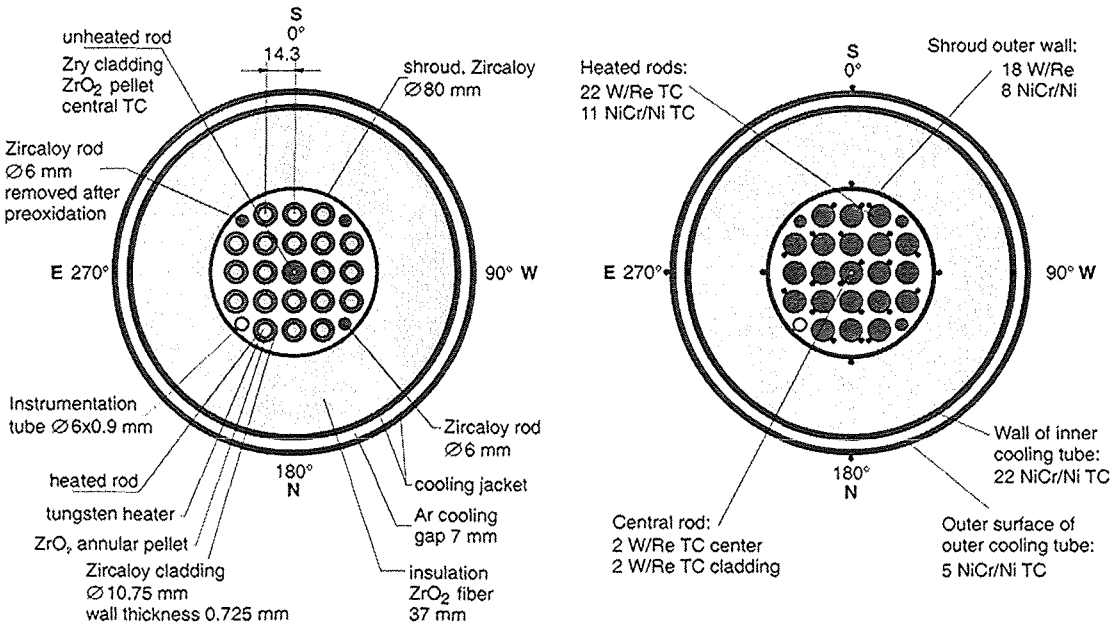

Fig. 3.3: Cross-section of the QUENCH test bundle with dimensions (left) and thermocouple instrumentation (right).

The test bundle is equipped with thermocouples attached to the cladding at different elevations between -250 mm and 1350 mm and in four different orientations. Also the thermocouples of the shroud are mounted in four different orientations (Fig. 3.3), with elevations of the shroud thermocouples ranging between -250 mm and 1250 mm. In the lower bundle region, i. e. up to 550 mm elevation, NiCr/Ni thermocouples with stainless steel sheath and an outside diameter of 1.0 mm are used for measurements of the rod cladding and shroud temperatures. The thermocouples in the hot zone are high-temperature resistant thermocouples with W-5Re/W-26Re wires, HfO_2 insulation, and a duplex sheath of tantalum (inside)/ Zircaloy (2.1 mm outside diameter).

Hydrogen is analysed by two different instruments: (1) a mass spectrometer located behind the test section, (2) a "Caldos" hydrogen detection system located downstream the condenser. Due to the different locations of the hydrogen measurement devices (see Fig. 3.1) the mass spectrometer responds almost immediately whereas the delay time for the response of the Caldos system is around 100 s.

Bundle type		PWR
Bundle size		21 rods
Number of heated rods		20
Number of unheated rods		1
Pitch		14.3 mm
Rod outside diameter		10.75 mm
Cladding material		Zircaloy-4
Cladding thickness		0.725 mm
Rod length	heated rods (extension) unheated rods (extension)	2480 mm (-690 mm to 1790 mm) 2842 mm (-827 mm to 2015 mm, incl. extension piece)
Heater material		Tungsten (W)
Heater length		1024 mm
Heater diameter		6 mm
Annular pellet	heated rods unheated rods	ZrO_2; ∅ 9.15/6.15 mm; L=11 mm ZrO_2; ∅ 9.15/2.5 mm; L=11 mm
Pellet stack	heated rods unheated rods	0 mm to ~ 1020 mm 0 mm to 1553 mm
Grid spacer	material length location of lower edge	Zircaloy-4, Inconel 718 Zry 42 mm, Inc 38 mm -200 mm Inconel 50 mm Zircaloy-4 550 mm Zircaloy-4 1050 mm Zircaloy-4 1410 mm Zircaloy-4
Shroud	material wall thickness outside diameter length (extension)	Zircaloy-4 2.38 mm 84.76 mm 1600 mm (-300 mm to 1300 mm)
Shroud insulation	material insulation thickness elevation	ZrO_2 fiber ~ 37 mm -300 mm to 1000 mm
Molybdenum-copper electrodes: length of upper electrodes length of lower electrodes diameter of electrodes: - prior to coating - after coating with ZrO_2		 766 mm (576 Mo, 190 mm Cu) 690 mm (300 Mo, 390 mm Cu) 8.6 mm 9.0 mm
Cooling jacket	material inner tube outer tube	1.4541 stainless steel ∅ 158.3 / 168.3 mm ∅ 181.7 / 193.7 mm

Table 3.1: Design characteristics of the QUENCH test bundle.

Test QUENCH-01

The objective of test QUENCH-01 [3] (conducted in February 1998) was the investigation of the physico-chemical behaviour of partially oxidised PWR fuel rods during reflood, therefore the Zircaloy cladding was pre-oxidised to a

maximum oxide layer thickness of 300 µm and then quenched from a maximum temperature of 1870 K. Test QUENCH-01 (Figure 3.4) consisted of (a) a heatup phase, (b) a phase at ca. 1000 K in which well-defined amounts of helium were injected into the test section at 700 mm elevation to determine delay times for the hydrogen transport to the mass spectrometer and the Caldos system, (c) a second heatup period, (d) a pre-oxidation phase, (e) a transient phase, and (f) a quench phase. All phases except the quench phase were conducted with an argon (3 g/s) plus steam (3 g/s) flow.

The pre-oxidation phase started after a ramp rate of 0.5 K/s and lasted for 8280 s at maximum temperatures of about 1400 K - 1600 K to obtain the required maximum oxide layer thickness of 300 µm at the 900 mm elevation. The electrical power was adjusted such that the hydrogen production rate, measured on-line with the mass spectrometer, was fairly constant. This control allowed to minimise the pre-oxidation time for such a large bundle and at the same time to avoid a premature temperature escalation. At about 6000 s into the pre-oxidation phase one of the solid Zircaloy rods was withdrawn from the hot bundle to check immediately the extent of oxidation achieved by means of an eddy current device. Figure 3.5 shows the axial temperature profile at that time. At the end of the pre-oxidation phase the test bundle was ramped at 0.5 K/s to a maximum rod cladding temperature of 1870 K (extrapolated at 950 mm) and a maximum shroud temperature of 1800 K at the 950-mm elevation.

Initiation of the quench phase was done in the following way. The steam and argon flow through the test section were turned off, argon was injected at the upper end of the test bundle, and the lower plenum was filled with quench water at a high rate of 80 g/s. Thirty seconds later the electrical power was reduced from 20 kW to 4 kW (representing the decay heat level) within 15 s, and the bundle was flooded with 52 g/s H_2O for 89 s, until water reached the bottom of the upper plenum. The injection rate corresponds to a velocity of 1.7 cm/s in the bundle, based on the quench water flow F 104 of 187 l/h and the coolant channel cross section of 30 cm^2. The experiment was terminated by shutting off the electric power and the quench water and argon flow. Altogether the amount of water injected at a rate of 80 g/s and 52 g/s was 2.4 l and 4.6 l, respectively, so that the total amount of water injected was 7.0 l.

Altogether 19 high-temperature thermocouples had failed. Five TCs had been damaged during handling, i.e. prior to the test. 14 TCs had failed during the experiment due to the severe oxidation (5 TCs during pre-oxidation, 4 TCs during the transient, and 5 TCs during the quench phase).

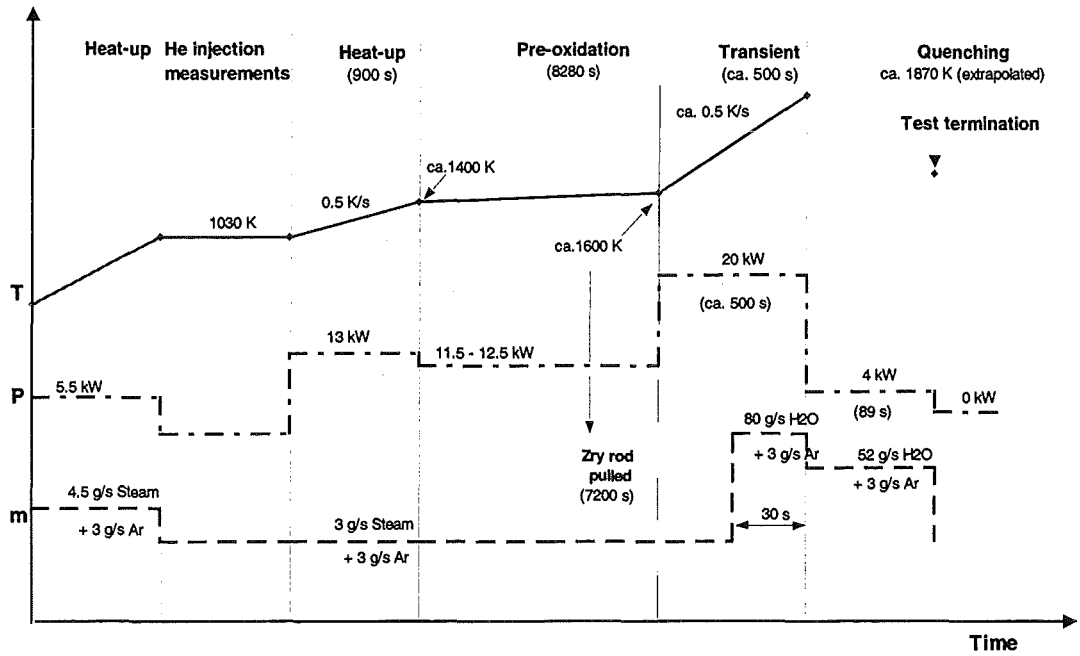

Fig. 3.4: QUENCH-01 test conduct.

Figure 3.6 gives the temperature history of the transient phase at 950 mm with a maximum temperature of about 1800 K. The centreline thermocouple TCRC13 shows similar behaviour as that of the shroud thermocouples. During quenching, however, the shroud thermocouples exhibit a slightly faster response than TCRC13. As all cladding thermocouples failed at this elevation the maximum cladding temperature is not known and had to be extrapolated at the 950 mm elevation resulting in 1870 K. At the shroud a maximum temperature of 1800 K was reached at 1150 mm, an elevation well above the shroud insulation where radial heat losses are larger than in the insulated region. The high heatup rate of 1.5 K/s at 1150 mm suggests that the shroud material had experienced a slight temperature escalation.

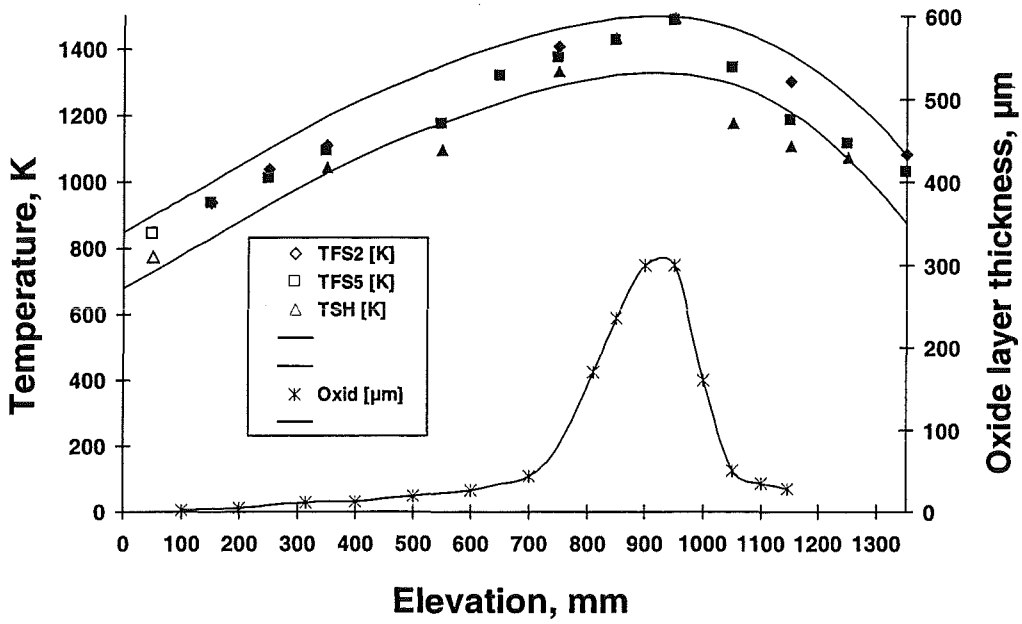

Fig. 3.5: Test QUENCH-01. Axial temperature profile at 6000 s and axial oxide layer thickness profile.

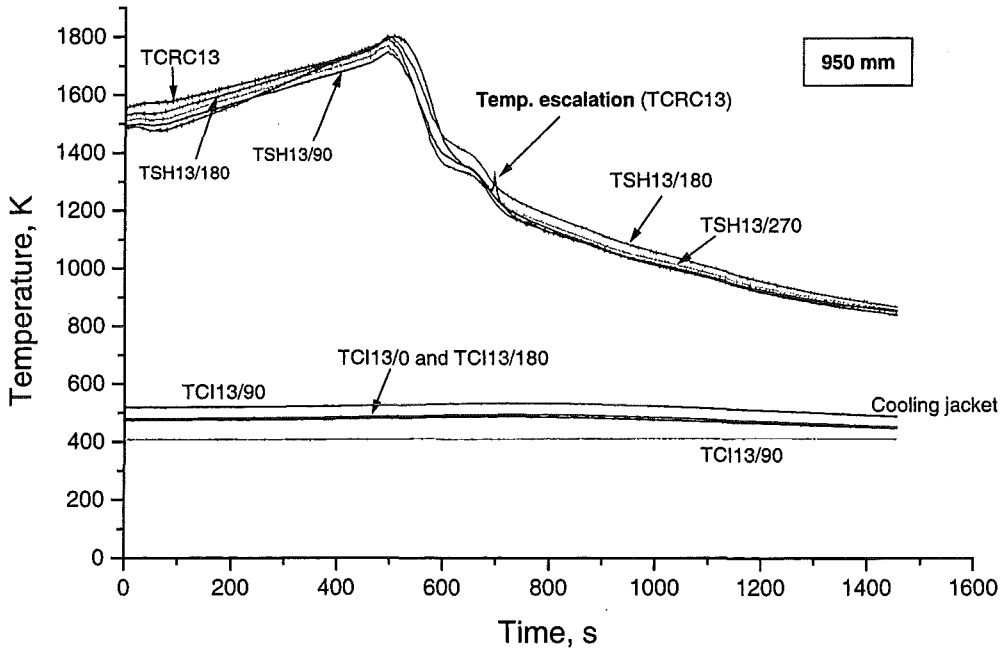

Fig. 3.6: Transient and quench phases of the QUENCH-01 test.

As a consequence of the shutoff of the argon/steam flow (initiation of the quenching) the rod temperatures increased at lower elevations up to the middle of the heated zone but dropped at the upper elevations.

During the reflood phase the bundle appeared to quench steadily with no evidence of any temperature excursion. Toward the end of the flooding phase when all rod cladding temperatures were already at the lowest level the thermocouple signals of the upper elevations exhibit a renewed temperature peak (Figure 3.7). The shroud temperatures of the upper regions do not show this behaviour.

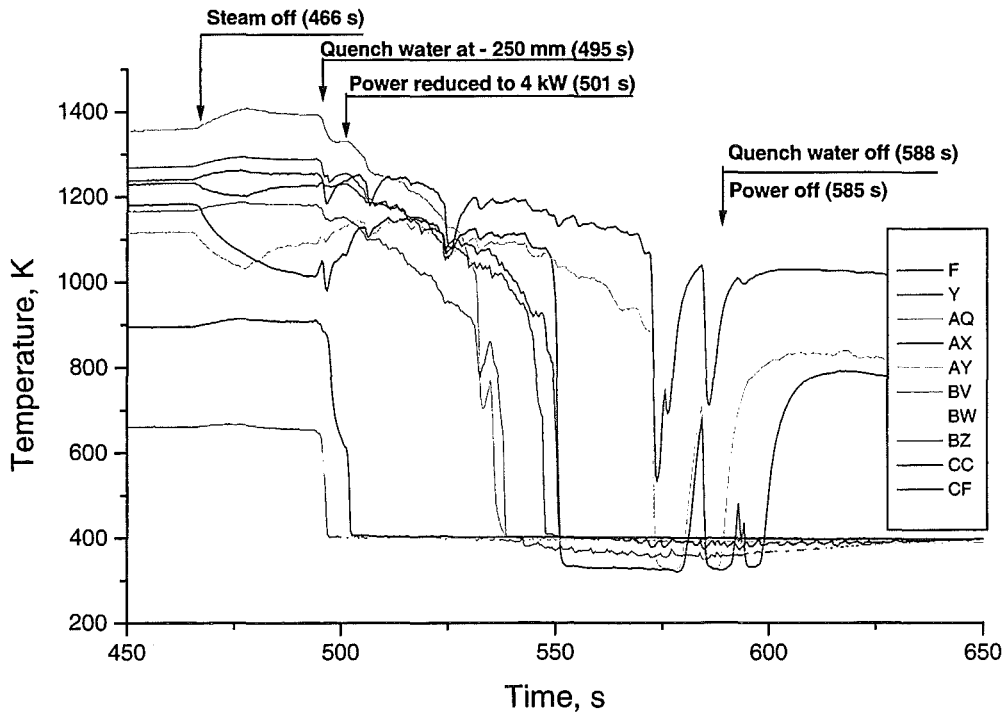

Fig. 3.7: Temperatures at different elevations during the quench phase of the QUENCH-01 test.

Cooling of the test bundle occurs in two stages, firstly a cooling period (period before the water level is at a given axial location) with a moderate cooldown rate then secondly a very pronounced cooldown. The latter period is caused by a drastic improvement in heat transfer. The beginning of this period is called "quench temperature" and "onset of quenching", respectively. Quench temperature indicates a first local wetting of the rods at the locations of cladding thermocouples. The quench temperature "seen" by the shroud

thermocouples occurs later in time as is demonstrated for the 50-mm elevation in Figure 3.14.

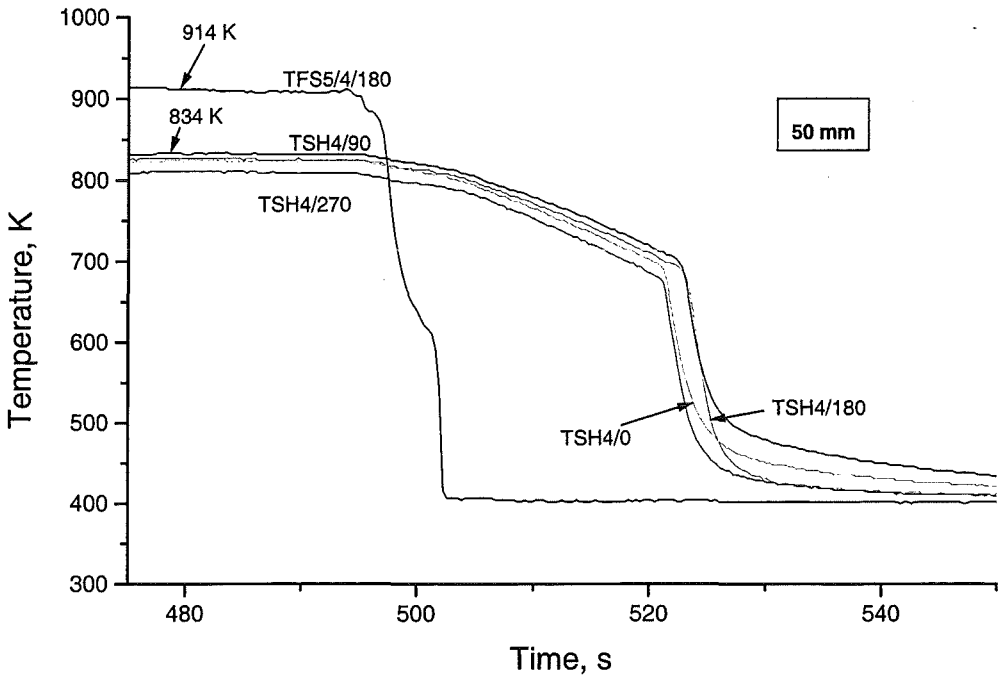

Fig. 3.14: Wetting behaviour of cladding and shroud thermocouples in the quench phase of QUENCH-01 test.

The precursory cooling (before quenching) is not affected by the rod surface thermocouples. This "onset of cooling" occurs simultaneously, namely within one second, for all axial positions. This happened exactly at the time when the quench water level (saturation temperature) was at -250 mm elevation. The pertinent temperatures are given in Table 3.2. The quench temperatures determined by the cladding temperature measurements were between 641 K at the -250 mm and 1199 K at the 1150 mm elevations. Taking the quench temperatures from the shroud thermocouple readings somewhat lower quench temperatures are obtained from the bottom of the test section (-250 mm) to 550 mm (middle of the heated zone). In the upper bundle section quench temperatures measured by the shroud thermocouples seem to be even higher than those evaluated from the cladding thermocouples. Cladding thermocouples at the instrumentation levels 12, 13, and 15, however, failed so that a direct comparison is not possible.

Cladding Thermo-couple	Elevation Rod number	Onset of cooling Time(s)	Temp.(K)	Onset of quenching Time(s)	Temp.(K)	Max. cooldown during quenching (K/s)
TFS 2/1	- 250 mm (rod 4)	494	653	495	641	240
TFS 2/2	- 150 mm (rod 6)	494	768	495	757	160
TFS 2/3	- 50 mm (rod 8)	477	839	494	817	100
TFS 5/4/180	50 mm (rod 21)	495	907	497	877	100
TFS 2/5	150 mm (rod 2)	494	1043	520	782	130
TFS 5/5	150 mm (rod 16)	495	1035	513	874	110
TFS 2/6	250 mm (rod 4)	494	1179	531	897	200
TFS 5/6	250 mm (rod 18)	494	1144	531	866	100
TFS 2/7	350 mm (rod 6)	495	1282	543	942	430
TFS 5/7	350 mm (rod 19)	495	1247	547	919	260
TFS 3/8	470 mm (rod 5)	495	1384	558	972	150
TFS 5/9	570 mm (rod 10)	495	1391	532	1013	210
TFS 5/10	670 mm (rod 12)	495	1571	568	984	140
TFS 5/14	1050 mm (rod 18)	495	1600	569	1199	100
TFS 5/16	1250 mm (rod 21)	495	1227	572	1064	410
TFS 2/17	1350 mm (rod 6)	*	*	549	1060	320
TFS 5/17	1350 mm (rod 10)	*	*	569	929	430

Table 3.2: Evaluation of the cooldown data in QUENCH-01 test.

The determination of the quench rate was performed using pairs of thermocouples located on the same test rod in taking the distance between a pair of thermocouples on the same test rod and relating it to the times of the onset of quenching. The quench rates evaluated for thermocouple pairs fixed at one rod, namely at rods 4, 6, 10, 18, and 21 were between 1 cm/s (rod 6, -150/350 mm) and 2.9 cm/s (rod 10, 570/1350 mm). The quench rates evaluated from temperatures (onset of quenching) of thermocouple pairs fixed at different rods, at elevations closest to each other lie then between ca. 0.4 and 7 cm/s with the majority of the rates between ca. 0.4 and 1 cm/s. The quench rates determined from the shroud thermocouple signals at elevations

closest to one another lie in the same range, i. e. between 0.4 and 4.7 cm/s. In any case, the quench rates seem to have the tendency to be larger at the upper elevations. The maximum cooldown rates, i.e. temperature decreases that occur during quenching, on the basis of the cladding thermocouple responses were determined to be between 100 and 430 K/s with the higher rates at the upper elevations of 1250/1350 mm (see Table 3.2).

Due to partial condensation of the steam near the MS sampling position at the off-gas pipe of the facility, the steam flow rate could not be evaluated quantitatively as was explained in the section describing the hydrogen measurement devices. The concentrations of nitrogen and oxygen were measured to be below 0.02 and 0.002 vol%, respectively, during the whole test.

The integral hydrogen releases at low temperatures (< 1000 K) during the heatup phase and during the delay time measurements was 0.5 g and 0.4 g, respectively.

During the pre-oxidation phase, the hydrogen measurement was used to control the oxidation process and the electrical power on-line. The rate and the integral value of hydrogen release were calculated continuously and compared with the results of the SCDAP/RELAP5 pre-test calculations. The power was increased stepwise in order to compensate the lower oxidation rate with increasing oxide layer thickness. This procedure worked very well, the maximum oxide layer thickness at the end of the pre-oxidation phase was measured to be 300 µm, which was exactly the target value. The hydrogen production rate was at a constant value of about 3 - 4 mg/s during the whole pre-oxidation phase. Only at about 4700 s a local temperature escalation which was rapidly suppressed by a decrease of the electrical power (see central diagram in Figure 3.9) caused a slightly enhanced hydrogen release.

Figure 3.9 shows the hydrogen production (rate and integral value) measured by the mass spectrometer and the CALDOS system together with some relevant data of the facility during the pre-oxidation, transient and quench phases. Altogether, 38 g of hydrogen were produced and released during

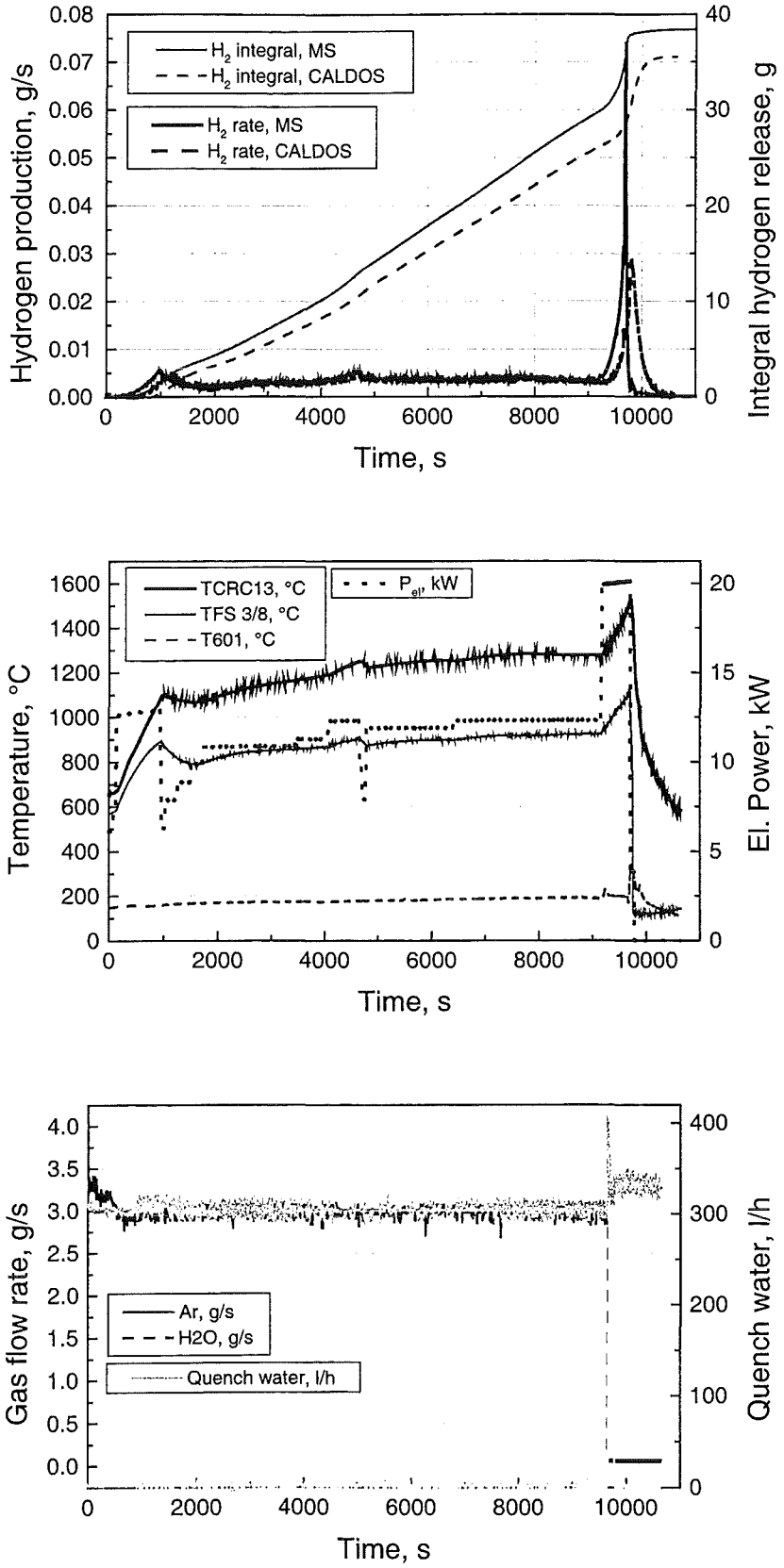

Fig. 3.9: Hydrogen measurements and data of the facility in pre-oxidation, transient and quench phases of the QUENCH-01 test.

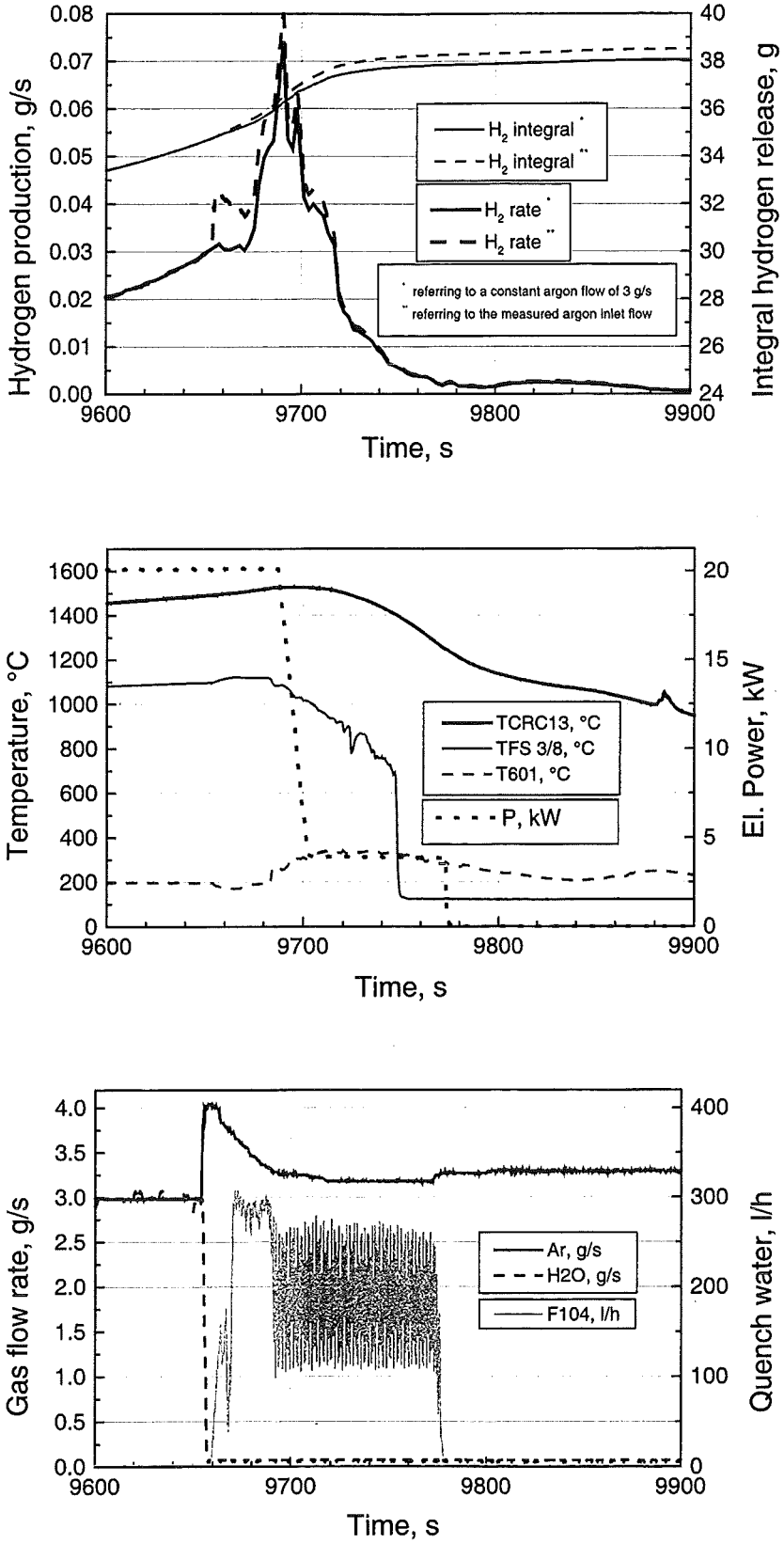

Fig. 3.10: Hydrogen measurements and data of the facility in the quench phase of the QUENCH-01 test.

these three phases. The hydrogen production rate and the integral value measured by the mass spectrometer correspond very well with data from the CALDOS system (34 - 35 g, see Table 3.3). The maximum hydrogen rate was 0.08 g/s during the transient/quench phase.

Figure 3.10 presents the same data as Figure 3.9, but zoomed in on the end of the transition phase and the quenching. The upper diagram shows two curves for the H_2 rate and integral H_2 release each of them according to two different evaluation algorithms, i.e. one curve is based on constant 3 g/s argon flow rate; and the other one is based on the measured argon flow rate which was slightly increased during the initiation of the quench phase (see lower figure). The hydrogen peak is initiated by an enhanced steam production due to the quench water flow into the lower head of the test section. Three sub-peaks can be identified. The first and largest peak is turned around by the start of the power reduction from 20 kW to 4 kW. The third and smallest hydrogen increase is connected with the end of the power reduction. The intermediate one may be caused by a temporary increase of the temperature of the upper part of the bundle at elevation 1250 and 1350 mm.

Test phase	Mass spectrometer	Caldos system
1st heatup	0.5 g	-
He injection	0.4 g	-
2nd heatup & pre-oxidation	30 g	27 g
Transient & quench	8 g	8 g
Σ	39 g	35 g

Table 3.3: Hydrogen release measured by mass spectrometer and Caldos system during QUENCH-01 test.

In general, the hydrogen production during the quench phase of about 3 g was very low compared to the results obtained during the commissioning tests (about 40 g).

To view the bundle after the test a window had to be cut into the shroud. The post-test appearance of the test bundle shows no signs of any melt but significant oxidation of the bundle between 700 and 1100 mm elevation (Figure 3.11). In this region the oxide layer is of gray colour and some larger

cracks in the cladding have formed (Figure 3.12). The central rod that lacks the support of the central heating element (tungsten rod) is broken and pellets are found outside the rod cladding. The grid spacer (Zircaloy) at 1050 mm is destroyed and parts of it relocated downward. The shroud is intact and undeformed. The region of the shroud above the heated zone that is without insulation exhibits a bronze-like colour. This is the region where a slight temperature escalation of the shroud might have taken place. All rod cladding thermocouples in the hot region are destroyed.

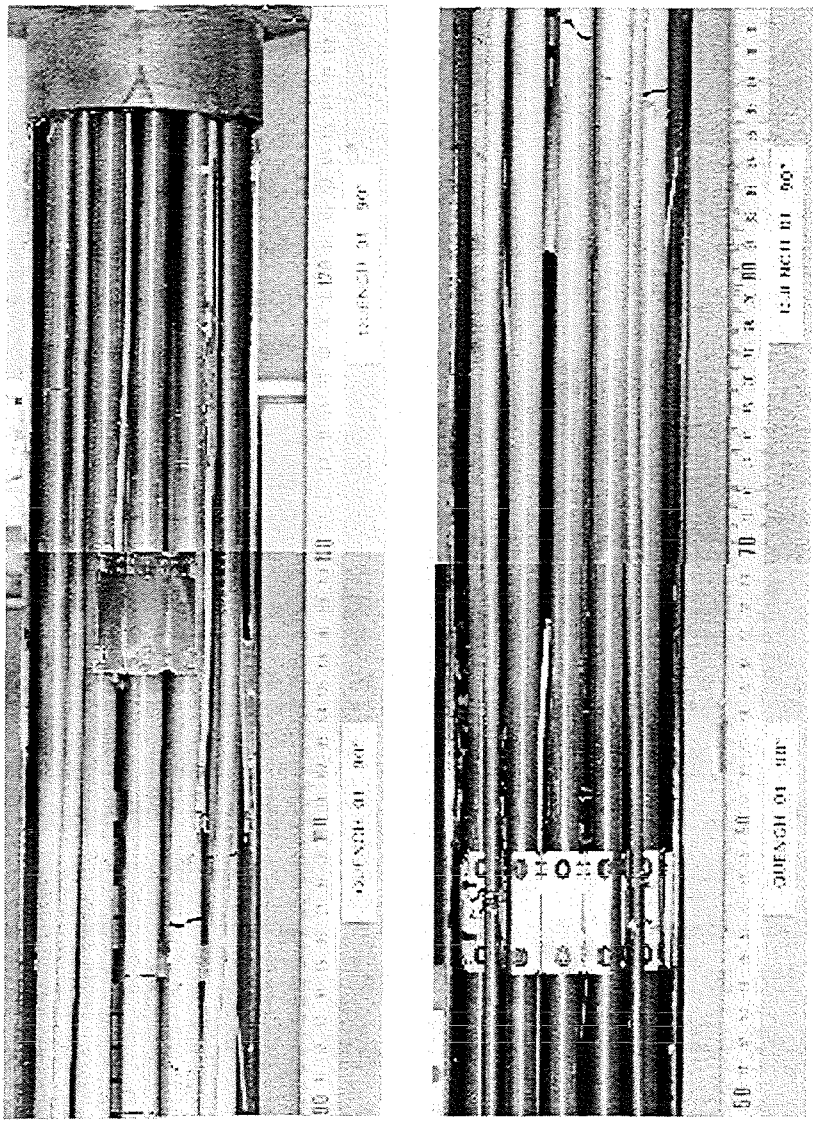

Fig. 3.11: Post-test appearance of the bundle QUENCH-01. Formation of cracks in the oxygen-embrittled Zircaloy cladding during flooding.

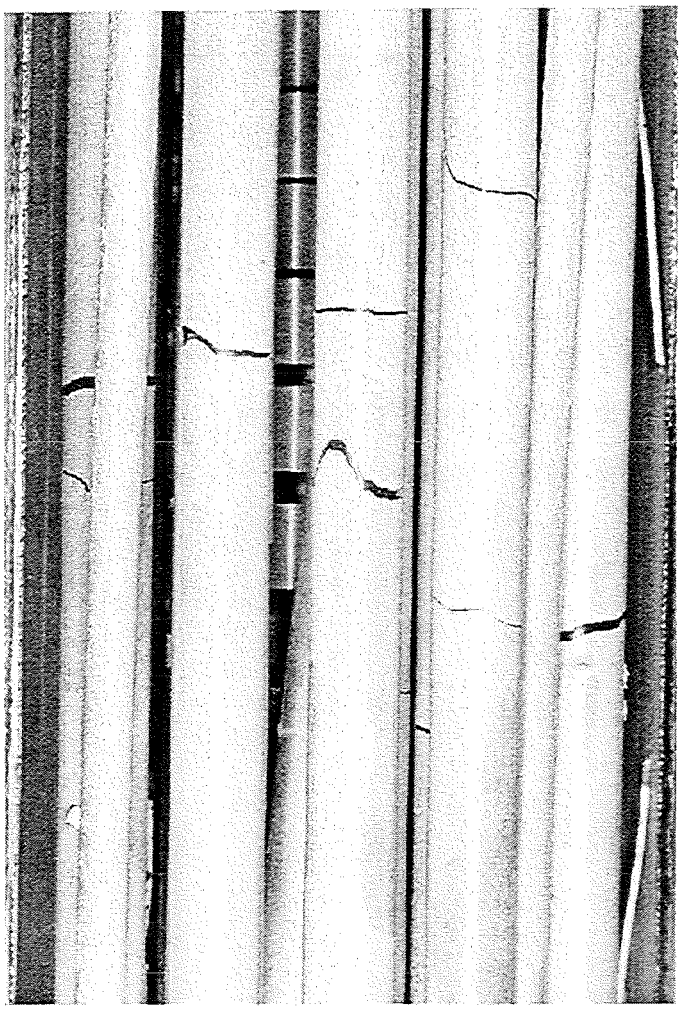

Fig. 3.12: Cladding breaches in the region of 900 mm elevation of the bundle in the QUENCH-01 test.

Prior to the encapsulation of the test bundle fuel rod simulator #18 was removed from the bundle for further investigations, especially for the determination of the axial oxide layer thickness distribution and for the analysis of the hydrogen absorbed in the remaining Zircaloy-4 metal. For this reason the cladding tube was sectioned and specimens were taken every 100 mm. Additionally, three specimens each from the shroud and from a 6 mm corner rod were taken at elevations 700, 900 and 1100 mm.

The results of both measurements are shown in Figure 3.13. The oxide layer thickness distribution is discussed in detail later and is here only used for comparison reasons. Both curves obtained from the cladding tube (hydrogen absorbed and oxide layer thickness vs. axial elevation) show a similar shape, the hydrogen curve is only slightly shifted to higher elevations. The maximum value of the hydrogen absorbed is about 5 at-% which is far away from

saturation with respect to Sieverts' law but near saturation of the α-phase with respect to the phase diagram Zr-H. It seems that most of the hydrogen is absorbed at that elevation where it is produced by steam oxidation of Zircaloy-4. No indications were found for hydrogen uptake at higher colder parts of the bundle. Furthermore, it was estimated that no significant relocation of the hydrogen due to axial diffusion in the metal phase should have happened during quenching.

Some hydrogen was absorbed by the shroud and the 6 mm corner rods with a maximum amount of about 2.5 at-% in the hot zone.

An extrapolation of the data obtained at one cladding tube and three specimens each from the shroud and the 6 mm rod gives a value of about 1 g hydrogen absorbed by the whole bundle, which is only 3 % of the hydrogen totally produced during the test QUENCH-01.

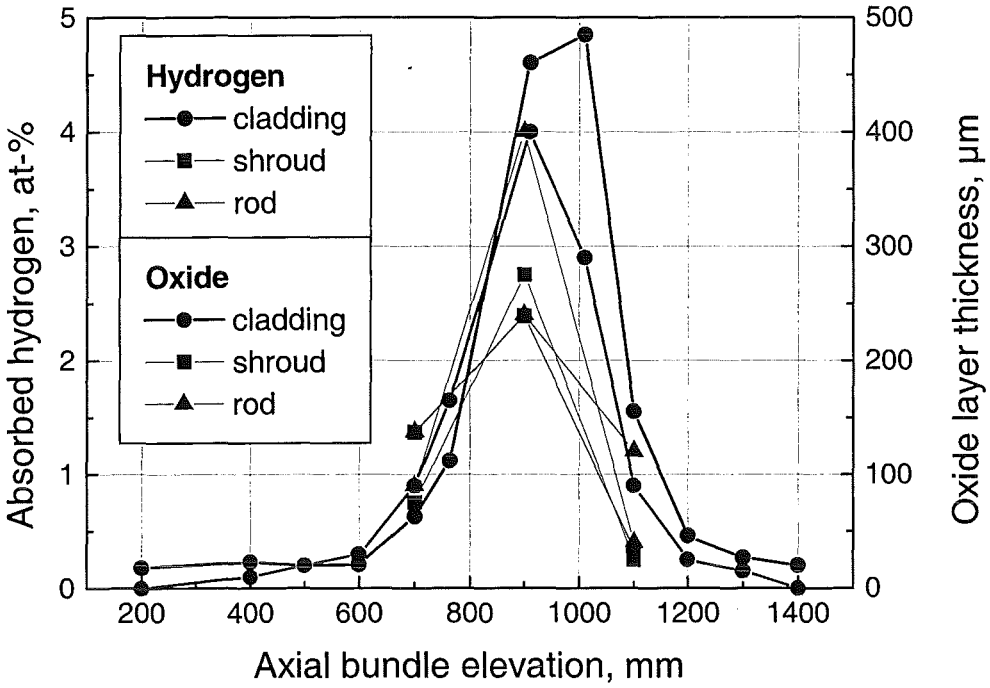

Fig. 3.13: Oxide layer thickness and absorbed hydrogen in the remaining Zircaloy-4 metal of cladding, shroud and corner rod in the QUENCH-01 test.

The physico-chemical state of the Zircaloy cladding material was examined and evaluated by optical microscope and by scanning electron microscope examinations. Of special interest was the determination of the oxide layer

thicknesses of the Zircaloy cladding tubes and the shroud, the formation of through-wall cracks in the cladding tubes and the oxidation of the crack surfaces.

Figure 3.14 shows as an example details of the heated rods and the unheated central rod as well as the 6 mm Zircaloy rods at higher elevation (913 mm) within the hot zone. The Zircaloy cladding tubes are partially oxidised and cracked.

The formation and number of through-wall cracks depends on the thickness of the ZrO_2 oxide layer which determines the thicknesses of the oxygen-stabilised α-Zr(O) and the transformed β'-phase; the latter is the only ductile part of the "sandwich" structure. Figures 3.15 and 3.16 show the extent of the cladding oxidation at three different axial bundle elevations of 763, 913, and 1000 mm. As a result of the axial temperature distribution within the bundle, the thicknesses of the various phases are different. No or only a few through-wall cracks form at ZrO_2 layer thicknesses $\leq$ 200 µm (Figures 3.15 and 3.16) since the remaining β'-phase is still present and sufficient thick to prevent the crack formation.

Figure 3.16 shows in addition the oxidation of the crack surfaces which must have formed during flooding. Figure 3.17 shows different appearances of cracked cladding tubes at the cross-section elevation 913 mm. The reason for the formation of the needle-like structures in the α-Zr(O) has still to be clarified. SEM/EDX examinations of the chemical composition of needles indicate that they consist of ZrO_2.

At some locations a strong internal localised cladding tube oxidation could be observed, independent on the examined bundle elevations. Figure 3.18 (unheated rod) shows a similar external oxide layer cracking together with a rather strong internal cladding oxidation. Also at the elevation of 763 mm the crack surfaces are oxidised. In addition, a pore-like structure in the cladding tube can be observed. The reason for the formation of these channels and the subsequent oxidation of their surfaces are not yet clarified. The white metallic phases in some parts of the cladding tube consist of a (Zr, Cr, Fe) alloy of variable chemical composition which contains different amounts of oxygen.

The physico-chemical behaviour of the Zircaloy cladding tubes at the upper bundle elevation of 1000 mm is shown in Figures 3.19 and 3.20. One can recognise also localised internal cladding oxidation with through-wall cracks through the external and internal oxide layers. Figure 3.21 shows details of the crack morphology.

The bundle elevation of 1163 mm is outside the heated region. At this elevation the extent of cladding oxidation is small, therefore, no through-wall cracks have formed. At all elevations the central cladding tube is more oxidised than the other cladding tubes.

Beside the cladding tubes also the Zircaloy shroud was oxidised on its internal (≈ 380 µm, at the 913 mm bundle elevation) and external (≤ 5 µm) surface.

The Zircaloy rod (6 mm ∅) which was taken out of the hot bundle after pre-oxidation before quenching was examined with respect to oxide layer thickness over its total length. The result is shown in Figure 3.21 and compared with the oxide layer thickness of another Zircaloy rod which remained in the bundle over the whole test sequence. One can recognise that the maximum oxidation occurred at the bundle elevation of about 900 mm and that there is a pronounced oxide layer thickness increase during the transient heatup and quench process.

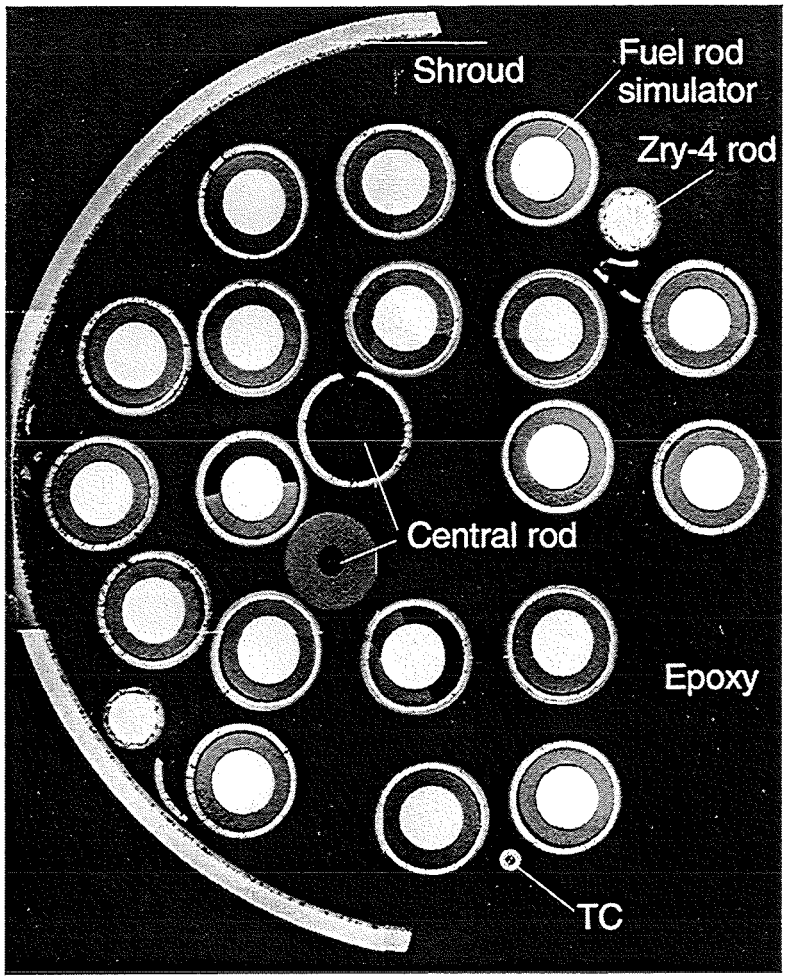

Fig. 3.14: Horizontal cross section of the QUENCH-01 test bundle at elevation 913 mm.

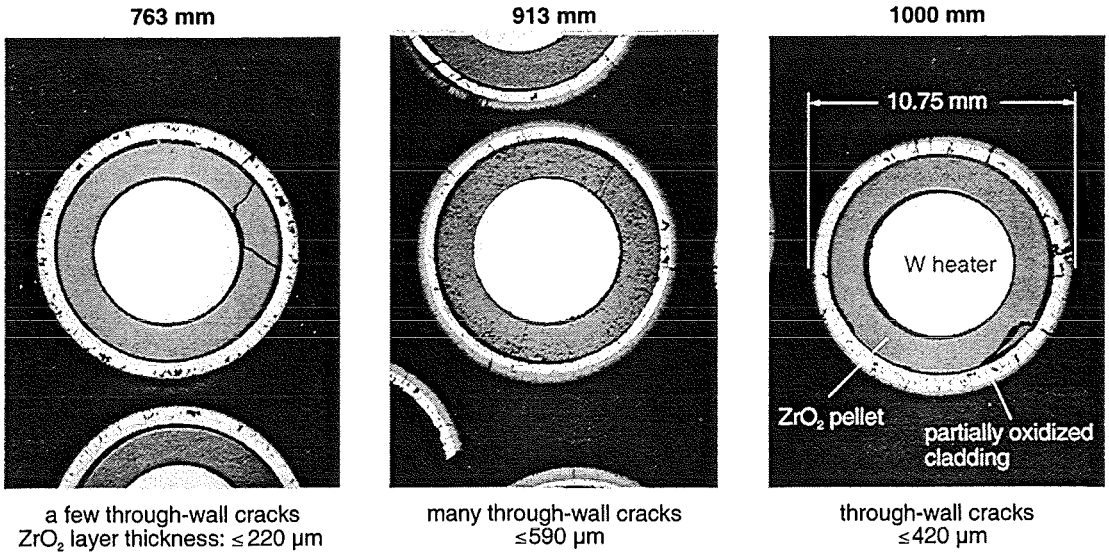

Fig. 3.15: Macroscopic appearance of one fuel rod simulator at different bundle elevations in the QUENCH-01 test.

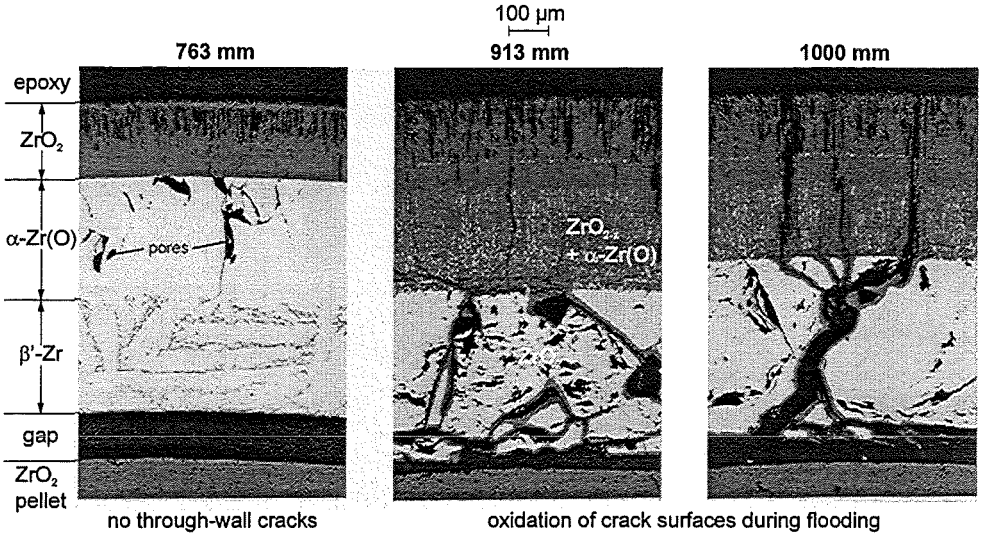

Fig. 3.16: Oxidation of Zircaloy cladding at different axial bundle elevations in the QUENCH-01 test.

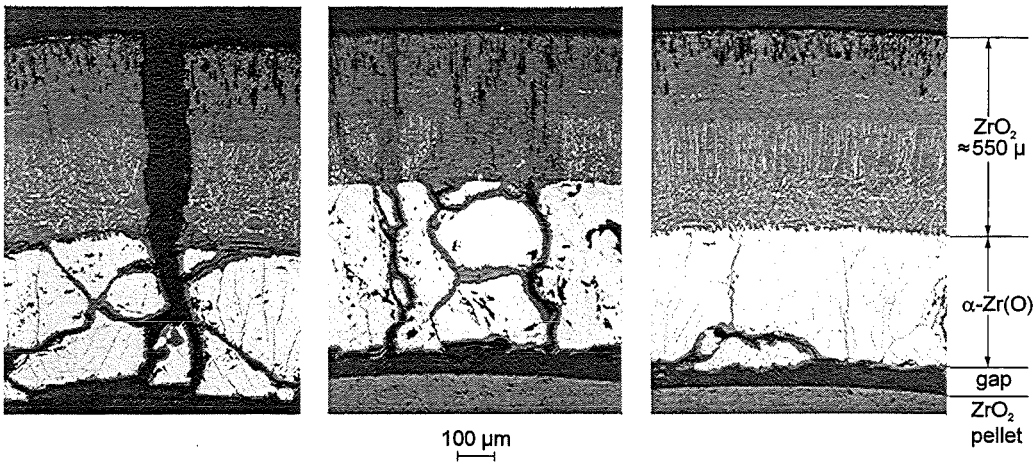

Fig. 3.17: Oxidation of crack surfaces formed during flooding in the QUENCH-01 test at bundle elevation 913 mm.

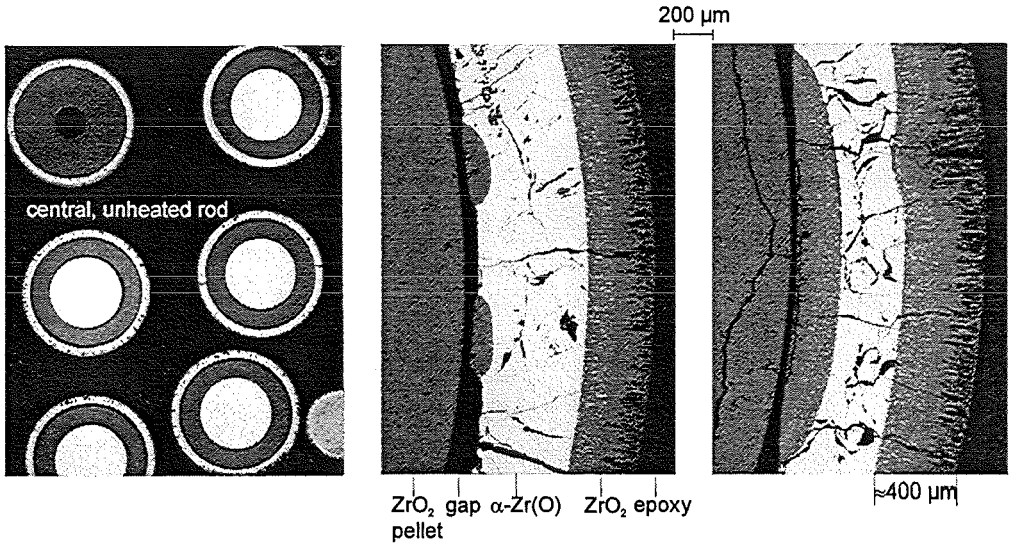

Fig. 3.18: External and internal Zircaloy cladding tube oxidation of the central rod in the QUENCH-01 test at bundle elevation 763 mm.

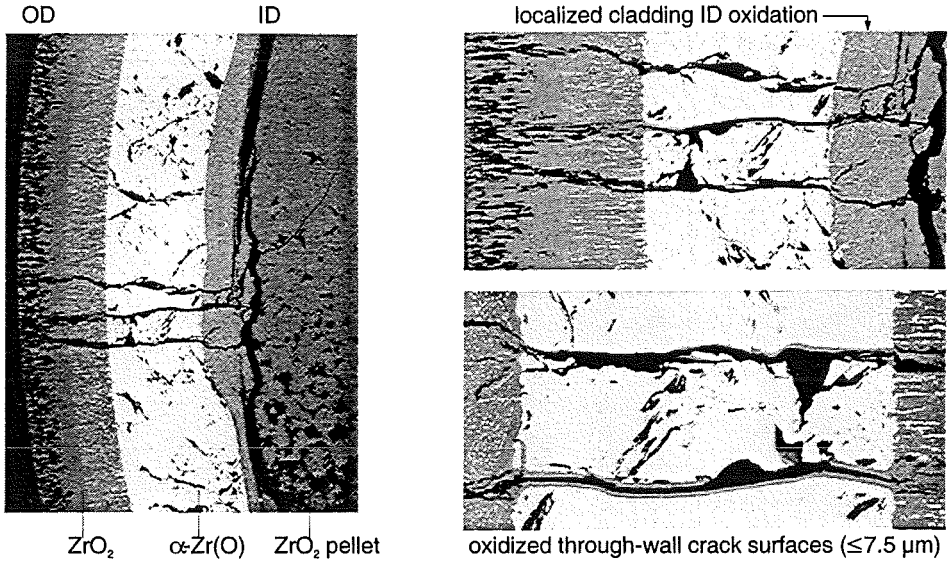

Fig. 3.19: Localised, increased oxidation of the cladding inner surface in the QUENCH-01 test at bundle elevation 1000 mm.

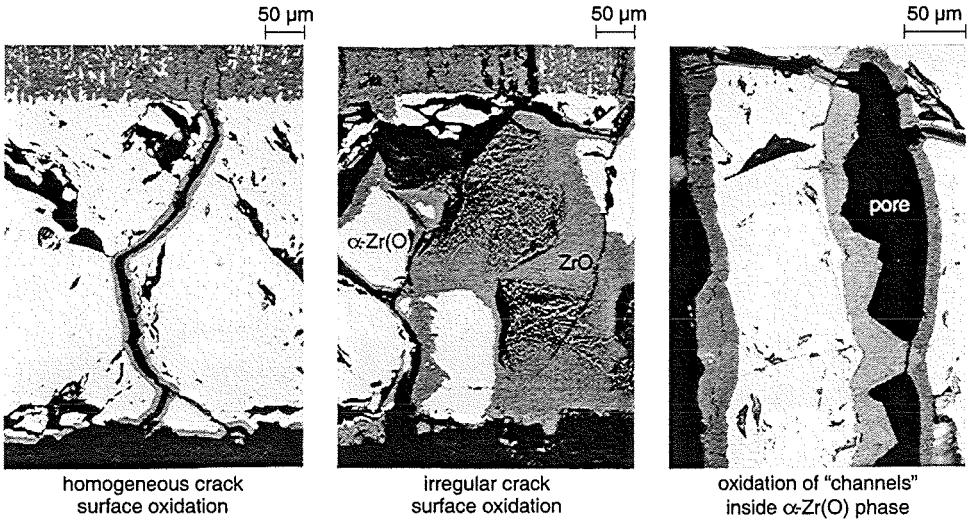

Fig. 3.20: Oxidation of crack surfaces formed during flooding in the QUENCH-01 test at bundle elevation 1000 mm.

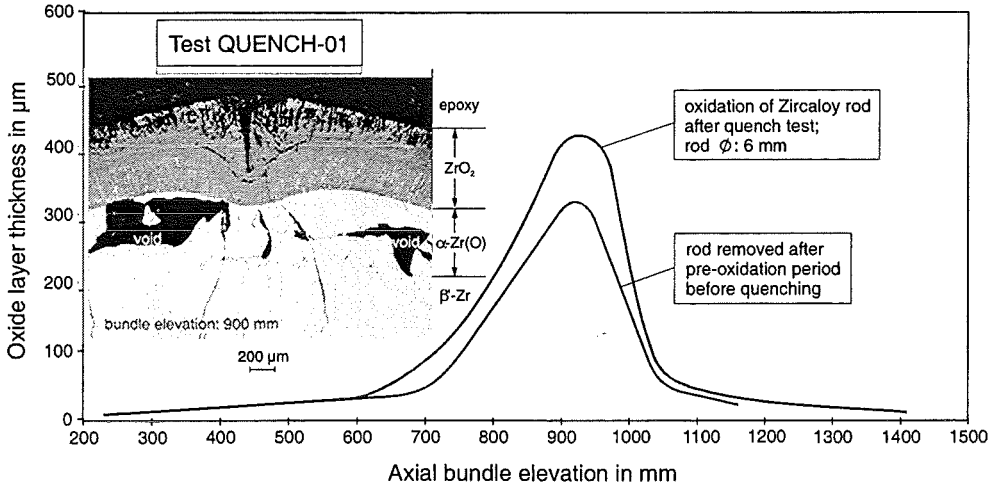

Fig. 3.21: Oxide layer thickness of the Zircaloy rods before and after the QUENCH-01 test.

Test QUENCH-02

The second bundle experiment QUENCH-02 [4] was a reference test to investigate the behaviour of partially oxidised PWR fuel rods, e.g. without additional pre-oxidation, on reflood. The bundle configuration was the same as in test QUENCH-01.

The bundle was heated by a series of stepwise increases of electrical power from room temperature to ~900 K in an atmosphere of flowing argon and steam. During this time the operation of the hydrogen measurement system (mass spectrometer and Caldos device) was checked. The bundle was stabilised at this temperature in a mixture of 3 g/s argon and 3 g/s steam for 4800 s, with the electrical power being 3.75 kW. At the end of the thermal stabilisation period the bundle was ramped with an average heatup rate of 0.45 K/s (0.9 K/s at 1470 K) in the argon/steam mixture until an uncontrolled temperature excursion due to the exothermal zirconium-steam reaction began at the 950 mm level, which had then reached ~1820 K. From this level the high temperature front spread downwards to 850 mm, then upwards to 1050 mm, and 1150 mm (150 mm above the heated zone), and finally again downwards to 750 mm. The escalations started at different temperatures, e. g. 1820 K at 950 mm (TFS2/13), 1700 K at 850 mm (TFS3/12), and 1495 K at 1150 mm elevation (TFS2/15), because the axial temperature distribution determines the extent of oxidation at the different levels. The temperature escalation of the shroud at the 950 mm level occurred almost simultaneously with the escalation of the rods at the 850 mm elevation. The temperature excursion of the shroud at the 850 mm level followed about 25 s later with the maximum heatup rate of approx. 48 K/s (TSH12/0). For comparison, the maximum escalation rate of the rods amounted to approx. 23 K/s (TFS5/12). At the end of the transient phase the electrical power input was 16.35 kW.

At about 2270 K the pre-planned reflood sequence was initiated, with water being injected firstly at the high rate of 89 g/s to fill the lower plenum. The temperature of the water at the lower plenum was near the saturation temperature. The steam (3 g/s) and argon (3 g/s) flow through the test section were turned off. During quenching argon (3 g/s) is injected at the upper bundle head, i.e. above the heated zone of the test section, to provide a carrier gas

for the hydrogen to be transported to the analysing systems. The electrical power was stabilised at 19 kW and held at this level for 77 s. The water injection was reduced to 47 g/s after 30s (at this time it was estimated that the lower plenum had been filled, up to the level of -250 mm). The water mass flow of 47 g/s resulted in a local flooding rate of 1.6 cm/s. When the bundle had become half full (water level at 550 mm), the bundle electrical power was reduced to 4 kW (to simulate decay heat levels) within 15 s. Reflood of the main test section to 1300 mm (above the heated zone) was completed in 263 s, after which the experiment was terminated by shutting off the electrical power. The amount of water injected at a rate of 89 g/s and 47 g/s was 2.7 l and 11 l, respectively, so that the total amount of water injected was 13.7 l.

During the reflood phase strong secondary temperature excursions were observed starting from 1700 – 2270 K.

The cooling of the test bundle began in the heated zone between 1000 K and 2200 K at 150 mm and 1150 mm elevation, respectively. The quench temperatures in the heated zone were between 950 K (150 mm) and 1470 K at the 1150 mm elevation (Figure 3.22).

The hydrogen production started when the escalation period (level 950 mm) began reaching a maximum H_2 concentration of 42 % in the offgas (Figure 3.23). The maximum hydrogen production rate was 2.5 g/s. The total hydrogen release measured by the mass spectrometer is 190 g with most of it associated with the reflood phase (Figure 3.22 and Table 3.4). This hydrogen production is comparable to that observed in previous tests under similar conditions, e. g. CORA experiments. The maximum hydrogen production rate, however, is about twice the highest value in the CORA experiments (CORA-17: 1.3 g/s, total H_2 = 150 g).

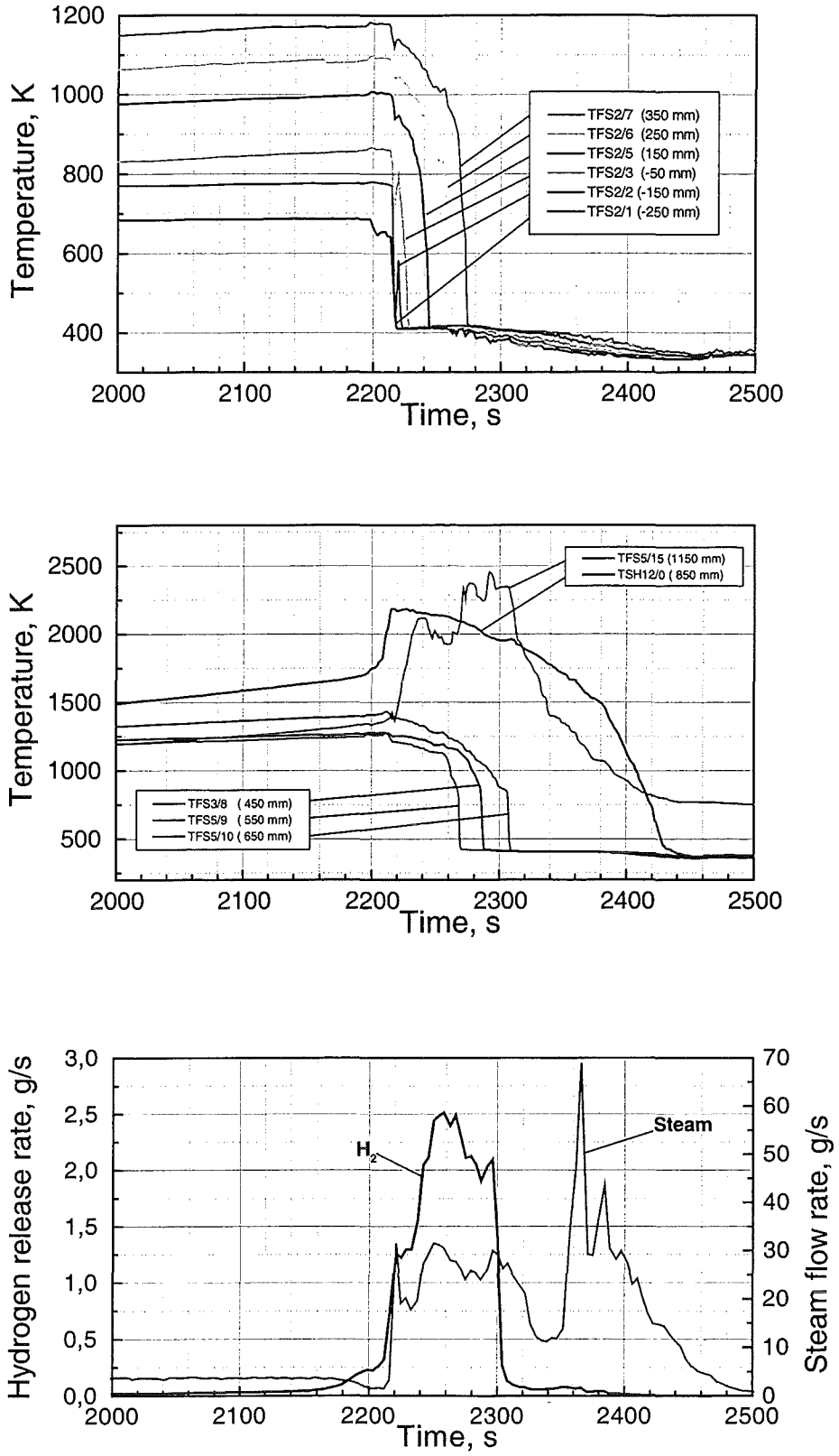

Fig. 3.22: Hydrogen generation, cladding temperatures and shroud temperature, and steam flow as a function of time during QUENCH-02 test.

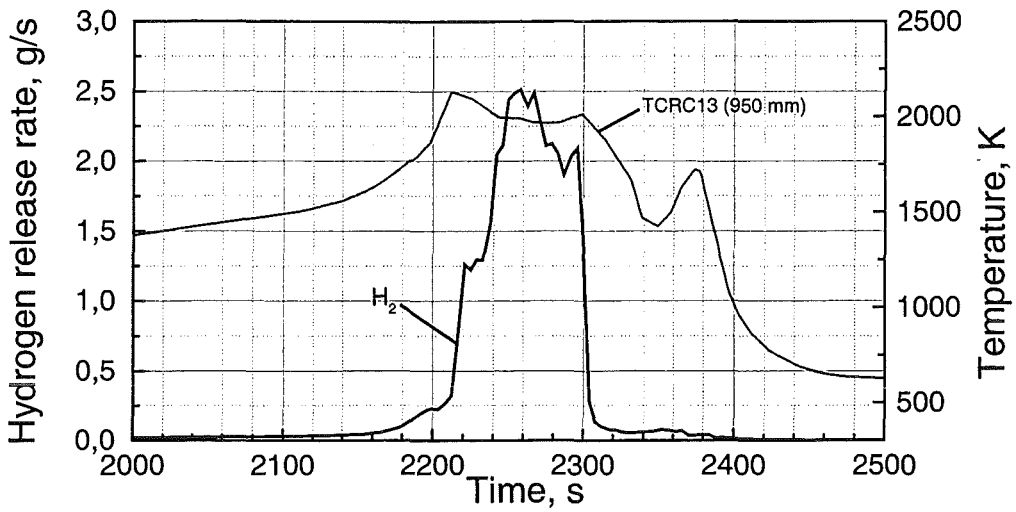

Fig. 3.23: Hydrogen release rate and temperature history of QUENCH-02 test.

Test phase	Hydrogen mass, g
Pre-oxidation	-
Transient	20
Reflooding	170
Total released	190
Total absorbed	~5
Max. rate, g/s	2.5

Table 3.4: Hydrogen release measured by mass spectrometer during QUENCH-02 test.

On the basis of hydrogen production, the chemical power was calculated and compared to the electric power input in Figure 3.24. The contribution of the exothermal energy to the total energy in test QUENCH-02 is enormous.

The hydrogen absorbed in the remaining Zircaloy-4 metal was analysed in the LAVA facility. Two-centimeter long cladding segments taken from the fuel rod simulator #17 were heated for 20 minutes to some 1800 K under a well-defined argon flow. The hydrogen released was measured by a mass spectrometer.

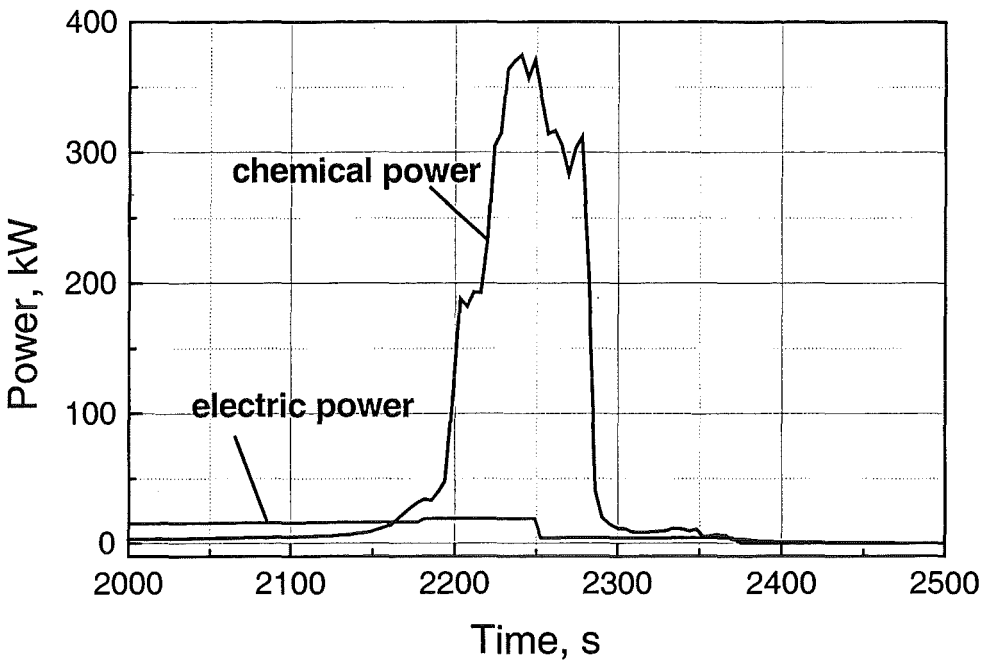

Fig. 3.24: Electric bundle power input as compared to chemical power (due to the Zircaloy/steam reaction) for the QUENCH-02 test.

The results of the measurements are shown in Figure 3.25. The axial distribution of hydrogen absorption in the Zircaloy-4 cladding of the rod from the QUENCH-02 bundle again correlates with the axial oxide layer thickness distribution. The range includes the region where most of the H_2 was produced, but is slightly extended to higher levels. The maximum concentration of about 15 at-% hydrogen was found in the cladding at the upper end of the hot zone and in the shroud in the middle part of the hot zone. In this region between 950 mm and 1200 mm no data were obtained for the rod cladding which had been oxidised completely. Extrapolation of the data obtained from one cladding tube and from the shroud specimens results in approx. 5 g of hydrogen absorbed by the whole bundle (Table 3.4).

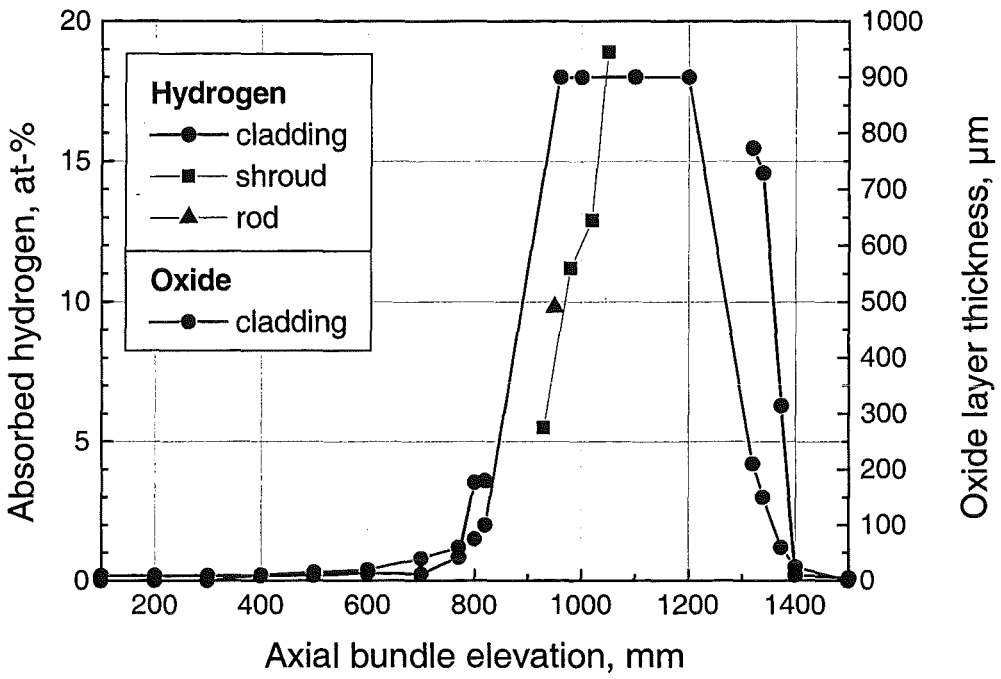

Fig. 3.25: Hydrogen absorbed from the remaining Zircaloy metal as measured in QUENCH-02 test.

The post-test appearance of the test bundle is shown in Figure 3.26. The Zircaloy cladding is heavily oxidised and partially broken away during the quench process. Below and above 870 mm elevation parts of the bundle were molten and had formed a blockage zone upon solidification. The shroud appears to have generated a kind of bubble where molten material accumulated. The remnants of the upper part of the shroud indicate a deformation caused by melting. Embrittlement of the shroud and rod cladding of the QUENCH-02 test bundle is by far more severe than in the QUENCH-01 test bundle.

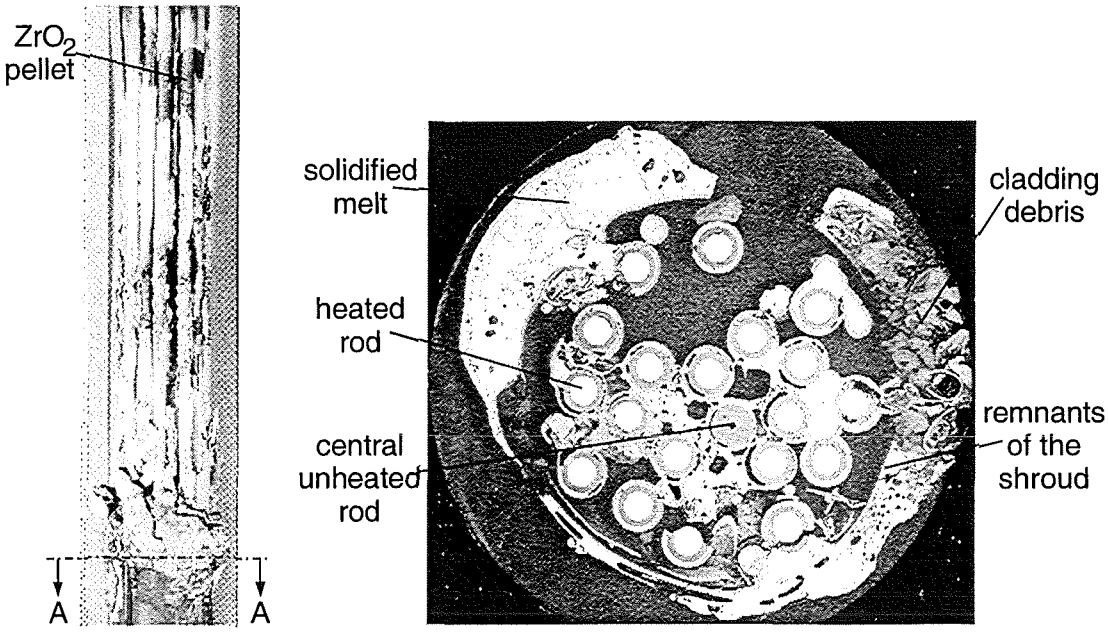

Fig. 3.26: Post-test appearance of the bundle QUENCH-02 and cross-section A-A of the elevation 868 mm. Extensive bundle degradation in the upper hot region and formation of bundle blockages due to relocation of molten materials.

4. CONCLUSIONS FROM EXPERIMENTAL PROGRAM

Small-scale quench experiments:

- Formation of macroscopic through-wall cracks can be observed in steam quenched experiments with ZrO_2 layer thickness larger than 200 µm. Oxidation of crack surfaces increases with decrease of the specimen temperature at the onset of quenching.
- In contrary to the water-quenched experiments (pre-oxidised in an Ar/O_2 gas mixture) in the steam-cooled experiments it was not possible to determine the cooldown-related amount of hydrogen as a result of the preferred crack surface oxidation.
- Deviation from the regular cooldown curve during the quench phase was observed in all experiments with quench temperatures less than 1600 °C when the ZrO_2 layer thickness was larger than 200 µm. No temperature increase was observed in experiments with 1600 °C even for large ZrO_2 layer thicknesses.

- In general, the results show that after reaching certain oxide layer thickness (about 200 µm) and crack density, the amount of hydrogen absorbed in the metallic part of the Zircaloy tube increases considerably.
- In experiments with 1600 °C initial temperature at onset of cooldown even for large oxide layer thickness (>300 µm) the amount of absorbed hydrogen is still relatively low in comparison with similar specimens cooled from 1100, 1200 and 1400 °C. Only for very large oxide layer thickness (~380 µm) this amount is significant.
- The amount of the absorbed hydrogen correlates not only with the extent of the pre-oxidation at the onset of cooldown, but also with the total crack length.
- The uptake of the hydrogen in Zircaloy and its additional release during oxidation of the metal and during the quench phase can influence the kinetics of hydrogen release and has therefore to be studied quantitatively in more detail.
- The possibility, that the deviation from the regular cooldown curve could be triggered by the exothermal hydrogen absorption process, needs to be investigated further in the future.

Hydrogen absorption tests:

- The hydrogen solubility of Zircaloy-4 decreases with increasing oxygen content in the α- as well as in the β-phase.
- No differences in the hydrogen absorption behaviour between Zircaloy-4 and Zr1%Nb were found.
- During steam oxidation a limited amount of hydrogen is absorbed in situ.
- The different transient behaviour during absorption and desorption, respectively, which was experimentally observed, could be well described by a mathematical model developed by the Russian IBRAE team.

The major results of the first QUENCH experiments:

- Oxide layer on the cladding tube surface prevent the test bundle QUENCH-01 from a temperature escalation. In test QUENCH-02 with no additional pre-oxidation of the cladding the bundle experienced a temperature escalation with heating rates around 20 K/s and 50 K/s for the rod cladding and the shroud, respectively. The escalation started prior to flooding of the test bundle.
- The maximum temperature in test QUENCH-01 was ~1870 K, that in experiment QUENCH-02 ~2500 K.
- The temperature escalation and the enhanced steam generation due to flooding strongly supports the hydrogen generation rate.
- In experiment QUENCH-01 (without a temperature escalation), the bulk of H_2 was produced in the pre-oxidation phase (30 g).
- In experiment QUENCH-02 (with a temperature escalation) an amount of 190 g of hydrogen was generated during the whole test.
- The maximum hydrogen production rate was measured during test QUENCH-02, i. e. 2.5 g/s as compared to 0.08 g/s in test QUENCH-01.
- The "onset of cooling" of the rod cladding (prior to rewetting) occurs simultaneously for all axial positions and exactly at the time when the quench water level is at -250 mm.
- The post-test condition with respect to embrittlement of the rod cladding and the shroud is more severe for the QUENCH-02 test bundle than for the QUENCH-01 test bundle.
- Parts of the QUENCH-02 test bundle were molten and had formed localised blockage zones in the coolant channels whereas the QUENCH-01 test bundle shows no sign of melting.

5. REFERENCES

[1] P. Hofmann, A. Miassoedov, L. Steinbock, M. Steinbrück, M.S. Veshchunov, A.V. Berdyshev, A.V. Boldyrev, A.V. Palagin, V.E. Shestak. "Quench Behavior of Zircaloy Fuel Rod Cladding Tubes. Small-Scale Experiments and Modeling of the Quench Phenomena". FZKA 6208, INV-COBE(98)-D018.

[2] P. Hofmann, V. Noack, M.S. Veshchunov, A.V. Berdyshev, A.V. Boldyrev, L.V. Matweev, A.V. Palagin, V.E. Shestak, "Physico-Chemical Behavior of Zircaloy Fuel Rod Cladding Tubes During LWR Severe Accident Reflood", FZKA 5846, Forschungszentrum Karlsruhe, 1997, INV-COBE(97)-D004.

[3] P. Hofmann, W. Hering, C. Homann, W. Leiling, A. Miassoedov, D. Piel, L. Schmidt, L. Sepold, M. Steinbrück, "QUENCH-01, Experimental and Calculational Results," FZKA 6100, Forschungszentrum Karlsruhe, 1998, INV-COBE(98)-D010.

[4] P. Hofmann, S. Horn, W. Leiling, D. Piel, L. Schmidt, L. Sepold, M. Steinbrück, "QUENCH-02 Test Data Report", FZK Internal Report PSF 3303, Forschungszentrum Karlsruhe, 1998, INV-COBE(98)-D015.

[5] M. Steinbrück (Ed.), 4th International QUENCH Workshop, Germany, Karlsruhe, October 6-8, 1998, Compilation of Handouts, Internal Report PSF 3312.

II. Speculations on mechanisms for temperature escalations in LWR fuel rod bundles under quench conditions

(H. Steiner, IMF III)

Abstract

Temperature escalations are an important phenomenon in quench tests as they lead to enhanced oxidation and hydrogen production as well as to severe degradation of fuel rod bundles. They have been observed in tests of the CORA and The QUENCH program. With the help of experience gained from separate effects tests mechanisms are discussed which might trigger the temperature escalations under heating-up or cooling-down situations.

Zusammenfassung

Temperatureskalationen sind ein wichtiges Phänomen in Abschreckversuchen, da sie zu verstärkter Oxidation und Wasserstoffproduktion führen sowie zu einer starken Zerstörung der Brennstabbündel. Sie wurden sowohl bei verschiedenen CORA-Versuchen als auch bei denen des neu begonnen QUENCH-Programms beobachtet. Im Lichte der Erfahrung aus Einzeleffekt-Untersuchungen werden mögliche Mechanismen diskutiert, die Temperatureskalationen auslösen können und zwar sowohl für Aufheiz- als auch für Abkühlsituationen.

1. Introduction

The occurrence of unexpected temperature escalations in some quench tests of the CORA program was a strong motive for the initiation of a new out-of-pile quench test program at FZK with small bundles of fuel rod simulators [1]. With four tests having been done in the meantime, a first review of the outcome of these tests with regard to temperature escalation mechanisms might be of help for the further test conduct.

2. Phenomenological aspects

Temperature escalations occurred in the quench tests of the CORA program under heating-up as well as under cooling-down situations, with the latter phenomenon the more unexpected one. In the tests of the QUENCH program, done so far, temperature escalations have only appeared in heating-up situations. Temperature escalations are observed on fuel rod thermocouples as well as on shroud thermocouples,, starting sometimes at temperatures as low as about 800 °C. Some typical examples are shown in Fig. 1.

Thus, there seem to be different mechanisms at work. The aim is to identify and understand them. Normally, one would look for hints from post test examinations. But the temperature escalations have led locally to severe destructions of the test bundles. Thus, we have little hope to find any hints from PTE. Progress in this respect could eventually be made with separate effects tests, as with the single rod quench test done at IMF I.

There might also be obtained some hints from the thermocouple readings. If there is a very steep increase of the temperature, the arrival of relocated hot material can be suspected.

3. Mechanisms in a cooling-down situation

The single rod quench tests done at IMF I [2] have provided valuable insight into the mechanical behavior of pre-oxidized Zry claddings under a cooling-down situation. The parameters which are decisive for the mechanical behavior are oxidation temperature and oxide scale thickness. At oxidation temperatures above 1100 °C, mechanically stable oxide scales are obtained. Spalling is unimportant in this case, but the occurrence of through-wall cracks at cooling-down has to be noted. Most probably, these through-wall cracks are due to the phase change tetragonal/monoklin in the oxide , occurring below 1100 °C [3].

Due to this rather low temperature, locally the through-wall cracks have a limited oxidation potential. But the steam can now penetrate into the fuel rods and eventually reach positions with higher clad temperatures, where in principle a temperature escalation may be triggered. This situation is depicted in Fig. 2.

The main question is whether a sufficient amount of steam can penetrate into the fuel rods and whether hot clad positions can be reached in due time. The experience of QUENCH-01 [4] demonstrates that it might be difficult to trigger a temperature escalation under this scenario.

Some single rod quench tests with oxidation temperatures below 1100 °C have shown massive spalling of the oxide scale as a result of the break-away oxidation regime. At some axial locations of QUENCH-01 this regime should have been reached as the oxidation time was sufficient. But no indications for massive spalling have been reported in [4].

4. Mechanisms in a heating-up situation

Temperature escalations in heating-up situations have been observed on fuel rod simulator thermocouples, as well as on shroud thermocouples. We will discuss them separately, although there might be mechanisms which are representative for both.

a) Fuel rod simulators

Mechanical effects may be a major cause for temperature escalations. Stresses in the oxide scale can arise by chemical processes like oxidation, by phase changes, bending, temperature gradients etc. With higher temperatures creep processes become important. Thus, there is an effective stress relaxation for long-term processes like oxidation and therefore process which can lead to abrupt change of the stress state like phase changes are first candidates for mechanical effects.

In heating-up situations there is the monoklin/tetragonal phase change in the oxide at about 1100 – 1200 °C and the tetragonal/cubic phase change at about 1500 °C if the oxide contains some α-phase fraction. Temperature escalations starting from these temperature regions have been observed in QUENCH-02 [5] and QUENCH-03 [6].

High tensile stresses arise in the oxide scale at the monoklin/tetragonal phase change, which lead to cracking in the scale. As the stresses in the metal phase are compressive and as there should still be a ductile β-phase no through-wall cracks are to be expected.

A temperature escalation can only be triggered if there is spalling of the scale to some extent, cracks alone are not sufficient. Bending of the fuel rod simulators or a cauliflower structure of the oxide scale which may develop for oxidation temperatures below 1100 °C [7], are possible causes for oxide scale spalling.

No data on the volume change occurring at the tetragonal/cubic phase transition can be found in the literature. If there is a significant volume change, through-wall cracks are to be expected and the steam can penetrate into the fuel rods. As this is a high temperature location and a temperature escalation is then highly probable. The Kr-signal of QUENCH-02 [5] indicates that this scenario might be realistic.

b) Shroud

Temperature escalations in the shroud have been observed in all the tests of the QUENCH program done so far. In the oxide scale of the shroud the same effects as that in the fuel rod simulators may play a role. It is not necessary to discuss this once more. But as the starting temperature of the escalations was sometimes very low in the shroud (800 °C and lower) there might be mechanisms of its own.

At such low temperatures, oxidation alone cannot lead to a temperature escalation and we have to look for other mechanisms. One possibility would be hydrogen uptake. The largest effect would be provided by hydrogen uptake of a clean Zry cladding but under certain circumstances hydrogen can also permeate through oxide scales.

The measurements of hydrogen uptake by clean surfaces reported in [8] and [9] can be described by the following expression for the hydrogen flux [10]:

$$j_H = \theta \bullet k_{abs} - C_H^2 \bullet k_{des} \qquad (1)$$

θ = surface coverage with H_2

k_{abs} = absorption rate constant

k_{des} = desorption rate constant

C_H = surface concentration of atomic hydrogen

Evaluation of the measurements reported in [8] and [9] provided values for $\theta \bullet k_{abs}$ and k_{des}. It appears that the temperature increase rate in the shroud is proportional to

the hydrogen partial pressure in the coolant channel (p_{H_2}) [11] and between 800 and 960 °C the temperature increase rates by hydrogen uptake alone are estimated to range between 4 $\bullet p_{H_2}$ and 8 $\bullet p_{H_2}$, if hydrogen is taken up only at the inner surface of the shroud [11].

The temperature of the shroud may also increase by radiation heat transfer. For a constant temperature difference between fuel rod simulators and the shroud the heat transfer rises with the 3rd power of the fuel rod temperature.

For thin oxide scales on the shroud between 0 and 10 µm the emissivity of the shroud increases from 0.2 to about 0.8 leading to an enhancement of the heat transfer by more than a factor 2 [11]. Thus, increase rates of the shroud temperature between 3 and 13 K/s due to radiation heat transfer have been estimated.

References:

[1] W. Hering, et al.: FZK-Nachrichten 4/97, p. 309 (1997)

[2] P. Hofmann, et al.: FFZKA 5846 (1997)

[3] H. Steiner, M. Heck: Nucl. Techn. Vol. 123, p. 209 (1998)

[4] P. Hofmann, et al.: FZKA 6100 (1998)

[5] L. Sepold, et al.: internal report

[6] L. Sepold, et al.: internal report

[7] G. Schanz, et al.: Proc. Met. Corrosion, Mainz (1981)

[8] G. Schanz, et al.; Fifth Intern. Meeting on Therm. Nuclear Reactor Safety, KFK 3880/2 (1984)

[9] M. Steinbrück, et al.: 3rd Intern. Quench Workshop, Karlsruhe (1997)

[10] H. Steiner: Reaktortagung (1999)

[11] H. Steiner: internal report

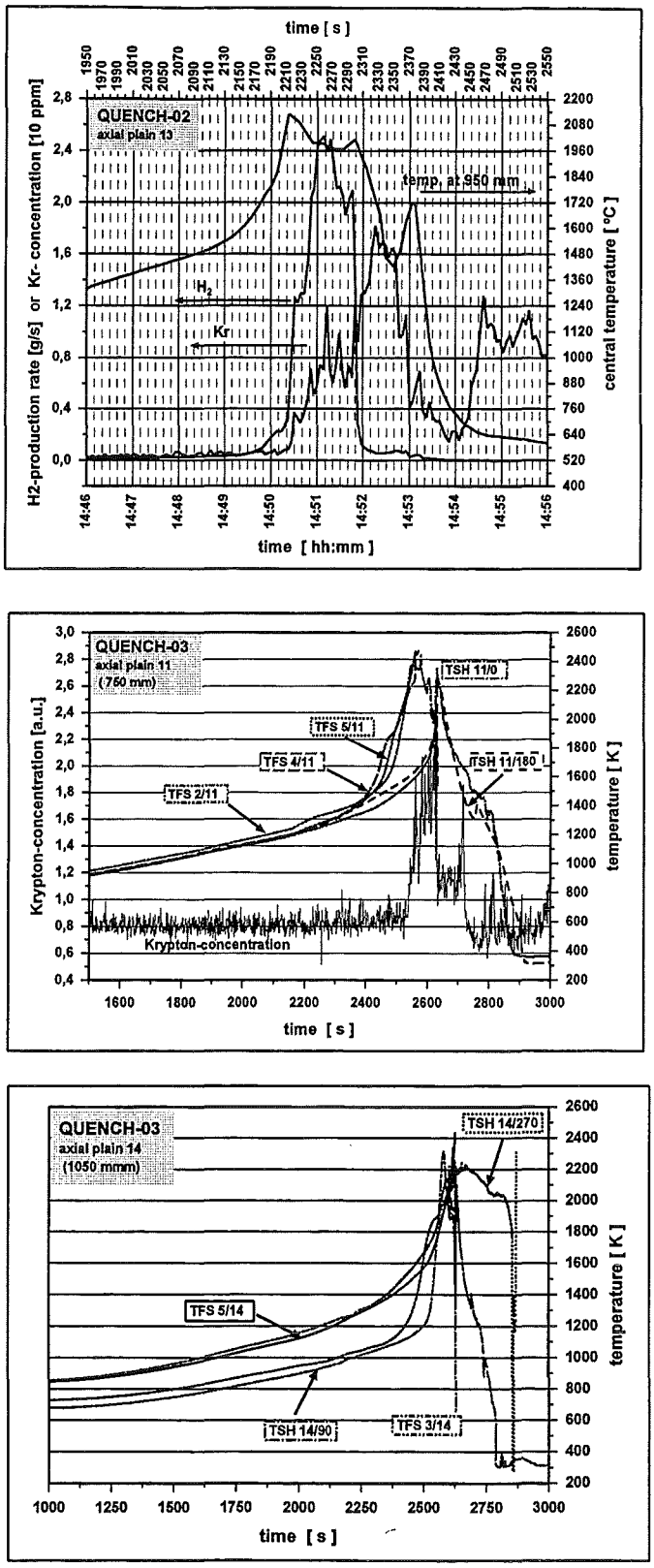

Fig. 1: Examples for temperature escalations in FZK QUENCH tests

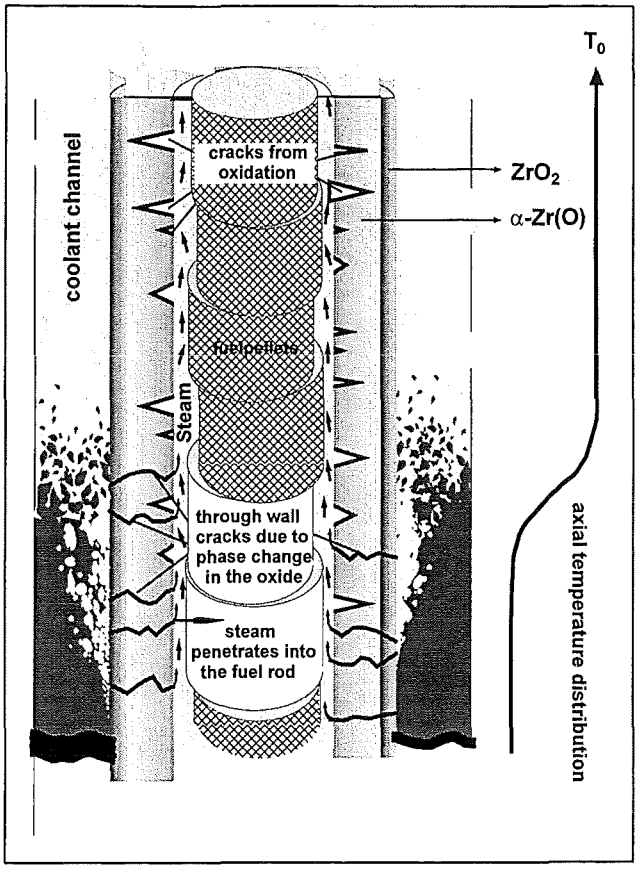

Fig. 2: Scenario for a temperature escalation in a cooling down situation

III. Analysen zum Ablauf kernzerstörender Unfälle

(W. Hering, Ch. Homann, W. Sengpiel, S. Smit, D. Struwe, IRS;
Ch. Messainguiral, CEA*)

Abstract

At the Forschungszentrum Karlsruhe (FZK) the Institute for Reactor Safety (IRS) performs accident analyses for the European Pressurized Water Reactor (EPR) by plant calculations with SCDAP/RELAP5 (S/R5) and RELAP5 (R5). The new S/R5 mod3.2 (S/R5m32) code version is still under validation, the improved FZK/IRS models have been implemented and tested. Validation is ongoing using CORA and Phebus experiments, the latter with respect to late phase conditions. Calculations for Phebus FP experiments showed some shortcomings in S/R5m32 so that the studies to evaluate the influence of burn-up on fuel dissolution are realized with S/R5m31.

For S/R5m32 EPR input decks have been revised and a new version has been created for the improved version during BDOP-Phase (EPR-2). For code comparison with MELCOR and MAAP, S/R5m32 calculations for the 50 cm^2 SBLOCA scenario were performed up to melt attack onto the heavy reflector. Detailed analyses to this melt process are performed with LOWCOR2, ICARE2, and FIDAP.

The support of the QUENCH activities at FZK/IRS effectively enhances the understanding and separation of physical and facility based effects. The different reflood models in RELAP5 mod 3.2.2β were validated against integral experiments. The improvement of the film boiling model is under way.

Zusammenfassung

Im Institut für Reaktorsicherheit (IRS) des Forschungszentrums Karlsruhe (FZK) werden Unfallanalysen für den EPR mit SCDAP/RELAP5 (S/5) und RELAP5 (R5) durchgeführt.

Im Berichtszeitraum wurden neue Programmversionen von R5 und S/R5 getestet, Fehler korrigiert und anschliessend mit den FZK/IRS Erweiterungen versehen. Der Validierungsprozess anhand von CORA und Phebus Versuchen ist noch nicht abgeschlossen.

---

* Von CEA-DRN (Frankreich) an FZK/IRS delegiert.

Anhand des Phebus FPT1 Versuchs wurde eine Modellentwicklung in S/R5m31 begonnen, um den Einfluß des Abbrandes auf die Brennstabauflösung zu qualifizieren.

Für die Kernschmelzanalysen wurden neue Input-Decks für den EPR und die leistungserhöhte Version (EPR-2) erstellt und Rechnungen zum kleinen Leck für den Code-Vergleich (50 cm^2) mit MAAP und MELCOR vorgezogen. Codeschwächen bezüglich des Aufschmelzens der radialen Kernumrandung des EPR wurden durch Einzeluntersuchungen mit ICARE2, LOWCOR2 und FIDAP ergänzt.

Die QUENCH Versuche wurden mit Vorausrechnungen zur Versuchssteuerung sowie mit Nachrechnungen zur Versuchsanalyse erfolgreich begleitet. Die neuen Flutmodelle in R5 mod3.2.2β werden anhand von Integralversuchen validiert, eine Verbesserung des Filmsiedemodels ist in Arbeit.

1 Unfallanalysen mit SCDAP/RELAP5

Im IRS werden für Störfallanalysen das mechanistische Programm SCDAP/RELAP5 (S/R5) /1/ in den Versionen MOD 3.1.F (S/R5m31) und MOD3.2 (S/R5m32) sowie - auf den Reaktorkern beschränkt - das französische Programm ICARE2 /2/ verwendet.

1.1 Modellierung des EPR in der BDOP[1] Phase

In Absprache mit Siemens/KWU wurde das zugrunde liegende Datenmodell (s. auch /3/) an die Bedingungen des leistungserhöhten EPR (intern EPR-2) angepaßt. Die radiale Aufteilung wurde, um den Vergleich mit MAAP Ergebnissen zu erleichtern, modifiziert. Der Heavy Reflektor (HR) des Kernbehälters sowie die Reaktor-Druckbehälter(RDB)-Wand wurden vereinfacht als zwei konzentrische Shroud-Komponenten dargestellt. Als Verlagerungspfad für radial austretende Schmelze wurde der Downcomer angenommen, da der Bypass im HR eine zu geringe Querschnittsfläche aufweist. In der frühen Phase der Kernzerstörung werden die Brennstäbe und die Shrouds durch radialen Strahlungsaustausch miteinander gekoppelt. Wird in einer axialen Zone das Auftreten von Debris oder eines Schmelzepools berechnet, so wird modellbedingt der Strahlungstransport zwischen den einzelnen Komponenten deaktiviert. Der Wärmetransport erfolgt dann nur durch Konvektion und Wärmeleitung sowie durch Wärmestrahlung an das Fluid. Die obere Kernplatte wurde durch ein „Upper Plenum Structure" (UPS) Element dargestellt.

---

1 BDOP: Basic Design Optimization Phase

Da bislang kein Strahlungsaustausch zwischen UPS Oberflächen möglich ist, wurden die restlichen Plenumseinbauten weiterhin mit RELAP „heat structures" realisiert. Der Primärkreis besteht aus 2 Loops, einem repräsentativen Loop mit dem Leck im kalten Strang (3xx), einem Loop, der die restlichen drei Kreise simuliert (4xx), dem Emergency Core Cooling (ECC) System und dem Druckhalter. Die Dampferzeuger wurden an die Erfordernisse der gesteigerten nuklearen Leistung angepaßt.

1.2 Rechnungen zum kleinen Leck

Im Berichtszeitraum wurde die neue Codeversion S/R5m32 getestet und um die notwedigen FZK/IRS Modelle erweitert. Die Validierung anhand von ausgewählten CORA- (s. Kap. 1.1.2.2) und Phebus-Versuchen (s. Kap. 1.1.2.3) ergab jedoch einige Unstimmigkeiten im Bereich der Kopplung von Thermohydraulik (R5) und SCDAP-Komponenten (Shroud), an deren Behebung noch gearbeitet wird. Zum Teil sind auch EPR spezifische Bauteile nicht mit den unterstellten Randbedingungen (S/R5 orientiert sich am AP-600) vereinbar.

Unter Berücksichtigung der gefundenen Unstimmigkeiten wurden Kernschmelzanalysen zum kleinen Leck (50 cm² SBLOCA) zum Vergleich mit der alten Version (S/R5m31) durchgeführt. Um numerische Instabilitäten, die beim Ausströmen des Treibgases Stickstoff in den Primärkreis auftreten, zu vermeiden, wurden die Akkumulatoren kurz vor der vollständigen Entleerung vom Primärkreislauf isoliert (abgeschiebert), so daß kein Treibgas in den Primärkreis gelangen kann. Dadurch wird jedoch der zeitliche Unfallablauf verändert, da kein Stickstoff mehr durch das Leck ausströmt. Wie in Abbildung 1 d erkennbar, wird bei gleicher Nachzerfallsleistung (-N-) der Beginn der Kernaufheizung (Tcore_max: -T-) etwa 40 min früher erreicht. Die Temperatureskalation aufgrund der Freisetzung von Leistung (P_oxid) aus der exothermen Zirkonium-Wasserdampf-Reaktion verschiebt sich um etwa um 35 min, da der Kern aufgrund von geänderten Wärmeübergangskoeffizienten schneller ausdampft. In Abbildung 1 c sind die Druckverläufe in Primär- und Sekundärkreislauf dargestellt. Der von S/R5m31 berechnete Druckanstieg im Primärsystem {p-prim(3.1)} deutet auf durch das Leck ausströmendes Wasser hin, das in S/R5m32 nicht berechnet wird.

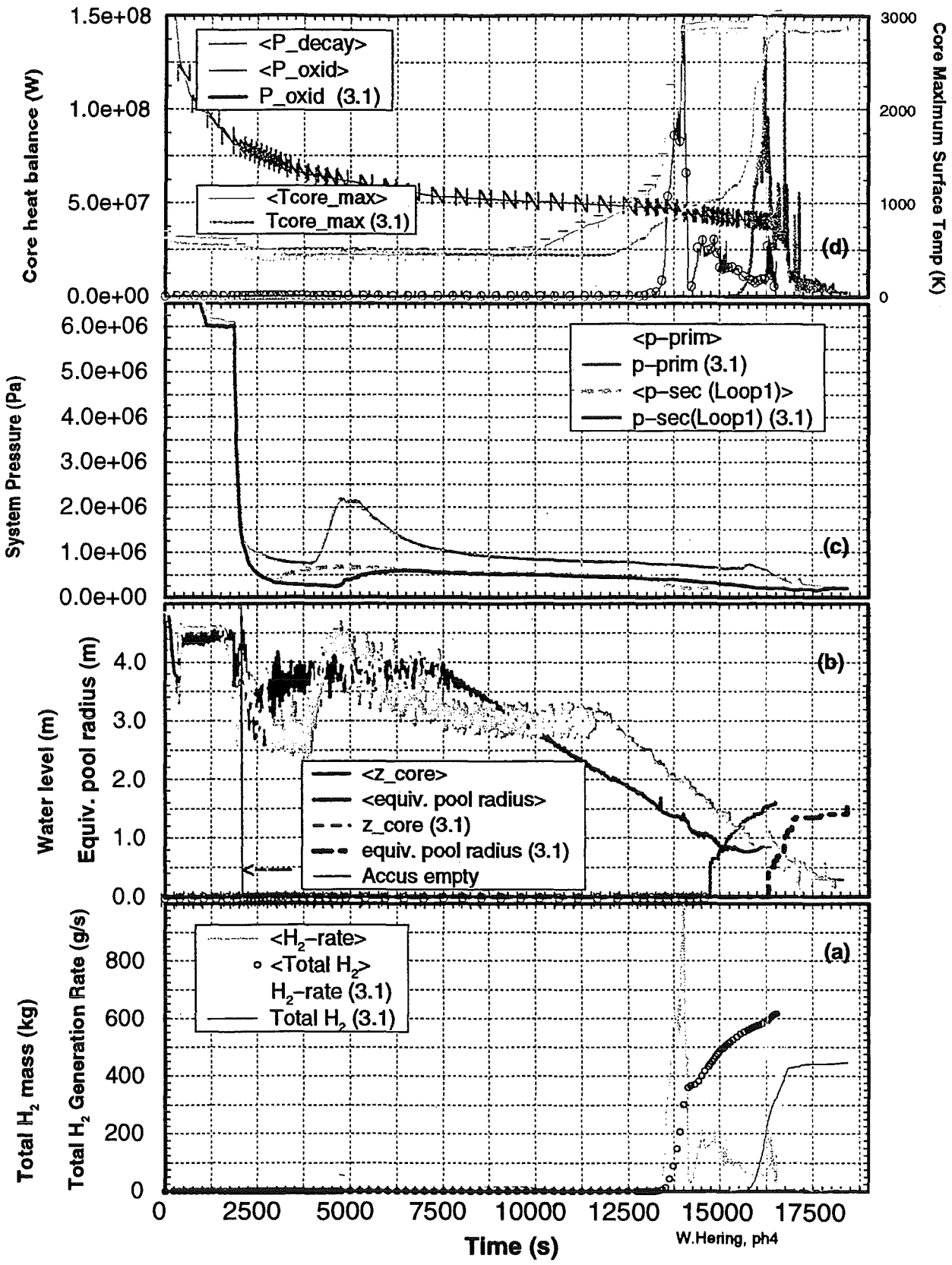

Abbildung 1 Unfallanalysen für das 50 cm² Leck berechnet mit S/R5 m3.1 und S/R5 m3.2. (a) Wasserstoffproduktionsrate (Symbole) und gesamte erzeugte H_2-Masse, (b) Wasserstand und äquivalenter Radius des Schmelzepools im Kern , (c) Primär- und Sekundärkreisdruck und (d) Leistungsbilanz und maximale Kerntemperatur (T).

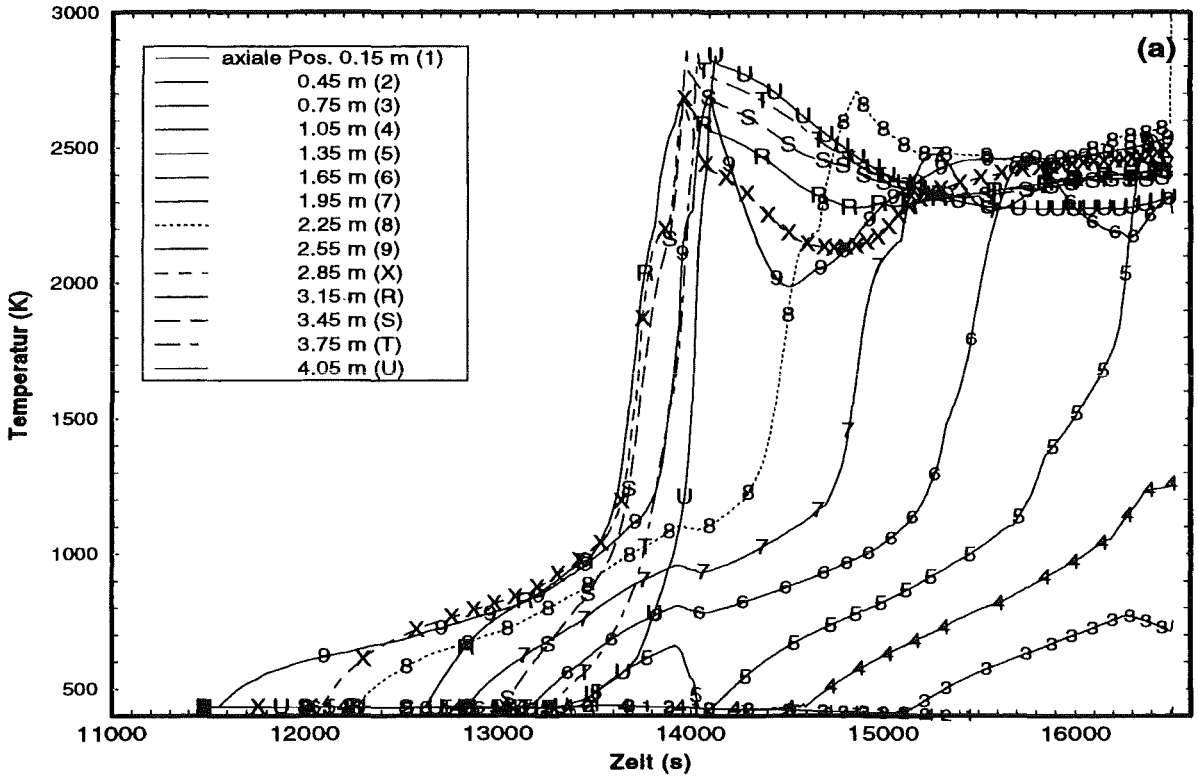

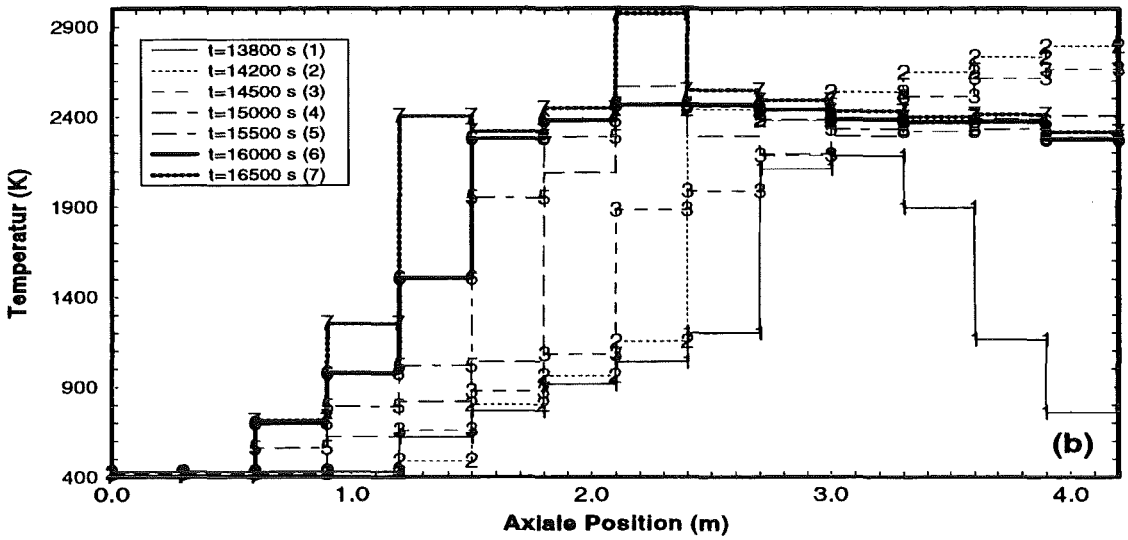

Abbildung 2: Temperaturentwicklung von Brennstäben bzw. Debris im äussersten Kanal als Randbedingungen für LOWCOR2 Rechnungen mit S/R5m32 (a) und axiales Temperaturprofil für verschiedene Zeitpunkte (b).

Die Auswirkung der neuen Wärmeübergangskorrelationen (s. Kap. 1.1.2) in RELAP5 führen bei in etwa gleichen Primärkreisdrücken (s. Abbildung 1 b) zu unterschiedlichen Kernfreilegungsgeschwindigkeiten (s. Abbildung 1 c, S/R5m32: 42 min/m, S/R5m31: 37 min/m). Eine endgültige Antwort kann erst ein Vergleich mit den Ergebnissen einer Rechnung mit EPR-spezifischen Akkumulatoren ergeben.

In der Oxidationphase (s. Abbildung 1 a) wird etwa gleich viel Wasserstoff freigesetzt wie bei der alten Version. Die maximale Produktionsrate stieg von 0.9 kg/s auf 1,35 kg/s, was auf den in S/R5m32 bilanzierten Anteil der Absorberstab - Führungsrohre und Wasserrohre zurückzuführen ist. Weitere Verbesserungen betreffen das Debris-Oxidationsmodell, wodurch jetzt der Anteil des freigesetzten Wasserstoffs nach der ersten Temperatur-Eskalation von 7% auf 43% ansteigt. Die Gesamtmenge an Wasserstoff bis der Schmelzepool im Kern den Rand (HR) erreicht, steigt von 450 kg auf 620 kg an. In Abbildung 2 sind die Temperaturen der Brennstäbe bzw. des Debris im äußersten Ring dargestellt.

Die Verbesserung des Übergangs von intakter Brennstabgeometrie in die Debris- bzw. Pool-Bildung in S/R5m 32 äußerst sich u. A. auch in einer niedrigeren anfänglichen Poolmasse und einer kontinuierlicheren die Ausbreitung in axialer und radialer Richtung.

Parallel zu dem SBLOCA wurde das Szenario „Abriss der Druckhalterleitung" (Surge line rupture) mit S/R5m32 untersucht. Jedoch gibt es auch hier numerische Probleme nach dem Entleeren der Akkumulatoren.

1.3 Wasserstoffquellterm

In Abbildung 3 sind die berechneten Wasserstoffmassen für alle Rechnungen (Abriss der Druckhalterleitung: SL-Rupture, kleines Leck im kalten Strang: SBLOCA, Ausfall der Eigenbedarfsversorgung: LOOP) mit verschiedenen Codes zusammengestellt. Die Korrekturen S/R5m32 der von uns gefundenen Fehler im Oxidationsmodell führen zu einer deutlich größeren Wasserstoffmasse. Die unterschiedlichen Zeiten des Oxidationsbeginns ergeben sich aus den unterstellten Randbedingungen, z.B. der Verfügbarkeit von Sicherheitssystemen.

Die Wasserstoffmassen bei den Reflood-Szenarien (S/R5m31) liegen im Bereich der Streuungen von S/R5 LOOP (no.lim) und S/R5-F:LOOP. Nach dem derzeitigen Modellstand wird beim Fluten während der Oxidationsphase zwar kurzzeitig sehr viel H_2 beim Quenchen freigesetzt, integral betrachtet liefert die zusätzliche Oxidation keinen signifikanten zusätzlichen Beitrag zur gesamten Wasserstoffmasse im Vergleich zum unbeeinflußten Unfallablauf /4/.

Die Analysen werden mit verbesserten Codeversionen fortgesetzt, (Übertragung der Code-Korrekturen von R5m3.2.2 in S/R5m32).

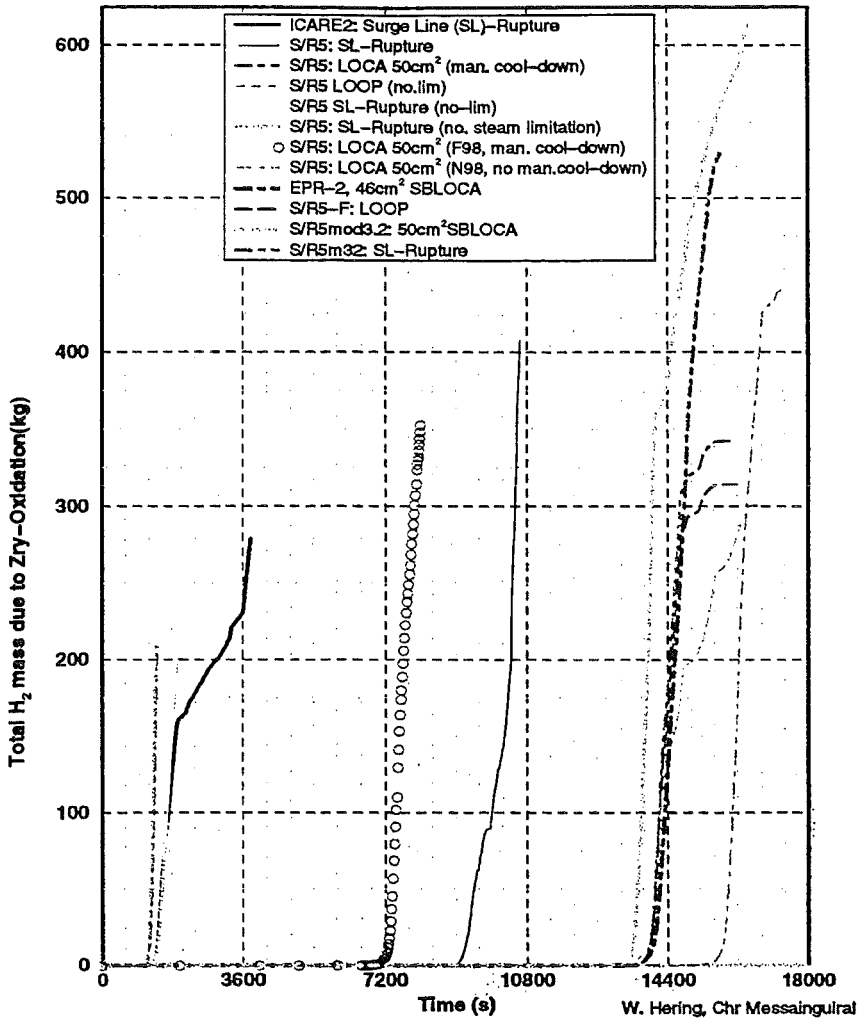

Abbildung 3: Zusammenstellung aller H_2-Massen aus Rechnungen mit S/R5m31F, S/R5m32 und ICARE2.

2 Validierung von RELAP5 und SCDAP/RELAP5

Zwei neue Versionen mußten im Berichtszeitraum installiert und validiert werden: RELAP5 mod3.2.2β (R5m3.2.2β) und S/R5mod32 (Release: hxt). Die zuerst erhaltene Code Version war sehr fehlerhaft und konnte erst nach umfangreicher, zeitintensiver Fehlerkorrektur angewendete werden. Die Fehlerkorrekturen und bei uns getestete FZK/IRS Erweiterungen wurden an INEEL gesandt mit der Bitte, eine offizielle Version mit allen verfügbaren Fehlerkorrekturen und Erweiterungen für Unterstützung der QUENCH-Versuche zu erstellen und an FZK und AEAT weiterzugeben. Im folgenden werden die durchgeführten Validierungsaktivitäten dargestellt. In der vorliegenden Form von S/R5 ist R5m32 integriert, das unter anderem noch Probleme bei nichtkondensierbaren Gasen und im Bereich des Fluten (Massenfehler) aufweist.

2.1 Validierung der Wärmeübergangskorrelationen in RELAP5 mod3.2.2

Im Rahmen des Code Assessment and Maintenance Programs (CAMP) der US Nuclear Regulatory Commission (USNRC) beteiligt sich das FZK/IRS zusammen mit Industriepartnern (SIEMENS/KWU, TÜV Süddeutschland und ABB-Mannheim) an der Qualifizierung des Flutmodells in R5. Bedingt durch die Entwicklung neuer Reaktorkonzepte (AP-600) in den USA wurde der Umfang thermohydraulischer Modelle in RELAP5 stark vorangetrieben, so daß ein wesentlicher qualitativer Sprung beim Übergang von der Codeversion R5m31 zur Version R5m32 zu verzeichnen ist. Im folgenden wird das Flutmodell in R5m3.2.2β mit dem im FZK/IRS verbesserten Chen-Übergangssiedemodell /5/ ,/6/ verglichen, das bereits erfolgreich anhand verschiedener Flutexperimente (Quench Rig, NEPTUN, FLECHT, LOFT /7/) getestet und validiert wurde.

Seit Mitte 1998 ist die neuste Version R5m3.2.2β mit dem vom PSI entwickelten Flutmodell freigegeben. Während bislang alle R5-Versionen ein einheitliches Wand-Fluid-Wärmeübertragungsmodell aufwiesen, welches sowohl für den Normalbetrieb als auch auf Flutprozesse anwendbar war. In R5m3.2.2β wurde ein gesondertes Modell zur Beschreibung des Wärmeübergangs zwischen einer gefluteten Struktur (z.B. Brennstäbe) und dem Fluid eingebaut. Dies führte auch zu weiteren Änderungen der Wand-Fluid-Wärmeübertragungsmodelle im „post-CHF"-Bereich (Übergangssieden, Filmsieden) für normale, d.h. nicht geflutete Strukturen.

Daneben umfassen die Modellerweiterungen in R5m32 folgende Änderungen:

- Wandkondensation bei Anwesenheit nicht kondensierbarer Gasen,
- mechanistisches Modell für Dampfabscheider und –trockner im Dampferzeuger,
- vertikale Zwangskonvektion für Bündelgeometrie mit und ohne Querströmung,
- thermische Schichtung,
- Verbesserung der Numerik zur Behandlung des Auftretens, des Transports und des Verschwindens nicht kondensierbarer Gase in einem Fluidvolumen,
- Verdampfung an horizontalen Rohren,
- Energiebilanz entlang Verbindungen (Junctions) mit großen Druckgradienten,
- Querströmungsmodell,
- Zwischenphasenwärmeübertragung bei Fluid-Gas-Gegenströmung,
- Reduzierung des Massenfehlers,
- Erhöhung der numerische Robustheit, etc.

Eine umfassende Qualifizierung der aufgelisteten Modelle findet in Rahmen vom CAMP parallel zu der vom SCIENTECH weitergeführten Codeverbesserungen statt.

Als erster Schritt zur Validierung des PSI-Flutmodells wurde der LOFT LP-LB-1 Test mit R5m3.2.2β nachgerechnet. In Abbildung 4 ist ein Vergleich der mit verschiedenen Codeversionen berechneten Hüllrohrtemperatur mit den Meßdaten von zwei Höhen (0.6858 und 0.7874 m) dargestellt. Darin ist zu sehen, daß sowohl das PSI- als auch das FZK-Flutmodell vergleichbare Temperaturverläufe berechnen. Dagegen ist die Temperaturvorhersage des INEEL-Flutmodells von R5mod3.1 nicht physikalisch. Es sind noch weitere Verbesserung im Bereich des Filmsiedens erforderlich, um die dort existierenden Diskrepanzen zwischen Experiment und Rechnung weiter zu reduzieren.

Als weiterführende Arbeiten ist neben der Implementierung des FZK-Flutmodells in R5mod3.2.2β die Fortführung der Qualifizierung und Verbesserung des Flutmodells unter Einbeziehung weiterer Experimente wie z. B. der PKL-Test und die FZK-Quenchversuche geplant.

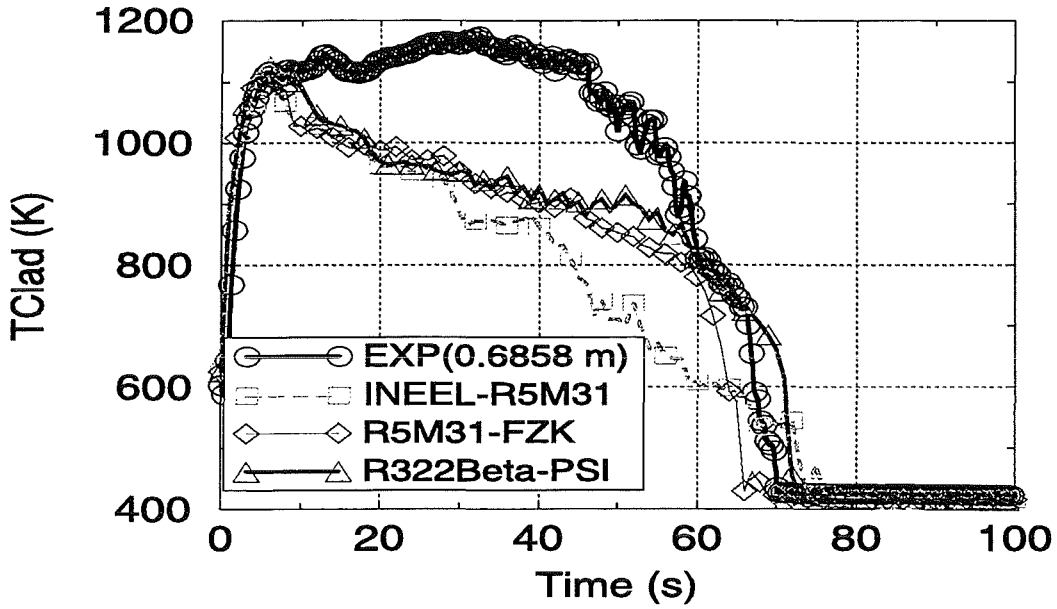

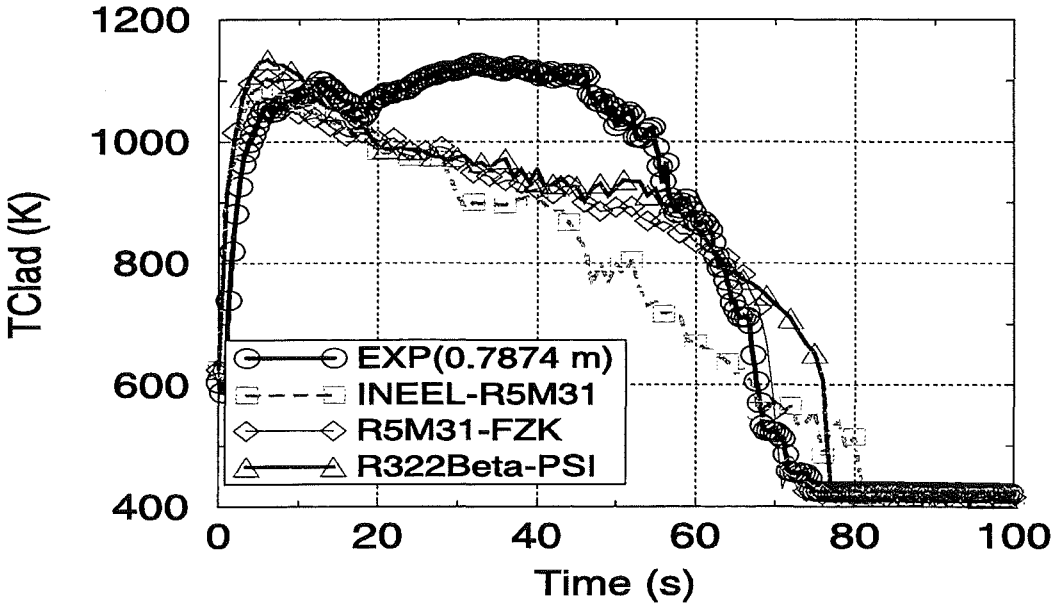

Abbildung 4 Vergleich der berechneten Temperaturen mit den experimentellen Daten aus dem Experiment LOFT LP-LB-1.

2.2 Codevalidierung anhand von CORA Experimenten

Die beiden S/R5 Codeversionen wurden anhand des großen CORA-Bündelversuchs CORA-7 mit 57 Stäben /8/ verglichen. In Abbildung 5 sind die experimentellen Temperaturen mit den entsprechenden Werten aus S/R5m31F und S/R5m32 in sechs verschiedenen Höhen dargestellt. Betrachtet man das integrale Verhalten, so fällt auf, daß der gemessene axiale Temperaturgradient nicht vollständig richtig berechnet werden kann. Dies liegt vor allem an der Quereinströmung bei z = 0.0m, deren hohe Strömungsgeschwindigkeiten (60 m/s) zu verbesserten Wärmeübergangskoeffizienten im Bündelbereich bis ca. 0.4 m führt. Dadurch wird die elektrische Heizleistung verstärkt im oberen Bereich des Bündels, auch in der Elektrodenzone freigesetzt, so daß aus einem vermeintlich lokalen Effekt über die elektrische Heizung ein globaler Effekt wird.

Der lokalen Effekt kann mit S/R5 oder R5 nicht direkt modelliert werden, eine mögliche Reduktion der Einströmtemperatur reduziert hingegen das gesamte Enthalpieniveau im Bündel und eine mögliche Erhöhung der radialen Wärmeverluste wirkt auf die gesamte Bündellänge.

Vergleicht man die berechneten Temperaturen, so zeigt S/R5m32 eine bessere thermische Kopplung zwischen den beheizten (H_321) und den unbeheizten Stäben (U_321) was auf die verbesserte Wärmeübergangskorrelation zurückgeführt werden kann. In Abbildung 5 b ist die Temperaturentwicklung in der oberen Elektrodenzone dargestellt. Durch die massiven Molybdän-Elektroden wird hier nur gering elektrische Heizleistung freigesetzt, so daß der Temperaturgradient sehr klein ist. Zudem ist in diesem Bereich keine Faserisolation mehr vorhanden, wodurch die radialen Verluste sehr gross sind.

Mit Einsetzen der Oxidation verschwindet dieser Temperaturgradient, da die Oxidationswärme auch die unbeheizten Stäbe direkt aufheizt, der verbesserte Wärmeübergang verhindert jedoch einen Temperaturanstieg, so daß anstelle von 105 g Wasserstoff (S/R5m31) nur noch ca. 80 g berechnet wurden. Im Experiment wurden ca. 114 g gemessen.

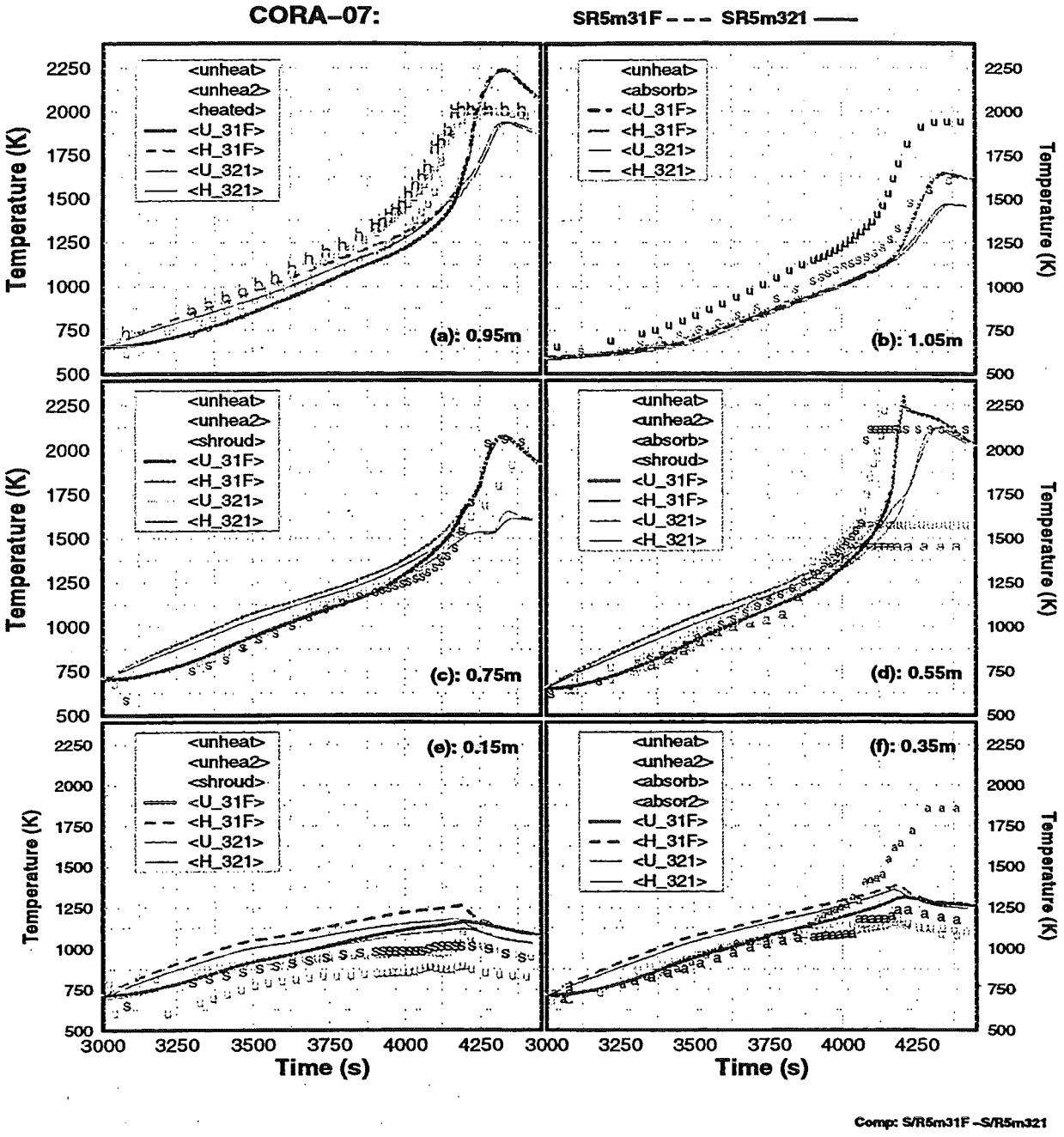

Abbildung 5 Vergleich der mit S/R5m31F und S/R5m32 berechneten Hüllrohrtemperaturen für den CORA-7 Versuch in sechs verschiedenen Bündelhöhen (a-f).

2.3 Einfluss des Abbrandes auf die Brennstoffauflösung

Ziel der Phebus FP in-pile-Versuchsserie ist, Daten über die Freisetzung von Spaltprodukten im Reaktor und deren Transport durch die Kreislaufkomponenten ins Containment zu gewinnen, sowie Informationen über den Ablauf eines Kernschmelzunfalls und die dabei auftretenden kernzerstörenden Prozesse und ihre Wechselwirkung zu bekommen /9/ .

In FPT0 /10/ wurde frischer Brennstoff (9 Tage in-situ vorbestrahlt) und in FPT1 abgebrannter Brennstoff (Abbrand ca. 23 GWd/tU) verwendet. Die entscheidenden Versuchsparameter, nuklearer Leistungsverlauf und Dampfeinströmrate, waren sehr ähnlich, so dass die Versuchsabläufe und Ereignissequenzen vergleichbar waren.

Dennoch zeigten die experimentellen Ergebnisse im Test Phebus FPT1, am Ende des Versuchs massive Verlagerungen und eine besonders starke Zerstörung der bestrahlten Brennstäbe im Vergleich zu den beiden eingesetzten frischen Brennstäben. Dies deutet auf ein sehr unterschiedliches Verlagerungsverhalten der Brennstäbe hin, das derzeit nicht mit den verfügbaren SFD Code-Systemen erklärt werden kann.

Im FZK/IRS wurde versucht, diesen offenbar Abbrand-abhängigen Effekt physikalisch zu erklären und in ein Modell für den Code S/R5 zu überführen. Nach unserer Auffassung liegt das besondere Verlagerungsverhalten abgebrannter Brennstäbe weniger an einer wie auch immer gearteten Verminderung der Schmelztemperatur des Brennstoffs als an der geänderten Struktur der Brennstofftabletten. Hoch abgebrannte Brennstäbe enthalten aufgrund von Leistungsrampen und der Bildung gasförmiger Spaltprodukte geborstene Tabletten, deren Risse im Fall der Wechselwirkung mit geschmolzenem Zircaloy des Hüllrohrs zu einer Vergrößerung der Wechselwirkungsoberfläche beitragen und die Reaktion beschleunigen. Im extremen Fall können die Brennstofftabletten sogar als auf nahezu Korngröße fragmentiert betrachtet werden. Dabei wird dann die gesamte Tablette von flüssigen Zircloy durchdrungen, so daß der Brennstoff in diesem Wechselwirkungsbereich eine Struktur wie verflüssigter Sand bekommt und letztlich durch vorhandene oder entstehende Öffnungen des Hüllrohrs in größeren Mengen austreten kann. Insbesondere der letzte Fall ist noch nicht durch Experimente oder durch anderweitige Erfahrung ausreichend abgesichert, so daß eine genaue Quantifizierung des Problems zur Zeit nicht möglich ist.

Dieser Extremfall ist vergleichsweise einfach im Code zu modellieren, indem die Korrelation für die Brennstoffauflösung durch schmelzflüssiges Zircaloy so verändert wird, daß die Brennstofftablette als komplett aufgelöst betrachtet werden kann. Dieses Modell soll zunächst nur als Abschätzung dieses extremen Szenarios dienen und mit Hilfe von Rechnungen zu Phebus FPT1 die Behandlung abgebrannter Brennstäbe verstehen lernen.

Die Abbildung 6 zeigt Rechenergebnisse (Brennstabtemperaturen, Wasserstoffproduktion, verlagertes Material und die Bildung eines Schmelzepools) im Vergleich mit Meßergebnissen aus dem Experiment Phebus FPT1. Zwei Rechnungen sind den Messungen gegenübergestellt, erstens eine Rechnung mit S/R5-Auflösungsmodell und zweitens eine Rechnung mit dem beschriebenen Auflösungsmodell. Hinsichtlich der Temperaturen und der Wasserstoffproduktion sind sich die Rechnungen sehr ähnlich und stimmen mit dem Experiment recht gut überein. Auch der Zeitpunkt der Bildung eines keramischen Schmelzepools wird von beiden Rechnungen übereinstimmend beschrieben. Signifikant ist der Unterschied bezüglich der verlagerten Massen. Die Rechnung mit dem speziellen Auflösungsmodell weist deutlich höhere Verlagerungen aus, wie es auch zu erwarten war, aber eben ohne die anderen wichtigen Zustandsgrößen des Experiments wesentlich zu beeinflussen. Erstaunlich, möglicherweise aber zufällig erscheint die gute Übereinstimmung der errechneten Masse an verlagerten Material mit den im Experiment gefundenen verlagerten Massen. Die Untersuchung des Einflusses des Abbrands auf das Verlagerungsverhalten im Fall von schweren Störfällen wird fortgesetzt im Hinblick auf höhere Abbrände.

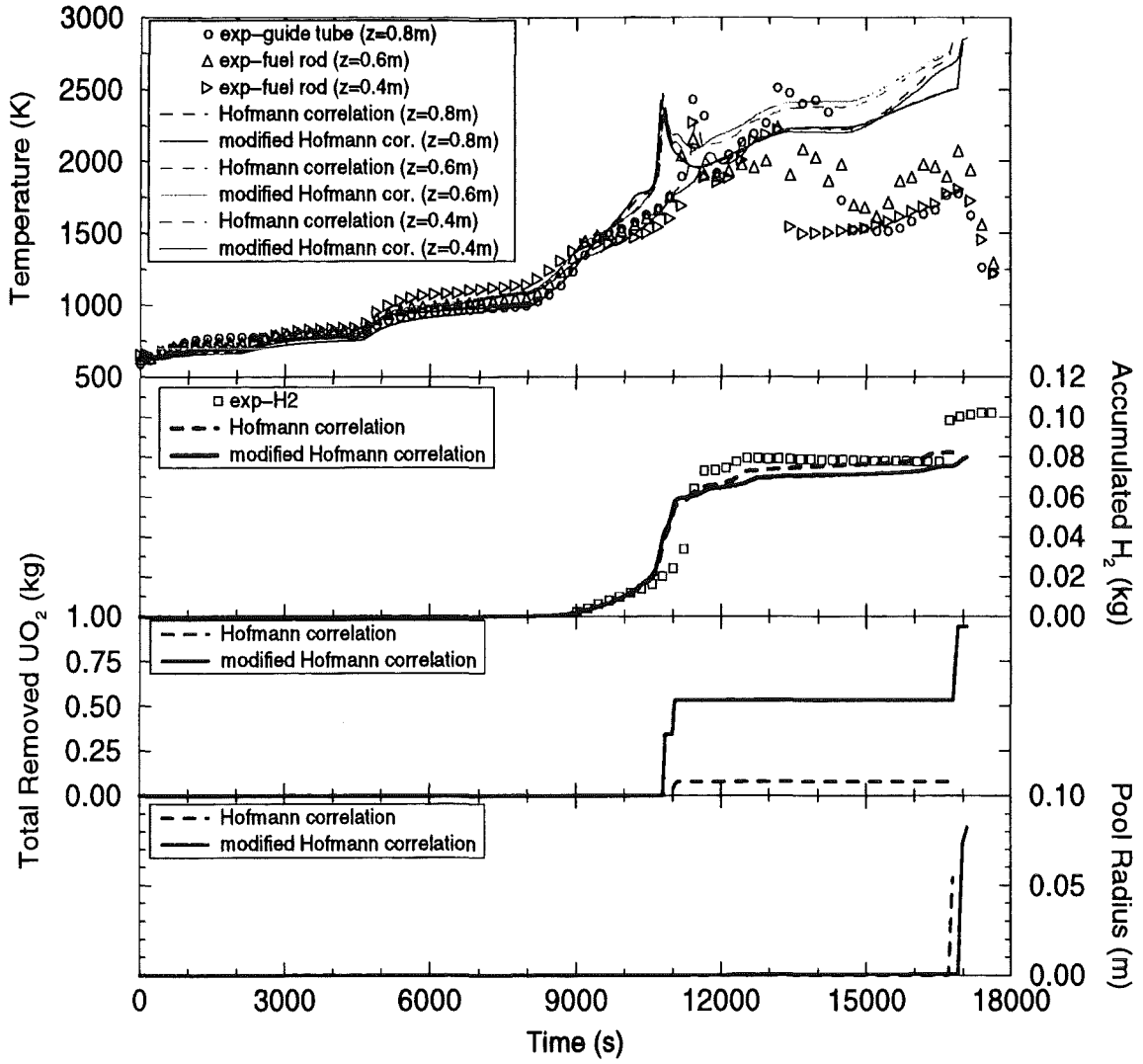

Abbildung 6 Simulation des möglichen Einflusses des Abbrandes auf die modellierte Brennstoff-Hüllrohr Wechselwirkung anhand Phebus FPT1.

3 Untersuchung des Aufschmelzverhaltens des HR

Aus den Kernschmelzanalysen mit Programmen wie S/R5, MAAP oder MELCOR kann man keine detaillierten Aussagen über lokales Aufschmelzen des HR erwarten, da zum einen das Interphase zwischen Kern und Kernumfassung sehr grob modelliert und mit Unsicherheiten behaftet ist, und sie zum anderen Zylindersymmetrie verwenden. Daher wird das Programm LOWCOR2 entwickelt, mit dem langfristigen Ziel, es als Modul an S/R5 zu koppeln.

LOWCOR2 löst die transiente Wärmetransportgleichung einschließlich Phasenänderung in zweidimensionalen kartesischen oder zylindrischen Koordinaten. Es basiert auf einem Differenzenverfahren 1. Ordnung mit einem speicherplatzoptimierten Gauss-Solver zur direkten Lösung einer Bandmatrix /11/ . Phasenwechsel in einer Zone des Maschengitters wird mit der Methode der effektiven Wärmekapazität behandelt. Das Entstehen neuer Ränder mit entsprechenden Randbedingungen bei Massenverlust durch lokales Aufschmelzen wird berücksichtigt. Die Berücksichtigung des Wiedererstarrens verlagerter Schmelzen und deren Einfluss auf Geometrie und thermische Randbedingungen ist in Arbeit. Das LOWCOR2-Modell und einige Anwendungsrechnungen werden in /12/ ausführlicher dokumentiert.

3.1 Detail Analysen mit LOWCOR2

Für das SBLOCA Szenario (s. Kap. 1.1.1.2) ist mit LOWCOR2 die thermische Belastung des HR infolge des Versagens der äusseren BE-Reihe mit Debris- und Schmelzepoolentstehung berechnet worden. Die Randbedingungen bis 16500s (s. Abb. 2) aus S/R5 m32 entnommen. Der Code versagte mit Beginn des Aufschmelzens des HR, wobei im Programm nur Konvektion und kein Strahlungstransport berechnet wurde (s. Kap. 1.1.1.1).

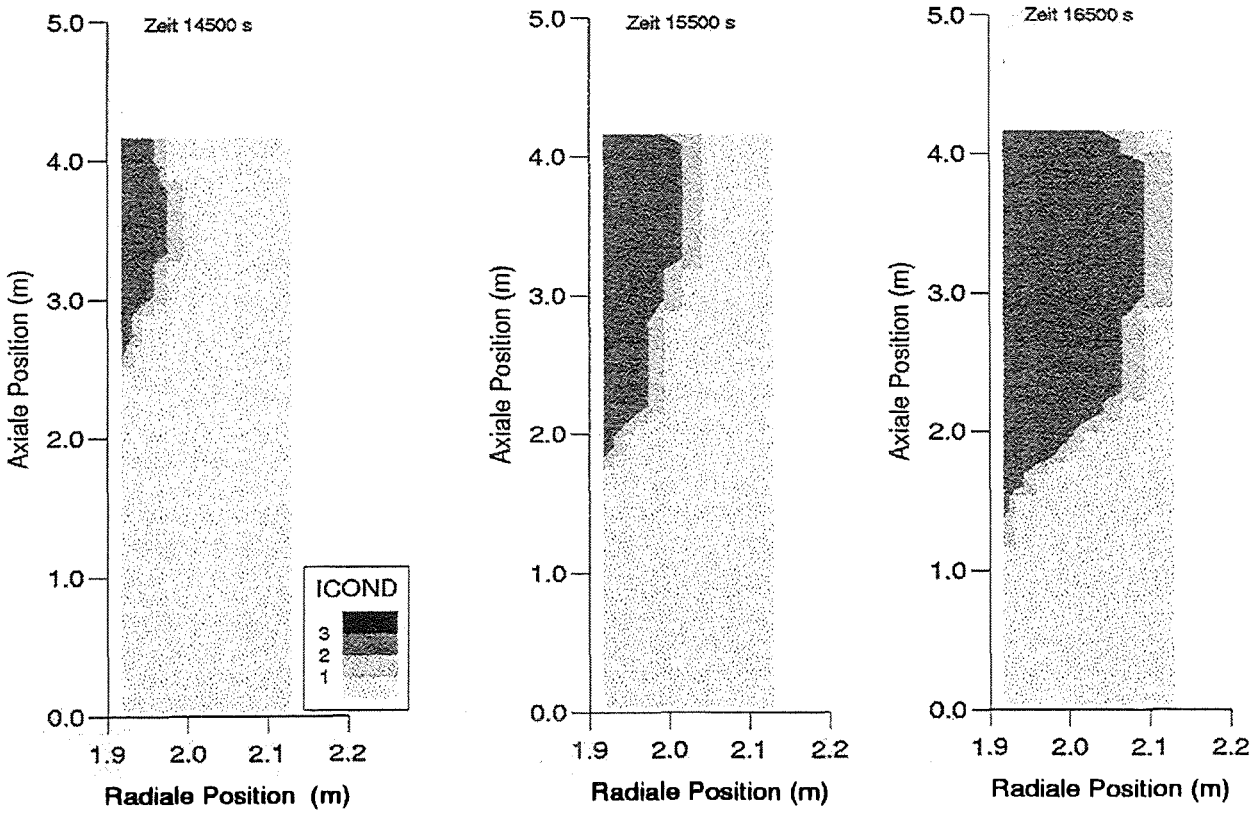

Abbildung 7 Zeitliche Entwicklung des Aufschmelzens des HR für das mit S/R5m3.2 gerechnete 50 cm² SBLOCA Szenario. (ICOND: Zustandsindex des Materials: 1: fest $T<T_{solidous}$, 2: „mushy" $T_{solidous} < T < T_{liqidus}$, 3: flüssig $T > T_{liqidus}$).

Unter Berücksichtigung des Strahlungstransport in radialer und axialer Richtung ergibt sich unten dargestellte Situation, wobei der verbesserte Wärmetransport über Strahlung zu niedrigeren Quelltemperaturen (BE) führen würde als in der Studie unterstellt.

Die Randbedingungen für den HR wurden den o. g. S/R5-Analysen entnommen: Die Aussenseite des HR führt Wärme durch Strahlung an den RDB ab ($T_{(RDB)}$ = 450 K), an der HR Oberseite (z = 4.20 m) findet Strahlungswärmeaustausch an eine Umgebungstemperatur von $T_{(umgb)}$ = 1000 K statt, die Unterseite des HR befindet sich auf $T_{(unten)}$ = 450 K, und die HR-Innenfläche wird infolge Wärmestrahlung von Brennstäben, Debris und Schmelzepool aufgeheizt. In Abbildung 2 sind Temperaturverläufe der Wärmestrahlungsquellen im äussersten Ring des Cores gegen die Zeit (a) und als axiales Profil dargestellt (b).

Abbildung 7 zeigt ein Beispiel der berechneten Schadensentwicklung für drei Zeitpunkte 14500 s, 15500 s und 16500 s. Entsprechend der auf der HR-Innenseite vorgegebenen zeitlichen und lokalen Temperaturentwicklung des niederschmelzenden Cores ist die Schadensentwicklung im betrachteten Zeitbereich auf die obere Hälfte des HR konzentriert; es dauert hier ca. 3000 s, bis der HR durchgeschmolzen ist.

Ein Aspekt, der bei der Betrachtung der Schadensentwicklung im HR von Bedeutung ist, betrifft den Übergang der 3D-Struktur, vorgegeben durch die BE-Anordnung am Aussenrand des Cores (s. Abbildung 8), in eine annähernd zylindrische Geometrie durch Abschmelzen der kantigen Innenstruktur des HR. Abbildung 9 zeigt im Querschnitt die charakteristische Innenkantengeometrie des HR, für die im angegebenen Ausschnitt in 3.15 m Höhe zur Zeit 14500 s das Temperaturfeld berechnet worden ist.

Die Schmelzefront wandert von der Innenkante nach aussen und glättet dabei die HR-Innenfläche, so dass annähernd Zylindergeometrie entsteht. Die Temperaturentwicklung im HR ist stark abhängig von Temperaturniveau und axialer Verlagerungsgeschwindigkeit von Debris und Pool sowie Unsicherheiten in den Strahlungs-Emmissionskoeffizienten und in der Art der Randbedingungen auf der HR-Innenseite (Kontaktmode von Debris und Pool mit HR). Diese und andere Fragen werden in /12/ in Form von Parameterstudien und Ingenieursabschätzungen weitergehend behandelt.

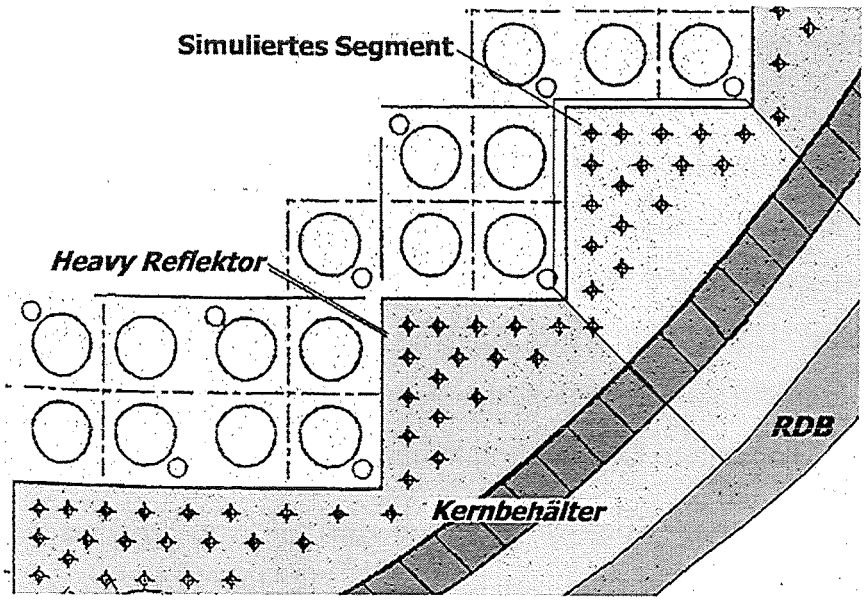

Abbildung 8 Querschnitt durch die massive Kernumfassung bestehend aus HR und Kernbehälter.

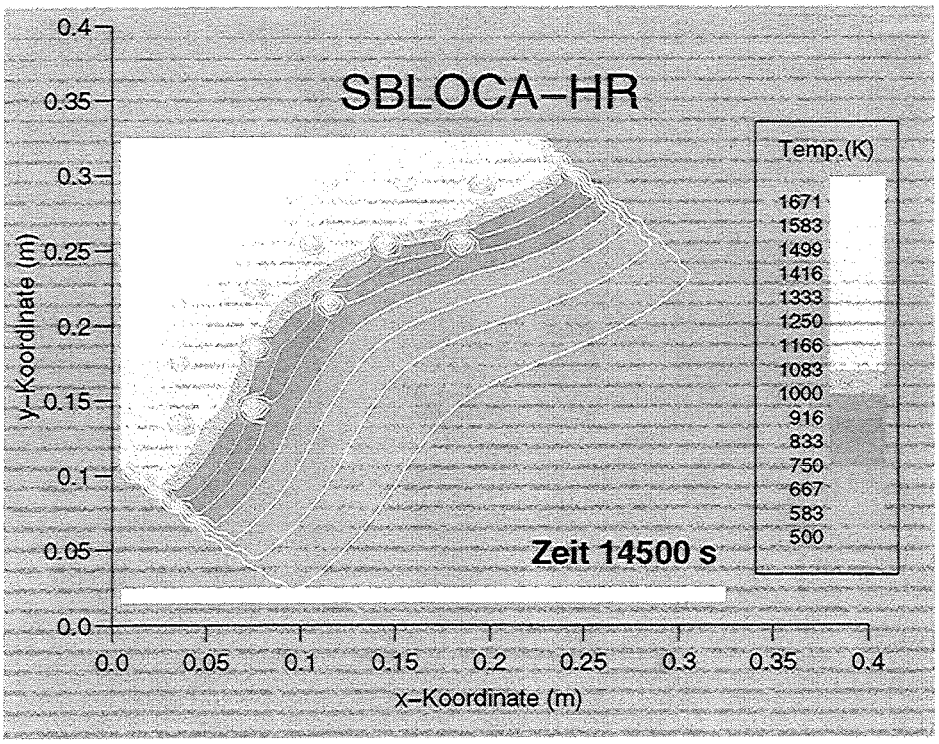

Abbildung 9 Radiales Aufschmelzen der Innenkanten des HR zum Zeitpunkt 1250 s (Original Geometrie s. Abbildung 8).

3.2 Analysen mit ICARE2 und FIDAP

ICARE2

Da im Berichtszeitraum die mit CATHARE angekoppelte ICARE2-Version noch nicht zur Verfügung stand, konnte die Aufheizung des HR mit ICARE2 nur für Bedingungen im Kern berechnet werden, die einen vernachlässigbar geringen konvektiven Wärmeaustausch aufweisen. Daher wurde mit S/R5m3.1.F bis in die Kernfreilegungsphase gerechnet und die Daten zum Zeitpunkt des Auftretens der ersten Schmelzen an ICARE2 übergeben /13/ . Die weitere Berechnung konnte dann mit ICARE2 weitergeführt werden.

In dieser Weise wurde das "Surge line rupture" Szenario von S/R5 bis 3900 s berechnet. Ab 2500 s tritt ein Schmelzepool im Kern auf. Die ICARE2-Berechnung fängt nach 2100 s an, das heißt, als einige Brennstäbe schon Debris-Zonen (lokale Blockaden) aufwiesen, aber die HR-Temperaturen noch deutlich unter dem Schmelzpunkt von Edelstahl sind.

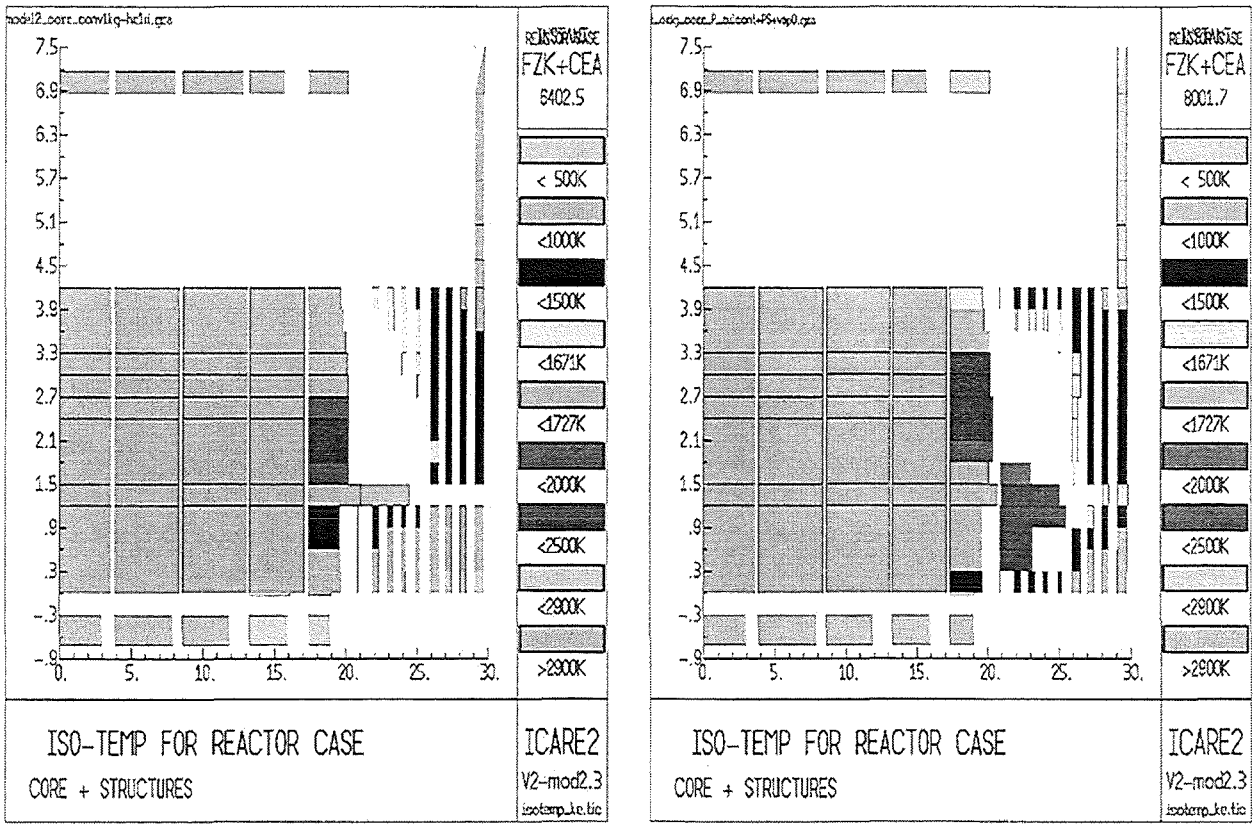

Abbildung 10 Ergebnisse der ICARE2 Rechnungen mit Anfangsbedingungen aus S/R5, Aufschmelzen des HRs mit unterschiedlichem konvektivem Wärmeaustausch im äußersten Kanal (Massenströme im Kühlkanal: 1 kg/s: links, 0: rechts).

Von 2100 s an rechnet ICARE2, bis die Stahlstrukturen in radialer Richtung bis zum Kernbehälter lokal durchgeschmolzen sind. Ab diesem Zeitpunkt ist eine Verlagerung der Kernschmelze im Downcomer denkbar (s. Abbildung 10).

Alternativ zur normalen Stabanordnung erlaubt ICARE2 auch die Modellierung eines Debris-Bettes. Dabei können folgende Wärmeaustauschmechanismen berücksichtigt werden: Wärmeleitung und Strahlung im Debrisbett und zwischen dem Bett und den Stahlstrukturen, sowie konvektiver Wärmeaustausch zwischen dem Bett auf der einen Seite und dem Pool sowie dem Dampf auf der anderen Seite. In Abbildung 10 sind die Ergebnisse der Debrisbettsimulation für zwei Randbedingungen an der Innenseite (links: 1 kg/s Dampfmassenstrom, rechts kein konvektiver Wärmeaustausch) zum Zeitpunkt des Durchschmelzens angegeben. Hierbei wurden der ganzen Kern (als Debris), der HR, die untere und obere Stahlplatte und den Druckbehälter modelliert.

FIDAP

FIDAP ist ein kommerzielles FEM Programm, das Wärmeaustausch und Massenströme sowohl in 2D als auch in 3D-Geometrie berechnet. Es kann für Reaktorrechnungen zur Untersuchung der Änderung der HR-Geometrie eingesetzt werden und ermöglicht die Modellierung der inneren Formkanten des HR, die sich aus der rechteckige Anordnung der Brennelemente ergeben. Da reaktorspezifische Programme immer den HR in zylindrische Geometrie modellieren, war ein Ziel unserer Studie mit FIDAP abzuschätzen, wie lang die Übergangszeit von ursprünglichen rechteckigen HR Geometrie zur zylindrischen im Fall des HR-Abschmelzens ist.

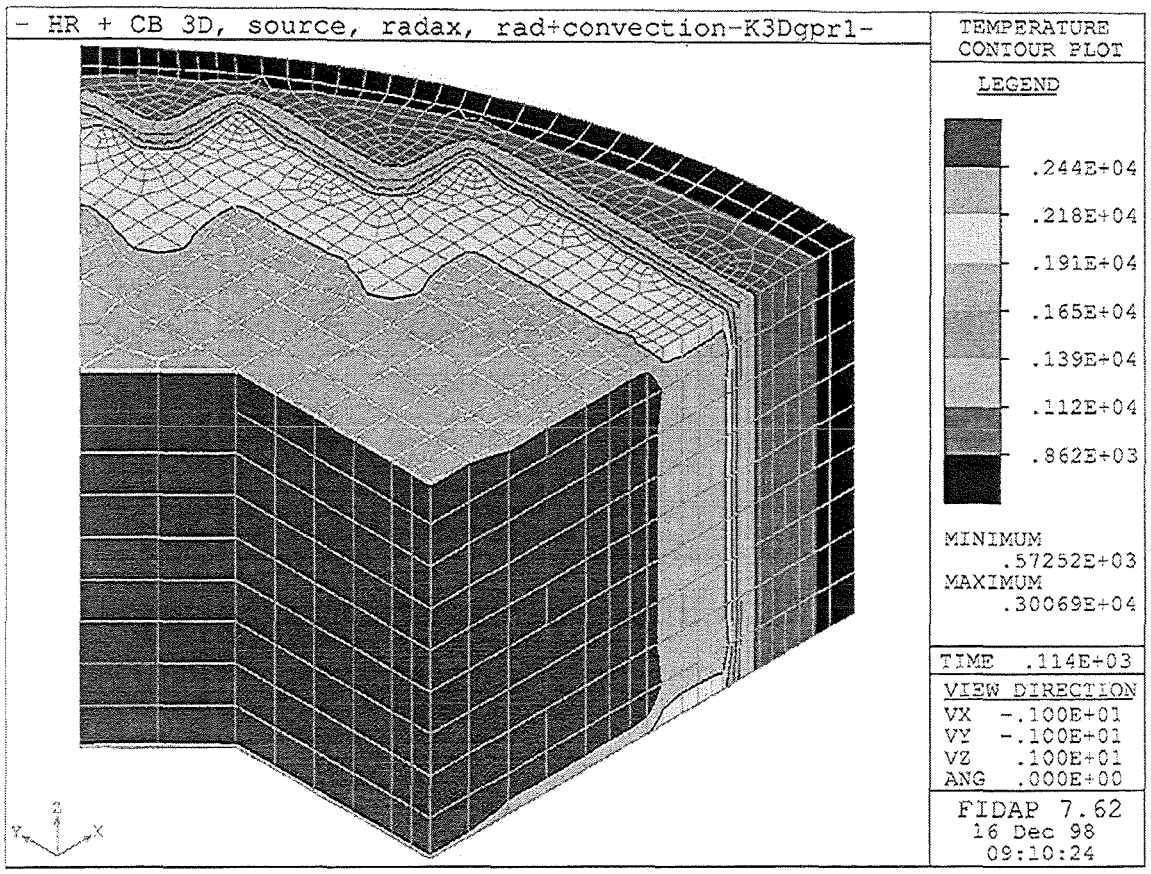

Abbildung 11 Modellierung des Kernbereiches als Debris und des HR in FIDAP für 3D Analysen.

Ferner wurde ein 3D-Modell aufgebaut, das 1/8 des Kernes und des HRs darstellt (s. Abbildung 8). Die dazu notwendig Maschenanzahl erfordert sehr lange Rechenzeiten, so dass dieses Modell nicht für Parameterstudien benutzt werden kann, aber als Referenzrechnung für 2-D Analysen in zylindrischer oder karthesischer Geometrie herangezogen werden kann. Hierzu muss noch ein geeignetes Szenario ausgewählt werden.

4 Quenchversuche

4.1 Zielsetzung

In der QUENCH-Anlage im FZK/IMF werden die physikalischen und chemischen Vorgänge bei einer Abschreckung des überhitzten Bündels mit Wasser oder einer schnellen Abkühlung durch Dampf untersucht. Im IRS werden diese Versuche durch numerische Analysen vor und nach den jeweiligen Experimenten, vor allem mit S/R5m31 unterstützt /13/ -/18/ .

Mit der validierten Modellierung aus dem Inbetriebsetzungstest IBS_02, bei dem das Fluid im Bündel reines Argon war, wurde für den Test IBS_03 (je 3 g/s Dampf und Argon) eine vergleichbare Übereinstimmung der gemessenen und berechneten Temperaturprofile in der Anlage wie für IBS_02 erreicht. Die Wasserstoffproduktion wird mit 17 g gegenüber den gemessenen 13 g überschätzt.

4.2 QUENCH-01

Im Experiment QUENCH-01 wurden die Stäbe bei möglichst gleichbleibender Temperatur bis zu einer maximalen Oxidschichtdicke von etwa 300 μm voroxidiert, danach folgten die Leistungstransiente und das Abschrecken des Bündels von unten mit Wasser. Unsere Vorausrechnungen gaben Abschätzungen für die elektrische Leistung und die Dauer der Voroxidationsphase. Während des Versuchs wurde die elektrische Leistung nach unseren Vorschlägen nach der aktuellen Wasserstoffproduktionsrate als sensitivem Maß für die Bündeltemperatur geregelt. Diese Nachregelung ist erforderlich, da mit dicker werdende Oxidschicht die Oxidation und die damit verbundene Leistungsfreisetzung abnehmen.

Aus den Nachrechnungen ergab sich, daß die Fluidtemperatur im Bündeleintritt durch das Thermoelement T 511 nicht genau genug gemessen wurde, so daß ein Wert aus einem Vergleich von gemessenen und gerechneten Stabtemperaturen am unteren Bündelende geschätzt werden muß. Außerdem zeigte sich, daß elektrische Widerstände außerhalb des Bündels, z. B. Übergangswiderstände der Gleitkontakte an den Enden der Brennstabsimulatoren, deutlich höher sind als in der CORA-Anlage, wo 1,6 mΩ/Stab angenommen wurden. Der genaue Wert für diese Widerstände muß bekannt sein, um die elektrische Leistungseinspeisung in das Bündel richtig zu berechnen. Eine Messung dieser Widerstände während der Vorbereitung eines Experimentes ist wegen des kleinen Wertes nicht möglich, so daß nur eine Abschätzung aus einer Parametervariation in den Rechnungen möglich ist. Mit einem Wert von 4,2 mΩ/Stab wird die Wasserstoffproduktion am Ende der Voroxidationsphase zu 33 g berechnet; gemessen wurden etwa 30 g.

Auch die zeitliche Entwicklung der Wasserstoffproduktion wird mit dieser Modellierung recht gut wiedergegeben (s. Abbildung 12 oben). Nur zu Beginn der Voroxidationsphase wird die Bündeltemperatur und damit die Wasserstoffproduktion überschätzt. Jedoch ist

selbst während der vorzeitigen Eskalation bei t = 4500 s, die durch eine Verringerung der elektrischen Leistung beendet werden konnte, die Übereinstimmung gut. Abbildung 13 oben zeigt die Übereinstimmung von gemessenen und gerechneten Temperaturen auf der ganzen Bündellänge zu der Zeit, als im Experiment ein Eckstab gezogen wurde, um die Oxidschichtdicke gegen Ende der Voroxidationsphase zu bestimmen. Das gemessene axiale Profil der Oxidschichtdicke ist steiler und schmaler als nach der Rechnung. Da jedoch die Oxidationsrate stark von der Temperatur abhängt und kleine Abweichungen sich über lange Zeiten zu großen Unterschieden summieren können, scheint diese Abweichung derzeit nicht bedenklich zu sein.

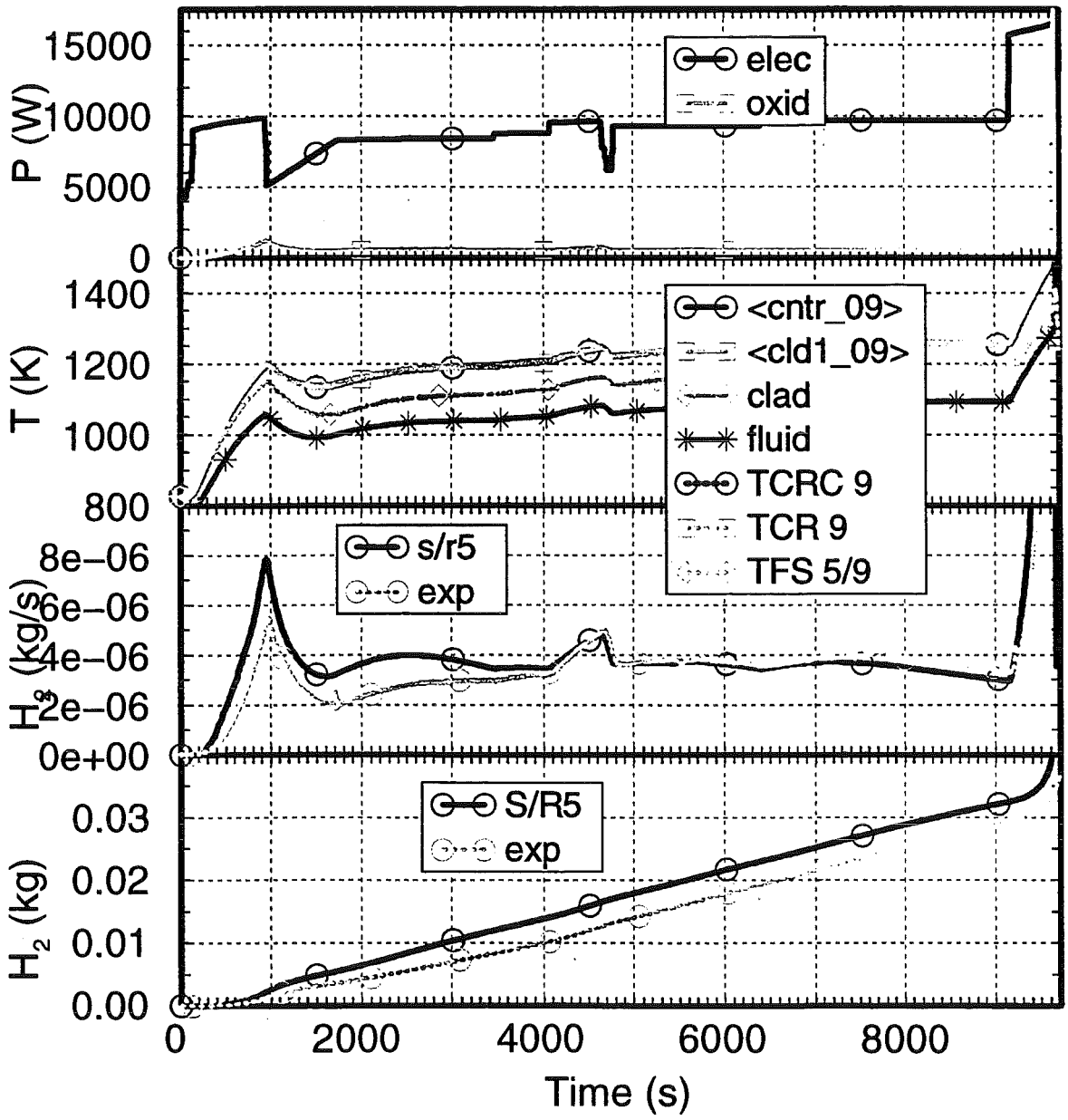

Abbildung12 Elektrische und chemische Leistung, Stabtemperaturen, Wasserstoffproduktionsrate und kumulierte Wasserstoffmenge als Funktion der Zeit für QUENCH-01.

Der Versuch zeigt, daß bei der Erhöhung der elektrischen Leistung um etwa 400 W bei t = 3450 s und t = 6400 s die Erhöhung der Temperatur im Bündel begrenzt war, während bei der Leistungserhöhung um etwa 1 kW bei t = 4060 s eine Temperatureskalation begann. Aus der Wasserstoffproduktionsrate ergibt sich, daß die freigesetzte chemische Leistung etwa bei 480 W liegt. Man kann aus diesen Werten vermuten, daß für die Voroxidationsphase die elektrische Leistung ohne Gefahr für eine Temperaturexkursion um den Betrag erhöht werden kann, der der chemischen Leistungsfreisetzung entspricht, aber nicht um den doppelten Betrag.

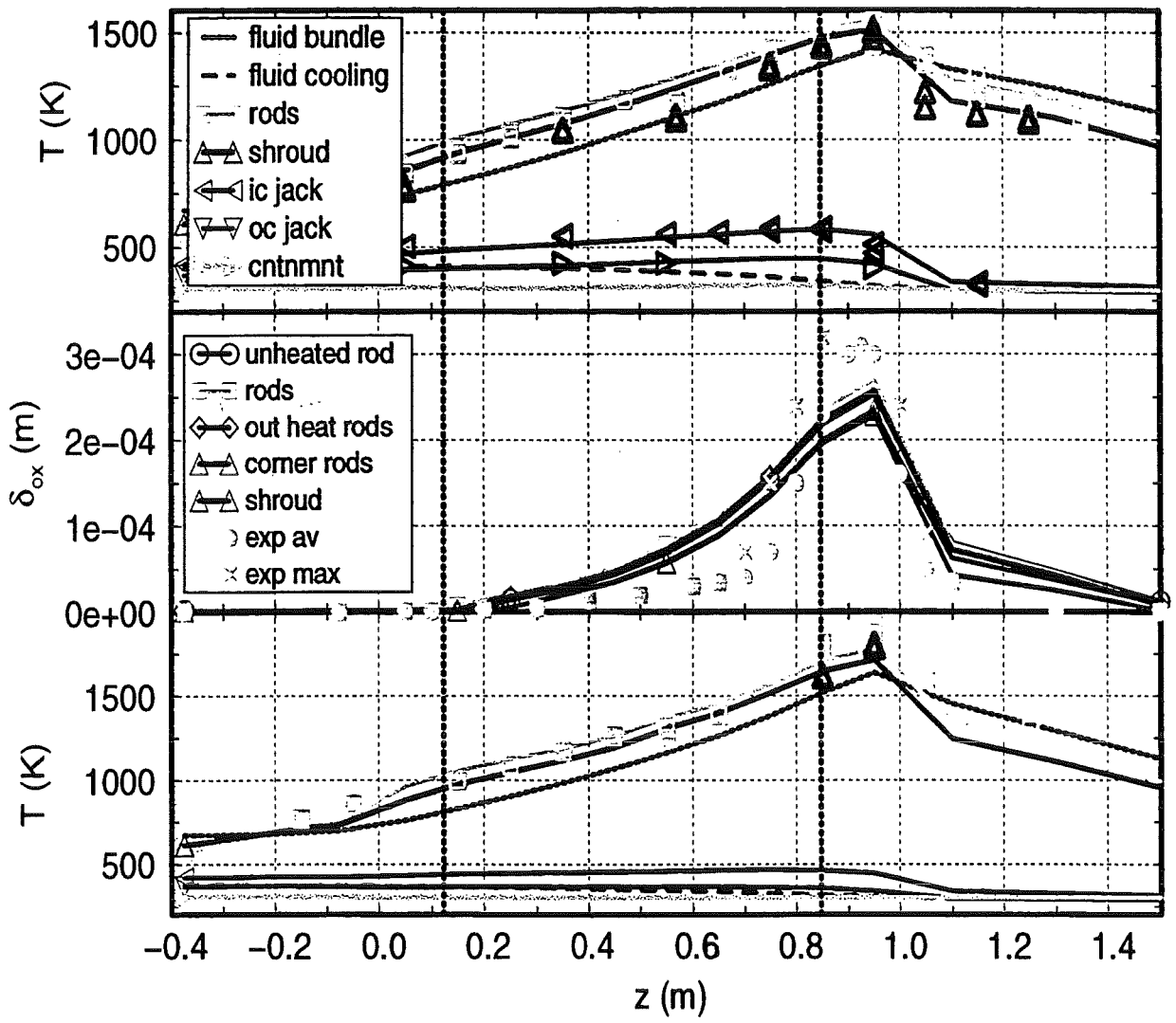

Abbildung13 Gemessene und gerechnete axiale Profile für Temperatur (oben) und Oxidschichtdicke (Mitte) für QUENCH-01 zu der Zeit, als der Eckstab gezogen wurde und gemessene und gerechnete Temperaturen 30 s vor dem Beginn der Abschreckung für QUENCH-02. Symbole beziehen sich auf Messungen, Kurven auf Rechnungen.

4.3 QUENCH-02

Im Versuch QUENCH-02 wurde das Bündel ohne Voroxidationsphase bei deutlich höherer Temperatur abgeschreckt (s. Abbildung 12 unten). Bei den Vorausrechnungen wurde der Anstieg der Bündeltemperatur während der Leistungstransiente als wichtiger Parameter auch für Einzelheiten der Versuchsdurchführung festgestellt, da die Zeit für ein Eingreifen der Operateure bei der gewünschten Leistungstransiente recht kurz ist.

Die Nachrechnung zeigt, daß bei gleicher Modellierung wie für QUENCH-01 die Temperaturen und damit auch die Wasserstoffproduktion gut übereinstimmen. Der Beginn der Temperatureskalation ist nach der Rechnung etwa 50 s später als im Experiment. Der Umfang der Eskalation wird in der Rechnung etwas unterschätzt.

Die bisherige Erfahrung zeigt, daß eine detaillierte Modellierung der Anlage erforderlich ist, um eine solche Übereinstimmung von gerechneten und gemessenen Ergebnissen in allen Bereichen der Anlage zu erreichen, wie sie in den Abbildungen für die beiden Experimente gezeigt wird. Weitere Arbeiten und Verbesserungen sollen mit der neuen Programmversion, S/R5m32, gemacht werden.

5 Literaturverzeichnis

/1/ Allison et al., SCDAP/RELAP5 mod3.1 Code Manual, Vol I - IV. NUREG/CR-6150, EGG-2720, Oct. 1993.

/2/ Gonzales R., Chatelard D., Jacq F., ICARE2 Version 2 Mod 1, Description of physical models, Note Technique DRS/SEMAR 92/43, 1996.

/3/ Mühl B., Untersuchungen zu auslegungsüberschreiteden Ereignissen (Unfällen) in Leichtwasserreaktoren, PSF-interner Bericht, März 1998.

/4/ Hering W., Status of Reflood Analyses for the LOOP Scenario using SCDAP/RELAP5, PSF report, 1999.

/5/ Sanchez, V., Elias, E., Homan, Ch., Hering, W., Struwe, D., Development and validation of a transition boiling model for RELAP5/MOD3 Reflood Simulation. Forschungszentrum Karlsruhe FZK, Germany. FZKA-5954, September 1997.

/6/ Sanchez, V. , Homann, Ch., Validation of a transition boiling model for RELAP5/MOD3 Reflood Simulation against the Integral Test LOFT LP-LB-1. Forschungszentrum Karlsruhe FZK, Germany. FZKA-.....in preparation. 1999

/7/ Sanchez, V., Homann, Ch., Validation of the improved RELAP5 transition boiling model against the full-length FLECHT-SEASET reflood test. Forschungszentrum Karlsruhe FZK, Germany. FZKA-..... in preparation. 1998.

/8/ Hagen S., Hofmann P., Noack V., Sepold L., Schanz G., Schumacher G., Large Bundle PWR test CORA-7: test Results, FZKA 6030, April 1998.

/9/ von der Hardt, P., Jones, A.V., Lecomte, C., Tattegrain, A., "Nuclear Safety Research: The Phebus Severe Accident Experimental Program", Nuclear Safety 35(2),1994.

/10/ Smit, S., Hering, W., Sengpiel, W., Analysis of Fuel Bundle Behaviour in Phebus FPT0 with SCDAP/RELAP5, FZKA 5882, 1998.

/11/ Dorr, B., Implementierung der GAUSS-Lösungsroutine zur direkten Lösung einer Bandmatrix in FLUTAN, Interner Bericht IRS 5/95, PSF 3244, 1995.

/12/ Hering, W., Messainguiral, Ch., Sengpiel, W., Investigation of the Meltdown Behaviour of Massive Radial Core Enclosures during LWR Accidents, FZKA-.....in preparation. 1999.

/13/ Messainguiral, Ch., Hering, W., Steel annular core structures; temperature evolution during a severe accident. Calculation with Icare2-V2-mod2~. Interner Bericht CEA/SERA/LAPE-FZK/IRS.

/14/ Haste, T.J. et al., Design Studies for FZK Degraded Core Bundle Quench Experiments, Report AEAT-1360, May 1997.

/15/ Hofmann, P. et al., Results of the QUENCH Commissioning Tests, FZKA 6099, August 1998

/16/ Hofmann, P. et al.: QUENCH-01, Experimental and Calculational Results, FZKA 6100, November 1998.

/17/ Hering W. et al.: "Status of Reflood Analyses for the LOOP Scenario using SCDAP/RELAP5 mod 3.1", in „Projekt Nukleare Sicherheitsforschung, Jahresbericht 1997", FZKA 6126, Forschungszentrum Karlsruhe, 1998.

/18/ Hiles, R.P. et al.: Scaling Studies and Support of FZK Bundle Quench Experiments, Report AEAT –4484 Issue 1, November 1998.

IV. Reaktionsverhalten von Zircaloy-4 in Luft

(W. Krauss, G.Schanz, IMF III)

Abstract

In support of the current EU project OPSA an experimental program on Zircaloy-4/air oxidation was initiated in extension of earlier studies. Short Zircaloy-4 tube sections were exposed to flowing synthetic air in temperature transient thermobalance tests: The parameters were the linear heat-up rate (5-40 K/min) and the ramp temperature (800-1400 °C). Mass increase and reaction rate were continuously registered and evaluated in temperature/time dependence. Oxide scale growth is accompanied by changes of specimen color and dimensions, scale cracking and spalling, thus revealing serious scale degradation, consistent with the kinetic results. The metallographic investigation confirms that nitrogen-induced morphological and mechanical phenomena determine the observed anomalies. Presently, ramps with isothermal holding periods are studied. Further experiments towards more realistic conditions (steam pre-oxidation, steam/air atmospheres, etc.) and analytical efforts are required.

Kurzfassung

Begleitend zum gegenwärtigen EU-Projekt OPSA wurde in Erweiterung früherer Untersuchungen ein experimentelles Programm zur Zircaloy-4/Luft Oxidation aufgenommen. Kurze Zircaloy-4 Rohrabschnitte wurden in transienten Thermowaage-Tests strömender synthetischer Luft ausgesetzt. Die Parameter waren die Aufheizrate (5-40 K/min) und die Rampentemperatur (800-1400 °C). Massenzunahme und Reaktionsrate wurden kontinuierlich registriert und in Temperatur/Zeitabhängigkeit ausgewertet. Das Oxidwachstum wird von Farb- und Dimensionsänderungen, sowie Aufreißen und Abplatzen der Schicht begleitet, im Einklang mit den kinetischen Ergebnissen. Die metallographische Untersuchung bestätigt, daß Stickstoff die morphologischen und mechanischen Phänomene verursacht. Das Programm wird gegenwärtig auf isotherme Versuchsphasen erweitert, die sich an die Temperaturrampen anschließen. Weitere Untersuchungen und begleitende analytische Arbeiten sind hinsichtlich realistischerer Bedingungen (Dampf-Voroxidation, Dampf/Luft-Mischatmosphären etc.) erforderlich.

Zielsetzung

Denkbare Szenarien für den Einbruch von Luft („Air Ingress") in einen Reaktorkern unter Störfallbedingungen werden gegenwärtig im Rahmen des EU-Projektes OPSA betrachtet, allerdings überwiegend als hypothetisch beurteilt. Jedenfalls wären bei solchen Szenarien gravierende Auswirkungen auf den Wasserstoff-Quelltherm, sowie die Spaltprodukt- und die Brennstoff-Chemie zu erwarten.

Aus der Literatur und eigenen, jedoch früher mit anderer Zielsetzung durchgeführten Studien ist bekannt, daß die Hochtemperatur-Oxidation von Zirkonium und seinen Legierungen an Luft vom Verhalten in Dampf dramatisch abweichen kann [1,2]. Insbesondere die neben der Oxidation ablaufende Reaktion mit der Luft-Komponente Stickstoff, führt zum Aufbau morphologisch veränderter und mechanisch geschädigter Reaktionsschichten anstelle von schützenden Oxid-Deckschichten, und deshalb zu komplexeren reaktionskinetischen Zusammenhängen. Es ist deshalb nicht zulässig, ein Reaktionsverhalten zu unterstellen, das ähnlich zur Dampfoxidation ist. Darüber hinaus tritt bei der Luft-Oxidation im Vergleich zur Dampfoxidation eine wesentlich höhere Energiefreisetzung auf.

Über grundlegende Untersuchungen zur Zircaloy-4/Luft-Oxidation wird im folgenden berichtet. Diese finden zunächst unter idealisierten und sauber definierten Bedingungen an kleinen metallischen (also nicht voroxidierten) Zircaloy-4 Proben statt. Der Übergang auf realitätsnähere Versuchsbedingungen, vor allem mit Dampf-Voroxidation und Oxidation in Dampf/Luft-Gemischen wäre der nächste Schritt. Insbesondere für eine weitergehende Auswertung und Bewertung der Ergebnisse ist eine begleitende Modellierung der beobachteten Reaktionsmechanismen erforderlich.

Versuchsausführung

Die Untersuchung des Reaktionsverhaltens von Zircaloy-4 in Luft wurde mit Einzeleffekttests unter transienten Temperaturbedingungen aufgenommen. Die Parameter der Testserien waren die Steilheit der zeitlich linearen Temperaturrampen (5-40 K/min) und die Endtemperaturen (800-1400°C). Der Abkühlungsprozess erfolgte

im Ofen unter Ausnutzung des natürlichen Abkühlverhaltens der Testanlage mit Kühlraten bis zu 50 K/min.

Zur Gewährleistung von reinen und reproduzierbaren Oberflächen wurden die Zircaloy-4 Hüllrohrabschnitte von 4 mm Länge in einer Ätzlösung aus HNO_3 und HF gebeizt, sorgfältig gespült und in deionisiertem Wasser gekocht. Die Experimente wurden in strömender, trockener, synthetischer Luft in einer Thermowaage ausgeführt. Der Vorteil dieser Experimentführung liegt bei der simultanen und kontinuierlichen Aufzeichnung von Probentemperatur, Massenzunahme und Reaktionsraten. Durch eine geeignete Probenmontage können sogar eventuell stattfindende Fragmentierungsprozesse registriert werden.

Ergebnisse

Morphologie, mechanisches Verhalten

Das makroskopische Aussehen von nicht voroxidierten Zry-4 Proben, die nur kurze Zeit bei niedriger Temperatur der Luftatmosphäre ausgesetzt waren, unterscheidet sich nur wenig von demjenigen der in Dampf oxidierten Proben. Sie weisen ebenfalls eine glatte Oberfläche mit schwarzer Färbung auf.

In Abb. 1 sind Zry-4 Rohrabschnitte wiedergegeben, die mit der konstanten Heizrate von 20 K/min (0,33 K/s) auf Endtemperaturen zwischen 1000°C und 1200°C aufgeheizt wurden und repräsentativ das dabei auftretende makroskopische Probenaussehen zeigen. Die bei der Luftoxidation gebildeten Reaktionsschichten nehmen sehr schnell eine bräunliche oder weißliche Färbung an. Dieses deutet auf Defekte im Schichtaufbau, z.B. Risse hin. Dickere Reaktionsschichten verlieren ihre Haftung zur metallischen Matrix und platzen bevorzugt beim Abkühlen oder, bei Transienten mit höheren vorgesehenen Umsetzungsgraden (ca. 2/3 der möglichen O_2-Aufnahme), bereits beim Aufheizen ab.

Die in Abb. 2 dargestellten Probenquerschliffe, die von Proben angefertigt wurden, die mit verschiedenen Heizraten auf die Endtemperatur von 1200°C erwärmt wurden, lassen den durch mechanische Spannungen ausgelösten Abplatzvorgang der Reak-

tionsschicht erkennen. Bei der langsam aufgeheizten Probe ist die Außenschicht bereits vollständig abgeplatzt. Selbst bei schnellen Transienten (40K/min) treten bereits große Spalte zwischen Matrix und Außenschicht auf. Durch geeignete Probenmontage in der zur Versuchsausführung eingesetzten Thermowaage konnte gezeigt werden, daß der makroskopisch sichtbare Abplatzprozeß während des Abkühlvorganges bei ca. 750 °C erfolgte und gleichzeitig eine erhöhte Reaktionsrate auftrat [3].

Reaktionskinetik

Die in der Thermowaage durchgeführten Versuche zeigen auch, daß weißlich gefärbte Proben mit dünneren Reaktionsschichten, die makroskopisch betrachtet noch haften, beim Abkühlen unterhalb von 900 °C vorübergehend wieder erhöhte Reaktionsraten zeigen. Dagegen weisen schwarze Proben diesen Anstieg der Reaktionsgeschwindigkeit nicht auf.

Während des Aufheizvorganges steigt die Reaktionsrate mit zunehmender Temperatur erwartungsgemäß stark an. Jedoch weisen die langsam aufgeheizten Proben entgegen der Erwartung höhere Reaktionsraten trotz größerer Reaktionsschichtstärken auf (Abb. 3). Dieses Probenverhalten deutet auf Defektbildung in den wachsenden Schichten und den Verlust der zunächst passivierenden Schichtwirkung hin.

Die Auswertung der Massenzunahme von in Luft reagierten Zry-4 Rohrsegmenten, wie in Abb. 4 dargestellt, zeigt, daß bei doppelten Heizraten oder äquivalent halber effektiver Reaktionszeit ungefähr die halbe Massenzunahme auftritt. Dieses Verhalten wurde bei transienten Versuchen beobachtet, die bis jetzt für verschiedene Endtemperaturen zwischen 900 und 1200°C ausgeführt wurden. Diesem Probenverhalten liegt somit keine parabolische Reaktionskinetik zugrunde, wie sie von der Dampfoxidation her bekannt ist. Eine modellmäßige Beschreibung des Schichtwachstums mit den für die Dampfoxidation entwickelten Codes ist nicht möglich.

Das bei der Reaktion mit Luft auftretende Schichtwachtum erfolgt schneller als mit Dampf und entspricht eher einem linearen als einem parabolischen Zeitgesetz. Um detailliertere Aussagen zur Kinetik erarbeiten zu können sollte die Auswertung der Versuchsdaten von modelltheoretischen Ansätzen begleitet und unterstützt werden.

Davon werden Hinweise erwartet, mit welchen Parametern weitere Versuche durchgeführt werden sollten.

Mikrostruktur

Mikrostrukturelle Untersuchungen wurden an allen in Luft reagierten Zry-4 Rohrabschnitten durchgeführt. Sämtliche Proben zeigen ein vielfältiges, aber konsistentes Verhalten. In Abb. 5 sind als Beispiel für die auftretenden Gefügestrukturen in Abhängigkeit von der Heizrate bzw. der effektiven Reaktionszeit bei transienten Bedingungen Querschliffe wiedergegeben. Die erste der drei dargestellten Proben zeigt eine noch überwiegend regelmäßige, dichte jedoch dünne Oberflächenschicht aus Oxid, stellenweise mit radialen Rissen und warzenförmig ausgebildeten Oxidnestern. Bei längeren Reaktionszeiten wächst eine häufig gleichmäßig dicke Reaktionsschicht, die Defekte in lateraler Richtung aufweist. Diese Schicht kann sich bei entsprechender Stärke von der Außenseite der metallischen Rohrmatrix ablösen, während die Schicht der Rohrinnenseite nicht abplatzt. Morphologische Details in Abb. 6 zeigen im Interferenzkontrast die α-Zr(O)- Schicht und die Nachoxidation der Risse, die in diese spröde Zwischenschicht hineinlaufen bzw. sie durchdringen.

Abb. 7 zeigt Ausschnitte aus der äußeren (oberes Bild) und der inneren (untere zwei Bilder) Oxidschicht eines Hüllrohres zur Beschreibung weiterer Details: Das obere und das untere Teilbild zeigen von der jeweiligen Oberfläche ausgehende Anrisse (radial orientiert), die teilweise in lateral gerichtete Risse auslaufen. Das mit Stengelstruktur beginnende Oxidwachstum setzt sich offensichtlich unter Bildung lateral ausgerichteter Risse bzw. Rißsysteme fort. Kleine, metallisch aussehende, eingeschlossene Partikel sind schon früher als Zirkoniumnitrid identifiziert worden, und für die Luftoxidation typisch. Gehäuft und als größere Partikel tritt diese Phase im Oxid eingeschlossen an und nahe der Grenze zur metallischen α-Zr(O)-Schicht auf. Im Zusammenhang damit werden offenbar laterale Anrisse im Oxid und radiale, in die α-Zr(O)-Phase einlaufende Anrisse gebildet.

Zusammenfassung

Das Oxidationsverhalten von Zircaloy-4 in Luft wird durch den zusätzlichen Reaktionspartner Stickstoff maßgeblich beeinflußt. In der Reaktionszone, d.h. an der Grenzfläche Oxidschicht – metallische Matrix, kommt es zur Bildung von Zirkoniumnitrid-Körnern. Dies führt im weiteren Verlauf der Reaktion zu einer mechanischen Schädigung der Oxidschicht durch die Bildung von reaktionsbeschleunigend wirkenden Schichtdefekten.

Die Ursache dafür ist nach der vorläufigen Interpretation der Zerfall der Nitridphase im Verlauf der Oxidation im Kontakt mit dem gleichzeitig anwesenden Sauerstoff. Der frei werdende Stickstoff könnte an der Grenze zum Metall erneut Nitrid bilden. Stickstoff würde somit als konkurrierender Reaktionspartner zu Sauerstoff auftreten, ohne auf Dauer einen großen anteiligen Umsatz zu erreichen. Statt dessen wäre eine Wirkung ähnlich der eines Katalysator für den Umsatz mit Sauerstoff gegeben.

Das Aussehen der gebildeten Oxidschicht, die Hohlräume, laterale und axiale Risse aufweist, ist sehr ähnlich zu dem späten Oxidationsverhalten von Zircaloy-4 in Dampfatmosphäre bei mittleren Temperaturen. Unter diesen Bedingungen werden in Dampf Oxidschichten gebildet, deren Schutzwirkung aufgrund von Schichtdefekten verloren geht. Dabei treten ähnlich komplizierte Auswirkungen auf die Oxidationskinetik auf. Auch dieses Verhalten ist bisher nicht zufriedenstellend modelliert worden.

Sowohl bei den transienten als auch bei den erst ansatzweise ausgeführten isothermen Reaktionsversuchen ist keine mit zunehmender Schichtstärke abnehmende, sondern eher eine zunehmende Reaktionsrate feststellbar. Diese Ergebnisse zeigen, daß die bei Luftoxidation gebildeten Schichten keine oder eine wesentlich schlechtere passivierende Wirkung haben als die bei der Dampfoxidation gewachsenen Schichten.

Ausblick

Die Untersuchungen zur Zircaloy/Luft Hochtemperaturoxidation sind zunächst von grundlegendem wissenschaftlichen Interesse, zumal das komplizierte Materialverhalten in einigen Punkten der ebenfalls noch nicht vollständig geklärten Breakaway-Oxidation von Zircaloy in Dampf ähnelt. Dieses Verhalten wiederum ist hinsichtlich der angestrebten verlängerten Einsatzdauer von Brennelementen von großem aktuellem Interesse. Es ist zwar nicht bekannt, ob das bei hohen Temperaturen ermittelte Verhalten auf den Bereich der Reaktorbetriebstemperatur übertragbar ist, viele morphologische Details, die an Oxidschichten nachweisbar sind, sprechen aber dafür.

Die Frage der Relevanz der Luftoxidation bei Störfallbetrachtungen, zweifellos das wichtigste Kriterium, ist leider noch nicht abschließend zu beurteilen. Von amerikanischer Seite durchgeführte Risikostudien zum Störfallszenarium Lufteinbruch („Air Ingress") sind im Rahmen des EU-Projektes OPSA aufgegriffen worden. Neben Sicherheitsanalysen wurden orientierende experimentelle Untersuchungen zum Oxidationsverhalten des Hüllmaterials in Einzelstab- und Kleinbündel Versuchen durchgeführt. Das Vorhaben wird in Kürze beendet sein. Seitens der kerntechnischen Industrie überwiegt die Beurteilung, daß ein Lufteinbruch im Verlauf eines Störfalls als hypothetisch einzustufen ist.

Bekanntlich kann selbst bei kleiner Eintrittswahrscheinlichkeit aber gravierenden Konsequenzen, wie sie hier in Modellversuchen dargelegt worden sind, das sich ergebende Risiko beträchtlich sein. Dementsprechend wäre zu prüfen, ob die Verminderung dieses zunächst noch unbestimmten Risikos weitere Untersuchungen rechtfertigt. Es ist durchaus wahrscheinlich, daß sich dies bereits dadurch erreichen läßt, daß man das Materialverhalten nicht unter idealisierten, sondern unter realitätsnäheren Bedingungen prüft. Dazu sind Versuche in reaktor- und störfalltypischen Gasmischungen, wie sie im Störfallverlauf auftreten könnten, unerläßlich. Die Schritte dahin sind die Ausführung von Versuchen in Luft an verschieden stark in Dampf voroxidierten Proben, die Ermittlung des Reaktionsverhalten in Dampf nach kurzzeitiger Stickstoffaussetzung d.h. Prüfung der Reaktion in Dampf auf einen eventuellen Stickstoff-bedingten Memory-Effekt bzw. die Ausheilung der von Stickstoff verursachten Schichtdefekte, sowie die Untersuchung eines H_2 Einflusses im teil-konsu-

mierten Dampf. Als begleitende Arbeit ist eine modelltheoretische Beschreibung der Luftoxidation erforderlich, die sich später in die Störfallanalyse der Dampfoxidation von LWR's integrieren läßt.

Literatur

[1] E.B. Evans et al.
Critical role of nitrogen during high temperature scaling of zirconium
Proc. Conf. Met. Soc. AIME, Boston, USA, 1972, pp248-281

[2] S. Leistikow, H.v. Berg
Investigation under nuclear safety aspects of Zircaloy-4 oxidation kinetics at high temperatures in air
2nd workshop of German and Polish research on high temperature corrosion of metals
Jülich, 2-4 Dec. 1987

[3] W. Krauss, G. Schanz
Zircaloy/air oxidation kinetics: current experiments towards future demands.
4th Internat.QUENCH Workshop, Karlsruhe, October 6-8, 1998

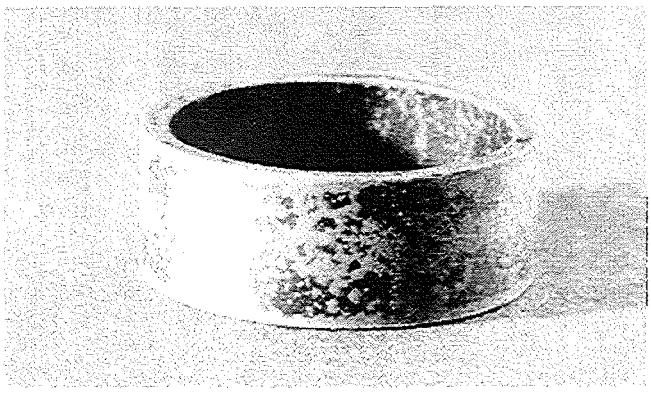

Heating rate 20 K/min, 1000 °C

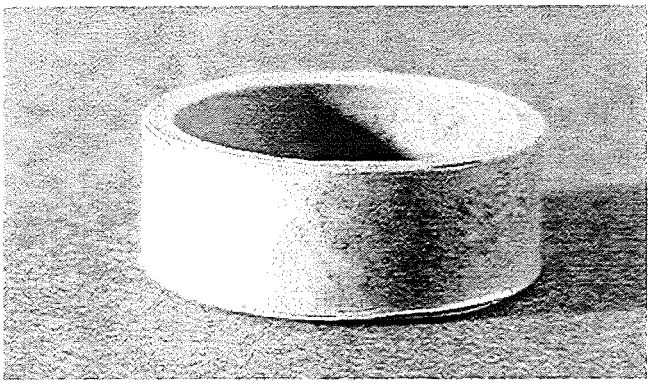

Heating rate 20 K/min, 1100 °C

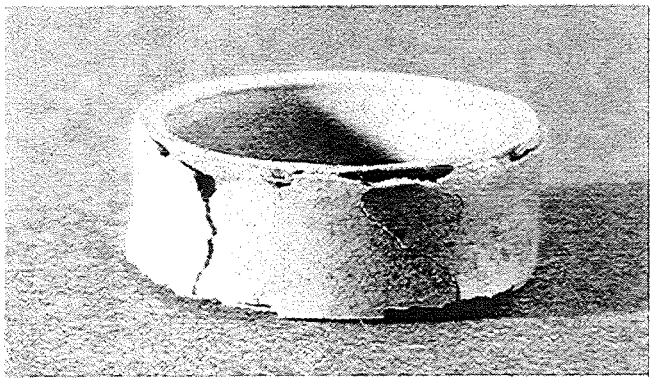

Heating rate 20 K/min, 1150 °C

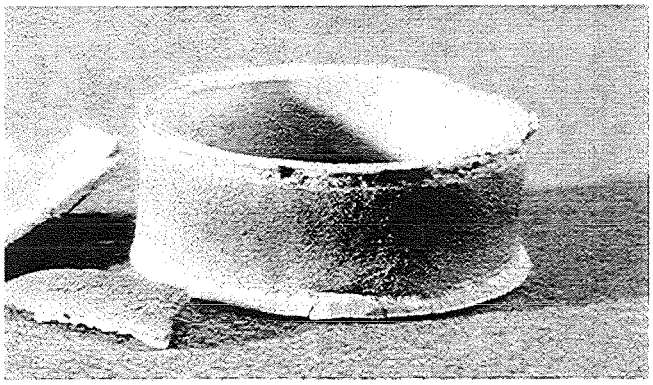

Heating rate 20 K/min, 1200 °C

Abb. 1 Makroskopische Darstellung von Zry-4 Rohrabschnitten nach transienter Luftreaktion in Abhängigkeit von der Endtemperatur. Dickere Reaktionsschichten verlieren ihre Haftung und platzen von der metallischen Matrix ab.

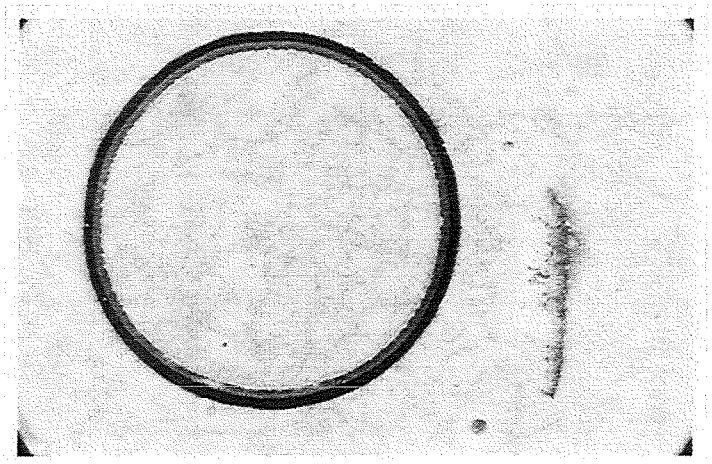

1200 °C, 20 K/min

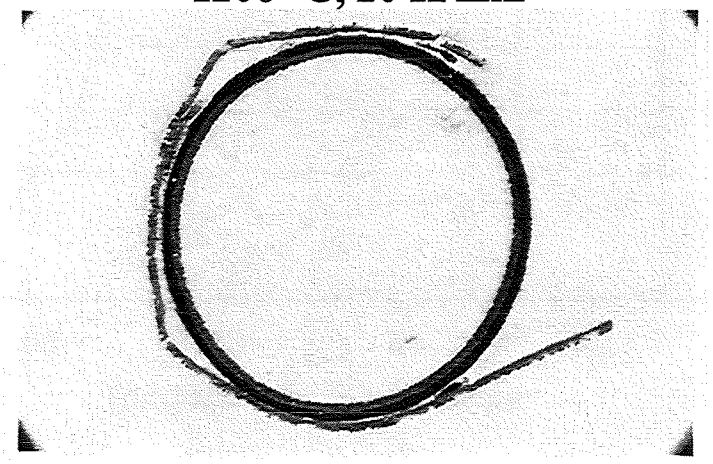

1200 °C, 30 K/min

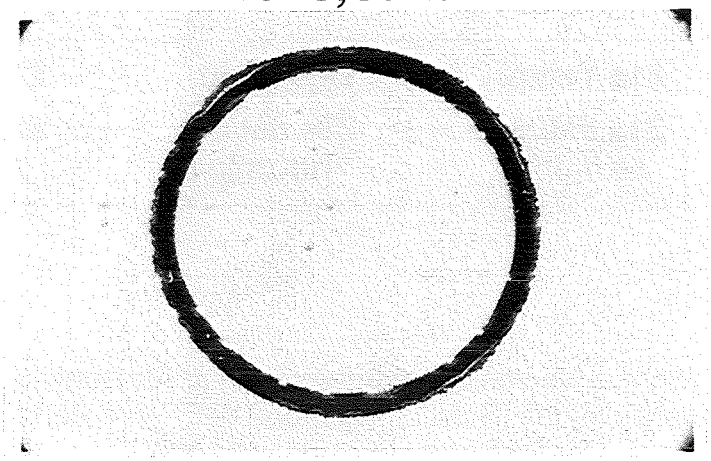

1200 °C, 40 K/min

Abb. 2 Querschliffe von Zry-4 Rohrproben, die mit verschiedenen Heizraten in Luft aufgeheizt wurden.

Oben: Äußere Oxidschicht vollständig abgeplatzt.
Mitte: Äußere Oxidschicht noch leicht haftend.
Unten: Bereits Spalte zwischen äußerer Oxidschicht und metallischer Matrix erkennbar

Vergrößerung ca. 6-fach.

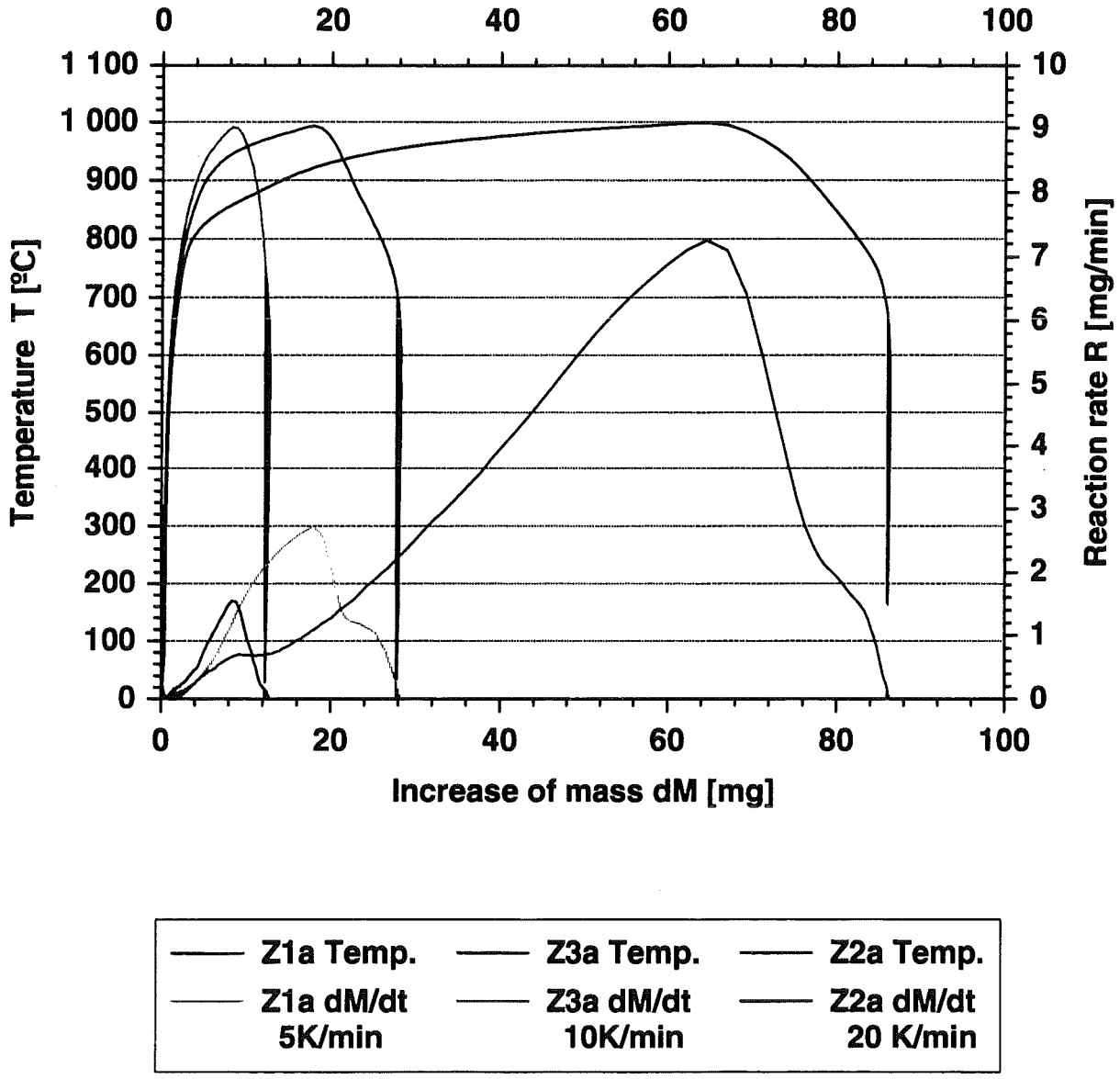

Abb. 3 Reaktionsraten von Zry-4 Rohrproben in Abhängigkeit vom Massenzuwachs (Schichtdicke) und der Probentemperatur bei transienter Probenaufheizung auf 1000 °C

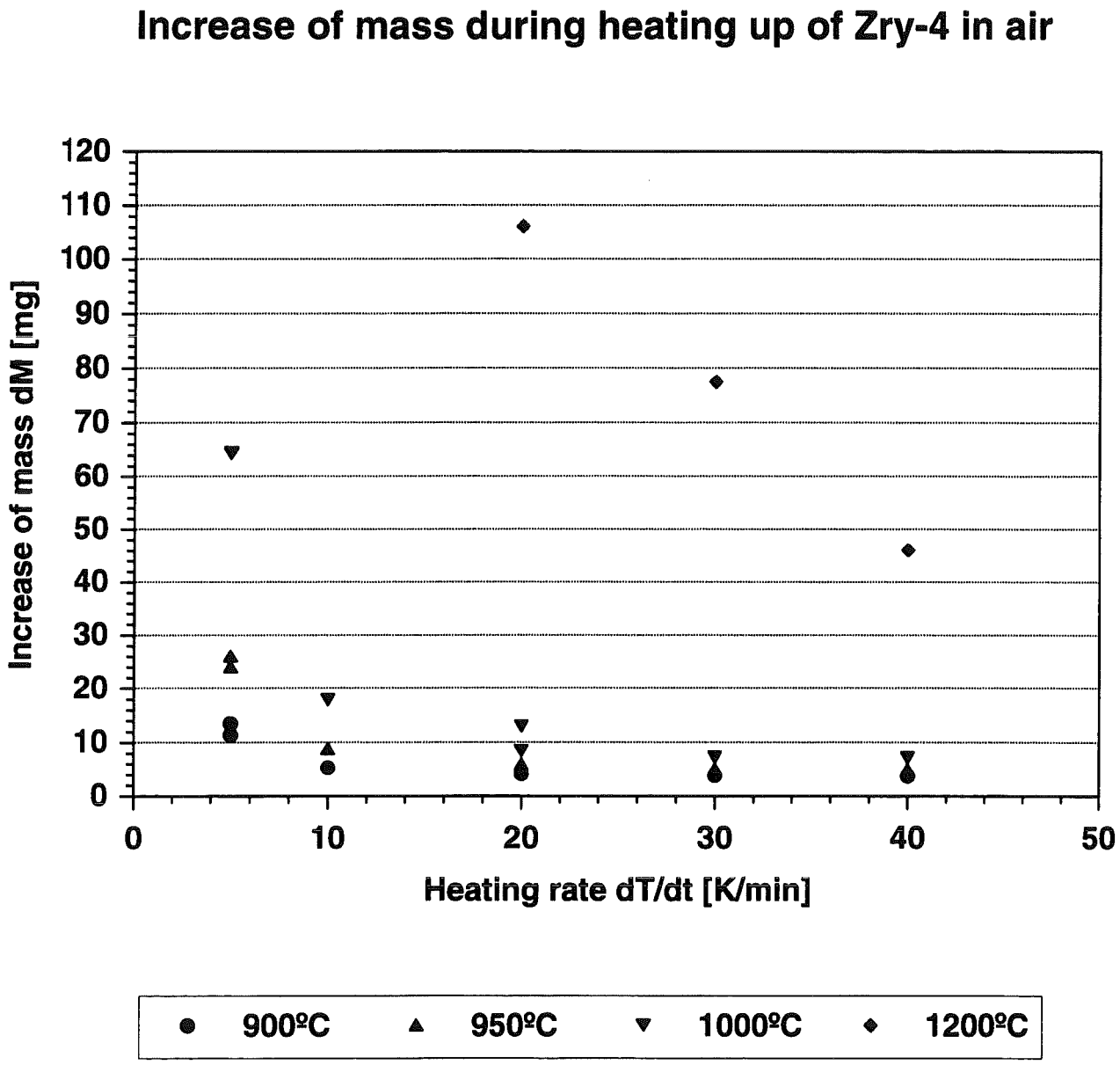

Abb.4 Massenzunahme von Zry-4 Rohrabschnitten in Abhängigkeit von der Heizrate (effektiver Reaktionszeit) und der Endtemperatur.
Die vollständige Oxidation des Ringes würde eine Massenzunahme von ca. 207 mg bewirken.

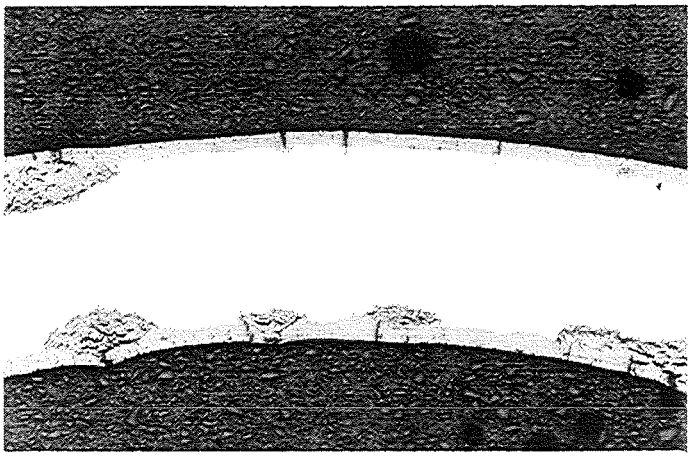

Heating rate 40 K/min

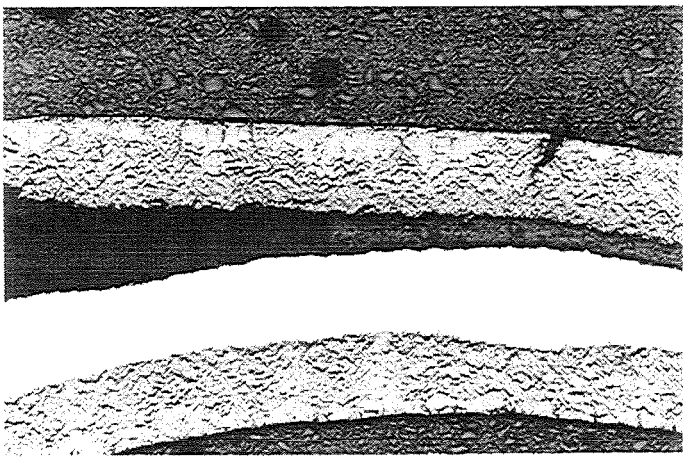

Heating rate 30 K/min

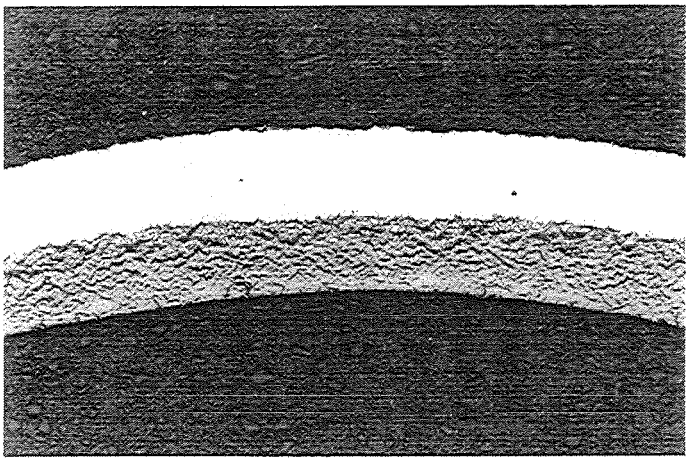

Heating rate 20 K/min

Abb. 5 Gefüge von Zry-4 Rohrproben nach transienter Reaktion in Luft bei 1200 °C in Abhängigkeit von der Aufheizrate bzw. der effektiven Reaktionszeit.
Hell: Metallische Matrix; Grau: Oxidschicht; Dunkel: Einbettmasse. Dickere Oxidschichten lösen sich von der Matrix teilweise (Mitte) bzw. vollständig (Unten) ab; Querschliffe mit Vergrößerung ca. 50 x.

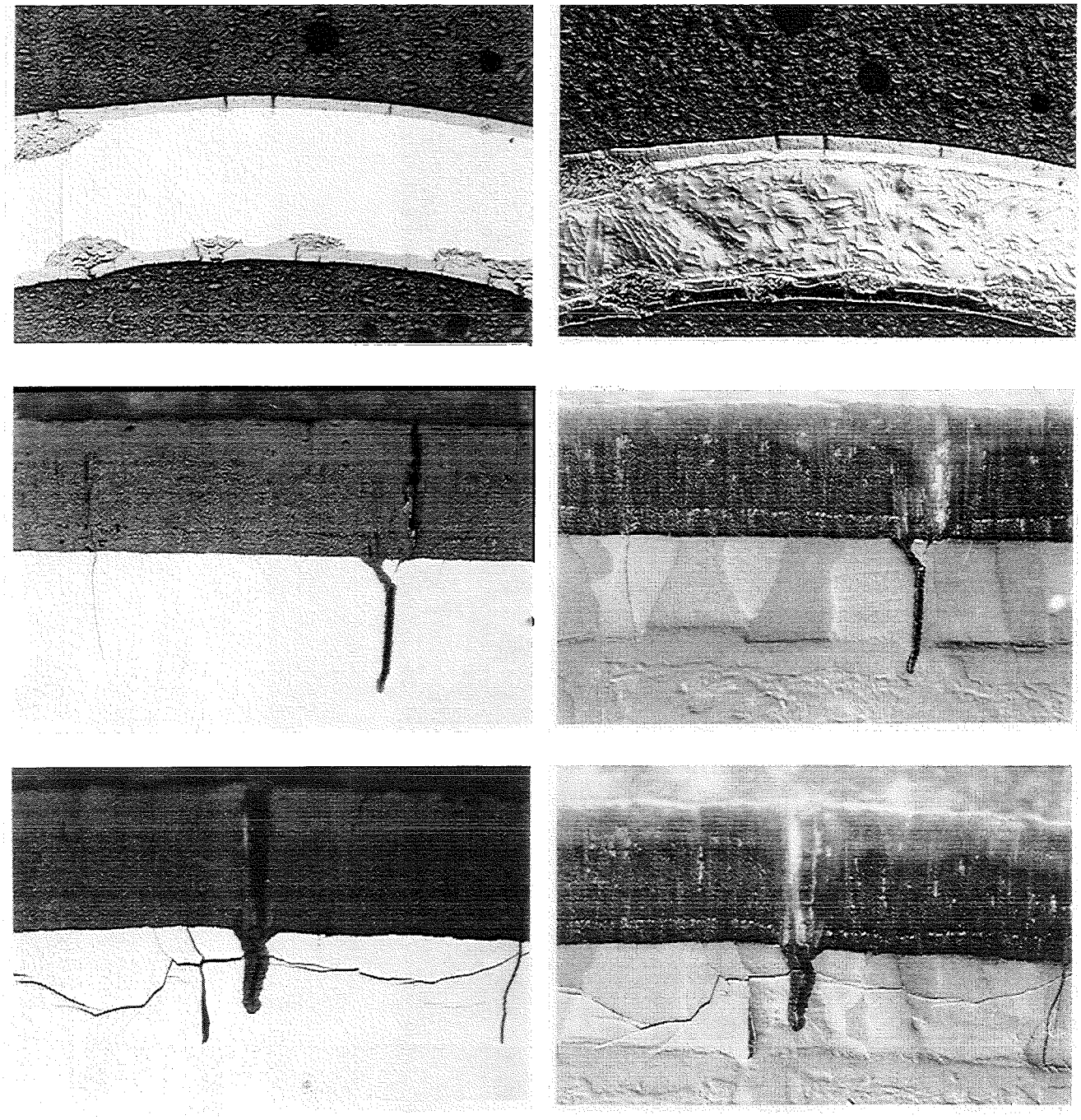

Abb. 6 Gefügedetails einer Zry-4 Rohrprobe nach transienter Aufheizung mit 40 K/min auf 1200 °C in Luft (siehe Abb. 5, oben).

Links: Hellfeld (normal) Rechts: Interferenzkontrast

Oben: Dünne Oxidschicht mit anfänglich stengeligem Gefüge und radialen Rissen sowie Ausbildung von Oxidnestern; ca. 50 x.

Mitte: Oxidschicht mit regulärer Wachstumsform und Sn-Ausscheidung. Metallische Matrix α-Zr(O) und primäres β-Zr. Radiale Anrisse zeigen noch keine Oxidationsspuren; ca. 500 x.

Unten: Oxidschicht mit ähnlicher Struktur jedoch mit Nachoxidation von radialen Rissen und Ausbildung von lateralen Rissen im spätern Versuchsablauf; ca. 500 x.

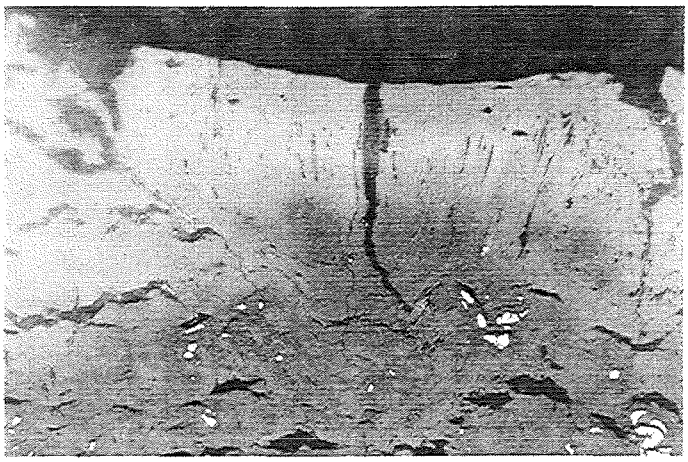

Outer tube surface, 500x

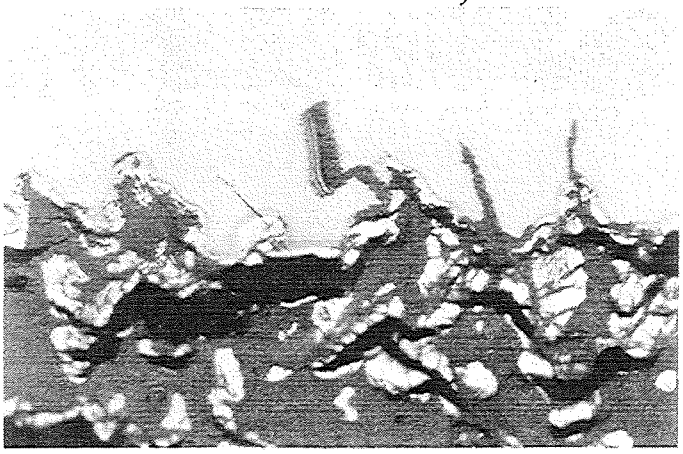

Boundary ZrO_2 / α-Zr, 1000x

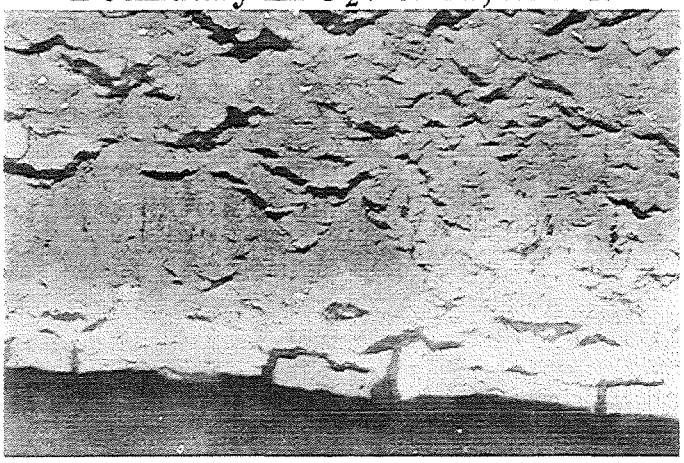

Inner tube surface, 500x

Abb. 7 Gefügedetails der Oxidschicht einer Zry-4 Rohrprobe; die mit 20 K/min auf 1150 °C in synthetischer Luft aufgeheizt wurde..

Oben: Oxidschicht auf äußerer Wand mit anfänglich stengeligem Gefüge und radialen Rissen sowie lateralen Defekten.

Mitte: Grenzbereich zwischen metallischer Matrix (oben) und Oxidschicht (unten) nahe der Rohrinnenwand mit eingelagerten ZrN-Körnern (weiß).

Unten: Oxidschicht auf der Innenwand mit ähnlicher Struktur wie auf der Außenwand

32.21.09 Entwicklung von Methoden zur Abschätzung und Minimierung der radiologischen Folgen von Reaktorunfällen

(G. Benz*, J. Ehrhardt, F. Fischer, Ch. Haller*, I. Hasemann, E. Hesselschwerdt, A. Lorenz, J. Päsler-Sauer, M. Rafat*, W. Raskob*, T. Schichtel*, O. Schüle, C. Steinhauer, INR)

Abstract

Uncertainty and sensitivity analyses with the program system COSYMA for assessing the radiological consequences of nuclear accidents have been performed in close co-operation with the University of Delft, NL, and the NRPB, UK. The results are evaluated on the submodule level and for the overall code system.

The first operational version PV 3.1 of the real-time on-line decision support system RODOS for off-site emergency management after nuclear accidents has been prepared in 1998. It is being enhanced and customised to the various regions of Europe in close co-operation with some 40 contract partners in East and West Europe. Its operational use at a central place in Germany and in emergency centres of other West and East European countries is in progress.

Zusammenfassung

Unsicherheits- und Sensitivitätsanalysen mit dem Programmsystem COSYMA zur probabilistischen Abschätzung der radiologischen Konsequenzen kerntechnischer Unfälle werden in Zusammenarbeit mit der Universität Delft, NL, und dem NRPB, UK, durchgeführt. Die Ergebnisse werden sowohl für Einzelmodule als auch für das gesamte Programmsystem ausgewertet.

Die operationelle Version PV 3.1 des Echtzeit- und On-line-Entscheidungshilfe-systems RODOS für den Notfallschutz nach kerntechnischen Unfällen wurde in 1998 fertiggestellt. Es wird in Zusammenarbeit mit etwa 40 Vertragspartnern in Ost- und Westeuropa erweitert und zur Anwendung in den verschiedenen Regionen Europas

---

* Fa. D.T.I., Dr. Trippe Ingenieurgesellschaft m.b.H., Karlsruhe

angepaßt. Sein operationeller Betrieb an zentraler Stelle in der Bundesrepublik Deutschland und in Notfallschutzzentralen anderer ost- und westeuropäischer Länder wird vorbereitet.

1. Probabilistische Abschätzungen von Unfallfolgen

Im Rahmen des Vertrages FI4P-CT95-0006 mit der Europäischen Kommission (EK) werden in Abstimmung mit der Universität Delft (NL) und dem NRPB (UK) in den Jahren 1997 bis 1999 Unsicherheits- und Sensitivitätsanalysen mit dem Programmsystem COSYMA durchgeführt.

Die Unsicherheitsanalysen erfolgen in mehreren Stufen. Zunächst werden die folgenden vier Hauptmodule separat untersucht. Nach dem Modul „Atmosphärische Ausbreitung und Ablagerung" in 1997 folgten im Berichtszeitraum die Module zum Verhalten von Radionukliden in Nahrungsketten, zur Berechnung von Strahlendosen durch interne und externe Exposition sowie zur Berechnung gesundheitlicher Schäden (deterministisch und stochastisch). Aufgrund der Ergebnisse der Einzelmodulanalysen werden die wichtigsten Parameter für die abschließenden Unsicherheitsanalysen mit dem gesamten Programmpaket COSYMA bestimmt. Sämtliche Analysen werden für drei typische Quellterme durchgeführt. Die Anzahl der ausgewerteten Zwischen- und Endergebnisse schwankt je nach Teilmodul und liegt maximal bei 191.

Die Datensätze der unsicheren Modellparameter wurden durch Stichprobenauswahl nach der Methode des Latin Hypercube Sampling erzeugt. Dosisfaktoren als auch Ingestionsdaten werden nicht direkt in COSYMA berechnet, sondern von externen Programmen in Form von Dateien zur Verfügung gestellt. Die Anzahl zu berücksichtigender Modellparameter war für die Dosis - und Nahrungskettenmodule sehr groß (159 bzw. 162). Für die entsprechenden Unsicherheitsanalysen wurden darum in Voranalysen mit den externen Programmen 360 bzw. 300 Dateien entsprechend der Stichprobenauswahl der zugehörigen unsicheren Parameter vorberechnet. Bei den Unsicherheits- und Sensitivitätsanalysen des Moduls zur Berechnung gesundheitlicher Schäden wurden 27 Modellparameter untersucht, wobei 100 COSYMA - Läufe durchgeführt wurden. Ausgewertet wurden die Fehlerbandbreiten (5%-95% Fraktilwerte) der Ergebnisse aller Einzelmodulanalysen sowie die Beiträge der verschiedenen Modellparameter zu ihren Unsicherheiten.

Aus der sich ergebenden Rangreihenfolge wurden die wichtigsten 186 Parameter abgeleitet, die am meisten zu den Ergebnisunsicherheiten beitragen; sie werden bei der Gesamtanalyse von COSYMA berücksichtigt werden. Die für die Endanalyse notwendigen Rechnungen, ihre Auswertung und die Gesamtdokumentation erfolgen in 1999.

2. Rechnergestützte Entscheidungshilfeinstrumentarien für den Notfallschutz

2.1 Gegenwärtiger Entwicklungsstand von RODOS

Mit Unterstützung der EK (Verträge FI4P-CT95-0007, FI4C-CT96-0006 und IC15-CT96-0318) wird das Entscheidungshilfesystem RODOS für den anlagenexternen Notfallschutz nach kerntechnischen Unfällen bis zur Einsatzreife entwickelt. Im RODOS Projekt sind im 4. Rahmenprogramm der EK seit Anfang 1996 etwa 40 Vertragspartner aus der Europäischen Union, den mittel- und osteuropäischen Staaten und den GUS Republiken mit FZK/INR als Hauptkoordinator involviert. In diesem Zusammenhang müssen auch zwei weitere Projekte der EK im Rahmen von TACIS/PHARE/ECHO Programmen in den Jahren 1999 und 2000 gesehen werden, die die beschleunigte Implementierung von RODOS in Notfallschutzzentralen der Ukraine, Polens, der Slovakischen Republik und Ungarns, sowie die Errichtung eines Informationsnetzes für den schnellen Austausch von radiologischen Informationen zwischen ost- und westeuropäischen Staaten zur Zielsetzung haben. Die vorbereitenden Arbeiten hierzu (Unterstützung bei der Erstellung von Ausschreibungs- und Angebotsunterlagen, Durchführung von Ausschreibungen) wurden in 1998 fortgeführt.

Mitte des Jahres 1998 wurden die Arbeiten zur Fertigstellung der operationellen RODOS Version PV3.1 abgeschlossen. In der Folge wurde die RODOS-Software während und nach dem RODOS Contractors' Meeting, Trnava (Slowakische Republik), 5. - 9. Oktober 1997, an die Vertragspartner verteilt; zuvor erfolgte die Implementierung in Portugal.

2.1.1 Betriebsabwicklungssystem OSY

Zu den wesentlichen Arbeiten am Betriebsabwicklungssystem gehörten die Implementierung und der Test der Real-time Datenbank einschließlich graphischer

Oberfläche und ihre Ankopplung an verschiedene Datennetze (z.B. FZK Meßmast, KFÜ-Daten, EURDEP) sowie die Neugestaltung des Hauptdialog-Layouts durch Gliederung bestimmter Funktionalitäten in entsprechende Funktionsgruppen und deren Visualisierung durch Icons. Darüber hinaus wurden eine Reihe weiterer Verbesserungen vorgenommen; zu den wesentlichen gehören die Zeitoptimierung der Datenmanager-Zugriffsfunktionen, die Entwicklung des RODOS-Datenbank-Generators und die Trennung von Programmdatenbank und Stammdatenbank.

Im ersten Halbjahr wurde das neue Release der Grafiksoftware vervollständigt. Diese neu entwickelte Grafik wurde in C++ codiert und ist durch ihr objektorientiertes Design leicht portierbar und einfach zu warten. Im Laufe des Jahres wurde dieses Konzept auch auf die übrigen Komponenten von RoGIS ausgedehnt, so daß nun eine auf UNIX Workstations und Windows 95/NT einsetzbare Software existiert.

Ausgehend von den Anregungen der Arbeitsgruppe RODOS/RESY (siehe Abschnitt 2.3) sowie im Rahmen der künftigen Zusammenarbeit mit LLNL (USA) und JAERI (Japan), bei denen die operationellen Entscheidungshilfesysteme ARAC und SPEEDI betrieben werden, wurde im zweiten Halbjahr 1998 der Prototyp einer Eingabeoberfläche für das WWW auf der Basis von JavaScript entwickelt. Sie erlaubt dem Benutzer auf einfache Art Rechenläufe von RODOS zu definieren. Die Ergebnisse solcher Rechnungen sind ebenfalls über das WWW abrufbar. Der Zugriff kann mit den verbreiteten Browsern (Netscape oder Internet Explorer) erfolgen.

Das vorhandene geographische Datenmaterial für Deutschland (NavTech u.a.) wurde erweitert um Übersichtskarten (Europa, Welt) aus ArcAtlas (ESRI). Daraus wurden Bodenbeschaffenheits -, Bodennutzungs -, und Bevölkerungsdaten entnommen und für das geographische Informationssystem RoGIS von RODOS aufbereitet.

2.1.2 Teilsystem ASY zur Ermittlung der radiologischen Lage

Wie in den Vorjahren waren die Arbeiten zur Integration von bei den Vertragspartnern entwickelten Softwarepaketen ein wesentlicher Teil des Arbeitsprogramms. Dabei handelte es sich insbesondere um die Vervollständigung der meteorologischen Modellkette LSMC mit vollen Funktionalitäten der Ausbreitungsmodelle ATSTEP und RIMPUFF und Einbau der „Deutsch - Französischen Parameter-

isierung" der Dispersionsvorgänge. Die Echtzeit - und On-line Funktionalitäten wurden sowohl für Daten meteorologischer Meßmaste als auch der numerischen Vorhersagemodelle realisiert. Der Zugriff zu den Landnutzungs- und Höhendaten in RODOS wurde hergestellt. In ausführlichen Testprozeduren wurde durch intensiven Kontakt mit den beteiligten Institutionen (RISØ (DK), GRS) die gesamte Modellkette für Ausbreitungsrechnungen im Nahbereich im Hinblick auf ihren operationellen Einsatz getestet und durch Beseitigung von Schwachstellen in Funktionalität und Modellierung ertüchtigt. Das Ausbreitungsmodell für den Fernbereich, MATCH, des SMHI (S) wurde an die Nahbereichsmodelle angekoppelt.

2.1.3 Teilsystem CSY zur Simulation von Schutz- und Gegenmaßnahmen

Die Integrations- und Erweiterungsarbeiten zu den Nahrungsketten- und Dosismodulen für terrestrische (FDMT) und aquatische (FDMA) Expositionspfade der GSF und den entsprechenden Modulen zur Behandlung von Strahlenschutzvorsorgemaßnahmen, LCMT und LCMA, des NRPB (UK) konnten weitgehend abgeschlossen werden. Die gesamte hydrologische Modellkette, die den Run-off/Wash-off von Radionukliden im Einzugsgebiet großer Flüsse, den Transport in Flußsystemen und das Verhalten in Seen beschreibt, wurde in RODOS implementiert und an die o.g. Nahrungskettenmodelle angekoppelt.

Für RODOS werden zusätzlich zwei neue terrestrische Nahrungskettenmodelle zur Behandlung von Tritium und zur Einbeziehung von Produkten aus Waldgebieten entwickelt. Bei der Entwicklung dieser beiden neuen Module wurde Wert darauf gelegt, daß die Strukturen mit denen des jetzigen Standardmoduls FDMT übereinstimmen. Die Entwicklung des Tritiummoduls wird unter Federführung rumänischer Vertragspartner zusammen mit dem INR durchgeführt.

Da die verschiedensten Module in RODOS ähnliche Rechnungen durchführen (z.B. Ablagerung von Radionukliden auf Pflanzenoberflächen), wurden im Laufe diese Jahres viele Rechenvorgänge harmonisiert. Unter anderem wurde zusammen mit der GSF ein gemeinsames Depositionsmodul entwickelt, das sowohl in den atmosphärischen Ausbreitungsmodellen als auch in den Nahrungskettenmodellen angewendet wird.

2.2 Entwicklung und Durchführung von Trainingskursen

Im Mai 1998 wurde der Kurs „Computergestützter Trainingskurs: Entscheidungsunterstützung für den anlagenexternen Katastrophenschutz in der Frühphase eines nuklearen Unfalls" am FEERC/SPA Typhoon in Obninsk (Rußland) mit Unterstützung des INR durchgeführt. Diese Veranstaltung war die Wiederholung eines gleichnamigen Kurses, der 1996 und 1997 im FTU abgehalten worden war. Ein neuer Kurs mit dem Titel „Computergestützter Trainingskurs: Entscheidungsunterstützung für den anlagenexternen Katastrophenschutz in den späteren Phasen eines nuklearen Unfalls" wird von EdF (F), IPSN (F) und ECN (NL) mit Unterstützung des INR vorbereitet und vom 12. - 16. April 1999 im FTU durchgeführt.

2.3 Errichtung und Betrieb von RODOS an zentraler Stelle

Im Rahmen des BMU - Vorhabens St.Sch. 4168 wird das RODOS System im Zeitraum 3/1998 bis 2/2000 zum operationellen Betrieb durch den Bund und die Länder an zentraler Stelle vorbereitet. Das Schwergewicht der Arbeiten im Berichtszeitraum lag auf der Erstellung des Konzeptberichts. Zur Abstimmung der technischen und administrativen Einzelheiten der Installation des RODOS Systems und des Zugriffs durch den Bund und die Länder fanden im Jahr 1998 insgesamt 5 Sitzungen der projektbegleitenden aus Vertretern des Bundes, der Länder und des INR bestehenden „Arbeitsgruppe RODOS/RESY" statt. In ihr wurden die Themenbereiche

- Anforderungen an den zentralen Betrieb von RODOS seitens der Strahlenschutzvorsorge und des Katastrophenschutzes,
- Festlegung der Betriebsarten (Normal-, Notfall- und Übungsbetrieb),
- Benutzeranforderungen und organisatorisch-administrative Ankopplung von RODOS an die Einsatzzentralen des Bundes und der Länder,
- Bereitstellung von Stammdaten, radiologischen und meteorologischen Meßdaten und meteorologischen Prognosedaten,
- Festlegung von Eingabe- und Ergebnisdaten (Standardinformation),
- Aufgabenbeschreibung zur Errichtung und zum Betrieb einer RODOS Zentrale, sowie
- Beschreibung der DV-technischen Realisierung des zentralen Betriebs

ausführlich behandelt. Parallel dazu fanden bilaterale Gespräche beim Bayerischen StMLU sowie beim BfS, ZdB Neuherberg und IAR Freiburg, zur Klärung von Einzelfragen statt.

Entgegen der ursprünglichen Zeitplanung liegt noch keine akzeptierte Endversion des Konzeptberichts vor. Infolgedessen verschiebt sich auch die Fertigstellung der softwaretechnischen und hardwaretechnischen Feinkonzepte und die daran gekoppelte Bestellung und Installation der Hardware- und Software-Komponenten. Allerdings wurden eine Reihe von Einzeluntersuchungen im Hinblick auf die Festlegung der technischen Spezifikationen durchgeführt; hierzu gehören

- Datenübertragung zwischen den zuständigen Bundes- und Länderbehörden,
- Datenübertragung zum Deutschen Wetterdienst,
- Redundanz bei der Plattenspeicherung,
- Recherche über eine geeignete Rechnertopologie.

2.4 Internationale Zusammenarbeit

Basierend auf bereits geschlossenen bzw. bevorstehenden Zusammenarbeitsvereinbarungen zwischen LLNL (ARAC), JAERI (SPEEDI) und dem Forschungszentrum Karlsruhe/INR als Vertreter des RODOS Consortiums werden Software - Tools entwickelt, die den schnellen Informationsaustausch über Rechenergebnisse und radiologische Informationen im Fall eines kerntechnischen Unfalls in Europa, USA und Asien via Internet erlauben.

Veröffentlichungen

Ehrhardt, J.; Weis, A.
Mid-term Report of the RODOS Project
FZKA-Bericht 6203, RODOS-R4-1998

Raskob, W.; Heling, R.; Popov, A.; Zheleznyak, M.
Untersuchung radioökologischer Modelle für Binnengewässer hinsichtlich ihrer Eignung für den Einsatz in IMIS
10. Fachgespräch zur Überwachung der Umwelradioaktivität 28.-30.4.1998 in Hamburg

Ehrhardt, J.; Rafat, M.; Schüle, O.
Operationeller Betrieb und Weiterentwicklung des Entscheidungshilfesystems RODOS
10. Fachgespräch zur Überwachung der Umwelradioaktivität 28.-30.4.1998 in Hamburg

Raskob, W.; Popov, A.; Zheleznyak, M.; Heling, R.
Radioecological Models for Inland Water Systems
FZKA- Bericht 6089

Ehrhardt, J.; Weis, A.
RODOS: Decision Support Sytems for Nuclear Emergencies
FZKA-Bericht 6089, RODOS-R3-1998

Jones, J.A.; Brown, J.; Gossens, L.; Kraan, B.; Cooke, R.; Ehrhardt, J.; Hasemann, I.; Fischer, F.
Uncertainty Analysis on COSYMA: Results from the Dispersion and Deposition and Health Effects Modules
SAMO: Second International Symposium on Sensitivity Analysis of Modul Output, 19. – 22.4.1998, Venedig

Jones, J.A.; Brown, J.; Gossens, L.; Kraan, B.; Cooke, R.; Ehrhardt, J.; Hasemann, I.; Fischer, F.
COSYMA: Accident Consequence Uncertainty Analysis: Procdure and First Results
ESREL 98 (European Safety and Reliability Conference), 16. –19.6.1998, Trondheim

32.21.10 Beteiligung am PHEBUS-Projekt

Theoretische Interpretation der experimentellen Ergebnisse

(W. Sengpiel, W. Hering, S.-O. Smit, IRS)

Abstract

FZK/IRS participates in the international PHEBUS FP project by analyses of the experiments and their interpretation concerning fuel rod behaviour and physico-chemical material interactions. The computer codes applied are SCDAP/RELAP5 and ICARE2. Calculations both for FPT0 and FPT1 revealed a number of code deficiencies and model uncertainties, especially in the late phase of FPT1; one of them refers to the experimental observation of severe fuel relocation in the temperature range between 2450 K and 2650 K, about 300 K below the $(U,Zr)O_2$ melting temperature.

This effect was relevant especially for the interpretation and analyses of the FPT1 experiment, which had been performed with irradiated fuel (burn-up of 24 MWd/kg U).

Assuming that augmented fuel relocation in the range from 2450 K to 2650 K is promoted by cracked fuel and thus can be interpreted to be a burn-up effect, a simple model has been introduced into SCDAP/RELAP5 based on a modification of the Hofmann correlation for the calculation of the amount of metallic (Zr-U-O) mixture. It is shown that by this simple model as a first step towards consideration of burn-up effects onto fuel rod degradation mechanisms, the agreement between experimental data and calculational results could be improved significantly.

Current analytical work refers to the calculation of FPT4 (planned for 1999) with ICARE2 and a code comparison for FPT2 (planned for 2000) using both SCDAP/RELAP5 and ICARE2.

Zusammenfassung

Die Beteiligung von FZK/IRS am PHEBUS FP - Projekt beinhaltet die Interpretation des phänomenologischen Ablaufs der Bündelzerstörung und der auftretenden physikalisch-chemischen Vorgänge mittels Experimentanalysen mit den Rechenprogrammen SCDAP/RELAP5 (S/R5) und ICARE2. Wegen der engen thematischen Verbindung mit dem PSF-Vorhaben 32.21.08 (Untersuchung zur Kernzerstörung/Analysen zum Ablauf kernzerstörender Unfälle) ist dort im Zusammenhang mit der Validierung

von S/R5 bereits auf PHEBUS FP-Experimentanalysen eingegangen worden. Im folgenden werden die wesentlichsten Erkenntnisse aus diesen Analysen kurz zusammengefaßt.

Die Analysen zu PHEBUS FPT0 sind vorläufig abgeschlossen und dokumentiert /1/. Die Beteiligung an Benchmarkanalysen innerhalb des PHEBUS-Projekts hat wesentliche Modellschwächen aller für Reaktorsicherheitsanalysen eingesetzter mechanistischer Codes offengelegt und die Bedeutung des Einflusses der PHEBUS FP-Testserie auf die Entwicklung von Rechenprogrammen für Analysen der Folgen schwerer Reaktorunfälle demonstriert /2/. Die größten Unsicherheiten in den Analysen sind bezogen auf Prozesse wie

- Zry-Oxidation (insbesondere von geschmolzenem und verlagertem Zry),
- Absorbermaterialeinfluß auf die Desintegration benachbarter Brennstäbe,
- Verlust der Stabilität oxidierter Hüllrohre bei hohen Temperaturen, die zur Freisetzung metallischer (Zr-U-O)-Schmelzen und/oder fester Pelletfragmente führt,
- signifikante Brennstoffverlagerungen unterhalb der $(U,Zr)O_2$ - Schmelztemperatur,
- Debrisbildung, Übergang zum Schmelzepool, Schmelzepoolausbreitung (sogenannte "späte Phase"),
- Wärmeverluste durch den Shroud (kein reaktortypischer Effekt).

Von besonderer Bedeutung für die Berechnung der Brennstabzerstörung und damit des Übergangs von intakter Geometrie zu Debris-/Poolgeometrie ist die Beobachtung von Brennstoffverlagerungen deutlich unterhalb der $(U,Zr)O_2$ - Schmelztemperatur (wie sie aus den Phasendiagrammen ermittelt wird). Während der Versuch PHEBUS FPT0 mit Brennstäben aus unbestrahltem Brennstoff durchgeführt wurde, hatte der Brennstoff des Versuchs FPT1 einen Abbrand von ca. 24 MWd/kg U; die Versuchsführungen waren vergleichbar /1/, /3/. On-line-Messungen und Datenanalysen für FPT1 haben erste massive Brennstoffverlagerungen im Temperaturbereich zwischen 2450 K und 2650 K ergeben, ca. 300K unter der Schmelztemperatur des $(U,Zr)O_2$-Gemisches. Es liegt deshalb nahe, einen Einfluß des Abbrandes - d.h. der Rißdichte in den Brennstoffpellets - auf (frühe) Verlagerungsmechanismen anzunehmen. Ein vorläufiges einfaches Modell, das in eine FZK/IRS-Version von S/R5 eingeführt wur-

de, geht davon aus, daß geschmolzenes Zry in die Risse der Pellets eindringt und zum einen wegen der vergrößerten Reaktionsfläche mehr Brennstoff lösen kann, und zum anderen infolge des Auflösungsprozesses im Pellet die Stabilität der Brennstoffsäule vermindert, so daß Brennstoffpartikel zusammen mit der Masse metallischer (Zr-U-O)-Schmelze verlagert werden. Dieser Effekt wurde in einem ersten Ansatz näherungsweise über eine Modifizierung der Hofmann-Korrelation zur Berechnung der gelösten UO_2 - Massen durch schmelzflüssiges Zry modelliert /3/. Abb. 1 illustriert diesen Vorgang der Entstehung einer 2-Phasenmischung als Folge der Pelletfragmentation und somit der verstärkten chemischen Auflösung von UO_2 mit Einschluß fester UO_2 - Partikel in der (Zr-U-O)-Schmelze schematisch. Ein Vergleich von Rechenergebnissen für FPT1 ohne und mit dem neuen Verlagerungsmodell zeigt, wie erwartet, eine qualitative Verbesserung mit großen Unterschieden in den verlagerten UO_2 - und den entstehenden Schmelzepool-Massen (s. PSF-Vorhaben 32.21.08/ Analysen zum Ablauf kernzerstörender Unfälle, Abb. 6). In den folgenden Abbildungen 2 bis 4 werden Brennstabtemperaturen, Shroudtemperaturen und kumulative H_2 - Massen mit gemessenen Werten verglichen (TCW: gemessene Brennstabtemperaturen, TUS: Temperaturen mit Ultraschallthermometer nahe Shroudinnenseite gemessen, (a) berechnete Brennstab- und Shroudinnenseitentemperaturen mit Original-Hofmann-Korrelation entspr. unbestrahltem Brennstoff, (b) berechnete Brennstab- und Shroudinnenseitentemperaturen mit modifizierter Hofmann-Korrelation entspr. Brennstoff mit starker Rißstruktur). Da in der Hochtemperaturphase die Thermoelemente im Bündel ausgefallen sind bzw. große Meßungenauigkeiten aufweisen und auch die TUS Fehlmessungen zeigen, ist ein Vergleich zwischen Meßwerten und Rechenergebnissen für die späte Unfallphase schwer, qualitativ ist aber die Übereinstimmung – die TUS-Messungen zugrunde gelegt – in den Brennstabtemperaturen für die späte Phase zufriedenstellend, in den Shroudtemperaturen auch quantitativ gut. Die Wasserstoffmasse am Ende des Experiments (Abb. 4) wird in den Rechnungen um ca. 20 % unterschätzt. Im Gegensatz zu großen Unterschieden in den verlagerten UO_2 - Massen wirken sich die verschiedenen Verlagerungsmodelle auf die berechneten Brennstab- und Shroudtemperaturen nicht signifikant aus.

Für Mitte 1999 ist das Experiment FPT4 geplant, im folgenden Jahr der Versuch FPT2. Für FPT4 sind Rechnungen mit ICARE2 durchgeführt worden, für FPT2 laufen im Rahmen eines Codevergleichs Rechnungen mit S/R5 und ICARE2. FPT2 wird

wie FPT1mit bestrahltem Brennstoff durchgeführt werden, so daß nach Vorliegen der experimentellen Ergebnisse zusätzliche Daten für die Beurteilung und Modellierung des Verhaltens bestrahlten Brennstoffs herangezogen werden können.

Literatur

[1] S.-O. Smit, W. Sengpiel, W. Hering, "Investigation of the Phebus FPT0 bundle degradation with SCDAP/RELAP5", FZKA 6083, April 1998

[2] I. Shepherd et al.,"Intermediate Analysis of Phebus FP Test FPT-0: Bundle Degradation and Release (The Ability of Codes to Reproduce Core Behaviour in FPT-0)", Technical Note No. I.98.206, 1998 (interner Bericht für Teilnehmer am PHEBUS FP-Programm)

[3] S.-O. Smit, "Investigation of the Phebus FPT1 bundle degradation experiment with SCDAP/RELAP5", FZKA-Bericht, erscheint 1999

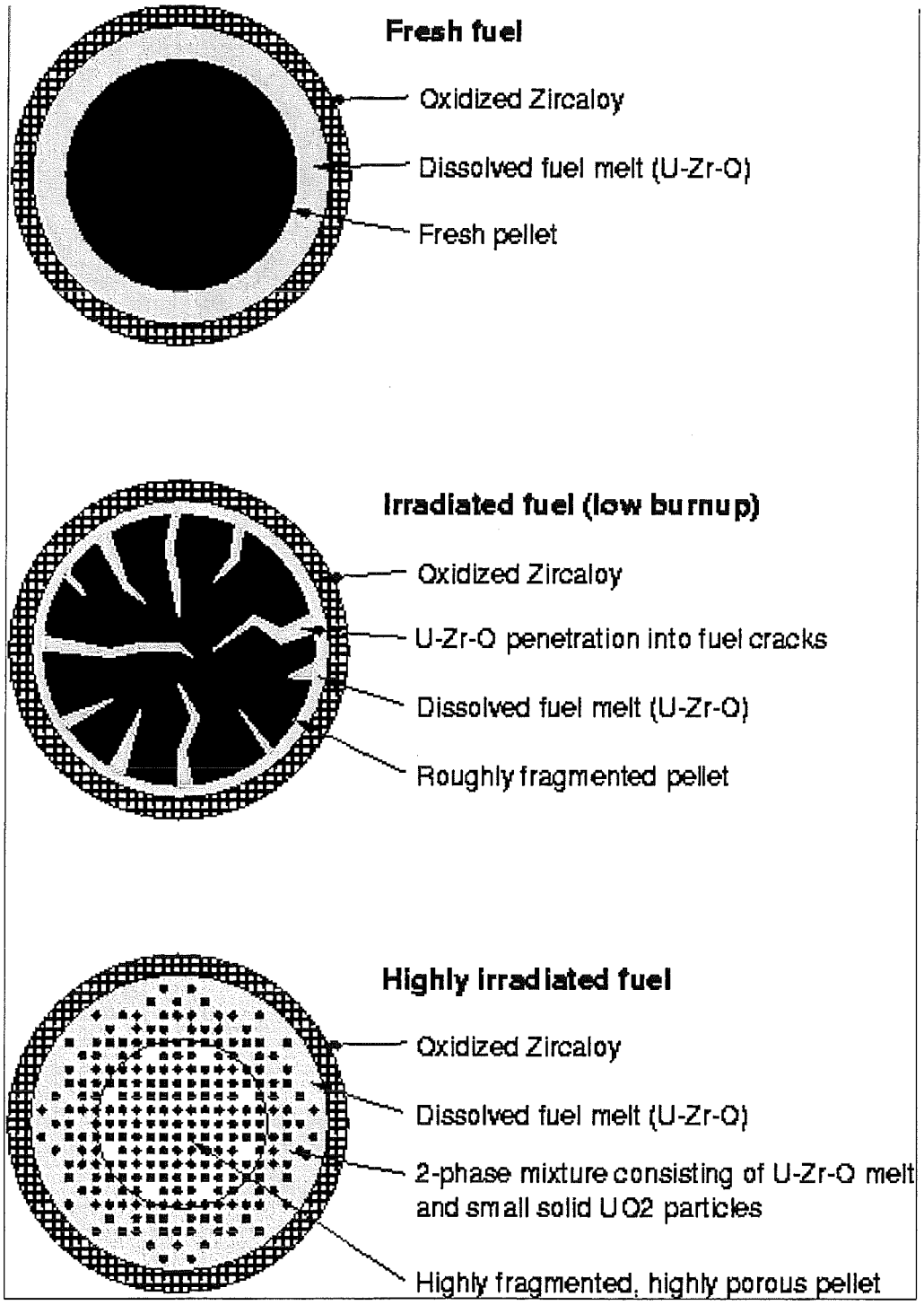

Abb. 1: Schema der Modellierung der UO_2 - Auflösung und resultierender Destabilisierung der Brennstoffsäule bei abgebranntem Brennstoff

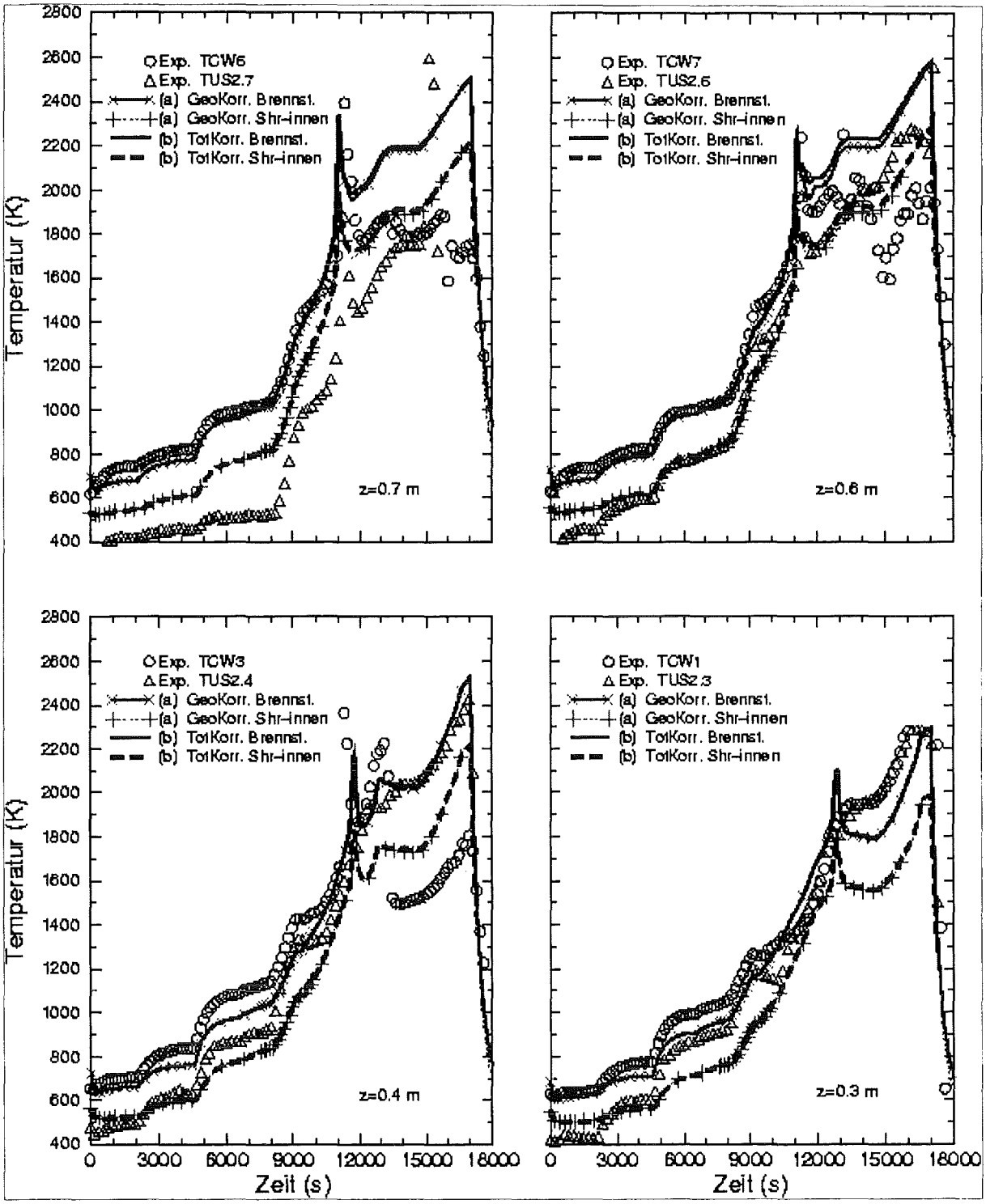

Abb. 2: Gemessene (TCW,TUS) und gerechnete Brennstabtemperaturen an verschiedenen axialen Positionen ((a): mit Original-Hofmann-Korrelation, (b) mit modifizierter Hofmann-Korrelation, Brennst. = Brennstaboberfläche, Shr-innen = Shroudinnenfläche)

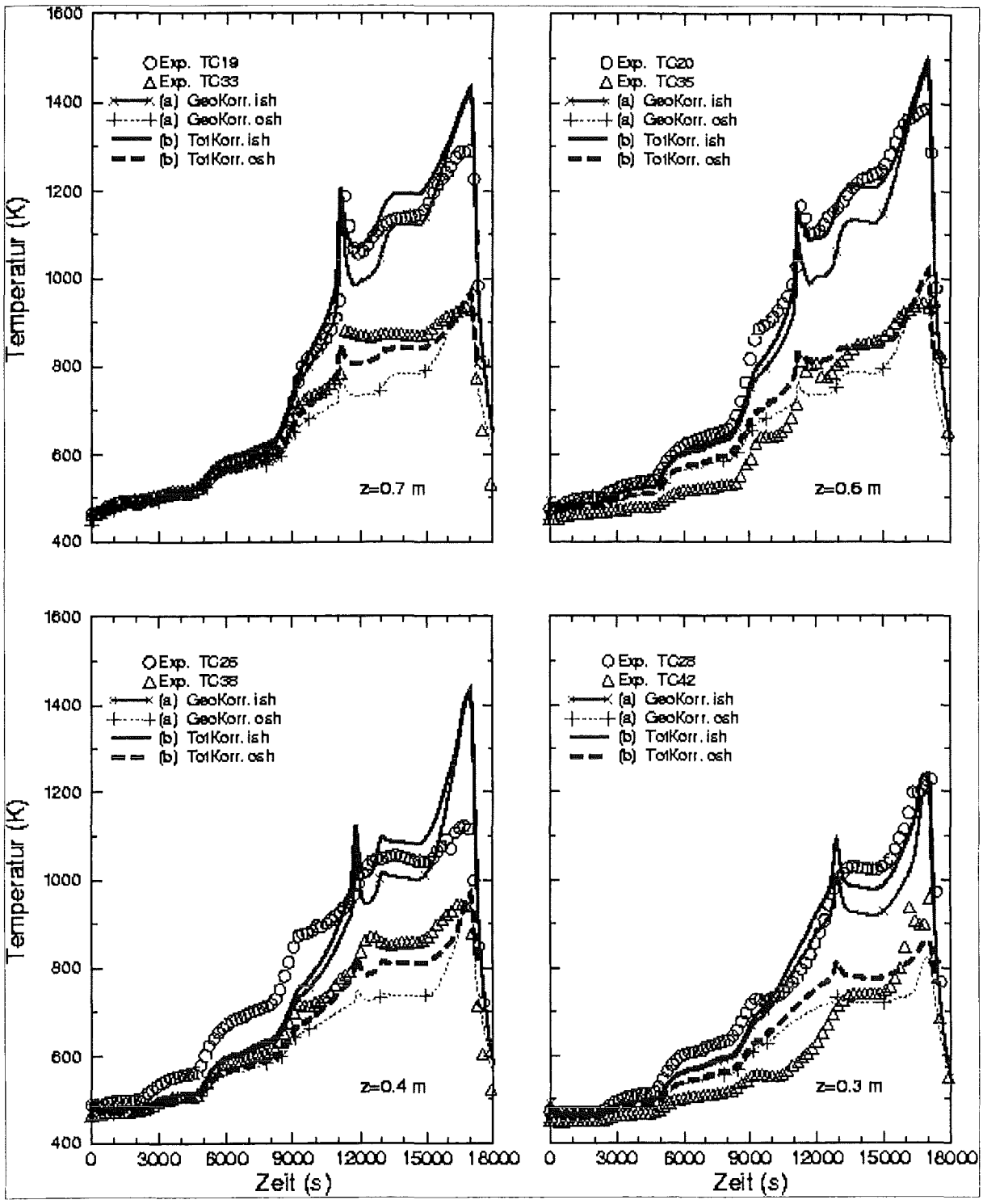

Abb. 3: Gemessene (TC) und gerechnete Shroudtemperaturen an verschiedenen axialen Positionen ((a) mit Original-Hofmann-Korrelation, (b) mit modifizierter Hofmann-Korrelation, ish/osh = innere/äußere Meßstelle im Shroud)

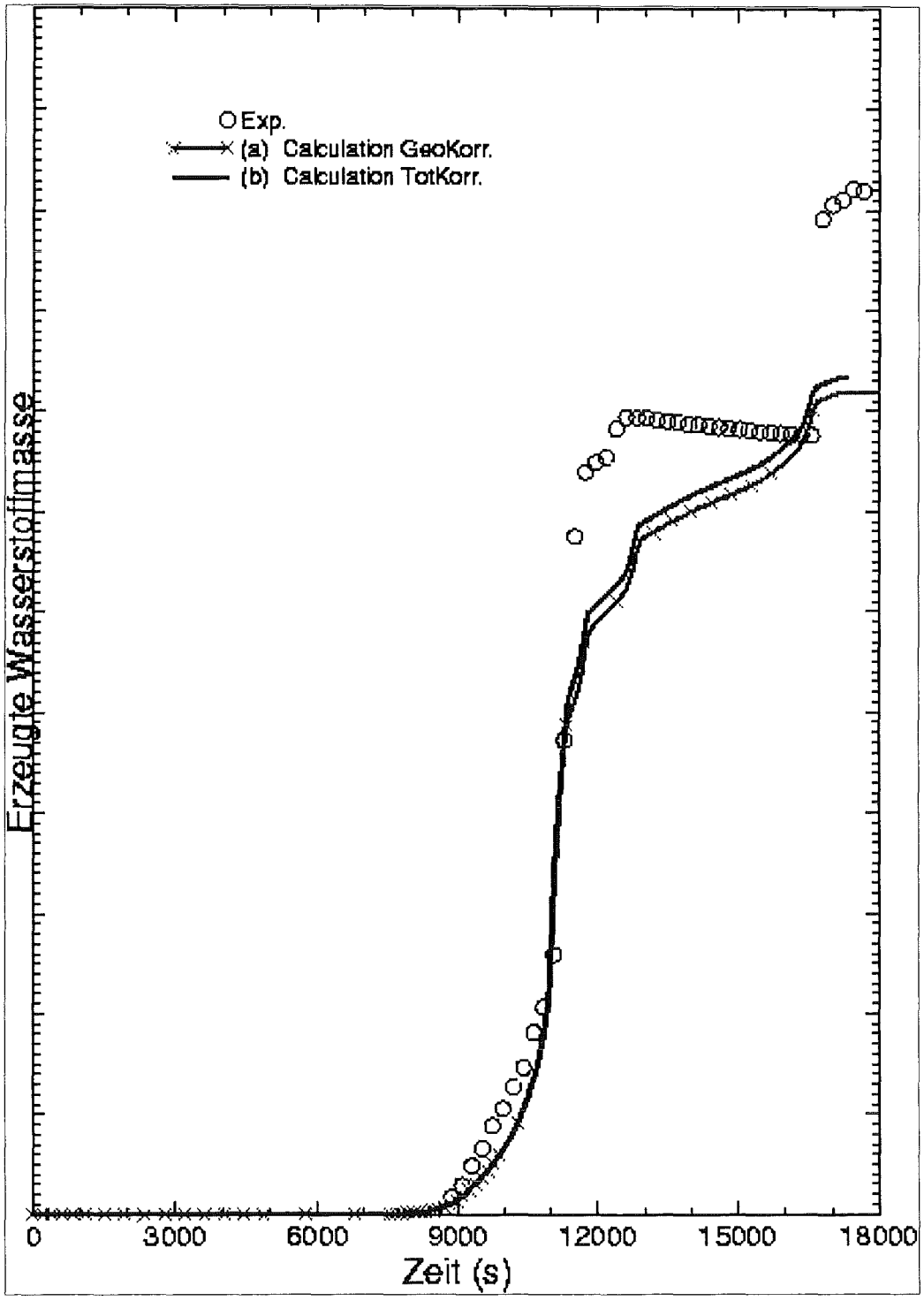

Abb. 4: Gemessene und gerechnete kumulative Wasserstoffmassen (ohne Einheit, (a) mit Original-Hofmann-Korrelation, (b) mit midifizierter Hofmann-Korrelation)

32.22 INNOVATIVE SYSTEME

32.22.02 Passive Nachwärmeabfuhr

I. Entwicklung von Thermofluiddynamikprogrammen und ingenieurtechnische Anwendungen

(G. Grötzbach, L. Carteciano, M. Wörner, A. Blahak, B. Dorr, S. Mitran, W. Olbrich, W. Sabisch, IRS; M. Alef, E. Aronskaia, T. Dunker, U. Gentner, St. Genz, N. Lehmann, A. Müller, D. Seldner; HIK; X. Jin; Siemens/KWU)

Zusammenfassung

Das Rechenprogramm FLUTAN wird für die Analyse der Nachwärmeabfuhr in neu konzipierten Reaktorsystemen und zu den Kühlungsmöglichkeiten in Tanks von beschleunigergetriebenen unterkritischen Anordnungen weiterentwickelt und validiert. Das Turbulenzmodell für Auftriebströmungen in FLUTAN wurde durch verfeinerte Modelle für den Auftriebsproduktionsterm in der Dissipationsgleichung und für den Dissipationsterm in der Wärmestromtransportgleichung weiter verbessert und validiert. Zur Validierung der lokalen Gitterverfeinerung in FLUTAN wurden SUCOS-2D Experimente nachgerechnet. Das entwickelte Konzept zur Diskretisierung der Transportgleichungen in komplexen Geometrien mit Hilfe von körperangepaßten Koordinaten wird vorgestellt. Schließlich wird der Stand der Methodenentwicklung zur direkten numerischen Simulation von Blasenströmungen mit dem Rechenprogramm TURBIT-VoF diskutiert.

Abstract

The FLUTAN Code is developed and validated for analyses of after heat removal in new reactor systems and will also be used for cooling of accelerated driven systems. The validation of the turbulence model for buoyant flows in natural convection and the validation of an implicit method for the local refinement of a structured grid are discussed for the case of a complex geometry. The newly developed method for the discretization of transport equations in complex geometry using body fitted coordinates is shortly given. Finally, the current status of the development of a new method is discussed which will

provide direct numerical and large eddy simulation capabilities of bubbly flows in the computer code TURBIT-VoF and later on also in the commercial code CFX.

A. Weiterentwicklung des Rechenprogramms FLUTAN für thermo- und fluiddynamische Anwendungen

Das Rechenprogramm FLUTAN [1] wird derart weiterentwickelt, daß das Programm für die Analyse der Nachwärmeabfuhr in neu konzipierten Reaktorsystemen (32.21.05) oder der Kühlungsmöglichkeiten in Tanks von beschleunigergetriebenen unterkritischen Anordnungen (32.23.03) eingesetzt werden kann. Die Weiterentwicklung betrifft zum einen die Entwicklung von physikalischen Modellen zur Naturkonvektion [2,3], zum anderen die Verbesserung der Effizienz der verwendeten numerischen Methoden [4]. In diesem Teil des Berichtes wird über die Weiterentwicklung von FLUTAN detailliert berichtet.

Gängige Turbulenzmodelle, wie das k-ε-σ_t Modell, sind für die Simulation von Naturkonvektion nicht zuverlässig genug, da ihr Gültigkeitsbereich durch die Annahmen der isotropen Wirbeldiffusivität und der Reynolds-Analogie zwischen Impuls- und Wärmetransport auf Zwangskonvektion begrenzt ist. Es wurde daher ein Turbulenzmodell für Auftriebsströmungen, TMBF [3], entwickelt und in FLUTAN implementiert, das für Misch- und Naturkonvektion geeignet ist. Das TMBF besteht aus einem Modell erster Ordnung für den Impulstransport, wie dem k-ε Modell, und aus einem Modell zweiter Ordnung für die Berechnung der Wärmeflüsse.

Mit Hilfe der analytischen Methode der Zweipunkt-Korrelationstechnik wurden von Ye et al. [5] verbesserte und für einen breiteren Anwendungsbereich gültige Schließungsansätze für den Auftriebsproduktionsterm in der Dissipationsgleichung und den Dissipationsterm in der Wärmestromtransportgleichung entwickelt. Diese Modelle wurden in FLUTAN implementiert. Die neuen Modelle sind in der untenstehenden Tabelle angegeben, für die bisherigen Modelle sei auf die in [3] zitierten Referenzen verwiesen. Bei den neuen Modellen wurde der Wert 0,7 des Exponenten aus Ergebnissen von Direkten Numerischen Simulationen (DNS) turbulenter Naturkonvektion optimiert.

Term	Bisherige Modellierung	Neue Modellierung
$P_{\varepsilon b}$	$\frac{\varepsilon}{k} c_{\varepsilon 1}(P_k + G_k)(1 + c_{\varepsilon 3} Ri_f)$	$-\frac{1}{2}\nu\beta g_i \frac{\partial^2 \overline{U_i'T'}}{\partial x_i^2} + \frac{\varepsilon}{k}\left(c_{\varepsilon 1} P_k + \left(\frac{\mathrm{Pr}}{R}\right)^{0,7} G_k\right)$
$\varepsilon_{U_i'T'}$	$-\frac{1+\mathrm{Pr}}{2\sqrt{\mathrm{Pr}}\sqrt{R}}\left(\frac{\varepsilon}{k}\right)\exp(-c_{T5}(\mathrm{Re}_t + Pe_t))\overline{U'_i T'}$	$\frac{\nu+\kappa}{4}\frac{\partial^2 \overline{U_i'T'}}{\partial x_i^2} - \frac{1}{2}\left(1+\frac{1}{\mathrm{Pr}}\right)\left(\frac{\mathrm{Pr}}{R}\right)^{0,7}\left(\frac{\varepsilon}{k}\right)\overline{U'_i T'}$

Die in FLUTAN implementierten neuen Modelle für $P_{\varepsilon b}$ und $\varepsilon_{U_i'T'}$ wurden für Naturkonvektion validiert und mit den Ergebnissen der alten Modellierungen verglichen [6]. Es wurde eine Auftriebsströmung simuliert, die sich an einer flachen vertikalen beheizten Wand ausbildet. Das Experiment wurde von Tsuji und Nagano durchgeführt [7]. Die Meβdaten sind im Internet verfügbar [8]. In dem Experiment wurde die Temperatur der 4m hohen, 0,5m breiten und 2mm dicken Wand räumlich und zeitlich konstant auf 60°C gehalten. Die Temperatur der umgebenden Luft ist ungefähr 16°C. Die Messungen wurden in vier verschiedenen Höhenebenen durchgeführt: z=1,44 m, z=1,92 m, z=2,54 m und z=3,24 m. In diesem gesamten Bereich ist die Strömung turbulent. Die Meßebene z=1,44 m wird als Eintrittsebene für das zweidimensionale Rechengebiet (81x250 Maschen) benutzt. Das Rechengitter endet mit der Ebene z=3,94 m. In der z-Richtung ist das Gitter regelmäβig mit einer Maschenweite von Δz=1 cm geteilt. Die Größe der Maschen senkrecht zur Wand erstreckt sich von 0,1 mm (Wandnähe) bis 1,5 mm.

Die Rechnung mit den neuen Modellierungen stimmt sehr gut mit den Meßwerten der mittleren Geschwindigkeit und Temperatur überein (siehe Abb. 1 und 2). Die Ergebnisse für die turbulente kinetische Energie und den vertikalen turbulenten Wärmefluß sind nicht zufriedenstellend, sie sind aber besser als die Ergebnisse mit den alten Standard-Modellierungen (siehe Abb. 3 und 4). Der Vergleich mit experimentellen Daten zeigt, daß eine weitere Verbesserung der Übereinstimmung bezüglich dieser Turbulenzgrößen weitere Modellverbesserungen erfordert. Dennoch wurde bereits mit den eingebrachten neuen Modellen der Gültigkeitsbereich des TMBF erweitert und verbessert, so daß kerntechnische Problemstellungen zur einphasigen Naturkonvektion in verschiedenen neu konzipierten Reaktoranlagen mit FLUTAN mit weiter verbesserter Genauigkeit untersucht werden können.

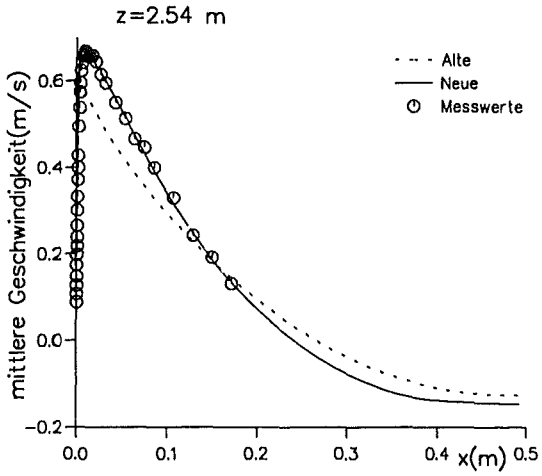

Abb.1: Profil der Vertikalgeschwindigkeit

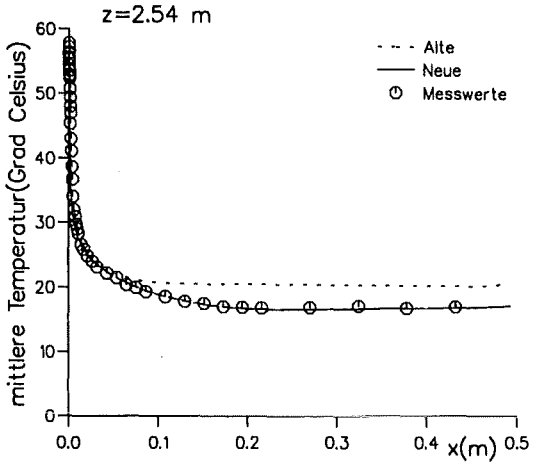

Abb.2: Profil der mittleren Temperatur $\overline{T}$

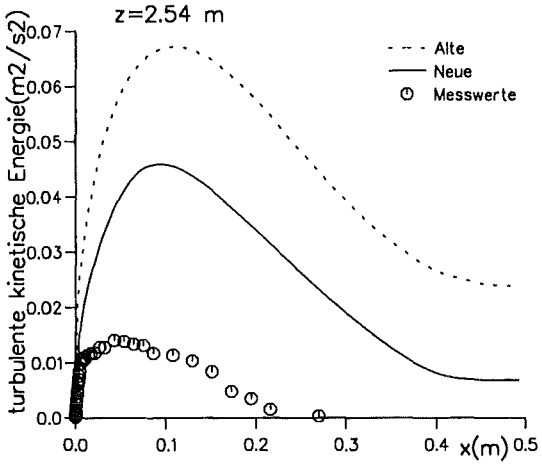

Abb.3: Profil der turb. kin. Energie k

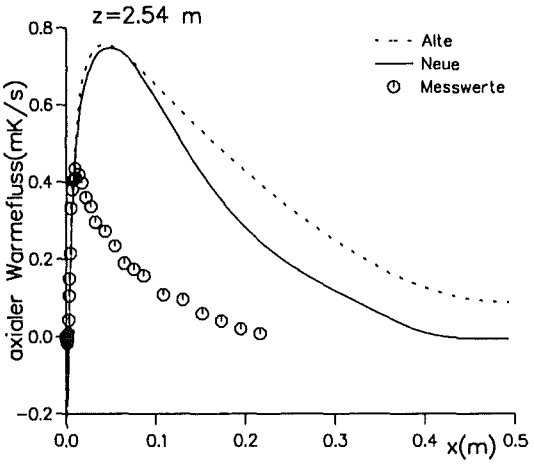

Abb.4: Profil des vertikalen turbulenten Wärmeflusses

Das in FLUTAN implementierte implizite Verfahren zur lokalen Verfeinerung (LGV) in einem strukturierten Gitter [4] wurde weiter untersucht [9]. Mit der lokalen Gitterverfeinerung können die Maschen verfeinert werden, die direkt durch eine starke lokale Änderung der abhängigen Variablen betroffen sind. Dieses Verfahren erlaubt prinzipiell eine optimale Auflösung und bietet auch eine sehr effiziente Möglichkeit, ein lokales Ereignis auf einem strukturierten Gitter adäquat aufzulösen.

Die LGV wurde in dieser Arbeit auf den Fall einer komplexen Geometrie in Naturkonvektion angewendet. Als Beispiel wurde eine Nachrechnung des zweidimensionalen Experimentes SUCOS-2D ausgewählt [10]. In der Abbildung 5 sind die verfeinerten Gebiete im zweidimensionalen Gitter dargestellt. Dabei wurden die Temperatur- und Geschwindigkeitsgrenzschicht lokal verfeinert, Gebiete also, in denen hohe Geschwindig-

keits- und Temperaturgradienten vorhanden sind. Durch die Anwendung der LGV wurde eine bessere Übereinstimmung mit den Meßwerten von SUCOS in wichtigen Gebieten des Experiments erreicht, wo die Temperatur und Geschwindigkeitsgrenzschichten besser aufgelöst werden. Der berechnete Wert der Sumpftemperatur unterhalb des schrägen Sumpfdaches, die das Experiment charakterisiert, liegt mit 31°C mit der lokalen Gitterverfeinerung näher an dem experimentellen Wert von 28,3°C als der berechnete Wert von 34°C ohne lokaler Gitterverfeinerung (siehe Abbildung 6). Die Rezirkulation unter dem rechten Rand des linken Kamins (dieses Gebiet wird lokal verfeinert) wird mit der LGV ausgeprägter simuliert als ohne LGV (siehe Abbildung 7). Damit sind mit lokaler Gitterverfeinerung mit wesentlich weniger Maschen ähnlich genaue Ergebnisse erzielbar, wie ohne lokaler Gitterverfeinerung auf wesentlich feineren Gittern. Dies beweist, daß bei technischen Strömungen, wie der Naturkonvektion in SUCOS, durch die LGV eine wesentliche numerische Effizienzsteigerung erzielt werden kann. Die Untersuchung hat allerdings auch gezeigt, daß die Implementierung der LGV noch vervollständigt werden muß.

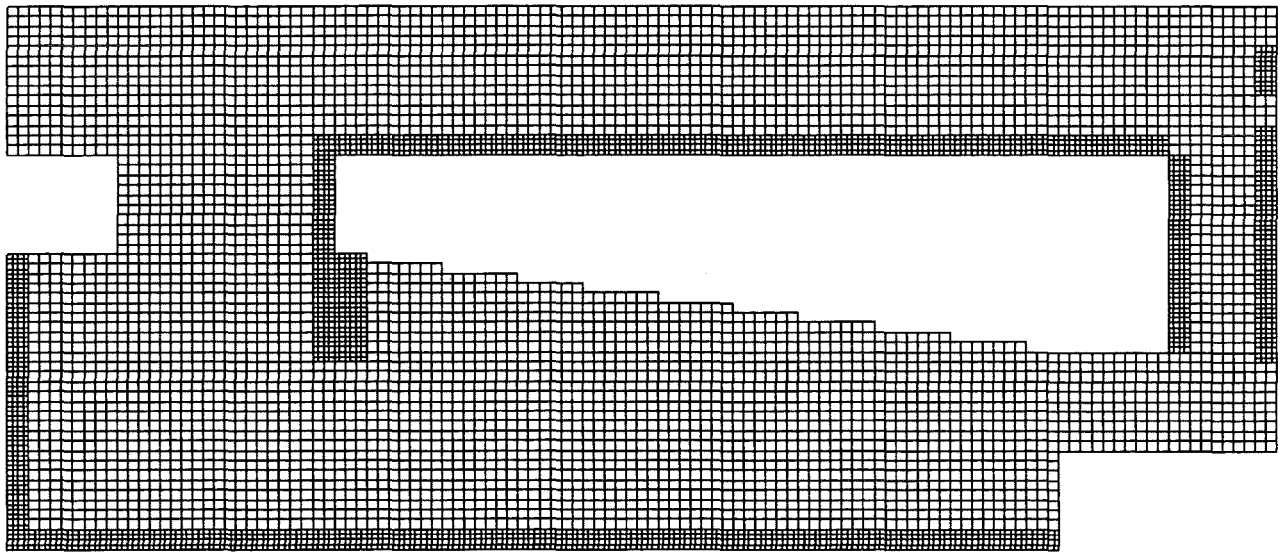

Abb. 5: Die verfeinerten Gebiete im Gitter für ein SUCOS-2D Experiment.

Im Rahmen einer Doktorarbeit, die von SIEMENS-KWU finanziert wird, wird ein Verfahren zur Diskretisierung der Transportgleichungen in komplexen Geometrien mit Hilfe von körperangepaßten Koordinaten entwickelt [11]. Damit soll eine effiziente und genaue Lösung bei der Gestaltung krummliniger Oberflächen, die bisher in FLUTAN nur durch

stufige Ränder modelliert werden können, angestrebt werden. Die Stufendarstellung ist aus Genauigkeitsgründen zu vermeiden. Das vorgeschlagene Verfahren stellt eine dreidimensionale Koordinatentransformation für das Gleichungssystem in FLUTAN dar. Dabei wird ein versetztes nichtorthogonales Gitter verwendet. Die kartesischen Geschwindigkeitskomponenten wurden aufgrund ihrer Anschaulichkeit und leichteren Diskretisierung der transformierten Transportgleichungen eingesetzt. Alle drei kartesischen Geschwindigkeitskomponenten werden an jeder Oberfläche eines Kontrollvolumens aus den dazugehörigen Impulsgleichungen berechnet. Der Vorteil bei diesem Verfahren ist, daß die in einem krummlinigen Koordinatensystem auftretenden zusätzlichen Terme in den Transportgleichungen für Impuls, Energie und Turbulenzgrößen nicht auftreten. Außerdem paßt sich diese Methode dem vorhandenen Rechenalgorithmus und der Datenstruktur in FLUTAN gut an. Die bei diesem Verfahren notwendigen krummlinigen, nichtorthogonalen Gitter werden von CFX-Meshbuild generiert. Es wurde ein Konvertierungsprogramm entwickelt, das eine mit dem blockstrukturierten CFX-Meshbuild generierte Geometrie in eine von FLUTAN gelesene Geometrie umsetzt.

In Zusammenarbeit mit HIK wird die Möglichkeit einer weiteren Beschleunigung des Rechenprogramms und besonders einer Erweiterung des nutzbaren Speichers durch eine

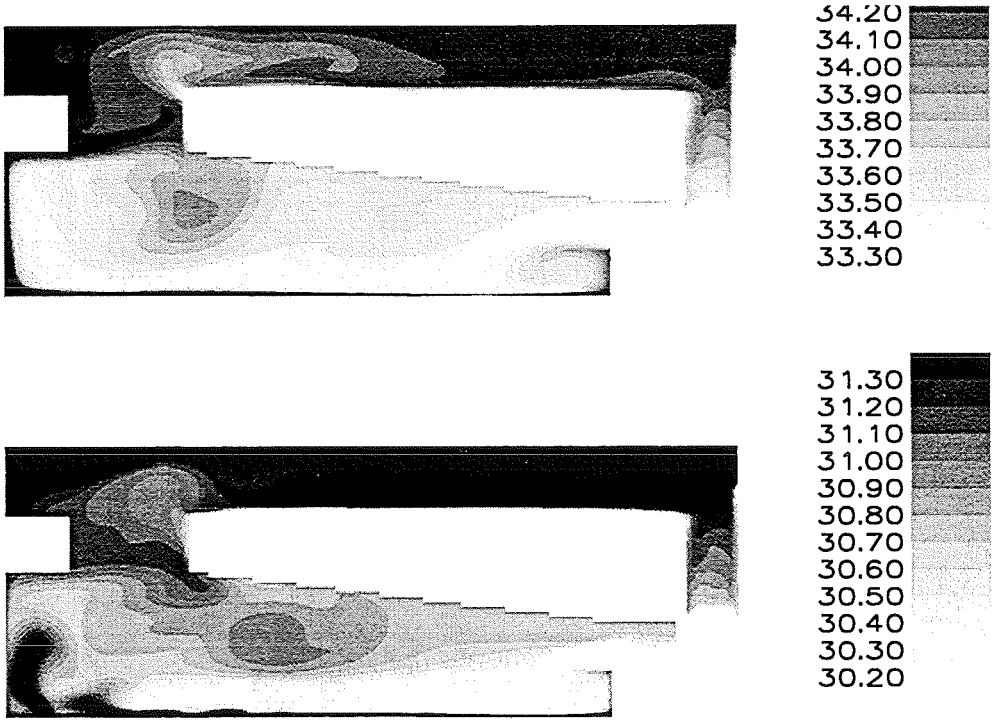

Abb.6: Temperaturfelder bei einer transienten Rechnung im ganzen Gebiet ohne lokaler Verfeinerung (oben) und mit lokaler Verfeinerung (unten).

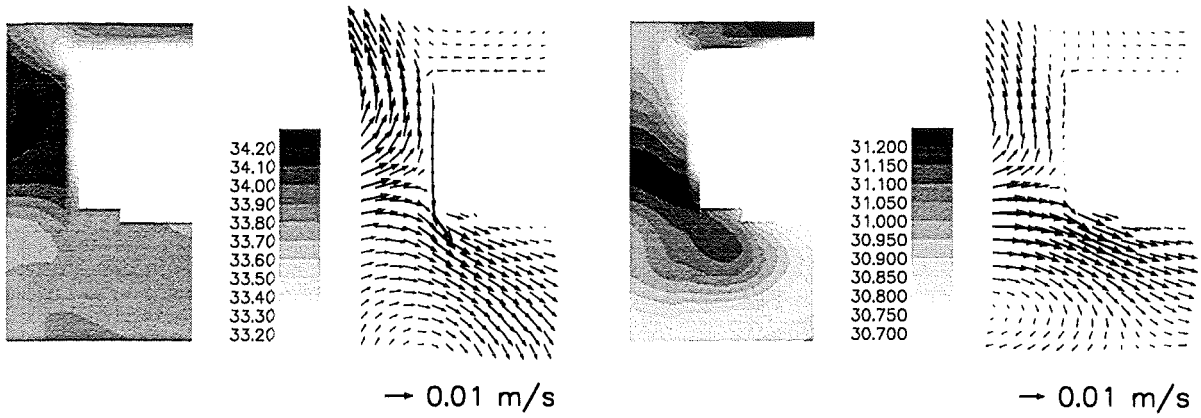

Abb.7: Temperatur- und Geschwindigkeitsfelder ohne lokaler Verfeinerung (links) und mit Verfeinerungsgrad 1 (rechts) am rechten Rand des linken Kamins.

Parallelisierung des FLUTAN-Programms mit High Performance FORTRAN untersucht. Wegen der Datenstruktur des hochgradig vektorisierten FLUTAN-Programms und Unzulänglichkeiten der verfügbaren Compiler gestalten sich diese Arbeiten äußerst schwierig.

Das Rechenprogramm FLUTAN soll auch für die numerische Analyse der Kühlungsmöglichkeiten in Tanks von beschleunigergetriebenen unterkritischen Anordnungen (32.23.03) angewendet werden. Dafür muß die in FLUTAN implementierte Stoffdatenbibliothek um die Stoffdaten für Blei ergänzt werden. Die von K. Thurnay, INR, zusammengestellten Stoffdaten für flüssiges Blei wurden programmiert und getestet. Das Programmpaket umfaßt die Stoffdaten für die Dichte, spezifische Wärme, Wärmeleitfähigkeit und Viskosität. Die Daten sind auf das Molgewicht bezogen; die in Polynomform gegebenen Daten hängen von der Enthalpie ab, sind jedoch unabhängig vom Druck. Die Implementierung der erweiterten Stoffdatenbibliothek in FLUTAN wurde mit einer Überprüfung abgeschlossen.

Damit wurde im Berichtszeitraum folgender Stand erreicht: Das FLUTAN-Rechenprogramm wird für die Analyse der Nachwärmeabfuhr in neu konzipierten Reaktorsystemen eingesetzt und ist für die Analyse der Kühlungsmöglichkeiten in Tanks von beschleunigergetriebenen unterkritischen Anordnungen vorbereitet. In diesem Bericht wurde die Entwicklung und die Validierung der folgenden physikalischen und numerischen Modelle diskutiert :

- Ein Turbulenzmodell für Auftriebsströmungen wurde für Naturkonvektion erweitert und validiert;
- Ein implizites Verfahren zur lokalen Gitterverfeinerung wurde für den Fall einer komplexen Geometrie in Naturkonvektion ausgetestet. Als Beispiel wurde das zweidimensionale Experiment SUCOS-2D ausgewählt.
- Ein Konzept zur Diskretisierung der Transportgleichungen in komplexen Geometrien mit Hilfe von körperangepaßten Koordinaten wurde entwickelt und wird derzeit realisiert.

B. Numerische Simulation turbulenter Naturkonvektion

Die Arbeiten am Rechenprogramm TURBIT zur numerischen Simulation von Turbulenz in Kanalströmungen dienen dazu, die im Rechenprogramm FLUTAN verwendeten Turbulenzmodelle auf eine breitere Basis zu stellen. Insbesondere soll mit Hilfe der Simulationsergebnisse der Anwendungsbereich von Turbulenzmodellen auf Naturkonvektion in verschiedenen Fluiden methodisch erweitert und überprüft werden.

Die von TURBIT mit der Methode der direkten numerischen Simulationen (DNS), bei der alle Skalen von Geschwindigkeits- und Temperaturfeld durch das Maschennetz aufgelöst werden, für Rayleigh-Bénard-Konvektion in verschiedenen Fluiden und für die Konvektion in einer Fluidschicht mit volumetrischer innerer Wärmequelle zuvor bereitgestellte Datenbasis wurde weiter ergänzt [12] und analysiert [13]. Basierend auf der Zweipunkt-Korrelationstechnik wurde für den molekularen Vernichtungsterm $\varepsilon_{U_3'T'}$ in der Transportgleichung des vertikalen turbulenten Wärmeflusses, der in gängigen statistischen Turbulenzmodellen für Naturkonvektion eine wichtige Rolle spielt, ein zuvor auf empirischer Basis aus den DNS-Daten abgeleitetes Modell [5] analytisch begründet und weiter verbessert [14]. Das vorgeschlagene Modell setzt sich aus zwei Anteilen zusammen. Der inhomogene Anteil berücksichtigt unmittelbar den Einfluß fester Wände, ohne - wie sonst in Modellen aus der Literatur üblich - komplizierte empirische Wandkorrekturfunktionen einzuführen. Der homogene Anteil des Modells lehnt sich an existierende Modelle an, geht aber insofern über diese hinaus, als dem Einfluß der Stoffeigenschaften des Fluides und der Turbulenzintensität Rechnung getragen wird. Die Abbildung vergleicht für

Rayleigh-Bénard-Konvektion in Luft das mit dem neuen Modell vorhergesagte Profil von $\varepsilon_{U_3'T'}$ mit den DNS Daten. Es ist ersichtlich, daß das neue Modell insbesondere den komplexen Verlauf von $\varepsilon_{U_3'T'}$ in Wandnähe sehr gut wiedergibt.

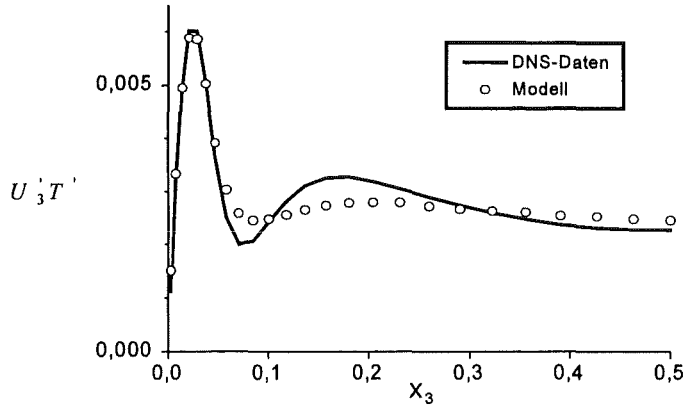

Abb.8: Dissipationsterm $\varepsilon_{U_3'T'}$ in der Gleichung für den vertikalen turbulenten Wärmestrom über dem dimensionslosen Wandabstand x_3. Vergleich von Modell (o) mit DNS-Daten (—) für Rayleigh-Bénard-Konvektion in Luft.

Die 1997 im World Wide Web eingerichtete DNS Datenbank zur Naturkonvektion in horizontalen Fluidschichten wurde aktualisiert und um Ergebnisse zur Fluidschicht mit interner Wärmequelle erweitert. Die Ergebnisse stehen damit der Fachwelt unter der Adresse http://www.fzk.de/irs/turbit zur Verfügung. Sie werden als Vergleichs- und Verifikationsdaten für Rechnungen mit statistischen Turbulenzmodellen verwendet.

Die Weiterentwicklung von TURBIT konzentrierte sich auf die Bereitstellung von weiteren Analysemöglichkeiten und auf das Postprocessing der Daten

C. Theoretische Untersuchungen für turbulente Zweiphasenströmungen

Ziel dieses Vorhabens ist die Bereitstellung von numerischen Methoden und physikalischen Modellen, mit denen lokale Vorgänge in turbulenter Zweiphasenströmung unter Einbeziehung der Information über die zeitliche Entwicklung der Phasengrenze detailliert simuliert werden können. Die Arbeiten bauen zunächst auf grundlegenden Untersuchungen zu turbulenten Blasenströmungen auf. Die Ergebnisse und Erfahrungen werden verwendet, um die Methode und physikalischen Modelle mittelfristig in

anwendungsorientierten Rechenprogrammen für allgemeine Zweiphasenströmungen verfügbar zu machen.

Die neue Methode für die numerische Berechnung von Zweiphasenströmung stellt eine Erweiterung des von einphasigen Strömungen her bekannten Konzeptes der Grobstruktursimulation [15] dar. Die generelle Konzeption der Methode und die Grundzüge der mathematischen Formulierung wurden u.a. bereits im letzten Jahresbericht vorgestellt [10,16]. Wesentlich ist, daß für den durch das Rechengitter aufgelösten Anteil eine lokale, momentane Beschreibung von Turbulenz und Evolution der Phasengrenzfläche erfolgt. Im Vergleich zu dem aktuell in der Literatur am häufigsten eingesetzten Zwei-Fluid Modell ergibt sich der Vorteil, daß die Strömungsform, d.h. die Art der topologischen Verteilung der Phasen, ein Ergebnis der Simulation ist. Damit muß die Strömungsform nicht mehr bereits a priori zwecks Auswahl geeigneter physikalischer Modelle für die Austauschprozesse zwischen den Phasen bekannt sein.

Im Berichtszeitraum stand die Realisierung der Methode in Rechenprogrammen im Vordergrund. Diese konzentriert sich dabei in einem ersten Schritt auf den methodischen Grenzfall eines sehr feinen Rechengitters, bei dem sowohl die kleinsten Wirbel als auch die kleinsten Blasen aufgelöst werden („DNS-RBS" = direct numerical simulation - resolved bubble simulation). Die Realisierung im Rechenprogramm TURBIT-VoF (VoF = Volume of Fluid Methode zur Verfolgung und Rekonstruktion der Phasengrenzfläche) ist weit fortgeschritten. Da bei praxisrelevanten Phasenpaarungen wie z.B. Wasser-Luft große Dichteunterschiede auftreten, sind an das numerische Verfahren besondere Anforderungen zu stellen. Es wird ein hochauflösendes Verfahren (E-ENO) implementiert, das zum einen eine unphysikalische Verschmierung der Phasengrenze vermeidet, und andererseits auch in einphasigen Bereichen der Strömung die für eine numerische Simulation der Turbulenz notwendige Genauigkeit sicherstellt. Zur Integration der Gleichungen in der Zeit wurde ein 3. Ordnung Runge-Kutta-Verfahren implementiert, dessen Genauigkeitsordnung bei Bedarf recht einfach erhöht werden kann.

Zur Beschreibung der zeitlichen Entwicklung der Phasengrenzfläche und deren numerischen Rekonstruktion im Rahmen der Volume-of-Fluid Methode wurde der EPIRA - Algorithmus [17] entwickelt und in TURBIT-VoF programmiert. EPIRA steht für „Exact Plane

Interface Reconstruction and Advection". Wie der Name andeutet, wird mit diesem Algorithmus eine die Phasengrenzfläche repräsentierende Ebene, die im Rechengitter beliebig orientiert sein kann, von EPIRA stets exakt rekonstruiert und mit dem Geschwindigkeitsfeld advektiert. Testrechnungen mit EPIRA für die Advektion einer sphärischen Einzelblase in einem gleichförmigen Geschwindigkeitsfeld zeigen, daß das Verfahren absolut Volumenerhaltend ist. Abb. 9 (links) verdeutlicht, daß bei einer Auflösung von nur acht Maschen pro Blasendurchmesser die Blase nach 160 Zeitschritten merklich von der Kugelform abweicht. Bei einer Verdopplung der Auflösung (Abb. 9, rechts) ergibt sich dagegen nach dann 360 Zeitschritten ein nur sehr geringer Fehler.

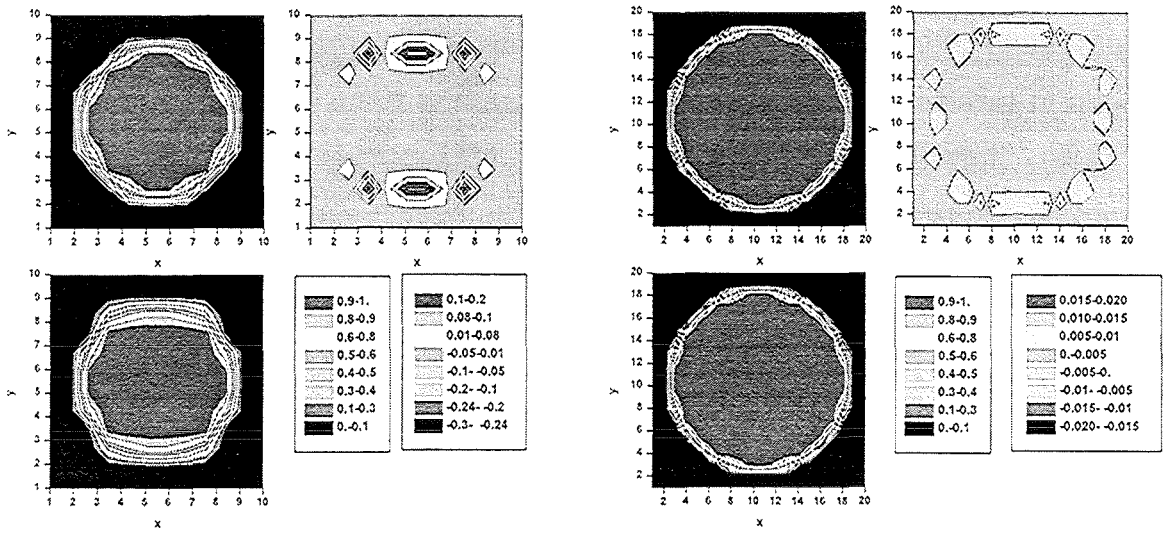

Abb. 9: Advektion einer Blase mit EPIRA. Blasendurchmesser *d* aufgelöst mit 8 Maschen (linke Abb.-Hälfte) bzw. mit 16 Maschen (rechte Abb.-Hälfte). Oben links: Anfangsverteilung der Volumenfraktion in der Mittelebene; unten links: Volumenfraktion nach Advektion um 10 *d* entsprechend 160 bzw. 320 Zeitschritten (jeweils linke Farbskala); oben rechts: Differenz der Volumenfraktionen (jeweils rechte Farbskala).

Im Gegensatz zu EPIRA können gängige dreidimensionale Rekonstruktionsverfahren aus der Literatur ebene Phasengrenzflächen nicht in allen Fällen richtig rekonstruieren. Die verbesserte Rekonstruktion mit EPIRA bietet somit die Möglichkeit bei bestimmter Genauigkeit eine einzelne Blase effektiv mit weniger Maschen zu diskretisieren, oder andererseits in einem Gitter mit einer bestimmten Maschenanzahl die Wechselwirkung einer größeren Anzahl von Blasen zu untersuchen. Die Entwicklung von EPIRA ist damit ein wichtiger Baustein zur Durchführung von numerischen Simulationen von Blasen-

schwärmen mit TURBIT-VoF. Die verbesserte Genauigkeit der Phasengrenzflächen-Rekonstruktion mit EPIRA kann desweiteren für eine verbesserte Beschreibung der Oberflächenspannungskräfte ausgenutzt werden.

Zur Zeit werden die verschiedenen Programmerweiterungen zur Realisierung der Methode weiter ausgetestet. Nach erfolgreichem Abschluß dieser Phase sind Anwendungsrechnungen zu Einzelblasen mit unterschiedlicher Form und unterschiedlichem Aufstiegsverhalten geplant. Der Vergleich mit entsprechenden experimentellen Ergebnissen dient der Verifikation und Validierung der Methode, und der Vorbereitung von Simulationen für komplexere Blasenströmungen.

Die Realisierung der allgemeinen Grobstruktursimulationsmethode für Zweiphasenströmungen in technisch interessierenden Behältern und Kanälen erfolgt im Umfeld des kommerziellen Softwarepakets CFX. Die hierzu notwendigen methodischen Erweiterungen und physikalischen Modelle werden über benutzereigene Unterprogramme an das CFX Basispaket angebunden, das im wesentlichen als Gleichungslöser dient. Analog zu TURBIT-VoF und unter Verwendung der dort gewonnenen Erfahrungen wird zunächst die „DNS-RBS"-Methode realisiert, bevor zum allgemeinen, technisch relevanten Fall übergegangen wird, bei dem eine Aufteilung von Turbulenz und Phasengrenzfläche in einen durch das Rechengitter aufgelösten und einen sogenannten Feinstrukturanteil vorgenommen werden muß. Neben anderen Erweiterungen wurde insbesondere der zweidimensionale FLAIR-Algorithmus zur Verfolgung und Rekonstruktion der Phasengrenze an CFX gekoppelt. Aufgrund des Abganges eines Mitarbeiters aus dem Team sind die entsprechenden Arbeiten langsamer vorangeschritten als ursprünglich geplant.

Für die neue Methode der Grobstruktursimulation von Zweiphasenströmungen ergibt sich ein Bedarf an neuen lokalen physikalischen Modellen. Die für die Entwicklung solcher Modelle notwendigen Daten sollen zum Teil aus Experimenten gewonnen werden; die Anforderungen an geeignete Experimente wurden formuliert. Zum anderen Teil werden die Daten aus analytischen und numerischen Betrachtungen abgeleitet, siehe unten. In einem ersten Schritt werden aus integralen Betrachtungen abgeleitete Modelle eingeführt, die bei Vorliegen der experimentellen Informationen zu verfeinern sind.

In engem Zusammenhang mit diesem Forschungsvorhaben steht ein gemeinsames Forschungsprojekt zwischen IRS und der Fakultät für Luft- und Raumfahrttechnik der Polytechnischen Universität Bukarest. Von den rumänischen Partnern wurde, basierend auf den analytischen Methoden der Potentialtheorie und der Grenzschichttheorie, ein Rechenprogramm entwickelt, das die Blasenform in Abhängigkeit verschiedener physikalischer Einflußgrößen unter der Annahme rotationssymmetrischer Blasen berechnet. Derzeit wird das Programm um die Berechnung des Geschwindigkeitsfeldes erweitert. Damit wird ein Werkzeug verfügbar, das insbesondere zur Entwicklung von physikalischen Modellen für die lokale Relativgeschwindigkeit beider Phasen geeignet ist. In einem zweiten Themengebiet werden theoretische Ansätze zur Formulierung von Feinstrukturmodellen für turbulente Blasenströmungen untersucht. Schließlich wird vom Forschungspartner ein Rechenprogramm entwickelt, das durch die Verwendung unstrukturierter und dynamisch verfeinerter Gitter eine vollständige Beschreibung der Vorgänge an Blasenoberflächen in turbulenter Strömung zum Ziel hat. Auch hier wird angestrebt, mittels Simulationen mit dem Programm die aus Experimenten [18] nur schwerlich beschaffbaren Informationen bereitzustellen. Diese werden dann zur Entwicklung von physikalischen Modellen eingesetzt, die schließlich in die Methode der Grobstruktursimulation von Zweiphasenströmungen einfließen werden.

Literatur

1 G. Willerding, W. Baumann,
FLUTAN 2.0 - Input Specifications.
Forschungszentrum Karlsruhe, FZKA 5712, Mai 1996

2 W. Baumann, L. N. Carteciano, D: Weinberg,
Thermal propagation effects in a vertical turbulent flow behind a jet block – A benchmark exercise.
Journal of Hydraulics Research, special issue of Section II.3: Fluid Phenomena in Energy Exchanges, 1997, Vol. 35, pp. 843-864

3 L. N. Carteciano, D. Weinberg, U. Müller,
Development and Analysis of a Turbulence Model for Buoyant Flows.
Proc. of the 4th World Conf. on Experimental Heat Transfer, Fluid Mechanics and Thermodynamics, Brussels, Belgium, June 2-6, 1997. Vol. 3, pp. 1339-46. Pisa Edition ETS.

4 T. Ammann,
An implicit method for the local refinement of a structured grid.
GAMM Jahrestagung, 6.-9. April 1998, Bremen, Abstract in Internet http://www.zarm.uni-bremen.de/gamm98/num_abs/a517.html

5 Q.-Y. Ye, M. Wörner, G. Grötzbach,
Modelling Turbulent Dissipation Correlations for Rayleigh-Bénard Convection Based on Two-point Correlation Technique and Invariant Theory,
Forschungszentrum Karlsruhe, FZKA 6103, 1998.

6 C. Prudhomme,
Validierung eines Turbulenzmodells für Auftriebströmungen in Naturkonvektion.
Diplomarbeit, Inst. für Kerntechnik und Reaktorsicherheit, Univ. Karlsruhe, 1998.

7 T. Tsuji, Y. Nagano,
Turbulence Measurements in a Natural Convection Boundary Layer along a Vertical Flat Plate,
Int. J. Heat Mass Transfer, 10 (1988), pp. 2101-2111.

8 ERCOFTAC Fluid Dynamics Database, http://www.fluindigo.mech.surrey.ac.uk.

9 M. Grumler,
Validierung eines impliziten Verfahrens zur lokalen Verfeinerung eines strukturierten Gitters.
Diplomarbeit, Inst. für Kerntechnik und Reaktorsicherheit, Univ. Karlsruhe, 1998.

10 G. Grötzbach, M. Wörner, A. Blahak, L. Carteciano, B. Dorr, W. Olbrich, W. Sabisch, Q. Ye, Alef, St. Genz, G. Janßen, M. Linder, N. Lehmann, A. Müller, D. Seldner, X. Jin,
Entwicklung von Thermofluiddynamikprogrammen und ingenieurtechnische Anwendungen,
Projekt Nukleare Sicherheitsforschung, Jahresbericht 1997, Forschungszentrum Karlsruhe, FZKA 6126, September 1998, pp. 486 - 504

11 X.Z. Jin,
Konzept zur Realisierung körperangepaßter, nichtorthogonaler Gitter in FLUTAN.
Forschungszentrum Karlsruhe, Interner Berich, IRS Nr. 20/98, PSF Nr. 3314

12 Bunk, M., Wörner, M.,
Direkte numerische Simulation turbulenter Rayleigh-Bénard-Konvektion in Quecksilber.
FZKA 5915, Forschungszentrum Karlsruhe, April 1998

13 M. Wörner, G. Grötzbach,
Pressure transport in direct numerical simulations of turbulent natural convection in horizontal fluid layers, International Journal of Heat and Fluid Flow, Vol 19, pp. 150-158, 1998.

14 M. Wörner, Q.-Y. Ye, G. Grötzbach,
Consistent modelling of fluctuating temperature-gradient-velocity-gradient correlations for natural convection, Proc. 4th Int. Symp. on Engineering Turbulence Modelling and Measurements, 24.-26. Mai 1999, Corsica, France.

15 Grötzbach, G., Wörner, M.,
Direct numerical and large eddy simulations in nuclear applications.
2nd Engineering Foundation Conference in Turbulent Heat Transfer, May 31 – June 4, 1998, UMIST and University of Manchester, Vol. II, pp. 8-31 – 8-48

16 W. Sabisch, M. Wörner, G. Grötzbach, D. G. Cacuci,
Methode und erste Ergebnisse zur Direkten Numerischen Simulation von Blasen mit TURBIT-VOF.
Tagung des Fachausschusses Mehrphasenströmungen der Gesellschaft für Verfahrenstechnik und Chemieingenieurwesen (GVC), Bad Kissingen, 1.-3. März 1999

17 W. Sabisch, M. Wörner, G. Grötzbach, D.G. Cacuci,
An Improved Volume of Fluid Method for Numerical Simulation of Clusters of Bubbles, Proc. 9th Workshop on Two-phase Flow Predictions, 13.-16. April 1999, Halle, Deutschland.

18 W. Cherdron, G. Grötzbach, M. Samstag, W. Sengpiel, M. Simon, I. Tiseanu,
Experimental Investigations of Air/Water Bubbly Flow in Vertical Pipes.
Third International Conference on Multiphase Flow, Lyon, June 8 - 12, 1998, Proc. on CD-ROM.

II. Experimentelle Untersuchungen von Wechelwirkungsmechanismen und Phasentransportprozessen in Zweiphasenströmungen

(J. Aberle, W. Cherdron, G. Grötzbach, V. Heinzel, P. Philipp, H. Sauter, W. Sengpiel, M. Simon, I. Tiseanu, IRS)

Einleitung

Zweiphasenströmungen kommen in vielen energietechnischen Einrichtungen oder verfahrenstechnischen Apparaten vor. Für deren Auslegung werden Rechenprogramme eingesetzt, die Vorhersagen über den Druckverlust und den Wärmeübergang liefern. Diese benötigen vorab Eingaben über die zu erwartenden Strömungsformen bzw. Phasenverteilungen. Eines der Vorhaben im Institut betrifft daher die Entwicklung eines Rechenprogramms zur Grobstruktursimulation von turbulenten Strömungen und in Fortsetzung von turbulenten Zweiphasenströmungen, um u. a. die Phasenverteilungen bestimmen zu können (siehe Teil I dieses Vorhabens). Die Vorgehensweise bei der Programmentwicklung sieht eine Wechselwirkung mit experimentellen Arbeiten vor. Diese sind einmal Beobachtungen der Blasen- oder Gasverteilungen in vertikalen Rohrströmungen mit Luft/Wasser. Neu aufgenommen wurden Untersuchungen an Einzelblasen im Pool d. h. in ruhender Flüssigkeit. Die Arbeiten im Berichtsjahr betrafen vor allem die Entwicklung von geeigneten Meß- und Beobachtungstechniken.

Entwicklung und Anwendung eines hochauflösenden 3D-Röntgen-Computertomographen zur Analyse von Zweiphasenströmungen

An der vertikalen Meßstrecke des TWOFLEX-I Kreislaufs wurden die Gas- oder Blasenverteilung in radialer und axialer Richtung mittels eines im Institut früher entwickelten Röntgentomographen [1] in vertikalen auf- und abwärts gerichteten Rohrströmungen vermessen. Der Tomograph besteht aus einer Röntgenquelle und einem Detektor, die sich auf einer gemeinsamen Plattform um das Meßrohr drehen. Aus der Intensität bzw. Schwächung der Röntgenstrahlen nach Durchgang durch die Meßstrecke wird nach Umfahren eines Umfangswinkels von 220° die Gasverteilung in der Strömung berechnet. Der

Tomograph ist ein nicht-invasives Meßinstrument, das die zeitlich gemittelte Gasverteilung bestimmt.

Der bereits genannte 2D-Röntgentomograph besitzt bedingt durch die Konstruktion der Detektoren und die mechanische Konstruktion der Drehplattform eine Begrenzung bezüglich der örtlichen Auflösung. Weiter ist die Dichteauflösung limitiert durch die 12 Bit AD-Wandlung der Datenerfassung. Untersuchungen der lokalen Gasverteilung in aufwärts gerichteten Blasenströmungen [2] haben gezeigt, daß steile Gradienten der Gasverteilung eine Auflösung im Submillimeterbereich erfordern. Aus diesem Grund wurde ein neuer Tomograph mit einer hohen örtlichen Auflösung entwickelt.

In dem Tomographen kommt ein digitaler Flächendetektor aus amorphem Silizium mit 512*512 Pixeln und einer Größe von 20*20 cm^2 zum Einsatz. Dies ermöglicht eine direkte 3D-Rekonstruktion der Dichteverteilung der Strömung innerhalb des Strahlkegels. Eine Röntgenquelle mit Maximalwerten von 160 kV und 10 mA erlaubt den zukünftigen Einsatz in Strömungen in Metallrohren. Der Detektor befindet sich zusammen mit einer Röntgenquelle auf einer Plattform, die sich um 360° um das Rohr dreht (Abbildung 1). Als Voraussetzung für eine hohe Ortsauflösung wurde die Rotationsplattform so konstruiert, daß ein präziser Umlauf mit geringen Toleranzen gewährleistet ist.

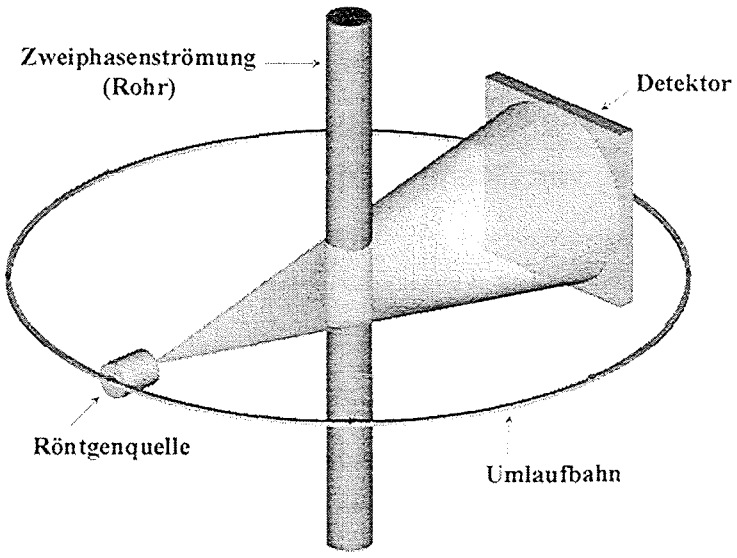

Abbildung 1: Prinzipskizze des 3D-Tomographen

Die Umlaufzeit ist zwischen 30 und 300 Sekunden einstellbar, um die zeitliche Mittelung an die Bedingungen der Strömung anpassen zu können. Dabei werden 200-300 Projektionen für ein Tomogramm aufgezeichnet. Abbildung 2 zeigt ein Foto des Tomographen. Es wurde eine Software für die Meßdatenerfassung und für die 3D-Rekonstruktion entwikkelt.

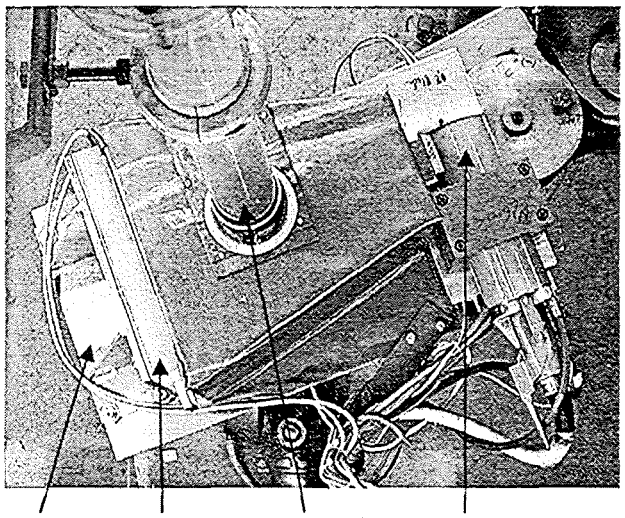

Abbildung 2: Röntgen-Tomograph zur Analyse von Blasenströmungen

Die Auflösung und Genauigkeit des Tomographen wurde durch Testkörper aus verschiedenen Materialien überprüft. Abbildung 3 zeigt die Zeichnung des zylindrischen Testkörpers aus Polyethylen mit Bohrungen. Im oberen Teil des Körpers befindet sich außen ein Aluminiumring, der zum einen zur Überprüfung von hohen Dichtegradienten dient und zum anderen die Fähigkeit des Tomographen zur Erfassung von Hohlräumen innerhalb von Metallrohren unter Beweis stellt. Ergebnisse von Rekonstruktionen von Daten des früheren Tomographen wurden zusammen mit Analysen der Gesamtverteilung in turbulenter Blasenströmung in [3] dokumentiert. Die 3D-Rekonstruktionen aus Messungen mit dem neuen Tomographen in Abbildung 4 zeigen, daß sowohl die Geometrie als auch das Material korrekt erfaßt werden.

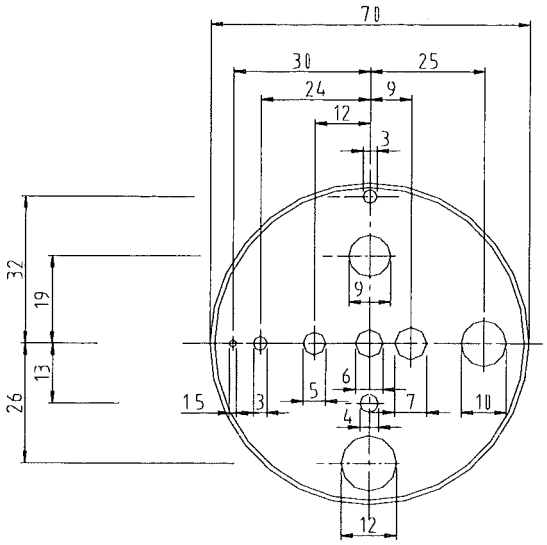

Abbildung 3: Testkörper aus Polyethylen

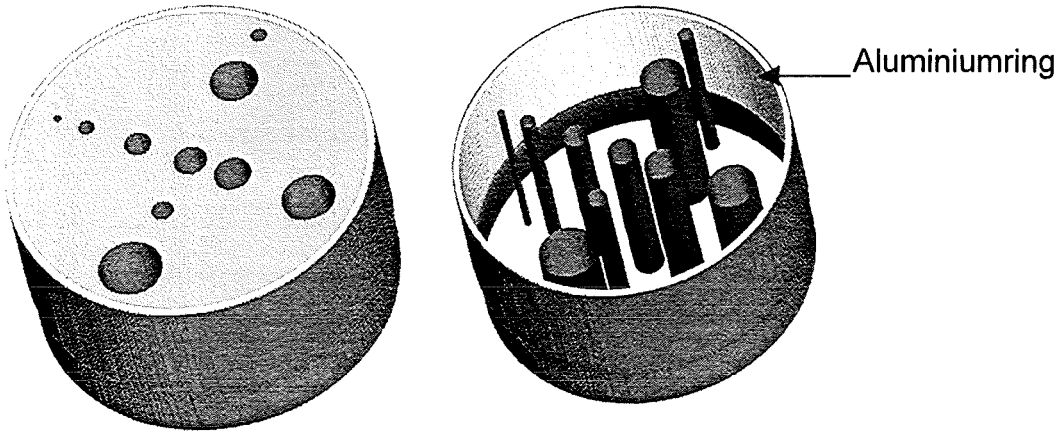

Abbildung 4: 3D-Rekonstruktion des Testkörpers: Isovolumen- und Isoflächendarstellung. Aluminium ist weiß-grau hervorgehoben, die Grenzfläche Material/Luft ist schwarz

Mit Hilfe solcher Probekörper wurde eine räumliche Auflösung von 0.4 mm nachgewiesen. Die Rekonstruktion und bildliche Darstellung des Probekörpers in Abbildung 4 legen die Fähigkeit der entwickelten Software zur Umsetzung der Detektorsignale und Bildanalyse zu einem 3D-Bild dar. Somit ist der Tomograph zur präzisen Bestimmung der lokalen Gasverteilung mit hoher Gaskonzentration geeignet. Entsprechend wurden Messungen in der TWOFLEX-I-Anlage in einem senkrechten Rohr aus Plexiglas mit einem Innendurchmesser von 70 mm und einer Länge von 5 m durchgeführt. Abbildung 5 zeigt die lokale Gasverteilung einer nach oben gerichteten Blasenströmung in einem Rohr in einer Meßebene ca. 3 m oberhalb des Blasengenerators. Ein radialer Blasentransport zur Rohrwand

aufgrund von Kutta-Joukowski-Kräften führt zu einem ausgeprägten Peak in der Nähe der Rohrwand. Der maximale lokale Gasgehalt beträgt das achtfache des mittleren volumetrischen Gasgehaltes. Das Ergebnis macht die Notwendigkeit einer hohen örtlichen Auflösung zur Erfassung des Gasgehaltes deutlich.

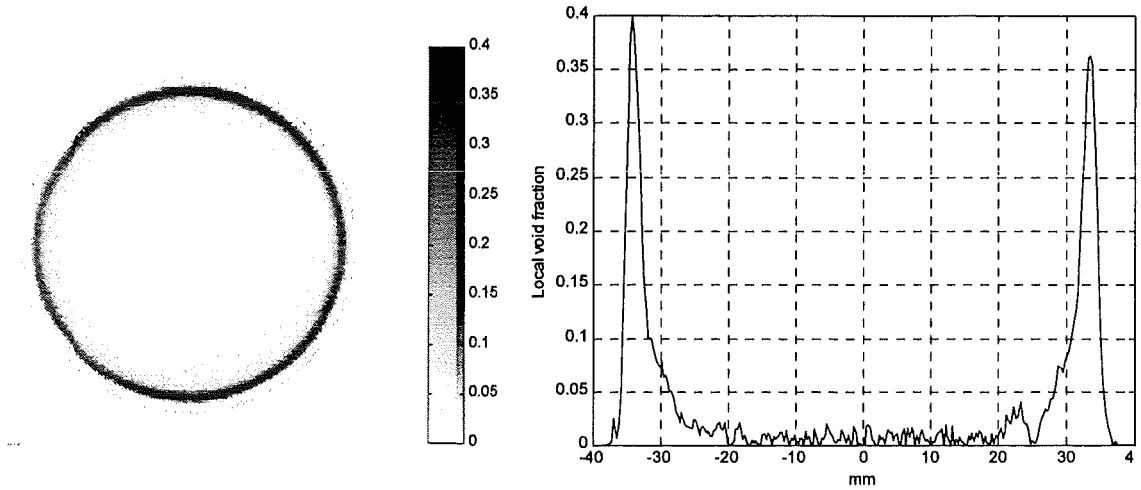

Abbildung 5: Lokale Gasverteilung einer aufwärtsgerichteten Blasenströmung mit symmetrischer Gaszufuhr durch 7 Düsen, ß=5%, j_l=1.8m/s, axiale Meßposition 40D

Die Fähigkeit zur dreidimensionalen Rekonstruktion wird für die Bestimmung des axialen Verlaufes der Gasverteilung genutzt. In Abbildung 6 ist für verschiedene axiale Positionen der lokale Gasgehalt zu sehen. Die Meßposition befindet sich 40D über der Gaseingabestelle, die für den gezeigten Fall einseitig einspeist. Die asymmetrische Gasverteilung an der Meßposition bleibt über eine Höhe von 15 cm erhalten, ohne daß es zu einem Netto-Blasentransport in radialer Richtung oder Umfangsrichtung kommt.

Sonden zur Detektion von Blasen

Neben der Tomographie werden Widerstandssonden eingesetzt, die in die Strömung ragen und Aussagen über die Anwesenheit von Gasblasen lokal an der Sondenspitze und je nach Sondenausführung über die vertikale Geschwindigkeitskomponente der Blasen liefern können.

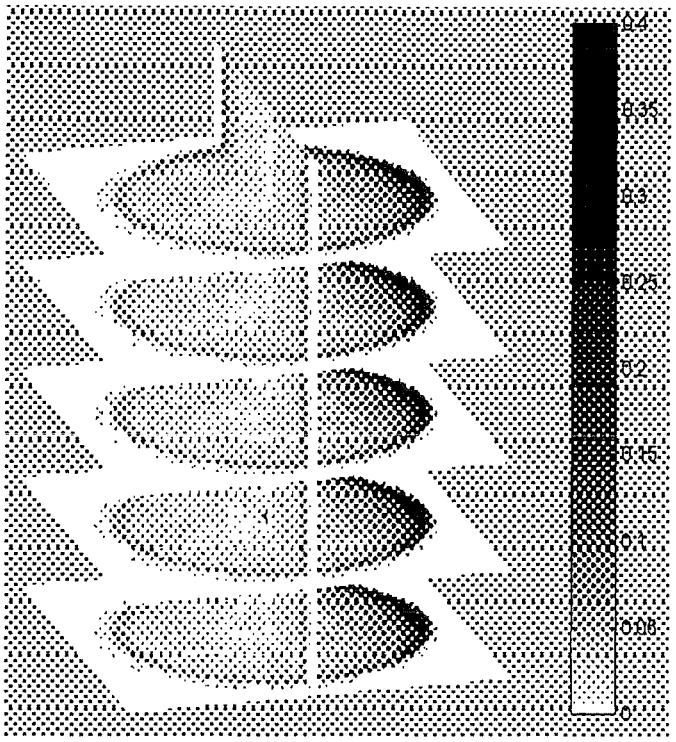

Abbildung 6: Lokale Gasverteilung einer aufwärtsgerichteten Blasenströmung mit unsymmetrischer Gaszufuhr durch eine exzentrische Düse, ß=3.25%, j_l=1.8m/s, Meßposition 40D über der Gaseingabestelle

Die vor nunmehr zehn Jahren am IRE entwickelte 2-Punkt–Widerstandssonde, damals zu den führenden Sensoren dieser Art zu rechnen, sollen nach dem inzwischen erreichten internationalen Standard wie auch nach eigenen Untersuchungen vom Konzept her erneuert werden. Schwachpunkte der bisherigen Ausführung sind der Aufbau, der keine geringe Wandnähe zuläßt, die Ausmaße der Sondenhalterung und deren Anfälligkeit gegen eindringendes Wasser. Beides liegt im Konzept der Tauschbarkeit des Meßkopfes begründet, auf die andere Entwickler inzwischen verzichten. Weiterhin ignoriert die Signalauswertesoftware sogenannte "missing events", d.h. Situationen, in denen nur einer der beiden Meßpunkte anspricht. Je nach Blasengröße und Strömungstyp charakterisieren diese Ereignisse jedoch statistisch den Betrag und die Häufigkeit von Horizontalkomponenten in der Aufstiegsgeschwindigkeit. Hierzu liegen inzwischen neuere Arbeiten vor, die dies entweder berücksichtigen oder durch 4 bzw. 5-Punkt Meßtechnik gezielt erfassen.
Ein eigener Ansatz zur Weiterentwicklung bestand in der Fertigung einer koaxialen 1-Punkt-2-Ringsonde zur Demonstration der Machbarkeit in einer schlanken Ausführung

(Abbildung 7). Bei einem Außendurchmesser des Sondenträgers von 2,5 mm bildet der Aufbau durch die 3 verklebt ineinander geschobenen Röhrchen einen steifen Verbund. Die koaxialen Sensorflächen ergeben ein lateral isotropes Ansprechverhalten, das durch die drei (mit Lichtleitereinbau vier) Kontaktflächen redundant unterstützt wird. Der Mittenleiter soll später durch eine leitfähig überzogene Lichtleiterfaser ersetzt werden, um bei elektrischen Störungen durch Diversität die Ereigniserkennung sicherer zu handhaben.

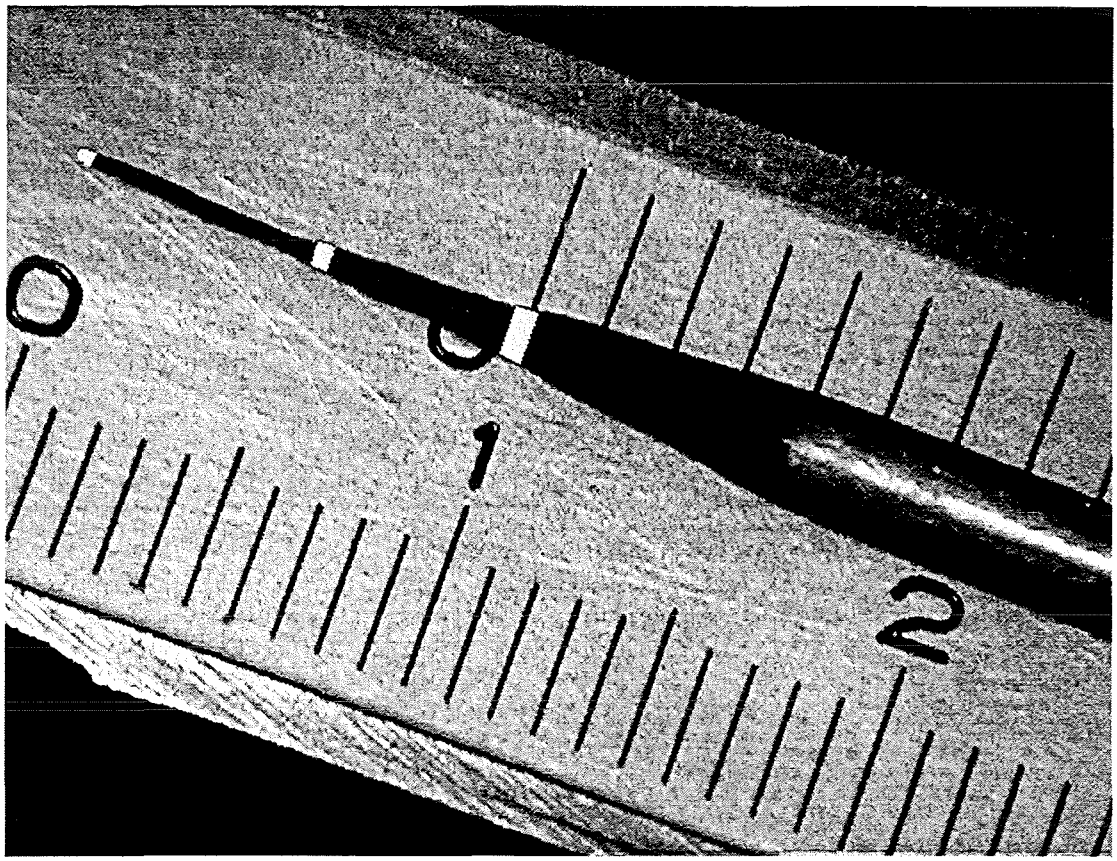

Abbildung 7: 1-Punkt-2-Ring-Sonde; die elektrisch leitenden (vergoldeten) Oberflächen sind in der Abbildung hervorgehoben

Beobachtung von Einzelblasen

Zu den Entwicklungsaufgaben der Grobstruktursimulation von Zweiphasenströmungen gehören u. a. die Formulierung von Feinstrukturmodellen, die sich mit den Strömungsverhältnissen um eine Blase und den Vorgängen an der Blasenoberfläche befassen (siehe Teil I). Sowohl zur Erstellung der Modelle als auch zu deren Validierung werden experimentelle Daten angefordert. Die dazu gewünschte Vollständigkeit der experimentellen

Bedingungen läßt sich nur bedingt der Literatur entnehmen. Daher ist im Fortschritt bei den Programmentwicklungen eine Wechselwirkung mit parallelen experimentellen Untersuchungen zweckmäßig.

Um einem solchen Bedarf kurzfristig entsprechen zu können, wurde die Entwicklung von geeignete Blasengeneratoren und Beobachtungstechniken aufgegriffen. Zum Aufbau des Blasengenerators wurden verschiedene konfektionierte Teile untersucht. Es wurde eine Gruppe von Kanülen ausgewählt und damit eine Basis für die Folgearbeiten geschaffen. In einem ersten Schritt soll ein Datensatz über Blasengröße und –aufstiegsgeschwindigkeit von Einzelblasen mit Luft/Wasser mit den jeweils dazu gehörenden Stoffwerten erstellt werden. Die Fortsetzung zielt auf die Ermittlung des Strömungsfeldes um Blasen, die in einem ruhenden Flüssigkeitspool aufsteigen.

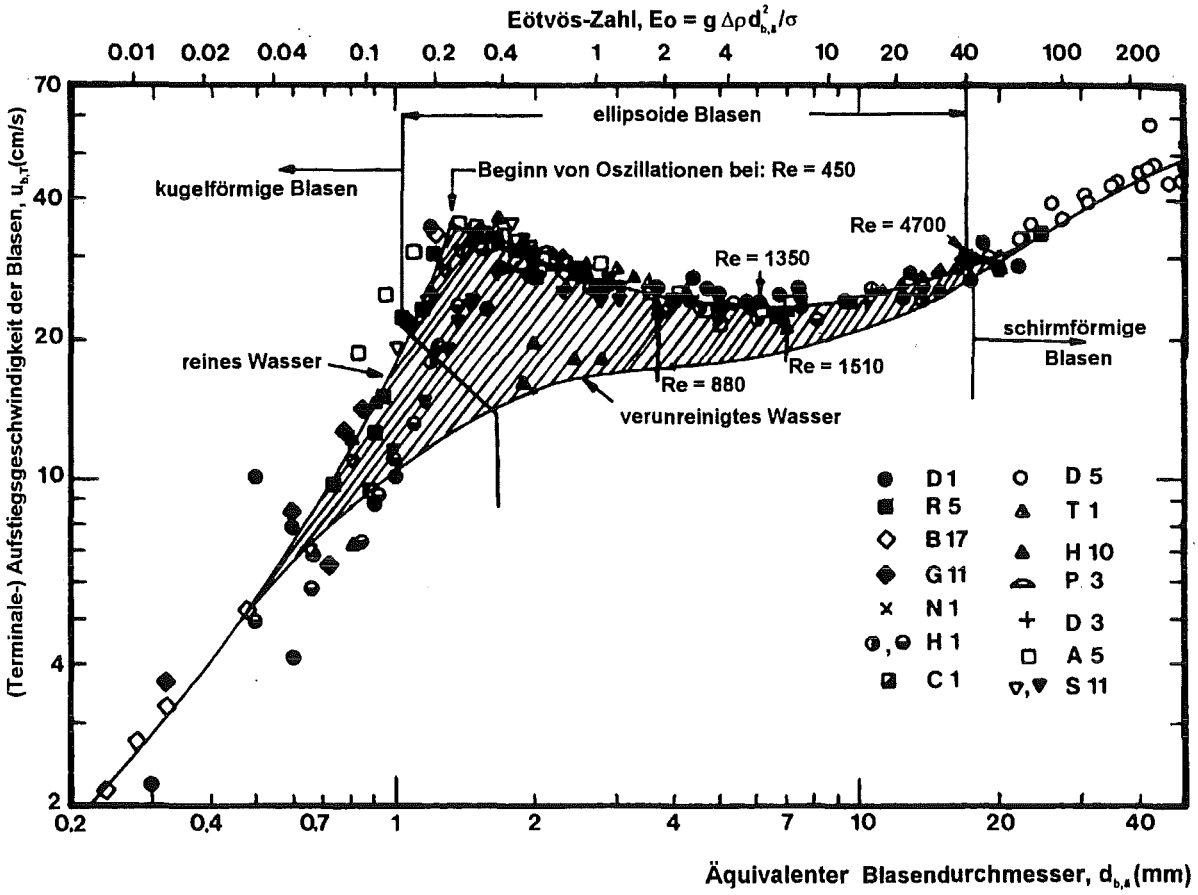

Abbildung 8: Terminale Aufstiegsgeschwindigkeit von Luftblasen in Wasser bei 20 °C in Abhängigkeit vom Blasendurchmesser bzw. der Eötvös-Zahl [4]

Der Zusammenhang von Blasengröße und –aufstiegsgeschwingigkeit ist in der Literatur an verschiedenen Stellen beschrieben. Abbildung 8 von R. Clift et. al. [4] zeigt diesen Zusammenhang mit Grenzkurven für reines und verschmutztes Wasser so wie experimentelle Werte. Die Streuung der experimentellen Daten, zum Teil liegen die Meßpunkte außerhalb der beiden Grenzkurven, können nach den Textangaben bei R. Clift et. al. nur teilweise mit der Kontamination des Wassers erklärt werden.

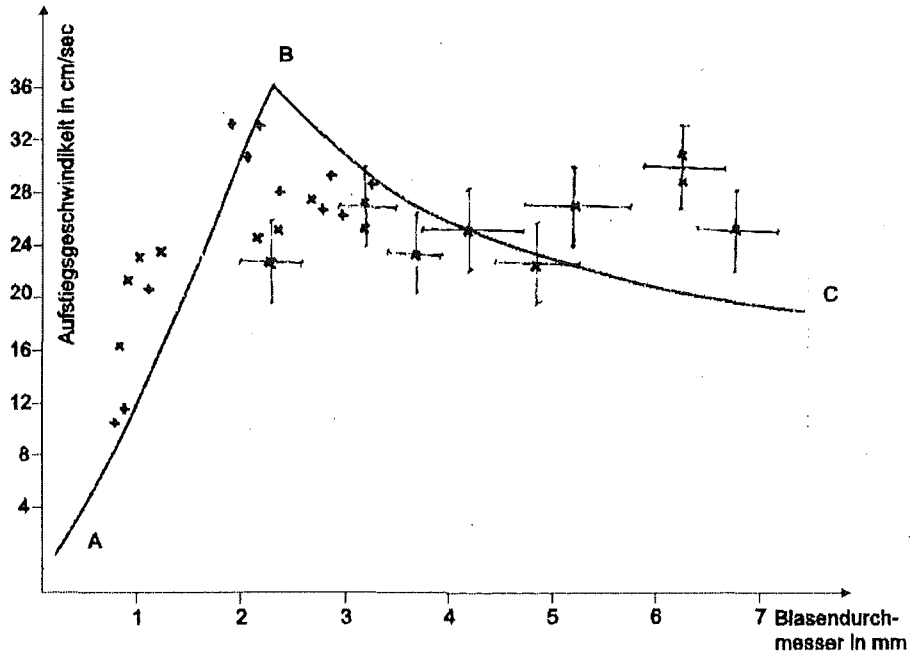

Abbildung 9: gemessene Blasenaufstiegsgeschwindigkeiten und Grenzkurve nach der Formel von H. Brauer [5] (entspricht der oberen Grenzkurve in Abbildung 8)

Abbildung 9 stellt die eigenen Messungen zusammen mit einer Grenzkurve nach einer Formel von H. Brauer [5] für reines Wasser dar. Der Streubereich der Meßpunkte bestätigt die zuvor übernommene Aussage. Die durchgeführten Messungen der Oberflächenspannung erklären die Abweichungen nicht. Vielmehr verweisen die beim Experimentieren gesammelten Erfahrungen auf Einflüsse durch den Experimentaufbau und die Beobachtungtechnik. Zumindest läßt sich schon im Hinblick auf die Anforderung „Einzelblase" aufzeigen, daß zu dem Wertepaar Blasengröße und –aufstiegsgeschwindigkeit Angaben über die zeitliche Folge oder Frequenz der erzeugten Blase gehören müssen.

Literatur

1 G. Class,
Entwicklung eines Computertomographen als Dichte-Meßverfahren an Luft-Wasser-Strömungen für NOVA,
Primärbericht 12.07.06.P02A, 1988.

2 I. Tiseanu, M. Simon,
High Resolution Cone-Beam Tomography for Two-Phase Flow Diagnostics.
2nd International Symposium on Two-Phase Flow Modelling and Experimentation, Pisa, Italy 23-26 May, 1999.

3 W. Cherdron, G. Grötzbach, M. Samstag, W. Sengpiel, M. Simon, I. Tiseanu,
Experimental Investigations of Air/Water Bubbly Flow in Vertical Pipes.
Third International Conference on Multiphase Flow, Lyon, June 8 - 12, 1998, Proc. on CD-ROM.

4 R. Clift, J. R. Grace, M. E. Weber,
Bubbles, Drops and Particles
Academic Press, New York, 1978, S. 172.

5 H. Brauer,
Grundlagen der Einphasen- und Mehrphasenströmungen, 1998
Verlag Sauerländer, Aarau und Frankfurt am Main 1971.

32.22.04 Strukturelle Integrität

Untersuchungen an austenitischen Stählen

(E. Daum, K. Ehrlich, A. Falkenstein, S. Heger, R. Hübner, M. Schirra, IMF I)

Abstract

The research area "Structural Integrity" comprises different activities. The examinations on structural materials concentrate on the creep behaviour of the austenitic steel 316L(N) - DIN 1.4909. The irradiation project PFR-M2 is aimed to determine the influence of different parameters on the volume swelling and the irradiation creep of different steels. Additionally, activation calculations are used to assess the long-term activation potential with the objective to specify new low activation alloys for use as structural materials in pressurized water reactors.

Zusammenfassung

In diesem Vorhaben sind verschiedene Aktivitäten des IMF I zusammengefaßt. Die Untersuchungen an Strukturmaterialien konzentrieren sich auf das Kriechverhalten des Stahls 316L(N) - DIN 1.4909 bei 550 und 600°C bei niedrigen, konstanten Spannungen bzw. bei ansteigender Spannung im Vergleich zu konstanter Spannung. Das Bestrahlungsprojekt PFR-M2 dient der Bestimmung des Einflusses verschiedener Parameter auf Volumenschwellen und In-pile Kriechen verschiedenster Stähle. Zusätzlich wird durch Aktivierungsrechnungen das Langzeitaktivierungspotential untersucht, mit dem Ziel, neue niedrigaktivierende Legierungen zur Verwendung als Strukturmaterialien in Druckwasserreaktoren zu spezifizieren.

1. Untersuchungen an Strukturmaterialien, Langzeitversuche am Strukturwerkstoff 316L(N)

1.1 Einleitung

Für das im europäischen Rahmen geplante Brüterprojekt wurde als Anlagenstrukturwerkstoff der 17/12/2 CrNiMo-Stahl 316L(N) - DIN 1.4909 gewählt. Das Zeitstandfestigkeits- und Kriechverhalten dieses Stahltyps ist im üblichen Spannungs- und Temperaturbereich experimentell hinreichend untersucht, u.a. durch eigene Ar-

beiten an 3 Chargen im Temperaturbereich 500 - 700°C und bis zu Zeiten von 70 000 Stunden. Im auslegungsrelevanten niedrigen Spannungsbereich bei 550 und 600°C ist ein völliger Mangel an Daten festzustellen, die z.B. eine Aussage zur Spannungsabhängigkeit der minimalen Kriechgeschwindigkeit oder zu den technisch wichtigen Zeit-Dehngrenzen erlauben würden.

Innerhalb der AGT9A/SG1 wurde die Bestimmung von Kriechdaten für die Aufstellung zuverlässiger konstitutiver Auslegungsformeln zum Werkstoffverhalten für unbedingt notwendig erachtet, und das Forschungszentrum / IMF I erklärte sich bereit, spezielle Langzeitversuche im Rahmen des meßtechnisch Möglichen durchzuführen

1.2 Stand der Untersuchungen

Im Jahresbericht 1996 [1] wurde detailliert über die Versuchsdurchführung, den Stand 40 000 h sowie über Ergebnisse von Versuchen mit stufenweisen Belastung im Vergleich zu den Versuchen mit konstanter Last berichtet.

Die Versuche mit konstanter Last bei 550° und 600°C Prüftemperatur haben mittlerweile 60 000 h Laufzeit erreicht bzw. überschritten. Die in Abb. 1.2 [1] und Fig. 2 [2] erstmals dargestellte Tendenz, daß z.B. die Spannungsabhängigkeit der minimalen Kriechgeschwindigkeit $\dot{\varepsilon}_{p\,min}$ im auslegungsrelevanten niedrigen Spannungsbereich sich deutlich ändert, wird erhärtet. Die Änderung geschieht zur nichtkonservativen Seite, d.h. es ergeben sich höhere Kriechgeschwindigkeitswerte, als bisher vom höheren Spannungsniveau extrapoliert wurden. Der Spannungsexponent n erniedrigt sich bei 550° und 600°C von >10 im bisher experimentell abgedeckten Spannungsbereich auf einen Wert ≤ 7. Der bisherige Stand der Untersuchungen zeigt, daß sich die niedrigen Versuchsspannungen (bei 550°C 100 - 180 MPa und bei 600°C 60 - 80 MPa) noch nicht eindeutig auf dem niedrigsten $\dot{\varepsilon}_{p\,min}$-Niveau stabilisiert haben, wird aus der Abb. 1.1 beispielhaft für die 550°C-Versuche hervorgeht. In diesem Bild sind die aus dem Kriechverlauf in 5000 bzw. 10 000 h Schritten ermittelten Werte für die lineare Kriechgeschwindigkeit in Abhängigkeit von der Versuchszeit dargestellt. Auch die technologisch wichtigen Zeit-Dehngrenzen (0,01 - 1% Dehnung) zeigen eine deutlich geänderte Abhängigkeit. Bis zum Versuchszeitraum von $\approx 10^4$ h werden die Dehngrenzen bis 0,5% z.T. deutlich früher als erwartet erreicht. Darüber hinaus wird die σ/t-Abhängigkeit wieder stärker und es besteht die Tendenz zu einem wesentlich

flacheren Verlauf der Zeit-Dehngrenzen-Kurven. Für eine eindeutige Aussage sind allerdings noch wesentlich längere Versuchszeiten erforderlich.

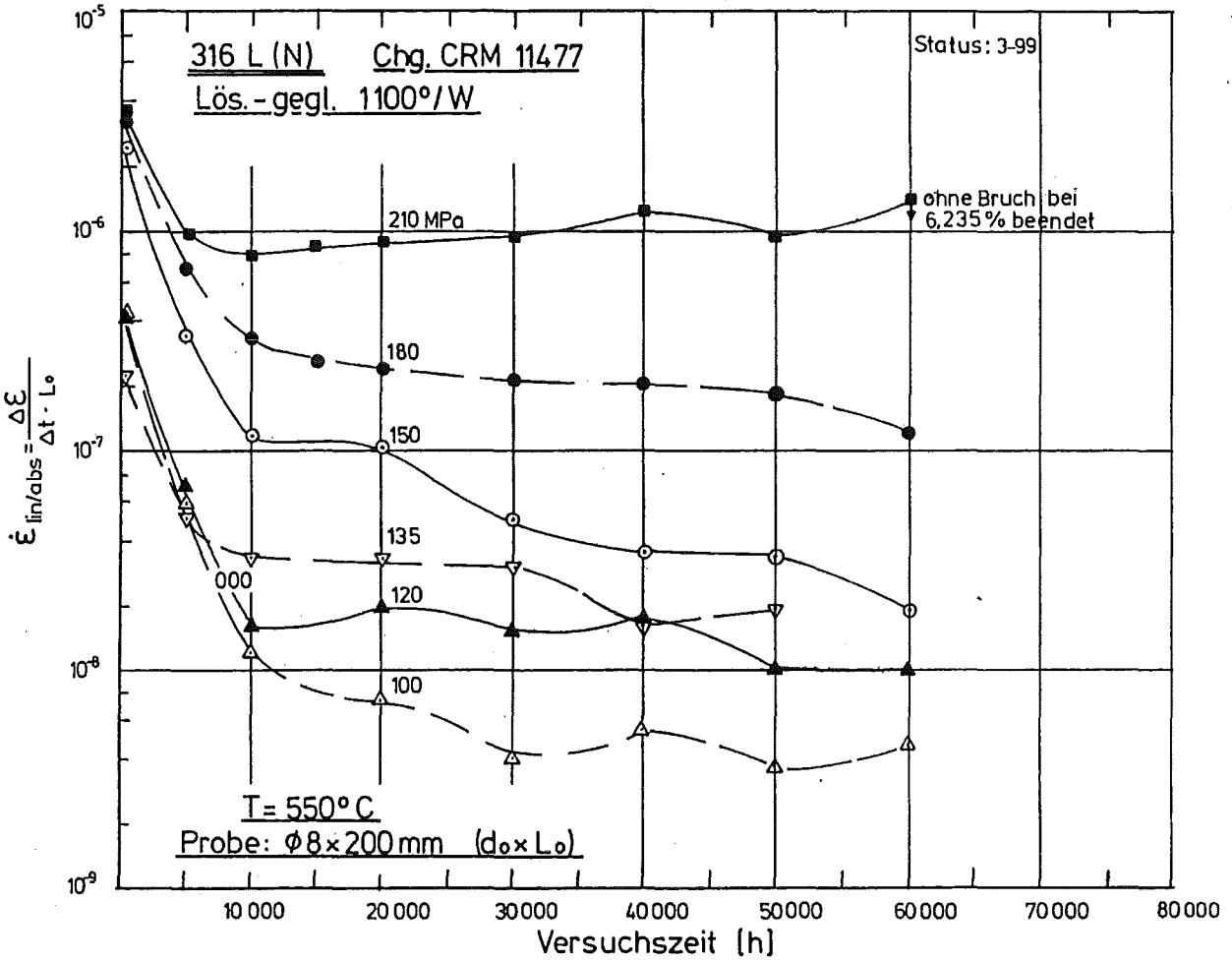

Abb. 1.1: Lineare Kriechgeschwindigkeit in Abhängigkeit von der Versuchszeit.

Veröffentlichungen

[1] FZKA 5963, Sept. 1997, Projekt Nukleare Sicherheitsforschung

[2] M. Schirra, " Studies on the creep behaviour of the structural material 316L(N) in the low-stress range at 550 and 600°C", Nuclear Engineering and Design, 188 (3), pp 381-384, May 1999

[3] T. Nakazawa, Y, Otoguro, H. Kimura, H. Kaguchi: M. Schirra, " Long Term Creep Rupture Properties and Precipitation in Type 316 Stainless Steels", Conf. San Diego, USA, 1. - 4.3.1999

2. Nachuntersuchungen am Werkstoff DIN 1.4864, Bestrahlungsprojekt PFR-M2

2.1. Einleitung

Zu den wichtigsten Eigenschaften von Struktur- und Hüllmaterialien gehören das Schwell- und In-pile Kriechverhalten. Im Bestrahlungsexperiment PFR-M2 sollen diese Eigenschaften für verschiedene Gruppen von Stählen systematisch untersucht werden. Zu diesem Zwecke wurden Druckröhrchen mit 6mm Durchmesser und 28mm Länge hergestellt und im Prototype Fast Reactor (PFR) in Dounreay, Schottland bei nominell 420, 500 und 600°C bestrahlt. Die Proben wurden mehrfach dem Reaktor entnommen um die Durchmesser- und Längenänderungen zu bestimmen. Die bei Beendigung der Bestrahlung akkumulierten maximalen Dosen betragen 106 dpa_{NRT} bei 420°C, 81 dpa_{NRT} bei 500°C und 61 dpa_{NRT} bei 600°C. Nach Beendigung der Bestrahlung wurden die Proben nach Karlsruhe transportiert, wo in den HZ die nichtzerstörenden Untersuchungen abgeschlossen wurden und mit den zerstörenden Untersuchungen begonnen wurde.

2.2 Stand der Untersuchungen

Neben anderen Faktoren wurde auch der Einfluß der Hauptlegierungselemente Ni und Cr auf Schwellen und Kriechen untersucht. Zu diesem Zweck wurde u.a. der kommerzielle Stahl DIN 1.4864 mit 15.6% Cr, 35.3 % Ni, 0,07% C, 1,56% Si und 1,16% Mn bestrahlt. Der thermomechanische Zustand der Proben war Lösungsglühen bei 1100°C und 20% Kaltverformung. Diese Legierung zeigte im Laufe der Bestrahlung ein bisher noch nicht beobachtetes Schwellverhalten (Abb. 2.1)

Bei 420°C nimmt die Schwellrate nach dem Beginn des Schwellens nicht kontinuierlich zu, was bei Austeniten immer beobachtet wird, sondern nimmt wieder ab. Aufgrund der Kriech-Schwellkopplung zeigen die mit Druck beaufschlagten Proben ein analoges Verhalten.

Bei 500°C tritt nur geringfügiges Schwellen ($\Delta D/D_0 < 0{,}1\%$ bei 53 dpa_{NRT}) so daß keine Aussage über eine Sättigung des Schwellen gemacht werden kann.

Zur Klärung dieses Phänomens wurden zusätzlich zu den bereits bestrahlten Proben einige Proben bei der letzten Bestrahlungskampagne bis 10 dpa_{NRT} bestrahlt. Somit

liegen sowohl Proben im Zustand vor dem Beginn des Schwellens, als auch Proben im Zustand nach der Sättigung der Schwellrate zur Nachuntersuchung vor.

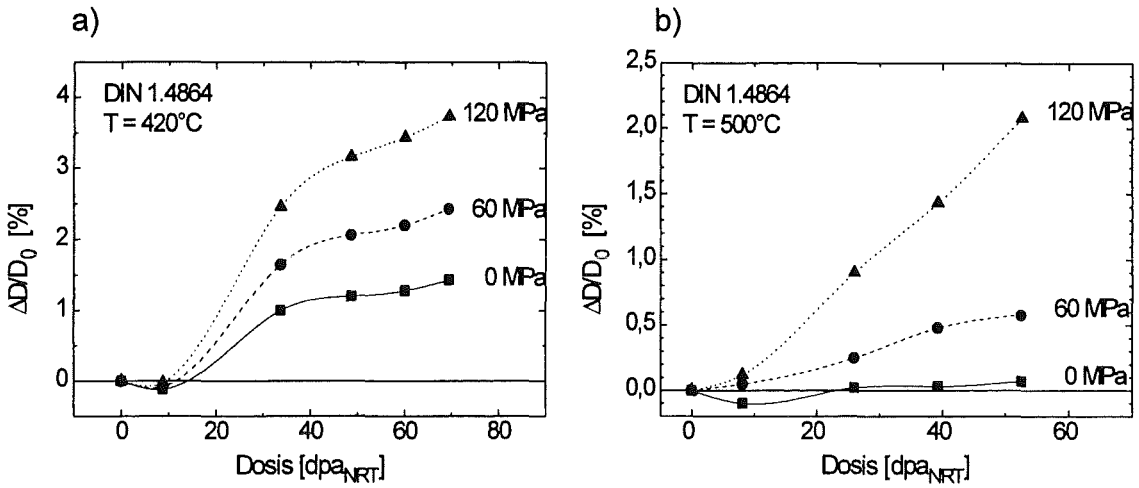

Abb. 2.1: Dosisabhängigkeit der Durchmesseränderung der Druckkapseln aus DIN 1.4864. a) 420°C, b) 500°C.

Die Nachuntersuchungen zur Bestimmung des Volumenschwellens, Dichtemessung und Analyse der Porenstruktur im TEM ergaben eine gute Übereinstimmung mit den Durchmesseränderungen. Für die drucklose Probe mit einer Bestrahlungsdosis von 69 dpa_{NRT} bei 420°C ergab sich:

Durchmesseränderung: $\Delta D/D_0 = 1/3\ \Delta V/V_0 = 1{,}43\% \Rightarrow \Delta V/V_0 = 4{,}29\%$

Dichteänderung: $\Delta\rho/\rho_0 = 4{,}8\%$

Analyse der Porenstruktur: $\Delta V/V = 5{,}6\%$

Der höhere Wert der Analyse der Porenstruktur erklärt sich durch die Verdichtung durch Erholung der Versetzungsstruktur und Bildung von Ausscheidungen, die zu Beginn der Bestrahlung auftritt und bei der Porenanalyse nicht berücksichtigt wird.

Die Analyse der Mikrostruktur zeigt sowohl bei 10 als auch bei 69 dpa_{NRT} eine hohe Dichte von kohärenten, intragranularen γ' (Ni_3Si) und $M_{23}C_6$ - Ausscheidungen. Dabei nimmt der mittlere Durchmesser der Ausscheidungen mit zunehmender Dosis zu. (10 dpa_{NRT}: $M_{23}C_6$: ~25 nm, γ': ~10 nm, 69 dpa_{NRT}: $M_{23}C_6$: ~50 nm γ': ~15 nm), während die Konzentration konstant bleibt. ($M_{23}C_6$: ~5 x 10^{14} cm^{-3}, γ': ~2 x 10^{15} cm^{-3}). Die Korngrenzen sind bei 10 dpa_{NRT} gering und bei 69 dpa_{NRT} massiv mit $M_{23}C_6$ belegt. In allen Proben finden sich außerdem große intragranulare $M_{23}C_6$ - Ausscheidungen (200 - 300 nm), die bereits in den unbestrahlten Proben vorhanden sind. Die Verset-

zungsdichte steigt durch die Bestrahlung bei 420°C von ~3 x 10^{10} cm^{-2} im unbestrahlten Zustand auf ~13 x 10^{10} cm^{-2} bei 10 dpa_{NRT} und ändert sich im Laufe der Bestrahlung nicht mehr.

Schließlich wurden von den Proben mit Hilfe der EDX-Analyse im TEM Konzentrationsprofile aufgenommen. Die Auflösung wird dabei vom Durchmesser des Elektronenstrahls bestimmt und betrug ca. 50 nm. In Abbildung 2.2 sind typische Konzentrationsprofile bei 10 und 69 dpa_{NRT} dargestellt.

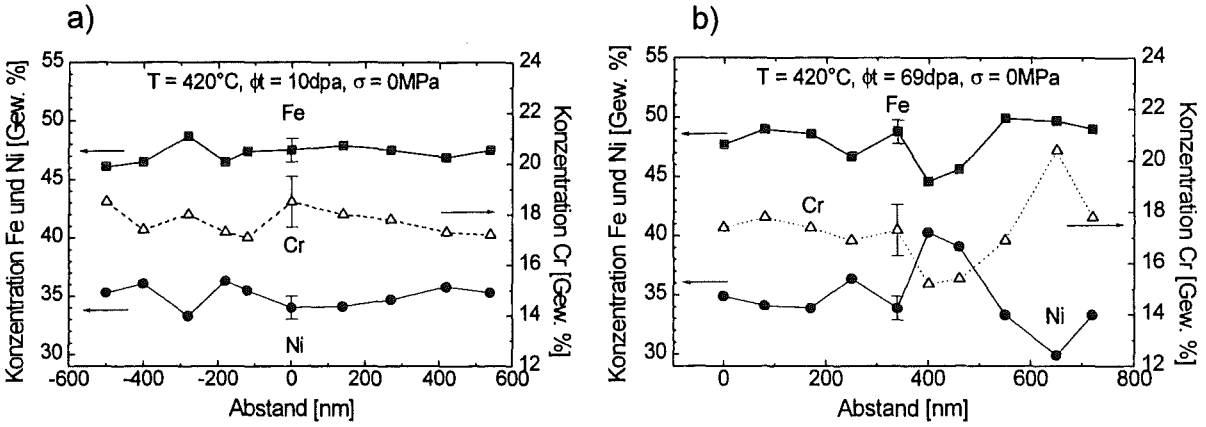

Abb. 2.2: Konzentrationsprofile der DIN 1.4864-Proben nach der Bestrahlung a) 10 dpa_{NRT} b) 69 dpa_{NRT}

Die Meßgenauigkeit beträgt ± 1 Gew. %. Man erkennt, daß bei einer Bestrahlungsdosis von 10 dpa_{NRT} die Konzentration der Hauptlegierungselemente nur geringfügig um die Mittelwerte schwankt. Im Gegensatz dazu treten bei 69 dpa_{NRT} sehr starke Schwankungen in den Konzentrationen auf. Dabei verhalten sich Fe und Cr analog, während Ni sich genau entgegengesetzt verhält, d.h. wenn der Fe-Gehalt hoch ist, ist auch der Cr-Gehalt hoch und der Ni-Gehalt ist niedrig. Daraus ist zu schließen, daß in der Probe nach der Sättigung der Schwellrate eine Entmischung vorliegt.

Aufgrund dieser Beobachtungen muß davon ausgegangen werden, daß die beobachtete Entmischung für das ungewöhnliche Schwellverhalten des DIN 1.4864 verantwortlich ist. Es ist anzunehmen, daß der noch nicht entmischte Werkstoff wie alle Austenite zu schwellen beginnt und daß es dabei durch Segregationsvorgänge zur Entmischung kommt. Warum allerdings der Werkstoff im entmischten Zustand eine so geringe Schwellrate aufweist ist zur Zeit noch ungeklärt. Der Effekt der spinodalen Entmischung von 35% Ni-Stählen wurde in der Literatur zwar bereits diskutiert, jedoch wurde bisher kein Zusammenhang mit dem Schwellverhalten festgestellt.

3. Modellrechnungen für die Langzeitaktivierung von Reaktordruckbehälterstählen

3.1. Einleitung

Eine wichtige Eigenschaft von Strukturmaterialien ist das Aktivierungsverhalten unter Neutronenbestrahlung, welches mittels Aktivierungsberechnungen systematisch untersucht werden soll. Dadurch können kritische Elemente mit hohem Langzeitaktivierungspotential identifiziert, Legierungen optimiert und niedrigaktivierende Legierungen spezifiziert werden.

3.2 Stand der Rechnungen

Die ersten durchgeführten Berechnungen [1, 2] für die innere Platierung eines typischen Reaktordruckbehälters bei 30 Jahren Lebensdauer zeigten für die Stähle 1.4541 (Ti-stabilisiert) und 1.4550 (Nb-stabilisiert), daß sich mit einer Begrenzung der Elemente Co auf 50 ppm und Nb auf 100 ppm eine niedrigaktivierende Legierung spezifizieren läßt. Die neuen Rechnungen [3] mit dem Programm FISPACT 97 und den Aktivierungsdaten EAF 97 dienen einer umfassenden Charakterisierung des Langzeitaktivierungspotentials und berücksichtigen auch Spuren- und Verunreinigungselemente.

Als besonders kritisch, zusätzlich zu Nb und Co, konnten seltene Erdenelemente wie Eu, Sm und Dy und schwere Elemente wie Ho, Hf und Ag identifiziert werden. Für diese Elemente sind zukünftig obere Verunreinigungsgrenzen auszuarbeiten, die in die Spezifikation von niedrigaktivierenden Reaktorstählen einfließen sollten.

Veröffentlichungen

[1] E. Daum and J. Bertsch, Reduction of Long-term Activation in Structural Components of Commercial Reactors - A Promising Task for Materials Optimization?, European Nuclear Conference, Transactions Vol. II, Berne, October 1994

[2] E. Daum and J. Bertsch, Investigation of the Long-term Activation of Austenitic Steels in Pressurized Water Reactors, Proceedings EUROMAT 96, October 21-23, 1996, Bournemouth, UK

[3] E. Daum, Interner Bericht, PKF-Nr. 106, April 1998

32.22.06 Untersuchungen zum Brennstoff- und Brennstabverhalten innovativer Systeme

(W. Pfrang, B. Porscha, D. Struwe, W. Zimmerer, IRS)

Diese Arbeiten umfassen den Beitrag des Forschungszentrums Karlsruhe zum CABRI-FAST bzw. zum CABRI-RAFT Programm, die in internationaler Zusammenarbeit mit dem französischen IPSN und dem japanischen JNC durchgeführt werden. Die in Frankreich durchgeführten Experimente dieses Programms zielen darauf ab, das transiente Verhalten von Brennstäben mit unterschiedlichen Entwurfsmerkmalen zu untersuchen und insbesondere die Versagensbedingungen in Abhängigkeit vom Brennstabzustand nach der Vorbestrahlung und von Kühlmitteldurchsatzänderungen bzw. Leistungstransienten zu ermitteln.

SAS4A Programmentwicklung

Für sicherheitsorientierte Untersuchungen wird das Programmsystem SAS4A eingesetzt. Dieses Programmsystem wird in Zusammenarbeit mit dem französischen IPSN und dem japanischen JNC-Institut kontinuierlich weiterentwickelt. Die Modelle der im Sommer 1997 freigegebenen Programmversion Ref96.Rel 1.0 wurden an Hand der experimentellen Ergebnisse der unterschiedlichen CABRI Programme überprüft. Es wurden im Detail Modellverbesserungen vorgenommen, um eine konsistente Interpretation dieser Experimente zu erreichen, ohne spezielle Modelladjustierungen für einzelne Experimente vornehmen zu müssen. Im Einzelnen bezogen sich diese Arbeiten auf Details des Brennstabdeformationsmodells DEFORM-4C, des Siedemodells und des PLUTO-2 Modells zur Beschreibung der Brennstoff-Natrium-Wechselwirkung. Darüber hinaus wurden die Materialdaten für die Hüllrohrmaterialien dem neuesten Kenntnisstand angepaßt. Mit diesen Verbesserungen ist es gelungen, eine zufriedenstellende Übereinstimmung zwischen den berechneten und den experimentell beobachteten Brennstabversagensbedingungen zu erreichen.

Result of Fuel Pin Failure Calculations

SAS4A.Ref96.R1-mod FZK

Experiment	Time into the power transient [ms]		Axial location [cm_{bfc}]		Peak fuel enthalpy (kJ/kg) 10^{-6}	Melt cavity press. MPa	mid wall clad temp. K
	exp.	calc.	exp.	calc.			
AI2[2]	230	(210)	43-49	(38-42)	1.31	76.7	1088
AI3	82	81.6 (-0.4)	43-45	43-47	1.41	94.2	958
BI2	79	77.7 (-1.3)	49-53	51-55	1.33	52.4	1155
BI4	88	89.5 (+1.5)	51-53	52-56	1.28	28.4	1360
BI6	63-64	63.6	42; 57	47-51	1.35	31.4	1332
BI3	69-82	78.8	43-51	43-47	1.08	1.8	>1700
BI5	55-60	59.3	35-53	43-47	1.04	0.9	>1700
AGS3[1]	525	519.7 (-5.3)	45-47	38-42	1.06	80.1	947
BGS3[1]	520-548	534	31-55	38-42	1.04	12.2	1600
BGS4[1]	500-555	538	28-64	47-51	1.06	14.8	>1700

[1] fuel melt fraction dominated [2] prescribed failure strain

Result of Fuel Pin Failure Calculations

SAS4A.Ref96.R1-mod FZK

Experiment	Time into the power transient [ms] exp.	calc.	Axial location [cm_{bfc}] exp.	calc.	Peak fuel enthalpy (kJ/kg) 10^{-6}	Melt cavity press. MPa	mid wall clad temp. K
E6	564-567	573 (+7.5)	50-54	55-59	1.13	67.4	1102
E2[1]	570	574 (+4)	48-52	46-50	0.96	80.3	1123
E3[1]	370 (475-500)	(380) 482	44-60 (30,70)	(50-58) 51-55	(0.83) 0.97	(16.5) 120	(1250) 1320
E13[1]	250-350	299	40-70	46-50	1.07	4.6	>1700
E11[1]	100-150	62	45-60	51-55	1.07	10.3	>1700
E12	76000	75730 (-270)	56-65	50-54	0.83	71.8	970
BCF1	28400	26500 (-1900)	~60	50-54	0.83	47.3	976
E7[2]	467	465.3 (-1.7)	53-56	46-50	1.42	55.5	1042
E8[2]	523-524	52.4	51-57	36-44 (50-54)	1.01	253	1290 (1334)
EFM1[1]	380-480	395	41-51	44-48	1.09	8.8	>1700

[1] fuel melt fraction dominated [2] prescribed failure strain

In gleicher Weise können heute für langsame Leistungstransienten die linearen Stableistungen verläßlich bestimmt werden, bei denen Brennstoffschmelzen einsetzt. Diese Kenngrößen sind für die sicherheitstechnische Bewertung neuer innovativer Brennelemententwürfe von großer Bedeutung.

Bei Experimenten, bei denen der Kühlmitteldurchsatz reduziert wird und bei denen zunächst Sieden einsetzt, versagt das Hüllrohr aufgrund der Innendruckbelastung durch den Spaltgasdruck, wenn die Hüllrohrtemperaturen auf Werte in der Nähe der Schmelztemperatur ansteigen. Es kommt zum Abblasen des Spaltgases in den Kühlkanal und als Folge verändern sich die Wärmeübertragungsbedingungen im Kühlkanal, da das Spaltgas zum einen zu einer Reduktion des Kondensationskoeffizienten führt und zum anderen die Druckverlustkoeffizienten des Gas/Dampf-Gemisches sich ändern. Der Umfang dieser Änderungen ist abhängig von der Geschwindigkeit, mit der das Spaltgas abgeblasen wird. In einem ersten Schritt wurden diese Vorgänge im Programm SAS4A auf der Grundlage eines vom JNC entwickelten, stark vereinfachten Modells simuliert. Prinzipiell werden die Phänomene richtig erfaßt. Die quantitative Überprüfung der Auswirkungen an mehreren Experimenten hat aber gezeigt, daß die Rückwirkungen auf die Zweiphasenströmung teilweise erheblich überschätzt werden. Es ist daher notwendig, das derzeit verfügbare Modell zu überarbeiten und die Vorgänge detaillierter zu erfassen.

Aus der Analyse der Ergebnisse von Experimenten mit Brennstäben hohen Abbrands haben sich Hinweise ergeben, daß der Wärmeübergangskoeffizient zwischen Brennstoff und Hüllrohr dann stärker ansteigt als berechnet, wenn der Kontaktdruck hoch ist und die Brennstofftemperaturen in den Randbereichen des Brennstoffs auf Werte in der Nähe der Schmelztemperatur ansteigen. Diese Beobachtung läßt vermuten, daß sich bei hohem Abbrand die Oberflächenstruktur des Brennstoffs gegenüber dem Ausgangszustand ändert und sich dann bei hohem Kontaktdruck und erhöhten Temperaturen andere Wärmeübertragungsverhältnisse einstellen. Daher wurde ein parametrisches Modell entwickelt, das diese Tendenzen in der Rechnung berücksichtigt, indem die Oberflächenrauhigkeit des Brennstoffs mit Werten des Abbrands größer als 5 at% gegenüber den Werten bei der Herstellung reduziert wurde. Dieses Modell wurde an Experimenten mit Brennstäben hohen Abbrands überprüft. Der Vergleich gerechneter Werte für die Kühlmitteltemperatur, die axiale Brennstabausdehnung und die Versagensbedingungen mit den entsprechenden Meßwerten liefert Hinweise auf die Qualifizierung des Modellansatzes. Die Ergebnisse dieses Vergleichs zeigen, daß der gewählte Weg zu einer Verbesserung der Nachrechnungen der experimentellen Befunde führt.

32.22.07 Containmentuntersuchungen für innovative Systeme

KAREX-Experimente zum radiologischen Quellterm infolge Resuspension

(J. Minges, W. Schütz, IRS; M. K. Koch, RUB-NES)

Zusammfassung

Die Wiederfreisetzung schwerflüchtiger Substanzen aus Flüssigkeiten (nasse Resuspension oder Reentrainment) kann als Langzeitbeitrag zum radiologischen Quellterm nach einem Unfall mit Kernzerstörung eine wichtige Rolle spielen. Im Rahmen des KAREX-Programms werden Laborversuche, Versuche im technischen Maßstab und modelltheoretische Entwicklungen zu dieser Thematik durchgeführt. Laborversuche im Bereich des Siedepunktes lieferten Resuspensionsfaktoren, die wesentlich niedriger sind als vergleichbare Werte aus früheren Jettropfenversuchen bei Raumtemperatur. Der neue Versuchsstand im technischen Maßstab wurde mit einem ersten Experiment zur Freisetzung von Silberjodid in Betrieb genommen. Frühere Experimente zum instantanen Quellterm wurden abschließend ausgewertet, auch im Hinblick auf ihre Aussagen zur Resuspension. Modelltheoretische Entwicklungen bei RUB wurden auf hohe Gasvolumenströme erweitert.

1. Überblick

Bei der Betrachtung radiologischer Quellterme sind Kurzzeit- und Langzeitbeiträge zu beachten. Normalerweise gilt das Interesse den „intensiven" Kurzzeitbeiträgen. Die Langzeitbeiträge haben meist geringe Massenstromdichten, aber sie können über lange Zeiträume (Monate, Jahre) aktiv sein und deshalb eine besondere Bedeutung erlangen. Ein wichtiger Langzeitbeitrag ist die Wiederfreisetzung von bereits abgeschiedenem Material.

Im KAREX-Programm sind Arbeiten zur Spaltproduktfreisetzung (Quellterm) nach einem schweren Störfall zusammengefaßt. Eine besondere Rolle spielt dabei die Wiederfreisetzung (Resuspension) schwerflüchtiger partikelförmiger Substanzen aus Wasser, insbesondere über Gas- und Dampfblasen. Im gefluteten Schmelzeausbreitungsraum des EPR muß nach einem Kernschmelzeunfall mit monatelanger bis jahrelanger Wiederfreisetzung gerechnet werden, ebenso aus dem Sumpfwasser bestehender Kernkraftwerke nach einem Kühlmittelverluststörfall.

Die Beiträge des IRS umfassen die KAREX-Laborversuche, die KAREX-Versuche im technischen Maßstab und modelltheoretische Arbeiten an der Ruhr-Universität Bochum (RUB).

2. Laborversuche

Vorausgegangen Laborversuche bei Raumtemperatur mit zerplatzenden Einzelblasen und der Bildung von Jet-Tropfen zeigten, daß die so resuspendierten Materialien (typischerweise Metallpulver mit Korngrößen von einigen Mikrometern) in einer Konzentration freigesetzt wurden, die mit wenigen Ausnahmen in der Größenordnung der Poolkonzentration lag ***/1/***. Im Berichtszeitraum wurden Laborversuche zur Freisetzung von Zn-Pulver im Bereich des Siedepunktes durchgeführt, d. h. bei hohen Gasvolumenströmen. Auch hier konnte ein relativ gleichmäßiger Materialaustrag nachgewiesen werden (siehe Abb.1). Bedingt durch den völlig anderen Freisetzungsmechanismus (siehe Abschnitt 5) ergaben sich erheblich geringere Resuspensionsfaktoren von 10^{-3} bis 10^{-5}, wobei unterhalb des Siedepunktes eine ansteigende Tendenz zu erkennen war.

3. Versuche im technischen Maßstab

Der neue KAREX-Versuchsstand für Versuche im technischen Maßstab wurde fertiggestellt und in Betrieb genommen (siehe Abb. 2). Der thermisch isolierte und beheizbare Versuchsbehälter hat einen Durchmesser von 0,6 m, eine Höhe von 1,1 m und besitzt am Boden eine Heizplatte, die bis zu 50 kW liefern kann. Ein erstes Experiment zur Resuspension von Silberjodid AgI wurde durchgeführt. AgI ist partikelförmig und unlöslich, im Gegensatz zu anderen Jodverbindungen wie z. B. CsI. Es wurde ein deutlicher Materialaustrag auf Filterproben nachgewiesen. Die quantitative Auswertung ist zur Zeit noch nicht abgeschlossen.

4. Auswertung früherer FAUST-Experimente

Die Experimente des früheren FAUST-Programms zum instantanen Quellterm („Unterwasserexplosion") wurden im Berichtszeitraum abschließend ausgewertet und dokumentiert ***/2/***. Ein wichtiges Resultat war, daß die instantane Materialfreisetzung deutlich geringer ist als bisher angenommen. Andererseits ergab sich aber, daß durch Resuspensionsprozesse mit einem verzögerten, zeitlich ansteigenden Quellterm gerechnet werden muß.

5. Modelltheoretische Arbeiten (RUB)

Zur Bestimmung des Radionuklidquellterms bei schweren Störfällen werden im Zuge der Entwicklung eines Spaltprodukt-Transportmodells bei RUB Modelle zur Beschreibung des Quellterms hervorgerufen durch Resuspension bei gasdurchströmten Wasservorlagen entwickelt **/3, 4/**.

Die bislang untersuchte Radionuklidfreisetzung infolge der Tropfenbildung beim Zerplatzen von Blasen an Flüssigkeitsoberflächen ist für solche Störfallszenarien von Bedeutung, bei denen nur geringe Gasmengen in Form einzelner Blasen in der Wasservorlage aufsteigen. Hohe Gasvolumenströme führen zu einem Wechsel zwischen Koaleszens und Zerfall von Blasen, woraus unterschiedlich große Blasen, die unstetig und ungeordnet in der Flüssigkeit aufsteigen, resultieren. In dieser Strömungsform – auch als turbulente Wirbelströmung bezeichnet – beruht die Tropfenbildung nicht mehr auf dem Zerplatzen einzelner Blasen an der Flüssigkeitsoberfläche, sondern auf einem Zerfall instabiler Flüssigkeitsbereiche infolge des Impulsaustausches zwischen Gas und Flüssigkeit.

Für eine Modellierung der Tropfenbildung ist es zunächst wichtig, ein Kriterium zu ermitteln, mit dem der Umschlagpunkt zwischen Einzelblasenströmung und turbulenter Wirbelströmung bestimmt werden kann. Die hierzu vorhandenen Modellansätze zur Bestimmung der Volumenstromdichte, bei deren Überschreitung eine turbulente Wirbelströmung vorliegt, liefern dabei deutlich variierende Ergebnisse, so daß es sinnvoll ist, den Umschlagpunkt experimentell detaillierter zu untersuchen.

Als Vorbereitung der Experimente zur Resuspension bei hohen Gasvolumenströmen und als eine Basis für die modelltheoretische Begleitung dieser Experimente wird in **/3/** ein Modell dargestellt, mit dem der Tropfenfreisetzungsmassenstrom als Funktion der Höhe über der Pooloberfläche bestimmt werden kann. Aufgrund der größtenteils mechanistisch basierten Modellierung liefern diese Ansätze erste Informationen über die wesentlichen Einflußparameter. Die Analyse der Modellansätze verdeutlicht jedoch auch die Notwendigkeit weiterer experimenteller Untersuchungen zur Validierung des Modells sowie zur Beseitigung von Schwachstellen der Modellansätze.

Literatur

/1/ J. Minges, W. Schütz, M. Tietjen
KAREX-Laborversuche zur Jettropfenbildung bei zerplatzenden Gasblasen und zur Resuspension schwerflüchtiger Substanzen
Interner Bericht IRS-Nr. 1/98, PSF-Nr. 3289, Januar 1998

/2/ J. Minges, W. Schütz
FAUST-Quelltermexperimente mit Stoßstromentladungen über UO_2-Proben
Interner Bericht IRS-Nr. 3/98, PSF-Nr. 3290, März 1998

/3/ A. Voßnacke, M. K. Koch, H. Unger
Modellansätze zur Bestimmung des Re-Entrainments bei hohen Gasvolumenströmen
Interner Bericht RUB-E-I-216 (Erster Bericht über die Arbeiten 1998), Oktober 1998

/4/ M. K. Koch, J. Starflinger, H. Unger, W. Schütz
Analysis of the jet-droplet and radionuclide release due to bubble bursting at liquid surfaces.
ICONE-6, Proc. of the 6. Int. Conf. on Nuclear Engineering, San Diego/Calif., May 10-15, 1998

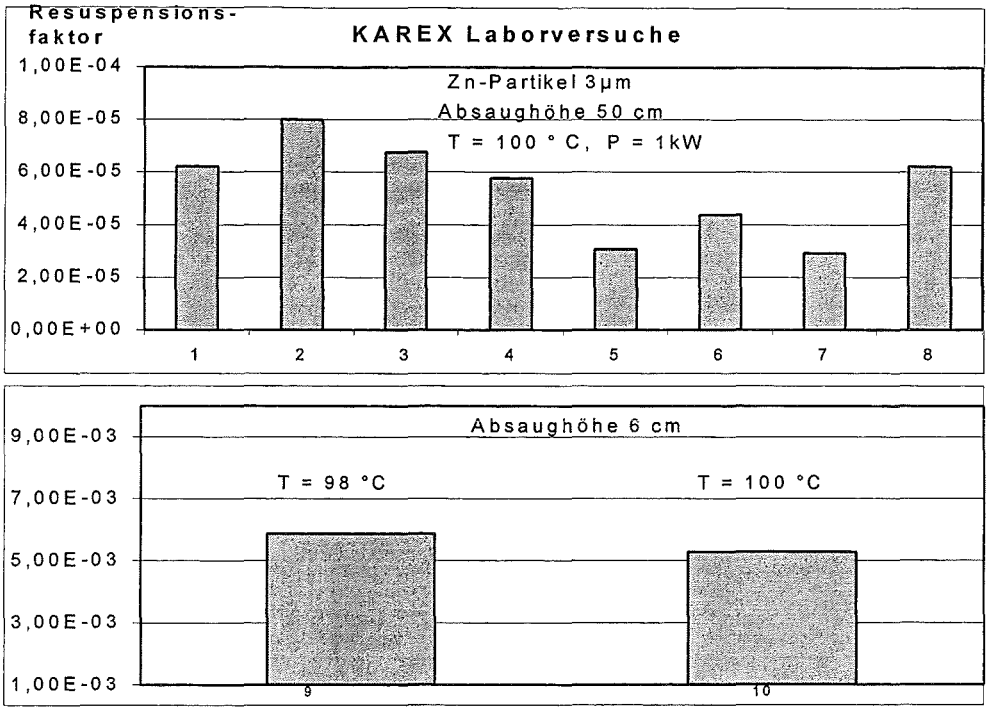

Abb. 1 Resuspensionsfaktoren für Zinkpulver aus KAREX-Laborversuchen im Bereich des Siedepunktes

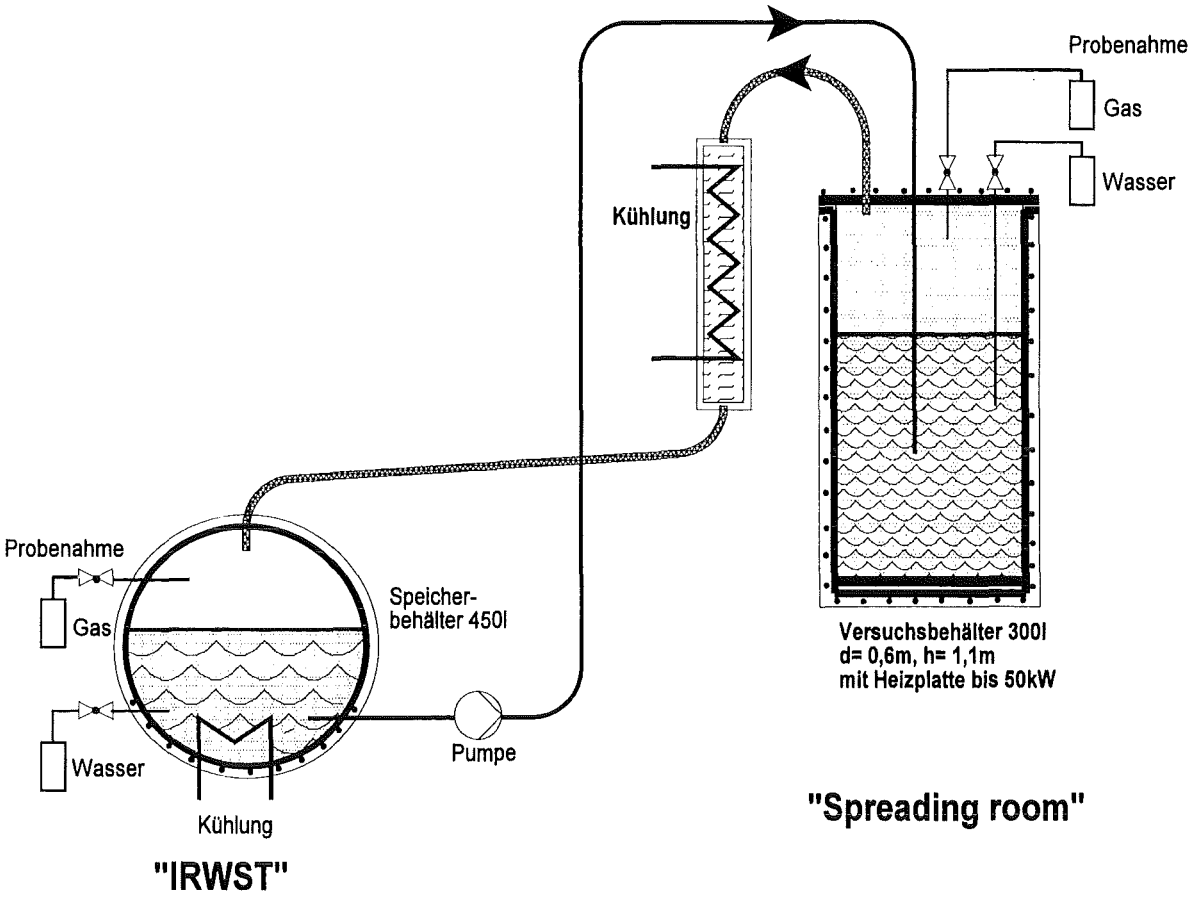

Abb. 2 Schema des neuen KAREX-Versuchsstandes im technischen Maßstab

32.23 STUDIEN ZUR AKTINIDENUMWANDLUNG

32.23.01 Neutronenphysikalische Untersuchungen zur Transmutation von Aktiniden und Spaltprodukten

I. Improving the Agreement between Many-Groups Transport and Few-Groups Diffusion Calculations by a Semi-Automatic Scheme for Deriving Adjusted Diffusion Coefficients

(S.Jaag, E.Kiefhaber, INR)

Abstract

Many-groups transport calculations are the most appropriate way for neutronic reactor calculations. But even with current powerful computer capabilities and using nodal instead of finite difference methods, such a procedure is too expensive for routine applications when compared to few-groups diffusion methods. The present study aims at the development of a numerical adjustment technique for establishing a closer correspondence between the many-groups transport and few-groups diffusion calculations. The method is based on the adaption of the few-groups diffusion coefficients. It will be demonstrated that such a correspondence can be achieved for a simplified CAPRA design without singularities.

Motivation and Introduction

A previous study [1] has shown that the former calculational route, *formulaire*, for neutronic calculations related to conventional LMFR concepts is no longer suitable for more complicated designs, like CAPRA, and calls for more sophisticated methods and tools. Among the conclusions gained in [1] is the fact that the 3-dim. coarse group diffusion calculations with VARIANT are sufficient for most purposes; however, for a reliable determination of Na-Void reactivities, transport calculations are still needed. Also mentioned in [1], was the lack of an improved formulaire for obtaining a suitable equivalence principle for adjusting the reactivities of control rods (or corresponding *heavy* diluent S/As) and of the reactivity worth of S/As filled with optically thin material,

such as *light* diluents or followers which are rather transparent for neutrons.

Even with today's powerful computer capabilities the most appropriate way for neutronic reactor calculations, i.e. the nodal many-groups transport calculations, are far too time consuming and the application of few-group diffusion still remains the first choice for routine applications in the framework of the *project route*. Therefore, a closer correspondence between the two calculational schemes is highly desirable. Naturally, such a correspondence can only be established for a particular type of reactor design.

Before dealing with the suggested equivalence relationships between transport and diffusion results for the *singularities*, it seems appropriate to aim at a closer similarity between the neutronics parameters for core layouts without any singularities. Having established such a similarity in a first step, the mentioned singularities will be dealt with in future work.

The desired equivalences will be derived on the basis of the nodal code package VARIANT [2] which provides both calculational options.

Basic Principles of the Diffusion Coefficient Adjustment Method for a Reactor without Singularities

As starting point, a many-groups (anisotropic) VARIANT transport calculation has to be performed for determining reference values forming the basis of the correspondence relations. The core dimensions and compositions should be in accordance with the envisaged design. Using the corresponding results of neutron balance evaluations one can derive a set of parameters, $A^{tr.,m}_{r,g}$, (where the upper index, *tr.,m*, stands for *m*any-groups *tr*ansport calculation) characterizing every reactor region, *r*, and group, *g*.

$$r = \begin{cases} 1 & : \text{ radial reflector} \\ 2 & : \text{ axial reflector} \\ 3 & : \text{ core} \end{cases} \qquad (1)$$

The physical nature of the parameters, $A^{tr.,m}_{r,g}$, is an essential aspect of the presented method and different choices are conceivable. In the present study a combination of leakage terms was chosen :

$$A_{r,g}^{tr.,m} = \begin{cases} L_{p,1,g} + L_{p,2,g} + L_{p,3,g} & : \mathrm{r}=1 \\ L_{z,2,g} + L_{z,3,g} & : \mathrm{r}=2 \\ L_{3,g} & : \mathrm{r}=3 \end{cases} \tag{2}$$

$L_{z,r,g}$ is the axial leakage, $L_{p,r,g}$ the planar (or horizontal) leakage, and $L_{r,g}$ the net leakage of the simplified reactor (in region r and group g). Other combinations for the parameters $A^{tr.,m}{}_{r,g}$ would also be justified and were also considered in the investigations, but the chosen parameters showed the best performance and account for the unavailability of an option allowing the application of direction-dependent diffusion coefficients in VARIANT.

The parameters $A^{tr.,m}{}_{r,g}$ can be collapsed to associated coarse group quantities $A^{tr.,m}{}_{r,G}$ using a suitable condensation scheme. For the same reactor configuration a coarse group diffusion calculation will give similar leakage parameters, $A^{di.,f}{}_{r,G}$. Both sets of parameters, $A^{tr.,m}{}_{r,G}$ and $A^{di.,f}{}_{r,G}$, will be similar but not identical. If the leakage parameters would exactly agree for all regions and groups both types of calculations would be almost equivalent. The agreement can be improved by modifying the few group diffusion constants. In order to do this in a systematic way, a straightforward matrix algorithm based on sensitivity coefficients and modification factors has been examined.

Let $A^{di.,f}{}_{r',G'}$ and $D_{r,G}$ and the leakage parameters and diffusion constants of the reactor regions r and r' in groups G and G', then one can derive the sensitivity coefficients

$$S_{r',G',r,G} = \frac{dA_{r',G'}^{di.,f}}{(dD/D)_{r,G}} \tag{3}$$

by a series of coarse group diffusion calculations, starting from a standard case, changing the diffusion constants for a certain energy group, G, in a specific region, r, by a reasonable amount, and evaluating the modified and the original neutron balance tables.

By solving the linear matrix equation:

$$S_{r',G',r,G} \cdot \left(\frac{\Delta D}{D}\right)_{r,G} = A^{tr.,m}_{r',G'} - A^{di.,f}_{r',G'} \tag{4}$$

a solution in form of a set of relative changes $(\Delta D/D)_{r,G}$ can be obtained. Despite the fact that the sensitivities will show a highly nonlinear behavior, it can be expected that the new set of adjusted diffusion coefficients

$$D'_{r,G} = D_{r,G} \cdot (1 + \left(\frac{\Delta D}{D}\right)_{r,G}) \tag{5}$$

will result in an improved agreement between the $A^{tr.,m}{}_{r,G}$ and $A^{di.,f}{}_{r,G}$ values.
In order to avoid unphysical solutions caused by the linearization of complicated functional relationships between $A^{di.,f}{}_{r',G'}$ and $D_{r,G}$, some restrictions on the changes of the diffusion constants revealed to be an important precaution:

$$c_{\min.,r,G} \cdot \min._{g \in G} D_{r,g} \quad \leq \quad D'_{r,G} \leq \quad c_{\max.,r,G} \cdot \max._{g \in G} D_{r,g} \tag{6}$$

The two constants $c_{min./max.,r,G}$ allow for additional flexibility of the adjustment method and will be described below.

Having available the modified coefficients, $D'_{r,G}$, a new diffusion calculation using these adjusted constants will show whether the corresponding parameters $A^{di.,f}{}_{r,G}$ are already close enough to the reference values $A^{di.,f}{}_{r,G}$. If the deviation is still larger than acceptable, the adjustment process can be repeated. After a very few iterations the remaining deviations are expected to become sufficiently small.

It was realized at a very early stage of the studies that the primitive method, as presented so far, was not able to yield physically reliable results, the new $D'_{r,G}$ sometimes exceeded all reasonable limits. Therefore, it was aimed at an optimization algorithm by a suitable adaption of the rank of the linear matrix equation: The new diffusion coefficients, $D'_{r,G}$, are computed as explained before, but, in case one of them exceeds the physical limits (Eqn. 6), the region/group with the minimal difference $A^{tr.,m}{}_{r,G}$-$A^{di.,f}{}_{r,G}$ will be removed from the matrix equation; it is anticipated, knowing that a perfect agreement cannot be achieved, that the corresponding diffusion coefficient, $D'_{r,G}$, and/or adjustment parameter, $A^{di.,f}{}_{r,G}$, cannot be improved. By applying this recipe,

the rank of the problem is lowered, the matrix equation is re-solved and the above procedure can be repeated until a physical result is obtained. The iterations terminate naturally when no new physical solution can be found within the physical limits.

It can be expected that the diffusion constant adaption factors, $(1+(\Delta D/D)_{r,G})$, can be applied unchanged to different reactors if the variations in the compositions remain only minor. Multiple use of the adaption factors is an attractive feature of the suggested new scheme.

Practical Realization of the Adjustment Method for a Simplified CAPRA Reactor without Singularities

A simplified reactor design without singularities and only one fuel region of an average enrichment was deduced from the CAPRA 4/94 layout. The axial dimensions were left unchanged. In order to reach criticality three fuel rings were necessary. For this reactor a 25-groups VARIANT transport calculation was performed providing the reference solution from which the leakage parameters, $A^{tr.,m}{}_{r,G}$, were derived. For the adjustment of the few-groups diffusion calculation a group scheme with 7 groups was chosen.

First, the condensed few-groups constants were used to perform a few-groups reference transport calculation; the results are needed to estimate reasonable limits, $c_{min./max.,r,G}$, for our adaption factors, $(1+(\Delta D/D)_{r,G})$, (compare Eqn. 6). Second, these condensed constants were used to derive the starting guess for the diffusion coefficients adjustment calculations.

The first column of Table1 compiles the parameter differences, $A^{tr.,m}{}_{r,G}$-$A^{di.,f}{}_{r,G}$ (Eqn. 2) between the 25gr. ref. case and the 7gr. diffusion approximation, the differences are expressed in *pcm*, i.e. normalized to the total fission production and multiplied by 10^5.

Definition of the Physical Limits for the Diffusion Coefficients

In the next step a physically reliable interval for the adjusted diffusion coefficients had to be determined. The first, straightforward, limitation follows from the maximum or minimum value found within the corresponding many-groups diffusion constants. In

order to accout for distortions caused by the condensation process itself, this limitation has to be weakened. It was decided that the additional factors $c_{min./max.,r,G}$, ,applied to the min./max. values (Eqn.6), will be derived from the results of a pre-adjustment process. This pre-adjustment follows exactly the same formalism as the *main* adjustment, as discussed so far. The only difference is the fact that the few-groups transport calculation is used as the reference for the leakage parameters. By admitting very weak limitation factors $c_{min.,r,G}$ = 0 and $c_{max.,r,G}$ = 2, the best consistency between the few-groups diffusion and the few-groups transport calculation is iterated. The so computed adaption factors, $(D'/D)_{r,G}$, provide a good estimate for $c_{min.,r,G}$ and $c_{max.,r,G}$. When a diffusion coefficient was not adjusted during the pre-adjustment, $D'_{r,G}=D_{r,G}$ the factor $c_{min./max.,r,G}$ is estimated via the leakage ratios $(A^{tr.,f}/A^{di.,f})_{r,G}$:

Under certain circumstances it might be possible that the above recipe results in limitation factors, $c_{min./max.,r,G}$, which are so close to unity that any adjustment of the corresponding diffusion coefficient is ruled out by Eqn.6. To avoid such a situation, the introduction of a minimum confidence interval seems to be recommended, e.g.: $(c_{max.,r,G}, - c_{min.,r,G}) > p$ (where, p can be of the order of a few percent).

Results

Table1 shows the improvement of the total reactivity and leakage parameters as a function of the iteration step. Only two iteration steps were necessary before the formalism stopped. Within the two steps the total reactivity difference between the multi-groups transport and the few-groups diffusion results dropped from more than 1100*pcm* to only about 50*pcm*. Also, the differences between leakage parameters were reduced significantly. The very good overall performance of the adaption method can be seen best when looking at the root mean square of the leakage parameter differences.

In addition to the reactivity differences, Table1 also shows the corresponding adaption factors as obtained by the adjustment formalism, only less than half of the diffusion coefficients were adjusted. The major adjustments had to be applied to the core region, the coefficients of the axial reflector remain almost unchanged.

		7 GR. DIFFUSION CALCULATION					
Iteration step		0		1		2	
Reactivity, pcm		-23		1465		1162	
Differences to the 25gr. Transport calculation							
Δpcm		-1140		348		45	
Region	Group	$A^{tr.,m}_{r,G} - A^{di.,f}_{r,G}$ and adaption factors $(D'/D)_{r,G}$					
Radial Reflector R=1	1	-2.78	-	-0.62	-	-1.24	-
	2	-224.28	-	-12.40	0.9046	-21.64	0.9046
	3	-1407.46	-	83.17	0.8516	-1.36	0.8535
	4	9.79	-	70.51	-	44.36	-
	5	40.80	-	46.37	-	43.83	-
	6	-6.90	-	3.26	-	-5.69	-
	7	23.12	-	22.95	-	11.87	-
Axial Reflector R=2	1	-2.53	-	-0.36	-	-0.88	-
	2	-36.18	-	-32.92	-	-34.77	-
	3	-271.96	-	10.46	0.7396	1.11	0.7396
	4	-34.81	-	-34.74	-	-38.87	-
	5	3.15	-	3.20	-	2.94	-
	6	-17.30	-	-19.61	-	-21.32	-
	7	-7.68	-	-14.09	-	-15.66	-
Core R=3	1	-969.70	-	243.36	0.7333	-0.51	0.7608
	2	-149.05	-	15.29	0.9924	-19.11	0.9924
	3	-244.68	-	182.30	1.1625	-9.07	1.2166
	4	180.56	-	-7.14	1.2609	28.70	1.2609
	5	52.35	-	76.49	-	80.23	-
	6	-62.96	-	-10.96	0.9389	1.18	0.9389
	7	92.54	-	-211.44	0.2858	-36.61	0.4711
Root mean square		389.18		87.60		28.46	
max. diff.		-1407.46		243.36		80.23	

Table 1: Reactivity and leakage parameters as a function of iteration steps together with their corresponding diffusion coefficient adjustment factors for the various reactor regions and coarse groups.

In order to validate the improvement which can be gained from the above adjustment process, the adaption factors, $(D'/D)_{r,G}$, were applied to a new simplified core with six diluents. The new core layout was the same as before, with the only difference that the number of fuel rings was increased up to 4, a measure necessary to compensate the reactivity-loss due to the insertion of 6 *typical* CAPRA diluents within the 3rd core ring (hexagon mid-sides). The 60 degrees symmetry was preserved. The result for the full core reactivity showed that the unadjusted 7 groups diffusion calculation underestimates the transport result significantly by more than 1700 *pcm*. When the adaption factors, $(D'/D)_{r,G}$, are applied to the diffusion coefficient of the reflectors and the core, a much better agreement is obtained, the discrepancy between many-groups transport and few-groups diffusion decreases by more than a factor of 3.

Computing costs

Adding the computation times of deriving the sensitivity matrix, the two transport reference calculations, and the iteration and pre-process for obtaining the limitation factors, $c_{min./max.,r,G}$, the total computing time sums up to about one hour on an IBM RISC 6000 workstation - a considerable effort. However, this initial expense for deriving adaption fators will pay off in the later design work because it is expected that these factors can always be used as long as no major design changes have to be taken into account. The computation time for a few-groups diffusion run, e.g. applying the obtained adaption factors, is only about 20 *s*

Treatment of Core-Singularities

Having got acceptable adaption factors for an unperturbed core configuration, we have to look how such an agreement can also be obtained for cores containing singularities like S/As filled with diluent (optically thin) or absorber (optically dense) material.

Again, starting with the simplified reactor layout it would be a quick step to a more general adjustment technique, also including the diffusion coefficient of the diluent/absorber S/A into the iteration process. Two different options can be imagined: first, an adaption of the diffusion coefficients of the diluent/absorber S/A, only, without a subsequent adjustment of the other reactor regions or, second, a more time-consuming

process including all reactor regions.

But, due to the remarkable influence of interface effects when dealing with singularities, it can be expected that a more refined treatment has to be applied. Additionally it has to be taken into account that the axial dimensions of optically thin singularities (many mean free paths) are typically 5-10 times larger than the lateral ones (neutron streaming). In this respect the previously mentioned lack of directional diffusion coefficients might become a serious shortcoming within the context of the adjustment method including singularities. It is highly recommended to include such an option in future versions of the VARIANT code.

Summary/Conclusions

The aim of the present study was to develop a semi-automatic scheme for the improvement of the reliability of few-groups diffusion calculations. The problem was solved for reactors without singularities by an iterative diffusion coefficient adjustment method:

The linear sensitivities of characteristic core parameters are determined as a function of the few-groups diffusion coefficients. When aiming at the highest possible consistency between the condensed core parameters obtained in many-groups transport calculations and the ones of few-groups diffusion calculations, one can derive a linear matrix equation. The solution of this equation results in a new set of few-groups diffusion coefficients. When taking these new coefficients as a starting guess for an improved calculation an iterative process can be defined; after convergence the solution leads to a few-groups diffusion calculation which shows an excellent agreement with the many-groups transport calculation. The comparison with the initial diffusion coefficients provide diffusion coefficient adaption factors which, then, can be applied to reactors which have similar core designs.

In order to avoid unphysical solutions caused by the linearization of the complicated functional relationships it was necessary to introduce a number of restrictions and a formalism for reducing the rank of the matrix equation.

For the example of a simplified CARPA core it was successfully demonstrated that the new method is well suited to achieve convincing consistencies between a many-groups transport and a few-groups diffusion calculation. Future work will have to be devoted to the problem of including singularities into the adaption process.

References

[1] S. Jaag and E. Kiefhaber, *Proc. of the 4th CAPRA Seminar*, Cadarache, 1997

[2] E.E. Lewis, C.B. Carrico, and G. Palmiotti, *Variational Nodal Formulation for the Spherical Harmonics Equations Nucl. Sci. and Eng.*, 122 (1996), 194

II. SIRENE : SAS4A Interface to Reactor Data Evaluated Using the Nuclear Code System ERANOS

(A. Rineiski, INR)

Abstract

The nodal diffusion and transport capability of ERANOS for 3-dimensional hexagonal-Z and rectangular geometry was extended to prepare neutronics parameters for the SAS4A safety analysis code. A new technique was developed that allows to compute the power and reactivity curves for 'fine' axial SAS4A nodes on the basis of the nodal fluxes obtained for 'coarse' VARIANT/TGV axial nodes. A scheme to prepare data for SAS4A, new ERANOS options, and a new associated post-processing code are described.

1. Objectives of the work

The nuclear code system ERANOS[1] is developed by France, Great Britain and Germany for Fast Reactor analysis and used as a basic tool for calculating neutronic parameters of modern Fast Burner Reactor cores (CAPRA[2]).

Recently, a new nodal diffusion/transport solver VARIANT/TGV[3] was included into ERANOS that made possible transport calculations of the neutron flux in the 3-D rectangular and hexagonal-Z reactor models. However, the power distributions and reactivity curves required for the safety analysis code SAS4A[4] could not be prepared directly by employing ERANOS with VARIANT/TGV.

Previously, SAS4A input was mainly prepared at FZK on the basis of the KAPROS[5] code system and an associated evaluation package by D. Thiem. In the future, all partners cooperating in CAPRA work should be enabled to prepare the SAS4A input parameters based on ERANOS (with VARIANT/TGV).

In this paper, SIRENE, the SAS4A Interface to Reactor data Evaluated using the Nuclear code system ERANOS, is described. It was developed at FZK/INR in cooperation with Dr. E. Kiefhaber/INR, DP. D. Thiem /INR, and Dr. D. Struwe/IRS.

2. The nuclear code system ECCO/ERANOS with VARIANT/TGV

The ECCO/ERANOS package includes the following parts:

- Calculation of basic nuclear data (cross-sections),
- Diffusion and transport calculations, power and perturbation calculations,
- Burnup calculations, detailed calculation of subassembly irradiation,
- Post-processing and printouts,
- The management of user libraries.

Most of the ERANOS modules create/modify/use the standard data structures called EDLs (Ensemble de Données LU) such as MICRO, MACRO, MEDIUM, CONCENTRATION, GEOMETRY, etc. There may be several different EDLs (with different names) of the same type. At the end of an ERANOS job, some EDLs may be saved in an archive for being retrieved from the archive later.

Before the VARIANT/TGV code was included into ERANOS, the ERANOS neutron flux calculations were mainly performed by H3D (HEX-Z diffusion finite-difference code) and BISTRO (RZ&XY transport Sn finite-difference code).

The VARIANT/TGV code is based on the Variational Nodal Method (VNM)[3], which was promoted in USA (by E. Lewis et. al.) and incorporated as a VARIANT module into the DIF3D[6] code system of ANL. Later, VARIANT was implemented into ERANOS as a TGV module.

VARIANT/TGV solves the real/adjoint neutron transport (or diffusion) equation in HEX-Z or XYZ geometry, with or without an external source.

According to VNM, the even-parity neutron flux $(\varphi(\Omega)+ \varphi(-\Omega))/2$ is approximated within the nodes by a linear combination of the basis functions which are the products of the spatial basis functions (Legendre polynomials) and angular basis functions (even spherical harmonics). At the node interfaces, the partial currents are approximated in a similar manner (with odd spherical harmonics).

The user can choose the expansion order both in space and in angle. The lowest angular expansion order corresponds to the diffusion approximation (P0 within the nodes, P1 on the node interfaces). Currently, the highest angular order is P5. In space, the within node flux may be approximated up to the 4th order (6th order in plane in HEX, HEX-Z), the interface currents up to the 2nd order.

VARIANT doesn't exchange data with the ERANOS EDLs directly. It uses the original (binary) DIF3D files as input (cross-sections, geometry,...) and output (flux, adjoint flux,...). The input files are created by ERANOS. After the calculations, VARIANT writes the real (or adjoint) flux into a NHFLUX (NAFLUX) file from which the scalar flux moments are read by ERANOS and written into an EDL. Then, this EDL may be used, for example, to simulate burnup. However, it cannot be used by the ERANOS modules which calculate the perturbation theory integrals, because these modules were originally developed to process the finite-difference fluxes.

Recently, a new KIN3D[7] module was included into VARIANT at Cadarache. It extends the capabilities of the code to solve the time-dependent transport (or diffusion) equations provided that changes in the cross-sections during the transient are known. It can also calculate the reactivity effects caused by changes in the cross-sections by employing the first order or exact perturbation theory approaches. Besides, the scalar products of the real and adjoint flux moments may be saved (in a binary file) and subsequently used by KIN3D again (instead of the real/adjoint flux moments).

3. Neutronic parameters for SAS4A

SAS4A employs the point-kinetics model to compute the reactor power during a transient. These computations are based on the reactivity and power curves which are usually calculated for the nominal conditions at the beginning of the transient (excepting the Doppler constants which are to be prepared for the both wet and dry core states and interpolated for the actual transient conditions).

To improve accuracy of the SAS4A simulations, these reactivity and power curves might be updated during the transient. That would require, however, employing of the transient

material and temperature distributions (determined by SAS4A) in the neutronic calculations, which would be performed (by ERANOS or a similar code) several times during a simulation. Such an option is postponed to the possible future implementation of a space-time kinetics module into SAS4A, that is desirable, in principle, but is beyond the frame of this work. Currently, the material density and temperature distributions in the reactor are to be provided completely by the ERANOS user.

During burnup, the reactivity and power curves (under nominal conditions) may change significantly. Therefore, several sets of the neutronics parameters (several inputs) for SAS4A (to simulate transients for several burnup states) should be prepared for the reactor in the general case. SAS4A takes into account impact of irradiation on the reactor material properties (for example, while computing probability of pin-failure), but it doesn't calculate changes in the fuel isotopic compositions; these changes during burnup have to be computed in advance by ERANOS formally independently of SAS4A.

SAS4A simulates the transient core behavior for a set of the thermal-hydraulics channels each of which usually represents an 'average' fuel pin of a group of S/As (these groups are chosen by the SAS4A user). For the CAPRA core, use of 21 channels was proposed, the material inside the diluent pins is currently ignored by SAS4A, the cladding of these pins being associated with the structure which represents a share of the duct wall per pin in a SAS4A thermal-hydraulics channel[8].

Each channel is subdivided axially into segments (generally speaking, independently in each channel) which are treated as nodes in the thermal-hydraulics (and other) models of SAS4A. During reactor operation and during the transient, these nodes change their heights (independently in each channel), but the related fuel masses remain constant until pin failure. Therefore, the core upper boundary position, which is the same for all channels of the cold fresh reactor, may change differently in different channels during a SAS4A simulation. Currently, this phenomenon is ignored by ERANOS, the axial expansion is assumed to be the same for all S/As.

The parameters, which are required by the SAS4A user, are of two types: the very SAS4A neutronic input parameters and a set of the additional parameters required for evaluations.

SAS4A input includes the parameters provided for each channel, each axial pin segment:

- relative power,
- wet and dry Doppler,
- coolant, cladding and fuel reactivity worths (per kg);

and the channel-independent parameters (provided for the whole reactor): the effective delayed neutron fractions, effective decay constants of the associated delayed neutron precursors and mean neutron lifetime.

Additional parameters are usually needed, such as

- maximum pin linear ratings,
- maximum pin powers,
- axial/radial form factors, etc.

in order

- to facilitate the choice of attributing the S/As to the SAS4A channels,
- to follow the power history of S/As,
- to evaluate the probability of pin failure during the specified S/A residence time
- to analyze the results of SAS4A transient simulations.

Optionally, these data are to be provided for each start/end of fuel (sub)cycle.

4. Two-step scheme

A two-step scheme was developed for preparing SAS4A data:

1. ERANOS is employed to create a SIRENE file that contains a large 'intermediate' set of neutronics parameters (power, reactivity contributions) for each S/A.

2. The SIRENE file is transformed into SAS4A input, the SAS4A channel and axial node specifications being employed. The SIRENE file is also used to compute the additional parameters which are required for evaluations. These calculations are done by a stand-alone post-processing program named SIPOST (which is not a part of ERANOS).

The proposed scheme has the following advantages:

- One (e.g. each SAS4A user) can simply process a SIRENE file to create SAS4A input employing different choices of attributing the S/As to the channels (even having no access to ERANOS).
- New types (such as DPAs or burn-up) may be included easily in the future due to the fairly simple structure of the file.
- A SIRENE file (with probably new types included) may be used to provide neutronics input for other thermal-hydraulics codes.
- A simple format facilitates use of SIRENE files on different computer platforms and the presentation of the SIRENE data in graphical form.

5. SIRENE file

This is an ASCII file which consists of data sections. The sections may be accumulated for different reactor states independently from each other. Each section is identified by TYPE and NAME. The following TYPEs can be produced currently:

- DENSITY_CHANGE (g/cm**3) = the material density changes related to changes in the cross-sections,
- POWER_CONTRIBUTIONS (W) = the nodal contributions to the total reactor power,
- POWER_DENSITY_MOMENTS (W/cm**3) = the nodal power density moments computed from the flux moments and power 'cross-sections' (which are calculated on the basis of the fission and capture cross-sections by the cross-section preparation modules of ERANOS),
- POINT_POWER_DENSITY(W/cm**3) = the power density values at the points defined by the user,
- REACTIVITY_CONTRIBUTIONS ($\Delta k/kk'$) = the nodal contributions to a reactivity value caused by the cross-section changes,
- REACTIVITY_COMPONENTS ($\Delta k/kk'$) = the nodal reactivity contributions and their components: leakage, absorption, production and scattering.

The section NAMEs are defined by the user. During post-processing, it is assumed (by default) that the NAMEs related to the 'material reactivity' and 'density change' sections are started from the COOL, CLAD, FUEL prefixes; the NAMEs related to wet Doppler are

started from the COLD, HOT, prefixes, the NAMEs related to dry (void) Doppler are started from the VCOLD, VHOT prefixes. If a SIRENE file contains sections with non-standard NAMEs or several sections with similar NAME prefixes (for example, COOL_FRESH, COOL_EOC1 reactivity sections), the user should specify NAMEs for the sections to be chosen during post-processing (see Section 12 for more details).

6. Reactivity and kinetics parameters: mathematical formulation

Hereafter, it is assumed that the transient starts at t=0, the reactor being at steady-state conditions earlier. During the transient, the time-dependent neutron flux is governed by the following system of equations:

$$\frac{1}{v_g(r,t)}\frac{\partial}{\partial t}\psi_g(r,\Omega,t)+\Omega\nabla\psi_g(r,\Omega,t)+\sigma_{t,g}(r,t)\psi_g(r,\Omega,t)=\frac{1}{4\pi}\sum_{g'}\sigma_{s,g'\to g}(r,t)\phi_{g'}(r,t)+$$
$$\frac{1}{4\pi}\{\chi_g(r,t)-\sum_i\chi_{i,g}\beta_i(r,t)\}\frac{1}{\gamma}\sum_{g'}\nu\sigma_{f,g'}(r,t)\phi_{g'}(r,t)+\frac{1}{4\pi}\sum_i\lambda_i\chi_{i,g}C_i(r,t)+\frac{1}{4\pi}Q_g(r,t), \quad (1)$$

$$\frac{\partial}{\partial t}C_i(r,t)=\beta_i(r,t)\frac{1}{\gamma}\sum_{g'}\nu\sigma_{f,g'}(r,t)\phi_{g'}(r,t)-\lambda_iC_i(r,t), \quad (2)$$

If Q=0 (no external source), γ is eigenvalue of the steady-state transport equation at t=0. If Q≠0, γ is equal to 1 (or to a parameter chosen by the user). Other notations are common.

The time-independent homogeneous adjoint neutron transport equation is solved at t=0:

$$-\Omega\nabla\psi^*_g(r,\Omega)+\sigma_{t,g}(r)\psi^*_g(r,\Omega)=\frac{1}{4\pi}\sum_{g'}\sigma_{s,g\to g'}(r)\phi^*_{g'}(r)+\frac{1}{4\pi k^*}\nu\sigma_{f,g}(r)\sum_{g'}\chi_{g'}(r)\phi^*_{g'}(r). \quad (3)$$

To obtain the point-kinetics equations and parameters (following the traditional procedure[9]), we multiply Eq. (1) by the adjoint flux, Eq.(3) by the real flux and perform integration, summation (hereafter, dVdΩdg=dX, dVdgdg′=dY, dVdg=dZ, ∫dg means summation over energy groups) and subtract the last equation from the first one:

$$\int dX\psi_g^*(r,\Omega)\frac{1}{v_g(r,t)}\frac{\partial}{\partial t}\psi_g(r,\Omega,t) =$$
$$-\int dX\{\psi_g^*(r,\Omega)\Omega\nabla\psi_g(r,\Omega,t) - \psi_g(r,\Omega,t)\Omega\nabla\psi_g^*(r,\Omega)) - \Delta\sigma_{t,g}(r,t)\psi_g^*(r,\Omega)\psi_g(r,\Omega,t)\}$$
$$+\int dY\{\Delta\sigma_{s,g'\to g}(r,t) + \frac{1}{\gamma}\chi_g(r,t)\nu\sigma_{f,g'}(r,t) - \frac{1}{k^*}\chi_g(r)\nu\sigma_{f,g'}(r)\}\phi_g^*(r)\phi_{g'}(r,t) \tag{4}$$
$$-\int dY\frac{1}{\gamma}\{\sum_i \chi_{i,g}\beta_i(r,t)\}\nu\sigma_{f,g'}(r)\phi_g^*(r)\phi_{g'}(r,t) + \int dZ\{\sum_i \lambda_i\chi_{i,g}C_i(r,t) + Q_g(r,t)\}\phi_g^*(r),$$

where $\Delta\sigma(r,t)=\sigma(r,t) - \sigma(r,0)$.

Employing a similar procedure with Eq. (2) and defining the normalization constant:

$$F = \frac{1}{\gamma}\int dY\{\chi_g(r,t)\nu\sigma_{f,g'}(r,t)\}\phi_g^*(r)\phi_{g'}(r,t), \tag{5}$$

one can obtain the well-known point kinetics equations:

$$\frac{dP(t)}{dt} = \frac{(\rho-\beta_{eff})}{\Lambda}P(t) + \sum_i \lambda_i C_i(t) + Q(t), \tag{6}$$

$$\frac{d}{dt}C_i(t) = \frac{\beta_{eff,i}}{\Lambda}P(t) - \lambda_i C_i(t), \tag{7}$$

where reactivity is defined (hereafter, time-dependence is omitted) as follows:

$$\rho = \frac{1}{F}[\int dX(\psi_g^*(r,\Omega)\Omega\nabla\psi_g(r,\Omega) - \psi_g(r,\Omega)\Omega\nabla\psi_g^*(r,\Omega))$$
$$-\int dX\Delta\sigma_{t,g}(r)\psi_g^*(r,\Omega)\psi_g(r,\Omega) + \int dY\Delta\sigma_{s,g'\to g}(r,t)\phi_g^*(r)\phi_{g'}(r) \tag{8}$$
$$+\frac{1}{k^*}\int dY\Delta\{\chi_g(r)\nu\sigma_{f,g'}(r)\}\phi_g^*(r)\phi_{g'}(r)] + \{1-\frac{\gamma}{k^*}\}.$$

The kinetics parameters (effective delayed neutron fractions and mean generation time) are defined as

$$\beta_{eff,i} = \frac{1}{\gamma F}\int dY\chi_{i,g}(r)\beta_i(r)\nu\sigma_{f,g'}(r)\phi_g^*(r)\phi_{g'}(r), \tag{9}$$

$$\Lambda = \frac{1}{F}\int dX\psi_g^*(\Omega,r)\frac{1}{v_g(r)}\psi_g(\Omega,r) = \gamma\cdot l, \tag{10}$$

where l is the mean neutron lifetime.

7. Reactivity coefficients for SAS4A

During the transient, the reactivity coefficients are treated by SAS4A as normalized (per mass or per temperature change) contributions (from the nodes of the SAS4A reactor model) to the reactivity value defined by Eq. (8) (without the {...}member); the cross-section changes in Eq. (8) being caused by changes in the coolant, clad, and fuel density (material reactivities) and in fuel temperature (contributions to the Doppler constant) values.

The following material reactivity worths [1/kg] are of interest:
$-\rho_{coolant}/\Delta_{coolant\_mass}$, $\rho_{clad}/\Delta_{clad\_mass}$, and $\rho_{fuel}/\Delta_{fuel\_mass}$ (void, clad, and fuel coefficients)

The wet and dry (void) Doppler constants are calculated as:
$(\rho_{hot} - \rho_{cold})/\ln(t_{hot}/t_{cold})$ and $(\rho_{void\ hot} - \rho_{void\ cold})/\ln(t_{hot}/t_{cold})$,
where t_{hot}, t_{cold} are two different values related to the fuel temperature.

Simulating a transient, SAS4A computes a reactivity contribution due to change in the coolant density value (in a node) by multiplying the related mass change by the related reactivity coefficient. The total reactivity value is calculated by summation of the contributions of all types from all nodes.

One can note again, that employing the **same** set of the reactivity coefficients to compute the reactivity values related to **different** reactor states (which occur during the transient) is certainly an approximation.

The reactivity effect calculations are based on the VARIANT/KIN3D perturbation theory option. This option was developed earlier to compute reactivity effects (eigenvalue changes) provided that the related cross-section changes are known and the neutron real and adjoint even-parity flux moments are available (calculated by VARIANT).

KIN3D calculates the reactivity effects (here, k^* is the eigenvalue related to the unperturbed state, k′ is that one related to the perturbed state) according to the following expression:

$$\frac{\Delta k}{k'k^*} = \frac{1}{\int dY\{\chi_g(r)\nu\sigma_{f,g'}(r)\}\phi_g^*(r)\phi_{g'}(r)}[\int dX\{\psi_g^*(r,\Omega)\Omega\nabla\psi_g(r,\Omega)$$
$$-\psi_g(r,\Omega)\Omega\nabla\psi_g^*(r,\Omega) - \Delta\sigma_{t,g}(r)\psi_g^*(r,\Omega)\psi_g(r,\Omega)\} + \int dY\Delta\sigma_{s,g'\to g}(r)\phi_g^*(r)\phi_{g'}(r) \qquad (11)$$
$$+\frac{1}{k^*}\int dY\Delta\{\chi_g(r)\nu\sigma_{f,g'}(r)\}\phi_g^*(r)\phi_{g'}(r)]$$

As one can see, the reactivity value and related nodal contributions (defined by Eq.(8) without the {...} term) can be computed as given by Eq. (11) and then multiplied by γ. For a subcritical reactor, the integral defined by Eq. (11) has no longer the meaning of an eigenvalue change, but it still might be used to compute reactivity.

In the SIRENE preparations, the unperturbed state is the nominal reactor state, and several intentionally perturbed states are obtained from the nominal state by changing one (or two for void Doppler) of the reactor parameters (coolant density, clad density, fuel density, temperature, temperature & coolant density) which are related to the corresponding reactivity coefficients (void, clad,...). The user is free in choosing a suitable degree of perturbation: to find the 'void' coefficients, concentration of coolant, may be changed by 10%, or coolant may be completely removed from the core. A perturbed state, however, should be chosen taking into account numerical accuracy of the cross-section computations and, therefore, it cannot be 'too' close to the unperturbed state.

Eqs. (8) - (10) were derived using the time-dependent real flux. Instead, the real flux moments, which are employed in the KIN3D calculations for SAS4A, are obtained by solving the steady-state neutron transport (or diffusion) equation for the nominal state or for a corresponding perturbed state. The most important thing is that the 'wet' real fluxes must be used to compute 'wet' Doppler, and the 'dry' real fluxes must be used to get 'dry' Doppler. However, in all reactivity and kinetics parameter calculations, the same adjoint flux must be used.

The reactivity parameters (Doppler, material worths) must be calculated for the core segments and for some segments up and below the core (for a breeder reactor, these segments belong to the blankets). The upper/lower segment contributions to the Doppler constant are equal to zero if these segments contain no heavy isotopes (and contributions

of other isotopes to Doppler are neglected). On the contrary, the fuel reactivity worths are always greater than zero and must be calculated assuming change in **fuel** concentration even in the non-fuel segments: these worths are used by SAS4A to compute the reactivity contributions related to fuel movement during the transient (axial expansion due to temperature changes, fuel movement during the post-failure phase of the transient).

Currently, SAS4A employs in each channel (1) the two (wet and dry) Doppler constants for the whole channel and (2) the normalized (sum is equal to unity) related nodal contributions which are assumed by SAS4A to be the same for the wet and dry states. However, the user should write into a SIRENE file the nodal contributions to the two Doppler constants.

8. Remapping of reactivity and power curves

In the general case, the reactor core models of VARIANT and SAS4A are different both in plane and in the axial dimension. Transformation of the reactor parameters computed by VARIANT to another subdivision in plane is fairly straightforward: one should just sum or average the S/A-wise data for the chosen group of S/As, this is done during post-processing. With respect to the axial dimension, the situation is more complicated (see Fig. 1).

The typical SAS4A axial mesh size is about 5 cm, the mesh being more detailed near (up and below) the upper core boundary. A coarser VARIANT axial mesh (of about 10 cm or more) might be usually recommended to take full advantage of the efficiency of VNM. Thus, it might be desirable to solve the neutron transport equations with the coarse axial nodes and than 'remap' the solutions (or their functionals) to a finer axial mesh.

VARIANT/TGV axial mesh:
Eulerian, channel-independent

SAS4A axial mesh:
Lagrangian, channel-dependent (in the general case)

Fig. 1 VARIANT axial mesh and SAS4A axial mesh (core with a few segments up and below)

If one has to recalculate several times the power/reactivity curves during the transient (this option is foreseen for the future), 'remapping' would be also needed for the material density and temperature distributions.

Lower part of the blanket (or a control rod)
Upper part of the core (or a rod follower)

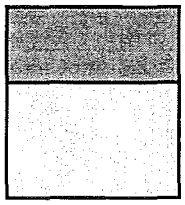

Fig. 2 Heterogeneous node where the cross-sections are stepwise functions

The 'remapping' implies, that the nodes, which are treated as homogeneous in the neutronic reactor model, have (in principle) a heterogeneous structure because they may include several (fully or only parts of) SAS4A nodes each of which changes its parameters (the material density and temperature values) during simulation in its own manner (finite-difference tools are much less subject to these problems because they usually employ many fairly small meshes).

VNM allows use of heterogeneous nodes. It was demonstrated for 2D XY models that the 'heterogeneous' response matrices might be computed by numerical integration and used

to calculate the neutron flux in a more accurate manner than by employing models with 'homogenized' nodes.

A new method was developed to calculate the response matrices for axially heterogeneous nodes without numerical integration, **provided** that the cross-sections are stepwise functions axially (see Fig. 2). The proposed technique allows also to compute the reactivity and power contributions from fine axial sub-nodes, on the basis of the 'coarse' nodal real and adjoint fluxes.

The full implementation of the method would be useful for possible future coupling of SAS4A with a spatial kinetics code based on VNM. Currently, the technique is used only to remap the coarse power and reactivity curves.

The mathematical formulation of the method and the results of corresponding verification for some benchmark cases are given in the original SIRENE report.

9. Modified and new ERANOS modules.

The following new options were included into the KIN3D module of VARIANT:

- The power density moments, nodal power and reactivity contributions (defined by Eq.(11)) can be written into a SIRENE file (optionally, for the fissile S/As only).
- The scalar products, power and reactivity contributions can be computed for 'fine' axial subnodes on the basis of the 'coarse' fluxes (the flux calculations with the heterogeneous nodes has not been implemented yet in VARIANT).
- For the reactivity calculations, a perturbed region of the reactor (defined initially by matching the macroscopic cross-sections for the unperturbed and perturbed states) can be changed by employing the following options: (1) the perturbed domain can be restricted axially to exclude, for example, the nodes where the material compositions are similar, but the cross-sections are different due to a chosen option of cross-section condensation; (2) the extended axial boundaries can be introduced to apply the core cross-section changes to the regions below and above the core. To compute the fuel worths, two options have to be employed: first, the 'blanket' regions are excluded; second, these regions are included, but with the a new (core) material assignment.

A new capability was implemented into the CALCUL_BETA_EFFECTIF module of ERANOS: a scalar product file (of the nodal real and adjoint flux moments computed by VARIANT) can be employed to calculate the kinetics parameters. Earlier, these calculations could be performed on the basis of the finite-difference fluxes only. The printout of the module remains unchanged: the effective delayed neutron fractions, effective decay constants and mean neutron lifetime.

For the nodal calculations, lifetime is calculated by KIN3D, saved in a scalar product file and just printed by CALCUL_BETA_EFFECTIF.

10. SIRENE file preparations

To prepare a SIRENE file, a lot of the ERANOS modules is employed. The general data flow is presented in Fig. 3.

Fig. 3 Data processing for SIRENE (EDLs, FILEs, *SIRENE SECTIONS*)

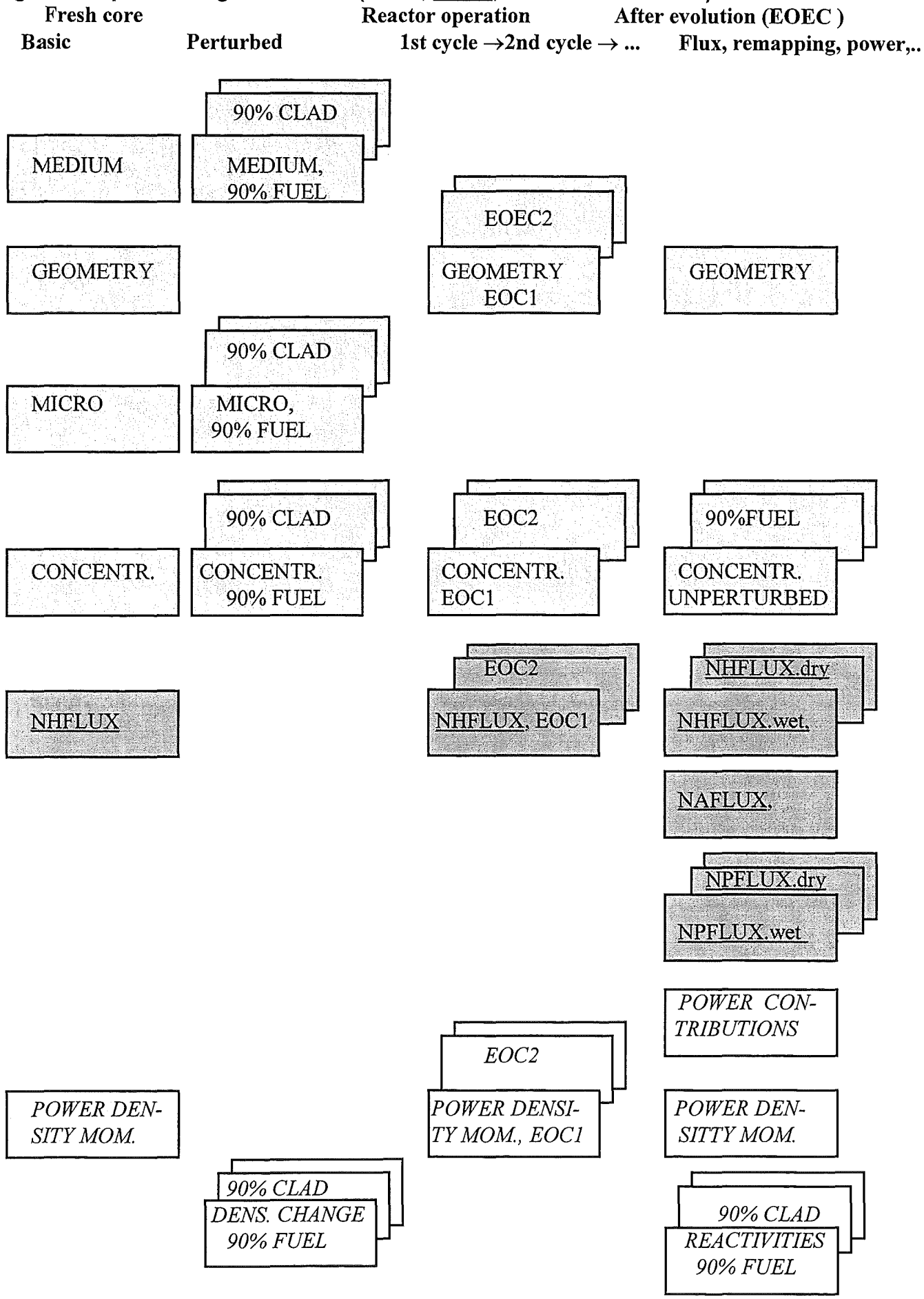

11. Post-processing

Post-processing is performed by the SIPOST program. Currently, SIPOST has two modes: CREATE_SAS4A_INPUT and EDIT_POWER. The SIPOST input parameters are provided in the ERANOS-like format.

11.1 CREATE_SAS4A_INPUT mode

In this mode, a complete set of the following SIRENE sections

- DENSITY_ CHANGE (with names starting from 'COOL', 'CLAD', 'FUEL', or others but with the same meaning),
- POWER_CONTRIBUTIONS,
- REACTIVITY_CONTRIBUTIONS (with names starting from the 'COOL', 'CLAD', 'FUEL', 'COLD', 'HOT', 'VCOLD', 'VHOT' prefixes or with others but with the same meaning)

must be available from a SIRENE file (REACTIVITY_COMPONENTS can be used instead of REACTIVITY_CONTRIBUTIONS).

The user defines the section NAMEs (if they are not standard or there are NAMEs with similar prefixes), the S/A numbers (2 numbers for each S/A: for example, {30, 30} for the central S/A in hexagonal geometry; {1, 1} for the S/A with minimal X and Y coordinates in rectangular geometry), axial subdivision, temperatures of the COLD and HOT states. The user may specify only the few first letters of a NAME. '*' indicates that any NAME can be chosen. If several SIRENE sections (of a given TYPE) match the same character string for "NAME", the last met (while looking through the file from the beginning to the end) section is chosen.

The S/A numbers (provided as input parameters for SIPOST) must match the numbers provided as a part of a SIRENE section. If the reactor model is a 120-degree (or a 180-degree sector), a SIRENE section will contain data for the 120-degree (180-degree) sector (optionally, without non-fissile S/As), and the user should define the S/A numbers for the same sector.

Axial subdivision may be different, in principle, for different channels. In the example, the same vertical mesh is used for all channels.

Different SIRENE sections may have different axial meshes, each of which may be more or less detailed than a SAS4A mesh (for a particular channel). The power and reactivity contributions, density changes are remapped during post-processing in a very simple manner: considering these axial distributions as histograms and integrating between the limits corresponding to the SAS4A node boundaries. Therefore, it is recommended to include all SAS4A axial mesh boundaries (as ADDITIONAL_AXIAL_PLANES) into the mesh, for which the power and reactivity distributions are prepared.

An axial mesh of a SIRENE section takes into account axial expansion. Therefore, the user may provide a 'cold' SAS4A mesh (which is transformed by the code into the 'expanded' mesh) or a 'hot' (already expanded) mesh. By default, the 'cold' option is chosen, the axial expansion coefficients are taken from the DENSITY_CHANGE sections (these sections always contain axial and radial expansion coefficients).

Since the values defined by Eq. (8) and Eq. (11) (without the {...} term) are different (with respect to the normalization constant if $\gamma \neq 1$) the user can opt how to define γ: (1) as k* , (2) as k or (3) as an arbitrary number provided by the user (see end of Section 8 for meaning of k and k* and for recommendations). By default, the first option is chosen. The third option (for example, 1.0) might be preferable if one has to consider a situation where the reactor model is not critical e.g. because the rods are not positioned properly, and that control rod movement does not change strongly the power and reactivity curves.

11.2 EDIT_POWER mode

In this mode, only POWER_DENSITY_MOMENTS must be available from a SIRENE file. The parameters 'for evaluations' (maximum pin powers, maximum linear ratings, ...) are calculated for each S/A, group of S/As (channel), and the whole reactor. In this mode, the SIRENE channel subdivision may differ from the SAS4A channel subdivision.

The following two types of pins are presently allowed only: fissile (fertile) and diluent pins. There may be only one fissile pin type in a fuel (fertile) S/A (but S/As related to different channels may contain different fissile pins). During the post-processing, power in a fuel S/A is assumed to be produced by the fissile pins only. However, the contributions from the fuel S/As to the **total** reactor thermal power are accurate (with γ-power contributions from **all** materials).

The pin power reconstruction is performed at fuel pin centers and based on the homogeneous (within each node) flux calculations and, therefore, reflects only the global behavior of the intranodal flux. The positions (in plane) of pin centers are calculated by employing the following parameters: the total number of pins, pin diameter and p/d ratio (assuming triangular/square pin grid in a hexagonal/square geometry). In the center of each fissile pin, axial power density moments (coefficients of polynomials of order 1, 2, 3 or 4) are calculated for each axial segment, the power density being assumed constant within each pin in plane. These moments are normalized (with respect to the total S/A power and used to compute the average and maximum power density values. The power edits can be made for an axial subregion of the reactor (this feature might be useful to exclude, for example, the axial blankets).

Since all dimensions in a SIRENE file take into account axial expansion, the user may determine the 'hot' dimensions (pin diameter, boundaries of the axial subregion) or the 'cold' dimensions. If the 'cold' option is chosen, the user may
(1) define NAME of a DENSITY_CHANGE section (the file must contain such a section in this case): the axial and radial expansion coefficients are retrieved from this section,
(2) or define cold S/A pitch and core (here, the region for which the POWER_DENSITY_MOMENTS are given) height: the axial and radial expansion coefficients will then be calculated by the code (by comparing them with hot S/A pitch and hot core height which are available from the SIRENE file).

12. Upgrading SIRENE for Square S/As, Lead Cooling, and ADS

When developing SIRENE within the framework of the CAPRA cooperation, the main objective was a fast burner reactor with hexagonal shaped S/As and sodium as coolant

medium. Offering the potential for better safety features, currently, alternative coolants are discussed for advanced LMFR designs. The candidates considered as the most attracting ones are lead and the lead-bismuth eutecticum. Due to their high atomic mass numbers, a tight hexagonal lattice (which was required for Na to avoid a softening of the spectrum) is no longer needed and can be replaced by a configuration of square S/As, e.g. used in most LWRs.

Therefore, the ERANOS/SAS4A interface SIRENE was extended to compute the power and reactivity curves in square geometry. For such a lead-cooled fast reactor an input has been created for ERANOS on basis of a report (prepared by Dr. Heusener et al. "Seminar on the Concept of the High Safety and Economy Lead-Cooled Fast Reactor, Moscow, October 1990"). One particular feature of this LFR design is its square arrangement of the fuel pins and the absence of wrapper tubes. Fig. 5 shows a quarter of the horizontal cross section of the core layout together with some typical features characterizing the suggested design. Since some technical details are not given in the report (such as Pu isotopic compositions), corresponding data from the input for a CAPRA design were used, and, therefore, some given parameters (such as fuel enrichment) were slightly modified to obtain a complete and consistent input. The applicability of the SIRENE interface for this lead fast reactor model was demonstrated.

Recently, also accelerator driven systems (ADSs) have regained considerable attention because of their claimed improved safety characteristics and the corresponding advantages in cases of postulated accidents. These ADSs are characterized by a intense external neutron source produced by spallation reactions (e.g. induced by a proton beam on a liquid lead target) and a subcriticality of the multiplying medium. To accomodate SIRENE to future safety-related studies of such new designs some extensions and amendments were also implemented in the code package.

All modifications were included in the documentation and the options were tested successfully in preliminary test runs.

12. Summary

An interface (SIRENE) between ERANOS and SAS4A was established. New options were implemented into the KIN3D module of VARIANT/TGV to produce a SIRENE file; a new code (SIPOST) was developed to transform SIRENE data into SAS4A input and a set of parameters required for evaluations (maximum linear ratings etc.).

A new technique was developed to compute response matrices for axially heterogeneous nodes without numerical integration. It is employed in KIN3D to compute the power and reactivity contributions from fine axial subnodes on the basis of the 'coarse' nodal fluxes for SIRENE.

Two new modules were included into ERANOS to facilitate SIRENE preparations. A module of ERANOS was extended to compute the kinetics parameters on the basis of the nodal solutions.

Currently, the material and temperature distributions in the reactor must be provided completely by the ERANOS user. A tighter SAS4A/ERANOS coupling is desirable to recompute the reactivity and power curves during the transient, thus, improving accuracy of SAS4A simulations. Implementation of the mentioned technique into VARIANT to calculate the neutron flux with axially heterogeneous nodes would be useful for these coupling.

Acknowledgments

The author is grateful to Dr. G. Heusener and Prof. G. Keßler for providing an opportunity to work at FZK. Dr. E. Kiefhaber read the paper very carefully and made many good suggestions to improve the presentation. Dr. G. Palmiotti (working currently at ANL/USA) kindly provided the VARIANT spatial basis functions. Mr. J. M. Rieunier of Cadarache helped a lot with ERANOS. The author thanks also the colleagues of INR for their help, advice and support during his stay at FZK.

References

1. J. Y. Doriath, C. W. McCallien, E. Kiefhaber, U. Wehmann, J.M. Rieunier, "ERANOS 1: The Advanced European System of Codes for Reactor Physics Calculations", Proc. Int. Conf., Karlsruhe, (1993).
2. A. Languille et al. , "Capra core studies - the oxide reference option", Proc. Int. Conf. on Evaluation of Emerging Nuclear Fuel Cycle Systems (GLOBAL'95), Versailles, France (1995).
3. E. Lewis, C. B. Carrico and G. Palmiotti, "Variational Nodal Formulation for the Spherical Harmonics Equations," Nucl. Sci. Eng., 122, p. 194 (1996); Latest improvements and extensions were communicated by J.-M. Rieunier, 1998, Cadarache, France.
4. D. R. Ferguson et al. , "The SAS4A LMFBR Accident Analysis Code System: A Progress Report", Proc. Int. Meeting on Fast Reactor Safety and Related Physics, Chicago, (1976).
5. N. Moritz, "Die FORTRAN-77 Version des Karlsruher Programmsystems KAPROS", KfK 3860, Karlsruhe, (1985); G. Buckel, W. Höbel, "Das Karlsruher Programmsystem KAPROS, Teil I, Übersicht und Vereinbarungen, Einführung für Benutzer und Programmierer", KfK 2317, Karlsruhe (1976); H. Bachmann, S. Kleinheins, "Das Karlsruher Programmsystem KAPROS, Teil Ia, Kurzes KAPROS-Benutzerhandbuch", KfK 2317, Karlsruhe (1976).
6. K.L. Derstine, "DIF3D", code abstract, Proc. Top. Meeting on Advances in Reactor Computations, Salt Lake City, p. 225, (1983).
7. A. Rineiski, "KIN3D: A space-time kinetics and perturbation theory module for TGV2", NT-97-203, Cadarache, France (1997).
8. D. Struwe. Private communication, (1997).
9. G. Bell and S. Glasstone, "Nuclear Reactor Theory", Van Nostrand Reinhold Company, (1970).
10. S. Jaag and E. Kiefhaber, "Definition of a Suitable Project Route for CAPRA Neutronic Calculations", INR-1964, Karlsruhe, (1997).

32.23.02 Abtrennverfahren für Aktiniden aus hochradioaktiven Abfällen

(Z. Kolarik, U. Müllich, A. Geist, INE)

Zusammenfassung

Die schwierige Trennung von Transplutoniden(III) von den Spaltlanthaniden(III) aus stark salpetersaurer Lösung kann extraktiv mit 2,6-Di-(5,6-dialkyl-1,2,4-triazin-3-yl)-pyridinen erfolgen. Insbesondere 2,6-Di-(5,6-dipropyl-1,2,4-triazin-3-yl)pyridin trennt aus bis zu 0,9 M HNO_3 Am(III) von Eu(III) mit einem Trennfaktor von ca. 130 und geeignenten Verteilungskoeffizienten als trisolvate Komplexe vom Typ $Am(NO_3)_3 \cdot HNO_3 \cdot 3B$ bzw. $Eu(NO_3)_3 \cdot HNO_3 \cdot 3B$.

Einleitung

Das Vorhaben wird im Rahmen des EU-Programms „Safety of Nuclear Reactors. A.2. Fuel Cycle Concepts (Partitioning and Transmutation)" unter der Vertragsnummer FI4I-CT96-0100 bearbeitet (Projekt „New Partitioning Techniques"; Vertrag seit 1.5.96, finanzielle Unterstützung EUR 100.000 für drei Jahre). Das Projekt befaßt sich mit der Ausarbeitung eines Prozesses zur Abtrennung von Minoren Aktiniden aus dem hochaktiven Flüssigabfall der Wiederaufarbeitung von Kernbrennstoffen. Gemäß der Arbeitsaufteilung innerhalb des EU-Programms liegt der Schwerpunkt unserer Arbeit an dem Vorhaben in der Untersuchung der Abtrennung von Transplutoniden(III) von den Spaltlanthaniden(III).

Das Ziel unserer Arbeiten ist die Synthese und Charakterisierung von Extraktionsmitteln für die selektive Extraktion von Transplutoniden(III) in Bezug auf Spaltlanthaniden(III). Die gewünschte Selektivität wird durch eine sogenannte „soft donor"-Bindung der abzutrennenden Metallionen über Stickstoffatome erreicht.

Es wurden neutrale, tridentat (d.h. über drei Stickstoffatome) solvatisierende Extraktionsmittel B synthetisiert, welche Aktiniden(III) und Lanthaniden (III) (M^{3+}) als neutrale Komplexe vom Typ $MA_3 \cdot nB$ in die organische Phase überführen. Charakterisierende Extraktionsversuche wurden mit Am(III) und Eu(III) als Vertreter der Transplutoniden(III) bzw. Spaltlanthaniden(III) durchgeführt.

2,6-Di-(5,6-dialkyl-1,2,4-triazin-3-yl)pyridine

Im Jahre 1998 wurden neue Dihetarylderivate von Pyridin, namentlich 2,6-Di-(5,6-dialkyl-1,2,4-triazin-3-yl)pyridine, synthetisiert und charakterisiert (siehe Abbildung).

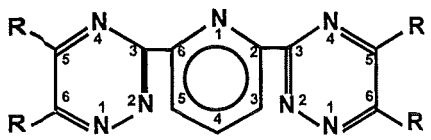

Structure B

R = Methyl, Ethyl, Propyl, Butyl, Isopropyl, Isobutyl, Phenyl, p-Tolyl, p-tert.-Butylphenyl

Die Verbindungen zeichnen sich durch teilweise sehr günstige Extraktionseigenschaften aus. So extrahiert beispielsweise eine 0,0267 M Lösung von 2,6-Di-(5,6-diethyl-1,2,4-triazin-3-yl)pyridin in einem aliphatischen Verdünnungsmittel (TPH) Am(III) als Bromhexanoat aus 0,1 M Salpetersäure mit einem Verteilungsverhältnis von über 1000 und einem Am(III)/Eu(III)-Trennfaktor von ca. 140.

Der zunächst enttäuschende Befund, daß die Extraktionsmittel in Gegenwart von Bromhexansäure chemisch instabil sind, verliert durch folgende Tatsache an Bedeutung: Die 2,6-Di-(5,6-dialkyl-1,2,4-triazin-3-yl)pyridine extrahieren Am(III) und Eu(III) sehr effektiv als Nitrate [1]. Dies ist aufgrund der Anwesenheit von Nitrat in den betrachteten Prozeßlösungen vorteilhaft. So extrahiert 2,6-Di-(5,6-dipropyl-1,2,4-triazin-3-yl)pyridin in TPH mit 2-Ethyl-1-hexanol als Modifier Am(III) als Nitrat aus (0,9 M HNO_3 + 1,0 M NH_4NO_3) mit einem Verteilungsverhältnis von 23 und einem Am(III)/Eu(III)-Trennfaktor von ca. 130.
Um die wäßrige Löslichkeit herabzusetzten, wurden n-Butyl- und Isobutylreste eingeführt. Dies verlangsamt jedoch die Extraktionskinetik drastisch. Die Einführung von Isopropylresten unterdrückt desweiteren die Am(III)/Eu(III)-Trennung fast vollständig.
Zur Erhöhung der chemischen Stabilität wurden die Alkylreste durch aromatische Substituenten ersetzt. Dies erhöht zwar die chemische Stabiltät, unterdrückt jedoch die Löslichkeit in aliphatischen Lösungsmitteln (R = Phenyl, p-Tolyl) bzw. die Am(III)/Eu(III)-Trennung (R = p-tert.-Butylphenyl).

Weitere Untersuchungen [2] beschränkten sich also auf 2,6-Di-(5,6-dipropyl-1,2,4-triazin-3-yl)pyridin (DPTP).

Aus der gefundenen Abhängigkeit des Verteilungskoeffizien des Komplexbildners selbst von seiner Konzentration folgt, daß DPTP in der organischen Phase selbstassoziiert. Der Komplexbildner liegt in dimerer und trimerer Form in der organischen Phase vor; der Grad der Selbstassoziation ist von der Salpetersäurekonzentration abhängig.
Untersuchungen des Einflusses verschiedener Verdünnungsmittel und Modifier auf Extraktionseffektivität und Trennfaktor von DPTP bezüglich Am(III)/Eu(III) zeigen die überlegenen Eigenschaften von TPH/2-Ethyl-1-hexanol als organische Phase.
Die Zusammensetzung der in der organischen Phase vorliegenden Komplexe wurde über die Abhängigkeit der Am(III)- und Eu(III)-Verteilungsverhältnisse von der Komplexbildner- (B) bzw. Nitratkonzentration bestimmt. Demnach werden Am(III) und Eu(III) als trisolvate Komplexe $Am(NO_3)_3 \cdot HNO_3 \cdot 3B$ bzw. $Eu(NO_3)_3 \cdot HNO_3 \cdot 3B$ in die organische Phase überführt.
Der hohe Trennfaktor wird durch die Anwesenheit von Eu(III)-Makrokonzentrationen (bis 0,1 M, im Gegensatz zu den sonst verwendeten Tracerkonzentrationen) nicht herabgesetzt. Auch die Bildung einer dritten Phase wird durch die höhere Beladung der organischen Phase mit Eu(III) nicht beobachtet, die gebildeten Komplexe sind also in der organischen Phase ausreichend löslich.

Schlußfolgerung

Es wurde mit DPTP, gelöst in TPH/2-Ethyl-1-hexanol, ein Extraktionssystem zur selektiven Abtrennung von Am(III) gegenüber Eu(III) aus stark salpetersaurer Lösung vorgestellt. Die vielversprechenden Eigenschaften machen eine weitere Verbesserung der Komplexbildner, insbesondere im Hinblick auf eine höhere chemische Stabilität, wünschenswert.

---

[1] Z. Kolarik, U. Müllich and F. Gassner, *Selective Extraction of Am(III) over Eu(III) by 2,6-Ditriazolyl- and 2,6-Ditriazinylpyridines,* Solvent Extr. Ion Exch. **17**, 23 (1999)

[2] Z. Kolarik, U. Müllich and F. Gassner, *Extraction of Am(III) and Eu(III) Nitrates by 2,6-Di(5,6-dipropyl-1,2,4-triazin-3-yl)pyridine,* to be published in Solvent Extr. Ion Exch. (1999)

32.23.03 Sicherheitsuntersuchungen zum dynamischen Verhalten von Kernen mit Aktinidenanteil

I. Safety Investigations for an Annular High Leakage Core

(D. Thiem, W. Maschek, INR; G. Heusener, PSF)

I. INTRODUCTION

Within the international CAPRA/CADRA program the feasibility of different reactor types is investigated for managing the Plutonium stockpile and burning Minor Actinides (MAs) and long lived fission products (LLFP) /1/. The reactor types investigated range from light water reactors (LWRs) to fast reactors (FRs) and to accelerator driven subcritical system (ADSs). For the burning of waste FRs and ADSs are the systems of choice. Investigations of these burner cores show significant design differences to conventional FR cores. This refers e.g. to the pin design and the 'fuel' which might be fabricated of MAs, the core size, the coolant etc. In the present work we are dealing with the potential of a FR core with conventional oxide fuel. As the integration of MAs into the core usually leads to a deterioration of safety parameters, special emphasis has been laid on the safety of this core. These investigations should contribute to the assessment how far the safety potential of 'critical' burner reactors can be improved and under which conditions an ADS might be the preferential system /2/.

II. CORE LAYOUT

The mentioned design specialties of burner cores have a significant impact on safety parameters and accident scenarios. This refers especially to the void worth, but also to the Doppler coefficients, the delayed neutron fraction and to the kinetics parameters, as e.g. the neutron lifetime. As a general trend, without any additional measures, especially the safety parameters of dedicated cores (pure MA fuel) are worse /3/ than those of the reference CAPRA oxide core. /4, 5, 6/. To obtain good safety coefficients, and utilizing conventional oxide fuel, an annular high leakage core (**AHLC**) has been investigated (Fig. 1). Burning of MAs is done in an heterogeneous way, by positioning the MA -

containing elements (Americium targets) outside the core in the central annulus and around the outer core periphery. In the current paper it is only dealt with neutronic and safety aspects of the annular core but not with problems, as target technology, e.g. the large He-production in Am containing pins. The basic design data of the 2000 MWth annular core are given in Tab.1. As can be seen from Fig.1 the core is only 60 cm high with the intention to increase the neutron leakage and reduce the void worth of the core.

III. SAFETY INVESTIGATIONS

The investigations for assessing the safety behavior of the core have been performed in 3 steps. Firstly, the different safety parameters as void worth, Doppler etc. have been calculated for different design options. Secondly, investigations have been performed for assessing the energetics and recriticality potential under core-melt conditions. In the last step preventive and mitigative measures are discussed which could minimize the risk of core-melt accidents and their consequences.

1) For the calculations of the sodium void worth the different regions of the core have been voided sequentially. To decrease the void worth, the core height is limited to 60 cm. Two additional measures for further void worth reduction were the placement of a sodium layer above the core /6, 7/ and the introduction of axial layers of absorber (B4C) above and below the core at different distances. Some results of this study are shown in Tab.2. The results of these analyses show that the reduction of the core height is not sufficient for obtaining a low void worth for the core. This can however be achieved by placing B4C layers axially close to the core. The Doppler values of the rather flat core are lower than for the CAPRA oxide core, the kinetics parameters are similar and the delayed neutron fraction β_{eff} is large with 350 pcm compared to the 200pcm or less for dedicated cores /3/. The insertion of Am targets in the central annulus only increases the core void reactivity by 10%.

To increase the Doppler values (Tab. 3) moderating materials could be introduced into the core. Static neutronic analyses indeed show that a large Doppler value can be achieved. Assessing the safety impact of this moderator insertion must however take into account the following aspects. For prevention of severe accidents a small

Doppler constant might be advantageous to rapidly reduce the power level. If core melting must be assumed a large Doppler constant would be needed, but due to analyses the moderator separates from the fuel and its effect is strongly reduced /8/. For the void worth similar differences between a more 'static' and 'dynamic' view exist. A void reduction may not have an overall risk minimizing aspect. For accident prevention, again a small core void is optimal, but in case a core melting can not be prevented, the initial power transient caused by voiding leads to fuel mobilization but to no permanent nuclear shutdown by fuel dispersal. The consequence is a further melt progression with the potential for fuel compaction and recriticalities. The impact of an additional sodium layer above the core for void reactivity reduction /7/ must also be viewed under these aspects. As analyses show, this additional sodium layer is superfluous in case axial absorber layers are introduced. A realistic assessment of the impact of safety coefficients can only be judged by dynamical analyses, covering preventive and mitigative points of view in a balanced way.

2) In the next step the energetics and recriticality behavior of the core under severe accident conditions has been checked. This is of importance as these cores usually have high enrichments of fissionable material and mobilization of the fuel can lead to compaction processes with reactivity insertions and power transients. In accordance with earlier analyses /8/ several compaction and fuel/steel separation scenarios have been investigated. The results show that the reactivity potentials and the compactive reactivity ramp rates are smaller (20%) compared to the reference CAPRA core. Transient analyses of recriticality scenarios with SIMMER-III, a coupled fluid-dynamics/thermohydraulics/neutronics code /9/ revealed an interesting fuel motion pattern under power conditions. The maximum nuclear power deposition takes place within the fuel region (not in the central diluent region) of the core. As a consequence the mobilized fuel is pushed both inwards to the internal target region and outwards in direction of the radial reflector. The inward fuel motion is transiently even more pronounced and leads to a delay of the shutdown of the nuclear excursion. Results show, that the overall energetics levels are however lower (15-25%) than for ordinary CAPRA oxide core /8/.

3) For the CAPRA cores investigations have shown that the recriticality risk can be diminished by a so-called 'CMR', a controlled material relocation, meaning that the molten fuel can easily escape through special elements from the core region leading to an early and permanent nuclear shut-down. In the CAPRA cores this is mainly accomplished via the internal diluents and the control rods. For the annular core the main relocation path is via the central MA target island, especially the first row of elements (18 in total) and the control rods. An optimization between safety requirements and burning efficiency of the internal target island has to be found.

IV. CONCLUSIONS

The safety potential of an annular high leakage core has been investigated. The results show that by specific measures the core void reactivity can be made rather small. The core seems to have good attributes on the prevention level. Analyses of core disruptive accident scenarios reveal energetics enhancing and mitigating effects, with a tendency of lower energetics than ordinary CAPRA cores. Mitigating measures against recriticalities could be installed, but a compromise has to be found between diluent and target positions in the inner annulus of the core. The analyses show that 'critical' cores still have a significant flexibility for safety optimization, while retaining their MA burning capability.

V. REFERENCES

/1/ B. Barré.: "The Future of CAPRA", 5th Int. CAPRA Sem., Karlsruhe, Germany (1998).

/2/ W. Maschek et al.: "Comparison of Severe Accident Behavior of Accel. Driven Subcrit. Systems and Conventional Critical Reactors", AccApp'98, Gatlinburg, USA (1998)

/3/ J. Tommasi et al.: "Minor Actinide Destruction in Dedicated Reactors", 5th Int. CAPRA Seminar, Karlsruhe, Germany (1998).

/4/ A. Languille et al.: "CAPRA Core Studies - the Oxide Reference Option", GLOBAL '95, Paris, France (1995).

/5/ W. Maschek et al.: "Risk Reduction of Core-Melt Accidents in Advanced CAPRA Burner Cores", ARS'97, Orlando,USA (1997).

/6/ S.Pillon et al.: "Current Status of the CAPRA Program.", ENC'98, Nice, France (1989).

/7/ D. Struwe et al.: Internal communication 1998.

/8/ W. Maschek et al.: "Core Disruptive Accident Analyses for Advanced CAPRA Cores", ICONE-4, New Orleans, USA (1996)

/9/ S. Kondo et al.: "SIMMER-III: An Advanced Comp. Progr. for LMFBR Severe Accident Analysis", ANP'92,Tokyo, Japan (1992).

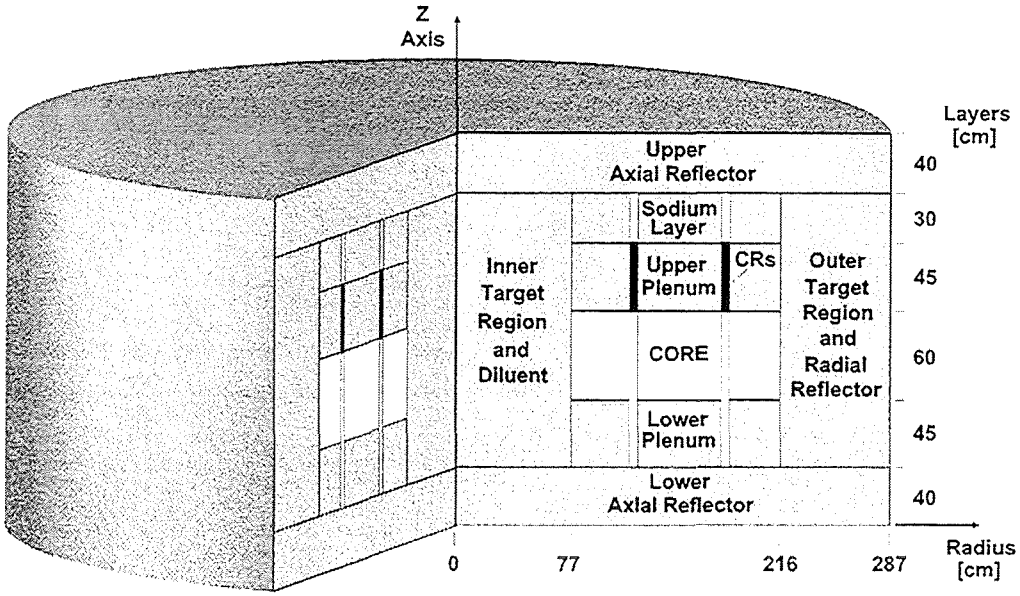

Fig. 1 Core layout of the annular high leakage (AHLC) core

Thermal power	**MW**	**2000**
Maximum linear rating	**W/mm**	**48**
Active core height	**mm**	**600**
Peak factor		**1.38**
Number of subassemblies		**240**
Number of inner ring Sas		**37**
Number of control rods		**12**
Inner core radius	**mm**	**770**
Outer radius inner core zone	**mm**	**1615**
Outer radius outer core zone	**mm**	**2151**
Number of pins per subassembly		**397**
Pin diameter	**mm**	**8.2**
Volume fraction fuel/steel/coolant	**%**	**32/18/50**
Fuel mass	**kg**	**20 400**
Pu – enrichment	**%**	**32.5**

Tab. 1 Design parameters of the annular high leakage core (AHLC)

Configuration: actually voided regions	Reference	B4C layers (Plenum)	B4C layers (Reflector)	B4C layers (Reflector) Central Am Island
Void region	dρ (pcm)	Dρ (pcm)	dρ (pcm)	dρ (pcm)
C1 + C2 wet	0	0	0	0
C1 + C2 voided	+ 1706	+ 290	+ 1389	+ 1419
C1 + C2 + upper + lower plenum voided	- 1074 core void value: total: + 1706 positive: + 1900 core+plena void value: total: - 1074 positive: + 1752	- 840 core void value: total: + 290 positive: + 1353 core+plena void value: total: - 840 positive: + 1305	- 3314 core void value: total: + 1389 positive: + 1754 core+plena void value: total: - 3314 positive: + 1555	-
C1 + C2 + upper +lower plenum + axial + sodium layer voided	- 1286		- 4166	-

Tab. 2 Void values for various configurations and voiding steps in the AHLC

Configuration	Reference	B4C layers (Plenum)	B4C layers (Reflector)
Void region	dρ (pcm)	dρ (pcm)	dρ (pcm)
C1 + C2 wet	- 413	- 202	- 373
C1 + C2 voided	- 301	- 110	- 255
C1 + C2 + upper + lower plenum	- 261	- 107	- 209
C1 + C2 + upper +lower plenum + axial + sodium layer			

Tab. 3 Doppler values for various configurations and voiding steps in the AHLC

II. Test Calculations for the Validation and Verification of the newly developed SIMMER-III Neutronics Module

(G. Buckel, E. Hesselschwerdt, E. Kiefhaber, S. Kleinheins, W. Maschek, INR)

Abstract

The TWOTRAN-like solver module /1/ contained in the neutronics part of the SIMMER-III code for the solution of the stationary and time dependent neutron transport equation was replaced by the more modern and powerful TWODANT Solver Module /2/ in order to improve considerably the convergence behaviour and the performance of the solution process with respect to computing times, as well. It could be demonstrated by comparison calculations outside of SIMMER-III that the TWODANT SOLVER module had for safety-relevant problems of liquid metal cooled fast reactors (LMFRs) far better characteristics with respect to robustness of the solution algorithms and to accuracy and reliability of the results compared to TWOTRAN.

The replacement of the code parts was successful also in so far as for all options contained in TWOTRAN corresponding feasibilities could be implemented in TWODANT. In order to avoid negative flux values in the solution of the neutron transport equation in the framework of SIMMER-III, three options had been included in TWOTRAN:

- using FIXUP-ON, negative flux values are replaced by zeroes;
- using POSDIF-ON, the conventional diamond differencing (DD) discretization method is replaced by a weighted diamond differencing method where the weighting factors are calculated code-internally so that negative angular fluxes can be avoided.
- Furthermore, when choosing the combination of options FIXUP-OFF and POSDIF-OFF, then negative fluxes are tolerated in the solution scheme.

The standard discretization method used in TWODANT corresponds to the conventional diamond differencing with negative flux fixup and is, therefore, equivalent to FIXUP-ON in TWOTRAN. In TWODANT the Adaptive Weighted

Diamond Differencing (AWDD) method can be used, where the values for the weighting factors have to be specified in the input. This method can be regarded as comparable to the POSDIF-ON option in TWOTRAN. (Differences and difficulties are described in /3/.) Employing AWDD and specifying all weighting factors in the input as –1.0 is equivalent to POSDIF-OFF and FIXUP-OFF in TWOTRAN.
The new neutronics version of the SIMMER-III package has been applied to four representative test problems, including static and transient cases, in order to validate and verify the code. Brief descriptions of these test problems and their results are reported.

Zusammenfassung

Bisher enthielt der Neutronikteil von SIMMER-III einen maßgeblich von TWOTRAN /1/ beeinflußten Programmteil zur Lösung der stationären und der zeitabhängigen Neutronen-Transportgleichung. Dieser Programmteil wurde durch den moderneren und in vieler Hinsicht leistungsfähigeren TWODANT – Lösungsmodul /2/ ersetzt, um sowohl das Konvergenzverhalten wesentlich zu verbessern als auch eine erhebliche Reduzierung der Rechenzeiten zu erzielen. Mit Vergleichsrechnungen außerhalb von SIMMER-III konnte für typische Anwendungsfälle bei Schnellen Reaktoren gezeigt werden, daß sich der TWODANT – Lösungsmodul im Vergleich zu TWOTRAN für sicherheitsrelevante Aufgabenstellungen wesentlich zuverlässiger und robuster verhält.
Der Ersatz des TWOTRAN – ähnlichen Programmteils war auch insofern erfolgreich, als alle darin enthaltenen Programmoptionen durch entsprechende Eingriffe in den TWODANT Lösungsmodul verfügbar gemacht werden konnten. Zur Vermeidung negativer Flußwerte bei der Lösung der Neutronen-Transportgleichung waren in der SIMMER-III – Umgebung der TWOTRAN Version drei Möglichkeiten enthalten:

- Bei Anwendung der FIXUP-ON Option wurden auftretende negative Flußwerte durch Nullen ersetzt.
- Bei Anwendung der POSDIF-ON Option sollte durch die Benutzung eines „gewichteten Diamond – Differencing" Diskretisierungsverfahrens, bei dem die Wichtungsfaktoren programmintern berechnet werden, vermieden werden, da negative Flußwerte auftreten.

- Außerdem würden durch die Kombination der Optionen FIXUP-OFF und POSDIF-OFF im Verlauf der Rechnung auftretende negative Flußwerte toleriert.

Die in TWODANT implementierte Standard – Diskretisierungsmethode entspricht dem konventionellen „Diamond Differencing" Diskretisierungsverfahren mit Nullsetzen auftretender negativer Flußwerte und entspricht damit der FIXUP-ON Option in TWOTRAN. Darüber hinaus kann in TWODANT die „Adaptive Weighted Diamond Differencing (AWDD) Methode" angewendet werden bei der die benötigten Wichtungsfaktoren in der Eingabe enthalten sein müssen. Diese Methode kann als vergleichbar mit der POSDIF-ON Option in TWOTRAN angesehen werden. (Zu Einzelheiten siehe /3/.) Die Verwendung von AWDD und das Setzen sämtlicher Wichtungsfaktoren auf den Wert – 1.0 ist äquivalent mit den Optionen FIXUP-OFF und POSDIF-OFF in TWOTRAN.
Die neue Neutronik – Version des SIMMER-III Programmpakets wurde zur Lösung von vier repräsentativen Testbeispielen für statische und auch transiente Aufgabenstellungen eingesetzt, um die Anwendbarkeit und Korrektheit des Rechenprogramms nachzuweisen. Der Bericht enthält die kurz gefa ten Beschreibungen der Testbeispiele und ihrer Resultate.

1 FCA (Fast Critical Assembly)

A series of fuel slumping experiments has been performed in JAERI's FCA facility, of which a cylindrical model of geometry and material arrangement is shown in Figure 1. Several disrupted core configurations were simulated in the FBR test region with 14% - Pu-enriched fuel. The test section was surrounded by the driver region with 29% - U235-enriched fuel and further blanket regions with natural or depleted U fuel.

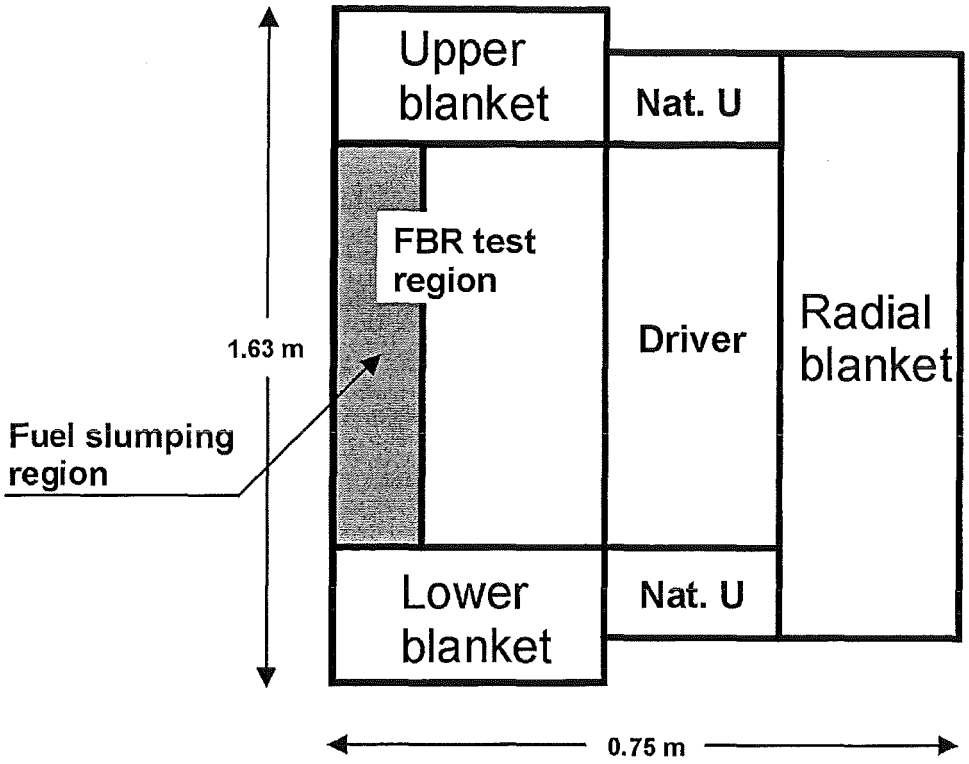

Figure 1: R-Z model of FCA VIII-2 experiments.

In a central part of the test region (3 by 3 drawers of 5.5cm x 5.5cm each), the fuel distribution was varied from a reference uniform distribution (A0) to three levels of compacted configurations (A1, A2, and A3) and to a fuel dispersed configuration (S). The patterns of fuel re-configurations are depicted in Figure 2, where a dark hatched region represents compacted fuel having twice as dense fuel as the reference fuel density simulating an intact core. Fuel slumping into a compact configuration, from A0 to A3 causes a positive reactivity change. Because of a large void region developed above the fuel region, the reactivity change must be evaluated by suitably treating negative reactivity effects due to increased neutron leakage. This means the use of neutron transport theory is inevitable in simulating the experiments. Although the scales of fuel re-distribution were only limited in the FCA experiments, reactivity changes from the reference configuration were measured sufficiently accurate.

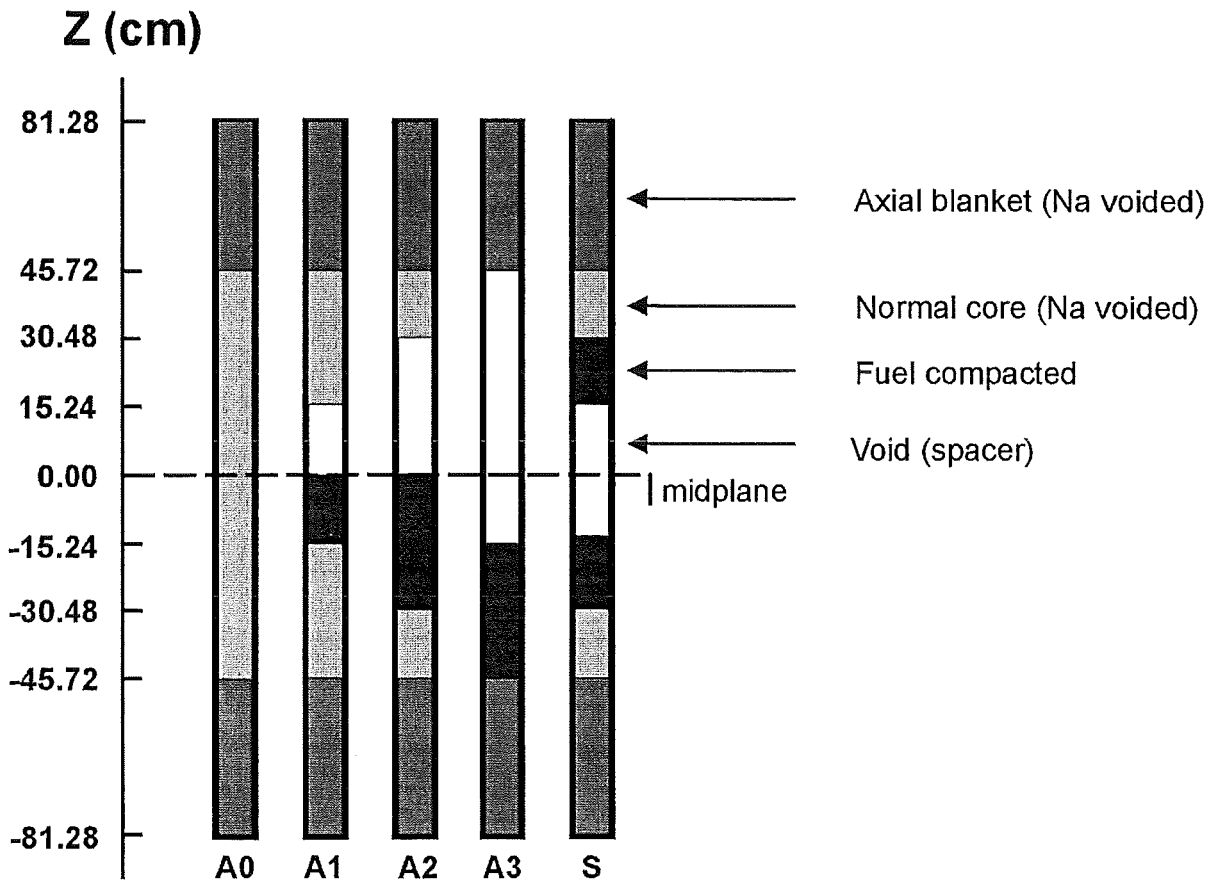

Figure 2: Fuel relocation pattern in FCA VIII-2 experiments

Two series of test calculations were done using different options with SIMMER/ TWOTRAN and SIMMER/TWODANT. The following table shows the result with POSDIF ON and the SIMMER/TWODANT corresponding option AWDD ON, the next table FIXUP ON and AWDD OFF. The calculations were performed with SIMMER-III, version 2d using ISOTXS- / BRKOXS-files prepared for 9 energy groups and 11 isotopes. The anisotropic scattering was approximated based on the Bell-Hansen-Sandmeier /4/ transport correction. The S_N-order was specified to N = 4.

	POSDIF ON			AWDD ON		
	SIMMER/TWOTRAN			SIMMER/TWODANT		
	adjoint	real	ρ	adjoint	real	ρ
A0	1.007070811	1.006210146		1.00702616	1.00574626	
A1	1.007560225	1.006699311	4.8298E-4	1.00751559	1.00623686	4.8477E-4
A2	1.008212480	1.007354450	1.1289E-3	1.00816797	1.00689455	1.1339E-3
A3	1.00841946	1.007556997	1.3283E-3	1.00836616	1.00709942	1.3360E-3
S	1.006592140	1.005721157	-4.8321E-4	1.00654697	1.00525523	-4.8567E-4

	FIXUP ON			AWDD OFF		
	SIMMER/TWOTRAN			SIMMER/TWODANT		
	adjoint	real	ρ	adjoint	real	ρ
A0	1.007071968	1.006725006		1.00707174	1.00648544	
A1	1.007561369	1.007212599	4.8087E-4	1.00756115	1.00697378	4.8183E-4
A2	1.008213624	1.007864715	1.1233E-4	1.00821340	1.00762738	1.1260E-4
A3	1.008412091	1.008064707	1.3201E-3	1.00841186	1.00782858	1.3241E-4
S	1.006593275	1.006237366	-4.8138E-4	1.00659306	1.00599712	-4.8228E-4

$$\rho = \frac{k' - k_{A0}}{k' k_{A0}}$$

$$k_{A0} = k_{eff}(A0_{real}), \qquad k' = k_{eff}(a),$$

$$k_{eff}(a) = k_{eff}(A1_{real}), k_{eff}(A2_{real}), k_{eff}(A3_{real}), k_{eff}(S_{real}), \quad \textit{respectively}$$

Effective multiplication factors calculated for individual configurations were converted into reactivity changes from the reference configuration (A0) and compared with experimental measurements in Figure 3. The predicted reactivity changes agreed fairly well with the experiments with deviations in C/E of less than 20% . The

TWODANT module is judged to be implemented into SIMMER-III correctly since the results of SIMMER-III using TWOTRAN and TWODANT modules agree almost completely as shown in this Figure. The effect of negative flux fixing up on the relative reactivity change seems to be negligible in this case although the maximum percentage of the fixing up operation in the AWDD-OFF case was around 20%.

For TWODANT the same calculational model was used as was originally specified for TWOTRAN. For these restricted investigations no refinement of the calculational model such as increasing the S_N order or reducing the mesh sizes, was considered.

Even the fairly good agreement between the SIMTRAN and SIMDANT results cannot be taken as a proof that the results can be considered as sufficiently accurate; primarily it only means that both results are affected by roughly the same uncertainty. The dominant feature is that the discretization error (although usually being sufficiently small) is about the same in both solution algorithms.

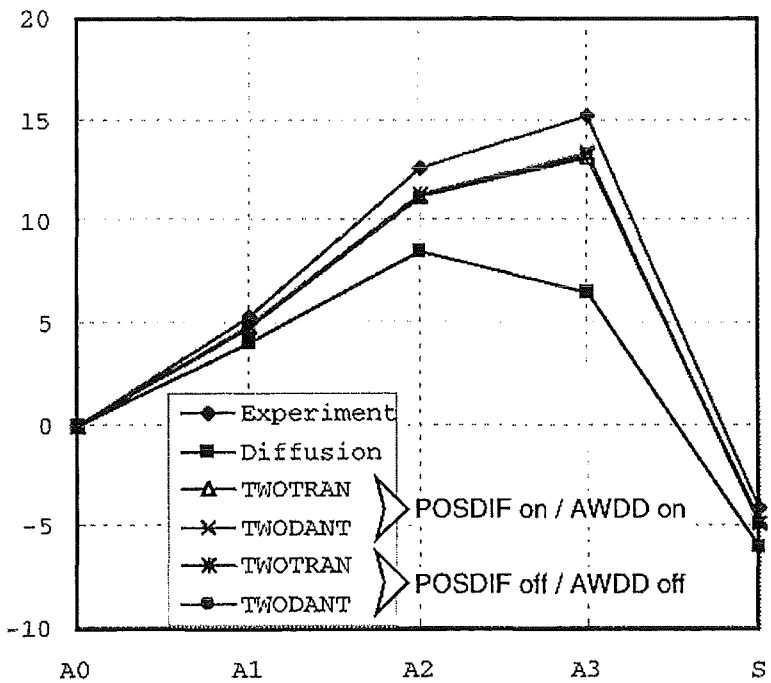

Figure 3: Predicted reactivity change by TWOTRAN and TWODANT module

2 SRA (Static Reactor Analyses)

Parametric cases are set up to investigate the reactivity change due to the hypothetical one-dimensional compaction in the core of a large scale LMFBR (see Figure 4). In the compacted configuration, an upper blanket region lies above the empty space produced by the compaction in the core. This problem is a good example for demonstrating the superiority of the new neutronics version based on the TWODANT code, because the former neutronics package in SIMMER-III based on TWOTRAN initially failed to converge for the compacted configuration.
(In order to describe the situation in more detail: initially, calculations performed with TWOTRAN didn't converge at all; subsequent calculations performed at FZK/INR did converge indeed, mainly as a result of using – instead of the default option, - the recommended option for the modified incomplete lower and upper decomposition bi-conjugate gradient scheme for the preconditioned conjugate gradient method for the rebalance equation matrix solver; but the results were still not reliable.)

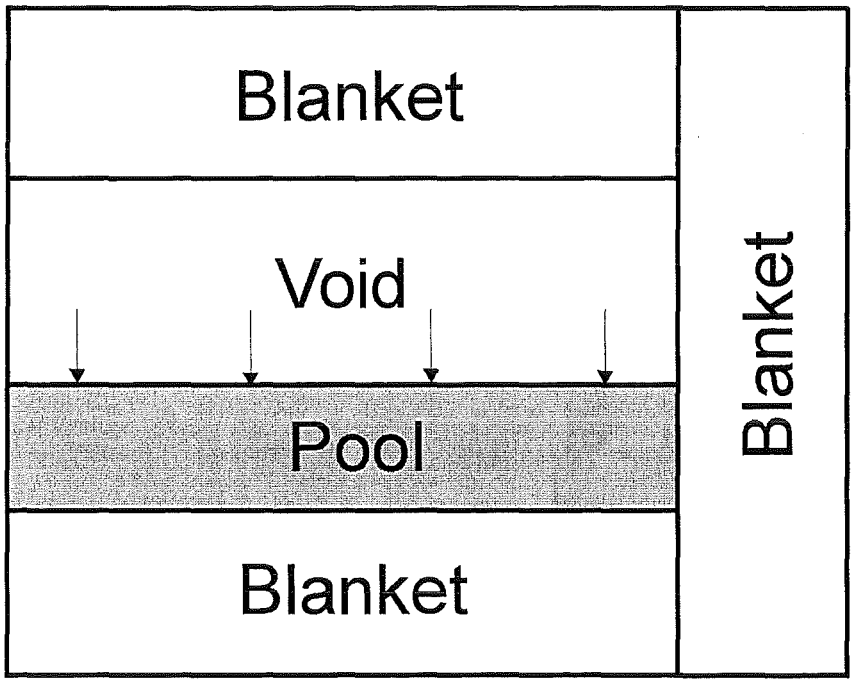

Figure 4: R-Z model of SRA (Static Reactor Analysis)

Two series of test calculations were done for the SRA case, too; the first one by using the options POSDIF ON and AWDD ON, respectively, the second one using

FIXUP ON and AWDD OFF, respectively. The calculations were performed with SIMMER-III, version 2d using ISOTXS- / BRKOXS- files prepared by the neutronics preprocessor MXS /5/ for 9 energy groups and 5 materials. The S_N-order was specified to N = 4.

POSDIF ON AWDD ON

	SIMMER / TWOTRAN		SIMMER / TWODANT	
	adjoint	real	adjoint	real
compact	0.98338562*)	0.97725826*)	1.04216938	1.04190530
uniform	0.98453313	0.98452505	0.98448339	0.98426495

FIXUP ON AWDD OFF

	SIMMER / TWOTRAN		SIMMER / TWODANT	
	adjoint	real	adjoint	real
compact	0.98342664*)	0.97700906*)	1.04235340	1.04236921
uniform	0.98453422	0.98451724	0.98453418	0.98452736

*) see explanation given at the beginning of this chapter.

The new neutronics module based on TWODANT converged successfully for the compacted configuration in this test problem whereas the former TWOTRAN module failed as well in the FIXUP ON case as in the POSDIF ON case. These results verified the robustness and superiority of TWODANT over TWOTRAN. The effect of the fixing up operation of negative fluxes is apparent from the difference in absolute value of the effective multiplication factor. However, the relative reactivity change between the compacted case and the uniform case is not affected by the choice of various differencing schemes, i.e. the reactivity change due to compaction is 0.05784185 in the AWDD-OFF case and 0.05764035 in the AWDD-ON case, which can be considered as negligibly small. Again no efforts were devoted to investigations using refined calculational models.

3 STN (Standard Test Problem for Neutronics)

This sample problem is intended to test the space- and energy-dependent neutron kinetics model and its coupling with the fluid dynamics. The considered problem set-up is a fictitious disrupted LMFR core of an intermediate size for simulating a short-time energetic recriticality event with 12 by 16 meshes. In order to drive a very rapid reactivity insertion, a slug of molten fissile fuel initially present at the bottom of the core axis is pushed toward the core midplane with its initial velocity 100 m/s. The geometric model and initial conditions used for this problem are shown in Figure 5. This reactor configuration and these initial conditions minimize the effect of non-linear feedback processes between the material motion and reactor kinetics. The resulting rapid positive reactivity insertion brings the core to prompt criticality. The power excursion terminates in a short period of several milliseconds due to a negative reactivity feedback mechanism of continued axial fuel motion in the core center beyond the core midplane.

The reactivity and power transient are plotted in Figures 6 - 9 for both the TWOTRAN and the TWODANT module, respectively. The discrepancy between the two codes is fairly small and one can conclude that the implementation of the transient terms into the TWODANT module and the coupling of SIMMER-III fluid dynamics and TWODANT have been performed successfully. In addition, the effect of the fixing up procedure of negative flux is larger than the effect of the difference between the neutronic modules. Both, TWOTRAN and TWODANT, produce a little bit larger amplitude peak around 6 ms with the fixing up procedure than with the positive differencing scheme or AWDD scheme. It may be worthwhile to mention that according to the FIXUP tables produced by TWODANT for the 12 * 16 mesh grid, large fixup percentages were observed at the radial core blanket interface, indicating that the results may not be fully reliable in this part of the core.

The calculations were performed with SIMMER-III, Version 2d using ISOTXS- / BRKOXS-files prepared by the neutronics preprocessor MXS /5/ for 7 energy groups and 5 materials. The S_N-order was specified to N = 4.

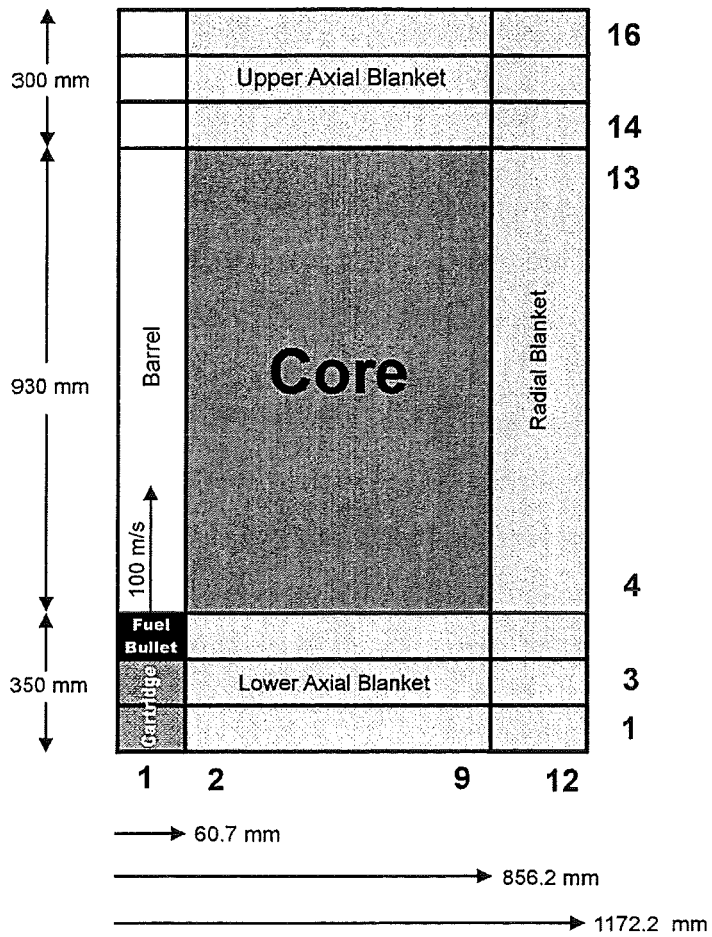

Figure 5: Configuration of the STN (Standard Test Problem for Neutronics)

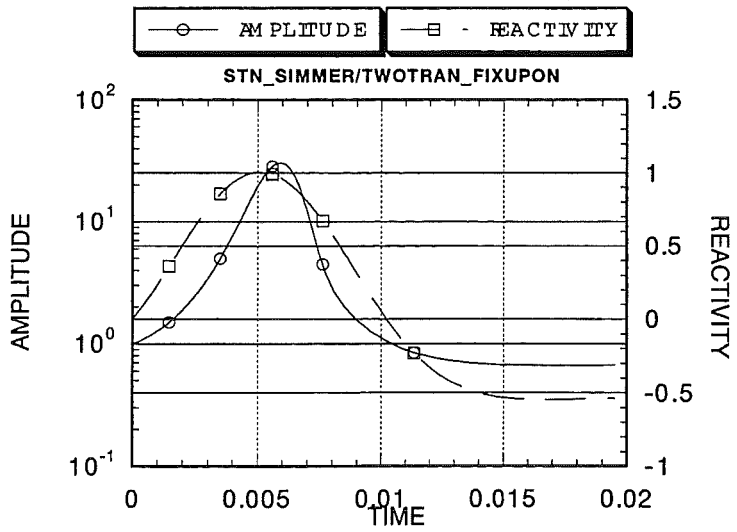

Figure 6: Plot of reactivity and power transient calculated by TWOTRAN using FIXUP ON

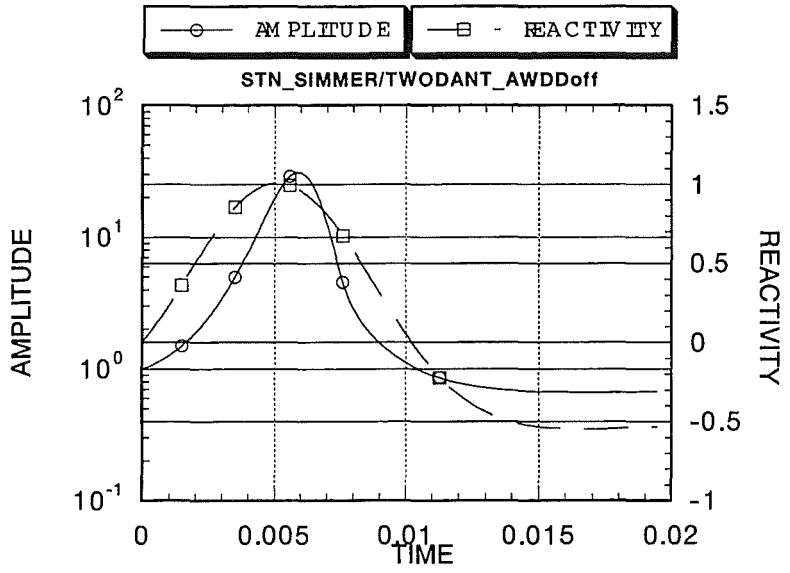

Figure 7: Plot of reactivity and power transient calculated by TWODANT using AWDD OFF

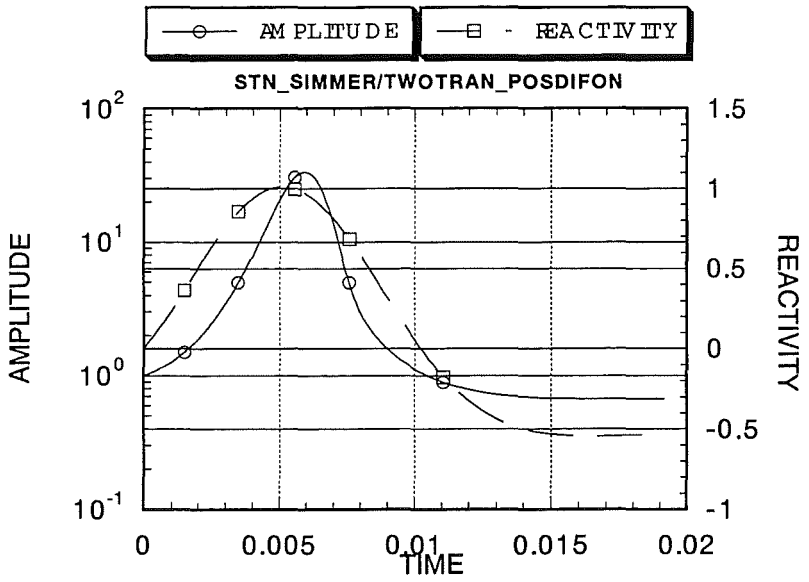

Figure 8: Plot of reactivity and power transient calculated by TWOTRAN using POSDIF ON

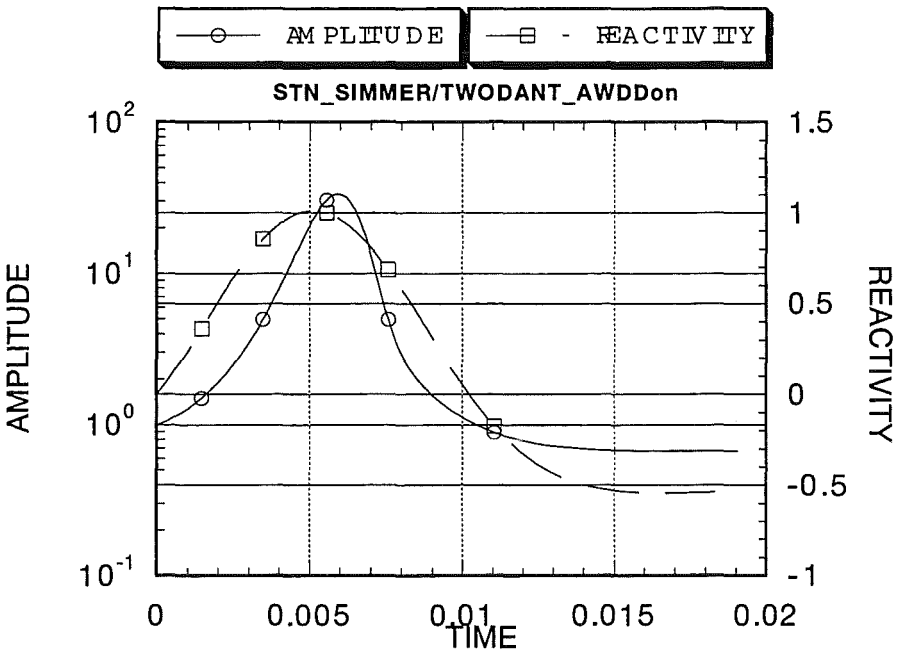

Figure 9: Plot of reactivity and power transient calculated by TWODANT using AWDD ON

4 TRA (Transient Reactor Analyses)

The final and integral test problem is the transient analysis of the early transition phase in a core disruptive accident. The objective of this test problem is to verify the applicability of the new code package and to find out whether plausible results can be obtained. The initial spatial distribution of the material, temperature, and pressure is taken from the final state of the initiating phase analysis by SAS4A using the interfacing code SAME-II. According to the hypothetical assumption of a large diameter of the fuel particles, the one-dimensional fall down of the relocated fuel causes a recriticality event around 1s which drives the subsequent recriticality phase by a sloshing of molten core material.

The calculations were performed with SIMMER-III, version 2d using ISOTXS- / BRKOXS-files prepared for 7 energy groups and 21 isotopes. The S_N-order was specified to N = 4.

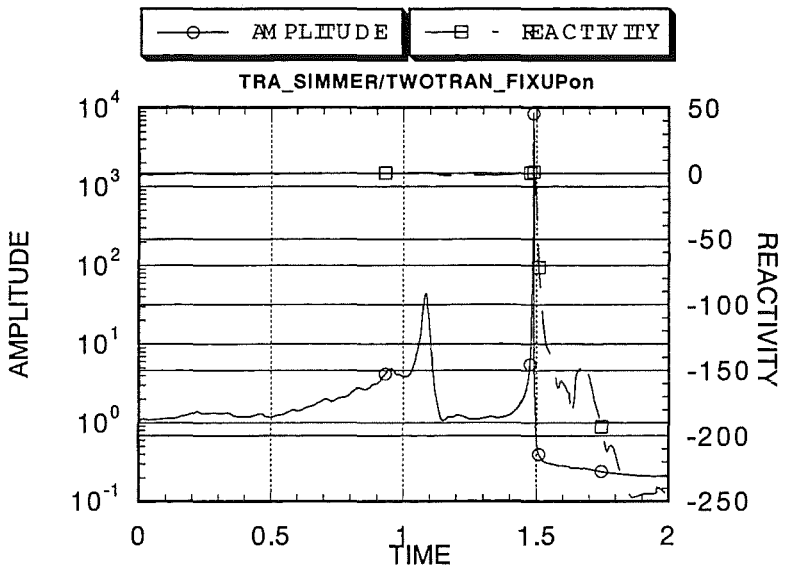

Figure 10: Power and reactivity plot of TRA case calculated by TWOTRAN using FIXUP ON

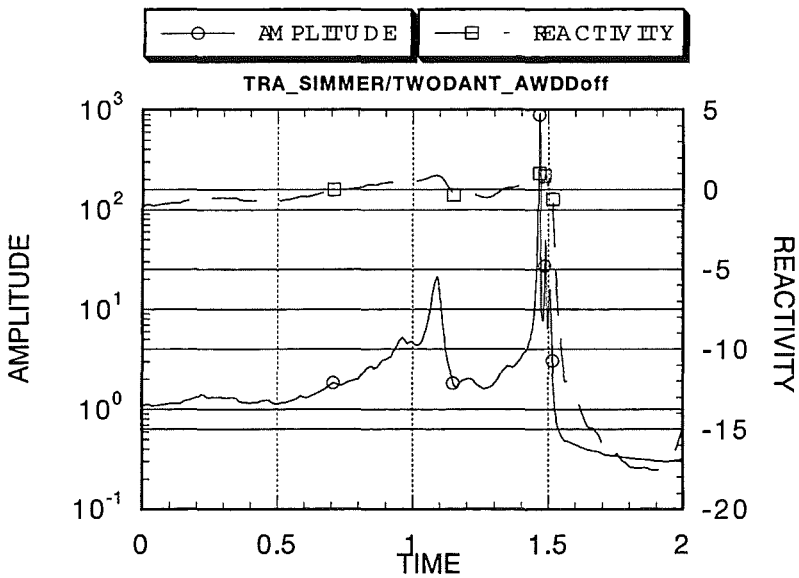

Figure 11: Power and reactivity plot of TRA case calculated by TWODANT using AWDD OFF

Please note: The scales used in Figures 10 and 11 are very different regarding amplitude as well as reactivity. The normalized amplitude peak at the first recriticality event shows an increase by a factor of 40 (Figure 10) and by a factor of 20 (Figure 11). It is nearly impossible to compare the trend of the reactivity values because of the different scales as ranging from –250 $ to +50 $ in Figure 10 and from –20 $ to +5 $ in Figure 11.

Therefore, the calculated power and reactivity transient shown in Figure 11 is only qualitatively similar to the result obtained when using the former SIMMER-III shown in Figure 10 in this sense that the first recriticality event takes place around 1.1s and this drives the second power burst by the sloshing pool. However, each recriticality event in the calculation by the TWODANT module is milder than for the TWOTRAN calculation. The cause of this discrepancy is not yet fully understood at the moment and has to be investigated in future studies.

When repeating at FZK the previous runs leading to Figures 10 and 11, it was observed that the results of the calculations for the TRA problem were affected by a deficiency namely the not fully converged inner iterations (essentially due to the input value ITLMIN = 10). The SIMMER code version used at that time didn't monitor this fact in the output protocol as it had done in former versions. Therefore, this failure, i.e. not achieving convergence, could not be identified by straightforward analysis of the output file. After detection of this shortcoming at FZK, the SIMTRAN calculations have been repeated and Figures 12 – 14 led to the following conclusions:

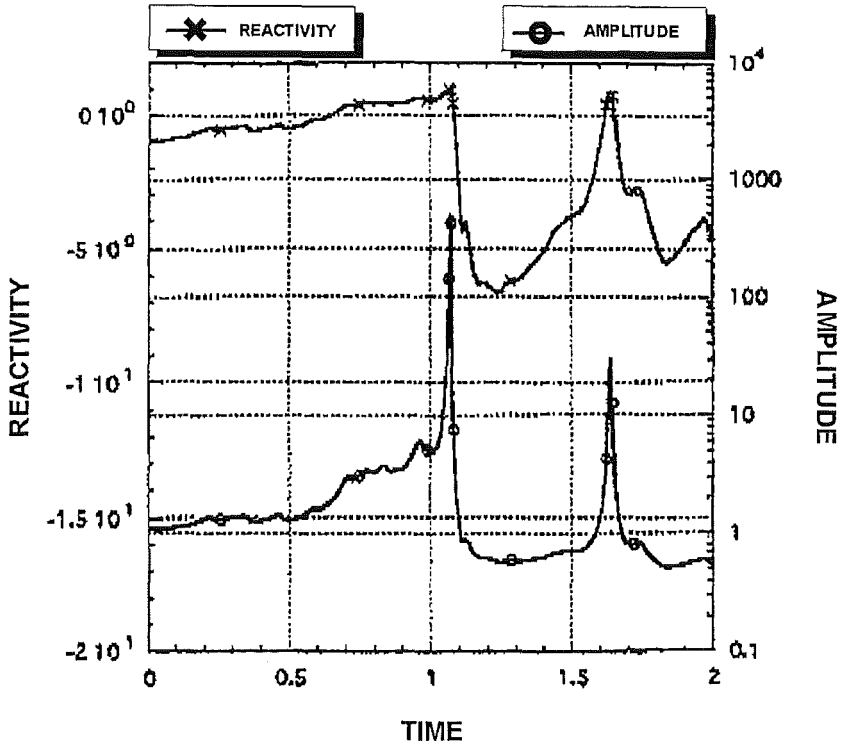

Figure 12: TWOTRAN POSDIF ON, FIXUP OFF (inner iteration failure)

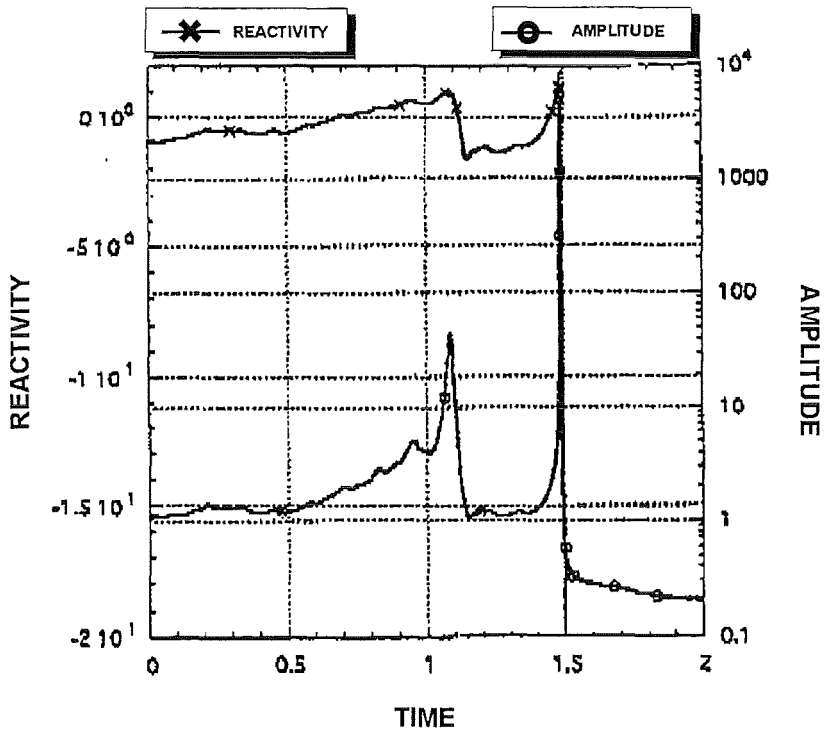

Figure 13: TWOTRAN POSDIF ON, FIXUP OFF (without inner iteration failure)

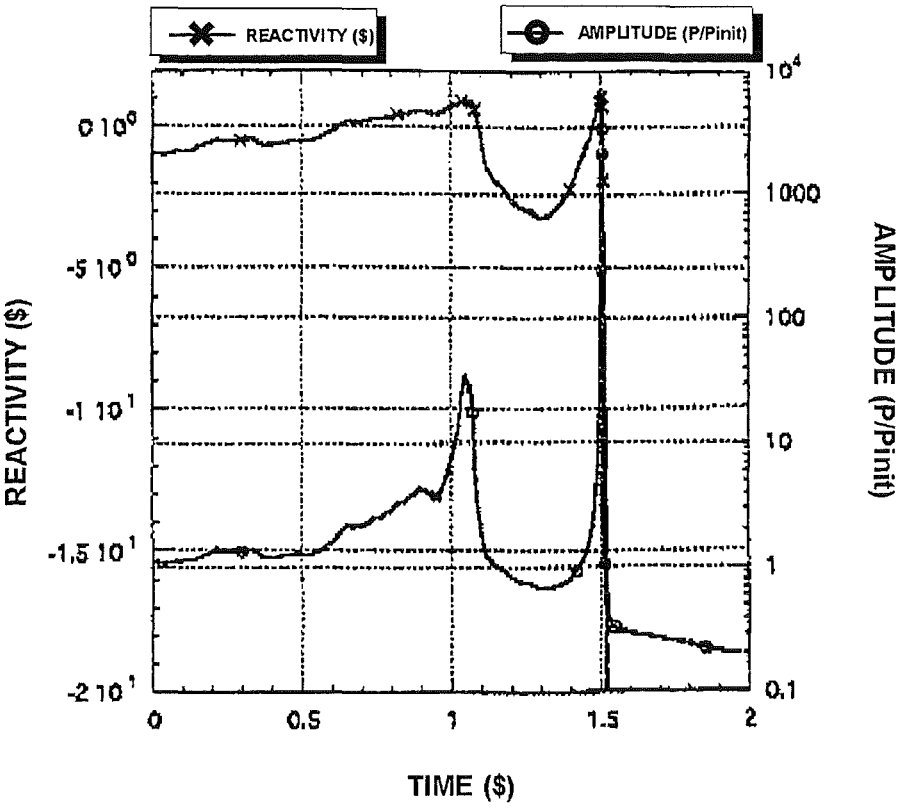

Figure 14: TWOTRAN POSDIF OFF, FIXUP ON (inner iteration failure)

Please note:The left-right position of the ordinate scales in Figs. 10-11 and Figs. 12-14, respectively, has been changed.

When comparing Figures 12 and 13 it is evident that the transient behavior of the SIMTRAN results was affected substantially by the non-convergence of the inner iteration process. Keeping in mind that Figure 14 shows results also obtained with a failure in the inner iteration process for the POSDIF OFF, FIXUP ON case, the correspondence with the results in Figure 13 without inner iteration failure for the POSDIF ON, FIXUP OFF case is rather surprising. But this fairly good agreement might be fortuitous and should not be considered as a validation of the reliability of these results.

Comparing SIMTRAN and SIMDANT results in Figures 11 and 13 it is important to observe, that now the scales are nearly comparable. Concerning the amplitude, the first recriticality event is calculated by both code versions at 1.1 s showing an

amplitude peak of approximately a factor of 30 (initially normalized to unity). The second recriticality event is calculated by SIMTRAN exactly at 1.5 s and by SIMDANT at 1.45 s. The maximum amplitude factor is calculated by SIMTRAN to $7*10^3$ and could be estimated in the SIMDANT calculation as to be not too different. (The scale ends in this case at $1*10^3$.) The reactivity curves show a similar trend up to the first recriticality event. Afterwards, the course of the reactivity and amplitude curves is different. Whereas the SIMDANT results reach a local minimum of approximately -0.5 $, SIMTRAN calculates a local minimum of -2 $. After the second criticality event SIMDANT ends at a reactivity value of –18 $ at 2 s, whereas SIMTRAN determines the reactivity curve with a rather steep gradient leading to values far below –20 $.

The intercomparison verifies that SIMDANT can be applied for complicated transient analyses and increases the confidence in the suitability of this upgraded tool. There are still some nonnegligible discrepancies remaining between the results shown in Figures 11 and 13, in particular in the peak amplitude at about 1.5 s and the time behavior of the reactivity and the amplitude afterwards. The origin of these differences is not clear presently. In particular it would be premature to conclude that they will essentially be caused by the different algorithms applied for the solution of the neutron transport equation.

It should be noted that in SIMMER highly transient dynamic processes with an interplay of neutronics and fluiddynamics are simulated. Any change in the neutronics quantities influences the fluid motion which - over a feedback loop - has an impact on the neutronics quantities again. This behavior reflects the reality of dynamical systems. In addition some types of threshold effects such as sudden pin failure, fission gas release, and fuel relocation processes could exaggerate discrepancies of results. Therefore, differences as those observed e.g. between Figure 11 and Figure 13 are not too unusual for results of codes dealing with accident analyses and that is one of the reasons why with these code systems a band width of results with a possible enclosing envelope should usually be calculated.

5 Conclusion

The test calculations demonstrated that in total the implementation of the TWODANT SOLVER module in the most recent version of SIMMER-III led to the desired and expected success of providing a more robust and reliable tool for safety analyses with the additional considerable advantage of a very stable performance and a significant reduction in overall computing time.

Comparing computing times, roughly a factor of about two has been observed during verification- and validation-tests in favor of the new SIMMER-III version. These experiences could be confirmed recently by our French colleagues /6/. For configurations showing poor convergence performance in the iteration process, the factor of two is improved remarkably. More detailed comparisons of computing times will be necessary and should be performed in the future.

The test calculations were supported and facilitated appreciably by improved diagnostic capabilities (negative flux fixup tables which can be visualized) entered in the new SIMMER-III version, assisting the analysis of the reliability of the neutronics results and making evident where a refinement of the mesh grid would be most suitable.

Acknowledgements

The authors gratefully acknowledge the support of their Japanese colleagues at JNC who supported the testing of the new SIMMER-III code package and provided the input for the sample problems

The authors also want to express their gratitude to the French colleagues at CEA/ Cadarache for making available rather early the results of their time-intercomparisons of calculations using different SIMMER versions.

13 References

/1/ K. D. Lathrop, F. W. Brinkley, "TWOTRAN-II: An Interfaced, Exportable Version of the TWOTRAN Code for TWO-Dimensional Transport", Los Alamos Scientific Laboratory, report LA-4848-MS, Los Alamos, New Mexico, (1973)

/2/ RSIC COMPUTER CODE COLLECTION, DANTSYS 3.0, One-, Two-, and Three-Dimensional, Multigroup, Discrete Ordindates Transport Code System, contributed by: Los Alamos National Laboratory, Los Alamos, New Mexico, (1995).

http://www-xdiv.lanl.gov/XTM/

/3/ G. Buckel, E. Hesselschwerdt, E. Kiefhaber, S. Kleinheins, W. Maschek, "A new SIMMER-III Version with improved Neutronics Solution Algorithms", FZKA 6290 (1999)

/4/ G. I. Bell, G. E. Hansen, H. A. Sandmeier, "Multiple Treatment of Anisotropic Scattering in SN Multigroup Transport Calculations", *Nucl. Sci. Eng.* ***28***, 376 (1967)

/5/ F. Parker, M. Ishikawa, L. B. Luck, "MXS Cross-Section Preprocessor User's Manual", Nureg/CR-4765, Los Alamos National Laboratory report LA-10856-M (March 1987)

/6/ O. Marchand, J. Louvet, Commissariat à l'Energie Atomique (CEA), Cadarache, France: Comparison TWODANT/TWOTRAN/ERANOS
Private communication, January 1999.

III. Extension of the SIMMER-III Code Neutronics for ADS Application

(A. Rineiski, B. Merk, W. Maschek, INR)

I. INTRODUCTION

In providing tools for the analysis of transients and accidents in accelerator driven systems (ADS), the neutronics module of the SIMMER-III code has been extended for the simulation of an external neutron source.

Though it is claimed that the ADS has an extraordinary safety potential /1/, this has to be proven in detail. Some first analyses especially in the severe accident area have shown, that for an ADS in its mode as energy amplifier some safety advantages might exist compared to critical sodium cooled fast reactors. This is related to lead as coolant and to the sub-criticality and the low enrichment of an ADS core in the amplifier mode /2, 3/ . These investigations must be further pursued and refined and especially extended to an ADS system with a high actinide load in the core. In critical reactors, the massive insertion of MAs has a profound impact on the safety behavior. In the case that e.g. 'dedicated fuel' consisting of minor actinides would be used it can be deduced from /4/, the burn-up behavior of minor actinide fuel might have consequences concerning the initial sub-criticality level and the required source variation.

II. SIMMER-III ACCIDENT CODE

To analyze severe transients and core disruptive accidents in Liquid Metal Reactors (LMRs) the SIMMER-III code /5/ is under development at JNC (Japan Nuclear Cycle Development Institute, O-arai Engineering Center) with cooperation of Forschungszentrum Karlsruhe and CEA (Comissariat a l'Energie Atomique, CEN Grenoble and CE Cadarache). SIMMER-III is a two-dimensional, three-velocity-field, multi-phase, multi-component, Eulerian, fluid-dynamics code coupled with a fuel-pin model and a space-, time- and energy-dependent neutron dynamics model.

The neutronics part provides nuclear heat sources based on the mass and energy distributions calculated by the other code elements. The transient neutron flux

distribution is calculated based on the improved quasistatic method /6/. For the space dependent part, a TWODANT based flux shape calculation scheme has been implemented recently /7/. The decay heat is separately taken into account. The basic geometric structure of SIMMER-III is a two-dimensional R-Z system, although optionally an X-Z or one-dimensional system can also be used.

As the code has been designed to describe all relevant phenomena of severe transients and core disruptive accidents in liquid metal cooled MA burner reactors, it was natural to extend the code application to accelerator driven systems with lead cooling. Some necessary changes had to be performed, as e.g. installing an equation of state for lead. Additional work is under way in assessing models e.g. as the pin model for different fuels and also the closure relations for lead as coolant.

An important change, which will be described below has been performed in the neutronics part of the code. The original neutronics describes a reactor system without external neutron sources. In the following the insertion of a source within the SIMMER-III framework is described. With this new neutronics feature coupled to an elaborate accident code, SIMMER-III represents a new and versatile tool for assessing safety issues of an ADS.

III. SOURCE IMPLEMENTATION INTO SIMMER-III

III.a Mathematical formulation

The time-dependent multigroup neutron transport equation (in the following presentation only one group of delayed neutrons is considered for simplicity, x denotes a space-angular position, $\Phi, Q, v, \nu, \chi_p, \chi_d$ are "multigroup" vectors, at steady-state $\chi = (1-\beta)\chi_p + \beta\chi_d$); M and F are operators):

$$\frac{1}{v}\frac{\partial \Phi}{\partial t} + M(t)\Phi(x,t) = (1-\beta)\chi_p F(t)\Phi(x,t) + \chi_d \lambda C(x,t) + Q(x,t)\,, \tag{1}$$

$$\frac{\partial C}{\partial t} = \beta F(t)\Phi(x,t) - \lambda C(x,t)\,, \tag{2}$$

is solved following the quasistatic scheme /8/. Space-time factorization:

$$\Phi(x,t) = N(t)\psi(x,t)\,, \tag{3}$$

is employed for each shape step assuming that (the time-independent weighting vector-function *W* is defined later)

$$<W(x),\frac{1}{v}\psi(x,t)>=\gamma=const\,, \tag{4}$$

$$N(t=0)=1.0. \tag{5}$$

The shape equations (time-dependence is omitted hereafter for *N, M, F* and all point-kinetics parameters):

$$\frac{1}{v}\frac{\partial\psi(x,t)}{\partial t}+\frac{1}{vN}\frac{dN}{dt}\psi(x,t)+M\psi(x,t)=(1-\beta)\chi_p F\psi(x,t)+\frac{1}{N}\chi_d\lambda C(x,t)+\frac{1}{N}Q(x,t)\,, \tag{6}$$

$$\frac{\partial C}{\partial t}=N\beta F(t)\psi(x,t)-\lambda C(x,t)\,, \tag{7}$$

are solved relatively rare (shape steps) compared to the amplitude (point-kinetics) equations

$$\frac{dN}{dt}=(\frac{\rho}{\Lambda}-\frac{\beta_{eff}}{\Lambda})N+\lambda c+q\,, \tag{8}$$

$$\frac{\partial c}{\partial t}=\frac{\beta_{eff}}{\Lambda}-\lambda C(x,t)\,, \tag{9}$$

where the point-kinetics parameters (one has not to define Λ explicitly here, only the ratios are needed)

$$\frac{\rho}{\Lambda}=\frac{1}{\gamma}<W(x),(\chi F-M)\psi(x,t)>\,, \tag{10}$$

$$\frac{\beta_{eff}}{\Lambda}=\frac{1}{\gamma}<W(x),\chi_d F\psi(x,t)>\,, \tag{11}$$

$$c=\frac{1}{\gamma}<W(x),\chi_d C(x,t)>\,, \tag{12}$$

$$q=\frac{1}{\gamma}<W(x),Q(x,t)>\,. \tag{13}$$

The described technique corresponds to the original SIMMER scheme with the only exception: the source term is included into Eqs. (1), (6), (8).

III.b Weighting functions

Within a shape step (started at t_0) the flux distribution in the reactor changes:

$$\psi(x,t)=\psi(x,t_0)+\delta\psi(x,t) \tag{14}$$

However, only the shape functions computed at the beginning the shape steps are available for calculating the point-kinetics parameters. Thus, the weighting function should reduce errors due to using an approximation to the flux shape within a shape step.

Substituting Eq. (14) into Eq. (10) and setting the first-order term containing $\delta\psi(x,t)$ to zero (setting this term to zero may not be the best option in a particular case; however, it is the best option in the general case) yields (because γ = *const*):

$$<W(x),(\chi F - M)\delta\psi(x,t)>= 0 \tag{15}$$

Since W is calculated in SIMMER only once, we will assume in the following that the operators *F* and *M* are defined at *t*=0.

For a critical reactor Eq. (15) is valid if *W* is neutron importance /18/, a solution of the adjoint equation (there is no 1/k factor here since fission is supposed to be already normalized):

$$M^{*}W(x) = (\chi F)^{*}W(x) \tag{16}$$

For a subcritical reactor (with source) Eq. (15) is valid if, for example, *W* is a solution of the α-adjoint equation (where α is an eigenvalue)

$$\frac{\alpha}{v}W(x) = (\chi F - M)^{*}W(x) \ , \tag{17}$$

because substitution of Eq. (17) into Eq. (15) yields

$$<W(x),(\chi F - M)\delta\psi(x,t)>= \alpha <W(x),\frac{1}{v}\delta\psi(x,t)> . \tag{18}$$

The right-hand side of the above equation is equal to zero due to Eq. (4).

A physical reason for choosing such a weighting function is the fact that *W* (defined by Eq. (17)) is the space-energy shape of the fundamental α-mode of the neutron importance /19/. The neutron importance in a subcritical system is time-dependent even at the steady-state conditions: with respect to the neutron population in the future, the earlier one takes into account the number and distribution of neutrons, the less important they are. One may also note that Eq. (16) is a particular case of Eq. (17) that is valid for a critical system. For very close-to-criticality levels, the weighting

functions defined by Eq. (17) will not be too much different from the "quasi-critical" weighting functions:

$$M^{*}W(x) = \frac{1}{k}(\chi F)^{*}W(x). \tag{19}$$

Other weighting functions - which are applicable to a subcritical system - may be certainly constructed too; currently, however, only the two weighting functions (defined by Eqs. (17) and (19)) are available in SIMMER.

One should note that the described weighting technique (which is the standard one for critical systems) does not assure that β_{eff}/Λ is also "first-order" accurate (the effective precursors are accurate if both ρ/Λ and β_{eff}/Λ are accurate). Moreover, for strong reactor perturbations using of a "steady-state" weighting function may give not very accurate point-kinetics parameters. However, following the common practice (for critical systems), these inaccuracies are accepted (they are reduced in SIMMER by performing γ-iterations).

III.c Calculation flow details

The problem is started from a steady-state (t=0) or from transient conditions (in the last case, time derivative is omitted in the shape equations at the initial time point).

A user-defined constant, γ_0, is employed throughout the whole run, (at both steady-state and transient conditions) for fission normalization (the generation cross-sections, $\nu\sigma_f$, are divided by this constant). That allows to meet a desired subcriticality level (which may differ from the one calculated by SIMMER in the absence of any normalization due to approximations employed in the code: a relatively small number of energy groups, coarse mesh, low Sn-order, etc.).

To obtain a weighting function, the adjoint equation (optionally k-eff or α-problem) is solved at t=0. The flux (shape) and source are normalized at t=0 to meet a specified (with respect to the initial power) level; this normalization is kept throughout the transient.

Space-energy shape of the source is time-independent and, for simplicity, is given by a product of an energy spectrum and a spatial distribution. The amplitude is supposed to be time-dependent: it is specified by the user in a special 'source - vs.-time' table (with linear dependence between the table points). The source angular distribution is isotropic.

While doing outer iterations to get the shape at the initial time point, the fission source term may be normalized by in a special way (by employing the $<W,(M-F)\psi>/<W,Q>$ ratio) to accelerate convergence in close-to-criticality reactor models. During the transient, the quasistatic constraint (see Eq. (4)) is used in the traditional (i.e. as for the critical case) way: to normalize the fission source and to check whether the new shape should be used to recalculate the point-kinetics parameters and the power trace during the last shape step (γ-iteration).

IV. TEST CALCULATIONS

To test the new options, the modified STN (Standard Test for Neutronics) problem of SIMMER-III /5/ was analyzed. The original (critical) problem setup is a fictitious disrupted LMFR core of an intermediate size for simulating a short-time energetic recriticality event. To drive a very rapid reactivity insertion, a slug of molten fissile fuel ("bullet") initially present at the bottom of the core center is pushed towards the core midplane with an initial velocity 100 m/s. The geometric model and initial conditions used for this problem are shown in Fig. 1.

A user-defined parameter, γ_0 (see the previous section) was used to simulate the transients at different subcriticality levels which corresponds to the k-eff values of 0.975 and 0.99. The source was placed in the two central reactor nodes (see Fig.1). In Fig. 2, 3 power and reactivity traces for the critical case and two subcritical cases are shown. The decrease of the transient power swing with going down from the criticality level is clearly demonstrated. The "critical" weighting function was used in all cases (we have compared critical and α-weighting for the 0.975 case and have not found any significant effect on the results; this is a consequence of the close-to-

criticality level and rather short shape steps which are necessary here to update the power shape).

Further calculations were also based on the STN problem. We employed here the two types of "bullets" – a fissile bullet and an "absorbing" (neutrons) bullet of greater size (to increase the reactivity swing) – for the critical and subcritical systems. Thus the impact of introducing strong negative and positive reactivities into the critical and subcritical systems was compared. The results are presented in Fig. 4, 5. As expected, the source-driven system demonstrates a much greater stability. The low response to the introduction of negative reactivity makes difficult, however, to reduce the power of the system without shutting off the source; this may result in unfavorable transient behavior for some types of accidents as e.g the unprotected loss of heat sink accident.

V. CONCLUSIONS

A new capability to simulate transients in subcritical systems with a strong neutron source was implemented in SIMMER; the recent incorporation of TWODANT in SIMMER-III provided a firm basis for the described developments.

The solution technique and related time-step control schemes provide the calculation results which are reasonable and internally consistent. Any comparison with another transient code has not yet been done, however. Efficient simulation of cases with a rapid source variation may require additional extensions and improvements.

A more wide class of transients (also related to the switch off and on of the source) will be analyzed. Further verification of the implemented capability is also planned. Employing of SIMMER for actual ADS is foreseen in the nearest future. That requires, however, certain extensions in the thermal-hydraulics part of SIMMER which are currently under development at FZK.

VI. ACKNOWLEDGMENTS

The authors highly appreciate the help, advice and support of Dr. G. Buckel, Mrs. E. Hesselschwerdt and Dr. E. Kiefhaber who performed earlier the TWODANT implementation into SIMMER. The first author is also grateful to Dr. G. Heusener and Prof. G. Kessler for providing an opportunity to work temporarily at FZK on this problem.

VII. REFERENCES

/1/ C. Rubbia et al.: A Tentative Programme towards a Full Scale Energy Amplifier, CERN/LCH/96-11 (EET) (1996)

/2/ H.U. Wider et al.: Severe Accident Studies in Fast Accelerator - Driven Systems, 2nd. Int Conf. on ADS Transmutation Technology and Application., Kalmar, Sweden (1996)

/3/ W. Maschek et al.: Some Safety Studies for Accelerator Driven Subcritical Systems, AccApp'98, Gatlinburg, USA (1998)

/4/ J. Tommasi et al.: Minor Actinide Destruction in Dedicated Reactors, 5th Int. CAPRA Seminar, Karlsruhe, Germany (1998)

/5/ S. Kondo et al.: SIMMER-III : An Advanced Computer Program for LMFBR Severe Accident Analysis, ANP'92, Tokyo, Japan (1992)

/ 6/ K. Ott et al.: Accuracy of the Quasistatic Treatment of Spatial Reactor Kinetics, Nucl. Sci. Eng., 36, 402 (1966)

/7/ G. Buckel et al.: A new Simmer-III Version with Improved Neutronics Solution Algorithms, FZKA 6290 (1999).

/8/ K.Ott et al.: Introductory Nuclear Reactor Dynamics, ANS, La Grande Park, IL, USA (1985)

/9/ J. Lewins: Importance The Adjoint Function, Pergamon Press, Oxford, UK (1965).

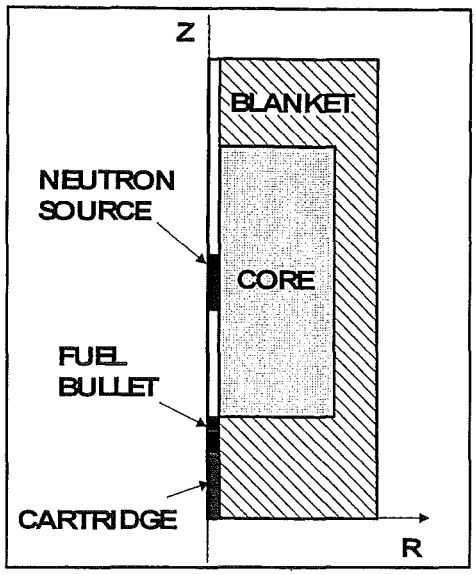

Figure 1: Geometry of the Standard Test problem for Neutronics (STN)

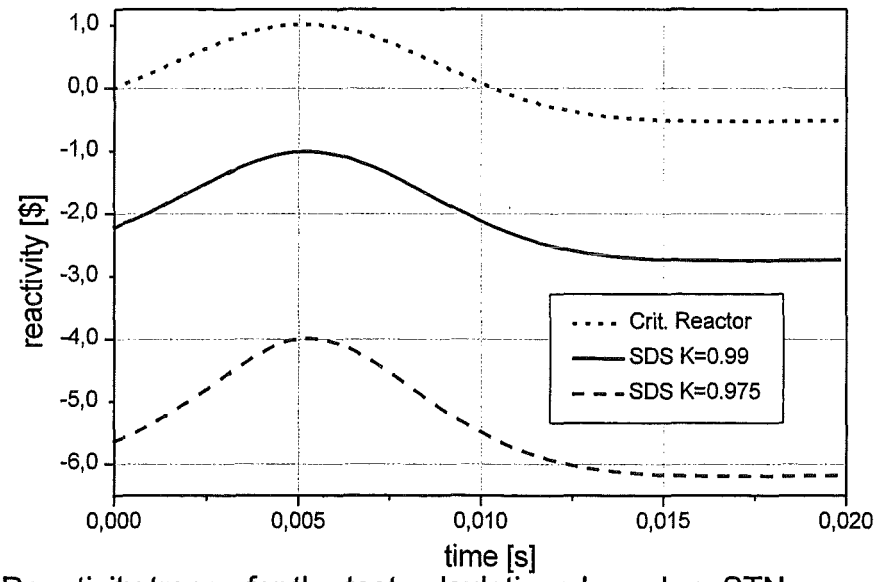

Figure 2: Reactivity traces for the test calculations based on STN

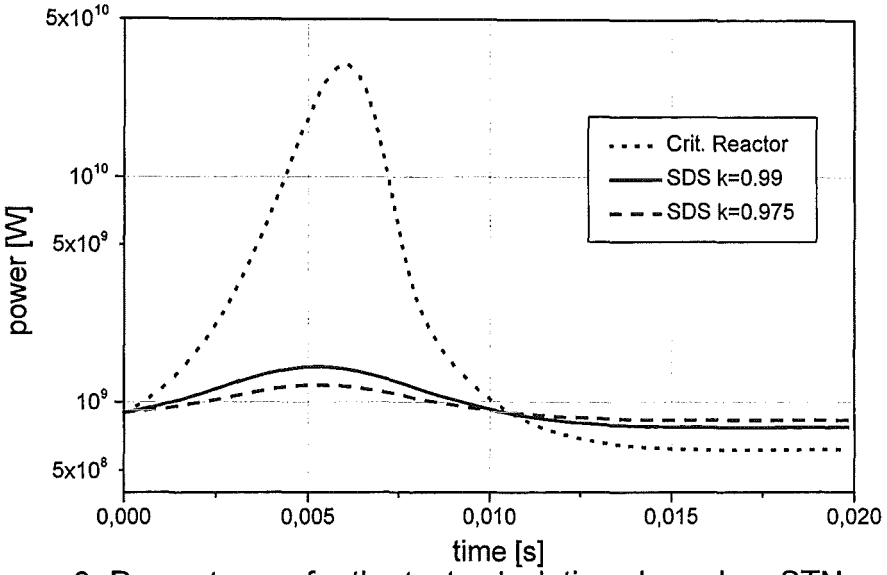

Figure 3: Power traces for the test calculations based on STN

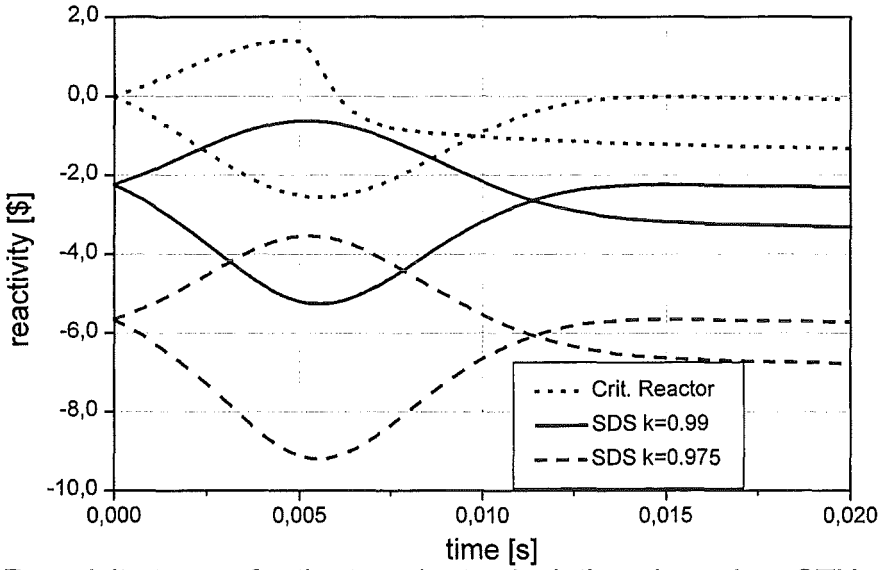

Figure 4: Reactivity traces for the transient calculations based on STN

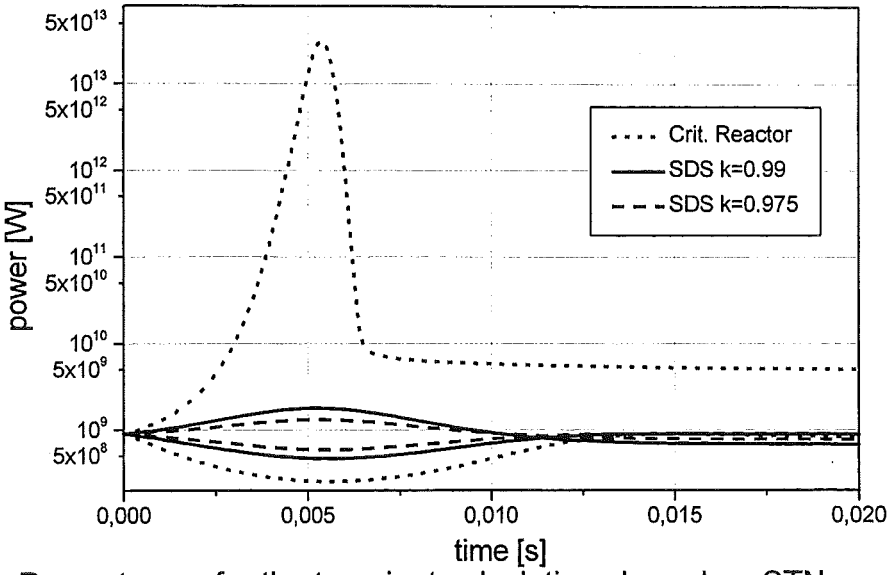

Figure 5: Power traces for the transient calculations based on STN

IV. New SAS4A Analyses of the CAPRA 4/94 Core Design for Actinide Burning and Transmutation

(D. Struwe, W. Pfrang, M. Schikorr, IRS; D. Thiem, INR)

INTRODUCTION

Within the CAPRA-project innovative core designs have been investigated for efficient actinide burning and transmutation. Balance of plant characteristics of the European Fast Reactor EFR [1] have been retained as a reference. One of the investigated design variants uses MOX fuel but the Pu-content is increased to about 40-45 percent for efficiently burning Plutonium. This CAPRA 4/94 core design has a similar size as the conventional EFR core and a thermal power output of 3600 MWth. To cope with the high Pu enrichment the core configuration represents a highly transparent structure [2]. This core design shows significant differences compared to conventional core designs which are reflected in altered fuel pin and subassembly design characteristics and safety parameters. These differences have an influence on accident analyses and especially on core melt accident scenarios. Therefore analyses have been performed to assess the behaviour of the hollow fuel pellet fuel pin design during power operation up to the envisaged high burn-up values and the energetics potential during unprotected transients. Consequence evaluations of an unprotected loss-of-flow transient (ULOF-accident) and an unprotected reactivity ramp rate transient (UTOP-accident) during the initiation phase have been selected as representative cases. Results of these analyses should give an impression of the change in the risk potential for beyond design basis accidents.

PIN BEHAVIOUR UP TO EOEC CONDITIONS

For simulation of the fuel pin behaviour during power operation up to end of equilibrium cycle conditions (EOEC-conditions) it becomes necessary to represent the specific features of the subassembly arrangement along core cross section in sufficient detail and to simulate the power history during the three batch loading scheme with subcycling of the diluent sub-assemblies appropriately. The core cross section was simulated with 21 fissile subassembly groups. The behaviour of fuel pins of these subassembly groups is represented by the behaviour of one representative fuel pin only. Impact of the behaviour of the homogeneously distributed unheated

pins in the fissile subassemblies is done only in a quite simplified manner by choosing the coolant channel area allocated to one fissile pin in an appropriate manner and neglecting the thermal inertia of the filling material in the unheated pins. This results in a ratio of the coolant channel cross section per heated fuel pin in the CAPRA-S/A-design of 0.84 which is 72% larger than the respective value of the EFR-S/A-design. Clad material of unheated pins together with wire wraps and hexcan structures are combined to a structure material coupled to the coolant cross section by appropriately defined wetted perimeters. The resulting hydraulic diameter of the CAPRA coolant channel is therefore smaller than the one of the EFR coolant channel.

The CAPRA hollow pellet fuel pin design concept leads to a value of the as fabricated fuel smear density of 77.7% which is considerably less than the 86.1% of the EFR hollow pellet fuel pin design concept. More pronounced differences in the two fuel pin design concepts appear when comparing the ratio of the hollow fuel pellet ring thickness to the outer fuel radius. The value of the CAPRA fuel pins amount to 0.59 while the EFR value amounts to 0.86. This poses a problem for a reliable calculation of the fuel pin behaviour during power operation because there is only little experimental experience available about the behaviour of these type of fuel pins if operated up to high burn-up values. Therefore it became necessary to evaluate the reliability of code calculations for description of the behaviour of hollow pellet fuel pin designs during power operation in view of existing experimental observations.

For this purpose power operation campaigns were recalculated which were performed in the framework of the CABRI-2 and CABRI-FAST projects [3]. In these projects three hollow pellet fuel pin designs were pre-irradiated in the Phenix reactor, i.e. the OPHELIE-6 fuel pins up to a peak burn-up of 5.8 at%, the SCARABIX fuel pins up to a peak burn-up of 6.4 at% and the QUASAR fuel pins up to a peak burn-up of 12 at%. Fuel pin design specification of the OPHELIE-6 and the SCARABIX fuel pins were close to the EFR fuel pin design values while the fuel pin specification of the QUASAR fuel pins are relatively close to the ones of CAPRA fuel pins. Comparison of the experimental results with calculations performed with the Rel. 1.0 code version of the SAS4A.Ref96 code [4] revealed reasonable agreement when

integral characteristics as fission gas release were considered. However, extending the comparison to more detailed data as fuel pellet stack dimensions and axial distributions of fission gas retention, non negligible differences between experimental observations and calculated results were identified. As a consequence of these findings several modelling aspects of the SAS4A fuel pin mechanics model DEFORM-4C were revised. These were

- the radial distribution of the solid fission product swelling,
- the temperature dependence of the fission gas induced fuel swelling
- the burn-up dependent fuel pellet stack expansion
- the calculational route to determine the behaviour of fully cracked fuel pellets
- the thermal expansion of solid fission products
- the JOG-material behaviour
- the impact of contact pressure effects on the fuel to clad heat transfer

When comparing the results of calculations with the revised DEFORM-4C model with the experimental observations better agreement was obtained especially with regard to the burn-up dependent axial fuel pellet expansion and the axial distribution of retained fission gases for the three irradiation campaigns considered.

The revised code version was used to investigate the fuel pin behaviour of the CAPRA 4/94 core design with mixed oxide fuel during power operation. The power variation of individual subassembly groups during the equilibrium cycle operation with simulation of the subcycling of heavy and light diluents was newly calculated. The burn-up behaviour of subassemblies was determined dependent on the actually established power distribution. As a result of these calculations a fully consistent power distribution along core cross section was provided for EOEC conditions. Peak linear ratings vary between 406 W/cm and 230 W/cm in outer subassembly positions. In the center part of the first and second enrichment zone linear ratings vary between about 300 W/cm and 400 W/cm dependent on the burn-up achieved. Gap conductance values decrease continuously with burn-up thus resulting in a rather flat distribution of average fuel temperatures varying between values of 1710 K up to 1840 K. The larger values are calculated for fuel pins with a burn-up of about 12 to 14 at%. Clad swelling becomes rather large especially for high burn-up pins. Integral

fission gas release values of fuel pins with about 12 at% burn-up amount to about 80 % which is consistent with the value of 72 % observed in the QUASAR pin irradiation which reached a peak burn-up value of 12 at% with slightly lower linear ratings during irradiation. The as fabricated central hole becomes slightly smaller with higher burn-up which is consistent with the experimental observation. On basis of the calculations no anomalies were identified which might indicate difficulties arising from the fuel pin behaviour during power operation. Peak values of the integral gas release amount to about 88 % which represents a kind of a saturation level for gas release fractions at high burn-up in accord with the experimental observations obtained from the different irradiation campaigns investigated in the different CABRI-programmes.

As cooling strategy the one provided by the project has been used for the analyses. This leads to rather large differences of coolant outlet temperatures in subassembly groups with different burn-up. The maximum difference in between subassembly groups being located close to each other in the core configuration amount to 30 up to 50 K which remains below the maximum allowed target value of 60 K. However, this difference in coolant outlet temperatures is rather large when compared to values normally achieved in conventional core design variants. Therefore consequences of thermal striping on internal reactor structures need to be considered carefully.

ANALYSES RESULTS FOR THE INITIATION PHASE OF ULOF-TRANSIENTS

For consequence evaluation of an unprotected loss-of flow transient in the CAPRA 4/94 core design new reactivity worth distributions of sodium, steel and fuel were calculated for the EOEC core conditions as well as values for the Doppler effect, the prompt neutron life time and the effective delayed neutron fractions. These calculations were based on a fully consistent evaluation of the equilibrium cycle power operation taking into consideration subcycling of the heavy and light diluents. The calculated maximum sodium void worth value amounted to 6 $ and the reactivity feedback related to a total steel removal would result in a positive reactivity feedback of 7.6 $. These newly calculated values are considerably higher than the ones provided earlier by the project due to the use of more appropriate calculation methods for the heterogeneous core configuration.

The transient core behaviour has been calculated using the EFR-approach to simulate the transient behaviour of core inlet and outlet plena and the one of the primary and secondary circuits. Primary and secondary coolant mass flow reduction was simulated as specified for EFR. To force the transient calculation into sodium boiling onset as consequence of a coolant mass flow reduction it became necessary to reduce the effectiveness of the negative control rod drive line expansion feedback when compared to the project reference data. Fuel pin axial expansion is calculated according to the balance-of-force model which has been qualified during theoretical interpretation of experiments performed in the different CABRI-programmes for quite a variety of different test conditions covering pure coolant mass flow transients, slow and very rapid power transients and the superposition of both type of transients. For other modelling aspects approaches were chosen which have been qualified during theoretical interpretation of results obtained within the different CABRI-programmes [5].

Transient variation of the power and the different reactivity feedback contributions as consequence of the coolant mass flow reduction up to boiling onset is shown in Fig. 1. Sodium boiling starts at 38.14 s into the transient at a normalised power level of 63 %. The net reactivity amounts to –15.7 c. It mainly represents the sum of the positive contribution due to the coolant heat-up, which amounts to 18.3 c positive, and the negative contribution due to the control rod drive line expansion feedback, which amounts to – 35,1 c. Reactivity feedback effects due to axial fuel pin expansion and the Doppler effect are negligibly small, because coolant heat-up resulted in a fuel temperature level which is close to the steady state value.

Boiling starts within 1 s in subassembly groups 6, 9 and 14 which simulate the transient behaviour of low burn-up subassemblies with steady state values of the peak linear rating of about 400 W/cm. As shown in Fig. 2 boiling is initiated in the upper axial reflector region and does not result in an immediate voiding of core fissile height. The two phase flow region expands firstly upward into the upper subassembly structure penetrating the upper B4C-shield and extending into the upper sodium plenum prior to penetrating down into fissile core height. This takes about 6 s. The reactivity feedback due to sodium boiling is negative initially. However, when voiding fissile core height the positive reactivity feedback is released within another five

seconds and amounts to a value of 32 c in case of the firstly boiling subassembly group 6. These contributions add up with positive contributions from other boiling subassembly groups so that a void induced benign power excursion develops.(see Fig. 3). This power excursion leads to first fuel pin failures in subassembly group 6 at 49.7 s into the transient which is 11.6 s after boiling onset. Up to that time into the transient the net reactivity has increased up to a value of 78.8 c and the normalised power level has reached a value of 5.3. The sodium void reactivity feedback up to that time amounts to 1.59 $ which is only about 26 % of the maximum value. This positive contribution is mitigated partially by negative contributions due to the control rod drive line expansion feedback (-36.8 c), the Doppler feedback (-27.6 c) and the fuel axial expansion feedback (- 24 c). However a small positive contribution is calculated to result from molten clad material relocation which started to develop firstly in the first boiling channel 9s after boiling onset. The core state close to the time of first fuel pin failure is shown in Fig. 4. Only for a few subassembly groups fissile core height is already voided, so that a continuous and accelerating release of the positive void reactivity feedback is to be expected after first fuel pin failure. At this point in time the positive reactivity ramp rate due to sodium boiling amounts only to values of 1 to 2 $/s. The subsequently calculated power excursion is shown in Fig. 5 and the transiently varying reactivity feedback contributions to the net reactivity variation in Fig. 6.

First fuel pin destruction occurs shortly after fuel melting onset in subassembly group 6 which is nearly completely voided and in which molten clad relocation has been initiated a few seconds earlier. The mode of failure corresponds to a kind of a fuel pin break-up, i.e. the fuel pin geometry is totally lost as consequence of the melt cavity pressure built-up, which amounts to a value of about 2.5 MPa. Subsequently fuel and molten clad material is relocated up- and downward in the coolant channel. The molten clad material relocation is initially more pronounced due to its lower viscosity. Therefore it results in an increase of the associated reactivity feedback which leads to a slight increase of the net reactivity and thus to a slight increase of the reactor power. However, fuel relocation becomes activated a few 10 ms afterwards as consequence of the release of retained fission gases which results in a more pronounced negative reactivity feedback leading to a continuous decrease of the normalised power.

As consequence of the nearly coherent fuel pin destruction in subassembly groups 14, 9, 3 and 17 within the next 30 ms a similar materials relocation behaviour is observed. However, the positive reactivity feedback due to molten clad material relocation is enhanced by a simultaneous increase of the sodium void reactivity feedback which results in a positive sodium void reactivity ramp of about 10 to 20 $/s. This positive reactivity feedback drives the net reactivity to values above superprompt critical. The normalised power increases rapidly to values of about 180. The associated fuel heat-up leads to a rapid release of retained fission gases. These fission gases result in a pressure built-up in the molten clad and fuel mixture which initiates a dispersive fuel relocation within the broken-up fuel pin geometry. This fuel relocation leads to a rapid reduction of the net reactivity and thus to a rapid reduction of the normalised power. The net reactivity is reduced so effectively that further sodium voiding and fuel pin break-up in other subassembly groups is not sufficient to drive the net reactivity back to values close to delayed critical. The core state at the end of the calculated transient is subcritical on a level of –3.3$.

The core state at this late time into the transient is shown in Fig. 7. It can be seen that core zone 1 is completely voided. Fuel pins in subassemblies with burn-up levels of 7 and 12 at% have failed and are destroyed along major parts of fissile core height. Core zone 2 is nearly completely voided as well. However, only the inner subassembly groups are destroyed. The outer part of core zone 2 remains intact up to that time into the transient. Sodium boiling is already far advanced but it will need some time to void fully fissile core height. However fuel relocation in failed subassembly groups is limited mainly to the original fissile core height and only little fuel is relocated into reflector regions above and below. Therefore it is not at all clear that the established configuration will remain permanently subcritical when pressure levels in the mobile fuel/clad mixture will decrease continuously as consequence of the continuously low power level. The established configuration defines initial and boundary conditions for transition phase analyses. Hexcan structures and dummy pins in subassemblies are heated up considerably and therefor further material relocation will quickly become two- and last not least three-dimensional. Analyses of further materials relocation need to be performed carefully to evaluate whether early access to controlled core material relocation paths along diluent subassemblies or control rod positions provides a possibility of preventing the occurrence of more or

less energetic recriticality events in the transition phase prior to achievement of permanent reactor shut-down.

The potential of a mechanical loading of reactor vessel structures at the end of the initiation phase of the transient has been evaluated. A characteristic quantity for the mechanical work energy potential is the isentropic expansion of vapour components of the core material mixture to the cover gas volume. This evaluation leads to negligibly small values only. However, parametric analyses have shown that this result depends strongly on the fuel pin characterisation at EOEC conditions, criteria used for determination of fuel pin failure propagation and the mobility of the fuel/fission gas mixture after break-up. Results presented here assume that fuel pins of the CAPRA subassemblies behave similarly as observed in the different CABRI programmes. This might be optimistic in view of the complicated and different structure of the CAPRA subassemblies with the numerous dummy pins distributed along subassembly cross-section. Therefore it seems necessary to evaluate the problem with experiments to be performed on a subassembly like scale.

ANALYSES RESULTS OF THE INITIATION PHASE OF A UTOP-TRANSIENT

Complementary to the analyses of an unprotected loss-of-flow transient consequences of an unprotected transient overpower transient in the CAPRA 4/94 core design were analysed. Objectives of these analyses were to determine power to melt values and to evaluate the margin to failure of the specific CAPRA fuel pin designs. These two items were identified of special importance as result of experimental observations for other hollow pellet fuel pin designs which were investigated in the different CABRI-programmes.

As initiating event an unprotected and unlimited reactivity ramp rate of 0.8 c/s was postulated to occur. Assuming a similar efficiency of the reactivity feedback due to control rod drive line expansion as in the ULOF-analyses this results in a power increase of about 1% P_N/s. Transient variation of the normalised power and the reactivity feedback contributions up to fuel pin failure is shown in Fig. 8. Up to fuel pin failure the normalised power reaches a value of 2.863. This corresponds to a peak linear rating in the highest rated subassembly group of 1169 W/cm. At these power levels the coolant starts to boil at subassembly outlet in the highest rated

subassembly groups which are the ones with a peak burn-up of around 6 to 8 at% burn-up.

Up to fuel pin failure the externally supplied reactivity amounts to 1.35 $. This reactivity disturbance is nearly balanced by three major reactivity feedback effects: the Doppler reactivity feedback (-0.724 $), the control rod drive line reactivity feedback (-0.511 $) and the axial fuel expansion reactivity feedback (-0.365 $). The only positive reactivity feedback effects are the ones due to sodium heat-up (+0.25 $) and due to axial clad expansion (+0.05 $). The net reactivity does hardly exceed a value of +5 c during transient time. This calculation demonstrates the inherent safety characteristics of the CAPRA 4/94 core design and the large margin to failure of the hollow pellet fuel pin design.

However, this hollow pellet fuel pin design results in power to melt values of the peak linear rating which are rather low. Calculated results are shown in Table I in dependence of linear ratings at steady state conditions and peak burn-up values. The power to melt values decrease with higher burn-up values, but the ratio between power to melt values and the steady state linear ratings increase for the higher burn-up pins. Therefore it is not at all obvious that this feature of a hollow pellet fuel pin design is a disadvantage when compared to the behaviour of a solid pellet fuel pin design. The very large margin to failure is more important and a clear advantage of the hollow pellet fuel pin design.

Post-failure results are shown in Fig. 9. Fuel accumulation around the initial failure site and a pronounced sodium voiding increases the net reactivity to values of 23 c positive. The respective power increases only little to values of 3.5 times nominal. Subsequently fuel sweep-out initiates a rather rapid reduction of the net reactivity. This reactivity effect related to a dispersive fuel relocation becomes more pronounced after initiation of fuel pin break-up. The net reactivity becomes reduced to values of –3.2 $ and the normalised power stabilises around 58 % of its nominal value. The core configuration enters into a situation similar to consequences of an accident resulting from a single subassembly blockage accident. Whether longterm coolability can be achieved or not is dependent on the question whether a subassembly to subassembly propagation is prevented due to the interwrapper

coolant flow and/or subassembly to subassembly heat transfer. This question would need to be analysed carefully but with other tools than SAS4A.

CONCLUDING REMARKS

Analyses have been performed to evaluate transient behaviour of the CAPRA 4/94 core design in case of a ULOF-accident and of a slow UTOP-accident applying the most recent code version of the SAS4A code system. Modelling improvements of the fuel pin mechanics model needed to be developed firstly to represent the fuel pin behaviour during power operation up to EOEC conditions more reliably than possible with the previously existing code version.

Consequence evaluations of the ULOF-accident indicate a tendency for an enhanced margin to sodium boiling onset when compared to the EFR core design. However, this tendency needs to be qualified taking into account the inter subassembly coolant flow behaviour and the subassembly to subassembly heat transfer including appropriately the diluent subassembly positions. Experimental validation on a subassembly scale is strongly recommended.

Results of transient analyses of a ULOF accident leading to fuel pin destruction and post-failure core materials relocation indicate a favourable behaviour of the CAPRA-core design during the initial phase of core destruction. There seems to be less potential for highly energetic power transients during the initiation phase than in the EFR core design. This favourable result holds when it is assumed that the dispersive fuel relocation within subassemblies develops similarly as observed in the single pin experiments performed within the different CABRI programmes. This assumption should be qualified by experimental investigations simulating the impact of diluent pins on the post-failure fuel relocation in a subassembly-like geometry.

In case of a ULOF-accident core configurations established at the time of first reactor shut-down reach a level of about –3.5 $ for the net reactivity but they might not represent a final state of reactor shut-down. One has to expect subsequent materials relocation in the early transition phase which could drive the net reactivity back to and above critical. This needs to be analysed carefully. Results of first attempts to consider this problem have already been reported and indicate that there are

reasonable chances that controlled materials relocation occur along diluent subassembly and/or control rod positions and thus could prevent entering into highly energetic recriticality events in the transition phase.

In case of a slow UTOP-transient inherently activated reactivity feedback mechanisms limit the net reactivity to small positive values so that the associated power increase remain small, i.e. at values of about 1%P_N/s only. The margin to failure of the hollow pellet fuel pin design is large. Fuel pin failure is to be expected only at peak linear ratings above 1200 W/cm. However, the power to melt values are small decreasing with higher values of the burn-up. They amount to values of 1.5 to 1.8 times the peak linear ratings at steady state. However, this cannot be interpreted as a disadvantage what concerns safety features of the hollow pellet fuel pin design. These findings should only be valued in relation to the more important large margin to failure which is achieved with the hollow pellet fuel pin design. Post-failure transients associated with a slow UTOP-accident do not indicate specific problems. The established core configuration might be coolable for longterm or the subsequent core behaviour is dominated by consequences of a thermally induced subassembly to subassembly propagation which needs to be investigated carefully.

REFERENCES

[1] Heusener G.; Hubert G., Michell C.H.,1994, EFR Safety Concept; ARS'94, Int. Top. Mtg. On Advanced Reastors Safety, Pittsburgh, USA

[2] Rouault J.A., Conti J.C., Garnier A., Languille A., Lo Pinto P., Pillon S.,1994, Physics of Plutonium Burning in Fast Reactors: Impact on Burner Cores Design, Prc. Top. Mtg. Advances in Reactor Physics, Knoxville; Tenessee, April 11 – 15, 1994, USA

[3] Heusener G., Kussmaul G., Struwe D., Cowking C., Melis J., Schmitz F., Dadillon J., Tattegrain A., Takahashi K.,1990, The CABRI Programmes – Motivations and Achievements, Int. Fast Reactor Safety Mtg., Snowbird, Utah, USA

[4] Imke U, Struwe D., Niwa H., Sato I., Camous F., Moxon D., 1994, Status of the SAS4A-code development for consequence analysis of core disruptive accidents, Proc. Int. Top. Mtg. Sodium Cooled Fast Reactor Safety, Obninsk, October 3 – 7, 1994, Russia

[5] Struwe D., Imke U., Pfrang W., Maschek W., Wolff J., Overview on Material Relocation Phenomena in Liquid Metal Fast Reactors as Consequence of Core Disruption, IWGFR /89 IAEA Mtg., O'Arai, Mito, Japan

Table I Power to melt values dependent on linear rating at steady state and burn-up in the CAPRA 4/94 core design for a 0.8 c/s reactivity ramp rate accident

Burn-up at%	Steady state linear rating W/cm	Power to melt W/cm
6 - 8	380 - 400	570 - 630
12 - 14	330 - 350	480 - 530
18 - 21	270 - 300	490 - 550

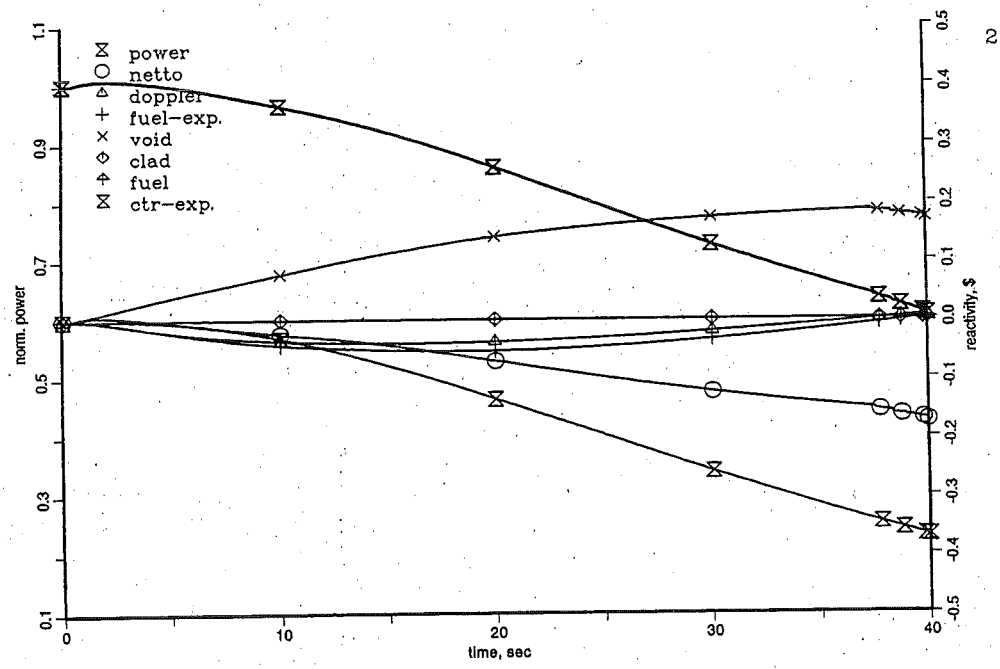

Fig. 1 Transient variation of characteristic core state variables during the initial phase of a ULOF-transient in the CAPRA 4/94 core design up to boiling onset

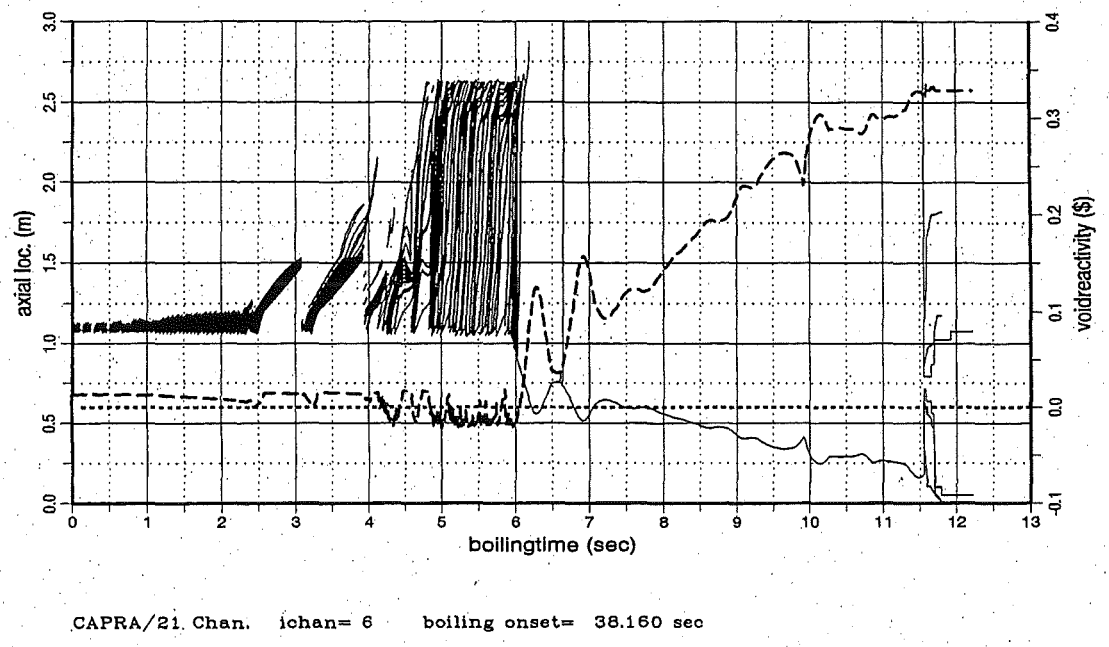

Fig. 2 Transient variation of the axial extent of the two-phase flow zone and the void reactivity feedback in the first boiling subassembly group 6 of the CAPRA 4/94 core design

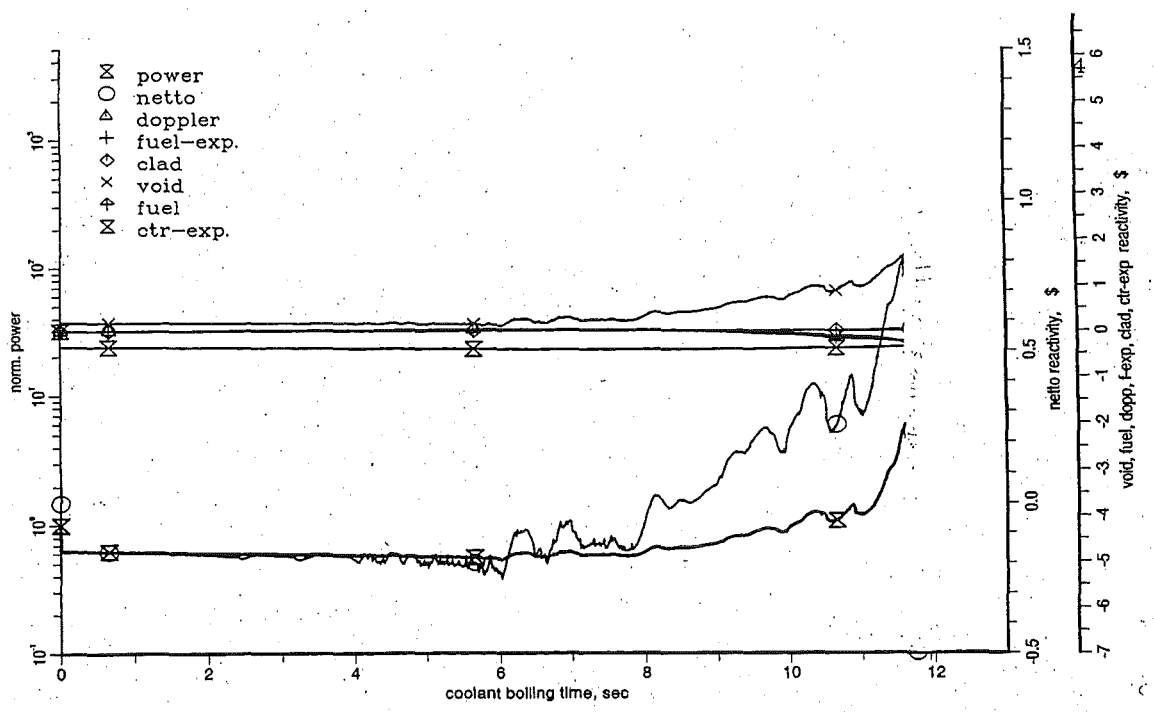

Fig. 3 Transient variation of characteristic core state variables during the boiling phase of a ULOF-accident in the CAPRA 4/94 core design up to first fuel pin disruption

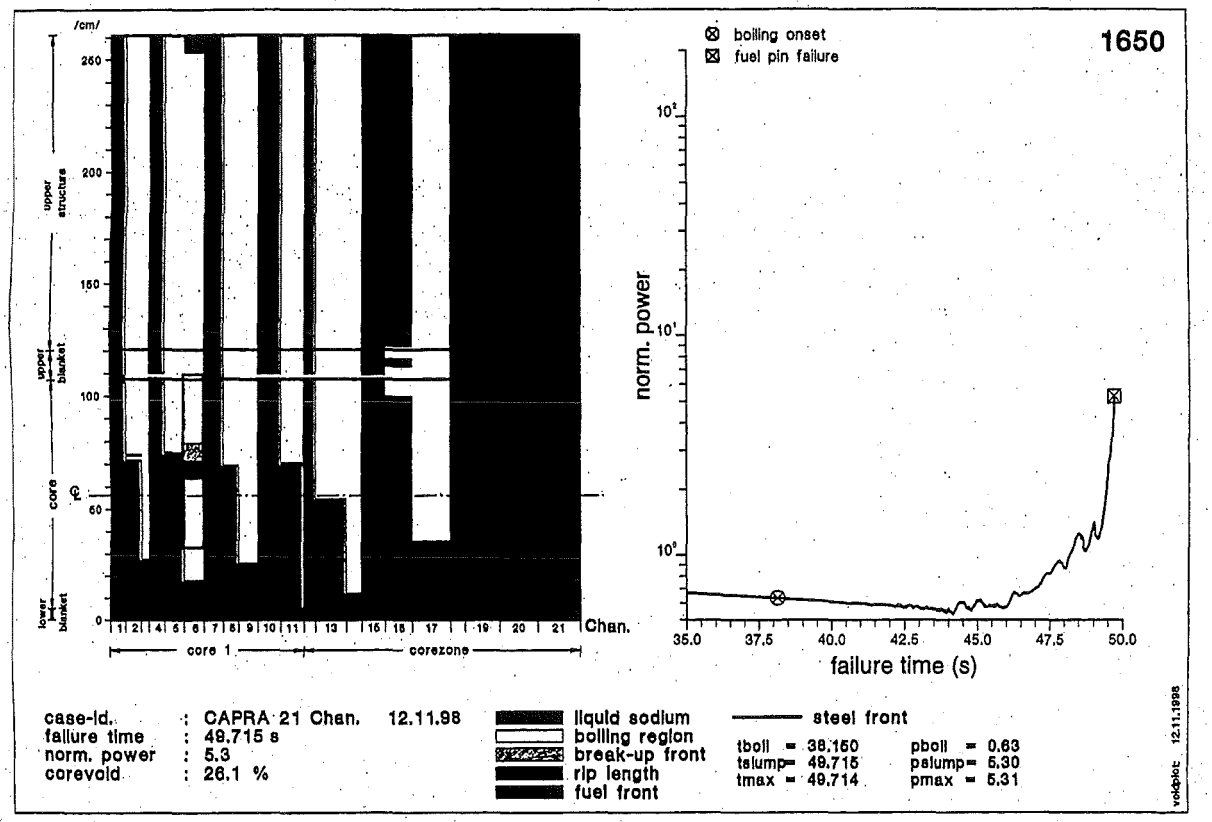

Fig. 4 CAPRA 4/94 core state close to the time into the transient when first fuel pin disruption is calculated in subassembly group 6

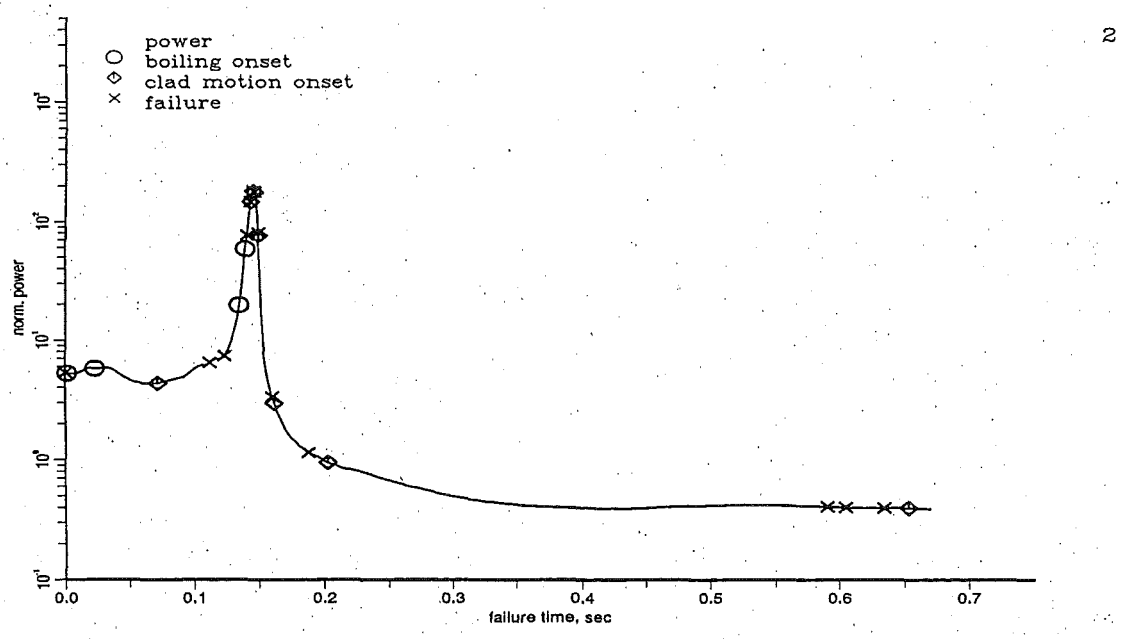

Fig. 5 Transient variation of the normalised power during the failure time of a ULOF-accident in the CAPRA 4/94 core design up to first reactor shut-down

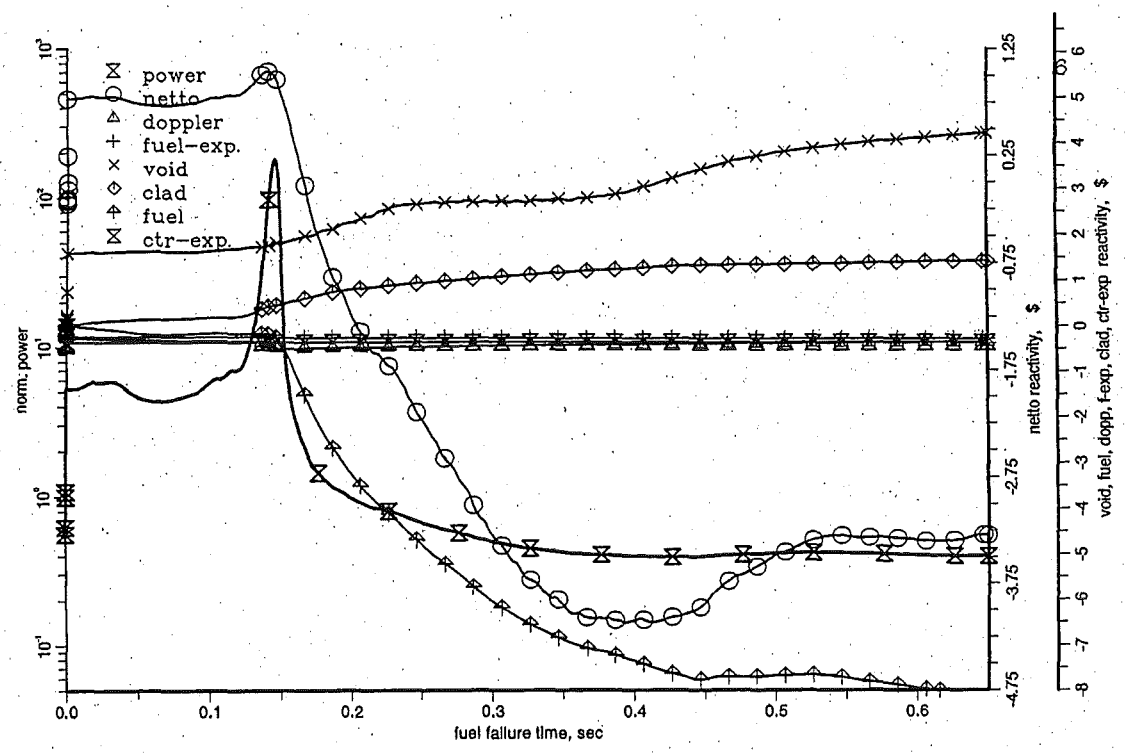

Fig. 6 Transient variation of characteristic core state variables during the failure time of a ULOF-accident in the CAPRA 4/94 core design up to first reactor shut-down

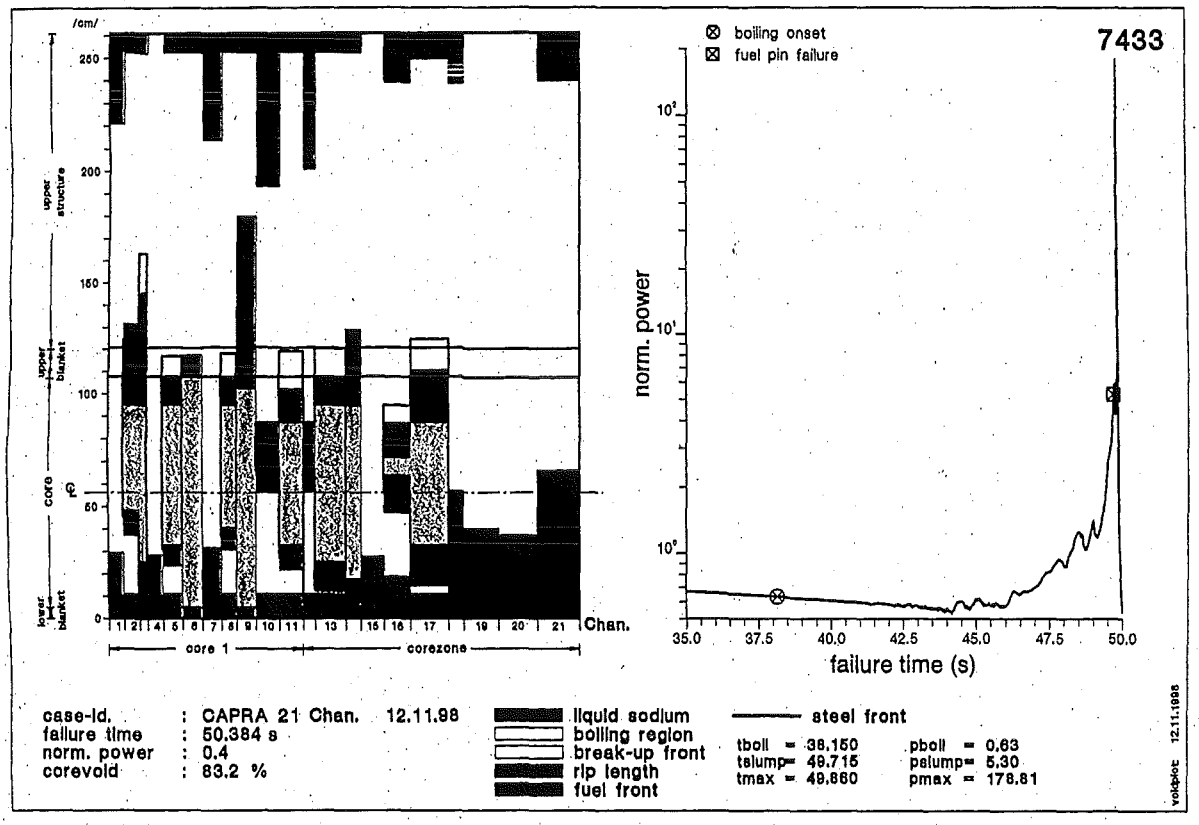

Fig. 7 Core state at the end of the initiation phase calculation of a ULOF-accident in the CAPRA 4/94 core design

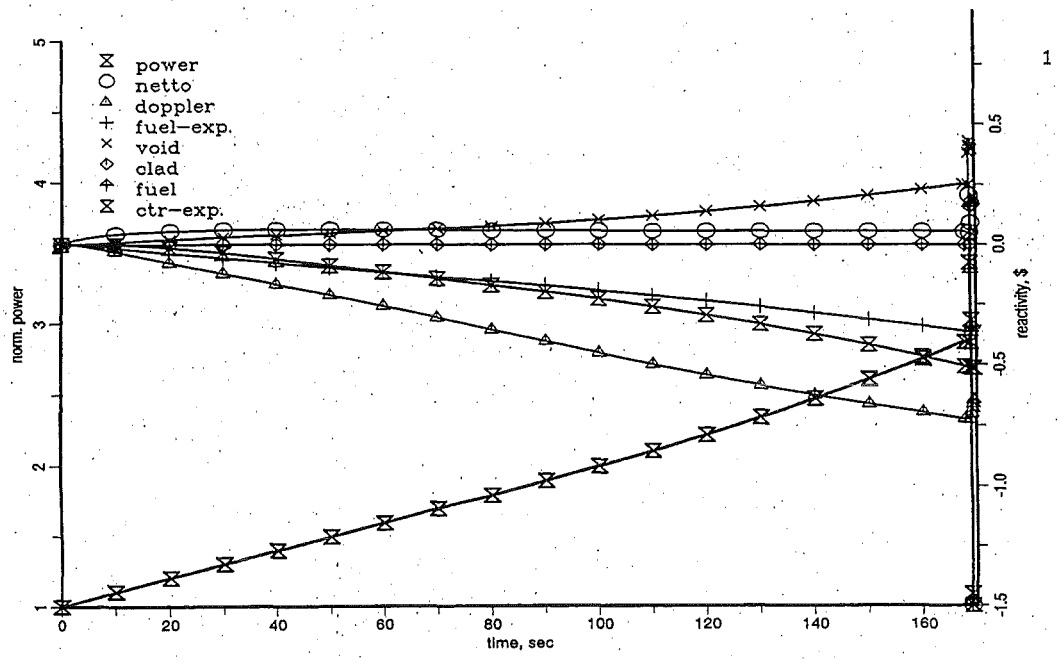

Fig. 8 Transient variation of characteristic core state variables during the initiation phase of a slow UTOP-accident in the CAPRA 4/94 core design

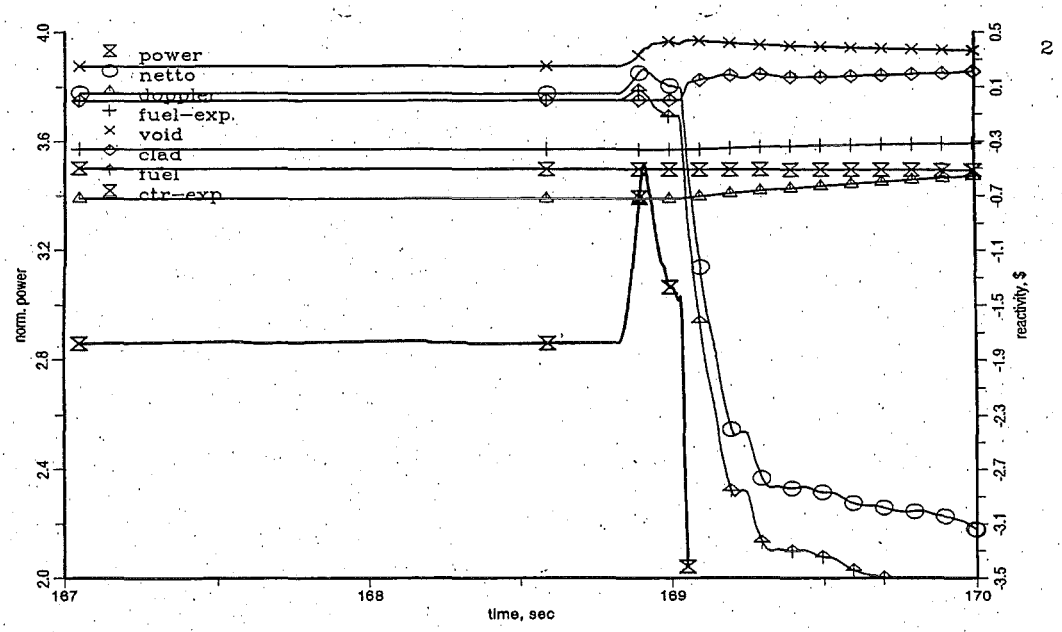

Fig. 9 Transient variation of characteristic core state variables during the post-failure phase of a slow UTOP-transient in the CAPRA 4/94 core design

32.23.04 Bestrahlungsexperimente zur Transmutation von Aktiniden im HFR

(H. Plitz, PSF)

Since 1993 FZK has been contributing to the CAPRA programme which aims to burn as much plutonium as possible for electricity production and to transmute or destroy minor actinides. A fast reactor typical reference core with annular mixed oxide fuel of uranium and plutonium with a maximum plutonium content of 45 % has been defined. The reference fuel pin concept was chosen because this is compatible with the PUREX process, already demonstrated on fresh 45 % Pu-content MOX fuel. The results on irradiated fuel will be obtained with fuel irradiated in experiments.

The High Flux Reactor (HFR) at Petten (NL) was chosen to perform an experimental irradiation programme within specially designed irradiation devices called TRABANT (Transmutation And Burning of Actinides iN TRIOX), which can contain 3 fuel pins which are independently cooled. In cooperation with CEA Cadarache, Institute for Transuranium Elements (ITU) and FZK an irradiation programme TRABANT was launched in 1994. The fuel pins were commonly designed and specified and 3 fuel pins for the first experiment TRABANT 1 were manufactured:

- a CAPRA reference high plutonium content (45 % Pu) oxide fuel pin manufactured by CEA Cadarache,
- another reference oxide fuel pin with 40 % Pu content plus 5 % Np manufactured by ITU, and
- a Pu without U oxide fuel pin with $(Ce_{0.56},Pu_{0.44})O_2$ solid pellets, containing two tightly separated short fuel columns of different O/M ratios and densities, manufactured by ITU. The upper fuel column with very low O/M ratio and density replaced the initially planned PuO_2-MgO fuel, which was not available in time. The pin design was then modified by shifting axially the partial fuel columns away from the high neutron flux regimes. The cladding material is an austenitic steel.

The main objective of the TRABANT experiments is to assess the irradiation behaviour of high Pu-content fuels up to a significant burn-up.

The heat rating requirements were defined to reach equivalent fuel temperatures as in fast neutron flux conditions, that is 520-570 W/cm for mixed oxide pins (equivalent to 400-450 W/cm in fast neutron flux), and 350-400 W/cm for pin 3. Corresponding clad temperatures are 873-903°K. The irradiation history is briefly summarised in /1/.

The pin 1 began irradiation separately in May 1995 up to 4.1 at% b.u., when a neutron radiograph revealed no abnormal behaviour. The irradiation then continued with the two other fresh pins (2 and 3), with higher linear powers than planned for pin 1 (up to 20 % more) and to a lesser extend for pin 3, until pin 1 reached 9.5 at% b.u and pin 2 about 4,5 at% b.u. The mandatory neutron radiograph inspection showed a failure of pin 1, fuel melting of pin 3, and nothing abnormal for pin 2. Perturbations of the sodium temperatures above the top of the fuel column indicated that the failure of pin 1 probably occurred before or at 7 at% b.u. The pins 1 and 3 were discharged from the reactor at 9.5 at % and 4.6 at%, respectively. The pin 2 continued up to 9.3 at% b.u. and was interrupted once to perform a neutron radiograph at about 7 at% b.u.

The pin failure of the CAPRA-type pin 1 was clearly to be seen in the neutrographs. Also the upper fuel column of fuel pin 3 was showing fuel melting, but no clad failure did occur. For pin 3, the cause of fuel melting is clearly du to the poor conductivity of the $(Ce,Pu)O_2$ fuel with low density and low O/M ratio submitted to higher operating powers.

According to the sodium temperature registration, the failure of pin 1 occurred at about 7 at% b.u., after running with very high linear powers, which has led to high fuel temperatures and perhaps to fuel melting.

Just before HFR reactor cycle 7 the 3-pin cluster TRABANT was turned is such a way that pin 1 attained by chance a power ramp up to 660 W/cm, which might be the cause for a clad failure occurring in cycle 7, but without being detected. The pin therefore continued to run with a clad failure during 3 more cycles (60 days) causing conditions still more severe (fuel/sodium reaction leading to lower fuel conductivity, fission gas release in sodium, etc.) Results of post-test examinations (neutrographs, gammascans, macrographs of ceramographics) indicate that a massive sodium/MOX

reaction did occur and was obviously maintained for another 3 irradiation cycles with 3 shut-offs and start-ups. Due to the axial fuel relocations and due to the massive thermal isolation of the reaction product uranate-plutonate (thermal conductivity only 10 % of MOX) even clad melting occurred.

The destructive post-test examinations are underway at ITU.

From the TRABANT 1 irradiation experiment the following can be concluded /1/:

- At higher burn-up, first results obtained on oxide fuel with 40 % Pu and 5 % Np content are very positive as they demonstrate that that very significant burn-ups (close to 10 at%) can be reached by a high plutonium content fuel without problems. However, the TRABANT 1 pin no. 1 (oxide pin with 45 % Pu), which run under severe conditions, has failed at about 7 at% b.u. The destructive examinations of these pins will give more evidence on the causes of the failure.
- The low O/M fuel column of $(Pu,Ce)O_{2-x}$ melted, thus confirming the poor thermal properties of this fuel. In spite of its apparent satisfactory behaviour, the high O/M high density $(Pu,Ce)O_2$ fuel could not be used in CAPRA cores due to its incompatibility with sodium shown through laboratory tests.

The TRABANT 2 irradiation has been prepared. 3 fuel pins were manufactured, all of the CAPRA type, i.e.

Pins	Pu content (%)	Density (% dt)	O/M
1	40	94.18	1.971
2	40	93.40	1.995
3	45	86.36	1.99

The TRABANT 2 irradiation device has already been ordered in 1997, the irradiation of these 3 fuel pins in TRABANT will start in HFR Petten in fall 1999.

References

/1/ High Plutonium Content Oxide Fuel for Pu Burning in Fast Reactors. CAPRA Irradiation Programme and First In-pile Experimental Results
E. Picard, J. Noirot, H. Plitz, R. Moss, G. Dassel, J. Rouault, A. Languille
Internat. Conf. On Future Nuclear Systems, GLOBAL '97, Oct. 5-10, 1997, Yokohama, Proc. pp 523-534.

32.23.05. Untersuchungen zu beschleunigergetriebenen, unterkritischen Anordnungen

I. Thermohydraulische Untersuchungen zur Auslegung des Kerns und des Spallationstargets einer ADS-Anordnung

(J.U. Knebel, X. Cheng, G. Janssens-Maenhout, K.J. Mack, H.J. Neitzel, IATF)

ABSTRACT

At the Forschungszentrum Karlsruhe GmbH a project study is performed in the framework of the Nuclear Safety Research Project (PSF) that investigates accelerator-driven subcritical reactor systems (ADS). The aim of this study is to critically evaluate the characteristics of a subcritical system, mainly concerning the potential of transmutation of minor actinides and long-lived fission products, to the feasibility and to safety aspects. The comparison with a critical system is done with respect to core design, neutronics, safety, system analyses, materials and corrosion.

Within this project study, this article describes the ADS design work and the supporting numerical and experimental efforts performed up to now at the former Institut für Angewandte Thermo- und Fluiddynamik, IATF (new name since April 1999: Institut für Kern- und Energietechnik, IKET). Finally, the KArlsruhe Lead LAboratory KALLA is introduced, the objectives of which are technological, thermal-hydraulic and corrosion investigations concerning the target module and the primary system of an ADS.

1. INTRODUCTION

An accelerator-driven subcritical reactor system (ADS) consists of three main parts: an accelerator for primary particles (protons), a target in which the protons produce free nucleons (neutrons) in a spallation reaction (external neutron source), and a subcritical blanket in which the fission reaction takes place, producing fission neutrons (internal neutron source) and thermal energy. The protons are infected into

the target through a vacuum beam pipe, the beam pipe being closed by a window at the end. The target is a heavy liquid metal (e.g. lead Pb or lead bismuth alloy Pb-Bi). The spallation neutrons produced in the target are completely independent of the subcritical blanket. A shut-down of the accelerator or an interruption of the proton beam immediately stops the fission reaction. Due to the subcriticality of the system advantages to safety are expected [1-2].

The main advantage of an ADS is its potential to transmute minor actinides and long-lived fission products, thus participating in closing the fuel cycle [3-6]. An ADS provides a powerful proton beam which produces a high number of neutrons, due to the spallation reaction in the heavy metal target. These neutrons are a good requirement for a transmutation machine.

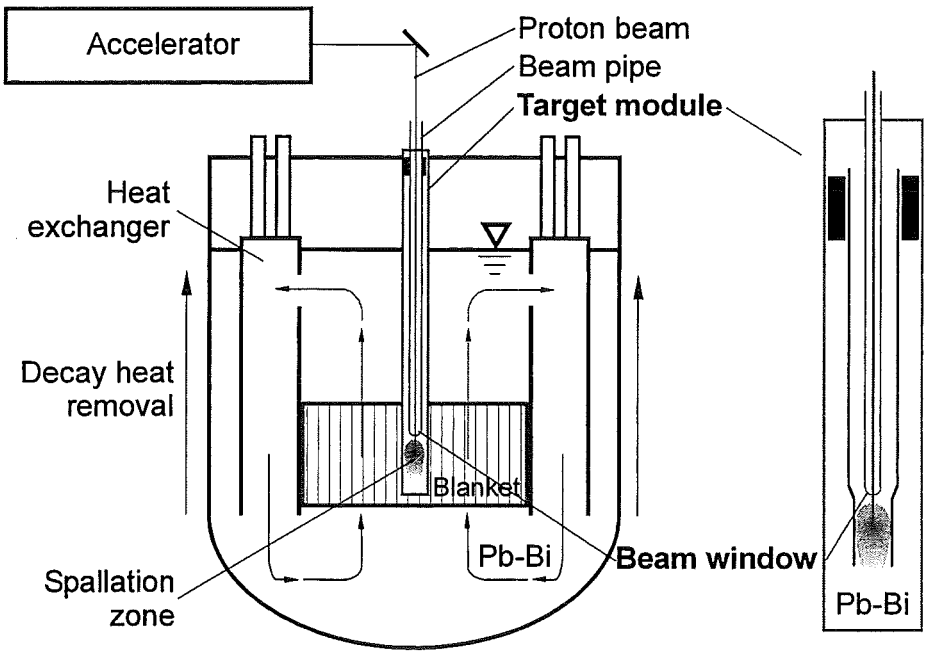

Figure 1: Sketch of an accelerator-driven subcritical reactor system (ADS).

Such a new reactor system involves the development of new technologies, e.g. a new reactor design using the heavy liquid metal Pb-Bi as spallation material and coolant, improved accelerators to drive the reactor, new fuel, new fuel fabrication and fuel reprocessing systems, new waste management arrangements [7].

2. FZK THREE-BEAMS CONCEPT

2.1 GENERAL DESIGN

The FZK three-beams concept for an ADS is associated with Professor Carlo Rubbia's conceptual design of an Energy Amplifier [4]. Some of the crucial problems of an ADS are an acceptable power distribution in the core and the design of the spallation target, mainly the heat removal from the window and the spallation zone. This holds for normal operation and for decay heat removal.

The FZK three-beams concept is a further development of Rubbia's conceptual design. Further general remarks on this multiple beam concept are discussed in [8]. The FZK concept considers a pool-type reactor with three separate spallation targets located in the mid region of the core. The coolant for the core is liquid lead. The fuel has a thorium based matrix with 10% U233. The spallation targets are closed modules, separated from the pool. Each target module has the cross-section of 7 fuel assemblies. The target material is liquid lead that, in addition, is used as coolant for the spallation region and for the beam window. The target module and the hemispherical beam window are similar to the design proposed in [9]. However, a perforated plate is introduced upstream of the beam window as described in [10]. The perforated plate introduces a flow resistance, forces the flow towards the window and leads to a better cooling of the window around the stagnation point where the highest temperatures are located. During normal operation both the core circuit and the target circuit are cooled by forced convection. In case of accident conditions the decay heat is removed by natural circulation inside the pool and natural circulation of air and radiation outside of the main vessel. In addition, immersion coolers for decay heat removal with an intermediate natural circulation circuit could be considered.

The nominal power is 1500 MWth. Each proton beam has a power of 4 MW, the proton energy being about 1 GeV and the beam current being about 4 mA, depending on the effective criticality factor. The general design characteristics together with the parameters of the core, the fuel elements and the fuel pins are summarised in Tab. 1.

Tab. 1: Main parameters of the FZK three-beams concept for an ADS.

General design:			
Pool type reactor		Separated target and core cooling	
1500 MW_{th} thermal power		Forced convection target & core cooling	
3 spallation targets: 4 MW (1GeV, 4mA)		Natural circulation decay heat removal	
Hemispherical beam window		Only one subassembly design	
Lead coolant for core and targets		Grid spacers	
Core configuration:		**Fuel element:**	
Number of fuel elements (6 hexagonal rounds)	106	Active core height	1500 mm
		Upper plenum height	900 mm
Number of breeder elements (2 hexagonal rounds)	90	Lower plenum height	900 mm
		Number of pins	397
Number of elements used by beam pipes	21 (3x7)	Pin diameter	8.2 mm
		Pitch	11.38 mm
Number of lead elements (1 hexagonal round)	54	Pitch / diameter	1.388
Coolant:		**Target module:**	
Fluid	liquid lead	Outer module diameter	0.6 m
Core inlet temperature	400°C	Outer beam pipe diameter	0.2 m
Core outlet temperature	550°C	Window diameter	0.2 m
Core heat-up	150 K	Perforated plate	option

2.2 REACTOR CORE DESIGN

Formfactor

The main objective of the FZK three-beams concept is to flatten the power distribution in the core and to allow for acceptable formfactors. This more complicated design has a positive consequence, e.g. the heat input into the window material can be reduced due to the power decrease of the proton beam. Thus, the cooling of the beam window for an ADS of 1500 MW_{th} becomes feasible. Similar results are found in the numerical simulation of the 1 MW spallation target of the ISTC 559 project [10]. By introducing an optimised perforated plate the maximum temperature increase in the stagnation point relative to the inlet temperature could be reduced by 559 K, the maximum temperature being 105 K above the inlet temperature.

In general, the power shape in a nuclear core is derived by the space dependent fission-rates, neutron flux times fission cross section. In an ADS that is far enough from criticality and that has one single neutron source in the core center, the neutron flux distribution has an exponential slope towards the neutron source [5]. The consequences of such a power distribution can be observed in the results of the IAEA ADS benchmark. The radial formfactors vary between 2.5 and 3.8 depending on the initial value for subcriticality, a detailed description is given in [11]. Such high formfactors are not acceptable for the practical operation of an ADS.

A much more favourable power density distribution is achieved with the FZK three-beams concept. In Fig. 2 the maximum specific heat is given versus the height for start-up and 250 days of operation, based on the parameters from Tab. 1. The maximum values are 405 W/cm and 442 W/cm, respectively. The radial formfactor is shown in Fig. 3. It has a nearly uniform value over the whole height. The overall formfactor for the FZK three-beams concept is 2.04 for start-up and 2.23 for 250 days of operation.

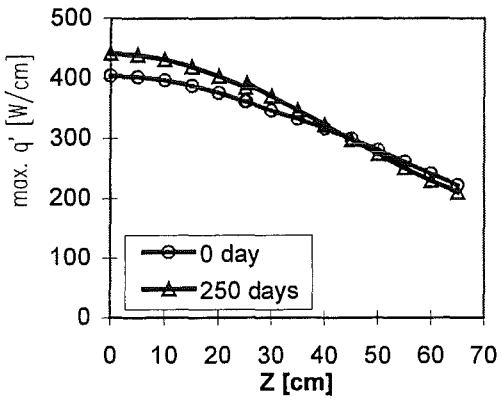

Figure 2: Max. specific heat vs height.

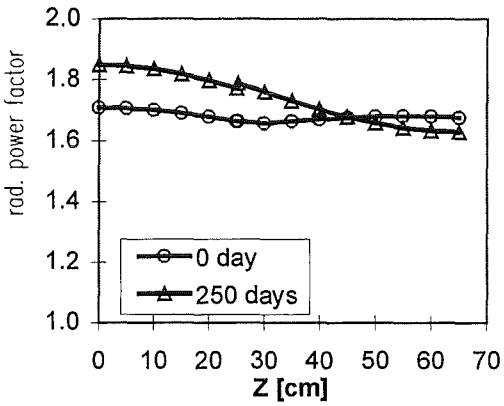

Figure 3: Radial formfactor vs height.

Design Criteria

By designing a reactor core attention has to be paid to keep the maximum temperatures of the fuel, the cladding and the coolant well below their limiting values, in order to avoid the melt-down of the fuel, corrosion failure and mechanical failure of the cladding material. Moreover, the pump capacity and the hydraulic performance of the system has to be taken into consideration. Figure 4 shows the design-relevant relationship between the maximum specific power (unit in W/cm) and the minimum

coolant velocity required. The curves are derived by using different design criteria. Relating to the design limitation of the coolant temperature $T_{f,max}$ or the cladding temperature $T_{ci,max}$, a nearly linear relationship between the specific power and the coolant velocity is obtained. An increase in the coolant velocity allows a higher specific power. At low velocity region, e.g. ≤ 3 m/s, the limitation of the coolant temperature or the cladding temperature plays a more important role than the limitation of the fuel temperature $T_{fu,max}$, whereas at high velocity region the maximum specific power is mainly restricted by the limitation of the fuel temperature.

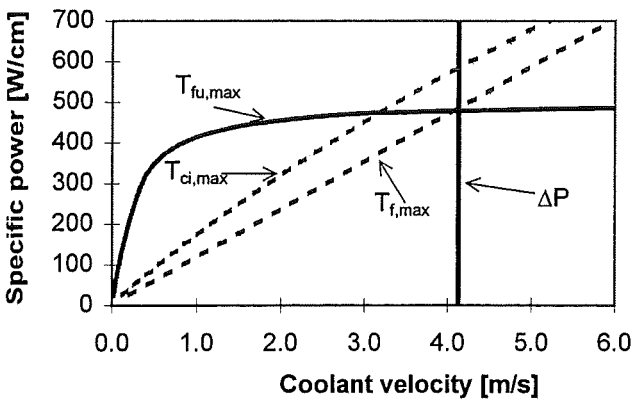

Figure 4: Design criteria:

$T_{fu,max}$ maximum temperature of the fuel (e.g. 2400°C),

$T_{ci,max}$ maximum temperature of the cladding (e.g. 650°C),

$T_{f,max}$ maximum temperature of the coolant (e.g. 550°C),

ΔP limitation of the pressure drop over the reactor core (e.g. 0.65 MPa).

Obviously, the higher the coolant velocity, the larger is the safety margin to the temperature limitations. However, the maximum coolant velocity is limited by the hydraulic performance of the pump.

Power Density Distribution

For the preliminary evaluation the lumped parameter approach has been applied to a critical subchannel. It is assumed that in the critical subchannel the maximum specific power, the maximum coolant temperature, the maximum cladding temperature and the maximum fuel temperature appears. An analysis with the lumped parameter approach has indicated that the temperature distribution of the coolant, the cladding and the fuel depends on the coolant velocity, the specific power, the geometric parameters and the thermal imbalance factor. The thermal imbalance factor is defined as the ratio of the heat input into the subchannel to the enthalpy gain of the coolant in the subchannel. Figure 5 shows the temperature

difference between the fuel rod center and the cladding outer surface versus the specific power (unit in W/cm). It is seen that at a specific power of 500 W/cm, a temperature difference of about 1800°C is obtained. Considering that the cladding outer surface temperature can be as high as 600°C, the fuel temperature will be 2400°C at a specific power of 500 W/cm. To have a sufficiently large safety margin to the fuel melting point, the maximum specific power should be kept below about 500 W/cm.

Figure 6 shows the power density distribution (unit in W/cm³) on the middle cross-section (z = 0) of the reactor core for the FZK three-beams concept. The neutronic results used are taken from [11]. The maximum power density is about 350 W/cm³ which corresponds to a maximum specific power of about 400 W/cm.

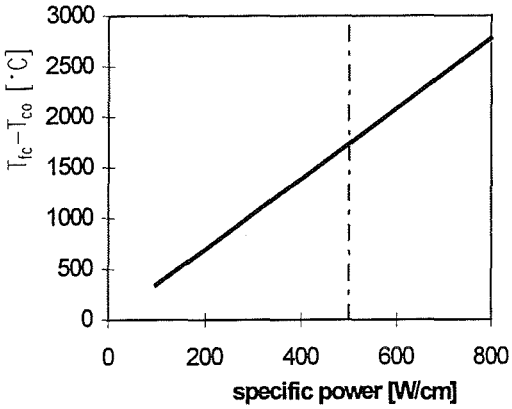

Figure 5: Temperature difference between the fuel center and the cladding outer surface.

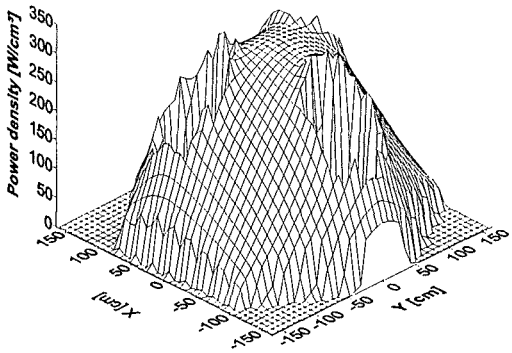

Figure 6: Power density distribution in the reactor core of the FZK three-beams concept.

Coolant and Cladding Temperature:

Figure 7 shows the maximum temperatures of the coolant and of the cladding versus the coolant velocity. The results are valid for a thermal imbalance factor of 1.0. It is seen that the coolant velocity has to be higher than 3 m/s, in order to guarantee a maximum cladding temperature below 650°C. A higher velocity, e.g. 4.0 m/s, is required to keep the coolant temperature on the subchannel outlet below 550°C. It has to be kept in mind that in a real case the thermal imbalance factor of the critical subchannel is larger than unity. This leads to a reduction in the coolant velocity required.

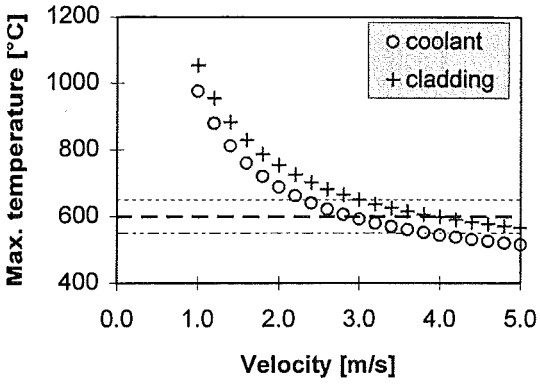

Figure 7: Maximum coolant and cladding temperatures vs coolant velocity.

Pressure Drop in Subchannels

The upper limit of the coolant velocity is determined by the pressure loss in the coolant circulation loop. Before the details of the circulation loop are well defined, the hydraulic analysis is restricted to the reactor core. Figure 8 presents the pressure drop in a subchannel, i.e. central subchannel, wall subchannel and corner subchannel, versus the coolant velocity. In this case the wall clearance is 1.5 mm. It is seen that the hydraulic resistance in the corner subchannel is about twice the hydraulic resistance in the central subchannel, and about 20% higher than in the wall subchannel. The coolant velocity in the corner subchannel will be about 10% lower than in the wall subchannel and about 40% lower than in the central subchannel. Moreover, the ratio of the heating perimeter to the flow area in a corner subchannel is about 6% higher than in a central subchannel. To avoid the occurance of the hot spot in corner subchannels, a larger wall clearance is necessary, e.g. 3.0 mm.

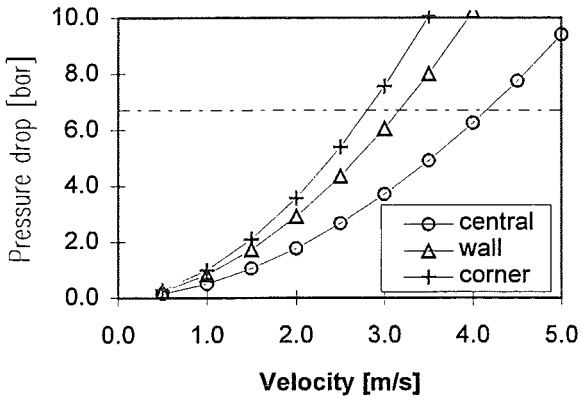

Figure 8: Pressure drop in subchannels vs coolant velocity.

2.3 REACTOR CORE COOLING BY NATURAL CIRCULATION

Reactor core cooling by natural circulation under normal operating condition has been proposed for some ADS concepts [5, 12]. In the following the feasibility of natural convection heat removal for the FZK three-beams concept is discussed. The buoyancy force in the convection loop is determined by

$$\Delta P_g = g \cdot h \cdot \Delta\rho \quad .$$

Here h is the convection height, defined as the elevation difference between the heat source and heat sink, $\Delta\rho$ is the density difference of coolant in the hot leg and the coolant in the cold leg. The density difference can be resulted by temperature difference, or by introducing fluids of different densities [12]. Introduction of a lighter fluid, e.g. gas, into the hot leg results in an increase of the buoyancy force and, thus, reduces the height of the convection system required. It simplifies the design of the reactor vessel. Nevertheless, an additional gas injection system leads to technical complexity which has to be investigated. In the present paper discussions are limited to systems without gas injection, i.e. buoyancy force results purely from thermal expansion of the coolant. Figure 9 shows the coolant velocity through the reactor core as a function of the convection height for two different values of pressure ratio. The pressure ratio is defined as the ratio of the pressure loss in the whole convection loop to the pressure loss over the reactor core. It is seen that at a convection height of 30 m and a pressure ratio of 1.5, the average coolant velocity in the reactor core is about 1.4 m/s, much smaller than the minimum velocity required for the FZK three-beams concept (fig. 4). For the FZK three-beams concept natural circulation is no technically feasible approach to remove the heat from the reactor core under normal operating conditions.

One possibility to allow heat removal by natural convection is to modify the design of the reactor core, e.g. by enlarging the fuel rod lattice. Figure 10 presents the average coolant velocity and the coolant temperature rise in the critical subchannel versus the pitch to diameter ratio. The maximum specific power is kept at 400 W/cm and the convection height is 30 m. It is seen that for tight lattices ($p/d \leq 1.35$) the coolant velocity decreases with decreasing the pitch to diameter ratio. In this region the effect of the hydraulic resistance dominates. For wide lattice ($p/d \geq 1.35$) coolant

velocity decreases with increasing the pitch to diameter ratio. A dominating effect of increasing flow area is obtained. A velocity maximum is obtained at a pitch to diameter ratio of about 1.35. This corresponds to a temperature rise of the coolant of about 500 K.

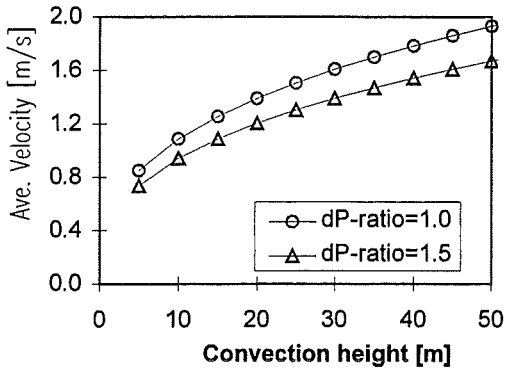

Figure 9: Coolant velocity in reactor core under natural convection conditions.

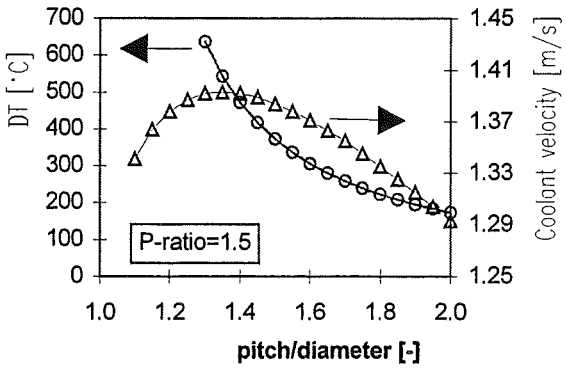

Figure 10: Coolant velocity and temperature rise under natural convection conditions, (400 W/cm, 30 m).

Figure 11 shows the effect of the pitch to diameter ratio on the convection height required. The specific power is kept unchanged at 400 W/cm. The pressure ratio is 1.5. It is seen that a pitch to diameter ratio larger than 1.8 is required to sufficiently remove the heat at a convection height of 30 m. For the FZK three-beams concept with a pitch to diameter ratio of 1.388, a convection height larger than 100 m would be needed.

Another way to avoid overheating in the reactor core under the natural convection condition is the reduction of the power density. This leads to a reduction of the total thermal power, when keeping the same geometricyl arrangement of the reactor core. Figure 12 shows the required convection height versus the thermal power for two different values of the pitch to diameter ratio. In both cases the fuel rod diameter is 8.2 mm. The pitches are 11.38 mm and 12.43 mm, respectively. At a convection height of 10 m, about 250 MW of thermal power can be removed by natural convection from the core with the pitch to diameter ratio 1.388, the reference value for the FZK three-beams concept. Therefore, natural convection will be a promising approach for decay heat removal.

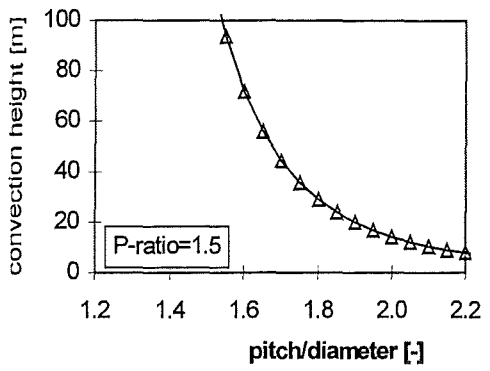

Figure 11: Convection height vs pitch to diameter ratio under natural convection conditions, (400 W/cm).

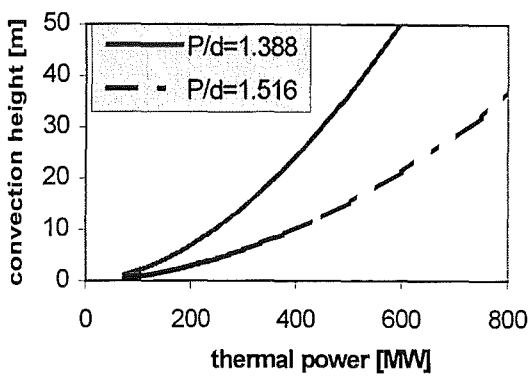

Figure 12: Convection height vs removable thermal power under natural circulation conditions, (400 W/cm).

3. SPALLATION TARGET

3.1 GENERAL DESIGN

One of the crucial problems of any ADS system is the design of the target module, mainly the heat removal from the window and the spallation zone. This holds for normal operation and for decay heat removal.

In the FZK three-beams concept the power of the proton beam of each spallation target is reduced to about 4 MW, one third of the single beam design proposed by C. Rubbia [5]. This reduces the thermal load of the beam window significantly, the challenge of beam window cooling and irradiation damage can be solved more easily, [13]. The target design is now underway: the FZK three-beams concept is similar to that of the EA-concept [14], as shown in fig. 13. The main dimensions of the target are summarized in Tab. 2.

Liquid lead or lead-bismuth eutectic is used as coolant. At the present stage it is not yet decided, whether the heat is removed by natural convection or by forced convection. The study is carried out both for natural and for forced convection. Under natural convection conditions a sufficiently large convection height should be chosen to achieve a high coolant flow rate and subsequently, to provide a safe heat removal from the spallation volume and from the beam window.

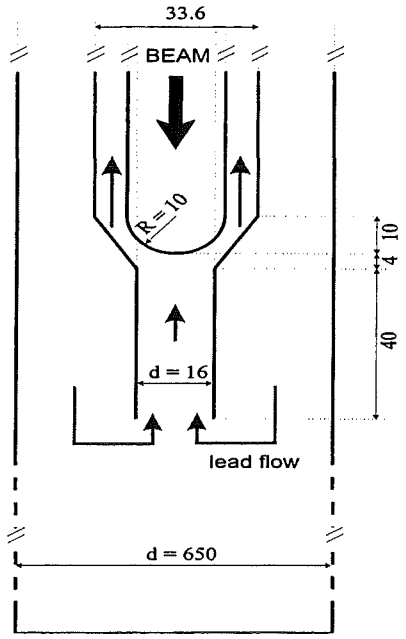

Figure 13: Spallation target design, unit in cm

Tab. 2: Main spallation target dimensions.

proton energy:	≈ 1 GeV
beam current:	≈ 4 mA
beam power:	≈ 4 MW
beam diameter:	15 cm
window diameter:	20 cm
window material:	steel
target material/coolant:	Pb or Pb-Bi
coolant circulation:	natural or forced convection
window thickness:	1.5 - 3.0 mm

For these calculations a pressure ratio of 6.7 is assumed. The pressure ratio is defined as the ratio of the pressure loss in the whole target loop to the pressure loss over the heat exchanger. Figure 14 shows the relationship between the coolant flow rate and the convection height. At a convection height of 10 m, a volume flow rate of about 70m³/h is obtained. Increasing the convection height to 20 m leads to an increase in the coolant flow rate of about 30%. Figure 15 shows the window excess temperature as a function of the coolant flow rate. The window excess temperature is defined as the difference between the window outer surface temperature and the coolant temperature at the spallation volume inlet. The results are obtained for a volume flow rate of 70 m³/h. A hot spot at the window center (stagnation point) is observed. The maximum temperature rise is as high as 320 K. The maximum temperature rise as a function of the coolant flow rate is presented in Fig. 16. Under natural convection conditions the coolant flow rate is lower than 100 m³/h, even with a convection height of 20 m. Therefore, forced convection is a more promising approach to keep the maximum temperature rise of the window as low as required, e.g. below 200 K.

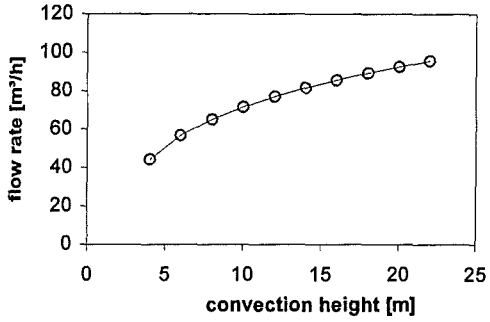

Figure 14: Coolant flow rate in the target vs convection height under natural convection conditions.

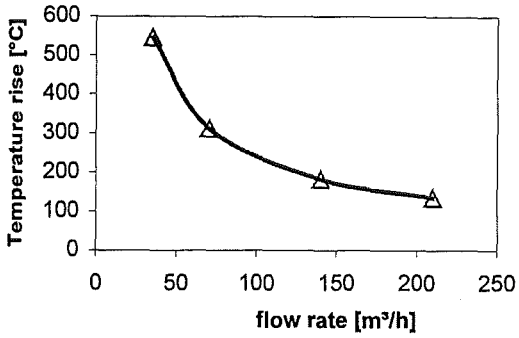

Figure 16: Maximum temperature rise in the window center (stagnation point) vs coolant flow rate.

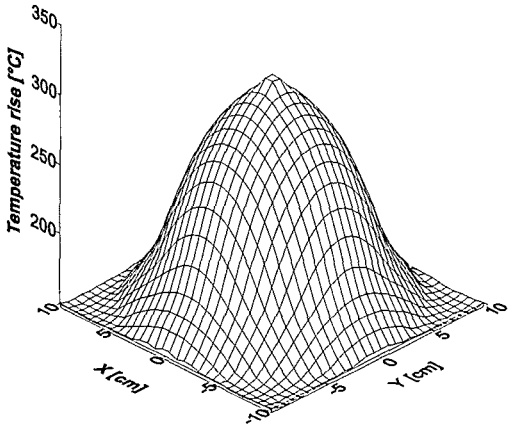

Figure 15: Excess temperature distribution on beam window outer surface, (flow rate 70 m³/h).

3.2 SIMULATION EXPERIMENTS

Parallel to the numerical investigations scaled water experiments are performed at IKE that simulate the hydraulic behaviour of a spallation target. Figure 17 shows the two-dimensional model of the improved FZK design of the ISTC 559 target module, developped in cooperation with IPPE Obninsk, [15]. The main purpose of these two-dimensional experiments is to gain an insight into the flow behaviour close to the window. The test section consists mainly of two flow channels (inner and outer channel) and the cylindrical head which simulates the beam window of the target. In some experiments a perforated plate (cf. Tab. 1) is placed close to the cylindrical head.

Experiments are performed for upward and downward flow and for different volume flow rates.The flow is visualised using the laser light sheet technique. Particles of diameter 0.5 mm are added to the flow. The flow field is recorded either by video

camera or by CCD camera. Figure 18 shows one example of the flow pattern around the cylindrical head recorded by the CCD camera. In this case, the water flows upward in the inner channel at a flow rate of 5 m^3/h. As expected, a stagnation point is observed when approaching the cylindrical head on the centerline. Figure 19 shows the flow pattern around the cylindrical head for the same volume flow rate (5 m^3/h), however for downward flow. The flow pattern is totally different from that of the upward flow: In the inner flow channel the fluid flows downwards near the wall and upwards in the center. A strong flow recirculation is observed downstream of the cylindrical head which reduces the heat transfer from the window and, therefore, has to be eliminated in a prototypical geometry.

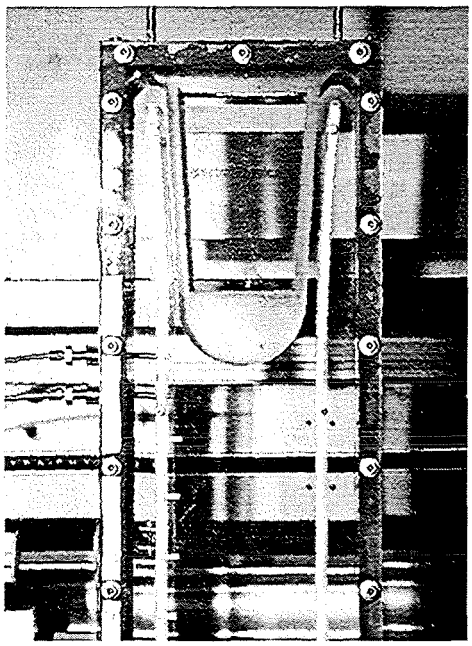

Figure 17: Two-dimensional model of the ISTC 559 target module, (improved FZK design).

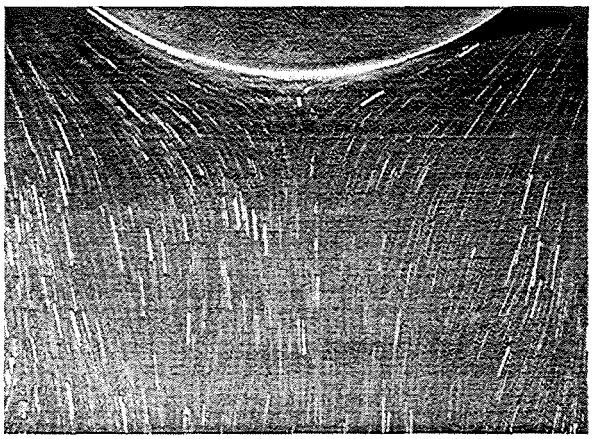

Figure 18: Flow pattern at upward flow condition, (Laser light sheet).

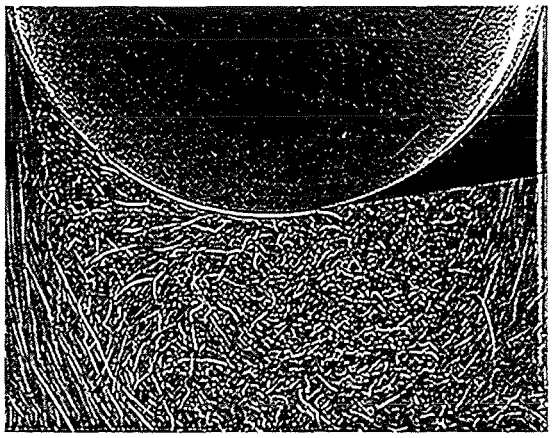

Figure 19: Flow pattern at downward flow condition, (Laser light sheet).

3.3 BENCHMARK EXERCISE

On the basis of the numerical considerations from chapter 3.1 and the experimental results from chapter 3.2, a first detailed geometrical design of a 4 MW_{th} spallation target for the FZK three-beams concept has been put up, see. Fig. 20. This design is currently discussed within the HLMTH Working Group, [16], as a possible pre-test numerical benchmark exercise. After the water experiments are completed, this design will be investigated in KALLA (cf. Chapter 4.) using Pb-Bi as working fluid.

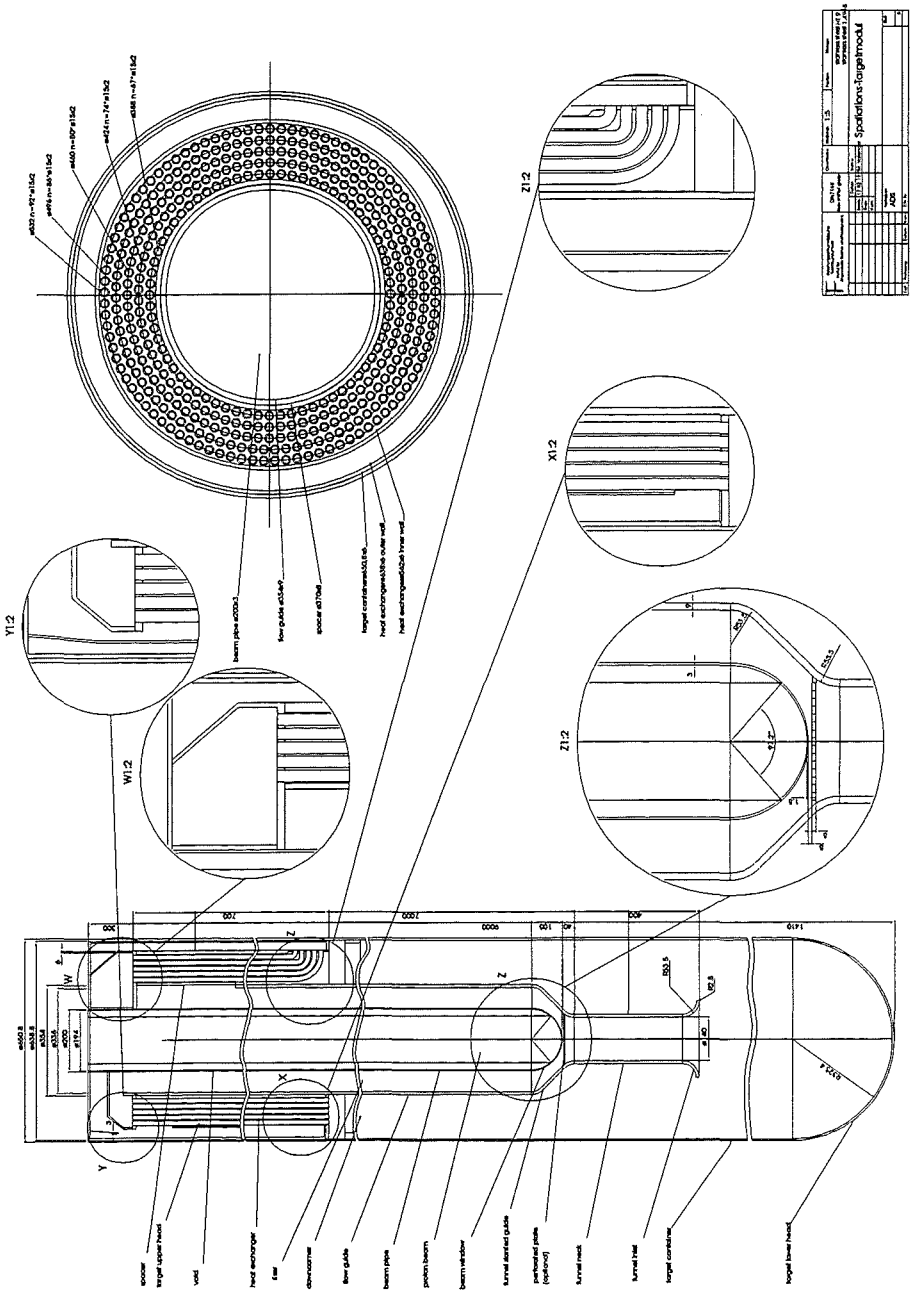

Figure 20: Spallation target module for the FZK three-beams concept.

4. KARLSRUHE LEAD LABORATORY KALLA

Currently, at the Forschungszentrum Karlsruhe the KArlsruhe Lead LAboratory KALLA is being planned and constructed. KALLA comprises three different experimental loops, each emphasizing on different specific objectives, briefly summarised in Tab. 3 together with the main data.

The *Technology Loop* concentrates on the establishment of an oxygen measurement and control technique, the most important prerequisite to safely operate a Pb or Pb-Bi loop, [17]. Measurement techniques are adapted to or specially developed for Pb and Pb-Bi. In addition, basic heat transfer experiments will be performed.

The *Thermalhydraulic Loop*, first, is designed for single-effect investigations of the thermally high-loaded beam window and the heat removal from a complete closed target module. Furtheron, detailed experiments can be done for a fuel element and a steam generator. Second, integral real-height investigations into the core heat removal and the decay heat removal from the pool can be performed.

The *Corrosion Loop* allows for fundamental investigations of corrosion mechanisms, the formation and the stability of protection layers and the performance of mechanical tests. The final aim is the development of available low-activation steels and structural materials.

Table 3: The KArlsruhe Lead LAboratory KALLA.

Technology Loop	**Thermalhydraulic Loop**	**Corrosion Loop**
	Investigations:	
Oxygen measurement Oxygen control Measurement techniques Heat transfer High-performance heaters	*Single-effect investigations:* Beam window Closed Target module Fuel element Steam generator Heat exchanger *Integral investigations:* Core heat removal Decay heat removal	Corrosion mechanisms Protection layers Mechanical tests
Fluid volume: 0.1 m^3 Temperature: max 550°C Flow rate: max 5 m^3/h	Fluid volume: 0.5 - 4.0 m^3 Temperatur: max 550°C Power: 0.3 - 4.0 MW Flow rate: max 100 m^3/h	Fluid volume: 0.03 m^3 Temperature: max 550°C Flow rate: max 3.5 m^3/h

5. MAIN PROGRESS

The article gives an overview of the 1998 work performed at Institut für Kern- und Energietechnik (IKE) that is related to an accelerator driven system (ADS), especially focussing on

- ADS design work: reactor core design and spallation target design for the FZK three-beams concept, comparison with a single-beam concept;
- Numerical efforts: reactor core: formfactors, power density distribution, coolant and cladding temperatures, pressure drops in subchannels; spallation target: beam window temperature, flow field;
- Experimental efforts: scaled water experiments, flow visualisation;
- KALLA: KArlsruhe Lead LAboratory designed for technological, thermal-hydraulic and corrosion investigations.

6. FUTURE ACTIVITIES

- Qualitative and quantitative water experiments (2D and 3D geometry) to investigate hydraulic and thermal-hydraulic behaviour of a beam window and a spallation target;
- Numerical calculation of all water experiments using CFD-codes, such as CFX and FIDAP;
- Construction of KALLA within the HGF-Strategy Fund Project;
- Taking in operation of the Technology Loop of KALLA, installation and calibration of an oxygen control system;
- Numerical design of a spallation target module for the FZK three-beams concept using CFD-codes, such as CFX and FLUTAN;
- Design of a Pb-Bi Pilot Target (MEGAPIE) to be tested in SINQ at PSI Switzerland under full load conditions; the work is performed in cooperation with CEA France and PSI Switzerland.

7. REFERENCES

[1] H. Wider
Safety of acclerator-driven nuclear waste burners
Proc. of the Jahrestagung Kerntechnik'98, May 1998, München, pp217-220

[2] W. Maschek, D. Thiem, G. Heusener
Safety assessment of a reactor core dedicated to burn minor actinides
Proc. of the Jahrestagung Kerntechnik'99, May 1999, Karlsruhe, pp.635-638

[3] G. Heusener, M. Salvatores
Use of heavy liquid metal: A perspective for critical/subcritical fast neutron concepts
HLMC'98, 5-9 October 1998, Obninsk, Russia

[4] Carminati, F., Klapisch, R., Revol, J.P., Roche, Ch., Rubio, J.A., Rubbia, C.,
An Energy Amplifier For Cleaner and Inexhaustible Nuclear Energy Production Driven by a Particle Beam Accelerator
CERN/AT/93-47 (ET), November 1, 1993

[5] C. Rubbia, Rubio, J.A., Buono, S., Carminati, F., Fiétier, F., Galvez, J., Gelès, C., Kadi, Y., Klapisch, R., Mandrillon, P., Revol, J.P., Roche, Ch.
Conceptual design of a fast neutron operated high power energy emplifier
CERN/AT/95-44(ET), September 1995

[6] T. Takizuka, et al.
Heavy liquid-metal cooling option of JAERI accelerator-driven transmutation systems
HLMC'98, 5-9 October 1998, Obninsk, Russia

[7] Pooley, D.
Opinion of the Scientific and Technical Committee (STC) on a nuclear energy amplifier, nuclear science and technology
European Commission, EUR 17616 EN, 1997

[8] Broeders, C.H.M.
Neutron Physics ADS Investigations at Forschungszentrum Karlsruhe
Proceedings of the International Workshop on Physics of Accelerator Driven Systems for Nuclear Transmutation and Clean Energy Production, Trento, September 29 - October 3, 1997

[9] Buono, S., Rubbia, C.
Preliminary Design of a Molten Lead Convection Driven Standalone Beam Target for the Energy Amplifier
CERN/ET Internal Note 96-023, October 17, 1996

[10] Knebel, J.U., Cheng, X.
Some Ideas on Liquid Metal Targets For Neutron Spallation Sources,
Jahrestagung Kerntechnk 1998, München, pp. 677-680, 1998

[11] Broeders, C.H.M.
A Comparison of Some Neutronics Characteristics of Critical Reactors and Accelerator Driven Subcritical Systems
5th Intern. Inf. Meeting on Actinide and Fission Product Partitioning and Transmutation, Mol Belgium, Nov. 25-27, 1998

[12] L. Cinotti
ADS_DEMO Overview: Motivation for a large test pool facility
Proceedings of Workshop on HLM Thermal-Hydraulics, ENEA Centre of Brasimone, April 12-13, 1999

[13] Cheng, X., Knebel, J.U.
Numerical Investigation on an ADS Target Module and the Primary Circuit of a Pool Type ADS system Using CFX and FLUTAN
Proceedings of Workshop on HLM Thermal-Hydraulics, ENEA Centre of Brasimone, April 12-13, 1999

[14] S. Buono, C. Rubbia
A comparison of different materials for the beam window of the energy amplifier
CERN/ET/Internal Note 96-26, August 1996

[15] Knebel, J.U., Cheng, X., Neitzel, H.J.
Untersuchungen zu beschleunigergetriebenen, unterkritischen Anordnungen
In: Projekt Nukleare Sicherheitsforschung Jahresbericht 1997, Wissenschaftliche Berichte FZKA 6126, pp. 562-568, 1998

[16] J.U. Knebel, X. Cheng, C. Broeders, H. Glasbrenner, J. Konys, K.-J. Mack, G. Müller, H.-J. Neitzel, G. Schumacher
Investigations at KALLA for an ADS System: Ongoing and Planned Experiments
Proceedings of Workshop on HLM Thermal-Hydraulics, ENEA Centre of Brasimone, April 12-13, 1999

[17] Knebel, J.U., Müller, G., Schumacher, G.
Gas-Phase Oxygen Control Processes for Lead/Bismuth Loops and Accelerator Driven Systems
Jahrestagung Kerntechnik 1999, Karlsruhe, pp.645-650, 1999

II. HGF-Strategiefonds-Projekt: Thermohydraulische und material-spezifische Untersuchungen zur Realisierung einer beschleunigergetriebenen Anordnung (ADS) zur Transmutation von Aktiniden

(J.U. Knebel, X. Cheng, G. Janssens-Maenhout, K.J. Mack, H. Neitzel, IATF; J. Konys, H. Glasbrenner, IMF III; G. Grötzbach, L.N. Carteciano, IRS; G. Müller, G. Schumacher, INR)

KURZFASSUNG

Im Berichtszeitraum wurde ein HGF-Strategiefonds-Projekt mit dem Kurztitel "Blei-Versuchskreislauf" ausgearbeitet, das von der Hermann von Helmholtz-Gemeinschaft Deutscher Forschungszentren (HGF) in der Sektion "Energieforschung und Energietechnologie" über eine Laufzeit von 1999-2002 mit einem Finanzvolumen von 7.0 Millionen DM (35 Personenjahre) gefördert wird.

Ziel des HGF-Strategiefonds-Projektes ist es, neue Methoden und Technologien zur Auslegung und Herstellung thermisch hochbelasteter Oberflächen, die von einem korrosiven schweren Flüssigmetall (eutektisches Blei-Wismut) gekühlt werden, zu entwickeln.

Das Ergebnis dieses Projektes ist ein wissenschaftlich-technisches Instrumentarium, um zunächst das Konzept und später die detaillierte Auslegung einer europäischen Demonstrationsanlage einer ADS-Anordnung zu ermöglichen. Die Arbeiten am Forschungszentrum Karlsruhe sind in ein breites europäisches Forschungs- und Entwicklungsprogramm zu beschleunigergetriebenen Anordnungen (ADS) eingebunden.

Das Projekt gliedert sich in drei Teilprojekte:

Teilprojekt 1: Thermohydraulische Untersuchungen,

Teilprojekt 2: Materialspezifische Untersuchungen,

Teilprojekt 3: Sauerstoffkontrolle.

HGF-STRATEGY FUND PROJECT: THERMAL-HYDRAULIC AND MATERIAL SPECIFIC INVESTIGATIONS INTO THE REALISATION OF AN ACCELERATOR-DRIVEN SYSTEM (ADS) TO TRANSMUTE ACTINIDES

ABSTRACT

During the last year a HGF-Strategy Fund Project entitled "Lead Loop" was worked out which is now funded by the Hermann von Helmholtz-Gemeinschaft Deutscher Forschungszentren (HGF) in the section "Energy Research and Energy Technology" over a time period from 1999 to 2002 with a financial support of 7.0 Million DM (35 man years).

The objectives of the HGF-Strategy Fund Project is the development of new methods and technologies to design and manufacture thermally highly-loaded surfaces which are cooled by a corrosive heavy liquid metal (lead-bismuth eutectic).

The results of this project is the basic scientific-technical tool which allows the conception and the design of a European Demonstrator of an ADS system. The work performed at Forschungszentrum Karlsruhe is embedded in a broad European research and development programme on ADS systems.

The project is divided in three sub-projects:

Sub-Project 1: Thermalhydraulic Investigations,

Sub-Project 2: Material specific Investigations,

Sub-Project 3: Oxygen control.

1. FORSCHUNGSPROGRAMM

1.1 KONKRETE ZIELE DES HGF-STRATEGIEFONDS-PROJEKTES

Ziel des Projektes ist es, neue Methoden und Technologien zur Auslegung und Herstellung thermisch hochbelasteter Oberflächen, die von einem korrosiven schweren Flüssigmetall (eutektisches Blei-Wismut) gekühlt werden, zu entwickeln. Die Vorgehensweise ist in drei Teilprojekte unterteilt:

Teilprojekt 1: Im Bereich der *Thermohydraulik* werden für das Fluid Blei-Wismut physikalische Gesetzmäßigkeiten zum konduktiven und konvektiven Wärmeübergang für die turbulente Umströmung einer thermisch hochbelasteten Oberfläche entwickelt und ein für Blei-Wismut validiertes thermohydraulisches Rechenprogramm zur Verfügung gestellt.

Teilprojekt 2: Im Bereich der *Materialforschung* werden physikalische Methoden zur Beschreibung der Korrosionsmechanismen und zur Lösung der Korrosionsproblematik für potentielle Struktur- und Fensterwerkstoffe, mit und ohne Schutzschichten, in flüssigem Blei-Wismut entwickelt.

Teilprojekt 3: Im Bereich der *Reaktionskinetik* wird auf der Basis von physikalisch / chemischen Überlegungen ein Verfahren zur Messung und Regelung des Sauerstoffpotentials in Blei-Wismut und somit zur Kontrolle der Korrosion der eingesetzten Werkstoffe entwickelt.

Die Strategie bei der Bearbeitung der drei Teilprojekte basiert sowohl auf einem theoretischen / numerischen Ansatz als auch auf einem experimentellen Ansatz.
Eine Betrachtung des komplexen Gesamtsystems unter Berücksichtigung von reaktionskinetisch kontrollierten und materialspezifisch definierten Randbedingungen erfolgte für eine thermohydraulische Fragestellung im Bereich der Wärmeübertragung an korrodierten Oberflächen und des Wärmetransports in Blei-Wismut bisher nur unzureichend.
Die Zusammenfassung der Ergebnisse der drei Teilprojekte bildet die Methode und die Technologie für die Realisierung von kritischen, systembestimmenden Einzelbauteilen einer beschleunigergetriebenen Anordnung (ADS), wie zum Beispiel

das Strahlfenster und das Targetmodul. Die sichere Auslegung dieser Bauteile hinsichtlich Wärmeabfuhr, Materialauswahl und Korrosionskontrolle ist eine Grundvoraussetzung für die integrale Funktionalität einer ADS-Anordnung.
Die in diesem Projekt erarbeiteten Methoden und Technologien werden in regelmäßig stattfindenden Arbeitsgruppen mit den in die Untersuchungen eingebundenen europäischen Partnern diskutiert und abgestimmt. Die wichtigsten Partner sind CEA und CNRS Frankreich, PSI Schweiz, ENEA und ANSALDO Italien, CIEMAT und LAESA Spanien, IPPE und PROMETEY Russland.

1.2 LÄNGERFRISTIGE UND STRATEGISCHE ZIELE

Das übergeordnete, längerfristige Ziel des Projektes ist es, mit den neuen Methoden und Technologien ein wissenschaftlich-technisches Instrumentarium zur Verfügung zu stellen, um zunächst das Konzept und später die detaillierte Auslegung einer europäischen Demonstrationsanlage einer ADS-Anordnung zu ermöglichen. Das Instrumentarium umfasst eine thermohydraulische und materialspezifische Datenbasis aus grundlegenden und anwendungsspezifischen Experimenten, ein für Blei-Wismut validiertes thermohydraulisches Rechenprogramm, eine Identifikation von Fenster- und Strukturmaterialien, Vorschriften zur Korrosionskontrolle und Werkstoffkonditionierung und zur Sauerstoffkontrolle in Blei-Wismut-Kreisläufen.
Die Demonstrationsanlage mit einer thermischen Leistung von etwa 100 MW_{th} ist ein Hauptmeilenstein zur langfristigen Realisierung einer prototypischen ADS-Anordnung mit einer thermischen Leistung von etwa 1500 MW_{th}.

Eine ADS-Anordnung besteht aus drei Hauptkomponenten: einem Beschleuniger für Protonen, einem Target, in welchem die Protonen in einer Spallationsreaktion Neutronen erzeugen (externe Neutronenquelle) und einem unterkritischen Blanket, in dem die Spaltungsreaktion unter Freisetzung von Spaltungsneutronen (interne Neutronenquelle) und von Wärme stattfindet. Die Protonen werden durch ein evakuiertes Strahlrohr, das im Allgemeinen am Ende durch ein Strahlfenster abgeschlossen ist, in das Target eingebracht. Das Target besteht aus einem schweren Flüssigmetall, zum Beispiel Blei oder eutektisches Blei-Wismut. Die im

Target erzeugten Spallationsneutronen sind unabhängig vom unterkritischen Blanket. Eine Unterbrechung des Protonenstrahls führt zu einer Unterbrechung der Spaltungsreaktion im Blanket. Aufgrund der Unterkritikalität des Blankets werden Vorteile hinsichtlich des Sicherheitsverhaltens erwartet. Eine schematische Darstellung einer ADS-Anordnung gibt Abb. 1.

Die strategische Zielsetzung einer ADS-Anordnung ist die Transmutation von langlebigem, radioaktivem Abfall und somit die Schließung des Brennstoffkreislaufs. Der in einer ADS-Anordnung verwertbare radioaktive Abfall unterteilt sich in zwei Gruppen: Die minoren Aktiniden wie zum Beispiel Neptunium, Americium und Curium und einige langlebige Spaltprodukte wie zum Beispiel Technetium 99 und Jod 129. Letztere könnten langfristig in die Biosphäre diffundieren und dort selektiv von Organismen aufgenommen werden.
Die ADS-Anordnung ist eine natürliche Ergänzung zu dem bestehenden Park an Leichtwasserreaktoren. Der Einsatz von ADS-Anordnungen verringert die Menge und die Radiotoxizität an radioaktivem Abfall, der in Endlager eingebracht werden muss.

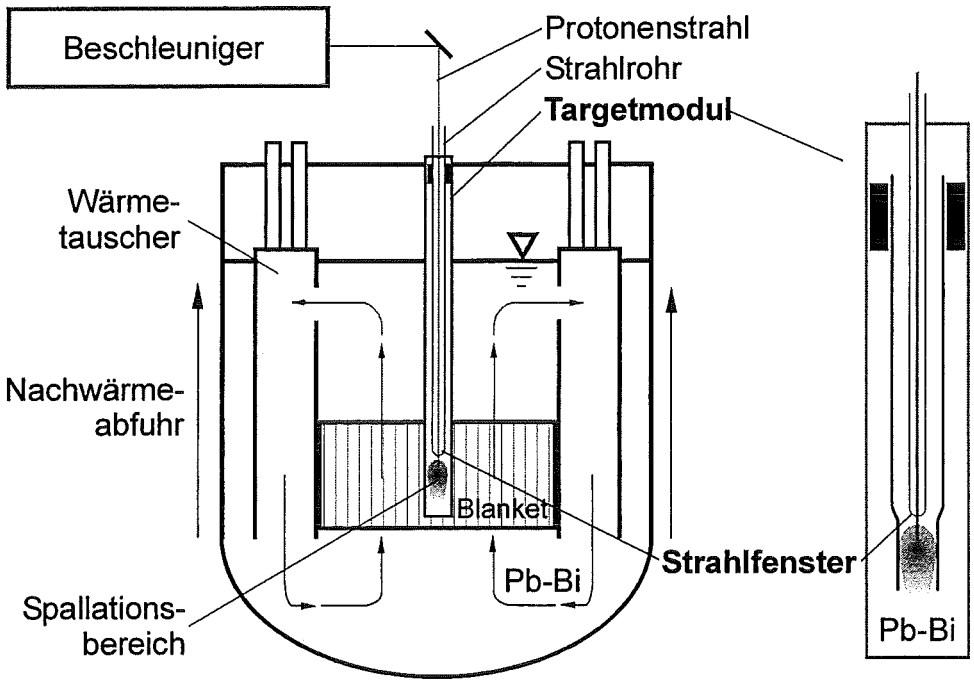

Abb. 1: Schematische Darstellung einer ADS-Anordnung.

1.3 WISSENSCHAFTLICHES VORGEHEN

Das wissenschaftliche Vorgehen des Projektes orientiert sich an drei kritischen, technischen Fragestellungen einer ADS-Anordnung, die weitere detaillierte Forschungs- und Entwicklungsaufgaben erfordern und deren Lösung eine Grundvoraussetzung für den erfolgreichen Betrieb einer ADS-Anordnung darstellen. Die drei Fragestellungen werden schwerpunktmäßig in folgenden Teilprojekten TP behandelt:

- TP1: Thermohydraulische Untersuchungen an thermisch hochbelasteten Flächen (Strahlfenster und Targetmodul) mit Blei-Wismut als Kühlmittel,
- TP2: Untersuchungen zur Korrosion und Verfahren zur Konditionierung metallischer Werkstoffe in Blei-Wismut,
- TP3: Sauerstoffmessung und Sauerstoffregelung in Blei-Wismut.

Die drei Teilprojekte ergänzen sich gegenseitig durch methodische Erkenntnisse und den Transfer erarbeiteter Technologie. Der unter industriellen und genehmigungstechnischen Gesichtspunkten geforderte sichere und langfristige Betrieb einer ADS-Anordnung setzt drei Punkte voraus: Beherrschung und Kontrolle der Korrosion der eingesetzten Materialien, Kenntnis der Thermohydraulik der Gesamtanordnung und Beschreibung der Wechselwirkung zwischen Korrosion und Thermohydraulik durch zum Beispiel über die Zeit veränderte Oberflächeneigenschaften und somit verändertem Wärmeübergang.

Die in den drei Teilprojekten ausgewählten Fragestellungen gehören zu den international wissenschaftlich sehr aktuellen Themen, für die es derzeit jedoch keine technisch etablierten und anwendbaren Lösungen gibt. Durch die Schwerpunktsetzung in den drei Teilprojekten wird dem Anliegen der HGF entsprochen, langfristig innovative Forschungsstrategien mit vorhandenem Forschungspotential zu verbinden und dieses zu einer neuen Qualitätsstufe auszubauen. Die Methoden zur Lösung werden mit den internationalen Partnern entwickelt und ausgetauscht. Ein wichtiger Partner ist dabei Russland, das große, bisher schwer zugängliche technologische Erfahrung im Umgang mit flüssigem Blei-Wismut besitzt.

Die Vorgehensweise des Projektes zum Erreichen des Forschungszieles ist in Abb. 2 dargestellt.

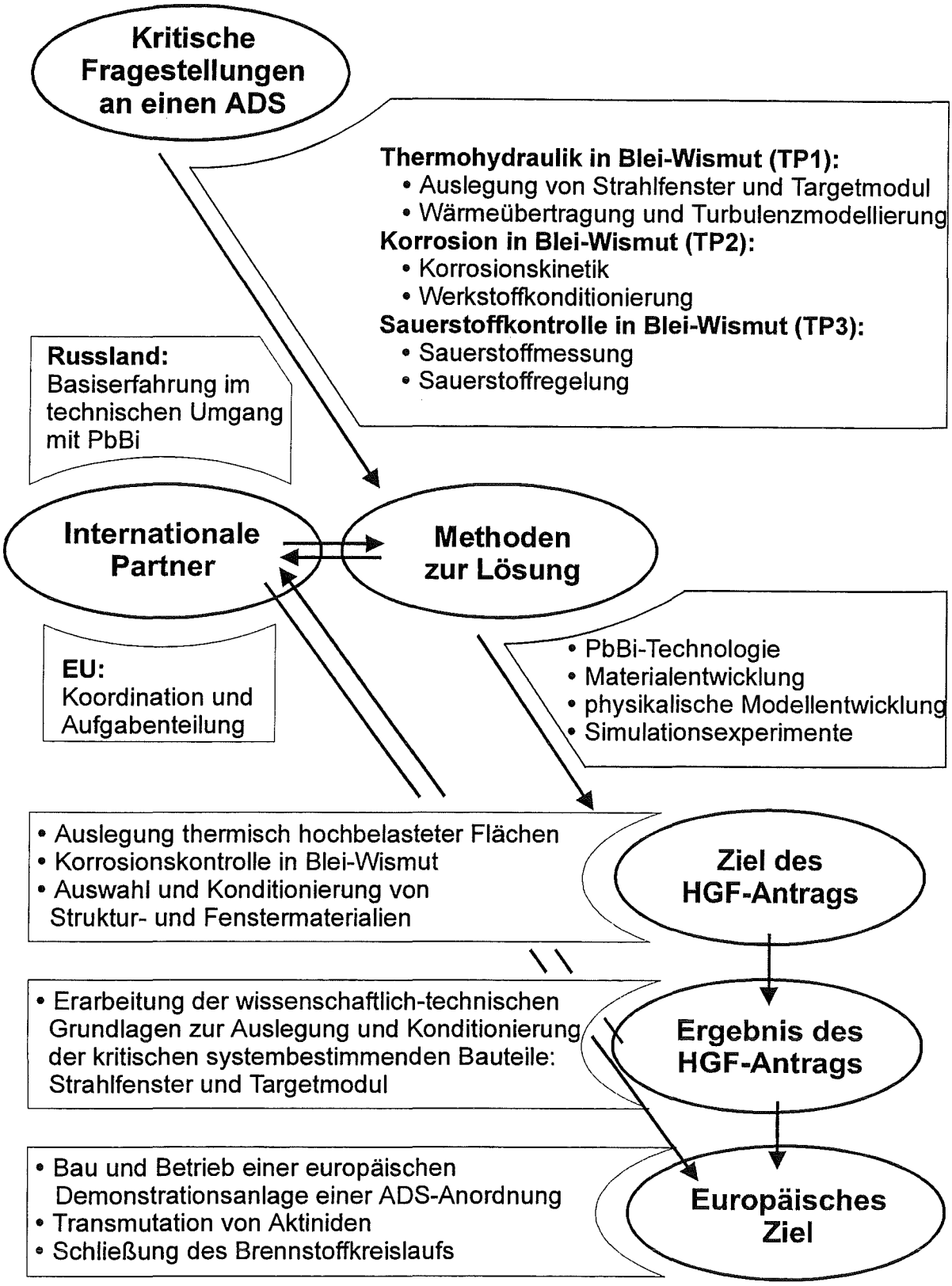

Abb. 2: Vorgehensweise des Projektes zum Erreichen des Forschungszieles.

2. WISSENSCHAFTLICHES DARSTELLUNG DES HGF-PROJEKTES

Der Projektstrukturplan (Abb. 3) zeigt schematisch die Gliederung des Projektes in die drei Teilprojekte. Die Teilprojekte sind in theoretische (physikalische Modellentwicklung und Simulationsrechnungen) und experimentelle Arbeitspakete unterteilt. Die für den Projektantrag relevanten Vorarbeiten, die am Forschungszentrum Karlsruhe oder durch andere Forschungseinrichtungen geleistet sind, werden im Projektstrukturplan ebenfalls dargestellt.

2.1 THERMOHYDRAULISCHE UNTERSUCHUNGEN (TEILPROJEKT 1)

Das Forschungsziel ist die Auslegung, die Fertigung und der Betrieb eines festen Strahlfensters, die Erstellung einer detaillierten thermohydraulischen Datenbasis, die Entwicklung physikalischer Modelle zur Beschreibung des Wärmeübergangs an thermisch hochbelasteten Oberflächen (Strahlfenster) und die Entwicklung eines validierten CFD-Rechenprogramms zur Strömungssimulation. Abschließend erfolgt die Auslegung eines geschlossenen Targetmoduls mit dem CFD-Rechenprogramm.
Im Rahmen des Teilprojekts 1 werden drei, aufeinander aufbauende Arbeitspakete abgearbeitet.

(AP1.) Auslegung eines Strahlfensters aufbauend auf Simulationsrechnungen und Modellexperimenten mit Modellfluid Wasser

(AP2.) Grundlegende Experimente in flüssigem Pb-Bi zur Wärmeübertragung und Modellentwicklung/Modellvalidierung

(AP3.) Simulationsexperiment zum optimierten Strahlfenster mit Fluid Blei-Wismut und Simulationsrechnung

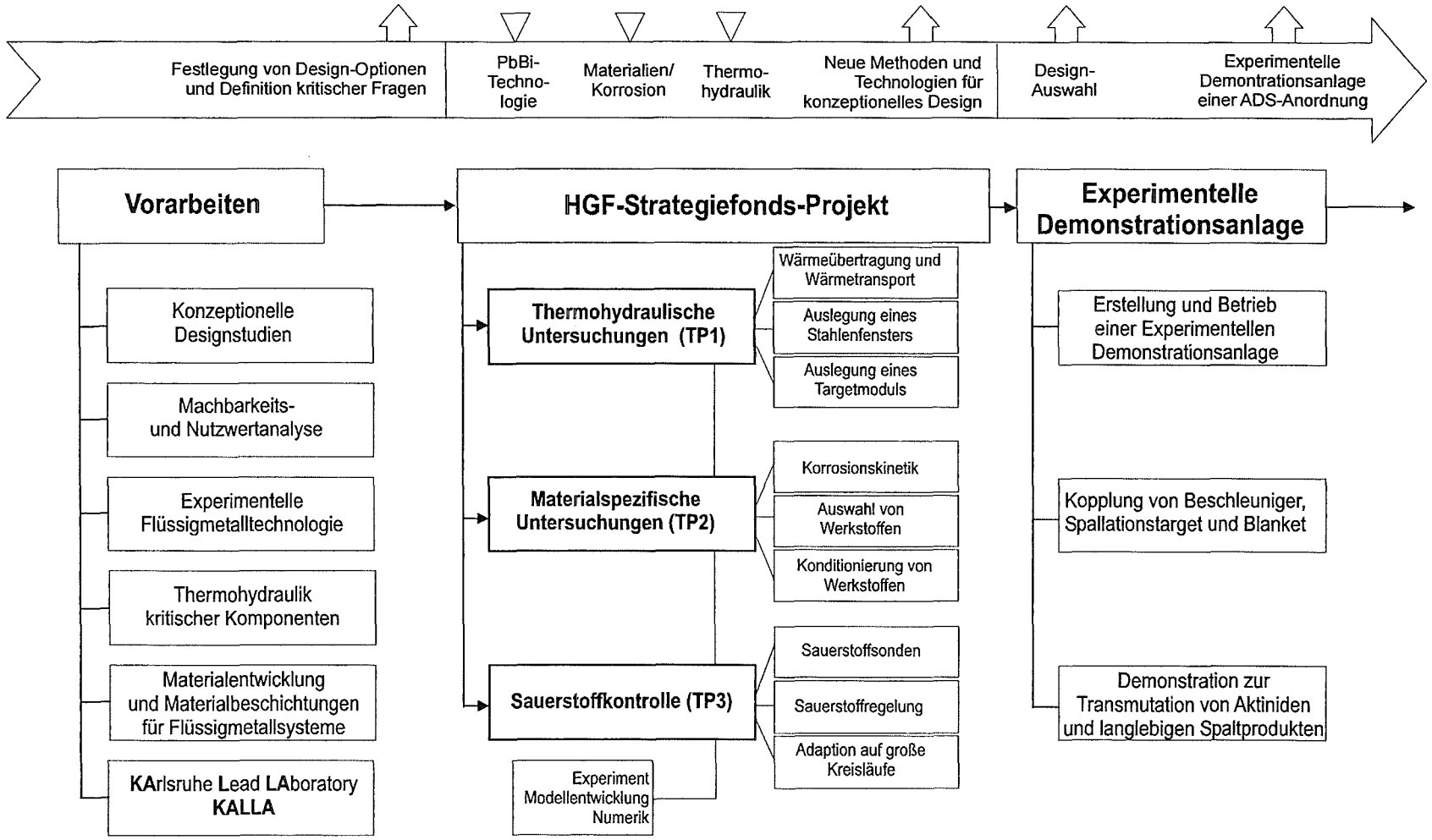

Abb. 3: Projektstrukturplan.

2.2 MATERIALSPEZIFISCHE UNTERSUCHUNGEN (TEILPROJEKT 2)

Das Forschungsziel ist es, die wissenschaftlich-technischen Grundlagen zum Korrosions- und Erosionsverhalten metallischer Struktur- und Fensterwerkstoffe in strömendem Blei-Wismut zu erarbeiten. Dabei wird bei den Strukturwerkstoffen das Hauptaugenmerk auf die nickelfreien, ferritisch-martensitischen Chromstähle sowie wegen der höheren Warmfestigkeit auch auf die hochchromhaltigen und hochnickelhaltigen Austenite gelegt. Um die Beherrschung der Korrosion von Strukturwerkstoffen zu gewährleisten, werden die wissenschaftlichen Grundlagen zu folgenden Fragestellungen erarbeitet:

- Chemisch-physikalische Wirkung von Inhibitoren in Pb-Bi,
- Langzeitbeständigkeit von Schichten, die durch Voroxidation erzeugt werden,
- Anwendbarkeit der Tauchaluminisierung mit anschließender Oxidation als Beschichtungsverfahren (Tauchanlage am FZK verfügbar),
- Eignung der GESA-Oberflächenveredlung durch Umschmelzen einer dünnen Oberflächenschicht mit einem gepulsten Elektronenstrahl (GESA-Anlage am FZK in Betrieb).

Diese Arbeiten schließen alle notwendigen Technologien mit ein, die eine sichere Handhabung und einen störungsfreien Betrieb eines Pb-Bi Kreislaufs gewährleisten. Im Rahmen des Teilprojekts 2 werden drei Arbeitspakete abgearbeitet.

(AP1.) Untersuchungen zum Korrosions- und Erosionsverhalten von Struktur- und Fensterwerkstoffen in strömendem Blei-Wismut

(AP2.) Untersuchungen zur Verbesserung der Korrosionsbeständigkeit durch Beschichtungen

(AP3.) Oberflächenmodifikation mittels gepulstem Elektronenstrahl (GESA)

2.3 SAUERSTOFFKONTROLLE (TEILPROJEKT 3)

Das Forschungsziel ist die Erarbeitung der wissenschaftlich-technischen Grundlagen zur Messung und zur Regelung des Sauerstoffpotentials in strömendem Blei-Wismut

und die Erstellung einer Vorschrift zur Verbesserung der Korrosionsbeständigkeit von Struktur- und Fensterwerkstoffen. Eine Sauerstoffkontrolle ist für den sicheren Langzeitbetrieb eines Pb-Bi Kreislaufs unerlässlich. Die Messung des Sauerstoffpotentials erfolgt mit einer Sauerstoffsonde. Die Sauerstoffsonde und das Referenzsystem werden hinsichtlich der Langzeitstabilität und der Temperaturwechselbeständigkeit der Sondenkeramik an flüssiges Pb-Bi angepasst. Die Sauerstoffkontrolle selbst erfolgt über die Gasphase durch Kontrolle des Wasserstoff/Wasserdampf-Verhältnisses. Abschließend wird die Übertragbarkeit dieses Verfahrens auf große Pb-Bi-Kreisläufe untersucht.
Im Rahmen des Teilprojekts 3 werden zwei Arbeitspakete abgearbeitet.

(AP1.) Sauerstoffmessung in strömendem Blei-Wismut

(AP2.) Sauerstoffkontrolle in strömendem Blei-Wismut

3. SCHWERMETALLLABORS KARLSRUHE LEAD LABORATORY KALLA

Die in den Teilprojekten 1 bis 3 beschriebenen experimentellen Untersuchungen werden im Schwermetalllabor KALLA (KArlsruhe Lead LAboratory) durchgeführt, das zur Zeit am Forschungszentrum Karlsruhe geplant und errichtet wird. Eine schematische Darstellung des Schwermetalllabors KALLA ist in Abb. 4 gegeben.
KALLA besteht aus drei Kreisläufen (Fluid: PbBi), die für folgende Einzeluntersuchungen ausgelegt sind:

- *Technologie-Kreislauf*: Messung und Kontrolle des Sauerstoffpotentials; Entwicklung und Erprobung von Strömungsmesstechnik (Geschwindigkeit: permanentmagnetische Potentialsonden MPP; Gasvolumenanteil: Voidsonden; Wandwärmestrom: beheizte Oberflächenelemente HETSS; Entwicklung und Erprobung von Hochleistungs-Wendelheizern; Wärmeübergangsmessungen unter Zwangskonvektion.
  Kennwerte: Volumen 0.1 m^3, Temperatur max 550°C, Volumenstrom max 5 m^3/h, Teststrecke für Wärmeübergangsmessungen: d_i=60mm, x/d_i=60.

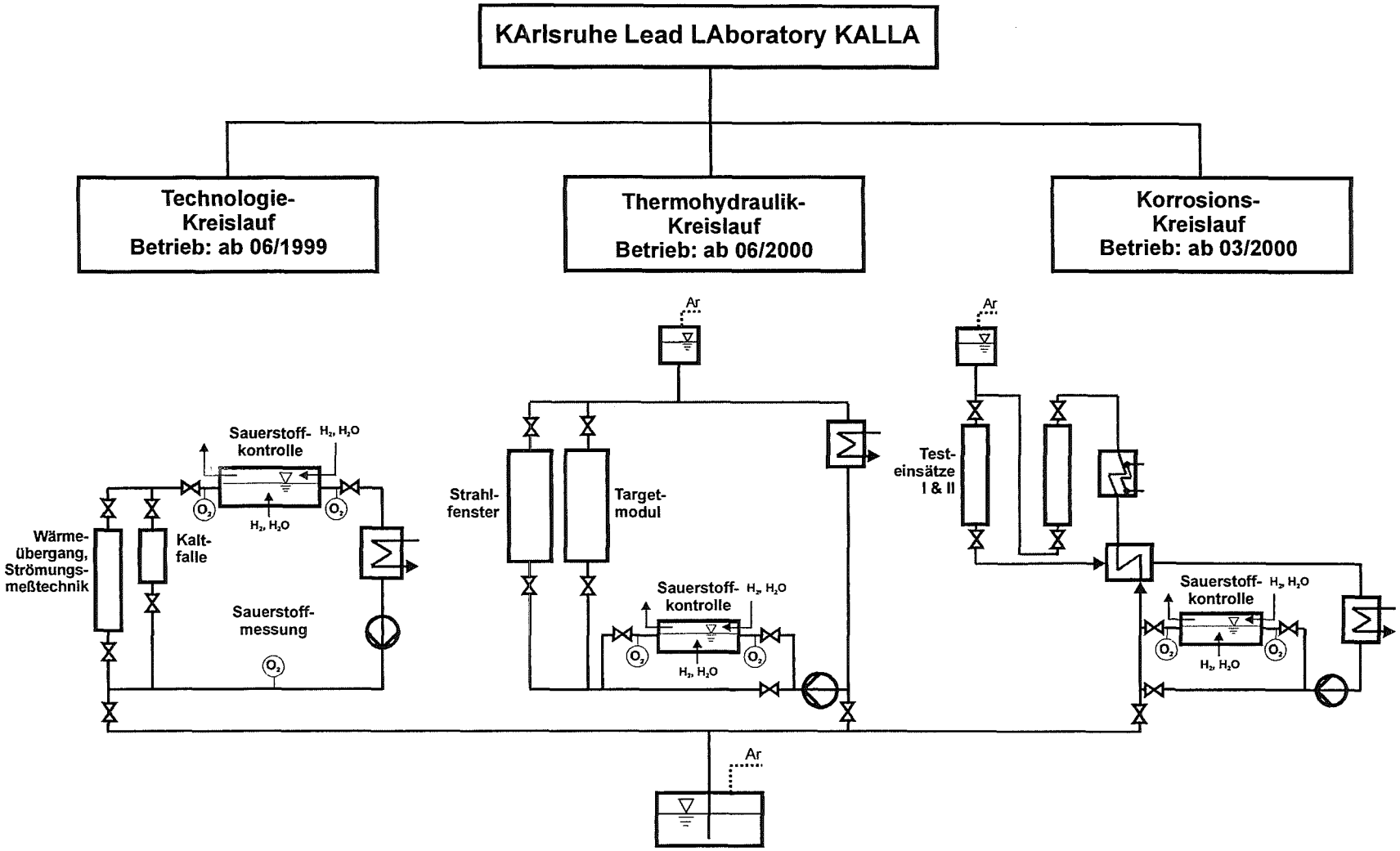

Schema 4: Schwermetalllabor KALLA (KArlsruhe Lead LAboratory).

- *Thermohydraulik-Kreislauf*: Einzeleffektuntersuchungen an einem Strahlfenster; (weiteres Potential des Kreislaufs außerhalb des Zeitrahmens dieses Strategiefonds-Projektes: Einzeleffektuntersuchungen an Targetmodul, Brennelement, Dampferzeuger und Integraluntersuchungen für eine Strömung im Primärsystem unter Normalbetrieb und unter Nachwärmeabfuhr).
  Kennwerte: Volumen max 4 m^3, Temperatur max 550°C, Volumenstrom max 100 m^3/h, Leistung max 4 MW.
- *Korrosions-Kreislauf*: Untersuchungen zur Korrosion und zu Schutzschichten an ausgewählten Stählen; (weiteres Potential des Kreislaufs außerhalb des Zeitrahmens dieses Strategiefonds-Projektes: mechanische Tests an ausgewählten Stählen).
  Kennwerte: Volumen 0.03 m^3, Temperatur max 550°C, Volumenstrom 3.5 m^3/h.

4. FORTSCHRITT UND ZUSAMMENFASSUNG

Das HGF-Strategiefonds-Projekt „Blei-Versuchskreislauf" wird von der HGF mit einem Finanzvolumen von 7 Millionen DM (35 Personenjahre) über eine Laufzeit von 1999 bis 2002 gefördert.

Das Projekt erarbeitet neue Methoden und Technologien zur Auslegung und Herstellung thermisch hochbelasteter Oberflächen, die von einem korrosiven schweren Flüssigmetall (eutektisches Blei-Wismut) gekühlt werden. Die Arbeiten stehen in unmittelbarem Zusammenhang mit der Auslegung einer europäischen Demonstrationsanlage einer beschleunigergetriebenen Anordnung (ADS) zur Transmutation von minoren Aktiniden und langlebigen Spaltprodukten. Eine ADS-Anordnung hat das Potential, die Menge und die Radiotoxizität an radioaktivem Abfall zu verringern und so einen entscheidenden Beitrag zur Schließung des Brennstoffkreislaufs zu leisten.

Der Aufbau des Technologie-Kreislaufs im Schwermetalllabor KALLA hat begonnen. Einen Stand der Arbeiten zeigt Abb. 5.

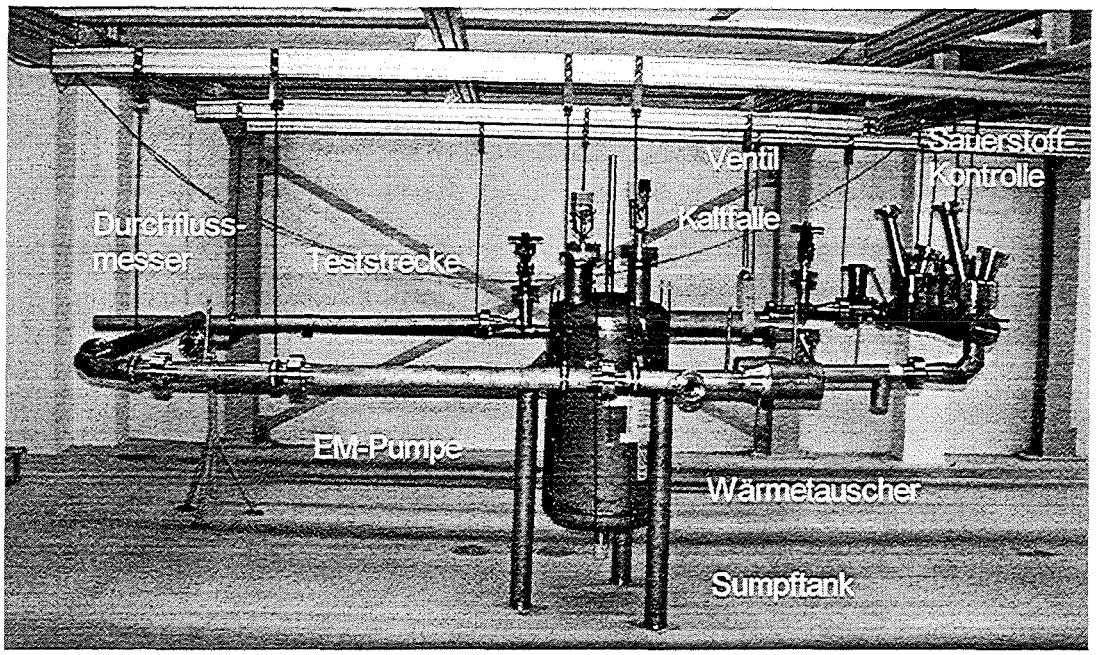

Abb. 5: Technologie-Kreislauf im Schwermetalllabor KALLA (aktueller Stand).

III. Flüssigkmetallkorrosion

(H. Glasbrenner, J. Konys, Z. Voß, O. Wedemeyer, IMF III)

Abstract

Eight different iron-chromium alloys are exposed to static lead at 600 °C for 3000 h, 5000 h and 10,000 h. Metallographical results of specimens exposed for 3000 h and 5000 h have shown that steels with lower chromium content were only little attacked. A more severe corrosion attack could be found in steels with higher chromium content. With longer exposure time the corrosion rate increases as well. Corrosion is probably related to the dissolution of steel components or partly leaching of elements out of the steel matrix. Further investigations are in progress.

Zusammenfassung

Acht verschiedene Eisen-Chrom-Legierungen werden bzw. wurden in statischem Blei bei 600 °C für 3000 h, 5000 h und 10,000 h ausgelagert. Erste metallographische Ergebnisse liegen von den 3000 h und 5000 h ausgelagerten Proben bereits vor. Legierungen mit einem niedrigen Cr-Gehalt zeigen nur einen geringen Korrosionsangriff. Stähle mit höherem Cr-Gehalt weisen einen deutlich stärkeren Korrsionsangriff auf. Mit zunehmender Auslagerungsdauer steigt die Korrosionsrate ebenfalls an. Vermutlich ist die Auflösung von Stahl oder das teilweises Herauslösen von Stahlelementen aus der Matrix maßgeblich für die stattfindende Korrosion. Weitere Untersuchungen mit EDX und REM müssen noch durchgeführt werden.

Introduction

Use of lead and lead-bismuth alloy is being considered as spallation target for the so-called hybrid reactors in which long-lived actinides should be transmuted. Pb and PbBi have a high neutron yield and are very transparent to neutrons of energies below 1 MeV. The molten metal should be used not only as target but also as coolant in the reactor system. It is known, that heavy metals Pb and Bi are much more aggressive corrodents than the alkali metals. For the development of an accelerator driven system (ADS) the corrosion problems of structural materials in the coolant must be solved. Until now there is only little or no experience in the field of corrosion except for military application in the former USSR, but unfortunately these results are unpub-

lished. Therefore, corrosion experiments are strongly required. The tests should be performed in a corrosion loop in which the liquid melt has a flow velocity in the order of 2 m/s and temperatures up to 550 °C. Such a loop is under design. Beforehand some corrosion experiments have been carried out with 8 different ferritic alloys with variying Cr and Al content in static Pb at 600 °C up to 10000 h. First results of specimens exposed for 3000 h and 5000 h are already at hand.

Experimental

Different types of steel have been selected for corrosion testing in Pb: 1.4713, Optifer IVa, Optifer IVc, MANET II, 1.4923, 1.4742, PM 2000 and Ducrolloy. All steels have no or only small amount of Ni. The Cr content varies between 6 – 8 wt% (1.4713) and 50.4 wt% (Ducrolloy). The chemical composition of these steels is given in table 1.

Table 1: Chemical composition of the steels investigated.

Steel	Fe	Cr	Mn	Others
1.4713	87.98-92.17	6-8	0-1	Al, V, W
Optifer IVa	89.20	8.5	0.57	Ta, V, W
Optifer IVc	89.16	9.05	0.52	Mo, Ta, W, Si
MANET II	86.75	10.37	0.76	Al, Mo, Ni, Si, V
1.4923	83.54-87.25	11-12.5	0.3-0.8	Mo, Ni, Si, V
1.4742	77.21-81.6	17-19	0-1	Al, Si
PM 2000	74.5	19	-	Al, Ti, Y2O3
Ducrolloy	44.14	50.4	-	Al, Ti, Y2O3

The geometry of the steels to be tested was sheet material in different sizes. The samples were polished, degreased in acetone and finally cleaned ultrasonically in ethanol. Afterwards the sheets were inserted into molten lead inside an alumina crucible in a glove box under purified dry Ar atmosphere ($p_{O2} \leq 10^{-6}$ bar, $p_{H2O} \leq 10^{-6}$ bar). The alumina crucibles were put in hermetically closed stainless steel capsules which then were placed in a chamber furnace and kept there at 600 °C for 3000 h, 5000 h and 10000 h. After the tests steel sheets were taken out of the liquid lead in a glove

box. There were still covered zones with Pb on the surface of the specimens. Remaining lead was not washed away to be sure that a possibly formed corrosion layer could be removed as well during this process. All specimens were metallographically examined in order to see how the molten lead has reacted with the different steels. Moreover lead was analysed to get information about dissolution of steel elements. Further investigation like EDX and REM still have to be done on the specimens. First metallographical results are already obtained on the 3000 h and 5000 h specimens. The 10000 h hour test is still running.

Results

Pb analyses have been made of each crucible in which specimens were exposed for 3000 h and 5000 h, reps. The results of the lead analysis after 3000 h exposure showed no difference compared to the values obtained for virgin lead used. No increase of any element could be observed. Pb analysis after 5000 h exposure showed a slightly increase of the iron content. The amount of the other steel elements in lead did not increase measurable.

Metallographical cross sections of Optifer IVc after 3000 h and 5000 h in lead are shown in Figure 1. It can be exactly seen that with longer exposure time the corrosion attack increases.

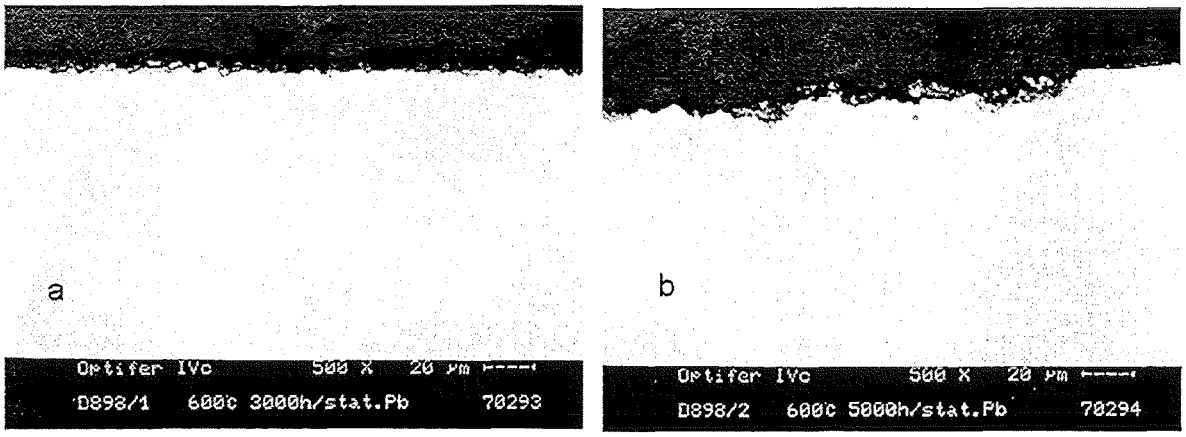

Figure 1: Metallographical cross sections of Optifer IVc after a) 3000 h and b) 5000 h exposure to static lead at 600 °C.

Metallographical results obtained on the cross sections of the exposed specimens lead to the following observation: Steels with lower chromium content were only little attacked. A more severe corrosion attack could be found in steels with higher chromium content. With longer exposure time the corrosion rate increases as well. Table 2 shows results of corrosion tests in stationary molten lead. The attack depth was determined on the cross section of each specimen. These values are just a rough estimation but a tendency can be clearly recognised.

Table 2: Observed maximum corrosive attack depth (µm) on specimens exposed to stationary lead at 600 °C

Steel	3000 h	5000 h
1.4713	about 2	about 4
Optifer IVa	about 4	about 10
Optifer IVc	about 4	about 10
MANET II	about 10	about 15
1.4923	about 12	about 16
1.4742	about 12	about 16
PM 2000	about 15	about 20
Ducrolloy	about 20	about 44

The most severe corrosion attack was found on the alloy Ducrolloy which has a high Cr content (50.4 wt%). One of the Ducrolloy specimen exposed to lead for 3000 h was already investigated with EDX. It could be clearly seen that the Cr content in the near surface region was decreased enormously (down to app. 13 wt%) compared to the virgin material because of the high solubility of Cr in lead [1].

Discussion and Conclusions

Corrosion tests in stationary lead are important as they give information about the principal kind of corrosion of steels. For a further evaluation of corrosion behaviour of alloys, the tests in circulating melt are, however, essential due to the phenomena of erosion and mass transport.

First results in stationary lead determined metallographically on cross sections of specimens exposed for 3000 h and 5000 h reps. the following observations could be made: Firstly, with increasing Cr content in the alloy the corrosion attack increases, secondly, with increasing exposure time the corrosion attack increases as well.
Corrosion by liquid metal is generally related to the solubility of the materials involved [2-4]. The solubility of chromium in lead is about 4 orders of magnitude higher than of iron [1]. This means that alloys with a low chromium content are more stable in liquid lead than steels with a high Cr content. This is in agreement with our observations. Anyway, EDX and REM analyses are necessary before making more detailed statements concerning the corrosion mode proceed. Probably the dissolution of steel elements in lead and / or the partly leaching out of one or more component out of the steel matrix are responsible for the corrosion attack. Further investigations on specimens exposed for 3000 h, 5000 h and 10,000 h to lead are in progress.

References

[1] C. Guminski, Metallkunde **81** (1990) 105.

[2] W.E. Berry in „Corrosion in Nuclear Applications", John Wiley and Sons, New York 1971, p. 308.

[3] H.U. Borgstedt, H.D. Röhrig, J. Nucl. Mater. **179-181** (1991) 596.

[4] R.C. Asher, D. Davies, S.A. Beetham, Cor. Sci. **17** (1977) 545.

IV. Calculations of the Energy Deposition in the Target of an ADS

(C. Broeders, I. Broeders, INR)

Abstract

The energy deposition in the target and in the target window of an accelerator-driven subcritical reactor has been calculated using the LAHET code system (LCS). Results of two studies will be discussed: In a first investigation we used a model based on the NEA/OECD ADS neutronic benchmark (liquid lead target, lead zones, core). The energy deposition in the target window was studied for windows of different materials. The proton source was a circular beam with radius 10cm and with parabolic profile. The proton energy was 1GeV, the beam current 10mA. The main goal of our second study was to obtain a first estimate of the spatial distribution of the energy deposited in the target and in the target window. In this case the material of the window was stainless steel, the target material was liquid lead. These calculations have been carried out for a 600MeV proton beam of radius 7.5cm with parabolic profile.

Introduction

The high energy protons that enter the accelerator driven system (ADS) deposit most of their kinetic energy in the target and an appreciable part also in the target window in front of the target. The programs LAHET/HTAPE of the LAHET Code System (LCS) [1] evaluate the different mechanisms of energy deposition and print out detailed results.

Energy deposition due to nuclear reactions of neutrons with $E_n \leq 20MeV$ and interactions of photons with $E_\gamma \leq 100MeV$ with atoms are calculated with MCNP [2] within the LCS code package.

The input of LAHET requires information on the nuclear models to be used for the simulation of the spallation processes. For our calculations we have used the default values except that we choose the option to use a preequilibrium model following the intranuclear cascade.

For the low energy cutoff of protons and heavier charged particles we also used

the default value which is 1MeV. Protons (and heavier charged particles) reaching their cutoff energy are assumed to deposit the remaining kinetic energy at the same spot. The default value of the low energy cutoff for pions is 0.149MeV, for muons it is 0.113MeV.

Energy deposition in the target window of an ADS

The model of the reactor that has been used in the calculations has been derived from the ADS neutronic benchmark [3] and is shown in Fig.1. The cylindrical liquid lead region with outer radius 32.5cm is surrounded by a core region $32.5 \leq r \leq 82.5cm$. The material composition in the core corresponds to the one of the inner core region of the ADS neutronic benchmark. The neutron beam enters from above through a vacuum tube.

Results of the calculations

Results of LAHET.

LAHET has been used together with the tally evaluation code HTAPE for the calculation of the energy deposition in the zones of the model given in Fig.1. MCNP is used for neutrons with energy below 20MeV and photons with energy below 100MeV. Both LAHET and MCNP use Monte Carlo methods. In this first study we were mainly interested in the energy deposition in the target window. In our model the window is hemispherical its outer radius is $r_{w_o} = 10cm$, the inner radius is $r_{w_i} = 9.8cm$. The lowest point of the outer edge of the window is 90.0cm in Figure 1. The proton source is a parallel beam with parabolic density over a radius. The radial dependence of the proton density in the beam is given by: $p(r) = \frac{2}{\pi r_0^2}[1 - \frac{r^2}{r_0^2}]$ and $p(r) = 0$ for $r \geq r_0$.
The beam radius r_0 is set equal to 10cm for the calculations discusssed in this section. The starting z-coordinate of the source is 20.0cm above the lowest point of the window, corresponding to 110.0cm in Figure 1. Most of the calculations described in this section have been carried out for proton energy 1GeV and proton current 10mA.

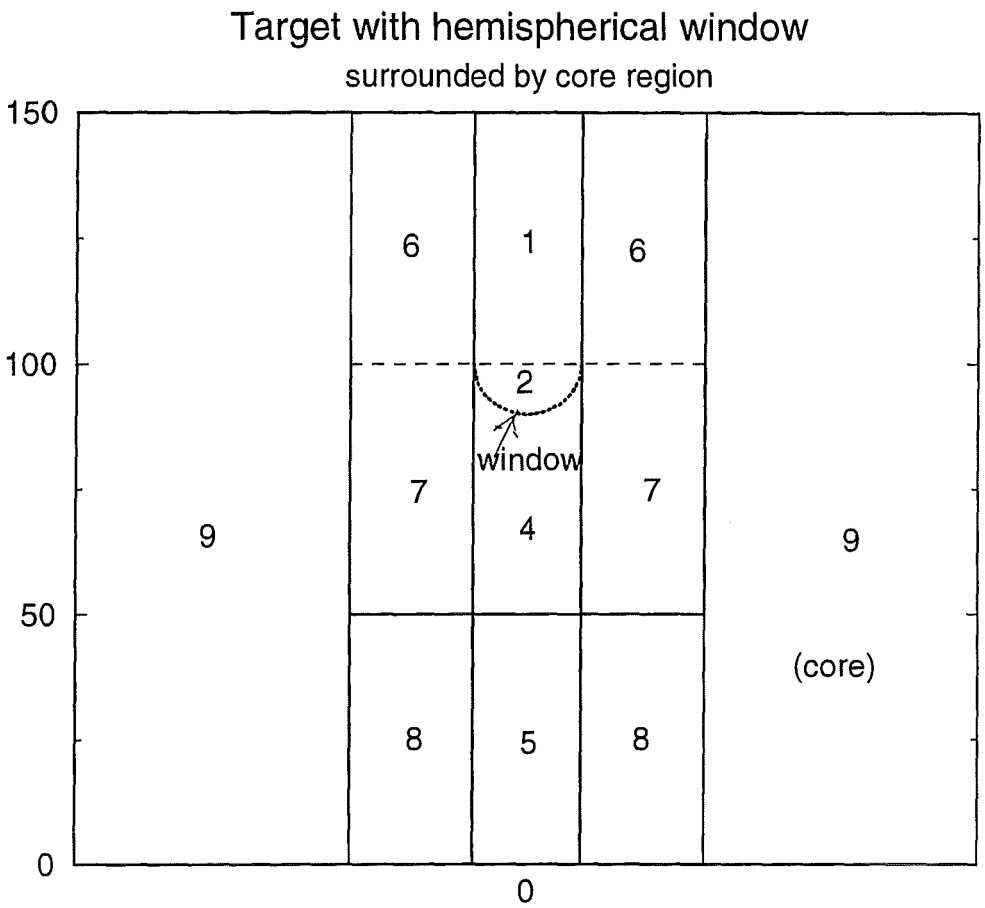

Figure 1: Geometry used for the calculation of the energy deposition in the window

zones 1,2:	**vacuumtube**
zone 3:	**hemispherical window** ($r_{w_o} = 10cm, r_{w_i} = 9.8cm$)
zones 4, 5, 6, 7, 8:	**liquid lead zones**
zone 9:	**core (material composition corrresponding to the inner core region of the ADS neutronic benchmark)**

proton beam enters from above in negative z-direction. (r=0)

In the following the results of the LAHET calculation (LAHET and HTAPE) are given for a tungsten window on top of a lead target. The density of tungsten was taken from [4]: ρ_W **at** $20^0C = 19.3g/cm^3$**. For the total layout see Figure 1. The characteristics of the proton beam are as described above. The Monte Carlo calculations have been carried out for 60.000 proton histories.**

The energy deposition is given in MeV/proton which corresponds to kW/mA.

Table 1: Energy deposition calculated by LAHET/HTAPE

Contribution of different reactions

	(W-window) [MeV/proton]		(Pb-target) [MeV/proton]	
	mean value	statistical error		
coulomb loss h-1	8.83099D+00	.008	4.12747D+02	.002
coulomb loss pi+-	2.00913D-01	.051	1.26629D+01	.012
coulomb loss mu+-	0.00000D+00	.000	0.00000D+00	.000
coulomb loss K+-	0.00000D+00	.000	0.00000D+00	.000
coulomb loss pbar	0.00000D+00	.000	0.00000D+00	.000
coulomb loss h-2	1.84320D-01	.052	4.50597D+00	.010
coulomb loss h-3	9.05429D-02	.062	2.61394D+00	.010
coulomb loss he-3	1.56417D-02	.160	2.56022D-01	.038
coulomb loss he-4	3.78479D-01	.045	1.24890D+01	.006
nuclear recoil	1.08541D-01	.071	9.32996D+00	.013
excitation	1.62954D-01	.026	9.36397D+00	.003
pi0 decay gammas	1.23938D+00	.064	3.08361D+01	.012
kin. eng. of e+,e-	0.00000D+00	.000	0.00000D+00	.000
positron mass	0.00000D+00	.000	0.00000D+00	.000
kin. eng. of muons	1.05227D-02	.084	4.50920D-01	.014
mu+ mass	2.52252D-01	.084	9.94349D+00	.013
mu- mass	3.52200D-04	.707	2.78921D-02	.082
total deposition	1.14749D+01	.012	5.05227D+02	.001

It is seen from the results that the main contribution to the energy deposition in the target and in the target window is due to Coulomb loss (ionization energy loss) of protons (about 77% in the window and about 82% in the target). Coulomb losses of other charged particles that are emitted in the spallation process contribute less than 8%. Nuclear recoil and nuclear excitation contribute less than 4%. γ's from decay of neutral pions contribute about 10% to the energy deposition. The contribution from muons is about 2%. (For the interpretation of the various schemes of energy deposition see also [5]).
The energy deposition in the window calculated by LAHET/HTAPE is 114.75 kW for a 10mA proton beam.

Results from the MCNP calculations
Contributions from neutron reactions with $E_n \leq 20MeV$ and from photon reactions with $E_\gamma \leq 100MeV$ are calculated with MCNP:
Energy deposition in the window:

- energy deposition from neutrons: 0.309kW for 10mA proton current
- energy deposition from photons: 11.67kW for 10mA proton current
- total energy deposition in the window: 126.73kW for a proton current of 10mA (114.75kW are from the LAHET/HTAPE calculation).

In Table 2 the energy deposition is shown for target windows of different materials and of the same assumed thickness. All calculations use the geometry given in Figure 1. Three partial results are given for the energy deposition: the result of LAHET/HTAPE as discussed above and the results of MCNP for reactions with neutrons ($E_n \leq 20MeV$) and for reactions with photons ($E_\gamma \leq 100MeV$). The contribution of the MCNP results to the total energy deposition is between 6% and 12%, mainly due to reactions with photons.

Spatial dependence of the energy density in the target and in the target window

In this section we investigate the spatial dependence of the energy density deposited in the target window and in the target. The results are meant as a first estimate of the energy deposition in the vicinity of the target window. The calculations have been carried out for a liquid lead target with a target window of steel 1.4970. The geometry of the target and the target window is very similar to the corresponding regions in Fig. 1. In the calculations discussed in this section the lead region is surrounded by a thin layer (thickness: 0.6cm) of steel 1.4970, the outer radius of this layer is 32.54cm. The total height of the target is 100cm. The geometry of the window is nearly hemispherical: The outer surface of the window is strictly hemispherical, $r_{w_o} = 10cm$, the inner window surface is the surface of an ellipsoid, such that the thickness is 0.15cm at the bottom of the window and 0.3cm at the upper edge. The distance

Table 2: Energy deposition in target window and target

window material	proton beam: energy/ current	energy deposition [kW] LAHET	MCNP neutrons	MCNP photons	total	energy density [Watt/cm^3]
tungsten (W)	1.0GeV/ 10mA	114.75 (.012)	0.31 (.0100)	11.67 (.0446)	126.73	1029
tungsten	0.6GeV/ 10mA	100.10 (.010)	0.18 (.0118)	6.00 (.0536)	106.28	863
W-Re W: 74 w% Re: 26 w%	1GeV/ 10mA	116.07 (.015)	5.50 (.0059)	11.57 (.0478)	133.14	1081
steel 1.4970	1GeV/ 10mA	62.54 (.020)	0.62 (.0103)	3.40 (.0650)	66.56	540
target material	**proton beam: energy/ current**	**energy deposition [MW] LAHET**	**MCNP neutrons**	**MCNP photons**	**total**	**energy density [Watt/cm^3]**
liquid Pb	1GeV/ 10mA	5.053 (.001)	.0129 (.0033)	0.579 (.0094)	5.644	415

outer radius of the window $r_{w_o} = 10cm$, thickness of the window $d_w = 0.2cm$

densities: $\rho_W = 19.3g/cm^3$, $\rho_{Re} = 21.02g/cm^3$, $\rho_{steel1.4970} = 7.80g/cm^3$

radial proton beam: $r_0 = 10cm$, parabolic profile $p(r) = \frac{2}{\pi r_0^2}[1 - \frac{r^2}{r_0^2}]$

between the lowest point of the window and the bottom of the target is 80cm. The 600MeV proton beam enters the target window through a vacuum tube (inner radius: 9.7cm, outer radius: 10cm, material steel 1.4970). The beam radius is $r_0 = 7.5cm$, the density distribution of the proton beam is parabolic over the radius. The Monte Carlo calculations have been carried out for 100.000 proton histories.

Presentation of the results

The results are given in Fig. 2 and Table 3. In order to enable comparison with calculations carried out at IPPE, Obninsk (for 800MeV protons) [6], the scale on the vertical (z-) axis was transformed such that r=0, z=0 is the center of the target window, and the z values are ascending from the proton source to the target, i.e. reversed to Fig. 1. Fig. 2 shows the presentation of these results carried out with the visualization program TECPLOT. This presentation corresponds to the results given in Table 3.

In the following we try an interpretation of the results: The flamelike shape of the energy density distribution shown in Fig. 2 is caused by the shape of the primary proton beam and by energy deposition from secondary particles emitted in the spallation process. The highest proton density is along the central axis of the beam, accordingly the highest energy deposition is along the central axis of the target. The parabolic pattern of the regions of nearly equal energy deposition is caused by the parabolic profile of the entering proton beam. The protons lose kinetic energy on their way through the target therefore the energy deposition caused by protons and secondary particles decreases with increasing distance from the proton source. The energy-range of a 600MeV proton beam in liquid lead is about 28cm (from proton energy-range tables printed out by LAHET). This means that along the beam axis the proton beam should reach a distance of about 28cm from the surface of the window. This is in good agreement with the result presented in Fig. 2.

References

[1] R.E. Prael and H. Lichtenstein: LA-UR-89-3014 Los Alamos National Laboratory (September 1989) and R.E. Prael LA-UR-97-4981 (December 1, 1997)

[2] Judith F. Briesmeister, Editor: LA-12625-M, Version 4B (March 1997)

[3] C. Broeders, I. Broeders: in Wissenschaftliche Berichte, FZKA 5963 (September 97) p. 464 - 472

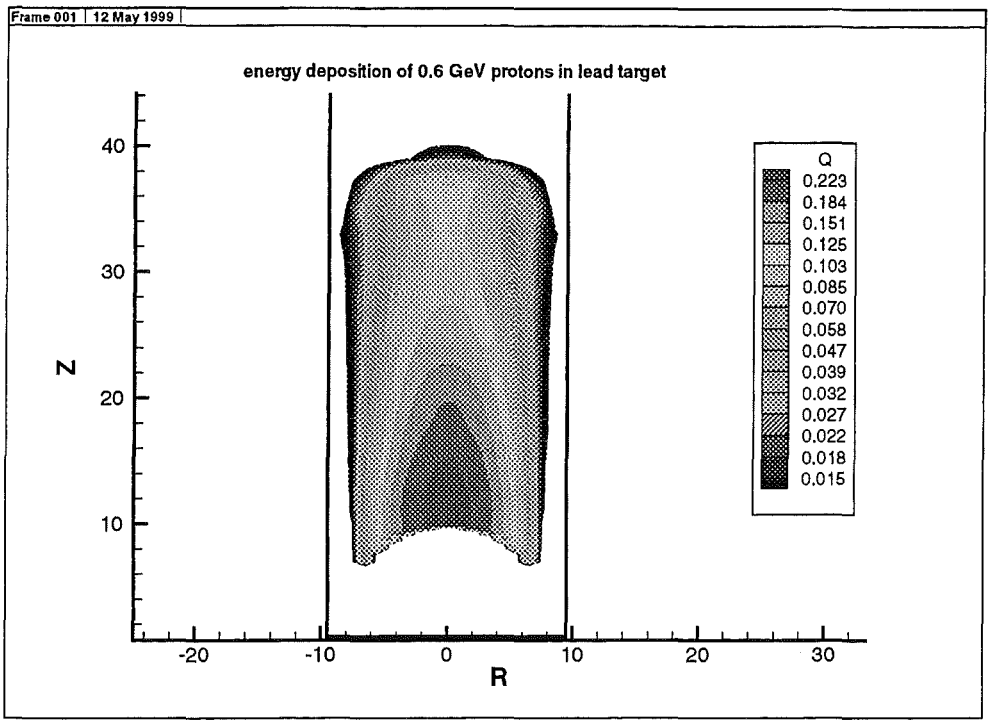

Figure 2: Energy deposition of a 600MeV proton beam in a liquid lead target (energy densities are given in $kW/(cm^3 \cdot mA)$). In the Figure the (nearly) hemispherical window is between z=0cm and z=10cm, the proton beam is entering from below. The figure is taken from a color plot where red represents the highest energy density.

[4] G. Pfennig, H.Klewe-Nebenius, W. Seelmann-Eggebert: Karlsruher Nuklidkarte November 1995

[5] P. Cloth, D. Filges et. al.: Jül-2203, (May 1988)

[6] X. Cheng, Private communication

Table 3: Spatial dependence of the energy deposition in the target window and the target of an ADS $[kW/cm^3/mA]$ $([MeV/cm^3/proton])$

r [cm]:	0 - 1	1 - 2	2 - 3	3 - 4	4 - 5
window	2.36916E-01	2.32205E-01	1.99195E-01	1.97541E-01	1.69046E-01
z [cm]					
0 - 2	0.00000E+00	0.00000E+00	0.00000E+00	0.00000E+00	0.00000E+00
2 - 4	0.00000E+00	0.00000E+00	0.00000E+00	0.00000E+00	0.00000E+00
4 - 6	0.00000E+00	0.00000E+00	0.00000E+00	0.00000E+00	0.00000E+00
6 - 8	0.00000E+00	0.00000E+00	0.00000E+00	0.00000E+00	0.00000E+00
8 - 10	2.51652E-01	2.32556E-01	2.00871E-01	1.82376E-01	1.48805E-01
10 - 12	2.37537E-01	2.28668E-01	2.16545E-01	1.89405E-01	1.50494E-01
12 - 14	2.34794E-01	2.23265E-01	2.12435E-01	1.80239E-01	1.44774E-01
14 - 16	2.26661E-01	2.09573E-01	1.93221E-01	1.64955E-01	1.31300E-01
16 - 18	2.00090E-01	1.90055E-01	1.75613E-01	1.51967E-01	1.18688E-01
18 - 20	1.90882E-01	1.72602E-01	1.60953E-01	1.38741E-01	1.09045E-01
20 - 22	1.65599E-01	1.58114E-01	1.47156E-01	1.24960E-01	9.98000E-02
22 - 24	1.48900E-01	1.45464E-01	1.32145E-01	1.15530E-01	9.19712E-02
24 - 26	1.38027E-01	1.32999E-01	1.20425E-01	1.05861E-01	8.32447E-02
26 - 28	1.26559E-01	1.22193E-01	1.09870E-01	9.76225E-02	7.66701E-02
28 - 30	1.16394E-01	1.13352E-01	1.01113E-01	9.02428E-02	6.95630E-02
30 - 32	1.12690E-01	1.06278E-01	9.43234E-02	8.27653E-02	6.44476E-02
32 - 34	1.04538E-01	1.01027E-01	9.05393E-02	7.93304E-02	6.23072E-02
34 - 36	1.12697E-01	1.03555E-01	9.22954E-02	8.27070E-02	6.56876E-02
36 - 38	1.25965E-01	1.13081E-01	9.88035E-02	8.46321E-02	6.04524E-02
38 - 40	1.95984E-02	1.73876E-02	1.21450E-02	7.85976E-03	3.89527E-03
40 - 42	1.45669E-03	1.10972E-03	1.05948E-03	8.94353E-04	8.86037E-04
42 - 44	7.19878E-04	9.19500E-04	7.79191E-04	6.49240E-04	6.53259E-04
44 - 46	5.99382E-04	6.02340E-04	5.26333E-04	6.34277E-04	5.92807E-04
46 - 48	3.42806E-04	7.46280E-04	4.73109E-04	5.52550E-04	3.39010E-04
48 - 50	4.18219E-04	3.66649E-04	3.93599E-04	3.15466E-04	3.89258E-04
50 - 55	2.45962E-04	2.96353E-04	2.85608E-04	3.52599E-04	2.73188E-04
55 - 60	1.39953E-04	1.06658E-04	1.93320E-04	1.51165E-04	2.18701E-04
60 - 65	1.96875E-04	1.23039E-04	1.26722E-04	1.42473E-04	1.56274E-04
65 - 90	3.34936E-05	4.80283E-05	3.25463E-05	4.33801E-05	4.58961E-05

Table 3: continued

r [cm]:	5 - 6	6 - 7	7 - 8	8 - 9	9 - 10
window	1.07077E-01	5.59767E-02	8.51664E-03	1.44369E-03	1.23430E-03
z [cm]					
0 - 2	0.00000E+00	0.00000E+00	0.00000E+00	0.00000E+00	9.70036E-04
2 - 4	0.00000E+00	0.00000E+00	0.00000E+00	1.10247E-03	8.85468E-04
4 - 6	0.00000E+00	0.00000E+00	0.00000E+00	9.67387E-04	6.28735E-04
6 - 8	0.00000E+00	4.95802E-02	7.33348E-03	1.58396E-03	5.69273E-04
8 - 10	1.07011E-01	5.80186E-02	1.01903E-02	2.57469E-03	9.25317E-04
10 - 12	1.07634E-01	5.67741E-02	1.20176E-02	3.29941E-03	1.44288E-03
12 - 14	1.01638E-01	5.41234E-02	1.27492E-02	3.75291E-03	1.96675E-03
14 - 16	9.36285E-02	5.02239E-02	1.29881E-02	4.30388E-03	2.14258E-03
16 - 18	8.64327E-02	4.60879E-02	1.41069E-02	5.00727E-03	2.47705E-03
18 - 20	7.86971E-02	4.25502E-02	1.43723E-02	5.49021E-03	2.69053E-03
20 - 22	7.11069E-02	3.90656E-02	1.46922E-02	5.72108E-03	2.89537E-03
22 - 24	6.47606E-02	3.55535E-02	1.48271E-02	5.98497E-03	3.19184E-03
24 - 26	5.82066E-02	3.30889E-02	1.47630E-02	6.40020E-03	2.87780E-03
26 - 28	5.33988E-02	3.11776E-02	1.54580E-02	7.05731E-03	3.07097E-03
28 - 30	4.97209E-02	3.00545E-02	1.58698E-02	7.66614E-03	3.41223E-03
30 - 32	4.77106E-02	2.89395E-02	1.63040E-02	8.57616E-03	3.73283E-03
32 - 34	4.65204E-02	3.00311E-02	1.74461E-02	1.11759E-02	4.26585E-03
34 - 36	5.09011E-02	3.46202E-02	2.16570E-02	4.86940E-03	5.78719E-03
36 - 38	4.07403E-02	2.39758E-02	1.20364E-02	6.93272E-04	2.13147E-03
38 - 40	1.94329E-03	1.12318E-03	7.53450E-04	5.91363E-04	6.53653E-04
40 - 42	8.33257E-04	6.86980E-04	6.23489E-04	4.16575E-04	4.65926E-04
42 - 44	7.68847E-04	5.06985E-04	5.64691E-04	4.01992E-04	3.62469E-04
44 - 46	5.97848E-04	4.94763E-04	4.30472E-04	2.99324E-04	3.47455E-04
46 - 48	4.78519E-04	3.83935E-04	3.49272E-04	3.84088E-04	3.36539E-04
48 - 50	4.00291E-04	3.53798E-04	2.81875E-04	2.25547E-04	2.41206E-04
50 - 55	2.60685E-04	2.30052E-04	2.49105E-04	1.54891E-04	2.22076E-04
55 - 60	1.49758E-04	1.71145E-04	1.55689E-04	8.16852E-05	1.47077E-04
60 - 65	8.30748E-05	8.94660E-05	8.62170E-05	4.12829E-05	1.18124E-04
65 - 90	4.52254E-05	3.97539E-05	4.58696E-05	0.00000E+00	4.31117E-05

V. Investigation on Oxygen Controlled Liquid Lead Corrosion of Surface Treated Steels

(A. Heinzel, R. Huber, G. Müller, G. Schumacher, F. Zimmermann, INR)

1. Introduction

Recently promising proposals were discussed on accelerator driven subcritical systems (ADS) for energy production and as actinide burners [1]. Those concepts include safety liquid metal cooling systems on the basis of Pb-Bi or Pb. However, corrosion problems with steel arise in using such coolants. Severe intergranular attack was observed for 316 steel and corrosion effects in the 100 µm range for Fe, Cr steels between 575 and 750 °C after 3250 h of exposure [2]. Compatibility tests with ferrous steels showed corrosion attack can be minimized if an oxide layer exists at the steel surface [3,4].

The highest solubility in lead is that of Ni for which the phase diagram [5] shows 2 at% at 550 °C. No data are available for Fe and Cr at this temperature. The respective phase diagrams give reasonable values only for temperatures above 1000 °C. Values of 1 at% Cr and 0.15 at% Fe can be obtained at 1200 °C [5]. At this temperature already 19 % of Ni is dissolved in lead. Since all the solubilities vary with temperatures, transport processes will take place which live from the higher solubility at high temperatures and precipitation at low temperatures. A temperature difference of 150 °C is about typical for lead cooling loops. With high flow velocities, in the range of 1 m/s, and long in pile times already small solubilities can lead to heavy corrosion effects.

One way to slow down corrosion of metals in liquid Pb would be to use metals with no or very low solubility in lead. Those metals could be W which is reported with a solubilities of < 0.0056 at% and Mo with < 0,011 at% at 1200 °C by Elliot [6]. Molybdenum was reported to be highly resistant, even at 1000 °C [3]. Good results were obtained also with FeCr alloy containing 8 at% Al that allows formation of a protection oxide scale also at low oxygen potentials [3]. Orlov [4] and Markov [7] stabilize the oxide protection layer by maintaining the necessary oxygen potential in liquid Pb or Pb-Bi with an oxygen control system. The concentration of oxygen should be below the saturation value at which PbO precipitates in the liquid lead.

An overview on the corrosion behavior of 2 steels in a loop with liquid lead at 550 °C as a function of oxygen concentration after 3000 h of exposure, is presented in Fig. 1 [7].

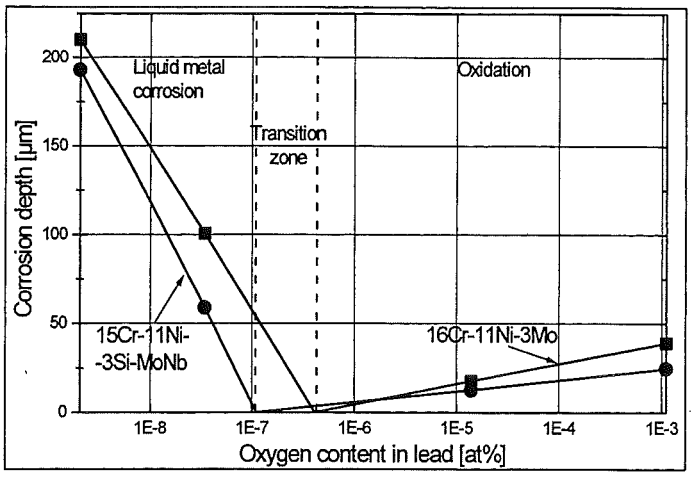

Fig. 1: Corrosion behavior of steels in flowing lead after 3000 h at 550 °C from [7]

At oxygen concentrations below 10^{-7} at% corrosion is determined by solution of alloy components in steel. It increases strongly with decreasing oxygen content. Above 10^{-6} at% oxygen corrosion is by oxidation of the surface that on the other hand protects the steel from dissolution of alloying components. No clear statement about the corrosion behavior can be given for the transition zone between 10^{-6} and 10^{-7} at% were dissolution as well as oxidation could be possible. From this discussion it becomes obvious that it is necessary to measure and control the oxygen concentration exactly to keep the conditions of the liquid lead in a range of low corrosion effects. After a certain time period oxygen in Pb or Pb-Bi will be depleted by oxide formation on the surface of the structure steel and thus the conditions will shift to the region with low oxygen concentration and hence strong corrosion effects, if there would be no oxygen control.

In experiments on surface treatment by a pulsed electron beam with the GESA installation [8] it was observed that formation of protective oxide scales can be improved by such treatment. With GESA a surface layer of metals can be molten on a large area (50 cm²) within 10 - 40 µs by just one pulse. The rapid solidification after the pulse with about 10^7 K/s results in a very fine grained structure. By the same process a metal that is precipitated on the surface can be alloyed into the molten layer. Both methods will be applied in this work to examine if the corrosion resistance of steels in liquid lead could be improved.

2. Determination of the conditions for test loops

In large loops the concentration of oxygen may be controlled by solid electrolyte cells that measure and feed oxygen into the liquid lead or lead bismuth. Such cells are sophisticated and require a special know how to build them. Another possibility is control by an atmosphere with a definite oxygen partial pressure that determines the chemical poten-

tial μ_{O_2} of oxygen within the liquid metal bath. To prevent PbO precipitation and to support Fe_3O_4 formation the following conditions must be established:

$$2\Delta G^0_{PbO} > \mu_{O_2} = RT \ln P_{O_2} > 1.5\Delta G^0_{Fe_2O_3} \qquad (1)$$

The standard values ΔG^0 of the free reaction enthalpies are known for the oxides in question and with these values the equilibrium partial pressure region of oxygen that retains the stable conditions can be determined. The easiest way to do this is to draw an Ellingham-Richardson-diagram that contains oxygen potentials as a function of temperature of the relevant oxides PbO, NiO, Fe_2O_3 and Cr_2O_3 and the lines for constant oxygen partial pressures and constant H_2/H_2O ratios as a function of temperature. The latter will be used to control the oxygen potential as follows:

$$P_{O_2} = \frac{P^2_{H_2O}}{P^2_{O_2}} \exp \frac{2\Delta G^0_{H_2O}}{RT} \qquad (2)$$

The Ellingham-Richardson-diagram in Fig. 2 demonstrates in which region the stable conditions exist and how they can be established. The ordinate shows the chemical potential of oxygen, the abscissa the temperature. Dashed lines in the diagram represent the isobars of the oxygen partial pressure and the lines of constant H_2/H_2O ratios in the gas atmosphere above the oxidizing species or above the liquid lead that dissolved oxygen, respectively. The important region in the diagram is the one between the lines of the oxygen potential for PbO and Fe_3O_4 in the temperature regime of 400 - 550 °C.

For working conditions with reduced corrosion we have to select a field of oxygen partial pressures the lines of which would not cross the PbO- and Fe_2O_3-lines within the temperature regime of 400-550°C. Lines of constant H_2/H_2O ratios within the boarders of this field show the ratios that must be established to maintain the appropriate oxygen partial pressures.

If we chose a H_2/H_2O ratio of 0.4 we will attain $Po_2 \cong 10^{-25}$ at 550 °C and $Po_2 \cong 10^{-29}$ at 400 °C. At both temperatures we still form iron oxide and no PbO in the case of stagnant Pb. If we consider a liquid metal loop, there will be no equilibration across the temperature region via the H_2/H_2O ratio but through the oxygen dissolved in Pb (Pb/Bi). In this case we have to consider the variation of the oxygen potential as a function of temperature for the oxygen concentration in liquid lead that exists in equilibrium with the H_2/H_2O ratio in the gas phase at 550 °C.

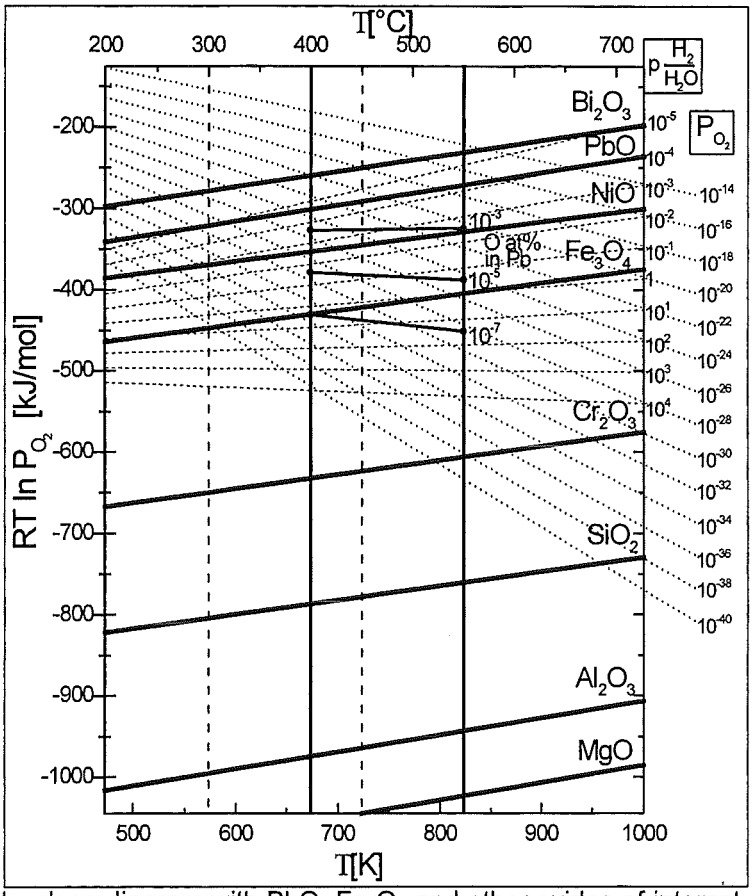

Fig. 2: Ellingham-Richardson-diagram with PbO, Fe_3O_4 and other oxides of interest. Loop temperature regions are marked for Pb by solid, and Pb-Bi by dashed vertical lines.

For the calculation of the oxygen concentration C_0 from the oxygen partial pressure P_{O_2} we need to know the activity coefficient γ_0 that we get from the following relation for the oxygen activity in lead a_O :

$$a_O = \gamma_O C_O = \frac{C_O}{C_{O,s}} = \left(\frac{P_{O_2}}{P_{O_2,s}}\right)^{\frac{1}{2}} \qquad (3)$$

The suffix s indicates the values that correspond to saturation conditions.

With saturation values for the oxygen concentration in lead of $4 \cdot 10^{-2}$ at% at 550 °C and $7.5 \cdot 10^{-3}$ at% at 400 °C [5] equilibrium oxygen concentrations in the range 400 - 550 °C were calculated and drawn in Fig. 2. The solid vertical lines at 400 and 550 °C mark the operating range for a lead cooled loop and the dashed lines at 300 and 450 °C the one for a lead - bismuth coolant. The lines of constant oxygen concentrations indicate safe regions with 10^{-3} - 10^{-5} at% oxygen for the high temperature Pb - loop and 10^{-4} - 10^{-6} at% for the low temperature Pb - Bi loop. Activity coefficients for Pb and Pb - Bi do not differ much in the region above about 50 at % of Pb [7]. Therefore the values calculated here for Pb can be extrapolated for Pb - Bi as an approximation.

The diagram in Fig. 2 also shows the advantage of controlling the oxygen partial pressure

by the H_2/H_2O ratio. It would not be possible with an oxygen partial pressure of 10^{-25} to replace oxygen that was used for oxidation of the surface of the specimen in lead. However with a H_2/H_2O ratio of 0.4 it is easy to replace the oxygen. With a gas flow of 200 cm^3/min it is possible to provide 10 cm^3 O_2/min which corresponds to about 1000 cm^2 Cr_2O_3-oxide layer of 1µ thickness. With this gas flow delivery of the amount necessary for solution of 10^{-6} at% oxygen in 1000 cm^3 Pb would take about one second, therefore, the controlling step is only the uptake of oxygen from the gas phase. Thus, not only small and medium loops could be managed by controlling them via the H_2/H_2O ratio in the gas phase if one can deliver the available oxygen through the surface to the lead, e.g. by bubbling.

3. Experimental

3.1 Materials

Samples of the martensitic steel OPTIFER and of the austenitic steel 1.4970 are prepared for the corrosion tests. The compositions of steels are given in Tab. 1.

C	Si	Mn	P	S	Cr	V	W	Ta
0,12	0,01	0,57	0,003	0,005	9,35	0,26	1,00	0,08

(a)

C	Si	Mn	P	S	Cr	Ni	Mo	Ti
0,10	0,45	1,90	0,007	0,005	15,5	14,6	1,14	0,37

(b)

Table1: Chemical composition of OPTIFER IVc (a) and 1.4970 (b) in wt%

The specimens were small plates of 15 x 10 x 2 mm dimension. Three conditions of specimens are provide:

a) original OPTIFER and 1.4970
b) OPTIFER and 1.4970 after surface treatment by a pulsed electron beam
c) OPTIFER and 1.4970 after surface alloying with Al by a pulsed electron beam

The original steel specimens were polished to improve conditions for analysis of the corrosion effects.

Pulsed electron beam treatment of thin surface layers was done using the pulsed electron beam facility GESA. Because of the rapid cooling rates of about 10^7 K/s and more, the solidified melt layer has very fine grains in the nanometer size range. This has been proofed to be a favorable structure for formation of protective oxide layers with good adhesion [8]. The micrograph of the cross section perpendicular to the surface structure of a treated OPTIFER specimen is presented in Fig. 3. No crystal structure is visible in the so-

lidified melt region on top of the coarse grained base material.

Fig. 3: Micrograph of the cross section of OPTIFER after GESA treatment

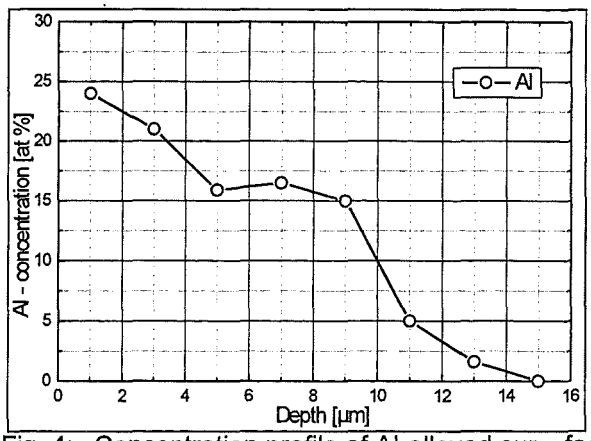

Fig. 4: Concentration profile of Al-alloyed sur- face layer on OPTIFER specimen F3

Surface alloying of the steel specimens was done by applying the electron pulse to the surface covered with a 18 µm thick Al-foil. During surface melting 20 to 25 % of the aluminum is dissolved in the melt layer, the remainder evaporates. The concentration profile of Al perpendicular to the surface is shown in Fig. 4. The micrograph of the cross section is identical to that of in Fig.3. Al penetrates the steel within the molten surface layer. The concentration profile is not typical for a diffusion process, but for a distribution by turbulences in the melt.

The structural changes due to melting and rapid solidification by the GESA-treated alloyed specimens are examined by X-ray diffraction. The spectra are recorded in Fig. 5.

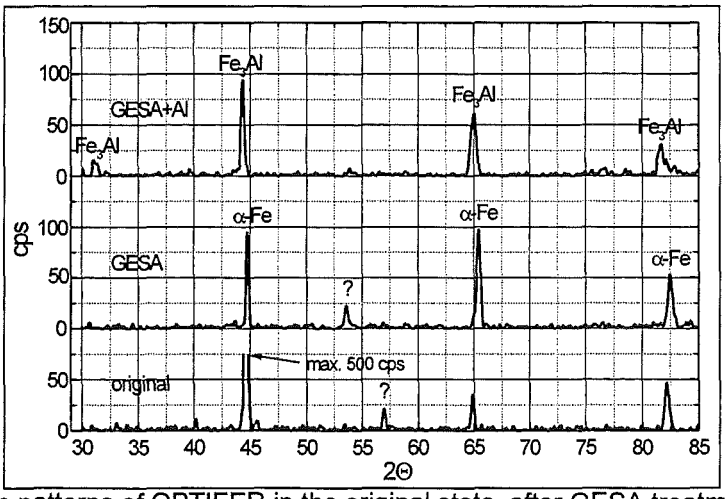

Fig. 5: X-ray diffraction patterns of OPTIFER in the original state, after GESA treatment and after surface alloying of Al

The lower spectrum represents the structure of original OPTIFER containing the major α - Fe peaks (ICPDS 6-696). The origin of the peak at 57° could not be resolved. The spectrum in the middle is that of the rapid solidified melt layer after electron pulse treatment. It shows the same peaks but with some preferential orientation. The unknown peak at 57°

disappeared while another came up at 53.6 which is also unknown. All the peaks are slightly shifted to higher angles. The spectrum on the top is obtained from OPTIFER alloyed with Al by electron pulse melting. It contains peaks that could be ascribed to FeAl as well as to Fe_3Al (ICPS 3320 and 45-1203) that can not be discriminated with our diffractometer. It must be assumed that the second order phase transformation FeAl to Fe_3Al is completed during the rapid cooling process.

3.2 Corrosion tests

A corrosion test stand was build up with control of the oxygen potential via the H_2/H_2O ratio in the gas phase as described above. Fig. 6 shows a scheme of this equipment. The reactor is a quartz tube inside an furnace that is controlled at 550 °C. A mixture of Ar and Ar5%H_2 allows to adjust the hydrogen concentration in the gas. The water vapor is added by passing the gas through water of a definite temperature. The maximum hydrogen concentration that can be introduced is 5 %, which is high enough and well below the lower explosion limit. In the actual experiments the ratio of Ar and Ar5%H_2 is 200 cm^3min^{-1} / 16 cm^3min^{-1} which gives a H_2/H_2O ratio of 0.4 at a water temperature of 7.4 °C. The lead in the furnace is not moved but stagnant and contained in 4 crucibles together with 4 metal specimens. Each crucible contains 40 g of high purity lead.

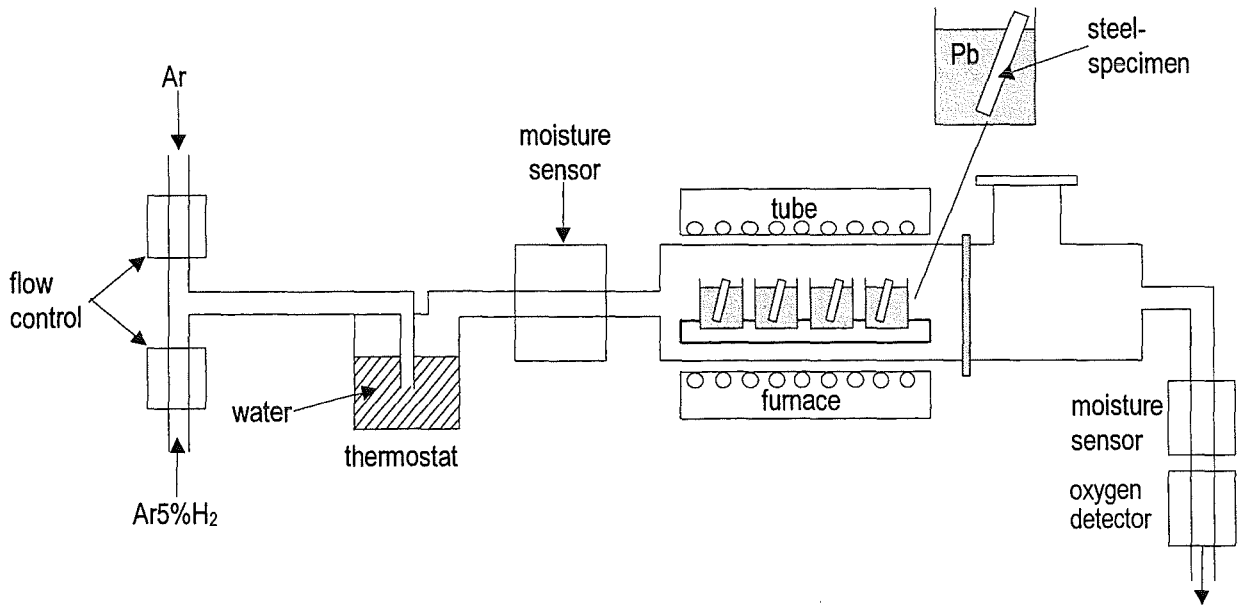

Fig. 6: Corrosion test stand with stagnant liquid lead

The ratios of gas flows are measured and controlled and the partial pressure of water vapor is measured before the gas enters the oven and after it leaves it. There, the gas passes also through an oxygen partial pressure measuring system.

The tests so far run a maximum time of 3000 h. The samples immerged about 1 cm deep

into the liquid lead. Specimens were examined by cutting them perpendicular to the surface and looking at the cross section by Microscope and SEM (Scanning Electron Microscope). The reaction zone and oxide layers at the surface were analyzed by an EDAX (Energy Dispersive Analysis of X-rays) analyzer that is attached to the SEM. The examinations are carried out after 800, 1500 and 3000 h of exposure.

3. Results

The specimens were taken from the reactor after the corrosion test in liquid lead of 550°C under controlled Ar-H_2 / H_2O - atmosphere for metallographic examination and concentration analysis. The specimens and test data are listed in Tab. 2.

Material data			test data			
Spec. No.	Type	Treatment	t_{tot} [h]	mag. scale [µm]	sp. zone [µm]	diff. zone [µm]
F1	OPTIFER	original	3000	20	15	10
F2		e - pulse	3000	16	15	8
F3		Al - alloyed	1500	none	none	none
A1	1.4970	original	3000	10	6	12(1)
A2		e - pulse	3000	6	6	3(1)
A3		Al - alloyed	1500	none	none	none

mag. = magnetite; sp = Fe (Fe, Cr)$_2$ O_4; e-pulse = pulsed electron beam, GESA;
(1) including grain boundary penetration

Table 2: Materials and test data after maximum exposure to lead at 550 °C oxygen concentration of $8 \cdot 10^{-6}$ at %

The cross section of the original OPTIFER specimen F1 after exposure is presented in Fig. 7 together with the concentration profiles as a function of the distance from the original specimen surface. The micrograph of the cross section shows the typical corrosion attack that represents three different zones. The zone at the top, that ends at the original specimen surface, consists of magnetite without appreciable Cr - concentration. It is obviously brittle, because many defects caused by spallation of scale parts exist. The layer in the middle contains Cr-Fe spinel, that roots in the pore belt. At some places the spinel layer is also missing more pronounced at other places. In the interior an oxygen diffusion zone can be observed in which oxides precipitate along the grain boundaries. The concentration profile in Fig. 7a indicates the zone structure also. Since quantitative determination of the oxygen content was not possible, the ordinate scale presents arbitrary values for oxygen that are proportional to the count rate of oxygen during the EDAX analysis. The measurement results in a maximum of oxygen at the scale surface followed by a constant oxygen concentration throughout the magnetite and spinel region, in the latter one on a slightly lower level. The concentration in the diffusion zone is about 20% of that

in the magnetite scale.

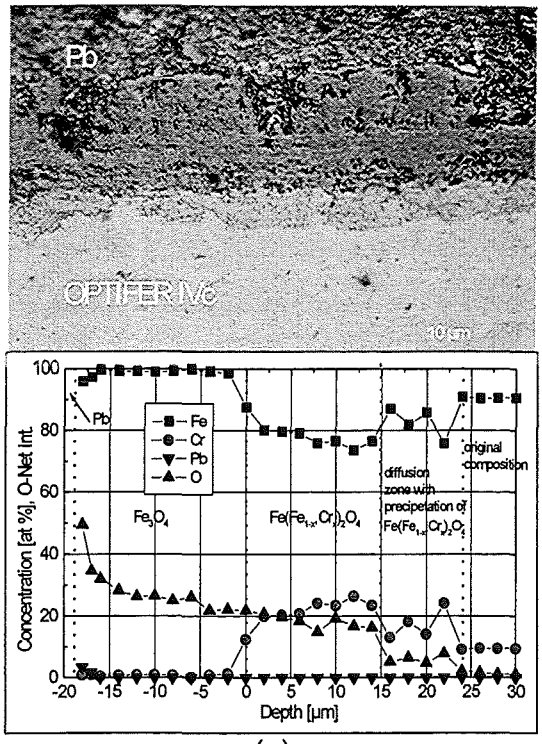

(a)

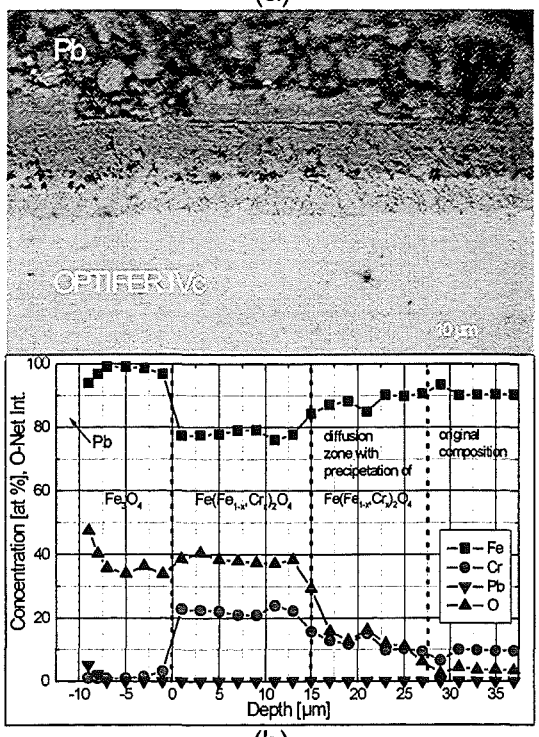

(b)

Fig. 7: Micrograph of cross section of OPTIFER original specimens and EDAX concentration profiles after 3000 h at 550 °C. Metallic elements sum up to 100%. Oxygen in arbitrary units proportional to the netto integral of the K_α -peak.
(a): original F1,(b): GESA treated F2.

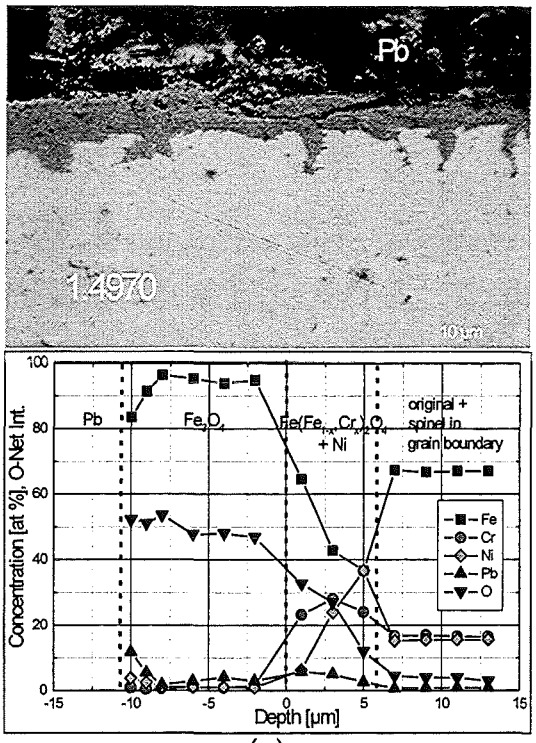

(a)

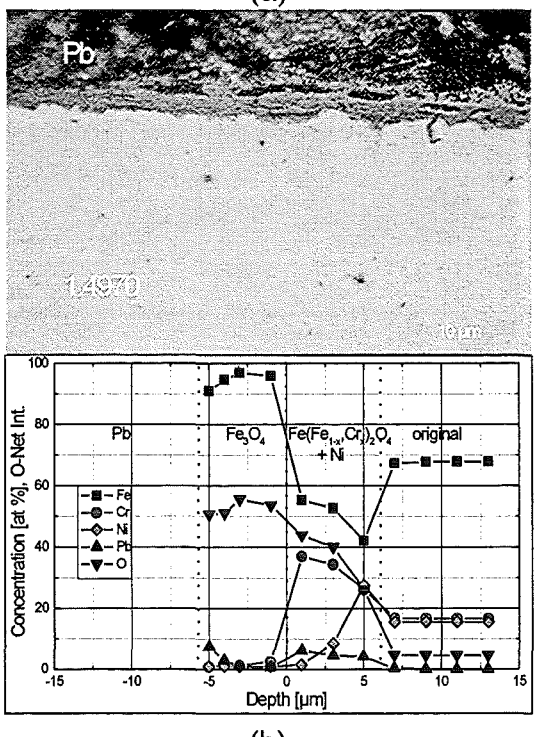

(b)

Fig. 8: Micrograph of cross section of 1.4970 original specimens and EDAX concentration profiles after 3000 h at 550 °C. Metallic elements sum up to 100%. Oxygen in arbitrary units proportional to the netto integral of the K_α -peak.
(a): original A1, (b): GESA treated A2.

Peaks in this zone indicate spinel precipitation in a grain boundary. Within the spinel zone the Cr - concentration reaches a maximum of twice the concentration in the bulk due to Fe depletion by the magnetite scale formation.

Specimen F2, that was treated by an electron pulse before the test shows the same features, as the one in the non treated specimen F1. Different is the size of the magnetite scale, which is smaller and more compact than on the untreated surface but is also partially spalled off, Fig. 7b. Furthermore, the spinel layer is completely retained without spallation.

The structure of the oxidation zone in the original austenitic specimen A1 is similar to that in the ferritic steel with layers of magnetite and Fe-Cr-spinel and an oxygen diffusion zone in the interior. But, the Fe-Cr-spinel zone contains Pb and oxygen penetrates along grain boundaries up to 20 µm deep into the metal matrix, Fig. 8. Remarkable is the strong depletion of Ni within the spinel zone, that was observed already after 800 h of exposure and did not change markedly since that time.

The oxygen diffusion zone is much smaller in the electron pulse treated specimen A2 than in A1,because it not show the deep grain boundary attack, Fig. 8. The Pb-containing spinel layer looks tighter and smaller and is strongly depleted in Ni. Most of the magnetite layer got also lost.

Completely different is the behavior of specimen F3 alloyed with Al during the electron pulse treatment on one half of the surface.

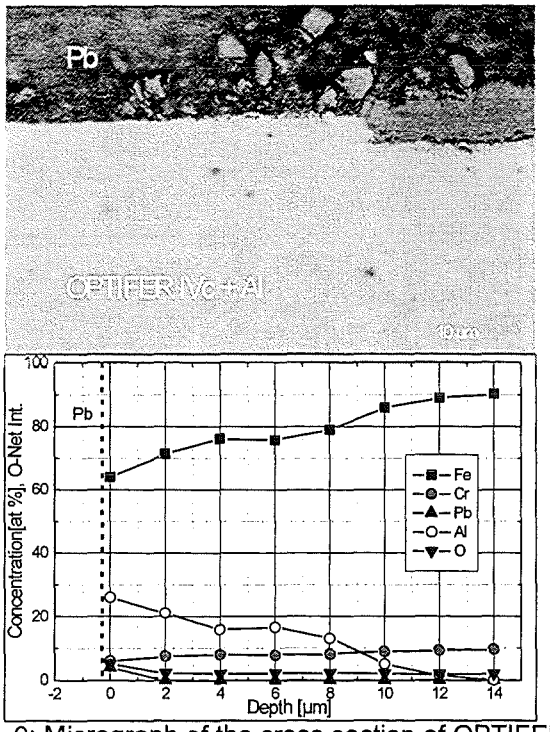

Fig. 9: Micrograph of the cross section of OPTIFER specimen F3 alloyed with Al on the left part and EDAX concentration profiles through the alloyed surface layer after 1500 h at 550 °C. Metallic elements sum up to 100%. Oxygen in arbitrary units proportional to the netto integral of the K_α -peak.

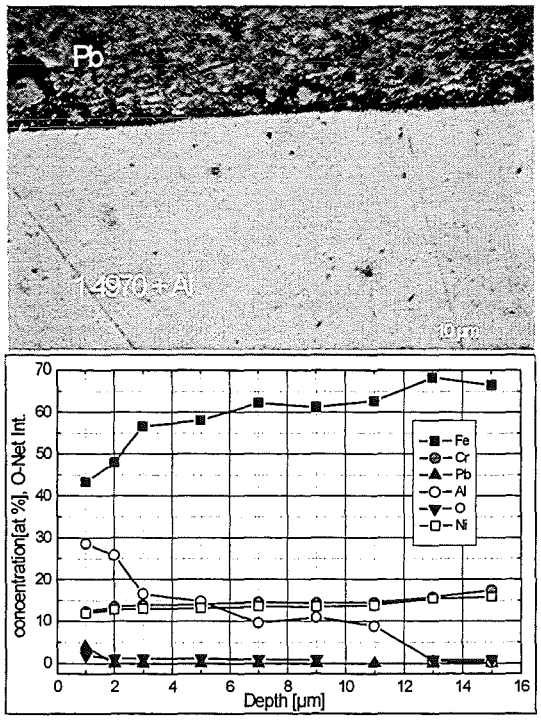

Fig. 10: 1.4970 alloyed with aluminum after 1500 h at 550 °C in liquid Pb.

There is no corrosion attack visible in the alloyed part at all after 1500 h exposure to liquid lead at 550 °C, Fig. 9. Also the concentration profiles do not give any indication of an interaction between lead or oxygen and the alloyed specimen part. Only the unalloyed part of the surface to the right is covered with thick oxide scales. It is obvious from this micrograph that the Fe -Cr spinel layer ends at the original specimen surface.
From the concentration profiles of the Al- alloyed austenitic specimen A3 there is no attack observable at all, Fig. 10. No oxygen penetration through the surface and no Ni-depletion took place. The micrograph does not show any signs of corrosion.

4. Discussion of results

The examination of the corrosion tests with OPTIFER and 1.4970 steel specimens proof hat the behavior of these materials in liquid lead differs with the treatment of the surface. Large oxidation layers are formed at the unalloyed OPTIFER surface. They are smaller at 1.4970.
No oxidation attack can be observed at both steel surfaces alloyed with Al.
Three distinct oxidation zones are developed at the unalloyed steel surface , an outer magnetite scale that is placed on top of the original surface, a $Fe^{2+}(Fe^{3+}_{1-x}, Cr^{3+}_{x})_2O_4$ spinel layer that lays beneath the original surface and below this one beyond a pore belt an oxygen diffusion zone with spinel formation along grain boundaries, Fig.11. From the concentration curves x-results in about 0.3 for OPTIFER and in a maximum value of 0.6 for 1.4970.

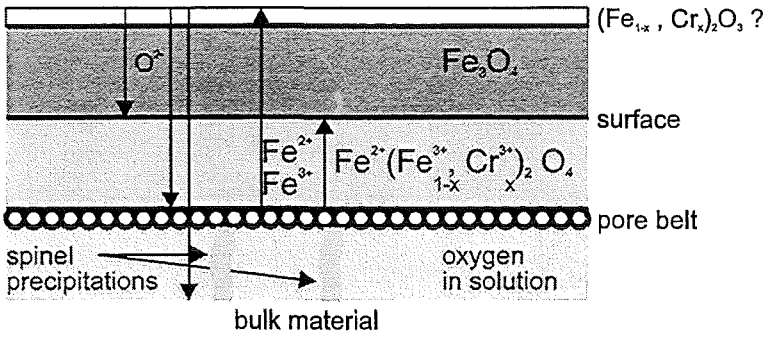

Fig. 11: Scheme of oxidation zones and ion migration

This agrees with descriptions by Hauffe [9] and Talbot [10] for oxidation of steels on air at temperatures below 570 °C. The only difference to our results obtained by experiments in liquid lead containing 8 10^{-6} at% oxygen consists in the practically Cr - free magnetite scale that develops on the steel - lead interface. This, however corresponds to the preferred stratified scale type described by Whittle and Wood [11] for iron - chromium alloys

with less than 18 % Cr.

Analog to the oxidation mechanism described [9, 10] as well anion- as cation-diffusion can be called responsible for the formation of the oxide layers. Oxygen penetrates the surface to form at first Fe-Cr-spinel that grows inwards [12]. Fe-ions migrate to the surface get oxidized and produce from there the magnetite scale. This scale starts exactly at the surface and does not contain more than 1 % of chromium. Oxygen migrates easily through the magnetite scale to the specimen surface, feeds the scale growth and partly diffuses into the spinel zone and solution zone. On the other hand iron ions migrate through the magnetite layer and oxidize at the surface of the magnetite scale. By this two processes the magnetite scale grows from both sides, like indicated in the scheme of the oxidation zones and the migrating ions in Fig. 11.

The behavior of 1.4970 specimens differ substantially from those of OPTIFER, although the stratified scale structure is the same. The magnetite scale is much smaller than that of OPTIFER if it is visible at all. The same concerns the spinel zone and the diffusion zone with exception of the deep grain boundary penetration of oxygen in the nontreated specimen A1 in Fig. 8. This is because of the higher oxidation resistance of high alloyed steels [13].

As opposed to the OPTIFER, 1.4970 shows Pb - inclusions in the interface region between the magnetite scale and the spinel layer that reaches frequently into the spinel, Figs. 8. This effect depends obviously on the presence of Ni in the initial stage of scale formation when Ni is dissolved by liquid lead that gets trapped by the growing magnetite scale and solidifies with about 2 at% of Ni [5]. After this process the Ni depletion does not change any more with increasing exposure time. Thus, the Ni depletion zones in Figs. 10a, b represent those established in the time before the first examination at 800 h of exposure.

The influence of electron pulse melting of a surface layer of the unalloyed materials on the corrosion behavior in liquid lead at 550 °C after 3000 h exposure time manifests in some more or less important effects. In OPTIFER it causes a smaller magnetite scale and better spallation resistance of the spinel zone while in 1.4970 the deep grain boundary penetration of oxygen is avoided. The reason for this behavior is thought to be the much finer grain structure in the specimen surface layer after melting and rapid solidification. However, if there will be a benefit of this effects for the corrosion behavior can not yet be said with confidence. Tests with much longer exposure times and experiments in loops will be necessary to attain to confidential statements.

In the comparison of OPTIFER and 1.4970, the austenitic material should be favored so far after 3000 h, especially when the surface is treated by GESA. The corrosion zone consisting of the spinel layer and the diffusion zone is much smaller after that time. Fig. 13 shows the growth of the corrosion zones in both steels with and without surface treatment. The points represent the mean values of 5 measurements each at a different position of the surface. At least for the first 3000 h it indicates the better performance of 1.4970 with advantages for the surface treated specimen. No visible advantage can be observed for the treated OPTIFER specimen. The fragile magnetite scale is not considered in the evaluation because it constitutes a corrosion product that lies above the original specimen surface and is lost in the greatest part of the surface area. This effect will be enhanced by the flowing lead in loops.

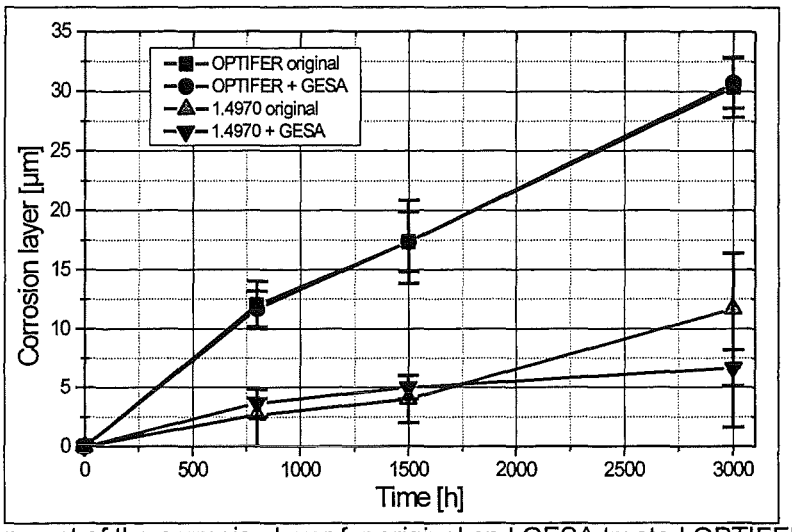

Fig. 13: Development of the corrosion layer for original and GESA treated OPTIFER and 1.4970.

The most striking effect is obtained with both, OPTIFER and 1.4970, when Al is alloyed into the surface layer during melting by GESA. The alumina layer that must have been formed at the surface during oxidation in lead with $8 \cdot 10^{-6}$ at% of oxygen should be very thin and could not be detected up to now. However, it constitutes such an effective barrier against corrosion that up to now after 1500 h not even a minimal attack occurred.

5. Conclusions

Oxide layers on steel can effectively prevent from leaching of the steel components by dissolution in liquid lead. To maintain the oxide layers over long exposure time it is necessary to control the oxygen concentration in lead. By this procedure the corrosion attack is changed from that of liquid metal corrosion to that of oxidation. Thus, it is needed to

find materials that from stable protective oxide scales under conditions in liquid lead.
Among the two materials OPTIFER, a martensitic steel, and 1.4970, an austenitic steel, the austenite shows better performance in liquid lead under oxygen control than OPTIFER. This is a consequence of the better oxidation resistance of 1.4970.
Electron pulse treatment improved the behavior of 1.4970 only because it suppresses deep grain boundary penetration of oxygen due to the fine grained structure that forms in melting and rapid solidification.
Alloying of aluminum into the surface by pulsed electron beam surface melting improves the corrosion oxidation behavior of both examined steel types in an impressive manner. No corrosion attack at all was observed after 1500 h of exposure. Therefore, liquid lead or lead-bismuth resistant candidates should be searched among the high temperature oxidation resistant steels that form stable oxide layers.
Oxidation scale formation under controlled gas atmosphere obeys the same principle mechanisms as in liquid lead with an oxygen concentration that corresponds to the same oxygen potential.
Oxygen in liquid lead loops can be controlled through the gas atmosphere via the hydrogen / water ratio.
Findings in this work are just as well applicable to Pb-Bi loops.

6. References

[1] C. Rubbia, J.A.Rubio, S. Buono, F. Carminati, Conceptual Design of a Fast Neutron Operated High Power Energy Amplifier, CERN/AT/95-44 (ET), September 29, 1995

[2] G. Y. Lai, ´High Temperature Corrosion of Engineering Alloys´, ASM Int. (1990)

[3] R. C. Asher, D. Davies, S. A. Beetham, Corrosion Science, 17 (1977) 545

[4] B. F. Gromov, Yu. I. Orlov, P. N. Martynov, K. D. Ivanov, V. A. Gulevski in ´Liquid Metal Systems´, Edited by H. U. Borgstedt and G. Frees, Plenum Press (1995) 339

[5] T.B. Massalski, Editor, ´Binary Phase Diagrams´ ASM Int. (1990)

[6] R. P. Elliott, ´Constitution of Binary Alloys´, First Supplement, McGraw-Hill Book Company, 1965

[7] V. Markov, Seminar on the Concept of Lead-Cooled fast Reactor, Cadarache september 22-23, 1997 (unpublished)

[8] G. Müller, G. Schumacher, D. Strauß, Surface and Coating Technology, 108-109 (1998) 43

[9] K. Hauffe, ´Oxidation of Metals´, Plenum Press 1965

[10] D. Talbot, J. Talbot, ´Corrosion Science and Technology´, CRC Press, 1998

[11] D. P. Whittle, G. C. Wood, J. Electrochem. Soc., 114/10 (1967) 986

[12] K. Kuroda, P. A. Labun, G. Welsch and T. E. Mitchell, ´Oxidation of Metals, 19, 3/4, (1983) 117

[13] S. K. Mitra, S.K. Roy and S. K. Bose, ´Oxidation of metals´, Vol. 34, Nos. 1/2, 1990

VI. Auslegungsorientierte Analysen

(E. Aronskaia, HIK; L. Carteciano, R. Dagan, B. Dorr, G. Grötzbach, W. Pfrang, M. Schikorr, P. Schmidt, D. Struwe, W. Zimmerer, IRS)

Beschleunigergetriebene, unterkritische Anordnungen weisen gegenüber kritischen Kernanordnungen eine Reihe von Besonderheiten auf, die bei der Auslegung und der Sicherheitsanalyse dieser Systeme besonders beachtet werden müssen. Im Mittelpunkt der derzeitigen Analysen steht ein Referenzkernentwurf auf der Grundlage von drei symmetrisch im Kernquerschnitt angeordneten Protonenquellen. Erste Analysen zur thermohydraulischen Auslegung dieser Kernanordnung wurden mit dem Programm THESYS durchgeführt. Betrachtet wurde der Zustand frischer Beladung und der Zustand, der sich nach einer Standzeit von 250 Tagen einstellt. Die über den Kernquerschnitt stark variierende Leistungsverteilung erfordert eine Aufteilung der Brennelemente in vier Kühlgruppen unterschiedlichen Kühlmittel-durchsatzes. Die Unterschiede der Kühlmittelaustrittstemperaturen sind relativ groß und die Änderungen über der Standzeit auch. Zukünftige Arbeiten müssen sich hier auf eine Optimierung der Auslegungsbedingungen konzentrieren.

Für die Brennstabauslegung wird eine Datenbasis für den Brennstoff (Th-, U- bzw. Pu-Mischoxid) benötigt. Erste Schritte in dieser Richtung wurden realisiert. Die Daten für die thermodynamische Auslegung liegen nun weitgehend vor. Daten zum mechanischen Verhalten derartiger Brennstoffe sind nur schwer zugänglich. Schon heute ist absehbar, daß eine belastbare Auslegung ein geeignetes experimentelles Programm für die ausgewählten Brennstoffe voraussetzt.

Zur sicherheitstechnischen Bewertung der Kernanordnungen wurde das Programm SAS4A derart erweitert, daß das dynamische Verhalten von unterkritischen Anordnungen mit der punktkinetischen Näherung näherungsweise erfaßt wird. Erste Analysen wurden durchgeführt, um Aussagen aus der Literatur zu den sicherheitstechnischen Vorteilen dieser Kernanordnungen zu überprüfen. Es hat sich gezeigt, daß die vielfach zitierten inhärenten Sicherheitseigenschaften nicht uneingeschränkt gelten und insbesondere von der Lage der Quelle und deren Energiespektrum abhängig sind. Die wesentliche Problematik sicherheitstechnischer Analysen liegt in der Bereitstellung von geeignet ermittelten Reaktivitätsrück-

wirkungskoeffizienten. In enger Zusammenarbeit mit dem INR wurden dazu erste Analysen durchgeführt. Es hat sich gezeigt, daß für ein unterkritisches System die bekannten, für kritische Reaktoren entwickelten Verfahren nicht unmittelbar einsetzbar sind. Analysen auf der Grundlage von Störungstheorie erster Ordnung sind kaum belastbar, da sich die Neutronenflußverteilungen in Abhängigkeit von Lage und Energiespektrum der Protonenquelle stark ändern. In diesem Bereich werden zur Zeit noch grundlegende Arbeiten durchgeführt.

Für die numerische Analyse der Kühlungsmöglichkeiten in Tanks von beschleunigergetriebenen, unterkritischen Anordnung soll das Rechenprogramm FLUTAN angewendet werden. Dafür mußte die in FLUTAN implementierte Stoffdatenbibliothek um die Stoffdaten für Blei ergänzt werden. Die vom INR zusammengestellten Stoffdaten für flüssiges Blei wurden programmiert und getestet. Das Programmpaket umfaßt die Stoffdaten für Dichte, spezifische Wärme, Wärmeleitfähigkeit und Viskosität. Die erweiterte Stoffdatenbibliothek wurde in FLUTAN implementiert und nach Überprüfung freigegeben.

Veröffentlichte Berichte

Schriftliche Veröffentlichungen

AHLBRECHT, M.; BORODIN, R.; BORZENKO, V.; EHRHARDT, J.; FRENCH, S.; SHERSHAKOV, V.; SOHIER, A.; TRKHTENGERTS, E.; VERBRUGGEN, A.
Decision support issues in RODOS: the needs of decision makers.
RODOS: Decision Support for Nuclear Emergencies
Wissenschaftliche Berichte, FZKA-6069 (März 98) S.94-99
RODOS R-3-1998 (43247)

ALBRECHT, G.; BRÜGGEMANN, H.; HUBER, F.; RAUPP, D.; SCHÜTZ, W.
Untersuchungen zum EPR-Konzept - KAJET-Versuche.
Projekt Nukleare Sicherheitsforschung. Jahresbericht 1997.
Wissenschaftliche Berichte, FZKA-6126 (September 98) S.267-71 (44205)

ALBRECHT, G.; HUBER, F.
KAJET experiments on pressurized melt jets and their interaction with substratum materials.
Jahrestagung Kerntechnik 98, München, 26.-28.Mai 1998
Bonn : INFORUM GmbH, 1998 S.149-52 (44091)

ALSMEYER, H.; ADELHELM, C.; BENZ, H.; CRON, T.; PASLER, H.; SCHÖCK, W.; SCHUMACHER, G.; TROMM, W.; SPENCER, B.W.; FARMER, M.T.
Das COMET-Kernfängerkonzept: Experimente mit Nachbeheizung und mit Uranschmelzen.
Jahrestagung Kerntechnik 98, München, 26.-28.Mai 1998
Bonn : INFORUM GmbH, 1998 S.157-60 (43031)

ALSMEYER, H.; CRON, T.; FOIT, J.J.; SCHMIDT-STIEFEL, S.; SCHNEIDER, H.; TROMM, W.; WENZ, T.; FERDERER, F.; ADELHELM, C.; DILLMANN, H.G.; PASLER, H.; SCHÖCK, W.; SCHUMACHER, G.; BENZ, H.; GREHL, C.; MERKEL, G.; RATAJCZAK, W.
COMET-Konzept.
Projekt Nukleare Sicherheitsforschung. Jahresbericht 1997.
Wissenschaftliche Berichte, FZKA-6126 (September 98) S.229-55 (44203)

ALSMEYER, H.; FARMER, M.; FERDERER, F.; SPENCER, B.; TROMM, W.
The COMET-concept for cooling of ex-vessel corium melts.
ICONE-6 : Proc.of the 6th Internat.Conf.on Nuclear Engineering, San Diego, Calif., May 10-15, 1998
New York, N.Y. : ASME, 1998, CD-ROM (44113)

ALSMEYER, H.; FIEG, G.; TROMM, W.; WERLE, H.
FZK investigations on ex-vessel melt behavior.
Brennelementtechnik, Kernauslegung, Reaktorbetrieb : Fachtagung der KTG-Fachgruppen 'Brennelemente' und 'Reaktorphysik und Berechnungsmethoden', Karlsruhe, 3.-4.Februar 1998
Tagungsbd. S.143-53 (42879)

ARNECKE, G.; JACOBS, H.; STEHLE, B.; THURNAY, K.; VÄTH, L.; BÖTTCHER, M.; IMKE, U.; LUMMER, M.
Theoretische Arbeiten zur Schmelze-Kühlmittel-Wechselwirkung.
Projekt Nukleare Sicherheitsforschung. Jahresbericht 1997.
Wissenschaftliche Berichte, FZKA-6126 (September 98) S.168-75 (44199)

BAUMANN, W.; ROCHHOLZ, H.; WILKENING, H.; BOTTONI, M.; NECKER, G.; ROYL, P.; TRAVIS, J.R.; SPORE, J.
Hydrogen distribution. Theoretical investigations with GASFLOW.
Projekt Nukleare Sicherheitsforschung. Jahresbericht 1997.
Wissenschaftliche Berichte, FZKA-6126 (September 98) S.27-70 (44192)

BAUMANN, W.; ROYL, P.
Validating the GASFLOW modelling of condensation with Phebus containment thermal hydraulics.
Projekt Nukleare Sicherheitsforschung. Jahresbericht 1997.
Wissenschaftliche Berichte, FZKA-6126 (September 98) S.71-81 (44193)

BEJAN, A.; DAN, N.; CACUCI, D.G.; SCHÜTZ, W.
On the thermodynamic efficiency of energy conversion during the thermal interaction between hot particles, water and steam.
Wissenschaftliche Berichte, FZKA-6020 (Juni 98) (43519)

BENNEK-KAMMERICHS, B.; EHRLICH, K.; FALKENSTEIN, A.; HEGER, S.; HÜBNER, R.; SCHIRRA, M.
Untersuchungen an austenitischen Stählen.
Projekt Nukleare Sicherheitsforschung. Jahresbericht 1997.
Wissenschaftliche Berichte, FZKA-6126 (September 98) S.508-11 (44222)

BLANK, H.; MAUSSNER, H.; MATZKE, H.J.; RAY, I.L.F.; EHRLICH, K.; MATERNA-MORRIS, E.; SCHNEIDER, W.
Nuclear materials.
Amelinckx, S. [Hrsg.]
Handbook of Microscopy : Applications in Materials Science, Solid-State Physics and Chemistry
Vol.3. Applications S.583-664
Weinheim : VCH, 1997 (43074)

BORGSTEDT, H.U.
The solubility of nickel in sodium calculated from corrosion tests in flowing liquid metal.
Zeitschrift für Metallkunde, 89(1998) S.199-202 (43162)

BREITUNG, W.; KOTCHOURKO, A.; VESER, A.; SCHOLTYSSEK, W.
Reactive flow simulation in complex 3D geometries using the COM3D code.
Severe Accident Research in Japan (SARJ), Tokyo, J, November 4-6, 1998, Proc. (V44651)

BREITUNG, W.; VESER, A.
Wasserstoffverbrennungsvorgänge. Zusammenfassung.
Projekt Nukleare Sicherheitsforschung. Jahresbericht 1997.
Wissenschaftliche Berichte, FZKA-6126 (September 98) S.1-6 (44190)

BROEDERS, C.H.M.
Investigations on fuel utilization and transuranium buildup in PWRs.
Zrodnikov, A.V. [Hrsg.]
ICENES '96 : The 8th Internat.Conf.on Emerging Nuclear Energy Systems, Obninsk, GUS, June 24-28, 1996 Proc. Vol.1 S.191-95
Obninsk : Inst.of Physics and Power Engineering, 1997 (39793)

BROEDERS, I.; BROEDERS, C.H.M.
Implementation, development, validation and first applications of different code chains for the investigation of accelerator-driven transmutation.
Zrodnikov, A.V. [Hrsg.]
ICENES '96 : The 8th Internat.Conf.on Emerging Nuclear Energy Systems, Obninsk, GUS, June 24-28, 1996 Proc. Vol.2 S.734-39
Obninsk : Inst.of Physics and Power Engineering, 1997 (39792)

BROEDERS, C.; BROEDERS, I.
Generation of a group constant library for neutron energy until 50 MeV. Tests and applications.
Projekt Nukleare Sicherheitsforschung. Jahresbericht 1997.
Wissenschaftliche Berichte, FZKA-6126 (September 98) S.580-86 (44236)

BUNK, M.; WÖRNER, M.
Direkte numerische Simulation turbulenter Rayleigh-Benard-Konvektion in Quecksilber.
Wissenschaftliche Berichte, FZKA-5915 (April 98)
http://hikwww4.fzk.de/hbk/literatur/ABSTRACTS/5915.htm (43139)

CACUCI, D.G.
Two-dimensional geometrical corner singularities in neutron diffusion. Part I: analysis.
Nuclear Science and Engineering, 128(1998) S.1-16 (42882)

CACUCI, D.G.; IONESCU-BUJOR, M.
Sensitivity analysis of thermodynamic properties of water: a prerequisite for deterministic sensitivity analysis of thermal-hydraulic codes.
ICONE-6 : Proc.of the 6th Internat.Conf.on Nuclear Engineering, San Diego, Calif., May 10-15, 1998
New York, N.Y. : ASME, 1998, CD-ROM (44115)

CACUCI, D.G.; KIEFHABER, E.; STEHLE, B.
Two-dimensional geometrical corner singularities in neutron diffusion. Part II: application to the SNR-300 benchmark.
Nuclear Science and Engineering, 128(1998) S.17-26 (42883)

CHENG, X.
Entwicklung experimentell gestützter analytischer Verfahren zur Auslegung der Containmentkühlung mit Luft durch Naturkonvektion.
Wissenschaftliche Berichte, FZKA-6056 (Februar 98)
http://hikwww4.fzk.de/hbk/literatur/ABSTRACTS/6056.htm
http://hikwww4.fzk.de/hbk/literatur/FZKA_Berichte/FZKA6056.pdf (43089)

CHENG, X.
Critical heat flux in tight 37-rod bundles.
ICONE-6 : Proc.of the 6th Internat.Conf.on Nuclear Engineering, San Diego, Calif., May 10-14, 1998
New York, N.Y. : ASME, 1998, CD-ROM (44753)

CHENG, X.; MÜLLER, U.
Turbulent natural convection coupled with thermal radiation in large vertical channels with asymmetric heating.
International Journal of Heat and Mass Transfer, 41(1998) S.1681-92 (43360)

CHENG, X.; NEITZEL, H.J.
Heat transfer of naturally induced turbulent convection in advanced reactor containment.
2nd EF Conf.in Turbulent Heat Transfer, Manchester, GB, May 31-June 4, 1998
Manchester : UMIST, 1998 Vol.II S.7-3 - 7-13 (43693)

CHENG, X.; NEITZEL, H.J.; SCHMIDT, H.; KNEBEL, J.U.
PASCO-Programm.
Projekt Nukleare Sicherheitsforschung. Jahresbericht 1997.
Wissenschaftliche Berichte, FZKA-6126 (September 98) S.304-09 (44209)

CHERDRON, W.; GRÖTZBACH, G.; ABERLE, J.; PHILIPP, P.; SAUTER, H.; SIMON, M.; TISEANU, I.
Experimentelle Untersuchungen von Wechselwirkungsmechanismen und Phasentransportprozessen in Zweiphasenströmungen.
Projekt Nukleare Sicherheitsforschung. Jahresbericht 1997.
Wissenschaftliche Berichte, FZKA-6126 (September 98) S.505-07 (44221)

CHERDRON, W.; GRÖTZBACH, G.; SAMSTAG, M.; SENGPIEL, W.; SIMON, M.; TISEANU, I.
Experimental investigation of air/water bubbly flow in vertical gaps.
ICMF '98 : Proc.of the 3rd Internat.Conf.on Multiphase Flow, Lyon, F, June 8-12, 1998
Adobe Systems Incorporated, 1998
CD-ROM (44173)

COGNET, G.; ALSMEYER, H.; MORRIS, S.; WITTMAACK, R.; SEHGAL, B.R.; BÜRGER, M.; DE CECCO, L.; OCELLI, R.; AZARIAN, G.; RANVAL, W.; SPINDLER, B.
Corium spreading and coolability (CSC project).
FISA-97 Symp.on EU Research on Severe Accidents, Luxembourg, L, November 17-19, 1997
Preprints S.141-51
Luxembourg : European Commission, 1997
(42317)

DOLENSKY, B.; GÖLLER, B.; HAILFINGER, G.; HIRT, A.; HOFFMANN, G.; JONATZKE, O.; JORDAN, T.; KRIEG, R.; LANG, K.H.; MALMBERG, T.; MESSEMER, G.; STRATMANNS, E.; VORBERG, G.
Mechanische Auswirkungen auf den Reaktordruckbehälter.
Projekt Nukleare Sicherheitsforschung. Jahresbericht 1997.
Wissenschaftliche Berichte, FZKA-6126 (September 98) S.310-19 (44210)

EFIMENKO, A.A.; DENKEVITS, A.V.; DOROFEEV, S.B.; BREITUNG, W.
Numerical investigation of missiles acceleration by hydrogen explosion.
Internat.Symp.on Hazards, Prevention, and Mitigation of Industrial Explosion, Colloquium on Gas, Vapor, Hybrid and Fuel-Air Explosions, Schaumburg, Ill., September 21-25, 1998
Proc. S.367-90 (44649)

EHRHARD, P.; BUNK, M.; FELLMOSER, F.; FIEG, G.; FOIT, J.J.; HUBER, F.; MÜLLER, U.; SIEGEL, U.; STEGMAIER, U.; WERLE, H.; WITTMAACK, R.
Spreading of the core melt on the spreading area of the EPR.
ICONE-6 : Proc.of the 6th Internat.Conf.on Nuclear Engineering, San Diego, Calif., May 10-15, 1998
New York, N.Y. : ASME, 1998, CD-ROM (42994)

EHRHARD, P.; BUNK, M.; FOIT, J.J.; MÜLLER, U.; SIEGEL, U.; FELLMOSER, F.; FIEG, G.; WERLE, H.; HUBER, F.; STEGMAIER, U.; WITTMAACK, R.
Spreading of the core melt on the spreading area of the EPR.
Projekt Nukleare Sicherheitsforschung. Jahresbericht 1997.
Wissenschaftliche Berichte, FZKA-6126 (September 98) S.272-86 (44206)

EHRHARDT, J.
The RODOS system: decision support for off-site emergency management in Europe.
RODOS: Decision Support for Nuclear Emergencies
Wissenschaftliche Berichte, FZKA-6069 (März 98) S.13-22
RODOS R-3-1998 (43242)

EHRHARDT, J.; BROWN, J.; FRENCH, S.; KELLY, G.N.; MIKKELSEN, T.; MÜLLER, H.
RODOS: real-time on-line decision support system for off-site emergency management in Europe.
SARM '97 : Internat.Topical Meeting on Severe Accident Risk and Management, Piestany, Slovakia, June 16-18, 1997 Trnava : VUJE, 1998 CD-ROM (41924)

EHRHARDT, J.; FAUDE, D.; FISCHER, F.; HASEMANN, I.; LORENZ, A.; PÄSLER-SAUER, J.; SCHICHTEL, T.; SCHÜLE, O.; STEINHAUER, C.; BENZ, G.; HALLER, CH.; RAFAT, M.; SAUDER, T.
Entwicklung von Methoden zur Abschätzung und Minimierung der radiologischen Folgen von Reaktorunfällen.
Projekt Nukleare Sicherheitsforschung. Jahresbericht 1997.
Wissenschaftliche Berichte, FZKA-6126 (September 98) S.469-79 (44218)

EHRHARDT, J.; RAFAT, M.; SCHÜLE, O.
Operationeller Betrieb und Weiterentwicklung des Entscheidungshilfesystems RODOS.
10.Fachgespräch zur Überwachung der Umweltradioaktivität, Hamburg, 28.-30.April 1998
Tagungsband S.345-50 (43256)

EHRHARDT, J.; WEIS, A.; [HRSG.]
RODOS: decision support for nuclear emergencies.
Wissenschaftliche Berichte, FZKA-6069 (März 98)
RODOS R-3-1998 (43241)

EHRHARDT, J.; WEIS, A.; [HRSG.]
Mid-term report of the RODOS-project. Report period: 1 January 1996 to 31 December 1997.
Wissenschaftliche Berichte, FZKA-6203 (Dezember 98) (44632)

EIGEMANN, M.; PFRANG, W.; PORSCHA, B.; STRUWE, D.; ZIMMERER, W.
SAS4A-Programmentwicklung.
Projekt Nukleare Sicherheitsforschung. Jahresbericht 1997.
Wissenschaftliche Berichte, FZKA-6126 (September 98) S.555-57 (44231)

ELIAS, E.; SANCHEZ, V.; HERING, W.
Development and validation of a transition boiling model for RELAP5/MOD3 reflood simulation.
Nuclear Engineering and Design, 183(1998) S.269-86 (44239)

ENGEL, G.; FELLMOSER, F.; FIEG, G.; MASSIER, H.; WERLE, H.; PROTHMANN, N.; RAUPP, D.; SCHÜTZ, W.; STEGMAIER, U.
Untersuchungen zum EPR-Konzept - KAPOOL- und KATS-Experimente.
Projekt Nukleare Sicherheitsforschung. Jahresbericht 1997.
Wissenschaftliche Berichte, FZKA-6126 (September 98) S.256-66 (44204)

ERBACHER, F.J.; CHENG, X.; NEITZEL, H.J.
Research at Forschungszentrum Karlsruhe on passive containment cooling by natural air convection and thermal radiation.
Jahrestagung Kerntechnik, Mannheim, 21.-23.Mai 1996
Bonn : INFORUM GmbH, 1996 S.273-76 (39261)

FELLMOSER, F.; FIEG, G.; MASSIER, H.; SCHÜTZ, W.; STEGMAIER, U.; WERLE, H.
Simulation experiments on the spreading behaviour of corium melts.
Jahrestagung Kerntechnik 98, München, 26.-28.Mai 1998
Bonn : INFORUM GmbH, 1998 S.135-39 (43429)

FELLMOSER, F.; FIEG, G.; MASSIER, H.; WERLE, H.
Simulation experiments on the corium melt behaviour in the EPR reactor cavity: KAPOOL-tests.
Jahrestagung Kerntechnik 98, München, 26.-28.Mai 1998
Bonn : INFORUM GmbH, 1998 S.141-44 (43430)

FISCHER, E.A.
An equation of state of plutonium nitride fuel.
Wissenschaftliche Berichte, FZKA-6081 (Mai 98)
http://hikwww4.fzk.de/hbk/literatur/ABSTRACTS /6081.htm (43416)

FREUND, D.; JACOBI, O.; HECK, M.; ERNST, W.; STEINER, H.
Bestrahlungsexperimente zur Transmutation von Aktiniden im HFR.
Projekt Nukleare Sicherheitsforschung. Jahresbericht 1997.
Wissenschaftliche Berichte, FZKA-6126 (September 98) S.558-61 (44232)

FRUTOS, R.; GIDO, R.G.; HENNEGES, G.; SCHMUCK, P.
Spaltproduktausbreitung vom Primärsystem an die Umgebung bei einem schweren Unfall im EPR.
Projekt Nukleare Sicherheitsforschung. Jahresbericht 1997.
Wissenschaftliche Berichte, FZKA-6126 (September 98) S.320-32 (44211)

GELFAND, B.E.; KHOMIK, S.V.; MEDVEDEV, S.P.; POLENOV, A.N.; BARTENEV, A.M.; BREITUNG, W.; VESER, A.
Investigation of hydrogen and air fast flame propagation and DDT in tube with multidimensional endplates.
Internat.Symp.on Hazards, Prevention, and Mitigation of Industrial Explosion, Colloquium on Gas, Vapor, Hybrid and Fuel-Air Explosions, Schaumburg, Ill., September 21-25, 1998
Proc. S.434-55 (44650)

GIDO, R.G.; HENNEGES, G.
Containment module for the source term estimation based on plant status (STEPS). The containment module models.
Projekt Nukleare Sicherheitsforschung. Jahresbericht 1997.
Wissenschaftliche Berichte, FZKA-6126 (September 98) S.333-63 (44212)

GLASBRENNER, H.
Flüssigmetallkorrosion.
Projekt Nukleare Sicherheitsforschung. Jahresbericht 1997.
Wissenschaftliche Berichte, FZKA-6126 (September 98) S.574-79 (44235)

GOOSSENS, L.H.J.; KRAAN, B.C.P.; COOKE, R.M.; JONES, J.A.; BROWN, J.; EHRHARDT, J.; HASEMANN, I.; FISCHER, F.
COSYMA accident consequence uncertainty analysis: procedure and first results.
Lydersen, S. [Hrsg.]
Safety and Reliability : Proc.of the European Conf. (ESREL '98), Trondheim, N, June 16-19, 1998 Vol.2 S.1411-18
Rotterdam [u.a.] : Balkema, 1998 (44580)

GRÖTZBACH, G.; WÖRNER, M.
Direct numerical and large eddy simulations in nuclear applications.
2nd EF Conf. in Turbulent Heat Transfer, Manchester, GB, May 31-June 4, 1998
Manchester : UMIST, 1998 Vol.II S.8-31 - 8-48 (43564)

GRÖTZBACH, G.; WÖRNER, M.; BLAHAK, A.; CARTECIANO, L.; DORR, B.; OLBRICH, W.; SABISCH, W.; YE, Q.; ALEF, M.; GENZ, ST.; JANSSEN, G.; LINDER, M.; LEHMANN, N.; MÜLLER, A.; SELDNER, D.; JIN, X.
Entwicklung von Thermofluiddynamikprogrammen und ingenieurtechnische Anwendungen.
Projekt Nukleare Sicherheitsforschung. Jahresbericht 1997.
Wissenschaftliche Berichte, FZKA-6126 (September 98) S.486-504 (44220)

HAGEN, S.; HOFMANN, P.; NOACK, V.; SEPOLD, L.; SCHANZ, G.; SCHUMACHER, G.
Large bundle PWR test CORA-7: test results.
Wissenschaftliche Berichte, FZKA-6030 (April 98)
http://hikwww4.fzk.de/hbk/literatur/ABSTRACTS /6030.htm (42667)

HAGEN, S.; HOFMANN, P.; NOACK, V.; SEPOLD, L.; SCHANZ, G.; SCHUMACHER, G.
Large bundle BWR test CORA-18: test results.
Wissenschaftliche Berichte, FZKA-6031 (April 98)
http://hikwww4.fzk.de/hbk/literatur/ABSTRACTS /6031.htm (42668)

HARTNAGEL, M.; KIRSTALER, M.; MEYER, L.; ROTH, A.; SCHWALL, M.; WACHTER, E.; WÖRNER, G.
DISCO, Experiment zur Dispersion von simuliertem Corium, die Versuchsanlage.
Projekt Nukleare Sicherheitsforschung. Jahresbericht 1997.
Wissenschaftliche Berichte, FZKA-6126 (September 98) S.192-200 (44201)

HENNIES, H.H.
Safe decommissioning by remote dismantling.
Internat.Topical Meeting on Safety of Nuclear Power Plants (TOPSAFE '98), Valencia, E, April 15-17, 1998
Proc. CD-ROM (44855)

HERING, W.; HOMANN, CH.; SENGPIEL, W.; STRUWE, D.
Severe core degradation analysis for an advanced reactor concept using SCDAP/RELAP5.
Proc.of the Internat.Topical Meeting on Advanced Reactors Safety, Orlando, Fla., June 1-5, 1997 Vol. 2, S.945-52
La Grange Park, Ill. : American Nuclear Soc., 1997 (42919)

HERING, W.; HOMANN, CH.; SENGPIEL, W.; SMIT, S.; STRUWE, D.; MESSAINGUIRAL, CH.
Analysen zu schweren Störfällen sowie Analysen kernzerstörender Unfälle.
Projekt Nukleare Sicherheitsforschung. Jahresbericht 1997.
Wissenschaftliche Berichte, FZKA-6126 (September 98) S.435-68 (44217)

HERING, W.; SENGPIEL, W.; SMITH, S.O.
Beteiligung am PHEBUS-Projekt. Theoretische Interpretation der experimentellen Ergebnisse.
Projekt Nukleare Sicherheitsforschung. Jahresbericht 1997.
Wissenschaftliche Berichte, FZKA-6126 (September 98) S.480-85 (44219)

HERING, W.; SENGPIEL, W.; STRUWE, D.
Calculation of bundle degradation in the Phebus FPT0 in-pile experiment with SCDAP/RELAP5.
Jahrestagung Kerntechnik, Mannheim, 21.-23.Mai 1996
Bonn : INFORUM GmbH, 1996 S.226-29 (39365)

HEUSENER, G.; SCHOLTYSSEK, W.
Progress in LWR severe accident research at the FZK.
Severe Accident Research in Japan (SARJ), Tokyo, J, November 4-6, 1998,
Proc. (V44727)

HIRT, A.
Rechenmodell zum Aufprall von Kernschmelze auf die oberen Einbauten und den Deckel eines Reaktordruckbehälters.
Wissenschaftliche Berichte, FZKA-6054 (April 98)
Dissertation, Universität Karlsruhe 1998 (43413)

HOELLE, C.
Experimentelle Untersuchung der turbulenten Nachlaufströmung über einer beheizten Kugel in vertikaler Anströmung.
Dissertation, Universität Stuttgart 1998
Wissenschaftliche Berichte, FZKA-6116 (August 98)
http://hikwww4.fzk.de/hbk/literatur/ABSTRACTS /6116.htm (43757)

HOFMANN, P.
State of knowledge on core degradation phenomena and principal remaining uncertainties.
ICONE-6 : Proc.of the 6th Internat.Conf.on Nuclear Engineering, San Diego, Calif., May 10-15, 1998
New York, N.Y. : ASME, 1998, CD-ROM (44437)

HOFMANN, P.; HERING, W.; HOMANN, C.; LEILING, W.; MIASSOEDOV, A.; PIEL, D.; SCHMIDT, L.; SEPOLD, L.; STEINBRÜCK, M.
QUENCH-01. Experimental and calculational results.
Wissenschaftliche Berichte, FZKA-6100 (November 98) (44705)

HOFMANN, P.; HOMANN, C.; LEILING, W.; MIASSOEDOV, A.; PIEL, D.; SCHMIDT, L.; SEPOLD, L.; STEINBRÜCK, M.
Results of the QUENCH commissioning tests.
Wissenschaftliche Berichte, FZKA-6099 (August 98) (43893)

HOFMANN, P.; MIASSOEDOV, A.; STEINBRÜCK, M.; METZGER, H.; MOCH, J.; PIEL, D.; SCHMIDT, L.; HORN, S.; MACKERT, E.; LEILING, W.; SEPOLD, L.
Inbetriebnahme-Versuche in der QUENCH-Anlage.
Projekt Nukleare Sicherheitsforschung. Jahresbericht 1997.
Wissenschaftliche Berichte, FZKA-6126 (September 98) S.380-417 (44214)

HUBER, R.; KIRSTAHLER, M.; KUHN, D.; MEYER, L.; ROTH, A.; SCHWALL, M.; WACHTER, E.; WÖRNER, G.
Experimente zur Vorvermischungsphase (QUEOS).
Projekt Nukleare Sicherheitsforschung. Jahresbericht 1997.
Wissenschaftliche Berichte, FZKA-6126 (September 98) S.149-58 (44197)

HÄSSLER, M.
Experimentelle Untersuchungen zum Wärmeübergang und Strömungswiderstand bei Filmsieden an sehr heißen Kugeln.
Dissertation, Universität Karlsruhe 1998
Wissenschaftliche Berichte, FZKA-6149 (August 98) (43742)

HÜBNER, R.; EHRLICH, K.
Swelling and in-pile creep of neutron irradiated 15Cr15NiTi austenitic steels in the temperature range of 400 to 600^{0}C.
Influence of High Dose Irradiation on Core Structural and Fuel Materials in Advanced Reactors : Proc.of a Technical Committee Meeting, Obninsk, Russia, June 16-19, 1997
Wien IAEA, 1998 S.223-30
IAEA-TECDOC-1039 (42223)

HÜBNER, R.; EHRLICH, K.
Einfluss minorer Legierungselemente auf das bestrahlungsinduzierte Schwellen des austenitischen Stahls DIN 1.4970 bei hohen Neutronendosen.
Jahrestagung Kerntechnik 98, München, 26.-28.Mai 1998
Bonn : INFORUM GmbH, 1998 S.737-40 (43359)

IONESCU-BUJOR, M.; CACUCI, D.
Deterministic sensitivity analysis of water material properties in coupled neutronics-thermal-hyraulic codes.
Proc.of the Internat.Conf.on the Physics of Nuclear Science and Technology, Hauppauge, N.Y., October 5-8, 1998 Vol.1 S.372-79
LaGrange Park, Ill. : American Nuclear Soc., 1998 (44440)

JAAG, S.; KIEFHABER, E.
Veränderung der Pu-Qualität durch Bestrahlung in Schnellen Reaktoren.
Projekt Nukleare Sicherheitsforschung. Jahresbericht 1997.
Wissenschaftliche Berichte, FZKA-6126 (September 98) S.531-35 (44227)

JACOBS, G.; WENDTLANDT, T.; BRUNSBACH, D.
Scaling analysis for DISCO.
Projekt Nukleare Sicherheitsforschung. Jahresbericht 1997.
Wissenschaftliche Berichte, FZKA-6126 (September 98) S.201-28 (44202)

JANSSENS-MAENHOUT, G.; KNEBEL, J.U.; MÜLLER, U.
Subcooled nucleate boiling in industrial cooling loops.
Jahrestagung Kerntechnik 98, München, 26.-28.Mai 1998
Bonn : INFORUM GmbH, 1998 S.79-82 (43071)

JANSSENS-MAENHOUT, G.; KNEBEL, J.U.; MÜLLER, U.
Subcooled nucleate boiling at low pressure and low heat flux.
ICMF '98 : Proc.of the 3rd Internat.Conf.on Multiphase Flow, Lyon, F, June 8-12, 1998
1998, CD-ROM (43436)

JONES, J.A.; BROWN, J.; GOOSSENS, L.; KRAAN, B.; EHRHARDT, J.; HASEMANN, I.; FISCHER, F.
Uncertainty analysis on COSYMA.
SARM '97 : Internat.Topical Meeting on Severe Accident Risk and Management, Piestany, Slovakia, June 16-18, 1997 Trnava : VUJE, 1998 CD-ROM (41925)

JORDAN, T.; MALMBERG, T.
Size effects on liquid impact and resulting structural response.
Bhandari, S. [Hrsg.]
Severe Accidents and Topics in the NESC Project : The 1998 ASME/JSME Joint Pressure Vessels and Piping Conf., San Diego, Calif., July 26-30, 1998
New York, N.Y. : ASME, 1998 S.33-38
PVP-Vol.362 (44092)

KAISER, A.; HUBER, F.; WILHELM, D.
Experiments on the behaviour of a hot melt injected into sodium.
Experimental Thermal and Fluid Science, 18(1998) S.48-69 (44812)

KAISER, A.; SCHÜTZ, W.; WILL, H.
Melt water interaction tests. (PREMIX tests PM10 and PM11).
Proc.of the OECD/CSNI Specialists Meeting on Fuel-Coolant Interactions (FCI), Tokai-Mura, J, May 19-21, 1997
JAERI-Conf 97-011 (Part II) (January 98) S.646-57
NEA/CSNI/R(97)26 (41535)

KAYSER, G.; WILHELM, D.
Mechanical problems after a fast reactor core melt-down.
Bhandari, S. [Hrsg.]
Severe Accidents and Topics in the NESC Project : The 1998 ASME/JSME Joint Pressure Vessels and Piping Conf., San Diego, Calif., July 26-30, 1998
New York, N.Y. : ASME, 1998 S.57-63
PVP-Vol.362 (44627)

KESSLER, G.
Anforderungen an das Sicherheitskonzept für neue Reaktoren SWR-1000.
SWR 1000 : Ein zukunftsweisendes Reaktorkonzept ; KTG-Conf., Königswinter, 5.November 1998
Bonn : INFORUM GmbH, 1998 S.27-41 (44390)

KESSLER, G.; FAUDE, D.
The future of fission reactors.
Ronen, Y. [Hrsg.]
ICENES '98 : Proc.of the 9th Internat.Conf.on Emerging Nuclear Energy Systems, Tel-Avis, IL, June 28 - July 2, 1998 Vol.2 S.634-36
Ramat-Gan : Dan Knassim Ltd., 1998 (44659)

KESSLER, G.; KUCZERA, G.
Nachhaltige Energieversorgung.
Atomwirtschaft-Atomtechnik, 43(1998) S.671-75 (44362)

KIEFHABER, E.; HESSELSCHWERDT, E.; BUCKEL, G.; MASCHEK, W.
Erstellung eines neuen, verbesserten SIMMER-III-Neutronik Moduls.
Projekt Nukleare Sicherheitsforschung. Jahresbericht 1997.
Wissenschaftliche Berichte, FZKA-6126 (September 98) S.546-54 (44230)

KNEBEL, J.U.
Summary of SUCOS investigations into passive decay heat removal after core melt-down.
Internat.Topical Meeting on Safety of Nuclear Power Plants (TOPSAFE '98), Valencia, E, April 15-17, 1998
Book of Abstracts S.131-32
Proc. CD ROM (V42999)

KNEBEL, J.U.
The sump cooling concept: an active/passive approach for decay heat removal in future LWR.
Jahrestagung Kerntechnik 98, München, 26.-28.Mai 1998
Bonn : INFORUM GmbH, 1998 S.73-77 (43070)

KNEBEL, J.U.; AXCELL, B.P.
Investigations of a turbulent buoyant sodium jet.
Inst.of Thermomechanics Academy of Sciences [Hrsg.] EUROMECH Colloquium 377 : Stability and Control of Shear Flows with Strong Temperature of Density Gradients, Praha, CR, May 20-22, 1998
Book of Abstracts S.7-17 (43472)

KNEBEL, J.U.; CHENG, X.
Some ideas on liquid metal targets for neutron spallation sources.
Jahrestagung Kerntechnik 98, München, 26.-28.Mai 1998
Bonn : INFORUM GmbH, 1998 S.677-80 (43069)

KNEBEL, J.U.; CHENG, X.; NEITZEL, H.J.
Thermohydraulische Auslegung einer beschleunigergetriebenen, unterkritischen Anlagenanordnung (ADS).
Projekt Nukleare Sicherheitsforschung. Jahresbericht 1997.
Wissenschaftliche Berichte, FZKA-6126 (September 98) S.562-68 (44233)

KNEBEL, J.U.; JANSSENS-MAENHOUT, G.; DAUBNER, M.
SUCO-Programm.
Projekt Nukleare Sicherheitsforschung. Jahresbericht 1997.
Wissenschaftliche Berichte, FZKA-6126 (September 98) S.289-303 (44208)

KNEBEL, J.U.; JANSSENS-MAENHOUT, G.; MÜLLER, U.
Boiling induced mixed convection in cooling loops.
Proc.of the 1st European-Japanese Two-Phase Flow Group Meeting and 36th European Two-Phase Flow Group Meeting, Portoroz, Slowenia, June 1-5, 1998
Paper A4 (43425)

KNEBEL, J.U.; KREBS, L.; MÜLLER, U.; AXCELL, B.P.
Experimental investigation of a confined heated sodium jet in a co-flow.
Journal of Fluid Mechanics, 368(1998) S.51-79 (43922)

KNEBEL, J.U.; REINDERS, R.; SCHEUERER, M.
Some applications of computational fluiddynamic codes in nuclear technology.
Jahrestagung Kerntechnik, München, 26.-28.Mai 1998 - Fachsitzung Entwicklung, Validierung und Anwendung thermohydraulischer Rechenprogramme
Bonn : INFORUM GmbH, 1998 CD-ROM (43437)

KOLARIK, Z.; MÜLLICH, U.
Abtrennverfahren für Aktiniden aus hochradioaktiven Abfällen.
Projekt Nukleare Sicherheitsforschung. Jahresbericht 1997.
Wissenschaftliche Berichte, FZKA-6126 (September 98) S.536-39 (44228)

KOTCHOURKO, A.
COM3D code development.
Projekt Nukleare Sicherheitsforschung. Jahresbericht 1997.
Wissenschaftliche Berichte, FZKA-6126 (September 98) S.127-28 (44195)

KOTCHOURKO, A.; BREITUNG, W.; VESER, A.; DOROFEEV, S.B.
Tube experiments and numerical simulation on turbulent hydrogen-air combustion.
Houwing, A.F.P. [Hrsg.]
Proc.of the 21st Internat.Symp.on Shock Waves, Great Keppel Island, AUS, July 20-25, 1997
CD-ROM Paper 3220 (41898)

KRIEG, R.
RPVSA: Behaviour of the reactor pressure vessel under mechanical and thermal loadings caused by core melt-down and steam explosion accidents - INV.
EUR-18322/1-EN (1998) S.127-32 (44097)

KRIEG, R.; MESSEMER, G.
Reactor pressure vessel response to a postulated internal steam explosion. Investigation by model experiments.
Bhandari, S. [Hrsg.]
Severe Accidents and Topics in the NESC Project : The 1998 ASME/JSME Joint Pressure Vessels and Piping Conf., San Diego, Calif., July 26-30, 1998
New York, N.Y. : ASME, 1998 S.11-18
PVP-Vol.362 (44089)

KUCZERA, B.
Kohle und Kernenergie. Anmerkungen zu Stoff- und Aktivitätsströmen bei der Elektrizitätserzeugung.
Atomwirtschaft-Atomtechnik, 43(1998) Nr.1, S.24-27 (42852)

KUCZERA, B.
Die Verglasungseinrichtung Karlsruhe (VEK), ein Beitrag zur endlagergerechten Entsorgung von flüssigem hochradioaktivem Abfall.
Kernenergienutzung und Endlagerung hochradioaktiver Reststoffe : Interner Workshop des Fachausschusses Kerntechnik, Düsseldorf, 3.April 1998
Düsseldorf, Verein Deutscher Ingenieure, 1998 S.53-61 (44852)

LEFHALM, C.H.; DAUBNER, M.; KNEBEL, J.U.
MEMESS V5. Das Modular Erweiterbare Meßwerte Erfassungs- und Steuerungssystem.
Wissenschaftliche Berichte, FZKA-6122 (Aug. 98)
http://hikwww4.fzk.de/hbk/literatur/ABSTRACTS /6122.htm (44033)

LÄMMER, H.
Thermoplastizität und Thermoviskoplastizität mit Schädigung bei kleinen und großen Deformationen.
Wissenschaftliche Berichte, FZKA-6053 (März 98)
Dissertation, Universität Karlsruhe 1998
http://hikwww4.fzk.de/hbk/literatur/ABSTRACTS /6053.htm
http://hikwww4.fzk.de/hbk/literatur/FZKA_Berichte/FZKA6053.pdf (43075)

LÄMMER, H.; RITTER, B.; TSAKMAKIS, CH.
Zur Bestimmung der Materialparameter des Modells der finiten Thermoviskoplastizität mit Schädigung.
Projekt Nukleare Sicherheitsforschung. Jahresbericht 1997.
Wissenschaftliche Berichte, FZKA-6126 (September 98) S.176-91 (44200)

MAGALLON, D.; BERTHOUD, G.; SCHÜTZ, W.; KOLEV, N.; ALEMBERTI, A.; SEHGAL, R.; BÜRGER, M.; COLOMBO, G.; TURLAND, B.; ZERO, S.
Characterisation of processes which govern quenching of molten corium in water including steam explosion.
Van Goethem, G. [Hrsg.]
FISA 97 - EU Research on Severe Accidents : Mid-Term Review Symp.on Shared-Cost and Concerted Actions in Reactor Safety, Luxembourg, L, November 17-19, 1997
Luxembourg : Office for Official Publ.of the European Communities, 1998 S.93-102
EUR-18258-EN (1998) (42918)

MASCHEK, W.; FLAD, M.
Core-melt accident consequence mitigation in advanced burner cores.
Jahrestagung Kerntechnik 98, München, 26.-28.Mai 1998
Bonn : INFORUM GmbH, 1998 S.665-69 (43432)

MASCHEK, W.; FLAD, M.
Neutronische Untersuchungen zur verstärkten Brennstoffentladung aus hochangereicherten CAPRA-Kernen.
Projekt Nukleare Sicherheitsforschung. Jahresbericht 1997.
Wissenschaftliche Berichte, FZKA-6126 (September 98) S.540-45 (44229)

MASCHEK, W.; FLAD, M.; ARNECKE, G.; LO PINTO, P.
Mitigation of core disruptive accident energetics in burner cores.
2nd Conf.on Global Environment and Energy Systems (GENES-2), Tsuruga, J, October 29 - November 1, 1996
Abstracts S.70-74
Progress in Nuclear Energy, 32(1998) S.639-46 (40138)

MASCHEK, W.; MERK, B.
Safety considerations for accelerator driven subcritical reactors.
Jahrestagung Kerntechnik 98, München, 26.-28.Mai 1998
Bonn : INFORUM GmbH, 1998 S.671-75 (43433)

MASCHEK, W.; MERK, B.
Vergleichende Untersuchungen zum Sicherheitspotential von unterkritischen, beschleunigergetriebenen Systemen.
Projekt Nukleare Sicherheitsforschung. Jahresbericht 1997.
Wissenschaftliche Berichte, FZKA-6126 (September 98) S.569-73 (44234)

MASCHEK, W.; MERK, B.; WIDER, H.U.
Comparison of severe accident behavior of accelerator driven subcritical and conventional critical reactors.
AccApp '98 : 2nd Internat.Topical Meeting on Nuclear Applications of Accelerator Technology, Gatlinburg, Tenn., September 20-23, 1998
La Grange Park, Ill. : American Nuclear Soc., 1998 S.101-07 (44241)

MASCHEK, W.; MORITA, K.; FLAD, M.
SIMMER-III analyses of enhanced fuel removal processes under core disruptive accident conditions.
ICONE-6 : Proc.of the 6th Internat.Conf.on Nuclear Engineering, San Diego, Calif., May 10-15, 1998
New York, N.Y. : ASME, 1998, CD-ROM (43435)

MATERNA-MORRIS, E.; EHRLICH, K.
Material properties of a high-dose irradiated martensitic Wrapper: steel 1.4914.
Influence of High Dose Irradiation on Core Structural and Fuel Materials in Advanced Reactors : Proc.of a Technical Committee Meeting, Obninsk, GUS, June 16-19, 1997
Wien : IAEA, 1998 S.129-38
IAEA-TECDOC-1039 (42967)

MEYER, L.; JACOBS, H.
Investigation of the premixing phase of steam explosions using very hot solid spheres.
Jahrestagung Kerntechnik 98, München, 26.-28.Mai 1998
Bonn : INFORUM GmbH, 1998 S.253-56 (43431)

MEYER, L.; SCHUMACHER, G.; JACOBS, H.; THURNAY, K.
Investigation of the premixing phase of a steam explosion with hot spheres.
Proc.of the Internat.Topical Meeting on Advanced Reactors Safety, Orlando, Fla., June 1-5, 1997 Vol. 1, S.503-13
La Grange Park, Ill. : American Nuclear Soc., 1997
Nuclear Technology, 123(1998) S.142-55 (41655)

MIASSOEDOV, A.
Hydrogen production. Application of the MELCOR code to analysis of the CORA-13 experiment.
Projekt Nukleare Sicherheitsforschung. Jahresbericht 1997.
Wissenschaftliche Berichte, FZKA-6126 (September 98) S.7-26 (44191)

MIASSOEDOV, A.; STEINBOCK, L.
Small-scale quench experiments.
Projekt Nukleare Sicherheitsforschung. Jahresbericht 1997.
Wissenschaftliche Berichte, FZKA-6126 (September 98) S.418-28 (44215)

MIKKELSEN, T.; THYKIER-NIELSEN, S.; ASTRUP, P.; SANTABARBARA, J.M.; SORENSEN, J.H.; RASMUSSEN, A.; ROBERTSON, L.; ULLERSTIG, A.; DEME, S.; MARTENS, R.; BARTZIS, J.G.; PÄSLER-SAUER, J.
MET-RODOS: a comprehensive atmospheric dispersion module.
RODOS: Decision Support for Nuclear Emergencies
Wissenschaftliche Berichte, FZKA-6069 (März 98) S.31-49
RODOS R-3-1998 (43244)

MINGES, J.; SCHÜTZ, W.; KOCH, M.K.
KAREX-Experimente zum radiologischen Quellterm infolge Resuspension.
Projekt Nukleare Sicherheitsforschung. Jahresbericht 1997.
Wissenschaftliche Berichte, FZKA-6126 (September 98) S.517-23 (44225)

MORITA, K.; FISCHER, E.A.
Thermodynamic properties and equations of state for fast reactor safety analysis. Part I: Analytic equation-of-state model.
Nuclear Engineering and Design, 183(1998) S.177-91 (44581)

MORITA, K.; FISCHER, E.A.; THURNAY, K.
Thermodynamic properties and equations of state for fast reactor safety analysis. Part II: properties of fast reactor materials.
Nuclear Engineering and Design 183(1998) S.193-211

MÜHL, B. [HRSG.]
Projekt Nukleare Sicherheitsforschung. Jahresbericht 1997.
Wissenschaftliche Berichte, FZKA-6126 (September 98) (43892)

PFRANG, W.; PORSCHA, B.; STRUWE, D.; ZIMMERER, W.
Untersuchungen zu Brennstoff- und Brennstabverhalten innovativer Systeme.
Projekt Nukleare Sicherheitsforschung. Jahresbericht 1997.
Wissenschaftliche Berichte, FZKA-6126 (September 98) S.515-16 (44224)

PILLON, S.; TOMMASI, J.; D'ALETTO, T.; SAINT JEAN, C.DE; SUNDERLAND, R.; NEWTON, T.D.; JUDD, A.M.; MASCHEK, W.
Current status of the CAPRA programme.
ENC '98 : World Nuclear Congress, Nice, F, October 25-28, 1998
Transactions Vol.III: Poster Papers S.645-54 (44312)

POPP, M.
Kompetenzerhaltung in der Kerntechnik.
Atomwirtschaft-Atomtechnik, 43(1998) S.599-600 (44056)

PÄSLER-SAUER, J.; SCHICHTEL, T.
The simulation of early emergency actions in RODOS.
RODOS: Decision Support for Nuclear Emergencies
Wissenschaftliche Berichte, FZKA-6069 (März 98) S.70-76
RODOS R-3-1998 (43246)

QU, J.; EHRHARDT, J.
Dose and cost considerations for relocation after nuclear accidents.
Health Physics, 75(1998) S.130-35 (44725)

RAFAT, M.; SCHÜLE, O.
The software architecture of the real-time on-line decision support system RODOS.
Nuclear Emergency Data Management : Proc.of an Internat.Workshop, Zürich, CH, September 13-14, 1995
Paris : OECD, 1998 S.31-42 (42885)

RASKOB, W.; HELING, R.; POPOV, A.; ZHELEZNYAK, M.
Untersuchung radioökologischer Modelle für Binnengewässer hinsichtlich ihrer Eignung für den Einsatz in IMIS.
10.Fachgespräch zur Überwachung der Umweltradioaktivität, Hamburg, 28.-30.April 1998
Tagungsband S.313-18 (43294)

RASKOB, W.; POPOV, A.; ZHELEZNYAK, M.J.; HELING, R.
Radioecological models for inland water systems.
Wissenschaftliche Berichte, FZKA-6089 (April 98) (43138)

RINEISKI, A.
SIRENE, ein Interface zwischen nuklearen Reaktorparametern aus ERANOS und dem Sicherheitsanalyse-Code SAS4A.
Projekt Nukleare Sicherheitsforschung. Jahresbericht 1997.
Wissenschaftliche Berichte, FZKA-6126 (September 98) S.524-30 (44226)

ROYL, P.; NECKER, G.; SPORE, J.W.; TRAVIS, J.R.
3D analysis of hydrogen recombination experiments in the Battelle model containment with the GASFLOW code.
Jahrestagung Kerntechnik 98, München, 26.-28.Mai 1998
Bonn : INFORUM GmbH, 1998 S.183-86 (44160)

SCHIRRA, M.; EHRLICH, K.
Development of a high-strength martensitic CrNiMoVNb steel with 10.5% Cr and 0.11% C (OPTIMAR type).
Advanced Heat Resistant Steels for Power Generation, San Sebastian, E, April 27-29, 1998
Conf.Preprints S.1-10 (44186)

SCHLECHTENDAHL, E.G.
Averaging invariance and its consequences for fluid dynamics.
Zeitschrift für Angewandte Mathematik und Mechanik, 78(1998) S.841-54 (44756)

SCHLEISIEK, K.; ABERLE, J.; HOMANN, CH.; SCHMUCK, I.; MASCHEK, W.; RAHN, A.; ROMER, O.; SCHMIDT, L.; BORMS, L.; VERWIMP, A.
The Mol-7C in-pile local blockage experiments: main results, conclusions, and extrapolation to reactor conditions.
Nuclear Science and Engineering, 128(1998) S.93-143 (42881)

SCHMITT, R.; PFEIFENROTH, M.
Charakterisierende Werkstoffuntersuchungen von Strukturmaterialien.
Projekt Nukleare Sicherheitsforschung. Jahresbericht 1997.
Wissenschaftliche Berichte, FZKA-6126 (September 98) S.512-14 (44223)

SCHOLTYSSEK, W.
Investigation of ex-vessel corium melt behavior in support of core catcher development.
Internat.Topical Meeting on Safety of Nuclear Power Plants (TOPSAFE '98), Valencia, E, April 15-17, 1998
Proc. CD ROM (V42855)

SCHULZ, B.; HAASE, G.
Thermophysikalische Eigenschaften von Kernschmelzen.
Projekt Nukleare Sicherheitsforschung. Jahresbericht 1997.
Wissenschaftliche Berichte, FZKA-6126 (September 98) S.287-88 (44207)

SCHÜLE, O.; RAFAT, M.; KOSSYKH, V.
The software environment of RODOS.
RODOS: Decision Support for Nuclear Emergencies
Wissenschaftliche Berichte, FZKA-6069 (März 98) S.23-30
RODOS R-3-1998 (43243)

SEEGMÜLLER, F.
Gitteradaption für Finite-Volumen-Verfahren auf kartesischen Gittern.
Projekt Nukleare Sicherheitsforschung. Jahresbericht 1997.
Wissenschaftliche Berichte, FZKA-6126 (September 98) S.129-48 (44196)

SEILER, R.; BERGER, H.D.; BÖHME, R.; CHAWLA, R.; HAGER, H.; WILLIAMS, T.
Comparison of calculated and measured parameters for a highly undermoderated MOX/D_2O lattice.
Ronen, Y. [Hrsg.]
ICENES '98 : Proc.of the 9th Internat.Conf.on Emerging Nuclear Energy Systems, Tel-Avis, IL, June 28 - July 2, 1998 Vol.1 S.51-58
Ramat-Gan : Dan Knassim Ltd., 1998 (44657)

SEPOLD, L.; HORN, S.; LEILING, W.
Ergebnisse der TE-Vorversuche zu den Experimenten in der Quench-Versuchsanlage.
Projekt Nukleare Sicherheitsforschung. Jahresbericht 1997.
Wissenschaftliche Berichte, FZKA-6126 (September 98) S.364-79 (44213)

SMIT, S.-O.; SENGPIEL, W.; HERING, W.
Investigation of the Phebus FPT0 bundle degradation with SCDAP/RELAP5
Wissenschaftliche Berichte, FZKA-6083 (April 98) (43522)

STACH, T.; MALMBERG, T.; KRIEG, R.
Scaled experiments for a simple deformable structure under liquid slug impact.
Structural Mechanics in Reactor Technology : Transactions of the 14th Internat.Conf., Lyon, F, August 17-22, 1997
Vol. 10 Div.P S.307-14
Lyon : IASMIRT, 1997 (42921)

STARFLINGER, J.; KOCH, M.K.; UNGER, H.; SCHÜTZ, W.
Analysis of the Jet-droplet and radionuclide release due to bubble bursting at liquid surfaces.
ICONE-6 : Proc.of the 6th Internat.Conf.on Nuclear Engineering, San Diego, Calif., May 10-15, 1998
New York, N.Y. : ASME, 1998, CD-ROM (44404)

STEINER, H.
Mechanical effects in single rod quench tests.
Projekt Nukleare Sicherheitsforschung. Jahresbericht 1997.
Wissenschaftliche Berichte, FZKA-6126 (September 98) S.429-34 (44216)

STEINER, H.; HECK, M.
Stresses in an oxidized zircaloy cladding under quench conditions: recalculation of single-rod quench tests.
Nuclear Technology, 123(1998) S.209-211 (43836)

STRUB, C.; AUTRUSSON, B.; GOELLER, B.; KRIEG, R.
Analysis of slug impact against the reactor pressure vessel head interpretation of BERDA test 07 with the finite element code PLEXUS.
Bhandari, S. [Hrsg.]
Severe Accidents and Topics in the NESC Project : The 1998 ASME/JSME Joint Pressure Vessels and Piping Conf., San Diego, Calif., July 26-30, 1998
New York, N.Y. : ASME, 1998 S.19-26
PVP-Vol.362 (44238)

TENCHINE, D.; BERTHOUX, M.; KNEBEL, J.U.; JACKSON, J.D.; AN, P.; NAVIGLIO, A.; CARUSO, G.
Thermalhydraulics of passive decay heat removal systems, POOLTHY.
Van Goethem, G. [Hrsg.]
FISA 97 - EU Research on Severe Accidents : Mid-Term Review Symp.on Shared-Cost and Concerted Actions in Reactor Safety, Luxembourg, L, November 17-19, 1997
Luxembourg : Office for Official Publ.of the European Communities, 1998 S.501-10
EUR-18258-EN (1998) (41817)

THURNAY, K.
Thermal properties of transition metals.
Wissenschaftliche Berichte, FZKA-6095 (Mai 98) (43419)

TRAVIS, J.R.; SPORE, J.W.; ROYL, P.; LAM, K.L.; WILSON, T.L.; MÜLLER, C.; NECKER, G.A.; NICHOLS, B.D.; REDLINGER, R.; HUGHES, E.D.; WILKENING, H.; BAUMANN, W.; NIEDERAUER, G.F.
GASFLOW: a computational fluid dynamics code for gases, aerosols, and combustion.
Vol.1 Theory and computational model.
Vol.2 User's manual.
Vol.3 Assessment manual.
LA-13357-M (October 98)
(FZKA-5994) (44666)

TROMM, W.
Experimentelle Untersuchungen zum Nachweis der langfristigen Kühlbarkeit von Kernschmelzen.
Wissenschaftliche Berichte, FZKA-6176 (November 98)
Dissertation, Universität Karlsruhe 1998
(44180)

TROMM, W.; ALSMEYER, H.; CRON, T.; FERDERER, F.
Transiente Experimente zur Untersuchung des Verhaltens später Schmelzen aus dem RDB für das COMET-Kernfängerkonzept.
Jahrestagung Kerntechnik 98, München, 26.-28.Mai 1998
Bonn : INFORUM GmbH, 1998 S.153-56 (43033)

TSAGRAKIS, I.; MALMBERG, T.; AIFANTIS, E.C.
Gradient plasticity and size effects.
Theocaris, P.S. [Hrsg.]
5th Nat.Congress on Mechanics, Ioannina, GR, August 27-30, 1998
Proc.Vol.2 S.953-60
The University of Ioannina, 1998 (44159)

VESER, A.; BREITUNG, W.; ENGEL, G.; STERN, G.
Hydrogen combustion.
Projekt Nukleare Sicherheitsforschung. Jahresbericht 1997.
Wissenschaftliche Berichte, FZKA-6126 (September 98) S.82-126 (44194)

VOSNACKE, A.; STARFLINGER, J.; SCHÜTZ, W.; KOCH, M.K.; UNGER, H.
Modelling of radionuclide resuspension due to bubble bursting at liquid surfaces.
Internat.Topical Meeting on Safety of Nuclear Power Plants (TOPSAFE '98), Valencia, E, April 15-17, 1998
Book of Abstracts S.91 CD-ROM
Proc. CD-ROM (44403)

WIESE, H.W.
Development and application of KORIGEN.
Brennelementtechnik, Kernauslegung, Reaktorbetrieb : Fachtagung der KTG-Fachgruppen 'Brennelemente' und 'Reaktorphysik und Berechnungsmethoden', Karlsruhe, 3.-4.Februar 1998
Tagungsbd. S.155-60 (43229)

WILL, H.; HUBER, F.; KAISER, A.; SCHÜTZ, W.
Experimente zur Vorvermischungsphase (PREMIX).
Projekt Nukleare Sicherheitsforschung. Jahresbericht 1997.
Wissenschaftliche Berichte, FZKA-6126 (September 98) S.159-67 (44198)

WÖRNER, M.; GRÖTZBACH, G.
Pressure transport in DNS of turbulent natural convection in horizontal fluid layers.
Hanjalic, K. [Hrsg.]
Turbulence, Heat and Mass Transfer : 2 ; Proc.of the 2nd Internat.Symp., Delft, NL, June 9-12, 1997
Delft : Delft Univ.Pr., 1997 S.351-60
Internat.Journal of Heat and Fluid Flow, 19(1998) S.150-158 (41386)

WÖRNER, M.; SCHMIDT, M.; GRÖTZBACH, G.
Direct numerical simulation of turbulence in an internally heated convective fluid layer and implications for statistical modelling.
Journal of Hydraulic Research, 35(1997) S.773-97 (43476)

YE, Q.Y.; WÖRNER, M.; GRÖTZBACH, G.
Modelling turbulent dissipation correlations for Rayleigh-Benard convection based on two-point correlation technique and invariant theory.
Wissenschaftliche Berichte, FZKA-6103 (August 98)
http://hikwww4.fzk.de/hbk/literatur/ABSTRACTS/6103.htm
http://hikwww4.fzk.de/hbk/literatur/FZKA_Berichte/FZKA6103.pdf (43703)

ZHELEZNYAK, M.; GOFMAN, D.; LYASHENKO, G.; MARINETS, A.; SHEPELEVA, T.; TKALICH, P.; HELING, R.; RASKOB, W.; POPOV, A.; BORODIN, R.; POKHIL, A.
Modelling of hydrological pathways in RODOS.
RODOS: Decision Support for Nuclear Emergencies
Wissenschaftliche Berichte, FZKA-6069 (März 98) S.50-59
RODOS R-3-1998 (43245)

Veröffentlichungen in elektronischen Medien

WÖRNER, M.; GRÖTZBACH, G.
DNS database of turbulent natural convection in horizontal fluid layers. Extension.
http://hbksun17.fzk.de:8080/IRS/eng/IRS3/TURBIT_DNS_database.html (E44095)

Vorträge, die nicht in gedruckter Form vorliegen

AMMANN, T.
An implicit method for the local refinement of a structured grid.
GAMM-Jahrestagung, Bremen, 6.-9.April 1998 (V43368)

CARTECIANO, L.N.; DORR, B.; GRÖTZBACH, G.
Theoretical interpretation of the thermal and fluiddynamical conditions in single phase SUCOS experiments with the FLUTAN code.
9th IAHR-Working Group Meeting on Advanced Nuclear Reactor Thermal Hydraulics, Grenoble, April 7-9, 1998 (V43402)

CHENG, X.; SLASSAREV, I.
Thermohydraulic investigations on liquid metal target systems.
Internat.Conf.on Heavy Liquid Metal Codants (HLMC '98), Obninsk, GUS, October 5-9, 1998 (V44051)

COURTAUD, M.; HEUSENER, G.; PELTIER, J.; STEINWARZ, W.
Research and development related to the EPR.
The European Pressurized Water Reactor EPR, KTG/SFEN Conf., Köln, October 19-21, 1997 (V42492)

EHRHARD, P.; BUNK, M.
Theory and experiments related to the spreading of solidifying melts.
Vortr.: University of Nottingham, GB, 8.Oktober 1997
Vortr.: 50th Annual Meeting of the Division of Fluid Dynamics of the American Physical Society, San Francisco, Calif., November 23-25, 1997
Vortr.: University of Colorado, Boulder, Colo., 2.Dezember 1997 (V43032)

GRÖTZBACH, G.
Analysen mit FLUTAN zur Sumpfkühlung eines neuen Druckwasserreaktors und begleitende Modellentwicklung.
Vortr.: Universität Stuttgart, 6.Februar 1998 (V42920)

GUMINSKI, C.; BORGSTEDT, H.U.
Solubility of metallic and non-metallic substances and solution chemistry in liquid alkali metals.
8th Internat.Symp.on Solubility Phenomena, Niigata, J, August 5-8, 1998 (V43812)

HENNIES, H.H.; KRUGLYAKOV, E.P.; RYUTOV, D.
The gasdynamic trap (GDT) - system as a promising engineering solution for a volumetric neutron source and an intermediate step to a fusion reactor.
9th Internat.Conf.on Emerging Nuclear Energy Systems (ICENES '98), Herzliya, IL, June 28 - July 2, 1998 (V44853)

HOFMANN, P.; HORN, S.; LEILING, W.; MIASSOEDOV, A.; PIEL, D.; SCHMIDT, L.; SEPOLD, L.; STEINBRÜCK, M.
Posttest appearance of test bundle QUENCH-02.
4th Internat.QUENCH Workshop, Karlsruhe, October 6-8, 1998 (V44474)

HOFMANN, P.; HORN, S.; LEILING, W.; MIASSOEDOV, A.; PIEL, D.; SCHMIDT, L.; SEPOLD, L.; STEINBRÜCK, M.
First results of test QUENCH-02.
4th Internat.QUENCH Workshop, Karlsruhe, October 6-8, 1998 (V44476)

HOFMANN, P.; HORN, S.; LEILING, W.; MIASSOEDOV, A.; PIEL, D.; SCHMIDT, L.; SEPOLD, L.; STEINBRÜCK, M.
Posttest conditions of test bundle QUENCH-01.
4th Internat.QUENCH Workshop, Karlsruhe, October 6-8, 1998 (V44478)

HOFMANN, P.; HORN, S.; LEILING, W.; MIASSOEDOV, A.; PIEL, D.; SCHMIDT, L.; SEPOLD, L.; STEINBRÜCK, M.
Experimental results of test QUENCH-01.
4th Internat.QUENCH Workshop, Karlsruhe, October 6-8, 1998 (V44480)

HOFMANN, P.; LEILING, W.; MIASSOEDOV, A.; PIEL, D.; SCHMIDT, L.; SEPOLD, L.; STEINBRÜCK, M.
Hydrogen release and absorption during the bundle test QUENCH-02.
4th Internat.QUENCH Workshop, Karlsruhe, October 6-8, 1998 (V44475)

HOFMANN, P.; LEILING, W.; MIASSOEDOV, A.; PIEL, D.; SCHMIDT, L.; SEPOLD, L.; STEINBRÜCK, M.
Hydrogen release and absorption during the bundle test QUENCH-01.
4th Internat.QUENCH Workshop, Karlsruhe, October 6-8, 1998 (V44479)

HOFMANN, P.; MIASSOEDOV, A.; STEINBRÜCK, M.
Zircaloy cladding tube behavior during quenching.
4th Internat.QUENCH Workshop, Karlsruhe, October 6-8, 1998 (V44481)

HOFMANN, P.; MIASSOEDOV, A.; STUCKERT, J.
UO_2 and ZrO_2 dissolution by molten Zircaloy. Experiments on the ZrO_2 shell failure criteria.
Corium Interactions and Thermochemistry Meeting, Paris, F, December 1-2, 1998 (V44815)

HOFMANN, P.; STEINBRÜCK, M.; MIASSOEDOV, A.; SCHMIDT, L.; PIEL, D.; SEPOLD, L.; LEILING, W.
Zircaloy cladding tube behavior of PWR fuel rods during quenching from high temperatures. (Quench test results).
Spring Meeting, Cooperative Severe Accident Research Program (CSARP), Bethesda, Md., May 5-8, 1997 (V44438)

HOFMANN, P.; STEINBRÜCK, M.; MIASSOEDOV, A.; METZGER, H.; SCHANZ, G.; SCHMIDT, L.; PIEL, D.; SEPOLD, L.; LEILING, W.
Metallographic post-test examination of the Quench-01 bundle.
4th Internat.QUENCH Workshop, Karlsruhe, October 6-8, 1998 (V44477)

HOFMANN, P.; STEINBRÜCK, M.; MIASSOEDOV, A.; SCHMIDT, L.; PIEL, D.; SEPOLD, L.; LEILING, W.
Hydrogen source term during flooding of a degraded core. The QUENCH program at FZK.
4th Internat.QUENCH Workshop, Karlsruhe, October 6-8, 1998 (V44483)

HOFMANN, P.; STUCKERT, J.
ZrO_2 dissolution by molten Zircaloy and clad failure.
4th CIT Project Meeting, Pisa, I, June 10-11, 1998 (V44816)

HOFMANN, P.; STUCKERT, J.
UO_2 dissolution by molten Zircaloy.
4th CIT Project Meeting, Pisa, I, June 10-11, 1998 (V44817)

HOFMANN, P.; STUCKERT, J.; BURBACH, J.
ZrO_2 dissolution by molten Zircaloy. (New test results).
4th Internat.QUENCH Workshop, Karlsruhe, October 6-8, 1998 (V44814)

HOMANN, C.; HERING, W.
IRS calculational support for QUENCH-01.
4th Internat.QUENCH Workshop, Karlsruhe, October 6-8, 1998 (V44671)

HOMANN, C.; HERING, W.
IRS calculational support for QUENCH-02.
4th Internat.QUENCH Workshop, Karlsruhe, October 6-8, 1998 (V44672)

HÜBNER, R.; EHRLICH, K.
Influence of minor alloying elements on microstructural evolution and void swelling of austenitic stells under neutron irradiation.
19th Internat. Symp. 'Effects of Radiation on Materials', Seattle, Wash., June 16-19, 1998 (V43871)

KNEBEL, J.U.; JANSSENS-MAENHOUT, G.; MÜLLER, U.
Boiling induced mixed convection in cooling loops.
Technical Committee Meeting on Experimental Tests and Qualification of Analytical Methods to Address Thermalhydraulic Phenomena in Advanced Water Cooled Reactors, Villigen, CH, September 14-17, 1998 (V44088)

KRAUSS, W.; SCHANZ, G.
Zircaloy/air oxidation kinetics: current experiments towards future demands.
4th Internat.QUENCH Workshop, Karlsruhe, October 6-8, 1998 (V44643)

KRIEG, R.; GÖLLER, B.; HAILFINGER, G.; JORDAN, T.; MALMBERG, T.; MESSEMER, G.; VORBERG, G.
Mechanical response of the reactor vessel during an in-vessel steam explosion.
Internat.Topical Meeting on Safety of Nuclear Power Plants (TOPSAFE '98), Valencia, E, April 15-17, 1998 (V44172)

KUCZERA, B.
Innovative Weiterentwicklung der Sicherheitsvorsorge in Kernkraftwerken.
DAG-Seminar der Bundesfachgruppe Wissenschaft und Forschung, Walsrode, 26.März 1998 (V43098)

KUCZERA, B.
Fortschritte bei den Karlsruher Stillegungsprojekten.
Jahrestagung Kerntechnik 98, München, 26.-28.Mai 1998 (V44765)

KUCZERA, B.
On the role and the potential of nuclear power in reducing greenhouse gas emissions.
4th Internat.Conf.on Greenhouse Gas Control Technologies, Interlaken, CH, August 30 - September 2, 1998
Book of Abstracts S.194 (V44857)

MALMBERG, T.
Similitude and size effect studies for steel and steel structures in reactor technology.
2nd Euroconf.and Internat.Symp.on Material Instabilities in Deformation and Fracture, Thessaloniki, GR, August 31 - September 4, 1997
Book of Abstracts S.34 (V42922)

RIVALIN, F.; STEINBRÜCK, M.
Hydrogen absorption by zircaloy at high temperatures: new test results.
4th Internat.QUENCH Workshop, Karlsruhe, October 6-8, 1998 (V44482)

SANCHEZ, V.H.; HERING, W.; HOMANN, CH.; SENGPIEL, W.; SMIT, S.; STRUWE, D.
Reactor safety investigations using RELAP5 and SCDAP/RELAP5.
4th Internat.QUENCH Workshop, Karlsruhe, October 6-8, 1998 (V44673)

SCHMUCK, P.
Analysis of severe accident sequences for an innovative PWR of the 1500 MWe class.
1998 Annual MCAP Meeting, Bethesda, Md., April 29 - May 1, 1998 (V43148)

SCHOLTYSSEK, W.; HOFMANN, F.; PLITZ, H.
R and D at FZK to minimize energetic threats to containments of future reactors.
ENC '98 : World Nuclear Congress, Nice, F, October 25-28, 1998 (V44728)

STEINBOCK, L.
Surface crack formation of oxidized zircaloy tubes during cool-down.
4th Internat.QUENCH Workshop, Karlsruhe, October 6-8, 1998 (V44759)

TISEANU, I.
High resolution X-ray tomography for two-phase flow imaging.
Graduiertenkolleg Energie- und Umwelttechnik, Universität Karlsruhe, 29.April 1998(V44171)

WINTRUFF, I.
Numerische Simulation des Stabilitätsverhaltens erstarrter Kernschmelzen.
Jahrestagung Kerntechnik 98, München, 26.-28.Mai 1998 (V44754)